INTERNATIONAL DOCTORAL SCHOOL OF THE USC

Manuel
Fernández Míguez

PhD Thesis

Dynamic Helical Polymers: Exploring the Complexity of Responses to Stimuli

Santiago de Compostela, 2025

Doctoral Programme in Chemical Science and Technology

ESCOLA DE DOUTORAMENTO
INTERNACIONAL DA USC

DOCTORAL THESIS

DYNAMIC HELICAL POLYMERS: EXPLORING THE COMPLEXITY OF RESPONSES TO STIMULI

Author

Manuel Fernández Míguez

Supervisors: Emilio Quiñoá Cabana and Félix Freire Iribarne

Tutor: Emilio Quiñoá Cabana

PHD PROGRAMME IN CHEMICAL SCIENCE AND TECHNOLOGY

SANTIAGO DE COMPOSTELA

2025

Abbreviations and Acronyms

$[\alpha]_{\lambda}^{T}$	Specific optical rotation
A	Area
α_{Agg}	Fraction of aggregated species
Abs	Absorbance
ACAC	Acetylacetone
AFM	Atomic force microscopy
AgNP	Silver Nanoparticle
Aib	α-Aminoisobutyric Acid
AIE	Aggregation induced emission
Ala	Alanine
ALPB	Analytical linearized Poisson–Boltzmann
ap	Antiperiplanar
Ar	Argon gas
Å	Angstrom
aug	Augmented (difuse funcions)
AuNP	Gold nanoparticle
B	Becke
bipy	Bipyridine
Boc	*tert*-Butyloxycarbonyl
Bodipy	4,4-Difluoro-4-bora-3a,4a-diaza-*s*-indacene
BTA	Benzene-1,3,5-tricarboxamide
c	Concentration
c	Speed of light
c-c	*Cis-cisoidal*
c-t	*Cis-transoidal*
C_{60}	Buckminsterfullerene
ca.	Circa
calcd.	Calculated
CAM	Coulomb-attenuating method

USC UNIVERSIDADE DE SANTIAGO DE COMPOSTELA

cc	Correlation consisted
CD	Circular dichroism
cod	*cis*,*cis*-1,5-Cyclooctadiene
CP	Circularly polarized
CPL	Circularly polarized luminescence
CREST	Conformer–rotamer ensemble sampling tool
CSP	Chiral stationary phase
CuNP	Copper nanoparticle
CyD	Cyclodextrin
ω	Dihedral angle
ΔE_{bind}	Binding energy
$\Delta E_{bind,n-1}$	The binding energy per incremental pair of molecules
ΔG	Gibbs or free energy difference
ΔH	Enthalpy change
ΔH_e	Elongation enthalpy difference
ΔH_{np}	Nucleation penalty enthalpy
ΔH_{nuc}	Nucleation enthalpy difference
ΔS	Entropy change
ΔS_e	Elongation entropy difference
ΔS_{nuc}	Nucleation entropy difference
ΔG_h	Helical free energy difference
$\Delta\varepsilon$	Molar circular dichroism
D	Diameter
D	Dipole strength
Đ	Dispersity
D3/4	Grimme's dispersion correction (third/fourth version)
Da	Dalton
DCM	Dichloromethane
deg	Degrees
DFT	Density functional theory

USC UNIVERSIDADE DE SANTIAGO DE COMPOSTELA

dia.	Diameter (nm)
DIPEA	*N*,*N*-Diisopropylethylamine
DLS	Dynamic light scattering
DMF	*N*,*N*-Dimethylformamide
DMSO	Dimethylsulfoxide
DNA	Deoxyribonucleic acid
DP	Degree of polymerization
DPA	Diphenylacetylene
DSC	Differential scanning calorimetry
ε	Molar absorptivity
θ	Angle or ellipticity
$[\theta]$	Molar ellipticity
$E_{R/L}$	Right- or left-handed electric field amplitudes
e	Elementary charge
e.g.	Latin expression “exempli gratia”; for example
et al.	Latin expression “et alia” and others
ECD	Electronic circular dichroism
EDC	1-Ethyl-3-(3-dimethylaminopropyl)carbodiimide
ELF	Electron localization function
EPR	Electronic paramagnetic resonance
equiv	Equivalents
ESI	Electrospray ionization
ETDM	Electric transition dipole moment
f	Copolymer composition
F	Monomer feed ratio
f	Oscillator strength
FG	Functional group
FT-IR	Fourier transform infrared
FWHM	Full width at half-maximum
g	Gram

USC UNIVERSIDADE DE SANTIAGO DE COMPOSTELA

g_{abs}	Anisotropy factor; Kuhn dissymmetry factor or ratio
g_{lum}	Luminescence dissymmetry factor or ratio
GFN2-xTB	Grimme's extended semiempirical tight-binding method
GHz	Gigahertz
Gly	Glycine
GPC	Gel permeation chromatography
h	Planck constant
h	Hours
HATU	2-(7-Aza-1H-benzotriazole-1-yl)-1,1,3,3-tetramethyluronium hexafluorophosphate
HOAt	1-Hydroxy-7-azabenzotriazole
HOBt	1-Hydroxybenzotriazole
HOMO	Highest occupied molecular orbital
HOPG	Highly oriented pyrolytic graphite
HPLC	High-performance liquid chromatography
HPMC	Helical polymer-metal complex
HRMS	High-resolution mass spectrometry
HSSP	Helix-sense-selective polymerization
I	Intensity
i.e.	Latin expression "id est"; that is / in other words
Ile	Isoleucine
J	Joule
K	Kelvin
K_B	Boltzmann constant
kcal	Kilocalories
kDa	Kilodaltons
K_e	Elongation constant
K_{eq}	Equilibrium constant
kg	Kilograms
kJ	Kilojoules
K_n	Nucleation constant

USC UNIVERSIDADE DE SANTIAGO DE COMPOSTELA

L	Liter
l	Path length
LB	Langmuir-Blodgett
LbL	Layer-by-layer
Leu	Leucine
LOD	Limit of detection
LS	Langmuir-Schaefer
LSPR	Localized surface plasmon resonance
LUMO	Lowest unoccupied molecular orbital
LYP	Lee-Yang-Parr
m	Magnetic Dipole moment operator; magnetic transition dipole moment vector
μ	Electric Dipole moment operator; electric transition dipole moment vector
μm	Micrometer
μM	Micromolar
M	*Minus*; counterclockwise; levorotatory
M	Molarity
m-	*Meta*-position
m.r.u.	Monomer / molecular repeating unit
MALDI	Matrix-assisted laser desorption/ionization
MB	Mass-balance
MCH	Methylcyclohexane
MD	Molecular dynamics
mdeg	Millidegrees
mg	Milligrams
MHz	Megahertz
min	Minutes
mL	Milliliters
mM	Millimolar
MM	Molecular mechanics

USC UNIVERSIDADE DE SANTIAGO DE COMPOSTELA

Mmol	Millimoles
M_n	Number-average molar mass
M^{n+}	Metal cation in oxidation state n
MNP	Metal nanoparticle
MO	Molecular orbital
MOF	Metal-organic frameworks
M_p	Peak molecular weight
MPA	α-Methoxyphenylacetic acid
MR	Majority Rules
ms	Milliseconds
mT	Milliteslas
MTDM	Magnetic transition dipole moment
MTPA	α-Methoxy-α-trifluoromethylphenylacetic acid
Mw	Molecular weight
M_w	Weight-average molar mass
M_z	Z-average molar mass
nbd	2,5-Norbadiene
NBO	Natural Bond Orbital
NCI	Non-covalent interaction analysis
Nm	Nanometer
NMR	Nuclear magnetic resonance
NTO	Natural Transition Orbitals
o-	*Ortho*-position
ºC	Degree Celsius
Oligo	Oligomer
OPE	Oligo(phenylene ethynylene)
OPV	Oligo(phenylene vinylene)
OR	Optical rotation
ORD	Optical rotation dispersion
P	*Plus*; clockwise; dextrorotatory

USC UNIVERSIDADE DE SANTIAGO DE COMPOSTELA

p-	*Para*-position
PA	Poly(acetylene)
PAA	Poly(acrylic acid)
PAH	Poly(allylamine) hydrochloride
PCM	Polarizable continuum model
PDI	Polydispersity index
PdNP	Palladium nanoparticle
PEC	Photochemical electrocyclization
PEG	Poly(ethylene glycol)
Pgme	Phenylglycine methyl ester
pH	Potential of hydrogen
Pheala	Phenylalanine
PI	Poly(isocyanate)
π	Pi bond
Poly	Polymer
pp	Pseudopotential
PPA	Poly(phenylacetylene)
ppm	Parts per million
PSS	Polystyrene standards
PtNP	Platinum nanoparticle
PVP	Poly(vinylpyrrolidone)
PVTZ	Polarized valence triple zeta
Φ_{PL}	Quantum Yield
R	Ideal Gas Constant
r	Monomer reactivity ratio
(*R*)	*Rectus*, Latin for right
R	Rotatory strength
rp	relative polarity of the solvent to the water
r.t.	Room temperature
RKS	Restricted Kohn–Sham

USC UNIVERSIDADE DE SANTIAGO DE COMPOSTELA

ROA	Raman optical activity
ROS	Reactive oxygen species
r_{value}	Helicity induction ratio or Sergeant efficiency value in SaS
σ	Cooperativity parameter
s	Seconds
(*S*)	*Sinister*, Latin for left
SaS	Sergeants and Soldiers Effect
SCAT	Celective photocyclic aromatization
SD	Standard deviation
SEC	Size exclusion chromatography
SEE	Screw sense excess
SEM	Scanning electron microscopy
SOMO	Singly occupied molecular orbital
sp	Synperiplanar
STM	Scanning tunneling microscopy
T	Temperature
t	Time
t-c	*Trans-cisoidal*
t-t	*Trans-transoidal*
t_{50}	Lag time
$t_{1/2}$	Half-life
$t_{ECD50\%}$	Time at 50% ECD intensity
TBAA	Tetra-*n*-butylammonium acetate
TBAB	Tetra-*n*-butylammonium benzoate
TBABr	Tetra-*n*-butylammonium bromide
TBACl	Tetra-*n*-butylammonium chloride
TBAF	Tetra-*n*-butylammonium fluoride
TBAN	Tetra-*n*-butylammonium nitrate
$TBAN_3$	Tetra-*n*-butylammonium azide
TBAOH	Tetra-*n*-butylammonium hydroxide

USC UNIVERSIDADE DE SANTIAGO DE COMPOSTELA

TD	Time-dependent
TD-DFT	Time-dependent density functional theory
TDM	Transition Dipole Moment
T_e	Elongation Temperature
TEA	Triethylamine
TEM	Transmission electron microscopy
TFA	Trifluoroacetic acid
TGA	Thermogravimetric analysis
THF	Tetrahydrofuran
TMS	Trimethylsilyl
TOF	Time-of-flight
TrMA	Triphenylmethyl methacrylate
TU	Thiourea
UKS	Unrestricted Kohn-Sham
UV-Vis	Ultraviolet-visible
v	Volume
Val	Valine
VCD	Vibrational circular dichroism
vdW	Van der Waals
VMD	Visual molecular dynamics
VT	Variable temperature
$\tilde{\nu}$	Wavenumber
λ	Wavelength
ψ	Wavefunction
X	Mole fraction of x in the mixture (x + y)
XPS	X-ray photoelectron spectroscopy
Y	Mole fraction of y in the mixture (x + y)
δ	Chemical shift
+	Diffuse function

USC
UNIVERSIDADE DE SANTIAGO DE COMPOSTELA

USC
UNIVERSIDADE
DE SANTIAGO
DE COMPOSTELA

Table of Contents

SUMMARY 1

RESUMO 11

CHAPTER 1. INTRODUCTION 21

1.1. Classification of Helical Polymers 30

1.1.1. Static Helical Polymers 30

1.1.2. Dynamic Helical Polymers 31

1.2. Poly(acetylene)s and Poly(phenylacetylene)s 32

1.2.1. Rh Catalyst 33

1.2.1.1. Classical Organic Catalysts 34

1.2.1.2. Water Compatible Catalysts 34

1.2.1.3. Catalysts for controlled degree of polymerization and end functionalization 35

1.3. Stability of Poly(phenylacetylene)s 36

1.3.1 Photochemical Stability 36

1.3.2. Thermal stability 37

1.3.3. Radical-mediated Isomerization 38

1.4. The Structural Elucidation of Poly(phenylacetylene)s Helices 39

1.4.1. PPA Architecture 39

1.4.2. Determination of the Polyene Backbone Configuration and Conformation 41

1.4.2.1. NMR Polyene Backbone Elucidation 42

1.4.2.2. DSC Polyene Backbone Elucidation 42

1.4.2.3. Polyene Backbone Photoelectrocyclazation: Elucidation of the Dihedral Angle ω_1 43

1.4.2.4. Polyene Backbone Photoelectrocyclazation: Elucidation of the Screw Sense Excess 44

1.4.2.5. Raman Polyene Backbone Elucidation 46

1.4.2.6. UV-Vis Absorption Polyene Backbone Elucidation 46

1.4.3. Theory of Spectroscopic Optical and Chiroptical Techniques 48

1.4.3.1. Linear Absorption Techniques 48

1.4.3.2. Oscillator Strength 49

1.4.3.3. Chiroptical Techniques: ECD and VCD 50

1.4.3.4. Theoretical anisotropy factor: Rotatory Strength and Dipole Strength 51

1.4.3.5. Experimental Anisotropy Factor 53

1.4.3.6. Computed Anisotropy Factor and Oscillator Strength by Time-Dependent Density Functional Theory 56

1.4.3.7. Exciton Coupling 58

USC UNIVERSIDADE DE SANTIAGO DE COMPOSTELA

1.4.3.8. Electronic Circular Dichroism Assignation to the Helical Sense in Poly(phenylacetylene)s *59*
1.4.3.9. Vibrational Circular Dichroism in Poly(phenylacetylene)s *60*
1.4.3.10. Optical Rotation *61*
1.4.3.11. Raman Optical Activity *63*
1.4.4. Atomic Force Microscopy **64**
1.5. SUPRAMOLECULAR ASSEMBLIES OF POLY(ACETYLENE)S AND POLY(PHENYLACETYLENE)S **66**
1.5.1. Fibers and Superhelical Assemblies **66**
1.5.2. Layer-by-Layer Supramolecular Assembly **69**
1.6. NANOPARTICLES BASED ON POLY(ACETYLENE)S POLY(PHENYLACETYLENE)S **70**
1.6.1. Surfactant: Polymer Emulsification and Monomer Emulsion Polymerization **71**
1.6.2. Polymer Spheres: Micelle **71**
1.6.3. Polymer Sphere: Nanoprecipitation **72**
1.6.4. Metal Crosslinking Nanostructuration: Helical Polymer-Metal Complexes **73**
1.7. HYBRID MATERIALS BASED ON PPAS AND METAL NANOPARTICLES **74**
1.7.1. Silver Nanoparticles and their Hybrids **75**
1.7.1.1. In-Situ Reduction Method *75*
1.7.2. Identification and Characterization of Nanoparticles **76**
1.7.3. Hybrid Poly(acetylene)s and Poly(phenylacetylene)s with Metal Nanoparticles **78**
1.8. DYNAMIC HELICAL POLYMERS PPAS: HELICAL INDUCTION, INVERSION AND ENHANCEMENT IN PPAS **82**
1.8.1. Helix Induction Mechanisms **82**
1.8.1.1. Teleinduction *83*
1.8.1.2. Chiral Harvesting *84*
1.8.1.3. Chiral Overpass *86*
1.8.1.4. Substituent Priority Overpass *87*
1.8.1.5. Domino Effect *88*
1.8.2. External Stimuli in Poly(phenylacetylene)s **89**
1.8.4. Internal Stimuli: Communication Mechanism in Copolymeric Poly(phenylacetylene)s **94**
1.9. SUPRAMOLECULAR HELICAL POLYMERS **98**
1.9.1. Supramolecular Polymerization: Growth Mechanisms **98**
1.9.2. Types of Aggregates: Characterization and Physical Properties **100**
1.9.3. Energy Landscape and Pathway Complexity **104**

USC UNIVERSIDADE DE SANTIAGO DE COMPOSTELA

1.9.3.1. Consecutive Pathway *104*
1.9.3.2. Competitive Pathway *106*
1.9.4. Chiral Supramolecular Aggregates Response to External Stimuli **107**
1.9.5. Chiral Amplification in Supramolecular Copolymers: Internal Stimuli **107**
1.9.5.1. Blocky Communication Mechanisms *108*
1.9.6. Non-Planar Cores and Multiple Helices **110**

CHAPTER 2. OBJECTIVES **113**

CHAPTER 3. RESULTS **121**

3.1. THERMAL ACTIVATION OF ASYMMETRY AMPLIFICATION EFFECTS IN HELICAL POLYMER-METAL COMPLEXES **123**
3.1.1. Precedents **125**
3.1.2. Discussion **127**
3.1.3. Conclusions **139**
3.2. COLORIMETRIC DETECTOR OF OXIDIZING METAL IONS BY ANILIDE-POLY(PHENYLACETYLENE)S **141**
3.2.1. Precedents **143**
3.2.2. Discussion **144**
3.2.3. Conclusions **152**
3.3. DISPUTE BETWEEN CHIRAL COMONOMERS TO INDUCE TUNABLE ASYMMETRY AMPLIFICATION EFFECTS IN DYNAMIC HELICAL COPOLYMERS **153**
3.3.1. Precedents **155**
3.3.2. Discussion **156**
3.3.3. Conclusions **182**
3.4. SYNERGISTIC CHIRAL AWAKENING: CASCADE SERGEANTS AND SOLDIERS EFFECT THROUGH DOUBLE-STEP ACTIVATION **185**
3.4.1. Precedents **187**
3.4.2. Discussion **188**
3.4.3. Conclusions **202**
3.5. OPTICAL AND CHIROPTICAL STIMULI-RESPONSIVE CHIRAL AGNPS@H-LEU-POLY(PHENYLACETYLENE) NANOCOMPOSITES IN WATER **205**
3.5.1. Precedents **207**
3.5.2. Discussion **209**
3.5.2.1. Stimuli-responsive studies of chiral AgNP(s)@Poly-(L)-1 ..... *219*
3.5.3. Conclusions **224**
3.6. DECIPHERING THE EMERGENCE OF AXIAL CHIRALITY AND STIMULI-RESPONSIVENESS IN PPAS: FROM OLIGOMERS TO POLYMERS **227**
3.6.1. Precedents **229**

USC UNIVERSIDADE DE SANTIAGO DE COMPOSTELA

3.6.2. Discussion **230**
3.6.3. Conclusions **244**
3.7. Size Dependent Stimuli-Responsive Properties of Foldamers and Helical Polymer of Chiral PPAs Obtained via Degree of Polymerization Control or by Controlled Helix Unwind **245**
3.7.1. Precedents **247**
3.7.2. Discussion **248**
3.7.3. Conclusions **261**
3.8. Intercalation Matters: Complex Communication in Supramolecular Copolymers **263**
3.8.1. Precedents **265**
3.8.2. Discussion **265**
3.8.2.1. Aggregation Studies *266*
*3.8.2.2. Computational evaluation of **1** and **2*** *268*
3.8.2.3. Supramolecular Polymerization Mechanism *270*
3.8.2.4. Communication Studies of Copolymers *273*
3.8.3. Conclusions **282**
CHAPTER 4. CONCLUSIONS **285**
CHAPTER 5. METHODOLOGY AND EXPERIMENTAL SECTION **291**
5.1. Experimental Section and Methodology Chapter 3.1. ..... **293**
5.1.1. Experimental Procedures **293**
5.1.2. Monomers and polymers **293**
5.1.3. VT-ECD studies of PPAs **294**
5.1.4. VT-ECD and VT-UV-Vis studies of poly-(*S*)-1/Li^+ Complex **295**
5.1.5. VT-ECD and VT-UV-Vis studies of small size poly-(*S*)-1/Li^+ Complex **297**
5.1.6. VT-ECD studies of poly-(*S*)-1 Li^+ Complex with temperature cycles **298**
5.1.7. VT-ECD studies of poly-(*S*)-1/Li^+ Complex with MeOH excess **298**
5.1.8. VT-ECD studies of poly-(*S*)-1/Li^+ Complex with THF cosolvent **299**
5.1.9. VT-ECD and VT-UV-Vis studies of poly-(*S*)-1/Ca^{2+} Complex **300**
5.1.10. VT-ECD and VT-UV-Vis studies of poly-(*S*)-3/Li^+ Complex **301**
5.1.11. VT-ECD and VT-UV-Vis studies of poly-(*S*)-3/Ca^{2+} Complex **302**
5.1.12. VT-ECD and VT-UV-Vis studies of poly-(*S*)-4/Li^+ and poly-(*S*)-4/Ca^{2+} Complexes **302**
5.1.13. VT-ECD and VT-UV-Vis studies of Poly-(*S*)-5/Li^+ Complex **304**
5.1.14. IR studies of poly-(*S*)-1/Li^+ and poly-(*S*)-1/Ca^{2+} at different temperatures **304**

USC UNIVERSIDADE DE SANTIAGO DE COMPOSTELA

5.1.15. VT-ECD studies of poly-(*S*)-1/Li^+ and poly-(*S*)-1/Ca^{2+} Complexes: Decomplexation in presence of ACAC metal scavenger 305

5.1.16. VT-ECD studies of poly[(*S*)-$1_{0.3}$-*co*-$6_{0.7}$]/Li^+ and poly[(*S*)-$1_{0.3}$-*co*-$6_{0.7}$]/Ca^{2+} 306

5.1.17. Van 't Hoff equation fit of the VT-ECD experimental data of poly-(*S*)-1/Li^+ Complex 307

5.1.18. Van 't Hoff equation fit of the VT-ECD experimental data of poly-(*S*)-3/Li^+ Complex 308

5.1.19. Theoretical Calculations 309

5.1.19.1 DFT calculation of the complexation of poly-(S)-1/Li^+ 310

5.1.19.2 DFT calculation of the complexation of poly-(S)-3/Li^+ 310

5.2. EXPERIMENTAL SECTION AND METHODOLOGY CHAPTER 3.2. 313

5.2.1. Materials and methods 313

5.2.2. Monomers and polymers 314

5.2.3. Synthesis of monomer M-7 315

5.2.4. Synthesis of poly-(R)-7 317

5.2.5. UV-Vis studies of anilide-PPAs connection in different high polar and low polar solvents in presence of $Fe(ClO_4)_3$ 318

5.2.6. FT-IR studies of poly-(*R*)-1 in presence of $Fe(ClO_4)_3$ 320

5.2.7. UV-Vis and CD studies of poly-(*R*)-1 in presence of $FeCl_3$ in inert conditions 321

5.2.8. IR experiments of poly-(*R*)-1 in presence of $FeCl_3$ salt 321

5.2.9. UV-Vis studies of anilide-PPAs connection in presence of different oxidizing metal ions 322

5.2.10. UV-Vis studies of anilide-PPAs connection in presence of $Fe(ClO_4)_3$ 325

5.2.11. CD and UV-Vis studies of benzamide-PPAs connection in presence of $Fe(ClO_4)_3$ 326

5.2.12. CD and UV-Vis studies of benzamide-PPAs connection in presence of $Fe(ClO_4)_3$ 329

5.2.13. EPR studies of anilide and benzamide-PPAs connection 330

5.2.14. CD and UV-Vis studies of M-(*R*)-1 in presence of $Fe(ClO_4)_3$ 331

5.2.15. CD and UV-Vis studies of poly-(*R*)-7 in presence of $Fe(ClO_4)_3$ 331

5.2.16. IR experiments of poly-(*R*)-7 in presence of $Fe(ClO_4)_3$ salt 332

5.2.17. UV-Vis studies of poly-(*R*)-1 in presence of different M^{2+} 333

5.2.18. UV-Vis studies of poly-(*R*)-1 and poly-(*R*)-3 titration with $Fe(ClO_4)_3$ 333

5.2.19. UV-Vis studies of poly-(*R*)-1 in presence of $Fe(ClO_4)_3$. 334

5.2.20. Density functional theory-based computations 334

USC UNIVERSIDADE DE SANTIAGO DE COMPOSTELA

5.2.21. Calculation of the limits of detection 336
5.2.22. UV-Vis studies of poly-(*R*)-1 in presence of H_2O_2 338
5.2.23. Time Dependent UV-Vis Studies 339
5.3. EXPERIMENTAL SECTION AND METHODOLOGY CHAPTER 3.3 341
5.3.1. Experimental Procedures 341
5.3.2. Monomers and polymers 342
5.3.3. Synthesis monomers (*S*)-1 and (*R*)-1 343
5.3.4. Synthesis of monomer (*S*)-2 and (*R*)-2 346
5.3.5. Synthesis of homopolymers Poly-(*S*)-1 and Poly-(*R*)-1 349
5.3.6. Synthesis of homopolymer Poly-(*S*)-2 and Poly-(*R*)-2 354
5.3.7. Synthesis of copolymers Poly-[(*S*)-1_r-*co*-(*R*)-2_{1-r}] 357
5.3.8. Synthesis of copolymers Poly-[(*R*)-1_r-*co*-(*R*)-2_{1-r}] 357
5.3.9. Synthesis of copolymers Poly-[(*S*)-1_r-*co*-(*S*)-2_{1-r}] 358
5.3.10. Synthesis of copolymers Poly-[(*R*)-1_r-*co*-(*S*)-2_{1-r}] 359
5.3.11. FT-IR studies of polymers and copolymers 371
5.3.12. Determination of the monomer reactivity ratios in copolymerization 372
5.3.13. ECD and UV-Vis studies of complexed homopolymers with monovalent and divalent metal ions 378
5.3.14. FT-IR studies of polymers and copolymers complexed with metal ions 379
5.3.15. VT-UV-Vis studies of Poly-[(*S*)-$1_{0.6}$-*co*-(*R*)-$2_{0.4}$] and Poly-[(*R*)-$1_{0.4}$-*co*-(*R*)-$2_{0.6}$] complexed with Li^+ and Ca^{2+} 379
5.3.16. VT-ECD studies of Poly-[(*S*)-$1_{0.7}$-*co*-(*R*)-$2_{0.3}$] and Poly-[(*S*)-$1_{0.3}$-*co*-(*R*)-$2_{0.7}$] complexed with Li^+ and Ca^{2+} 380
5.3.17. ECD of the homopolymer Poly-(*S*)-1 or Poly-(*R*)-1 mixtures with Poly-(*R*)-2 in $CHCl_3$ and complexed with Li^+ and Ca^{2+} 382
5.3.18. ECD, UV-Vis and g_{value} of Poly-[(*S*)-1_r-*co*-(*R*)-2_{1-r}] and Poly-[(*R*)-1_r-*co*-(*R*)-2_{1-r}] in $CHCl_3$ and complexed with Li^+ and Ca^{2+} 383
5.3.19. ECD and UV of Poly-[(*S*)-1_r-*co*-(*S*)-2_{1-r}] and Poly-[(*R*)-1_r-*co*-(*S*)-2_{1-r}] in $CHCl_3$ and complexed with Li^+ and Ca^{2+} 386
5.3.20. DSC Studies 388
5.3.21. Raman Studies 389
5.3.22. Abnormal chiral-to-chiral Sergeants and Soldiers Effect in the poly-[(*R*)-1_r-*co*-(*S*)-2_{1-r}] copolymer series 390
5.3.23. Absence of chiral-to-chiral communication in poly-[(*S*)-1_r-*co*-(*S*)-2_{1-r}] copolymer series 392

USC UNIVERSIDADE DE SANTIAGO DE COMPOSTELA

5.3.24. From Abnormal to Classic chiral-to-chiral Sergeants and Soldiers Effect in poly-[(*R*)-1_r-*co*-(*S*)-2_{1-r}] (r= 0.0-1.0) m.r.u./Li^+ 1.0/0.1 (mol/mol) ratio 394
5.3.25. From Abnormal chiral-to-chiral Sergeants and Soldiers Effect to Chiral Accord in poly-[(*R*)-1_r-*co*-(*S*)-2_{1-r}] (r= 0.0-1.0) m.r.u./Ca^{2+} 1.0/0.1 (mol/mol) ratio 396
5.3.26. From a mixture of Chiral Accord and Chiral Conflict effect to a selective Chiral Accord in poly-[(*R*)-1_r-*co*-(*R*)-2_{1-r}] (r= 0.0-1.0) m.r.u./Li^+ 1.0/0.1 (mol/mol) ratio 398
5.3.27. From a mixture of Chiral Accord and Chiral Conflict effect to Classic chiral-to-chiral Sergeants and Soldiers Effect in poly-[(*S*)-1_r-*co*-(*S*)-2_{1-r}] (r= 0.0-1.0) m.r.u./Ca^{2+} 1.0/0.1 (mol/mol) ratio 400
5.4. EXPERIMENTAL SECTION AND METHODOLOGY CHAPTER 3.4. 405
5.4.1. Experimental Procedures 405
5.4.2. Monomers and polymers 406
5.4.3. Synthesis monomer 3 407
5.4.4. Synthesis of homopolymers Poly-(*S*)-1 and Poly-(*R*)-1 409
5.4.5. Synthesis of homopolymers Poly-2 and Poly-3 411
5.4.6. Synthesis of copolymers Poly-[(*S*)-1_r-*co*-2_{1-r}] 413
5.4.7. Synthesis of copolymers Poly-[(*R*)-1_r-*co*-2_{1-r}] 414
5.4.8. Synthesis of copolymers Poly-[(*S*)-1_r-*co*-3_{1-r}] 414
5.4.9. Synthesis of copolymers Poly-[(*R*)-1_r-*co*-3_{1-r}] 415
5.4.10. Determination of the monomer reactivity ratios in copolymerization 427
5.4.11. DSC Studies. 432
5.4.12. Raman Studies 433
5.4.13. ECD and UV-Vis spectra of Poly-(*S*)-1 in different solvents or in the presence of metal ions 434
5.4.14. ECD and UV-Vis spectra of enantiomeric series Poly-[(*R*)-1_r-*co*-2_{1-r}] and Poly-[(*R*)-1_r-*co*-3_{1-r}] in DFM and $CHCl_3$ 436
5.5. EXPERIMENTAL SECTION AND METHODOLOGY CHAPTER 3.5. 439
5.5.1. Materials and Methods 439
5.5.2. Monomers and polymers 440
5.5.3. Synthetic procedure of intermediate derived from 4-ethynylaniline 441
5.5.4. Deprotection protocol and synthesis of (*L*)-1 443
5.5.5. Polymer synthesis 444
5.5.6. CD and UV-Vis of Monomer (*L*)-1 and addition of $AgClO_4$ followed by $NaBH_4$ 446
5.5.7. Screening of poly-(*L*)-1 at pH = 7 with $AgClO_4$ 446

USC UNIVERSIDADE DE SANTIAGO DE COMPOSTELA

5.5.8. ECD and UV-Vis studies of Poly-(*L*/*D*)-1/Ag^+ Complexes and AgNP@Poly-(*L*/*D*)-1 or AgNPs@Poly-(*L*/*D*)-1 nanocomposites 447

5.5.9. Synthesis of AgNP@Poly-(*L*)-1 with more equivalents of $AgClO_4$ 448

5.5.10. Thermal, Time and Photo Stability studies of Poly-(*L*)-1 and AgNPs@Poly-(*L*)-1 449

5.5.11. ECD and UV-Vis studies of the oxidation of AgNP@Poly-(*L*)-1 with $Fe(ClO_4)_3$, $Hg(ClO_4)_2$, and $Ce(SO_4)_2$ 450

5.5.12. ECD, UV-Vis and DLS studies of the oxidation of AgNPs@Poly-(*L*)-1 with $Fe(ClO_4)_3$, $Hg(ClO_4)_2$, and $Ce(SO_4)_2$ 451

5.5.13. ECD and UV-Vis studies of AgNPs@Poly-(*L*)-1 in the presence of ultrapure $FeCl_2$ and not ultrapure $Fe(ClO_4)_2$ 452

5.5.14. ECD and UV-Vis studies of AgNPs@Poly-(*L*)-1 in the presence of salts 453

5.5.15. ECD study of Poly-(*L*)-1 interaction with $Ba(ClO_4)_2$ 454

5.5.16. Chiroptical study of AgNPs@Poly-(*L*)-1 and of AgNP@Poly-(*L*)-1 nanocomposites in the presence of divalent perchlorate salts 454

5.5.17. UV-Vis of the nanocomposites after basification 455

5.5.18. UV-Vis and DLS of the nanocomposite following cycles of basification and acidification 455

5.5.19. Poly-(*L*)-1 at different pH 456

5.5.20. Scanning electron microscopy images of Poly-(*L*)-1/$AgClO_4$ pH = 7 456

5.5.21. Scanning electron microscopy images of AgNP@Poly-(*L*)-1 synthetized at pH = 2 457

5.5.22. Transmission electron microscopy images of AgNP@ Poly-(*L*)-1 synthetized at pH = 2 458

5.5.23. Scanning electron microscopy images of AgNPs@ Poly-(*L*)-1 synthetized at pH = 7 459

5.5.24. Scanning electron microscopy images of Poly-(L)-1/AgClO4 pH = 7 461

5.5.25. Scanning electron microscopy images of AgNPs@ Poly-(*L*)-1 synthetized at pH = 7 before after precipitation with NaOH 1M and recovery with HCl 1M..... 462

5.5.26. Scanning electron microscopy images of AgNP@ Poly-(*L*)-1 synthetized at pH = 2 before after precipitation with NaOH 1M and recovery with HCl 1M..... 463

5.5.27. UV-Vis and TEM studies of AgNP@Poly-(*L*)-1 nanocomposite prepared (a) at pH = 7 and measured at pH = 2 (b) prepared at pH = 2 and measured at pH = 7.. 465

5.5.28. Calculation of the limits of detection 465

5.6. EXPERIMENTAL SECTION AND METHODOLOGY CHAPTER 3.6. 469

5.6.1. Materials and methods 469

USC UNIVERSIDADE DE SANTIAGO DE COMPOSTELA

5.6.2. Monomers and polymers 470
5.6.3. Synthesis of polymers 470
5.6.4. Synthesis of oligomers 471
5.6.5. ECD and UV-Vis spectra of oligomers 491
5.6.6. Experimental g-value and Ising model fit 496
5.6.7. Irradiation PEC Studies 497
5.6.8. Color dependence with the DP in Anilides 502
5.6.9. Color and morphology dependence with the DP in Benzamides 503
5.6.10. VT-ECD spectra of oligomers 504
5.7. EXPERIMENTAL SECTION AND METHODOLOGY CHAPTER 3.7. 505
5.7.1. Materials and methods 505
5.7.2. Monomers and polymers 505
5.7.3. Synthesis of polymers 506
5.7.4. Synthesis of oligomers 507
5.7.5. ECD and UV-Vis spectra of oligomers oligo-(*S*)-1 516
5.7.6. Color dependence with the DP of oligomers oligo-(*S*)-1 517
5.7.7. ECD and UV-Vis of Polymers in Solvents 518
5.7.8. ECD and UV-Vis of Poly-(*S*)-1 under the addition of $CHCl_3$ to visualize the elongation of a compressed structure in THF 519
5.7.9. ECD and UV-Vis upon irradiation of oligo-(*S*)-1 DP=89, Poly-(*S*)-1, Poly-(*S*)-3 in THF 520
5.7.10. ECD and UV-Vis upon irradiation of oligo-(*S*)-1 DP=89, Poly-(*S*)-1, Poly-(*S*)-3 in Dioxane 522
5.7.11. ECD of oligo-(*S*)-1 DP=89 and Poly-(*S*)-1 in $CHCl_3$ 523
5.7.12. ECD and UV-Vis spectra of oligomers oligo-(*S*)-2 in Et_2O (3% $CHCl_3$) 524
5.7.13. ECD and UV-Vis spectra of oligo-(*S*)-1 525
5.7.14. Irradiation studies of oligo-(*S*)-1 at DP=9 in THF 526
5.7.15. Second step process comparison of oligo-(*S*)-1 between DP=9 and DP=89 527
5.7.16. Irradiation studies of poly-(*S*)-1 and poly-(*S*)-3 in THF 528
5.8. EXPERIMENTAL SECTION AND METHODOLOGY CHAPTER 3.8. 529
5.8.1. Experimental Procedures 529
5.8.2. Synthesis of tert-butyl (*S*)- and (*R*)-(1-(3,4,5-tris(dodecyloxy)benzamido)propan-2-yl)carbamate 530
5.8.3. Synthesis of (*S*) and (*R*)-*N*-(2-(4-(cyanomethyl)benzamido)propyl)-3,4,5-tris(dodecyloxy)benzamide 534

USC UNIVERSIDADE DE SANTIAGO DE COMPOSTELA

5.8.4. Synthesis of *N,N'*-((2*S*/*R*,2'*S*/*R*)-((4,4'-((1*Z*,1'*Z*)-[2,2'-bipyridine]-5,5'-diylbis(1-cyanoethene-2,1-diyl))bis(benzoyl))bis(azanediyl))bis(propane-2,1-diyl))bis(3,4,5-tris(dodecyloxy)benzamide) 538

5.8.5. Synthesis of *N,N'*-(((4,4'-((1*Z*,1'*Z*)-[2,2'-bipyridine]-5,5'-diylbis(1-cyanoethene-2,1-diyl))bis(benzoyl))bis(azanediyl))bis(ethane-2,1-diyl))bis(3,4,5-tris(dodecyloxy)benzamide) 542

5.8.6. IR experiments 544

5.8.7. Temperature dependent NMR experiments 545

5.8.8. Additional Spectra 545

5.8.9. AFM Studies 559

5.8.10. Density functional theory-based computations 560

CHAPTER 6. BIBLIOGRAPHY 565

APPENDIX 603

A.1. LIST OF PUBLICATIONS DERIVED FROM THIS DOCTORAL THESIS AND PARTIALLY REPRODUCED 605

A.2. CONFLICT OF INTEREST 621

A.3. RIGHTS AND PERMISSIONS OF THE IMAGES 621

USC
UNIVERSIDADE DE SANTIAGO DE COMPOSTELA

Summary

USC
UNIVERSIDADE
DE SANTIAGO
DE COMPOSTELA

USC
UNIVERSIDADE
DE SANTIAGO
DE COMPOSTELA

Summary

Recently, the interest in chiral materials is growing. Point chirality has been studied for decades, and small molecules are known to show properties that depend on the chirality. Recently, polymers that exhibit properties not seen in the smallest factor allow the mix of chirality with the emerging functions of these materials. Polyphenylacetylenes (PPAs) are good candidates due to their ability to form helical polymers. One of the main differences with other materials is that the chirality does not only remain on one helicity. These materials are known to form many helical assemblies, from a covalent helicity in the inner to external helices by supramolecular stacking of the pendants at the external helix. These PPAs, as they are ruled by supramolecular interactions in the periphery, behave as dynamic polymers. It gives these polymers a very good response to external stimuli such as temperature variations, metal ions, or pH changes, among others. Besides PPAs, supramolecular polymers follow similar rules and response. When interacting with external stimuli, properties such as chiral amplification, helicity induction, helicity memory, chiral inversion, among others arise. Due to this complete and complex control over the helix, the dynamic polymers have great potential for application in catalysis, sensor development, and chiral stationary phases for HPLC.

This thesis, entitled "Dynamic Helical Polymers: Exploring the Complexity of Responses to Stimuli," includes research projects focused on the study of the structure, properties and interaction with external stimuli of helical polymers poly(phenylacetylene)s (PPAs) and supramolecular polymers. In the following sections a summary of each Chapter:

Thermal Activation of Asymmetry Amplification Effects in Helical Polymer-Metal Complexes Chapter 3.1

In this chapter, we explored the thermal activation of metal complexation in dynamic helical polymers like poly(phenylacetylene)s (PPAs). These polymers exhibit unique properties where their helical structure can be influenced by external stimuli such as temperature, solvents, or metal ions. Our work demonstrated that the helical structure of a chiral PPA can be controlled by temperature and metal ions. By adding a metal ion salt to a chloroform solution of a chiral PPA, we created the complexed structure. Afterwards, lowering the temperature caused the metal ion to uncomplex, reverting the polymer to

USC UNIVERSIDADE DE SANTIAGO

its initial helical structure. This process was fully reversible and triggered asymmetry amplification effects by playing with the temperature.

To investigate this phenomenon, we selected anilide and benzamide PPAs that respond to metal ions by complexation of the pendants. We prepared solutions of these polymers and added metal ion salts to observe the changes in their helical structures. Using VT-ECD studies, we monitored the helical sense of the polymers as the temperature was varied. As the temperature was lowered, the metal ions decomplexed, and the polymers returned to their initial helical sense without complexation.

Colorimetric Detector of Oxidizing Metal Ions by Anilide-Poly(phenylacetylene)s Chapter 3.2

In this chapter, we explored the interactions of poly(phenylacetylene)s (PPAs) with oxidizing metal ions such as Cu^{2+}, Hg^{2+}, Fe^{3+}, Au^{3+}, and Ce^{4+}. From the library of PPAs only *para*- anilides showed a redox reaction, while benzamides or other substitution pattern lack the radical formation. Our findings indicated that anilide-PPAs are particularly sensitive to oxidizing metal ions, resulting in a color change of the solution from yellow to blue due to the delocalization of a radical species along the polyene backbone. We used UV-Vis spectroscopy to monitor the color change and the formation of a new band at ca. 600 nm due to the presence of a delocalized radical cation. Infrared (IR) spectroscopy was employed to confirm the coordination of the metal ions with the carbonyl groups of the PPAs. Electron Paramagnetic Resonance (EPR) studies were carried out to detect the presence of organic free radicals, and X-ray Photoelectron Spectroscopy (XPS) was used to determine the oxidation state of the metal ions before and after complexation with the PPAs. Additionally, computational studies supported our experimental findings. Our comprehensive approach allowed us to demonstrate the electron transfer from the PPA to the oxidizing metal ion upon coordination and provide a multiple response to different external stimuli with the same material (PPAs).

Dispute Between Chiral Comonomers to Induce Tunable Asymmetry Amplification Effects in Dynamic Helical Copolymers Chapter 3.3

USC DE COMPOSTELA

PPA copolymers exhibit interesting Communication Mechanisms denoted as Sergeants and Soldiers Effect (SaS), Majority Rules, Chiral Coalition, among others. Previous examples exist on the field of the Chiral-chiral Communication Mechanisms from our group. We aimed to advance our understanding by exploring switchable chiral-to-chiral Sergeants and Soldiers effects, investigating the possibility of interchanging the roles of the two components within the copolymer by introducing external stimuli. We prepared two chiral monomers followed by copolymerization in a random fashion. Then, ECD and UV-Vis studies revealed in low polar solvents (first stimulus) Abnormal Sergeants and Soldiers mechanisms depending on the diastereomeric relation of the copolymer. Afterwards, we measured the same copolymers in the presence of the metal ions (second stimulus) to promote the Chiral Soldier and new mechanisms arised. Additionally, we examined the potential to revert to the initial Communication Mechanism in solvent by applying Temperature as a third external stimulus, effectively neutralizing the Metal complexation stimulus. We observed that the Chiral Soldiers and Sergeants exhibited different sensitivities to solvents and metal ions, leading to various Communication Mechanisms such as Abnormal Sergeants and Soldiers Effect, Chiral Accord, and Chiral Conflict. This temperature-induced switch in the roles of the Chiral Soldiers and Sergeants demonstrated the complexity and tunability of the Communication Mechanisms in dynamic helical copolymers.

Synergistic Chiral Awakening: Cascade Sergeants and Soldiers Effect Through Double-Step Activation Chapter 3.4

In this chapter, we investigated the synthesis and characterization of random copolymers composed of chiral and achiral monomers with different substitution patterns. The study focused on understanding the Communication Mechanisms between chiral and achiral monomers that induce axially racemic structures in the corresponding homopolymers. The chiral monomer (*S*/*R*)-**1**, which has a *para*-substitution, was copolymerized with achiral monomers **2** (*para*-substituted) and **3** (*meta*-substituted). The goal was to explore how these different substitution patterns and solvent conditions influence the helical structure and chirality of the resulting copolymers. In DMF, the homopolymer of (*S*/*R*)-**1** exhibited a preferred helicity due to the stabilization of the *sp* conformation, making it a strong candidate to act as a Sergeant in the SAS. In contrast,

USC UNIVERSIDADE DE SANTIAGO DE COMPOSTELA

the homopolymers of **2** and **3** remained axially racemic in DMF and therefore the copolymerization of (*S*/*R*)-**1** with **2** or **3** showed a Classical SaS. Demonstrated the SaS they exert in copolymers we tested the same copolymer in $CHCl_3$, where all the pendants behave as Soldiers or induce axially racemic structures. Interestingly, the hydrophobic environment that **2** and **3** create activated (*S*)-**1** to become a Sergeant. Then, in a second step, this activated Sergeant induced SaS while being activated by the Soldier. Interestingly, the commanding of the Sergeant was limited to only the helical sense induction. While chiral amplification exists in all copolymers in $CHCl_3$, the elongation depends entirely on the molar ratio, obtaining very compressed or elongated structures with chiral induction.

Optical and Chiroptical Stimuli-Responsive Chiral AgNPs@H-Leu-Poly(phenylacetylene) Nanocomposites in Water Chapter 3.5

In this chapter, we explored the creation and properties of dynamic macroscopically chiral nanocomposites by combining silver nanoparticles (AgNPs) obtained by direct reduction with $NaBH_4$ in presence of dynamic helical poly(phenylacetylene)s (PPAs) that have (*L*)-Leucine pendants. These amino groups enable the nanocomposite of AgNPs@PPA to disperse in water and maintain high stability due to the interaction between the ammonium group and the AgNP. The equilibrium between NH_3^+ and NH_2 allows for a “blinking” contact between the PPA and the AgNPs, providing control over the dynamic helical behavior of the polymer. By adjusting on synthesis the pH to acidic or neutral conditions, we can control the morphology of the nanocomposite, resulting in nanospheres that contain either a single AgNP (pH=2) or several AgNPs (pH=7) with a diameter of approximately 30 nm detected by the localized surface plasmon resonance (LSPR) in UV-Vis and electron microscopy techniques. The mechanism of the reduction by $NaBH_4$ was described depending on the pH and affecting the ECD during its formation and the final nanocomposite structure. These nanocomposites combine the optical and chiroptical stimuli-responsive properties of both AgNPs and PPAs, allowing for reversible variations in the LSPR in UV-Vis band of the AgNPs through controlled aggregation. Additionally, the chiral coating selectively responds to Ba^{2+}, causing a helical inversion detected by ECD. The nanocomposite can also distinguish between oxidizing different

USC UNIVERSIDADE DE SANTIAGO DE COMPOSTELA

metal ions Ce^{4+}, Fe^{3+}, and Hg^{2+}, which produce distinct responses when oxidizing the AgNP to $Ag^{+\cdot}$

Deciphering the Emergence of Axial Chirality and Stimuli-Responsiveness in PPAs: From Oligomers to Polymers Chapter 3.6

In this chapter, we studied how the size of polymers and oligomers affects their folding and chiral behavior. We used well-defined poly(phenylacetylene)s (PPAs) with controlled lengths, made using Maeda's initiator method to obtain oligomers with a controlled size. Techniques like ECD, UV-Vis spectroscopy, and irradiation helped us analyze their structures. As the chain length (degree of polymerization, DP) decreased, folding became less efficient due to less interaction between pendants and bigger ratio of terminal effects, which led to more stretched structures and weaker chiral signals.

We also found that metal complexation mainly affected the center of the polymers, while the ends stayed mostly unchanged. Solvent polarity and strength influenced the shape, but the general trend remained: shorter chains showed more conjugation, a color shift from yellow to orange, and less folding. Using the Ising model with ECD data, we estimated chain sizes and saw that smaller oligomers tried to stay stretched to maintain their structure. Screw sense excess (SSE) was studied depending on the DP and number of terminal parts. In all the oligomers series SSE decreases proportionally, evidencing that the loss of ECD comes from the general increase of terminal effects compared to the total size. These results show how crucial polymer length and terminal effects are, and how PPA can fold using just a few residues as foldamers and not full helical polymer chain is needed.

Size Dependent Stimuli-Responsive Properties of Foldamers and Helical Polymer of Chiral PPAs Obtained via Degree of Polymerization Control or by Controlled Helix Unwind Chapter 3.7

In this chapter the focus was to understand the stability of the compressed structures that absorb at very low wavelength due to very strong supramolecular interactions of the external helix of PPAs. First, different amino acid derivatives were polymerized to form benzamide PPAs, which in ether solvents show a very compressed structure. These

USC UNIVERSIDADE

compressed polymers upon oligomerization undergo elongation and a dynamic helix inversion due to the reduction of the strong supramolecular interaction. Therefore, the *c-c* 3/1 structures at big degrees of polymerization undergo elongation and chiral inversion to a *c-t* helix 2/1. This dynamic behavior was remarkable, and upon oligomerization, as the forces were reduced, the stabilized helical sense was the same as in other electron donor solvents like DMF. Therefore, at low degree of polymerization (DP), solvents get inside the external helix and stabilize the most stable structure depending on the donor properties of the solvent. To mimic this oligomerization from the polymer with an external stimulus, we took advantage of the photochemical electrocyclization (PEC). Upon irradiation of the *c-t* 2/1 small oligomer, ECD and UV-Vis decreased. On the other hand, the irradiation of high DP compressed *c-c* 3/1 oligomers led to a very fast elongation to a *c-t* 2/1 detected by UV-Vis and inversion of helicity by ECD. Therefore, we formed cyclohexadienes at one terminal end to reduce the folded region and make it behave more like a small oligomer than a full polymer.

Intercalation Matters: Complex Communication in Supramolecular Copolymers Chapter 3.8

In this chapter, we explored the supramolecular polymerization and Communication Mechanisms in copolymers composed of an achiral and a chiral monomer, which co-assemble into stable H-type aggregates. Using variable-temperature UV-Vis and ECD spectroscopy, supported by IR, variable-temperature ^{1}H-NMR, and computational methods, we investigated the self-assembly behavior in both good ($CHCl_3$) and poor (MCH) solvents. In $CHCl_3$, the monomers showed distinct absorption bands, while in MCH, hypsochromic shifts and strong bisignate ECD signals confirmed effective aggregation and chiral H-type aggregate formation. These findings revealed the presence of hydrogen-bonded pseudocycles in the molecularly dissolved state ($CHCl_3$) and cooperative supramolecular polymerization (MCH). Computational studies using the CREST module of xTB and DFT calculations confirmed the formation of H-type aggregates and identified the *M*-type helix in the (*S*) monomer chirality as the more stable conformation due to steric effects. Simulated ECD spectra aligned with experimental data, validating the proposed structures.

USC UNIVERSIDADE DE SANTIAGO DE COMPOSTELA

Afterwards, multiple approaches were taken to form the supramolecular copolymers. In pure MCH, SaS exists with an r_{value} = 0.5, while in a mixture of solvents ($CHCl_3$/MCH), the same SaS was observed but with greater effectiveness. Time-dependent studies revealed that at room temperature in MCH, the copolymers remained stable, but upon increasing the temperature, the system underwent ECD inversion due to the formation of an Abnormal Sergeants and Soldiers Effect. Therefore, this is the first example of kinetic Communication Mechanisms that evolve into a different thermodynamic communication. Also, this kinetic structure was perfectly modulated, existing as kinetically trapped in pure MCH —requiring an increase in temperature to evolve— while in $CHCl_3$/MCH, the system evolved at room temperature. In the solvent mixture, the kinetic SaS behaved as metastable.

Furthermore, we have demonstrated that the system evolved by adaptation and without disassembly, following a consecutive pathway as determined by time-dependent experiments at different concentrations. We have been able not only to produce the first example of a kinetic mechanism but also to manipulate the properties of this kinetic Communication Mechanism.

USC
UNIVERSIDADE DE SANTIAGO DE COMPOSTELA

USC
UNIVERSIDADE
DE SANTIAGO
DE COMPOSTELA

Resumo

USC
UNIVERSIDADE
DE SANTIAGO
DE COMPOSTELA

USC
UNIVERSIDADE
DE SANTIAGO
DE COMPOSTELA

Resumo

Recentemente, o interese polos materiais quirais está medrando. A quiralidade puntual foi estudada durante décadas, e sábese que as moléculas pequenas amosan propiedades que dependen da quiralidade. Recentemente, os polímeros que exhiben propiedades non vistas nas estructuras máis pequenas permiten a mestura de quiralidade coas funcións emerxentes destes materiais. Os polifenilacetilenos (PPAs) son bos candidatos debido á súa capacidade para formar polímeros helicoidais. Unha das principais diferenzas con outros materiais é que a quiralidade non permanece só nunha helicidade. Estes materiais son coñecidos por formar múltiples ensamblaxes helicoidais, desde unha helicidade covalente no interior ata hélices externas mediante apilamento supramolecular dos colgantes na hélice externa. Estes PPAs, ao estaren rexidos por interaccións supramoleculares na periferia, compórtanse como polímeros dinámicos. Isto dálles a estes polímeros unha moi boa resposta a estímulos externos como variacións de temperatura, ións metálicos ou cambios de pH, entre outros. Ademais dos PPAs, os polímeros supramoleculares seguen regras e respostas similares. Cando interaccionan con estímulos externos, xorden propiedades como amplificación quiral, indución de helicidade, memoria de helicidade, inversión quiral, entre outras. Debido a este control completo e complexo sobre a hélice, os polímeros dinámicos teñen un gran potencial para aplicacións en catálise, desenvolvemento de sensores e fases estacionarias quirais para HPLC.

Esta tese, titulada "Polímeros Helicoidais Dinámicos: Explorando a Complexidade das Respostas a Estímulos", inclúe proxectos de investigación centrados no estudo da estrutura, propiedades e interacción con estímulos externos dos polímeros helicoidais poli(fenilacetileno)s (PPAs) e polímeros supramoleculares. Nas seccións seguintes faise un resumo de cada capítulo:

Activación Térmica dos Efectos de Amplificación da Asimetría en Complexos Polímero-Metal Helicoidais Capítulo 3.1

Neste capítulo, exploramos a activación térmica da complexación metálica en polímeros helicoidais dinámicos como os poli(fenilacetileno)s (PPAs). Estes polímeros exhiben propiedades únicas onde a súa estrutura helicoidal pode ser influenciada por estímulos externos como temperatura, disolventes ou ións metálicos. O noso traballo

USC UNIVERSIDADE DE SANTIAGO

demostrou que a estrutura helicoidal dun PPA quiral pode ser controlada mediante temperatura e ións metálicos. Ao engadir un sal de ión metálico a unha disolución en cloroformo dun PPA quiral, creamos a estrutura complexada. Posteriormente, ao baixar a temperatura, o ión metálico descomplexouse, revertendo o polímero á súa estrutura helicoidal inicial. Este proceso foi totalmente reversible e desencadeou efectos de amplificación da asimetría ao xogar coa temperatura.

Para investigar este fenómeno, seleccionamos PPAs de anilida e benzamida que responden aos ións metálicos mediante complexación dos colgantes. Preparamos disolucións destes polímeros e engadimos sales de ións metálicos para observar os cambios nas súas estruturas helicoidais. Mediante estudos VT-ECD, monitorizamos o sentido helicoidal dos polímeros ao variar a temperatura. Ao baixar a temperatura, os ións metálicos descomplexábanse, e os polímeros retornaban ao seu sentido helicoidal inicial sen complexación.

Detector Colorimétrico de Ións Metálicos Oxidantes mediante Anilida-Poli(fenilacetileno)s Capítulo 3.2

Neste capítulo, exploramos as interaccións dos PPAs con ións metálicos oxidantes como Cu^{2+}, Hg^{2+}, Fe^{3+}, Au^{3+} e Ce^{4+}. Da biblioteca de PPAs, só os anilidas *para* mostran unha reacción redox, mentres que as benzamidas ou outros patróns de substitución non presentan formación de radicais. Os nosos resultados indicaron que os anolida-PPAs son particularmente sensibles a ións metálicos oxidantes, resultando nun cambio de cor da disolución de amarelo a azul debido á deslocalización dunha especie radical ao longo do esqueleto de polieno. Usamos espectroscopía UV-Vis para monitorizar o cambio de cor e a formación dunha nova banda arredor dos 600 nm debida á presenza dun catión radical deslocalizado. A espectroscopía IR foi empregada para confirmar a coordinación dos ións metálicos cos grupos carbonilo dos PPAs. Realizáronse estudos de Resonancia Paramagnética Electrónica (EPR) para detectar a presenza de radicais libres orgánicos, e Espectroscopía de Fotoelectróns de Raios X (XPS) para determinar o estado de oxidación dos ións metálicos antes e despois da complexación cos PPAs. Ademais, estudos computacionais apoiaron os nosos achados experimentais. A nosa aproximación integral permitiunos demostrar a transferencia electrónica do PPA ao ión

USC UNIVERSIDADE DE SANTIAGO DE COMPOSTELA

metálico oxidante ao complexarse e proporcionar unha resposta múltiple a diferentes estímulos externos co mesmo material (PPAs).

Disputa entre comonómeros quirais para inducir efectos axustables de amplificación da asimetría en copolímeros helicoidais dinámicos Capítulo 3.3

Os copolímeros PPA exhiben mecanismos de comunicación interesantes denominados Efecto Sarxento e Soldados (SaS), Regras da Maioría, Coalición Quiral, entre outros. Existen exemplos no campo dos Mecanismos de Comunicación quiral-quiral do noso grupo. Pretendemos avanzar na nosa comprensión explorando efectos Sarxento e Soldados quiral-quiral conmutables, investigando a posibilidade de intercambiar os roles dos dous compoñentes dentro do copolímero introducindo estímulos externos. Preparáronse dous monómeros quirais seguidos por copolimerización de forma aleatoria. Despois, estudos de ECD e UV-Vis revelaron en disolventes pouco polares (primeiro estímulo) mecanismos Sarxento e Soldados Anormais dependendo da relación diastereoisomérica do copolímero. Posteriormente, medimos os mesmos copolímeros na presenza de ións metálicos (segundo estímulo) para promover o soldado quiral e xurdiron novos mecanismos. Ademais, examinamos o potencial para reverter ao mecanismo de comunicación inicial en disolvente aplicando un terceiro estímulo externo de temperatura, neutralizando efectivamente os efectos da complexación de metais. Observamos que os Sarxentos e Soldados Quirais mostraban diferentes sensibilidades a disolventes e ións metálicos, levando a varios mecanismos de comunicación como o Efecto Sarxento e Soldados Anormal, Acordo Quiral e Conflito Quiral. Este cambio inducido pola temperatura nos roles dos Sarxentos e Soldados Quirais demostrou a complexidade e axustabilidade dos mecanismos de comunicación en copolímeros helicoidais dinámicos.

Despertar Quiral Sinérxico: Efecto de Sergentes e Soldados en Cadea a través da Activación en Dobre Paso Capítulo 3.4

Neste capítulo, investigamos a síntese e caracterización de copolímeros aleatorios compostos por monómeros quirais e aquirais con diferentes patróns de substitución. O

USC DE COMPOSTELA

estudo centrouse en comprender os mecanismos de comunicación entre monómeros quirais e aquirais que inducen estruturas racémicas axiais nos homopolímeros correspondentes. O monómero quiral (*S*/*R*)-**1**, que ten unha substitución *para*, copolimerizouse con monómeros aquirais **2** (substituído *para*) e **3** (substituído *meta*). O obxectivo foi explorar como estes diferentes patróns de substitución e condicións de disolventes inflúen na estrutura helicoidal e na quiralidade dos copolímeros resultantes. En DMF, o homopolímero de (*S*/*R*)-**1** exhibiu unha helicidade preferida debido á estabilización da conformación *sp*, facéndoo un forte candidato para actuar como serxento no SAS. En contraste, os homopolímeros de **2** e **3** mantivéronse racémicos axiais en DMF e por iso a copolimerización de (*S*/*R*)-**1** con **2** ou **3** mostrou un SaS clásico. Para demostrar o SaS que exercen nos copolímeros, probamos o mesmo copolímero en $CHCl_3$, onde todos os pendentes se comportan como soldados ou inducen estruturas racémicas axiais. Curiosamente, o entorno hidrofóbico que crean **2** e **3** activou (*S*)-**1** para converterse nun serxento. Logo, nun segundo paso, este serxento activado inducíu SaS mentres era activado polo soldado. Curiosamente, o mando do serxento limitouse só á indución do sentido helicoidal. Mentres que a amplificación quiral existe en todos os copolímeros en $CHCl_3$, a elongación depende completamente da relación molar, obténdose estruturas moi comprimidas ou alongadas con inducción quiral.

Nanocompósitos Quirais AgNPs@H-Leu-Poli(fenilacetileno) con Resposta a Estimulos Óptica e Quiro-ópticamente en Auga Capítulo 3.5

Neste capítulo, exploramos a creación e propiedades de nanocompósitos macroscópicos dinámicos quirais combinando nanopartículas de prata (AgNPs) obtidas por redución directa con $NaBH_4$ en presenza de poli(fenilacetileno)s (PPAs) helicoidais dinámicos que teñen pendentes de (*L*)-Leucina. Estes grupos aminos permiten que o nanocompósito AgNPs@PPA se disperse en auga e manteña alta estabilidade debido á interacción entre o grupo amonio e a AgNP. O equilibrio entre NH_3^+ e NH_2 permite un contacto "parpadeante" entre o PPA e as AgNPs, proporcionando control sobre o comportamento helicoidal dinámico do polímero. Axustando durante a síntese o pH a condicións ácidas ou neutras, podemos controlar a morfoloxía do nanocompósito,

USC DE SANTIAGO DE COMPOSTELA

resultando en nanosferas que conteñen unha única AgNP (pH=2) ou varias AgNPs (pH=7) cun diámetro aproximado de 30 nm detectado polo resonancia de plasmon de superficie localizada (LSPR) en técnicas UV-Vis e microscopía electrónica. O mecanismo da redución por $NaBH_4$ descríbese dependendo do pH e afecta o ECD durante a súa formación e a estrutura final do nanocompósito. Estes nanocompósitos combinan as propiedades ópticas e quiro-ópticas estimuladas de AgNPs e PPAs, permitindo variacións reversibles na LSPR na banda UV-Vis das AgNPs mediante agregación controlada. Ademais, o recubrimento quiral responde selectivamente a Ba^{2+}, causando unha inversión helicoidal detectada por ECD. O nanocompósito tamén pode distinguir entre diferentes ións metálicos oxidantes Ce^{4+}, Fe^{3+} e Hg^{2+}, que producen respostas distintas ao oxidar a AgNP a Ag^{+}.

Descifrando a aparición da quiralidade axial e da resposta a estímulos en PPAs: de oligómeros a polímeros Capítulo 3.6

Neste capítulo, estudamos como o tamaño dos polímeros e oligómeros afecta a súa plegadura e comportamento quiral. Utilizamos poli(fenilacetileno)s (PPAs) ben definidos con lonxitudes controladas, feitos usando o método iniciador de Maeda para obter oligómeros con tamaño controlado. Técnicas como ECD, espectroscopía UV-Vis e irradiación axudáronnos a analizar as súas estruturas. A medida que a lonxitude da cadea (grao de polimerización, DP) diminuíu, a plegadura fíxose menos eficiente debido a menor interacción entre os pendentes e maior proporción de efectos terminais, o que levou a estruturas máis estiradas e sinais quirais máis débiles.

Tamén descubrimos que a complexación metálica afectaba principalmente o centro dos polímeros, mentres que os extremos permanecían maiormente sen cambios. A polaridade e forza do disolvente influíron na forma, pero a tendencia xeral permaneceu: cadeas máis curtas mostraron máis conjugación, un cambio de cor de amarelo a laranxa e menos plegamento. Usando o modelo de Ising con datos ECD, estimamos tamaños das cadeas e observamos que os oligómeros máis pequenos intentaban manterse estirados para conservar a súa estrutura. O exceso de sentido de rosca (SSE) estudouse dependendo do DP e do número de partes terminais. En todas as series de oligómeros, o SSE diminúe proporcionalmente, evidenciando que a perda de ECD vén do aumento xeral dos efectos terminais en comparación co tamaño total. Estes

USC UNIVERSIDADE DE COMPOSTELA

resultados amosan o importante que é a lonxitude do polímero e os efectos terminais, e como o PPA pode dobrarse usando só uns poucos residuos como foldámeros, sen necesidade dunha cadea helicoidal completa

Propiedades responsivas a estímulos dependentes do tamaño de foldámeros e polímero helicoidal de PPAs quirais obtidos mediante control do grao de polimerización ou por desenrolamento controlado da hélice Capítulo 3.7

Neste capítulo o foco foi entender a estabilidade das estruturas comprimidas que absorben en moi baixa lonxitude de onda debido a interaccións supramoleculares moi fortes da hélice externa dos PPAs. Primeiro, diferentes derivados de aminoácidos foron polimerizados para formar PPAs de benzamida, que en disolventes éteres mostran unha estrutura moi comprimida. Estes polímeros comprimidos, ao oligomerizarse, experimentan unha elongación e unha inversión dinámica da hélice debido á redución da forte interacción supramolecular. Polo tanto, as estruturas *c-c* 3/1 en graos altos de polimerización experimentan elongación e inversión quiral a unha hélice *c-t* 2/1. Este comportamento dinámico foi notábel, e ao oligomerizarse, ao diminuír as forzas, o sentido helicoidal estabilizado era o mesmo que noutros disolventes doadores de electróns como DMF. Así, a baixo grao de polimerización, os disolventes entran na hélice externa e estabilizan a estrutura máis estable dependendo das propiedades doadoras do disolvente. Para imitar esta oligomerización do polímero cun estímulo externo, aproveitamos a electrocilización fotoquímica (PEC). Ao irradiar o pequeno oligómero *c-t* 2/1, diminuíron o ECD e o UV-Vis. Por outra banda, a irradiación de oligómeros comprimidos *c-c* 3/1 de alto DP levou a unha elongación moi rápida a unha *c-t* 2/1 detectada por UV-Vis e á inversión da helicidade por ECD. Así, obtivemos un primeiro exemplo dun PEC dinámico en PPAs. Por iso, formamos ciclohexadienos nun dos extremos terminais para reducir a rexión dobrada e facer que se comporte máis como un pequeno oligómero ca como un polímero completo

A Importancia da Intercalación: Comunicación Complexa en Copolímeros Supramoleculares Capítulo 3.8

USC UNIVERSIDADE DE SANTIAGO DE COMPOSTELA

Neste capítulo exploramos a polimerización supramolecular e os mecanismos de comunicación en copolímeros compostos por un monómero aciral e outro quiral, que se ensamblan en agregados estables do tipo H. Usando espectroscopía UV-Vis e ECD a temperatura variable, apoiada por IR, ^{1}H-NMR a temperatura variable e métodos computacionais, investigamos o comportamento de autoensamblaxe tanto en disolventes bos ($CHCl_3$) como pobres (MCH). En $CHCl_3$, os monómeros mostraron bandas de absorción distintas, mentres que en MCH, desprazamentos hipsocrómicos e sinais ECD bisignados fortes confirmaron unha agregación efectiva e a formación de agregados quirais do tipo H. Estes resultados revelaron a presenza de pseudociclos unidos por enlaces de hidróxeno no estado molecularmente disolto ($CHCl_3$) e unha polimerización supramolecular cooperativa (MCH). Os estudos computacionais usando o módulo CREST de xTB e cálculos DFT confirmaron a formación de agregados do tipo H e identificaron a hélice tipo *M* na quiralidade (*S*) como a conformación máis estable debido a efectos estéricos. Os espectros ECD simulados aliñáronse cos datos experimentais, validando as estruturas propostas.

Logo, realizáronse múltiples enfoques para formar os copolímeros supramoleculares. En MCH puro, SaS existe cun $r_{value} = 0,5$, mentres que nunha mestura de disolventes ($CHCl_3$/MCH), observouse o mesmo SaS pero con maior efectividade. Os estudos dependentes do tempo revelaron que a temperatura ambiente en MCH, os copolímeros permanecían estables, pero ao aumentar a temperatura, o sistema sufriu unha inversión ECD debido á formación dun efecto anormal de Sergentes e Soldados. Así, este é o primeiro exemplo de mecanismos de comunicación cinéticos que evolucionan a unha comunicación termodinámica diferente. Ademais, esta estrutura cinética foi perfectamente modulada, existindo atrapada cineticamente en MCH puro — requiriendo aumento de temperatura para evolucionar— mentres que en $CHCl_3$/MCH o sistema evolucionou á temperatura ambiente. Na mestura de disolventes, o SaS cinético comportouse como metastable.

Ademais, demostramos que o sistema evolucionou por adaptación e sen desensamblaxe, seguindo unha vía consecutiva determinada por experimentos dependentes do tempo a diferentes concentracións. Non só fomos capaces de producir o primeiro exemplo dun mecanismo cinético senón tamén de manipular as propiedades deste mecanismo de comunicación cinética.

USC
UNIVERSIDADE DE SANTIAGO DE COMPOSTELA

USC
UNIVERSIDADE
DE SANTIAGO
DE COMPOSTELA

Chapter 1. Introduction

USC
UNIVERSIDADE
DE SANTIAGO
DE COMPOSTELA

USC
UNIVERSIDADE
DE SANTIAGO
DE COMPOSTELA

Chapter 1. Introduction

Section 1.6.3. of this chapter is reproduced with the permission of John Wiley and Sons from the following Angewandte Chemie International Edition publication:

Manuel Núñez-Martínez[+,a] Manuel Fernández-Míguez[+,a] Emilio Quiñoá,[a] Félix Freire,[a]* Size Control of Chiral Nanospheres Obtained via Nanoprecipitation of Helical Poly(phenylacetylene)s in the Absence of Surfactants, *Angew. Chem. Int. Ed.* **2024**, *63*, e202403313. DOI: 10.1002/anie.202403313.

[+]These authors contributed equally to this work.

Affiliations

[a]Centro Singular de Investigación en Química Biolóxica e Materiais, Moleculares (CiQUS) and Departamento de Química Orgánica, Universidade de Santiago de Compostela 15782 Santiago de Compostela (Spain)

USC UNIVERSIDADE DE SANTIAGO DE COMPOSTELA

Section 1.8. of this chapter is reproduced with the permission of Royal Society of Chemistry from the following Chemical Society Reviews publication:

María Lago-Silva,[a] Manuel Fernández-Míguez,[a] Rafael Rodríguez,[a] Emilio Quiñoá,[a] Félix Freire,[a]* Stimuli-responsive synthetic helical polymers, *Chem. Soc. Rev.* **2024**, *53*, 793-852. DOI: 10.1039/D3CS00952A.

Affiliations

[a]Centro Singular de Investigación en Química Biolóxica e Materiais, Moleculares (CiQUS) and Departamento de Química Orgánica, Universidade de Santiago de Compostela 15782 Santiago de Compostela (Spain)

USC UNIVERSIDADE DE SANTIAGO DE COMPOSTELA

Section 1.8.1.3. of this chapter is reproduced with the permission of John Wiley and Sons from the following Angewandte Chemie International Edition publication:

Rafael Rodríguez,[a] Elena Rivadulla-Cendal,[a] Manuel Fernández-Míguez,[a] Berta Fernández,[b] Katsuhiro Maeda,[c] Emilio Quiñoá,[a] and Félix Freire,[a]* Full Control of the Chiral Overpass Effect in Helical Polymers: *P*/*M* Screw Sense Induction by Remote Chiral Centers After Bypassing the First Chiral Residue, *Angew. Chem. Int. Ed.* **2022**, *61*, e202209953. DOI: 10.1002/anie.202209953.

Affiliations

[a]Centro Singular de Investigación en Química Biolóxica e Materiais, Moleculares (CiQUS) and Departamento de Química Orgánica, Universidade de Santiago de Compostela 15782 Santiago de Compostela (Spain)

[b]Departamento de Química Física, Universidade de Santiago de Compostela 15782 Santiago de Compostela (Spain)

[c]Graduate School of Natural Science and Technology, Kanazawa University, Kakuma-machi, Kanazawa 920-1192 (Japan)

USC UNIVERSIDADE DE SANTIAGO DE COMPOSTELA

Section 1.9.5.1. of this chapter is reproduced with the permission of John Wiley and Sons from the following Chemistry – A European Journal publication:

Lafayette N. J. de Windt,[a] Zulema Fernández,[b] Manuel Fernández-Míguez,[b] Félix Freire,[b]* Anja R. A. Palmans,[a]* Elucidating the Supramolecular Copolymerization of N- and C-Centered Benzene-1,3,5-Tricarboxamides: The Role of Parallel and Antiparallel Packing of Amide Groups in the Copolymer Microstructure, *Chem. Eur. J.* **2022**, *18*, e202103691. DOI: 10.1002/chem.202103691.

Affiliations

[a]Laboratory of Macromolecular and Organic Chemistry, Institute for Complex Molecular Systems, Eindhoven University of Technology P.O. Box 513, 5600 MB Eindhoven (The Netherlands).

[b]Centro Singular de Investigación en Química Biolóxica e Materiais, Moleculares (CiQUS) and Departamento de Química Orgánica, Universidade de Santiago de Compostela 15782 Santiago de Compostela (Spain).

USC UNIVERSIDADE DE SANTIAGO DE COMPOSTELA

Section 1.9.6. of this chapter is reproduced with the permission of John Wiley and Sons from the following Angewandte Chemie International Edition publication:

María Lago-Silva[+,a] Manuel Fernández-Míguez[+,a] Zulema Fernández,[a] María Magdalena Cid,[b] Emilio Quiñoá,[a] Rafael Rodríguez,[c*] Félix Freire,[c*] Coaxial Helices in Chiral Supramolecular Aggregates from Highly Hindered Chiral Allenes, Angew. Chem. Int. Ed. 2024, 64, e202421310. DOI: 10.1002/anie.202421310.

[+]These authors contributed equally to this work.

Affiliations

[a]Centro Singular de Investigación en Química Biolóxica e Materiais, Moleculares (CiQUS) and Departamento de Química Orgánica, Universidade de Santiago de Compostela 15782 Santiago de Compostela (Spain)

[b]Departamento de Química Orgánica, Universidade de Santiago de Compostela 15782 Santiago de Compostela (Spain)

[c]CINBIO and Departamento de Química Orgánica, Campus Lagoas-Marcosende, Universidade de Vigo E-36310 Vigo (Spain)

USC UNIVERSIDADE DE SANTIAGO DE COMPOSTELA

USC
UNIVERSIDADE
DE SANTIAGO
DE COMPOSTELA

Chapter 1. Introduction

Helices are intrinsically chiral structures, therefore, the two possible helical senses —right- and left-handed configurations— cannot be overlapped. This chiral motif is very common in nature and plays a fundamental role in multiple biological processes. The helical arrangement adopted by macromolecular biological polymers, such as coiled-coil protein bundles, deoxyribonucleic acid (DNA) superhelices, and hybrid protein-DNA structures, is essential for genetic information storage and replication, ion transport, molecular recognition, and asymmetric chemical transformations, among others.[1-3] The discovery of the protein α-helix[4] and the structural model of the DNA double helix[5] proposed by Watson and Crick in the 1950s (Figure 1) are two of the most important discoveries for molecular biology. Inspired by these findings, researchers have made significant efforts to simulate the biological helices by synthetic means. However, in recent decades, the focus has shifted toward designing new synthetic helical systems with unique properties and functions not found in natural counterparts. Unlike the biological molecules, the synthetic helices can exert new properties and functions, not only focused on the biological field, such as asymmetric catalysis, molecular recognition, and chiral separation techniques.[6-10]

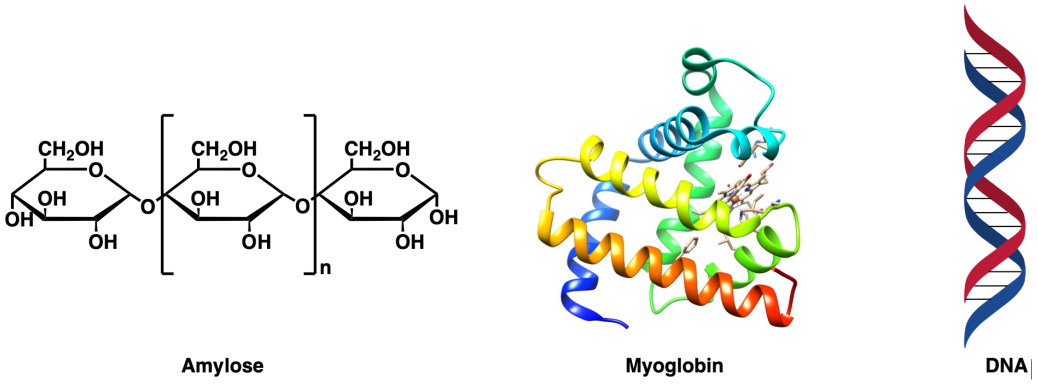


Figure 1. Natural helical polymers: amylose, myoglobin containing α-helices, and DNA.

The first successful synthesis of a helical polymer was obtained in 1955 by Natta, who developed isotactic poly(propylene) using a Ziegler-Natta catalyst. In the crystalline state the polymer displayed a helical conformation with a combination of both left-handed *M*-type helix and right-handed *P*-type helix orientations. However, in solution the helix was unstable, evolving into a random coil structure.[11] Despite this instability, Natta's

USC UNIVERSIDADE DE SANTIAGO DE COMPOSTELA

discovery opened the way for the development of more stable helical structures in solution.

Pino et al. described the synthesis of a series of poly(vinyl) polymers with a predominant helical orientation. It was obtained by polymerizing monomers that contained a chiral center, which influenced the helical preference of the resulting polymer. The predominancy of one helical sense was confirmed through optical rotation measurements.[12]

In 1974, Nolte and Drenth synthesized an isotactic poly(*tert*-butylisocyanide), in which they successfully isolated the *M* and *P* helical sense through chiral chromatography.[13] Shortly after, in 1979, Okamoto and coworkers selectively synthesized, for the first time, a homopolymer with a single helical sense using a chiral catalyst. In this case, the achiral monomer employed was triphenylmethyl methacrylate (TrMA), and they achieved a complete chiral transfer from the chiral catalyst to the monomers.[14]

In 1988, Green investigated a new family of helical polymers, the poly(isocyanates) (PIs). Unlike previous helical polymers, the helical sense of the PIs could be modified through external stimuli such as pH, solvents, chiral molecules, metals, or temperature.[15] These materials were classified as dynamic helical polymers due to their low energy barriers between the *M* and *P* type helices. Therefore, the two helical senses could coexist within the same polymer chain, or one could be selectively stabilized through the aforementioned stimuli.

1.1. Classification of Helical Polymers

The helical polymers can be classified into two different groups according to the energy barriers between the *M*-type and *P*-type helices.

1.1.1. Static Helical Polymers

Static helical polymers present one helicity that is induced during the polymerization by using chiral monomers or the use of chiral initiators or catalysts. The already formed polymers with one specific helical sense cannot interconvert, basically exist with a helical sense (Figure 3a) that will not change under any stimuli once they are synthesized.[10]

USC UNIVERSIDADE DE SANTIAGO

Thes presence of a high energy barrier is commonly due to the existence of very bulky substituents, which prevent the interconversion between the two possible forms of the polymer. Some examples are: poly(methacrylate)s (poly-**1**), poly(methylacrylamide)s (poly-**2**), poly(quinoxaline-2,3-dyl)s (poly-**3**) and poly(guanidine)s (poly-**4**) (Figure 2).

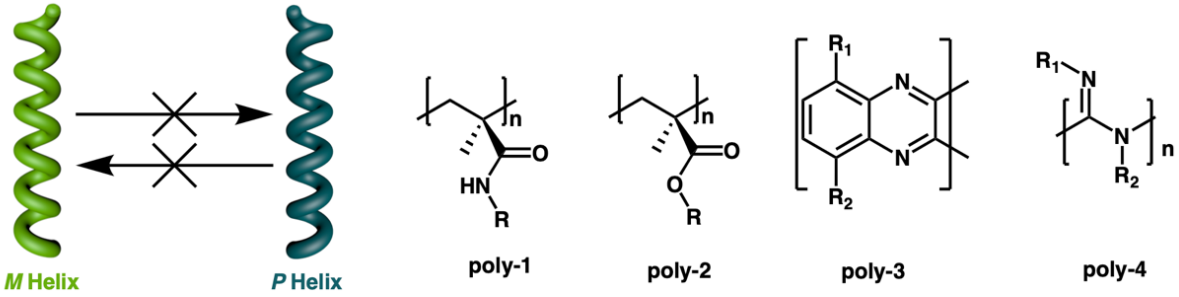


Figure 2. Static helical polymers and examples of polymers that exhibit this static behavior.

1.1.2. Dynamic Helical Polymers

Dynamic helical polymers are defined by their low energy barriers between *P*- and *M*-type helices, allowing for easy interconversion between these two helical orientations. This process occurs through conformational adjustments at the pendant groups and can be influenced by external stimuli, which selectively stabilize one helical sense over the other.[16] The equilibrium between *P* and *M* helices can be modulated by polymerizing an optically active monomer or by polymerizing an achiral monomer in the presence of a chiral solvent or additive. This approach results in a polymer with a preferred helical orientation, as the P/M equilibrium shifts to accommodate the chiral influence. Representative examples of dynamic helical polymers include poly(isocyanate)s (poly-**5**), poly(isocyanide)s (poly-**6**), poly(silane)s (poly-**7**), and poly(acetylene)s (poly-**8**) (Figure 3).

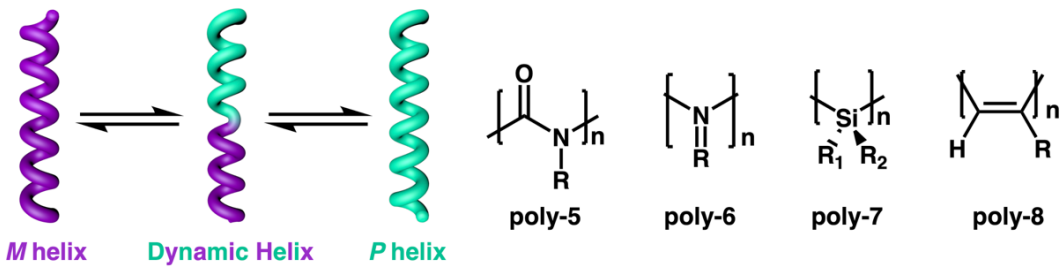


Figure 3. Dynamic helical polymers and examples of polymers that exhibit this dynamic behavior.

USC UNIVERSIDADE DE SANTIAGO DE COMPOSTELA

1.2. Poly(acetylene)s and Poly(phenylacetylene)s

Poly(acetylene)s (PAs) is a family of dynamic helical polymers characterized by their π-conjugated double bonds. These polymers are derived from the polymerization of acetylene monomers and have been extensively studied in recent decades due to their stability in both solid and solution states, and how easy they are to use.

They are characterized by a π-conjugated backbone and gained significant attention following the pioneering work started in the mid 70's of Heeger, MacDiarmid, and Shirakawa, who were awarded the Nobel Prize in Chemistry in 2000 for their groundbreaking research on using these materials as conductive polymers. At the same time notable contributions from researchers like Ciardelli et al., who synthesized various optically active π-conjugated and dynamic PAs through the polymerization of phenylacetylenes, further expanding their applications and understanding.[17,18]

Poly(phenylacetylene)s (PPAs), a family of PAs, represent one of the most investigated dynamic helical polymers by Yashima and coworkers from 1995. They studied how the PPAs by non-covalent interactions with chiral substrates induce a preferred helical sense.[19]

PPAs and PAs can be classified into four main configurations based on the arrangement of their conjugated double bonds: *cis-cisoidal* (*c-c*), *cis-transoidal* (*c-t*), *trans-cisoidal* (*t-c*), and *trans-transoidal* (*t-t*). Among these, only the *cis* configurations (*c-c* and *c-t*) allow the formation of helical structures, which are essential for their unique optical and chiroptical properties (Figure 4).[20-22]

Poly(phenylacetylene)s (PPAs) are particularly notable due to their high stereoregularity, stability in both solid and solution states, and versatility in applications such as Chiral Stationary Phases (CSPs) for High-Performance Liquid Chromatography (HPLC),[6,23,24] sensors,[8,25] and asymmetric catalysis.[26-28]

The synthesis of PAs or PPAs involves the polymerization of monomeric units containing an alkyne moiety, including phenylacetylenes, propiolic esters, propargyl esters, propargyl amides, or aliphatic acetylenes (Figure 4a).[29] PPAs, being the most extensively studied, are derived from poly(acetylene)s and exhibit high molecular weight and stereoregularity.[8,29,30] The polymerization process is highly dependent on the stereochemistry of the resulting double bonds, with *cis* configurations favoring helical folding (Figure 4b).[20-22]

USC UNIVERSIDADE DE SANTIAGO

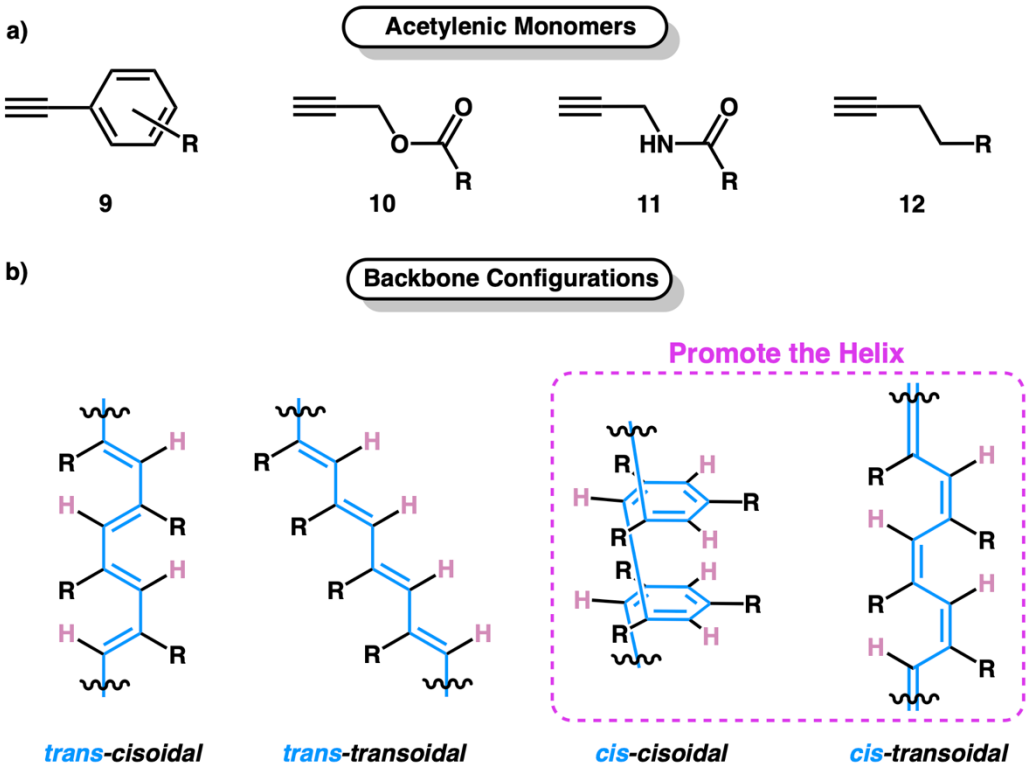


Figure 4. a) Chemical structures of monomers of the PA family (b) Possible configurations *trans* or *cis* at the polyenic backbone.

1.2.1. Rh Catalyst

In 1994 Noyori and coworkers developed powerful rhodium-based catalysts.[31-35] The development of rhodium-based catalysts resulted in high yields in the synthesis of PAs or PPAs with low polydispersity and high *cis*-stereoregularity. These catalysts carry out stereospecific and controlled living polymerization. The mechanism followed by this Rh(I) catalysts involves a head-to-tail 2,1-insertion mechanism. This mechanism is driven by steric repulsion between monomeric units, leading to the formation of highly ordered polymer chains (Figure 5).[36-38]

USC
UNIVERSIDADE DE SANTIAGO DE COMPOSTELA

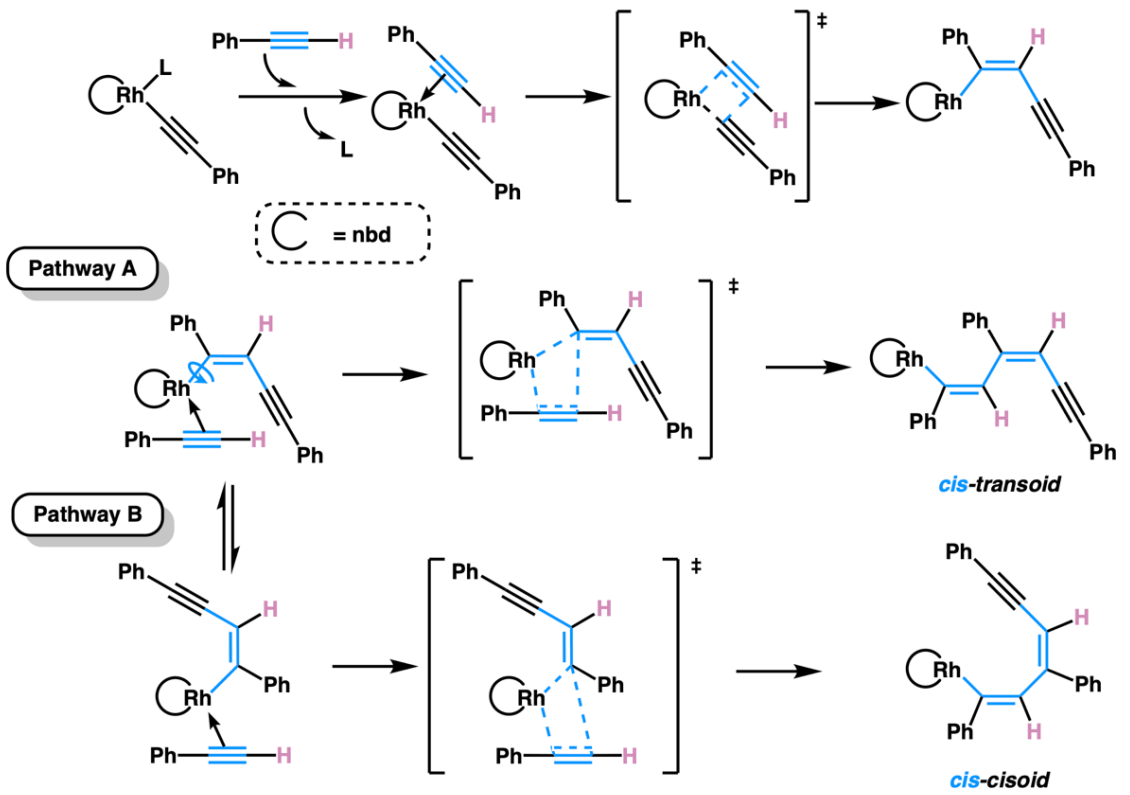


Figure 5. Polymerization mechanism of the PPAs catalyzed by Rh(I).

1.2.1.1. Classical Organic Catalysts

Classical rhodium-based catalysts developed by Tabata and coworkers,[39,40] such as $[Rh(nbd)Cl]_2/Et_3N$ (nbd: 2,5-norbornadiene) and $[Rh(cod)Cl]_2/Et_3N$ (cod: *cis*,*cis*-1,5-cyclooctadiene) have been widely used for the polymerization of helical polyphenylacetylenes.[36,41-45] Their compatibility with a variety of organic solvents and functional groups makes them highly versatile tools in PPA and PA synthesis.

1.2.1.2. Water Compatible Catalysts

Water-soluble PPAs present unique challenges due to the poisoning effect of rhodium catalysts by polar groups such as primary amines.[46-49] A key challenge is that conventional Rh(I) catalysts becomes poisoned when exposed to polar groups such as primary amines.[50-52] To avoid the poisoning, Tang and coworkers developed other rhodium catalysts: $[Rh(nbd)Cl]_2$, $[Rh(cod)Cl]_2$, and $Rh^+(nbd)[B(C_6H_5)_4]^-$ to polymerize phenylacetylenes with carboxylic acid or alcohol groups. [50,53,54] Similarly, Yashima and

coworkers explored the use of tertiary amines to prepare PPAs in water.[55-58] Even though, the primary and secondary amino groups in the polymerization of PPAs had low or moderate yields.[50-52] However, a recent publication by our group has demonstrated that $[Rh(cod)_2]^+BF_4^-$ can effectively polymerize phenylacetylenes bearing primary or secondary amino groups in aqueous conditions.[59]

1.2.1.3. Catalysts for controlled degree of polymerization and end functionalization

From the classical catalyst of Tabata many other examples that improve the activity and livingness of acetylene polymerizations, like $[(nbd)Rh(C{\equiv}CPh)(PPh_3)_2]$ and $(nbd)Rh\{C(Ph){=}CPh_2\}(PPh_3)$ with PPh_3, have been obtained. Recently, Maeda and coworkers introduced a novel rhodium-based multicomponent catalytic system for controlling PPA polymerization. They developed methods to obtain polymers or oligomers with precise control over dispersity, achieving highly monodisperse polymers by using a Rh(I) initiator.[54,60-62] This method also allows precise control over polymer molecular weight through the feed ratio of monomer to rhodium catalyst. Moreover, this method facilitated the synthesis of end-functionalized PPAs with high *cis*-stereoregularity. They reported a method involving 2 or 3 diphenylacetylene units in the initiator, which can be tuned to introduce different functional groups into the oligomers. This system includes $[Rh(nbd)Cl]_2$, boronic acid derivatives, diphenylacetylene, 50% aqueous KOH, and PPh_3.[61,63,64]

Additionally, the great reactivity and efficient living polymerization mechanism of this catalysts allows the obtention of block copolymers. Therefore, after full consumption of a first monomer, they could introduce a second monomer to continue the growth process and obtain block copolymers (Figure 6).[61]

Beside Maeda's catalyst, other example of catalysts like $(nbd)Rh\{C(Ph){=}CPh_2\}(PPh_3)$ with PPh_3 showed control over the block copolymerization.[65,66]

USC UNIVERSIDADE DE SANTIAGO DE COMPOSTELA

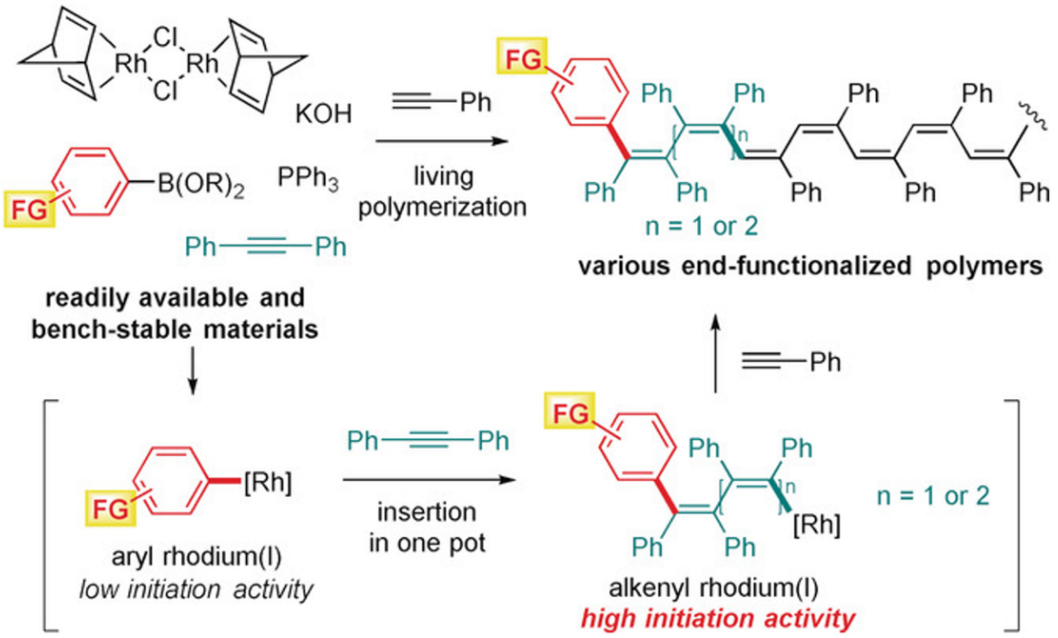


Figure 6. Fully controlled living polymerization of phenylacetylenes using a rhodium-based catalytic system, enabling the synthesis of end-functionalized poly(phenylacetylene)s by Maeda. FG = Functional Group. Reproduced from ref. 61 with permission from John Wiley and Sons, copyright 2020.

1.3. Stability of Poly(phenylacetylene)s

The stability of poly(phenylacetylene)s is key to their use in a range of applications. Understanding how they degrade or respond to conditions like light, heat, oxygen, or mechanical stress, not only helps to improve their performance and durability but also reveals information about their structure and behavior.

1.3.1 Photochemical Stability

The photochemical reactivity or stability of PPAs is examined by their response to light. Prof. Aoki and coworkers reported that PPAs undergo selective photocyclic aromatization (SCAT) under specific wavelengths of light, particularly visible light.[67,68] This process is highly controlled and results in the formation of 1,3,5-trisubstituted benzene derivatives with remarkable selectivity. The reaction proceeds through two main steps: a pericyclic photochemical 6π electrocyclic ring-closing or photochemical electrocyclation (PEC) (conrotatory Woodward-Hoffmann rules)[69] followed by aromatization (Figure 7).[70,71]

USC UNIVERSIDADE DE SANTIAGO DE COMPOSTELA

The stereochemistry and conformation of the PPA backbone are critical for this reaction to occur efficiently. Only PPAs with a *cis-cisoidal* configuration are capable of undergoing SCAT. It is required a precise alignment of their double bonds and lower distance than 4 Å, which facilitates the necessary molecular interactions. The reaction starts at the end of the polymers and extends orderly along the chain by a domino effect, avoiding the formation of byproducts unlike what happens in thermal degradation due to the random positions where cyclization occurs.[67] This photochemical pathway avoids the random formation of byproducts that often accompanies thermal processes (Figure 7).

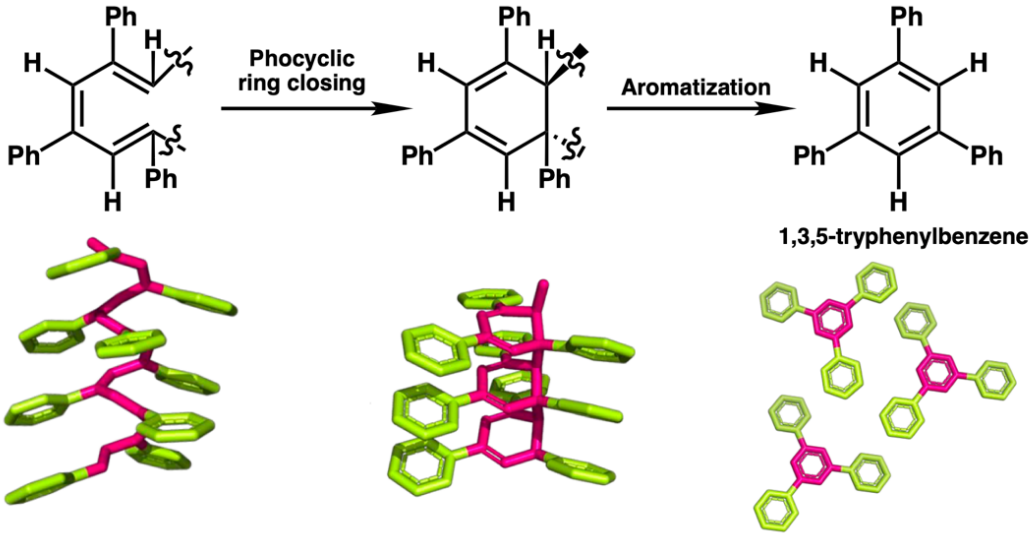


Figure 7. Photocyclic ring-closing and aromatization of polyenes, illustrating the selective photocyclic aromatization (SCAT) of PPAs under visible light. Reproduced from ref. 92 with permission from John Wiley and Sons, copyright 2021.

1.3.2. Thermal stability

The thermal degradation mechanism of the polyene backbone has been discussed by multiple research groups with different results.[72-75] However, Percec and coworkers demonstrate that the degradation mechanism is the same whether PPAs are in solution or solid phase. PPAs in the presence of heat go through a series of degradation processes: first a concerted 6π electrocyclization followed by aromatization.

The thermal degradation typically begins with an intramolecular electrocyclization of the polyenic backbone. Hence, conjugated double bonds in the polymer backbone rearrange into cyclic intermediates. These intermediates then produce aromatic compounds such as 1,3,5-trisubstituted benzene rings (Figure 8). Even so, PPAs can

follow a different pathway in the presence of oxygen and light. They may undergo faster degradation due to the oxidative effects of oxygen in $CHCl_3$. Cyclization occurs much more rapidly because of the HCl generated from $CHCl_3$ decomposition. Additionally, oxidative degradation produces many byproducts such as aldehydes and ketones. These byproducts result from secondary reactions, like [2+2] cycloadditions with singlet oxygen. For this reason, thermal degradation leads to the formation of many mismatched fragments.[76-79]

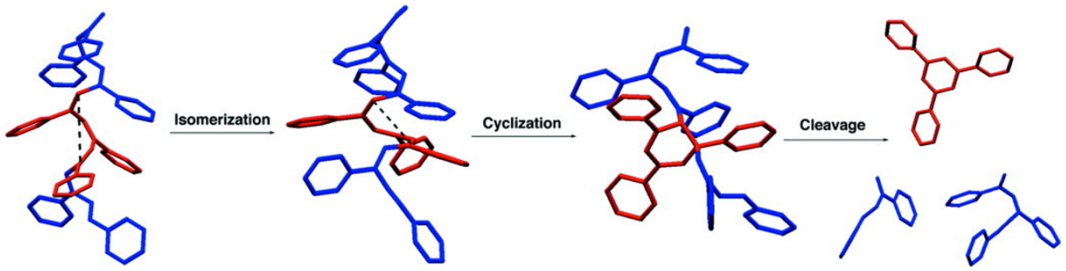


Figure 8. Thermal degradation of PPAs. Reproduced from ref. 76 with permission from John Wiley and Sons, copyright 2002.

1.3.3. Radical-mediated Isomerization

Radical-mediated isomerization represents another factor that affects the stability of PPAs, especially in the presence of mechanical stress or pressure. This process involves the generation of radical species within the polymer backbone, which can induce structural changes such as *cis-trans* isomerization. The formation of radicals can occur through multiple ways[80-82] such as mechanochemical grinding[44] or the application of pressure.[41,83]

Tabata's work elucidated these mechanisms, demonstrating that the compression of PPAs enhances the stability of the *trans* configuration through a radical mechanism (Figure 9). This process is supported by electronic paramagnetic resonance (EPR) measurements, which confirm the presence of radicals during isomerization[41,83] Additionally, mechanochemical treatments at low temperatures (e.g., 77 K) facilitated *cis-trans* isomerization in PPAs.[44]

USC UNIVERSIDADE DE SANTIAGO DE COMPOSTELA

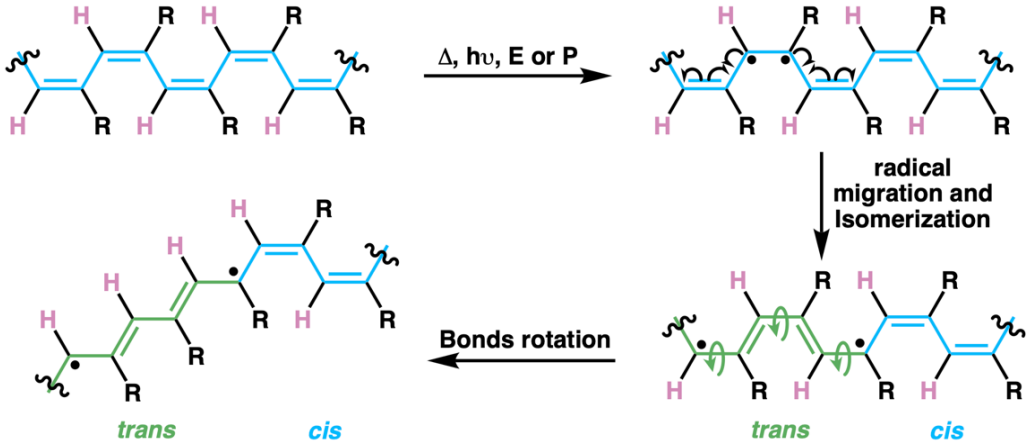


Figure 9. Schematic representation of the isomerization *cis-trans* by radical formation in PPAs described by Tabata.

1.4. The Structural Elucidation of Poly(phenylacetylene)s Helices

PPAs exhibit important secondary structures that affect the properties. Helicity is the primary structure of PPAs, and its determination is done by multiple techniques.

1.4.1. PPA Architecture

PPAs are dynamic helical polymers characterized by two coaxial helices —internal and external—, each playing distinct roles in their structural and functional properties. The internal helix is composed by a conjugated polyene backbone, while the external helix is formed by the stacking of pendant groups.[84]

The internal helicity is highly flexible and depends on the stacking of the external (pendant) helices. Since the olefins forming the internal helix lack supramolecular interactions, no specific stabilization dictates a preferred conformation. Instead, structure is governed by the external helix. The polyene backbone conformation is determined by the dihedral angle ω_1 between double bonds. When ω_1 takes negative values, the polymer adopts an *M*-type (levorotatory), negative helical sense. While positive ω_1 value corresponds to a *P*-type (dextrorotatory), positive helical sense (Figure 10). The helical sense of the internal backbone can be detected by Electronic Circular Dichroism (ECD), following the diene helicity rules established by Lorenzo Di Bari.[85] Due to the presence of multiple overlapping ECD signals (Cotton effects) from different dihedral angles: ω_1

USC UNIVERSIDADE DE SANTIAGO DE COMPOSTELA

for the internal helix, ω_4 for the external helix, and ω_3 between the polyene backbone and the first ring of the PPA. This Cotton assignation of the ECD pattern was obtained by computational calculations at various dihedral angles.[86]

The internal helix, being flexible, can elongate or compress depending on the ω1 values. When $\omega_1 < 90^o$, the polymer adopts a *cis-cisoidal* conformation, resulting in a compressed 3/1 helix (three residues per turn), where both helices rotate in the same direction. On the other hand, at $\omega_1 > 90^o$ the polymer gets stretched into a *cis-transoidal* conformation, forming a 2/1 helix (two residues per turn), where the internal and external helices rotate in opposite directions. These structural models have been confirmed by AFM for the external helix and ECD for the internal helix (Figure 10).

USC
UNIVERSIDADE DE SANTIAGO DE COMPOSTELA

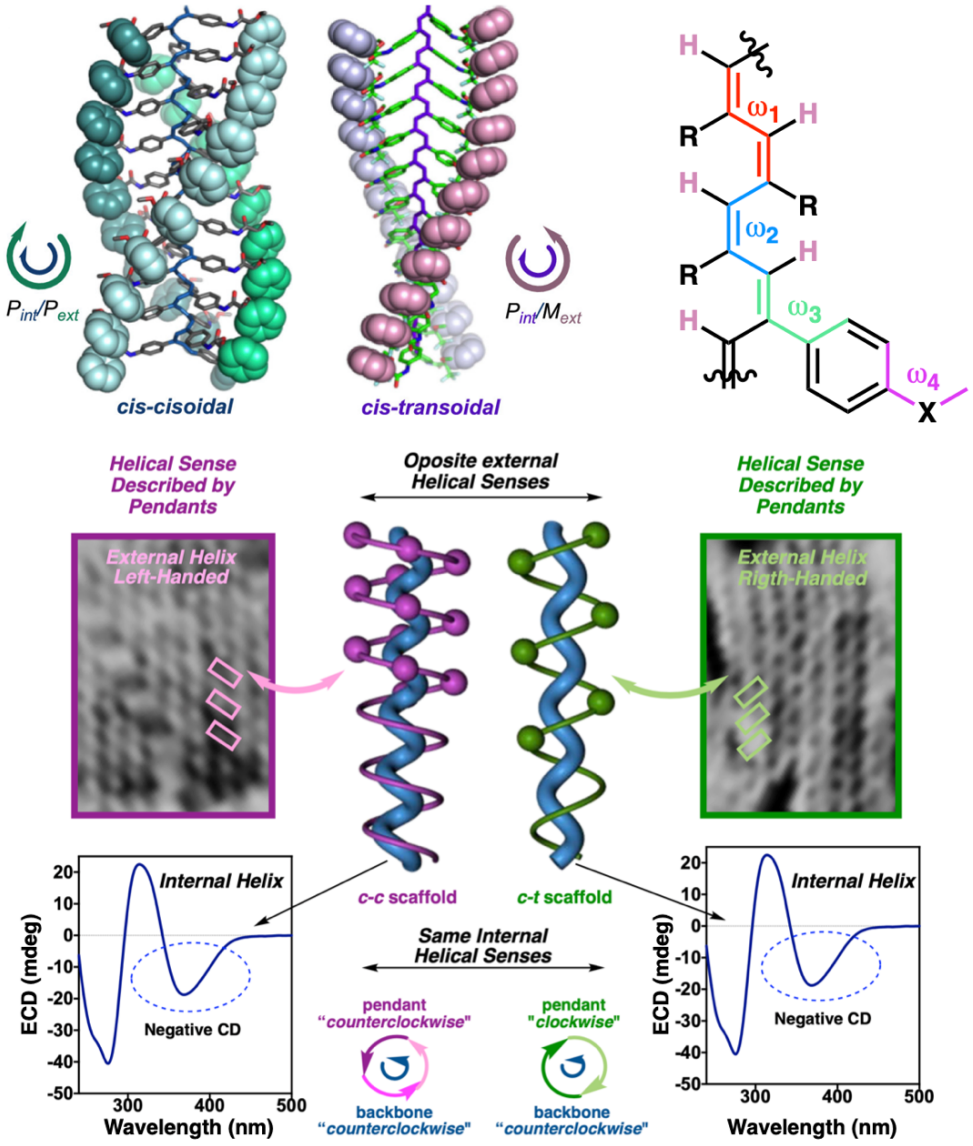


Figure 10. Schematic illustration of two possible helical scaffolds that a PPA can adopt, their dihedral angles and their relationship to ECD and AFM studies. Reproduced from ref. 86 with permission from American Chemical Society, copyright 2019.

1.4.2. Determination of the Polyene Backbone Configuration and Conformation

The polyene backbone of PPAs, also known as the internal helix, can adopt four different configurations: *cis-cisoidal*, *cis-transoidal*, *trans-cisoidal*, and *trans-transoidal*. However, only the *cis* configurations promote helix formation. The degree of elongation of these helices depends on the dihedral angle ω_1 between conjugated double bonds. Specifically, when ω_1 is smaller than 90º, the polymer adopts a *c-c* scaffold, whereas when ω_1 is larger than 90º, a *c-t* scaffold is favored. These structural differences can be elucidated using different spectroscopic and analytical techniques.

USC UNIVERSIDADE DE SANTIAGO

1.4.2.1. NMR Polyene Backbone Elucidation

Percec and coworkers introduced ^{1}H-NMR spectra to differentiate between *c-c*, *c-t*, *t-c*, and *t-t* polyene backbones by combining experimental and theoretical studies.[20,21,87,88] ^{1}H-NMR allows us to distinguish between *cis* and *trans* scaffolds by analyzing the chemical shift of the vinyl proton. In *trans* polyenes, this proton typically resonates between 6.20 and 7.20 ppm. In contrast, *cis* polyenes exhibit vinyl proton resonance between 5.60 and 5.80 ppm.

Moreover, the conjugated phenyl group directly connected to the polyenic backbone experiences an upfield shift of the aromatic signals in ^{1}H-NMR when polymerized compared to the phenyl group connected to the alkyne in the monomer. Due to the rigidity of the phenyl ring and the polyenic backbone, the ^{1}H-NMR signals exhibit broadening as a result of limited flexibility. Additionally, the internal region may show greater broadening than the protons from the pendant groups or the outer part of the helix, due to its reduced mobility. Based on this information, the percentage of cis double bonds in PPAs can be estimated using the equation (1) (where A_{cis} is the area of the vinyl proton peak (5.60–5.80 ppm), A_{total} is the total area of the observed ^{1}H-NMR spectrum, and H_{total} refers to the number of protons in the pendant groups).

$$percentage_{cis} = \frac{A_{cis}}{A_{total} \cdot H_{total}} \cdot 100 \quad \textbf{(1)}$$

1.4.2.2. DSC Polyene Backbone Elucidation

Differential Scanning Calorimetry (DSC) allows the differentiation between *c-c* and *c-t* scaffolds.[89-91] The thermograms of *c-c* scaffolds typically exhibit a single exothermic peak around 240 ºC, corresponding to the isomerization from *c-c* to *t-t*. In contrast, *c-t* scaffolds display two exothermic peaks: one at approximately 140 ºC (due to the *c-t* to *c-c* conversion) and another at 240 ºC (from *c-c* to *t-t*) (Figure 11). However, DSC results can sometimes be complicated by the presence of additional exothermic peaks that arise from pendant group interactions, making the technique less reliable in certain cases.

USC UNIVERSIDADE DE SANTIAGO DE COMPOSTELA

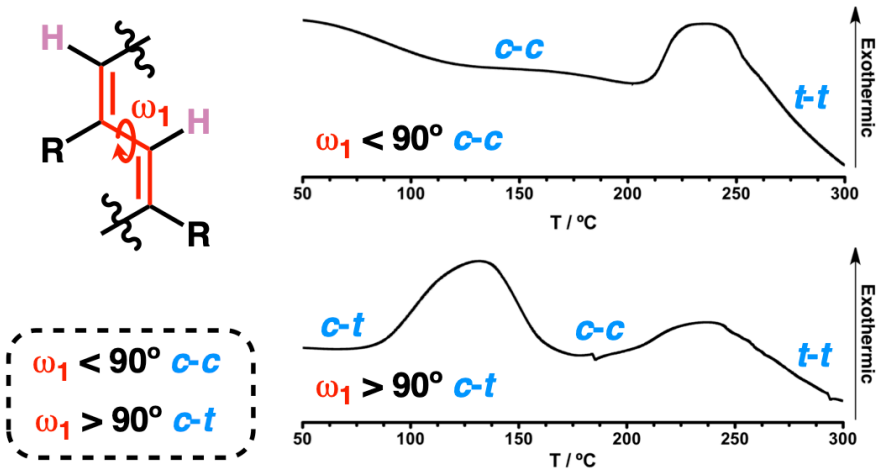


Figure 11. Examples of DSC thermograms of *c-c* and *c-t* scaffolds. Reproduced from ref. 84 with permission from Royal Society of Chemistry (Copyright Clearance Center), copyright 2013.

1.4.2.3. Polyene Backbone Photoelectrocyclazation: Elucidation of the Dihedral Angle ω_1

Recently, an alternative technique using visible-light irradiation has been introduced as a method to determine whether a PPA adopts a *c-c* or *c-t* scaffold. This approach takes advantage of differences in photochemical electrocyclization rates, which vary depending on the structural scaffold of the polyene backbone. By irradiating a solution of anilide or benzamide PPA with visible light ($\lambda > 350$ nm) and monitoring the decay of the CD signal over time, we can obtain the half-life ($t_{1/2}$) of the photochemical electrocyclation (PEC). Importantly, this method not only distinguishes between *c-c* and *c-t* configurations but also provides the dihedral angle ω_1 of the polyenic backbone. The results indicate that PPAs with a more compressed structure (*c-c*, $\omega_1 < 90^o$) undergo faster photochemical electrocyclization as described by Liu.[67,68] While more elongated structures (*c-t*, $\omega_1 > 90^o$) exhibit significantly longer $t_{1/2}$ values (Figure 12). This allows to approximate the degree of helical elongation of a given PPA in solution, and therefore, its overall secondary structure.[92]

USC UNIVERSIDADE DE SANTIAGO DE COMPOSTELA

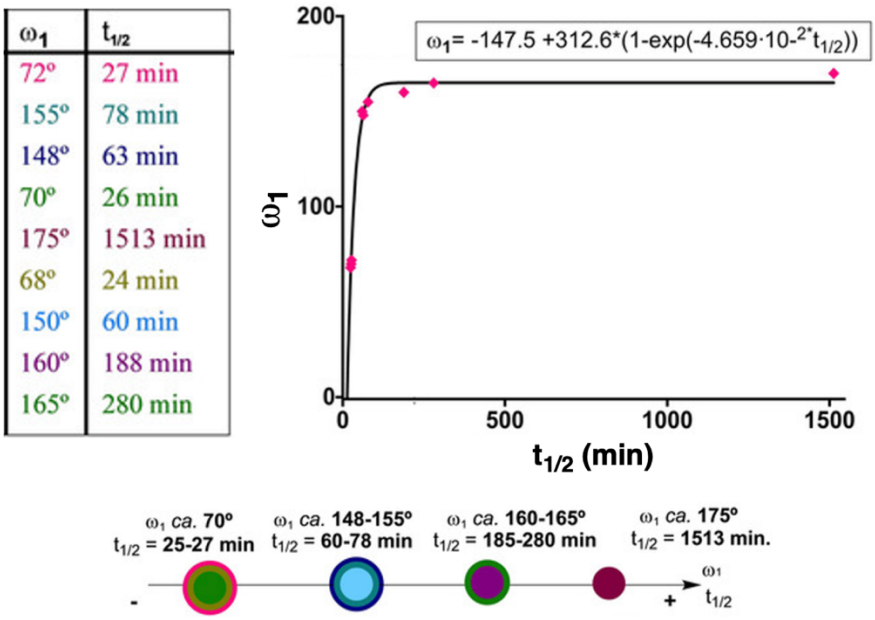


Figure 12. Variation of the PPA ω_1 vs. $t_{1/2}$ of the backbone photochemical electrocyclization process and the corresponding fit to an exponential equation. Reproduced from ref. 92 with permission from John Wiley and Sons, copyright 2021.

1.4.2.4. Polyene Backbone Photoelectrocyclazation: Elucidation of the Screw Sense Excess

Helix reversal is a structural feature observed in helical polymers in their solid state by atomic force microscopy (AFM), but it is difficult to detect in solution. In a study of our group,[70] a collection of well-folded PPAs and various copolymer series composed of enantiomeric comonomers, which exhibit chiral conflict effects, were utilized. The findings reveal that the PEC of a PPA is influenced by the helical structure of the PPA backbone and its folding degree. Therefore, the determination of the screw sense excess (SSE) of the PPAs can be obtained applying an equation. The screw sense excess equation depends on the dihedral angle, so for each monomer, copolymers were made with its enantiomer, and the excess was calculated (Figure 13).

USC UNIVERSIDADE DE SANTIAGO DE COMPOSTELA

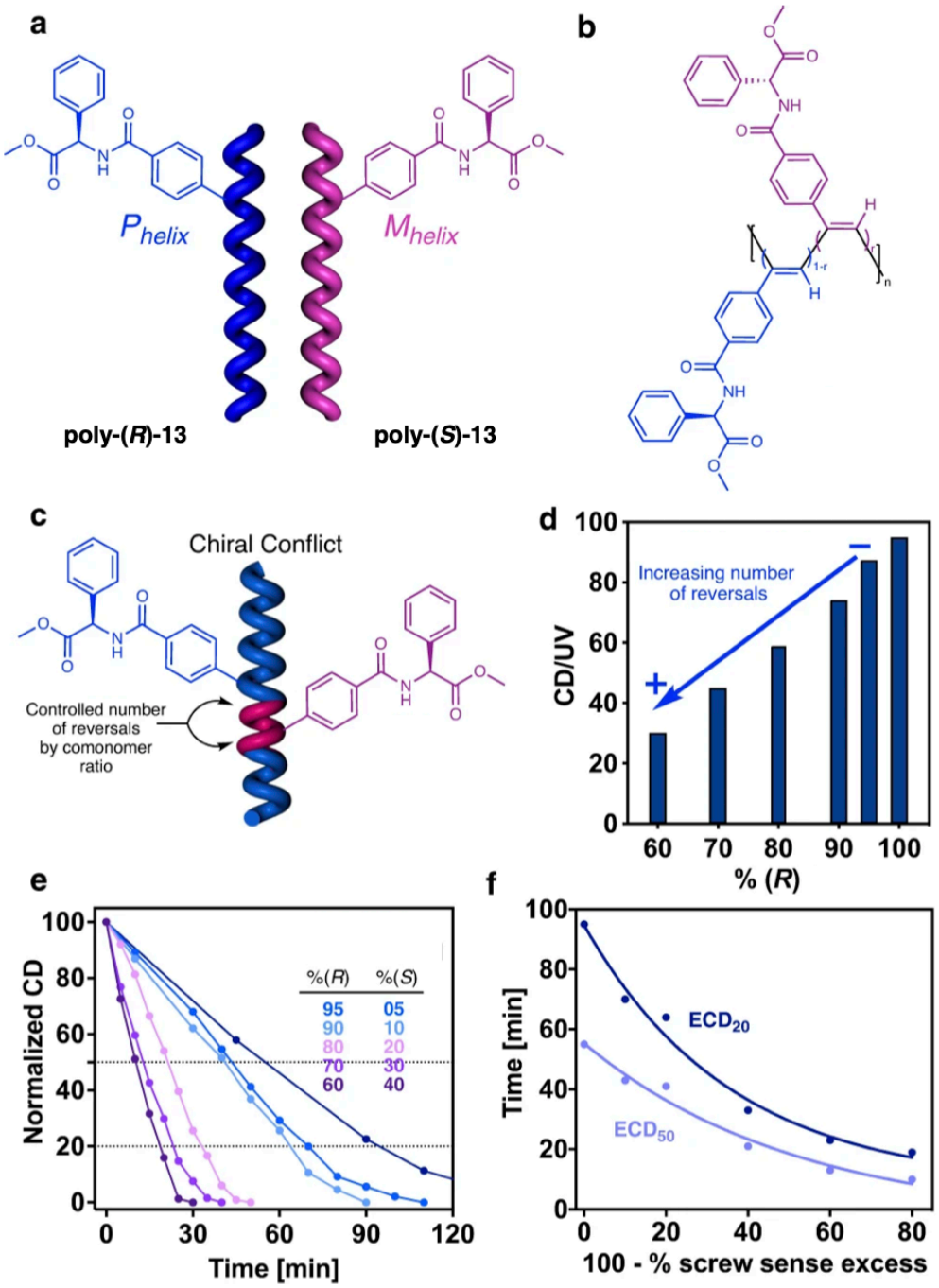


Figure 13. a) Chemical structure and helix sense of the polymer with (*R*) and (*S*) enantiomers of the monomer. b) Chemical structure of the copolymer. c) Illustration of the chiral conflict phenomenon. d) Change in ECD/UV-Vis signal (ECD@368 nm) with varying percentages of the (*R*) enantiomer in the copolymer series. e) Decay of normalized ECD signal (ECD@368 nm) over time for the copolymer series under visible light. f) Time taken to reach 50% and 20% ECD signal during photochemical electrocyclization vs. percentage of reversals in the copolymer series. Reproduced from ref. 70 with permission from Springer Nature, copyright 2023.

USC UNIVERSIDADE DE SANTIAGO DE COMPOSTELA

1.4.2.5. Raman Polyene Backbone Elucidation

To complement these studies, Raman spectroscopy is another powerful method for characterizing the configuration of the polyene backbone. *Cis*-configurations are identified by characteristic vibrational bands at ~1580 cm^{-1} ($C{=}C_{cis}$), ~1335 cm^{-1} ($C{-}C_{cis}$), and ~965 cm^{-1} ($C{-}H_{cis}$), while *trans* configurations exhibit shifts at ~1475 cm^{-1} ($C{=}C_{trans}$) and ~1200 cm^{-1} ($C{-}C_{trans}$).[83,93] Additionally, Fourier Transform Infrared (FT-IR) spectroscopy can help differentiate between ~1015 cm^{-1} ($C{-}H_{trans}$) and ~740 cm^{-1} ($C{-}H_{cis}$) vibrational modes.[94,95]

1.4.2.6. UV-Vis Absorption Polyene Backbone Elucidation

UV-Vis (Ultraviolet-Visible) spectroscopy provides information about the degree of elongation of the polymer. A bathochromic shift (redshift) in the polyene absorption band typically around 400 nm indicates an increase in conjugation and elongation of the polymer, while a hypsochromic shift (blueshift) suggests a decrease in conjugation and a compression of the polymer.[96-100]

In UV-Vis spectroscopy, the HOMO (highest occupied molecular orbital) is bonding, with electron density between atoms, while the LUMO (lowest unoccupied molecular orbital) is antibonding, with a node where electron density cancels out. The energy gap between them determines absorption.

In ethene, the π-HOMO has no nodes, while the π^*-LUMO has one node, creating a large HOMO-LUMO gap and absorption at ~165 nm. In butadiene, the conjugation of π-electrons across four carbon atoms leads to molecular orbital splitting. Instead of just one bonding (HOMO) and one antibonding (LUMO) orbital like in ethene, butadiene forms four π-molecular orbitals: two bonding (π_1, π_2) and two antibonding (π_3^*, π_4^*) (Figure 14a).

The HOMO in butadiene (π_2) results from constructive overlap of p orbitals with one node, while the LUMO (π_3^*) is antibonding and has two nodes, increasing its energy. This splitting reduces the HOMO-LUMO gap compared to ethene, meaning butadiene absorbs light at a longer wavelength (ca. 217 nm) (Figure 14b).[85,101]

USC UNIVERSIDADE

As conjugation extends in PPAs orbital splitting increases, and the energy gap decreases, shifting absorption into the visible region (bathochromic shift). On the

contrary, compression of the polymer backbone decreases conjugation, increasing the HOMO-LUMO gap and causing a hypsochromic shift. The *c-c* structure, as it is more compressed, has less overlap of the orbitals and therefore the conjugation decreases increasing the HOMO-LUMO gap compared to the more conjugated *c-t* conformation (Figure 14b).[102]

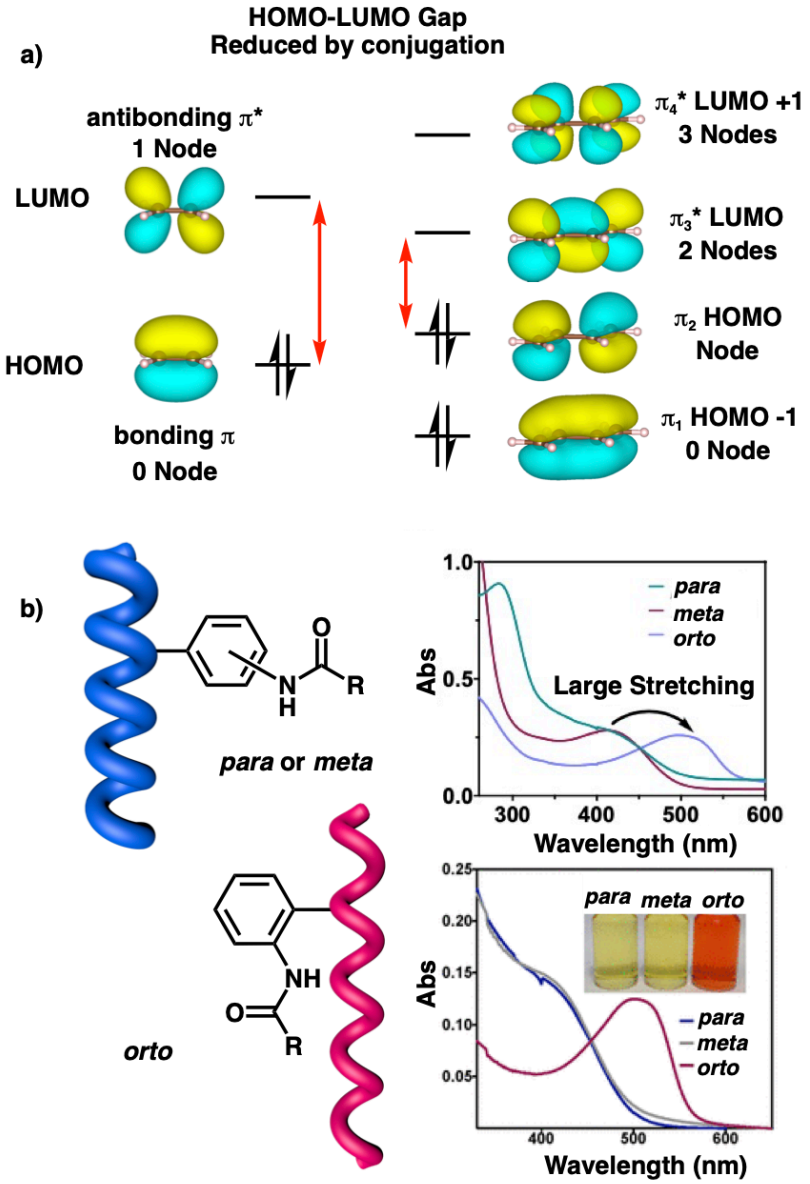


Figure 14. a) MOs calculated in wb97xd with the basis set aug-cc-pvtz. b) Behavior of anilide PPAs with pendant groups in *para*-, *meta*-, and *ortho*-positions. The *ortho*-position stretches the helix due to steric effects, altering the UV-Vis absorption profile compared to the *para*- and *meta*- positions. Reproduced (b) from ref. 102 with permission from American Chemical Society, copyright 2016.

USC
UNIVERSIDADE DE SANTIAGO DE COMPOSTELA

1.4.3. Theory of Spectroscopic Optical and Chiroptical Techniques

Chiroptical spectroscopy, including techniques like Electronic Circular Dichroism (ECD), Vibrational Circular Dichroism (VCD), Raman Optical Activity (ROA), and Optical Rotatory Dispersion (ORD), depend on the principles of linear spectroscopy. Techniques such as UV-Vis and infrared absorption provide fundamental information of the molecular transitions by measuring light absorption or scattering. Chiroptical methods extend these principles by examining how chiral molecules interact differently with polarized light, revealing unique structural and conformational details that are specific to chirality.

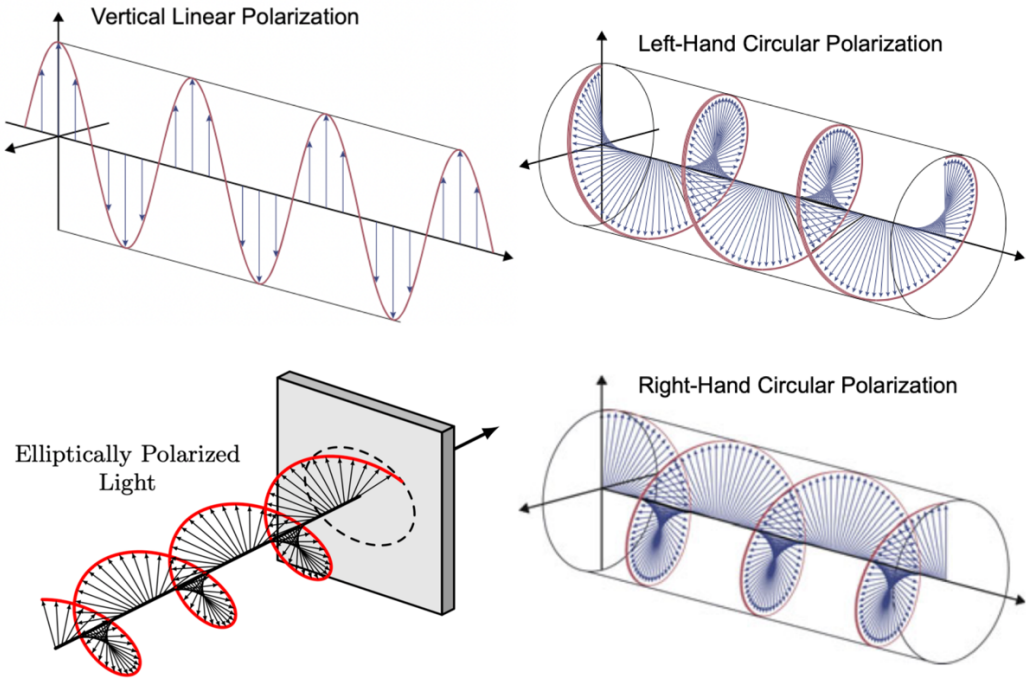


Figure 15. The different main types of polarization of electromagnetic waves. The oscillations of the electric field are used to describe the polarization type. Reproduced from ref. 103 with permission from Springer Nature (Copyright Clearance Center), copyright 2022.

1.4.3.1. Linear Absorption Techniques

Linear absorption techniques, such as UV-Vis and infrared spectroscopy, are fundamental in studying molecular transitions.

UV-Vis Absorption technique involves electronic transitions where chromophores (light-absorbing groups) interact with electromagnetic radiation. The absorption of light in the UV-Vis region corresponds to electronic transitions, where electric transition dipole

USC UNIVERSIDADE DE SANTIAGO

moments (ETDM) arise due to the interaction of chromophores with light. These transitions are governed by the electric dipole selection rules, which dictate the allowed transitions based on symmetry and electronic configuration.

Infrared Absorption technique focuses on vibrational transitions of the molecules. Infrared spectroscopy reveals vibrational modes associated with specific functional groups, providing a molecular fingerprint. The vibrational ETDM is analogous to the electronic ETDM but it is related to changes in molecular vibrations rather than electronic states.

Both achiral and chiral molecules respond to linearly polarized light in a similar manner, with excitations dictated by charge or electric shifts. However, chiral molecules exhibit additional properties when interacting with circularly polarized light, leading to the development of chiroptical techniques (Figure 15).[103]

1.4.3.2. Oscillator Strength

To quantify the absorption and intensity of electronic or vibrational transitions, we use the concept of oscillator strength.[104-106] The oscillator strength, f_{0n}, is a dimensionless quantity that represents the probability of a photon causing a transition in the molecule between two states, ground (0) to excited state (n). The oscillator strength is related to the electric transition dipole moment by the dipole moment operator μ in equation (2). At the same time, the dipole strength D_{0n} is defined as the absolute square value of the electric transition dipole moment vector, μ, where ψ_0 and ψ_n are the wavefunctions of ground and the n excited state, respectively, equation (3). Where m_e is the electron mass, c is the speed of light, $\tilde{\nu}$ is the wavenumber of the transition, h is Planck constant, and e is the elementary or electron charge.

$$f_{0n} = \frac{8\pi^2 \tilde{\nu}_{0n} m_e c}{3he^2} |\langle \psi_0 | \hat{\mu} | \psi_n \rangle|^2 \quad \textbf{(2)}$$

$$D_{0n} = |\langle \psi_0 | \hat{\mu} | \psi_n \rangle|^2 = |\mu_{0n}|^2 \quad \textbf{(3)}$$

USC UNIVERSIDADE DE SANTIAGO DE COMPOSTELA

The oscillator strength is a measure of the probability of an electronic or vibrational transition and is proportional to the square value of the electric transition dipole moment. This relationship allows us to estimate the strength or intensity in spectroscopy of molecular electronic transitions.

For an electric transition dipole moment to exist, there must be an overlap of the molecular orbitals involved in the transition. This overlap is crucial for the interaction between the molecule and the electromagnetic field and determines the value of the ETDM.[105,106]

1.4.3.3. Chiroptical Techniques: ECD and VCD

Chiroptical techniques, such as Electronic Circular Dichroism (ECD) and Vibrational Circular Dichroism (VCD), rely on the interaction of chiral molecules with circularly polarized light. These techniques provide unique insights into molecular structure and environment by measuring the differential absorption of left and right circularly polarized light (Figure 16). A key difference from linear spectroscopic methods is the involvement of the magnetic transition dipole moment (MTDM), which emerges in chiral scenarios due to the chiral arrangement of electric movements within the molecule.

ECD is used in the electronic region of the spectrum. It measures the difference in absorption between left and right circularly polarized light by chiral molecules. The resulting ECD spectrum provides information about electronic transitions and the molecular environment, influenced by both the electronic ETDM and the electronic MTDM.[107]

VCD is used in the infrared region. It measures the difference in absorption of circularly polarized light due to vibrational transitions. VCD spectra offer provides information into the vibrational modes of chiral molecules. The resulting VCD spectrum provides information about vibrational transitions, influenced by both the vibrational ETDM and the vibrational MTDM.[107]

USC UNIVERSIDADE DE SANTIAGO DE COMPOSTELA

1.4.3.4. Theoretical anisotropy factor: Rotatory Strength and Dipole Strength

Rotatory strength, R_{0n} dictates the preferential absorption of circularly polarized light. It is given by the Rosenfeld equation the scalar product of the ETDM and MTDM between the ground state ψ_0 and an excited state ψ_n by equation (4). [108]

$$R_{0n} = Im(|\langle\psi_0|\hat{\mu}|\psi_n\rangle| \cdot |\langle\psi_0|\hat{m}|\psi_n\rangle|) = |\mu_{0n}| \cdot |m_{0n}| \cdot \cos(\theta) \quad \textbf{(4)}$$

Where θ is the angle between the electric transition dipole moment μ_{0n} and the magnetic transition dipole moment m_{0n}. The rotatory strength determines the chiroptical properties of molecules, the intensity of the ECD or VCD signal. The intensity and sign of the chiroptical signal depend on the relative orientation of the ETDM and MTDM. If μ_{0n} and m_{0n}. are orthogonal (θ = 90º), R_{0n} = 0, results in no chiroptical signal. On the other hand, when μ_{0n} and m_{0n} are parallel or antiparallel, the signal is maximized, leading to strong positive or negative Cotton effects in the CD spectrum. The Cotton effect refers to the characteristic shape of CD signals, which can be positive or negative depending on the relative orientation of μ_{0n} and m_{0n}.

As discussed by Schellman another important quantity is the dipole strength, D_{0n}, that provides a measure of the overall strength of the transition, incorporating both electric and magnetic contributions in equation (5).[109]

$$D_{0n} = |\langle\psi_0|\hat{\mu}|\psi_n\rangle|^2 + |\langle\psi_0|\hat{m}|\psi_n\rangle|^2 = |\mu_{0n}|^2 + |m_{0n}|^2 \quad \textbf{(5)}$$

A useful quantity for measuring the strength of circular dichroism transitions is the anisotropy factor, g_{abs}, also known as the Kuhn dissymmetry factor or ratio. It is a dimensionless quantity introduced by Kuhn in 1930 and is defined by equation (6).[110,111]

USC UNIVERSIDADE DE SANTIAGO DE COMPOSTELA

$$g_{abs} = \frac{4R_{0n}}{D_{0n}} \quad \textbf{(6)}$$

This factor quantifies the chiroptical properties of a molecule by relating the rotatory strength R_{0n} to the dipole strength D_{0n}. The anisotropy factor is independent of concentration and path length. It is expressed in terms of the electric transition dipole moment μ_{0n}, the magnetic transition dipole moment m_{0n}, and the angle θ between these two vectors by equation (7).

The sign of g_{abs} depends only on the angle θ between m_{0n} and μ_{0n}. If $\theta > 90^{o}$, g_{abs} is negative, while $\theta < 90^{o}$ results in positive g_{abs}. The anisotropy factor is zero if m_{0n} and μ_{0n} are perpendicular or if the transition has no electric or magnetic transition dipole moment. A maximum anisotropy factor can be observed when m_{0n} and μ_{0n} are parallel or antiparallel with opposite magnitudes and same module.

To simplify g_{abs}, the dipole strength D_{0n} is approximated by $|\mu_{0n}|^2$, leaving out cases of electric dipole forbidden transition with magnetic dipole allowed transitions.[112,113]

$$g_{abs} = \frac{4|\mu_{0n}| \cdot |m_{0n}| \cdot \cos(\theta)}{|\mu_{0n}|^2 + |m_{0n}|^2} \approx \frac{4|m_{0n}| \cdot \cos(\theta)}{|\mu_{0n}|} \quad \textbf{(7)}$$

In emission, the chiral technique is circularly polarized luminescence (CPL). Luminescence dissymmetry factor g_{lum} is equal to g_{abs} with the dipole strength involving the two transition dipole moments (TDM) components. The same physical theory applies but for transitions from the excited (n usually 1) to the ground state (0) by equation (8). In most organic emitters, the magnitude of μ_{n0} is far greater than the magnitude of m_{n0} and g_{lum} can be approximated in equation (8).[114]

$$g_{lum} = \frac{4|\mu_{n0}| \cdot |m_{n0}| \cdot \cos(\theta)}{|\mu_{n0}|^2 + |m_{n0}|^2} \approx \frac{4|m_{n0}| \cdot \cos(\theta)}{|\mu_{n0}|} \quad \textbf{(8)}$$

USC UNIVERSIDADE DE SANTIAGO DE COMPOSTELA

1.4.3.5. Experimental Anisotropy Factor

In circular dichroism, the presence of a chiral molecule causes one circular polarization (left or right) to be absorbed more than the other. This creates an elliptical polarization (Figure 15). The normal vector to this polarization ellipse tilts by an angle θ compared to the original linear polarization direction. This tilt angle θ represents the effect of differential absorption and can be measured (Figure 16).[115-117]

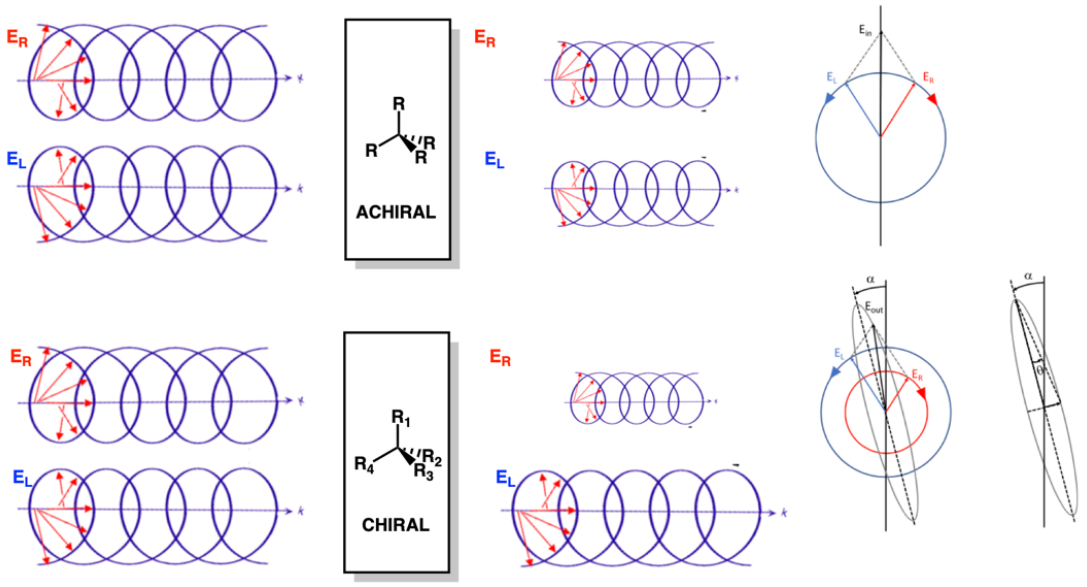


Figure 16. *Above: Equal absorption of right- and left-handed circular polarized light (only electric contribution) by an achiral molecule. Below: Differential absorption by a chiral molecule, leading to ellipticity (Circular Dichroism). The effect is exaggerated; typically, this angle is measured in millidegrees and is much smaller and harder to perceive.*

θ is also known as the ellipticity (in radians), which is the angle resulting from the differential absorption of left- and right-handed circularly polarized light (RCP and LCP). The ellipticity is given by equation (9), where E_R and E_L are the electric field amplitudes of the right- and left-handed circularly polarized light, respectively.

$$\tan\theta = \frac{E_R - E_L}{E_R + E_L} \qquad \textbf{(9)}$$

The poynting vector defines the dependence between electric and magnetic field and it can be derived to obtain the intensity relation with the electric field, equation (10).[118]

USC DE COMPOSTELA

$$I = \frac{1}{2}\, c \cdot \varepsilon \cdot E^2 \tag{10}$$

For small angles, which is typical in chiroptical measurements, θ (rad) ≈ tanθ and substituting the equation (10) on equation (9) we obtain the ellipticity equation (11) in terms of intensity.

$$\theta\ (rad) = \frac{{I_R}^{1/2} - {I_L}^{1/2}}{{I_R}^{1/2} + {I_L}^{1/2}} \tag{11}$$

Using the Lambert-Beer law, which relates absorbance Abs to intensity in equation (12), where I_0 is the initial intensity, and I is the transmitted intensity. This can be rewritten as equation (13).

$$Abs = \log_{10}\left(\frac{I_0}{I}\right) \tag{12}$$

$$I = \mathrm{I}_0 \cdot 10^{-Abs} = \mathrm{I}_0 \cdot e^{-Abs ln10} \tag{13}$$

By substituting equation (13) into the expression for θ of equation (11), and considering that e is raised to a small value, we obtain equation (14).

$$\theta\ (rad) = \frac{e^{-\frac{Abs_R}{2}ln10} - e^{-\frac{Abs_L}{2}ln10}}{e^{-\frac{Abs_R}{2}ln10} + e^{-\frac{Abs_L}{2}ln10}} = \frac{e^{\frac{Abs_R - Abs_L}{2}ln10} - 1}{e^{\frac{Abs_R - Abs_L}{2}ln10} + 1} \tag{14}$$

For small differences in absorbance $\Delta Abs = Abs_R - Abs_L << 1$, we can use a Taylor series expansion to approximate the ellipticity. To convert ellipticity from radians to

USC UNIVERSIDADE DE SANTIAGO DE COMPOSTELA

millidegrees, we use the conversion factor: 1 radian = 180·π·1000 millidegrees (mdeg) in equation (15) or 1 radian = 180·π degrees (deg) in equation (16).

$$\theta\ (mdeg) = \Delta Abs \cdot \frac{Ln10}{4} \cdot \frac{180}{\pi} \cdot 1000 = \Delta Abs \cdot 32982.102\ (mdeg) \quad \textbf{(15)}$$

$$\theta\ (deg) = \Delta Abs \cdot \frac{Ln10}{4} \cdot \frac{180}{\pi} = \Delta Abs \cdot 32.982102\ (deg) \quad \textbf{(16)}$$

The differential absorbance ΔAbs is related to the molar circular dichroism $\Delta\varepsilon$ through the Lambert-Beer law in equation (17), where c is the molar concentration and l is the path length. Therefore, the molar circular dichroism or difference of molar extinction coefficients for LCP and RCP light $\Delta\varepsilon$ in $(M^{-1} \cdot cm^{-1})$ can be expressed as equation (18).

$$\Delta Abs = c \cdot l \cdot \Delta\varepsilon \quad \textbf{(17)}$$

$$\Delta\varepsilon\ (M^{-1} \cdot cm^{-1}) = \frac{\theta\ (mdeg)}{c(M) \cdot l(cm) \cdot 32982.102(mdeg)} \quad \textbf{(18)}$$

To obtain the ellipticity independent of the concentration and path length we can use the molar ellipticity $[\theta]$ in $(deg \cdot cm^2/dmol)$ in equation (19). If we substitute equation (16) in (19) and ΔAbs from equation (17) we obtain equation (18).

$$[\theta](deg \cdot cm^2/dmol) = \frac{100 \cdot \theta\ (deg)}{c\ (M) \cdot l(cm)} \quad \textbf{(19)}$$

USC UNIVERSIDADE DE SANTIAGO DE COMPOSTELA

$$[\theta] = \frac{100 \cdot \Delta Abs \cdot 32.982102(\text{deg})}{c(M) \cdot l(cm)} = \Delta\varepsilon(M^{-1} \cdot cm^{-1}) \cdot 3298.2102(deg) \quad \textbf{(20)}$$

In UV-Vis spectroscopy, the absorbance Abs is related to the molar absorptivity ε through the Lambert-Beer law in equation (21). The Kuhn dissymmetry factor g_{abs} is a chiroptical parameter that provides insights into the chiral properties of molecules. It is defined as the ratio of the differential molar absorptivity in ECD to the molar absorptivity in UV-Vis. The g_{abs} expressed in equation (22) can be substituted with $\Delta\varepsilon$ from equation (18) and ε from equation (21) to obtain the experimental calculation of g_{abs} in equation (22).

$$Abs = c \cdot l \cdot \varepsilon \quad \textbf{(21)}$$

$$g_{abs} = \frac{\Delta\varepsilon}{\varepsilon} = \frac{\theta\ (mdeg)}{Abs \cdot 32982.102} \quad \textbf{(22)}$$

1.4.3.6. Computed Anisotropy Factor and Oscillator Strength by Time-Dependent Density Functional Theory

Technological advances and improvements in theoretical methods have made quantum-chemical calculations the standard to predict and simulate optical and chiroptical spectra. These methods are indispensable for understanding the optical and chiroptical properties of large molecules, where the primary challenge lies in accurately describing excited states. While traditional ab initio methods such as Hartree-Fock and post Hartree-Fock techniques (e.g., MP2, CCSD) provide high accuracy, their computational cost limits their applicability to large systems. Time Dependent Density Functional Theory (TD-DFT) methods are particularly efficient, offering an optimal balance between accuracy and computational cost.[86,119-122]

When simulating an ECD spectrum, several critical factors must be considered. ECD spectroscopy is highly sensitive to molecular geometry, so the first step is to accurately optimize the molecular structure. This ensures that the simulated spectrum reflects the

USC UNIVERSIDADE DE SANTIAGO

true structural characteristics of the molecule. However, for large molecular systems, optimizing geometry using DFT can be computationally demanding. In such cases, alternative methods like semi-empirical calculations, molecular mechanics (MM), or molecular dynamics (MD) simulations are often employed to obtain an optimized geometry. These methods involve some trade-offs in accuracy compared to DFT.

Describing excited states accurately requires considering electron correlation effects, which often involves using large basis sets and advanced computational methods to capture all the interactions between electrons. Dunning basis sets,[123,124] such as aug-cc-pVTZ, are frequently employed for small molecules to ensure high-quality results. These basis sets include diffuse and polarization functions, which are essential for capturing precise electron distributions in excited states. Long range corrected functionals like CAM-B3LYP[125] or wB97XD[126] are commonly used in TD-DFT calculations to correct the deficiencies of traditional exchange correlation functionals, which tend to decay too rapidly at long ranges, making them unsuitable for modeling electron excitations to high orbitals. Including dispersion corrections in DFT calculations is also favorable, especially when optimizing structures with stacked chromophores, as dispersion interactions contribute significantly.

For large systems like oligomers, computational efficiency limits the calculations. Smaller basis sets, such as Pople basis sets with double zeta (e.g., 6-31G or 3-21G),[127,128] are often used, with polarization functions if needed. The CAM-B3LYP functional is known for providing good correlation with experimental data, while wB97XD, although more computationally intensive, offers more accurate by including dispersion corrections.

To simulate ECD and UV-Vis spectra, the computed rotatory strengths are converted from atomic units to 10^{-40} cgs units.[116,129] These rotatory strengths are then broadened using a Lorentzian function to simulate the spectral shape. Calculations of oscillator and rotatory strengths are typically performed using software packages like Gaussian and ORCA. These tools enable the simulation of optical and chiroptical spectra with high accuracy.

USC
UNIVERSIDADE DE SANTIAGO DE COMPOSTELA

1.4.3.7. Exciton Coupling

Exciton coupling is a phenomenon in chiroptical spectroscopy defined by Nina Berova and Lorenzo Di Bari that occurs when two or more chromophores are spatially close but not conjugated.[130] This interaction leads to the splitting of energy levels and the creation of new electronic transitions, observable in techniques like ECD. As chromophores approach each other, their electronic states interact, resulting in the degeneration of individual states and the formation of new transitions. This interaction is particularly significant when the chromophores are identical and spatially close, allowing for simultaneous excitation.

The classical definition of exciton coupling applies to oblique aggregates, where the chromophores are perpendicular, and the axis is not centered. In these cases, the coupling results in a symmetric bisignate signal in the CD spectrum, with both transitions being strongly allowed (Figure 17a).[131,132] This occurs because the total electric transition dipole moments (ETDMs) are the same at different wavelengths (Figure 17b), with one parallel and the other antiparallel to the magnetic transition dipole moment (MTDM). Depending on the sign of the dihedral angle between the chromophores, the bisignate signal will be either positive/negative (+/-) or negative/positive (-/+), and the parallel or antiparallel nature of the TDMs will change accordingly (Figure 17c and Figure 17d). The bisignate signal is characterized by two peaks of opposite signs, reflecting the exciton coupling between the chromophores.[133,134]

USC UNIVERSIDADE DE SANTIAGO DE COMPOSTELA

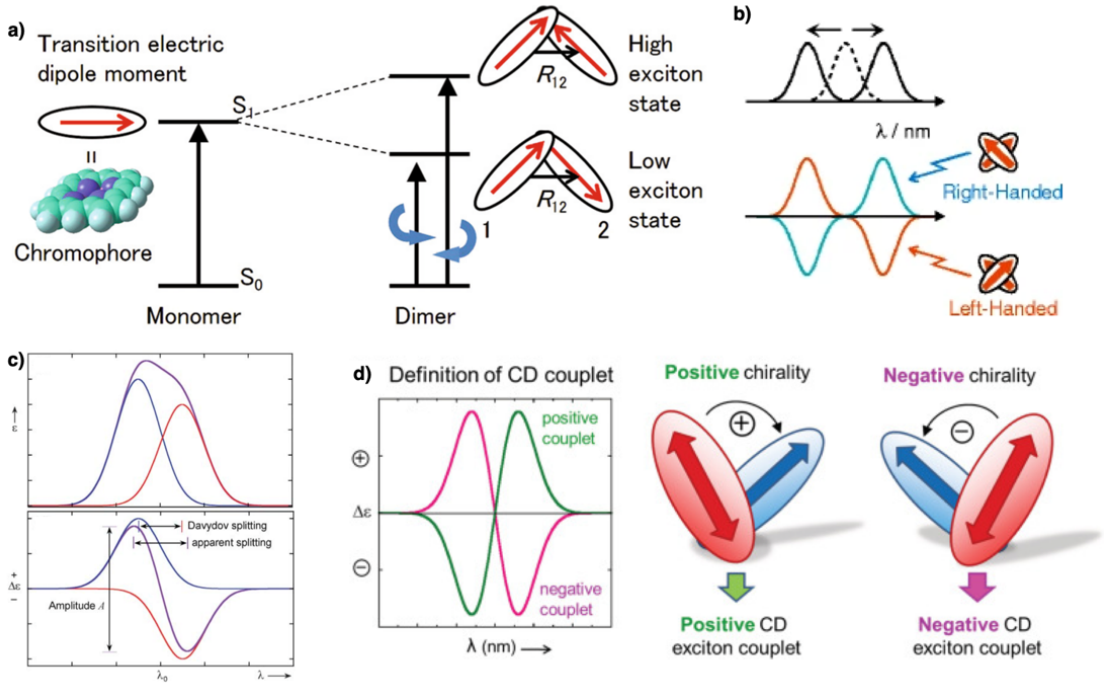


Figure 17. a) Schematic representation of two exciton-coupled chromophores undergoing electric dipole allowed transitions and their electric transition dipole moments (TDMs) together with splitting of the excited states of two degenerate exciton coupled chromophores compared with the monomer. b and c) Expected UV-Vis absorption and ECD spectra. d) Definition of CD exciton couplet, its sign and the corresponding ECD. Reproduced (a) from ref. 134 with permission from Springer Nature (Copyright Clearance Center), copyright 2020. Reproduced (b) from ref. 131 with permission from Springer Nature, copyright 2009. Reproduced (c) from ref. 130 with permission from Royal Society of Chemistry (Copyright Clearance Center), copyright 2007. Reproduced (d) from ref. 132 with permission from John Wiley and Sons (Copyright Clearance Center), copyright 2022.

1.4.3.8. Electronic Circular Dichroism Assignation to the Helical Sense in Poly(phenylacetylene)s

The electronic circular dichroism spectra of poly(phenylacetylene)s (PPAs) are determined using TD-DF calculations, which reveal the influence of main dihedral angles on the Cotton effects observed in the spectra. For *cis-transoidal* PPAs, the first Cotton effect is dominated by excitations involving molecular orbitals (MOs) related to the polyene backbone ω_1, reflecting the helical sense of the polymer's internal helix. Positive ECD signals of the polyenic backbone are assigned to *P*-type helices, while negative ECD signals correspond to *M*-type helices.[119] In *cis-cisoidal* arrangements, contributions from MOs in both the polyene and aryl rings produce the first Cotton effect, leading to distinct ECD signatures with either three or four alternating Cotton effects, depending on the dihedral angles ω_1 and ω_3. The angle ω_1 describes the helical sense of the polyene

USC DE COMPOSTELA

backbone, while ω_3 represents the angle between the polyenic bond and the phenyl ring. These angles determine the helical sense of the polyene and the orientation of the aryl ring relative to the polyene. When ω_1 and ω_3 rotate in opposite directions for *cis-transoidal*, a ECD spectrum with three alternating Cotton effects is observed, correlating with the polyenic helical sense. If they rotate in the same direction in *cis-cisoidal*, four alternating Cotton effects are produced, with the second Cotton effect indicating the helical sense (Figure 18). The *cis-cisoidal* PPAs follow the same rule as *cis-transoidal* PPAs for assigning the helical sense of the inner helix using ECD. Additionally, ω_4 describes the dihedral angle between the phenyl ring and its substituents. The first excitation at approximately 280 nm corresponds to transitions involving ω_4.[86]

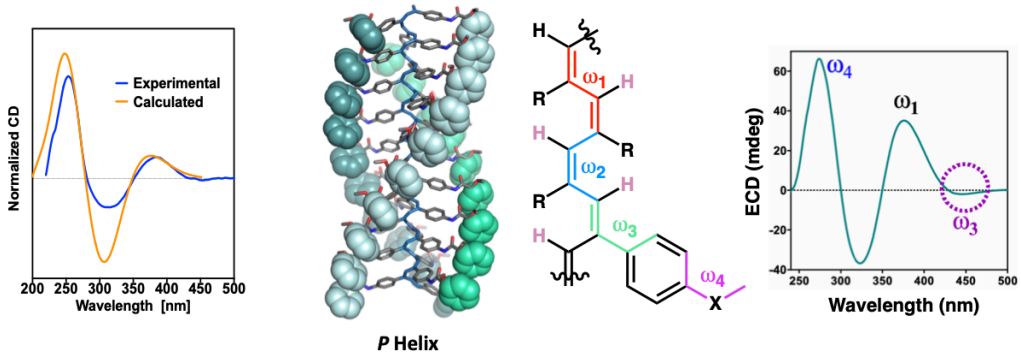


Figure 18. Experimental vs Calculated (TD-DFT) ECD for *P* helix of PPAs. Assignation of the calculated ECD cotton bands to the omega dihedral angles of the PPA. Reproduced from ref. 86 with permission from American Chemical Society, copyright 2019.

1.4.3.9. Vibrational Circular Dichroism in Poly(phenylacetylene)s

In a publication by our group, vibrational circular dichroism (VCD) on poly(phenylacetylene)s (PPAs) revealed opposite signals between enantiomers of the pendants, similar to ECD. VCD is useful to determine conformations of the pendant groups. In this example, it could determine the *syn* or *anti* conformation of pendant groups, which can induce opposite helical senses in the PPA. Additionally, VCD showed that PPAs act as chiral templates, inducing chirality in the surrounding DMSO solvent, affecting its vibrational signals (Figure 19). The study demonstrated by VCD that the DMSO solvent becomes chiral organized using poly-(*S*/*R*)-**13** as a template.[135]

USC UNIVERSIDADE DE SANTIAGO DE COMPOSTELA

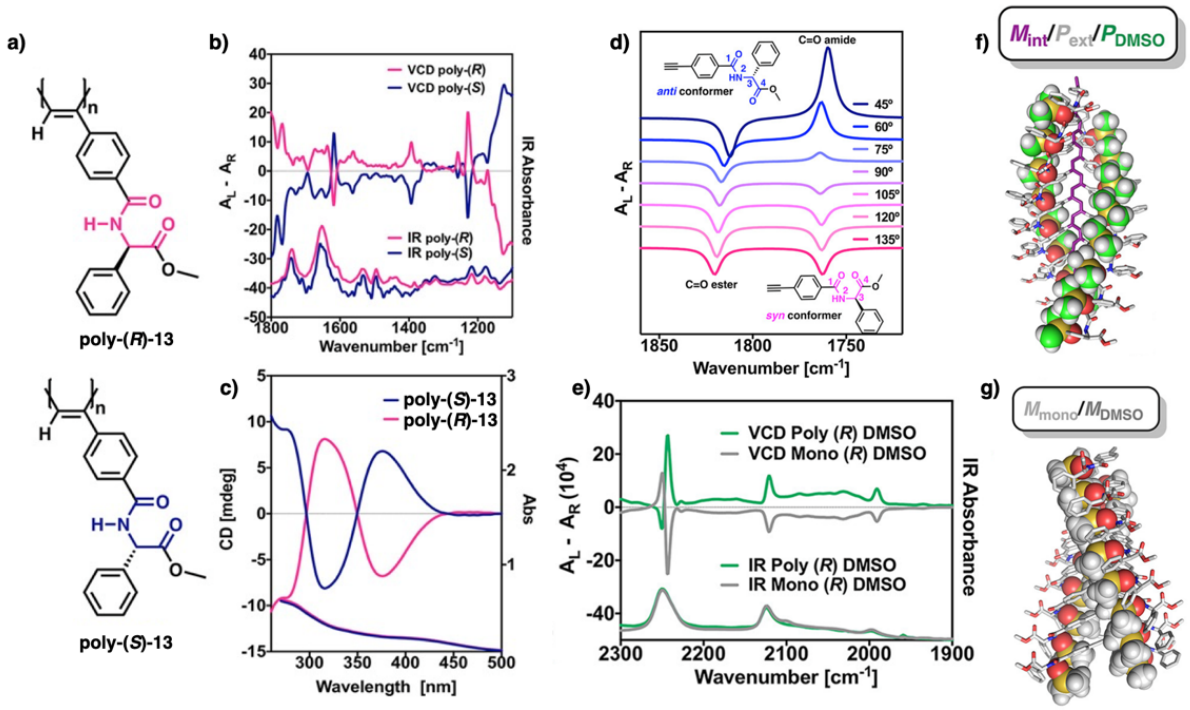


Figure 19. a) *Anti* conformation of poly-(*R*)-**13** and poly-(*S*)-**13**. (b) VCD (top) and infrared (bottom) spectra of poly-(*R*)-**13** (red) and poly-(*S*)-**13** (blue) in DMSO-d6. (c) ECD (top) and electronic absorption (bottom) spectra of poly-(*R*)-**13** (red) and poly-(*S*)-**13** (blue) in 0.1 mg/mL DMSO-d6. (d) Calculated (CAM-b3lyp/cc-pvtz) spectra of the monomer m-(R)-1 at different N–C–C–O dihedral angles. (e) Infrared and VCD spectra of (f) poly-(*R*)-**13** and (g) m-(*R*)-**13** recorded in 100 mg/mL DMSO-d6 solutions. Schematic illustration of the helical arrangement of DMSO molecules around (f) the poly-(*R*)-**13** scaffold and (g) m-(*R*)-**13** (DMSO molecules are highlighted in space filling). Reproduced from ref. 135 with permission from American Chemical Society, copyright 2018.

1.4.3.10. Optical Rotation

Optical rotation (OR) measures the degree to which polarized light is rotated as it passes through a solution of an optically active compound using a polarimeter. This rotation occurs due to the different refractive indices of left and right circularly polarized light in the sample, a phenomenon known as birefringence.

The interaction with light in OR is similar to that in ECD. In ECD, a light source with an equal population of right and left circularly polarized light is used. When this light interacts with a chiral molecule, one type of circularly polarized light is absorbed more than the other, leading to a difference in absorption (Figure 16).

In contrast, OR employs a light source composed of linearly polarized light. This linearly polarized light can be decomposed into left- and right-circularly polarized components of equal amplitude. As this linearly polarized light passes through the

USC DE SANTIAGO DE COMPOSTELA

sample, it experiences rotation due to the different refractive indices of the circularly polarized components (Figure 20). The resulting rotation of the linear polarization plane can be visualized as a combination of the two circularly polarized components, similar to the concept in ECD but without differential absorption. To avoid interference from absorption, since organic molecules tend to absorb between 190 and 400 nm, optical rotation is usually measured using a light source at 589 nm (the sodium D line). This allows detection of the signal arising only from the rotation of light with the chiral structure of the molecules without the chiral absorption.

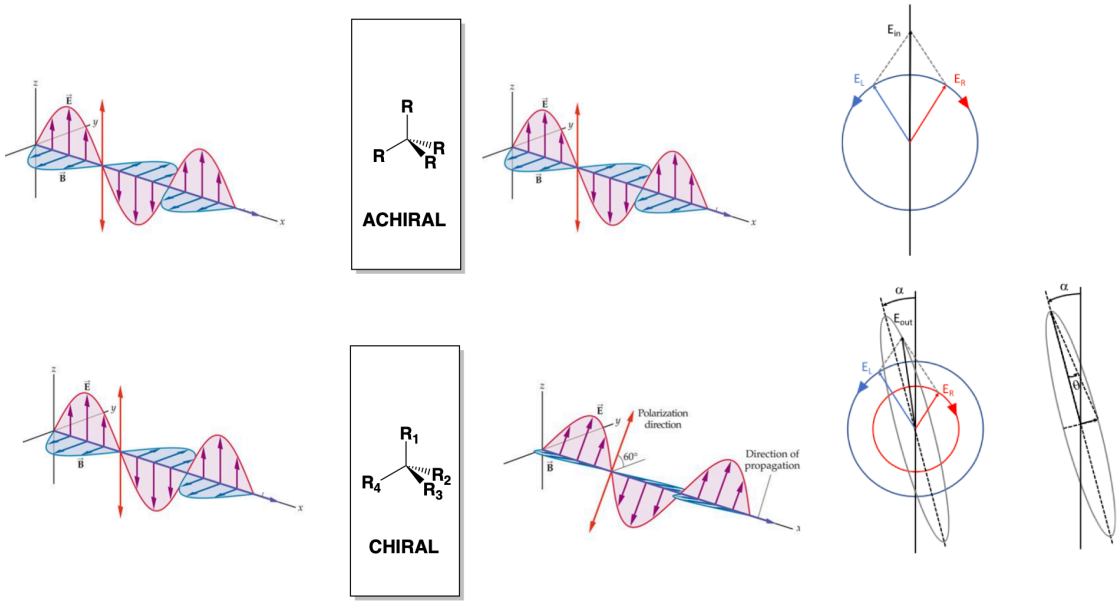


Figure 20. Linearly polarized light can be viewed as a superposition of opposite circularly polarized components of equal amplitude and phase. Above: null rotation of linearly polarized light passing through an achiral molecule. Below: Differential rotation of linearly polarized light passing through a chiral molecule, resulting in a rotation of the polarization plane leading to optical rotation (OR). The effect is exaggerated; typically, this angle is measured in millidegrees and is much smaller and harder to perceive.

The angle of rotation in OR depends on several factors, including the solvent, temperature, concentration of the optically active compound, and the length of the cell through which the light passes. The standardized measurement of this rotation is expressed as specific rotation and takes into account these variables in equation (23).[136] However, this technique has low sensitivity and requires a large sample size. In macromolecules like polymers, the specific rotation is typically an order of magnitude higher than that of their corresponding monomeric units.

USC UNIVERSIDADE DE SANTIAGO DE COMPOSTELA

$$[\alpha]_{\lambda}^{T} = \frac{\alpha_{obs}}{c \cdot l} \quad \textbf{(23)}$$

Optical Rotatory Dispersion (ORD) is the variation of optical rotation with the wavelength. It provides more detailed information about the structure and conformation of chiral molecules by measuring optical rotation at different wavelengths. ORD spectra can reveal the presence of multiple chiral centers or conformational changes.

1.4.3.11. Raman Optical Activity

Raman Optical Activity (ROA) is a spectroscopic technique that measures the difference in Raman scattering intensity between left and right circularly polarized light. It provides information about the chirality and conformation of molecules by analyzing vibrational transitions. For *cis* PPAs, specific Raman bands associated with the C=C, C-Ph, and C-C bonds of the polymer backbone can be observed in ROA spectra. These bands exhibit opposite signs in ROA for opposite helical senses, similar to ECD (Figure 21). However, assigning the helical sense using ROA is more complex than with ECD because the ROA sign is highly dependent on the dihedral angle ω_3. This dependence complicates the direct correlation of ROA signals with the helical sense, as seen in ECD.[137]

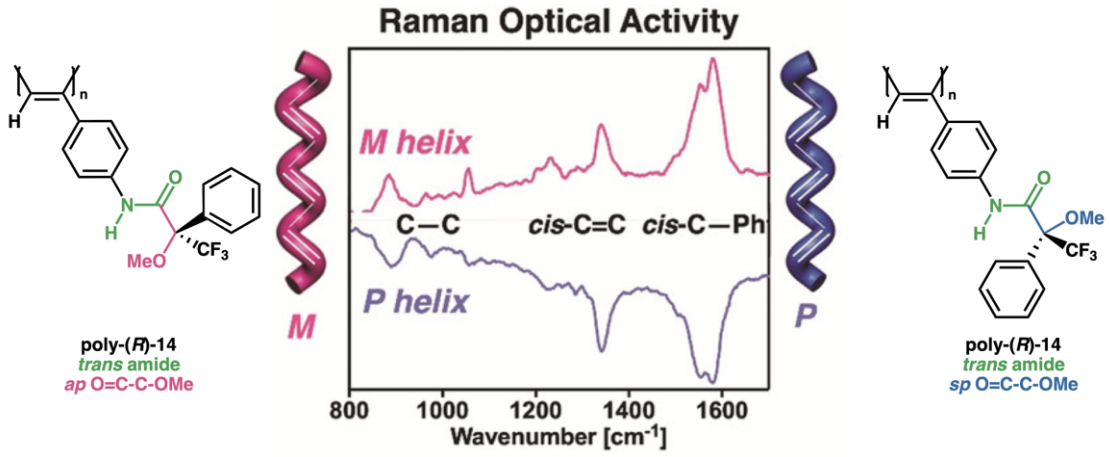


Figure 21. Poly-(*R*)-**14** with the amide in trans: ap conformation in apolar solvent $CHCl_3$ (left) and *sp* conformation in polar solvent $CHCl_3$/DMSO 4:1 v/v (right). VCD spectra in the middle show opposite signals, indicating opposite helices. Reproduced from ref. 137 with permission from John Wiley and Sons (Copyright Clearance Center), copyright 2020.

USC UNIVERSIDADE DE SANTIAGO DE COMPOSTELA

1.4.4. Atomic Force Microscopy

Atomic Force Microscopy (AFM) is a high-resolution technique that generates three-dimensional topographic images of surfaces at the molecular or atomic level. It works by scanning the surface of a sample with a sharp tip attached to a flexible cantilever, measuring the forces between the tip and the surface to create a detailed map of the topography.[138,139] In the study of helical polymers, AFM reveals details such as packing angle, helical pitch, and helical sense of the external helix formed by the pendant groups. However, obtaining high-resolution images requires well-ordered, self-assembled monolayers, which depend on careful sample preparation. Key factors include the solvent, deposition method (e.g., drop casting, spin coating), and substrate, which can influence intramolecular interactions and helical conformation.[140]

Prof. Yashima and coworkers were pioneers in the use of AFM to analyze the helical structure of a PPA copolymer with an achiral bulky C_{60} and an optically active amine. They used drop casting on mica and highly oriented pyrolytic graphite (HOPG) substrates, demonstrating the impact of the substrate on polymer conformation. On mica, the hydrophobic C_{60} groups aggregated due to repulsive interactions with the hydrophilic substrate, while on HOPG, extended and individual copolymer chains were observed (Figure 22a).[141]

Later, Prof. Yashima and coworkers applied spin coating to promote the assembly of polymer chains into well-defined 2D crystals. This method involves deposition, spin-up, spin-off, and evaporation, that allows controlled solvent evaporation and uniform monolayer formation. Using this approach, they successfully prepared monolayers of PPAs with long alkyl chain pendants, which self-assembled through chain interdigitation. AFM images revealed detailed structures, such as a helical pitch of 2.34 nm and a packing angle of 40° in a polymer, indicative of a *c-t* helix. Combining AFM with ECD and other structural techniques, they confirmed the presence of a right-handed internal helix (Figure 22b).[142]

Yashima's protocol has been extensively applied to various polymer systems, including those with different pendant topologies and complex polymer-metal systems. Alternative techniques, such as the Langmuir-Blodgett (LB) method,[143-146] have also been developed for forming monolayers at air/water interfaces. This technique has been demonstrated by Tang and coworkers using poly(phenylacetylene)s (PPAs) with

USC UNIVERSIDADE DE SANTIAGO DE COMPOSTELA

amphiphilic properties. The hydrophilic part of these PPAs attaches to mica, introducing the mica into the water pool (Figure 22c).[146] Another approach, the Langmuir-Schaefer (LS) method, involves a different approximation.[143,144] In this method, the PPAs are also amphiphilic and at the air/water interface, similar to the LB method. However, a hydrophobic surface of HOPG, is brought into contact with the air/water interface through the air phase to exfoliate the PPAs by hydrophobic interactions (Figure 22d).[102,147]

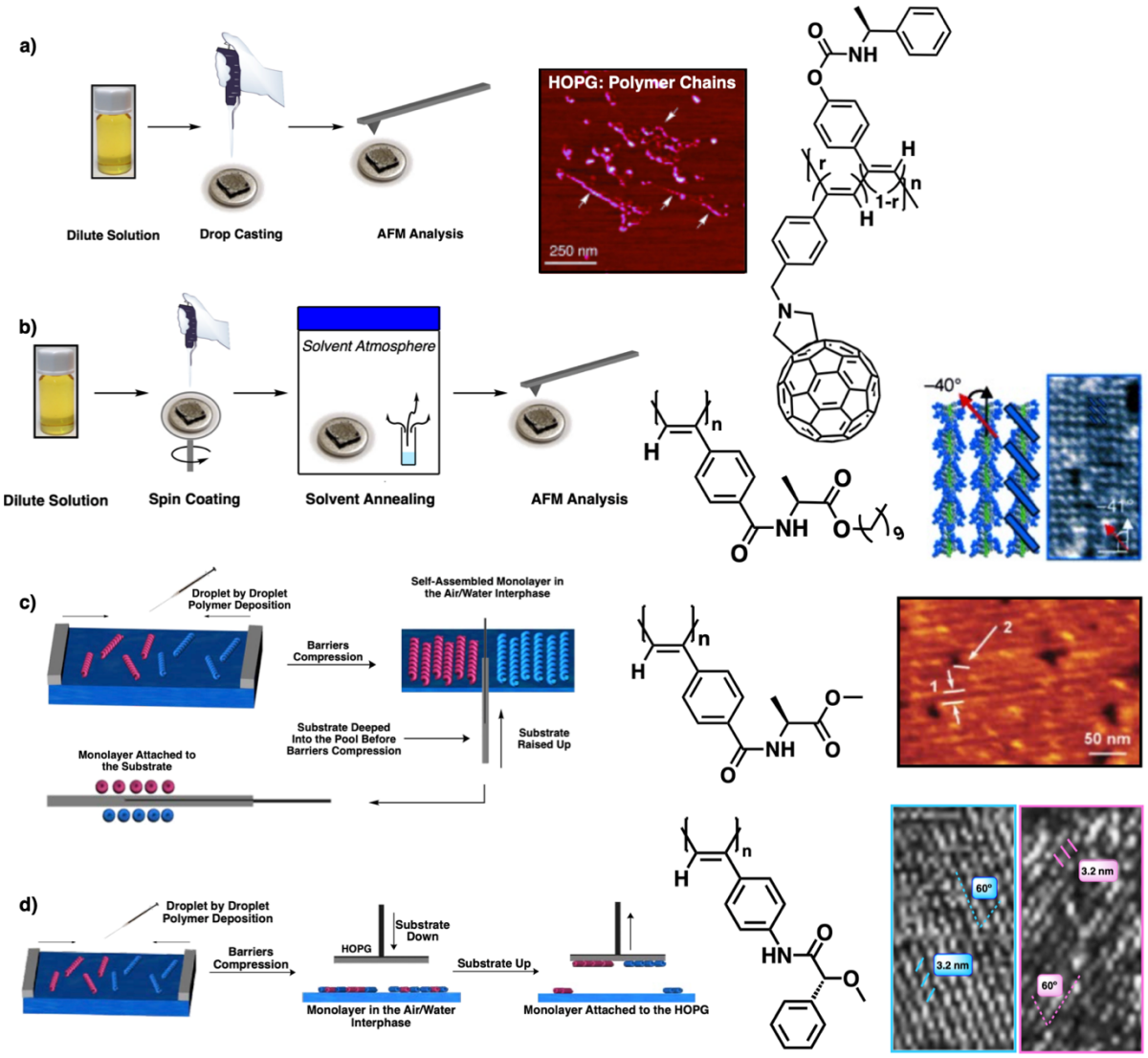


Figure 22. Schematic representation and AFM images of a) drop casting procedure, b) spin coating procedure, c) Langmuir-Blodgett method, d) Langmuir-Schaefer method. Reproduced (a) from ref. 141 with permission from John Wiley and Sons (Copyright Clearance Center), copyright 2002. Reproduced (b) from ref. 142 with permission from John Wiley and Sons (Copyright Clearance Center), copyright 2006. Reproduced (c) from ref. 145 with permission from American Chemical Society, copyright 2012. Reproduced (d) from ref. 147 with permission from Royal Society of Chemistry (Copyright Clearance Center, Inc.), copyright 2016.

USC UNIVERSIDADE DE SANTIAGO DE COMPOSTELA

1.5. Supramolecular Assemblies of Poly(acetylene)s and Poly(phenylacetylene)s

The historical development of supramolecular chemistry has been marked by major scientific milestones. In 1953, Prof. Hermann Staudinger was awarded the Nobel Prize for his pioneering work on macromolecules,[148] laying the foundation for polymer science. Later, in 1987, Profs. Donald J. Cram, Jean-Marie Lehn, and Charles J. Pedersen received the Nobel Prize for their contributions to molecular recognition and supramolecular chemistry, emphasizing the critical role of non-covalent interactions in the formation of complex molecular architectures.[149,150]

Supramolecular assembly refers to the organization of multiple molecules through non-covalent interactions. This process occurs when a significant number of molecules come together via self-assembly, often leading to self-organization into more complex structures. These assemblies can vary in size from nanometers to micrometers and form films, membranes, layers, spheres, and other formations. The nature and spatial arrangement of the interactions involved —such as hydrogen bonding, π-π stacking, ionic forces, and electrostatic attractions— determine the final structure. Additionally, supramolecular chirality arises when molecular spatial arrangements reflect the inherent chirality of their components.[8,151-153]

1.5.1. Fibers and Superhelical Assemblies

Helical polymers can self-organize into supramolecular architectures through interactions between their pendant functional groups. Therefore, pendant groups must be appropriately approximated to facilitate intermolecular bonding. One case reported by our group involves the first example of a reversible stereocomplex based on PPAs. When a polymer containing the α-methoxy-α-trifluoromethyl-α-phenylacetamide (MTPA) pendant group is dissolved in THF, the pendant groups predominantly adopt a *cis* amide conformation.[84] When enantiomeric versions of this polymer are mixed, supramolecular interactions between their pendant groups lead to the formation of fibers. At high concentrations, these aggregates form gel-like materials, with reversibility influenced by external factors such as temperature and solvent polarity. For instance, highly polar solvents that induce *trans* conformation on the amide (e.g., methanol) can disrupt the

USC UNIVERSIDADE DE SANTIAGO DE COMPOSTELA

hydrogen-bond between polymeric chains and disassembly the stereocomplex (Figure 23).[154]

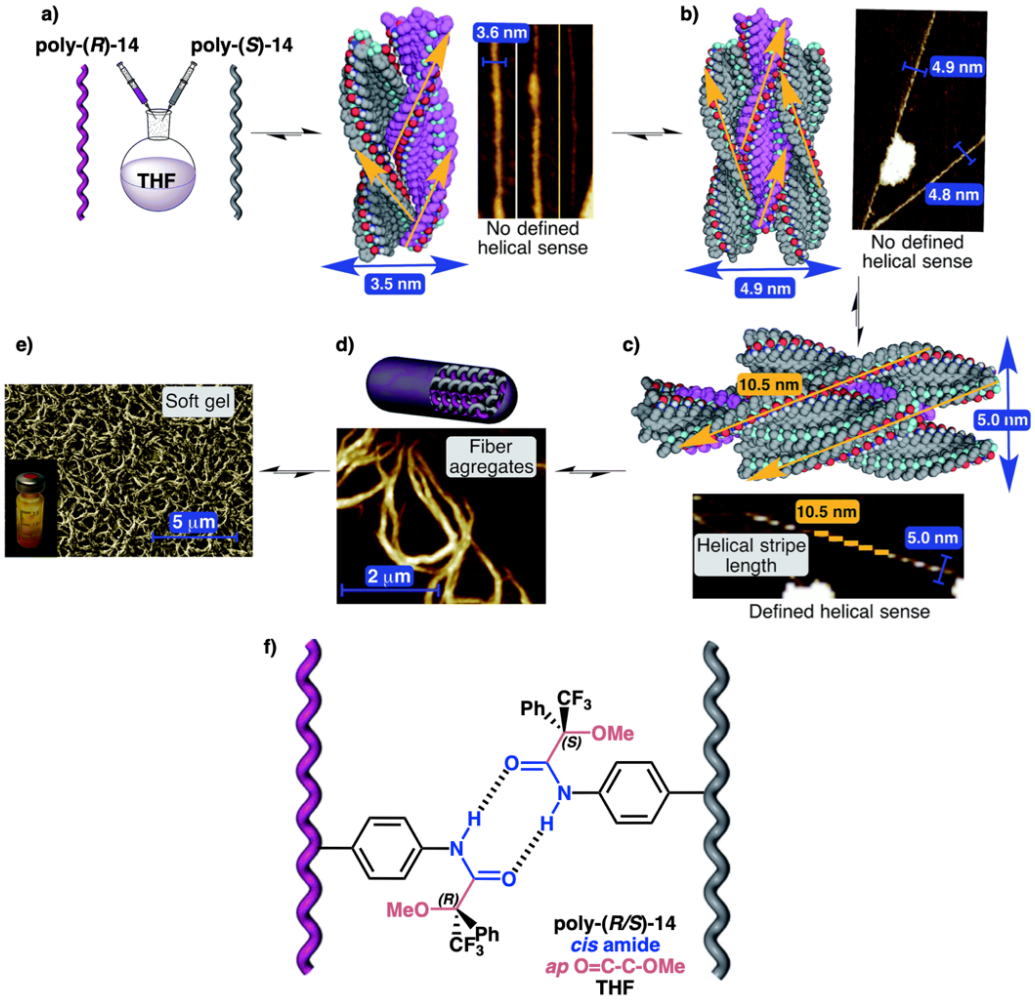


Figure 23. Structure of the stereocomplex. (a-c) Side views of dimer, trimer, and pentamer models of PPAs with the corresponding AFM images showing fiber widths. (d) Conceptual representation of stereocomplex fiber formation between complementary helices. (e) Microscopic (SEM) and macroscopic images of the soft gel structure in THF. (f) Two polymers, (*R*) and (*S*), with hydrogen bonds between them, amide in *cis*, and *ap* conformation in THF. Reproduced from ref. 154 with permission from Royal Society of Chemistry, copyright 2015.

Another example was reported by Shinohara, Shigekawa, and coworkers, who utilized Scanning Tunneling Microscopy (STM) to observe the presence of double helices based on PPAs. When an optically active PPA with menthocarbonylamino groups (poly-**21**) was deposited on HOPG, double-helical structures were observed. Interestingly, the polymer molecules on HOPG exhibited mobility under the STM, demonstrating the dynamic nature of these supramolecular interactions (Figure 24).[155]

USC UNIVERSIDADE DE SANTIAGO DE COMPOSTELA

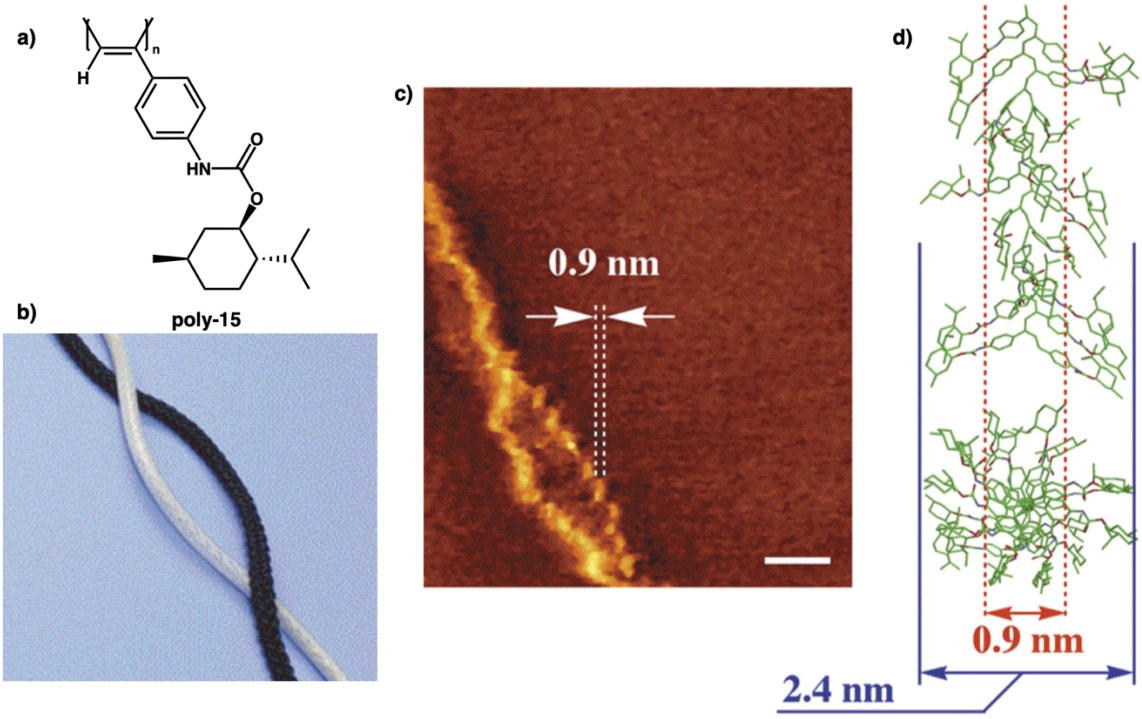


Figure 24. a) Chemical structure of poly-**15**. b) String model of the intertwining polymer chains. c) STM height image of poly-**15**. d) Optimized structure of 20-mer poly-**15** in *c-t* by molecular mechanics. Reproduced from ref. 155 with permission from American Chemical Society, copyright 2001.

Another remarkable example comes from Yashima and coworkers, who studied PPAs bearing β-cyclodextrin (β-CyD) pendants. These macromolecules self-organized into higher-order helical structures on a micrometer scale. Remarkably, the presence of chiral amines influenced the handedness of the resulting superstructure (Figure 25).[156]

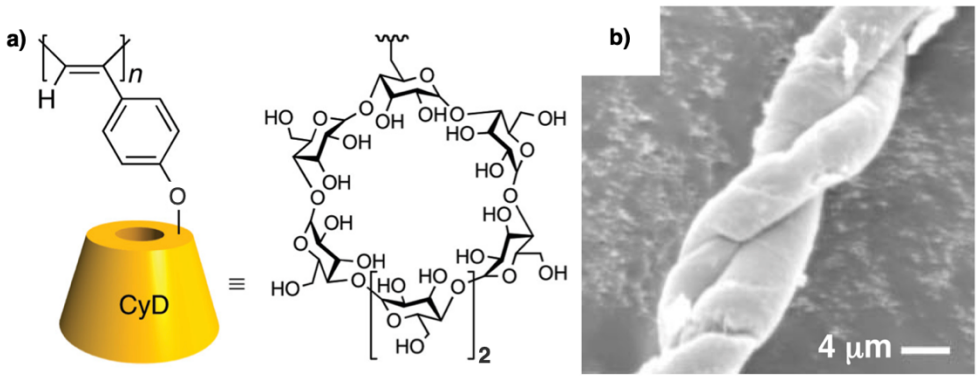


Figure 25. a) Structure of a CyD-Bound Poly(phenylacetylene). b) SEM image of the self-assembled helical aggregate. Reproduced from ref. 156 with permission from American Chemical Society, copyright 2011.

USC UNIVERSIDADE DE SANTIAGO DE COMPOSTELA

Similarly, Tang and coworkers explored the supramolecular interactions in PPAs containing different amino acid methyl esters, such as alanine, leucine, valine, and phenylglycine, as pendant groups. Their nuclear magnetic resonance (NMR) analysis indicated that at high concentrations in low-polarity solvents, pendant groups exhibited intermolecular hydrogen bonding. AFM imaging further demonstrated that when these polymers were dissolved in a low-polarity solvent like THF and slowly evaporated on a mica surface, fiber-like aggregates were formed. These findings suggest that supramolecular interactions arise from hydrogen bonding between amide groups of different chains (C=O---H-N). Moreover, in PPAs with free carbonyl groups at the pendant, aggregation appears to result from associations between the amide and carbonyl groups of separate helical chains.[157]

Interestingly, another example by Tang and coworkers of PPAs incorporating amino acid derivatives behaved differently in polar solvents such as methanol. In these environments, the polymers tend to form micelle-like aggregates, with the polymer backbone residing in the core and the amino acid pendants arranged in the outer shell. These amphiphilic PPAs exhibit amphiphilicity due to their hydrophobic backbone and hydrophilic pendant groups. The abundance of amino acid residues on the micelle surface promotes additional hydrogen bonding, leading to the formation of larger micellar aggregates or extended fiber-like supramolecular structures.[158]

1.5.2. Layer-by-Layer Supramolecular Assembly

Yashima and coworkers demonstrated the ability to construct optically active multilayers via macromolecular helicity memory. They designed polyelectrolytes bearing phosphonate or ammonium groups, which were initially complexed with chiral amines or carboxilyc acids to induce a preferred helical sense. By alternately depositing these helical polyelectrolytes with oppositely charged polyelectrolytes —such as poly(allylamine) hydrochloride (PAH) or poly(acrylic acid) (PAA)— they successfully structured multilayers while transmitting the initial chirality (Figure 26).[159]

USC UNIVERSIDADE DE SANTIAGO DE COMPOSTELA

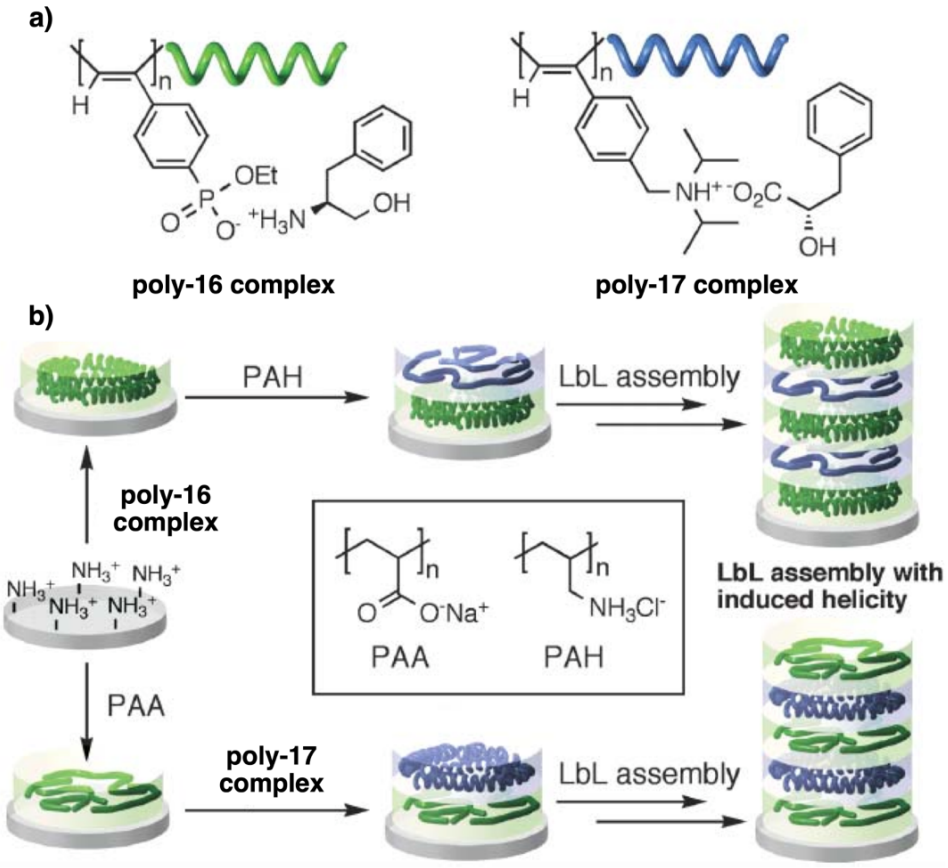


Figure 26. Layer-by-layer (LbL) self-assembly of charged poly(phenylacetylene)s with induced helicity. (a) Helical sense induced in poly-**16** and poly-**17**-HCl upon complexation with chiral molecules. (b) LbL assembly with achiral polyelectrolytes (PAA or PAH) forms multilayer films with induced helicity. Reproduced from ref. 159 with permission from Royal Society of Chemistry (Copyright Clearance Center), copyright 2005

1.6. Nanoparticles based on Poly(acetylene)s Poly(phenylacetylene)s

Polymer nanoparticles are able to form nanospheres and nanocapsules composed of various polymers, ranging in size from 10 nm to 1000 nm. Nanospheres are solid, spherical structures often utilized for surface adsorption of molecules, while nanocapsules are colloidal particles with a hollow core enclosed by a polymeric shell, making them ideal for encapsulation with the ability to control the size, shape, and chirality.[160]

USC UNIVERSIDADE DE SANTIAGO DE COMPOSTELA

1.6.1. Surfactant: Polymer Emulsification and Monomer Emulsion Polymerization

Deng and coworkers exemplified the synthesis of core polymer and shell surfactant micelle (emulsifier) by two different approximations to obtain the polymer particles as an emulsion.

The first approximation resides on mixing PAs in the presence of surfactants where smaller nanoparticles were obtained at higher concentrations of the surfactant (Figure 27).[160-163]

The other approach was followed by the polymerization of emulsions of the monomers. For this, the polymerization takes place in situ, in a heterogenous system formed by a mixture of aqueous phase and organic phase. The surfactant and the initiator had to be soluble in water while the monomer solubilized in the organic phase in order to transfer in a controlled manner the monomers to the growing polymeric chain inside the micelle (Figure 27).[160,162-164]

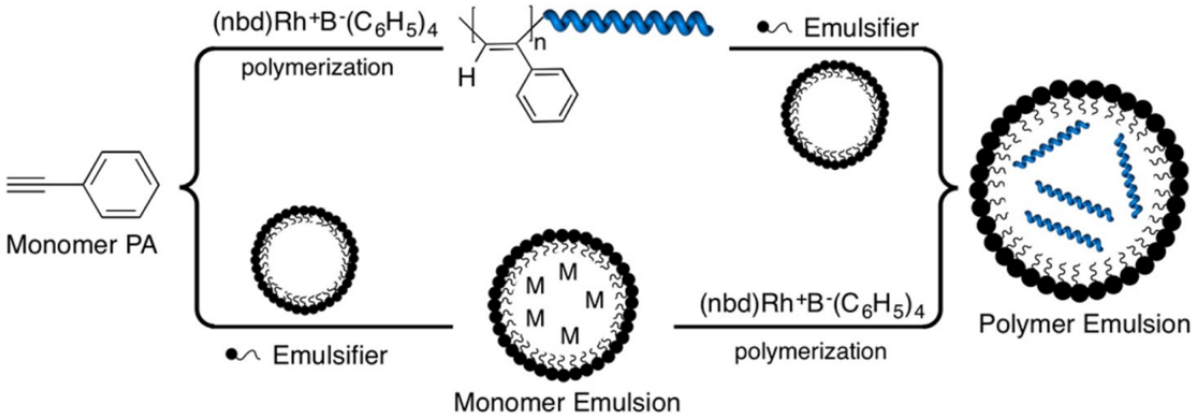


Figure 27. Schematic representation of polymer nanoparticle formation via emulsion of preformed polymers or emulsion polymerization. Reproduced from ref. 160 with permission from American Chemical Society, copyright 2016.

1.6.2. Polymer Spheres: Micelle

Deng and coworkers studied helix-sense-selective polymerizations (HSSPs) of achiral acetylene monomers in chiral micelles for the direct formation of optically active helical polymer emulsions. Through an emulsion-based approach, chiral micelles were formed with the Rh catalyst embedded in the system. After that, achiral acetylenes were introduced, undergoing HSSPs to form polyacetylene (PA) in the presence of

$[(nbd)RhCl]_2$. The hydrophobic PA chains remained attached to the Rh catalyst, which was anchored to the chiral polar surfactant, ensuring the transfer of chirality to the growing polymer (Figure 28).[165,166]

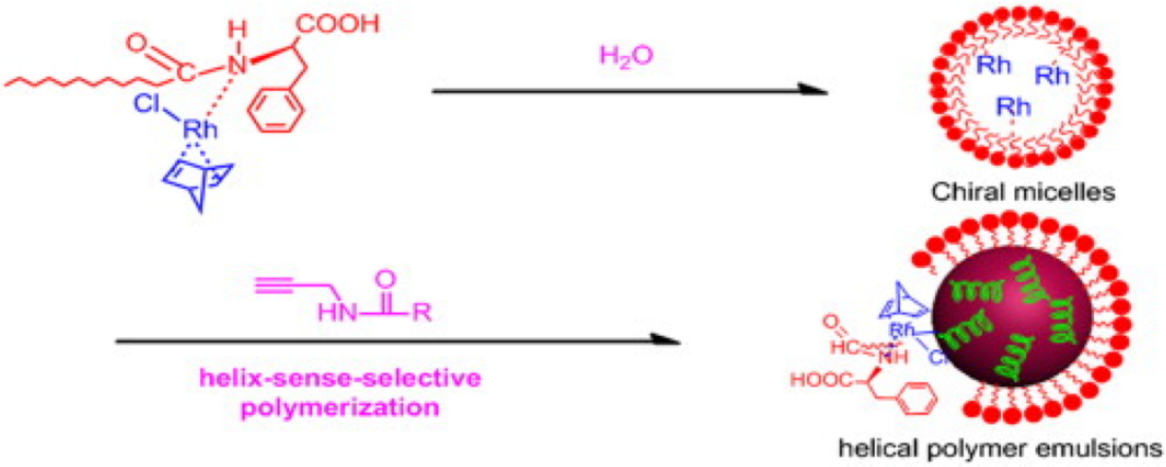


Figure 28. Schematic representation of HSSP of achiral acetylene in chiral micelles. Reproduced from ref. 166 with permission from Elsevier (Copyright Clearance Center), copyright 2014

1.6.3. Polymer Sphere: Nanoprecipitation

Nanoprecipitation is a widely used technique for drug encapsulation, overcoming limitations of conventional dosage forms. It involves polymer precipitation in solution upon adding a poor solvent, following four steps: supersaturation, nucleation, growth by condensation, and coagulation. This method is reproducible and scalable, suitable for both hydrophobic and hydrophilic compounds.[167]

Deng and coworkers developed a novel strategy using a chiral solvent (α-pinene) to induce helical polyacetylene formation from achiral monomers. Adjusting solvent composition enabled control over polymer morphology from fibers to spheres. α-pinene acts both as a chiral source and a poor solvent for precipitation polymerizations. Essentially, α-pinene induces polymer chains to precipitate from the solvent, preventing the formation of regular gels.[168]

Our research group has reported an example of PPAs that form nanoparticles in THF/water or acetone/water with controlled size depending on their secondary structure. Flexible PPAs (*para*- and *meta*-substituted $\omega_1 < 165^o$) produce stable (time and temperature), low-polydisperse nanospheres, while rigid ones (*ortho*-substituted $\omega_1 > 165^o$) aggregate uncontrollably. Moreover, these nanoparticles can encapsulate different

molecules or particles such as fluorescent dyes or quantum dots. Also, the release of cargo can be activated by light to release the dyes by photochemical electrocyclization of the polyene backbone (Figure 29).[169]

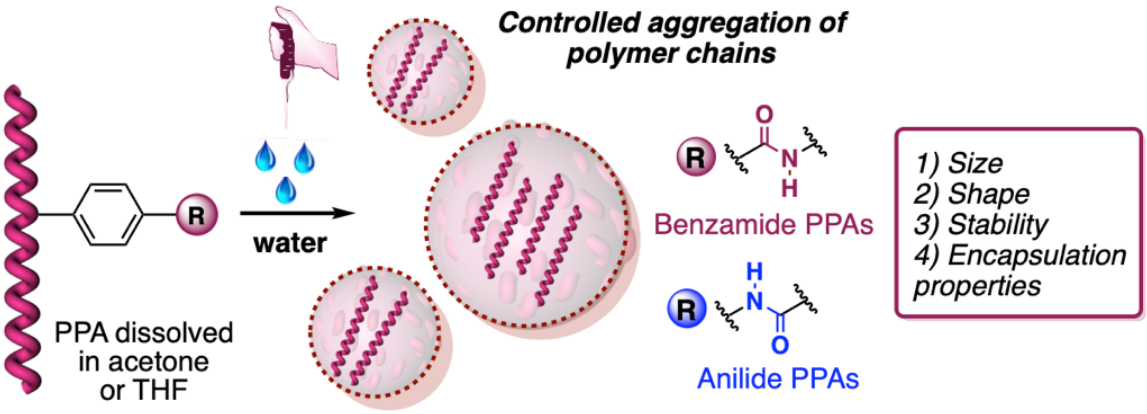


Figure 29. Illustration of the nanoprecipitation protocol to prepare chiral nanospheres. Reproduced from ref. 169 with permission from John Wiley and Sons, copyright 2024.

1.6.4. Metal Crosslinking Nanostructuration: Helical Polymer-Metal Complexes

PPAs can form nanoparticles through non-covalent interactions with metal cations acting as supramolecular cross-linking agents. Our research group reported the formation of PPA polymeric nanospheres using this approach. The introduction of metal ions not only induced chiral amplification but also facilitated the self-assembly of the polymer into nanospheres forming Helical Polymer-Metal Complexes (HPMC). The size and chiral properties of these nanostructures can be tuned by modification of the polymer/metal ratio, the solvent, and the valence of the metal ion.

PPAs can form alternative nanostructures such as nanotubes or toroidal structures depending on the solvent. When a high boiling point cosolvent is introduced, nanotubes emerge, whereas toroidal structures are favored when the solubility of the PPA is reduced by the cosolvent. Additionally, modifying the valence of the metal ion alters the chiral characteristics of the surface in the nanostructure (Figure 30). These versatile assemblies have demonstrated remarkable encapsulation capabilities, allowing the incorporation of iron oxide magnetic nanoparticles, quantum dots, and organic fluorescent dyes.[42,43,170,171]

USC UNIVERSIDADE DE SANTIAGO DE COMPOSTELA

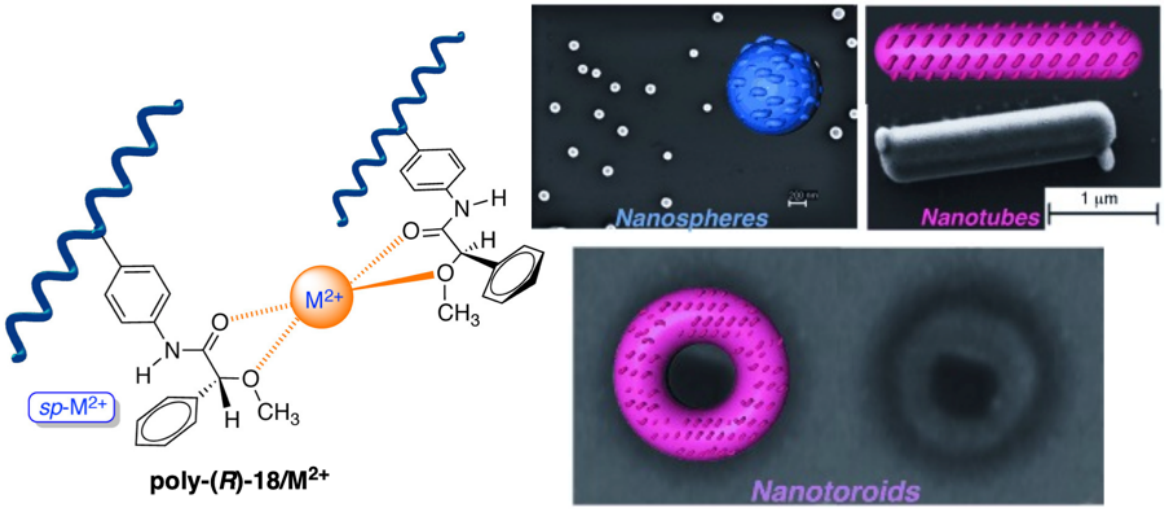


Figure 30. Schematic illustration of the crosslinking behavior of metal ions between PPAs and the chiral nanostructures that can be formed: nanospheres, nanotubes and toroids. Reproduced (left) from ref. 42 with permission from American Chemical Society, copyright 2012. Reproduced (right) from ref. 170 with permission from John Wiley and Sons (Copyright Clearance Center), copyright 2014

1.7. Hybrid Materials Based on PPAs and Metal Nanoparticles

Hybrid materials are formed by the combination of two different components, resulting in systems with unique properties derived from both materials. These hybrids have attracted significant attention due to their potential applications in various fields such as energy storage,[172] asymmetric catalysis,[173] sensing,[174] and medicine.[175] The properties or enhanced functionalities of hybrid materials arise from the synergy between their components.

Among hybrid systems, metal nanoparticles (MNPs) are widely studied for their tunable optical, electronic, and catalytic properties, such as gold nanoparticles (AuNPs),[176] silver nanoparticles (AgNPs),[177] and other metal nanoparticles such as platinum (PtNPs),[178] palladium (PdNPs),[179] and copper (CuNPs)[180] have been widely studied. Their size, shape, and surface chemistry can be easily controlled through different synthetic methodologies, and their functionalization with organic molecules or polymers to form hybrid materials.

USC UNIVERSIDADE DE SANTIAGO DE COMPOSTELA

1.7.1. Silver Nanoparticles and their Hybrids

Silver nanoparticles are of particular interest due to their antimicrobial activity against bacteria,[181] fungi,[182,183] and viruses.[184,185] This effectiveness comes from several mechanisms, such as disrupting cell membranes,[186] generating reactive oxygen species (ROS) that damage cellular components like DNA, proteins, and lipids,[187-189] interacting with intracellular elements by releasing silver ions (Ag^+) that bind to thiol groups in proteins, and inhibiting biofilm formation to reduce antibiotic resistance.[190-191] These properties make AgNPs widely applicable in medical coatings,[192] wound dressings,[193] antibacterial textiles,[194] and pharmaceuticals.[195-197]

The synthesis of silver nanoparticle-based hybrid materials helps to improve their stability, functionality, and applicability across various fields, including sensing, catalysis, and biomedicine. The formation of these hybrids typically follows two approaches: in-situ reduction and the incorporation of previously synthesized AgNPs.

1.7.1.1. In-Situ Reduction Method

This method involves directly forming AgNPs within a hybrid matrix by reducing silver precursors in the presence of stabilizing agents. Commonly used silver salts, such as silver nitrate ($AgNO_3$) and silver perchlorate ($AgClO_4$), serve as the source of Ag^+ ions. Afterwards, various reducing agents facilitate the conversion of Ag^+ to metallic silver (Ag^0).

Chemical Reduction: sodium borohydride ($NaBH_4$) is widely used due to its strong reducing power, enabling the rapid formation of small, uniform AgNPs, [reactions (24) and (25)].[198,199] The surfactants can also cause the reduction of Ag^+ or to grow already formed seeds, they are mild reductors in presence of heat or light and stabilizing agents like trisodium citrate and ascorbic acid.[200]

Photochemical Reduction: ultraviolet light, in combination with photosensitizers, can reduce silver ions without the need for additional chemical reducing agents.[201,202]

Biological Reduction: biomolecules from plant extracts or microorganisms can act as both reducing and stabilizing agents, offering an green synthetic alternative.[203]

USC UNIVERSIDADE DE SANTIAGO DE COMPOSTELA

$$n \cdot Ag^{+} + n \cdot e^{-} \rightarrow Ag_n \quad \textbf{(24)}$$

$$n \cdot BH_4^{-}(aq) + 3n \cdot H_2O \rightarrow n \cdot B(OH)_3(aq) + 3n \cdot H_2 + n \cdot H^{+} + n \cdot e^{-} \quad \textbf{(25)}$$

The choice of matrix material significantly influences the properties of the final hybrid. Careful control of the reduction process ensures the uniform dispersion of AgNPs within the matrix while preventing aggregation.

Polymers: polyvinylpyrrolidone (PVP)[204] and polyethylene glycol (PEG)[205] are often used to stabilize nanoparticles and prevent aggregation.

Carbon-Based Materials: graphene[206] and carbon nanotubes[207] provide conductive platforms, enhancing the electrical properties of the hybrid.

Silica: silica matrices[208] offer thermal stability and biocompatibility, making them suitable for biomedical applications.

Metal-Organic Frameworks (MOFs): these porous structures can encapsulate AgNPs, making them useful for catalysis and gas storage applications.[209]

1.7.2. Identification and Characterization of Nanoparticles

A key feature of metal nanoparticles is their localized surface plasmon resonance (LSPR), a phenomenon that occurs when the collective oscillation of free electrons in the nanoparticle is excited by light.[210] This effect generates a strong absorption band in the UV-Vis spectrum, whose position and intensity depend on the size, shape, composition, and surrounding medium of the MNP. The plasmonic properties of MNP based hybrids are particularly relevant for applications in sensing, chiral recognition, and optoelectronic devices.[211-215]

The plasmon can also indicate a decrease in the effective nanoparticle size or a change in surface electron polarization. AgNPs exhibit a characteristic LSPR peak around 400 nm.[210,216,217] Smaller AgNPs produce narrow, well-defined peaks, while larger nanoparticles shift to broader peaks at longer wavelengths.

USC DE COMPOSTELA

Variations in intensity or peak broadening can be associated with modifications in colloidal stability and nanoparticle dispersion.

A shift in the LSPR band suggests an increase in the local refractive index or controlled aggregation of the nanoparticles. Not only does the size of the nanoparticles affect the plasmon band, but the approximation of other nanoparticles (dipole approximation) also causes plasmon coupling, creating a shift to longer wavelengths (Figure 31). This makes the analysis of size using the plasmon band possible only in the absence of aggregation or nanoparticle approximation.[218,219]

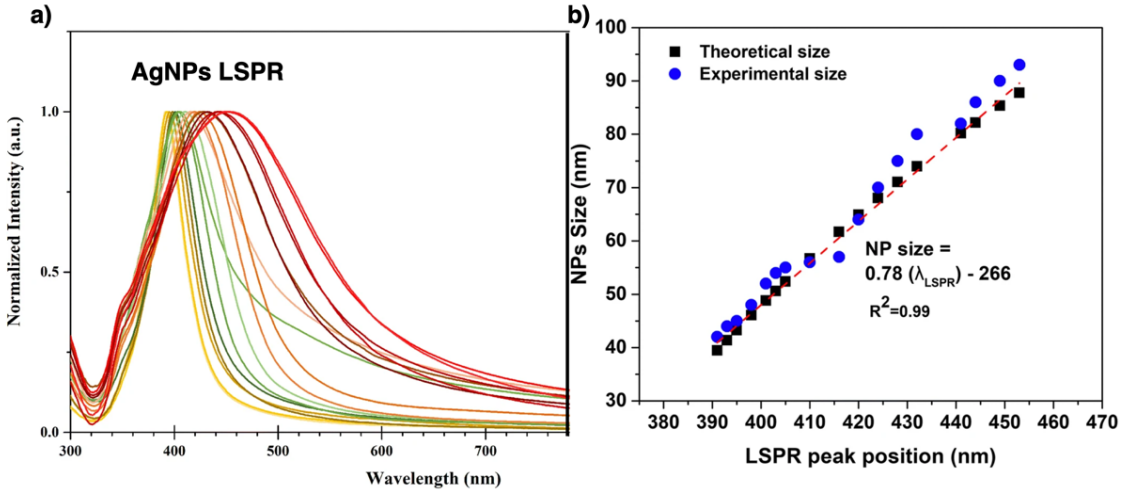


Figure 31. a) UV-Vis spectra of AgNPs with controlled sizes and their corresponding LSPR. b) Dependence of the LSPR absorption on the size of the AgNPs and the linear regression fit. Reproduced from ref. 216 with permission from Springer Nature, copyright 2020

To characterize these hybrid materials, transmission or scanning electron microscopy (TEM or SEM) are powerful tools for visualizing the morphology, distribution, and possible supramolecular organization of nanoparticles in the presence of helical polymers.[220-222]

Additional techniques such as dynamic light scattering (DLS),[223] X-ray photoelectron spectroscopy (XPS),[224-225] thermogravimetric analysis (TGA),[226] ECD,[227-230] provide the hydrodynamic diameter distribution, surface composition, thermal stability, and chiroptical properties, respectively.

USC UNIVERSIDADE DE SANTIAGO DE COMPOSTELA

1.7.3. Hybrid Poly(acetylene)s and Poly(phenylacetylene)s with Metal Nanoparticles

Typically, MNPs like gold (AuNPs) and silver (AgNPs) are stabilized by non-chiral polymers, but recent advances have introduced optically active polyacetylenes as protective ligands that not only stabilize nanoparticles but also influence their chiral and self-assembly properties. Deng and coworkers developed AuNP-based hybrid materials using poly(*N*-propargylamide) PA, a helical polymer that acts as both a stabilizing ligand and a chirality inducer. They demonstrated that these hybrid materials exhibit selective interactions with chiral molecules like (*R*)-(+)- and (*S*)-(-)-1-phenylethylamine.[231] A similar approach has been explored using PAs with Fe_3O_4 nanoparticles.[232]

In our group dynamic helical poly(phenylacetylene) (PPA) copolymers were hybridized with AuNPs. The studies revealed that the introduction of thiolated monomers into the PPA backbone affects the helical arrangement to obtain tunable chiral nanocomposites. By adjusting the thiol content in PPA copolymers, different nanoparticle morphologies from well-dispersed AuNPs to fiber-like structures were obtained. This study demonstrated that these materials could be manipulated by external stimuli like solvent polarity or metal ion coordination. Moreover, by incorporating Ba^{2+} as a crosslinking agent, macroscopically chiral nanospheres with controlled size and low polydispersity were obtained (Figure 32).[233]

USC UNIVERSIDADE DE SANTIAGO DE COMPOSTELA

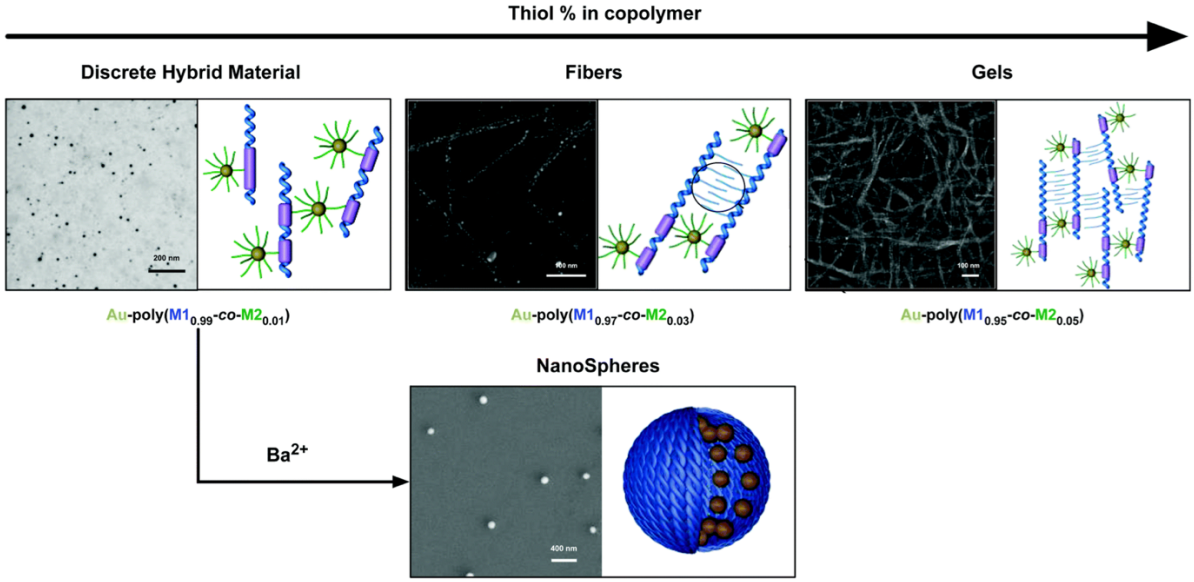


Figure 32. Electron microscopy images and illustration of nanoassemblies formed by the copolymer, showcasing the crosslinking ability of AuNPs and the self-assembling properties of the PPA. Reproduced from ref. 233 with permission from Royal Society of Chemistry (Copyright Clearance Center), copyright 2020

A further refinement in this area involved the development of AgNP hybrid with PPA anilide homopolymers, where silver nanoparticles were stabilized via weak amide-Ag interactions instead of traditional strong thiol bonds. This modification preserved the dynamic helical properties of PPA while allowing for the controlled placement of AgNPs along the polymer chain at regular intervals corresponding to the helical pitch (Figure 33a and Figure 33b).[234]

This structure allowed reversible helix switching in response to external stimuli. Another example using Au^{3+} showed also with anilide PPAs the alignment of AuNPs (Figure 33c).[235]

USC UNIVERSIDADE DE SANTIAGO DE COMPOSTELA

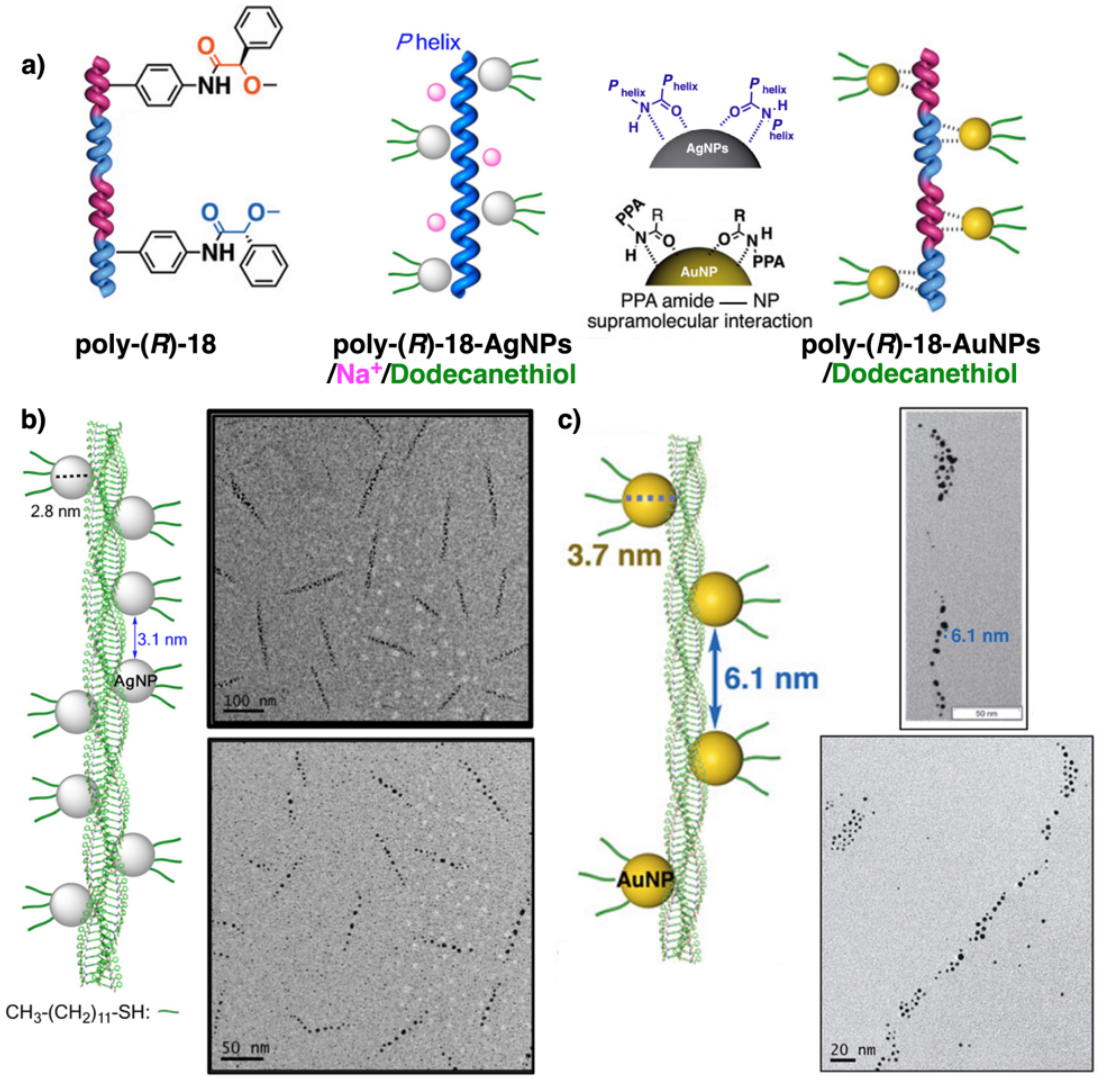


Figure 33. a) Molecular structure and schematic represenation of poly-(*R*)-**18**, poly-(*R*)-**18**-AgNPs/Na^+/dodecanethiol and poly-(*R*)-**18**-AuNPs/dodecanethiol. Molecular models and TEM images of a PPA with b) AgNPs/Na^+/dodecanethiol. c) AuNPs/dodecanethiol. Reproduced (left) from ref. 234 with permission from American Chemical Society, copyright 2021. Reproduced (right) from ref. 235 with permission from John Wiley and Sons, copyright 2021.

A similar approach was extended to dual-metal systems, where PPA copolymers containing both methionine and alanine-based pendant groups were used to create hybrid nanostructures with AgNPs and AuNPs. Furthermore, these nanocomposites experienced reversible helical inversions upon interaction with metal ions (Figure 34).[236]

USC UNIVERSIDADE DE SANTIAGO DE COMPOSTELA

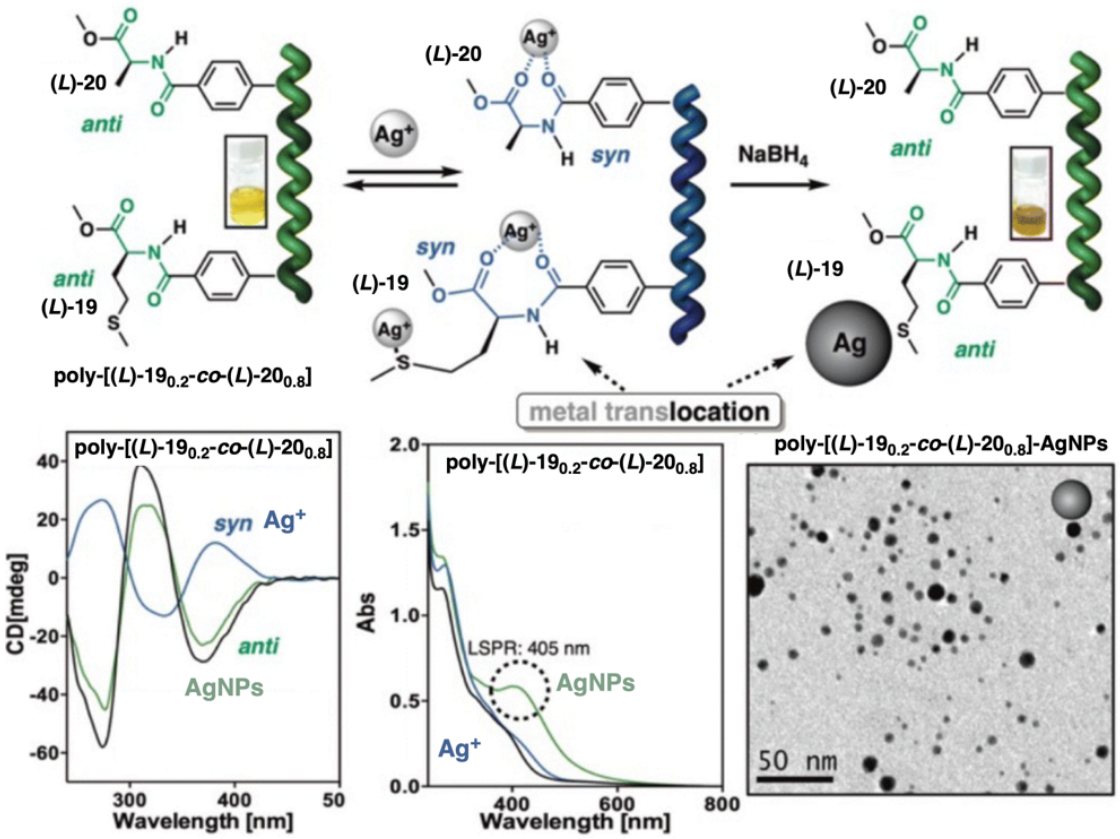


Figure 34. Preparation of poly-[(L)-19-co-(L)-20]-AgNPs and associated chiroptical responses. CD and UV-vis spectra of the polymer, polymer/Ag+, and polymer-AgNPs. TEM image of polymer-AgNPs. Reproduced from ref. 236 with permission from Royal Society of Chemistry (Copyright Clearance Center), copyright 2022

Finally, an ON/OFF stereocomplexation was introduced, where enantiomeric helical polymer-MNP nanocomposites were designed to form fiber-like aggregates upon interaction. These stereocomplexes were stabilized by a hydrogen-bonding network between complementary helices. Furthermore, the self-assembly were reversible through external stimuli. To form the stereocomplex two different copolymer with the corresponding enantiomer selected poly-[(*R*)-**14**$_{0.98}$-*co*-**21**$_{0.02}$] and poly-[(*S*)-**14**$_{0.98}$-*co*-**21**0.02]. Then, two hybrid materials were produced poly-[(*R*)-**14**$_{0.98}$-*co*-**21**$_{0.02}$]/AgNP and poly-[(*S*)-**14**$_{0.98}$-*co*-**21**$_{0.02}$]/AuNP and mixed in 50/50 v/v in THF to form the stereocomplexes of two different hybrid materials (Figure 35).[237]

USC UNIVERSIDADE DE SANTIAGO DE COMPOSTELA

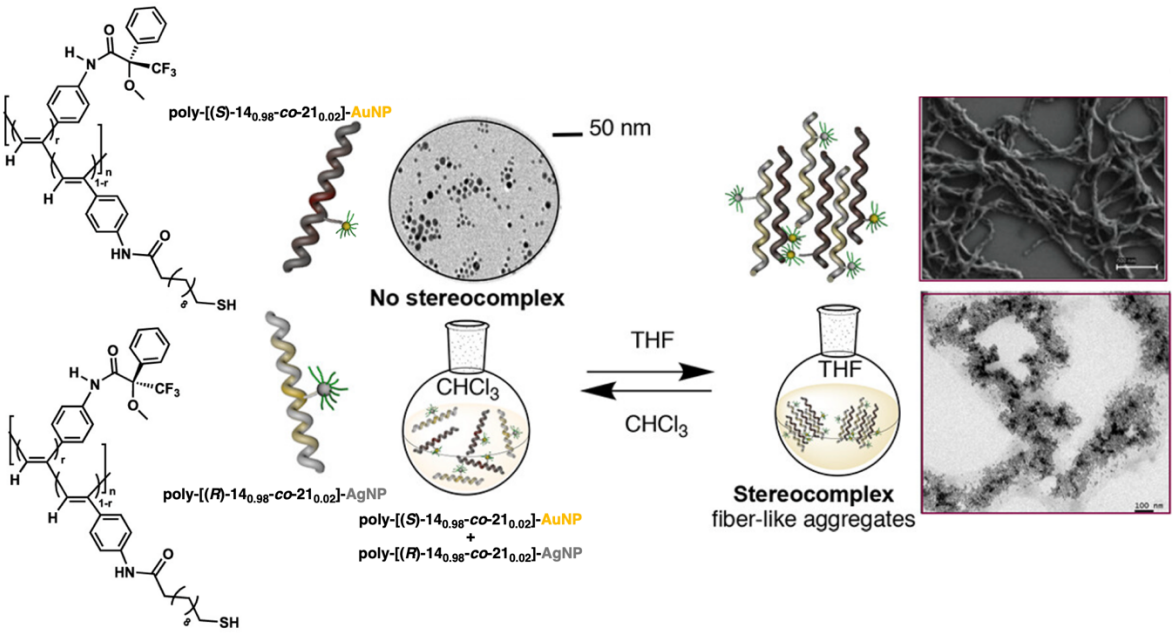


Figure 35. Graphic illustration and electron microscopy studies of the ON/OFF stereocomplex-nanocomposite formation of a 50/50 v/v mixture of poly-[(*S*)-**14**$_{0.98}$-*co*-**21**$_{0.02}$]-AuNP/ poly-[(*R*)-**14**$_{0.98}$-*co*-**21**$_{0.02}$]-AgNP nanocomposites in THF. Reproduced from ref. 237 with permission from American Chemical Society, copyright 2023

1.8. Dynamic Helical Polymers PPAs: Helical Induction, Inversion and Enhancement in PPAS

Variations in chiral helical polymers in the conformational composition of chiral pendant groups (Figure 36a) by the presence of external stimuli,[16] such as solvent polarity or the addition of metal ions, can result in either helical sense enhancement or helical inversion effect (Figure 36b). On the other hand, if the helical polymer is achiral,[48,238] a phenomenon of asymmetry induction (helical induction) arises from interactions between the polymer and external chiral molecules, such as chiral amines used as external stimuli (Figure 36c).

1.8.1. Helix Induction Mechanisms

Chirality in Poly(phenylacetylene)s arises from the external helix. Depending on the pendant different mechanisms induce helicity into the polyenic backbone.

USC UNIVERSIDADE DE SANTIAGO DE COMPOSTELA

1.8.1.1. Teleinduction

The most frequently helix induction mechanism that governs the screw sense excess adopted by chiral and achiral polymers is teleinduction.[239] In this mechanism, changes in the spatial distribution of substituents in the chiral centres or in the species associated with the pendant groups result in stimuli being transmitted through space to the polymer backbones, which adopt specific conformations that generate *P* or *M* helical structures (Figure 36).

Interestingly, other helix induction mechanisms operating from the pendants to the main chains of polymers have been explored in recent years.

USC UNIVERSIDADE DE SANTIAGO DE COMPOSTELA

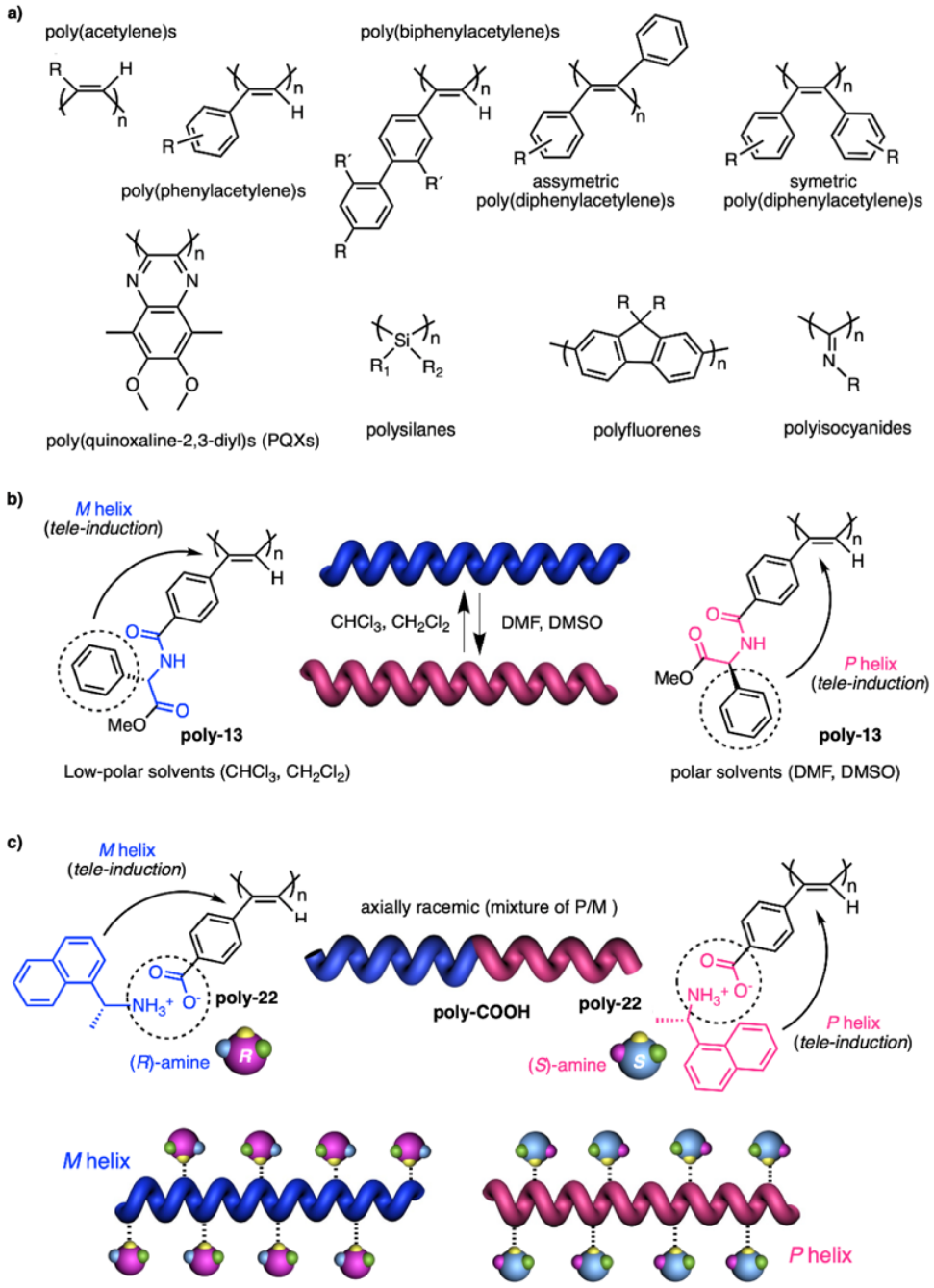


Figure 36. a) Some families of dynamic helical polymers. b) Helix inversion of a chiral poly(phenylacetylene) bearing 4-benzamide of (*S*)-phenylglycine methyl ester as pendant group by tuning its conformational composition using solvent polarity as external stimulus. c) Chiral amplification of an achiral poly(phenylacetylene) bearing 4-benzoic acid as pendant using chiral amines as external stimuli. Reproduced from ref. 25 with permission from Royal Society of Chemistry, copyright 2023

1.8.1.2. Chiral Harvesting

It is based on the introduction of a chiral source at a remote position separated from the backbone by achiral spacers. In such a case, the information transmission mechanism can follow two different paths. The induction of: (i) a conformational change

in the flexible achiral spacer,[240] or (ii) a tilting degree in the supramolecular arrangement of the rigid achiral spacers along the helix.[241] Both mechanisms are triggered by changes in the conformational composition of a chiral group placed in a remote position, which are transmitted to the achiral spacer and further harvested by the polymer backbone that adopts a *P* or an *M* screw sense excess. There are examples for the two mechanisms, PPAs that bear achiral and flexible Aib residue[240] and planar and rigid oligo(phenylene-ethynylene) (OPE)[241] as spacers (Figure 37).

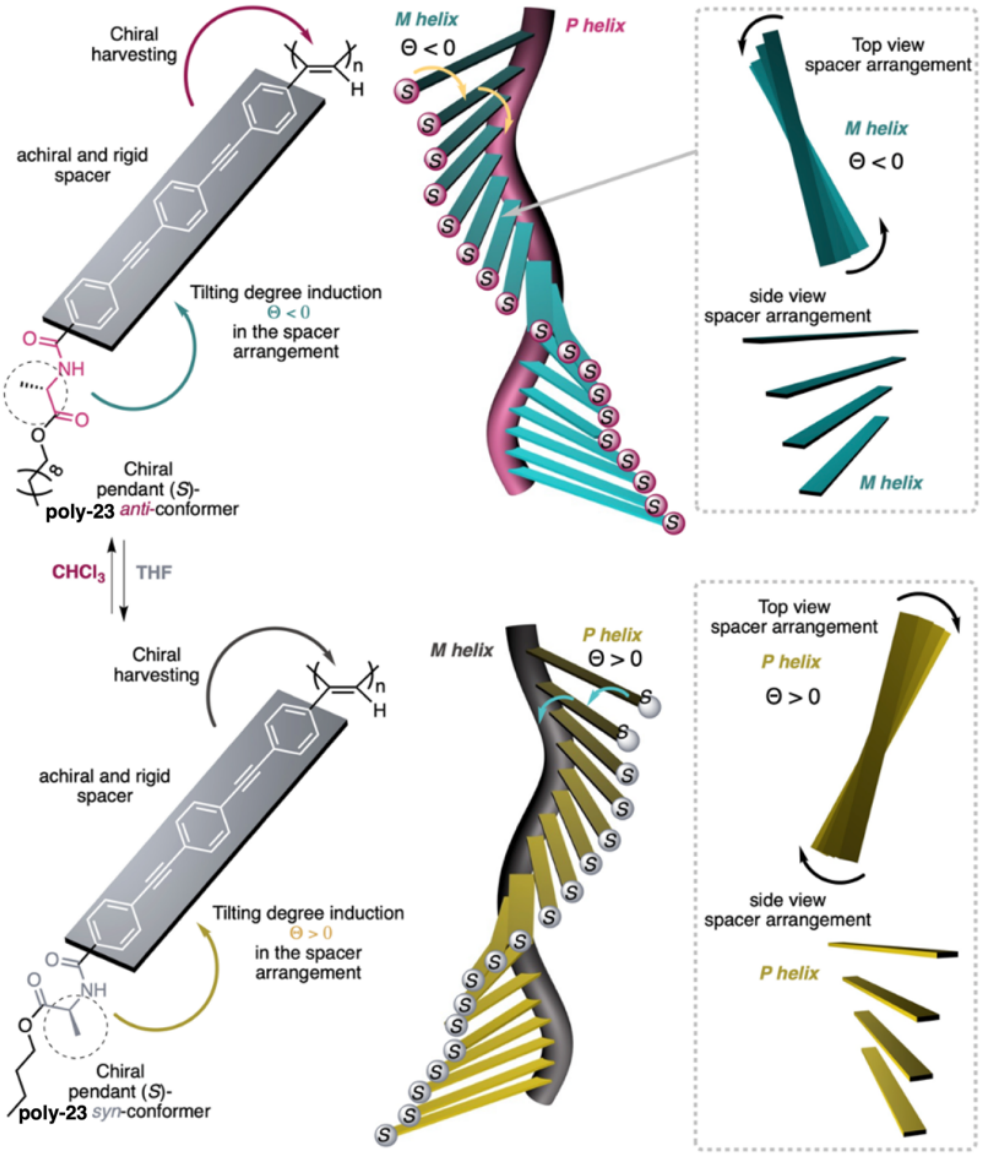


Figure 37. Screw sense induction of helical polymers through chiral harvesting using rigid achiral spacers. Reproduced from ref. 25 with permission from Royal Society of Chemistry, copyright 2023

USC UNIVERSIDADE DE SANTIAGO DE COMPOSTELA

1.8.1.3. Chiral Overpass

Usually, when the pendant of a helical polymer is composed by two or more chiral centers, the one closest to the backbone of the polymer is more likely to control its handedness, while the other center has low-to-null impact on the structural features of the helical structure.[242] Interestingly, the possibility of playing with the conformational composition of these multi-chiral side chains makes possible to activate a chiral-overpass effect.[243,244] For example, a polymer bearing the anilide of (*S*)-alanine-(*R*)-methoxyphenylacetate —(*S*)-Ala-(*R*)-MPA— as pendant,[244] two different conformations, extended and bent, can occur (Figure 38). Thus, if the pendant adopts an extended conformation, (*S*)-alanine, located closer to the poly(phenylacetylene) main chain, commands a preferred macromolecular structure (screw sense and elongation) in the PPA (*M* helix, Figure 38). On the other hand, by fixing a bent structure at the pendant, it is possible to place the second chiral residue close to the backbone, which is now responsible for the screw sense preference adopted by the macromolecular helical polymer (*P* helix, Figure 38).[243,244] However, if the (*S*)-Ala-(*S*)-MPA pendant is used, *M* helices are obtained in both extended and bent conformations (Figure 38). Through computational calculations, the stabilization of a beta sheet in DMSO and a gamma turn in $CHCl_3$ was confirmed. VCD studies performed experimentally on these two structures showed an exact VCD pattern matching the computed calculations. For the computed VCD of the betta sheet an extended pendant structure betta sheet of an oligomer was used showing the exact VCD than $CHCl_3$. Additionally, the gamma turn of one pendant, without interaction with other pendants, showed the exact VCD than DMSO.

USC
UNIVERSIDADE DE SANTIAGO DE COMPOSTELA

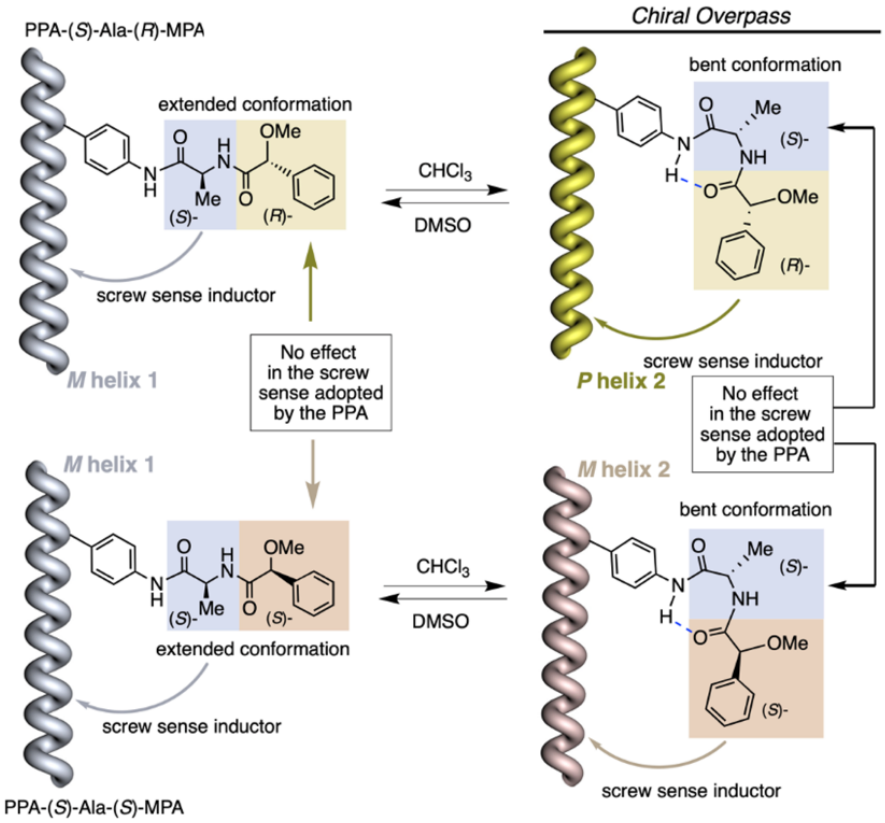


Figure 38. Schematic illustration of the chiral overpass effect in poly(phenylacetylene)s. b) Chiral amplification of a poly(phenylacetylene). Reproduced from ref. 25 with permission from Royal Society of Chemistry, copyright 2023

1.8.1.4. Substituent Priority Overpass

This helix induction mechanism is found in dynamic helical polymers bearing conformationally locked chiral pendants such as chiral allenes.[245] In these systems, the relative spatial orientation of the substituents is always the same, and it is not possible to modulate it by altering the conformational composition of the chiral moiety. In such cases, to invert the helical sense of the polymer it is necessary to modify the relative volume of one of the substituents.

As a result of this volume change, a new substituent located in a different position will be responsible for producing variations in the macromolecular structure and inducing the screw sense preference. To show this effect, poly-**24** was chosen as illustrative example.[245] This polymer bears an allene pendant (Figure 39) in which its two consecutive double bonds place their four substituents in two perpendicular planes. If these substituents are different, the allene becomes chiral, as in poly-**24**, which shows P

USC UNIVERSIDADE DE SANTIAGO DE COMPOSTELA

axial chirality. In poly-**24**, the screw sense is governed by the *tert*-butyl group located closest to the backbone (substituent a). However, if a secondary or tertiary amine are added to a solution containing poly-**24**, a supramolecular interaction is established between the alcohol group (substituent b) of the allene and the amine, increasing the size of this substituent. As a result, substituent b, placed in a different spatial orientation than substituent a, now controls the helical sense that poly-**24** adopts, resulting in a helix inversion process.

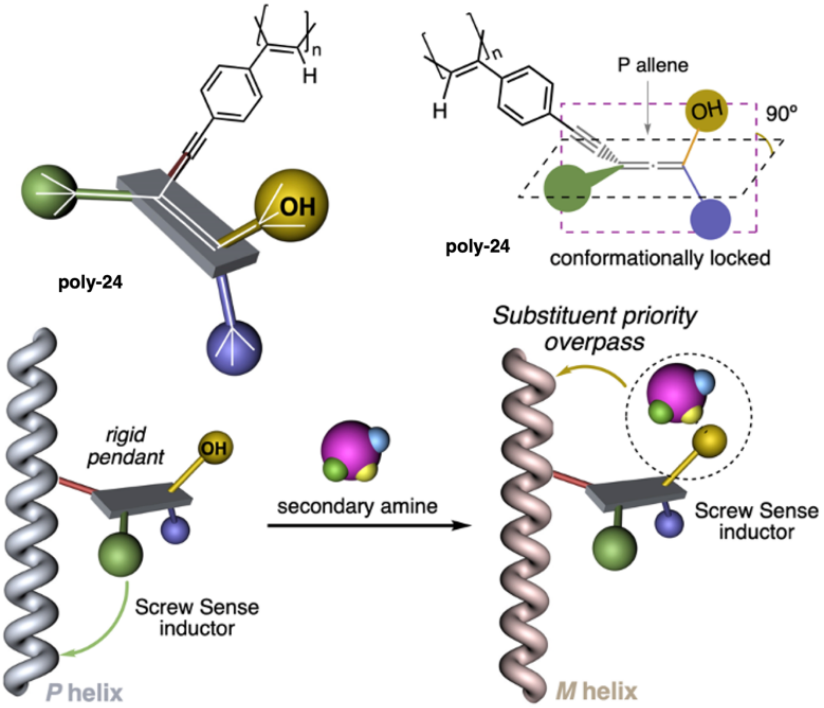


Figure 39. Chiral amplification of a poly(phenylacetylene) bearing a chiral allene as pendant using chiral amines as external stimuli. Reproduced from ref. 25 with permission from Royal Society of Chemistry, copyright 2023

1.8.1.5. Domino Effect

The domino effect involves introducing a chiral residue at the terminal position of an achiral oligomer[246,247] or polymer,[248] leading to a preferred helical sense. There are examples of oligomers where this residue can be achiral but responds to chiral stimuli, becoming chiral upon interaction. This dynamic behavior allows the helical sense to be switched by manipulating the terminal part.[249]

In an example from our group,[248] an achiral poly(phenylisocyanate) with a chiral terminal (*R*)-α-methoxyphenylacetic acid (MPA) poly-**25** derivative that stabilizes a *sp*

conformation in $CHCl_3$, induces a preferred helical sense —*M*-type helix— of the poly(phenylisocyanate). By modifying the solvent environment, the conformation of the terminal residue can be altered. In $CHCl_3$, low polarity and non electron donor solvents stabilize the *ap* conformation in the (*R*)-MPA moiety, resulting in a *P*-type helix. On the other hand, in THF, polar and electron donor solvents promote the *sp* conformation, leading to an *M*-type helix. This dynamic switching showed domino effect, where the chiral information propagates through the structure. The conformation could also be modulated by the addition of Li^+, which stabilizes the *ap* conformation, and recovered by adding a metal scavenger in a switchable fashion (Figure 40).

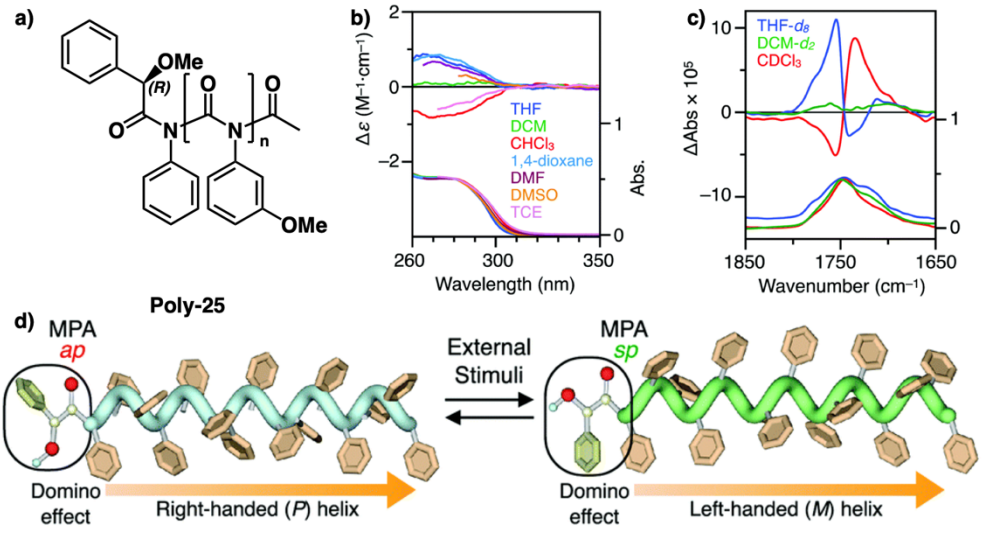


Figure 40. a) Molecular structure of poly-**25** c) ECD and UV-Vis of poly-**25** in different solvents. c) VCD and IR of poly-**25** in different solvents. d) Schematic illustration of the switchable domino effect along a polymer chain. Reproduced from ref. 248 with permission from Royal Society of Chemistry (Copyright Clearance Center), copyright 2019

1.8.2. External Stimuli in Poly(phenylacetylene)s

The literature presents various examples illustrating how helical structures adopted by PPAs can be modified. These modifications include helix inversion, amplification of asymmetry, or variations in the helical scaffold, achieved through interactions with different stimuli such as temperature,[47,89,91,96,250-256] anions,[257-264] cations,[6,16,42,43,170,171,265-269] redox conditions,[81] light,[270] chiral solvents,[238] and pH.[59] Most examples involve modulating pendants that respond to these stimuli, affecting the helix by stabilizing a different helical sense, elongation, or structure.

USC UNIVERSIDADE DE SANTIAGO DE COMPOSTELA

Zhang and Wan demonstrated a temperature-driven conformational change in a 3,5-dibenzoate PPA poly-**26**. They manipulated the cis/trans conformational composition of the tertiary amide using temperature, thereby modifying the pendants and influencing the internal helix.[251] In another example by the same authors, they reported a 3,5-dibenzoate PPA that can transition between compressed and stretched helical scaffolds in chloroform. At high temperatures, n-π* interactions between carbonyl groups are deactivated, leading to elongated *cis-transoidal* helices, while at lower temperatures, these interactions stabilize compressed *cis-cisoidal* structures (Figure 41).[256]

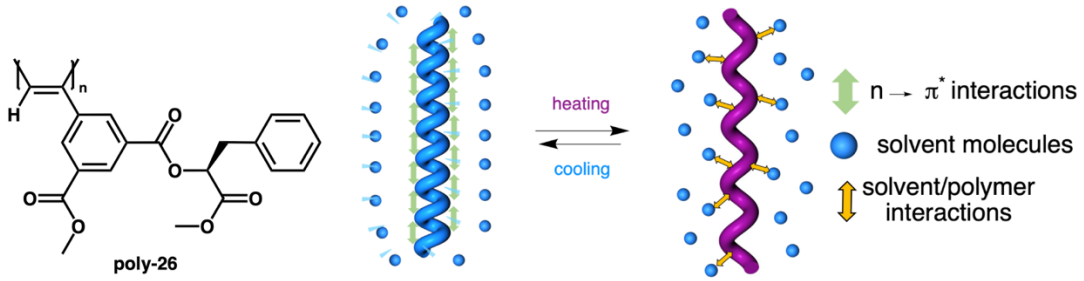


Figure 41. Chemical structure of poly-**26** and schematic represntation of its thermoresponsive behaviour. Reproduced from ref. 25 with permission from Royal Society of Chemistry, copyright 2023

To create a selective anion detector based on a dynamic helical polymer, such as a PPA, the design of the monomer is crucial, as with many other stimuli. For instance, Kakuchi designed a chiral PPA that bears, as a pendant, an amino acid connected to the backbone through a urea group —(*L*)-leucine, (*L*)-glutamic acid, (*L*)-aspartic acid, (*L*)-phenylalanine, (*L*)-isoleucine, and (*L*)-alanine; PPA-Leu, PPA-Glu, PPA-Asp, PPA-Phe, PPA-Ile, and PPA-Ala, respectively.[257,260] Thus, while the chiral amino acid is used to induce a specific helical sense in the PPA, the acidic urea groups are used to interact with anions. The anion/ chiral pendant interaction causes a conformational change in the monomer repeating unit, which is harvested by the polyene backbone producing an elongation and/or a helical sense change. All these polymers showed modulable helicities by external stimuli. Interestingly, the addition of various anions as ammonium salts, such as tetra-*n*-butylammonium acetate (TBAA), benzoate (TBAB), nitrate (TBAN), azide ($TBAN_3$), fluoride (TBAF), chloride (TBACl) and bromide (TBABr), to solutions containing the different polymers showed different ECD responses depending on polymer and anion (Figure 42a for PPA-Leu). Therefore, the anionic signaling property of these polymers depends on both the size of the anion and the amino acid selected as

USC UNIVERSIDADE DE SANTIAGO DE COMPOSTELA

the pendant group. For instance, while the addition of CH_3COO^- to a solution of PPA-Leu, PPA-Ala, and PPA-Ile induces a *P* helix in the polymer ($ECD_{500\ nm} > 0$), an *M* helix is induced in PPA-Phe, PPA-Asp, and PPA-Glu ($ECD_{500\ nm} < 0$) (Figure 42b). Similar effects were observed with other anions, such as C_6H_5COO, F, Cl, and Br, indicating that these polymers can be used for distinguishing anionic hosts due to the resulting unique patterns.

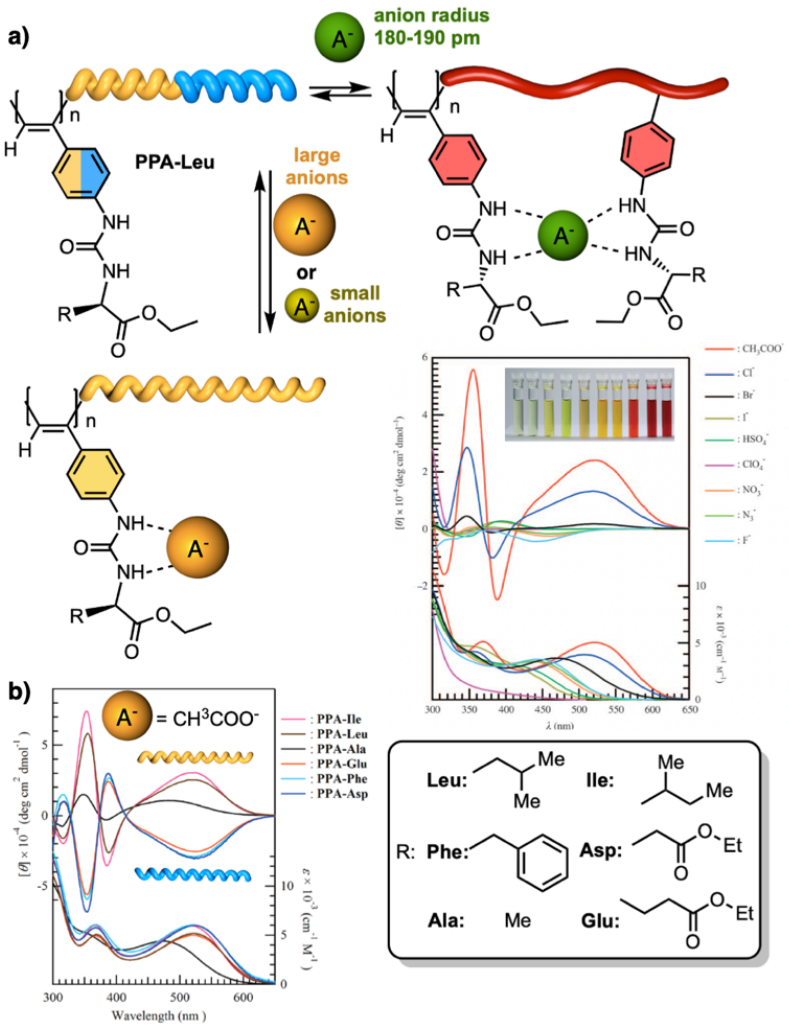


Figure 42. a) Schematic representation of size-selective detection for anions based on a PPA. ECD (upper) and UV-Vis absorption (lower) spectra of poly-PPA-Leu upon addition of several anions (1 equiv of anion to a 3.3 mmol·L^{-1} THF solution of poly-PPA-Leu) b) CD (upper) and UV-vis (lower) spectra of urea-functionalized polymers with CH_3COO^-. Reproduced from ref. 25 with permission from Royal Society of Chemistry, copyright 2023

Our group demonstrated the use of a chiral MPA group as a pendant to control the helical sense of a PPA with monovalent or divalent metal ions. In this MPA polymer monovalent ions induce an M helix by stabilizing an *ap* conformer, while divalent ions

induce a *P* helix by fixing a *sp* conformation (Figure 43a Figure 43b). Nanospheres were prepared with tunable size and chirality by controlling the metal-polymer ratio (Figure 43c). The addition of a cosolvent altered the coordination, enabling precise tuning between *P* and *M* helical senses. This protocol has paved the way for numerous applications. One notable achievement by Maeda and our group is the development of a three-state switchable chiral stationary phase using the polymer of MPA. This material can adopt distinct chiral states in response to the presence of monovalent or divalent metal ions, enabling the inversion of enantiomer elution times (Figure 43d).[6,42,43,170,266-268]

Our group also explored the coordination of metal ions with PPAs containing amino acids as pendants to induce helical changes. It was found that an *anti-syn* conformational change in PPAs with benzamides of (*L*)-phenylglycine methyl ester can be triggered in low-polarity solvents, leading to helical inversion. Therefore, if a metal ion is added to the two carbonyl groups of the pendant when they are oriented in anti in low polarity solvents, a chelate is produced between the metal ion and the amino acid that orients the two carbonyls in *syn*.[16,171,269]

USC
UNIVERSIDADE DE SANTIAGO DE COMPOSTELA

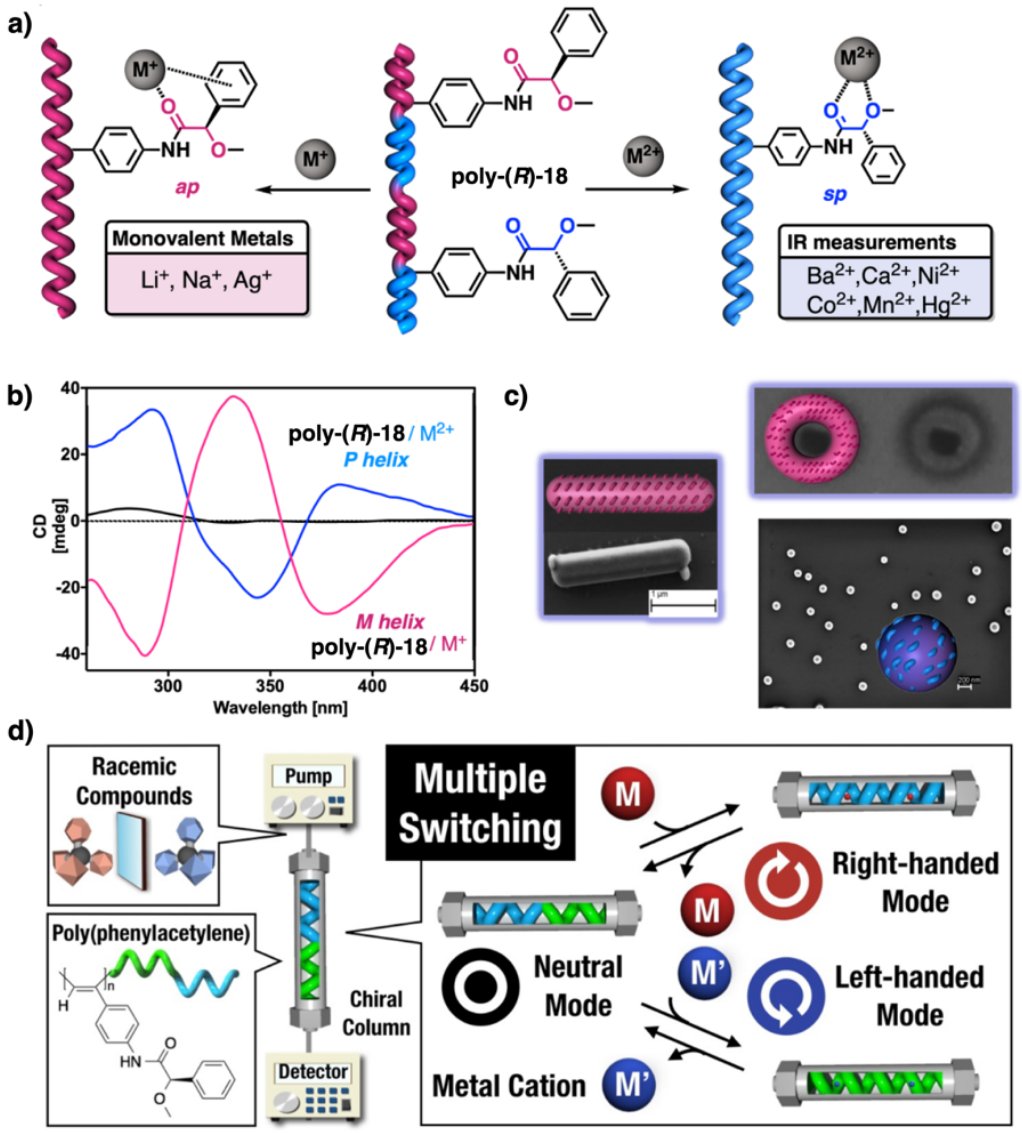


Figure 43. a) Schematic illustration and (b) ECD spectra of the helical sense induction in poly-(R)-18 by monovalent and divalent metal ions. c) Different nanostructures obtained for poly-(R)-18/Mn+ d) Application of poly-(R)-18/Mn+ as multiple-switch chiral stationary phase. Reproduced from ref. 25 with permission from Royal Society of Chemistry, copyright 2023

Our group also synthesized water-soluble helical amine-PPAs with pH-responsive behavior, such as poly-**27**.[59] Importantly, the location of the amino group within the polymer determines the mechanism and direction of the helical response. At acidic pH, the preferred helical conformation is stabilized by a hydrogen bond between the ammonium and carbonyl groups, while at higher pH values, when the amino group is deprotonated, an antiperiplanar orientation is preferred between both groups, placing the substituents of the chiral center in different locations and therefore, promoting opposite

USC UNIVERSIDADE DE SANTIAGO DE COMPOSTELA

helical senses. Helix inversion could be observed in MeOH, but not in water, due to solubility problems of the neutral form of poly-**27** (Figure 44).

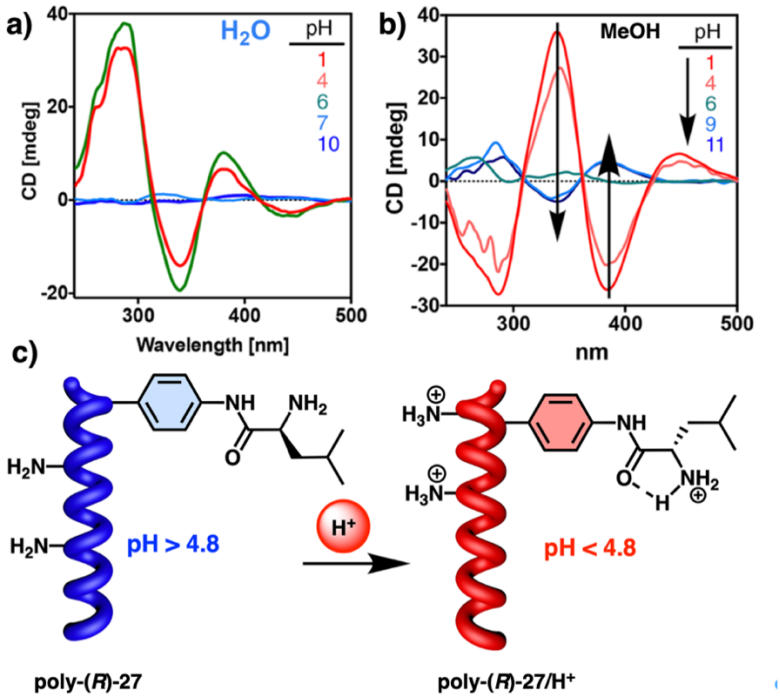


Figure 44. CD spectra for poly-**27** at different pH in a) water and b) MeOH. c). Conformational composition of amino-PPAs in basic and acidic media. [amino-PPA]=0.5 mg/mL. Reproduced from ref. 25 with permission from Royal Society of Chemistry, copyright 2023

1.8.4. Internal Stimuli: Communication Mechanism in Copolymeric Poly(phenylacetylene)s

The previous examples involve homopolymers with a single type of monomer, which are the most abundant helix induction mechanisms. However, these helix induction mechanisms can also occur in dynamic helical random copolymers made by two different monomers. In this case, in addition to the helical sense induction effect produced by the pendants in the polymer backbone, it is necessary to consider other Communication Mechanisms between the different components of the random copolymer, which can be either chiral/achiral or chiral/chiral. In general, in these systems, one of the monomers must adopt a preferred conformation that activates a specific conformation in the other comonomer (chiral or achiral). Thus, depending on the chiral composition of the comonomers, different effects can be triggered.

USC UNIVERSIDADE DE SANTIAGO DE COMPOSTELA

Sergeants and Soldiers Effect (Sergeant: chiral (*R* or *S*), minor component; Soldier: achiral, major component).[271-274] The Sergeant orders the Soldier to adopt a conformation that promotes the same helical scaffold (sense and elongation) induced by the Sergeant (Figure 45).

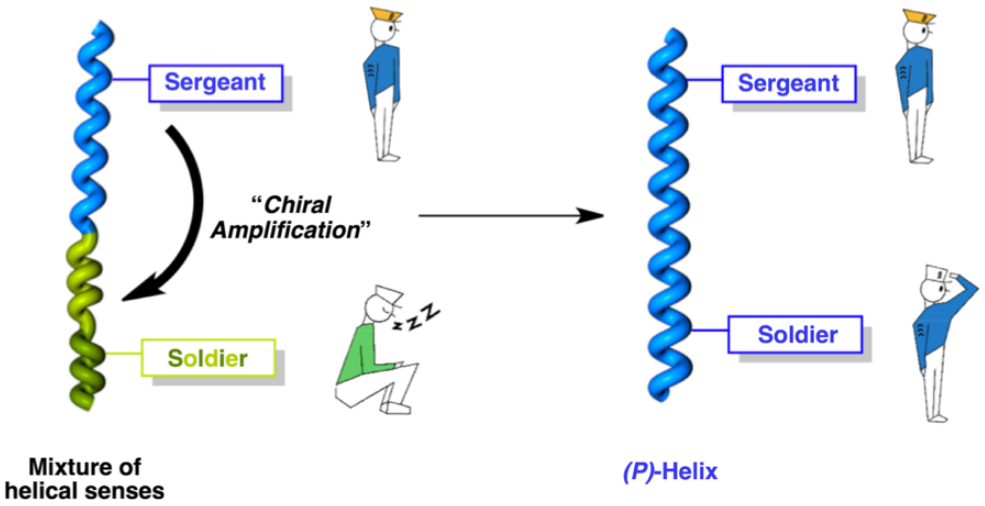


Figure 45. Schematic representation of the Sergeants and Soldiers Effect.

Abnormal Sergeants and Soldiers Effect (Sergeant: chiral, minor component (*R* or *S*); Soldier: achiral, major component).[275] The Sergeant activates a conformation in the Soldier that promotes a different helical scaffold than the one adopted by the Sergeant (sense and/or elongation).

Chiral to chiral Sergeants and Soldiers Effect (Sergeant: chiral, minor component (*R* or *S*); Soldier: chiral (*R* or *S*), major component).[276] The Sergeant commands a specific conformation on the Soldier, which differs depending on the absolute configuration of the chiral Soldier (Figure 46a). Thus, the two enantiomeric configurations of the Soldier can adapt to the scaffold induced by the Sergeant. For example, a PPA bearing the 4-anilide of (*R* or *S*)-methoxyphenylacetic acid (poly-**11**) behaves axially racemic (ECD = 0, mixture of *P* and *M* helices) even though the pendant is chiral.[276] This fact is due to the presence of two conformers in equilibrium at the pendant, *ap* and *sp*, which place the substituents of the chiral moiety in different spatial locations, inducing opposite helical senses in the PPA (Fig. 5a). Interestingly, replacement of the phenyl group by an anthryl ring (poly-**12**) shifts the conformational composition of the pendant towards the *ap* conformer (Figure 46a).[274] When the monomers of poly-**12** (Sergeant) and poly-**11**

USC DE COMPOSTELA

(Soldier) are copolymerized to create poly[(*S*)-**12**(Sergeant)$_r$-*co*-(*S*)-**11**(Soldier)$_{1-r}$] and poly[(*R*)-**12**(Sergeant)$_r$-*co*-(*S*)-**11**(Soldier)$_{1-r}$] copolymer series (b), it was observed that both series adopt opposite helical senses, *P* and *M*, commanded by the (*S*)- or (*R*)-chirality of the Sergeant respectively. The (*S*)-Soldier fits into the *P* and *M* helical scaffolds adopting the *ap* or *sp* conformations respectively.[276]

Chiral Coalition (Sergeant: chiral, minor component; Soldier: chiral, major component).[277] In this case, the role of the Sergeant is to behave like a chiral dopant, triggering a specific conformation in the Soldier that is different depending on the chirality of the Soldier. As a result, poly[(*S*)-Sergeant$_r$-*co*-(*S*)-Soldier$_{1-r}$] and poly[(*R*)-Sergeant$_r$-*co*-(*S*)-Soldier$_{1-r}$] adopt the same helical structure, which is commanded by the chirality of the Soldier, e.g., poly[(*S*)-**5**$_r$-*co*-(*S*)-**11**$_{1-r}$] and poly[(*R*)-**5**$_r$-*co*-(*S*)-**11**$_{1-r}$] (Figure 46b).[277] However, the Sergeant is necessary to trigger a specific conformation in the Soldier, otherwise, without its presence, the Soldier homopolymer behaves like an axially racemic helix.

Majority Rules [Sergeant: chiral; Soldier: chiral (Sergeant's enantiomer)].[278] In this case, the screw sense preferences of copolymer series made by two enantiomeric monomers (identical chemical structure, mirror image relationship) are biased towards *P* or *M* helices, commanded by a slight enantiomeric excess of one of the enantiomers. For instance, in poly[(*R*)-Sergeant$_{0.56}$-*co*-(*S*)-Soldier$_{0.44}$], made by enantiomeric monomers of 2,6-dimethylheptyl isocyanate (56% (*R*)-enantiomer/44% (*S*)-enantiomer; ee 12%), the helix adopted by the copolymer is identical to that adopted by the (*R*)-homopolymer.[278]

Chiral Accord and Chiral Conflict.[279-281] Other interesting phenomena can occur in chiral dynamic helical copolymers although there is not amplification of asymmetry due to the lack of communication between the two chiral components. Thus, if the two comonomers of the copolymer induce independently the same helical sense, a chiral accord emerges,[280] whereas if both comonomers induce opposite helical senses, a chiral conflict is produced.[280-281]

USC UNIVERSIDADE DE SANTIAGO DE COMPOSTELA

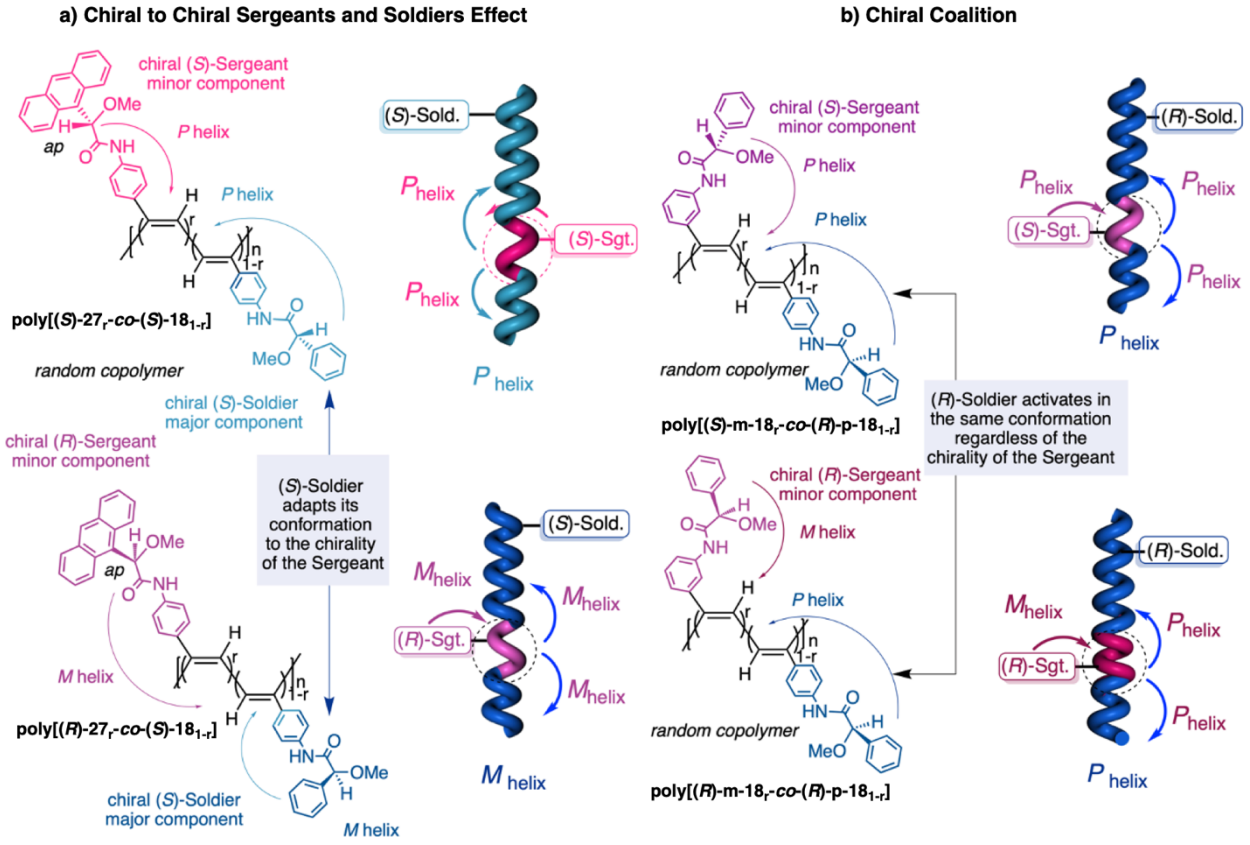


Figure 46. Schematic illustration of (a) Chiral to Chiral Sergeants and Soldiers Effect and (b) Chiral Coalition. Reproduced from ref. 25 with permission from Royal Society of Chemistry, copyright 2023

While classical studies of these polymers have focused on random copolymers, block copolymers are gaining attention for their potential to induce Communication Mechanisms. However, examples are limited because block copolymers offer only one point for inducing communication, whereas random copolymers have multiple intercalation points, making communication induction easier. The research from Fumio Sanda highlights these mechanisms, demonstrating chirality transfer in block copolymers. The work from Sanda shows that block copolymers can exhibit chiroptical properties and transfer chirality from one block to another, influenced by the Majority Rules.[66] Additionally, the investigation from Sanda of the Sergeants and Soldiers Effect (SaS) reveals how chiral units in block copolymers provoke chiral amplification of the helical structure of achiral blocks.[65,282]

USC UNIVERSIDADE DE SANTIAGO DE COMPOSTELA

1.9. Supramolecular Helical Polymers

Supramolecular helical polymers form through non-covalent interactions, such as hydrogen bonding and π-π stacking, which make them highly reversible and dynamic. These interactions allow monomers to assemble and disassemble, with stability dependent on environmental factors like concentration and temperature.

Inspired by the role of supramolecular interactions in biomolecules, scientists have studied these polymers to understand their self-assembly processes.[283] Supramolecular polymers exhibit unique properties, such as responsiveness to external stimuli and self-healing capabilities,[284] due to the dynamic nature of non-covalent bonds. Their formation is influenced by thermodynamics, kinetics, and growth factors.[285]

Controlling the helical structure of these polymers can be achieved through rational monomer design and adjustments to environmental conditions or polymer composition. This adaptability leads to properties like chiral amplification or helical inversion.[286]

1.9.1. Supramolecular Polymerization: Growth Mechanisms

Supramolecular polymerization is a process that is composed by two steps. Initially, monomers combine to form a nucleus that is known as the nucleation step. Following this, additional monomers are added to the already formed nucleus during the elongation step, ultimately forming the supramolecular polymer. The dynamics of this process can vary based on the association constants for nucleation and elongation ($K_n = K_e$). When these constants are equal, the growth is termed isodesmic, indicating that each monomer addition is equally favorable

When the association constants for nucleation and elongation differ, the growth process can be classified into two distinct types. In cooperative growth, the nucleation constant is lower than the elongation constant ($K_n < K_e$), meaning that once nucleation occurs, elongation is favored, leading to a rapid assembly of the polymer. Conversely, in anticooperative growth, the nucleation constant is higher than the elongation constant ($K_n > K_e$), which means that while nucleation may occur easily, the subsequent elongation is less favored, resulting in a slower polymer formation.[287-289]

The self-assembly mechanism of supramolecular helical polymers is often investigated using temperature-dependent ECD and UV-Vis spectroscopy. These

techniques measure the spectroscopic signal at a specific wavelength, which is then normalized as a function of temperature to produce a cooling curve. In the case of isodesmic growth, where the nucleation and elongation constants are equal, the cooling curve follows a sigmoidal shape with $\sigma = 1$, indicating uniform monomer addition throughout the process. Cooperative processes, characterized by $\sigma < 1$, exhibit steeper cooling curves, while anticooperative processes, with $\sigma < 1$, display smoother curves compared to isodesmic growth (Figure 47).[290]

The cooling curves provide the thermodynamic parameters using the mass-balance (MB) model,[291] which considers the exchange of monomers between polymers and their molecularly dissolved state. The fraction of aggregated species (α_{Agg}) is determined from these parameters, which describe the equilibrium in both the nucleation phase (characterized by K_n, ΔH_n, and ΔS_n) and the elongation phase (characterized by K_e, ΔH_e, and ΔS_e). These phases are distinguished by a characteristic temperature (T_e). Equation (26) simplifies the fitting process by assuming ΔS_e equals ΔS_n. Additionally, the model incorporates a nucleation penalty (ΔH_{np}) in Equation (27). ΔH_{np} quantifies how the nucleation step influences aggregate formation, which is directly related to the σ value.

Instead of using temperature variations to study the self-assembly process, solvent denaturation experiments can be performed. In these experiments, two samples of the molecule are prepared: one in a good solvent where the monomers remain molecularly dissolved, and another in a bad solvent where aggregation occurs. Then the samples with varying molar fractions of the good and bad solvents are measured. By measuring these mixtures, we can obtain denaturation curves that can be fitted to obtain the cooperativity of the system.[292]

USC
UNIVERSIDADE DE SANTIAGO DE COMPOSTELA

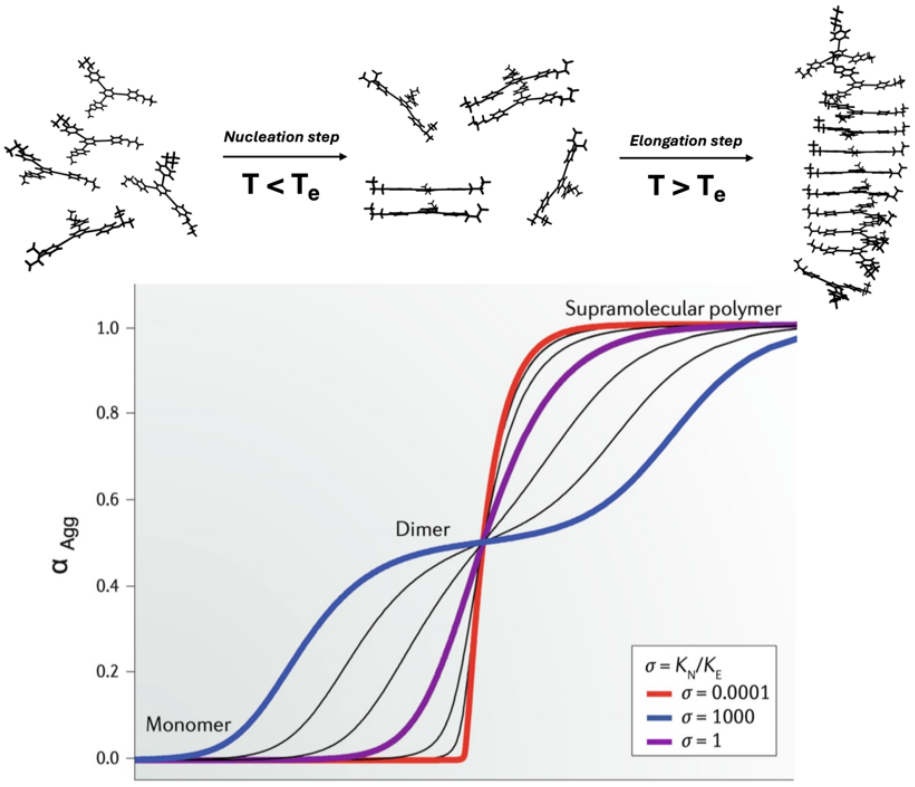


Figure 47. Supramolecular polymerization mechanisms for p scaffolds controlled by thermodynamics. The fraction of aggregated π surfaces $\alpha_{Agg\text{-}\pi}$ as a function of the normalized concentration or temperature with different σ values and a nucleus size of two. Reproduced from ref. 290 with permission from Springer Nature, copyright 2019

$$\sigma = \frac{K_n}{K_e} = e^{-\Delta H_{np}/RT} \quad \textbf{(26)}$$

$$\Delta H_{np} = \Delta H_e - \Delta H_n \quad \textbf{(27)}$$

1.9.2. Types of Aggregates: Characterization and Physical Properties

The principle in molecular exciton theory that describes how the arrangement of electronic ETDMs in aggregates affects their optical properties is the Kasha's Rules. These rules helps to predict the absorption and fluorescence characteristics of aggregates based on the relative orientation of their ETDMs.[293,294]

USC DE COMPOSTELA

In H-aggregates, the ETDMs are aligned in a face-to-face or side-by-side manner. According to Kasha's Rules, this arrangement leads to a blue shift (hypsochromic shift) in the absorption spectrum compared to the monomer. The lower excited state in H-aggregates is optically forbidden, which results in reduced fluorescence efficiency. The higher excited state is optically allowed, contributing to the observed blue shift in absorption in UV-Vis spectra (Figure 48).

J-aggregates, on the other hand, have their ETDMs aligned in a head-to-tail configuration. Kasha's Rules predicts that this alignment causes a red shift (bathochromic shift) in the absorption spectrum relative to the monomer. The lower excited state in J-aggregates is optically allowed, leading to enhanced fluorescence efficiency. This makes J-aggregates particularly useful in applications requiring strong fluorescence and efficient energy transfer (Figure 48).

X-aggregates, also known as cross-dipole aggregates, occur when the ETDMs are arranged in a crossed or perpendicular manner. In these aggregates, the energy splitting between the excited states becomes minimal as the rotation angle approaches 90º. According to Kasha's Rules, this minimal splitting results in spectral properties similar to those of monomers, including high fluorescence efficiency due to reduced exciton interactions (Figure 48).[295]

By adjusting the angles between 0 and 90 degrees in center of chiral molecules, it is possible to take advantage of both H-type and X-type aggregate properties. H-aggregates exhibit a splitting of energy levels, which can lead to a blue shift in absorption but reduced fluorescence. In contrast, X-aggregates can maintain high fluorescence efficiency and monomer absorption UV-Vis. By finding an intermediate angle, one can potentially balance these properties, achieving both energy level splitting, and therefore a bisignate in ECD and strong fluorescence in order to achieve CPL emissive H-type derivative aggregates.

USC
UNIVERSIDADE DE SANTIAGO DE COMPOSTELA

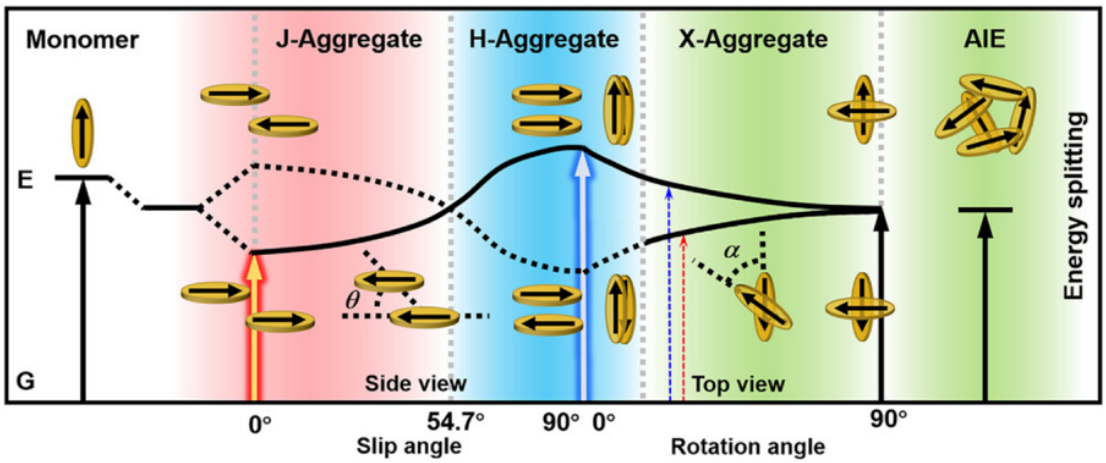


Figure 48. Excited states energy splitting diagram for molecular aggregates with J-, H- or X- Aggregates and AIE configuration. Reproduced from ref. 295 with permission from John Wiley and Sons (Copyright Clearance Center), copyright 2021

Oblique aggregates represent a less common arrangement where the TDMs are positioned at an oblique angle, typically between 60º and 120º. Kasha's Rules indicates that this configuration leads to two excitonically split absorption bands of nearly equal intensity. Oblique aggregates exhibit a broadened absorption profile, which is beneficial for light harvesting, and their equal intensity absorption bands are useful in quantum information science. The unique optical properties of oblique aggregates make them valuable for specific applications, although they are less frequently encountered compared to H- and J-aggregates (Figure 49).[296]

USC UNIVERSIDADE DE SANTIAGO DE COMPOSTELA

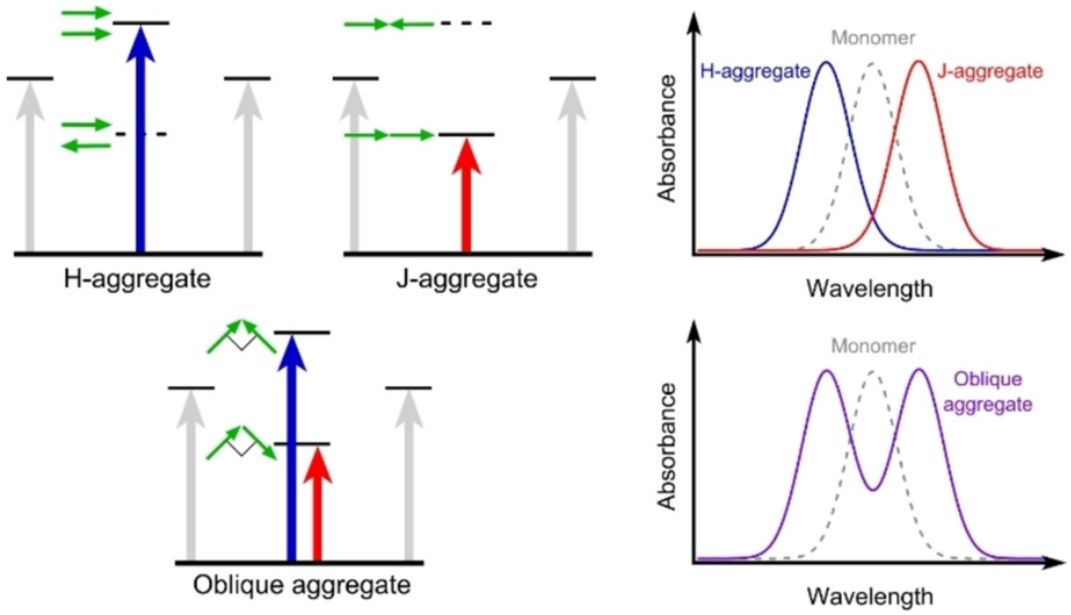


Figure 49. (Left) Diagrams for H-, J-, and oblique dimers with transition dipole moments. (Right) Absorption spectra for these aggregates and the monomer. Reproduced from ref. 296 with permission from John Wiley and Sons, copyright 2022

Understanding these concepts is key to design supramolecular aggregates. If the goal is to achieve emission or fluorescence, J-type aggregates are preferred as they stabilize the exciton interaction of the first excitation. This orbital overlap of ground and excited states, which stabilizes the excitation between symmetric or asymmetric orbitals, favors not only the excitation to the first state but also the emission from this state. In the case of H-type aggregates, emission is unfavorable because the first excitation does not involve orbital overlap, making it favorable only for the second excitation. If obtaining H-type aggregates is important for the system, the key is to introduce chirality, creating a polymer with a more favorable first excitation and, therefore, fluorescence. This aggregate lies midway between J-type and H-type aggregates, providing decent emission even without preferential exciton interaction from the first excitation (Figure 50).

USC
UNIVERSIDADE DE SANTIAGO DE COMPOSTELA

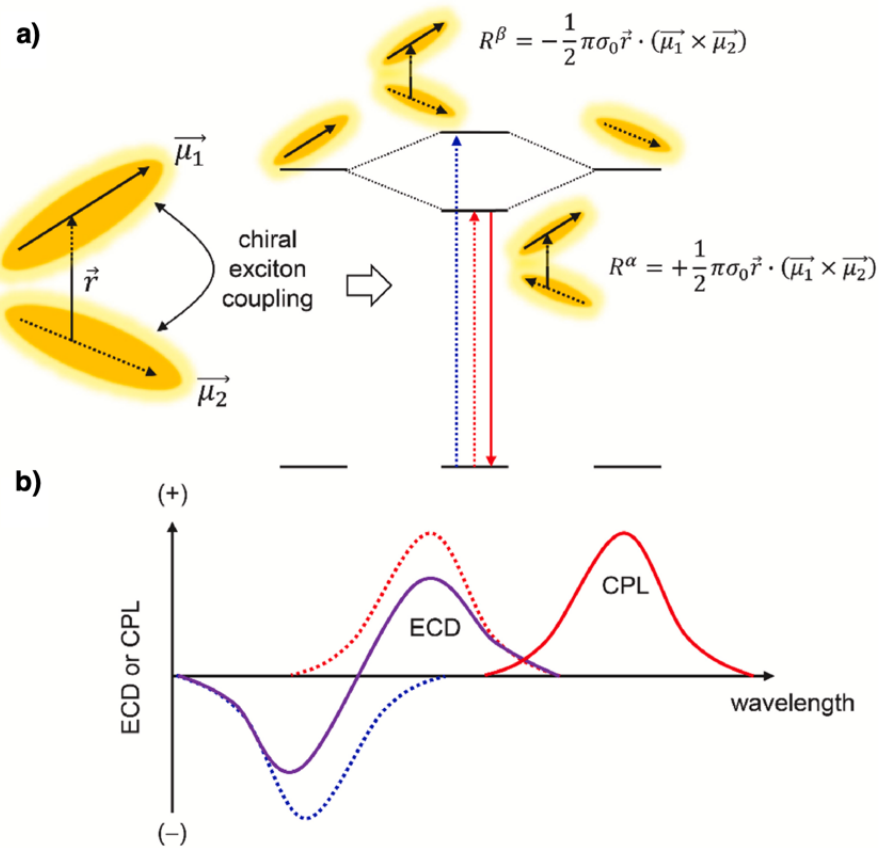


Figure 50. a) Asymmetric exciton coupling between two identical luminophores. b) Corresponding ECD (solid violet) and CPL (solid red) spectra, with dotted curves representing individual electronic absorption spectra. Reproduced from ref. 114 with permission from Elsevier (Copyright Clearance Center), copyright 2023

1.9.3. Energy Landscape and Pathway Complexity

Pathway complexity in supramolecular polymerization involves both thermodynamic and kinetic factors. Due to the difficulty of the complex pathway, research focused mainly on the thermodynamic aspects, which describe the most stable final structure in single component[297] or structures in polymorphisms.[298,299]

1.9.3.1. Consecutive Pathway

In consecutive pathways, the formation of the final structure involves multiple sequential steps, each influenced by kinetic factors. Würthner and coworkers have reported an example of a merocyanine dye (*R*)-**28** that initially forms dimers, which then convert into H1-aggregates, and finally into H2-aggregates.[300-302] This hierarchical

USC
DE SANTIAGO
DE COMPOSTELA

process shows how intermediate on-pathway kinetic products (H1-aggregates) are necessary steps toward the thermodynamically stable final product (H2-aggregates) (Figure 51).

Lag time (t_{50}) is the time required to assemble 50% of the monomers. In systems where the lag time decreases with increasing monomer concentration, the system follows a consecutive pathway. These systems require one or more on-pathway kinetic aggregates that will be interconverted into the most stable thermodynamic structure through structural rearrangement or the formation of higher-ordered architectures. If this transformation occurs at room temperature, the kinetic structure is considered metastable. On the other hand, if the transformation needs the addition of energy by increase of temperature, we denote this aggregate as kinetically trapped (Figure 51f).

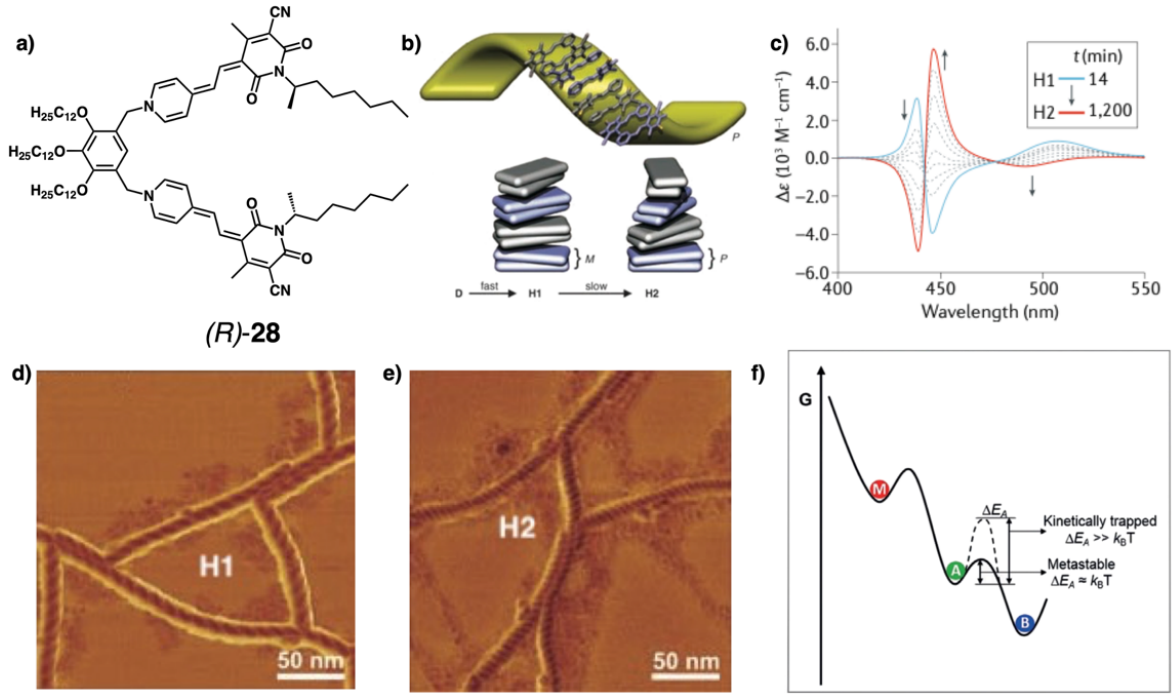


Figure 51. a) Chemical structure of (*R*)-**28** b) Schematic illustration of the left- to right-handed [(*M*) -> (*P*)] rearrangement between close neighboring dyes during the H1 -> H2 transition. c) Time-dependent CD spectra showing the transition from the initially formed H-aggregated species (H1) into the thermodynamically more stable H-aggregated species (H2) for dye (*R*)-**28** in a mixture of THF/MCH = 30:70 at 20 ºC (c_T = 10 μM). d and e) AFM phase imaging for (R)-**28** after 14 minutes, and 22 hours respectively. f) Energy landscape illustrating consecutive pathway. Reproduced from ref. 300 with permission from John Wiley and Sons (Copyright Clearance Center), copyright 2005

USC UNIVERSIDADE DE SANTIAGO DE COMPOSTELA

1.9.3.2. Competitive Pathway

In competitive pathways, different aggregation processes exist for the same monomers. In 2012, Prof. Meijer and coworkers incorporated the competition between kinetic and thermodynamic parameters in supramolecular polymerizations.[303,304] They used oligophenylene vinylenes (OPVs) derivatives, such as (*S*)-**29**.[305] This monomer can form a thermodynamically stable (*M*)-helix when cooled slowly, representing the thermodynamic pathway. However, under rapid cooling, a kinetically favored (*P*)-helix forms first (off-pathway), which is metastable. This (*P*)-helix must disassemble into monomers before it can convert into the thermodynamically stable (*M*)-helix due to the competitive pathway. This disassembly process increases the lag time with increased concentration (Figure 52).

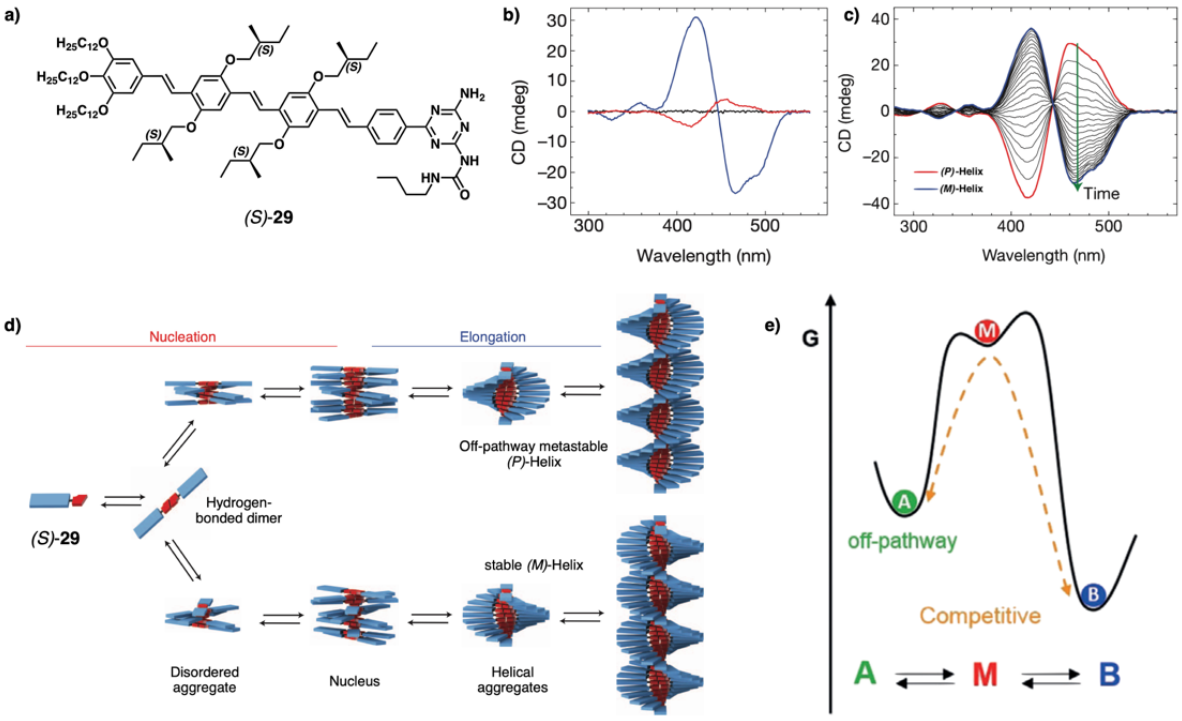


Figure 52. a) Chemical structure of (*S*)-**29**. b) ECD spectra of (*S*)-**29** in MCH in disassembled state (black line, 343 K), thermodynamically stable (M)-Helix (blue line, 273 K, 1K/min temperature drop) and mixture of stable (*M*)-helix and metastable (P)-Helix (red line, 273 K, fast temperature drop in ice bath). c) Stopped-flow ECD spectra acquired during conversion of (*S*)-**29** from metastable (P)-helix towards (*M*)-helix upon annealing at 298 K (mixing time < 10 ms, Δt = 1 s). d) Schematic representation of the aggregation pathways of (*S*)-**29**, including the growth of the two competing assemblies. e) Energy landscape illustrating competitive pathway. Reproduced from ref. 304 with permission from Springer Nature, copyright 2012

USC UNIVERSIDADE DE SANTIAGO DE COMPOSTELA

1.9.4. Chiral Supramolecular Aggregates Response to External Stimuli

Helical supramolecular polymers are not covalently bonded, so the presence of external stimuli can lead to the formation of a completely new aggregate. For example, cations can give rise to metallosupramolecular aggregates[306,307,308,309,310,311] and anions can stabilize new kinds of aggregates.[312] Additionally, oxidation,[313-315] light,[316-318] or pH,[319-322] among others[323] can isomerize or change the monomer structure or metal in metallosupramolecular aggregates, which produce a different stable type of aggregate (Figure 53).[25]

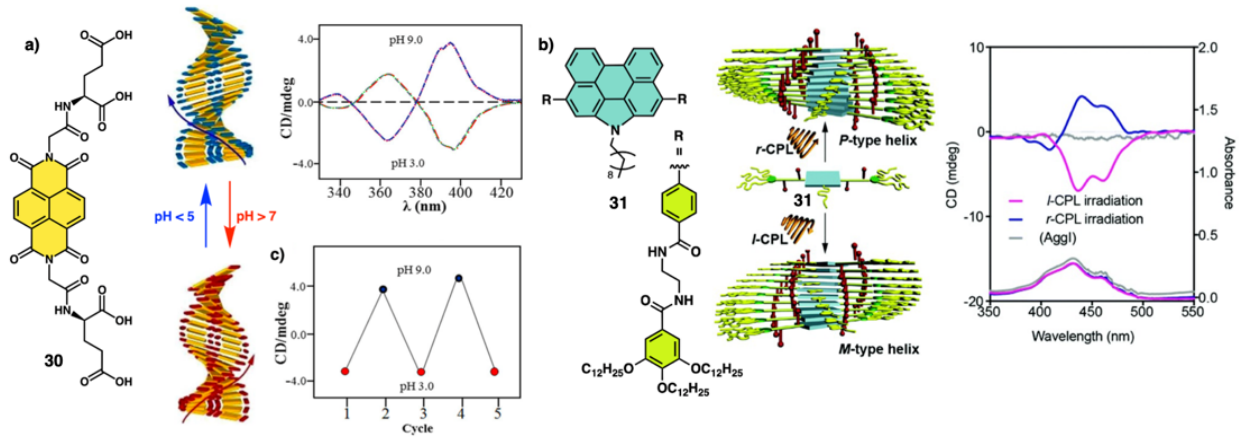


Figure 53. a) Structure of **30**, showing pH-tunable *P*/*M* helical senses and ECD spectra at pH 3 and 9. pH chiroptical switch of 30 after cycles at pH 3 and 9. b) Structure of **31**, asymmetry induction by CP light, and ECD spectra of resulting helical structures. Reproduced (a) from ref. 320 with permission from Springer Nature, copyright 2018. Reproduced (b) from ref. 323 with permission from Royal Society of Chemistry (Copyright Clearance Center), copyright 2020.

1.9.5. Chiral Amplification in Supramolecular Copolymers: Internal Stimuli

BTAs are the most extensively studied supramolecular polymers. They exhibit Majority Rules (MR) and Sergeants and Soldiers Effect (SaS) from point chirality in helical copolymers.[324] These molecules form supramolecular polymers stabilized by three hydrogen bonds between amide groups, with a distance of 2.1 Å. To optimize this interaction, the amide groups are tilted at 60º, leading to a helical assembly further stabilized by π-π stacking of 3.5 Å between aromatic groups.

USC UNIVERSIDADE DE SANTIAGO DE COMPOSTELA

SaS experiments, where chiral monomers can induce a predominant helical sense in a mixture of (*P*)- and (*M*)-helices, have shown promising results with BTAs. For example, the chiral molecule (*S*)-**33** can bias a racemic aggregate formed from achiral monomer **32** (Figure 54) towards an excess of one helical sense. The cooperative effect between monomers allows the stabilization of a single helical sense with a minimal number of Sergeants (10%).

BTAs have also been used to achieve MR Communication Mechanisms, demonstrating their ability to show chiral amplification. The MR effect can be examined by mixing two enantiomers, (*S*)-**23** and (*R*)-**23**, in varying ratios. Plotting the net helicity against the enantiomeric excess (Figure 54) reveals the induction of a single helical sense at an enantiomeric excess of 40%.

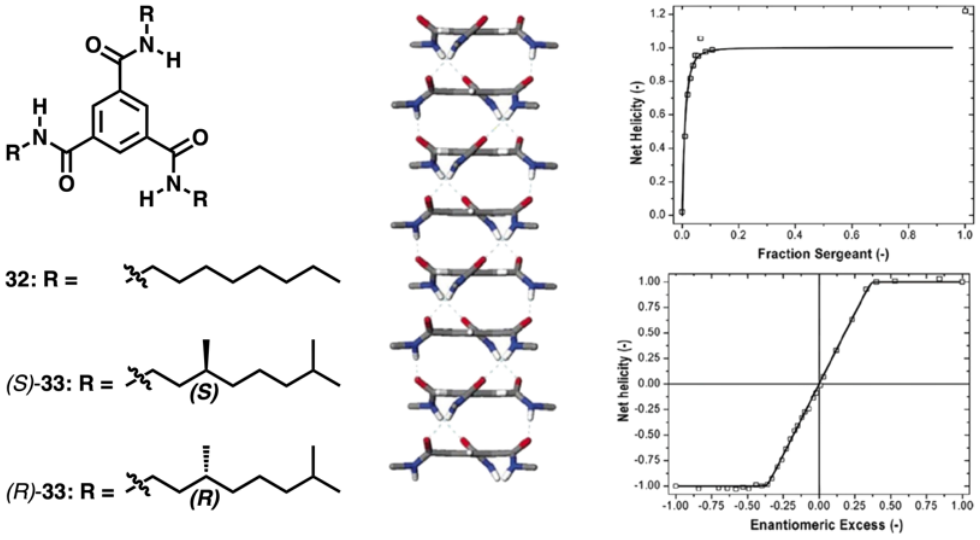


Figure 54. Chemical structure of BTAs **32** and **33**. Model of the right-handed helix for C_3-symmetrical BTAs. Net helicity variation in SaS and MR experiments with **22**, (*S*)-**23**, and (*R*)-**23**. Reproduced from ref. 324 with permission from American Chemical Society, copyright 2010

1.9.5.1. Blocky Communication Mechanisms

Classical Communication Mechanisms exist for random copolymers, but other situations can occur, such as Communication Mechanisms in blocky copolymers. We have studied the supramolecular copolymerization of *N*- and *C*-centered benzene-1,3,5-tricarboxamides (*N*- and *C*-BTAs) in methylcyclohexane solution and the solid state, revealing a distinct aggregation copolymerization that sets it apart from classical random copolymers. This structure exhibits a blocky architecture, differentiating it from random

USC DE COMPOSTELA

copolymers. While random supramolecular polymers often exhibit well-known Communication Mechanisms such as Majority Rules (MR) and Sergeants and Soldiers Effect (SaS), the interaction between *N*- and *C*-BTAs results in a unique blocky microstructure. This blocky arrangement is characterized by weaker, antiparallel hydrogen bonds between different BTA units, contrasting with the more uniform interactions seen in random copolymers (Figure 55a).[325]

In solution, the blocky microstructure is stabilized by an amide hydrogen-bond network, where both parallel and antiparallel hydrogen bonds contribute to the overall stability. DFT calculations reveal that any size of blocky copolymers, composed of 50% chiral *N*-BTAs (Sergeant) and 50% achiral *C*-BTAs (Soldier), is more stable than alternating or random arrangements for oligomers of eight units. This indicates that when copolymerization occurs, the BTAs tend to arrange in a blocky fashion. Furthermore, the smaller the block size, the greater the stability of the blocky copolymer. These findings highlight that blocky copolymers exhibit enhanced stability compared to other arrangements. This blocky arrangement was confirmed by a thermodynamic approach of the cooling curves with 5% of hetero-interactions while the others are homo-interactions, and therefore blocky structures in the copolymer. They also showed the Communication Mechanism Sergeants and Soldiers Effect upon cooling (Figure 55b).

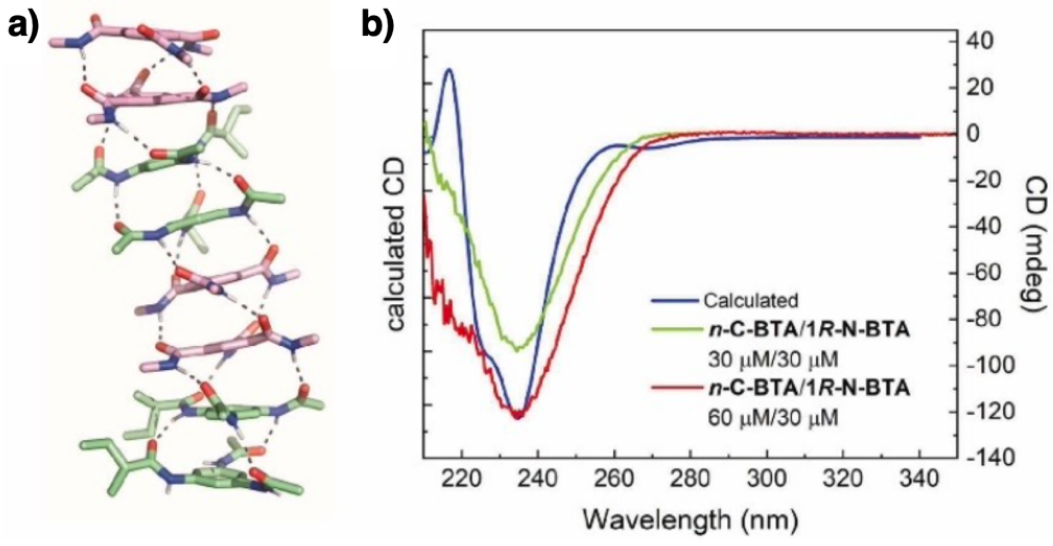


Figure 55. a) 3D structure of the optimized geometry for the lowest-energy copolymer. b) Comparison of the calculated (blue line) ECD spectra of an N-BTA/C-BTA octamer (blocky structure, 3 mismatches) with the measured spectra of copolymers comprising 1*R*-N-BTA (30 μM) and 30 μM n- C-BTA (green line) or 60 μM *n*-C-BTA (red line). Reproduced from ref. 325 with permission from John Wiley and Sons, copyright 2021

USC UNIVERSIDADE DE SANTIAGO DE COMPOSTELA

1.9.6. Non-Planar Cores and Multiple Helices

In the field of helical supramolecular polymers, it is possible for more than one helix to exist within a single structure. A central axis can give rise to two, three, or even more symmetric helices. Furthermore, the use of non-planar cores allows helices to exist with different symmetries.

For instance, consider the self-assembly of chiral allenes (Figure 56a), which follow a cooperative mechanism to form a supramolecular chiral aggregate. This aggregate consists of two coaxial helices: an internal helix described by the allene stack and an external helix composed of a 4-helix described by the four allene substituents. This supramolecular aggregate possesses six axially chiral elements within its structures: the allene, the allene stack (internal helix), and the stacks of the four allene substituents (external 4-helix).

Interestingly, slight variations in the magnitude of the tilting degree, while maintaining its *P*- or *M*-orientation (internal helix), can alter the orientation of the 4-axial motifs at the external helix. For example, (*P*)-**34** produces a supramolecular helix with a tilting angle (θ) of approximately 15º (P_{int}) and a $M_1/P_2/M_1'/P_2'$ orientation of the four axial motifs at the periphery (Figure 56b). On the other hand, (*P*)-**35** produces a supramolecular helix with a θ of approximately 23º (P_{int}) and a $P_1/P_2/P_1'/P_2'$ orientation of the four axial motifs at the external helix (Figure 56c). As a result, the ECD spectra and the AFM images of the (*P*)-**34** and (*P*)-**35** supramolecular aggregates, dominated by the **34** and **34'** substituents of the chiral allene, indicate opposite handedness, although the chirality of the building block and the orientation of the allene stack are the same.[326]

USC UNIVERSIDADE DE SANTIAGO DE COMPOSTELA

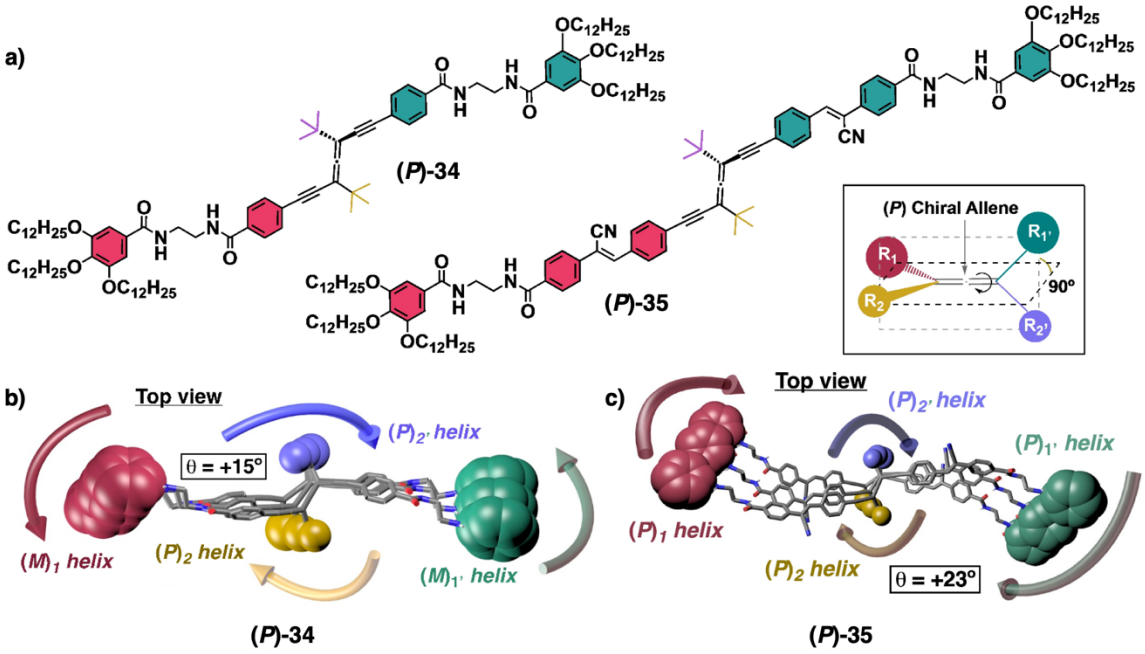


Figure 56. a) Chemical structures of chiral allenes (*P*)-**34** and (*P*)-**35**. b) Top view of a (P)-34 trimer stack optimized by DFT (B3LYP/6-31g**) highlighting the $M_1/P_2/M_1'/P_2$ 4-helix array. c) Top view of a (*P*)-**35** trimer stack optimized by DFT (B3LYP/6-31g**) highlighting the $P_1/P_2/P_1'/P_2$ 4-helix array. Reproduced from ref. 326 with permission from John Wiley and Sons, copyright 2024

USC UNIVERSIDADE DE SANTIAGO DE COMPOSTELA

USC
UNIVERSIDADE
DE SANTIAGO
DE COMPOSTELA

Chapter 2. Objectives

USC
UNIVERSIDADE
DE SANTIAGO
DE COMPOSTELA

USC
UNIVERSIDADE
DE SANTIAGO
DE COMPOSTELA

Chapter 2. Objectives

Helical polymers are of great interest due to their chirality control by dynamism. Polyphenylacetylenes (PPAs) are particularly interesting as they can induce helicity with dynamic properties in the helical sense and elongation. PPAs are covalent polymers with a polyenic backbone as an inner helix, while the external helix exhibits supramolecular stacking that is dynamic and can be explored to obtain novel materials with significant applications.

Similar to PPAs, supramolecular polymers stabilized by weak bonds can also respond to external stimuli. The nanostructuration of these systems is an important property as external stimuli can affect the packing, leading to new nanostructures and aggregates with novel properties.

The goal of this doctoral thesis is to explore the dynamic behavior and stability of PPAs and supramolecular polymers in presence of various external and internal stimuli. Another key focus is the formation of hybrid materials combining PPAs with metal nanoparticles, since their proximity can significantly affect the dynamic properties.

This work aims to investigate how different stimuli —such as temperature, metal nanoparticles in aqueous environments, metal ions, or internal factors like the copolymerization of chiral-chiral monomers— affect polymer dynamism. The degree of polymerization will be studied to determine if it alters the dynamic response of the system. Additionally, photochemical electrocyclization of oligomers will be explored as a potential route to trigger structural changes, while oxidative conditions (e.g., through metal ions) will be examined for their ability to induce radical formation.

Thermal Activation of Asymmetry Amplification Effects in Helical Polymer-Metal Complexes Chapter 3.1

Poly(phenylacetylene)s are known for their excellent dynamism in the presence of external stimuli. Salts have been described to interact with the pendant groups through the cation to stabilize specific conformations. In this work, we aim to describe how physical properties influence these interactions to understand the coordination between the cation and the pendant groups. The main goal is to determine whether this coordination is governed by thermodynamic parameters. In this sense, the correct

USC UNIVERSIDADE DE SANTIAGO DE COMPOSTELA

understanding of the system allows inducing coordination by playing with a second stimulus, the temperature. Therefore, we aim to modulate the first coordination stimulus with a second temperature stimulus to obtain a double stimuli-responsive sensor. PPAs that already respond to metals and then to temperature will be used to play with this coordination and apply it to copolymer series.

Publication associated with this objective: Manuel Fernández-Míguez, Emilio Quiñoá, Félix Freire,* *Angew. Chem. Int. Ed.* **2025**, *18*, e202503949.

Colorimetric Detector of Oxidizing Metal Ions by Anilide-Poly(phenylacetylene)s Chapter 3.2

Divalent or monovalent metals interact with pendants of PPA to give a chiroptical response. We aim to discover how other oxidation states of metals interact and to study if very oxidizing metals can induce a redox interaction with the PPA to give radicals. In this sense, we want to describe another use as a sensor for this homopolymer, not only for specific oxidation states but also for the oxidizing environment by the formation of organic radical compounds and therefore sensing by optical methods. The limit of detection has to be tested in order to obtain a material that provides better sensitivity than the already published examples, which is at the same time multisensory by optical and chiroptical techniques.

Publication associated with this objective: Manuel Núñez-Martínez[+], Manuel Fernández-Míguez[+], Emilio Quiñoá, Félix Freire,* *Nanoscale* **2025**, *17*, 4439–4443.

[+]These authors contributed equally to this work.

Dispute Between Chiral Comonomers to Induce Tunable Asymmetry Amplification Effects in Dynamic Helical Copolymers Chapter 3.3

Chiral-to-chiral Communication Mechanisms have already been explored, showing very good and unexpected results that demonstrated incredible communications in literature. Also, the activation of chiral monomers that act as Soldiers before activation and become Sergeants after activation by external stimuli was explored. In this project,

USC DE COMPOSTELA

we aim to create a chiral-chiral system in which one of the chiral monomers can be activated. In this idea, we will have in the same copolymer before activation a Sergeant-Soldier system. After activation, we could move to a Sergeant-Sergeant system in which we can expect the absence of communication or a new mechanism in which the role of the first Sergeant can be degraded. Therefore, we want to explore if we can obtain the first example of role degradation of a Sergeant in the same system only by external stimuli interaction. Also, we want to take advantage of the chapter 3.1 and apply temperature to this copolymer to play with the role of the Sergeants and promote and degrade the monomer role as we want in a switchable manner.

Synergistic Chiral Awakening: Cascade Sergeants and Soldiers Effect Through Double-Step Activation Chapter 3.4

Following the last play with roles in Sergeants and Soldiers Effect in chapter 3.3, we aim to use two Soldiers instead of two Sergeants. Two achiral Soldiers are known to have an absence of communication as there cannot be any chiral induction due to the symmetry of the system. Herein, in this project, we want to use an achiral Soldier copolymerized with a Chiral Soldier. In homopolymers, no chirality exists; nevertheless, we want to investigate if the copolymerization of this axially racemic system can exert new Communication Mechanisms. Also, we want to investigate if the communication between monomers affects not only the helical sense/chirality but also the elongation. In this sense, we want to investigate if these two Soldiers, in case of communication, show any difference in the command on the elongation, playing with monomers that induce very different levels of compression.

Optical and Chiroptical Stimuli-Responsive Chiral AgNPs@H-Leu-Poly(phenylacetylene) Nanocomposites in Water Chapter 3.5

MNPs tend to aggregate, and to overcome this problem, we can use organic coatings to produce nanocomposites. Numerous studies in the literature attribute the protection of MNPs to weak supramolecular interactions with the organic coating. Inspired by this, and by previous examples from the group on PPA-MNP hybrids in organic solvent, the primary objective of this chapter is to prepare the first example of

USC UNIVERSIDADE DE SANTIAGO DE COMPOSTELA

water-soluble AgNPs@PPA nanocomposites using supramolecular interactions. The objective is to use PPA water-soluble polymers that contain NH_2/NH_3^+, which allows the modification of this population with the pH. These PPAs are also dynamic, adding another layer of control. All together, we have the perfect example of different ways to modulate the mechanism of the synthesis of the nanocomposites and play with their response to external stimuli.

Publication associated with this objective: Manuel Fernández-Míguez, Manuel Núñez-Martínez, Esteban Suárez-Picado, Emilio Quiñoá, Félix Freire,* Optical and Chiroptical Stimuli-Responsive Chiral AgNPs@H-Leu-Poly(phenylacetylene) Nanocomposites in Water, *ACS Nano* **2024**, *18*, 28822–28833.

Deciphering the Emergence of Axial Chirality and Stimuli-Responsiveness in PPAs: From Oligomers to Polymers Chapter 3.6

The oligomerization of PPAs has been reported in the literature using various methods. In this work, our goal is to generate multiple oligomer series from different monomers at varying degrees of polymerization, in order to study how chain length influences ECD and UV-Vis spectra. We will also apply fitting models to predict how size affects these properties and to estimate the chain length of already synthesized polymers or oligomers. Additionally, we aim to investigate how an increased proportion of terminal groups —resulting from shorter chain lengths— impacts these characteristics. Finally, we will explore reversals via photochemical electrocyclization (PEC) by irradiating the oligomers and using established equations to determine the screw sense excess, assessing how it varies with the degree of polymerization.

Size Dependent Stimuli-Responsive Properties of Foldamers and Helical Polymer of Chiral PPAs Obtained via Degree of Polymerization Control or by Controlled Helix Unwind Chapter 3.7

After the correct description of oligomers in the last chapter 3.6, we aim to study how the oligomerization of very compressed structures affects the dihedral angle ω_1. It is expected that big polymers with a very small proportion of terminal parts and a big amount of hydrogen bonds and π-π stacking have a more compressed and better

USC UNIVERSIDADE DE SANTIAGO

interacting structure than small oligomers where the solvent can get inside. Also, irradiation is known to form benzenes in the polyenic backbone, therefore reducing the folded size of a polymer to behave as an oligomer. We want to investigate if the irradiation in PEC studies can induce oligomer like formation, and how the dynamic response to irradiation and oligomerization affects the helical sense and molecular stretching.

Intercalation Matters: Complex Communication in Supramolecular Copolymers Chapter 3.8

Supramolecular helical polymers are obtained from the non-covalent interaction of building blocks. The presence of these reversible and weak interactions provides these polymers with a dynamic character, not observed in their covalent counterparts. With this information in mind and taking advantage of the study of communication processes in copolymers exhibiting Sergeants and Soldiers Effect, we decided to evaluate the self-assembly properties of bipyridine with bisamides. The chiral and achiral monomers will be composed of a short chiral moiety and a π-conjugated core that aggregate by π-stacking and hydrogen bonding. While multiple thermodynamic structures can exist through polymorphism, our objectives include investigating complex pathways of the copolymers by playing with the energy landscape to achieve both kinetic and thermodynamic control. No previous examples exist for pathway complexity of Communication Mechanisms in supramolecular copolymers. By manipulating solvents, we aim to influence kinetic species to explore metastable or kinetically trapped Communication Mechanisms. Additionally, we will search for not only classic Communication Mechanisms between Soldiers and Sergeants, such as the Sergeants and Soldiers Effect, but also other Communication Mechanisms by time-dependent, and temperature-dependent studies.

USC
UNIVERSIDADE DE SANTIAGO DE COMPOSTELA

USC
UNIVERSIDADE
DE SANTIAGO
DE COMPOSTELA

Chapter 3. Results

USC
UNIVERSIDADE
DE SANTIAGO
DE COMPOSTELA

USC
UNIVERSIDADE
DE SANTIAGO
DE COMPOSTELA

3.1. Thermal Activation of Asymmetry Amplification Effects in Helical Polymer-Metal Complexes

The results of this chapter have been published by Angewandte Chemie International Edition as:

Manuel Fernández-Míguez,[a] Emilio Quiñoá,[a] Félix Freire,[b]* Thermal Activation of Asymmetry Amplification Effects in Helical Polymer-Metal Complexes, *Angew. Chem. Int. Ed.* **2025**, *64*, e202503949. DOI: 10.1002/anie.202503949.

Affiliations

[a]Centro Singular de Investigación en Química Biolóxica e Materiais, Moleculares (CiQUS) and Departamento de Química Orgánica, Universidade de Santiago de Compostela 15782 Santiago de Compostela (Spain)

[b]CINBIO and Departamento de Química Orgánica, Campus Lagoas-Marcosende, Universidade de Vigo E-36310 Vigo (Spain)

The information of this Chapter has been reproduced with permission from John Wiley and Sons.

Abstract

Dynamic helical polymers such as poly(phenylacetylene)s (PPAs) exhibit different asymmetry amplification effects, e.g. helix inversion or screw-sense induction, in the presence of different external stimuli such as temperature, solvents or metal ions that usually operate independently through interaction with the pendant on the monomer repeating units. In this work, we will demonstrate that the helical structure of a chiral PPA can be tamed by playing with two different external stimuli such as temperature and metal ions. Thus, when a metal ion salt is delivered to a chloroform solution of a chiral PPA to generate a chiral PPA monomer repeating unit (m.r.u.)/M^{n+} complex in a ratio of 1.0/<0.5 mol/mol, a temperature-responsive material is obtained. Interestingly, when the temperature is lowered to about 278-283 K, the metal ion uncomplexes, which recovers the initial helical structure adopted by the PPA. This complexation/decomplexation between the chiral PPA and the metal ions is fully reversible and triggers different asymmetry amplification effects —helix inversion, screw-sense induction or Sergeants and Soldiers, among others—, allowing the creation of a temperature-responsive helical polymer-metal complex (HPMC) from a metal-responsive helical polymer.

USC UNIVERSIDADE DE SANTIAGO

USC
UNIVERSIDADE
DE SANTIAGO
DE COMPOSTELA

3.1.1. Precedents

Dynamic helical polymers are an interesting family of helical polymers due to their stimuli-responsive properties, where the helical sense, the elongation, or both structural parameters can be altered by the presence/absence of an external stimulus. Of these polymers, poly(phenylacetyelene)s (PPAs)[9,25,29,30,54,71,160,169,237,241,245,327-337] have been widely studied due to the high flexibility of the polyene backbone —low activation energy barrier between the P and M screw senses—, and the versatility of the phenylacetylene polymerization reaction with Rh(I) catalysts, which allow obtaining the polymers in high yield and high content of cis double bonds independently of the functional groups (polar and non-polar) introduced as substituents in the monomer.[36]

Thus, to create a stimuli-responsive helical polymer based on a PPA, it is necessary to design a monomer whose conformational composition or macromolecular structure is altered by a given stimulus. Thus, anilide,[338] sulfonamide[339,340], or urea[341] groups have been used to interact with anions,[257-261,342-346] while aza crown ethers,[347,348,349] cyclodextrins[350-353], or amide groups[354-356] have been used to interact with cations. PPAs bearing chiral amino or chiral acid groups on the pendant have been used to create pH-responsive helical polymers, where the conformational composition in the pendant is altered by the protonation/deprotonation of the functional group.[59,334] Achiral PPAs bearing amino or acid functional groups have been used to interact with chiral molecules (acids or amines), where the *P* or *M* screw-sense excess adopted by the PPA depends on the absolute configuration of the chiral molecule used as external stimulus.[159,357-360]

Temperature-responsive helical polymers have been created using thermoresponsive tertiary amines,[238,361] peptides[362], or dendrons[363] as pendants, where temperature changes led to conformational changes in the pendant resulting in structural changes in the helical PPA.[91,250,253,364,365]

In general, homochiral PPAs are designed to interact with a specific external stimulus (input) producing an asymmetry amplification effect in the helical scaffold that can be easily monitored by electronic circular dichroism (ECD) (output). To sense two different external stimuli, such as metal ions and temperature, using a single chiral PPA, the best approach is to design a copolymer in which the two components interact selectively with either metal ions or temperature. However, to follow this approach it is

USC UNIVERSIDADE DE SANTIAGO DE COMPOSTELA

necessary to consider the different Communication Mechanisms that arise between the two components of the copolymer in the presence and absence of the different stimuli.

Herein, we will demonstrate that, in general, a metal ion-responsive chiral PPA can be rendered temperature-sensitive once complexed with a metal ion (Figure 57).

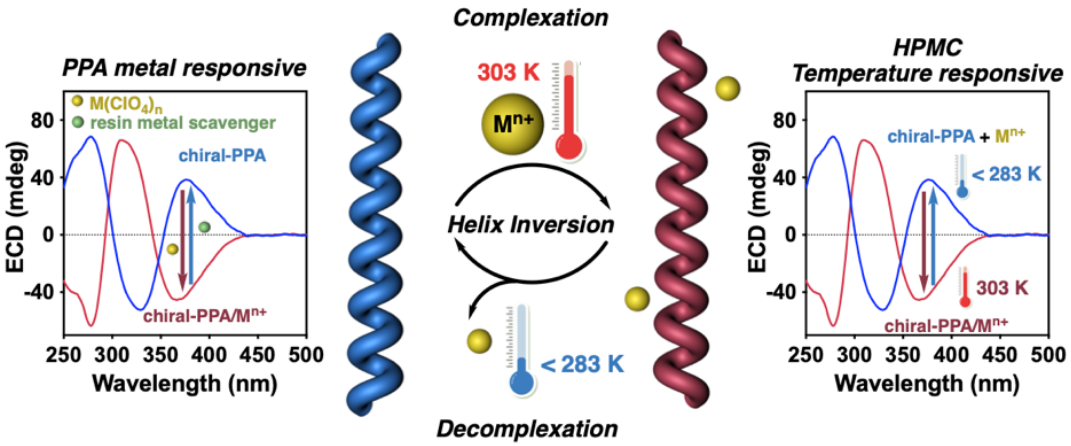


Figure 57. Helix inversion of a dynamic helical polymer induced by complexation with metal ions or by metal decomplexation of a helical polymer-metal complex induced by temperature changes.

In chiral PPAs, the helical structure adopted by the polymer and its screw-sense excess is dictated by the presence of a preferred conformation at the chiral pendant group, which through steric effects promotes the formation of a *P* or *M* helical structure. This helical construction is usually stabilized by additional π-π and/or H-bonding interactions between the pendant groups at the n^{th} and $(n+2)^{th}$ (*cis-transoidal*) or n^{th} and $(n+3)^{th}$ (*cis-cisoidal*) positions. However, the low energy barrier between the *P* and *M* helical screw senses adopted by the PPA backbone allows to trigger asymmetry amplification effects through a cooperativity effect when the conformational composition at the pendant groups of a few monomer repeating units is altered by the presence of an external stimulus such as metal ions.[42,43,70,171,267,269,281,366,367]

Nevertheless, if a second external stimulus such as temperature can activate/deactivate (On/Off) the interaction of the PPA with the first stimulus, *i.e.* metal ions —complexation/decomplexation—, a dual stimuli-responsive helical polymer-metal complex (HPMC) can be created from a stimuli-responsive helical polymer. To generate a temperature-responsive helical polymer-metal complex based on a metal ion-responsive chiral PPA it is necessary to consider the structural changes produced in the helical polymer after complexation with metal ions —*i.e.* helical inversion—, the

polymer/Mn+ ratio in the helical polymer-metal complex, the supramolecular forces that stabilize the helix, and the cooperativity effect.

3.1.2. Discussion

To test our hypothesis, five different chiral PPAs with metal-responsive properties have been selected from the literature: two anilide-PPAs —poly-(*S*)-**1** and poly-(*R*)-**2**— and three benzamide-PPAs —poly-(*S*)-**3**-**5**— (Figure 58).[92,102,169,171] These polymers show different asymmetry amplification effects when confronted with metal ions, such as screw-sense induction or helix inversion effects.

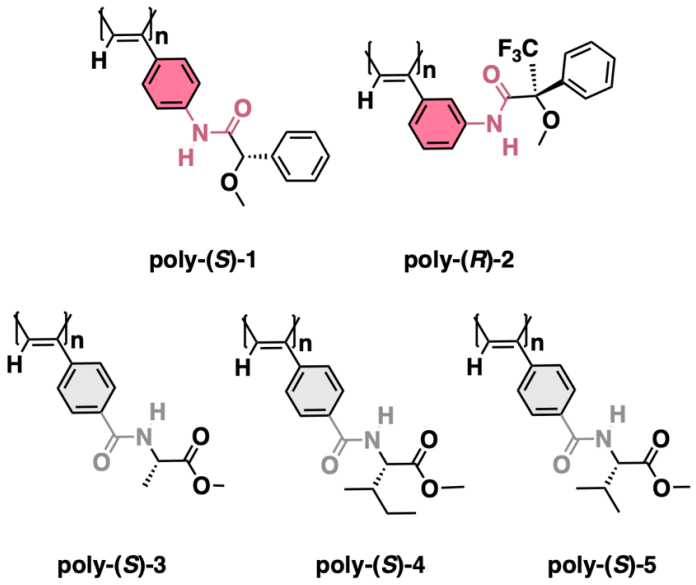


Figure 58. Chemical structures of anilide- and benzamide-PPAs used in this study.

Furthermore, these polymers comprise the necessary requirements to perform these studies:

i) Well-known conformational changes in the pendants caused by the presence/absence of metal ions.

ii) Asymmetry amplification effects, where small amounts of metal ions are needed to trigger them.

iii) Well-known secondary structures where the helical scaffolds are stabilized by a combination of steric effects and supramolecular forces.

USC DE SANTIAGO DE COMPOSTELA

The different chiral PPAs [poly-(*S*)-**1**, poly-(*R*)-**2**, poly-(*S*)-**3**, poly-(*S*)-**4**, poly-(*S*)-**5**] were prepared according to literature.

Among the anilide-PPAs, the most interesting polymer for carrying out these studies is poly-(*S*)-**1**. This polymer shows an axially racemic structure —electronic circular dichroism (ECD) = 0 in the vinylic region (400 nm)— when dissolved in chloroform due to an equal population of P and M helices in equilibrium. This fact is due to the existence of two preferred conformers in the pendant group —synperiplanar (*sp*, *M*-helix, $ECD_{400}<0$) or antiperiplanar (*ap*, *P*-helix, $ECD_{400}>0$) carbonyl and methoxy groups— that induce opposite helical senses (Figure 59). However, this polymer shows the ability to interact with monovalent (Li^+, Na^+, Ag^+) and divalent (Ba^{2+}, Ca^{2+}, Mg^{2+}, Zn^{2+}, Mn^{2+}, Ni^{2+}, Co^{2+}, Pb^{2+}) metal ions in different ways, triggering opposite asymmetry amplification effects.

Thus, while monovalent metal ions stabilize the ap conformer in the pendant through coordination to the carbonyl group and a cation-π interaction with the aryl ring of the pendant, divalent metal ions stabilize the *sp* conformation through chelation with the carbonyl and methoxy groups of the pendant (Figure 59).[42,43,171,267,366] Furthermore, these asymmetry amplifications with monovalent and divalent metal ions occur with a small amount of the external stimulus, *i.e.*, at a poly-(*S*)-**1** m.r.u./M^{n+} 1.0/< 0.5 mol/mol ratio, indicating that the asymmetry amplification occurs through a cooperativity effect. This fact indicates that not all pendant groups in the polymer chain need to interact with the external stimulus. This interaction occurs between a few of monomer repeating units and metal ions, which propagates the new helical sense induced by the external stimulus to the rest of the polymer chain.

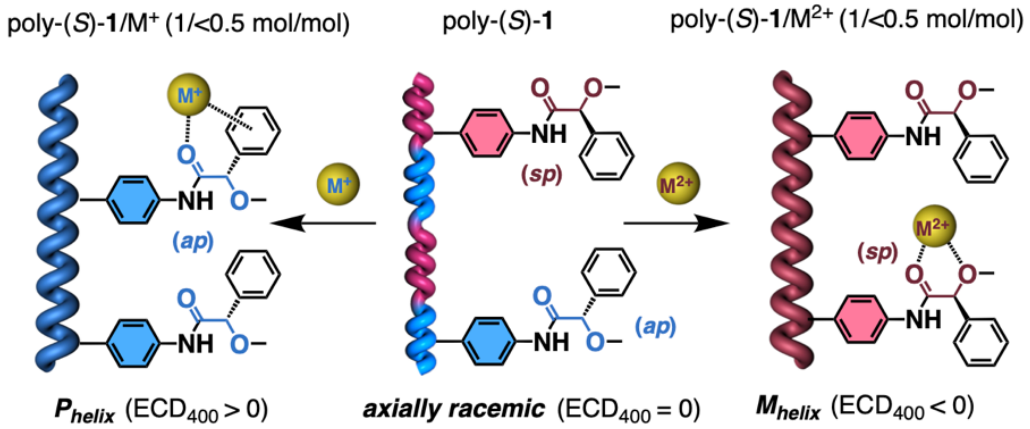


Figure 59. *P* and *M* screw-sense excesses induced in poly-(*S*)-**1** (axially racemic) after complexation with monovalent and divalent metal ions.

Thus, several vials containing a chloroform solution of poly-(*S*)-**1** (c= 0.3 mg/mL) were prepared and different equivalents of a methanolic solution of $LiClO_4$ and $Ca(ClO_4)_2$ (10 mg/mL) were added to obtain poly-(*S*)-**1**/M^{n+} in mol/mol ratios of 1.0/0.4 and 1.0/0.2 respectively. As expected, at 303 K the poly-(*S*)-**1**/Li^+ complex induced a *P* helix (ECD_{400}> 0) in the polymer, while the poly-(*S*)-**1**/Ca^{2+} complex induced the opposite helical sense (*M* helix, ECD_{400}< 0).

Next, variable temperature (VT) ECD studies were carried out over a range of 303-268 K. Interestingly, as the temperature is decreased, the ECD spectra decay to zero in the vinyl region (ECD_{400}= 0), indicating the presence of an axially racemic poly-(*S*)-**1**. The ECD traces obtained below 278 K for poly-(*S*)-**1**/Li^+ and poly-(*S*)-**1**/Ca^{2+} are identical to that obtained for a chloroform solution of poly-(*S*)-**1** in the absence of metal ions, indicating decomplexation of metal ions at low temperature.

Heating-cooling cycles of chloroform solutions of poly-(*S*)-**1**/Li^+ and poly-(*S*)-**1**/Ca^{2+} —in 1.0/0.4 mol/mol (λ= 379 nm) and 1.0/0.2 mol/mol (λ = 390 nm) ratios respectively— were carried out at 0.1 K·min^{-1} (Figure 60 and Figure 61) showing, in all cases, non-sigmoidal curves indicative that the asymmetry amplification towards the *P* (poly-(*S*)-1/Li^+) and *M* (poly-(*S*)-**1**/Ca^{2+}) screw senses follows a cooperative process. Moreover, a negligible thermal hysteresis was found between the heating a cooling curves obtained for poly-(*S*)-**1**/Li^+ and poly-(*S*)-**1**/Ca^{2+} complexes (Figure 60d and Figure 61d), denoting that the asymmetry amplification by coordination with metal ions occurs under thermodynamic control. The complexation and decomplexation process triggered by temperature changes is fully reversible. At 303 K, complexation with metal ions induces the same excess of *P* or *M* screw-senses. Below 278 K, decomplexation occurs, restoring the axially racemic helix.

USC UNIVERSIDADE DE SANTIAGO DE COMPOSTELA

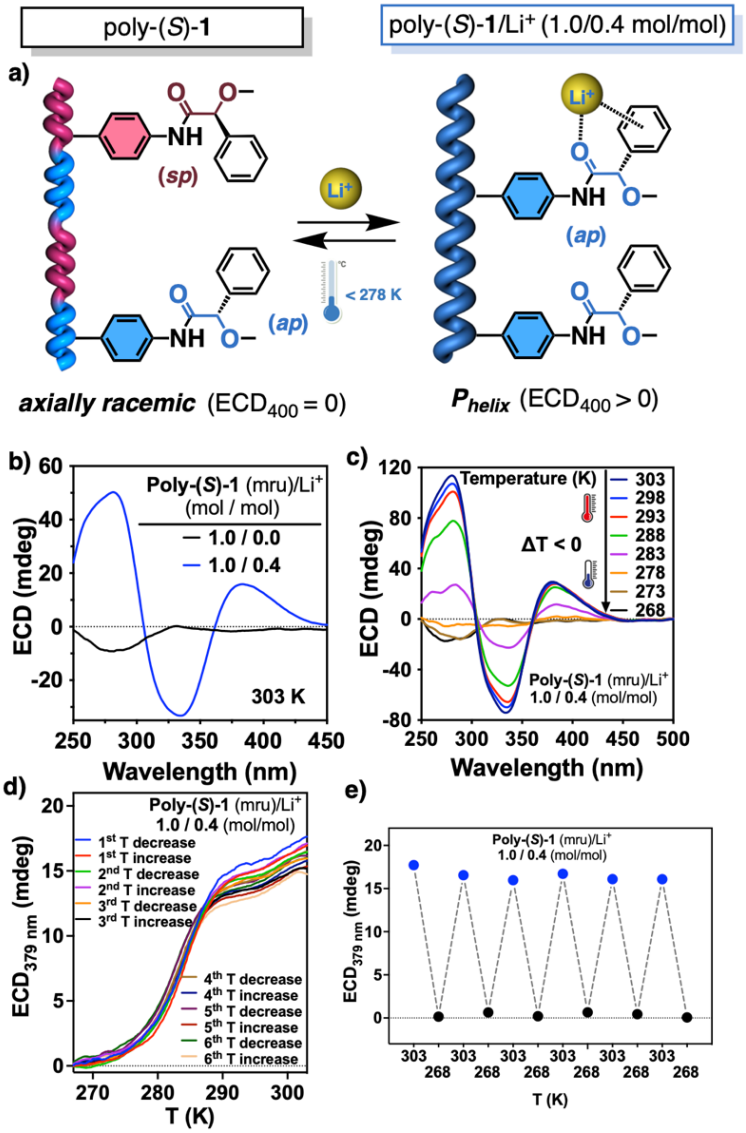


Figure 60. a) Graphical representation and (b) ECD studies of the Li⁺-responsiveness of poly(*S*)-**1** to generate poly(*S*)-**1**/Li⁺ complex in a 1.0/0.4 mol/mol ratio, (c) followed by temperature response studies of the HPMC. d) Heating/cooling cycles of a poly(*S*)-**1**/Li⁺ complex monitored by ECD. e) ECD vs temperature studies for a poly(*S*)-**1**/Li⁺ complex showing the reversibility of the process after several cycles. ([Poly-(*S*)-**1**]= 0.3 mg/mL $CHCl_3$, $Li(ClO_4)$= 10 mg/mL MeOH, 0.1 K·min^{-1}, poly(*S*)-**1**/Li⁺ at 1.0/0.4 mol/mol ratio).

To demonstrate that the metal ion is released from the polymer at low temperatures, IR experiments at different temperatures and VT-UV-Vis studies were carried out for poly-(*S*)-**1** m.r.u./Li⁺ and poly-(*S*)-**1** m.r.u./Ca^{2+} complexes in 1.0/0.4 mol/mol and 1.0/0.2 mol/mol ratios respectively. Interestingly, the UV-Vis spectra of poly-(*S*)-**1** m.r.u./Li⁺ and poly-(*S*)-**1** m.r.u./Ca^{2+} at 303 and 268 K are different, being those obtained at 268 K analogous to that obtained for poly-(*S*)-**1** in the absence of metal ions. Furthermore, comparison of the IR spectra obtained for the polymer-metal complexes at room

USC DE COMPOSTELA

temperature and 268 K, with those obtained for poly-(*S*)-**1** in the absence of the metal ions, shows that in poly-(*S*)-**1**/Li^+ and poly-(*S*)-**1**/Ca^{2+} complexes the carbonyl group is coordinated to the metal ion at room temperature (red shift of the C=O band), while no effect is observed at 268 K (Figure S18 and Figure S19).

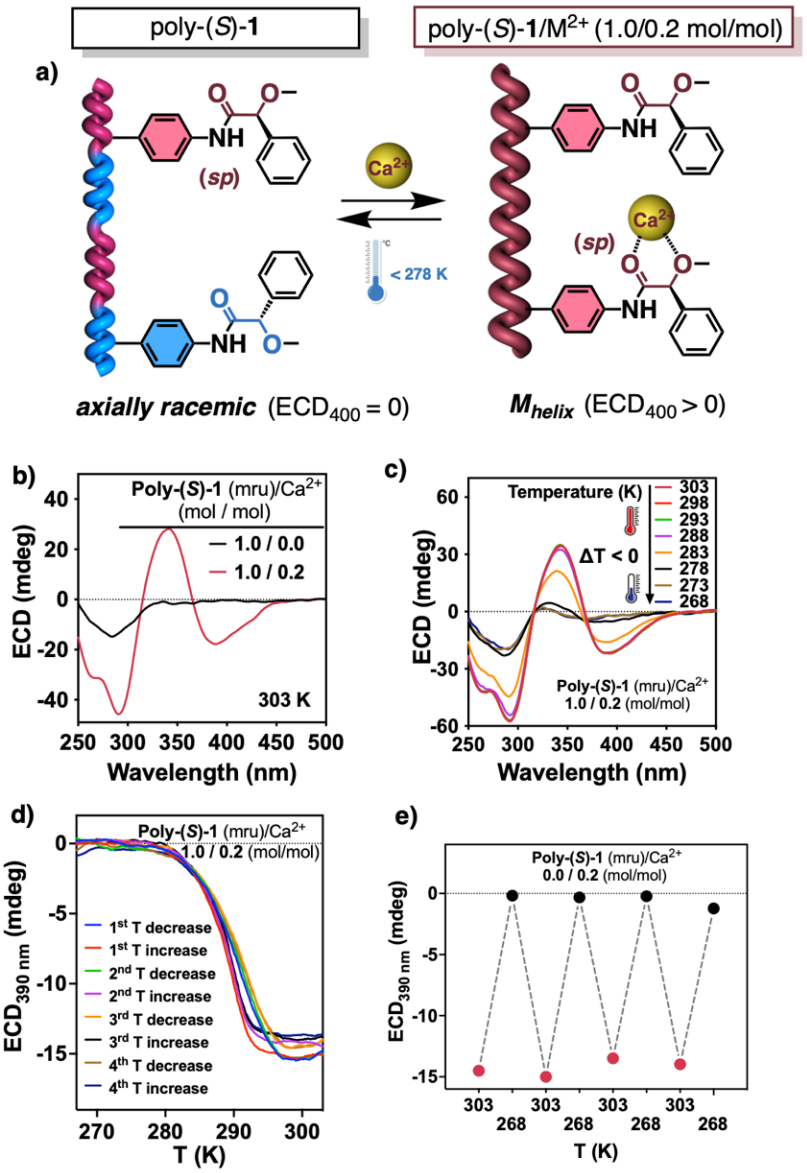


Figure 61. a) Graphical representation and (b) ECD studies of the Ca^{2+}-responsiveness of poly(*S*)-**1** to generate poly(*S*)-**1**/Ca^{2+} complex in a 1.0/0.2 mol/mol ratio, (c) followed by temperature response studies of the HPMC. d) Heating/cooling cycles of a poly(*S*)-**1**/Ca^{2+} complex monitored by ECD. e) ECD vs temperature studies for a poly(*S*)-**1**/Ca^{2+} complex showing the reversibility of the process after several cycles. ([Poly-(*S*)-**1**]= 0.3 mg/mL $CHCl_3$, $Ca(ClO_4)_2$= 10 mg/mL MeOH, poly(*S*)-**1**/Ca^{2+} 1.0/0.2 mol/mol ratio).

To further corroborate that metal decomplexation occurs at low temperatures, acetylacetone (acac) (2000 equiv) was added to a chloroform solution poly-(*S*)-**1** m.r.u./Ca^{2+} complexes in a 1.0/0.2 mol/mol ratio. Interestingly, while at room temperature

USC UNIVERSIDADE DE COMPOSTELA

the *P* and *M* helices induced in the polymer by the metal ions are not affected by the presence of acac, when the temperature is decreased to 278 K, the ECD becomes null, being impossible to recover the initial *P* or *M* helix when heated again to 303 K (Figure 62). This fact indicates that when the metal ion is detached from the polymer in the HPMC, the acac traps the metal ions in the solution and therefore they are no longer available to form HPMC.[42,171,366]

USC
UNIVERSIDADE DE SANTIAGO DE COMPOSTELA

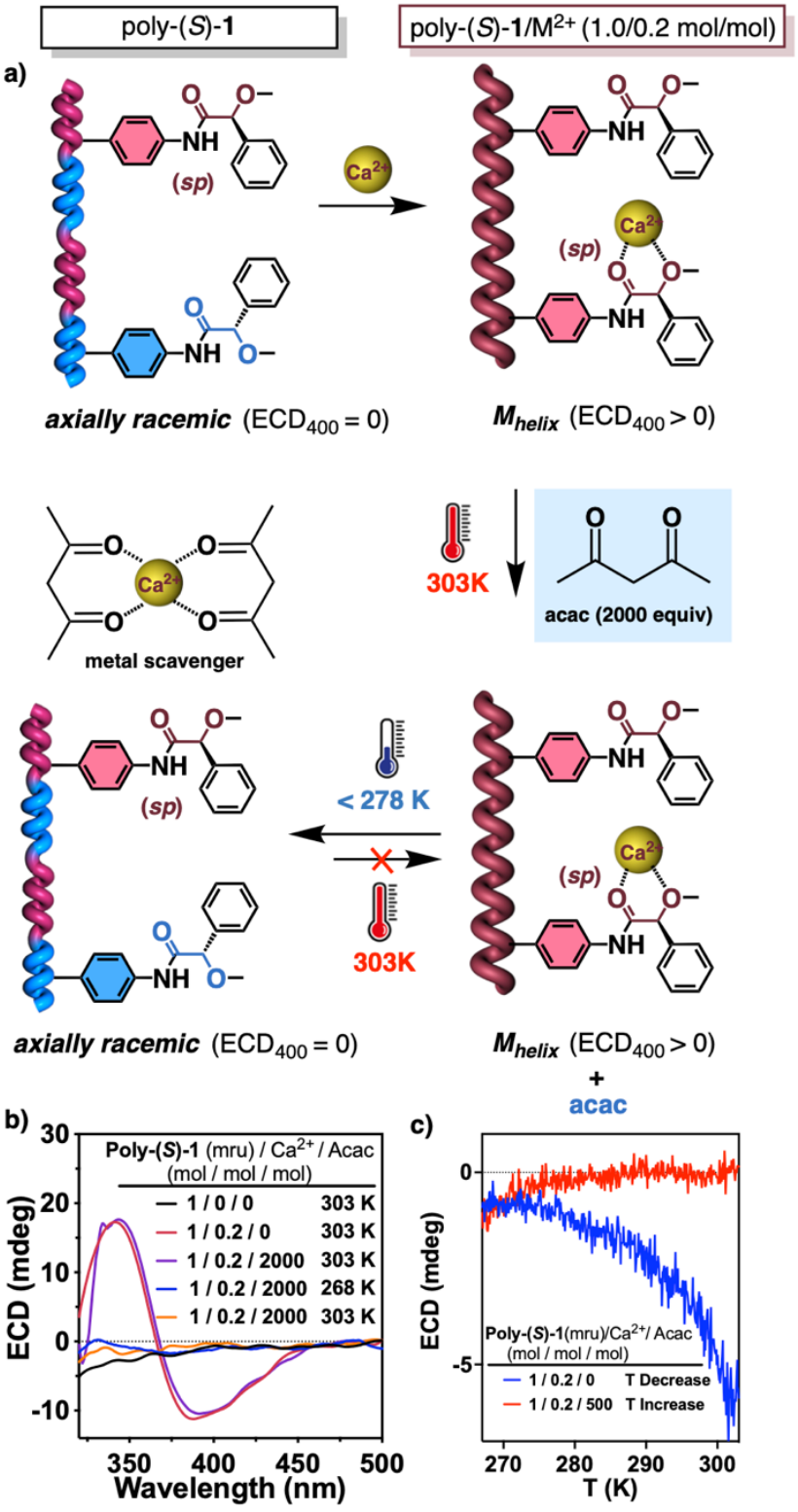


Figure 62. a) Graphical representation and (b-c) ECD studies of the response of poly(*R*)-**1** to Ca^{2+} to form poly(*S*)-**1**/Ca^{2+} at 1.0/0.2 mol/mol ratio followed by the addition of 2000 equiv of acac at room temperature and a temperature change to 283 K to determine the complexation/decomplexation of poly(*S*)-**1**/Ca^{2+} upon temperature changes. ([Poly-(*S*)-**1**]= 0.3 mg/mL $CHCl_3$, $Ca(ClO_4)_2$= 10 mg/mL MeOH, 0.1 K·min^{-1}, poly(*S*)-**1**/Ca^{2+} at 1.0/0.2 mol/mol ratio).

USC
DE SANTIAGO
DE COMPOSTELA

With all this information in hand we can state that complexation of poly-(*S*)-**1** with metal ions is a temperature-dependent equilibrium process, being the non-coordinated form of the polymer [poly-(*S*)-**1**] the most enthalpically stable structure favored at low temperatures, while the formation of HPMC is mainly entropically favored at higher temperatures. Thus, the VT-ECD data for poly-(*S*)-**1**/Li^+ was fitted to the van't Hoff equation[368-372] to obtain the thermodynamic parameters of the proposed equilibrium —ΔH= 275.09 kJ·mol^{-1} and ΔS= 0.9134 kJ·mol^{-1}·K^{-1}— (Figure 63).

Thus, the helical structure adopted by a chiral-PPA such as poly-(*S*)-**1**, an anilide-PPA, consisting of a *cis-cisoidal* helix, is stabilized by H-bond and π-π interactions between the anilide groups and the aryl rings at the n^{th}, n^{th}+3 positions. On the other hand, the axially racemic helical sense (mixture of *P* and *M* helices in equal population) adopted by poly-(*S*)-**1** is a consequence of two major conformers in the chiral pendant that place the carbonyl and methoxy groups antiperiplanar (*ap*) and synperiplanar (*sp*) orientations, respectively. These two conformers of the pendants introduce different steric effects, which induce opposite helical senses in the polyene backbone resulting in an axially racemic polymer. When a metal ion is added to a polymer solution, the conformational composition in the pendant changes, adopting either a preferred *ap* or *sp* conformation by interaction with monovalent or divalent metal ions, respectively. This conformational change in the pendant results in an asymmetry amplification at poly-(*S*)-**1**, which adopts a *P* helix in the presence of monovalent metal ions while an *M* helix is induced by divalent metal ions. Moreover, the supramolecular interactions that stabilize the initial helices are disrupted in the presence of metal ions. As the temperature decreases, intramolecular H-bond and π-π supramolecular interactions that stabilize the initial helical structure —enthalpic helix— are favored, leading to the decomplexation of the metal ion. To corroborate this hypothesis DFT calculations were performed on a model system consisting of the poly-(*S*)-**1**/Li^+ complex and a mixture of poly-(*S*)-**1** and Li^+ with no interaction between the two components. To reduce the number of atoms, our model system for the helical poly-(*S*)-**1** consists of three twisted conjugated double bonds describing a helical structure and where two pendant groups were introduced, one in *ap* conformation and the other in *sp* conformation, describing an n^{th}, n^{th}+3 helical structure stabilized by intrapendant supramolecular forces. Li^+ was computed as lithium perchlorate in methanol (3 MeOH molecules), while for the poly-(*S*)-**1**/Li^+ complex, to the model compound for poly-(*S*)-**1**, an additional Li^+ ion was coordinated to one of the

USC UNIVERSIDADE DE SANTIAGO DE COMPOSTELA

pendants. Moreover, the two pendant groups were introduced with a preferred *ap* conformation.

ClO_4^- counterion and methanol molecules were also considered in the HPMC to maintain the same number of atoms in the coordinated and non-coordinated form of the poly-(*S*)-**1** and Li(ClO_4) mixture. Then, the geometry and frequency calculations were optimized using the wb97xd functional method and the 6-311++g(d,p) basis set for the three model systems: poly-(*S*)-**1**, lithium perchlorate in methanol, and HPMC (see ESI).[373] Theoretical calculations show the same trend for the thermodynamic parameters with positive values of ΔH and ΔS —ΔH= 18.56 kJ·mol^{-1} and ΔS= 0.1150 kJ·mol^{-1}·K^{-1}—. The values obtained, experimentally and theoretically, are different in magnitude due to the different size of the molecules compared. Although the proposed and fitted chemical equilibrium models are the same, experimentally there are effects such as cooperativity that the simplified equilibrium model fails to capture. Interestingly, the representation of the theoretical and experimental Gibbs energy difference as a function of temperature shows the same trend, with ΔG being positive at low temperatures and negative at high temperatures (Figure 63).

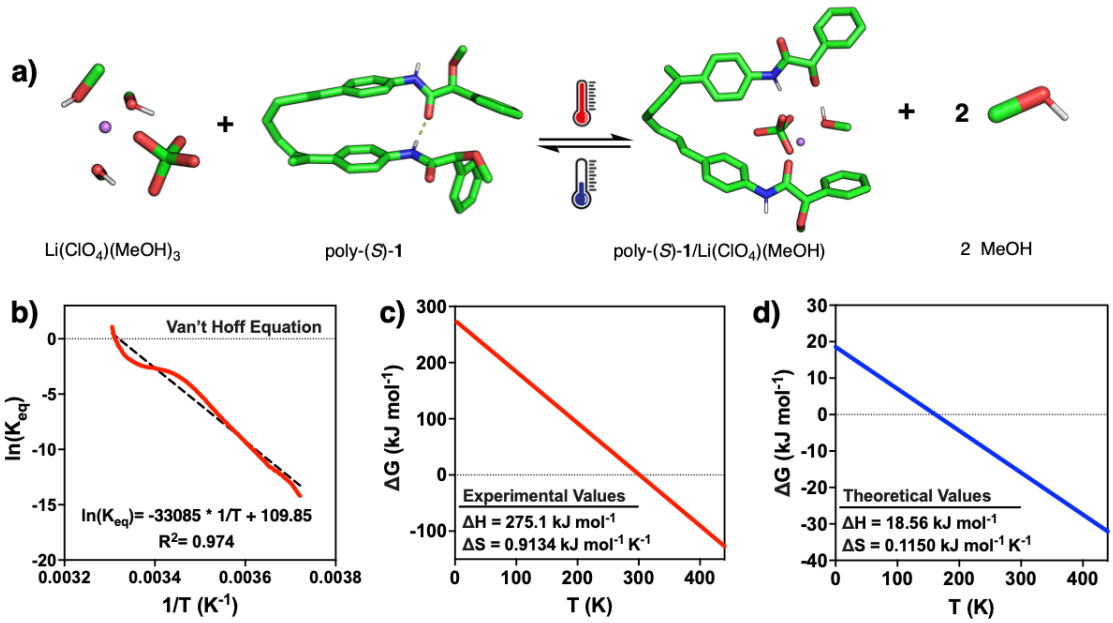


Figure 63. a) Proposed chemical equilibrium of the complexation and decomplexation and DFT optimized structures. b) van't Hoff equation fit of a VT-ECD cooling curve of poly-(*S*)-**1**/Li$^+$. c) Free energy values calculated from the entropy and enthalpy of the van't Hoff fit. d) Free energy values calculated from the entropy and enthalpy of the DFT calculations.

USC UNIVERSIDADE DE SANTIAGO DE COMPOSTELA

To extend this thermal behavior to other HPMCs based on chiral PPAs showing different asymmetry amplification effects, VT-ECD studies were carried out for solutions of poly-(*R*)-**2**, poly-(*S*)-**3**, poly-(*S*)-**4**, and poly-(*S*)-**5** in chloroform and their corresponding HPMCs. ECD studies of chloroform solutions of these polymers (c= 0.3 mg/mL) at 303 K show that they all adopted a preferred screw-sense due to the presence of a major conformer in solution.

This screw-sense excess is enhanced at lower temperatures due to a further stabilization of the preferred conformer, which can be easily monitored by ECD by an increase in the magnitude of the ECD spectra (Figure S2). By adding a perchlorate salt (c= 10mg/mL MeOH), such as $Ag(ClO_4)$, to a chloroform solution of poly-(*R*)-**2** (c= 0.3 mg/mL), and $Li(ClO_4)$ or $Ca(ClO_4)_2$ to chloroform solutions of poly-(*S*)-**3**, poly-(*S*)-**4**, poly-(*S*)-**5** (c= 0.3 mg/mL), the corresponding HMPCs were obtained in 1.0/0.4 mol/mol ratios. ECD studies revealed a helix inversion of the chiral PPAs, as evidenced by ECD traces with opposite signs compared to the corresponding homopolymer in the absence of metal ions.

ECD measurements were then performed at 268 K for the chloroform solutions of the different HPMCs. In all cases, the ECD spectra obtained correspond to that obtained for the homopolymer in the absence of the metal ion, indicating that in all HPMCs the decomplexation of the metal ion occurs at low temperatures (see Figure 64 for Ag^+ and Li^+ and experimental section for Ca^{2+}). Furthermore, when the temperature is increased up to 303 K, HPMC is recovered indicating the reversibility of the process (see Figure 64 for Ag^+ and Li^+ and experimental section for Ca^{2+}), demonstrating that in all these cases, chiral PPAs act as metal ion-responsive polymers that can be converted into thermo-responsive helical polymers once they are complexed with a metal ion.

USC UNIVERSIDADE DE SANTIAGO DE COMPOSTELA

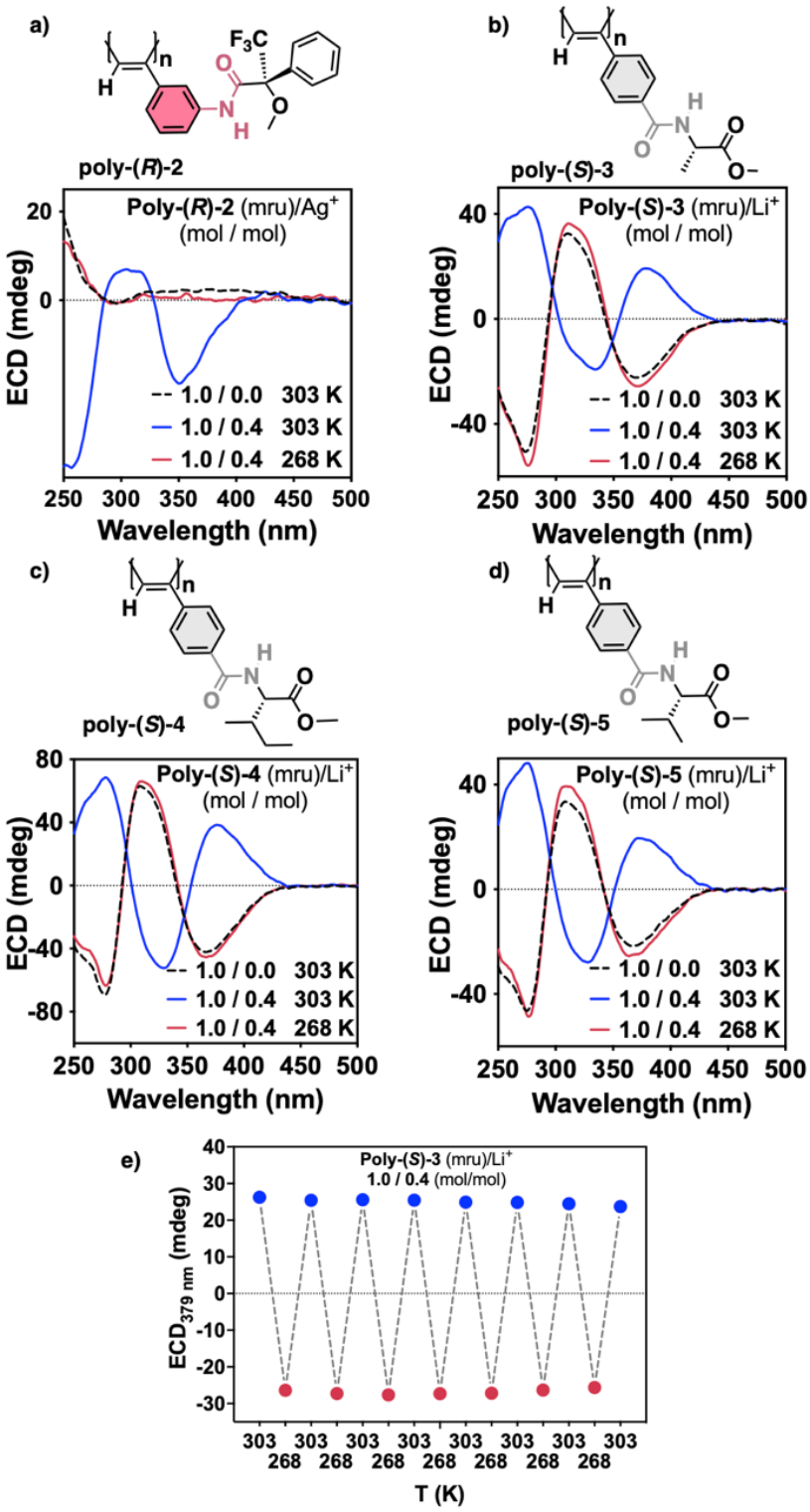


Figure 64. a) Ag^+ response of poly(*R*)-**2** and temperature response of poly(*R*)-**2**/Ag^+ complex in 1.0/0.4 mol/mol ratio. b-d) Li^+ response of poly(*S*)-**3**-**5** and temperature response of poly(*S*)-**3**-**5** /Li^+ complexes in 1.0/0.4 mol/mol ratios. e) Seven consecutive ON/OFF cycles of the poly(*S*)-**3** /Li^+ complex formation by temperature changes. [PPA c= 0.3 mg/mL $CHCl_3$, $MClO_4$= 10 mg/mL MeOH (M^+= Ag^+, Li^+) 0.1 $K{\cdot}min^{-1}$].

USC
UNIVERSIDADE DE SANTIAGO DE COMPOSTELA

Furthermore, to demonstrate that this thermal behavior of PPA-based HPMCs can be extrapolated to systems other than homopolymers, where other asymmetry amplification effects are found, such as the Sergeants and Soldiers Effect (SaS) in copolymers, decomplexations studies were performed on a copolymer where the SaS effect is triggered by the presence of a metal ion.

To perform these studies, poly[(*S*)-**1**$_{0.5}$-*co*-**6**$_{0.5}$] was chosen as a model compound (Figure 65). From literature it is known that this copolymer behaves as axially racemic when dissolved in $CHCl_3$.[367] However, by adding $Li(ClO_4)$ or $Ca(ClO_4)_2$ to a chloroform solution of poly[(*S*)-**1**$_{0.5}$-*co*-**6**$_{0.5}$] (c=0.3 mg/mL), to prepare a HPMC in a poly[(*S*)-**1**$_{0.5}$-*co*-**6**$_{0.5}$]m.r.u./M^{n+} 1.0/0.2 mol/mol ratio, it is possible to induce either a *P* or an *M* helical sense in the copolymer due to the fixation of different preferred conformations in the chiral moiety [*ap* with Li^+ (*P* helix, ECD_{400}> 0) and *sp* with Ca^{2+} (*M* helix, ECD_{400}< 0)]. Thereafter, the chiral information is effectively transmitted to the achiral component of the copolymer through a SaSt (Figure 65) as inferred from the ECD studies.

VT-ECD shows, as expected, that the axially racemic copolymer is recovered at 265 K, while measuring the ECD spectra again at 303 K, the *P* helix is recovered for the poly[(*S*)-**1**$_{0.5}$-*co*-**6**$_{0.5}$]/Li^+ complex and the *M* helix for the poly[(*S*)-**1**$_{0.5}$-*co*-**6**$_{0.5}$]/Ca^{2+} complex.

USC UNIVERSIDADE DE SANTIAGO DE COMPOSTELA

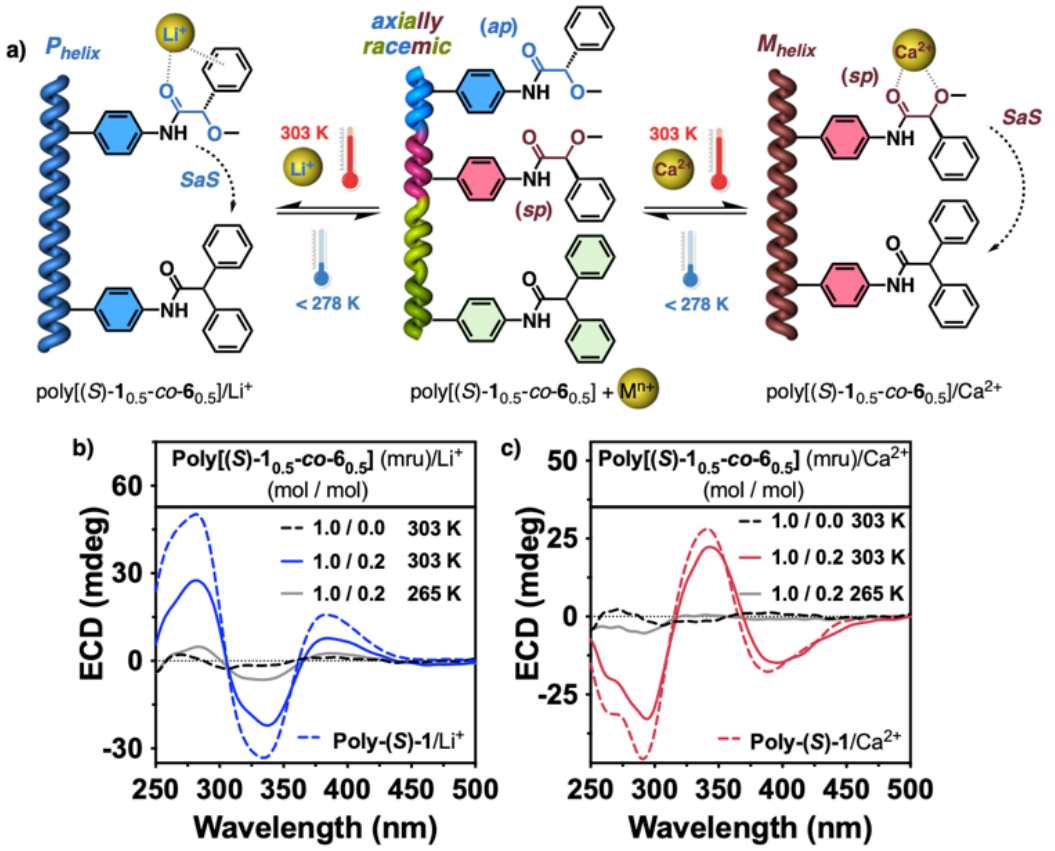


Figure 65. a) *P* and *M* helical induction of the axially racemic poly[(*S*)-**1**$_{0.5}$-*co*-**6**$_{0.5}$] copolymer by interaction with monovalent (Li^+) and divalent (Ca^{2+}) metal ions. b) Li^+-responsiveness of poly[(*S*)-**1**$_{0.5}$-*co*-**6**$_{0.5}$] and temperature responsiveness of poly[(*S*)-**1**$_{0.5}$-*co*-**6**$_{0.5}$]/Li^+ compared with poly-(*S*)-**1**/Li^+ 1.0/0.2 mol(m.r.u.)/mol. c) Ca^{2+}-responsiveness of poly[(*S*)-**1**$_{0.5}$-*co*-**6**$_{0.5}$] and temperature responsiveness of poly[(*S*)-**1**$_{0.5}$-*co*-**6**$_{0.5}$]/Ca^{2+} compared with poly-(*S*)-**1**/Ca^{2+} 1.0/0.2 mol(m.r.u.)/mol [PPA c= 0.3 mg/mL $CHCl_3$, $M(ClO_4)_n$= 10 mg/mL MeOH (M^{n+}= Ca^{2+}, Li^+) 0.1 K·min^{-1}].

3.1.3. Conclusions

In conclusion, in this work we have demonstrated, using different polymers, that metal ion-responsive chiral-PPAs can be used as temperature-responsive materials when complexed to metal ions under the right conditions forming HPMCs. Thus, while the chiral-PPA suffers an asymmetry amplification effect upon complexation with a metal ion at room temperature (303 K), this asymmetry amplification can be reverted to the initial state by decreasing the temperature of the HPMC solution.

Interestingly, this thermal responsive behavior of HPMCs was demonstrated for diverse chiral-PPAs with distinct functional groups, and where different asymmetry amplification effects, such as helix inversion, screw-sense enhancements or racemization, are triggered by complexation/decomplexation with metal ions. This

USC UNIVERSIDADE DE SANTIAGO

thermal behavior is also observed in PPA copolymers where a SaS can be triggered On/Off by adding metal ions followed by temperature changes. These results open a new scenario in the preparation of stimuli-responsive materials based on other stimuli-responsive materials, and where the driving force is a switchable deactivation of the first stimulus response by a second stimulus.

USC
UNIVERSIDADE DE SANTIAGO DE COMPOSTELA

3.2. Colorimetric Detector of Oxidizing Metal Ions by Anilide-Poly(phenylacetylene)s

The results of this chapter have been published by Nanoscale as:

Manuel Núñez-Martínez[+,a] Manuel Fernández-Míguez[+,a] Emilio Quiñoá,[a] Félix Freire,[a]* Colorimetric detector of oxidizing metal ions by anilide-poly(phenylacetylene)s, *Nanoscale* **2025**, *17*, 4439–4443. DOI: 10.1039/D4NR03662J.

[+]These authors contributed equally to this work.

Affiliations

[a]Centro Singular de Investigación en Química Biolóxica e Materiais, Moleculares (CiQUS) and Departamento de Química Orgánica, Universidade de Santiago de Compostela 15782 Santiago de Compostela (Spain)

The information of this Chapter has been reproduced with permission from Royal Society of Chemistry.

Abstract

Poly(phenylacetylene)s (PPAs) bearing para-substituted anilide pendant groups are sensitive to the presence of oxidizing metal ions such as Cu^{2+}, Hg^{2+}, Fe^{3+}, Au^{3+}, or Ce^{4+} due to a redox reaction between the anilide-PPA and the metal ion. Using a library of six different PPAs containing diverse chiral pendant groups connected to the PPA backbone through the N (anilide) or C (benzamide) atoms of an amide group used as a linker, it was found that anilide-PPAs are sensitive to oxidizing metal ions. In these polymers, and through a redox reaction, a radical species is delocalized along the polyene backbone, resulting in a color change of the solution from yellow to blue. UV-Vis, ECD, IR, EPR, XPS and computational studies were carried out to demonstrate the electron transfer from PPA to the oxidizing metal once the metal coordinates with the anilide of the polymer.

USC UNIVERSIDADE DE SANTIAGO DE COMPOSTELA

USC
UNIVERSIDADE
DE SANTIAGO
DE COMPOSTELA

3.2.1. Precedents

Dynamic helical polymers, such as poly(phenylacetylene)s (PPAs),[9,25,29,30,54,160,327-333,374] are macromolecular helical switches whose *P* or *M* helix sense and elongation can be modulated by the presence of external stimuli such as pH, temperature, chiral additives, anions among others.[43,70,171,243] Other interesting external stimuli to play with the response dynamic helical polymers are metal ions.[375] Heavy metal contamination of water and soil is a major problem found worldwide, which is associated to severe health problems. Thus, during the last years several analytical methods have been used to detect and remove these metals.[376-378] Helical polymers such as PPAs have been designed to interact with these chemical agents form helical polymer-metal complexes (HPMCs), where coordination of the metal ions with the pendant groups can occur in different ways —coordination, chelation—. As a result, various conformations in the pendant can be stabilized either by a single metal under various conditions, or by different metals, giving rise in one case or the other to the selective adoption of a *P* or *M* helical structure with different degrees of stretching. Moreover, it is also possible to play with the translocation of the metal in the pendant group by tuning the oxidation state of the metal, which can also lead to helical structural changes (sense, elongation). HMPCs have been used not only to detect metals or tune the helical structures of PPAs but have also been used to create nanospheres and PPA@metal nanoparticle (MNP) nanocomposites with dynamic macroscopic chiralities.[234,236,237,334] The selective *P* or *M* screw sense induction of PPAs by different metal ions have been used to create a three-state switchable chiral stationary phase, where by using a single chiral column (stationary phase) and different metal ion salts in the mobile phase it is possible to change the retention time of different racemates depending on the helical sense adopted by the PPA.[6] Moreover, PPAs have been also employed as chiral catalyst in asymmetric synthesis.[379,380]

In this work we want to explore the interactions of PPAs with oxidizing metal ions such as Cu^{2+}, Hg^{2+}, Fe^{3+}, Au^{3+}, and Ce^{4+} and where the PPA should act as a reducing agent. These metals, e.g. Hg^{2+}, Cu^{2+}, or Fe^{+3} are associated to healthy problems such as mental and neurological functions (Hg^{2+}),[381,382] Alzheimer, gastrointestinal problems and osteoporosis (Cu^{2+}),[383,384] respiratory problems, nervous system or affect the reproductive or digestive systems (Fe^{3+}).[385,386]

USC UNIVERSIDADE DE SANTIAGO DE COMPOSTELA

3.2.2. Discussion

From the literature, it is known that PPAs can produce radical species along the polymer backbone[44,80-82] when subjected to high pressures[44] or mechanochemical grinding.[83] Hence, we hypothesized that PPAs containing a suitable pendant group can interact with oxidizing metals to form a PPA radical cation that can be further delocalized along the polyene backbone. To perform these studies, a library of six different chiral PPAs (Figure 66) was chosen due to their stimuli-responsive properties towards metal ions. Thus, while in the case of poly-(**4**-**6**) the P/M helical sense can be controlled by the presence/absence of metal ions, regardless of the valence of the metal ion, poly-**1** can adopt a *P* or *M* helix in the presence of metal ions with different valence (Figure 67).[43,171] Poly-(**1**-**6**) polymers were prepared according to the literature. Vials containing solutions of poly-(**1**-**6**) in THF (c= 0.1 mg/mL) were then prepared and 1 equiv of $Fe(ClO_4)_3$ (10 mg/mL, THF) was added to each. Interestingly, vials containing anilide-PPAs, poly-(**1**-**3**), immediately showed a color change from yellow to deep blue. The other vials containing benzamide-PPAs [poly-(**4**-**6**)] did not show any color change after the addition of $Fe(ClO_4)_3$.

This color change was ascribed to the presence of a delocalized radical ion along the polyene chain. IR studies revealed, as expected, the coordination of Fe^{3+} ions with carbonyl groups ($\tilde{\nu}$ = 10 cm^{-1}) (Figure S32).

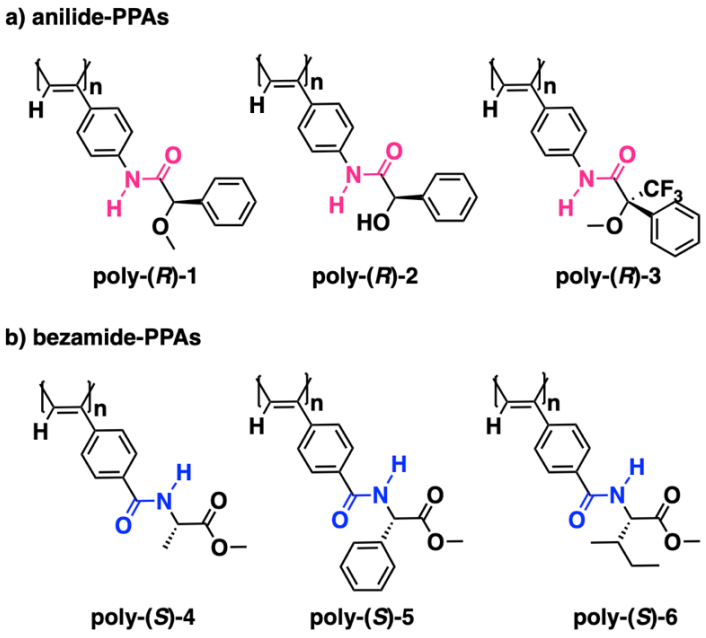


Figure 66. Chemical structure of (a) anilide- and (b)- benzamide-PPAs.

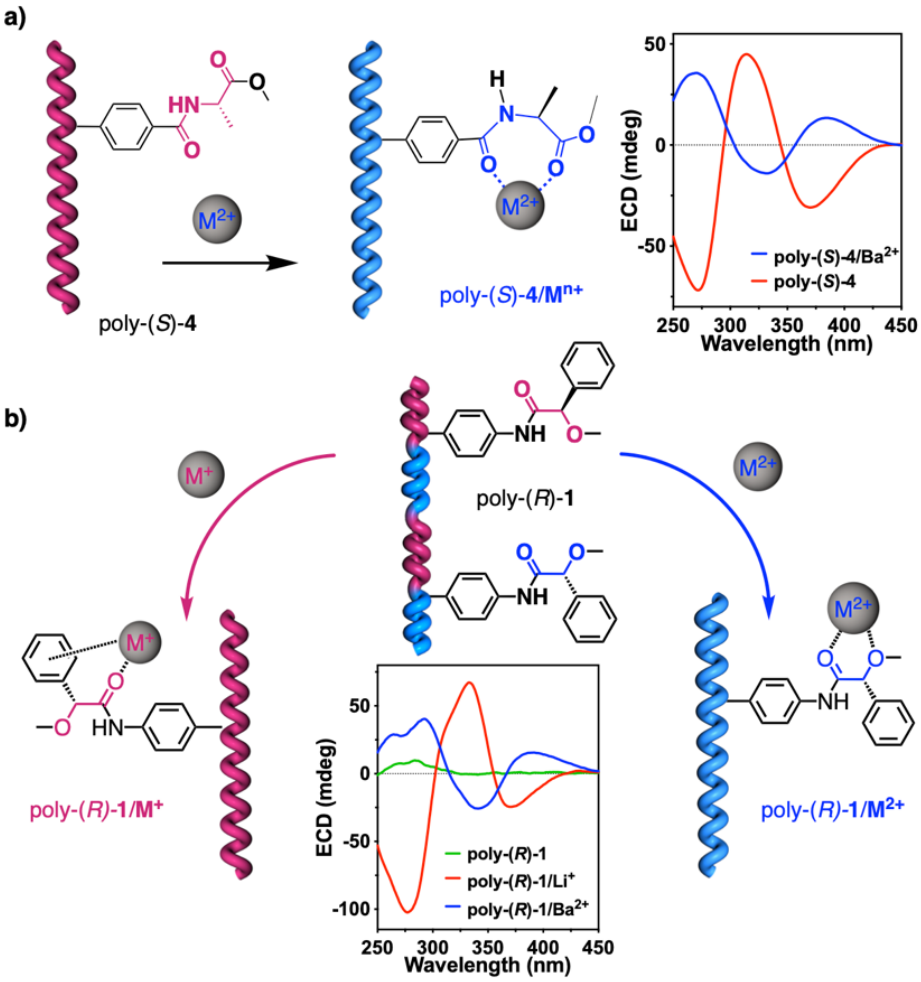


Figure 67. Stimuli-responsive helical behavior of (a) poly-(*S*)-**4** and poly-(*R*)-**1** in the presence of 0.1 equivalent of metal ions.

The existence of the radical ion was inferred from EPR studies (THF), which show a broad signal with a g value of 2.0039 confirming the presence of organic free radicals (Figure 68b). UV-Vis-studies (THF), show the disappearance of the polyene band at ca. 400 nm and the generation of a new band at ca. 600 nm (Figure 68c). This band corresponds to a delocalization of the radical along the polyene backbone which is accompanied with an irreversible *cis*-to-*trans* isomerization of the double bonds (Figure 68a). As a result, the helical structure of anilide-PPAs is lost, which can be monitored by ECD in those chiral anilide-PPAs that show a screw sense excess, such as poly-(**2**-**3**), where the ECD signal disappears once Fe^{3+} is added (Figure 68e and Figure S38).

USC UNIVERSIDADE DE SANTIAGO DE COMPOSTELA

Fe^{3+} is a strong oxidizing agent,[387,388] so, to confirm that a redox process is taking place between the anilide-polymers and the Fe^{3+} ions, X-ray photoelectron spectroscopy (XPS) studies were carried out to determine the oxidation state of the iron before and after the addition of an anilide-polymer. As a control, XPS studies were carried out on commercially available iron salts —$Fe(ClO_4)_3$ and $Fe(ClO_4)_2$— to obtain the XPS spectra of the oxidation states of Fe^{3+} and Fe^{2+}. Next, XPS studies were performed for the poly-(*R*)-**1**/Fe^{3+} complex. Interestingly, the spectrum matches that obtained for $Fe(ClO_4)_2$, indicating that Fe^{3+} is reduced to Fe^{2+} after complexation with the anilide-polymer (Figure 68d) generating a radical cation in the polymer.

USC UNIVERSIDADE DE SANTIAGO DE COMPOSTELA

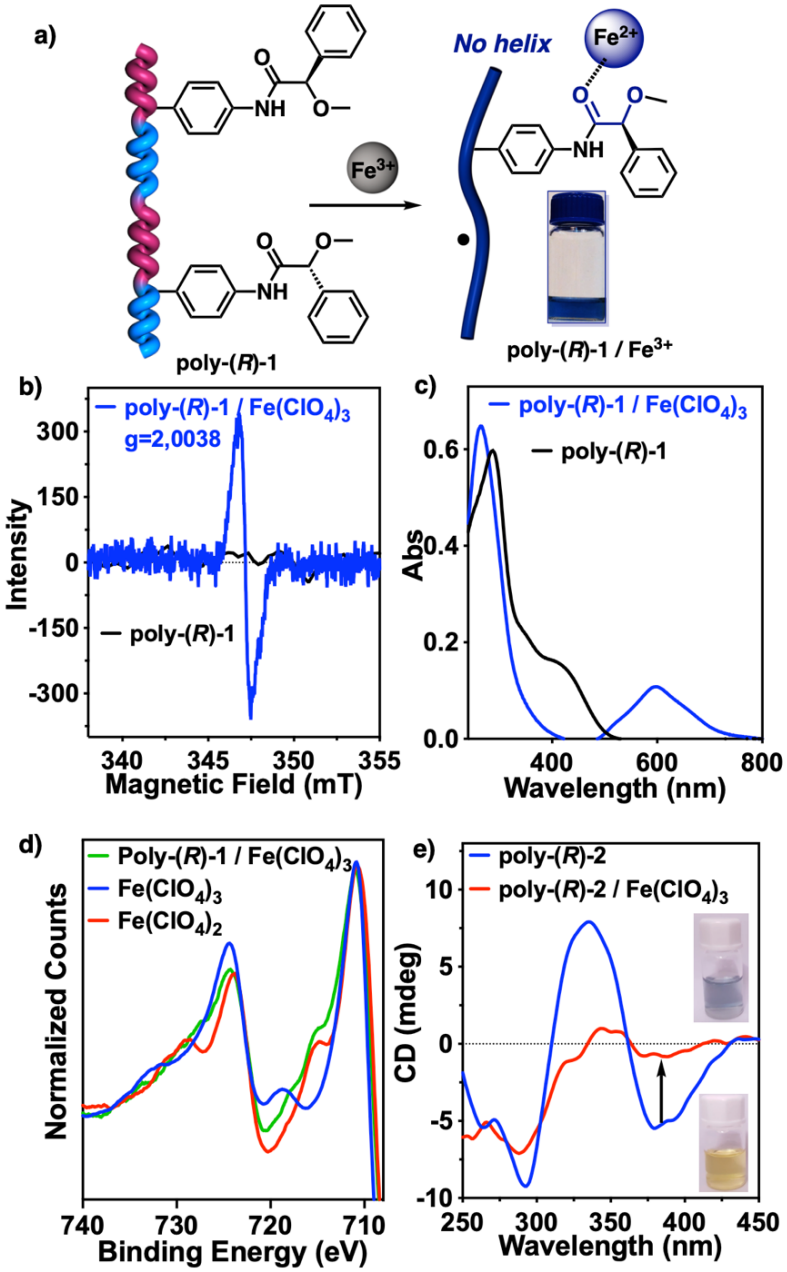


Figure 68. a) Conceptual illustration showing the formation of poly-(*R*)-**1**/Fe^{3+} complex and the delocalized radical along the backbone. b) EPR studies of poly-(*R*)-**1** and poly-(*R*)-**1**/Fe^{3+} complex in 1.00/0.01 (mol/mol) ratio (THF). c) UV-Vis studies of poly-(*R*)-**1** and poly-(*R*)-**1**/Fe^{3+} complex in 1.00/0.05 (mol/mol) ratio [poly-(*R*)-**1**]= 0.1 mg/mL, THF. d) XPS studies of $Fe(ClO_4)_2$, $Fe(ClO_4)_3$ and poly-(*R*)-**1**/Fe^{3+} complex indicating the presence of Fe^{2+} after the oxidation of Fe^{3+}. e) CD experiments of poly-(*R*)-**2** and poly-(*R*)-**2**/Fe^{3+} complex in 1.00/0.50 (mol/mol) ratio.

To demonstrate, that to trigger the redox process is necessary the oxidizing metal ion (Fe^{3+}) and an anilide-PPA, the same experiment was done for monomer M-(*R*)-**1**. Thus, $Fe(ClO_4)_3$ was added to a THF solution of M-(*R*)-**1**, which does not produce any color change in the solution. Moreover, EPR studies confirm the absence of radical

species in a THF solution of the M-(*R*)-**1**/Fe^{3+} complex (Figure S44). This study indicates that the redox reaction is not triggered by the anilide group itself, it needs to be linked to a phenylacetylene backbone.

Next, to determine the role of the anilide-connector in the redox reaction between an anilide-PPA and Fe^{3+} ions, we proceed to methylate the amide group of poly-(*R*)-**1** obtaining poly-(*R*)-**7** (see experimental section for details of the synthesis). The addition of 1 equiv of Fe(ClO4)3 (10 mg/mL, THF) to a THF solution of poly-(*R*)-**7** (c= 0.1 mg/mL) did not produce any color change in the polymer solution (Figure 69a and Figure 69c). IR studies indicate coordination of the metal ion to the carbonyl group due to a shift in the carbonyl band ($\tilde{\nu}$ (C=O) = 50 cm^{-1}) (Figure 69d). Moreover, EPR studies for a THF solution of poly-(*R*)-**7**/Fe^{3+} did not show the presence of radical species in the solution (Figure S43) and UV-Vis studies did not show any effect on the polyene band at ca. 400 nm (Figure 69b), which confirms the absence of a radical cation delocalized along the polyene backbone. These studies indicates that the redox process between an anilide PPA and the Fe^{3+} ions is triggered by a synergistic effect between the anilide group used as pendant and the PPA backbone, and not by just one of these two components of the helical polymer.

Thereafter, to determine the role of the anilide/Fe^{3+} interaction in the redox reaction, we added the oxidant metal ion salt to solutions of the poly-(*R*)-**1** in non-coordinating and coordinating solvents such as $CHCl_3$ and DCM or DMF and DMSO, respectively. From these studies it was observed that a color change from yellow to blue also takes place in the presence of non-coordinating solvents, while in coordinating no color changes are observed due to the lack of interaction between the polymer and the metal ion (Figure S31). These studies confirms that coordination between the anilide and the oxidizing metal ion is necessary to activate the redox reaction. The use of other oxidizing molecules such as hydrogen peroxide does not produce any effect on the polymer, indicating the need of interaction between the oxidizing agent and the polymer to trigger the redox reaction (see SI).

USC UNIVERSIDADE DE SANTIAGO DE COMPOSTELA

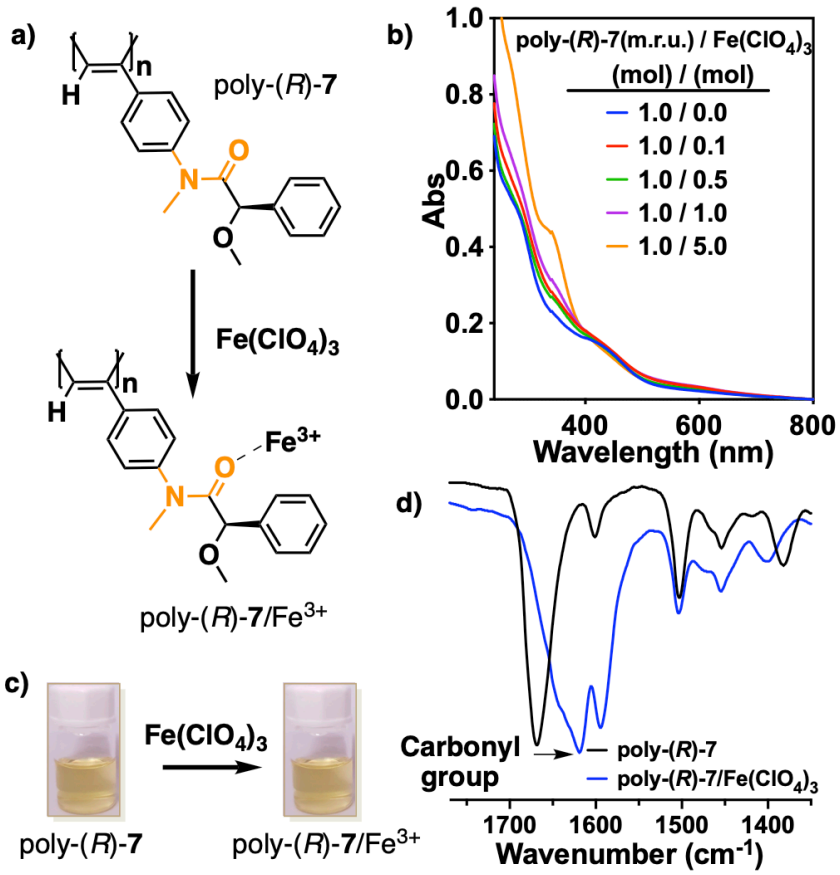


Figure 69. a) Illustration showing the formation of poly-(*R*)-**7**/Fe^{3+} complex. b) UV-Vis studies of poly-(*R*)-**1** and poly-(*R*)-**1**/Fe^{3+} complex [poly-(*R*)-**1**]= 0.1 mg/mL, THF. c) Images of vials containing solutions of poly-(*R*)-**7** and poly-(*R*)-**7**/Fe^{3+} complex in THF. d) FT-IR spectra of poly-(*R*)-**7** and poly-(*R*)-**7**/$Fe(ClO_4)_3$.

Afterwards, theoretical calculations were carried out to corroborate the *cis* to *trans* isomerization of the double bonds and the consequent delocalization of the cation radical in the polyene backbone. Thus, DFT calculations —using the uB3LYP functional and the 6-31G* basis set with charge 1+ and doublet multiplicity— were performed first using the Gaussian16 software on an n= 8 oligomer of poly-(*R*)-**1** with trans-configuration of double bonds. Analogous calculations were carried out for an n= 9 oligomer of poly-(*R*)-**1** with a cis-configuration of double bonds (see ESI). Spin density and SOMO orbitals show that the cation radical delocalizes from the pendant to the polyene backbone in the trans isomers (Figure 70a, Figure S51 and Figure S52). On the other hand, spin density of the cis-isomer isolates the radical at one edge of the oligomer, without delocalization (Figure S50).[389-392] TD-DFT were then run to simulate the UV-Vis spectra using the u/rCAM-B3LYP functional and the 6-31G* basis set from the optimized geometries in DFT (see

USC UNIVERSIDADE DE SANTIAGO DE COMPOSTELA

SI). As expected, the experimental absorption band of the radical cation at 600 nm coincides with the calculated one (Figure 70c) Furthermore, EPR calculations performed in Orca software using the UKS B3LYP functional and the EPR-II basis set predicted the same g values and EPR spectra as the experimental ones (Figure 70b and Figure S51).

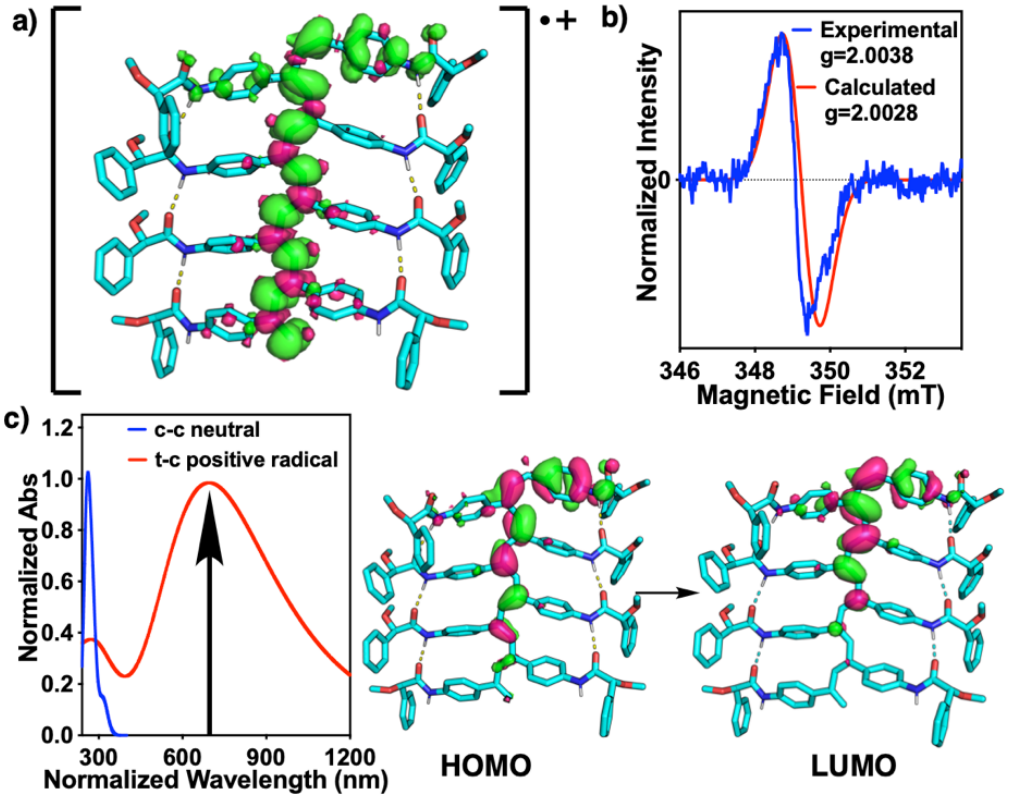


Figure 70. a) Spin density of a radical cation oligomer with a *trans-cisoidal* structure b) Comparison between the experimental EPR of poly-(*R*)-**1**/Fe^{3+} and that calculated for the *trans-cisoidal* oligomer. c) Simulated UV-Vis spectra of the neutral *cis-cisoidal* oligomer and the radical cation *trans-cisoidal* oligomer. Transition attributed to the band at ca. 700 nm in the radical cation *trans-cisoidal* oligomer.

Finally, to extend the stimuli-responsive behavior of anilide-PPAs to other oxidizing metal ions, metal salts containing oxidizing metals such as Cu^{2+}, Hg^{2+}, Au^{3+}, and Ce^{4+} were added to THF solutions of poly-(*R*)-**1** (0.1 mg/mL). In all cases, a color change from yellow to blue was observed with the appearance of a new band in the UV-Vis spectra at ca. 600 nm, confirming the presence of a delocalized radical cation along the polyene backbone. Again, these results show that anilide-PPAs are sensitive to the presence of oxidizing metal ions (Figure 71, Figure S35, and Figure S36). Titration experiments of a THF solution of poly-(*R*)-**1** with different equivalents of metal salts containing either Cu^{2+}, Hg^{2+}, Au^{3+} or Fe^{3+} were done to obtain the limit of detection (LOD) of the different poly-

USC UNIVERSIDADE DE SANTIAGO DE COMPOSTELA

(*R*)-**1**/M^{n+} complexes (Figure S36). From these studies it was found that the LOD for poly-(*R*)-**1**/ Cu^{2+} is 2.37 ppm; poly-(*R*)-**1**/ Hg^{2+} is 8.41 ppm; poly-(*R*)-**1**/ Au^{3+} is 1.65 ppm and poly-(*R*)-**1**/ Fe^{3+} is 1.32 ppm when the concentration of poly-(*R*)-**1** is 0.1 mg/mL THF (see Figure S53, Table S1, and Table S2).

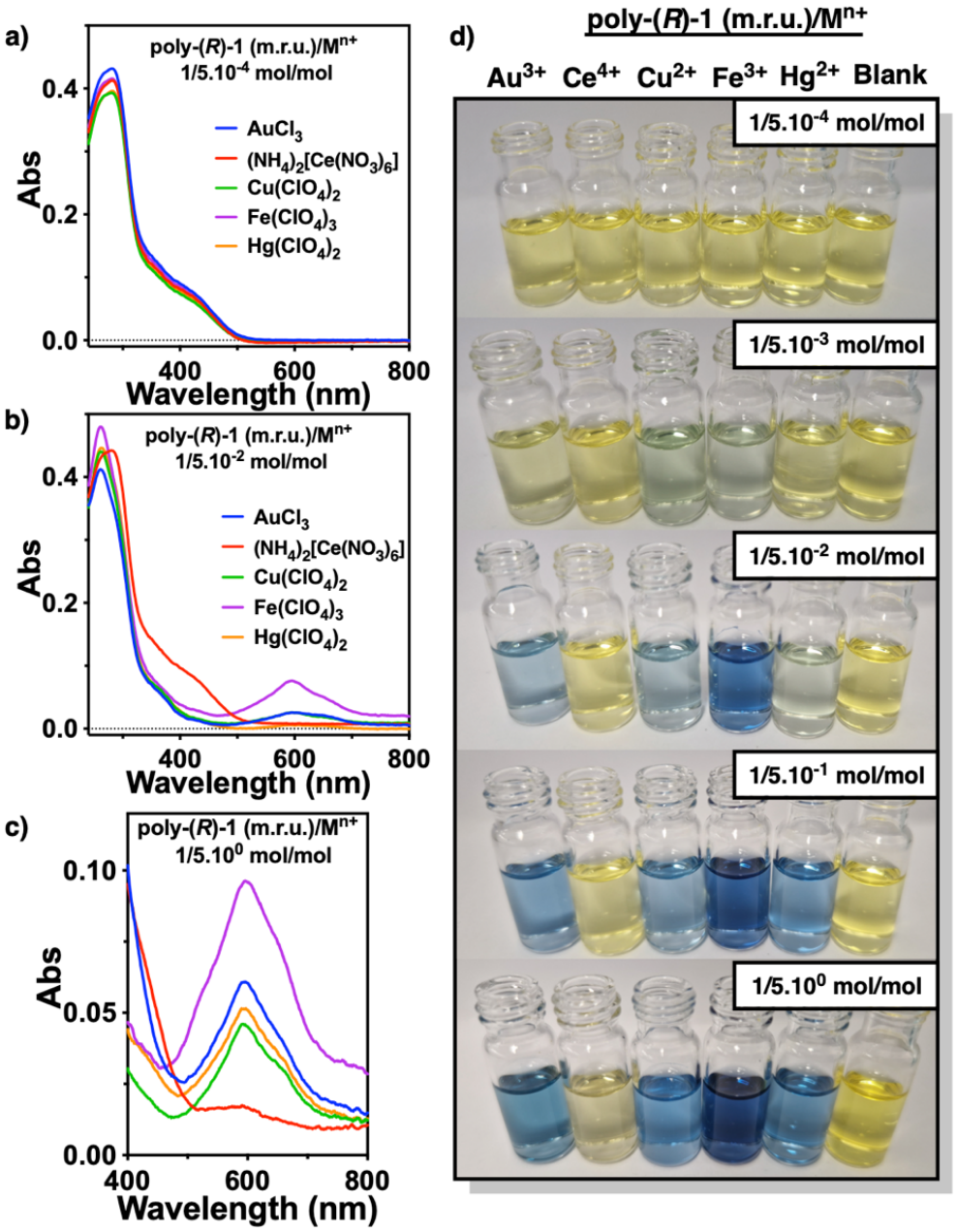


Figure 71. a-c) UV-Vis of poly-(*R*)-**1** (0.1 mg mL-1, THF) in presence of different equiv of $Cu(ClO_4)_2$, $Fe(ClO_4)_3$, $Hg(ClO_4)_2$, and $AuCl_3$ (10.0 mg·mL^{-1} and 1.0 mg·mL^{-1}, THF) or $(NH_4)_2[Ce(NO_3)_6]$ (10.0 mg·mL^{-1} and 1.0 mg·mL^{-1}, MeOH). d) Image of vials containing different THF solutions of several poly-(*R*)-**1**/M^{2+} complexes at different mol/mol ratios.

USC UNIVERSIDADE DE SANTIAGO DE COMPOSTELA

3.2.3. Conclusions

In conclusion, we have shown that anilide-PPAs are sensitive to the presence of oxidizing metal ions such as Cu^{2+}, Hg^{2+}, Fe^{3+}, Au^{3+}, and Ce^{4+}. The coordination of the metal ions with the carbonyl group of the anilide is accompanied with an oxidation of the PPA, which produces a radical cation that delocalizes along the polyene backbone ($PPA^{\cdot+}$), while the metal ion is reduced. Delocalization of the polyene radical generates an irreversible cis to trans isomerization of the double bonds that results in the loss of the helical structure.

Furthermore, this delocalization of the radical cation along the polyene gives rise to an observable and effective colorimetric response from a yellow to deep blue solution. Therefore, dynamic helical polymers, such as anilide-PPAs, can be considered multi-stimuli-responsive materials that can respond differently to various families of metal ions. For instance, poly-(*R*)-**1** adopts an *M* helix in the presence of monovalent metal ions, a *P* helix with divalent metal ions, and has a colorimetric response when interacting with oxidizing metal ions. This work should therefore be inspiring for scientists working with stimuli-responsive materials, where a single design can sense diverse stimuli in different ways.

USC
UNIVERSIDADE DE SANTIAGO DE COMPOSTELA

3.3. Dispute Between Chiral Comonomers to Induce Tunable Asymmetry Amplification Effects in Dynamic Helical Copolymers

Abstract

Conformational communication mechanisms activated by external stimuli are responsible for controlling the *P* and *M* screw sense excess in foldamers and helical polymers. Furthermore, important biological mechanism such as signaling involve conformational communication mechanisms along proteins, triggered by an external stimulus. In dynamic helical copolymers made of one chiral and one achiral component, the comonomer that dictates the helical sense of the copolymer is the chiral one; however, in copolymers made of two chiral components, more complex communication mechanisms can arise. Therefore, if there is a lack of communication between comonomers, a Chiral Accord or a Chiral Conflict occurs if both components induce the same or opposite screw senses in the helix. Moreover, if one of the chiral components has a preferred conformer in the pendant while the other possesses an equilibrium between different conformers, a chiral-to-chiral communication mechanism can be triggered, resulting in a Classic or Abnormal Sergeants and Soldiers Effect. In this work, we take a step forward and explore those chiral copolymers formed by two chiral components, where each comonomer presents an equilibrium between two different conformers in the pendant. In this case, by selecting a specific stimulus and choosing the correct diastereomeric composition in the chiral copolymer, different asymmetry amplification effects can be triggered, such as the Classic and Abnormal Chiral-to-Chiral Sergeants and Soldiers Effect, the Chiral Accord Effect or the Chiral Conflict Effect. Interestingly, the asymmetry amplification effect can be further tuned by another second external stimulus that promotes the initial Chiral Soldier to Chiral Sergeant and relegates the initial Chiral Sergeant to Chiral Soldier. This tunable chiral-to-chiral communication effects, where the role of different chiral components can be swapped by different external stimuli, will help to understand more complex chiral-to-chiral communication mechanisms, such as signaling or the preparation of dynamic chiral materials with applications such as chiral stationary phases in HPLC, asymmetric catalysis, chiral recognition, and so on.

USC UNIVERSIDADE

USC
UNIVERSIDADE
DE SANTIAGO
DE COMPOSTELA

3.3.1. Precedents

Stimuli-responsive materials, such as dynamic helical polymers, have been studied in recent decades due to the possibility of tuning their helical sense or elongation (output) through the action of an external stimulus (input). The low energy barrier between the two helical senses (*P*, plus; *M*, minus), and the cooperativity of the asymmetry amplification process make these materials excellent candidates for exploring stimuli-responsiveness. In general, to create a dynamic helical polymer, such as a poly(phenylacetylene) (PPA),[25,70,71,86,92,169,234,235,237,241,243-245,281,334-337,393-395] a stimuli-responsive group is introduced into the monomer repeating unit, and the ability of the polymer to interact with the external stimuli is monitored by circular dichroism (CD) and UV-Vis.[6,8,29,30,42,43,171,233,236,243,253,261,267,269,329,366,396-404] However, to improve the responsiveness of the dynamic helical polymer, it is necessary to understand how chiral information is transmitted from the chiral pendant group to the polymer backbone and how asymmetry amplification along the polymer is triggered.

This knowledge is also needed to improve other potential applications of these materials, such as their ability to act as asymmetric ligands for chiral catalyst, or as chiral stationary phases in high-performance liquid chromatography (HPLC).[6,8] In most cases, to have good control over the helix induction and asymmetry amplification processes, it is necessary to play with the conformational composition of the chiral pendant groups and, therefore, with the spatial orientation of the substituents of those chiral pendants that are responsible for triggering tele-induction or conformational communication effects. An additional degree of complexity emerges in copolymers, where two different monomers are present in the copolymer main chain.

In a pioneering work, Green demonstrated that it is possible to obtain a screw sense excess in dynamic helical copolymers made of an achiral and a chiral monomer as obtained for the corresponding chiral homopolymer.[26,276-279,367,405-407] In these copolymers, a small fraction of the chiral component (Sergeant) can induce a screw sense excess in the achiral one (Soldier). Thus, if the screw sense adopted by the copolymer is that adopted by the Sergeant in the corresponding chiral homopolymer, an asymmetry amplification mechanism based on the Sergeants and Soldiers Effect occurs, whereas if the copolymer adopts the opposite helical sense to that induced in the homopolymer of the Sergeant, an Abnormal Sergeants and Soldiers Effect is present.[26,271-275,327] In line with these studies, other asymmetry amplification mechanisms

USC UNIVERSIDADE DE SANTIAGO

were found when both copolymer components are chiral, *i.e.*, Majority Rules (the two components are enantiomers), Chiral Coalition or chiral-to-chiral Sergeants and Soldiers Effect (the two components are structurally different).[276,277,279,367] In all cases, one of the copolymer components acts as Sergeant, while the other acts as Soldier, without it being possible to reverse the role of the two components.

In this work, we will demonstrate that the helix induction mechanism between two chiral components can be bidirectional, that is, the two chiral components of the copolymer can adopt either the role of Sergeant or Soldier through a dispute for the component with the lower energy conformation. Therefore, depending on the external stimuli employed, the lower-energy conformer of the copolymer can be present in the pendant of one of the chiral components or in the pendant of the other. This novel asymmetry amplification phenomenon could be denoted as the Chiral Dispute Effect.

To design a chiral copolymer with this behavior, it is necessary to introduce two structurally different chiral monomers, with a controlled conformational composition between two conformers that can be orthogonally altered by different external stimuli. For instance, if solvent polarity largely stabilizes a conformer of component 1, without affecting the conformational composition of component 2, a Sergeant to Soldiers effect from 1 to 2 could emerge. However, if the addition of a metal largely stabilizes a conformer of component 2 by chelation, without affecting the conformational composition of component 1, a Sergeant to Soldiers effect from 2 to 1 should occur.

3.3.2. Discussion

To demonstrate this hypothesis, the 4-ethynylanilides of (*R*)-(-)- and (*S*)-(+)-α-methoxy-α-phenylacetic acid were selected as chiral monomers (*R*)-**1**/(*S*)-**1** (component 1), while the 4-ethynylanilides of (*R*)-(+)- and (*S*)-(-)-α-methoxy-α-(trifluoromethyl)phenylacetic acid were chosen as monomers (*R*)-**2**/(*S*)-**2** (component 2). The difference between monomers **1** and **2** lies in a -CF_3 group present in (*R*/*S*)-**2**, which is replaced by an H atom in (*R*/*S*)-**1** (Figure 72a).

The corresponding homopolymers [poly-(*R*/*S*)-**1**, poly-(*R*/*S*)-**2**] show orthogonal response towards external stimuli (Figure 72b). Thus, poly-(*R*/*S*)-**1** are barely sensitive to low polarity solvents, presenting an equilibrium between two conformers in a ca. 1:1 ratio —(O=)C-C(-O) bonds either antiperiplanar (*ap*-OMe, conformer 1) or synperiplanar

USC UNIVERSIDADE DE SANTIAGO

(*sp*-OMe, conformer 2) oriented—. However, in those low polar solvents, they are sensitive to monovalent and divalent metal ions that stabilize *ap*-OMe and *sp*-OMe conformers at the (O=)C-C(-O) bonds, respectively (Figure 72c).

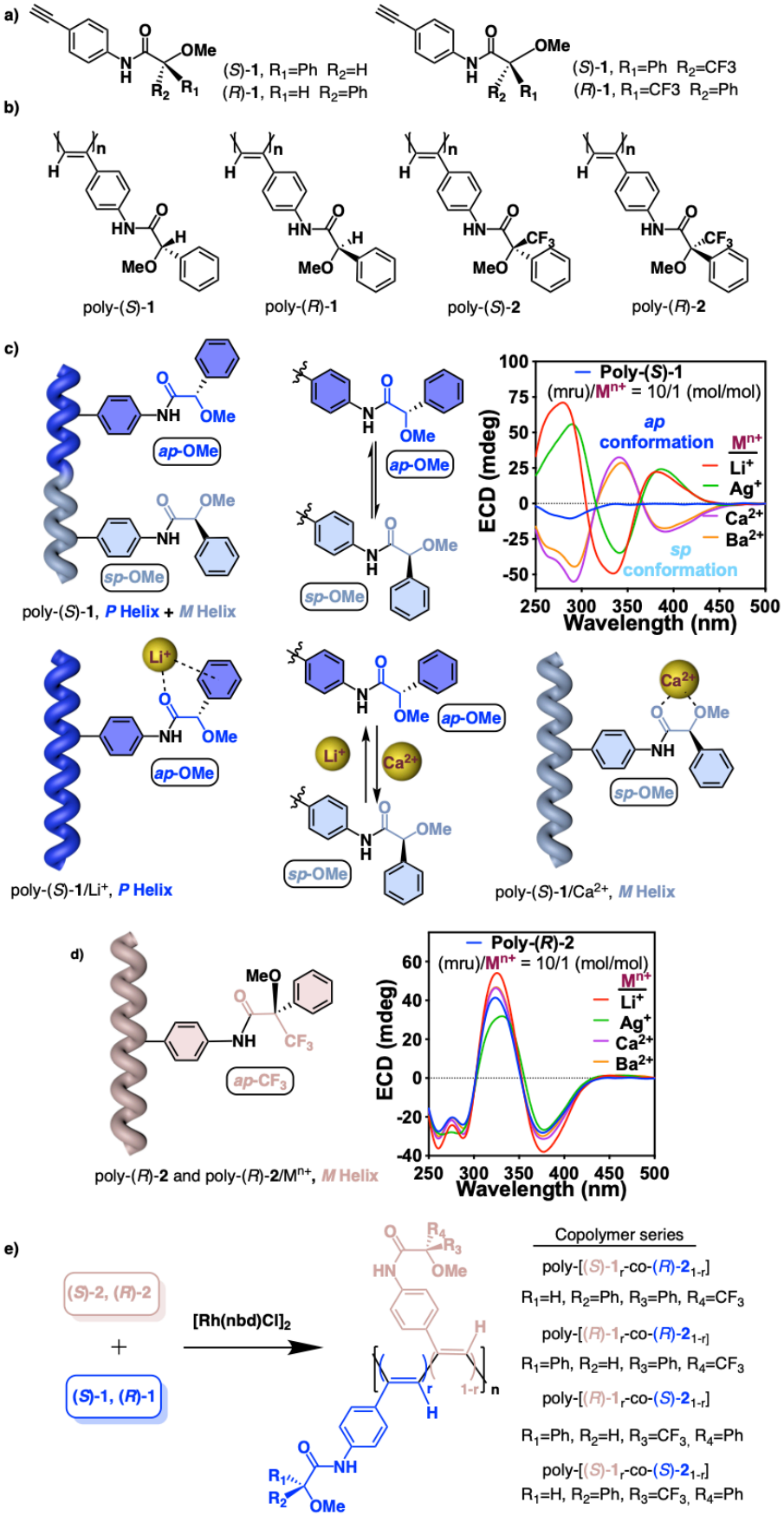
Hence, monovalent metal ions coordinate to the carbonyl group and establish an extra cation-π interaction with the aryl ring at the pendant, while divalent metal ions chelate the carbonyl and methoxy groups (Figure S35).[42,43,171,267,269,366] As a result, poly-(*S*)-**1** adopts a *P* helix in the presence of monovalent metal ions (first Cotton band negative in the electronic circular dichroism spectrum, $ECD_{380\ nm} > 0$), while an *M* helix is induced in poly-(*S*)-**1** in the presence of divalent metal ions ($ECD_{380\ nm} < 0$) (Figure 72c). As expected, the opposite helical senses are adopted by poly-(*R*)-1 in the presence of metal ions (monovalent: *M* helix, $ECD_{380\ nm} < 0$; divalent: *P* helix, $ECD_{380\ nm} > 0$) due to their enantiomeric relationship (Figure S89).

This amplification of asymmetry follows a cooperative process, where just a tiny amount of the metal ion is needed to induce a screw sense excess in the polymer through an effective chiral communication mechanism between complexed and uncomplexed monomer repeating units.

On the other hand, poly-(*R*/*S*)-**2** are poorly sensitive to monovalent and divalent metal ions (Figure 72d and Figure S90) in low polarity solvents, while they are greatly affected by the donor and polar parameters of the solvents, where four different helical structures can be induced. In our case, we are interested in the helical structure adopted by poly-(*R*/*S*)-**2** in non-donor/low-polar solvents such as $CHCl_3$ (Figure 72d). The reason is because in this solvent, poly-(*R/S*)-**2** have a strong conformational preference in their pendant groups, while poly-(*R*/*S*)-**1**, as already discussed, show an equilibrium between two conformers in their pendants in similar population, producing axially racemic helices. Thus, poly-(*R*/*S*)-**2** in $CHCl_3$ adopt a preferred *ap*-CF_3 conformation at the (O=)C-C(CF_3) bonds, resulting in the adoption of an *M* helix, ($ECD_{380\ nm} < 0$) for poly-(*R*)-**2** and a *P* helix, ($ECD_{380\ nm} > 0$) for poly-(*S*)-**2** (Figure 72d and Figure S100).[84]

The orthogonal response to $CHCl_3$ and metal ions of poly-**1** and poly-**2** makes them great candidates for exploring the communication mechanisms in series of diastereomeric random copolymer series of both components —poly-[(*R*)-$\mathbf{1}_r$-*co*-(*R*)-$\mathbf{2}_{1-r}$], poly-[(*S*)-$\mathbf{1}_r$-*co*-(*S*)-$\mathbf{2}_{1-r}$], poly-[(*R*)-$\mathbf{1}_r$-*co*-(*S*)-$\mathbf{2}_{1-r}$], and poly-[(*S*)-$\mathbf{1}_r$-*co*-(*R*)-$\mathbf{2}_{1-r}$]— (Figure 72e).

USC UNIVERSIDADE DE SANTIAGO DE COMPOSTELA



USC UNIVERSIDADE DE SANTIAGO DE COMPOSTELA

Figure 72. a) Structures of (*S*)-**1**, (*R*)-**1**, (*S*)-**2**, and (*R*)-**2**. b) Structures of poly-(*S*)-**1**, poly-(*R*)-**1**, poly-(*S*)-**2**, and poly-(*R*)-**2**. c) c) Illustration of the helical structure, conformational equilibrium between *ap*-OMe and *sp*-OMe in the (O=)C-C(-O) bonds and ECD spectra adopted by poly-(*S*)-**1** (0.3 mg/mL) in $CHCl_3$ in the presence and the absence of $LiClO_4$ or $Ca(ClO_4)_2$ (0.1 equiv, 10 mg/mL MeOH). d) Illustration of the helical structure, stable conformation *ap*-CF_3 of the (O=)C-C(CF_3) bonds and ECD spectra adopted by poly-(*R*)-**2** (0.3 mg/mL) in $CHCl_3$ in the presence and the absence of $LiClO_4$ or $Ca(ClO_4)_2$ (0.1 equiv, 10 mg/mL MeOH). e) Monomer and copolymer structures used in this study.

Thus, the four copolymer series —poly-[(*R*)-**1**$_r$-*co*-(*R*)-**2**$_{1-r}$], poly-[(*S*)-**1**$_r$-*co*-(*S*)-**2**$_{1-r}$], poly-[(*R*)-**1**$_r$-*co*-(*S*)-**2**$_{1-r}$], and poly-[(*S*)-**1**$_r$-*co*-(*R*)-**2**$_{1-r}$] (r=0.9-0.1)—, containing monomers **1** and **2** in both (*R*)- and (*S*)-configuration, were prepared following the classical procedure for PPAs. Thus, the two comonomers were copolymerized in the presence of a Rh(I) catalyst (see experimental section for details).

The ratio of the two monomers (r= 0.9-0.1) present in the copolymers was confirmed by ^{1}H-NMR and quantitative ^{13}C-NMR inverse-gated decoupled spectra (Figure S75, Figure S76, and Figure S81 to Figure S84), while the generation of random copolymers was demonstrated by using the Kellen-Tüdös method (see experimental section 5.3.12. Determination of the monomer reactivity ratios in copolymerization).[154,408,409] In all the copolymer series, both NMR (vinyl protons at δ= 5.7–5.8 ppm, details in experimental section) and Raman (peaks around 1580, 1360, and 980 cm^{-1}, Figure S109) spectroscopies confirmed the presence of cis double bonds at the polyene backbones.[157,410-412] Moreover, DSC analyses showed for these copolymers the classical thermograms for *cis-cisoidal* polyene backbones (Figure S106, Figure S107, and Figure S108).[67,96,100] The copolymer molecular weights were measured by GPC using THF and polystyrene standards. In all cases, the size of the polymers was within the range Mn=250-650 kDa, with a dispersity (Đ) between 1.2 and 1.7 (Table S7, Table S8, Table S9, Table S10, and Table S11).

Next, folding studies of the copolymer series were performed to decipher the chiral-to-chiral communication mechanisms that emerge in the copolymer series. Thus, ECD studies were done first performed for chloroform solutions of the different polymers of the different poly-[(*R*)-**1**$_r$-*co*-(*R*)-**2**$_{1-r}$], poly-[(*S*)-**1**$_r$-*co*-(*S*)-**2**$_{1-r}$], poly-[(*R*)-**1**$_r$-*co*-(*S*)-**2**$_{1-r}$], and poly-[(*S*)-**1**$_r$-*co*-(*R*)-**2**$_{1-r}$] (r=0.9-0.1) copolymer series at 0.3 mg/mL. These spectra were compared with those obtained for the corresponding parent homopolymers [poly-(*R*/*S*)-**1** and poly(*R*/*S*)-**2**] to elucidate the presence or absence of chiral-to-chiral

USC UNIVERSIDADE DE SANTIAGO DE COMPOSTELA

communication mechanisms. For clarity, the discussion of the results has been divided into the four different diastereomeric copolymer series.

Chiral-to-chiral communication studies (stimulus 1= chloroform)

Abnormal chiral-to-chiral Sergeants and Soldiers Effect in the poly-[(*S*)-$\mathbf{1}_r$-*co*-(*R*)-$\mathbf{2}_{1-r}$] copolymer series: ECD studies for homopolymer poly-(*S*)-**1** show a negligible ECD signal at 380 nm, which indicates a mixture of *P* and *M* helices due to an equal population of the *ap*-OMe and *sp*-OMe conformers in its pendant group. However, poly-(*R*)-**2** shows a strong negative Cotton band ($ECD_{380\ nm} < 0$) indicative of an *M* screw sense excess as a consequence of a preferred *ap*-CF_3 conformation in its pendant group (Figure 73a).

ECD studies of the poly-[(*S*)-$\mathbf{1}_r$-*co*-(*R*)-$\mathbf{2}_{1-r}$] (r= 0.9-0.1) copolymer series under the same conditions as the corresponding homopolymers (0.3 mg/mL $CHCl_3$) show a different response than these, indicating the presence of a communication mechanism between the two chiral components of the copolymer.

In this case, a chiral-to-chiral communication occurs from (*R*)-**2** (Sergeant) to (*S*)-**1** (Soldier). This fact is due to a non-linear decrease of the first Cotton effect ($ECD_{380\ nm}<0$) and the g_{value} when the ratio of (*S*)-**1** (Soldier) increases in the copolymer series (Figure 73b and Figure 73e). More precisely, an Abnormal chiral-to-chiral Sergeants and Soldiers Effect is observed. On this occasion, 10% of the (*R*)-**2** comonomer (Sergeant), which folds into an *M* helix [(*R*)-**2** monomer = *ap*-CF_3 conformation), can command the 90% of the (*S*)-**1** comonomer (Soldier) to fold into a *P* helix [$ECD_{382\ nm} > 0$].

From previous studies, it is known that monomer (*S*)-**1** commands a *P* helix in a polymer chain when it adopts an *ap*-OMe conformation (Figure 72c). To corroborate this assumption, perchlorate salts of monovalent and divalent metal ions such as $LiClO_4$ (10 mg/mL MeOH) and $Ca(ClO_4)_2$ were added to vials containing a chloroform solution of the copolymer poly-[(*S*)-$\mathbf{1}_{0.9}$-*co*-(*R*)-$\mathbf{2}_{0.1}$] (0.3 mg/mL $CHCl_3$) to form poly-[(*S*)-$\mathbf{1}_r$-*co*-(*R*)-$\mathbf{2}_{1-r}$]/M^{n+} in a 1.0/0.1 mol/mol ratio (Figure 73c and Figure 73d). This copolymer was chosen from the copolymer series because it contains a large amount of the Soldier [(*S*)-**1**], which shows metal ion valence stimuli-responsiveness.

As expected, the ECD trace of the poly-[(*S*)-$\mathbf{1}_r$-*co*-(*R*)-$\mathbf{2}_{1-r}$]/Li^+ has an ECD pattern analogous to that obtained for poly-[(*S*)-$\mathbf{1}_r$-*co*-(*R*)-$\mathbf{2}_{1-r}$] in the absence of the metal ion salt. Moreover, the ECD trace of the poly-[(*S*)-$\mathbf{1}_r$-*co*-(*R*)-$\mathbf{2}_{1-r}$]/Ca^{2+} shows a helix inversion

with respect to that obtained for poly-[(*S*)-**1**$_r$-*co*-(*R*)-**2**$_{1-r}$] in the absence of the metal ion salt (Figure 73d). This different stimuli-responsiveness of the copolymers to metal ions confirms that monomer (*S*)-**1** adopts a preferred *ap*-OMe conformation when is copolymerized with (*R*)-**2**, which is further stabilized by monovalent metal ions and rotates toward a *sp*-OMe conformer by complexing with divalent metal ions (Figure 73c).

Next, density functional theory (DFT) calculations were performed on a fragment of a *cis-cisoidal* helix to demonstrate the stabilization of a *P* helix in poly-[(*S*)-**1**$_r$-*co*-(*R*)-**2**$_{1-r}$] (r=0.1-0.9) copolymer series. Thus, (*R*)-**2** pendants adopt a preferred *ap*-CF_3 and (*S*)-**1** pendants adopt a preferred *ap*-OMe conformation. To reduce the number of atoms, we focus our attention on a dimer containing the residues at the nth, nth +3 positions which are in the same helix crest. In this model system, while monomer (*R*)-**2** was introduced into an *ap*-CF_3 conformation of the (O=)C-C(-CF_3) bonds, monomer (*S*)-**1** was introduced into either an *ap*-OMe and *sp*-OMe conformations for the (O=)C-C(-O) bonds. Then geometry optimizations and frequency calculations were performed using wb97xd functional method and the 6-31+g(d,p) basis set in implicit solvent (PCM=$CHCl_3$) in Gaussian 16 (G16RevC.01).[126,127,413-418] Non-Covalent Interaction (NCI) analysis was also performed with the Multiwfn software package[419,420] to recognize the supramolecular interactions between pendants from the last checkpoint file calculation from Gaussian 16. These studies show that within a *P* helix, a π-π stacking between the phenyl ring of adjacent pendants occurs when (*R*)-**2** adopts an *ap*-CF_3 conformation and the (*S*)-**1** monomers adopt an *ap*-OMe conformation within the copolymer (Figure 73f).

Next, we proceed to calculate the energy of the helix induction process (ΔG_h) following Sato's model[406] for the Classic Sergeants and Soldiers Effect (SaS) in random copolymers, which is based on the Ising model initially defined by Green.[273,421-424] In this model, both the degree and the direction of the helical induction rely on the structure of the neighboring monomer units, which can be either chiral or achiral in a copolymer that follows a Classic Sergeant and Soldiers Effect. Using this model, they were able to obtain the energy preference of a monomer repeating unit of a copolymer to adopt a certain helical sense (ΔG_h) in the Classic and the Abnormal SaS effects.[406] In copolymers, to obtain the ΔG_h value, it is necessary to consider which are the neighboring residues of a given monomer within the copolymer sequence. Thus, when a chiral residue is adjacent to another chiral residue, the energy to adopt a screw sense preference in the helix must consider that the two chiral monomers have the same propensity to induce the same

USC DE COMPOSTELA

screw sense preference $\Delta G_{h,CC}$ (C = chiral), while when a chiral residue is followed by an achiral residue or vice versa, $\Delta G_{h,CA}$ (C = chiral, A = achiral) and $\Delta G_{h,AC}$, the screw sense induction energy must consider the communication mechanism from the chiral to the achiral residue. In this model, it is assumed that the communication between both the chiral and achiral comonomers does not depend on the component sequence, *i.e.*, chiral-achiral or achiral-chiral, and considers that the energy for the two different combinations is equal, $\Delta G_{h,CA}$=$\Delta G_{h,AC}$. Finally, within the copolymer, it is also possible to have two consecutive achiral residues ($\Delta G_{h,AA}$). In this case, both monomers induce the *P* or *M* helix in equal population and therefore, the energy induction towards one of them is null, indicating an absence of screw sense induction preference ($\Delta G_{h,AA}$=0). By using this Sato's model, it is possible to obtain the energy preferences of a classic or abnormal SaS effect.[26,407]

However, when two chiral monomers are present in the copolymer chain, it is necessary to consider that in addition to the Classic or Abnormal SaS, absence of asymmetry amplification processes can occur such as the Chiral Conflict or the Chiral Accord effects. Thus, to introduce the new communication mechanisms between chiral monomers, for instance the chiral-to-chiral Classic and Abnormal SaS effects, and even the lack of communication between them through a Chiral Accord or a Chiral Conflict effects, we have redefined the g_{max} value [equation (30)] and the energy of the helix induction process [ΔG_h, equation (29)] of Sato's model [equation (28)].

As there are two potential candidates to act as Sergeants within a fully chiral copolymer —which could have opposite ECD signals in the corresponding homopolymers—, instead of defining two partition functions for *P*-type and *M*-type helices, we have introduced g_{max} obtained from absolute values of the components and normalized data in equation (30). As a result, the ΔG_h obtained from equation (28) is dependent on the sign of the g_{value}, allowing us to know which screw sense is favored during the asymmetry amplification process. Thus, if ΔG_h is negative, the screw sense induced through a chiral-to-chiral communication mechanism is *M*, while if this value it is positive, the screw sense induced is *P*.

USC UNIVERSIDADE DE SANTIAGO DE COMPOSTELA

$$g_{abs} = tanh\left(\frac{N\Delta G_h}{2RT}\right) \cdot g_{max} \quad \textbf{(28)}$$

$$\Delta G_h = X^2 \Delta G_{h,xx} + XY \Delta G_{h,xy} + Y^2 \Delta G_{h,yy} \quad \textbf{(29)}$$

$$g_{max} = \frac{X \cdot |g_{max\,x}| + Y \cdot |g_{max\,y}|}{X + Y} \quad \textbf{(30)}$$

The energy induction (ΔG_h) calculated from equation (28) considers which are the neighboring residues of a certain monomer within the copolymer sequence. Thus, ΔG_h is a combination of ($\Delta G_{h,xx}$) (x= chiral comonomer 1), ($\Delta G_{h,yy}$) (y= chiral comonomer 2), ($\Delta G_{h,xy}$) (x= chiral comonomer 1, y= chiral comonomer 2) and ($\Delta G_{h,yx}$) (x= chiral comonomer 1, y= chiral comonomer 2) [equation (29)]. However, in this model we assume that the communication between both chiral monomers does not depend on the copolymer sequence, *i.e.*, chiral1-chiral2 (xy), chiral2-chiral1 (yx), being therefore $\Delta G_{h,xy}$=$\Delta G_{h,yx}$. We define X as the molar fraction of the Sergeant and Y as the molar fraction of the Soldier defined by Y=1-X. In the absence of communication mechanisms, there are neither sergeants nor soldiers present, and the assignment becomes arbitrary. Also, the energy calculations of the helix induction process become highly sensitive to errors when communication mechanisms are missing, and many data points must be considered to achieve an accurate fit.

Therefore, from this modified Sato's model, it is possible to extract all the ΔG_h components ($\Delta G_{h,xx}$, $\Delta G_{h,yy}$, and $\Delta G_{h,xy}$) for different chiral-to-chiral communication processes, such as the Classic and Abnormal chiral-to-chiral SaS effects or the Chiral Conflict and Chiral Accord effects. Moreover, it is also possible to elucidate the chiral-to-chiral communication mechanism from the value obtained from equation (31) (Comm= communication value), which always considers monomer x as the Sergeant. Thus, if this value is positive (Comm >0), a Classic Sergeant and Soldiers Effect is produced, while if this value is negative (Comm <0), an Abnormal Sergeants and Soldiers Effect is triggered in the copolymer. On the other hand, if this value is close to zero (Comm ≈ 0), a lack of communication between the two comonomers occurs, resulting in a Chiral Accord or a Chiral Conflict effects.

USC UNIVERSIDADE DE SANTIAGO DE COMPOSTELA

$$Comm = \frac{\Delta G_{h,xy}}{\Delta G_{h,xx} - \Delta G_{h,yy}} \quad \textbf{(31)}$$

By fitting the g_{values} of the Poly-[(*S*)-**1**$_r$-*co*-(*R*)-**2**$_{1-r}$] (r=0-1) copolymer series to equation (28), the different ΔG_h values were obtained: $\Delta G_{h,(S)\mathbf{1}(S)\mathbf{1}}$=-2.38 J/mol, $\Delta G_{h,(R)\mathbf{2}(R)\mathbf{2}}$ = -24.72 J/mol, and $\Delta G_{h,(S)\mathbf{1}(R)\mathbf{2}}$= +49.60 J/mol, which yields a communication value obtained from equation (31) of Comm= -2.22. In equation (31) we introduced (*R*)-**2** as x (x= Sergeant). This chiral-to-chiral communication value (Comm < 0) indicates the existence of an Abnormal Sergeants and Soldiers Effect (Figure 73e).

USC UNIVERSIDADE DE SANTIAGO DE COMPOSTELA

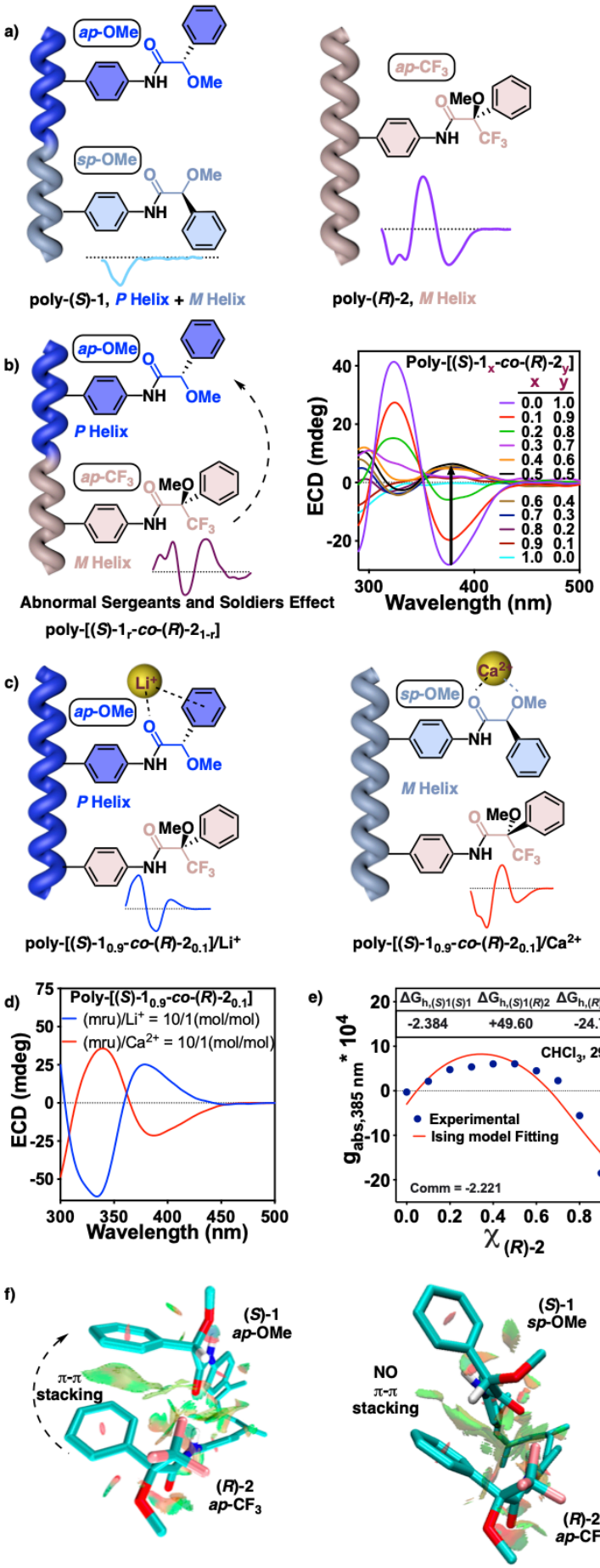

a)
ap-OMe
sp-OMe
poly-(S)-1, P Helix + M Helix
ap-CF3
poly-(R)-2, M Helix
b)
P Helix
M Helix
Abnormal Sergeants and Soldiers Effect
poly-[(S)-1r-co-(R)-21-r]
Poly-[(S)-1x-co-(R)-2y]
ECD (mdeg)
Wavelength (nm)
c)
Li+
Ca2+
poly-[(S)-10.9-co-(R)-20.1]/Li+
poly-[(S)-10.9-co-(R)-20.1]/Ca2+
d)
(mru)/Li+ = 10/1(mol/mol)
(mru)/Ca2+ = 10/1(mol/mol)
e)
ΔGh,(S)1(S)1 ΔGh,(S)1(R)2 ΔGh,(R)2(R)2
-2.384 +49.60 -24.72
CHCl3, 293 K
Experimental
Ising model Fitting
Comm = -2.221
gabs,385 nm * 10^4
χ(R)-2
f)
(S)-1 ap-OMe
π-π stacking
(R)-2 ap-CF3
(S)-1 sp-OMe
NO π-π stacking
(R)-2 ap-CF3

Figure 73. a) ECD pattern, helical sense, and equilibrium of the conformations or major conformation in the pendants of poly-(*S*)-**1** and poly-(*R*)-**2** in $CHCl_3$. b) ECD studies of the poly-[(*S*)-$\mathbf{1}_r$-*co*-(*R*)-$\mathbf{2}_{1-r}$] series. c, d) illustration of the helical sense adopted by the polyenic backbone of poly-[(*S*)-$\mathbf{1}_{0.9}$-*co*-(*R*)-$\mathbf{2}_{0.1}$] in the presence of a major conformation and ECD spectra of (*S*)-**1** by complexation with 0.1 equiv of $LiClO_4$ and $Ca(ClO_4)_2$ (10 mg/mL MeOH). e) Plot of the g_{abs} at indicated wavelength for poly-[(*S*)-$\mathbf{1}_r$-*co*-(*R*)-$\mathbf{2}_{1-r}$] series against copolymer composition and the corresponding curve fitting based on modified Sato's model to obtain the free energy parameters. f) Optimized structures and NCI calculations (wb97xd/6-31+g**, PCM=$CHCl_3$) of the dimers containing the residues at the nth, nth +3 in a *P* helix with conformation of the Sergeant (*R*)-**2** in *ap*-CF_3 and the two options of the Soldier (*S*)-**1** in *ap*-OMe and *sp*-OMe. Concentration of homopolymers and copolymers = 0.3 mg/mL $CHCl_3$.

Abnormal chiral-to-chiral Sergeants and Soldiers Effect in poly-[(*R*)-$\mathbf{1}_r$-*co*-(*S*)-$\mathbf{2}_{1-r}$] copolymer series: In this enantiomeric copolymer series, analogous chiral-to-chiral Abnormal Sergeants and Soldiers Effect is observed. The helical sense induced in the poly-[(*R*)-$\mathbf{1}_r$-*co*-(*S*)-$\mathbf{2}_{1-r}$] copolymer series are opposite to those observed for the poly-[(*S*)-$\mathbf{1}_r$-*co*-(*R*)-$\mathbf{2}_{1-r}$] copolymer series due to their enantiomeric relationship (see section 5.3.22. Abnormal chiral-to-chiral Sergeants and Soldiers Effect in the poly-[(R)-1r-co-(*S*)-21-r] copolymer series).

Absence of chiral-to-chiral communication in poly-[(*R*)-$\mathbf{1}_r$-*co*-(*R*)-$\mathbf{2}_{1-r}$] copolymer series: Next, we proceed to analyze the diastereomeric poly-[(*R*)-$\mathbf{1}_r$-*co*-(*R*)-$\mathbf{2}_{1-r}$] (r=0.9-0.1) copolymer series in $CHCl_3$. In this case, the ECD trace obtained for the different copolymers within this series diminishes linearly when the ratio of the soldier (*R*)-**1** increases. This fact indicates that both components of the chiral copolymer behave similarly to their corresponding chiral homopolymers [poly-(*R*)-**1**: $ECD_{380\ nm} \approx 0$, mixture of *P* and *M* helices; poly-(*R*)-**2**: $ECD_{380\ nm} < 0$, *M* helix] which denotes a lack of interaction, and therefore, an absence of communication between both components of the copolymer (Figure 74a and Figure 74b).

There are two effects in this phenomenon: the Chiral Conflict, where each comonomer induces the opposite helical senses [(*R*)-**1**: *P* helix; (*R*)-**2**: *M* helix] and the Chiral Accord, where the two comonomers induce the same helical sense [(*R*)-**1**: *M* helix; (*R*)-**2**: *M* helix]. However, the helix induction of each comonomer is that observed in the corresponding homopolymer, without being affected by the presence of the other comonomer within the copolymer main chain (lack of communication). Therefore, while comonomer (*R*)-**2** shows an *ap*-CF_3 conformation in the (O=)C-C(-CF_3) bond, inducing an *M* helix in the copolymer, comonomer (*R*)-**1** adopts an equal mixture of *ap*-OMe (*M*

USC UNIVERSIDADE DE SANTIAGO DE COMPOSTELA

helix) and *sp*-OMe (*P* helix) conformers, which induce Chiral Accord and a Chiral Conflict, respectively (Figure 74b).

To corroborate this hypothesis, perchlorate salts of monovalent and divalent metal ions such as $LiClO_4$ (10 mg/mL MeOH) and $Ca(ClO_4)_2$ were added to vials containing a chloroform solution of the copolymer poly-[(*R*)-**1**$_r$-*co*-(*R*)-**2**$_{1\text{-}r}$] (r=0.9) (0.3 mg/mL $CHCl_3$), which has a negligible ECD trace (no communication effect), to form poly-[(*R*)-**1**$_r$-*co*-(*R*)-**2**$_{1\text{-}r}$]/M^{n+} in a 1.0/0.1 mol/mol ratio.

As expected, the ECD trace of the poly-[(*R*)-**1**$_r$-*co*-(*R*)-**2**$_{1\text{-}r}$]/Li^+ shows an asymmetry amplification of the *M* helix adopted by poly-[(*R*)-**1**$_r$-*co*-(*R*)-**2**$_{1\text{-}r}$], due to the stabilization of the *ap*-OMe conformer in (*R*)-**1** (major component), which induces an *M* helix, while (*R*)-**2** (minor component) adopts the *ap*-CF_3 conformer and commands an *M* helix (Figure 74c and Figure 74d).

On the other hand, the ECD trace of the poly-[(*R*)-**1**$_r$-*co*-(*R*)-**2**$_{1\text{-}r}$]/Ca^{2+} shows a helix inversion when compared to that obtained for poly-[(*R*)-**1**$_r$-*co*-(*R*)-**2**$_{1\text{-}r}$] in the absence of the metal ion salt. This fact is due to the stabilization of the *sp*-OMe conformer at (*R*)-**1** (major component), which induces the *P* helix, and therefore a helix inversion regarding the *ap*-CF_3 conformation at (*R*)-**2** (minor component), which induces an *M* helix in the copolymer (Figure 74c and Figure 74d). This different stimuli-responsiveness of the copolymers to metal ions confirms that monomer (*R*)-**1** adopts a mixture of *ap*-OMe and *sp*-OMe conformations when is copolymerized with (*R*)-**2**, which has a preferred *ap*-CF_3 conformation (Figure 74b).

By applying a modification of Sato's model, it was possible to obtain the $\Delta G_{h,(R)\mathbf{1}(R)\mathbf{1}}$, $\Delta G_{h,(R)\mathbf{2}(R)\mathbf{2}}$ and $\Delta G_{h,(R)\mathbf{1}(R)\mathbf{2}}$ which are -1.89, -36.48, and +4.29 J/mol respectively. These energy helix induction energies for each possible pair of comonomer within the copolymer chain allow us to obtain a value for the communication process, in this case Comm= -0.12 [x= (*R*)-2], close to zero, which indicates a lack of communication between both comonomers (Figure 74e).

USC UNIVERSIDADE DE SANTIAGO DE COMPOSTELA

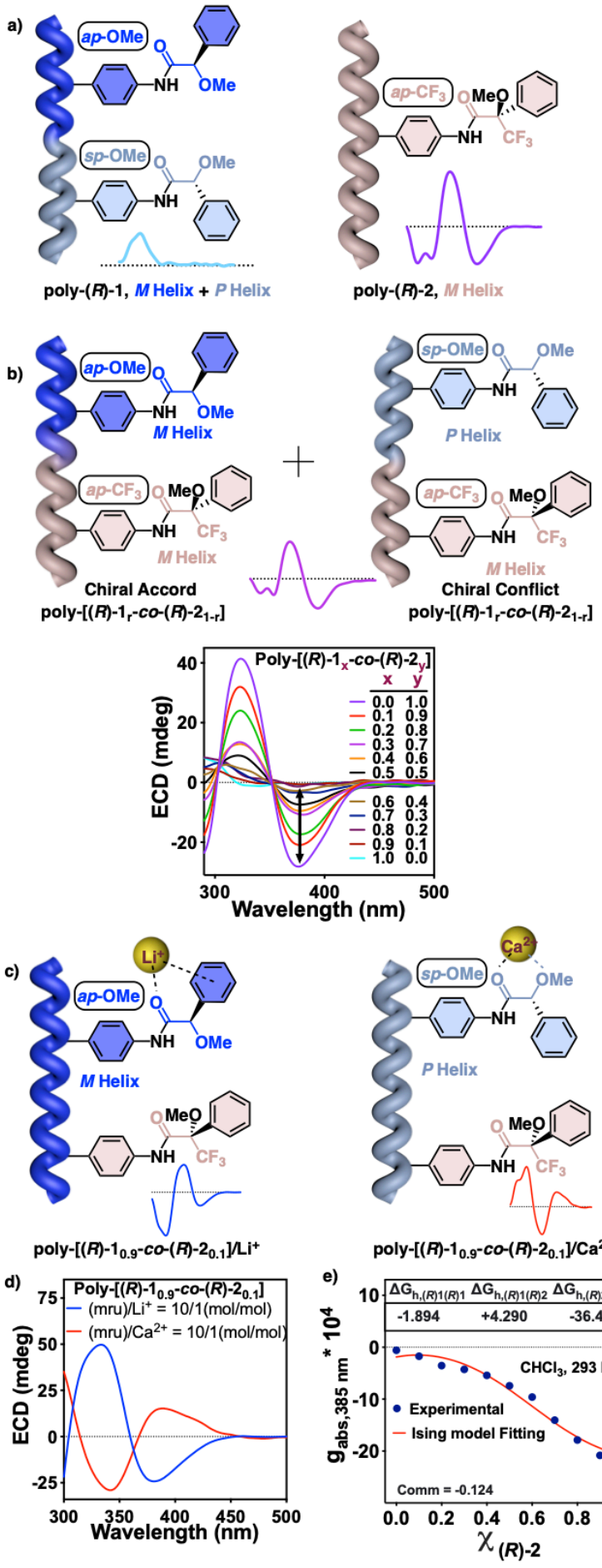

a)
ap-OMe
sp-OMe
poly-(R)-1, M Helix + P Helix
ap-CF3
poly-(R)-2, M Helix
b)
M Helix
P Helix
Chiral Accord
poly-[(R)-1r-co-(R)-21-r]
Chiral Conflict
poly-[(R)-1r-co-(R)-21-r]
Poly-[(R)-1x-co-(R)-2y]
ECD (mdeg)
Wavelength (nm)
c)
Li+
Ca2+
poly-[(R)-10.9-co-(R)-20.1]/Li+
poly-[(R)-10.9-co-(R)-20.1]/Ca2+
d)
(mru)/Li+ = 10/1(mol/mol)
(mru)/Ca2+ = 10/1(mol/mol)
e)
ΔGh,(R)1(R)1
ΔGh,(R)1(R)2
ΔGh,(R)2(R)2
-1.894
+4.290
-36.48
CHCl3, 293 K
Experimental
Ising model Fitting
Comm = -0.124
gabs,385 nm * 10^4
χ (R)-2

Figure 74. a) ECD pattern, helical sense, and equilibrium of the conformations or major conformation at the pendants of poly-(*R*)-**1** and poly-(*R*)-**2** in $CHCl_3$. b) ECD studies of the poly-[(*R*)-**1**$_r$-*co*-(*R*)-**2**$_{1-r}$] series. c, d) illustration of the helical sense adopted by the polyenic backbone of poly-[(*R*)-**1**$_{0.9}$-*co*-(*R*)-**2**$_{0.1}$] in the presence of a major conformation and ECD spectra of (*R*)-**1** by complexation of 0.1 equiv of $LiClO_4$ and $Ca(ClO_4)_2$ (10 mg/mL MeOH). e) Plot of the g_{abs} at indicated wavelength for poly-[(*R*)-**1**$_r$-*co*-(*R*)-**2**$_{1-r}$] series against copolymer composition and the corresponding curve fitting based on modified Sato's model to obtain the free energy parameters. Concentration of homopolymers and copolymers = 0.3 mg/mL $CHCl_3$.

Absence of chiral-to-chiral communication in poly-[(*S*)-1$_r$-*co*-(*S*)-2$_{1-r}$] copolymer series: In this enantiomeric copolymer series to the immediately preceding ones —poly-[(*R*)-**1**$_r$-*co*-(*R*)-**2**$_{1-r}$] (r=0.9-0.1)—, the lack of communication between the two chiral components is observed again. This result is expected due to the enantiomeric relationship between the series (see section 5.3.23. Absence of chiral-to-chiral communication in poly-[(S)-1r-co-(*S*)-21-r] copolymer series).

Therefore, these studies indicate that attending to the absolute configuration of the diastereomeric copolymer series, different chiral-to-chiral communication mechanisms are produced between the two components in chloroform. Thus, while poly-[(*S*)-**1**$_r$-*co*-(*R*)-**2**$_{1-r}$] and its enantiomeric poly-[(*R*)-**1**$_r$-*co*-(*S*)-**2**$_{1-r}$] copolymer series show an Abnormal chiral-to-chiral Sergeants and Soldiers Effect, the diastereomeric poly-[(*R*)-**1**$_r$-*co*-(*R*)-**2**$_{1-r}$] and its enantiomeric poly-[(*S*)-**1**$_r$-*co*-(*S*)-**2**$_{1-r}$] copolymer series show a mixture of Chiral Conflict and Chiral Accord effects.

Modulation of chiral-to-chiral communication studies by a second external stimulus (metal ions)

Next, we want to explore the dynamic behavior of these copolymer series towards a second stimulus, *i.e.*, a metal ion. As it was mentioned above, a chloroform solution of poly-(*S*)-**1** shows different asymmetry amplification effects in the presence of monovalent or divalent metal ions. This is due to the stabilization of either an *ap*-OMe or *sp*-OMe conformations at the chiral pendant by interaction with metal monovalent or divalent metal ions respectively. As a result, poly-(*S*)-**1** adopts a preferred *P* helix in the presence of monovalent metal ions, while an *M* helix is induced in the presence of divalent metal ions. Anologous stimuli-responsiveness is observed for poly-(*R*)-**1** although the helical senses induced by monovalent and divalent ions are opposite to those observed for poly-

USC UNIVERSIDADE DE SANTIAGO DE COMPOSTELA

(*S*)-**1** due to their enantiomeric relationship (poly-(*R*)-**1**/M^+, *M* Helix; poly-(*R*)-**1**/M^{2+}, *P* Helix).

Interestingly, poly-(*R*)-**2** and poly-(*S*)-**2** do not suffer alterations in their folding by the presence of metal ions. The presence of a CF_3 group at the monomer repeating unit, makes this pendant less prompt to coordinate to metal ions than monomer **1**. Thus, through a selective interaction of monomer **1** with monovalent and divalent metal ions in the poly-[(*R*)-$\mathbf{1}_r$-*co*-(*R*)-$\mathbf{2}_{1-r}$], poly-[(*S*)-$\mathbf{1}_r$-*co*-(*S*)-$\mathbf{2}_{1-r}$], poly-[(*R*)-$\mathbf{1}_r$-*co*-(*S*)-$\mathbf{2}_{1-r}$], and poly-[(*S*)-$\mathbf{1}_r$-*co*-(*R*)-$\mathbf{2}_{1-r}$] (r=0.9-0.1) copolymer series, we will explore how the chiral-to-chiral communication mechanisms present in the different copolymer series are altered by varying the conformational composition of one of the components of the copolymer series.

Therefore, ECD studies were performed for chloroform solutions —at 0.3 mg/mL— of the different polymers of the poly-[(*S*)-$\mathbf{1}_r$-*co*-(*R*)-$\mathbf{2}_{1-r}$], poly-[(*R*)-$\mathbf{1}_r$-*co*-(*S*)-$\mathbf{2}_{1-r}$], poly-[(*R*)-$\mathbf{1}_r$-*co*-(*R*)-$\mathbf{2}_{1-r}$], and poly-[(*S*)-$\mathbf{1}_r$-*co*-(*S*)-$\mathbf{2}_{1-r}$] (r=0.9-0.1) copolymer series in the presence of $LiClO_4$ (10mg/mL MeOH) and $Ca(ClO_4)_2$ (10 mg/mL MeOH) to form poly-[(*R*/*S*)-$\mathbf{1}_r$-*co*-(*R*/*S*)-$\mathbf{2}_{1-r}$] m.r.u./Li^+, and a poly-[(*R*/*S*)-$\mathbf{1}_r$-*co*-(*R*/*S*)-$\mathbf{2}_{1-r}$] m.r.u./Ca^{2+} complexes at a 1.0/0.1 (mol/mol) ratios. The results obtained are compared to the data obtained in the absence of metal ions to analyze the communication mechanism triggered in the presence of metal ions. For clarity, the discussion of results has been divided into the four different diastereomeric copolymer series.

From Abnormal to Classic chiral-to-chiral Sergeants and Soldiers Effect in poly-[(*S*)-$\mathbf{1}_r$-*co*-(*R*)-$\mathbf{2}_{1-r}$] (r= 0.0-1.0) m.r.u./Li^+ 1.0/0.1 (mol/mol) ratio: ECD studies show that in all the poly-[(*S*)-$\mathbf{1}_r$-*co*-(*R*)-$\mathbf{2}_{1-r}$] (r=0.9-0.1) copolymer series, a strong positive Cotton band is present at 380 nm [$ECD_{380\ nm} > 0$] (Figure 4b). This ECD signature corresponds to the one induced by the (*S*)-**1**/Li^+ pendant group (*ap*-OMe conformer), but opposite to the one commanded by the chiral monomer (*R*)-**2** (*ap*-CF_3 conformer) (Figure 75a). In this case, in all comonomer ratios, (*R*)-**2** induces a helical sense opposite to the one induced in the absence of a monovalent metal ions. This fact indicates that within this copolymer series, (*R*)-**2** changes its conformation once the metal ion is coordinated to the monomer (*S*)-**1**. Therefore, monomer (*S*)-**1** becomes a Sergeant once the $LiClO_4$ salt is added, relegating the monomer (*R*)-**2** to the Soldier position (Figure 75b).

USC UNIVERSIDADE DE SANTIAGO DE COMPOSTELA

DFT computational studies performed on a dimeric model (see above for details) show that π-π supramolecular interactions emerge when the copolymer adopts a *P* helix ($ECD_{380\ nm} > 0$), comonomer (*S*)-**1** being present in an *ap*-OMe conformation, while (*R*)-**2** adopts the *sp*-OMe conformation. This π-π interaction is not present when (*S*)-**1** adopts an *ap*-OMe conformation and (*R*)-**2** also adopts an *ap*-OMe. Therefore, a conformational change takes place at comonomer (*R*)-**2** when the Li^+ ion is complexed to (*S*)-**1** (Figure 75f).

It is worth noting that the Sergeant and Soldier roles of comonomers (*R*)-**2** (Sergeant) and (*S*)-**1** Soldier within this poly-[(*S*)-$\mathbf{1}_r$-*co*-(*R*)-$\mathbf{2}_{1-r}$] (r=0.9-0.1) copolymer series are swapped after complexation with the monovalent metal ion, where comonomer (*S*)-**1** becomes a Sergeant, relegating the comonomer (*R*)-**2** to the Soldier role. As far as we know, we have demonstrated for the first time that the role of the comonomers in a chiral-to-chiral Sergeants and Soldiers effect can be reversed by the addition of an external stimulus.

By applying a modification of Sato's model, it was possible to obtain the $\Delta G_{h,(S)\mathbf{1}(S)\mathbf{1}}$, $\Delta G_{h,(R)\mathbf{2}(R)\mathbf{2}}$, and $\Delta G_{h,(S)\mathbf{1}(R)\mathbf{2}}$ which are +50.25, -27.45, and +191.60 J/mol, respectively. These energy helix induction energies for each possible comonomer pair within the copolymer chain allow us to obtain a value for the communication process, in this case (Comm= +2.47 [Sergeant x= (*S*)-**1**]), which indicates the presence of a chiral-to-chiral Classic Sergeants and Soldiers Effect (Figure 75e).

Finally, the reversibility of the process was studied by decreasing the temperature of the helical polymer metal complex (HPMC) solution. From literature it is known that the metal ion can be decomplexed from a PPA pendant by decreasing the temperature.[404] Thus, ECD studies at 298 and 268 K were done for a chloroform solution (c =0.3 mg/mL) of the poly-[(*S*)-$\mathbf{1}_r$-*co*-(*R*)-$\mathbf{2}_{1-r}$] m.r.u./Li^+ (r=0.6) copolymer complex (0.5 K/min) in a 1.0/0.1 mol/mol ratio (Figure 75d). From these studies it was found that it is possible to completely reverse the roles of the Sergeant and Soldier comonomers of chiral dynamic helical copolymers by playing in this case between a chiral-to-chiral Classic Sergeants and Soldiers Effect and a chiral-to-chiral Abnormal Sergeants and Soldiers Effect (Figure 75c).

USC UNIVERSIDADE DE SANTIAGO DE COMPOSTELA

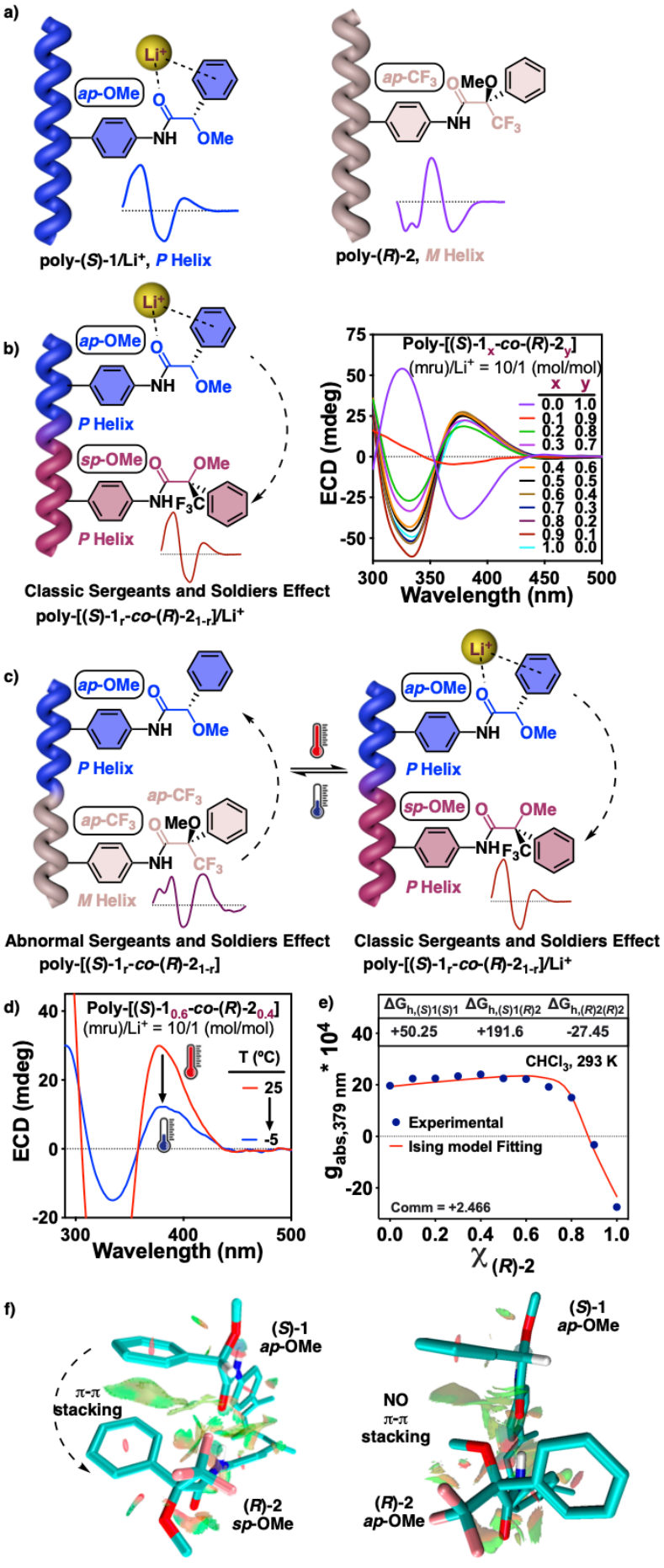

a)
poly-(S)-1/Li+, P Helix
poly-(R)-2, M Helix
b)
Classic Sergeants and Soldiers Effect
poly-[(S)-1r-co-(R)-21-r]/Li+
Poly-[(S)-1x-co-(R)-2y]
(mru)/Li+ = 10/1 (mol/mol)
ECD (mdeg)
Wavelength (nm)
c)
Abnormal Sergeants and Soldiers Effect
poly-[(S)-1r-co-(R)-21-r]
Classic Sergeants and Soldiers Effect
poly-[(S)-1r-co-(R)-21-r]/Li+
d)
Poly-[(S)-10.6-co-(R)-20.4]
(mru)/Li+ = 10/1 (mol/mol)
T (°C)
ECD (mdeg)
Wavelength (nm)
e)
ΔGh,(S)1(S)1 ΔGh,(S)1(R)2 ΔGh,(R)2(R)2
+50.25 +191.6 -27.45
CHCl3, 293 K
Experimental
Ising model Fitting
Comm = +2.466
gabs,379 nm * 10^4
χ (R)-2
f)
(S)-1 ap-OMe
π-π stacking
(R)-2 sp-OMe
NO π-π stacking
(R)-2 ap-OMe

Figure 75. a) ECD pattern, helical sense, and major conformations at the pendants of poly-(*S*)-**1** and poly-(*R*)-**2** in $CHCl_3$ complexed with 0.1 equiv $LiClO_4$ (10 mg/mL MeOH). b) ECD studies of the poly-[(*S*)-**1**$_r$-*co*-(*R*)-**2**$_{1-r}$] series complexed with 0.1 equiv $LiClO_4$ (10 mg/mL MeOH). c, d) illustration of the helical sense adopted by the polyenic backbone and VT-ECD spectra (0.5 ºC/min) of poly-[(*S*)-**1**$_r$-*co*-(*R*)-**2**$_{1-r}$]/Li^+ responding to temperature: at low temperature Sergeant complexation of (*S*)-**1** is deactivated, while at room temperature complexation is restored to switch the communication mechanism. e) Plot of the g_{abs} at indicated wavelength for poly-[(*S*)-**1**$_r$-*co*-(*R*)-**2**$_{1-r}$]/Li^+ series against copolymer composition and the corresponding curve fitting based on modified Sato's model to obtain the free energy parameters. f) Optimized structures and NCI calculations (wb97xd/6-31+g**, PCM=$CHCl_3$) of the dimers containing the residues at the nth, nth +3 in a *P* helix with conformation of the Sergeant (*S*)-**1** in *ap*-OMe and the two options of the Soldier (*R*)-**2** in *sp*-OMe and *ap*-OMe. Concentration of homopolymers and copolymers = 0.3 mg/mL $CHCl_3$.

From Abnormal to Classic chiral-to-chiral Sergeants and Soldiers Effect in poly-[(*R*)-1$_r$-*co*-(*S*)-2$_{1-r}$] (r= 0.0-1.0) m.r.u./Li^+ 1.0/0.1 (mol/mol) ratio: Similar results were obtained for the enantiomeric poly-[(*R*)-**1**$_r$-*co*-(*S*)-**2**$_{1-r}$] (r=0.9-0.1) copolymer series after complexation with Li^+ ions in a 1.0/0.1 mol/mol ratios. In this case, the same reversion of comonomer role in the chiral-to-chiral Sergeants and Soldiers effect was observed after addition of a monovalent metal ion as external stimulus. However, the screw sense induced after swapping the Sergeant and Soldier roles between the chiral comonomers (*R*)-**1** (*ap*-OMe, *M* helix) and (*S*)-**2** (*sp*-OMe, *M* helix) is an *M* helix, opposite to the previous one because of their enantiomeric relationship (see section 5.3.24. From Abnormal to Classic chiral-to-chiral Sergeants and Soldiers Effect in poly-[(R)-1r-co-(*S*)-21-r] (r= 0.0-1.0) m.r.u./Li+ 1.0/0.1 (mol/mol) ratio).

From Abnormal chiral-to-chiral Sergeants and Soldiers Effect to Chiral Accord in poly-[(*S*)-1$_r$-*co*-(*R*)-2$_{1-r}$] (r= 0.0-1.0) m.r.u./Ca^{2+} 1.0/0.1 (mol/mol) ratio: Next, similar studies were carried out adding a $Ca(ClO_4)_2$ to a chloroform solution of the poly-[(*S*)-**1**$_r$-*co*-(*R*)-**2**$_{1-r}$] (r=0.1-0.9) copolymer series to generate poly-[(*S*)-**1**$_r$-*co*-(*R*)-**2**$_{1-r}$]/Ca^{2+} complexes at a 1.0/0.1 (mol/mol) ratios.

ECD studies show that in all poly-[(*S*)-**1**$_r$-*co*-(*R*)-**2**$_{1-r}$] (r=0.9-0.1)/Ca^{2+} metal complex copolymer series, a strong negative Cotton band is present at 380 nm [$ECD_{380\ nm} < 0$] (Figure 76b). In this case, the ECD obtained for each copolymer is the result of an arithmetic sum of the ECD spectra obtained for the corresponding homopolymers in the presence of Ca^{2+} ions. This fact indicates that when monomer (*R*)-**1** is complexed to a divalent metal ion, it adopts the expected *sp*-OMe conformation inducing an *M* helical sense, while the conformer at comonomer (*S*)-**2** remains unaltered (*ap*-CF_3 conformer)

USC UNIVERSIDADE DE SANTIAGO DE COMPOSTELA

(Figure 76a). In these conformations, both comonomers induce the same *M* helical sense.

However, in the ECD and UV-Vis spectra, we can see that there are two different helical scaffolds, with different elongations but the same *M* helical sense (Figure 76b and Figure S97). A more compressed helix is obtained when the (*S*)-**1**/(*R*)-**2** comonomer ratio is between 0.0-0.4/1.0-0.6 mol/mol, while a more stretched helix is generated when the (*S*)-**1**/(*R*)-**2** comonomer ratio is 0.5-1.0/0.5-0.0 mol/mol. Thus, the elongation of the polymer depends on the copolymer composition (Figure S97). This fact indicates that the two components induce two different helical structures, although they have the same helical sense. Therefore, a lack of communication between the two components is present, resulting in a Chiral Accord effect.

DFT computational studies carried out with a dimeric model (see above for details) lack $\pi-\pi$ supramolecular interactions when the copolymer adopts an *M* helix ($ECD_{380\ nm}$<0), comonomer (*S*)-**1** being present in a *sp*-OMe conformation, while (*R*)-**2** is adopts an *ap*-CF_3 conformation. (Figure 76f).

By applying a modification of Sato's model, it was possible to obtain the $\Delta G_{h,(S)\mathbf{1}(S)\mathbf{1}}$, $\Delta G_{h,(R)\mathbf{2}(R)\mathbf{2}}$, and $\Delta G_{h,(S)\mathbf{1}(R)\mathbf{2}}$ which are -137.80, -46.83, and +6.39 J/mol, respectively. These energy helix induction energies for each possible pair of comonomer within the copolymer chain allow us to obtain a value for the communication process, in this case Comm= -0.07 [x=(*S*)-**1**]), a value close to zero which indicates the absence of a chiral-to-chiral communication mechanism (Figure 76e).

Low temperature ECD studies (268 K) of the poly-[(*S*)-$\mathbf{1}_r$-*co*-(*R*)-$\mathbf{2}_{1-r}$] (r=0.6)/Ca^{2+} complex (0.5 K/min) in a 1.0/0.1 mol/mol ratio (Figure 76d) show the reversibility of the process were the Sergeants and the Soldiers roles in the SaS effect can be reverted. This reversibility of the process allows us to activate/deactivate selectively by temperature different chiral communication effects such as the chiral-to-chiral Classic Sergeants and Soldiers Effect or the Chiral Accord effect (Figure 76c).

USC UNIVERSIDADE DE SANTIAGO DE COMPOSTELA

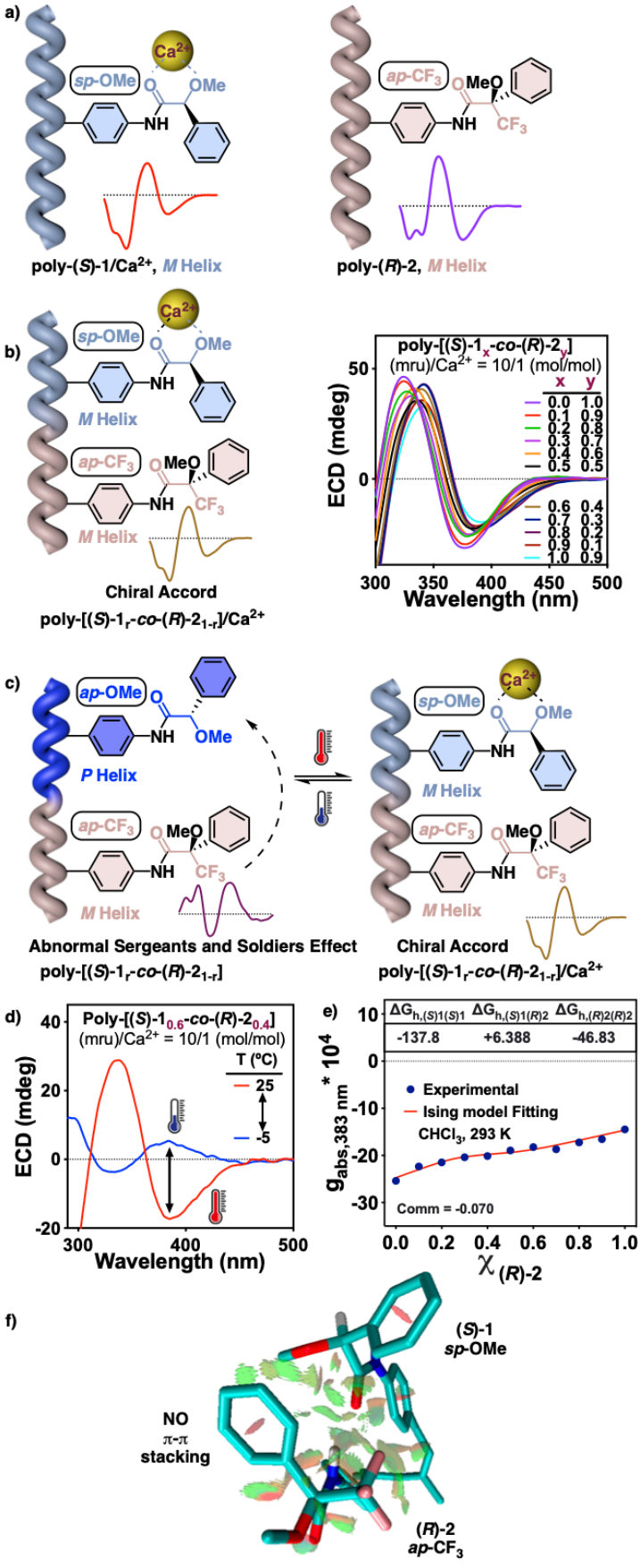

a)
sp-OMe
Ca2+
OMe
NH
poly-(S)-1/Ca2+, M Helix
ap-CF3
MeO
CF3
poly-(R)-2, M Helix
b)
M Helix
Chiral Accord
poly-[(S)-1r-co-(R)-21-r]/Ca2+
poly-[(S)-1x-co-(R)-2y]
(mru)/Ca2+ = 10/1 (mol/mol)
ECD (mdeg)
Wavelength (nm)
c)
ap-OMe
P Helix
Abnormal Sergeants and Soldiers Effect
poly-[(S)-1r-co-(R)-21-r]
d)
Poly-[(S)-10.6-co-(R)-20.4]
T (°C)
25
-5
e)
ΔGh,(S)1(S)1
ΔGh,(S)1(R)2
ΔGh,(R)2(R)2
-137.8
+6.388
-46.83
Experimental
Ising model Fitting
CHCl3, 293 K
Comm = -0.070
gabs,383 nm * 10^4
χ (R)-2
f)
(S)-1
sp-OMe
NO
π-π
stacking
(R)-2
ap-CF3

Figure 76. a) ECD pattern, helical sense, and major conformations at the pendants of poly-(*S*)-**1** and poly-(*R*)-**2** in $CHCl_3$ complexed with 0.1 equiv $Ca(ClO_4)_2$ (10 mg/mL MeOH). b) ECD studies of the poly-[(*S*)-**1**$_r$-*co*-(*R*)-**2**$_{1-r}$] series complexed with 0.1 equiv $Ca(ClO_4)_2$ (10 mg/mL MeOH). c, d) illustration of the helical sense adopted by the polyenic backbone and VT-ECD spectra (0.5 ºC/min) of poly-[(*S*)-**1**$_r$-*co*-(*R*)-**2**$_{1-r}$]/Ca^{2+} responding to temperature: at low temperature (*S*)-**1** complexation is deactivated, while at room temperature complexation is restored to switch the communication mechanism. e) Plot of the g_{abs} at indicated wavelength for poly-[(*S*)-**1**$_r$-*co*-(*R*)-**2**$_{1-r}$]/Ca^{2+} series against copolymer composition and the corresponding curve fitting based on modified Sato's model to obtain the free energy parameters. f) Optimized structure and NCI calculations (wb97xd/6-31+g**, PCM=$CHCl_3$) of the dimer containing the residues at the nth, nth +3 in an *M* helix with conformation of (*S*)-**1** in *sp*-OMe and (*R*)-**2** in *ap*-CF_3. Concentration of homopolymers and copolymers = 0.3 mg/mL $CHCl_3$.

From Abnormal chiral-to-chiral Sergeants and Soldiers Effect to Chiral Accord in poly-[(*R*)-1$_r$-*co*-(*S*)-2$_{1-r}$] (r= 0.0-1.0) m.r.u./Ca^{2+} 1.0/0.1 (mol/mol) ratio: The same Chiral Accord effect was observed in the enantiomeric poly-[(*R*)-**1**$_r$-*co*-(*S*)-**2**$_{1-r}$] copolymer series after complexation with divalent metal ions, although in this case two helices with a *P* screw sense excess are obtained [$ECD_{380\ nm} > 0$]. this fact is due to their enantiomeric relationship with the poly-[(*S*)-**1**$_r$-*co*-(*R*)-**2**$_{1-r}$] (r=0.9-0.1)/Ca^{2+} metal complex copolymer series (see section 5.3.25. From Abnormal chiral-to-chiral Sergeants and Soldiers Effect to Chiral Accord in poly-[(R)-1r-co-(*S*)-21-r] (r= 0.0-1.0) m.r.u./Ca2+ 1.0/0.1 (mol/mol) ratio).

From a mixture of Chiral Accord and Chiral Conflict effect to a selective Chiral Accord in poly-[(*R*)-1$_r$-*co*-(*R*)-2$_{1-r}$] (r= 0.0-1.0) m.r.u./Li^+ 1.0/0.1 (mol/mol) ratio: $LiClO_4$ was added to vials containing chloroform solutions of the poly-[(*R*)-**1**$_r$-*co*-(*R*)-**2**$_{1-r}$] (r=0.9-0.1) copolymer series to form poly-[(*R*)-**1**$_r$-*co*-(*R*)-**2**$_{1-r}$] (r=0.9-0.1)/Li^+ complexes in a 1.0/0.1 mol/mol ratios. ECD studies show that in all the poly-[(*R*)-**1**$_r$-*co*-(*R*)-**2**$_{1-r}$] (r=0.9-0.1)/Li^+ metal complex copolymer series, a strong negative Cotton band is present at 380 nm [$ECD_{380\ nm} < 0$] (Figure 77b). The ECD traces obtained for the different copolymers in the series are those expected from the corresponding behavior of the parent homopolymers in the presence of $LiClO_4$ and considering the (*R*)-**1**/(*R*)-**2** comonomer ratio (Figure 77a and Figure 77b). Therefore, a lack of communication between both monomers is found in the presence of Li^+.

However, by looking at the conformations adopted by (*R*)-**1** complexed to a monovalent metal ion (*ap*-OMe) and (*R*)-**2** (*ap*-CF_3), and the screw sense induced for both conformers (*M* helix sense), we can state that a Chiral Accord effect is ruling the helical sense in the copolymer series. Thus, ECD and UV-Vis spectra show that there

USC DE COMPOSTELA

are two different helical scaffolds, with different elongations but with the same *M* helical sense (Figure S98).

Therefore, the asymmetry amplification effect is being altered by the presence of Li^+, from a mixture of Chiral Conflict and Chiral Accord effects towards a pure Chiral Accord effect.

DFT computational studies carried out in a dimeric model (see above for details) lack π–π supramolecular interactions when the copolymer adopts an *M* helix ($ECD_{380\ nm}$<0), comonomer (*R*)-**1** being present in an *ap*-OMe conformation, while (*R*)-**2** adopts an *ap*-CF_3 conformation. (Figure 77f).

By applying a modification of Sato's model, it was possible to obtain the $\Delta G_{h,(R)\mathbf{1}(R)\mathbf{1}}$, $\Delta G_{h,(R)\mathbf{2}(R)\mathbf{2}}$, and $\Delta G_{h,(R)\mathbf{1}(R)\mathbf{2}}$ which are -64.10, -28.29, and +0.17 J/mol, respectively. These energy helix induction energies for each possible pair of comonomers within the copolymer chain allow us to obtain a value for the communication process, in this case Comm= -0.01 [x=(*R*)-**1**]), a value close to zero, which indicates the absence of a chiral-to-chiral communication mechanism characteristic of Chiral Conflict or Chiral Accord effects (Figure 77e).

Low temperature ECD studies (268 K) of the poly-[(*R*)-$\mathbf{1}_r$-*co*-(*S*)-$\mathbf{2}_{1-r}$] m.r.u./Li^+ (r=0.6) complex (0.5 K/min) in a 1.0/0.1 mol/mol ratio (Figure 77d) show a fully reversibility between the Chiral Conflict and Chiral Accord induced in the absence of metal ions (decomplexation) and the Chiral Accord effects (complex) (Figure 77c).

USC UNIVERSIDADE DE SANTIAGO DE COMPOSTELA

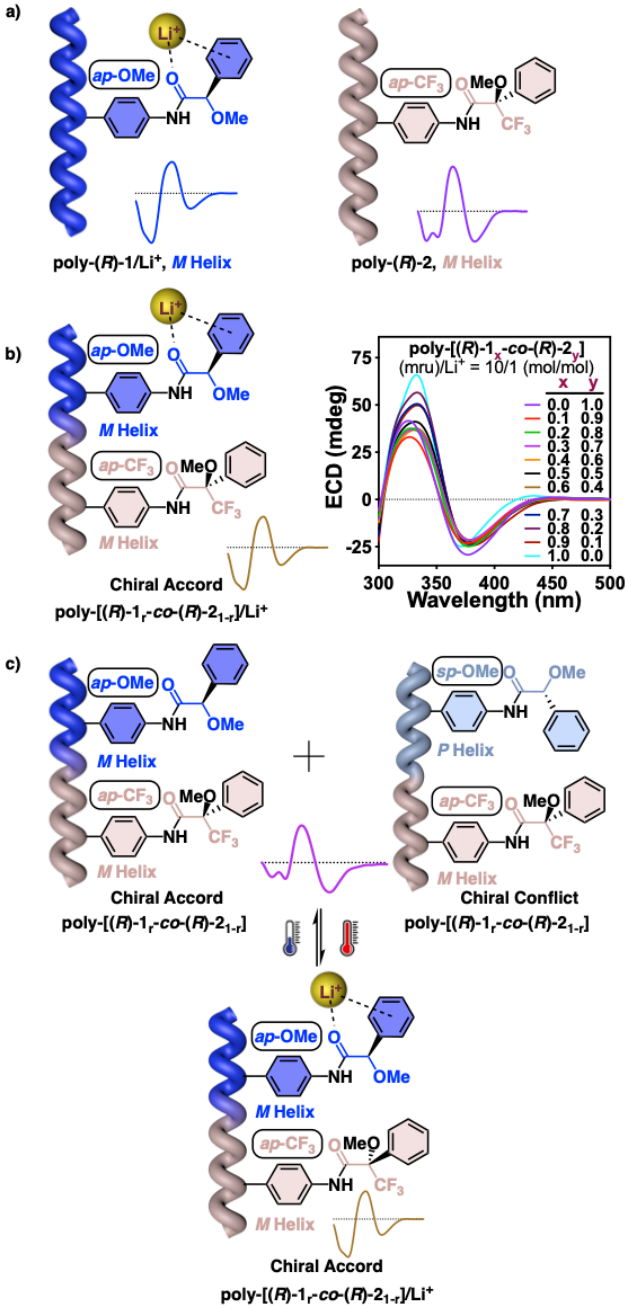

a)
poly-(R)-1/Li+, M Helix
poly-(R)-2, M Helix
b)
M Helix
Chiral Accord
poly-[(R)-1r-co-(R)-21-r]/Li+
poly-[(R)-1x-co-(R)-2y]
(mru)/Li+ = 10/1 (mol/mol)
ECD (mdeg)
Wavelength (nm)
c)
Chiral Accord
Chiral Conflict
P Helix
d)
Poly-[(R)-10.6-co-(R)-20.4]
T (°C)
e)
Experimental
Ising model Fitting
CHCl3, 293 K
Comm = -0.005
f)
(R)-1
ap-OMe
NO
π-π
stacking
(R)-2
ap-CF3

Figure 77. a) ECD pattern, helical sense, and major conformations at the pendants of poly-(*R*)-**1** and poly-(*R*)-**2** in $CHCl_3$ complexed with 0.1 equiv $LiClO_4$ (10 mg/mL MeOH). b) ECD studies of the poly-[(*R*)-**1**$_r$-*co*-(*R*)-**2**$_{1-r}$] series complexed with 0.1 equiv $LiClO_4$ (10 mg/mL MeOH). c, d) illustration of the helical sense adopted by the polyenic backbone and VT-ECD spectra (0.5 ºC/min) of poly-[(*R*)-**1**$_r$-*co*-(*R*)-**2**$_{1-r}$]/Li^+ responding to temperature: at low temperature (*R*)-**1** complexation is deactivated, while at room temperature complexation is restored to switch the communication mechanism. e) Plot of the g_{abs} at indicated wavelength for poly-[(*R*)-**1**$_r$-*co*-(*R*)-**2**$_{1-r}$]/Li^+ series against copolymer composition and the corresponding curve fitting based on modified Sato's model to obtain the free energy parameters. f) Optimized structure and NCI calculations (wb97xd/6-31+g**, PCM=$CHCl_3$) of the dimer containing the residues at the nth, nth +3 in an *M* helix with conformation of (*R*)-**1** in *ap*-OMe and (*R*)-**2** in *ap*-CF_3. Concentration of homopolymers and copolymers = 0.3 mg/mL $CHCl_3$.

From a mixture of Chiral Accord and Chiral Conflict effect to a selective Chiral Accord in poly-[(*S*)-1$_r$-*co*-(*S*)-2$_{1-r}$] (r= 0.0-1.0) m.r.u./Li^+ 1.0/0.1 (mol/mol) ratio: The same Chiral Accord effect is obtained for the enantiomeric poly-[(*S*)-**1**$_r$-*co*-(*S*)-**2**$_{1-r}$] (r=0.9-0.1)/Li^+ metal complex copolymer series [$ECD_{380\ nm} > 0$, *P* helix], although in this case the screw sense induced is the opposite to the one induced by the poly-[(*R*)-**1**$_r$-*co*-(*R*)-**2**$_{1-r}$] (r=0.9-0.1)/Li^+ metal complex copolymer series due to their enantiomeric relationship (see section 5.3.26. From a mixture of Chiral Accord and Chiral Conflict effect to a selective Chiral Accord in poly-[(*R*)-1r-co-(*R*)-21-r] (r= 0.0-1.0) m.r.u./Li+ 1.0/0.1 (mol/mol) ratio).

From a mixture of Chiral Accord and Chiral Conflict effect to to Classic chiral-to-chiral Sergeants and Soldiers Effect in poly-[(*R*)-1$_r$-*co*-(*R*)-2$_{1-r}$] (r= 0.0-1.0) m.r.u./Ca^{2+} 1.0/0.1 (mol/mol) ratio: $Ca(ClO_4)_2$ was added to vials containing chloroform solutions of poly-[(*R*)-**1**$_r$-*co*-(*R*)-**2**$_{1-r}$] (r=0.9-0.1) copolymer series to form poly-[(*R*)-**1**$_r$-*co*-(*R*)-**2**$_{1-r}$] (r=0.9-0.1)/Ca^{2+} complexes in 1.0/0.1 mol/mol ratios. ECD studies show that in all poly-[(*R*)-**1**$_r$-*co*-(*R*)-**2**$_{1-r}$] (r=0.9-0.1)/Ca^{2+} metal complexes, a strong positive Cotton band is present at 380 nm [$ECD_{380\ nm} > 0$], which is identical to the one induced by the monomer (*R*)-**1** interacting with the a divalent metal ion —poly-(*R*)-**1**/Ca^{2+} [$ECD_{380\ nm} > 0$], *sp*-OMe conformer—, and opposite to the one commanded by the chiral monomer (*R*)-**2** [poly-(*R*)-**2** ($ECD_{380\ nm} < 0$), *ap*-CF_3 conformation] (Figure 78a and Figure 78b).

Interestingly, the ECD signal remains positive at all comonomer ratios, indicating the presence of a very effective chiral-to-chiral communication effect, where monomer (*R*)-**1** now complexed to a Ca^{2+} ion, is the one that becomes a Sergeant, relegating the monomer (*R*)-**2** to the Soldier position. Thus, monomer (*R*)-**2** must change its

USC UNIVERSIDADE DE SANTIAGO DE COMPOSTELA

conformation at the pendant group from *ap*-CF_3 to *sp*-OMe to follow the *P* helix commanded by comonomer (*R*)-**1**/Ca^{2+} (*sp*-OMe conformer).

DFT computational studies carried out in a dimeric model (see above for details) show that $\pi-\pi$ supramolecular interactions emerge when the copolymer adopts a *P* helix ($ECD_{380\ nm}$>0), when both comonomers adopt a *sp*-OMe conformation at the pendant, while this interaction is not present if (*R*)-**2** is introduced into an *ap*-OMe conformation. These results corroborate the conformational change at (*R*)-**2** to behave as chiral Soldier (Figure 78f).

By applying a modification of Sato's model, it was possible to obtain the $\Delta G_{h,(R)\mathbf{1}(R)\mathbf{1}}$, $\Delta G_{h,(R)\mathbf{2}(R)\mathbf{2}}$, and $\Delta G_{h,(R)\mathbf{1}(R)\mathbf{2}}$ which are +42.74, -45.78, and +194.00 J/mol, respectively. These energy helix induction energies for each possible pair of comonomers within the copolymer chain allow us to obtain a value for the communication process, in this case, Comm= +2.19 [Sergeant x=(*R*)-**1**]), a value distinct to zero, which indicates the presence of a chiral-to-chiral communication mechanism within the asymmetry amplification process. In this case it is a chiral-to-chiral Classic Sergeants and Soldiers Effect (Figure 78e).

Low temperature ECD studies (268 K) of the poly-[(*R*)-$\mathbf{1}_r$-*co*-(*R*)-$\mathbf{2}_{1-r}$] m.r.u./Ca^{2+} (r=0.4) complex (0.5 K/min) in a 1.0/0.1 mol/mol ratio (Figure 78d) show a fully reversibility between the Chiral Conflict and the chiral-to-chiral Sergeants and Soldiers Effect (Figure 78c), demonstrating that a Chiral Dispute effect with different results effect can be produced between the two chiral monomers in the poly-[(*R*)-$\mathbf{1}_r$-*co*-(*R*)-$\mathbf{2}_{1-r}$] (r=0.9-0.1) copolymer series by the orthogonal action of external stimuli.

USC UNIVERSIDADE DE SANTIAGO DE COMPOSTELA

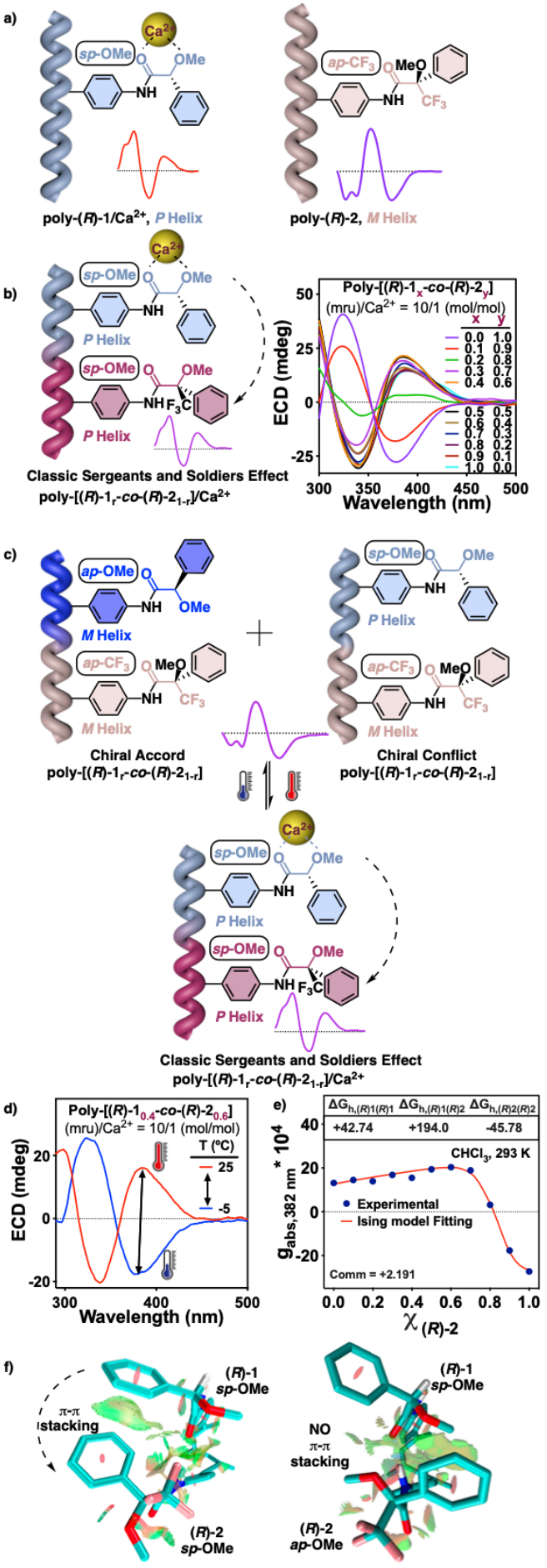

a)
sp-OMe
OMe
NH
Ca2+
poly-(R)-1/Ca2+, P Helix
ap-CF3
MeO
CF3
poly-(R)-2, M Helix
b)
P Helix
Classic Sergeants and Soldiers Effect
poly-[(R)-1r-co-(R)-21-r]/Ca2+
Poly-[(R)-1x-co-(R)-2y]
(mru)/Ca2+ = 10/1 (mol/mol)
ECD (mdeg)
Wavelength (nm)
c)
ap-OMe
M Helix
Chiral Accord
Chiral Conflict
d)
Poly-[(R)-10.4-co-(R)-20.6]
T (°C)
e)
ΔGh,(R)1(R)1 ΔGh,(R)1(R)2 ΔGh,(R)2(R)2
+42.74 +194.0 -45.78
CHCl3, 293 K
Experimental
Ising model Fitting
Comm = +2.191
gabs,382 nm * 10^4
χ (R)-2
f)
π-π stacking
(R)-1 sp-OMe
(R)-2 sp-OMe
NO π-π stacking
(R)-2 ap-OMe

Figure 78. a) ECD pattern, helical sense, and major conformations at the pendants of poly-(*R*)-**1** and poly-(*R*)-**2** in $CHCl_3$ complexed with 0.1 equiv $Ca(ClO_4)_2$ (10 mg/mL MeOH). b) ECD studies of the poly-[(*R*)-**1**$_r$-*co*-(*R*)-**2**$_{1-r}$] series complexed with 0.1 equiv $Ca(ClO_4)_2$ (10 mg/mL MeOH). c, d) illustration of the helical sense adopted by the polyenic backbone and VT-ECD spectra (0.5 ºC/min) of poly-[(*R*)-**1**$_r$-*co*-(*R*)-**2**$_{1-r}$]/Ca^{2+} responding to temperature: at low temperature Sergeant complexation of (*R*)-**1** is deactivated, while at room temperature complexation is restored to switch the communication mechanism. e) Plot of the g_{abs} at indicated wavelength for poly-[(*R*)-**1**$_r$-*co*-(*R*)-**2**$_{1-r}$]/Ca^{2+} series against copolymer composition and the corresponding curve fitting based on modified Sato's model to obtain the free energy parameters. f) Optimized structures and NCI calculations (wb97xd/6-31+g**, PCM=$CHCl_3$) of the dimers containing the residues at the nth, nth +3 in a *P* helix with conformation of the Sergeant (*R*)-**1** in *sp*-OMe and the two options of the Soldier (*R*)-**2** in *sp*-OMe and *ap*-OMe. Concentration of homopolymers and copolymers = 0.3 mg/mL $CHCl_3$.

From a mixture of Chiral Accord and Chiral Conflict effect to Classic chiral-to-chiral Sergeants and Soldiers Effect in poly-[(*S*)-1$_r$-*co*-(*S*)-2$_{1-r}$] (r= 0.0-1.0) m.r.u./Ca^{2+} 1.0/0.1 (mol/mol) ratio: As happens in their enantiomeric copolymer metal complex series [poly-[(*S*)-**1**$_r$-*co*-(*S*)-**2**$_{1-r}$] (r=0.9-0.1)/Ca^{2+}], a Chiral Dispute effect is observed with a swap of the Sergeants and Soldiers roles for monomer (*S*)-**2** and (*S*)-**1** once the divalent metal ion is added to the copolymer solutions (see section 5.3.27. From a mixture of Chiral Accord and Chiral Conflict effect to Classic chiral-to-chiral Sergeants and Soldiers Effect in poly-[(S)-1r-co-(*S*)-21-r] (r= 0.0-1.0) m.r.u./Ca2+ 1.0/0.1 (mol/mol) ratio).

3.3.3. Conclusions

By using the diastereomeric series of a dynamic helical copolymer made by two chiral comonomers —poly-[(*R*)-**1**$_r$-*co*-(*R*)-**2**$_{1-r}$], poly-[(*S*)-**1**$_r$-*co*-(*S*)-**2**$_{1-r}$], poly-[(*R*)-**1**$_r$-*co*-(*S*)-**2**$_{1-r}$], and poly-[(*S*)-**1**$_r$-*co*-(*R*)-**2**$_{1-r}$] (r=0.9-0.1)— with orthogonal stimuli-responsive properties, we have demonstrated that it is possible to trigger different chiral communication mechanisms along the copolymer chains such as chiral-to-chiral Classic and Abnormal Sergeants and Soldiers Effects, Chiral Accord, and Chiral Conflict Effects. The activation of the different asymmetry amplification effects depends on the absolute configuration of both components and the external stimuli employed. Of these fascinating results on chiral-to-chiral communication mechanisms along chiral dynamic helical copolymers, the most astonishing is the bidirectionality of the Sergeants and Soldiers Effect. Depending on the stimulus employed, it is possible to fully invert the Sergeants and Soldiers effect, swapping the Sergeant and Soldier roles within the copolymer. Moreover, we also found that these asymmetry amplification effects exchanging the

USC DE SANTIAGO DE COMPOSTELA

Sergeant and Soldiers Effect are also fully reversible when another stimulus such as temperature is present. This work constitutes the first step towards understanding complex asymmetry amplification effects in multi-chiral systems and will allow the creation of new stimuli-responsive materials with potential applications in fields such as asymmetric synthesis, molecular recognition, or as chiral stationary phases in HPLC, were both the axial chirality of the helix and the chirality of the different components can play an important role.

USC UNIVERSIDADE DE SANTIAGO DE COMPOSTELA

USC
UNIVERSIDADE
DE SANTIAGO
DE COMPOSTELA

3.4. Synergistic Chiral Awakening: Cascade Sergeants and Soldiers Effect Through Double-Step Activation

Abstract

In dynamic helical copolymers, the conformational communication mechanisms and the cooperativity of the asymmetry amplification processes triggered between the two comonomers—chiral(**1**)/achiral(**2**), chiral(**1**)/chiral(**2**)— can result in different effects such as the Classic or the Abnormal Sergeants and Soldiers Effect, Majority Rules, Chiral Coalition, Chiral Accord, or Chiral Conflict effects. Importantly, a previous knowledge of the conformational composition at the pendants, and its ability to be specifically shifted towards one conformer or another by certain external stimuli will allow us to trigger different asymmetry amplification effects within a copolymer series. In this work we will show how the intrinsic composition of the copolymer series (comonomers ratio), can also act as an internal stimulus to trigger different asymmetry amplification effects in a specific environmental condition (temperature and solvent). Specifically, we will show how the hydrophobicity introduced in the copolymer chain by increasing the ratio of one monomer (monomer **a**) in the copolymer, will activate a specific conformation in the other comonomer (monomer **b**), who will command the monomer **a** to adopt a specific helical structure (sense and elongation).

USC
UNIVERSIDADE DE SANTIAGO DE COMPOSTELA

USC
UNIVERSIDADE
DE SANTIAGO
DE COMPOSTELA

3.4.1. Precedents

Helices are key structural motifs found in biomolecules like DNA and proteins, whose structure is directly related to their function. Thus, creation of novel secondary structures allows obtaining materials with new functionalities. Dynamic helical polymers such as chiral poly(phenylacetylene)s (PPAs) have been studied extensively during the last decades due to the possibility of tuning their elongation and screw sense excess by the presence of different external stimuli. These stimuli-responsive properties of PPAs find applications as chiral stationary phases in HPLC, molecular recognition, or asymmetric catalysis among other applications.[6,71,337,379,380,404]

The ability of dynamic helical PPAs to modulate their screw sense resides in the low energy barrier between the *P* and *M* orientations of their polyene backbone, which can be selectively induced by acting on the conformational composition of the pendant groups through external stimuli such as light, heat, chiral molecules, or ions among others. In these polymers, helix induction follows a cooperative mechanism, where the conformational change produced by an external stimulus at the pendant groups of a reduced number of monomer repeating units is rapidly transmitted to the rest of the monomers present in the polymer chain.[6,25,43,59,70,84,86,92,102,119,135,147,169,171,233-237,240-245,248,253,265,266,269,334-337,393-398,425-428]

In copolymers, a more complicated mechanism is triggered. In such systems, a conformational communication mechanism is triggered between the two comonomers, where changes in the conformational composition at one of the copolymer components can provoke a conformational change in the other component and transmitted effectively to the whole copolymer chain via a cooperative mechanism.

Depending on the chirality of the two components, different conformational communication mechanisms can be triggered. Thus, if one component is chiral and the other is achiral, a Classic or Abnormal Sergeants and Soldiers Effect can be produced due to a communication mechanism from the Sergeant (chiral component) to the Soldier (achiral component). However, if both components are chiral, the communication can flow from one chiral component to the other or vice versa, depending on the stimuli used, which can selectively stabilize the conformer of one of the chiral components (Sergeant). In these chiral-to-chiral communication effects the Classic and abnormal Sergeants and Soldiers Effects are found, as well as Chiral Coalition or Majority Rules. If this

USC UNIVERSIDADE DE SANTIAGO DE COMPOSTELA

communication is not produced between the two components, keeping their helix induction effects as in their corresponding homopolymers, Chiral Conflict or Chiral Accord can be present in the copolymer helix.[26,248,271-279,281,367,375,406,407,421-424,429]

Herein, we will demonstrate that it is possible to use the different hydrophobicity/hydrophilicity of the two comonomers that form the helical copolymer as an internal stimulus to trigger different asymmetry amplification effects at different comonomer ratios within the copolymer series. To do that we designed a PPA copolymer made by a chiral monomer and an achiral one, where the conformational communication must flow from the chiral monomer towards the achiral one to induce asymmetry amplification effects such as the Classic or Abnormal Sergeants and Soldiers Effect. However, if the chiral component has a conformational composition at the pendant group between different conformers that induce opposite helical senses, the information that flows from the chiral component (Sergeant)[42,267,366] to the achiral one (Soldier) becomes confused and no asymmetry amplification should be triggered. Nonetheless, if both comonomers have different hydrophobicity/hydrophilicity, their ratio within the copolymer chain can be used as an internal stimulus to fix a preferred conformation at the chiral monomer and trigger an asymmetry amplification effect within the copolymer.

3.4.2. Discussion

To test our hypothesis, we designed a copolymer made from the 4-ethynilanilides of (*R*)-(-)- and (*S*)-(+)-α-α-methoxy-α-phenylacetic acid [chiral monomers (*R*)- or (*S*)-**1**, Sergeants], and the 4-ethynilanilide and 3-ethynilanilide of α-α-diphenylacetic acid [achiral monomers **2** and **3**, Soldiers] (Figure 79a). These monomers meet the requirements needed to perform the asymmetry amplification studies based on their different hydrophobic/hydrophilic behavior: while the achiral monomers (**2** and **3**) bear hydrophobic aryl rings at the pendant, the chiral monomer [(*R*/*S*)-**1**] bears heteroatoms on the pendant, such as an oxygen atom. Moreover, the chiral homopolymers poly-(*S*)-**1** and poly-(*R*)-**1** generate, in low-polar solvents, such as chloroform, axially racemic mixtures of helical polymers (*P* and *M* helices in equal populations). Therefore, small bias in the copolymer ratio can be enough to alter the polarity of the media and trigger through a cooperative effect an asymmetry amplification effect.

USC UNIVERSIDADE DE SANTIAGO DE COMPOSTELA

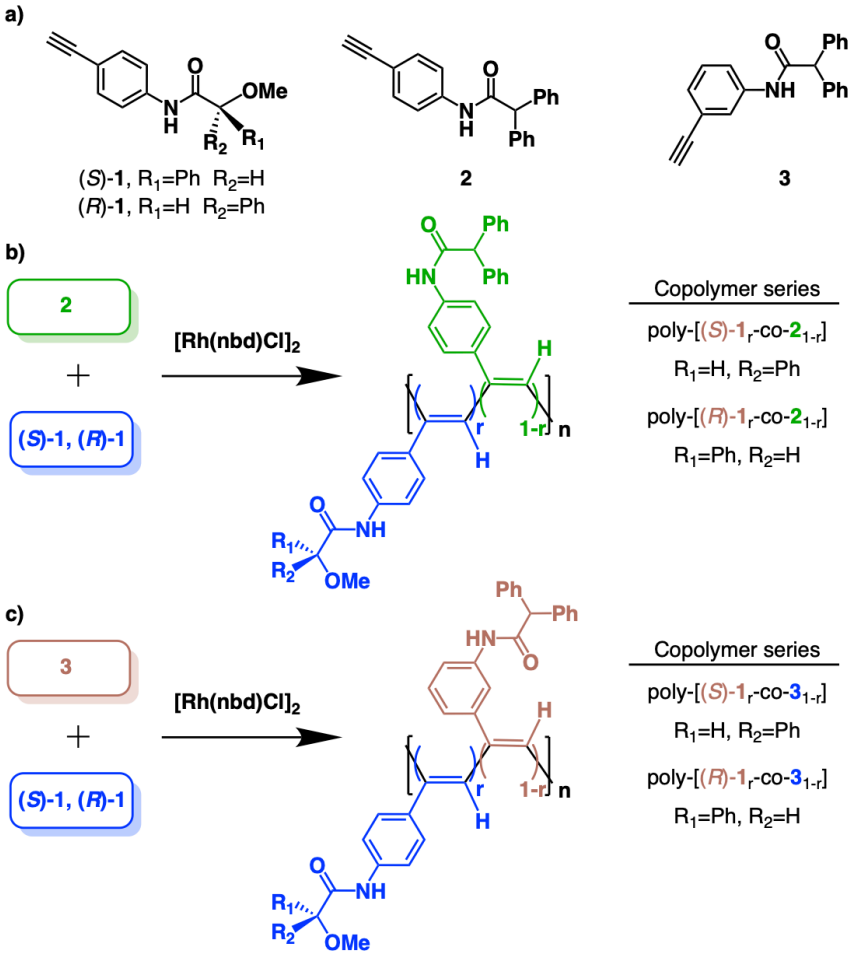


Figure 79. a) Structures of (*S*)-**1**, (*R*)-**1**, **2**, and **3**. b, c) Monomer and copolymer structures used in this study.

Thus, homopolymers: poly-(*S*)-**1**, poly-(*R*)-**1**, poly-**2**, poly-**3**, and the copolymer series: Poly-[(*S*)-$\mathbf{1}_r$-*co*-$\mathbf{2}_{1-r}$], Poly-[(*R*)-$\mathbf{1}_r$-*co*-$\mathbf{2}_{1-r}$], Poly-[(*S*)-$\mathbf{1}_r$-*co*-$\mathbf{3}_{1-r}$], and Poly-[(*R*)-$\mathbf{1}_r$-*co*-$\mathbf{3}_{1-r}$] (r = 0.1-0.9) were prepared by using a Rh(I) catalyst (Figure 79b and Figure 79c). The ratio of the two comonomers (r=0.1-0.9) present in the copolymers was confirmed by ^{1}H-NMR (Figure S123, Figure S124, Figure S125, Figure S126, Figure S127, Figure S128, Figure S129, and Figure S130), while the generation of random copolymers was demonstrated using the Kellen-Tüdös method (see experimental section 5.4.10. Determination of the monomer reactivity ratios in copolymerization).[154,408,409] In all copolymer series, both NMR (vinyl protons at δ=5.7–5.8 ppm, details in Supporting Information) and Raman (with peaks around 1580, 1360, and 980 cm^{-1}, Figure S137) spectroscopies confirmed the presence of *cis* double bonds at the polyene backbones.[57,410-412] Moreover, DSC analyses showed for these copolymers the classical

USC DE COMPOSTELA

thermogram for *cis-cisoidal* polyene backbones (Figure S134, Figure S135, and Figure S136).[67,96,100] The copolymers and homopolymers molecular weights were measured by GPC using THF and polystyrene standards. In all cases the size of the polymers fell in the range Mn=74-234 kDa, with a dispersity (Đ) between 1.2 and 1.9 (Table S19, Table S20, Table S21, Table S22, and Table S23). Homopolymers, poly-(*S*)-**1** and poly-(*R*)-**1**, show an axially racemic behavior in $CHCl_3$ due to a conformational equilibrium between an antiperiplanar (*ap*) and synperiplanar (*sp*) conformations of the (O=)C-C(-O) bonds in equal population. In both conformers, the largest group at the pendant, responsible for the helix induction effect, is oriented into opposite directions. As a result, an equal mixture of *P* and *M* helices are formed, obtaining an axially racemic polymer with an absence of Cotton band in the ECD spectrum at the vinylic region ($ECD_{380\ nm} = 0$) (Figure 80a). However, axially racemic behavior can be shifted towards a *P* or *M* screw sense excess by the action of monovalent (Li^+, Ag^+) or divalent (Ca^{2+}, Ba^{2+}) metal ions used as external stimuli. Thus, while monovalent metal ions stabilize the *ap* conformation at the pendant, inducing a *P* helix in poly-(*S*)-**1**/M^+ ($ECD_{380\ nm} > 0$) and an *M* helix in poly-(*R*)-**1**/M^+ ($ECD_{380\ nm} < 0$) complexes (Figure 80a); divalent metal ions stabilize the *sp* conformation at the pendant, inducing an *M* helix in poly-(*S*)-**1**/M^{2+} ($ECD_{380\ nm} < 0$) and a *P* helix in poly-(*R*)-**1**/M^{2+} ($ECD_{380\ nm} > 0$) complexes (Figure 80a).[42,43,248,267,281,366,367] The opposite helical senses induced in poly-(*S*)-**1** and poly-(*R*)-**1** by adding either monovalent or divalent metal ions is a consequence of their enantiomeric relationship.

The *sp*/*ap* conformational equilibrium at the pendant can be also shifted towards the *sp* conformer when the polarity of the solvent increases. Thus, in DMF, poly-(*S*)-**1** adopts an *M* helix ($ECD_{380\ nm} < 0$), while poly-(*R*)-**1** shows a *P* helix screw sense excess ($ECD_{380\ nm} > 0$) (Figure 80b).[43] On the other hand, achiral homopolymers, poly-**2** and poly-**3**, do not show any screw sense excess due to the absence of any source of chirality in the monomer repeating units (($ECD_{380\ nm} = 0$). Subsequently, ECD folding studies were carried out for the different poly-(*S*)-**1**, poly-(*R*)-**1**, poly-**2**, poly-**3**; and the copolymer series: Poly-[(*S*)-$\mathbf{1}_r$-*co*-$\mathbf{2}_{1-r}$], Poly-[(*R*)-$\mathbf{1}_r$-*co*-$\mathbf{2}_{1-r}$], Poly-[(*S*)-$\mathbf{1}_r$-*co*-$\mathbf{3}_{1-r}$], and Poly-[(*R*)-$\mathbf{1}_r$-*co*-$\mathbf{3}_{1-r}$] (r = 0.1-0.9) copolymer series and compared to the homopolymers to explore the communication mechanisms between comonomers and the different asymmetry amplification effects triggered.

USC UNIVERSIDADE DE SANTIAGO DE COMPOSTELA

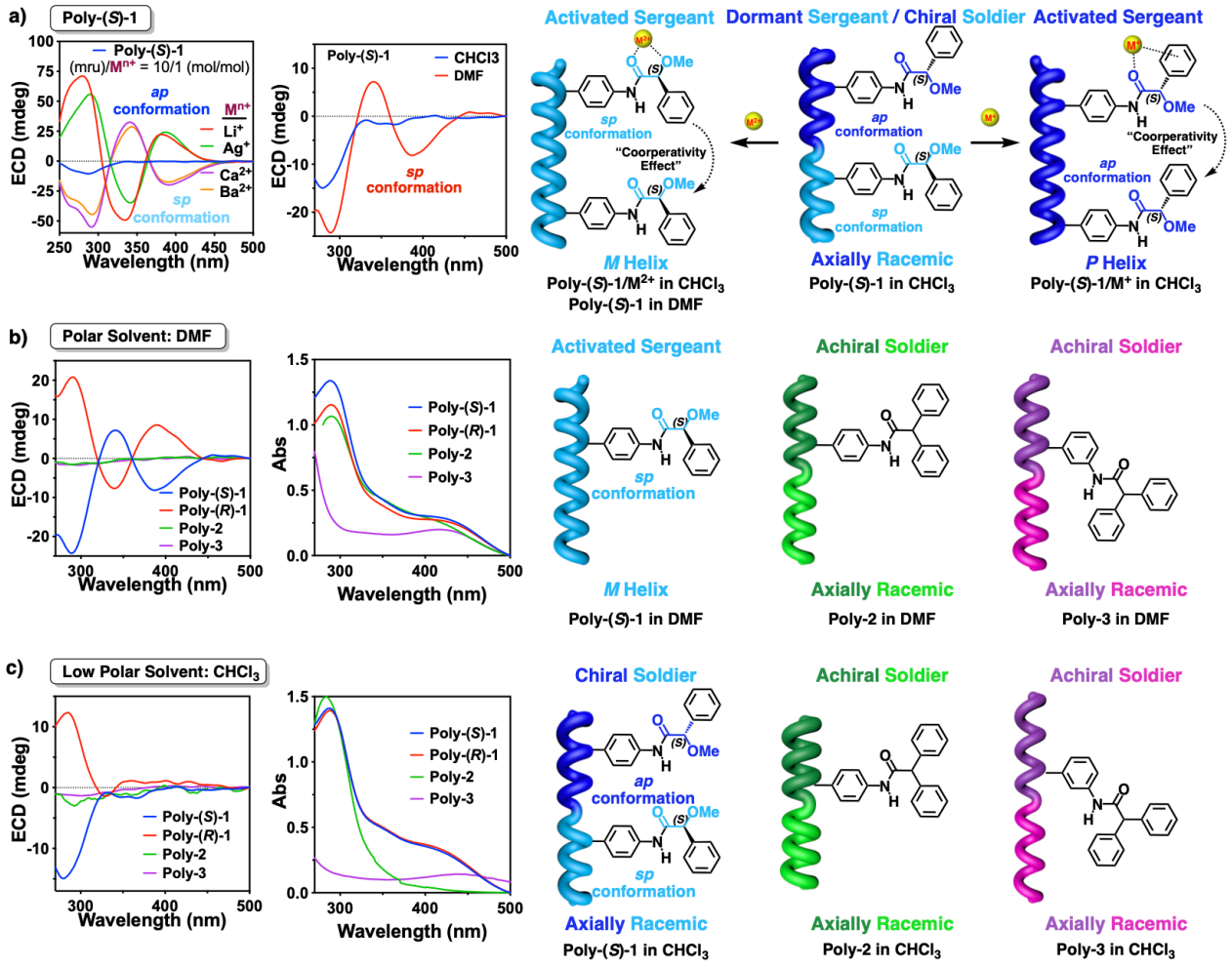


Figure 80. Schematic representation, ECD and UV-Vis spectra of a) Poly-(*S*)-**1** in $CHCl_3$ or DMF in the absence and the presence of 0.1 equivalents of $LiClO_4$, $AgClO_4$, $Ca(ClO_4)_2$, and $Ba(ClO_4)_2$ (10 mg/mL MeOH), b) Poly-(*S*)-**1**, Poly-(*R*)-**1**, Poly-**2**, and Poly-**3** in DMF, and c) Poly-(*S*)-**1**, Poly-(*R*)-**1**, Poly-**2**, and Poly-**3** in $CHCl_3$. Concentration of Homopolymers = 0.3 mg/mL.

First, we analyzed the communication mechanism in Poly-[(*S*)-$\mathbf{1}_r$-*co*-$\mathbf{2}_{1-r}$] and Poly-[(*S*)-$\mathbf{1}_r$-*co*-$\mathbf{3}_{1-r}$] copolymer series in DMF. As we mentioned above, in this solvent, monomer (*S*)-**1** adopts a preferred *sp* conformation, which can trigger a Classic or Abnormal Sergeants and Soldiers Effect by inducing a specific *P* or *M* helical sense into the achiral monomers.

ECD studies of the Poly-[(*S*)-$\mathbf{1}_r$-*co*-$\mathbf{2}_{1-r}$] (r= 0.9-0.1) copolymer series in DMF (0.3 mg/mL) showed the presence of the Classic Sergeant and Soldier Effect promoted by a low *sp* energy conformation at the (*S*)-**1** Sergeant. The g_{values} of the polyenic backbone followed non-linearlity with the chiral monomer content, and the minimum Sergeant fraction r_{value} needed to achieve the same g_{value} as the homopolymer was found to be

USC UNIVERSIDADE DE SANTIAGO

approximately 0.5 —50% Sergeant induces the other 50% of Soldiers to adopt an *M* helix—, confirming effective Sergeants-and-Soldiers communication (Figure 81a). In addition, it is worth noting that an amplification of 50% of the *M* helix occurs when 20% of the Sergeant is present within the copolymer helix (Figure 81a).

USC
UNIVERSIDADE DE SANTIAGO DE COMPOSTELA

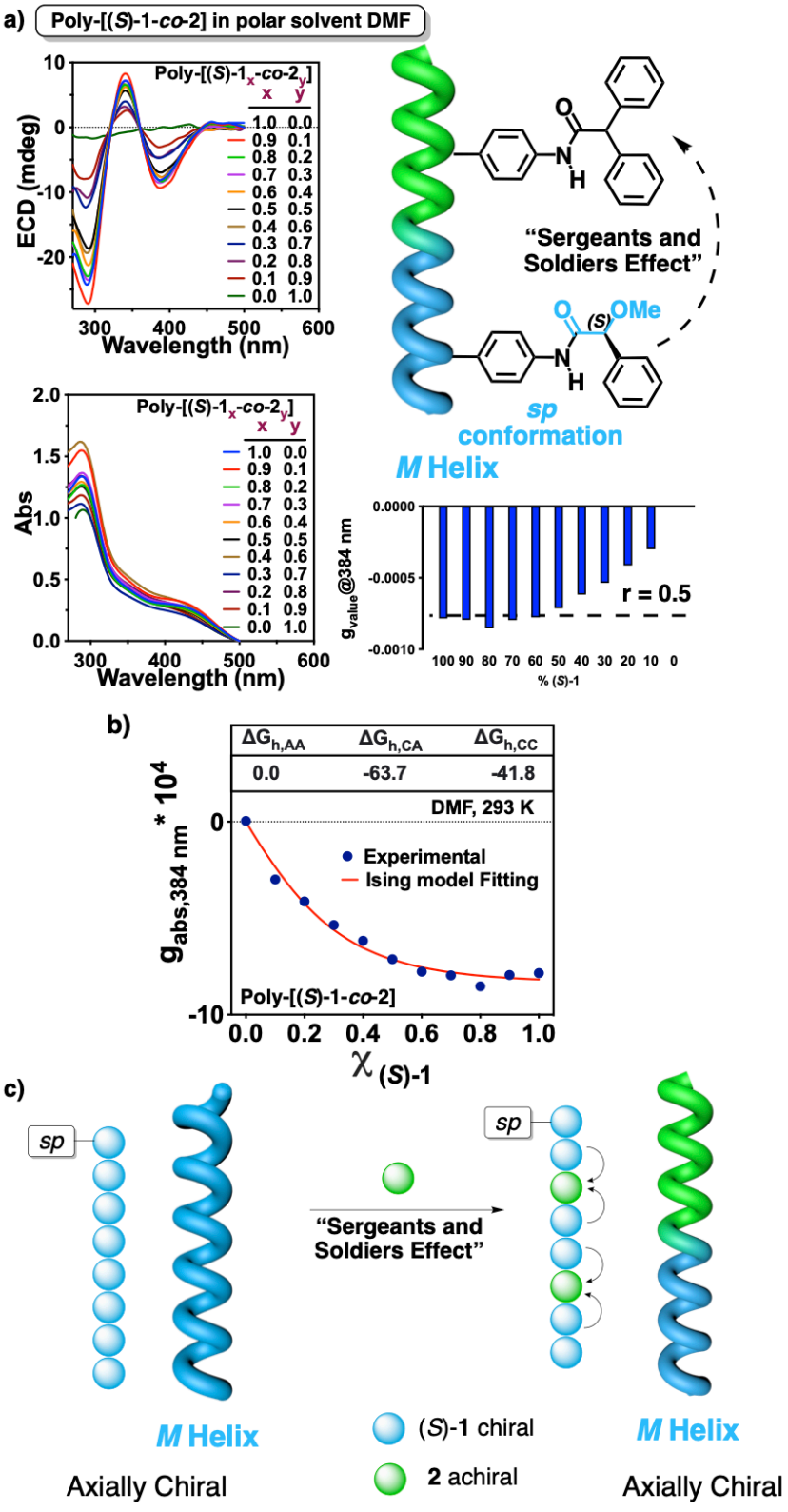


Figure 81. a) Schematic representation, g_{value}, ECD, and UV-Vis spectra in DMF for copolymer series (c = 0.3 mg/mL) Poly-[(*S*)-**1**$_r$-*co*-**2**$_{1-r}$]. b) g_{value} and Ising model fit with ΔG in J/mol of Poly-[(*S*)-**1**$_r$-*co*-**2**$_{1-r}$] in DMF. c) Schematic representation of the communication mechanism.

Next, we proceed to calculate the energy of the helix induction process (ΔG_h) following Sato's model[406] for the Classic Sergeants and Soldiers Effect (SaS) in random copolymers, which is based on the Ising model initially defined by Green.[273,421-423] In this model, both the degree and the direction of the helical induction rely on the structure of the neighboring monomer units, which can be either chiral or achiral in a copolymer that follows a Classic Sergeant and Soldiers Effect. By using this model, they could obtain the energy preference for a monomer repeating unit of a copolymer to adopt a certain helical sense (ΔG_h) in the Classic and the Abnormal SaS effects.[406] In copolymers, to obtain the ΔG_h value, it is necessary to consider which are the neighboring residues of a certain monomer within the copolymer sequence. Thus, when a chiral residue is adjacent to another chiral residue, the energy to adopt a screw sense preference in the helix must consider that the two chiral monomers have the same propensity to induce the same screw sense preference $\Delta G_{h,CC}$ (C = chiral), while when a chiral residue is followed by an achiral residue or vice versa, $\Delta G_{h,CA}$ (C = chiral, A = achiral) and $\Delta G_{h,AC}$, the screw sense induction energy must consider the communication mechanism from the chiral towards the achiral residue. In this model, it is assumed that the communication between both the chiral and achiral comonomers does not depend on the component sequence, *i.e.* chiral-achiral or achiral-chiral and considers that the energy for the two different combinations is equal, $\Delta G_{h,CA}$=$\Delta G_{h,AC}$. Finally, within the copolymer it is also possible to have two consecutive achiral residues ($\Delta G_{h,AA}$) in this case, both monomers induce the *P* or *M* helix in equal population and therefore the energy induction towards one of them is null, indicating an absence of screw sense induction preference ($\Delta G_{h,AA}$=0).[26,407] By using this Sato's model, it is possible to obtain the energy preferences of a Classic or Abnormal SaS effect.

We have introduced a variation in Sato's model, employing the g_{max} obtained from absolute values of the components and normalized data in equation (34). As a result, the ΔG_h obtained from equation (32) is dependent on the sign of the g_{value}, allowing us to know which screw sense is favored during the asymmetry amplification process. Thus, if ΔG_h is negative, the screw sense induced through a chiral-to-chiral communication mechanism is *M*, while if this value it is positive, the screw sense induced is the *P* one.

USC UNIVERSIDADE DE SANTIAGO DE COMPOSTELA

$$g_{abs} = tanh\left(\frac{N\Delta G_h}{2RT}\right) \cdot g_{max} \quad \textbf{(32)}$$

$$\Delta G_h = X^2 \Delta G_{h,xx} + XY\Delta G_{h,xy} + Y^2 \Delta G_{h,yy} \quad \textbf{(33)}$$

$$g_{max} = \frac{X \cdot |g_{max\,x}| + Y \cdot |g_{max\,y}|}{X + Y} \quad \textbf{(34)}$$

The energy induction (ΔG_h) calculated from equation (33) considers which are the neighboring residues of a certain monomer within the copolymer sequence. Thus, ΔG_h is a combination of ($\Delta G_{h,xx}$) (x= chiral comonomer 1), ($\Delta G_{h,yy}$) (y= achiral comonomer 2), ($\Delta G_{h,xy}$) (x= chiral comonomer 1, y= achiral comonomer 2) and ($\Delta G_{h,yx}$) (x= chiral comonomer 1, y= achiral comonomer 2) (equation 2). However, in this model this model we assume that the communication between the chiral and the achiral comonomers does not depends on the copolymer sequence, *i.e.* chiral1-achiral2 (xy), achiral2-chiral1 (yx), being therefore $\Delta G_{h,xy}$=$\Delta G_{h,yx}$. We define X as the molar fraction of the sergeant and Y as the molar fraction of the soldier defined by Y=1-X. In the absence of communication mechanisms, no Sergeants or Soldiers are present, and the assignment becomes arbitrary. Also, the energy of the helix induction process calculations becomes highly sensitive to error in lack of communication mechanisms, and many data points must be considered for accurate fitting.

Therefore, from these modified Sato's model, it is possible to extract all the ΔG_h components ($\Delta G_{h,xx}$, $\Delta G_{h,yy}$, and $\Delta G_{h,xy}$) for different chiral to chiral communication processes, such as the Classical and Abnormal chiral to chiral SaS effect or the Chiral Conflict and Chiral Accord effects. Moreover, it is also possible to elucidate the chiral-to-chiral communication mechanism from the value obtained from equation (35) (Comm= communication value), which always considers monomer x as the sergeant. Thus, if this value is positive (Comm >0), a Classic Sergeant and Soldiers Effect is produced, while when this value is negative (Comm <0) and Abnormal Sergeants and Soldiers Effect is triggered within the copolymer. On the other hand, if this value is close to zero (Comm ≈ 0) a lack of communication between the two comonomers is produced.

USC UNIVERSIDADE DE SANTIAGO

$$Comm = \frac{\Delta G_{h,xy}}{\Delta G_{h,xx} - \Delta G_{h,yy}} \quad \textbf{(35)}$$

Negative values of $\Delta G_{h,CC}$=-41.8 J/mol and $\Delta G_{h,CA}$=-63.7 J/mol were obtained for the Poly-[(*S*)-**1**$_r$-*co*-**2**$_{1-r}$] (**1** = C; **2** = A) copolymer series in DMF, indicating that the same negative g_{values} and therefore left-handed helical structure (*M*-type helix) is induced by the chiral Sergeant (*S*)-**1** and the achiral Soldier **2** (Figure 81b), that results in a Commun value of 1.52, (Commun > 0), which indicates an asymmetry amplification through a SaS effect.

On the other hand, in the Poly-[(*S*)-**1**$_r$-*co*-**3**$_{1-r}$] (r= 0.1-0.9) copolymer series, no communication is observed between the chiral comonomer [(*S*)-**1**] and the achiral one (**3**). ECD studies show a linear dependance in the g_{value} of the polyenic backbone with the molar ratio of each of the monomers (Figure 82), indicating the absence of supramolecular chirality transfer. This fact is explained due to the different aromatic substitution patterns of monomers **1** and **3**, where the pendants are spatially misaligned, preventing efficient overlap or interaction.

Similar effects are observed for the in poly-[(*R*)-**1**$_r$-*co*-**2**$_{1-r}$] and poly-[(*R*)-**1**$_r$-*co*-**3**$_{1-r}$] copolymer series in DMF, although in these cases a *P* helix is present due to their enantiomeric relationship with the poly-[(*S*)-**1**$_r$-*co*-**2**$_{1-r}$] and poly-[(*S*)-**1**$_r$-*co*-**3**$_{1-r}$] copolymer series (Figure S141).

USC UNIVERSIDADE DE SANTIAGO DE COMPOSTELA

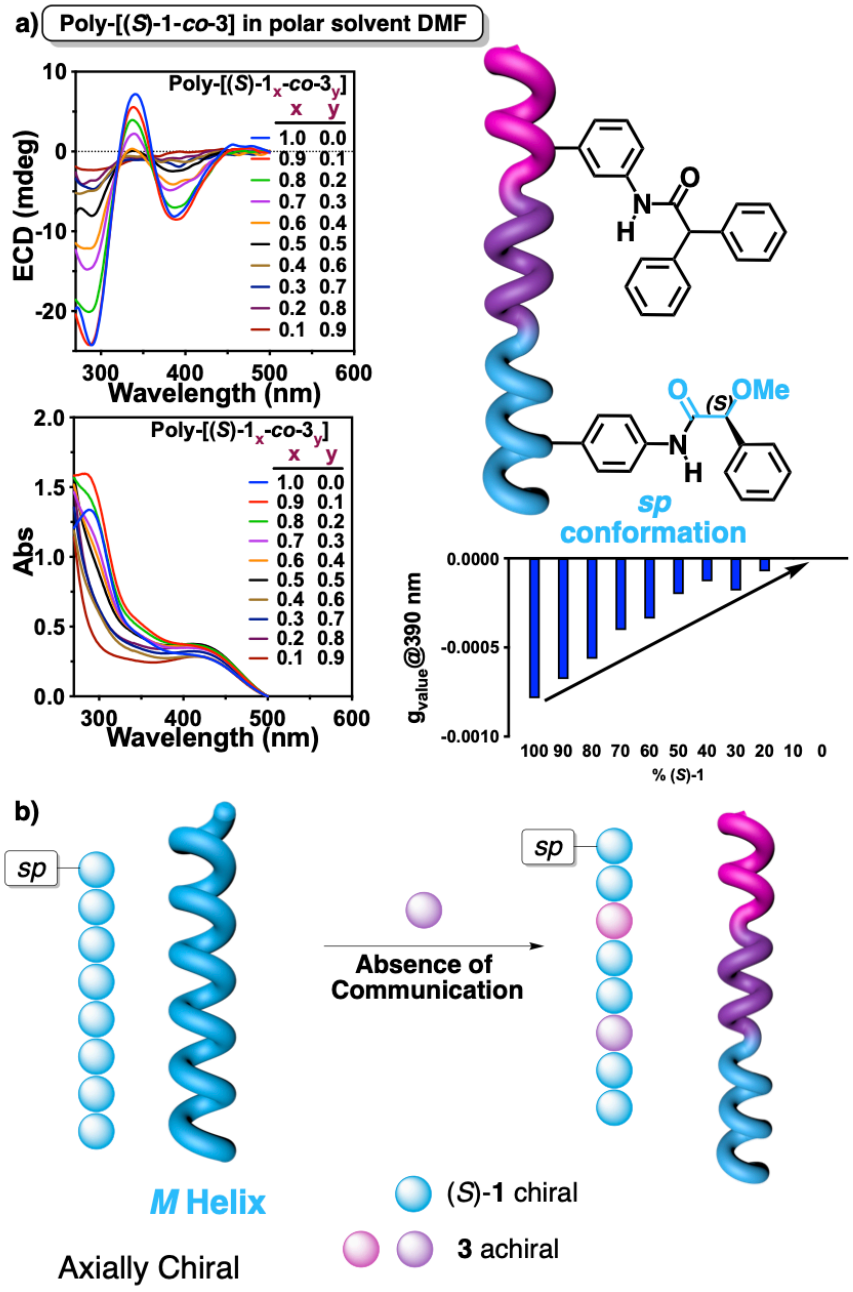


Figure 82. a) Schematic representation, g_{value}, ECD, and UV-Vis spectra for copolymer series (c = 0.3 mg/mL) Poly-[(*S*)-**1**$_r$-*co*-**3**$_{1-r}$] in DMF. b) Schematic representation of the communication mechanism.

Next, the communication mechanism in Poly-[(*S*)-**1**$_r$-*co*-**2**$_{1-r}$] and Poly-[(*S*)-**1**$_r$-*co*-**3**$_{1-r}$] copolymer series in $CHCl_3$. As we mention above, in this solvent, monomer (*S*)-**1** adopts a mixture of *sp* and *ap* conformers that led to a mixture of *P* and *M* helices in the homopolymer. Therefore, its copolymerization with achiral monomers **2** and **3** should result in no effects in their null induction effects towards a certain screw sense.

USC UNIVERSIDADE DE SANTIAGO DE COMPOSTELA

However, by looking at the ECD spectra of the Poly-[(*S*)-**1**$_r$-*co*-**2**$_{1-r}$] copolymer series, it is possible to observe that a conformational communication mechanism emerges when both comonomers are copolymerized (Figure 5a). Interestingly, at high ratios of the sergeant, r= 0.9-0.6 in the Poly-[(*S*)-**1**$_r$-*co*-**2**$_{1-r}$] (r= 0.1-0.9) copolymer series and intense positive ECD signal at the vinylic region, indicating the presence of a *P* helix screw sense excess in the copolymer (Figure 83b). This fact indicates, that when the achiral comonomer **2** is introduced in the copolymer series, its presence provoke change in the conformational composition of monomer (*S*)-**1** towards a preferred ap conformation of the (O=)C-C(-O) bonds, that results in the triggering of a Sergeants and Soldiers Effect, commanding the achiral monomer to be folded into a *P* helix.

Therefore, a cascade of effects is present in this copolymer series. Thus, the presence of low polar residues within the copolymer chain activates the *ap* conformer at the chiral residues which in return command the achiral comonomers to adopt a specific screw sense in the helix. The extension of this SaS effect is very high, where 10% of the chiral monomer is necessary to induce a *P* helix into the rest of the copolymer chain, which is made by 90% of the achiral monomer **2** (Figure 83c and Figure 83d).

Interestingly, these SaS effect is triggered into two different scaffolds. Thus, when the (*S*)-**1**/**2** ratio is 0.9-0.8/0.1-0.2, a *P* stretched helix with the maximum of the polyene band located at 382 nm is observed, however, when the ratio of the achiral comonomer increases, a more compact helix is obtained with the maximum of the polyene band located at 328 nm (Figure 83c). This 54 nm shift of the polyene band is attributed to the copolymer composition, adopting stretched helices at high ratios of the chiral component and more compressed helices at low ratios. However, in all cases, a SaS effect is present, where the copolymers of the Poly-[(*S*)-**1**$_r$-*co*-**2**$_{1-r}$] (r= 0.1-0.9) adopts a *P* screw sense excess.

To obtain the energy values of this asymmetry amplification process is necessary to consider that the stretching commanded by the Sergeant is not transmitted to the Soldier. In this case, only the screw sense excess is fully transmitted along the different copolymers of the copolymer series. Thus, two different regions in the ECD spectra are needed to be considered to obtain the energy values of the process. Therefore, the g_{values} for copolymers poly-[(*S*)-**1**$_r$-*co*-**2**$_{1-r}$] (r= 0.9-0.7) were measured at 384 nm, while the g_{values} for copolymers poly-[(*S*)-**1**$_r$-*co*-**2**$_{1-r}$] (r= 0.6-0.1) were measured at 328 nm (Figure 83d). Moreover, we must assume that as the homopolymers cannot stabilize any of the two

possible helical senses, the $\Delta G_{h,AA}$=$\Delta G_{h,CC}$=0. Thus, the energy of the process $\Delta G_{h,CA}$=$\Delta G_{h,AC}$ includes the stabilization energy of the *ap* conformer in (*S*)-**1** by the presence of **2**, and the asymmetry amplification induced by (*S*)-**1** over **2**. The $\Delta G_{h,CA}$ obtained by applying a variation of the Sato's model is $\Delta G_{h,CA}$=+233.6 J/mol. This positive value indicates that a right-handed helical structure (*P*-type helix) is induced into the copolymer by the Cascade SaS effect (Figure 83e). The energy is so large due to the combination of two effects occurring simultaneously (activation and amplification), and because the parents homopolymers (chiral and achiral) do not produce any screw sense excess.

USC UNIVERSIDADE DE SANTIAGO DE COMPOSTELA

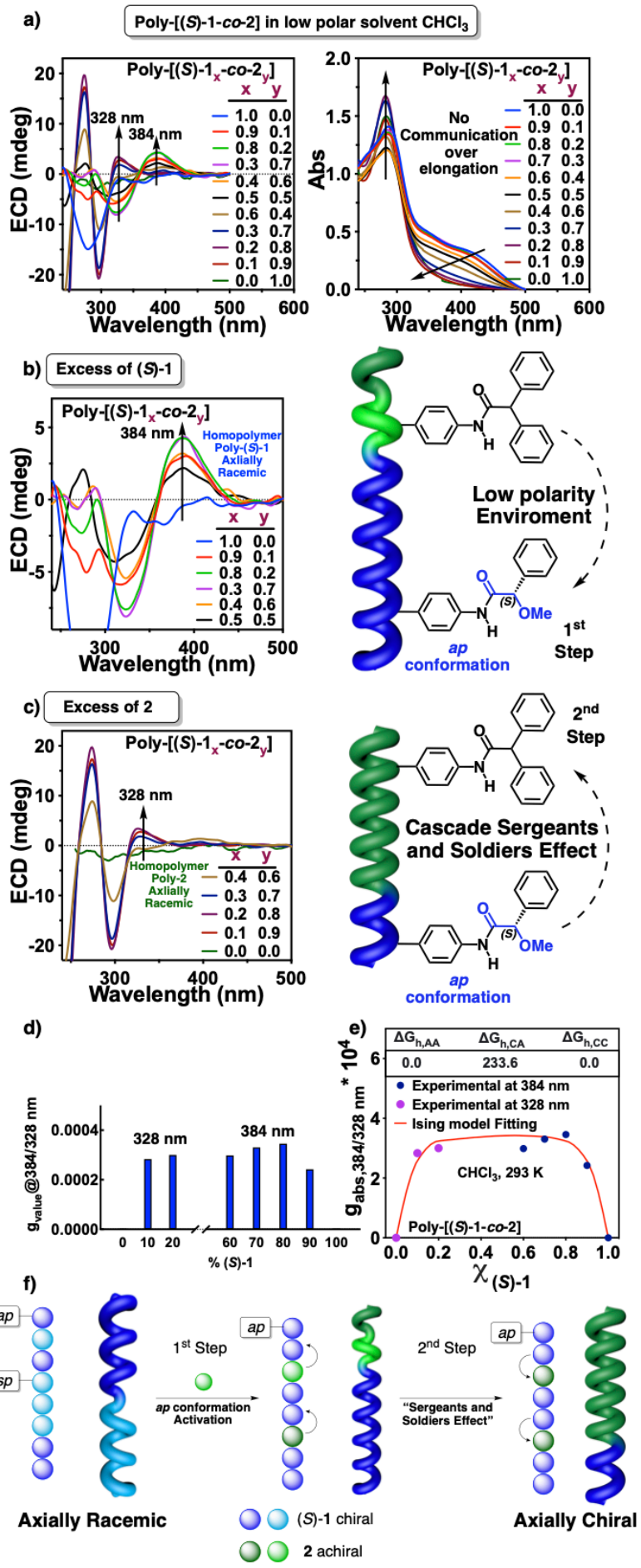

a)
Poly-[(S)-1-co-2] in low polar solvent CHCl3
Poly-[(S)-1x-co-2y]
328 nm
384 nm
ECD (mdeg)
Wavelength (nm)
No Communication over elongation
Abs
b)
Excess of (S)-1
Homopolymer Poly-(S)-1 Axially Racemic
Low polarity Enviroment
1st Step
ap conformation
c)
Excess of 2
Homopolymer Poly-2 Axially Racemic
2nd Step
Cascade Sergeants and Soldiers Effect
d)
gvalue@384/328 nm
% (S)-1
e)
ΔGh,AA
ΔGh,CA
ΔGh,CC
0.0
233.6
0.0
Experimental at 384 nm
Experimental at 328 nm
Ising model Fitting
CHCl3, 293 K
Poly-[(S)-1-co-2]
gabs,384/328 nm * 10^4
χ (S)-1
f)
ap
sp
1st Step
ap conformation Activation
2nd Step
"Sergeants and Soldiers Effect"
Axially Racemic
(S)-1 chiral
2 achiral
Axially Chiral

Figure 83. a) ECD and UV-Vis spectra in $CHCl_3$ for copolymer series (c = 0.3 mg/mL) Poly-[(*S*)-**1**$_r$-*co*-**2**$_{1-r}$]. b) ECD spectra in $CHCl_3$ for copolymer series (c = 0.3 mg/mL) Poly-[(*S*)-**1**$_r$-*co*-**2**$_{1-r}$] in excess of (*S*)-**1**. c) ECD spectra in $CHCl_3$ for copolymer series (c = 0.3 mg/mL) Poly-[(*S*)-**1**$_r$-*co*-**2**$_{1-r}$] in excess of **2**. a) g_{value} in $CHCl_3$ for copolymer series (c = 0.3 mg/mL) Poly-[(*S*)-**1**$_r$-*co*-**2**$_{1-r}$] measured at 384 nm in excess of (*S*)-**1**, and at 328 nm in excess of **2**. e) g_{value} and Ising model fit with ΔG in J/mol of Poly-[(*S*)-**1**$_r$-*co*-**2**$_{1-r}$] in $CHCl_3$. f) Schematic representation of the communication mechanism.

Finally, communication studies were carried out for the Poly-[(*S*)-**1**$_r$-*co*-**3**$_{1-r}$] copolymer series in $CHCl_3$. Considering the absence of a net helicity in the corresponding parent homopolymers, copolymerization of comonomer (*S*)-**1** with achiral monomer **3** it should still promote an axially racemic helix. However, by looking at the ECD spectra of the Poly-[(*S*)-**1**$_r$-*co*-**3**$_{1-r}$] copolymer series, it is possible to observe that a conformational communication mechanism emerges when both comonomers are copolymerized (Figure 84). Interestingly, in all the copolymers of the copolymer series a *P* helix is induced, indicating that the presence of an achiral hydrophobic comonomer within the copolymer series stabilized the *ap* conformer at the chiral (*S*)-**1** comonomer. However, the screw sense excess depends on the ratio of the chiral comonomer present within the copolymer, which indicates the absence of a Cascade Effect, where the asymmetry amplification through a SaS is not produced. Thus, while the presence of the achiral monomer within the copolymer series and its hydrophobic behavior can activate the *ap* conformation at the chiral residue, and the adoption of a *P* helix, this information is not transmitted back to the achiral residues due to the mismatch between a *para*- and *meta*-substituted pendant groups within a helical scaffold. Interestingly, we can also see that the higher screw sense excess is present when the chiral/achiral comonomers are present in a 0.8/0.2 ratio, indicating the polarity change produced by introducing 10% of achiral residues in the copolymer is not enough to activate the 90% of the chiral residues present in the helix (Figure 84).

Similar effects are observed for the in poly-[(*R*)-**1**$_r$-*co*-**2**$_{1-r}$] and poly-[(*R*)-**1**$_r$-*co*-**3**$_{1-r}$] copolymer series in $CHCl_3$, although in these cases an *M* helix is present due to their enantiomeric relationship with the poly-[(*S*)-**1**$_r$-*co*-**2**$_{1-r}$] and poly-[(*S*)-**1**$_r$-*co*-**3**$_{1-r}$] copolymer series (Figure S140).

USC UNIVERSIDADE DE SANTIAGO DE COMPOSTELA

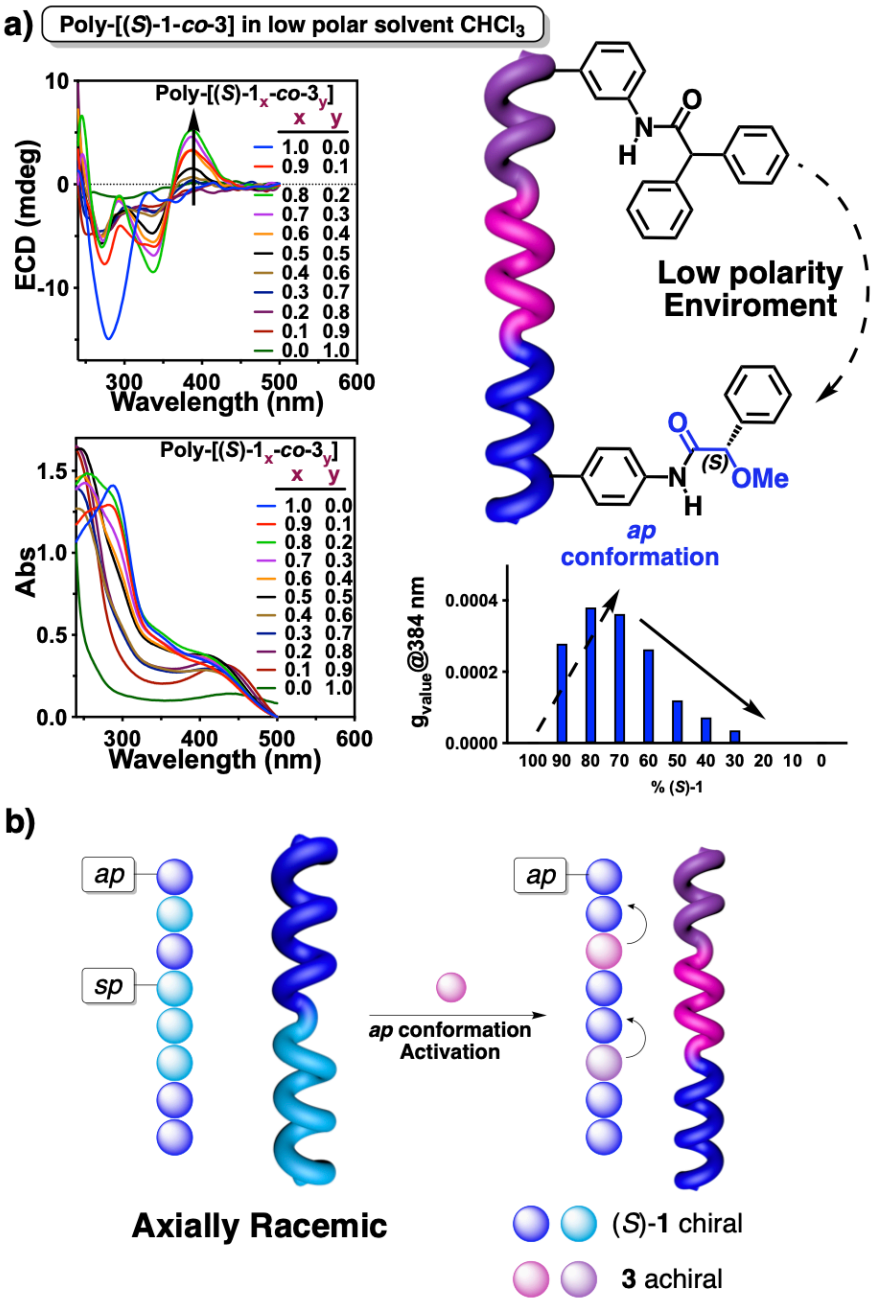


Figure 84. a) Schematic representation, g_{value}, ECD, and UV-Vis spectra for copolymer series (c = 0.3 mg/mL) Poly-[(*S*)-**1**$_r$-*co*-**3**$_{1-r}$] in $CHCl_3$. b) Schematic representation of the communication mechanism.

3.4.3. Conclusions

The dynamic behavior of helical polymers such as PPAs makes this family of helical polymers a unique platform to analyze helix induction and conformational communication mechanism. In this work we have demonstrated that copolymerization of two monomers,

USC UNIVERSIDADE DE SANTIAGO DE COMPOSTELA

one chiral [(*R*)- or (*S*)-**1**] and another achiral (**2**), and where the corresponding homopolymers produces axially racemic helices, can generate copolymers — poly-[(*S*)-**1**$_r$-*co*-**2**$_{1-r}$] and poly-[(*R*)-**1**$_r$-*co*-**2**$_{1-r}$]— that adopt a preferred *P* or *M* helix. In this case, the achiral comonomer **2** acts as an internal stimulus. Its hydrophobicity creates a low polar microenvironment surrounding the chiral comonomer, (*R*)- or (*S*)-**1**, resulting in the adoption of a preferred *ap* conformation at the (O=)C-C(-O) bonds, which induces a preferred *P* helix for (*S*)-**1** and an *M* helix for (*R*)-**1**. This activation of the chiral comonomers triggers in turs a second effect in the copolymer series, *i.e.* a Sergeants and Soldiers effect, where the achiral comonomer (Soldier) induces the same screw sense than the chiral one (Sergeant). In another examples, poly-[(*R*)-**1**$_r$-*co*-**3**$_{1-r}$] and poly-[(*S*)-**1**$_r$-*co*-**3**$_{1-r}$] copolymer series, we have demonstrated that the activation of the chiral comonomer **1** is also produced by copolymerization with the achiral comonomer **3**, which creates a low polar microenvironment surrounding the chiral comonomer **1**. However, in these copolymer series, the mismatch between the *para*- and *meta*-pendant groups within the helical scaffold provokes a lack of communication between both monomers and the absence of a second asymmetry amplification effect. This work opens a new scenario in the conformational communication mechanisms of comonomers within copolymers. The molecular structure of a comonomer can be used to modulate the conformational composition of the other comonomer, that induces a specific helical sense and which in turn can trigger an asymmetry amplification effect such as the Sergeants and Soldiers Effect over the other comonomer. These findings have applications in fields such as helical polymers, foldamers and supramolecular polymers, allowing to explore a new way of controlling the helical motif present in these systems and look for new applications.

USC UNIVERSIDADE DE SANTIAGO DE COMPOSTELA

USC
UNIVERSIDADE
DE SANTIAGO
DE COMPOSTELA

3.5. Optical and Chiroptical Stimuli-Responsive Chiral AgNPs@H-Leu-Poly(phenylacetylene) Nanocomposites in Water

The results of this chapter have been published by ACS Nano as:

Manuel Fernández-Míguez,[a] Manuel Núñez-Martínez,[a] Esteban Suárez-Picado,[a] Emilio Quiñoá,[a] Félix Freire,[a]* Optical and Chiroptical Stimuli-Responsive Chiral AgNPs@H-Leu-Poly(phenylacetylene) Nanocomposites in Water, *ACS Nano* **2024**, *18*, 28822–28833. DOI: 10.1021/acsnano.4c08622.

Affiliations

[a]Centro Singular de Investigación en Química Biolóxica e Materiais, Moleculares (CiQUS) and Departamento de Química Orgánica, Universidade de Santiago de Compostela 15782 Santiago de Compostela (Spain)

The information of this Chapter has been reproduced with permission from American Chemical Society.

Abstract

Dynamic macroscopically chiral nanocomposites are prepared by combining silver nanoparticles (AgNPs) and dynamic helical poly(phenylacetylene)s (PPAs) bearing pendants functionalized with amino groups. These amino groups provide the nanocomposite with the ability to disperse in water along with high stability due to the interaction between the ammonium group and the AgNP. Moreover, the equilibrium between NH_3^+/NH_2 produces a "blinking" contact between the PPA and the AgNPs, which allows to have a total control of the dynamic helical behavior of the polymer. The use of acidic or neutral pH allows controlling the morphology of the nanocomposite, which consist of a nanosphere that has trapped inside it a single AgNP (pH= 2) or several AgNPs (pH= 7) with ca. 30 nm of diameter. These nanocomposites combine the optical and chiroptical stimuli-responsive properties of both components, AgNPs and PPAs. Thus, the controlled aggregation of the nanocomposite produced variations in the LSPR band of the AgNPs in a reversible manner. In turn and given that the chiral coating is selective to Ba^{2+}, the presence of this metal ion caused a helical inversion of the chiral coating of the nanocomposite detected by electronic circular dichroism. Moreover, it is possible to distinguish between three metal ions in different oxidation states, such as

USC UNIVERSIDADE DE SANTIAGO

Ce^{4+}, Fe^{3+} and Hg^{2+}, which produce different responses of the nanocomposite when oxidizing the AgNP to Ag^{+}.

USC
UNIVERSIDADE DE SANTIAGO DE COMPOSTELA

3.5.1. Precedents

Silver nanoparticles (AgNPs) have attracted the attention of the scientific community due to their applications in various fields such as medical therapy,[430] sensors,[431] and catalysis,[432] among others. However, to keep these AgNPs stable over time in specific environmental conditions, it is necessary to coat them with a certain organic molecule or polymeric coating.[433-436] Thus, their natural tendency to aggregate and oxidize is disrupted by steric or electrostatic effects.[437] Moreover, by playing with the structure and functional groups of the coating agents, extra functionalities can be introduced in the hybrid material that could combine the properties of both systems (MNPs and coating)[438] generating chiral plasmonic nanostructures.[439-442]

Helical biopolymers including DNA,[442] peptides[444] and polysaccharides[445] have been used to decorate AgNPs. However, their pool of building blocks (chirality, functional groups) in biopolymers is limited because Nature only used a limited number of molecules to create organisms, such as the 20 natural amino acids or the 4 nucleotides. Furthermore, these biomacromolecules are generally static, a fact that makes it not possible to tune their helical sense or elongation in the presence of external stimuli.

Our group has been working lately on the preparation of hybrid materials that combine the properties of MNPs (M= Au or Ag) and stimuli-responsive helical polymers such as poly(phenylacetylene)s (PPAs).[234-237] These polymers are dynamic from a structural point of view, a fact that allows their secondary structure (elongation and/or helical sense, scaffold) to be modulated by the presence of external stimuli such as temperature, solvents, metal ions and pH, among others.[8,25,30,70,71,92,169,240,243,245,261] These characteristics make them excellent candidates to protect MNPs and obtain hybrid materials (MNPs@PPAs) that combine the dynamic chiroptical properties of PPAs and the optical properties of MNPs.

However, to date these studies were carried out only in organic media (e.g., $CHCl_3$, DCM), due to the limitation of creating water-soluble PPAs with the ability of interact with MNPs. The main reason is that the Rh(I) catalyst used during the polymerization reaction is poisoned by monomers containing amino groups. This problem was recently overcome by performing the polymerization reaction with protonated ammonium phenylacetylene monomers (NH_3^+-PA).[59] In this acidic condition, the Rh(I) catalyst is not poisoned, allowing the creation of water-soluble amino-PPAs required to prepare water-soluble

USC UNIVERSIDADE DE SANTIAGO DE COMPOSTELA

MNPs@PPA nanocomposites. Furthermore, by using amino-PPAs and playing with the pH it is possible to adjust the NH_3^+/NH_2 ratio along the helical polymer. These amino and ammonium groups are in equilibrium and the positive charges, from a macroscopic point of view, exchange from one amino group to another along the polymer scaffold.[446-448] Therefore, the NH_3^+—AgNP contacts, which stabilize the metal nanoparticle, are dynamic and move along the polymer-metal nanoparticle interface, without blocking the flexibility of the pendant groups attached to the AgNP. As a result, the polymer is expected to vary its helical structure —elongation, helix sense— when it interacts with external stimuli in the nanocomposite, similarly to its behavior in the molecularly dissolved state.

In this work we will explore the formation, chiroptical properties and morphology of dynamic aqueous AgNPs@PPAs nanocomposites by reducing an amino-PPA/Ag^+ complex at acidic and neutral pH (2 and 7 respectively, Figure 85) and their stimuli-responsive properties in water against different stimuli such as pH, divalent metal ions and oxidizing agents.

USC
UNIVERSIDADE DE SANTIAGO DE COMPOSTELA

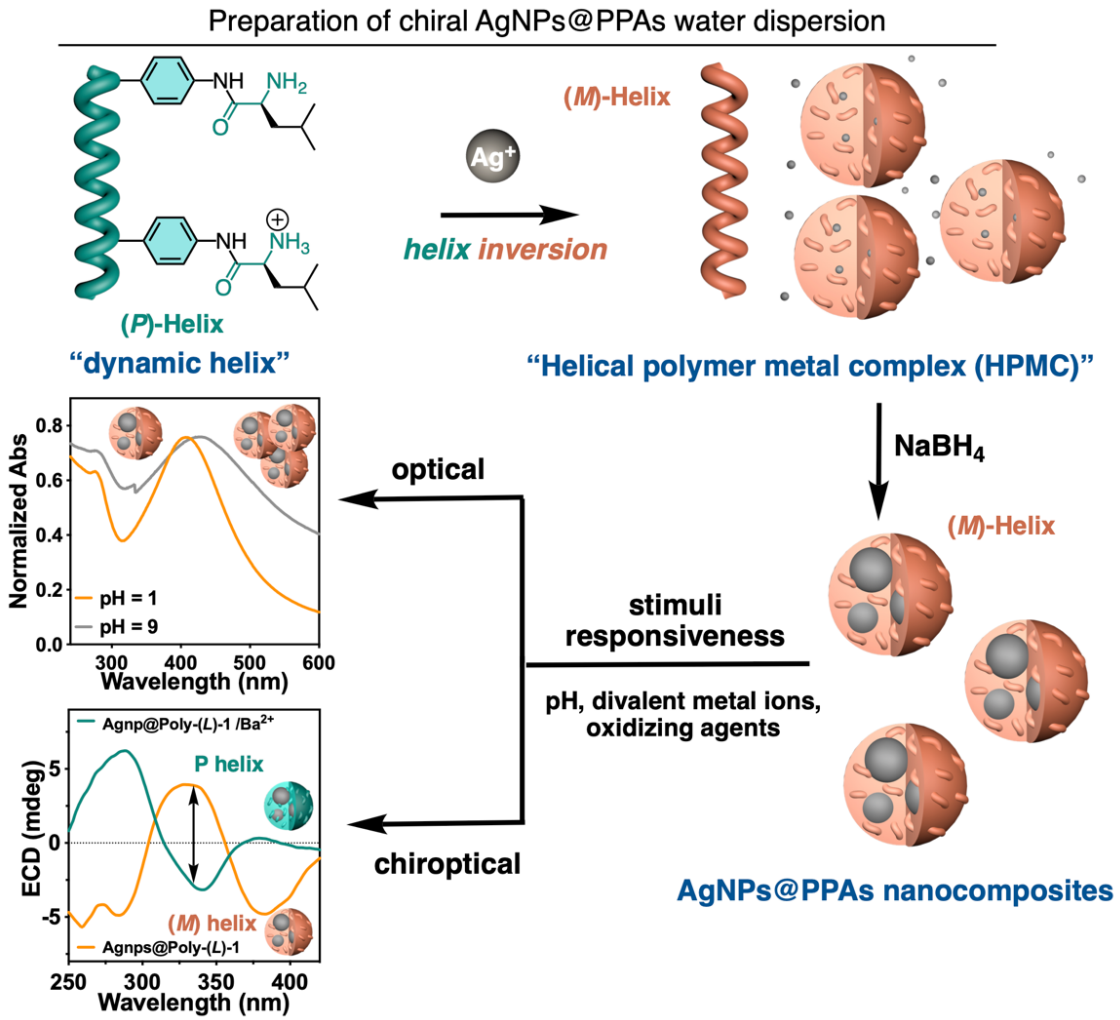


Figure 85. Graphical illustration for the preparation AgNPs@PPAs nanocomposites dispersed in water and the stimuli-responsive properties addressed in this work.

3.5.2. Discussion

To prepare a chiral AgNPs@PPA nanocomposite that can be dispersed in water, we designed an amino-phenylacetylene monomer bearing the 4-ethynyl anilide of (*L*)- or (*D*)-leucine with a deprotected amino group (Figure 86a). These monomers were prepared following peptide chemistry (see SI) and were further protonated with HCl (1 equiv) to generate the corresponding ammonium salt (Figure 86b).

These protonated monomers were polymerized with $[Rh(cod)_2]BF_4$ in water to obtain the desired polymers (Poly-(*L*)-**1**/HCl and Poly-(*D*)-**1**/HCl) with low polydispersity and high content of *cis*-configuration of double bonds (Figure 86c). These polymers show good water solubility at different pH, e.g., pH=2 and pH= 7, where the NH_2/NH_3^+ ratio will

be different along the polymeric scaffolds. Both protonated and deprotonated forms of the amino group are needed to prepare the desired chiral AgNPs@PPA nanocomposite, with the NH_2 groups being necessary to form complexes with Ag^+ ions, while the ammonium groups are essential to provide water solubility. Under these conditions (pH= 2 and pH= 7), Poly-(*L*)-**1** shows a *P* screw sense excess inferred from ECD (ECD380 nm> 0), while Poly-(*D*)-**1** shows an *M* screw sense excess ($ECD_{380\ nm}$< 0) due to their enantiomeric relationship (Figure 87c, Figure 87d, and Figure S151). The adoption of a *P* helix by Poly-(*L*)-**1** and an *M* helix by Poly-(*D*)-**1** is due to the presence of a preferred antiperiplanar conformation between the carbonyl and NH_2/NH_3^+ groups in the pendant (Figure 87a and Figure 87b), which places the side chain of the amino acid, *i.e.*, the isobutyl group, in such a way that it induces a *P* helix in the main chain of the polyene (Figure 87a).

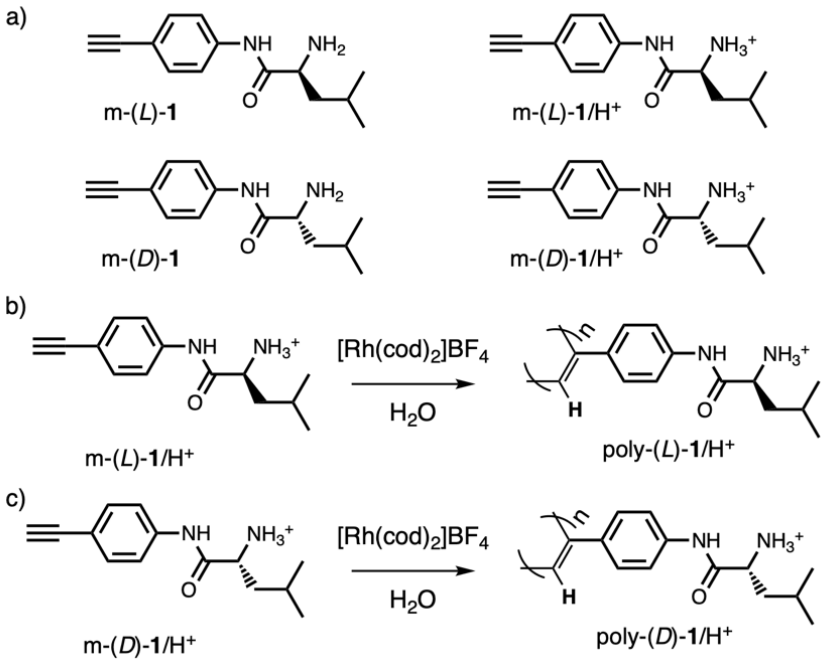


Figure 86. Chemical structure of (a) m-(*L*)-**1**, m-(*D*)-**1** and (b) their protonated forms. c) Scheme of the polymerization reaction to obtain Poly-(*L*)-**1**/H^+ and Poly-(*L*)-**1**/H^+.

Next, the ability of Poly-(*L*)-**1** to form complexes with Ag^+ ions at different pHs was verified by adding $AgClO_4$ (1.5 equiv, c= 10 mg/mL MQ H_2O) to an aqueous solution of Poly-(*L*)-**1** at pH= 7 and pH= 2 (Figure 87a and Figure 87b). Interestingly, when complexation is carried out at pH= 7 (Figure 87a), a helix inversion from *P* ($ECD_{380\ nm}$>

USC UNIVERSIDADE DE SANTIAGO DE COMPOSTELA

0) to *M* ($ECD_{380\ nm}$< 0) is observed (Figure 87c). This is a consequence of a change in conformation in the pendant group, from an antiperiplanar orientation between the carbonyl and amino (NH_2) groups to a synperiplanar orientation after chelation of both functional groups with a silver(I) ion (Figure 87a). This antiperiplanar to synperiplanar conformational switch places the amino acid side chain, *i.e.*, the isobutyl group, in two very different spatial orientations, producing a helix inversion effect.

However, at pH= 2, the addition of $AgClO_4$ to a Poly-(*L*)-**1** solution produces a slight decrease in the *P* screw sense excess (Figure 87b and Figure 87d). This result can be explained by considering the ratio of NH_2/NH_3^+ groups within Poly-(*L*)-**1** at these pHs. Thus, while at pH=7, the amount of neutral amino groups, which can coordinate silver ions, is high (major component), at acidic pH (pH= 2), this number is very low (minor component), the helix being mostly populated by ammonium groups that have lost the ability to coordinate with Ag^+ ions. Interestingly, these helical polymer metal complexes (HPMC, Poly-(*L*)-**1**/Ag^+), prepared at pH=7 and pH= 2, form nanospheres in water as inferred from dynamic light scattering (DLS) (Figure 87e) and scanning electron microscopy (SEM) studies (Figure 87f and Figure S164 to Figure S167).

HPMC nanospheres are generated due to the ability of silver ions to act as cross-linking agents. Their size is larger at pH= 7 due to the greater number of Ag^+ that form complexes with the amino groups (NH2) of different polymer chains, which are more abundant at pH= 7 than at pH= 2.

Analogous studies were carried out with Poly-(*D*)-**1**, showing identical stimuli-responsive properties but opposite helical senses due to their enantiomeric relationship (Figure S151).

USC UNIVERSIDADE DE SANTIAGO DE COMPOSTELA

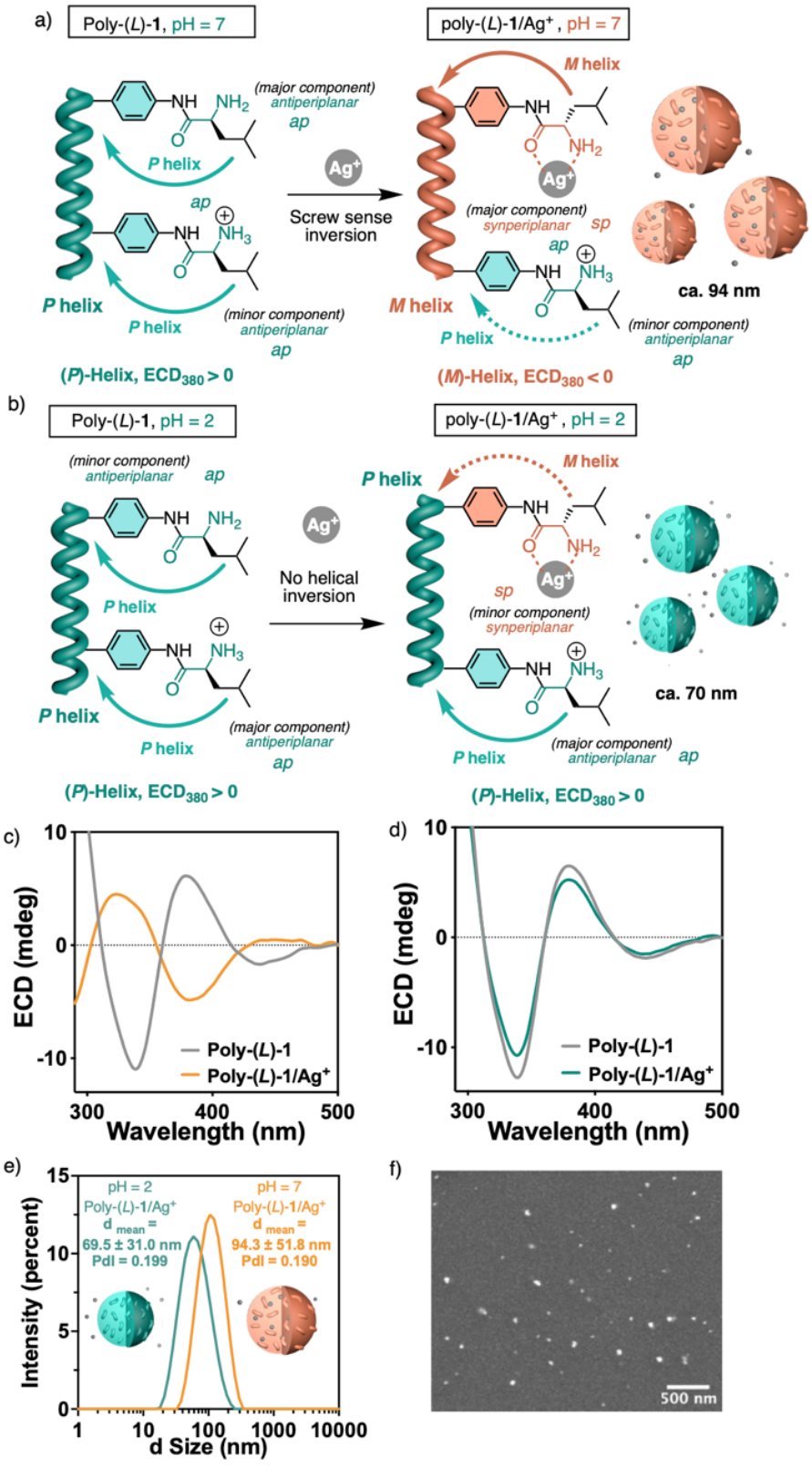


Figure 87. a) Schematic illustration of the Poly-(*L*)-**1** helix inversion after complexation with 1.5 equiv of Ag^+ at pH= 7 and (b) pH= 2 and the formation of HPMC particles. ECD spectra of Poly-(*L*)-**1** and Poly-(*L*)-**1**/Ag^+ at (c) pH= 7 and (d) pH= 2. e) DLS studies of Poly-(*L*)-**1**/Ag^+ 1/1.5 mol/mol prepared at pH= 7 and pH= 2. f) SEM image of Poly-(*L*)-**1**/Ag^+ nanospheres at pH= 7. [Poly-(*L*)-**1**]= 0.3 mg/mL H_2O, [$AgClO_4$]= 10 mg/mL H_2O.

Next, AgNPs@Poly-(*L*)-**1** nanocomposites were prepared at pH= 7 (Figure 88a) and pH=2 (Figure 89a) from the Poly-(*L*)-**1**/Ag^+ complexes (1/1 mol/mol ratio) by adding 0.45 equiv of $NaBH_4$ as reducing agent. The mixtures were kept under vigorous stirring for 60 minutes, and color of the solutions changed from yellow to brown, indicative that reduction of silver ions was taking place. Immediately thereafter, a metal scavenger resin (Quadrapure TU) was added to the solution mixtures to remove unreacted Ag^+ ions and Na^+ from the reducing agent.

ECD studies at pH= 7 show that the formation of the AgNPs@Poly-(*L*)-**1** nanocomposite, after metal ion reduction, does not affect the preferred *P* screw sense adopted by Poly-(*L*)-**1**/Ag^+ —$ECD_{380\ nm}$< 0 for Poly-(*L*)-**1**/Ag^+ and AgNPs@Poly-(*L*)-**1**)— (Figure 88b). UV-Vis studies of AgNPs@Poly-(*L*)-**1** show the localized surface plasmon resonance (LSPR) band centered at 427 nm, indicative of AgNPs formation (Figure 88c). Moreover, a variation in the size of the aggregate during the formation of the composite, from 94 to ca. 250 nm, is observed by DLS and SEM. These studies also reveal the presence of spherical particles for the AgNPs@Poly-(*L*)-**1** nanocomposite (Figure 88d, Figure 88e and Figure S171). These nanospheres are filled with several AgNPs whose size is ca. 30 nm (Figure 88f), as could be observed in the images obtained through transmission electron microscopy —TEM— studies. The large number of AgNPs within the nanosphere that forms AgNPs@Poly-(*L*)-**1** is attributed to the presence of several nucleation points (amino groups complexed with silver ions: NH_2—Ag^+) along the helix at pH= 7. Considering the morphology of the helical polymer metal complex and the nanocomposite, it is necessary for the reducing agent to diffuse inside the Poly-(*L*)-**1**/Ag^+ nanosphere to create the nucleation sites.

Moreover, FT-IR studies show that in addition to the ammonium groups, the AgNPs are also stabilized by the carbonyl group of the anilide (Figure S152). As a result, these nanocomposites show good thermal and temporal stability once the solvent is removed and they are redispersed in water, which confirms that Poly-(*L*)-**1** is a good protecting agent for obtaining AgNPs (Figure S153a).

USC UNIVERSIDADE DE SANTIAGO DE COMPOSTELA

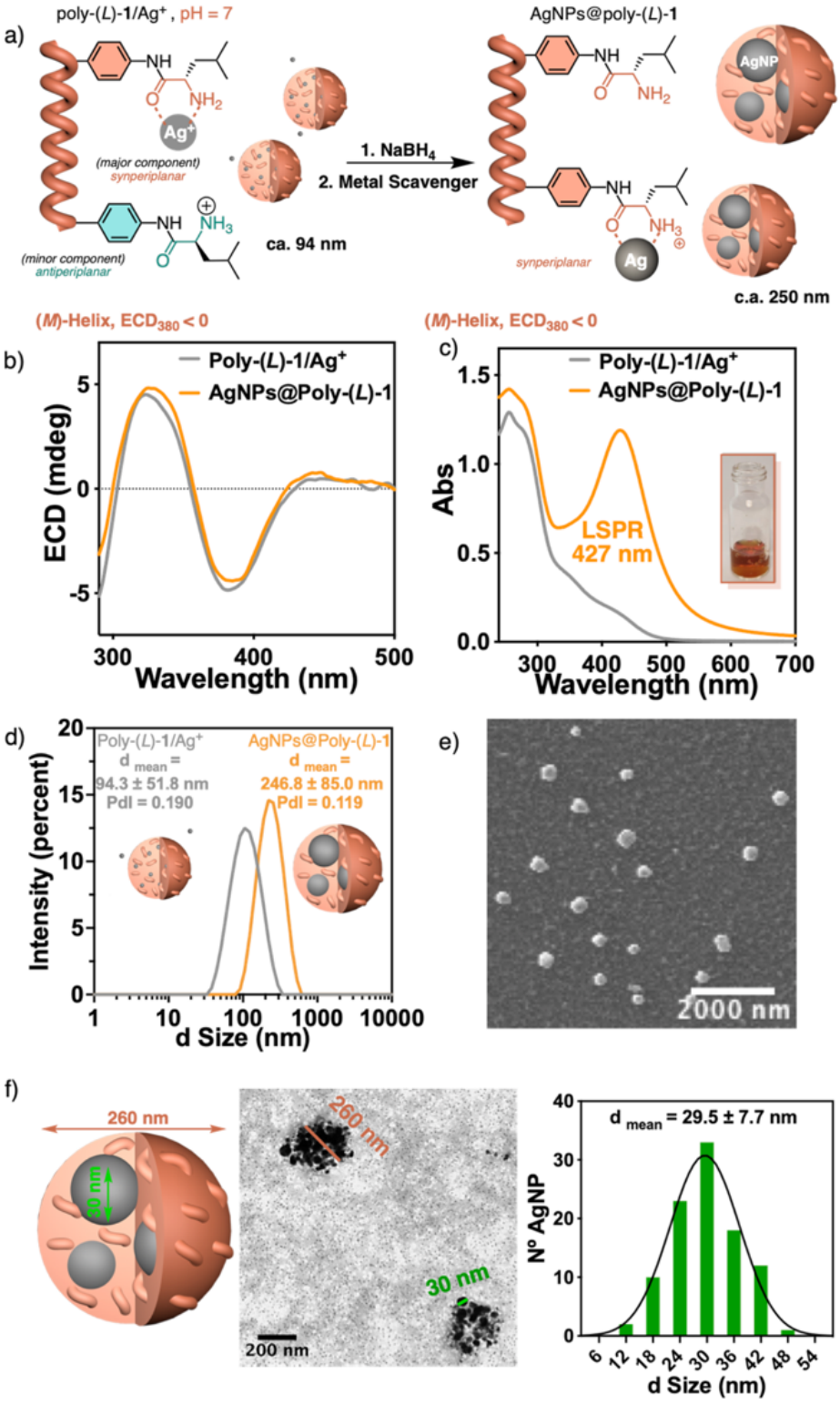


Figure 88. a) Schematic illustration of the formation of AgNPs@Poly-(*L*)-**1** nanocomposite at pH= 7. Comparison of (b) ECD and (c) UV-Vis spectra of Poly-(*L*)-**1**/Ag+ and AgNPs@Poly-(*L*)-**1** at pH= 7. d) DLS studies of Poly-(*L*)-**1**/Ag+ and AgNPs@Poly-(*L*)-**1**. e) SEM and (f) TEM studies of AgNPs@Poly-(*L*)-**1** at pH= 7 (gaussian size distribution of 100 AgNPs).

USC UNIVERSIDADE DE SANTIAGO DE COMPOSTELA

In addition, photostability studies show that poly-(*L*)-**1** is more stable to light irradiation when the nanocomposite is prepared at pH= 7 than when it is molecularly dissolved (Figure S153). Similarly, VT-ECD studies show how, in a molecularly dissolved state, the screw sense excess is lost at 340 K, while in the nanocomposite it remains unaltered at the same temperature (Figure S153).

Interestingly, when the AgNPs@Poly-(*L*)-**1** nanocomposite is prepared at pH= 2 (Figure 89a), ECD studies show a helical inversion of the Poly-(*L*)-**1**/Ag+ complex after reduction of the silver ion to form the AgNP@Poly-(*L*)-**1** nanocomposite (Figure 89b). At this pH, there are many ammonium groups in the polymer that do not interact with Ag^+ ions (Figure 89a). However, once the metal ion is reduced to Ag(0), the ammonium groups have high affinity for the metal in the ground state (Figure 89a). Thus, the chelation of carbonyl and ammonium to Ag(0) nanoparticles changes the preferred conformation of the pendant group, which evolves from antiperiplanar to synperiplanar during the reduction of the metal ion, placing the helix directing group (isobutyl) in different spatial orientations. As a result, this conformational switch produced a helix inversion of the PPA that allowed us to monitor the reduction of Ag(I) to Ag(0) by ECD (Figure 89b). Therefore, Poly-(*L*)-**1** in addition to stabilizing the metal nanoparticles, can be used to monitor the reduction of Ag(I) to Ag(0) in water.

UV-Vis studies of AgNP@Poly-(*L*)-**1** show the localized surface plasmon resonance (LSPR) band centered at 412 nm, indicative of the formation of AgNPs (Figure 4c). This plasmon band is hypsochromically shifted by 15 nm compared to the plasmon band of AgNP@Poly-(*L*)-**1** obtained at pH= 7. DLS studies show a small variation in the aggregate size during the formation of the nanocomposite from 70 to 83 nm (Figure 4d), in agreement with electron microscopy studies, SEM and TEM, which show the presence of spherical particles for AgNP@Poly-(*L*)-**1** whose average size is ca. 80 nm (Figure 89e, Figure 89f and Figure S166). Interestingly, TEM studies reveal that within each nanosphere of the AgNP@Poly-(*L*)-**1** nanocomposite prepared at pH=2, there is only one AgNP whose size is ca. 30 nm (Figure 89f).

Considering the different morphology of the AgNP@Poly-(*L*)-**1** nanocomposites prepared at pH= 7 and pH =2, it is possible to explain the UV-Vis data considering a different environment for the AgNPs in both nanocomposites. More precisely, a bathochromic shift is observed for the plasmon band of the nanocomposite prepared at

USC UNIVERSIDADE DE SANTIAGO DE COMPOSTELA

pH= 7 with respect to the band observed at pH= 2, although the size of the AgNPs is ca. 30 nm in both cases.

This variation in the morphology of the AgNP@Poly-(*L*)-**1** nanocomposites prepared at pH= 7 and pH= 2 is related to the different number of amino groups coordinated to the metal ion before adding the reducing agent. Thus, while at pH= 7 the number of amino groups within the polymer is greater than at pH= 2, the number of Ag^{+} coordinated to these amino groups is also greater. These amino/Ag+ interactions are the nucleation sites within the nanosphere, which produce more AgNPs growth sites within the nanocomposite at pH= 7 than at pH= 2. As a result, the morphology of the dispersed nanocomposites depends on the pH used to prepare them.

These nanocomposites prepared at pH= 2 show good thermal and temporal stability once the solvent is removed and redispersed again in water, confirming that Poly-(*L*)-**1** is a good protective agent to obtain AgNPs (Figure S153b).

USC UNIVERSIDADE DE SANTIAGO DE COMPOSTELA

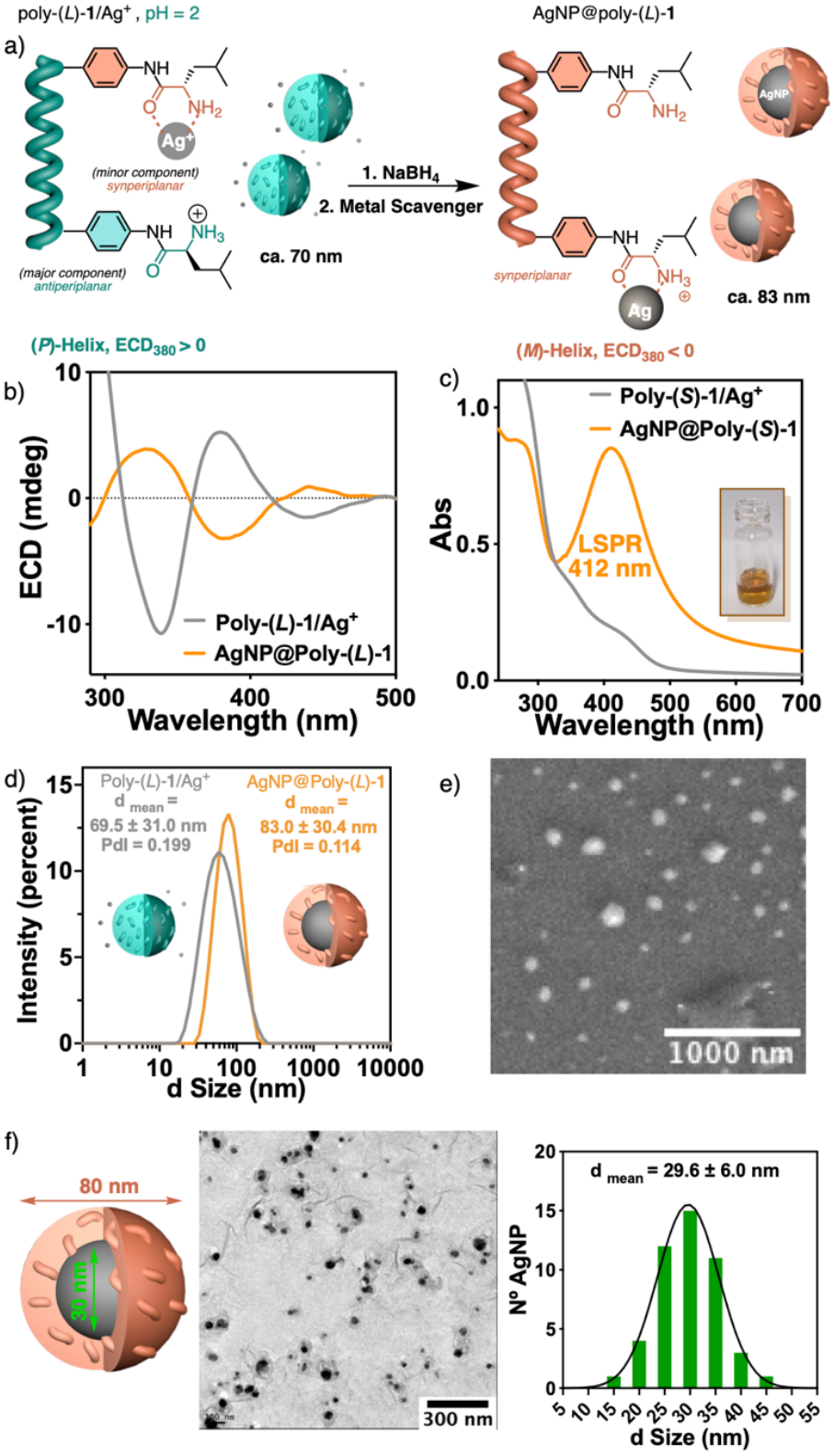


Figure 89. a) Schematic illustration of the formation of AgNP@Poly-(*L*)-**1** nanocomposite at pH= 2. Comparison of (b) ECD and (c) UV-Vis spectra of Poly-(*L*)-**1**/Ag⁺ and AgNP@Poly-(*L*)-**1** at pH= 2. d) DLS studies of Poly-(*L*)-**1**/Ag⁺ and AgNP@Poly-(*L*)-**1**. e) SEM and (f) TEM studies of AgNP@Poly-(*L*)-**1** at pH= 2 (gaussian size distribution of 50 AgNPs).

UNIVERSIDADE DE SANTIAGO DE COMPOSTELA

Density Functional Theory calculations (see SI) confirm the experimentally elucidated formation mechanism of AgNP(s)@Poly-(*L*)-**1**. Thus, in the absence of any metal ion, DFT calculations [B3LYP-D3/6-311+G(d,p)] indicate that the preferred conformation in the leucine derivative, regardless of the protonation state of the amino group, is the antiperiplanar one —carbonyl and amino/ammonium groups oriented antiperiplanar— (Figure 90a, Figure 90b, and Table S27). However, after addition of the Ag+ ion, DFT calculations [B3LYP-D3/6-311+G(d,p) for all atoms except silver, which used B3LYP-D3/cc-pVDZ(-pp)][449-450] show that chelation of the metal ion with the carbonyl and amino (NH_2) groups, through a synperiplanar orientation between them, is the most stable conformer. Additionally, according to the Gibbs free energy shift, the interaction with the deprotonated form in the synperiplanar orientation is the most stable. EFL and NCI analysis[451] were used to analyze the non-covalent interactions. EFL confirmed that there are not covalent interactions, while NCI studies indicated strong non-covalent interactions between the amide carbonyl and the amino group with the Ag^+ ion (Figure 90c, Figure 90d, and Figure S181).

Similar computational DFT calculations [B3LYP-D3/6-311+G(d,p) for all atoms except silver, which used B3LYP-D3/cc-pVDZ(-pp)] were performed by exchanging the Ag^+ ion for an AgNP consisting of Ag^0_7 faces.[452-454] In this case, the synperiplanar orientation between the carbonyl and NH_3^+ is preferred for interacting with an AgNP showing a larger Gibbs free energy shift than the deprotonated (NH_2) form (Figure 90a). ELF and NCI studies indicated a strong non-covalent interaction between the ammonium group with Ag(0) and Van der Waals interactions between the amide and the hydrogen in alpha position with the Ag(0) (Figure 90e, Figure 90f, and Figure S41).[455]

USC UNIVERSIDADE DE SANTIAGO DE COMPOSTELA

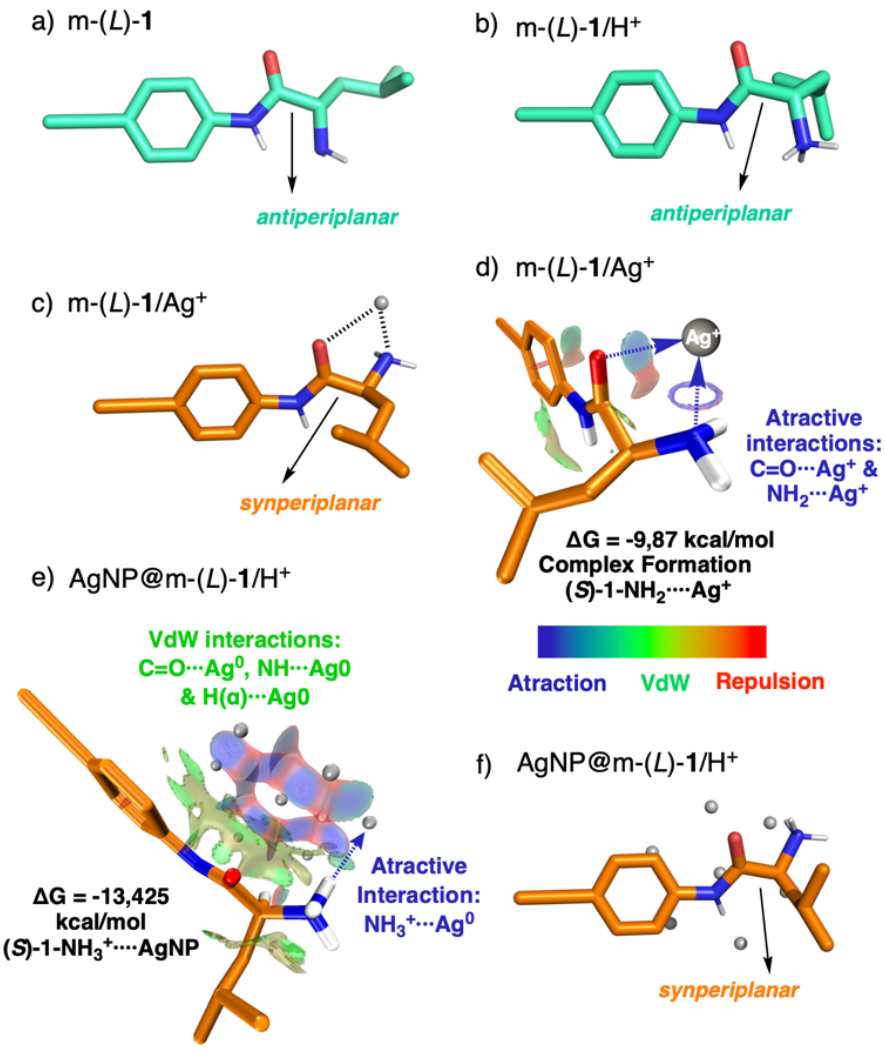


Figure 90. Preferred conformations of a) m-(*L*)-**1** and b) m-(*L*)-**1**/H⁺. c) Preferred conformation of m-(*L*)-**1** in presence of Ag⁺. d) Graphical illustration showing the attractive non-covalent interactions of m-(*L*)-**1**/Ag⁺ obtained by NCI analysis. e) Graphical illustration showing the attractive non-covalent interactions of m-(*L*)-**1**/H⁺/AgNP obtained by NCI analysis. f) Preferred conformation of m-(*L*)-**1**/H⁺ in presence of AgNPs. All structures were optimized by DFT B3LYP-D3/6-311+G(d,p) for all atoms and cc-pVDZ(-pp) for Ag.

3.5.2.1. Stimuli-responsive studies of chiral AgNP(s)@Poly-(L)-1

The stimuli responsiveness of the AgNP(s)@Poly-(*L*)-**1** nanocomposite prepared at two different pHs (7 and 2) was studied considering the stimuli responsive properties of the two components of the nanocomposite, the dynamic helical polymer (Poly-(*L*)-**1**) and the metal nanoparticle (AgNP).

External stimulus: pH. Poly-(*L*)-**1** adopts a preferred *P* helix ($ECD_{380\ nm} > 0$) at neutral pH —NH_2/NH_3^+ ratio> 1—, while an *M* helical sense ($ECD_{380\ nm} < 0$) is induced in the polymer at acidic pH —NH_2/NH_3^+ ratio< 1—. Thus, the chiroptical properties of the

USC UNIVERSIDADE DE SANTIAGO

two nanocomposites were checked by varying the pH of the water dispersions of the two AgNP@Poly-(*L*)-**1** nanocomposites (0.3 mg/mL) in ranges between 1 and 6.5. Interestingly, it was found that pH variations in the water dispersion of the AgNP(s)@Poly-(*L*)-**1** nanocomposites do not affect the axial chirality adopted by Poly-(*L*)-**1**. This fact is due to the stabilization of the nanocomposite through NH_3^+—Ag(0) interactions, which are maintained at different pHs and which keep the free amino groups, through a conformational Communication Mechanism, in an antiperiplanar orientation regardless of their protonation states. This result differs from studies carried out for a solution of Poly-(*L*)-**1**, where changes in pH alter the NH_2/NH_3^+ ratio and the preferred synperiplanar and antiperiplanar conformations adopted by the pendant —synperiplanar for NH_2 and antiperiplanar for NH_3^+—. However, although changes in the pH do not affect the chirality of the nanocomposites, their dispersion ability is reduced when the amount of NH_2 increases (pH> 6). As a result, the plasmon band of the AgNP(s)@Poly-(*L*)-**1** nanocomposites (LSPR= 428 nm of AgNPs@Poly-(*L*)-**1** prepared at pH= 7, LSPR= 413 nm of AgNP@Poly-(*L*)-**1** prepared at pH= 2) is red-shifted when the pH is higher than 7 —e.g., LSPR at pH= 9 is 444 nm for AgNPs@Poly-(*L*)-**1** previously prepared at pH= 7 and 430 nm for the AgNP@Poly-(*L*)-**1** nanocomposite previously prepared at pH= 2—. This bathochromic shift is due to the agglomeration of the nanocomposite at basic pH (Figure 91a and Figure 91b). This aggregation process is fully reversible, recovering the initial LSPR value at acidic pH and works perfectly after several pH cycles, as demonstrated by UV-Vis, DLS and SEM studies (Figure 91c, Figure S162, and Figure S175 to Figure S178).

USC UNIVERSIDADE DE SANTIAGO DE COMPOSTELA

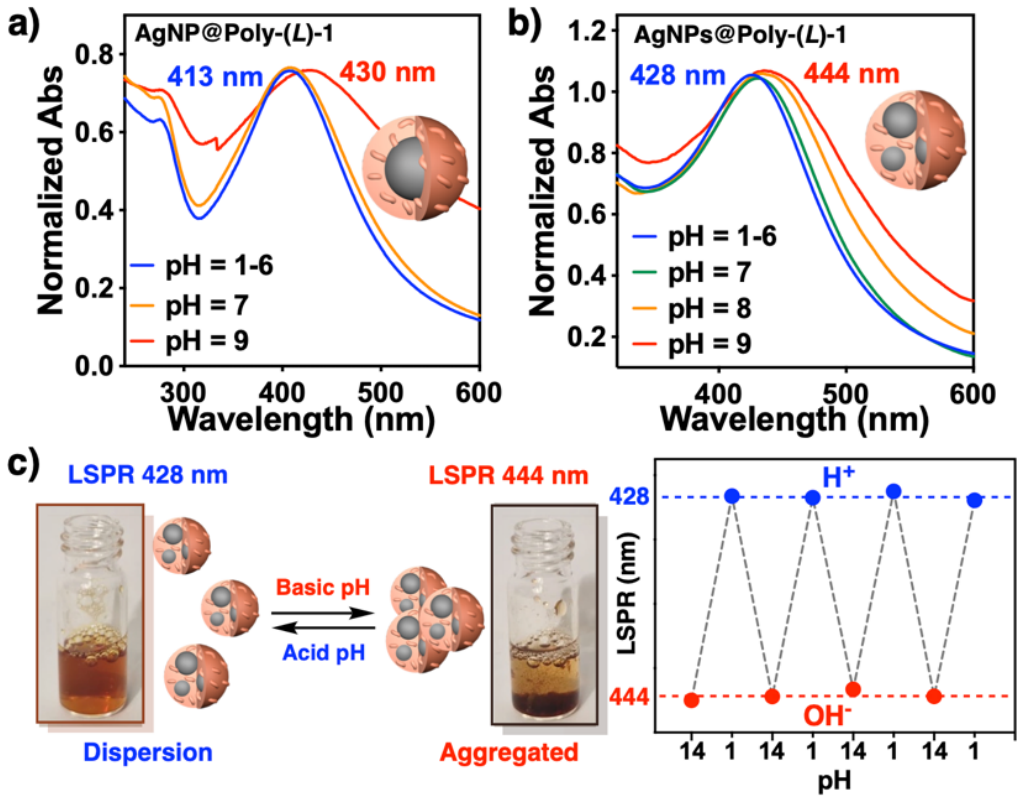


Figure 91. UV-Vis after basification with NaOH (1M) of a) AgNP@Poly-(*L*)-**1** (previously prepared at pH= 2) and b) AgNPs@Poly-(*L*)-**1** (previously prepared at pH= 7) (c= 0.3 mg/mL of Poly-(*L*)-**1**). c) Representation of the behavior of AgNPs@Poly-(*L*)-**1** with increasing pH after the addition of NaOH (aggregated) and with decreasing pH after the addition of HCl (dispersed).

External stimulus: divalent metal ions (M^{2+}). Poly-(*L*)-**1** can interact with Ag+ as previously demonstrated. Thus, we decided to explore its ability to interact with other metal ions such as divalent metal ions (M^{2+}). Hence, the chiroptical properties of an aqueous solution of Poly-(*L*)-**1** were explored in the presence of different divalent metal ions which were delivered to the solution as perchlorate salts [$M(ClO_4)_2$; M^{2+}= Mg^{2+}, Ca^{2+}, Mn^{2+}, Fe^{2+}, Co^{2+}, Cu^{2+}, Ba^{2+}, and Pb^{2+}]. Interestingly, it was observed that in all cases, when the metal ion is added in a 1/1 mol/mol Poly-(*L*)-**1**/$M(ClO_4)_2$ ratio, a helix inversion occurs due to a chelation between the carbonyl, the amino and the divalent metal ion that favors a synperiplanar conformation in the leucine pendant group (Figure 92a). Interestingly, and only in the case of Poly-(L)-1/Ba^{2+}, when the amount of metal ion added is 2 equivalents, a second helix inversion is observed (Figure 92a and Figure S159). This fact indicates that in the case of the other metal ions, or when the Poly-(*L*)-**1**/Ba^{2+} complex is in a 1/1 mol/mol ratio, the chelated form is the most favored, which orients the pendant group synperiplanar. On the other hand, when 2 equivalents of Ba^{2+} are

added to a solution of poly-(*L*)-**1** —Poly-(*L*)-**1**/Ba^{2+} complex in a 1/2 mol/mol ratio— an evolution towards a different complex occurs. In this special case, the adoption of an antiperiplanar conformation in the pendant is stabilized by the coordination of one of the Ba2+ to the carbonyl, while the other ion is coordinated to the amino group. As a result, a helix inversion from *M* to *P* occurs in the PPA (Figure 92a).

Analogous studies were carried out for the two nanocomposites prepared at pH= 2 and pH= 7.

Thus, different perchlorates [$M(ClO_4)_2$; M^{2+}= Mg^{2+}, Ca^{2+}, Mn^{2+}, Fe^{2+}, Co^{2+}, Cu^{2+}, Ba^{2+}, and Pb^{2+}] were added to dispersions of these nanocomposites in water in 1/1 and 1/2 mol/mol AgNP(s)@Poly-(*L*)-**1**/$M(ClO_4)_2$ ratios. In these cases, Poly-(*L*)-**1** adopts an *M* helix in the nanocomposites, consequence of the interactions between carbonyl and ammonium groups with AgNPs. Thus, when 1 equivalent of $M(ClO_4)_2$ is used, no effects are observed in the chirality of the nanocomposite. Both AgNPs and M^{2+} ions induce the same helical sense in the polymer used to coat the MNPs. However, when two equivalents of the metal salt are added, a helical inversion is selectively observed in the case of AgNP(s)@Poly-(*L*)-**1**/$Ba(ClO_4)_2$, similar to the effect observed in the case of Poly-(*L*)-**1**. Analogous results were found for both nanocomposites prepared at pH= 2 and pH= 7, indicating that these nanomaterials can be employed to selectively sense Ba^{2+} in aqueous media.

USC UNIVERSIDADE DE SANTIAGO DE COMPOSTELA

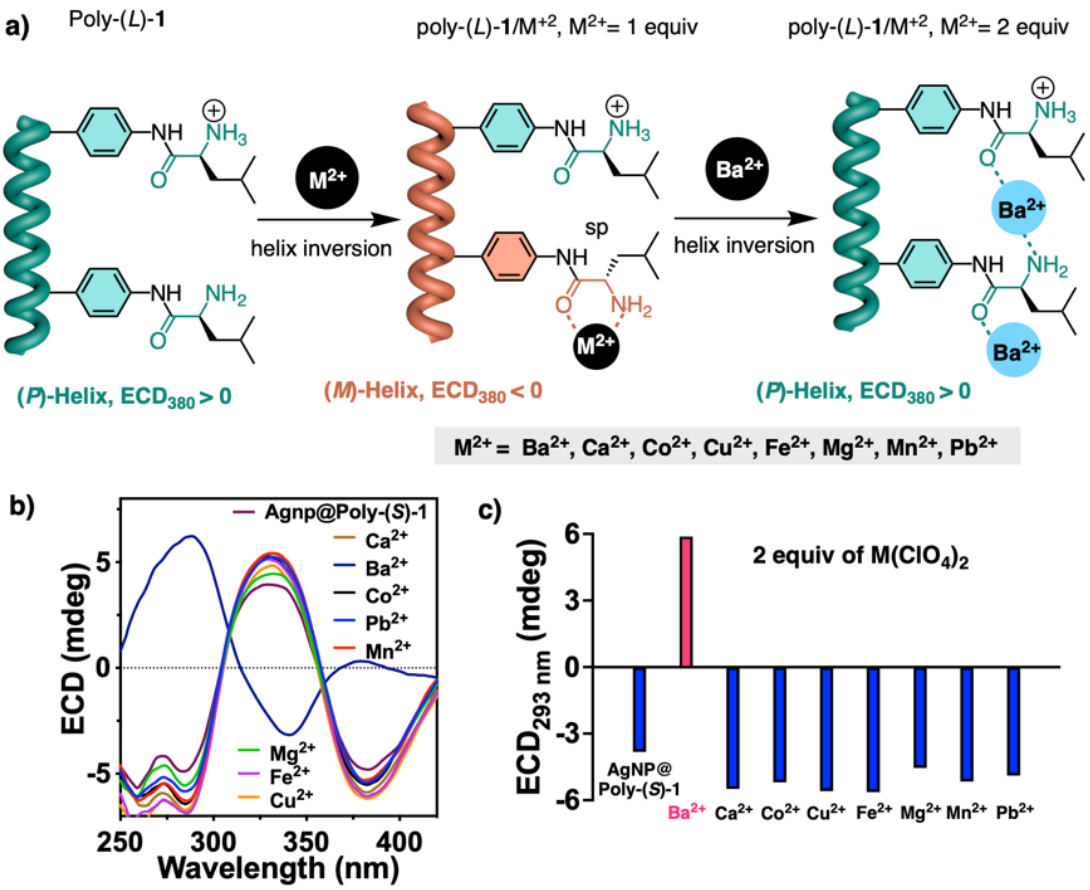


Figure 92. a) Graphical illustration of the conformational changes suffered by Poly-(*L*)-**1** in the presence of 1 equivalent of M^{2+} and 2 equivalents of Ba^{2+}. b) ECD studies of AgNP@Poly-(*L*)-**1** and AgNP@Poly-(*L*)-**1**/M^{2+} in 1/2 mol/mol ratios. c) Graph bar highlighting the response of the ECD band at 293 nm of AgNP@Poly-(*L*)-**1** and AgNP@Poly-(*L*)-**1**/M^{2+} in 1/2 mol/mol ratios.

External stimulus: Oxidizing metal ions. The optical properties of the two nanocomposites can be altered by the presence of oxidizing metal ions such as Fe^{3+}, Hg^{2+}, and Ce^{4+} in different ways (Figure 93a).[456-459] Thus, while the presence of Fe^{3+} and Ce^{4+} ions in an aqueous dispersion of AgNP(s)@Poly-(*L*)-**1** promotes a strong depletion of the LSPR band due to the oxidation of the AgNPs, the presence of Hg^{2+} causes a blue shift accompanied by a depletion of the LSPR band due to the formation of a Hg^0 layer on the surface of the AgNPs once they are oxidized to Ag^+. Thus, by observing the LSPR bands of the AgNP(s)@Poly-(*L*)-**1** nanocomposites, it is possible to distinguish Hg^{2+} from the other ions (Figure 93b, Figure 93c, and Figure 93d).[458] Fortunately, Poly-(*L*)-**1**/Ce^{3+} has a greater tendency to aggregate when compared to Poly-(*L*)-**1**/Fe^{2+}, a result that allow us to discern between these two metals and therefore between the three oxidizing ions Fe^{3+}, Hg^{2+}, and Ce^{4+}.

USC UNIVERSIDADE DE COMPOSTELA

In all cases, the macroscopic *M*-chirality observed in the AgNP(s)@Poly-(*L*)-**1** nanocomposite is also found in the Poly-(*L*)-**1**/M^{n+} complexes due to the stabilization of the synperiplanar conformation in the pendant by chelation between the metal ion (reduced oxidizing metal and oxidized silver) and the carbonyl and amine in the Poly-**1** pendant of the nanocomposite (Figure 93a).

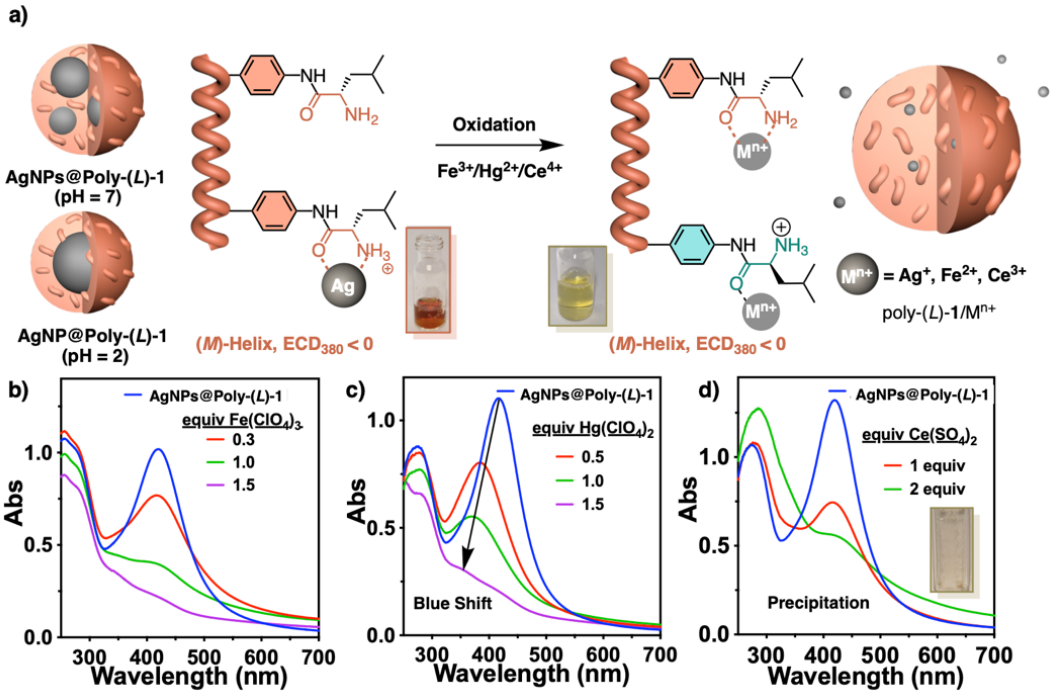


Figure 93. a) Graphical illustration of the AgNP(s)@Poly-(*L*)-**1** nanocomposites response towards oxidizing metal ions. UV-Vis titration studies of the AgNPs@Poly-(*L*)-**1** nanocomposite with (b) $Fe(ClO_4)_3$, (c) $Hg(ClO_4)_2$, and (d) $Ce(SO_4)_2$.

3.5.3. Conclusions

In this work, water-soluble and stimuli-responsive nanocomposites have been prepared by combining AgNPs and a dynamic helical poly(phenylacetylene) (PPA). The designed PPA contains, as a pendant, the anilide of the amino acid leucine [Poly-(*L*)-**1**], which has its N-terminus unprotected. Thus, the presence of amino groups provides the nanocomposite with the ability to disperse in water and strong Ag(0)—NH_3^+ interactions, necessary to stabilize the AgNPs in the aqueous medium. To prepare the nanocomposite, a Poly-(*L*)-**1**/Ag^+ complex is first formed which is subsequently reduced to the desired AgNPs@Poly-(*L*)-**1** nanocomposite. Interestingly, depending on the pH used to prepare the nanocomposite, different morphologies are obtained. Thus, if the nanocomposite is prepared at neutral pH (*i.e.*, 7), the nanocomposite consists of a ca.

USC UNIVERSIDADE DE SANTIAGO

250 nm nanosphere containing several 30 nm AgNPs inside. On the contrary, if the nanocomposite is prepared at acidic pH (*i.e.*, 2), nanospheres with size of ca. 100 nm are formed containing a single 30 nm AgNP in their interior. The two nanocomposite morphologies show similar stimuli-responsive properties to pH and metal ions. Thus, variations in the pH lead to controlled aggregation/dispersion of the nanocomposite resulting in variations of the LSPR band of AgNPs. This process is fully reversible, and the system works perfectly after several pH cycles. Furthermore, it was found that the AgNPs@Poly-(*L*)-**1** nanocomposite can detect and identify Ba^{2+} from a series of eight different divalent metal ions [M^{2+}= Mg^{2+}, Ca^{2+}, Mn^{2+}, Fe^{2+}, Co^{2+}, Cu^{2+}, Ba^{2+}, and Pb^{2+}] delivered as perchlorate salts. Finally, we also found that the AgNPs@Poly-(*L*)-**1** nanocomposite can selectively distinguish between three different oxidizing metal ions such as Fe^{3+}, Hg^{2+}, and Ce^{4+}. These metal ions oxidize AgNPs to Ag(I) within the nanocomposite, but with different responses. Thus, both Fe^{3+} and Ce^{4+} cause a strong depletion of the LSPR bands of AgNPs, but in the case of Ce^{4+} it is also accompanied by precipitation of the final product. On the other hand, the presence of Hg^{2+} ions produce a depletion of the LSPR band that is accompanied by a blue shift. In this way, water-soluble chiral AgNP(s)@PPA nanocomposites have been prepared that combine the optical and chiroptical properties of both components. The stability of these systems, in combination with the stimuli-responsive properties of the nanocomposites allow the preparation of aqueous stimuli-responsive materials with potential applications in sensing, chirality, chemical biology, or medicinal chemistry, among others.

USC UNIVERSIDADE DE SANTIAGO DE COMPOSTELA

USC
UNIVERSIDADE
DE SANTIAGO
DE COMPOSTELA

3.6. Deciphering the emergence of axial chirality and stimuli-responsiveness in PPAs: From oligomers to polymers

Abstract

In this study, by using five different polymers and oligomers with a variety of polymerization degrees (DP), the folding mechanism of a dynamic helical polymer is deciphered. Thus, when the oligomer reaches a minimum size of 3-4 residues, the internal monomer repeating units adopt a twisted conformation in solution that generates an ECD trace identical to the corresponding homopolymers. Interestingly, when the size of the polymer increases, the internal residues incorporated at the polymer chain adopts the same twisted conformation that, at a certain polymer length, results in a helix. Interestingly, by using different external stimuli such as metal ions or solvents it was observed that the dynamic behavior of the foldamers (short oligomers) is identical to the one observed in the polymers (DP>100). In all cases, at certain polymer or oligomer concentrations, the number of polymer or oligomer chains present in the solution varies, and therefore the number of terminal residues adopting a random coil structure, which is always two, one at each terminal end. As a result, we can state that in PPA polymers and foldamers the internal residues are folded into an identical conformation equilibrium that shows the same stimuli responsive properties. Therefore, these studies open a new scenario in the preparation of dynamic chiral materials, where the size of the polymer dictates the final shape of the material, from a twisted foldamer to a helical polymer, which can determine their functionality in fields such as asymmetric synthesis or molecular/macromolecular recognition, among others.

USC
UNIVERSIDADE DE SANTIAGO DE COMPOSTELA

USC
UNIVERSIDADE
DE SANTIAGO
DE COMPOSTELA

3.6.1. Precedents

In 1998 Prof. Samuel H. Gellman defined foldamer as an oligomer of modest length that shows a well-defined conformational preference in solution.[460] As a result, this macromolecule will be folded into a specific secondary structure that could resemble those structural motifs found in nature such as helices, turns, or sheets, or it could be folded into other complex structures such as knots. In all cases, the first step in foldamer chemistry is to identify a new backbone, made by non-natural residues, with suitable folding propensities. This backbone must have the ability to be decorated with different functional groups to endow the foldamer with different functions that show applications in fields such as catalysis, molecular recognition, or stimuli-responsiveness. Finally, these oligomers should be prepared efficiently with the aim of finding real applications in industry, medicine, or catalysis.

Dynamic helical polymers, such as chiral poly(phenylacetylene)s (PPAs) are a family of polymers that has the helix as a structural motif even in solution. PPAs are obtained from polymerization of the corresponding phenylacetylene monomer (PA),[8,21,29,461,462] which can be decorated with different functional groups to endow the material with a specific function.[36,50,59,463] Usually, PPAs are used as stimuli-responsive materials due to the possibility of tuning their helical sense and/or elongation by the presence of external agents such as chiral molecules, pH, temperature, light, metal ions, anions, or solvents.[25,42,43,84,171,233,235,236,245,248,266,267,281,335] This is possible due to a low energy barrier between the *P* and *M* screw senses of the polymer helix. In the foldamers field, dynamic foldamers are also found, which consist of synthetic folded molecules that show the ability of changing their conformation in response to an external stimulus. An interesting example is the dynamic helical foldamers described by Prof. Jonathan Clayden and Prof. Yosihito Inai which showed the ability of tuning the *P*/*M* screw sense excess of peptide mimetics composed primarily of achiral α-aminoisobutyric acid residues.[246,464-468]

The main difference between dynamic helical polymers and foldamers lies in the length of the backbone or the polymer main chain. In case of dynamic helical polymers such as chiral PPAs, the classical polymerization conditions led to the formation of large polymers, which prevents the formation of short oligomers that allow us to explore their folding and stimuli-responsive properties. Recently, Dr. T. Taniguchi, Prof. T. Nishimura and Prof. K. Maeda developed a well-controlled living polymerization of phenylacetylenes in which the molecular weight of the resulting poly(phenylacetylene)s

USC UNIVERSIDADE DE SANTIAGO

oligomers or polymers can be readily controlled by adjusting the initial feed ratio of the monomer and the catalyst, resulting in polymers or oligomers with narrow molecular-weight distributions (M_w/M_n=1.02–1.09).[54,60,61,469] This living polymerization of PPAs produces stereoregular polyene backbones, with a high cis content of double bonds. Interestingly, this polymerization introduces to the initiating end of the polymer components from aryl boronic acid derivatives and 2 or 3 diphenylacetylene units (Figure 94a). Therefore, by using this synthetic approach we can prepare different chiral PPA oligomers (n=3-100), whose folding and stimuli responsive properties will be compared to the corresponding PPAs obtained by using the classical polymerization protocol. Thus, from these studies we aim to extract the oligo(phenylacetylene) size (n-mer) needed for a chiral PPA to start folding into a helical structure, and the minimum oligomer size needed to be folded in a similar percentage as the corresponding parent homopolymer obtained from the classical polymerization protocol.

3.6.2. Discussion

To perform these studies, a library of 5 chiral PPAs with well-known secondary structures was selected. This PPA collection includes PPAs that bear the 4-anilide of (*R*)-methoxyphenylacetic acid (poly-(*R*)-**1**), the 4-anilide of (*S*)-α-methoxy-α-(trifluoromethyl)phenylacetic acid (poly-(*S*)-**2**), the 4-benzamide of (*S*)-leucine methyl ester (poly-(*S*)-**3**), the 4-benzamide of (*S*)-alanine methyl ester (poly-(*S*)-**4**), and the 4-benzamide of (*S*)-valine methyl ester poly-(*S*)-**5** (Figure 94b-c). All these polymers show a dynamic helical behavior and it is possible to tune the *P*/*M* screw sense excess by using solvents with different polarity or donor character, or metal ions as external stimuli.

Thus, long length poly-(*R*)-**1**, poly-(*S*)-**2**, poly-(*S*)-**3**, poly-(*S*)-**4**, and poly-(*S*)-**5** were prepared using $[Rh(nbd)Cl]_2$ as the catalyst,[36] while oligomers —oligo-(*R*)-**1**, oligo-(*S*)-**2**, oligo-(*S*)-**3**, oligo-(*S*)-**4**, and oligo-(*S*)-**5** — with different lengths that fell in the range N = 4-100 were prepared following Maeda's protocol.[54,60,61,469] In this work the 4-(methylthio)phenylboronic acid was employed as initiator. The methylthioether group (SMe) provides a distinctive NMR signal in the ^{1}H-NMR spectra of the different oligomers —oligo-(*R*)-**1**, oligo-(*S*)-**2**, oligo-(*S*)-**3**, oligo-(*S*)-**4**, and oligo-(*S*)-**5**; N= 4-100— which allows us to estimate the DP from the relative integral between the pendant and SMe protons. The 4-(methylthio)phenylboronic acid was used in combination with

USC UNIVERSIDADE DE SANTIAGO DE COMPOSTELA

norbornadiene rhodium (I) chloride dimer $[Rh(nbd)Cl]_2$, potassium hydroxide (KOH), triphenylphosphine (PPh_3), diphenylacetylene (DPA), and the corresponding PA monomer [m-(*R*)-**1**, m-(*S*)-**2**, m-(*S*)-**3**, m-(*S*)-**4**, m-(*S*)-**5**] to obtain the desired oligomers which contain 2 or 3 DPA units at the initiating end (Figure 94a).

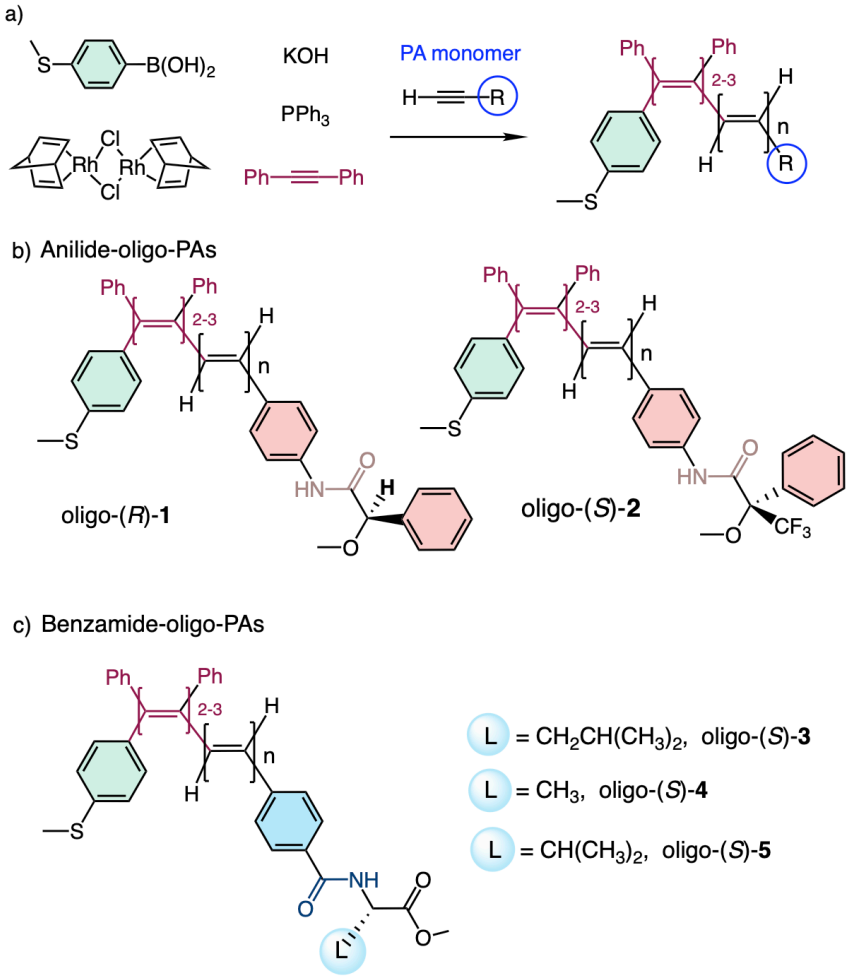


Figure 94. a) Schematic representation of the oligomerization reaction. Oligomers with (b) anilide and (c) benzamide linkage.

By using different monomer (m-(*R*)-**1**, m-(*S*)-**2**, m-(*S*)-**3**, m-(*S*)-**4**, m-(*S*)-**5**)/Rh ratios it is possible to obtain oligomers with different degree of polymerization (Figure 95 and SI). In our case, five oligomers were prepared for each oligomer series, with DP of ca. 5, 10, 20, 40, and 80. The DP of the different oligomers obtained is similar to the [monomer]/[Rh(I)] catalyst ratio employed, as confirmed by ^{1}H-NMR studies (Figure S189 to Figure S218). Moreover, GPC experiments showed that all the oligomers of the different oligomer series show very low dispersity (Đ<1.05) (Figure 95 and Figure S188).

USC DE COMPOSTELA

Next ECD studies of the polymers — poly-(*R*)-**1**, poly-(*S*)-**2**, poly-(*S*)-**3**, poly-(*S*)-**4**, and poly-(*S*)-**5**— and oligomers —oligo-(*R*)-**1**, oligo-(*S*)-**2**, oligo-(*S*)-**3**, oligo-(*S*)-**4**, and oligo-(*S*)-**5**; N ca. 5, 10, 20, 40, and 80— were carried out in $CHCl_3$, THF, and DMF (c= 0.3 mg/mL), solvents with different donor ability and where all the polymers selected in this study show different helical behavior.

USC
UNIVERSIDADE DE SANTIAGO DE COMPOSTELA

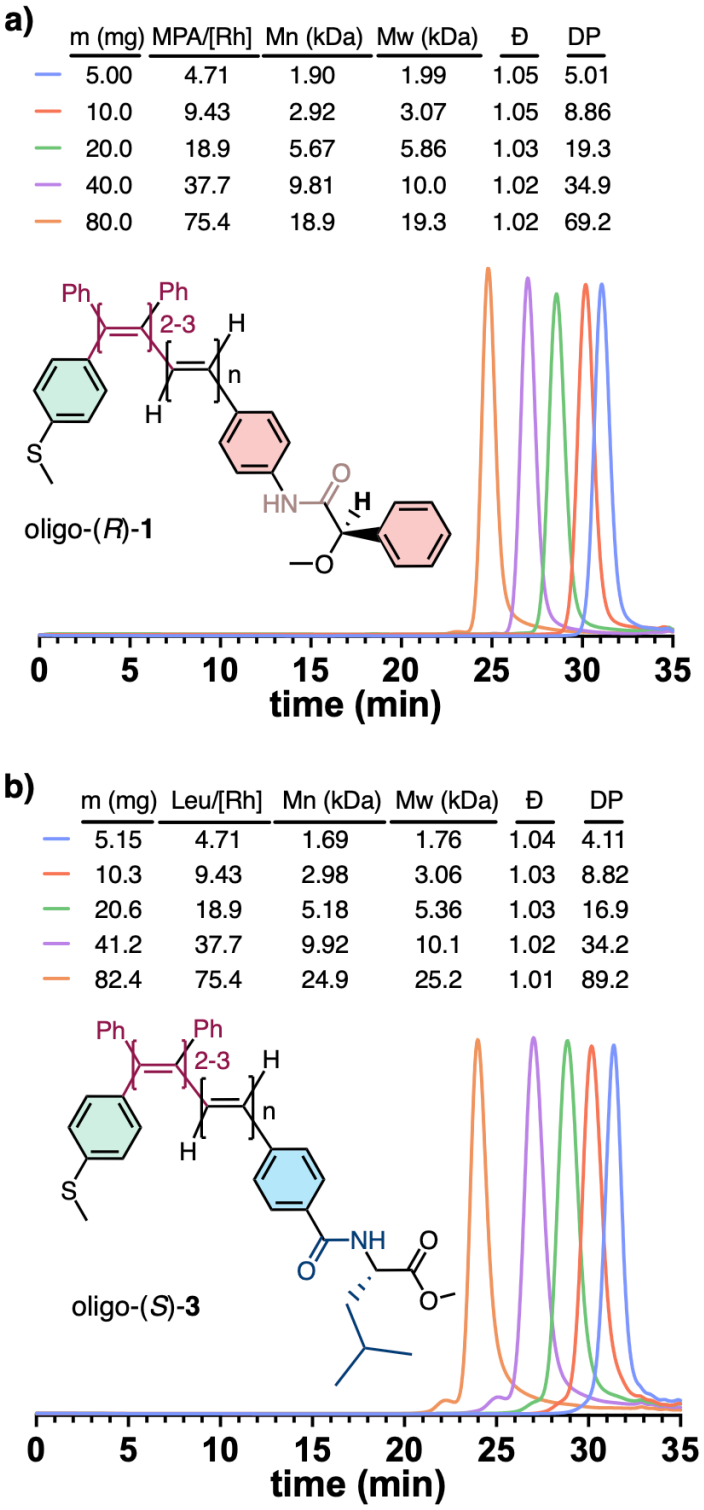


Figure 95. a) GPC traces of (a) oligo-(*R*)-**1** anilide oligomer series (DP = 5, 9, 19, 35, and 69) and (b) oligo-(*S*)-**3** benzamide oligomer series (DP = 4, 9, 17, 34, and 89).

By comparing the ECD spectra of the different oligomer series in the different solvents —oligo-(*R*)-**1**, oligo-(*S*)-**2**, oligo-(*S*)-**3**, oligo-(*S*)-**4**, and oligo-(*S*)-**5**; N ca. 5, 10, 20, 40, and 80— and the corresponding polymers — poly-(*R*)-**1**, poly-(*S*)-**2**, poly-(*S*)-**3**,

poly-(*S*)-**4**, and poly-(*S*)-**5**—, we can clearly see that when the DP of the oligomer is close to 40, the folding of the oligomer is very similar to the folding of the corresponding homopolymer. However, from these studies we can observe that in all cases that when the DP is ca. 20, the folding of oligomers is approximately 75% with respect to the corresponding polymers. Interestingly, although the folding of the oligomers decreases when the size of the oligomer is shortened —DP ca. 10, 40% folded; DP ca. 5, 20% folded—, it is possible to observe that very short oligomers made of just 5 chiral phenylacetylene monomer units show some folding (Figure 96). Curiously, although a polymer shows different extension in the degree of folding in different solvents, the variation of the folding within the oligomer series is similar regardless of the solvent used. This fact indicates that the equilibrium between the random coil and the folding state depends on the DP, but it is independent of the external stimuli used, such as solvent polarity (Figure 96).

USC
UNIVERSIDADE DE SANTIAGO DE COMPOSTELA

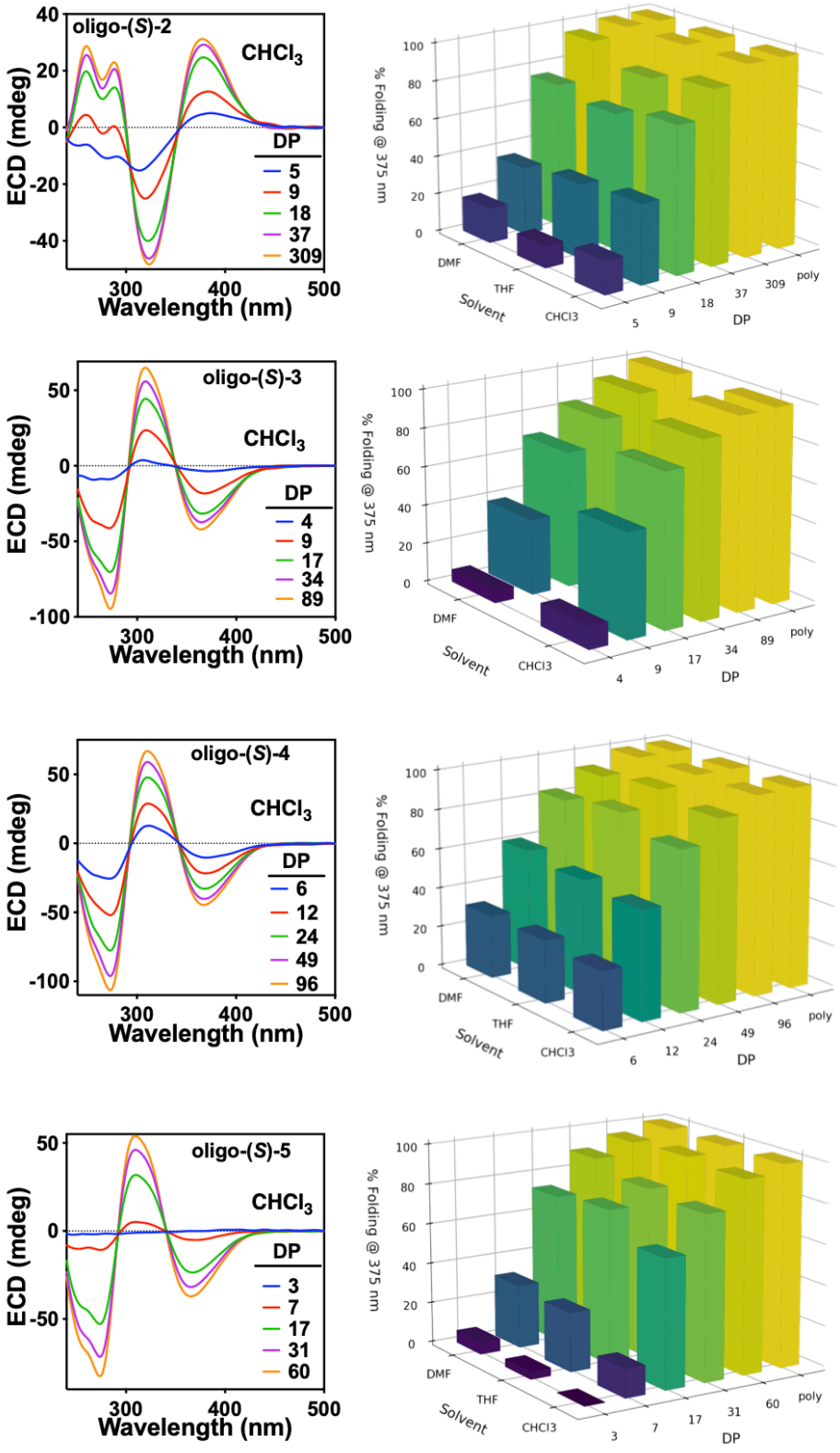


Figure 96. ECD spectra of the oligo-(*S*)-**2**, oligo-(*S*)-**3**, oligo-(*S*)-**4**, and oligo-(*S*)-**5** oligomer series in $CHCl_3$. Folding degree of oligomers for the different oligomer series in different solvents considering the polymer as the fully folded reference.

UNIVERSIDADE DE SANTIAGO DE COMPOSTELA

To corroborate this hypothesis, $LiClO_4$ (10 mg/mL MeOH) was added to chloroform solutions of poly-(*R*)-**1**, poly-(*S*)-**3**, poly-(*S*)-**4**, poly-(*S*)-**5**, and their corresponding oligomer series —oligo-(*R*)-**1**, oligo-(*S*)-**2**, oligo-(*S*)-**3**, oligo-(*S*)-**4**, and oligo-(*S*)-**5**; N ca. 5, 10, 20, 40, and 80— to prepare the corresponding poly- or oligomer/Li^+ complexes in a 1.0/0.5 mol/mol ratio (Figure S219 to Figure S223). These polymers show Li^+ response, where an asymmetry amplification is produced in the helical PPA after complexation with Li^+ ions.[43,171,267,269,334,337,366,367,404] For instance, poly-(*S*)-**4** undergoes a helix inversion from *M* to *P* once is complexed to Li^+ in chloroform (Figure 97). Remarkably, the extension of the helix inversion is directly related to the DP, where the folding associated to this new external stimulus depends on the polymer length. Thus, as occurs in the absence of Li^+, in the poly-(*S*)-**4**/Li^+ complex, when the oligomer DP is ca. 20, the folding of the oligomer/Li^+ complexes is 75% respect to the corresponding helical polymer metal complex. Interestingly, it is observed that the folding of the oligomers decreases when the size of the oligomer is shortened —DP ca 10, 40% folded; DP ca 5, 20% folded—, in a similar trend that in the absence of the external stimulus (Li^+).

USC UNIVERSIDADE DE SANTIAGO DE COMPOSTELA

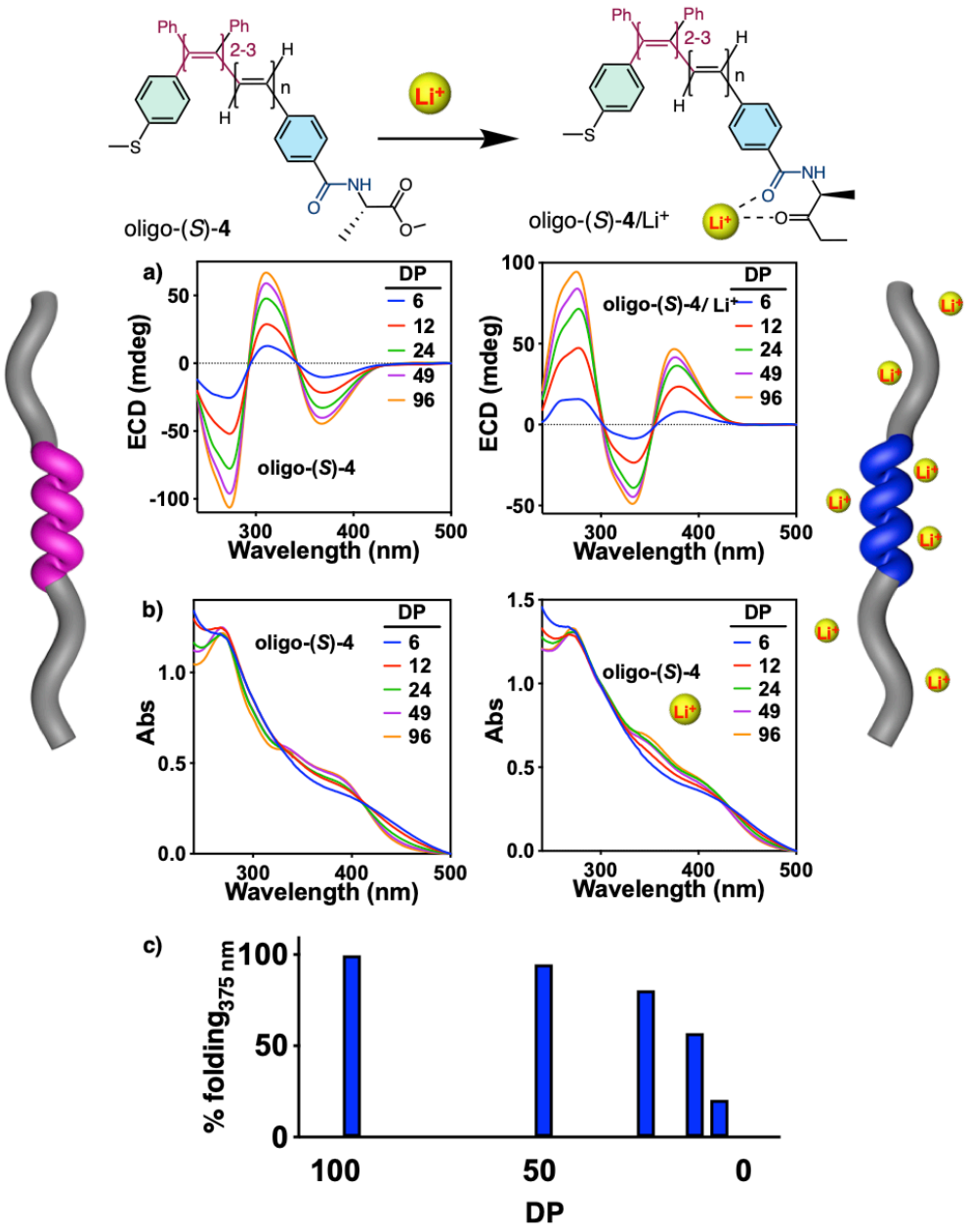


Figure 97. Spectra of oligo-(*S*)-**4** (DP = 6, 12, 24, 49, and 96) (c=0.3mg/mL $CHCl_3$) before and after the complexation of 0.5 equiv of $LiClO_4$ (10 mg mL^{-1} MeOH) a) UV-Vis spectra, b) ECD spectra, and c) % Folding at 375 nm in the complexed form.

Moreover, by looking at the UV-Vis spectra of the different polymers and the corresponding oligomer series it is also possible to extract interesting structural information.

For instance, comparison of the UV-Vis spectra of polymers—poly-(*S*)-**2**, poly-(*S*)-**3**, poly-(*S*)-**4**, and poly-(*S*)-**5**— and the corresponding oligomers — oligo-(*S*)-**2**, oligo-(*S*)-

3, oligo-(*S*)-**4**, and oligo-(*S*)-**5**; N ca. 5, 10, 20, 40, 80— in chloroform reveal the presence of an isosbestic point at 420 nm, which occurs because the polyene band at 380 nm decreases when the DP of the oligomer is reduced, while a new band at 460 nm increases (Figure 98a and Figure S219a to Figure S223a). The presence of this UV-Vis band at 460 nm and the absence of any signal in the same region of the ECD spectra (Figure 96), suggests this band at 460 nm corresponds to a random coil structure, whose percentage and intensity in the UV-Vis spectra increases when the DP of the oligomer decreases.

The same trend is observed when an external stimulus such as Li^+ ions are added to the polymer and oligomers solutions (Figure S222b and Figure S223b).

Notably, when comparing the UV-Vis spectra of the oligo-(*R*)-**1** oligomer series, negligible changes are observed in the UV-Vis spectra. This is attributed to the random coil structure adopted by poly-(*R*)-**1** and their corresponding oligomers as inferred from the absence of a helical trace in their corresponding ECD spectra (Figure S219).

In contrast, when the polymers adopt more elongated scaffolds, such as the helical structures adopted by poly-(*R*)-**1**, poly-(*S*)-**2**, poly-(*S*)-**3**, poly-(*S*)-**4**, poly-(*S*)-**5**, and their corresponding oligomers in THF or DMF, the isosbestic point is not observed, because in such cases the UV-band of the polyene and the random coil structures appear in the same region ca. 430 nm (Figure 98b and Figure S219 to Figure S223).

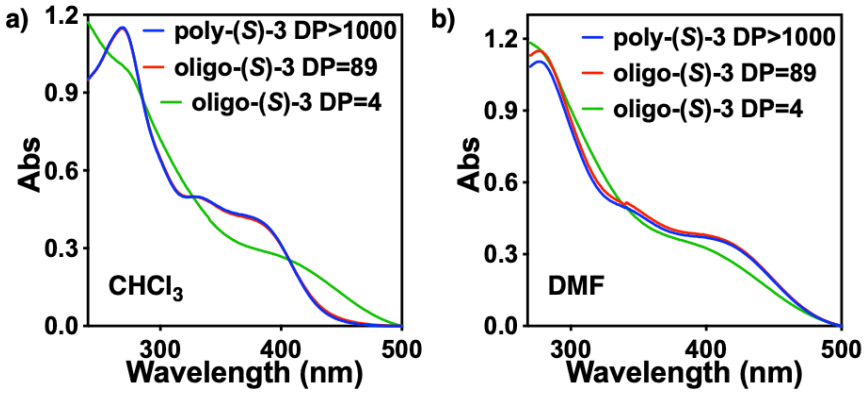


Figure 98. UV-Vis spectra of poly-(*S*)-**3**, and oligo-(*S*)-**3** (DP=89 and 4) in a) $CHCl_3$ and b) DMF.

These results indicate that in helical polymers such as PPAs, there is a minimum polymer chain length (DP = 5), where the polymer starts to fold. The folding starts when the number of intramolecular forces that stabilize the helix (H-bond, dipole-dipole, steric

effects, …) are the minimum needed to stabilize the helix versus other random coiled structures. Interestingly, if the polymer chain increases, the folding of the polymers gets higher. This folding/DP relationship is independent of external stimuli and depends only on the PPA. This result indicates that depending on the polymer length, the fragment that is folded and the fragment that appears as a random coil is different. Similar to what happens in peptides, the PPA folding occurs in the middle of the helix at a certain polymer length, while the terminal ends are adopting a random coil structure. When the polymer grows, the folded region becomes larger, while the frayed ends are reduced.

The PPA folding/DP relationship makes it possible to apply the approximation used by Prof. Green of the Ising model to extract the energy of the helix induction process from equation (36).[273,421,423]

By plotting the g_{abs} versus the DP of an oligomer series, and fitting them to equation (36), it is possible to observe that in all cases —oligo-(*R*)-**1**, oligo-(*S*)-**2**, oligo-(*S*)-**3**, oligo-(*S*)-**4**, and oligo-(*S*)-**5**— negligible increase of the g_{abs} after DP 50 for all oligomers (Figure 99). This fact indicates that the maximum helicity in chiral PPAs is obtained for oligomers with DP > 50. From the fitting, the ΔG_h obtained corresponds to the energy of the helix induction process, which is approximately + or - 250 J/mol for oligo-(*S*)-**2**, oligo-(*S*)-**3**, oligo-(*S*)-**4**, and oligo-(*S*)-**5** (Figure 99 and Figure S224). The sign of the ΔG_h value indicates if the helix induction is towards a *P* (positive) or an *M* (negative) helix when g_{max} is represented in absolute values $|g_{max}|$. Once ΔG_h is obtained from the g_{abs} value of an oligomer with unknown DP, it is possible to determine its DP by applying equation (37) (N = DP).

$$g_{abs} = tanh\left(\frac{N\Delta G_h}{2RT}\right) \cdot |g_{max}| \quad \textbf{(36)}$$

$$N = tanh^{-1}\left(\frac{g_{abs}}{g_{max}}\right) \cdot \left(\frac{2RT}{\Delta G_h}\right) \quad \textbf{(37)}$$

USC UNIVERSIDADE DE SANTIAGO DE COMPOSTELA

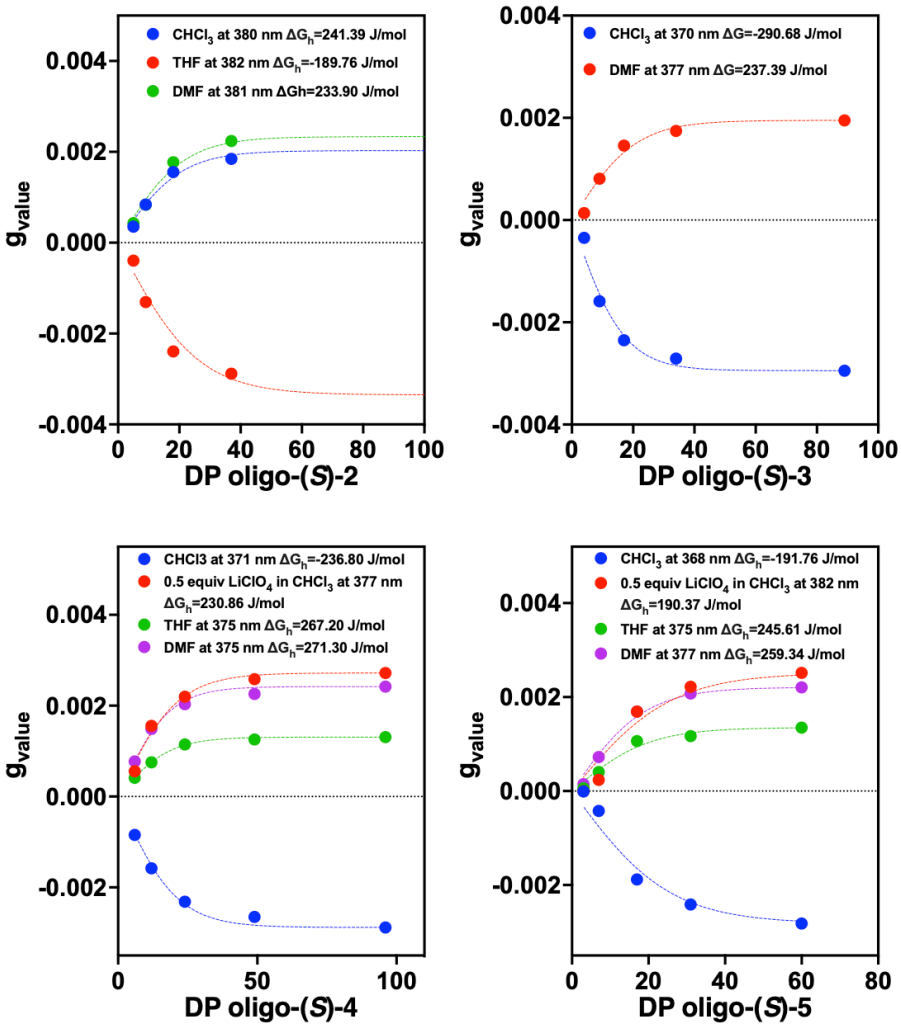


Figure 99. Graphs of g_{value} versus DP for oligo-(*S*)-**2** (DP = 5, 9, 18, 37, and 309), oligo-(*S*)-**3** (DP = 4, 9, 17, 34, and 89), oligo-(*S*)-**4** (DP = 6, 12, 24, 49, and 96), and oligo-(*S*)-**5** (DP = 3, 7, 17, 31, and 60).

From literature, it is known that irradiation of PPA solutions with visible light ($\lambda > 350$ nm) promotes the photochemical electrocyclization (PEC) which is preceded by unfolding of the polyene backbone. The rate of the unfolding process by light, which can be monitored easily by ECD allows to extract important structural parameters of a chiral PPA, such as the dihedral angle between conjugated double bonds (ω_1), and the screw sense excess (SSE) which is directly related to the PPA folding.[70,92] Thus, PEC of PPA oligomers can be used to corroborate that the PPA folding degree depends on the DP. Thus, the ECD signal decay under visible light of the different oligomers of the oligo-(*S*)-**2**, oligo-(*S*)-**3**, and oligo-(*S*)-**4** oligomer series (N= ca. 5, 10, 20, 40, and 80) were plotted versus time to afford the PEC rate constant and the $t_{1/2}$ as the relevant parameters using

USC UNIVERSIDADE DE SANTIAGO DE COMPOSTELA

a first order reaction fitting.[70,92] Following the previous reported procedure we estimate the value of $ECD_{50\%}$ from the graphs ($t_{ECD50\%}$) due to different patterns that cannot fit first order fitting for all cases. To determine the screw sense excess (%SSE) and therefore the folding degree, the $t_{ECD50\%}$, and the $ECD_{50\%}$ were fitted to an equation that depends on the elongation (ω_1) of the helical scaffold adopted by the PPA. Thus, the data obtained for chloroform solutions of oligo-(*S*)-**3** and THF solutions of oligo-(*S*)-**4** oligomer series was fitted to equation (38) to obtain the SSE. This equation was used because both polymers adopt in these solvents a *cis-transoidal* backbone with ω_1 ca 145-150º [c-$t_{145-150}$]. see SI for the rest of the oligomer series.

$$t_{ECD50\%(c-t_{145-150})} = 59.84 \cdot e^{(-0.01906 \cdot (100 - \%SSE_{t_{ECD50\%}}))} - 4.530 \qquad \textbf{(38)}$$

The SSE values obtained from equation (38) can be also correlated with the number of terminal residues at a certain concentration of an oligomer. Therefore, if we are measuring the ECD at 0.3 mg/mL $CHCl_3$ depending on the DP of the oligomer, the number of oligomer chains, and therefore, the number of terminal monomers at the different oligomer chains is going to be different in the different solutions of oligo PPAs with different DP.

The number of terminal monomers present in solution at different DPs can be calculated by equation (39).

$$[terminals]\left(\frac{number}{mL}\right) = 2 \cdot \frac{[Oligomer]\left(\frac{g}{mL}\right)}{M_n\left(\frac{g}{mol}\right)} \cdot N_A \left(\frac{number}{mol}\right) \qquad \textbf{(39)}$$

The previous $\%SSE_{tECD50\%}$ in equation (38) were obtained by irradiation studies. Nonetheless, the %SSE can be obtained from the g_{values} without irradiation. For that, the maximum %SSE is normalized between the g_{max} and the $\%SSE_{tECD50\%}$ obtained when the DP of the oligomer is higher than 50 (equation (40), Figure 100a-b). In this sense only the bigger oligomer must be irradiated to normalize the $\%SSE_{gvalue}$.

USC UNIVERSIDADE DE SANTIAGO DE COMPOSTELA

$$\%SSE_{g_{value}} = g_{value} \cdot \frac{\%SSE_{t_{ECD50\%},max}}{g_{max}} \quad \textbf{(40)}$$

Then, the %SSE from irradiation in equations (38) or g_{value} in equation (40) were plotted versus the number of terminal residues present in an oligomer solution at a certain concentration obtained from equation (39). The graphs show that for oligo-(*S*)-**3** and oligo-(*S*)-**4** oligomer series the folding of a PPA decreases (%SSE reduction) when the DP of a PPA is reduced, which is also associated with an increase of terminal groups at a certain concentration of the polymer or oligomer (Figure 100a-b).

The %SSE decay (slope) observed for the oligo-(*S*)-**3** and oligo-(*S*)-**4** oligomer series with the number or terminal residues is different because in this plot is being considered the %SSE of the initial polymers. Thus, while oligo-(*S*)-**3** with DP >50 are almost fully folded (%SSE ca. 100%), in case of oligo-(*S*)-**4** oligomer series, the oligomers with DP>50 show a %SSE ca 40%. To visualize only the loss of %SSE due to the oligomer DP, and not also due to the intrinsic folding of the polymer, the %SSE were normalized to its possible maximum value according to equation (41) (Lost $\%SSE_{gvalue}$).

$$Lost\ \%SSE_{g_{value}} = \frac{\%SSE_{g_{value}} - \%SSE_{t_{ECD50\%},max}}{\%SSE_{t_{ECD50\%},max}} \cdot 100 \quad \textbf{(41)}$$

By plotting the lost $\%SSE_{gvalue}$ versus the number of terminals it is possible to determine the effect of the terminal ends in the folding of PPA.

USC UNIVERSIDADE DE SANTIAGO DE COMPOSTELA

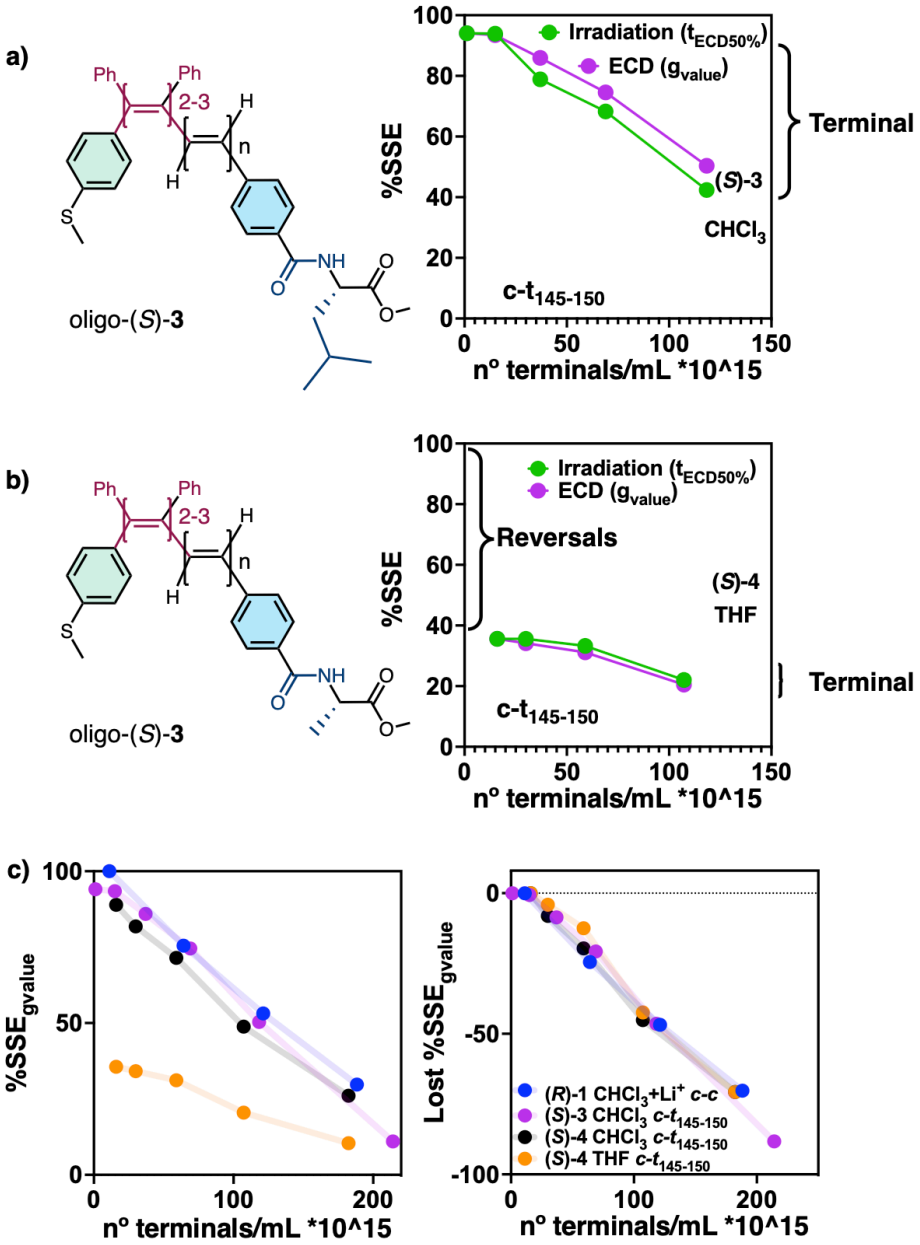


Figure 100. a) % screw sense excess calculated by irradiation and g_{value} as a function of the number of terminals per mL (c = 0.3 mg/mL) for a) a *c-t* benzamide oligo-(*S*)-**3** (DP = 4, 9, 17, 34, and 89) in $CHCl_3$, b) a *c-t* benzamide oligo-(*S*)-**4** (DP = 6, 12, 24, 49, and 96) in THF. c) Graph showing the %SSE calculated from g_{value} for oligo-(*S*)-**1**/Li^+ in $CHCl_3$, oligo-(*S*)-**3** in $CHCl_3$, oligo-(*S*)-**4** in $CHCl_3$, and oligo-(*S*)-**4** in THF.

By This normalized loss of $\%SSE_{gvalue}$ shows a linear trend dependent on the number of terminal groups which is very similar for the different oligomer series (Figure 100c). The same trend is also observed even when a second external stimuli such as Li^+ is added to form the corresponding HPMC. This result indicates that the asymmetry amplification observed by ECD in a helical polymer such as a PPA depends directly on

USC DE SANTIAGO DE COMPOSTELA

its DP and therefore in the number of polymer chains found in solution at a certain concentration with its corresponding monomers at the frayed ends which are not going to be properly folded into a helix.

3.6.3. Conclusions

In this work we have deciphering through 5 different examples how a dynamic helical polymer folds during the elongation of the polymer chain from a short oligomer (DP = 4) until reach a long length polymer state (DP > 100). All the folding studies were done at the same concentration to keep the number of monomer repeating units constant in the solution. Thus, in short oligomers there are going to be a larger number of polymer chains than in the long ones. By looking at the ECD spectra we could observe a signal decay from long polymers towards short ones. However, by considering that the number of polymer chains varies with the DP of the polymer at a certain monomer concentration, and therefore the number of terminal residues placed at the end of the polymer chain, we could observe that the ECD signal promote by the internal residues is all the time the same. This fact indicates elongation does not change the folding degree of the internal residues; the variation is just the result of an increase in the number of terminal residues. Moreover, the stimuli responsive properties of short oligomers and polymers is the same, depending on the number of terminal residues and not being affected by the polymer length. Therefore, these results indicates that PPAs start folding into a twisted structure when there is a minimum polymer length of 3 residues, where a monomer is surrounded by other two monomers. Hence, when the polymer growth, the other residues that are incorporated into the internal region of the polymer helix adopts the same twisted conformation that creates a helix as the polymer chain growths.

USC
UNIVERSIDADE DE SANTIAGO DE COMPOSTELA

3.7. Size Dependent Stimuli-Responsive Properties of Foldamers and Helical Polymer of Chiral PPAs Obtained via Degree of Polymerization Control or by Controlled Helix Unwind

Abstract

Chiral poly(phenylacetylene)s (PPAs) are a family of chiral materials that show a well-folded and dynamic behavior in a wide range of polymer length. Thus, while short foldamers made of just 4 residues in length are folded into twisted structures of the polyene chain, larger PPAs continuously growing into twisted structures that result in the formation of helices. In this work, we will show that chiral foldamers and polymers of a chiral phenylacetylene (PA), such as the 4-ethynylbenzamide of leucine methyl ester [(*S*)-**1**], can show different stimuli responsive properties associated to their different twisted and helical structures, respectively. In this case, we will show that while foldamers of oligo-(*S*)-**1** (DP < 20) are highly solvated in THF, establishing H-bond interactions between the pendants and the solvent resulting in the formation of stretched *P* twisted structures, larger oligo-(*S*)-**1** (DP > 40) foldamers and polymers (DP > 100) are less solvated in THF, adopting highly compressed *M* helical structures. These different stimuli responsive properties of foldamers and polymers of chiral PAs open a new scenario in the application of these materials in fields such as asymmetric synthesis or molecular recognition among others. Moreover, this structure (screw sense and elongation)/ polymerization degree relationship allowed us to decipher from a visual point of view the photochemical electrocyclization (PEC) of chiral helical PPAs in solution. It was possible to demonstrate that the triene photochemical electrocyclization reaction starts at one polymer chain end, introducing cyclohexadiene units at the main chain and continuously growth along the polymer, the rest of the chiral polyphenylacetylene chain remains folded. Interestingly, the folding properties of the remaining PPA fragment corresponds to the ones obtained for a chiral PPA oligomer of the same size, keeping its stimuli responsive properties even with the presence of cyclohexadiene units as part of the polymer main chain.

USC
UNIVERSIDADE DE SANTIAGO DE COMPOSTELA

USC
UNIVERSIDADE
DE SANTIAGO
DE COMPOSTELA

3.7.1. Precedents

Nature, with just a few building blocks defined by evolution constrains developed very sophisticated macromolecular machines —switches or molecular motors— that are involved in many important biological processes. In most cases, the presence of an external stimulus (input) within a specific biological media triggers a conformational communication mechanism in a biomacromolecule, whose conformational change provokes a response triggering or inhibiting for instance a reaction within the cell (output).[335,470-474] Foldamers and helical polymers possessing a dynamic scaffold have gained the attention of the scientific community during the last decade due to the possibility of creating basic models that can be used to understand more complex communication mechanisms present in biological systems such as cell signaling.[25,475-480] Dynamic helical polymers and foldamers are made by non-natural residues, and therefore the scientists working in these fields do not have any restriction when designing monomers that should adopt preferred conformation when they oligomerized or polymerized that led to a specific 3D structure in solution which have the ability of being modulated towards a different one by the action of an external stimulus. Thereby, helix induction and conformational communication mechanisms in dynamic non-natural foldamers or helical polymers have gained the attention of the scientific community during the last decade due to the possibility of creating basic models that can be used to understand the communication mechanisms in more complex biological systems such as cell signaling. Thus, Prof. Clayden and coworkers studied conformational communication mechanisms in peptide mimetics made mainly of aminoisobutiric amino acids (Aib) which are equipped at the C or N termini with a stimuli responsive molecule (chiral or achiral).[25,464,465,481-485] By using these systems, they could explore how the structural information is transmitted from the terminal end of the peptide mimetic towards the other one. In the field of helical polymers, Prof. Yashima and coworkers make a great contribution in triggering different asymmetry amplification effects by the action of different external stimuli such as chiral molecules, pH, solvents, or temperature and how the induced helix can be memorized.[25,28,48,238,254,486,487,488] Another important contribution to the dynamic helical polymers field is the asymmetry amplification mechanisms developed by Prof. Green and coworkers in copolymers, such as the sergeants and soldiers effect or the majority rules.[271-274,278,421,423,429] In addition to these representative studies, other research groups have addressed very interesting studies in asymmetry

USC DE SANTIAGO DE COMPOSTELA

amplification effects, helix induction mechanisms, or conformational communication mechanisms.[248,276,277,279,281,367]

Herein, we want to explore how local microenvironments associated to the length and microstructure of helical polymers can affect the folding (*P*/*M* screw sense excess and/or elongation) of a dynamic helical polymer such as a chiral poly(phenylacetylene).[42,43,84,102,171] Recently, our group found that when two phenylacetylene monomers (PAs) with different hydrophobic/hydrophilic behavior are copolymerized, depending on the ratio between the two comonomers, the local hydrophobic/hydrophilic behavior can be altered (Chapter 3.4. Synergistic Chiral Awakening: Cascade Sergeants and Soldiers Effect Through Double-Step Activation). This microenvironment change is enough to promote a conformational change at one of the monomers which in turn can trigger an asymmetry amplification effect through a Sergeants and Soldiers Effect. On the other hand, we also recently found that in chiral PPAs, the length of the polymer chain does not affect their folding and dynamic helical behavior (Chapter 3.6. Deciphering the emergence of axial chirality and stimuli-responsiveness in PPAs: From oligomers to polymers). Thus, chiral PPA foldamers made of 5 residues in length are folded into a twisted structure. The introduction of more residues into the polymer chain does not affect the folding and dynamic properties of the foldamer or the polymer. The introduction of more residues in the polymer chain makes that the twisted conformation adopted by the internal monomers growth until it reaches a helical structure. However, the folding degree of the internal residues is not affected or even their stimuli responsive properties. Considering all this information, the microenvironmental stimuli-responsive properties of a dynamic helical polymer and the emergence of a twisted conformation in very short chiral PPA foldamers, which persists foldamers or polymers of higher molecular weight, we decided to explore how chiral the dynamic helical properties of PPAs associated to local environmental changes during the polymer chain growth from foldamers to polymers.

3.7.2. Discussion

To test our hypothesis, a chiral PPA that bears the 4-benzamide of leucine methyl ester [poly-(*S*)-**1**] as pendant was chosen as model compound. This polymer is highly sensitive to solvent polarity changes, adopting three different scaffolds with different

USC UNIVERSIDADE DE SANTIAGO DE COMPOSTELA

elongation and/or screw senses. Thus, poly-(*S*)-**1** adopt in low polar solvents such as dioxane, tetrahydrofuran or diglyme (relative polarity towards water < 0.24)[489] a highly compressed *cis-cisoidal M* helix, where the polyene band appears in the ECD spectrum as a negative Cotton band centered at ca. 290 nm ($ECD_{290\ nm}$<0). In this solvent, the polyene band appears at very low wavelengths closer to the olefin absorption, which indicates poor conjugation between alternated double bonds (Figure 101b). This is associated to a high twisting degree of the dihedral angle between conjugated double bods of the polyene backbone (ω_1< -70º). Interestingly, in more polar solvents such as $CHCl_3$ (0.24 < relative polarity towards water < 0.33), poly-(*S*)-**1** adopts a more stretched *M* helix, where a negative Cotton band associated to the polyene band appears at 390 nm ($ECD_{390\ nm}$<0) (Figure 101b). This 100 nm shift of the polyene band towards higher wavelengths indicates more effective conjugation of alternating double bonds at the polyene backbone. In $CHCl_3$, poly-(*S*)-**1** adopts a *cis-transoidal* helix with a ω_1 ca. -145º, a more stretched helix than in THF, and where the p orbitals of the polyene backbone are partially overlapped (Figure 101b). Finally, when poly-(*S*)-**1** is dissolved in more polar solvents such as acetone or DMF (relative polarity towards water > 0.35), a helix inversion from *M* to *P* is observed in the polyene backbone, which is accompanied with a stretching of the polyene backbone (Figure 101b). In this solvent a positive Cotton band centered at 425 nm is observed ($ECD_{425\ nm}$<0). This result indicates the presence of a more elongated helix (ω_1 ca. -155º), with the p orbitals of the polyene backbone show better overlap and therefore a higher conjugation of the π electrons.

The *P*/*M* dynamic behavior of poly-(*S*)-**1** and the different elongation of the polymer is explained by the different conformational preference at the benzamide of (*S*)-leucine methyl ester used as pendant. In low polar solvents, such as THF or chloroform the two carbonyl groups adopt an antiperiplanar conformation (*anti*). In this conformer, the pendant adopts an extended conformation, reducing its bulkiness: As a result, poly-(*S*)-**1** can adopt a compressed helix, being more compressed for

less polar solvents (THF) and more stretched for more polar solvents ($CHCl_3$). The helical sense is dictated by the spatial orientation of the isobutyl in and *anti*-conformation at the benzamide of the (*S*)-leucine methyl ester used as pendant (Figure 101c).

In more polar solvents such as DMF, the conformational composition at the pendant changes. In polar solvents, the benzamide of the (*S*)-leucine methyl ester used as pendant adopts a preferred *syn* conformation between the two carbonyl groups. This

bent conformation increases the steric hinderance at the pendant and promotes a stretching of the helix to release the steric hindrance emerged during the anti to *syn* conformational change (Figure 101c).

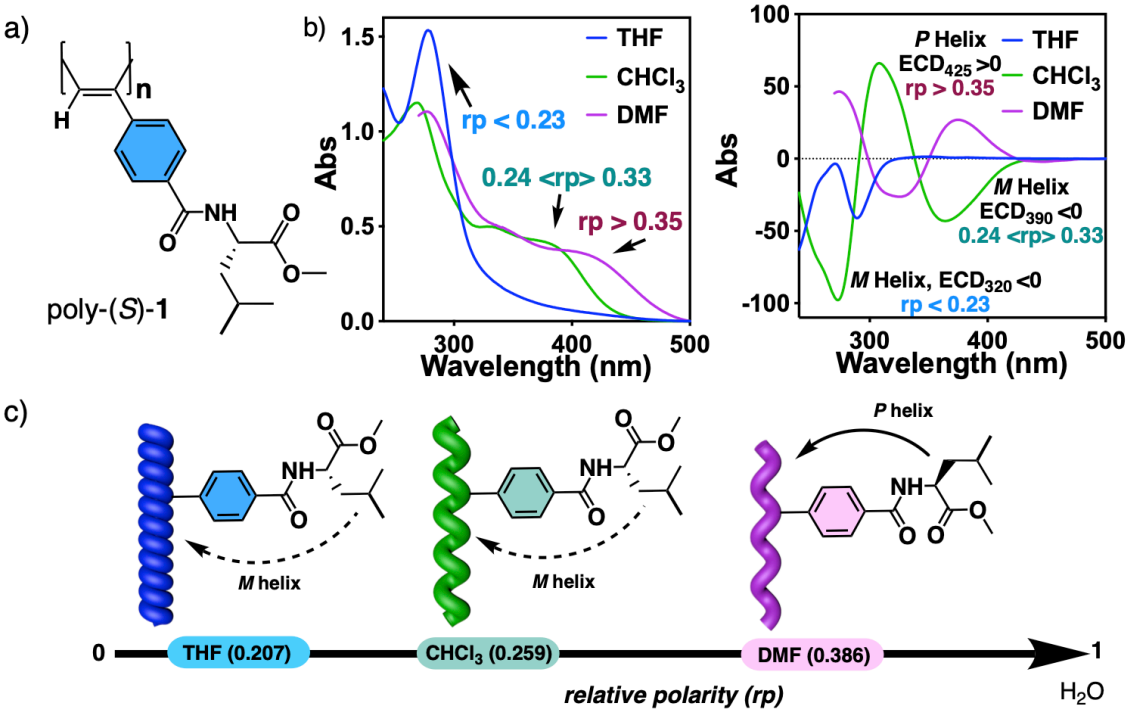


Figure 101. a) Chemical Structures of the PPAs poly-(*S*)-**1**. b) UV-Vis and ECD spectra of poly-(*S*)-**1** in different solvents (c=0.3 mg/mL). c) Schematic representation of the conformation adopted by the pendants in the benzamide-based PPAs as a function of the relative polarity (rp) of the solvent to water.

Next, PPA oligomers of (*S*)-**1** with size that fell in the range n = 4-100 were prepared following Maeda's protocol.[54,60,61,63,469] In our case, as phenylboronic acid we employed the 4-(methylthio)phenylboronic, which possesses a methylthioether group (SMe) providing to the boronic acid distinctive ^{1}H-NMR signals that allowed us to estimate the DP from the relative integral between the pendant and SMe protons (Figure S242 to Figure S247). The 4-(methylthio)phenylboronic acid was used in combination with norbornadiene rhodium (I) chloride dimer $[Rh(nbd)Cl]_2$, potassium hydroxide (KOH), triphenylphosphine (PPh_3), diphenylacetylene (DPA) and the corresponding (*S*)-**1** monomer to obtain the desired corresponding oligomers which possess at the initial end 2 or 3 DPA units (Figure 102). To control the DPs, and therefore the oligomer size, different [monomer]/[Rh(I)] molar ratios were employed. GPC and NMR studies show the presence of oligomers with very low dispersity (Đ<1.05), whose size is like the different

[monomer]/[Rh(I)] molar ratios employed (DP or N from GPC = 4, 9, 17, 34, and 89) (Figure 102). To analyze the structure and the dynamic helical behavior of poly-(*S*)-**1** in the oligomer and polymer size, ECD studies were carried out for solutions of these macromolecules in THF, $CHCl_3$, and DMF (c = 0.3 mg/mL).

These studies show a very interesting behavior in the dynamic helical properties within the oligo-(*S*)-**1** oligomer series. As expected from previous studies, the folding in chiral PPAs starts in very short oligomers, such as 4 residues. This fact indicates that the folding into a twisted structure starts when a monomer (internal monomer) is surrounded by other two monomers (terminal monomers). The ECD signature of foldamers with very low DP is identical to the ECD trace obtained for the corresponding polymer, although with different intensity. Previous studies from our group demonstrated that this variation in intensity is not associated to a different degree of folding in the oligomer series. The decrease of ECD signal as the oligomer size is reduced it is explained by the presence of a larger number of terminal monomers when the oligomer size decreases (Chapter 3.6. Deciphering the emergence of axial chirality and stimuli-responsiveness in PPAs: From oligomers to polymers).

USC UNIVERSIDADE DE SANTIAGO DE COMPOSTELA

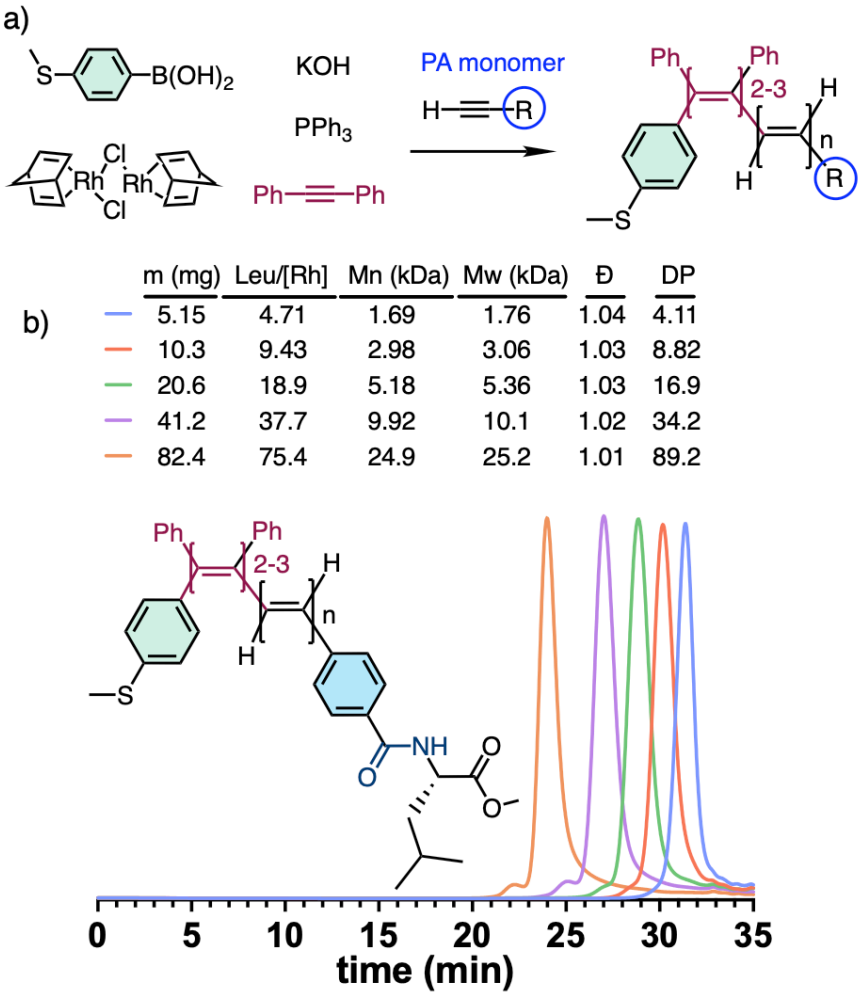


Figure 102. a) Schematic representation of the initiator synthesis and oligomerization process. b) Synthesized oligomers oligo-(*S*)-**1**.

For instance, at identical oligomer solution concentration, an oligomer with DP = 4 show 25 times the number of polymer chains (N X 25) than an oligomer with DP = 100 (N). This fact means that the number of terminal residues present in the solution of the oligomer with DP = 4 is 25 times (number of terminals: 50 x N) the number of oligomer chains found in an oligomer with DP = 100 (number of terminals = 2 x N). The terminal residues are folded into a random coil structure and not into the twisted one. As a result, as the number of terminal residues increases by shortening the polymer chain, the ECD signal decreases.

These results are observed for the oligo-(*S*)-**1** oligomer series in $CHCl_3$ and DMF. Thus, in $CHCl_3$, where poly-(*S*)-**1** adopts a compressed *cis-transoidal M* helix (ω_1 ca. -

USC DE SANTIAGO DE COMPOSTELA

145º) as the oligomer decreases from DP = 89 until DP = 4, the intensity of the ECD trace is reduced (Figure 103a). Moreover, this loss in intensity of the ECD spectra is accompanied by a decrease in the UV-vis band at 390 nm and the appearance of a new band at 420 nm associated to a random coil structure of the terminal monomer repeating units, creating an isosbestic point, that indicates the presence of the two structures (twist and random coil) (Figure 103c). Similar results are obtained for the oligo-(*S*)-**1** oligomer series in DMF. In this solvent poly-(*S*)-**1** adopts a stretched *cis-transoidal P* helix (ω_1 ca. +155º). If the polymer size decreases until reach an oligomer of 4 residues, the intensity of the ECD spectra gradually decrease following the same pattern than in $CHCl_3$, which is associated to the presence of more terminal residues in solution. In this case, the overlapping between the helical folding and random coil UV bands makes it not possible to observe the isosbestic point. However, a decrease of the UV-Vis band at ca. 420 nm it is observed, which can be correlated with the presence of more terminal residues in the oligomer chains (Figure 103b and Figure 103d).

Therefore, the folding studies of the oligo-(*S*)-**1** oligomer series in $CHCl_3$ and DMF show the same results that were observed in a previous work. The folding of chiral oligo-PPAs starts in very short oligomers (N = 4) adopting twisted structures in solution (foldamer), which by growing of the oligomer chain results into a helix. Interestingly, the screw sense excess and the dynamic behavior of the internal residues is the same in a short oligomer than in a long one. The only difference between helical foldamers and helical polymers of PPAs is the number of terminal residues present in the solution at the concentration of the monomer repeating units. This different ratio between internal and terminal residues affects to the intensity of the ECD spectra but not to the conformational composition on the internal residues, which adopt an anti-conformer in $CHCl_3$ and a *syn* conformer in DMF.

USC UNIVERSIDADE DE SANTIAGO DE COMPOSTELA

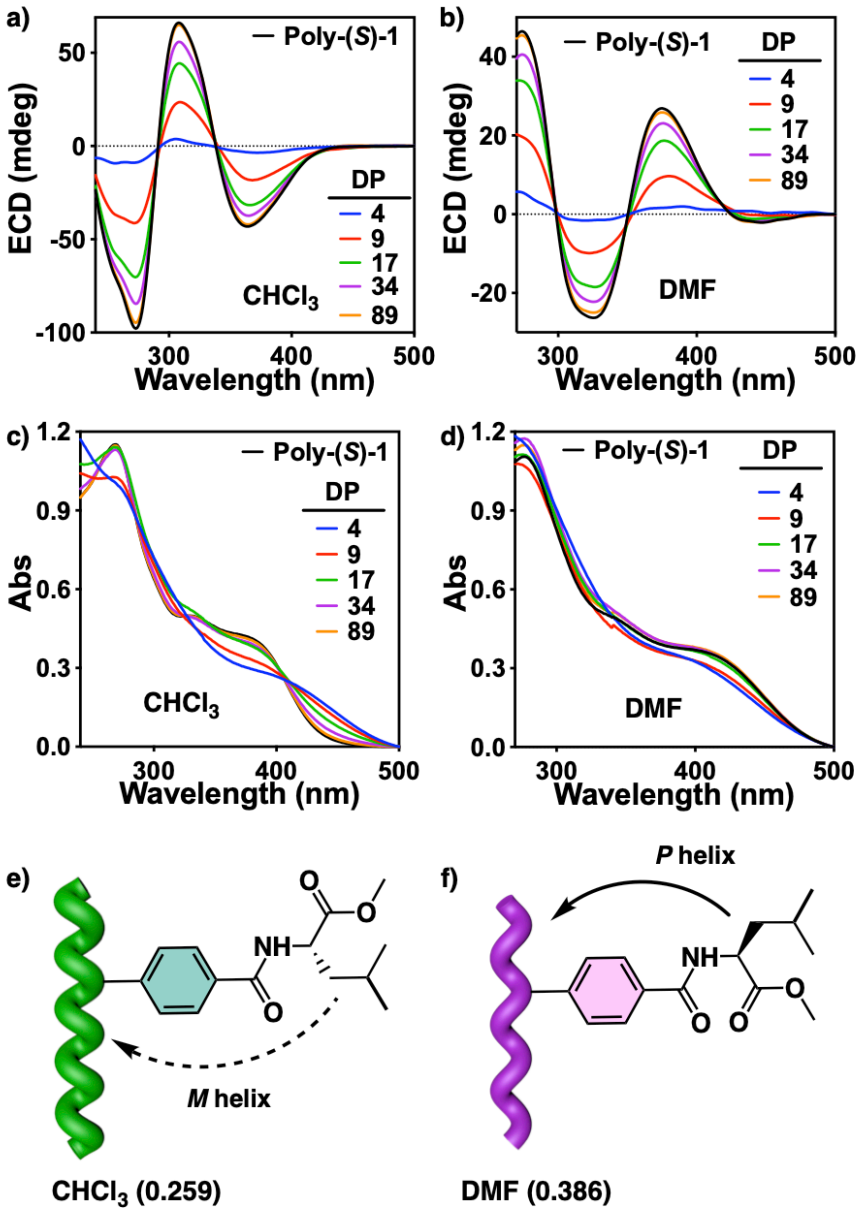


Figure 103. ECD spectra of poly-(*S*)-**1** and oligo-(*S*)-**1** in a) $CHCl_3$ b) DMF. UV-Vis spectra of poly-(*S*)-**1** in a) $CHCl_3$ b) DMF. Schematic representation of the helical sense and stretch of the poly-(*S*)-**1** or oligo-(*S*)-**1** and the conformation adopted by the pendants in the benzamide-based PPAs as a function of the relative polarity (rp) of the solvent to water for e) $CHCl_3$ b) DMF. Concentration of polymers and oligomers c=0.3 mg/mL.

However, an interesting effect was observed for the oligo-(*S*)-**1** oligomer series in THF. In this case, for long polymers, the pendant group adopts an *anti*-conformation due to the low polarity of the THF, which results in a highly compressed *M* helix (ω_1< -70º; $ECD_{290\ nm}$<0) (Figure 104a). However, when the oligomer has DP of 17 or lower, a change in the helical structure adopted by oligo-(*S*)-**1** (DP = 17, 8, 4) (Figure 104b). In

this case, an *M* to *P* helix inversion is produced, which is accompanied with a stretching of the helix. This result indicated that depending on the oligomer length, the oligo-(*S*)-**1** oligomer series behaves differently in THF. Thus, while at DP > 35, the polymer senses the polarity of the solvent, at DP < 17, the benzamide groups at the pendants can establish H-bond interactions with the oxygen of the THF, responding therefore to the donor character of the solvent rather than the polarity. Therefore, as the oligo-(*S*)-**1** decreases in size, the pendant groups are more exposed to the solvent, establishing H-bond interactions between the benzamide group at the pendant and the THF. This interaction was observed for oligo-(*S*)-**1** with high DP and solvents with polar and donor parameters such as DMF (Figure 103b). This pendant/solvent interaction is accompanied with an anti to *syn* conformational change at the pendant group, that results in the adoption of a *P* stretched helix (Figure 104b and Figure 104d).

Similar studies were carried out for oligo-(*S*)-**2** in Et_2O, which show a DP/stimuli responsive behavior similar to poly-(*S*)-**1** (Figure S263).

USC UNIVERSIDADE DE SANTIAGO DE COMPOSTELA

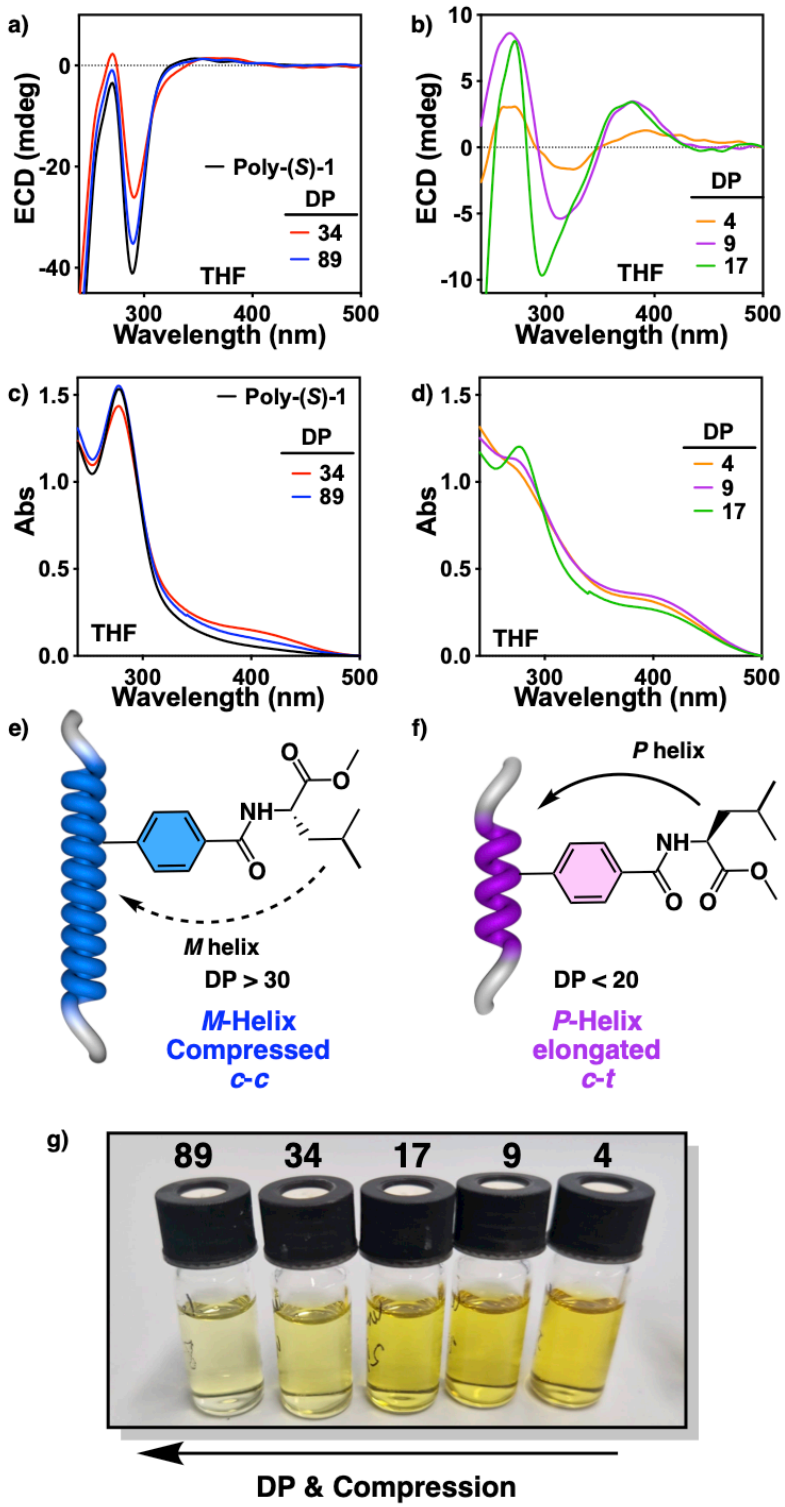


Figure 104. ECD spectra in THF (c=0.3 mg/mL) of a) poly-(*S*)-**1** and oligo-(*S*)-**1** (DP=34 and 89) b) oligo-(*S*)-**1** (DP=4, 9, and 17). UV-Vis spectra in THF (c=0.3 mg/mL) of a) poly-(*S*)-**1** and oligo-(*S*)-**1** (DP=34 and 89) b) oligo-(*S*)-**1** (DP=4, 9, and 17). Schematic representation of the helical sense and stretch of the oligomers and the conformation adopted by the pendants in the benzamide-based PPAs as a function of the relative polarity (rp) of the solvent to water for e) poly-(*S*)-**1** and oligo-(*S*)-**1** (DP=34 and 89) f) oligo-(*S*)-**1** (DP=4, 9, and 17). g) photograph of the oligomer series oligo-(*S*)-**1** with DP=4, 9, 17, 34, and 89 (c=0.5 mg/mL THF).

Taking advantage of this dynamic *P*/*M* screw sense dependence with the oligo-(*S*)-**1** DP in THF [*M* compressed helix ($ECD_{285\ nm}$< 0) for DP= 4, 9, and 17; *P* stretched helix ($ECD_{420\ nm}$> 0) for DP= 34, 89] the mechanism of the photochemical electrocyclization (PEC) in chiral helical PPAs. In a pioneering work, Prof. Percec and coworkers demonstrated that cis-poly(phenylacetylene) backbone thermally degrades towards the formation of 1,3,5-triphenylbenzene (1,3,5-C_6H_3-Ph_3).[72-79] This process includes a first *cis-cisoidal* isomerization of the polyene backbone, which is followed by the formation of cyclohexadiene structures via a 6π electrocyclization of triene sequences and the final extrusion of the 1,3,5-C_6H_3-Ph_3. They found that the 6π electrocyclization of the polyene backbone is much faster than the extrusion of the 1,3,5-C_6H_3-Ph_3 units. Later, Prof. Aoki and coworkers demonstrated that extrusion of 1,3,5-triphenylbenzene derivatives can be achieved via a photochemical electrocyclization (PEC) of chiral helical PPAs.[67,68] Although the thermal and photochemical electrocyclization of PPAs consist of a two-step process (6π electrocyclic reaction + extrusion of 1,3,5-triphenyl substituted benzene units), the thermal and photochemical mechanisms of the ring closing reactions are different. The thermal ring closing reaction follows a disrotatory process, while the photochemical ring closing reaction occurs via a conrotatory process.[69] In both cases, the ring closing reaction is much faster than the extrusion by aromatization of 1,3,5-triphenylbenzene units, although the controlled irradiation of PPAs under visible light leads to 1,3,5-triphenyl substituted benzenes in a highly selective intramolecular process. Recently, our group employed the PEC under visible light to elucidate the elongation degree (ω_1) of the polyene backbone and its screw sense excess (SEE).[92] To do that we focus our attention on the first step of the PEC process which consists of the *cis-cisoidal* isomerization of the polyene backbone followed by the 6π photochemical electrocyclic reaction. In those works, we focused our attention on the time needed for chiral PPAs with different elongation degrees and screw sense excess in order to isomerize and carry out the 6π electrocyclic reaction that led to the formation of cyclohexadiene structures within the polyene backbone that results in the loss of their helical structure. Thus, it was found that compressed helices (*cis-cisoidal*) isomerize much faster than stretched ones (*cis-transoidal*) and, as the number of reversals is increased in the polymer structure (reduction of the SEE) the isomerization also gets faster.[70] Herein, by using THF solutions of the oligo-(*S*)-**1** oligomer series we can study in detail the mechanism of the isomerization and 6π electrocyclic reaction within a chiral helical PPA.

USC UNIVERSIDADE DE SANTIAGO

Thus, a THF solution under argon atmosphere of oligomer (*S*)-**1** with DP = 89 (c = 0.3 mg/mL), which shows a highly compressed *M cis-cisoidal* helix ($ECD_{285\ nm} < 0$), was irradiated with visible light ($\lambda > 350$ nm). Fascinatingly, during the loss of helical structure due to the isomerization and 6π electrocyclic reaction to form the cyclohexadiene structures within the polymer chain a two-step process was found (Figure 105). First, a fast ECD signal decay of the polyene band at 285 nm is observed due to the presence of a *cis-cisoidal* polyene backbone (Figure 105a and Figure 105b). However, as the ECD trace of the compressed helix disappears ($ECD_{285\ nm} < 0$), a new ECD trace of a more stretched helix with opposite helical sense emerged ($ECD_{425\ nm} > 0$) (Figure 105c and Figure 105d). Interestingly, this ECD trace corresponds to the one obtained for THF solutions of oligomer of oligo-(*S*)-**1** with DP < 20 (Figure 104b, Figure 104d, and Figure 104f), which are sensitive to the donor character of THF rather than its low polarity as happens with oligo-(*S*)-**1** with DP > 30 (Figure 104a, Figure 104c, and Figure 104e). After ca. 6 min of irradiation, the ECD spectra observed in the THF solution of oligomer (*S*)-**1** with DP = 89 corresponds just to the stretched helix, which show a slower ECD signal decay in agreement with the presence of a *cis-transoidal* helix in solution (Figure 105d). A similar effect is observed in the UV-Vis spectra of a THF solution of oligomer (*S*)-**1** with DP = 89 (c = 0.3 mg/mL) irradiated with visible light ($\lambda > 350$ nm). Instead of obtaining a decrease of the polyene band with time, the decrease of the polyene band at 285 nm during the first 5 min is accompanied with the emergence of a new band at 420 nm, which corresponds to the elongated helix (Figure 105b).

USC
UNIVERSIDADE DE SANTIAGO DE COMPOSTELA

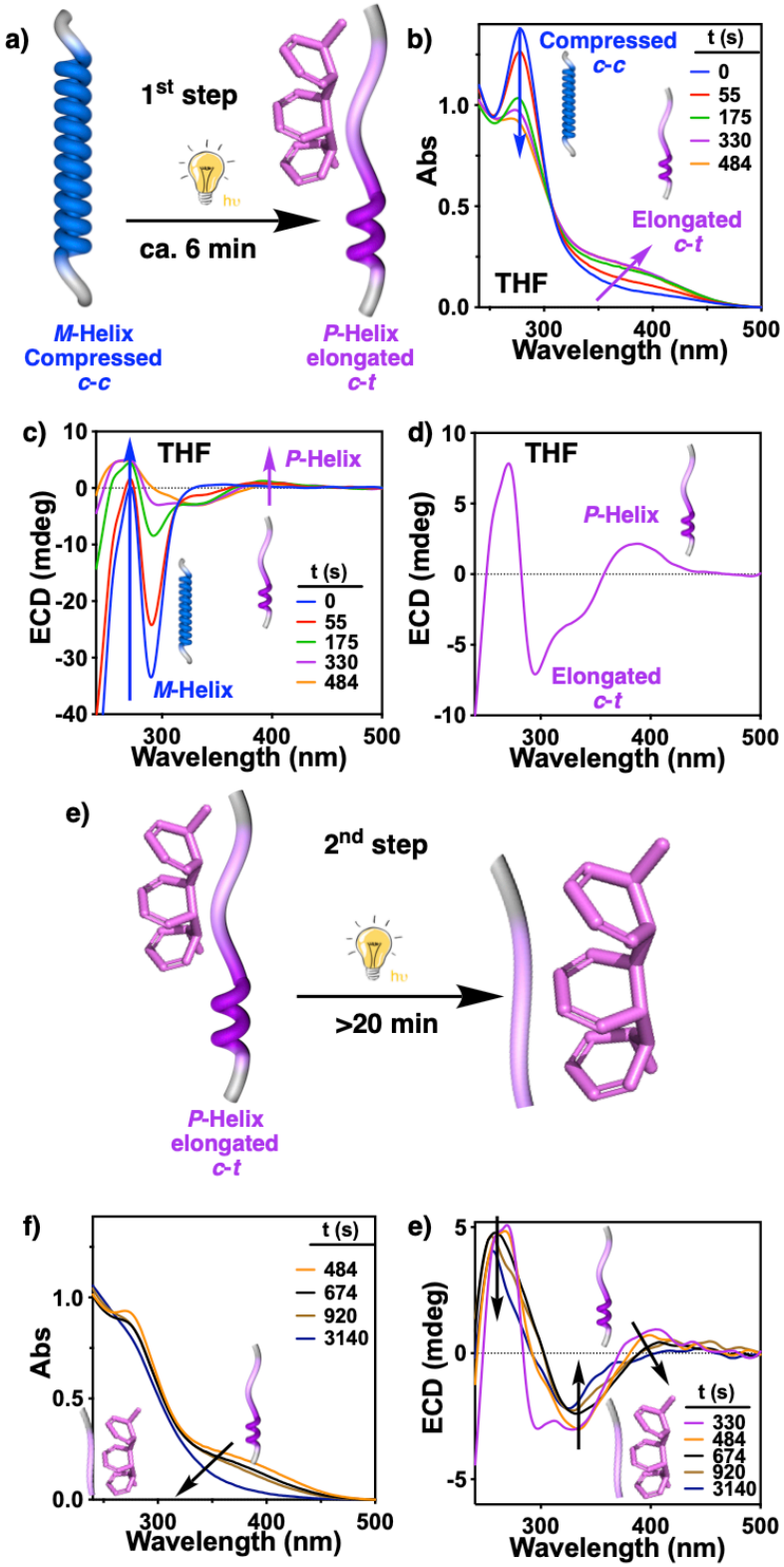


Figure 105. a) Schematic representation of the first step elongation, b) UV-Vis and c) ECD spectra of the irradiation PEC (short pass filter / Vis 550 nm 25 dia) over time of the oligo-(*S*)-**1** with DP=89 (c=0.3 mg/mL THF). d) ECD spectrum of the resulting polymer after 330 seconds. e) Schematic representation of the second step degradation, f) UV-Vis, g) ECD spectra of the irradiation PEC (short pass filter / Vis 550 nm 25 dia) over time of the oligo-(*S*)-**1** with DP=89 (c=0.3 mg/mL THF).

It was confirmed that removing THF and adding $CHCl_3$ triggered a helicity inversion —from a *P*-type helix to an *M*-type helix (Figure 106). The part that remains folded and behaves like smaller oligomers is still dynamic and responds to external stimuli. Then, continuous irradiation with visible light ($\lambda > 350$ nm) of the THF solution produces the reduction of the new polyene band (Figure 105f), indicating the loss of the PPA helical structure (Figure 105e). From these studies, important conclusions can be extracted from the PEC process of chiral PPAs. The isomerization of triene sequences and formation of the cyclohexadiene structures via 6π photochemical electrocyclic reactions starts gradually from a chiral helical polymer chain end. The formation of the cyclohexadiene derivatives does not affect the folding of the rest of the polyene backbone, which is gradually unwind as a consequence of the PEC process under visible light.

Irradiation studies in THF of another polymer, poly-(*S*)-**3**, showed similar results (Figure S259 and Figure S267). Likewise, irradiation in dioxane of both poly-(*S*)-**1** and poly-(*S*)-**3** gave comparable results (Figure S261).

USC
UNIVERSIDADE DE SANTIAGO DE COMPOSTELA

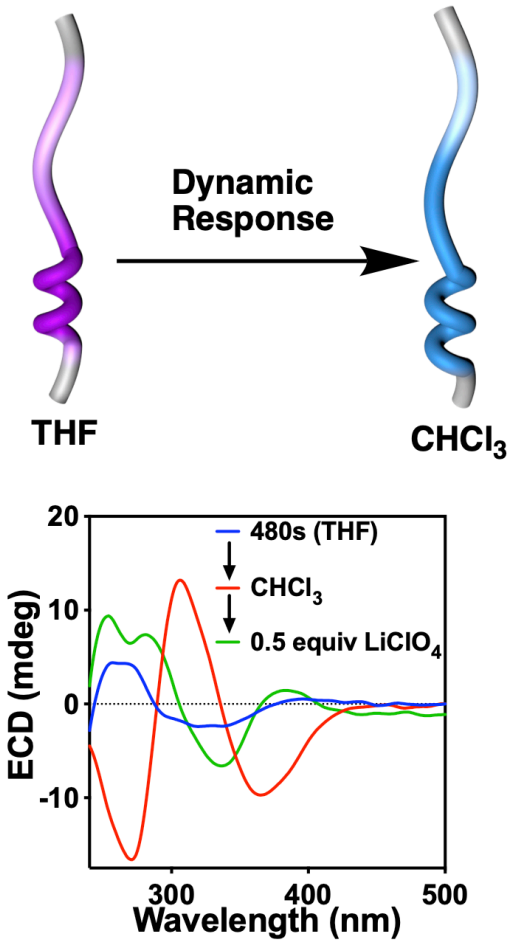


Figure 106. a) Schematic representation and ECD spectra of the dynamic response to external stimuli of the irradiated oligo-(*S*)-**1** with DP=89 (c=0.3 mg/mL THF) for 480 seconds.

3.7.3. Conclusions

In conclusion, we have demonstrated that short oligomers and long polymers of chiral PPAs can show different stimuli responsive properties towards the same external stimuli, in this case THF. In this work, poly-(*S*)-**1**, a chiral PPA that bears the 4-benzamide of leucine methyl ester was chosen as model compound to perform the folding studies of oligomers and polymers with different chain length. Thus, while short oligomers (DP < 20) fold into a P stretched helix, due to a high solvation of the foldamer, large oligomers and polymers of poly-(*S*)-**1** (DP >30) fold into more compact and compressed helical structures. Thus, while short oligomers establish H-bond interactions with the THF, to stabilize a syn conformation at the pendant (*P* helix) and sense therefore the donor parameter of THF, large oligomers stabilize in THF an *anti*-conformation at the pendant

USC
UNIVERSIDADE DE SANTIAGO DE COMPOSTELA

(*M* helix) due to the presence of weaker London interactions with the solvent, sensing therefore the low polarity of the solvent.

Moreover, these studies also allowed us to decipher how the PEC affects the helical structure of a chiral PPA once the unwinding of the helix starts at one polymer end. Thus, while the chemical perturbation (cyclohexadiene formation) or unwinding of the polyene helix starts at one polymer end, the remaining polyene chain is folded into a helical structure whose stimuli responsive properties will depend on the length of the polyene fragment that remains unaffected after visible light exposure ($\lambda > 350$ nm).

USC
UNIVERSIDADE DE SANTIAGO DE COMPOSTELA

3.8. Intercalation Matters: Complex Communication in Supramolecular Copolymers

Abstract

This study explores the supramolecular polymerization and Communication Mechanisms within a copolymer system comprising an achiral monomer, **1**, and a chiral monomer, (*S*)-**2**, which together form stable H-type aggregates. Using variable-temperature UV-Vis and ECD spectroscopy alongside computational methods, we elucidate the supramolecular polymerization mechanism and reveal a unique pathway-dependent Sergeants and Soldiers Effect (SaS). While Classic SaS behavior dominates in pure MCH, controlled cooling or time dependence in a $CHCl_3$/MCH mixture enables an Abnormal SaS, where (*S*)-**2** induces an opposite helical sense in the aggregate. Computational studies and modeling confirm that this unusual behavior is driven by steric effects, with steric hindrance restricting monomer exchange and aggregate growth in one direction while stabilizing growth in the opposite direction with the opposite helical sense to the Sergeant. These findings demonstrate the capacity to tune chiral induction in supramolecular copolymers, offering new insights into Communication Mechanisms and pathway complexity in noncovalent systems.

USC
UNIVERSIDADE DE SANTIAGO DE COMPOSTELA

USC
UNIVERSIDADE
DE SANTIAGO
DE COMPOSTELA

3.8.1. Precedents

Dynamic by nature, scientists have developed artificial self-assembling systems known as supramolecular polymers. These macromolecular structures are held together by non-covalent interactions such as hydrogen bonds, π-stacking, metal coordination, or metal-metal interactions. Their self-assembly processes and diverse structures have gained significant scientific interest.[285,290,490-495]

By utilizing building blocks with various structures, a wide array of supramolecular scaffolds with unique properties can be created. Planar building blocks, often consisting of flat aromatic cores like benzene tricarboxamides (BTAs),[291,325,496-501] peryleneimides,[292,502-509] BODIPYs,[510-515] porphyrins,[516-521] and oligophenyleneethynylenes (OPEs)[522-526] are commonly used in supramolecular helical polymers. These planar, π-extended units are typically modified with paraffinic or glycolated side chains to ensure solubility in the desired aggregating media.

Introducing chirality into these side chains can promote the formation of supramolecular helical scaffolds, with the handedness determined by the chiral center's absolute configuration. Structures with amides on side chains are known for efficient stacking and controlled aggregation, making bisamides a preferred choice.[326,527] To induce chirality, adding a point chirality is common. However, incorporating chiral points into solubilizing alkyl chains can complicate the system, leading to complex pathways.[527] To simplify, chiral points are often placed close to the aggregation centers.[528]

Communication Mechanisms, particularly the Sergeants and Soldiers Effect in covalent copolymers,[8,30,276] in supramolecular systems have been extensively studied in thermodynamic equilibrium for one-component systems[151,529] or polymorphisms.[530] Some examples also exist for Abnormal Sergeants and Soldiers Effect.[530] However, the complex pathways[304] involving kinetic Communication Mechanisms remain understudied. The goal is to use well-known systems that form aggregates in thermodynamic equilibrium to induce kinetic structures upon copolymerization.

3.8.2. Discussion

To perform these studies, we have designed a 2,2'-bipyridine system substituted at 5,5' positions with cyanostilbene units endowed with achiral/chiral aggregating side

USC DE SANTIAGO DE COMPOSTELA

chains (Figure 107). The designed molecules employed in this work —**1**, (*S*)- and (*R*)-**2**— were prepared following the synthetic scheme depicted in the experimental section and fully characterized by NMR and MALDI TOF (Figure S268 to Figure S274).

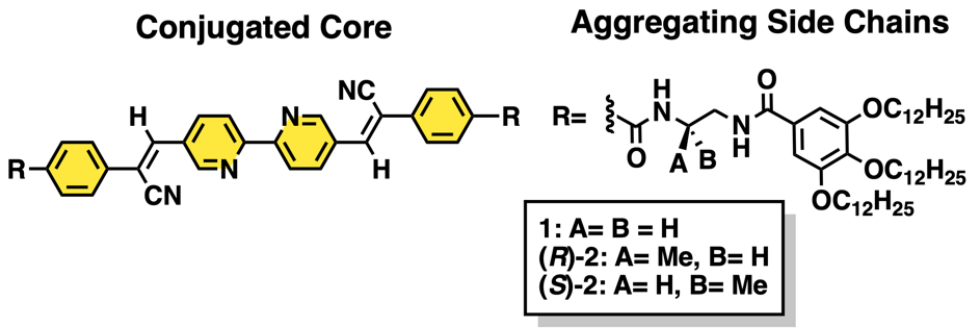


Figure 107. Chemical structures of the molecules employed in this work.

3.8.2.1. Aggregation Studies

The self-assembly ability of **1** and (*S*)- and (*R*)-**2** was investigated by means of a series of spectroscopic techniques in "good" (chloroform, $CHCl_3$) and "poor" (methylcyclohexane, MCH) solvents that stabilize molecularly dissolved and aggregated states, respectively.

Aggregation analyses started with UV-Vis studies. In $CHCl_3$ **1** (c_T = 100 μM) showed a maximum centered at λ= 383 nm. In MCH (c_T = 100 μM) the UV-Vis spectrum confirmed the effective aggregation of **1**, showing a hypochromic effect and a blue shift showing a maximum now centered at λ = 357 nm and the emergence of a new band at λ = 444 nm (Figure 108b), attributed to a H-type aggregate. Given the achiral nature of **1**, ECD studies (c_T = 100 μM, MCH) of showed a null ECD spectrum (Figure 108a).

Analogous experiments were performed for (*S*)-**2**. UV-Vis studies for (*S*)-**2** (c_T = 100 μM) in $CHCl_3$ show a maximum band center at λ = 383 nm (Figure 108b), while in MCH at the same concentration showed a UV-Vis spectrum with maximum now centered at λ = 364 nm together with the additional small band centered at λ = 446 nm (Figure 108b), attributed to a chiral H-type aggregate. Remarkably, the blue shift is smaller in the case of the chiral derivative (*i.e.*, Δλ= 7 nm), due to the adoption of a tilting degree between the aromatic cores of H-type aggregates. The presence of the methyl group in the diamide linker induces a rotating angle throughout the stacking to alleviate the steric hindrance. Therefore, the reduced exciton interactions —due to reduced less effective

USC UNIVERSIDADE DE SANTIAGO

π-π interactions between molecular transition dipoles— and less parallel Electric transition dipole moments of the monomers shift the absorption of the UV-Vis between the achiral aggregate and the monomer absorption bands (Figure 108b).[295]

ECD studies for (*S*)-**2** (c_T = 100 μM) in $CHCl_3$ showed a negligible signal (Figure 108a) given the molecularly dissolved of the molecule in this condition. However, in MCH a strong bisignate ECD spectrum showing consecutive maxima at λ = 376 nm, zero-crossing point at λ = 362 nm and minima at λ = 350 nm with maximum g_{abs} = 0.0056 at first cotton effect. As expected, (*R*)-**2** showed mirror image ECD spectra given its enantiomeric nature (Figure S277).

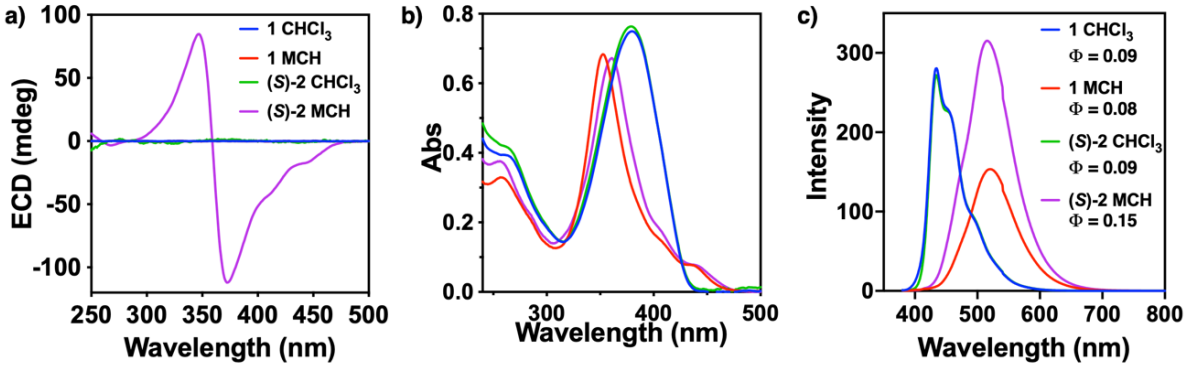


Figure 108. a) ECD and b) UV-Vis spectra of **1** and (*S*)-**2** in $CHCl_3$ and MCH (c_T= 100 μM). c) Emission spectra and quantum yield of **1** and (*S*)-**2** in $CHCl_3$ and MCH (c_T = 10 μM, λ_{exc} = 370 nm, sensitivity low, emission slit = 5.0 nm and excitation slit=2.5 nm).

Additionally, IR and VT-^{1}H-NMR experiments were performed to gain more insight into the supramolecular polymerization process. IR experiments for **1** and (*S*)-**2** in $CHCl_3$ show stretching bands of carbonyl and NH of the amide for **1** centered at 1651 cm^{-1} (C=O), 3449 (NH) and 3341 cm^{-1} (NH), indicative of the presence of intramolecular 7-membered hydrogen bonded pseudo-cycles. In MCH, these bands are shifted towards lower frequencies, C=O amide at 1634 cm^{-1} ($\Delta\tilde{\nu}$ = 17 cm^{-1}); NH bands merging into a single band centered at 3300 cm^{-1}, ($\Delta\tilde{\nu}$ = 149 and 41 cm^{-1}, respectively) (Figure S275). This shifting of the IR bands is indicative of the formation of an effective 4-fold array of hydrogen bonds, thus triggering effective aggregation in MCH (Figure S275). Analogous results were obtained for (*S*)-**2** as depicted in the experimental section (Figure S275). Variable temperature ^{1}H-NMR experiments (VT-^{1}H-NMR) were carried out for both **1** and (*S*)-**2** in mixture composed by 40%$CDCl_3$/60%MCH-d14. These studies show a concomitant deshielding of the amide protons with decreasing temperature, while the

USC UNIVERSIDADE DE SANTIAGO

other signals of the molecule remain virtually unaltered. Behavior indicative of the formation of 7-membered pseudocycles stabilized by intramolecular hydrogen bonds (Figure S276).[504,531]

The presence of an aggregation-induced emission (AIE) moiety (*i.e.*, cyanostilbene) in the structures of **1** and (*S*)-**2** allows monitoring the aggregation process by emission experiments.[532-535] Thus, while (*S*)-**2** shows weak blue emission in $CHCl_3$ with a maximum at λ = 440 nm and a quantum yield of Φ_{PL} = 0.09, a strong green emission is observed in MCH, characteristic of an aggregated cyanostilbene unit, with a maximum at λ = 524 nm and Φ_{PL} = 0.18 (Figure 108c). The achiral derivative **1** showed virtually identical emission spectrum than (*S*)-**2** for the in $CHCl_3$ (molecularly dissolved state). However, **1** in MCH, due to the formation of a more effective H-aggregate stacking than the chiral (*S*)-**2** devoid of a tilting degree between components, showed a slight quench of emission (maximum at λ = 524 nm, Φ_{PL} = 0.08 in MCH, Figure 108c).). The Cofacial parallel stacking scenario described by Kasha and coworkers[293,294] have shown quenched fluorescence as observed for the achiral aggregate **1**. While the rotation of the chiral aggregate reduces the quenching of the perfectly stacked H type aggregate due to reduced π-π interactions between molecular transition dipoles. Therefore, the first excitation and, consequently, the emissive state are in this case more allowed, hence increasing the emission of the chiral aggregate.[295]

*3.8.2.2. Computational evaluation of **1** and **2***

The formation of the 7-membered pseudocycles stabilized by intramolecular hydrogen bond pseudocycle was confirmed using the CREST module of xTB with the semiempirical Grimme's extended semiempirical tight-binding method (GFN2-xTB) and an implicit solvent model (alpb) for chloroform for both monomers **1** and (*S*)-**2** (Figure S275i and Figure S275j).[292,536]

To confirm the formation of an H-type aggregate, computational calculations were performed on a simplified dimer of bipyridine bearing the cyanostilbene and the first amide group. The most stable dimer structure was obtained using the CREST module (GFN2-xTB), employing an implicit solvent model (alpb) for *n*-hexane. This structure reveals an H-type aggregate with the bipyridine nitrogens in *trans* conformation, nitrile groups in an *anti*-orientation and alternating fashion between the monomers (Figure

109a). To further confirm the structure, DFT optimization and frequency calculations were performed using the wb97XD/6-31+g(d,p) functional with a PCM solvent model for methylcyclohexane (MCH) to optimize the dimer core in the ground state. This was followed by TD-DFT calculations on the ground-state optimized structure.

The lowest-energy excitation shows the electric transition dipole moments (TDMs) of the monomers in an anti-parallel orientation, effectively canceling each other and resulting in very low oscillator strength, characteristic of H-type aggregates as per Kasha's Rules.[537] The second excitation shows parallel electric TDMs of the monomers, resulting in an increased total electric TDM and therefore higher oscillator strength. This head-to-head electric TDM arrangement and the higher energy of the allowed transition confirm the H-type aggregate formation (Figure 109a).

To determine the most stable helical sense, a trimer of (*S*)-**2**, devoid of the alkyl chains, was optimized using GFN2-xTB with the alpb solvent model for *n*-hexane. First, the *M*-type helix was obtained. To avoid comparing opposite helical senses at different local or global minima, the *M*-type helix was mirrored to obtain the *P*-type helix keeping the correct point chirality (*i.e.*, (*S*)) of the methyl group, and the structure was next optimized. This approach ensures that the core structure remains consistent, allowing any energy difference to reflect only the disposition of the methyl group. The *P*-type helix showed a higher energy (ΔE = 5.8 kJ/mol) due to steric interactions, with the methyl groups pointing towards the adjacent side chain of the neighboring monomer. In stark contrast, the *M*-type helix presents the methyl groups oriented towards an open space, situation that is sterically alleviated further stabilizing the structure (Figure 109).[527,528]

Additionally, ECD spectra simulations for these *P*- and *M*-type trimers of (*S*)-**2** were performed using TD-DFT calculations with the cam-B3LYP functional and the 3-21G basis set in a PCM solvent model for methylcyclohexane.[128,538] The *M*-type helix of (*S*)-**2** not only proved to be more stable but also accurately replicated the experimental bisignate (-/+) pattern. The *P*-type helix —besides being less stable— produced an ECD pattern with an opposite (+/-) bisignate (Figure 109c and Figure 109d, respectively).[395,522]

USC
UNIVERSIDADE DE SANTIAGO DE COMPOSTELA

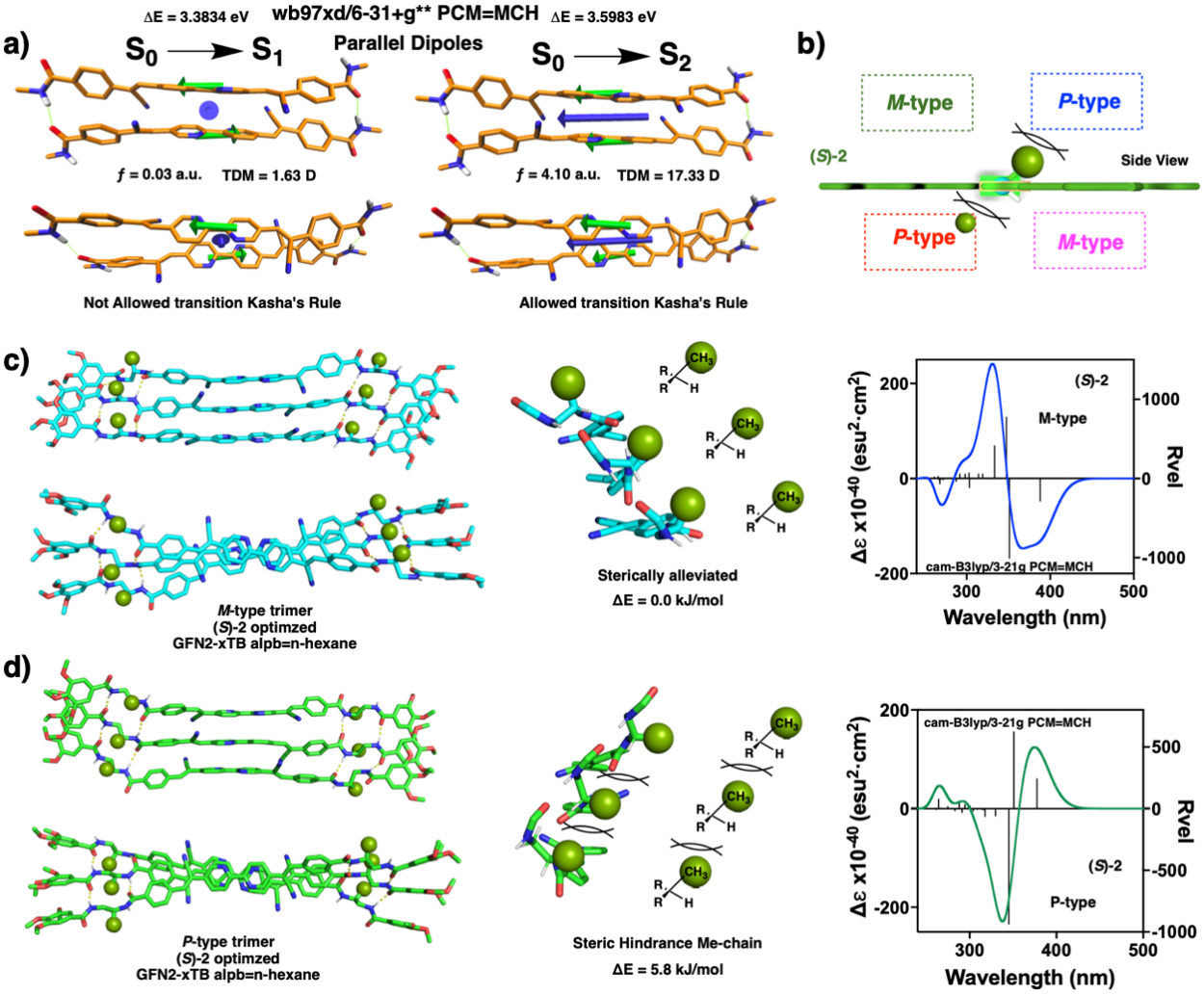


Figure 109. a) Crest most stable dimer in GFN2-xTB (alpb=n-hexane) followed by DFT optimization and then TD-DFT calculation (wb97xd/6-31+g**, PCM=MCH) of the first and second excitations. b) graphical illustration of the proposed model of the steric hindrance promoted by the (*S*) chiral center in the diamide linker in *P* type helices and sterically alleviated in *M* type helices. Optimized trimers of (*S*)-**2** in GFN2-xTB, Energy difference and simulated ECD by TD-DFT (Optimized by xtb, cam-B3LYP/3-21g, PCM=MCH) of the modelled as a mirror image before optimization of (c) *M*-Type helix and (d) *P*-type Helix.

3.8.2.3. Supramolecular Polymerization Mechanism

The aggregated structures generated by **1**, (*R*)- and (*S*)-**2** showed remarkable thermal stability, being completely stable in MCH even upon heating up to 373 K. Therefore, classic melting experiments in these conditions resulted unsuccessful to obtain the thermodynamic parameters for the supramolecular polymerization process (Figure S281). Hence, a $CHCl_3$/MCH mixture was used to promote full disassemble of the aggregates of **1** and (*S*)-**2** upon heating (Figure 110 and Figure S281). To elucidate the supramolecular polymerization mechanism of **1** and (*S*)-**2**, VT-UV-Vis and VT-ECD

experiments were conducted. Cooling VT-UV-Vis curves for a solution of (*S*)-**2** in 28/72 ($CHCl_3$/MCH), monitored at λ = 383 nm, were recorded at a rate of 1 K/min at various concentrations (70, 50, and 30 μM) (Figure 110a). For derivative **1**, VT-UV-Vis experiments revealed incomplete disassembly in the previous conditions (28/72 $CHCl_3$/MCH) upon heating. To stabilize the monomeric form, the proportion of $CHCl_3$ was increased to a 38/62 ($CHCl_3$/MCH) mixture. This behavior is attributed to the enhanced π-π stacking interactions of cores, where the absence of tilt leads to stronger interunit bonding, thereby requiring more energy to disassemble the components. Heating-cooling UV-Vis curves of a solution of **2** in 38/62 ($CHCl_3$/MCH), monitored at λ = 383 nm, were also recorded at 1 K/min at three different concentrations (90, 60, and 30 μM) (Figure 110e). These experiments afforded for both compounds non-sigmoidal curves, indicative of cooperative supramolecular polymerization processes (Figure 110b and Figure 110f). Following the one-component model developed by ten Eikelder, Meijer, and coworkers, the complete set of thermodynamic parameters, including the cooperativity factor σ was obtained, hence confirming the cooperative nature of the supramolecular polymerization processes (Table 1).[539,540]

Table 1. Thermodynamic parameters of the supramolecular polymerization process of **1** and (*S*)-**2**.

Compound	ΔH_e (kJ mol^{-1})	ΔS (kJ mol^{-1} K^{-1})	ΔH_n (kJ mol^{-1})	T_e (K)[a]	σ[b]
1	$-7.83\cdot10^{1}$	$-1.66\cdot10^{-1}$	$-61.4\cdot10^{1}$	310, 315, 319	$9.17\cdot10^{-4}$
(*S*)-**2**	$-9.18\cdot10^{1}$	$-1.80\cdot10^{-1}$	$-69.8\cdot10^{1}$	344, 350, 354	$1.39\cdot10^{-4}$

[a] Derived at c_T= 30, 60 and 90 μM. 38% CHCl3/62% MCH for **1** and c_T= 30, 50, and 70 μM. 28% CHCl3/72% MCH for (*S*)-**2**.

[b] Calculated at 298 K.

To validate the cooperative supramolecular polymerization mechanisms, 16-mers of **1** and (*S*)-**2** were modeled based on previously optimized structures of the simplified

dimer and the (*S*)-**2** *M*-type trimer. The cooperativity of the supramolecular aggregation process was examined using the methodology previously reported by Ortí and Sánchez.[292] For this, 16-mers of **1** and (*S*)-**2** were optimized using GFN2-xTB,[292,541] followed by the extraction of upper and lower terminal building blocks to create oligomers of decreasing sizes (n = 12, 10, 8, 6, 4, 2) to diminish terminal effects (Figure 110c and Figure 110g, respectively).[542,543] The energies of these oligomers were subsequently obtained by single-point energy calculations.[503,541,544,545]

The binding energy per incremental pair of molecules ($\Delta E_{bind,n-1}$) was estimated from these single-point energy calculations (see SI), revealing a decay in binding energy for both **1** and (*S*)-**2**, characteristic of a cooperative supramolecular polymerization process, that is indeed fully consistent with the experimental data (Figure 110d and Figure 110h).

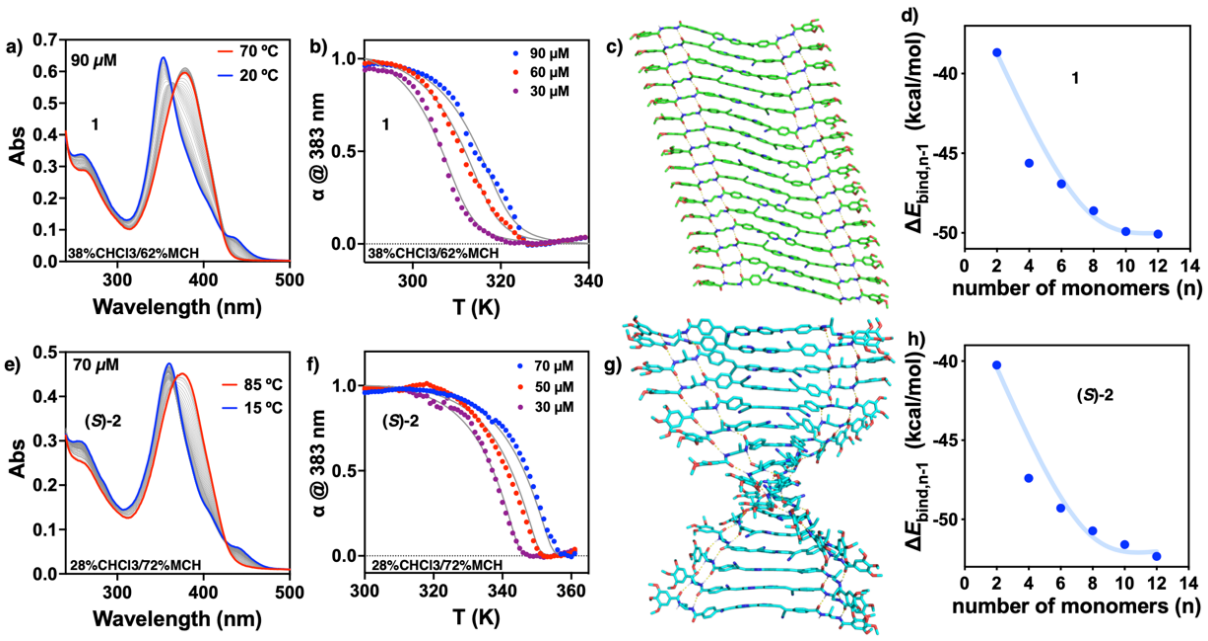


Figure 110. a) VT-UV-Vis cooling curves for **1**. b) secondary plot of aggregation and cooperative fit curves (black lines) at different concentrations (λ = 383 nm, 1 K/min, MCH). c) 16-mer optimized by GFN2-xTB (alpb=*n*-hexane) of **1** and d) corresponding decrease of energy binding per monomer addition calculated by single point calculations of different oligomer sizes from the 16-mer. e) VT-UV-Vis cooling curves for (*S*)-**2**. f) secondary plot of aggregation and cooperative fit curves (black lines) at different concentrations (λ = 383 nm, 1 K/min, MCH). g) 16-mer optimized by GFN2-xTB (alpb=n-hexane) of (*S*)-**2** and h) corresponding decrease of energy binding per monomer addition calculated by single point calculations of different oligomer sizes from the 16-mer.

To visualize the morphology of the aggregates atomic force microscopy (AFM) studies have been performed. 10μL of 100 μM MCH solution of (*S*)-**2** was spin-coated onto freshly cleavage highly oriented pyrolytic graphite (HOPG). AFM studies reveal the

USC UNIVERSIDADE DE SANTIAGO DE COMPOSTELA

formation of fibber-like structures with as depicted in Figure 111a. High resolution AFM images reveal the presence of individual helical chains that appear parallel oriented (Figure 111b). Interestingly, these images also allowed to directly visualize the handedness of the helical structures, being in these case *M*-oriented ones (Figure 111a and Figure 111b). These *M*-oriented helices obtained by AFM imaging are in fully agreement with the predicted structures obtained by theoretical calculations in the previous section (Figure 109c and Figure 110g).

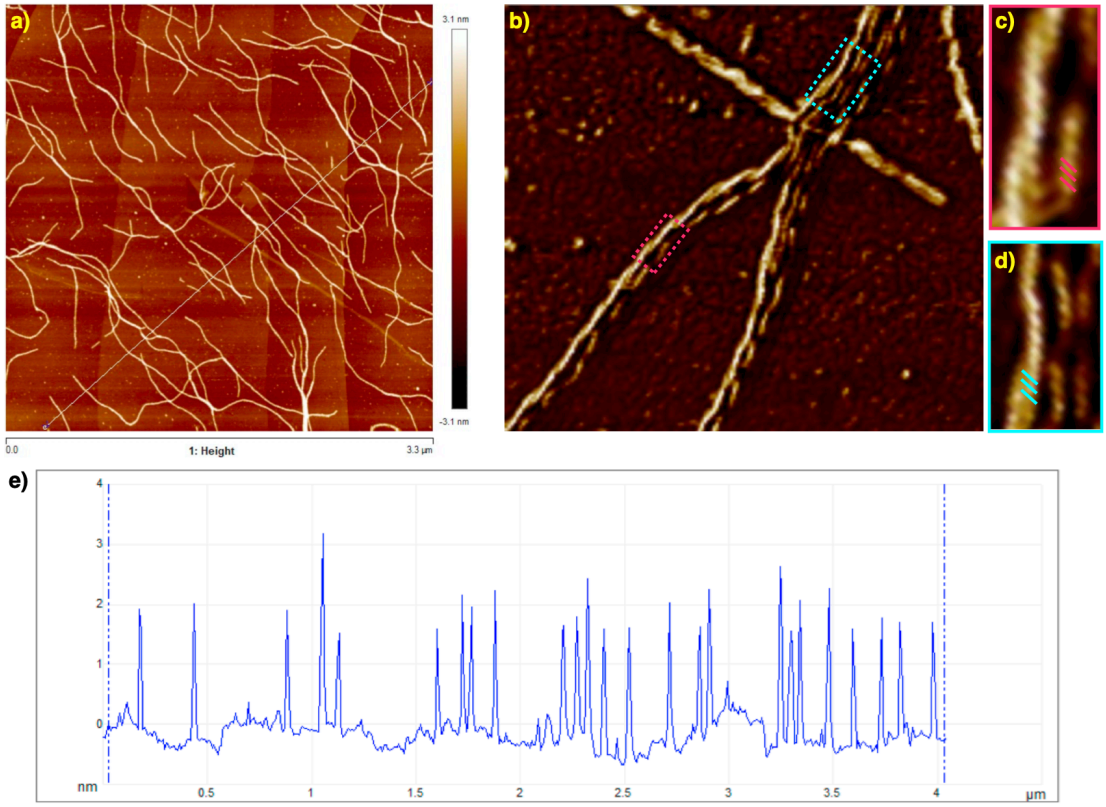


Figure 111. a) Large scale AFM image showing the presence of fibber-like structures for (*S*)-**2**. b) Zoomed image showing parallel-packed helical structures. c) and d) zooms from image of Figure 111b showing individual *M*-type helical structures. e) AFM Height profile from image of Figure 111a.

3.8.2.4. Communication Studies of Copolymers

To investigate the Communication Mechanism and the ability of monomers to interchange between preformed polymeric chains, we prepared two solutions (c_T = 100 µM) of the homopolymers **1** and (*S*)-**2** in MCH. These solutions were then mixed at varying ratios in 10% increments to observe potential communication effects. The resulting mixtures displayed a linear decrease in both the ECD signal and calculated

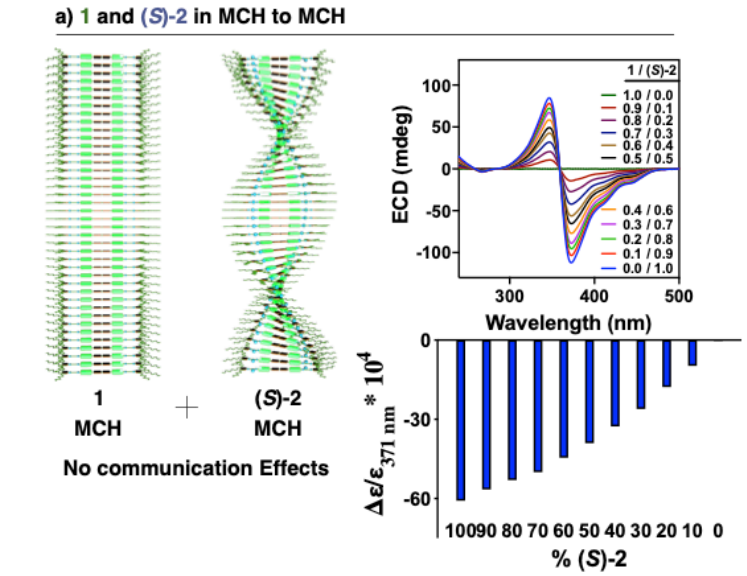
USC DE COMPOSTELA

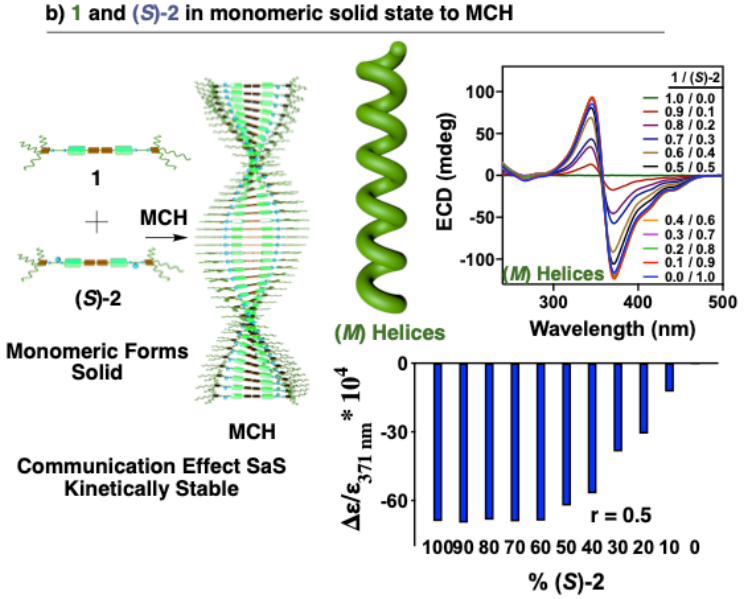
gabs values at λ = 371 nm with the increasing percentage of the achiral counterpart (Figure 112a). The observed absence of asymmetry induction indicated two possible scenarios: a copolymerization process lacking communication between components (*i.e.*, **1** and (*S*)-**2**) or that homopolymer fibers in MCH are highly stable and consequently resist disassembly into monomers, situation that prevents exchange of components between supramolecular polymers due to strong monomer-monomer interactions.

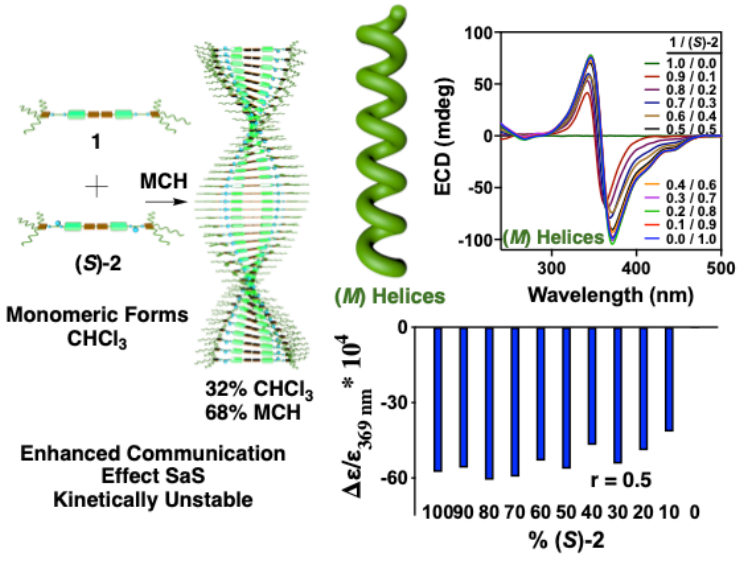
To induce efficient copolymerization in pure MCH and to confirm absence of copolymerization in the last example, we explored a different approach for copolymer preparation. Therefore, solutions of the monomers in $CHCl_3$ (c_T = 100 μM) were mixed at different ratios followed by solvent evaporation. MCH was subsequently added to obtain copolymers in pure MCH (c_T = 100 μM). In this case, as the polymerization occurred simultaneously for both comonomers, the generated copolymers exhibited asymmetry induction following a classic Sergeants and Soldiers Effect. Here, the Sergeant (*S*)-**2** induced homochirality and favored an *M*-type helical structure in the Soldiers (monomer **1**) as inferred by ECD experiments. Given that (*S*)-**2** and **1** form only H-type aggregates, a single Communication Mechanism was observed. Under these conditions (c_T= 100 μM, T= 25°C) a communication value of r=0.5 was achieved according to the g_{abs} values measured at λ = 371 nm (Figure 112b).

To induce copolymerization with better intercalation we used the solvent mixture 32/68 ($CHCl_3$/MCH), c_T = 100 μM. The copolymers showed an improved asymmetry induction, achieving now r = 0.2 (g_{abs} values monitored at λ = 369 nm) simply by changing the solvents (Figure 112c). The presence of $CHCl_3$ increased the mobility of the monomers in solution, promoting more efficient interchange between polymeric chains. This monomer mobility enhanced the operating Communication Mechanism by allowing better intercalation between Sergeants and Soldiers, thus reducing the self-sorting into homopolymers or large blocks involving a single monomer.

USC UNIVERSIDADE DE SANTIAGO DE COMPOSTELA







USC
UNIVERSIDADE DE SANTIAGO DE COMPOSTELA

Figure 112. a) Graphical illustration of homopolymers **1** and (*S*)-**2** in MCH mixed at varying ratios, showing a linear decrease in ECD spectra and g_{abs} (λ = 371 nm) at varying ratios Soldier/Sergeant **1**/(*S*)-**2**, indicating no communication (c_T = 100 μM). b) Graphical illustration of copolymerization in pure MCH by mixing monomers in $CHCl_3$, concentrating the solution, and adding MCH. The simultaneous polymerization resulted in a Sergeants and Soldiers Effect with r = 0.5, ECD spectra and g_{abs} (λ = 371 nm) at varying ratios Soldier/Sergeant **1**/(*S*)-**2** (c_T = 100 μM). c) Graphical illustration of enhanced copolymerization in $CHCl_3$/MCH (32/68), achieving r = 0.2 improved monomer intercalation, ECD spectra, and g_{abs} (λ = 369 nm) at varying ratios Soldier/Sergeant **1**/(*S*)-**2** (c_T = 100 μM).

As previously observed in the thermodynamic studies, mixing $CHCl_3$ and MCH leads to full disassemble of the polymers upon heating. We used this solvent mixture —32/68 ($CHCl_3$/MCH), c_T = 100 μM— to disassemble the polymers into monomers upon heating to 95°C, allowing thermodynamically controlled aggregation upon cooling at 1 K/min of the monomers into copolymeric structures (Figure 113a). In the case of an excess of Soldiers, the system remained unaltered and exhibited the same Sergeants and Soldiers Effect as before. The Sergeant and Soldier Effect remained stable over time previous and after the Heating-cooling cycle (Figure 112c, Figure 113a, and Figure 113b).

Extraordinarily, in the presence of an excess of Sergeant (*S*)-**2**, we observed an inversion of helicity to *P*-type helices compared to the structure before the variable temperature (VT) process from *M*-type helices. This resulted in a switch from a (-/+) bisignate to a strong (+/-) ECD signal (*M* and *P* helices, respectively), even with as little as 2% Sergeant (*S*)-**2** present (Figure 112c, Figure 113a, and Figure 113c). The inversion of the ECD signal and g_{abs} values at λ = 369 nm occurred only at excess of Sergeant (Sergeant >50%) with temperature modulation, representing an Abnormal Sergeants and Soldiers effect where the Sergeant (*S*)-**2** induced the opposite helical sense in the Soldiers **1**. To further confirm this helix inversion process, we have performed AFM studies of Poly-[$\mathbf{1}_{0.8}$-*co*-(*S*)-$\mathbf{2}_{0.2}$] —upon the above describe heating cooling cycle— to directly visualize the handedness of the obtained helical structures. The high resolution AFM images showed parallel packed *P*-type helices that are in fully agreement with the obtained ECD data as depicted in Figure 113c, Figure S293, and Figure S294.

This study presents the first example of two monomers that promote only one type of polymer (*i.e.*, H-type aggregates) — achiral **1** and chiral (*S*)-**2** — that show complex communication pathways upon copolymerization. Initially, a kinetic, Classical Sergeants and Soldiers Effect (SaS) is observed, which can evolve into a thermodynamic Abnormal

USC UNIVERSIDADE DE SANTIAGO DE COMPOSTELA

SaS over time or with temperature simply by playing with the appropriate Soldier/Sergeant ratio.

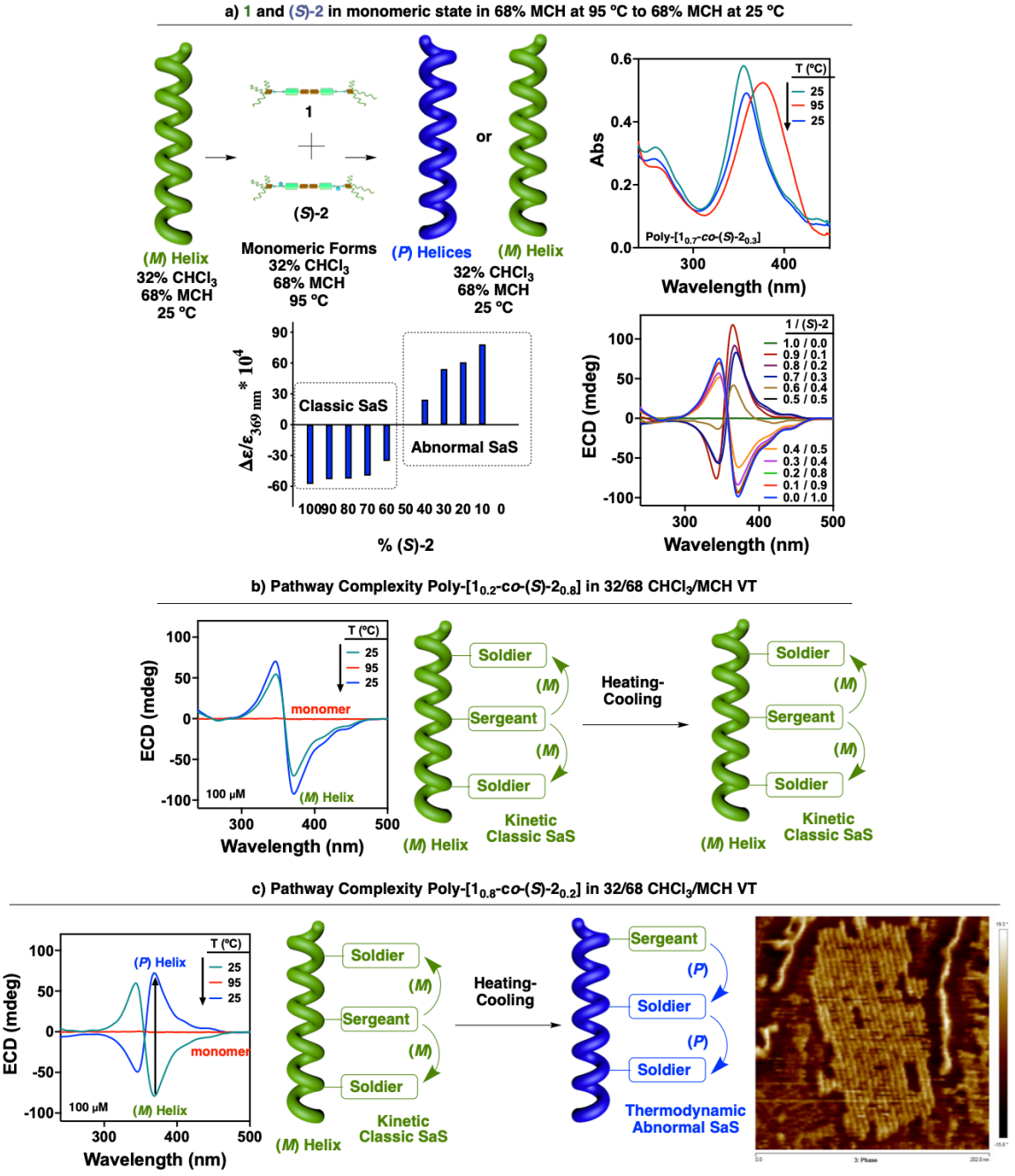


Figure 113. a) Graphical illustration of the heating and cooling at 1 K/min at different ratios with VT-UV-Vis representing the disassembly into monomers at 95 °C and copolymerization at 25 °C after Cooling (c_T = 100 µM, 32/68 $CHCl_3$/MCH). g_{abs} and ECD spectra of the copolymers at different ratios Soldier/Sergeant **1**/(*S*)-**2**. b) ECD and the schematic representation of the Classical Sergeants and Soldiers Effect unaffected by the VT process for the excess of Sergeant Poly-[**1**$_{0.2}$-*co*-(*S*)-**2**$_{0.8}$]. c) ECD and the schematic representation of the Classical Sergeants converting into Abnormal SaS after heating colling process for the excess of Soldier Poly-[**1**$_{0.8}$-*co*-(*S*)-**2**$_{0.2}$]. AFM image showing *P*-type helical structures of Poly-[**1**$_{0.8}$-*co*-(*S*)-**2**$_{0.2}$].

USC UNIVERSIDADE DE SANTIAGO DE COMPOSTELA

Time-dependent studies at room temperature on copolymers with an excess of Sergeant (Poly-[**1**$_{0.2}$-*co*-(*S*)-**2**$_{0.8}$], c_T= 50 μM 32/68 $CHCl_3$/MCH) did not show any evolution over time (Figure 114a). This was confirmed by heating and cooling experiments, which demonstrated the existence of only a Classical Sergeants and Soldiers Effect in the presence of excess Sergeant (Figure 113b).

In the case of an excess of Soldiers, we observed an evolution after the heating and cooling process (Figure 113c). To investigate the pathway complexity between the two Communication Mechanisms and determine if the communication follows a consecutive or competitive pathway, time-dependent studies at different concentrations (c_T = 10 μM, 50 μM, and 150 μM, 32/68 $CHCl_3$/MCH) at room temperature were conducted to observe the evolution from *M*- to *P*-type helices. These studies were performed for Poly-[**1**$_{0.8}$-*co*-(*S*)-**2**$_{0.2}$] to ensure a good extent of asymmetry induction in both Communication Mechanisms (Classic and Abnormal SaS effects). By performing ECD evolution measurements at different concentrations, we observed that the evolution is indeed consecutive, indicated by a slower progression at lower concentrations (Figure 113b).[546] Therefore, the asymmetry induction mechanism switched from the Classic SaS, which is kinetic and metastable, following a consecutive pathway into the Abnormal SaS, which is the thermodynamic one.

USC UNIVERSIDADE DE SANTIAGO DE COMPOSTELA

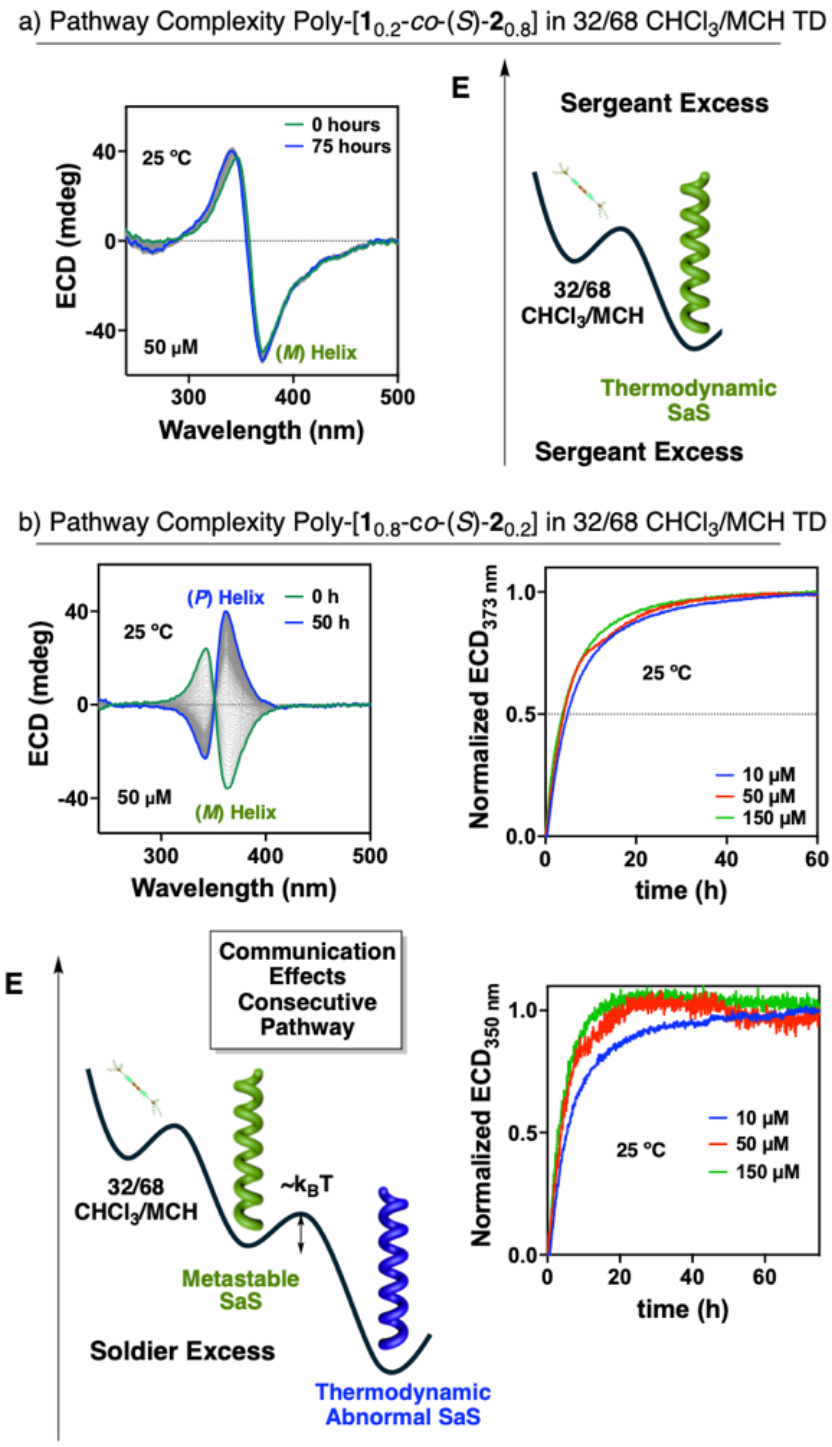


Figure 114. a) TD-ECD of Poly-[**1**$_{0.2}$-*co*-(*S*)-**2**$_{0.8}$] (c_T= 50 μM 32/68 $CHCl_3$/MCH) and energy landscape of the SaS communication mechanism in copolymer presenting excess of Sergeants (32/68 $CHCl_3$/MCH). b) TD-ECD of Poly-[**1**$_{0.8}$-*co*-(*S*)-**2**$_{0.2}$] (c_T= 10, μM, 50 μM, and 150 μM in 32/68 $CHCl_3$/MCH) and Energy landscape of the SaS communication mechanism in copolymers presenting excess of **1** (32/68 $CHCl_3$/MCH).

USC UNIVERSIDADE DE SANTIAGO DE COMPOSTELA

By playing with the conditions, we can modulate the activation energy between the kinetic Classic SaS and the thermodynamic Abnormal SaS in the excess of Soldiers (80 % Soldiers **1** 20% Sergeants (*S*)-**2**, c_T= 100 μM MCH). In MCH, the kinetic SaS is stable over time at room temperature (Figure 115a). On the other hand, if we increase the temperature, the system overcomes the energy barrier at 65 °C, and we obtain the Abnormal SaS in time dependent studies (Figure 115b). Therefore, the system is kinetically trapped in MCH (Figure 115c) while in CHCl3/MCH it was metastable and evolved with time at room temperature. Thus, by simply adjusting the conditions, we can modulate the system evolution as desired.

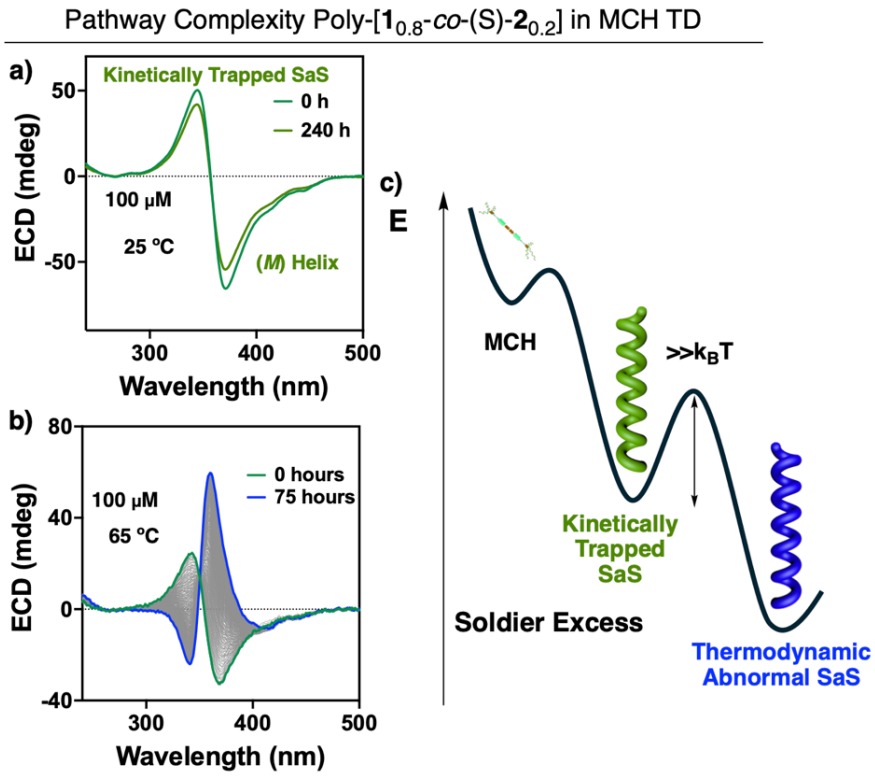


Figure 115. TD-ECD of Poly-[**1**$_{0.8}$-*co*-(*S*)-**2**$_{0.2}$] (c_T= 100 μM in MCH) at a) 25 ºC and b) 65 ºC. c) Energy landscape of the SaS Communication Mechanism in excess of Soldiers in MCH.

Only a small proportion of Sergeant is required to achieve maximal communication following the Abnormal SaS. The g_{abs} value at just 10% Sergeant is as significant as that of the homopolymer of the Sergeant but with the opposite sign (Figure 113a). Therefore, the Sergeant must be well-distributed among Soldiers, intercalating to facilitate the evolution from *M* to *P* type. This process is consecutive, not competitive, and does not involve disassembly. Hence, to evolve the sergeants not only need to be isolated by

Soldiers to avoid Sergeant-Sergeant interactions but also maintaining the minimum amount of Sergeant that orders the system.

To further explore this hypothesis, we optimized four distinct dimers of **1** and (*S*)-**2** with configurations GFN2-xTB with the alpb solvent model for *n*-hexane. These included dimers of one Soldier **1** and one Sergeant (*S*)-**2**, configured in both *P*- and *M*-type helices, with the methyl group of (*S*)-**2** either in the same side as **1** or in the opposite one. When larger blocks of Sergeant are present, either due to poor monomer exchange between polymers or an excess of Sergeant, *M*-type helices form, as seen in the previously calculated trimer of Sergeants (*S*)-**1** structures (Figure 109c). In these *M*-type helices, copolymerization with achiral monomer **2** occurs either from the top or bottom of the Sergeant (*S*)-**1**, with energies of ΔE = 11.72 kJ/mol KJ and ΔE = 1.84 kJ/mol respectively (Figure 116). However, in the *P*-type helices, copolymerization is significantly favorable compared with the other ΔE = 0.00 kJ/mol from bottom and ΔE = 8.45 kJ/mol from top, a configuration that another Sergeant cannot adopt due to steric hindrance (Figure 109d and Figure 116). This unique spatial positioning allows now the Soldiers to stabilize the *P*-type helix, explaining why only a small amount of Sergeant is required to induce the Abnormal SaS and why maximal monomer interchange is necessary ($CHCl_3$/MCH) to prevent large blocks of Sergeant that would, otherwise, induce *M*-type helices in the Soldiers (MCH).

USC
UNIVERSIDADE DE SANTIAGO DE COMPOSTELA

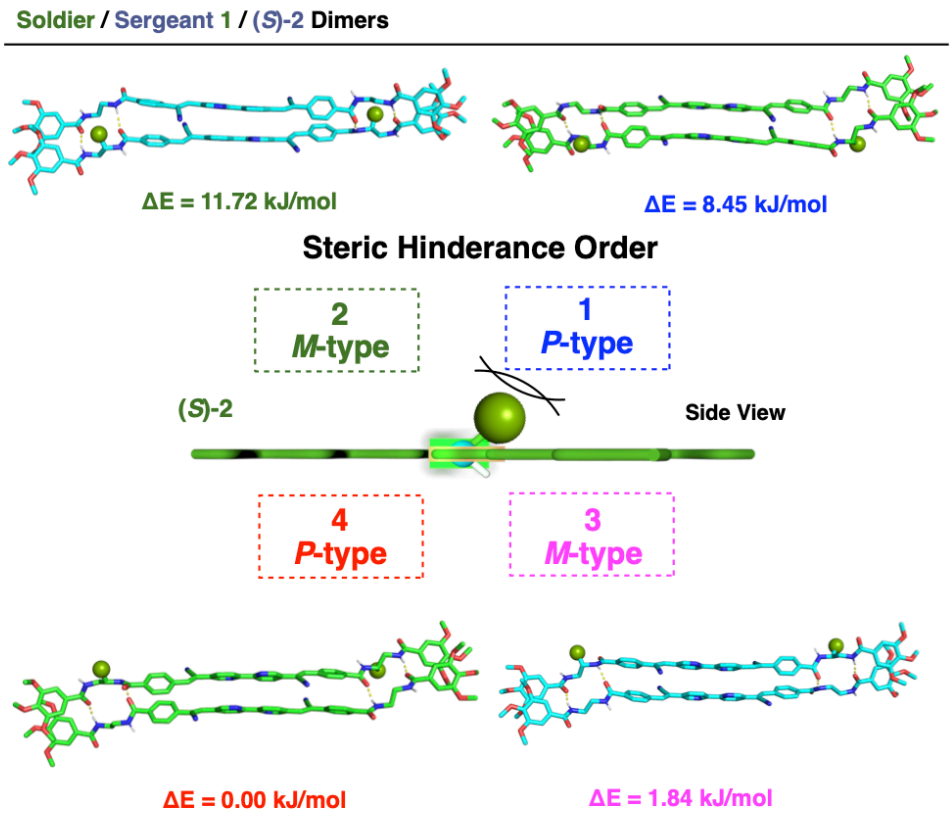


Figure 116. The four optimized dimers of **1**-(*S*)-**2** and the corresponding energy difference calculated with GFN2-xTB (alpb=*n*-hexane).

3.8.3. Conclusions

This work demonstrates the intricate supramolecular Communication Mechanisms achievable in a system of chiral and achiral monomers forming single-component H-type aggregates. Through experimental and computational analyses, we confirmed that **1** and (*S*)-**2** form stable copolymeric aggregates with a Classical SaS in pure MCH, where copolymerization induces homo-chirality in the *M*-type helix. However, by introducing a $CHCl_3$/MCH mixture and controlling thermal conditions, we achieved an Abnormal SaS, where the (*S*)-**1** Sergeant induces an opposite *P*-type helicity in the copolymer. Computational studies reveal that this Abnormal SaS arises due to steric constraints, which enable the achiral monomers to form helices that would be sterically hindered in a homopolymer of the Sergeant.

Additionally, we observed a consecutive pathway complexity in the chiral Communication Mechanism, where distinct pathways lead to kinetically or

thermodynamically favored outcomes, depending on conditions such as time or temperature. This pathway complexity enhances the system's ability to fine-tune chiral induction, offering deeper insights into complex Communication Mechanisms within noncovalent copolymeric systems.

USC
UNIVERSIDADE DE SANTIAGO DE COMPOSTELA

USC
UNIVERSIDADE
DE SANTIAGO
DE COMPOSTELA

Chapter 4. Conclusions

USC
UNIVERSIDADE
DE SANTIAGO
DE COMPOSTELA

USC
UNIVERSIDADE
DE SANTIAGO
DE COMPOSTELA

Chapter 4. Conclusions

This Doctoral thesis has explored the dynamic behavior and applications of chiral poly(phenylacetylene)s (PPAs) as advanced stimuli-responsive materials. The research has been structured to investigate various aspects of these polymers, from their thermal responsiveness to their interactions with metal ions, and their applications in nanocomposites and supramolecular Communication Mechanisms. Also, Communication studies have been performed on PPAs and fully supramolecular copolymers.

Thermal Activation of Asymmetry Amplification Effects in Helical Polymer-Metal Complexes Chapter 3.1

In Chapter 3.1, we demonstrated that metal ion-responsive chiral-PPAs can function as temperature-responsive materials when complexed with metal ions, forming helical poly(phenylacetylene)-metal complexes (HPMCs). These HPMCs exhibit reversible assembly and disassembly in temperature ramps. This response is of great interest, as it can be applied as a sensor of temperature and also opens the possibility for the study of dynamic responses of this system to multiple stimuli. Hence, this dynamic complexation was tested in copolymers with Sergeants activated by metal complexation that exhibit Communication Mechanisms that, at different temperatures, can activate or deactivate the interaction between monomers. This work highlights how a double stimulus behaves, where the second stimulus (temperature) needs the presence of the first complexation. We have presented a reported material of PPA that responds to metal ion that becomes a new material that responds to temperature changes once it is complexed.

Colorimetric Detector of Oxidizing Metal Ions by Anilide-Poly(phenylacetylene)s Chapter 3.2

Chapter 3.2 focused on the sensitivity of anilide-PPAs to oxidizing metal ions such as Cu^{2+}, Hg^{2+}, Fe^{3+}, Au^{3+}, and Ce^{4+}. The coordination of these metal ions with the carbonyl group of the anilide leads to an oxidation of the PPA. This electron withdrawal produces a radical cation delocalization along the conjugated polyene backbone. The

USC UNIVERSIDADE DE SANTIAGO

process induces an irreversible *cis* to *trans* isomerization of the double bonds, leading to the loss of the helical structure and a colorimetric response from yellow to deep blue. This chapter highlights how sensitive the PPAs are to the oxidizing metal with very low LOD depending on the metal ion. Together with their ability to detect non-oxidizing metal ions, these PPAs demonstrate their usefulness in sensing multiple stimuli.

Dispute Between Chiral Comonomers to Induce Tunable Asymmetry Amplification Effects in Dynamic Helical Copolymers Chapter 3.3

In Chapter 3.3, we presented the first switchable chiral-to-chiral Sergeants and Soldiers effects in dynamic helical copolymers and switchable degradation of Sergeants to become Soldiers. By introducing external stimuli such as solvent, metal ions and temperature changes, the roles of Chiral Soldiers and Sergeants on the copolymer were interchanged. This role reversal revealed distinct Communication Mechanisms, including Abnormal Sergeants and Soldiers Effect, Chiral Accord, Chiral Conflict, and the Unexpected Sergeants and Soldiers Effect. The modified Ising model provided a robust framework for understanding these complex interactions.

Synergistic Chiral Awakening: Cascade Sergeants and Soldiers Effect Through Double-Step Activation Chapter 3.4

Chapter 3.4 explored the helical behavior of several copolymer series based on different pendant substitutions and elongation. In the study, copolymers composed of chiral and achiral monomers that induce axially racemic structures were studied. Even when the monomers cannot induce homochirality in the helix, the copolymerization of the chiral with achiral monomers showed an excess of one helical sense. For this to happen, they followed two different steps: in the first step, achiral monomers act as a low polar environment that stabilized a conformation in the chiral monomers; then a second step arose where the activated chiral monomers, in the presence of the apolar environment, performed a Sergeants and Soldiers Mechanism. This double-step Communication Mechanism, where Soldiers activate the Sergeant, who then dictates the helicity of the polymer, was called the Cascade Sergeants and Soldiers Effect. As the

USC DE COMPOSTELA

Sergeants are not previously activated, no commanding over the elongation exists. Therefore, we can modulate the copolymer composition in order to induce chirality in very compressed or stretched structures.

Optical and Chiroptical Stimuli-Responsive Chiral AgNPs@H-Leu-Poly(phenylacetylene) Nanocomposites in Water Chapter 3.5

In Chapter 3.5, water-soluble and stimuli-responsive nanocomposites were developed by combining AgNPs with a dynamic helical poly(phenylacetylene) (PPA), Poly-(*L*)-**1**, which carries Leucine amino acid with unprotected -NH_2. These groups enable water dispersion and Ag(0)—NH_3^+ stabilization. The nanocomposite is formed by reducing a Poly-(*L*)-**1**/Ag^+ complex. Interestingly, pH controls morphology: at pH 7, 250 nm nanospheres with multiple 30 nm AgNPs form, while at pH 2, 100 nm spheres with a single AgNP are obtained. Both respond to pH and metal ions, showing reversible aggregation/dispersion and LSPR changes. The system can detect Ba^{2+} among eight M^{2+} ions in ECD and differentiate in UV-Vis spectra Fe^{3+}, Hg^{2+}, and Ce^{4+} by distinct LSPR responses due to AgNP oxidation. Thus, chiral, water-soluble AgNPs@PPA nanocomposites have been prepared, combining optical and chiroptical properties, with potential in sensing, chirality, and chemical biology.

Deciphering the Emergence of Axial Chirality and Stimuli-Responsiveness in PPAs: From Oligomers to Polymers Chapter 3.6

Chapter 3.6 shows how oligomer size strongly influences folding efficiency and chiral properties. We found that shorter polymers have the same folding, while the increase on the proportion of the terminal effects in the total size results in lower ECD signals and % Screw Sense Excess (%SSE). By using the Ising model with short oligomers, we clarified the energetics behind helical stabilization and estimate the DP from the g_{value}. Metal complexation further confirmed that only the polymer core can be tuned, as terminal regions lack chiral induction. Also, irradiation studies reveal that, regardless of the initial number of reversals, decreases in normalized SSE only depend only on the DP. The results highlight the key role of polymer length and terminal effects in controlling chiral

USC UNIVERSIDADE DE SANTIAGO DE COMPOSTELA

structure, and how the PPA can fold with just a few residues acting as foldamers if they have terminal parts, without the need for fully helical polymeric structures.

Size Dependent Stimuli-Responsive Properties of Foldamers and Helical Polymer of Chiral PPAs Obtained via Degree of Polymerization Control or by Controlled Helix Unwind Chapter 3.7

Chapter 3.7 demonstrated the dynamic behavior of compressed structures upon oligomerization in poly(phenylacetylene)s (PPAs). The findings revealed that the compression of the inner helix is influenced by the degree of polymerization (DP) and the chemical structure of the polymers. We observed a dynamic isomerization and helicity inversion in response to irradiation, leading to a two-step PEC process of the ring closing. This behavior was consistent across different polymers and solvents, highlighting the dynamic nature of these materials. Upon decreasing the DP, small oligomers have fewer interacting forces and more interaction with the solvent. Thus, we see the dynamic transformation to the most stable structure of the pendants in those solvent conditions and the helical sense depending on the donor behavior of the solvent.

Intercalation Matters: Complex Communication in Supramolecular Copolymers Chapter 3.8

Finally, Chapter 3.8 demonstrated the intricate supramolecular Communication Mechanisms achievable in a system of chiral and achiral monomers forming single-component H-type aggregates. Through experimental and computational analyses, we confirmed that these monomers form kinetic and thermodynamic copolymeric aggregates with Classical and Abnormal SaS, depending on the solvent and thermal conditions. We observed metastable or kinetically trapped states of the kinetic communication Classical Sergeants and Soldiers Effect that we could make stable in the kinetically trapped state at room temperature or evolve at room temperature in the metastable structure. The final thermodynamic structure is an Abnormal Sergeants and Soldiers Effect. This presents the first case of a kinetic Communication Mechanism that evolves into a different communication effect in thermodynamic communication.

USC UNIVERSIDADE DE SANTIAGO DE COMPOSTELA

Chapter 5. Methodology and Experimental Section

USC
UNIVERSIDADE
DE SANTIAGO
DE COMPOSTELA

USC
UNIVERSIDADE
DE SANTIAGO
DE COMPOSTELA

5.1. Experimental Section and Methodology Chapter 3.1.

5.1.1. Experimental Procedures

Commercially available chemicals have been used as delivered. Solvents were purchased as reagent grade and distilled if necessary. Anhydrous solvents were either purchased as ultra-dry solvent from Acros Organics® or received from solvent purification system. For the coupling and polymerization reactions, dry THF was obtained from MBRAUN SPS 800 solvent purification system.

NMR experiments were carried out in a Bruker AV-III (500 MHz). Size exclusion chromatography studies were performed on Alliance 2695 HPLC System (Waters) liquid chromatography system equipped with a UV 2489 detector (Waters). The samples were eluted by three Phenogel columns connected to each other with stationary phases of 103, 104 and 105 Amstrong and packed with a solid support of a cross-linked styrene and p-divinylbenzene copolymer.

ECD measurements were done in a Jasco-720 spectropolarimeter. UV-Vis spectra were registered in a Jasco-730 spectrophotometer.

FT-IR measurements were carried out on a Bruker IFS-66v.

DFT calculations were performed in the HPC Finis Terrae II (FT2) supercomputing infrastructure from CESGA inside a node of 64 cores of AMD and 256 GB of RAM.

5.1.2. Monomers and polymers

The preparation of monomers (M-**1**, M-**2**, M-**3**, M-**4**, M-**5**, and M-**6**) and polymers (poly-(*S*)-**1**, poly-(*R*)-**2**, poly-(*S*)-**3**, poly-(*S*)-**4**, and poly-(*S*)-**5**) can be found in references.[92,102,169,367] A smaller polymer poly-(*S*)-**1** of M-**1** was synthetized following the procedure.[169] A copolymer poly[(*S*)-$\mathbf{1}_{0.5}$-*co*-$\mathbf{6}_{0.5}$] was synthetized following the procedure.[367]

USC UNIVERSIDADE DE SANTIAGO DE COMPOSTELA

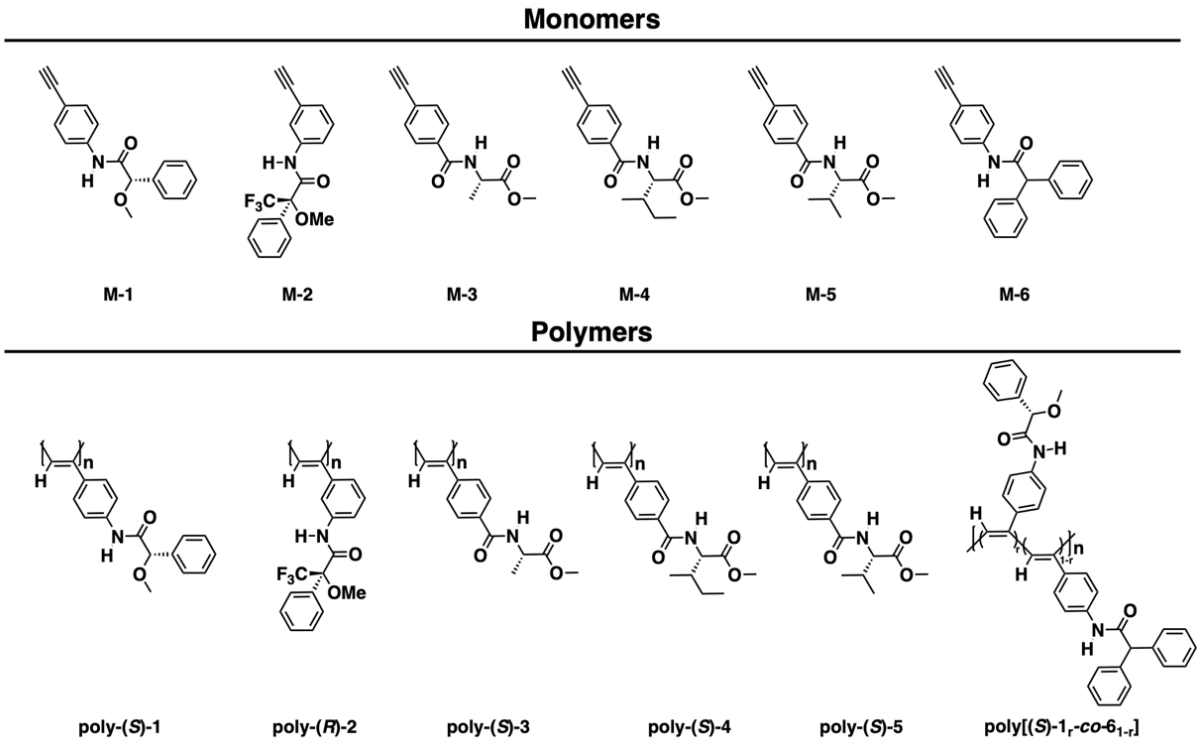


Figure S1. Structures of monomers and PPAs with anilide and bezamide connection.

5.1.3. VT-ECD studies of PPAs

Temperature-dependent Circular Dichroism (VT-ECD) were performed in a solution of poly-(*S*)-**1**, poly-(*R*)-**2**, poly-(*S*)-**3**, poly-(*S*)-**4**, poly-(*S*)-**5**, and poly[(*S*)-$\mathbf{1}_{0.5}$-*co*-$\mathbf{6}_{0.5}$] in $CHCl_3$ (c = 0.3 mg·mL^{-1}) in a cooling curve with full scan of the spectra (1.0 K·min^{-1}).

USC UNIVERSIDADE DE SANTIAGO DE COMPOSTELA

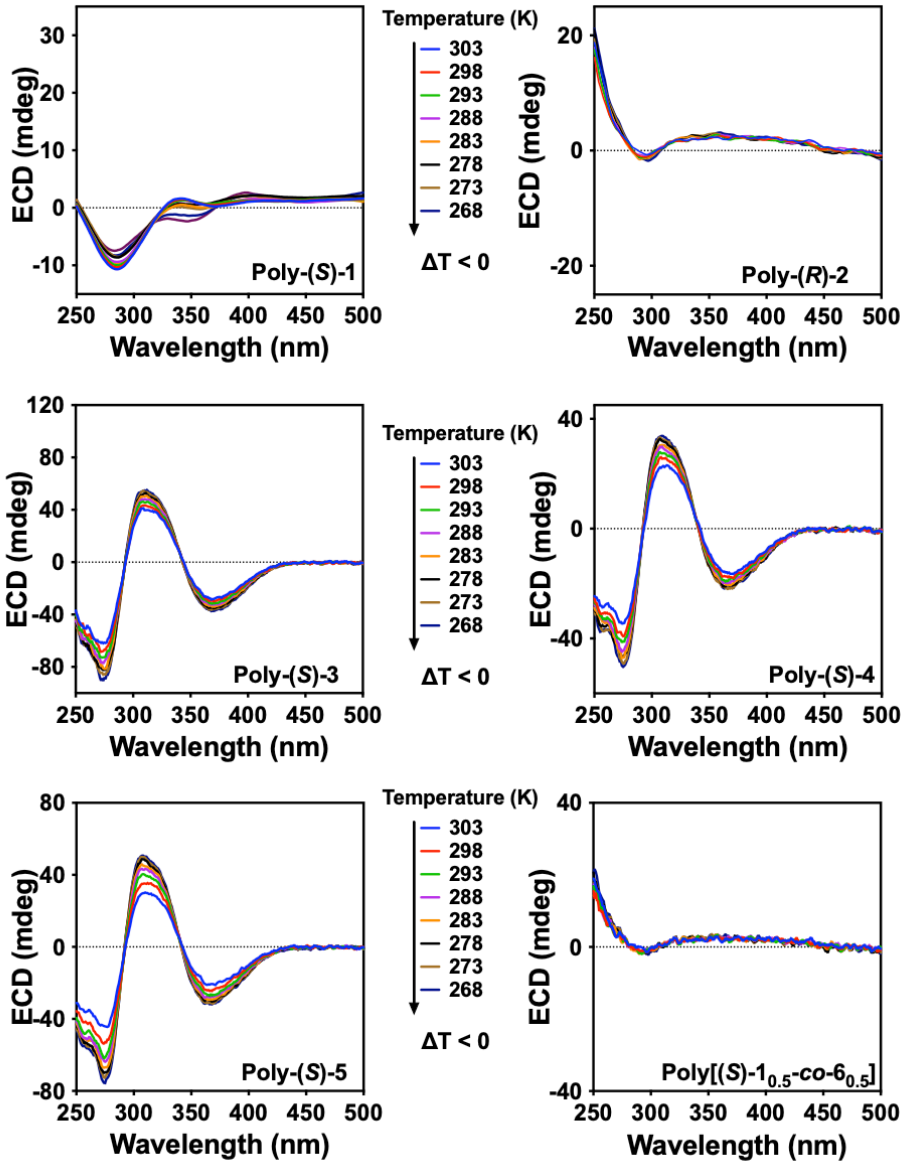


Figure S2. VT-ECD of poly-(*S*)-**1**, poly-(*R*)-**2**, poly-(*S*)-**3**, poly-(*S*)-**4**, poly-(*S*)-**5**, and poly[(*S*)-**1**$_{0.5}$-*co*-**6**$_{0.5}$] (0.3 mg·mL^{-1} $CHCl_3$) depending on the temperature (1.0 K·min^{-1}).

5.1.4. VT-ECD and VT-UV-Vis studies of poly-(*S*)-1/Li$^+$ Complex

VT-ECD and VT-UV-Vis were performed to a solution of poly-(*S*)-**1** in $CHCl_3$ (c = 0.3 mg·mL^{-1}) with full scan of the spectra (1.0 K·min^{-1}) after the addition of 0.4 equiv of $LiClO_4$ from a solution of 10 mg·mL^{-1} MeOH.

USC UNIVERSIDADE DE SANTIAGO DE COMPOSTELA

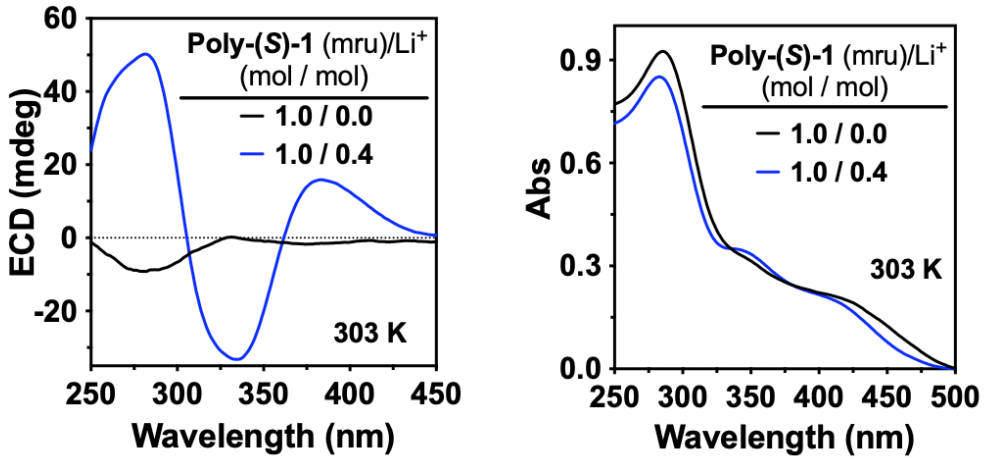


Figure S3. VT-ECD and VT-UV-Vis of poly-(*S*)-**1** (0.3 mg·mL^{-1} $CHCl_3$) in presence of $LiClO_4$ (10 mg·mL^{-1} MeOH).

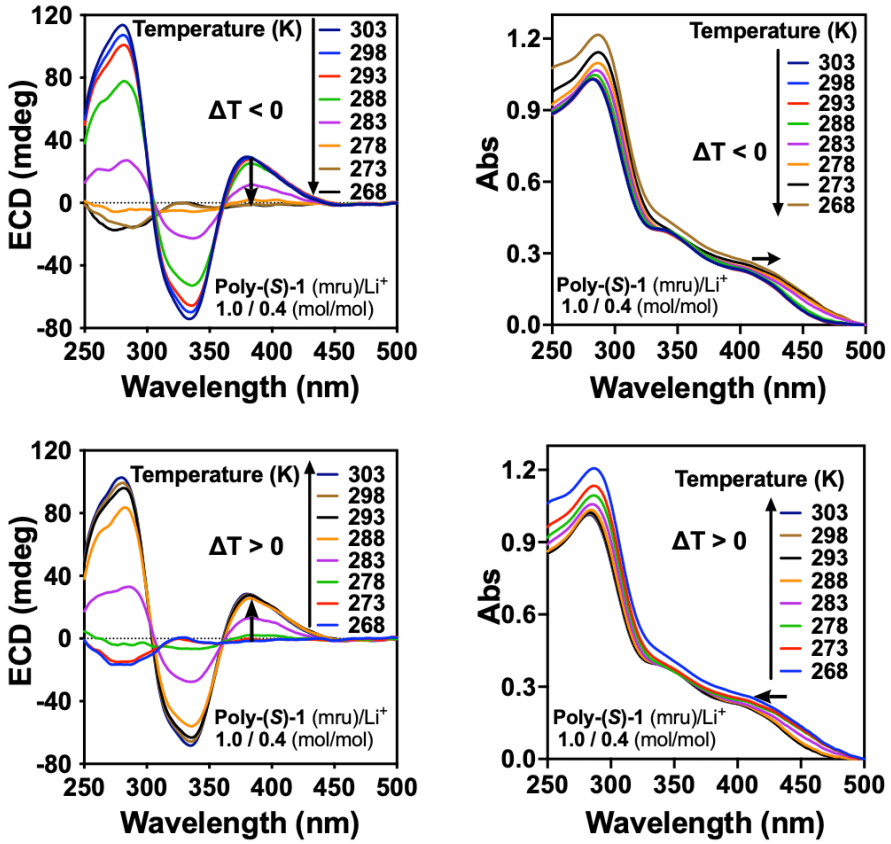


Figure S4. VT-ECD of poly-(*S*)-**1** (0.3 mg·mL^{-1} $CHCl_3$) in presence of 0.1 equiv of $LiClO_4$ (10 mg·mL^{-1} MeOH) cooling and heating curves at 1.0 K·min^{-1}.

USC
UNIVERSIDADE DE SANTIAGO DE COMPOSTELA

5.1.5. VT-ECD and VT-UV-Vis studies of small size poly-(*S*)-1/Li^+ Complex

VT-ECD and VT-UV-Vis were performed to a solution of poly-(*S*)-**1** of small size with M_n = 6708 KDa (GPC) DP=23 monomers in $CHCl_3$ (concentration = 0.3 mg·mL^{-1}) with full scan of the spectra (0.1 K·min^{-1}) after the addition of 0.4 equiv of $LiClO_4$ from a solution of 10 mg·mL^{-1} MeOH.

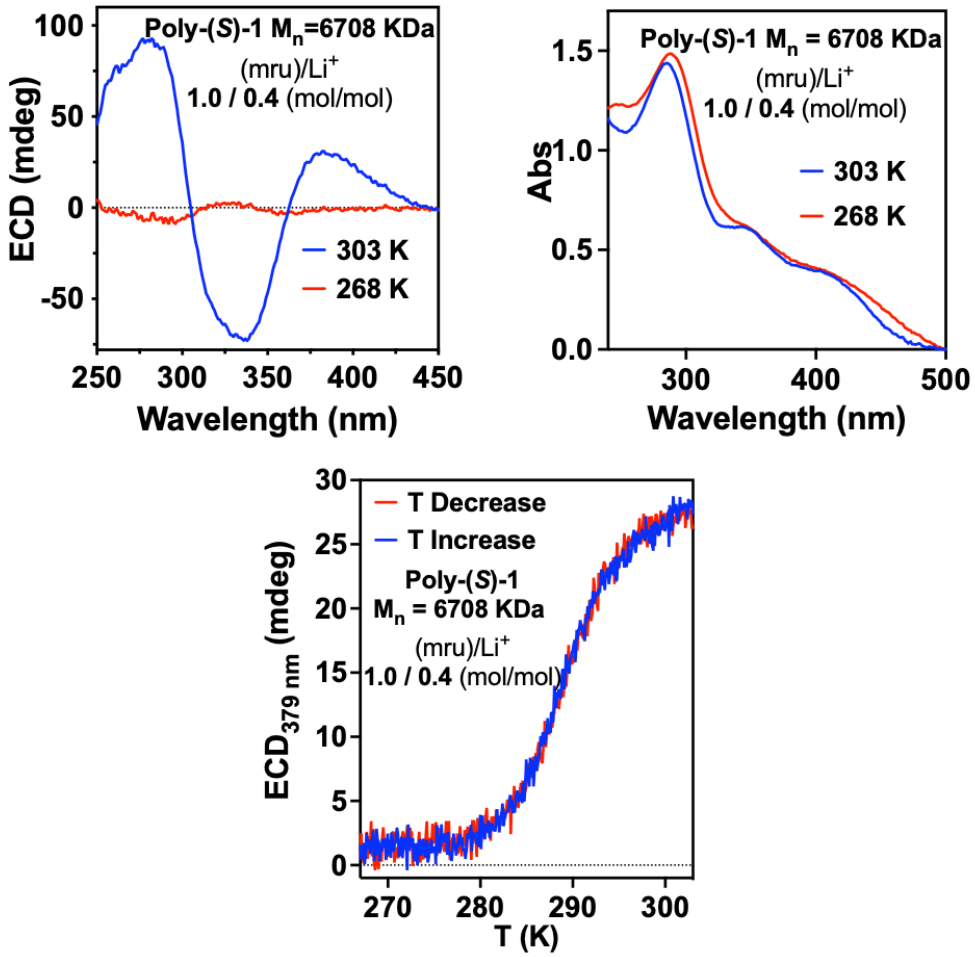


Figure S5. VT-ECD and VT-UV-Vis of poly-(*S*)-**1** of M_n=6708 KDa (0.3 mg·mL^{-1} $CHCl_3$) in presence of $LiClO_4$ (10 mg·mL^{-1} MeOH).

USC UNIVERSIDADE DE SANTIAGO DE COMPOSTELA

5.1.6. VT-ECD studies of poly-(*S*)-1 Li^+ Complex with temperature cycles

VT-ECD were performed at 379 nm to a solution of poly-(*S*)-**1** in $CHCl_3$ (c = 0.3 mg·mL^{-1}) at 0.1 K·min^{-1} after the addition of 0.4 equiv of $LiClO_4$ from a solution of 10 mg·mL^{-1} MeOH.

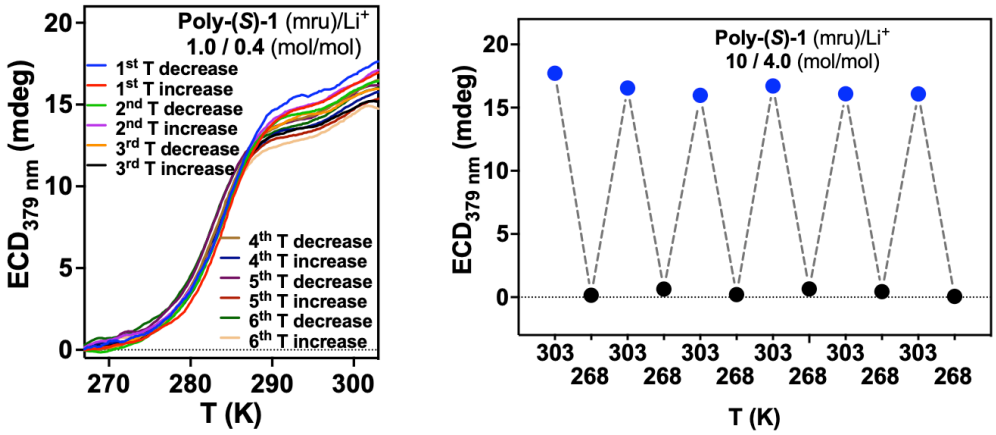


Figure S6. VT-ECD signal of poly-(*S*)-**1** (0.3 mg·mL^{-1} $CHCl_3$) in presence of 0.4 equiv of $LiClO_4$ (10 mg·mL^{-1} MeOH) at cycles of 0.1 K·min^{-1}.

5.1.7. VT-ECD studies of poly-(*S*)-1/Li^+ Complex with MeOH excess

VT-ECD (0.5 K·min^{-1}) were performed at 379 nm to a solution of poly-(*S*)-**1** (c = 0.3 mg·mL^{-1} $CHCl_3$) after the addition of 0.4 equiv of $LiClO_4$ from a solution of 10 mg/mL MeOH and 20 μL of MeOH.

USC UNIVERSIDADE DE SANTIAGO DE COMPOSTELA

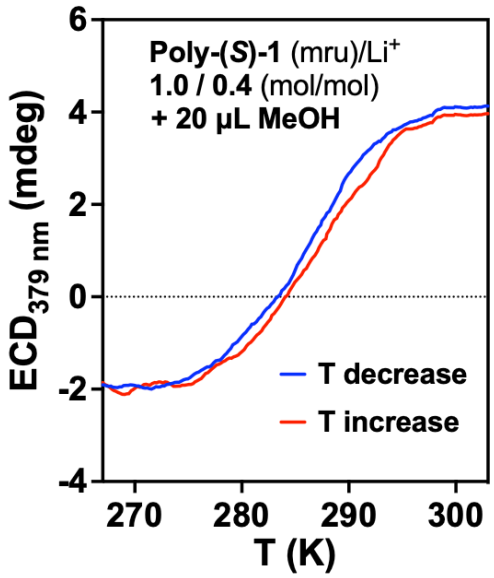


Figure S7. VT-ECD signal at 379 nm (0.5 K·min^{-1}) of poly-(*S*)-**1** (0.3 mg·mL^{-1} $CHCl_3$) in presence of 0.1 equiv of $LiClO_4$ (10 mg·mL^{-1} MeOH) and excess of MeOH.

5.1.8. VT-ECD studies of poly-(*S*)-1/Li$^+$ Complex with THF cosolvent

VT-ECD (0.5 K·min^{-1}) of a solution of poly-(*S*)-**1** (c= 0.3 mg·mL^{-1} $CHCl_3$) after the addition of 0.4 equiv of $LiClO_4$ from a solution of 10 mg·mL^{-1} THF

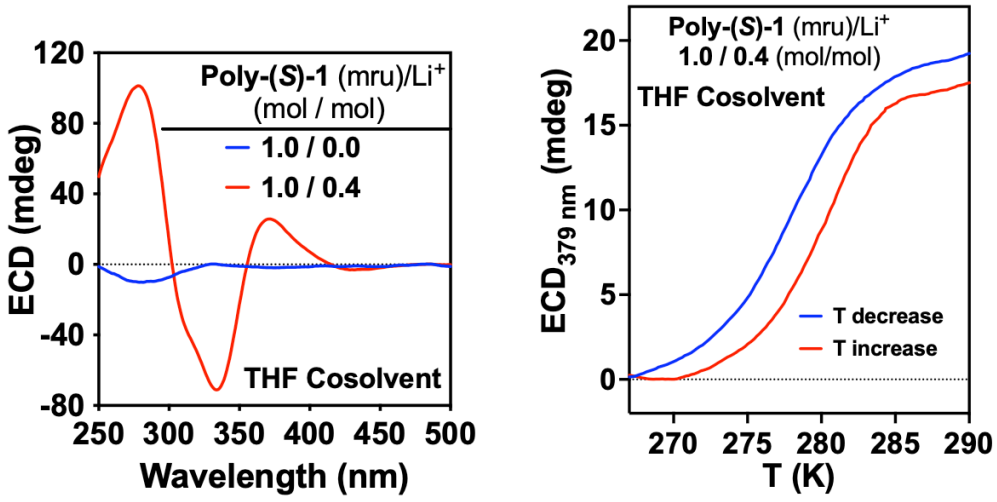


Figure S8. VT-ECD (0.5 K·min^{-1}) of poly-(*S*)-**1** (0.3 mg·mL^{-1} $CHCl_3$) in presence of 0.4 equiv of $LiClO_4$ (10 mg·mL^{-1} THF).

USC UNIVERSIDADE DE SANTIAGO DE COMPOSTELA

5.1.9. VT-ECD and VT-UV-Vis studies of poly-(*S*)-1/Ca^{2+} Complex

VT-ECD and VT-UV-Vis were performed for a solution of poly-(*S*)-**1** in $CHCl_3$ (c = 0.3 mg·mL^{-1}) after the addition of 0.2 equiv of $Ca(ClO_4)_2$ from a solution of 10 mg·mL^{-1} MeOH. ECD signals were measured at 390 nm at 0.1 K·min^{-1}.

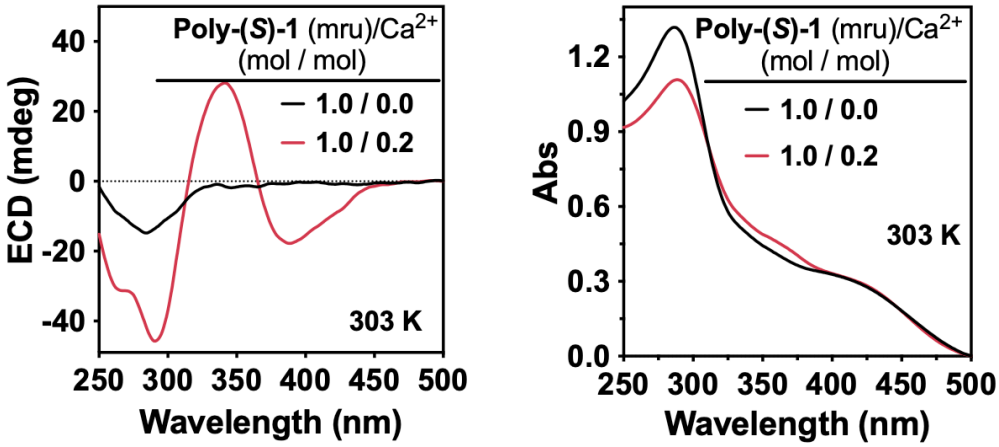


Figure S9. VT-ECD and UV-Vis (0.1 K·min^{-1}) of poly-(*S*)-**1** (0.3 mg·mL^{-1} $CHCl_3$) in presence of 0.2 equiv of $Ca(ClO_4)_2$ (10 mg·mL^{-1} MeOH).

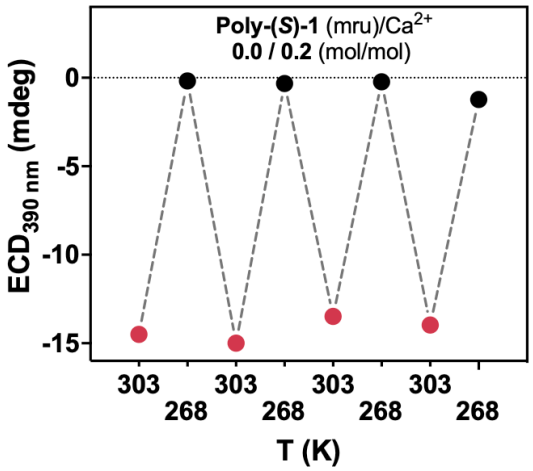


Figure S10. VT-ECD cycles (0.1 K·min^{-1}) of poly-(*S*)-**1** (0.3 mg·mL^{-1} $CHCl_3$) in presence of 0.2 equiv of $Ca(ClO_4)_2$ (10 mg·mL^{-1} MeOH).

USC UNIVERSIDADE DE SANTIAGO DE COMPOSTELA

5.1.10. VT-ECD and VT-UV-Vis studies of poly-(*S*)-3/Li$^+$ Complex

VT-ECD and VT-UV-Vis were performed for a solution of poly-(*S*)-**3** in $CHCl_3$ (c= 0.3 mg·mL^{-1}) after the addition of 0.4 equiv of $LiClO_4$ from a solution of 10 mg·mL^{-1} MeOH. ECD signals were measured at 390 nm at 0.1 K·min^{-1}.

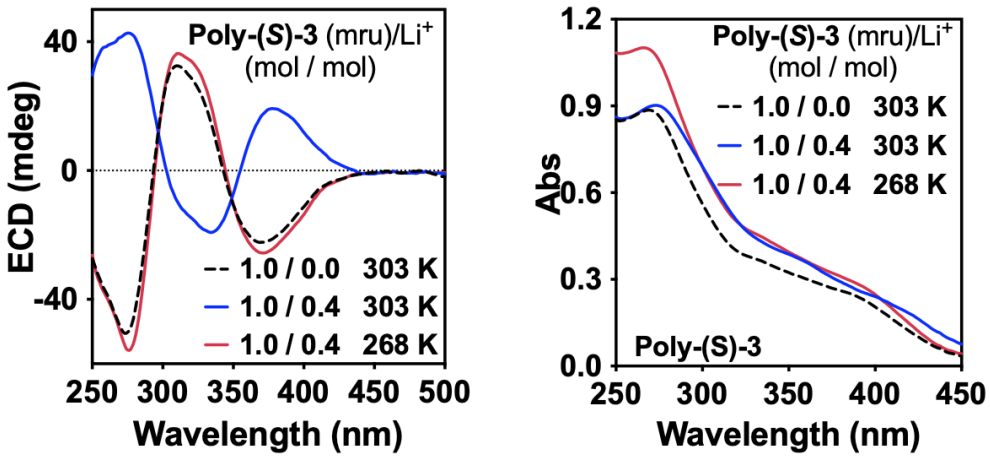


Figure S11. VT-ECD and UV-Vis of poly-(*S*)-**3** (0.3 mg·mL^{-1} $CHCl_3$) in presence of 0.4 equiv of $LiClO_4$ (10 mg·mL^{-1} MeOH) at temperature ramps of 0.1 K·min^{-1}.

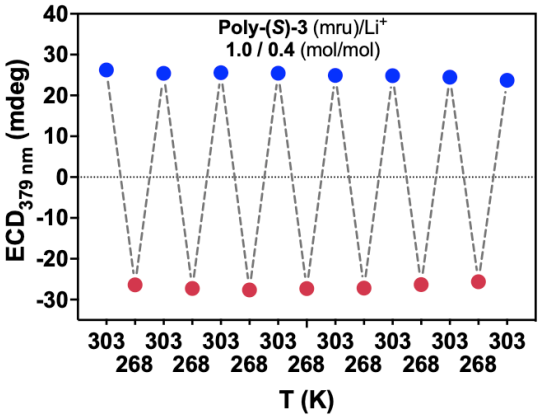


Figure S12. VT-ECD (0.1 K·min^{-1}) signal at 379 nm of poly-(*S*)-**3** (0.3 mg·mL^{-1} $CHCl_3$) in presence of 0.4 equiv of $LiClO_4$ (10 mg·mL^{-1} MeOH).

USC UNIVERSIDADE DE SANTIAGO DE COMPOSTELA

5.1.11. VT-ECD and VT-UV-Vis studies of poly-(*S*)-3/Ca^{2+} Complex

VT-ECD and VT-UV-Vis were performed for a solution of poly-(*S*)-**3** in $CHCl_3$ (c = 0.3 mg·mL^{-1}) after the addition of 0.4 equiv of $Ca(ClO_4)_2$ from a solution of 10 mg·mL^{-1} MeOH. ECD signals were measured at 390 nm at 0.1 K·min^{-1}.

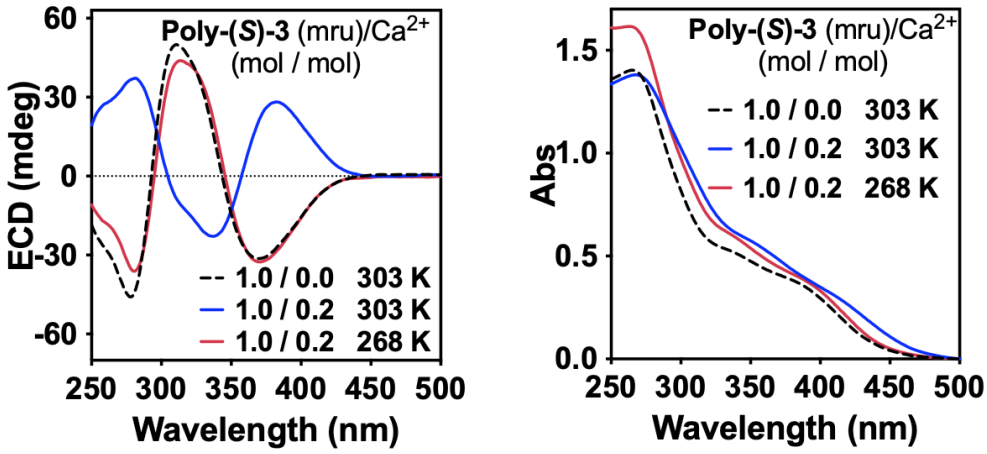
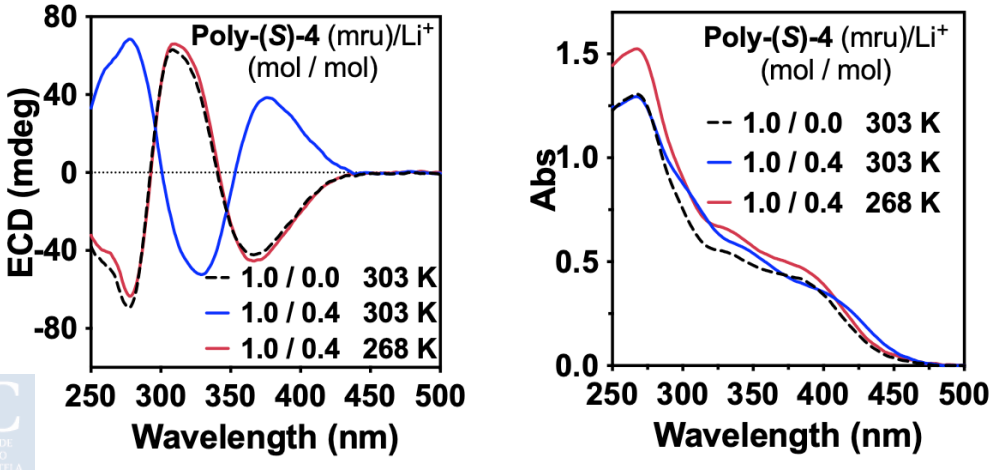


Figure S13. VT-ECD and UV-Vis of poly-(*S*)-**3** (0.3 mg·mL^{-1} $CHCl_3$) in presence of 0.2 equiv of $Ca(ClO_4)_2$ (10 mg·mL^{-1} MeOH) at temperature ramps of 0.1 K·min^{-1}.

5.1.12. VT-ECD and VT-UV-Vis studies of poly-(*S*)-4/Li^+ and poly-(*S*)-4/Ca^{2+} Complexes

VT-ECD and UV-Vis (0.1 K·min^{-1}) were performed to a solution of poly-(*S*)-**4** in $CHCl_3$ (c = 0.3 mg·mL^{-1}) after the addition of 0.3 equiv of $LiClO_4$ and $Ca(ClO_4)_2$ from a solution of 10 mg·mL^{-1} MeOH.



USC UNIVERSIDADE DE SANTIAGO DE COMPOSTELA

Figure S14. VT-ECD and UV-Vis of poly-(*S*)-**4** (0.3 mg·mL^{-1} $CHCl_3$) in presence of 0.4 equiv of $LiClO_4$ (10 mg·mL^{-1} MeOH) at temperature ramps of 0.1 K·min^{-1}.

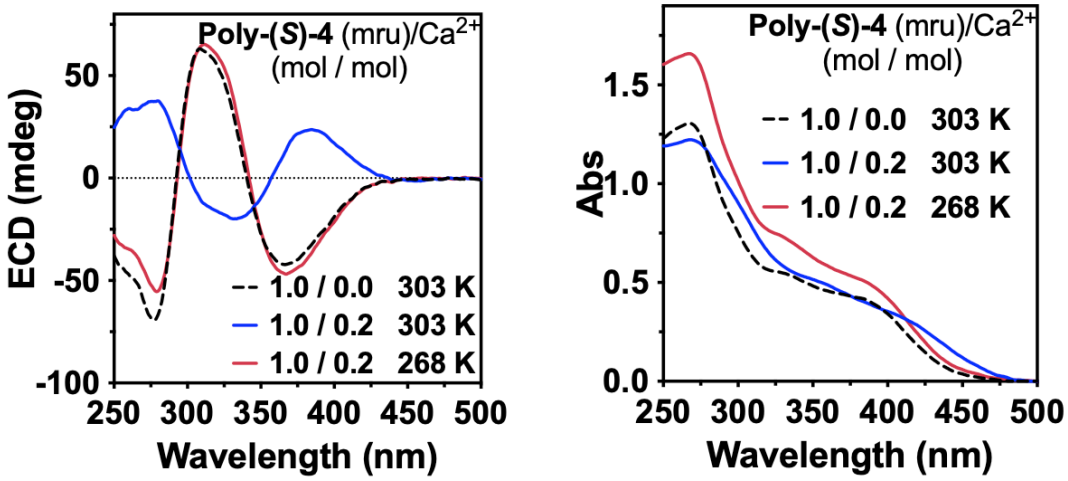


Figure S15. VT-ECD and UV-Vis (0.1 K·min^{-1}) of poly-(*S*)-**4** (0.3 mg·mL^{-1} $CHCl_3$) in presence of 0.2 equiv of $Ca(ClO_4)_2$ (10 mg·mL^{-1} MeOH).

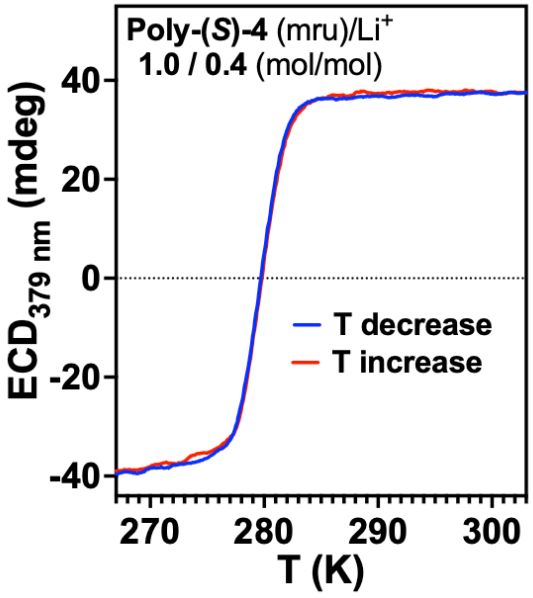


Figure S16. VT-ECD (0.1 K·min^{-1}) signal of poly-(*S*)-**4** (0.3 mg·mL^{-1} $CHCl_3$) in presence of 0.4 equiv of $LiClO_4$ (10 mg·mL^{-1} MeOH).

USC
UNIVERSIDADE DE SANTIAGO DE COMPOSTELA

5.1.13. VT-ECD and VT-UV-Vis studies of Poly-(*S*)-5/Li^+ Complex

VT VT-ECD and VT-UV-Vis (0.1 K·min^{-1}) were performed with a dispersion of poly-(*S*)-**5** in $CHCl_3$ (c = 0.3 mg·mL^{-1}) after the addition of 0.3 equiv of $LiClO_4$ from a solution of 10 mg/mL MeOH.

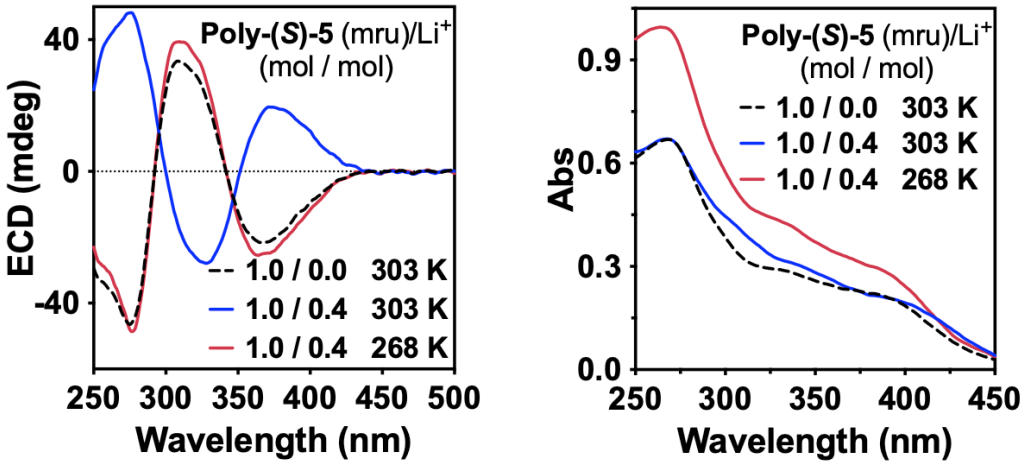


Figure S17. VT-ECD and UV-Vis (0.1 K·min^{-1}) of poly-(*S*)-**5** (0.3 mg·mL^{-1} $CHCl_3$) in presence of 0.4 equiv of $LiClO_4$ (10 mg·mL^{-1} MeOH).

5.1.14. IR studies of poly-(*S*)-1/Li^+ and poly-(*S*)-1/Ca^{2+} at different temperatures

FT-IR spectra of poly-(*S*)-**1** were recorded at room temperature in the absence and presence 0.1 equiv of $LiClO_4$ and $Ca(ClO_4)_2$ from a solution of 10 mg·mL^{-1} MeOH. To investigate the polymer structure at low temperature after metal decomplexation, a temperature ramp was performed using VT-ECD (0.1 K·min^{-1}) to confirm metal dissociation. Subsequently, the sample was flash-frozen in liquid nitrogen and measured by FT-IR.

USC UNIVERSIDADE DE SANTIAGO DE COMPOSTELA

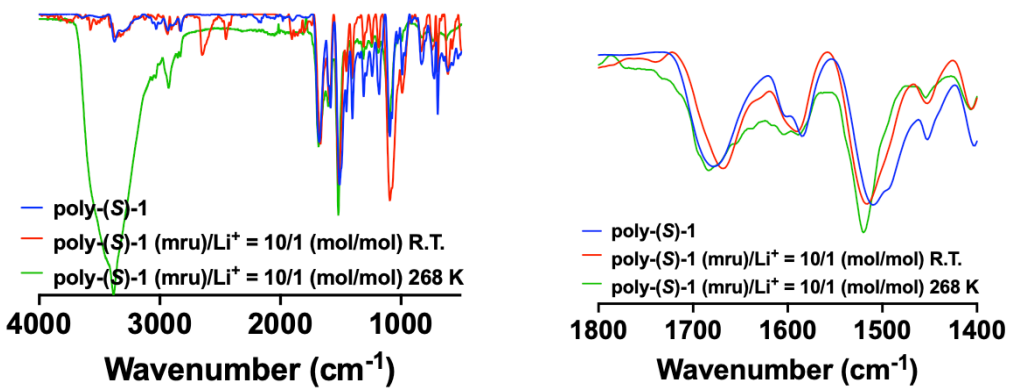


Figure S18. FT-IR spectra of poly-(*S*)-**1** at room temperature in the absence and presence of 0.1 equiv of $LiClO_4$ (10 mg·mL^{-1} MeOH) and after flash-freezing in liquid nitrogen following a VT-ECD (0.1 K·min^{-1}) temperature ramp.

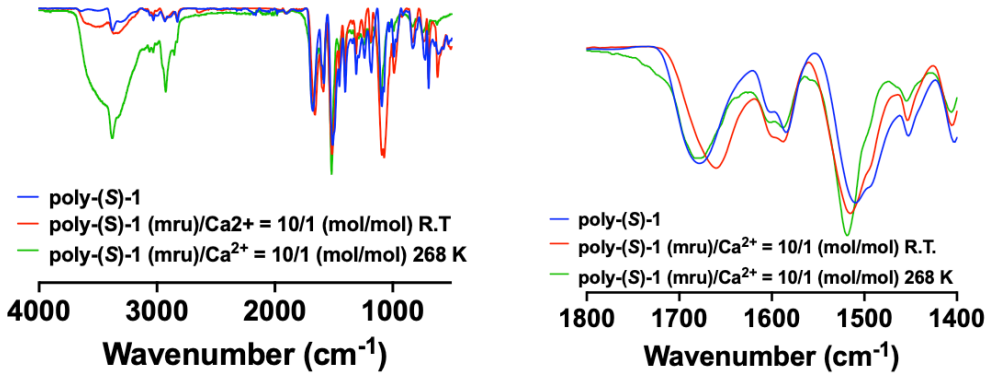


Figure S19. FT-IR spectra of poly-(*S*)-**1** at room temperature in the absence and presence of 0.1 equiv of $Ca(ClO_4)_2$ (10 mg·mL^{-1} MeOH) and after flash-freezing in liquid nitrogen following a VT-ECD (0.1 K·min^{-1}) temperature ramp.

5.1.15. VT-ECD studies of poly-(*S*)-1/Li$^+$ and poly-(*S*)-1/Ca^{2+} Complexes: Decomplexation in presence of ACAC metal scavenger

VT-ECD (0.1 K·min^{-1}) were performed to a solution of poly-(*S*)-**1** in $CHCl_3$ (c = 0.3 mg·mL^{-1}) after the addition of 0.2 equiv of $Ca(ClO_4)_2$ from a solution of 10 mg·mL^{-1} MeOH in presence of ACAC. ECD were performed to a solution of poly-(*S*)-**1** in $CHCl_3$ (c = 0.3 mg·mL^{-1}) after the addition of 0.4 equiv of $LiClO_4$ from a solution of 10 mg·mL^{-1} MeOH and different equivalents of ACAC.

USC UNIVERSIDADE DE SANTIAGO DE COMPOSTELA

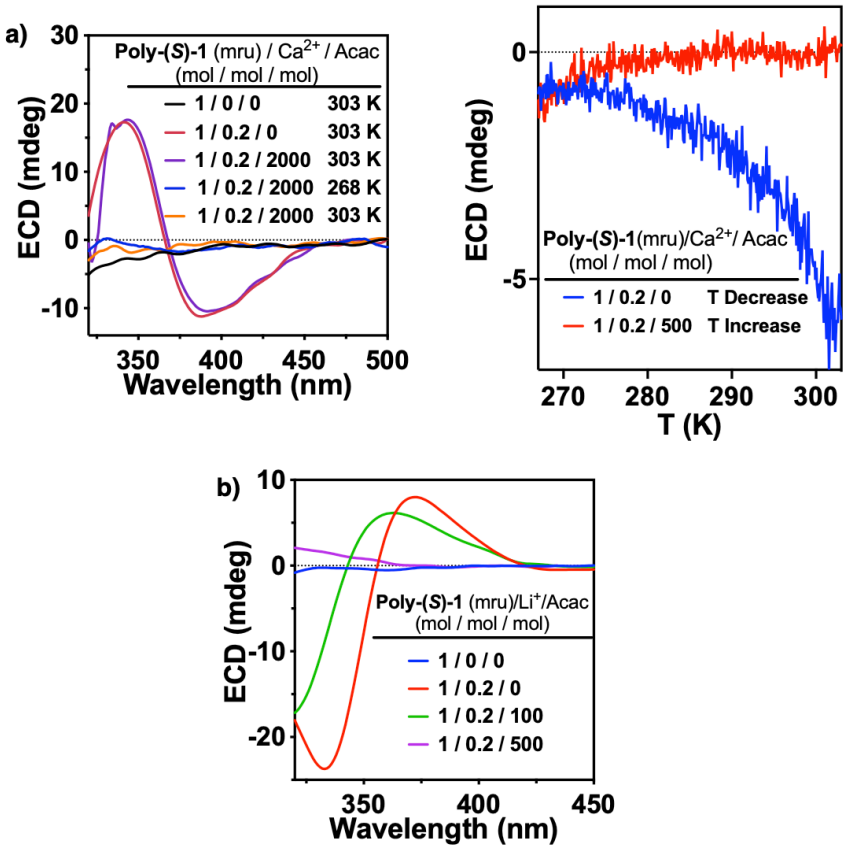


Figure S20. (a) VT-ECD and of poly-(*S*)-**3** (0.3 mg·mL^{-1} $CHCl_3$) in presence of 0.2 equiv of $Ca(ClO_4)_2$ (10 mg·mL^{-1} MeOH) and ACAC at temperature ramps of 0.1 K·min^{-1}. (b) VT-ECD of poly-(*S*)-**3** (0.3 mg·mL^{-1} $CHCl_3$) in presence of 0.4 equiv of $LiClO_4$ (10 mg·mL^{-1} MeOH) and different equivalents of ACAC (303 K).

5.1.16. VT-ECD studies of poly[(*S*)-$1_{0.3}$-*co*-$6_{0.7}$]/Li^+ and poly[(*S*)-$1_{0.3}$-*co*-$6_{0.7}$]/Ca^{2+}

VT-ECD (0.1 K·min^{-1}) were performed to a solution of poly-(*S*)-**1** in $CHCl_3$ (c = 0.3 mg·mL^{-1}) after the addition of 0.2 equiv of $Ca(ClO_4)_2$ from a solution of 10 mg·mL^{-1} MeOH in presence of ACAC. ECD were performed to a solution of poly-(*S*)-**1** in $CHCl_3$ (c = 0.3 mg·mL^{-1}) after the addition of 0.4 equiv of $LiClO_4$ from a solution of 10 mg·mL^{-1} MeOH and different equivalents of ACAC.

USC UNIVERSIDADE DE SANTIAGO DE COMPOSTELA

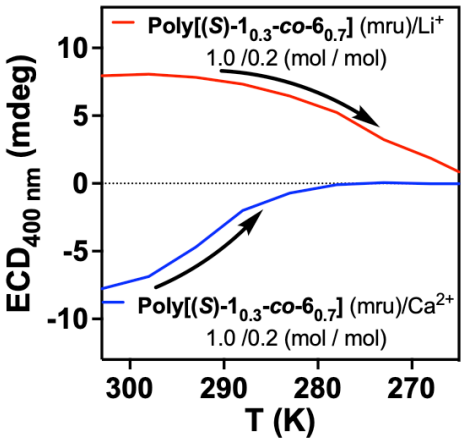


Figure S21. VT-ECD cooling curves at 400 nm of poly[(*S*)-1$_{0.3}$-*co*-6$_{0.7}$]/Li$^+$ and poly[(*S*)-1$_{0.3}$-*co*-6$_{0.7}$]/Ca^{2+} (0.3 mg·mL^{-1} $CHCl_3$) in presence of 0.2 equiv of $LiClO_4$ or $Ca(ClO_4)_2$ (10 mg·mL^{-1} MeOH).

5.1.17. Van 't Hoff equation fit of the VT-ECD experimental data of poly-(*S*)-1/Li$^+$ Complex

From the ECD signal we can extract the concentration of the different structures assigning the maximum ECD for the full conversion of the initial Lithium to the polymer metal complex. This full complexation is confirmed due to the maximum shift of UV-Vis signal in Figure S4 of the UV-Vis polyenic signal at 15 ºC. The null ECD signal is due to the full presence of lithium in the cosolvent and the pendants of the polymer without complexation. The methanol is calculated from the different complex formed from the initial value. Values adjusted to linear regression Van't Hoff equation substituting equation (S1) in equation (S2) at different Temperatures. $[MeOH]_i$= 0.088966292 mmol/mL, $[Pendant]_i$= 0.001130625 mmol/mL, and $[MeOH_3LiClO_4]_i$ = 0.000339189 mmol/mL.

$$K_{eq} = \frac{[Poly/Li][Pendant\ B][MeOH]^2}{[Li(ClO_4)(MeOH)_3]\,[PendantA - PendantB]} \quad \textbf{(S1)}$$

$$ln(K_{eq}) = -\frac{\Delta H}{R} * \frac{1}{T} + \frac{\Delta S}{R} \quad \textbf{(S2)}$$

USC UNIVERSIDADE DE SANTIAGO DE COMPOSTELA

$$\Delta G = \Delta H - \Delta S * T \quad \textbf{(S3)}$$

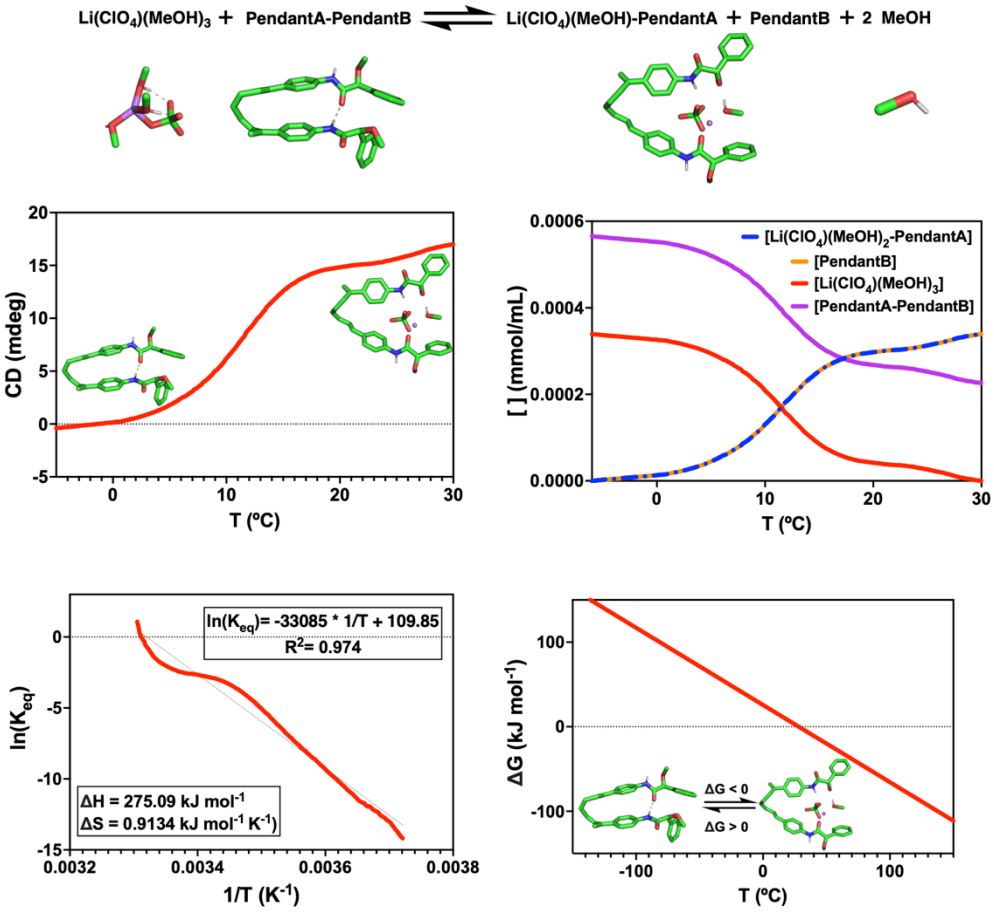


Figure S22. Experimental VT-ECD of poly-(*S*)-**1** in presence of 0.1 equivalents of $Li(ClO_4)$, calculated concentrations at each temperature and Van't Hoff Fitting.

5.1.18. Van 't Hoff equation fit of the VT-ECD experimental data of poly-(*S*)-3/Li^+ Complex

From the ECD signal we can extract the concentration of the different structures assigning the maximum ECD for the full presence of the initial Lithium to the polymer metal complex. The null ECD signal is due to the full presence of lithium in the cosolvent and the pendants of the polymer without complexation. The methanol is calculated from the different complex formed from the initial value. Values adjusted to linear regression Van't Hoff substituting equation (S1) in equation (S2) at different Temperatures.

USC UNIVERSIDADE DE SANTIAGO DE COMPOSTELA

$[MeOH]_i$= 0.123564295 mol/mL, $[Pendant]_i$= 0.0012982 mol/mL, and $[MeOH_3LiClO_4]_i$ = 0.000471096 mol/mL.

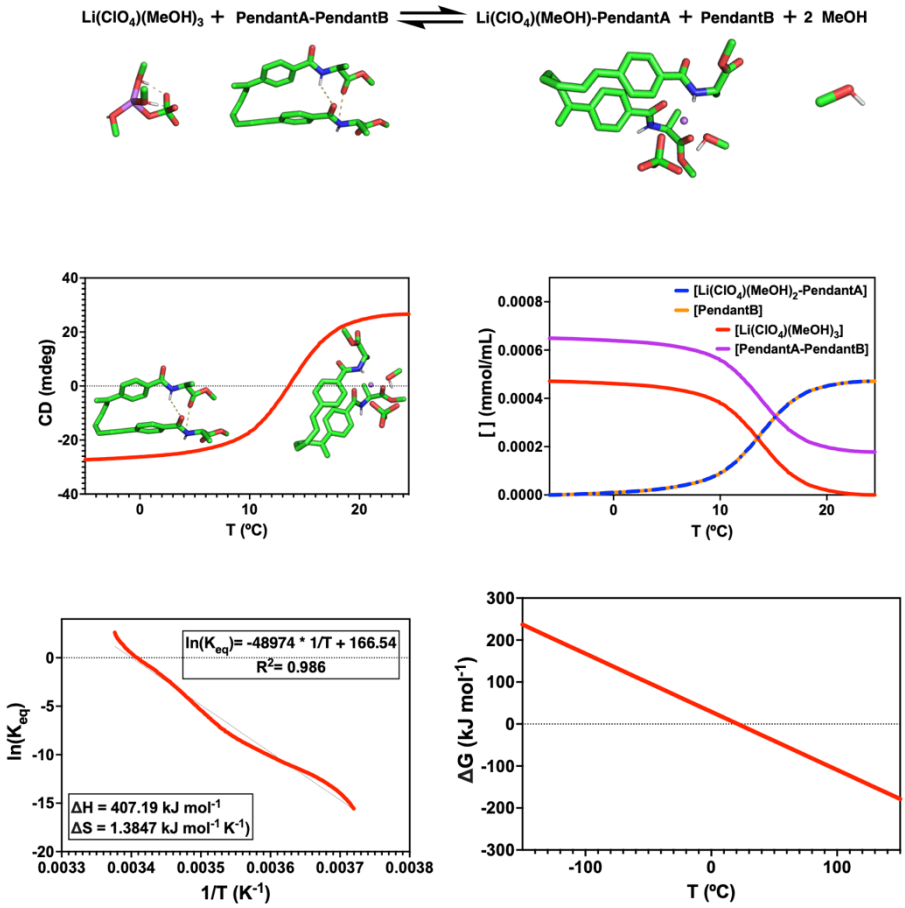


Figure S23. Experimental VT-ECD of poly-(S)-3 in presence of 0.1 equivalents of Li(ClO4), calculated concentrations at each temperature and Van't Hoff Fitting.

5.1.19. Theoretical Calculations

All the considerations before drawing the models were that Li^+ prefers coordination with 3 MeOH molecules and one perchlorate, as determined by an optimization performed in an explicit solvent box containing 8 MeOH, 1Li^+, 1 perchlorate, and 8 $CHCl_3$ molecules. This optimization was carried out using Gaussian-16 (G16RevC.01)[413] with the B3LYP functional[415] with the 6-31+G(d,p) basis set.

For the (*S*)-**1**/Li^+ complex, it was observed that only one MeOH molecule remained in the inner coordination sphere, while the other two were displaced. This was confirmed through calculations using the wb97xd[126] functional and the 6-311++G(d,p) basis set,

where Li^+ preferentially interacted with the carbonyl group and the aromatic ring via cation-π interactions. Meanwhile, the perchlorate and one methanol molecule interacted with the methoxy group of the upper pendant. These findings justify the structural model used for further calculations and the ap conformation of (*S*)-**1** in presence of monovalent metal ions. In the case of (*S*)-**3**, the interaction with Li^+ occurs between the two carbonyl groups, stabilizing the syn conformation.

5.1.19.1 DFT calculation of the complexation of poly-(S)-1/Li⁺

All computations were carried out for 2-mers poly-(*S*)-**1** with $Li(ClO_4)(MeOH)_3$ bound and unbound using Gaussian-16 (G16RevC.01). Geometry optimizations were performed by using the DFT method wb97xd and the 6-311++g(d,p) basis set. Frequency calculations of the optimized geometries revealed no imaginary frequencies, indicating that the calculated structures correspond, at least, to local minima on the potential energy surface. From the frequency calculation of the difference structures, we obtained the difference in energy of the Enthalpy and Entropy at 298 K. We represented the approximated Free Energy, neglecting other effects, to visualize its variation with temperature.

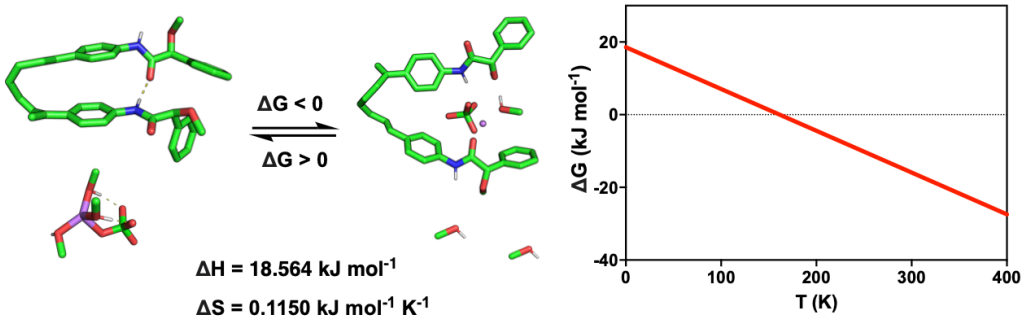


Figure S24. Optimized Structures of 2-mers poly-(*S*)-**1** with $Li(ClO_4)(MeOH)_3$ bound and unbound. Representation of the difference in calculated Free Energy at different Temperatures.

5.1.19.2 DFT calculation of the complexation of poly-(S)-3/Li⁺

All computations were carried out for 2-mers poly-(*S*)-**3** with $Li(ClO_4)(MeOH)_3$ bound and unbound using Gaussian-16 (G16RevC.01). Geometry optimizations were performed by using the DFT method wb97xd and the 6-311++g(d,p) basis set. Frequency calculations of the optimized geometries revealed no imaginary frequencies,

indicating that the calculated structures correspond, at least, to local minima on the potential energy surface. From the frequency calculation of the difference structures, we obtained the difference in energy of the Enthalpy and Entropy at 298 K. We represented the approximated Free Energy, neglecting other effects, to visualize its variation with temperature.

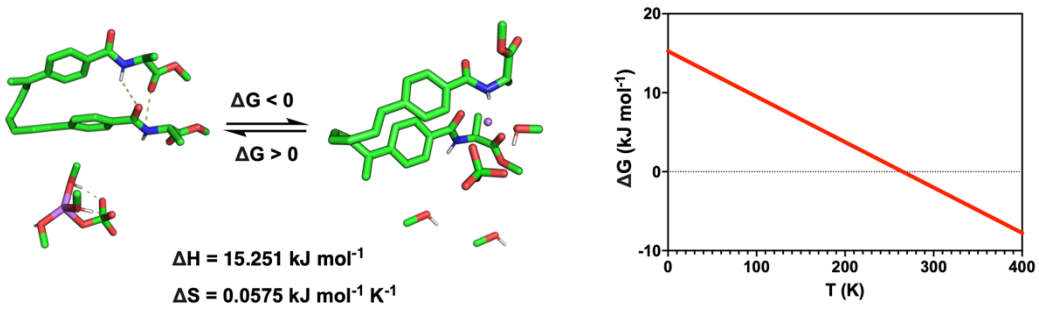


Figure S25. Optimized Structures of 2-mers poly-(*S*)-**3** with $Li(ClO_4)(MeOH)_3$ bound and unbound. Representation of the difference in calculated Free Energy at different Temperatures.

USC UNIVERSIDADE DE SANTIAGO DE COMPOSTELA

USC
UNIVERSIDADE
DE SANTIAGO
DE COMPOSTELA

5.2. Experimental Section and Methodology Chapter 3.2.

5.2.1. Materials and methods

Commercially available chemicals have been used as delivered. Solvents were purchased as reagent grade and distilled if necessary. Anhydrous solvents were either purchased as ultra-dry solvent from Acros Organics® or received from solvent purification system. For the coupling and polymerization reactions, dry THF was obtained from MBRAUN SPS 800 solvent purification system. Water was purified by Millipore water purification system. $Fe(ClO_4)_3$ (98.000% purity), $FeCl_3$ (99.990% purity), $AuCl_3$ (99.9%), $Cu(ClO_4)_2$ (98% purity), $Hg(ClO_4)_2$ (99.998% purity), $(NH_4)_2[Ce(NO_3)_6]$ (98.5% purity) salts were purchased from Sigma Aldrich.

NMR experiments were carried out in a Varian Inova 2 (250 MHz resonance 1H). Size exclusion chromatography studies were performed on Alliance 2695 HPLC System (Waters) liquid chromatography system equipped with a UV 2489 detector (Waters). The samples were eluted by three Phenogel columns connected to each other with stationary phases of 10^3, 10^4 and 10^5 Amstrong and packed with a solid support of a cross-linked styrene and p-divinylbenzene copolymer.

CD measurements were done in a Jasco-720 spectropolarimeter. UV spectra were registered in a Jasco-730 spectrophotometer.

FT-IR measurements were carried out on a Bruker IFS-66v while Raman measurements were carried out in a Renishaw confocal Raman spectrophotometer (Invia Reflex model), equipped with two lasers (diode laser 785 nm and Ar laser 514 nm).

EPR experiments were carried out in a Bruker EMX with a frequency around 9.443 GHz and using perylene in H_2SO_4 as internal reference. XPS analysis of the samples was performed using a Thermo Scientific K-Alpha ESCA instrument equipped with aluminum Kα monochromatized radiation at 1486.6 eV X-ray source. Due the no conductor nature of samples was necessary to use an electron flood gun to minimize surface charging. Neutralization of the surface charge was performed by using both a low energy flood gun (electrons in the range 0 to 14 eV) and a low energy Argon ions gun.

USC UNIVERSIDADE DE SANTIAGO DE COMPOSTELA

The XPS measurements were carried out using monochromatic Al-Kα radiation (hn = 1486.6 eV). Photoelectrons were collected from a take-off angle of 90º relative to the sample surface. The measurement was done in a Constant Analyser Energy mode (CAE) with a 100 eV pass energy for survey spectra and 20eV pass energy for high resolution spectra. Charge referencing was done by setting the lower binding energy C 1s photo peak at 284.8.0 eV C1s hydrocarbon peak. Surface elemental composition was determined using the standard Scofield photoemission cross sections.

5.2.2. Monomers and polymers

The preparation of monomers (M-**1**, M-**2**, M-**3**, M-**4**, M-**5**, M-**6**, and M-**7**) polymers (poly-**1**, poly-**2**, poly-**3**, poly-**4**, poly-**5**, poly-**6**, and poly-**7**) can be found in literature.[84,102,171]

USC
UNIVERSIDADE DE SANTIAGO DE COMPOSTELA

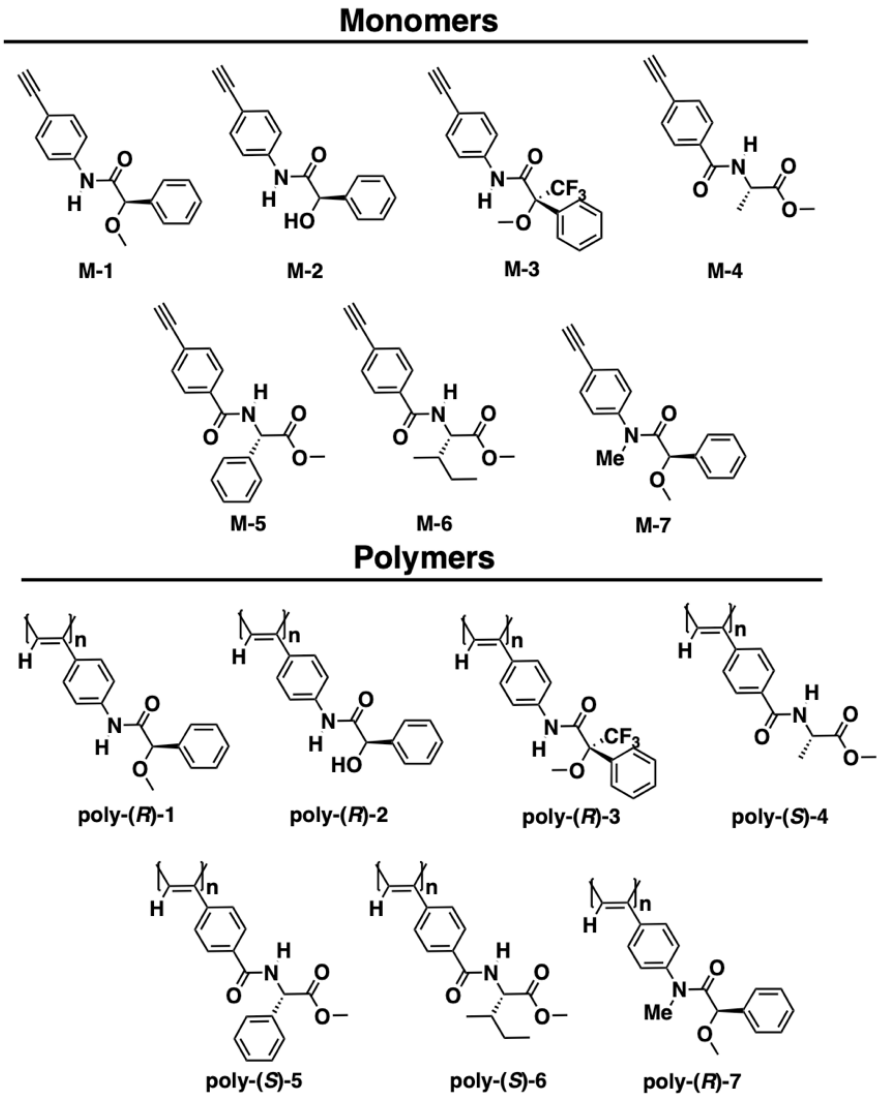
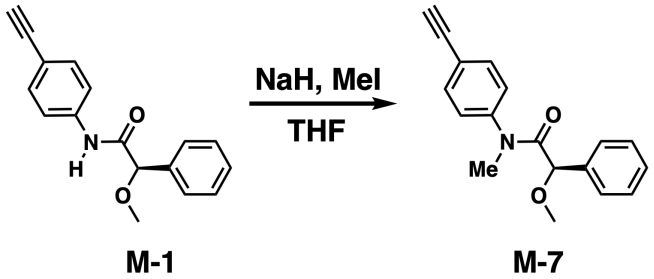


Figure S26. Structures of PPAs with anilide and bezamide connection.

5.2.3. Synthesis of monomer M-7



Sodium hydride (0.016 g, 0.416 mmol) was dissolved in dry THF (4 mL, 0 ºC) and M-1 (0.100 g, 0.376 mmol) dissolved in 10 mL in dry THF was added drop by drop. After

30 min, iodomethane (0.069 g, 0.489 mmol) was added and the reaction mixture was stirred overnight at room temperature. Once the reaction was completed (checked by TLC), all the mixture was poured into ethyl acetate and washed with water three times. Afterward the organic layer was separated, dried (Na_2SO_4) and concentrated. The crude product was purified by column chromatography over silica gel using hexane/ethyl acetate (7:3 as an eluent). The solvent was removed in vacuum to obtain compound M-**7** as colorless oil (Yield 0.082 g, 79%)

Spectroscopic data:

^{1}H-NMR (250 MHz, CDCl3) δ_H (ppm): 3.14 (1H, s), 3.21 (3H, s), 4.63 (1H, s), 6.93 (2H, d), 7.10 (2H, s), 7.24 (3H, s), 7.44 (2H, d).

^{13}C-NMR (62.5 MHz, CDCl3) δ_C (ppm): 29.6, 37.8, 56.8, 80.8, 82.8, 122.1, 128.1, 128.4, 128.6, 133.3, 136.1, 143.0, 169.7.

HRMS (ESI) m/z calcd. for $C_{18}H_{17}NO_2$ $[M+H]^+$: 280.1259, found: 280.1332.

$[\alpha]_D^{20}$ = = +76 (13 mg·mL^{-1}, $CHCl_3$)

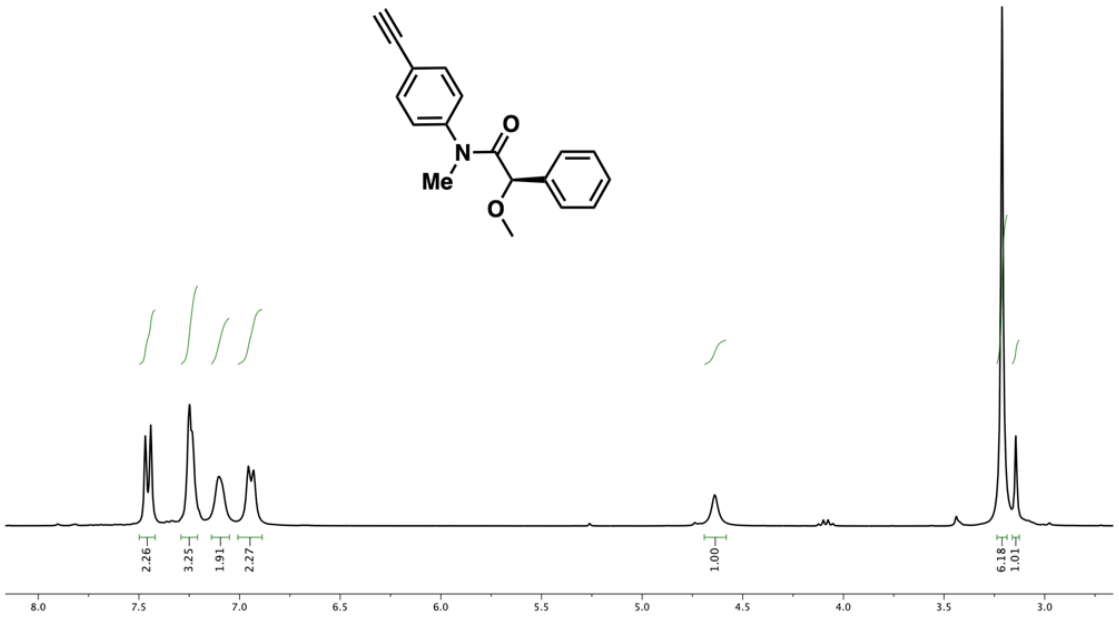


Figure S27. ^{1}H-NMR of monomer M-**7**.

USC UNIVERSIDADE DE SANTIAGO DE COMPOSTELA

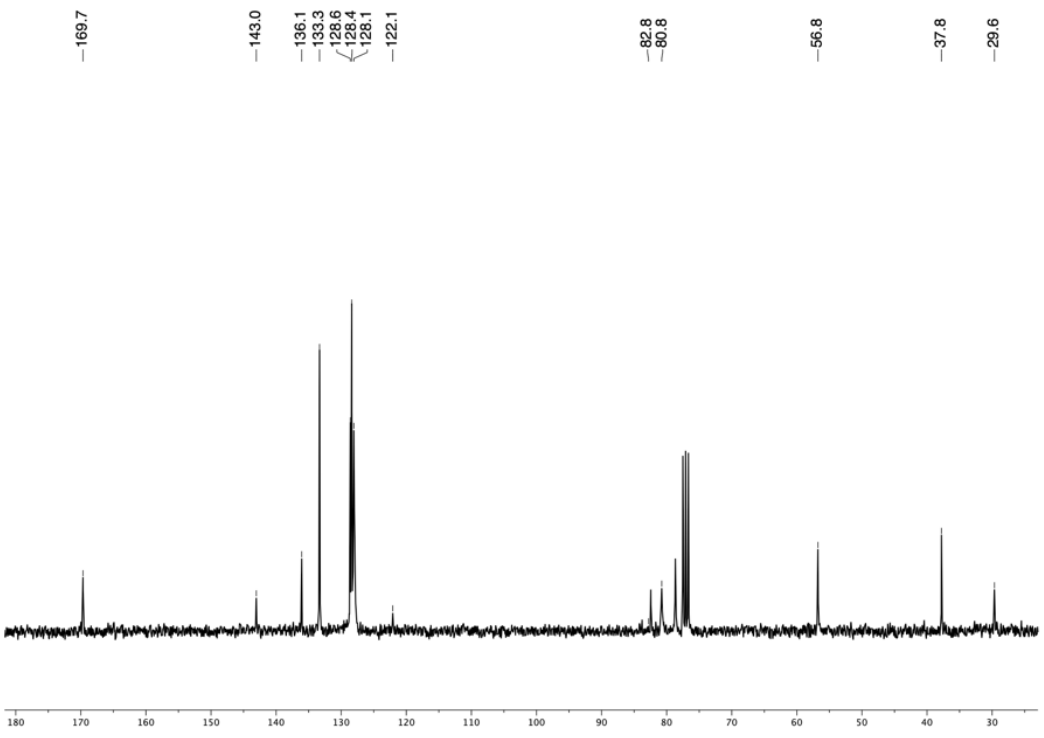
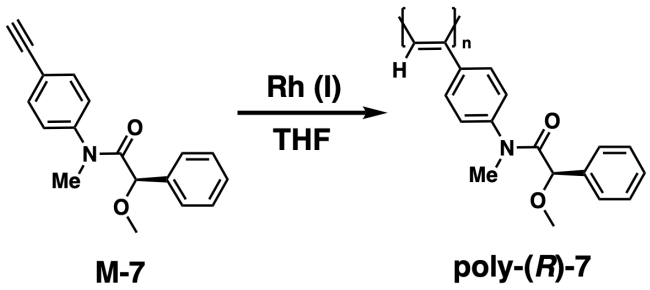


Figure S28. ^{13}C-NMR of monomer M-**7**.

5.2.4. Synthesis of poly-(R)-7



M-7 **poly-(*R*)-7**

The reaction flask (sealed ample) was dried under vacuum and Ar flushed for three times before the corresponding monomer M-**1** (100 mg) was added as a solid. Then, the flask was dried with a vacuum line and flushed with Ar (three times). Dry THF (0.72 mL) was added with a syringe and Et_3N dropwise. A solution of catalyst, [Rh(nbd)Cl]2 (1.65 mg) was added at 30 ºC. The reaction mixture was stirred at 30 ºC for 24 h. The resulting polymer was diluted in CH_2Cl_2 and precipitated in a large amount of MeOH, centrifugated twice and reprecipitated using hexane and centrifugated again (92% of yield).

USC UNIVERSIDADE DE SANTIAGO DE COMPOSTELA

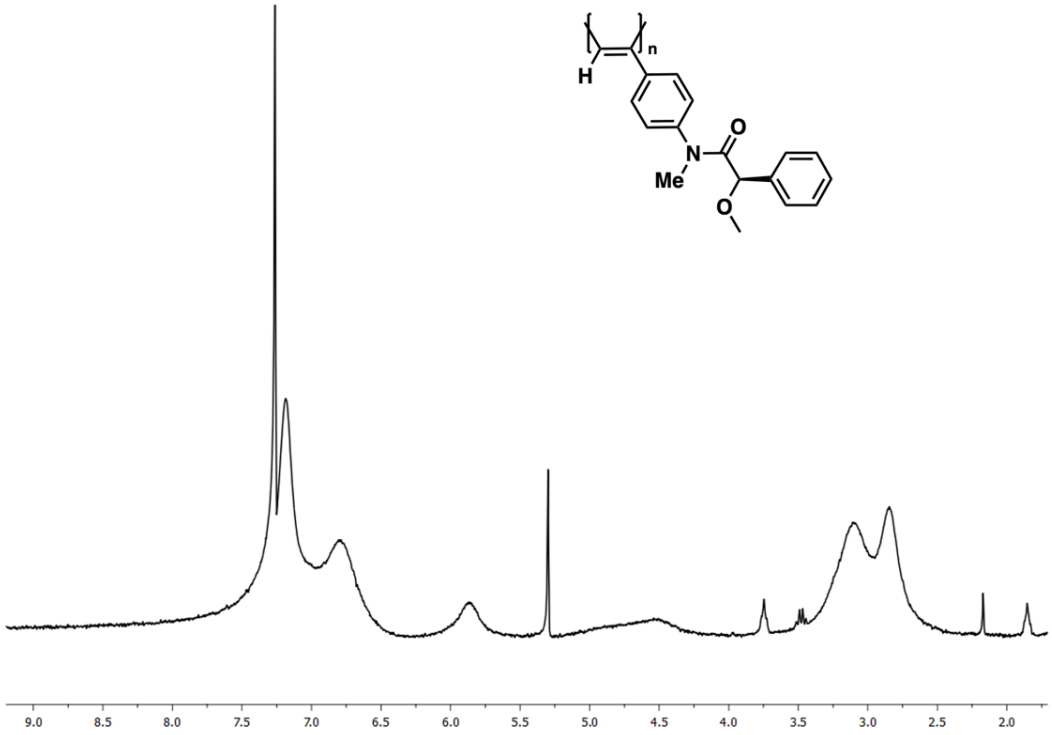


Figure S29. ^{1}H-NMR of poly-(*R*)-**7**

5.2.5. UV-Vis studies of anilide-PPAs connection in different high polar and low polar solvents in presence of $Fe(ClO_4)_3$

UV-Vis were performed for poly-(*R*)-**1** (0.1 mg·mL^{-1}) in different high polar (DMF and DMSO) and low polar solvents (THF and $CHCl_3$) using $Fe(ClO_4)_3$ which concentration was 10.0 mg·mL^{-1} THF.

USC UNIVERSIDADE DE SANTIAGO DE COMPOSTELA

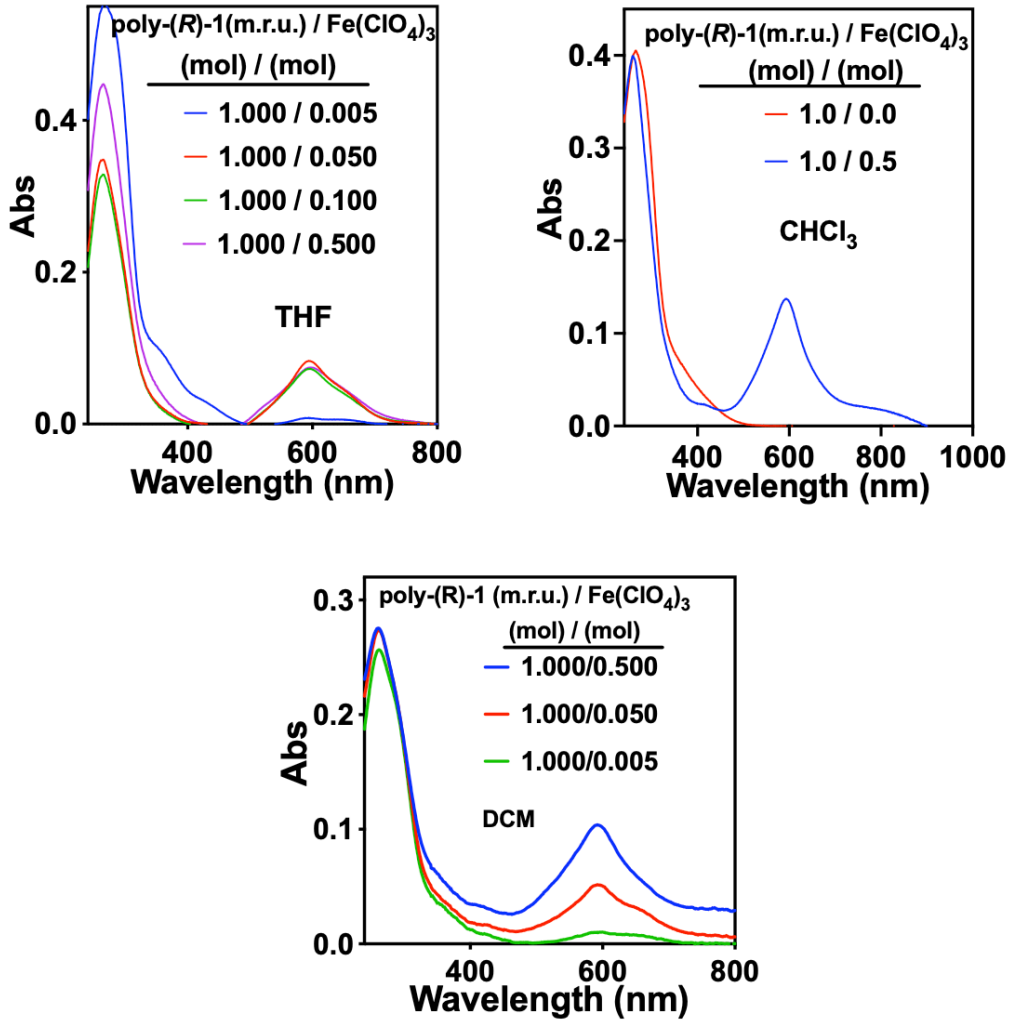


Figure S30. UV-Vis of poly-(*R*)-**1** (0.1 mg·mL^{-1}) in THF, $CHCl_3$ and DCM in presence of $Fe(ClO_4)_3$ (10 mg·mL^{-1}, THF).

USC UNIVERSIDADE DE SANTIAGO DE COMPOSTELA

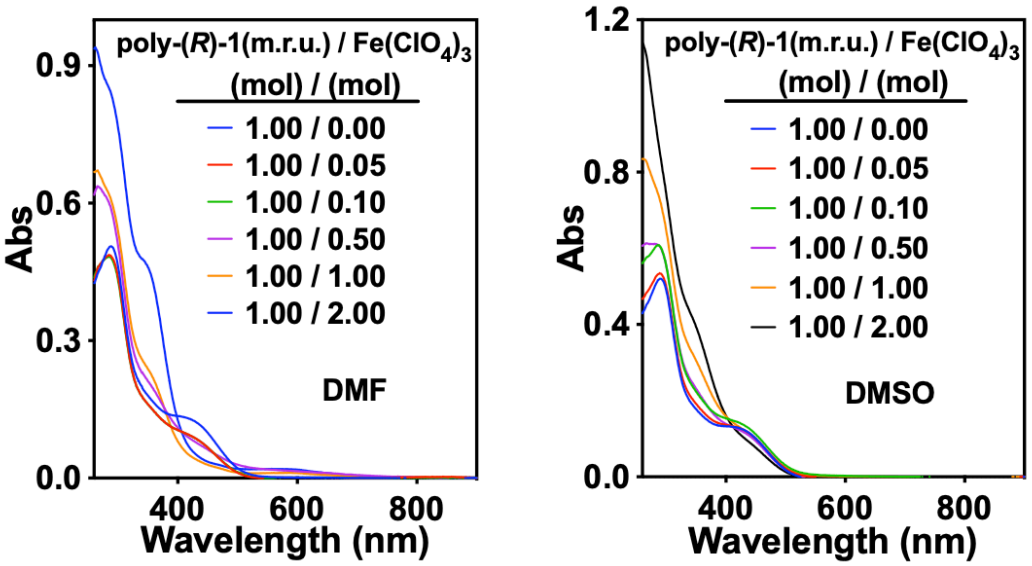


Figure S31. UV-Vis of poly-(*R*)-**1** (0.1 mg·mL^{-1}) in DMF and DMSO in presence of $Fe(ClO_4)_3$ (10 mg·mL^{-1}, THF).

5.2.6. FT-IR studies of poly-(*R*)-1 in presence of $Fe(ClO_4)_3$

A solution of $Fe(ClO_4)_3$ (0.5 equiv, 10.0 mg·mL^{-1} in THF) was added to a solution of poly-(*R*)-**1** in THF (0.3 mg·mL^{-1}) and then the FT-IR spectrum was registered. The experiments confirmed the coordination of Fe^{3+} ions to the carbonyl groups in poly-(*R*)-**1**.

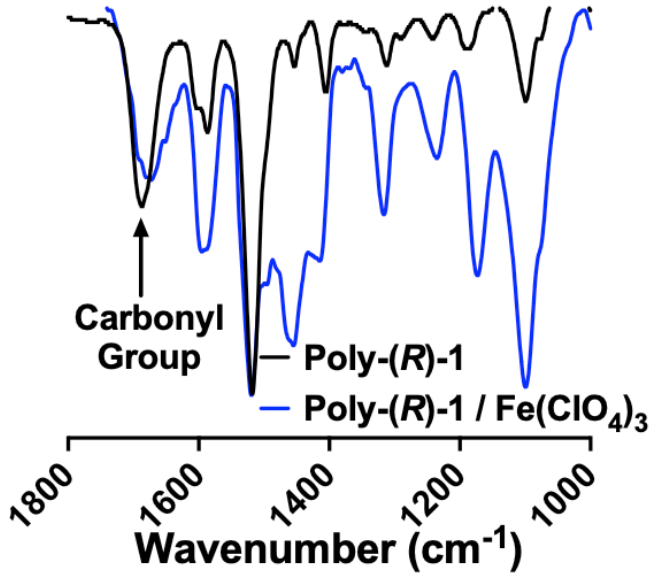


Figure S32. FT-IR spectra of poly-(*R*)-**1** and poly-(*R*)-**1**/$Fe(ClO_4)_3$.

5.2.7. UV-Vis and CD studies of poly-(*R*)-1 in presence of $FeCl_3$ in inert conditions

UV-Vis and CD were performed for poly-(*R*)-**1** in THF in Argon using $FeCl_3$ which concentration 10.0 mg·mL^{-1} THF.

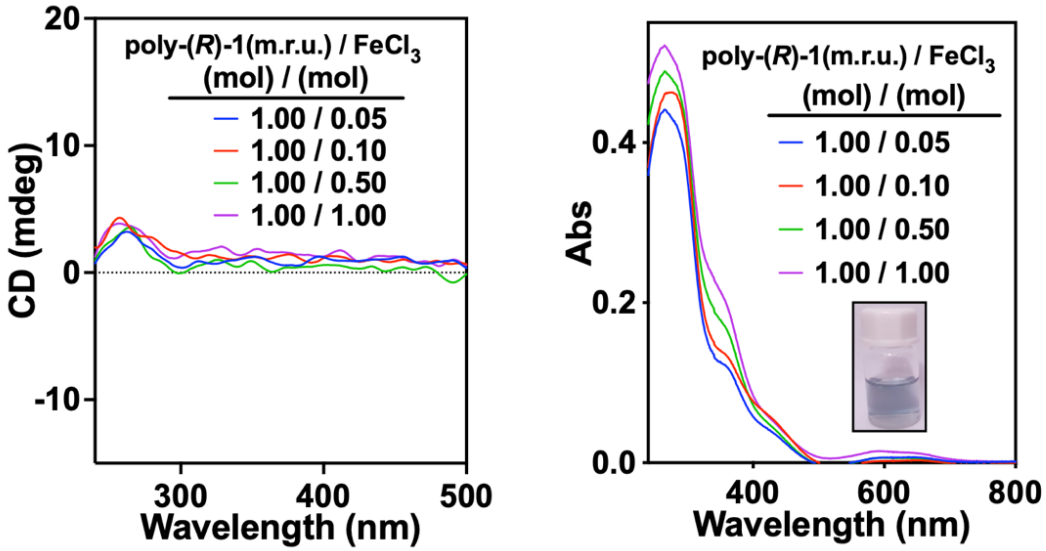


Figure S33. CD and UV-Vis of poly-(*R*)-**1** (0.1 mg·mL^{-1} THF) in Argon in the presence of $FeCl_3$ (10 mg·mL^{-1}, THF).

5.2.8. IR experiments of poly-(*R*)-1 in presence of $FeCl_3$ salt

A solution of $FeCl_3$ (0.5 equiv, 10.0 mg·mL^{-1} in THF) was added to a solution of poly-(*R*)-**1** in THF (0.3 mg·mL^{-1}) and hen the FT-IR spectra were registered.

USC UNIVERSIDADE DE SANTIAGO DE COMPOSTELA

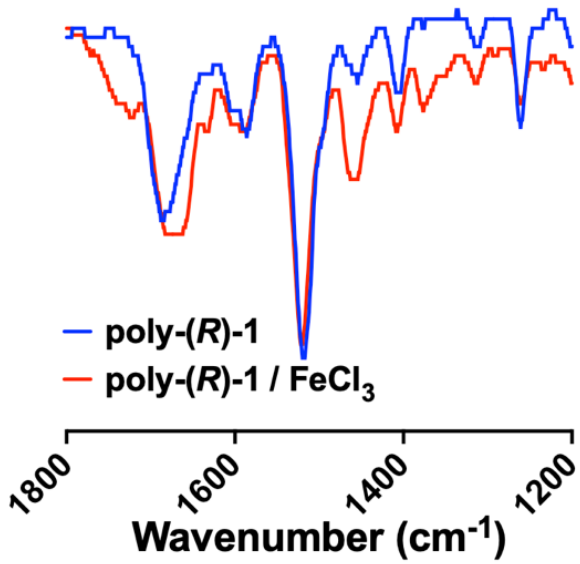


Figure S34. FT-IR spectra of poly-(*R*)-**1** and poly-(*R*)-**1**/$FeCl_3$.

5.2.9. UV-Vis studies of anilide-PPAs connection in presence of different oxidizing metal ions

UV-Vis were performed for poly-(*R*)-**1** (0.1 mg·mL^{-1}) in THF using $Cu(ClO_4)_2$, $Fe(ClO_4)_3$, $Hg(ClO_4)_2$, and $AuCl_3$ which concentration was 1.0 mg·mL^{-1} and 10.0 mg·mL^{-1} in THF. Also $(NH_4)_2[Ce(NO_3)_6]$ was added with concentration 1.0 mg·mL^{-1} and 10.0 mg·mL^{-1} in MeOH.

USC UNIVERSIDADE DE SANTIAGO DE COMPOSTELA

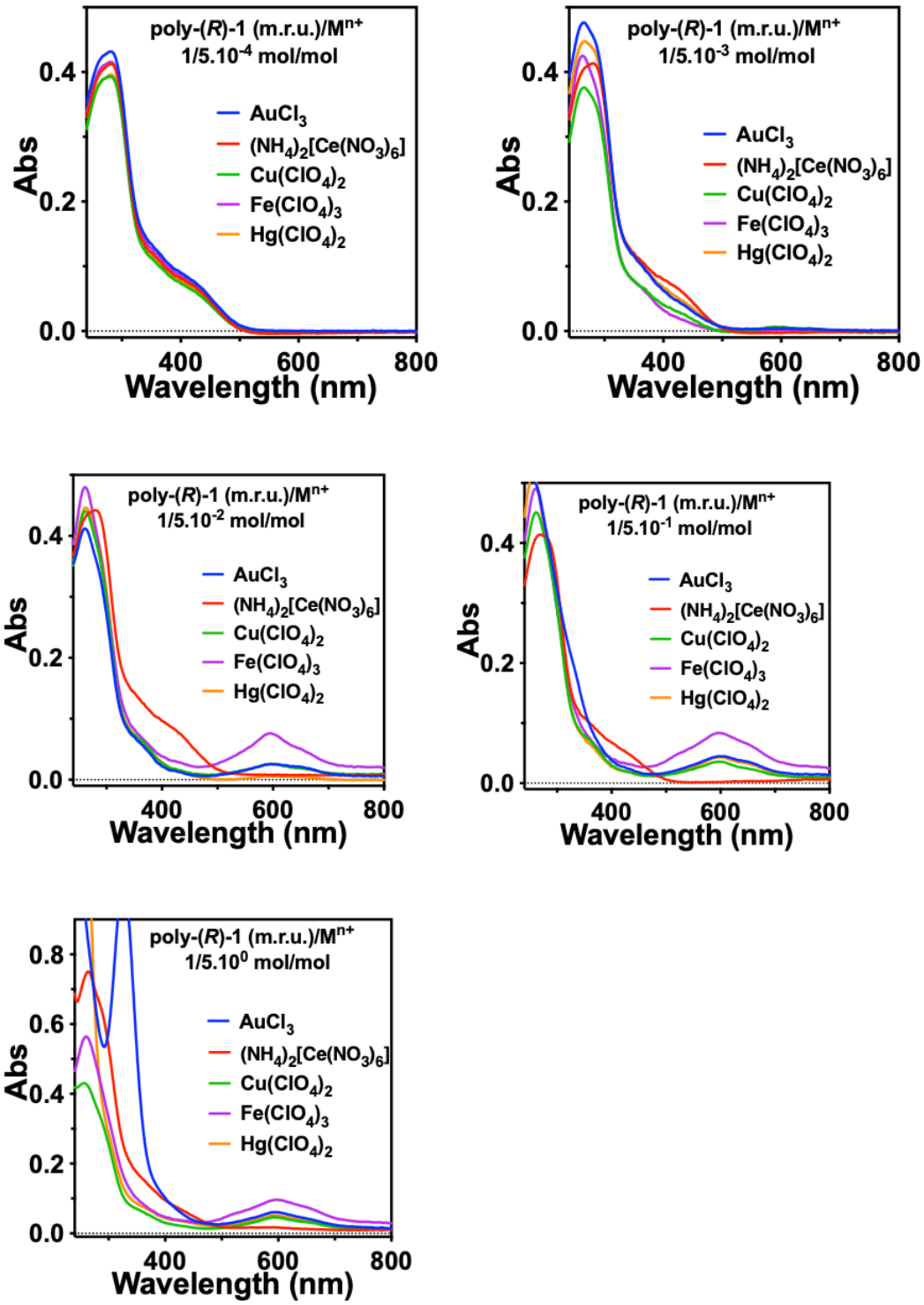


Figure S35. UV-Vis of poly-(*R*)-**1** (0.1 mg·mL^{-1}) in THF in presence of different amounts of $Cu(ClO_4)_2$, $Fe(ClO_4)_3$, $Hg(ClO_4)_2$, and $AuCl_3$ (10 mg·mL^{-1} and 1.0 mg·mL^{-1} THF) or $(NH_4)_2[Ce(NO_3)_6]$ (10 mg·mL^{-1} and 1 mg·mL^{-1} MeOH).

USC UNIVERSIDADE DE SANTIAGO DE COMPOSTELA

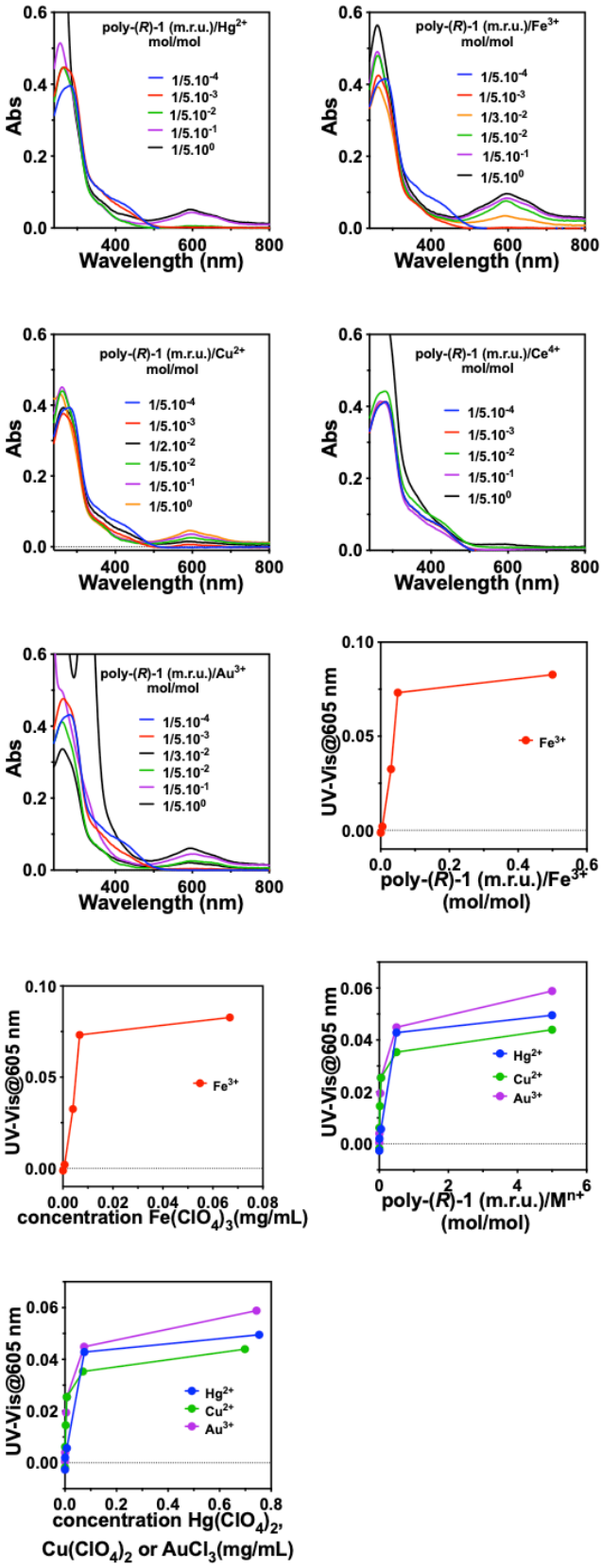


Figure S36. UV-Vis and response of the radical band at 605 nm of poly-(*R*)-**1** (0.1 mg·mL^{-1}) in THF in presence of different equivalents of $Cu(ClO_4)_2$, $Fe(ClO_4)_3$, $Hg(ClO_4)_2$, and $AuCl_3$ (10 mg·mL^{-1} and 1 mg·mL^{-1} THF) or $(NH_4)_2[Ce(NO_3)_6]$ (10 mg·mL^{-1} and 1.0 mg·mL^{-1} MeOH).

5.2.10. UV-Vis studies of anilide-PPAs connection in presence of $Fe(ClO_4)_3$

CD studies and UV-Vis were performed with poly-(*R*)-**2** and poly-(*R*)-**3** (0.3 mg·mL^{-1}, THF or $CHCl_3$) using $Fe(ClO_4)_3$ which concentration was 10.0 mg·mL^{-1}.

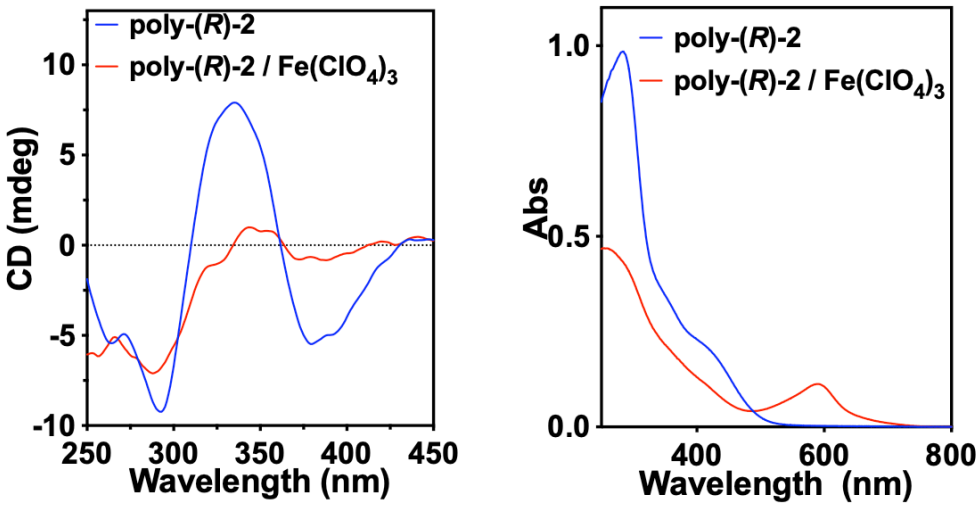


Figure S37. CD and UV-Vis experiments of poly-(*R*)-**2** (0.3 mg·mL^{-1}, THF) in presence of 0.5 equiv of Fe^{3+} (10 mg·mL^{-1}, THF).

USC UNIVERSIDADE DE SANTIAGO DE COMPOSTELA

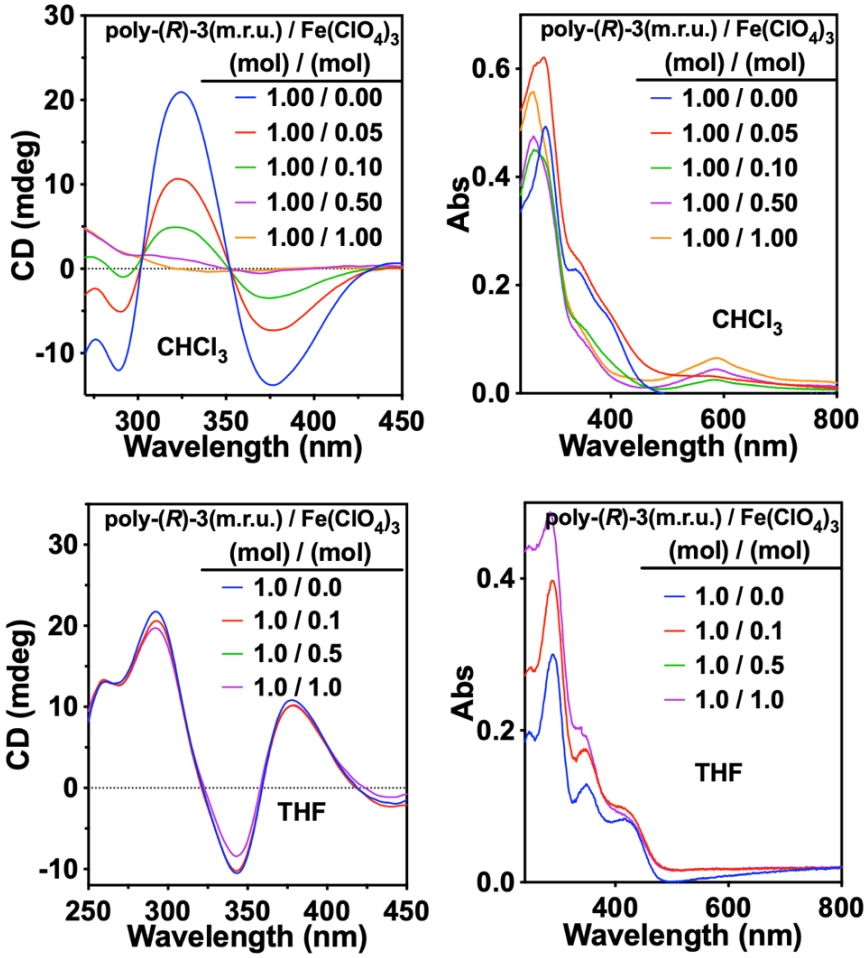


Figure S38. CD and UV-Vis experiments of poly-(*R*)-**3** (0.3 mg·mL^{-1}, $CHCl_3$ and THF) in presence of $Fe(ClO_4)_3$ (10 mg·mL^{-1}, THF).

5.2.11. CD and UV-Vis studies of benzamide-PPAs connection in presence of $Fe(ClO_4)_3$

CD studies and UV-Vis were performed with a poly-(*S*)-**4**, poly-(*S*)-**5**, and poly-(*S*)-**6** (0.3 mg·mL^{-1}, THF) using $Fe(ClO_4)_3$ which concentration was 10.0 mg·mL^{-1}.

USC UNIVERSIDADE DE SANTIAGO DE COMPOSTELA

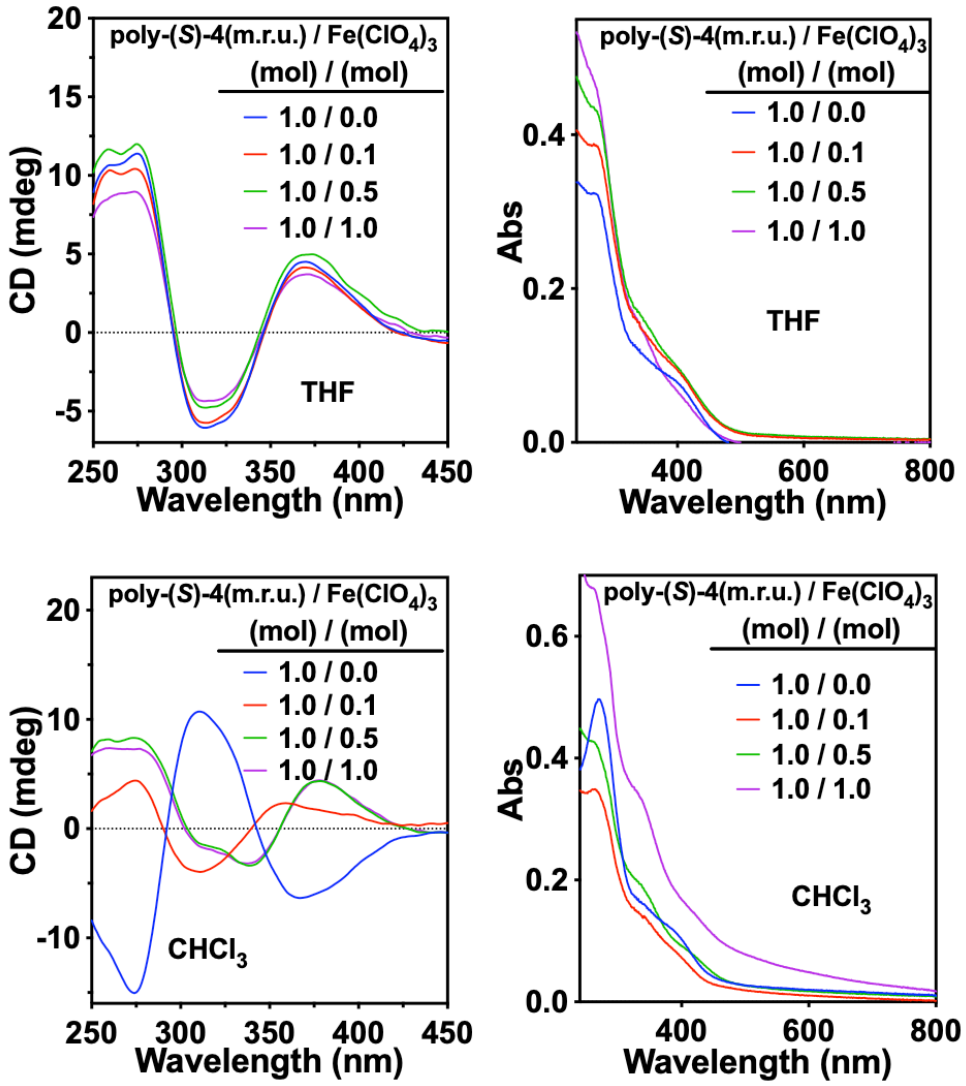


Figure S39. CD and UV-Vis experiments of poly-(*S*)-**4** (0.3 mg·mL^{-1}, THF and $CHCl_3$) in presence of $Fe(ClO_4)_3$ (10 mg·mL^{-1}, THF).

USC
UNIVERSIDADE DE SANTIAGO DE COMPOSTELA

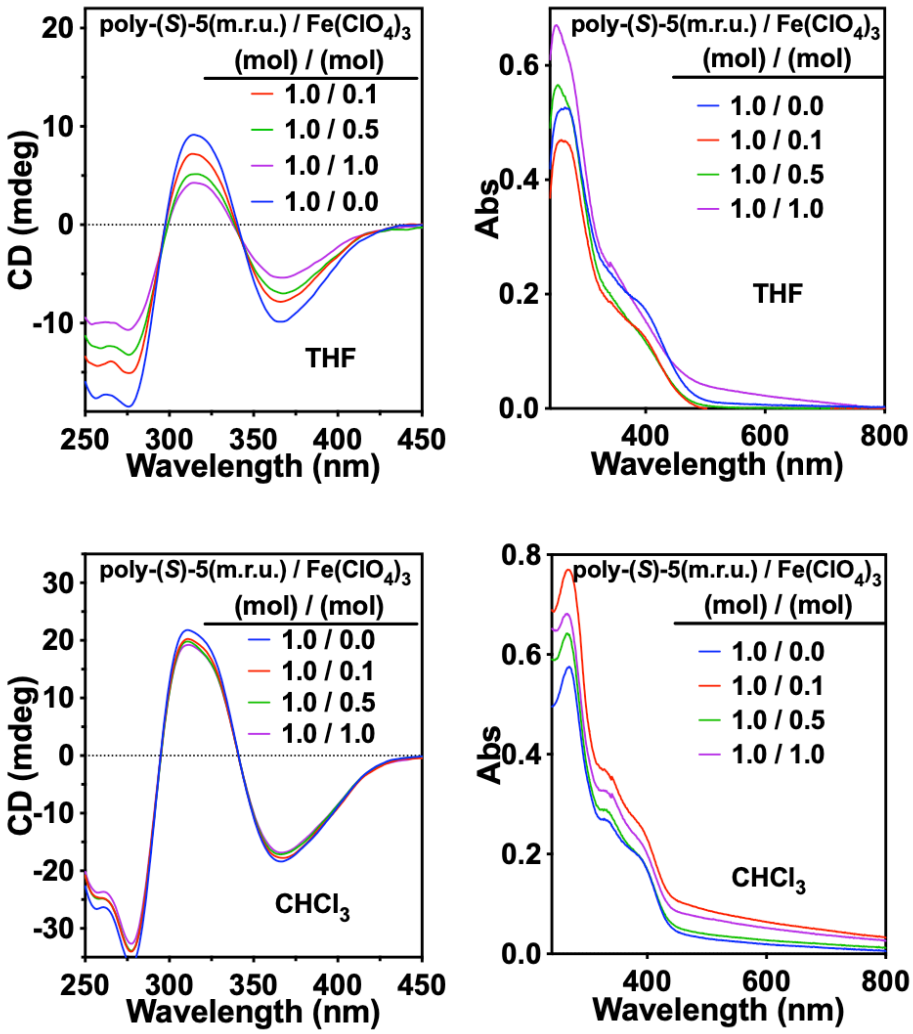


Figure S40. CD and UV-Vis experiments of poly-(*S*)-**5** (0.3 mg·mL^{-1}, THF and $CHCl_3$) in presence of $Fe(ClO_4)_3$ (10 mg·mL^{-1}, THF).

USC UNIVERSIDADE DE SANTIAGO DE COMPOSTELA

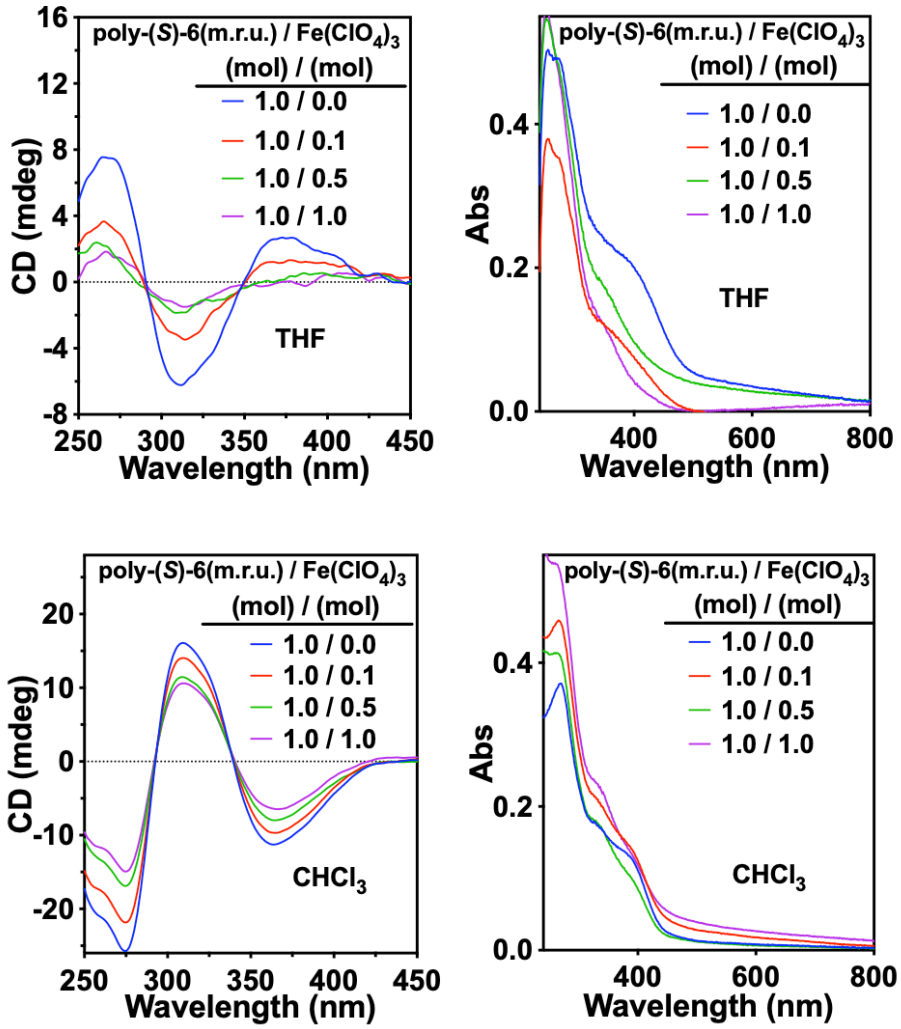


Figure S41. CD and UV-Vis experiments of poly-(*S*)-**6** (0.3 mg·mL^{-1}, THF and $CHCl_3$) in presence of $Fe(ClO_4)_3$ (10 mg·mL^{-1}, THF).

5.2.12. CD and UV-Vis studies of benzamide-PPAs connection in presence of $Fe(ClO_4)_3$

CD studies and UV-Vis were performed with of poly-(*S*)-**4** (0.3 mg·mL^{-1}, $CHCl_3$ and THF) using $Fe(ClO_4)_3$ which concentration was 10.0 mg·mL^{-1} in THF.

USC UNIVERSIDADE DE SANTIAGO DE COMPOSTELA

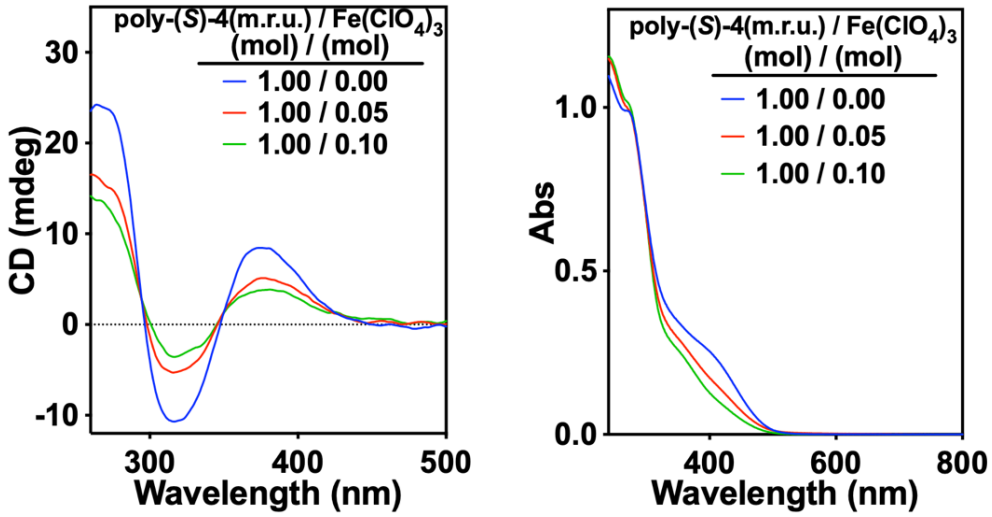


Figure S42. CD and UV-Vis studies of poly-(*S*)-**4** (0.3 mg·mL^{-1}, THF) in presence of $Fe(ClO_4)_3$ (10 mg·mL^{-1}, THF).

5.2.13. EPR studies of anilide and benzamide-PPAs connection

EPR experiments were carried out to study the presence of radicals in poly-(*R*)-**3**, poly-(*R*)-**5**, poly-(*S*)-**5**, poly-(*R*)-**7**, M-**1**, and (3 mg·mL^{-1}, THF) after addition of $Fe(ClO_4)_3$ (10 mg·mL^{-1}, THF).

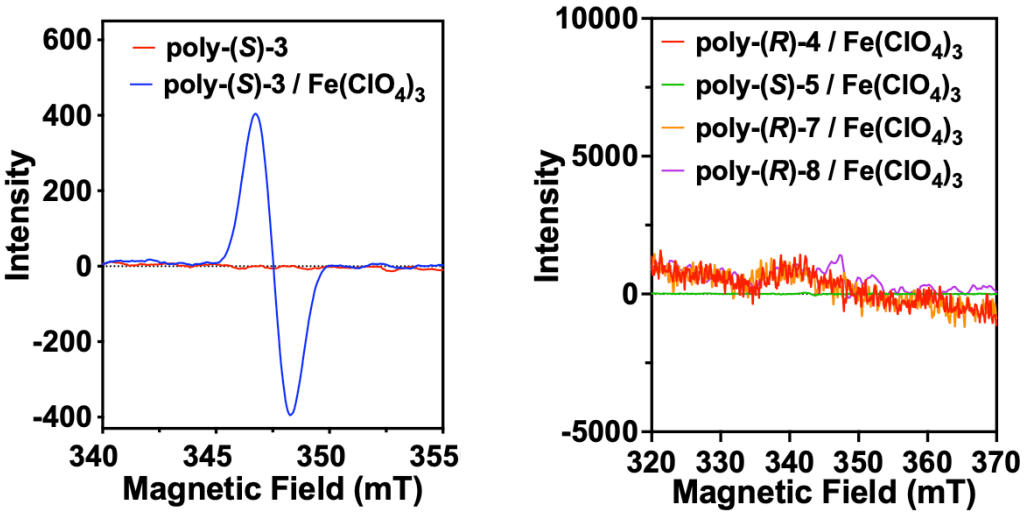


Figure S43. EPR experiments of M-**1**, poly-(*R*)-**3**, poly-(*R*)-**4**, poly-(*S*)-**5**, and poly-(*R*)-**7** (3.0 mg·mL^{-1}, THF) in presence of $Fe(ClO_4)_3$ (0.01 equiv, 10.0 mg·mL^{-1} in THF).

USC UNIVERSIDADE DE SANTIAGO DE COMPOSTELA

5.2.14. CD and UV-Vis studies of M-(*R*)-1 in presence of $Fe(ClO_4)_3$

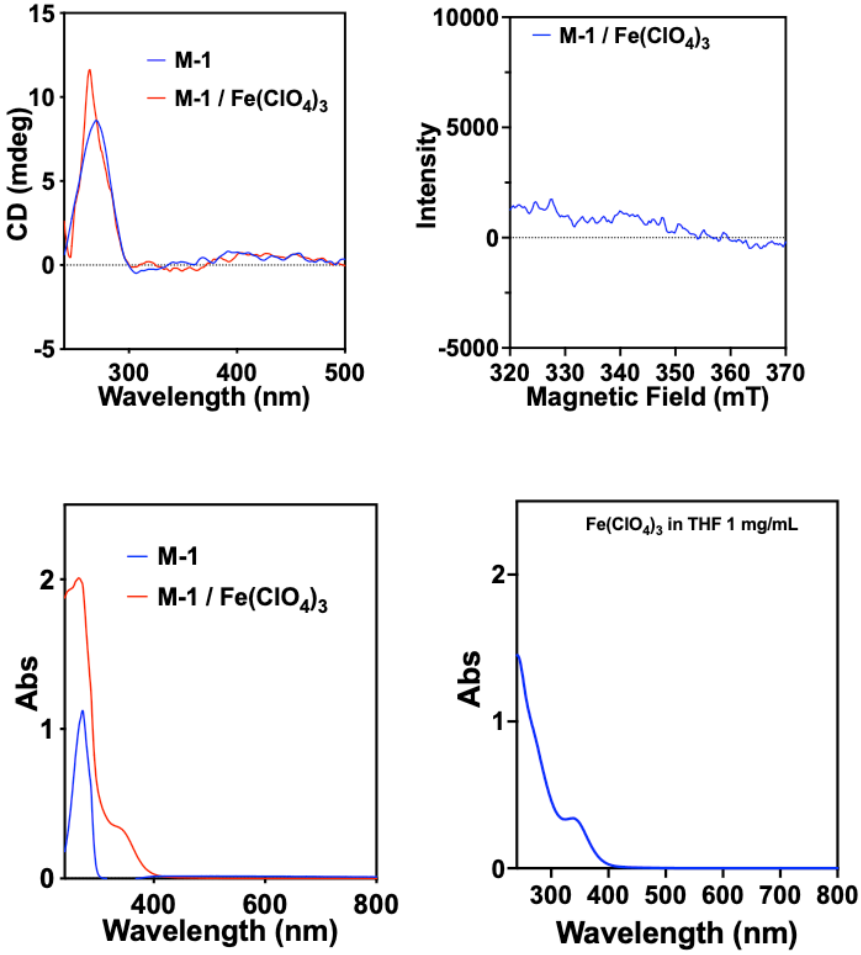


Figure S44. CD, UV-Vis studies of M-**1** (0.3 mg·mL^{-1}, THF) in presence of $Fe(ClO_4)_3$ (1 mg·mL^{-1}, THF). UV-Vis spectrum of $Fe(ClO_4)_3$ in THF. EPR studies of M-**1** (3.0 mg·mL^{-1}, THF) in presence of $Fe(ClO_4)_3$ (0.01 equiv, 10.0 mg·mL^{-1}, THF)

5.2.15. CD and UV-Vis studies of poly-(*R*)-7 in presence of $Fe(ClO_4)_3$

CD and UV-Vis studies of poly-(*R*)-**7** (0.1 mg·mL^{-1}, THF) were carried out in in presence of $Fe(ClO_4)_3$ (10 mg·mL^{-1}, THF).

USC UNIVERSIDADE DE SANTIAGO DE COMPOSTELA

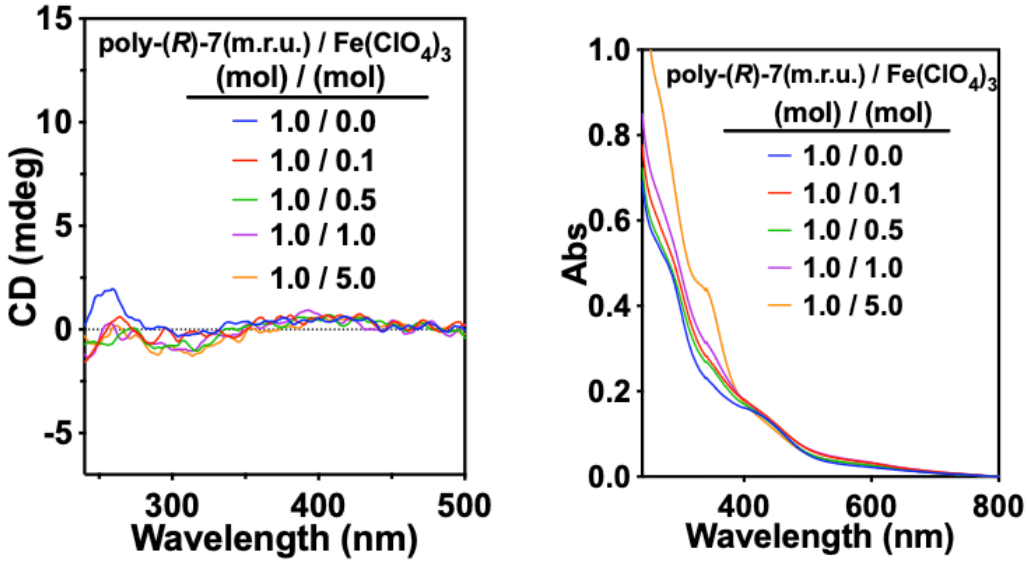


Figure S45. CD and UV-Vis studies of poly-(*R*)-**7** (0.1 mg·mL^{-1}, THF) in presence of different amounts of $Fe(ClO_4)_3$ (10 mg·mL^{-1}, THF).

5.2.16. IR experiments of poly-(*R*)-7 in presence of $Fe(ClO_4)_3$ salt

A solution of $Fe(ClO_4)_3$ (0.5 equiv, 10.0 mg·mL^{-1} in THF) was added to a solution of poly-(*R*)-**7** in THF (0.3 mg·mL^{-1}) and then the FT-IR spectra were registered. The experiments confirmed the coordination of Fe^{2+} and Fe^{3+} to the carbonyl groups in poly-(*R*)-**7**.

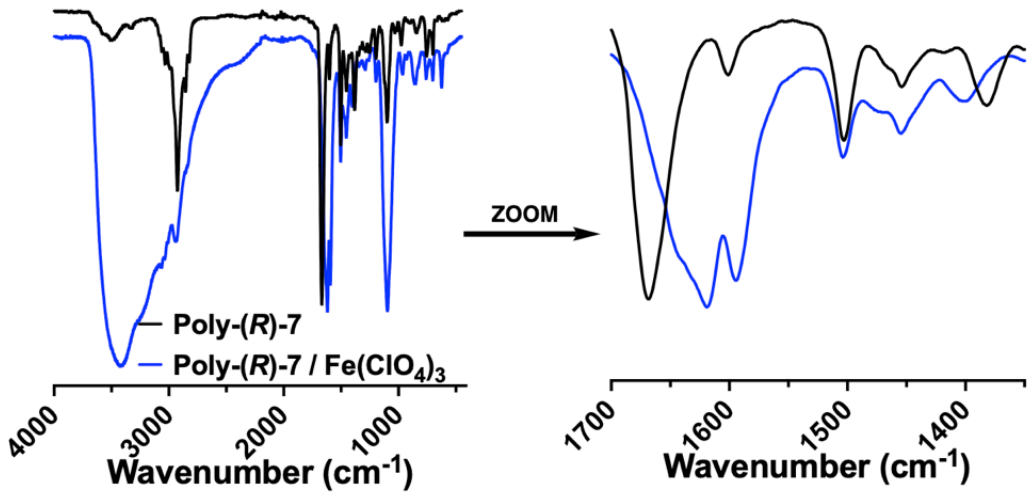


Figure S46. FT-IR spectra of poly-(*R*)-**7** and poly-(*R*)-**7**/$Fe(ClO_4)_3$.

USC UNIVERSIDADE DE SANTIAGO DE COMPOSTELA

5.2.17. UV-Vis studies of poly-(*R*)-1 in presence of different M^{2+}

UV-Vis were performed for poly-(*R*)-**1** (0.1 mg·mL^{-1}, THF) using $M(ClO_4)_2$ which concentration was 10.0 mg·mL^{-1}.

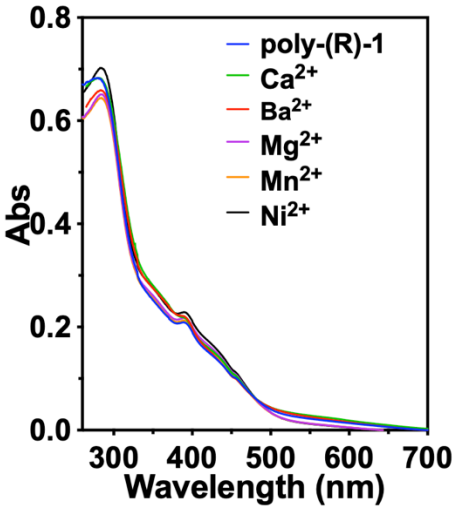


Figure S47. UV-Vis experiments of poly-(*R*)-**1** (0.1 mg·mL^{-1}, THF) in presence of 0.1 equiv of $M(ClO_4)_2$ (10 mg·mL^{-1}, THF).

5.2.18. UV-Vis studies of poly-(*R*)-1 and poly-(*R*)-3 titration with $Fe(ClO_4)_3$

UV-Vis were performed for poly-(*R*)-**1** and poly-(*R*)-**3** (0.1 mg·mL^{-1}, $CHCl_3$) using $Fe(ClO_4)_3$ which concentration was 1.0 mg·mL^{-1} in THF.

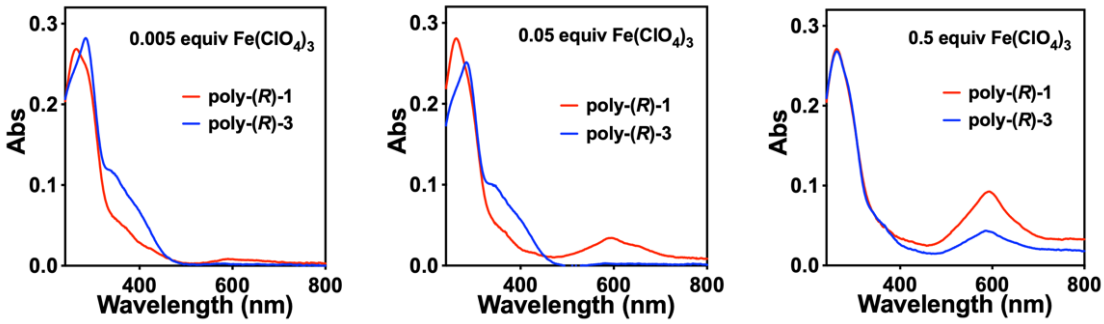


Figure S48. UV-Vis experiments of poly-(*R*)-**1** and poly-(*R*)-**3** (0.1 mg·mL^{-1}, $CHCl_3$) in presence of $Fe(ClO_4)_3$ (1.0 mg·mL^{-1}, THF).

USC
UNIVERSIDADE DE SANTIAGO DE COMPOSTELA

5.2.19. UV-Vis studies of poly-(*R*)-1 in presence of $Fe(ClO_4)_3$.

UV-Vis were performed for poly-(*R*)-1 (0.1 mg·mL^{-1}) using 0.01 equiv of $Fe(ClO_4)_3$ (1.0 mg·mL^{-1}, THF) in mixtures of $CHCl_3$/THF (v/v).

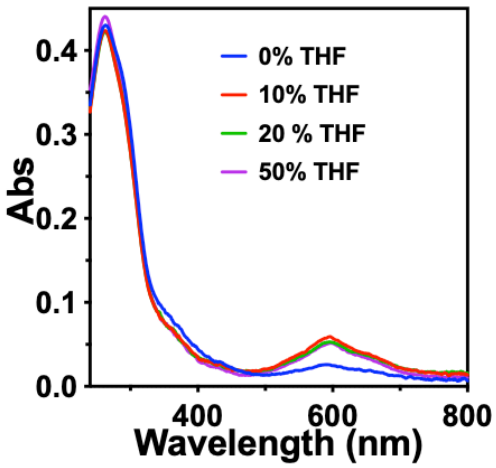


Figure S49. UV-Vis experiments of poly-(*R*)-**1** (0.1 mg·mL^{-1}, THF/$CHCl_3$) in presence of 0.01 equiv of $Fe(ClO_4)_3$ (1.0 mg·mL^{-1}, THF).

5.2.20. Density functional theory-based computations

Gaussian-16 (G16RevC.01)[413] was used to compute n=8 oligomers of poly-(*R*)-**1** with *trans*-configuration of double bonds, and the same calculation were carried out for a n=9 oligomer of poly-(*R*)-**1** with a *cis*-configuration of double bonds. The restricted closed-shell and unrestricted open-shell B3LYP[415] functionals together with the basis set 6-31G(d)[127] were used to perform the DFT calculations.[547] Geometry optimizations and frequency calculations of the oligomers were performed with charge +1 and doublet multiplicity in the unrestricted open-shell calculations while charge 0 and singlet multiplicity was used the restricted closed-shell calculations without imaginary frequencies and spin contamination. TD-DFT calculations were performed using the cam-b3lyp functional with the 6-31G(d) basis set. UV-vis spectra were simulated with 150 excitations, unrestricted calculations have 0.33 ev of peak half-width at half height and the restricted one for the non-radical structure has 0.20 ev.

For the EPR/ESR calculations, orca 4.1.2[548] in the UKS B3LYP with the EPR-II basis set[549] were performed for the g tensor with the absence of the A-tensor (hyperfine coupling). Prop files were processed in easyspin 5.2.35[550] These approximations were

USC DE COMPOSTELA

calculated with the garlic function, which computes isotropic and fast-motional EPR spectra of radicals in solution. The simulation was performed at 298 K, Lorentzian linewidths of 1mT and the experimental field sweep frequencies of 9.790 GHz.

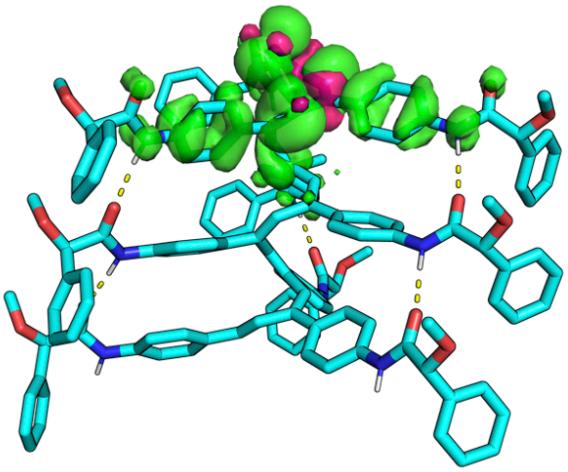


Figure S50. Calculated Spin Density of the cation radical *cis-cisoidal* structure without delocalization of the radical.

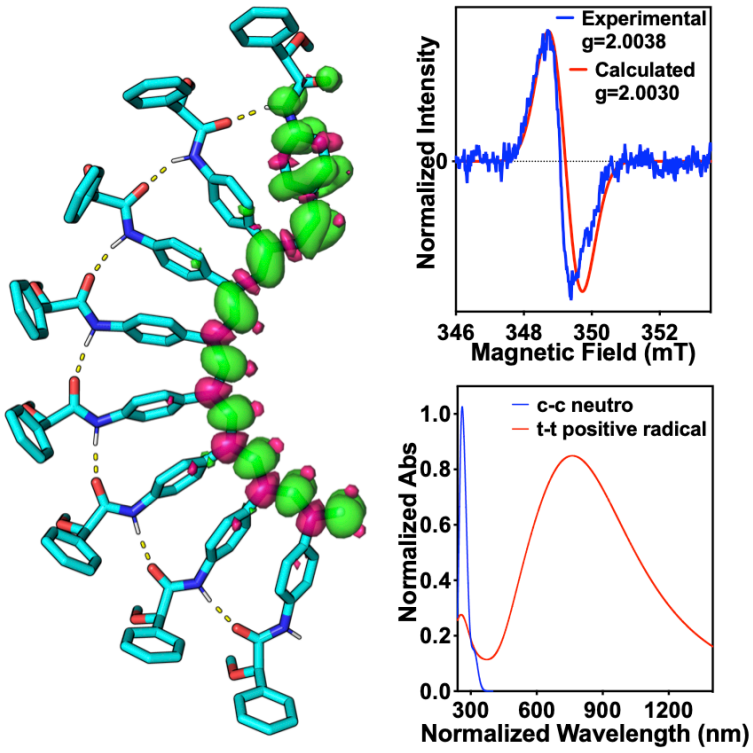


Figure S51. Calculated Spin density, EPR and UV-Vis (compared with neutral *cis-cisoidal* structure) of the cation radical *trans-transoidal* structure.

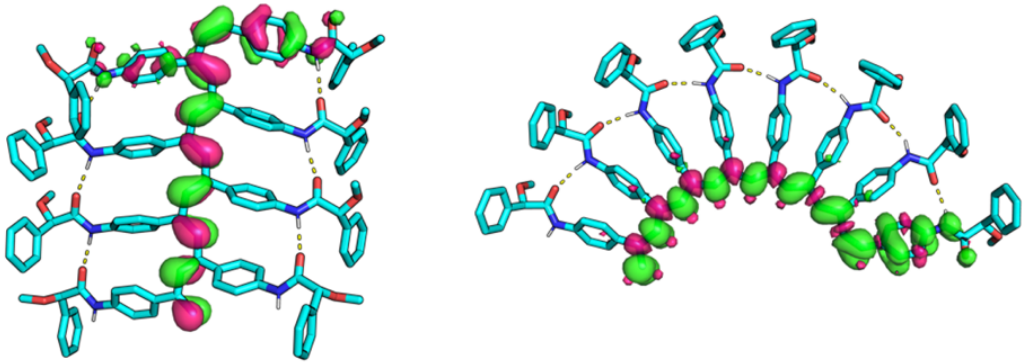


Figure S52. Calculated HOMO(/SOMO) of the radical cation *trans-cisoidal* and *trans-transoidal* configuration of the double bonds.

5.2.21. Calculation of the limits of detection

The limit of detection (LOD) for the radical formation in poly-(*R*)-**1** (100 mg/L, THF) was calculated in presence of various oxidants: $Cu(ClO_4)_2$, $Fe(ClO_4)_3$, $Hg(ClO_4)_2$, and $AuCl_3$. First, standard deviations of the residuals ($SD_{residuals}$) and the intercept ($SD_{intercept}$) using equation (S4) and equation (S5) were calculated.

$$SD_{residuals} = \sqrt{\frac{\sum_{i=1}^{n}(y_i - \hat{y}_i)^2}{n-2}} \quad \textbf{(S4)}$$

$$SD_{intercept} = SD_{residuals} * \sqrt{\frac{\sum_{i=1}^{n} x_i{}^2}{n * \sum_{i=1}^{n}(x_i - \bar{x})^2}} \quad \textbf{(S5)}$$

Where y_i and $\hat{y}_i$ are the absorbance in UV-Vis at 609 nm corresponding to radical formation in the PPA and predicted absorbance, x_i represents the concentration of oxidants in (mg/L), $\bar{x}$ is the mean of x_i, and n is the number of data points. The resulting values for $SD_{residuals}$and $SD_{intercept}$, along with the slopes (m) obtained from the linear regression, are summarized in Table S1.

USC UNIVERSIDADE DE SANTIAGO DE COMPOSTELA

For the linear regression, only the data from the initial concentrations (Figure S36) were used, where the UV-Vis absorbance of the radical polymer at 605 nm showed a linear response corresponding to radical formation. At higher oxidant concentrations, the polymer became saturated, and the absorbance no longer increased, deviating from linearity. The resulting fits, limited to the linear region, are displayed in Figure S53.

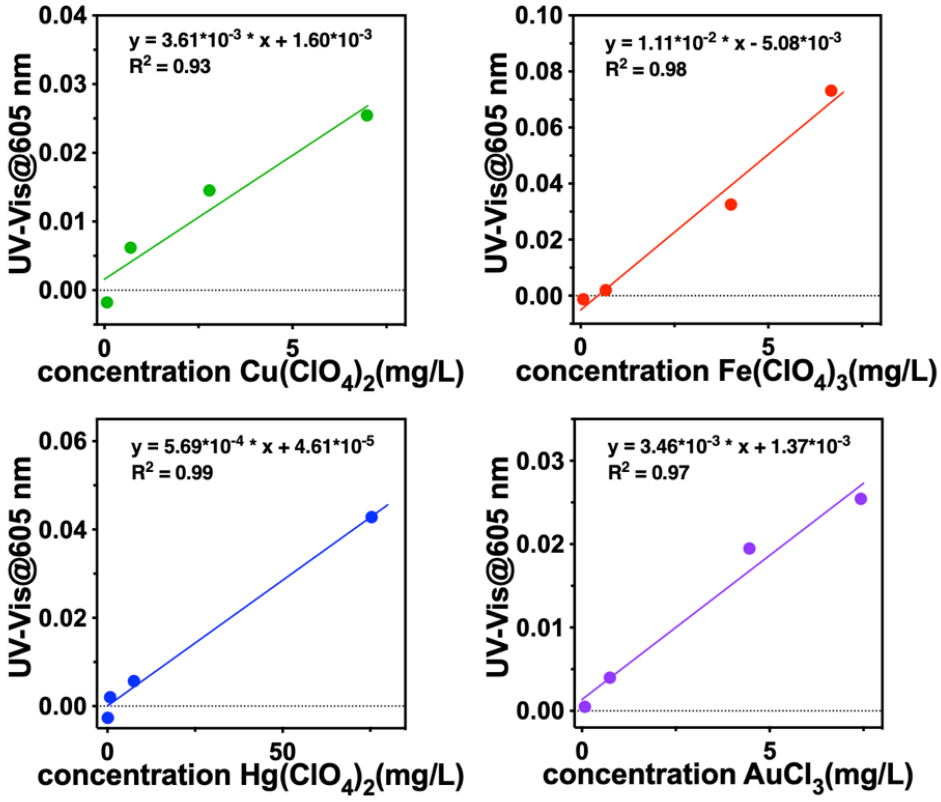


Figure S53. UV-Vis absorbance at 605 nm of the polymer (0.1 mg/mL in THF) at varying concentrations of $Cu(ClO_4)_2$, $Fe(ClO_4)_3$, $Hg(ClO_4)_2$, and $AuCl_3$, with linear fits for the initial range, including the equation and R^2. Saturation occurs at higher concentrations

Table S1. Regression Parameters and Standard Deviations.

Oxidant	$SD_{residuals}$ (Abs)	$SD_{intercept}$, (Abs)	m (Abs L/mg)
$Cu(ClO_4)_2$	$3.71x10^{-3}$	$2.59x10^{-3}$	$3.61x10^{-3}$
$Fe(ClO_4)_3$	$6.07x10^{-3}$	$4.44x10^{-3}$	$1.11x10^{-2}$
$Hg(ClO_4)_2$	$2.42x10^{-3}$	$1.45x10^{-3}$	$5.69x10^{-4}$
$AuCl_3$	$2.36x10^{-3}$	$1.72x10^{-3}$	$3.46x10^{-3}$

USC UNIVERSIDADE DE SANTIAGO DE COMPOSTELA

Using these values, the LOD was calculated according to equation (S6).

$$LOD = \frac{SD}{m} \quad \textbf{(S6)}$$

Where SD is $SD_{intercept}$, and m is the slope. The results, expressed in both ppm (m/v) (mg/L) and ppm (m/m) (mg/kg) using the density of THF (0.888 kg/L), are presented in Table S2.

Table S2. Calculated Limits of Detection (LOD).

Oxidant	$LOD_{intercept}$ (m/v) (mg/L)	$LOD_{intercept}$ (m/m) (mg/kg)
$Cu(ClO_4)_2$	2.37	2.67
$Fe(ClO_4)_3$	1.32	1.49
$Hg(ClO_4)_2$	8.41	9.47
$AuCl_3$	1.65	1.85

5.2.22. UV-Vis studies of poly-(*R*)-1 in presence of H_2O_2

A solution of $Fe(ClO_4)_3$ (0.5 equiv, 10.0 mg·mL^{-1} in THF) was added to a solution of poly-(*R*)-**7** in THF (0.3 mg·mL^{-1}) and then the FT-IR spectra were registered. The experiments confirmed the coordination of Fe^{2+} and Fe^{3+} to the carbonyl groups in poly-(*R*)-**7**.

USC UNIVERSIDADE DE SANTIAGO DE COMPOSTELA

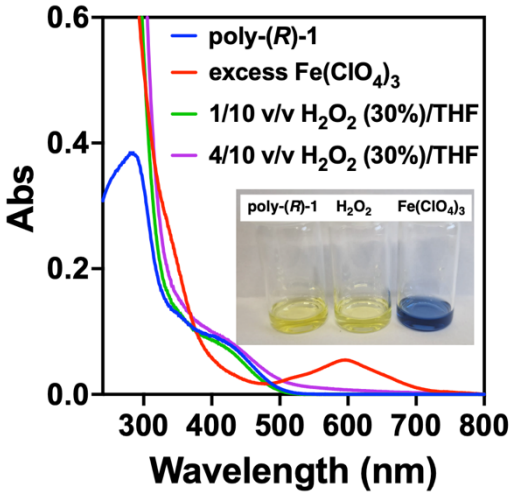


Figure S54. UV-Vis absorbance of poly-(*R*)-**1** in 1 mL THF (0.1 mg/mL), in the presence of excess of $Fe(ClO_4)_3$, and excess of H_2O_2 (30%).

5.2.23. Time Dependent UV-Vis Studies

Time dependent (TD) UV-Vis studies were carried out for a THF solution of poly-(*R*)-**1** (0.1 mg/mL) after addition of an oxidizing metal salt. Thus, variations in the UV-Vis band at 600 nm corresponding to the organic radical were plotted versus time after injection of 0.5 and 0.05 equiv. of $Fe(ClO_4)_3$ (Figure 30a), $Cu(ClO_4)_2$ (Figure 30b), $Hg(ClO_4)_2$ (Figure 30c), and $AuCl_3$ (Figure 30d). In all cases the presence of a new UV band at 600 nm is observed once the metal salt is added. However, from these studies we observed that poly-(*R*)-**1** shows the best response towards Fe^{3+}, where the UV band is one order of magnitude higher than when the other metal ions are used. In case of Cu^{2+}, Hg^{2+}, and Au^{3+} the UV band at 600 nm corresponding to the organic radical increases with time but does not reach the value obtained with Fe^{3+}.

USC UNIVERSIDADE DE SANTIAGO DE COMPOSTELA

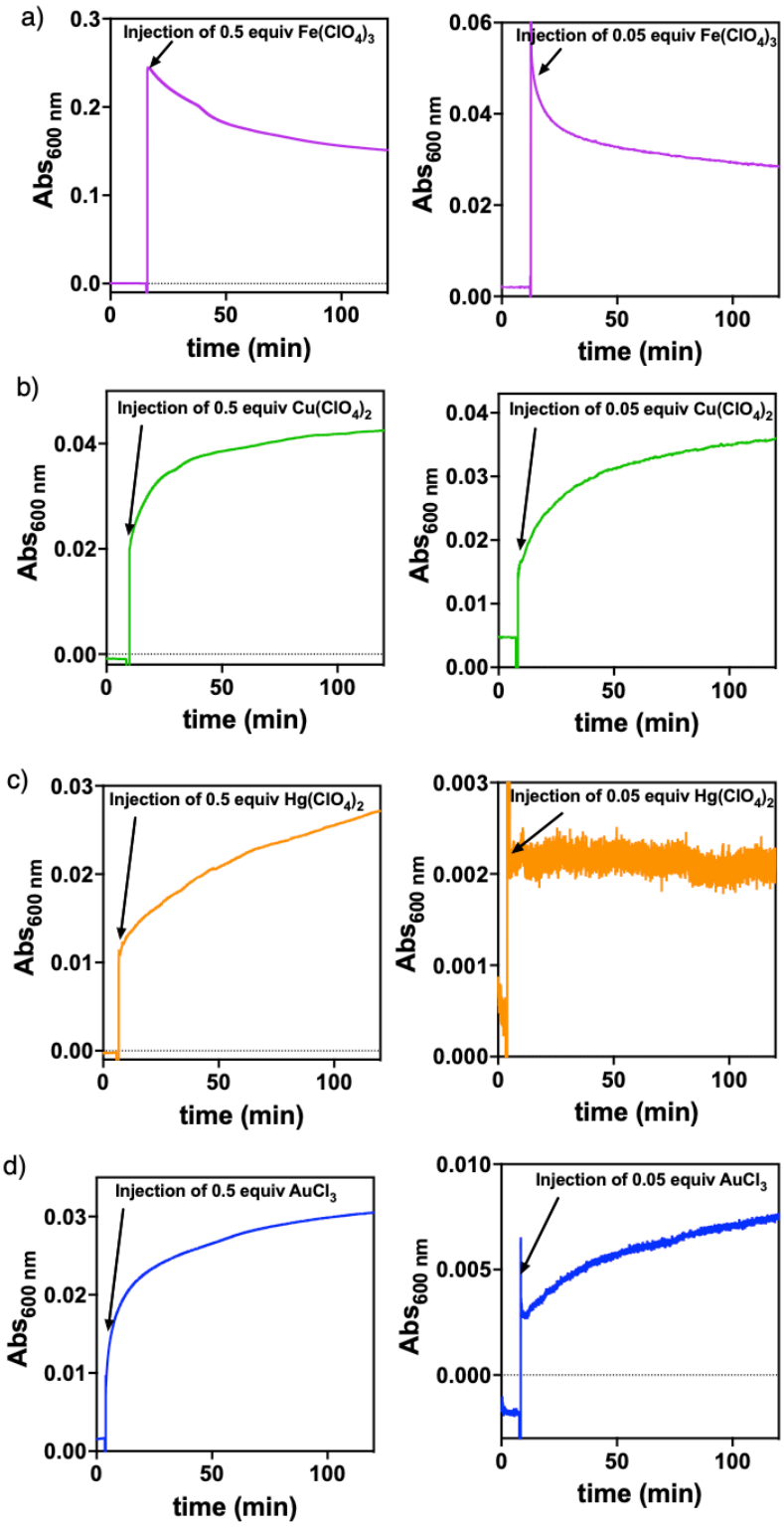


Figure S55. TD-UV-Vis studies of a THF solution of poly-(*R*)-**1** (0.1 mg/mL) in the presence of 0.5 and 0.05 equiv of (a) $Fe(ClO_4)_3$, (b) $Cu(ClO_4)_2$, (c) $Hg(ClO_4)_2$, and (d) $AuCl_3$.

USC UNIVERSIDADE DE SANTIAGO DE COMPOSTELA

5.3. Experimental Section and Methodology Chapter 3.3

5.3.1. Experimental Procedures

Commercially available chemicals have been used as delivered. Solvents were purchased as reagent grade and distilled if necessary. Anhydrous solvents were either purchased as ultra-dry solvent from Acros Organics® or received from solvent purification system. For the coupling and polymerization reactions, dry THF was obtained from MBRAUN SPS 800 solvent purification system. The reactions were done in inert atmospheres.

Column chromatography was performed with silica gel 230-400 mesh (Merck).

Thin-layer chromatography of silica 60F254 Merck was visualized in UV at a wavelength of 254 nm and by heat with Hanessian.

Size exclusion chromatography (SEC/GPC) studies were performed on Alliance 2695 HPLC System (Waters) liquid chromatography system equipped with a UV 2489 detector (Waters). The samples were eluted by three Phenogel columns connected to each other with stationary phases of 103, 104 and 105 Amstrong and packed with a solid support of a cross-linked styrene and p-divinylbenzene copolymer.

The average molecular weights (M_n and M_w) of all polymers were estimated by GPC with THF as eluent at flow rate 1.0 mL/min at concentration 0.5 mg/mL using narrow polystyrene standards (PSS) as calibrants.

The UV/Vis absorption spectra were acquired in the Jasco V-730 spectrophotometer in the range of wavelengths from 240 nm to 500 nm. All samples were prepared at a fixed concentration of 0.3 mg polymer/mL solvent inside quartz glass cuvettes with a light path of 1 mm.

The CD spectra were acquired in the Jasco 720 spectrophotometer in the range of wavelengths from 240 nm to 500 nm. All samples were prepared at a fixed concentration of 0.3 mg polymer/mL solvent inside quartz glass cuvettes with a light path of 1 mm.

The ^{1}H-NMR, ^{13}C-NMR spectra were obtained in a Varian Mercury 300 MHz spectrometer, using CDCl3 solvent. Normal and quantitative ^{13}C-NMR using inverse-gated decoupling of polymers were obtained in a Bruker Avance DRX-500.

USC UNIVERSIDADE DE SANTIAGO DE COMPOSTELA

The IR spectra were obtained using the FT-IR PerkinElmer Spectrum Two equipped with the UATR addon.

5.3.2. Monomers and polymers

For preparation and characterization of monomers (*S*)-**1**, (*R*)-**1**, (*S*)-**2**, and (*R*)-**2** see below.

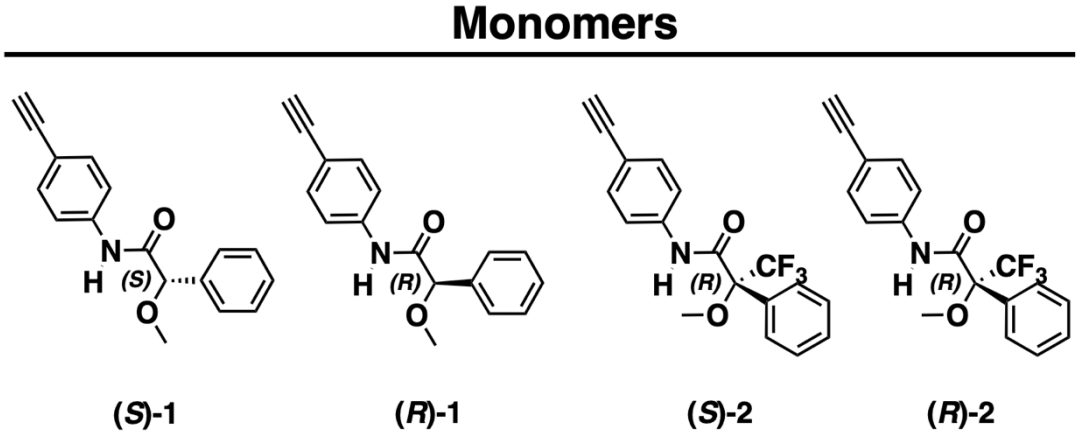
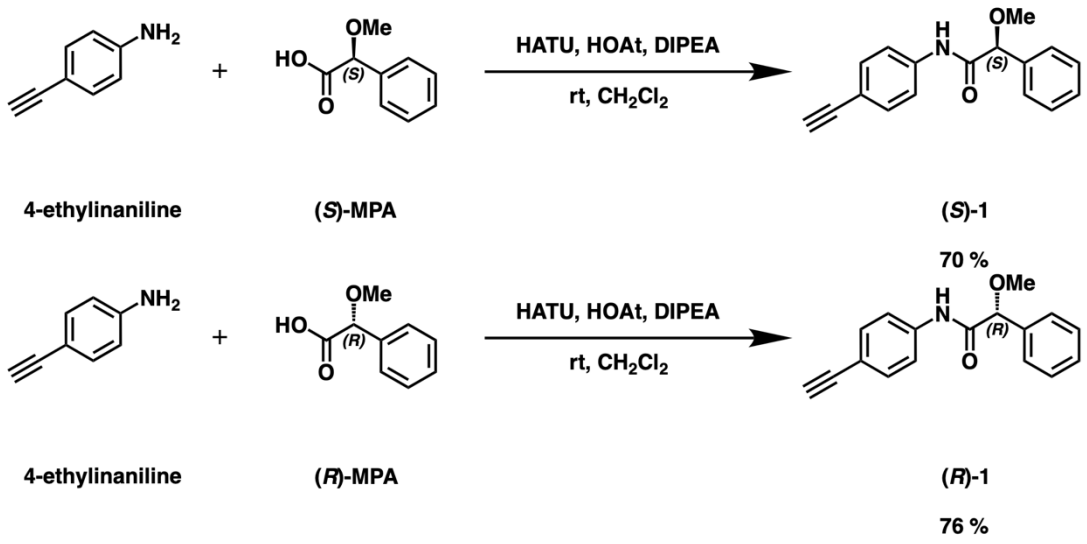


Figure S56. Structure of the monomers.

USC UNIVERSIDADE DE SANTIAGO DE COMPOSTELA

5.3.3. Synthesis monomers (*S*)-1 and (*R*)-1



(2-(7-Aza-1H-benzotriazole-1-yl)-1,1,3,4-tetramethyluronium hexafluorophosphate) (HATU, 2.75 g, 7.22 mmol, 1.20 equiv), 1-hydroxy-7-azabenzotriazole (0.98 g, 7.22 mmol, 1.20 equiv), (*S*)-(+)- or (*R*)-(-)-methoxyphenylacetic acid (1.00 g, 6.02 mmol, 1.00 equiv.) and diisopropyltriethylamine (DIPEA, 0.63 mL, 3.61 mmol, 1.20 equiv) were dissolved in 30 mL of dry CH_2Cl_2, and the mixture was stirred for 10 min. to activate the acid. Then, 4-ethynylaniline (0.85 g, 7.22 mmol, 1.20 equiv) was added and the reaction mixture was stirred overnight. Then, the organic solution was washed with HCl 1M, a saturated solution of $Na(HCO_3)$ and a saturated solution of NaCl. The combined organic layers were dried over anhydrous Na_2SO_4, filtered and the solvent was evaporated at reduced pressure. The crude product was chromatographed on silica gel with hexane/ethyl acetate (8/2) as eluent [1.11 g (*S*)-**1** and 1.21 g (*R*)-**1**], 70% and 76% yield respectively of pure products.

Spectroscopic data:

$[\alpha]_D^{20}$ = +15 (c = 1.3 mg/mL, $CHCl_3$, (*S*)-**1**).

$[\alpha]_D^{20}$ = -15 (c = 1.2 mg/mL, $CHCl_3$, (*R*)-**1**).

^{1}H-NMR (300 MHz, $CDCl_3$) δ_H (ppm): 8.64 (s, 1H, -NH-, amide), 7.58 (d, 2H, -CH=, ortho to amide), 7.43 (m, 5H, -CH=, phenyl), 7.38 (d, 2H, -CH=, meta to amide), 4.74 (s, 1H, Hydrogen in α to the amide), 3.44 (s, 3H, -OCH3), 3.06 (s, 1H, HC≡C-).

^{13}C-NMR (75 MHz, $CDCl_3$) δ_C (ppm): 57.3, 76,9, 83.4, 83.8, 117.8, 119.3, 127.1, 128.7, 133.0, 136.4, 137.8, 168.6.

USC UNIVERSITAT DE SANTIAGO DE COMPOSTELA

HRMS (ESI) m/z calcd. for (*S*)-**1** $C_{17}H_{15}NO_2$ $[M+H]^+$: 266.1176, found: 266.1176

HRMS (ESI) m/z calcd. for (*R*)-**1** $C_{17}H_{15}NO_2$ $[M+H]^+$: 266.1176, found: 266.1179

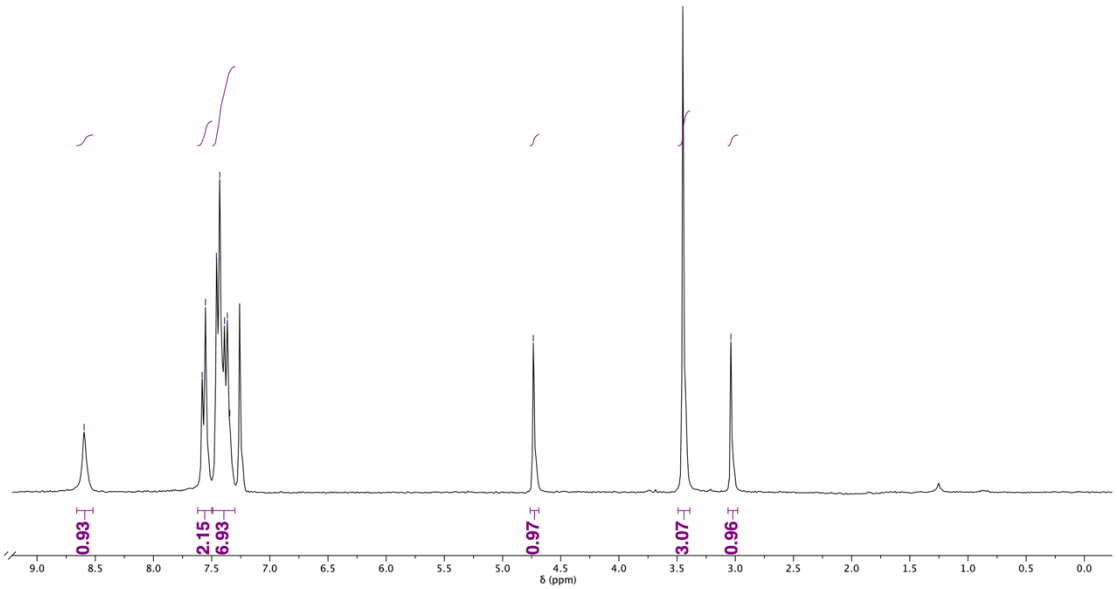


Figure S57. ^{1}H-NMR spectrum of (*S*)-**1** ($CDCl_3$, 300 MHz).

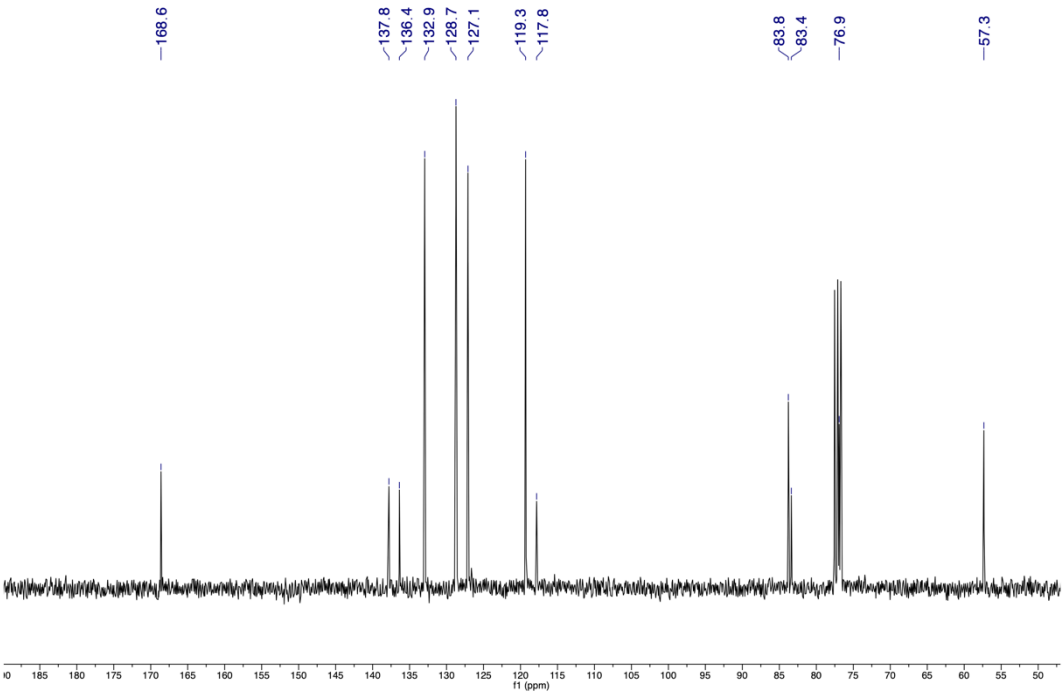


Figure S58. ^{13}C-NMR spectrum of (*S*)-**1** ($CDCl_3$, 75 MHz).

USC UNIVERSIDADE DE SANTIAGO DE COMPOSTELA

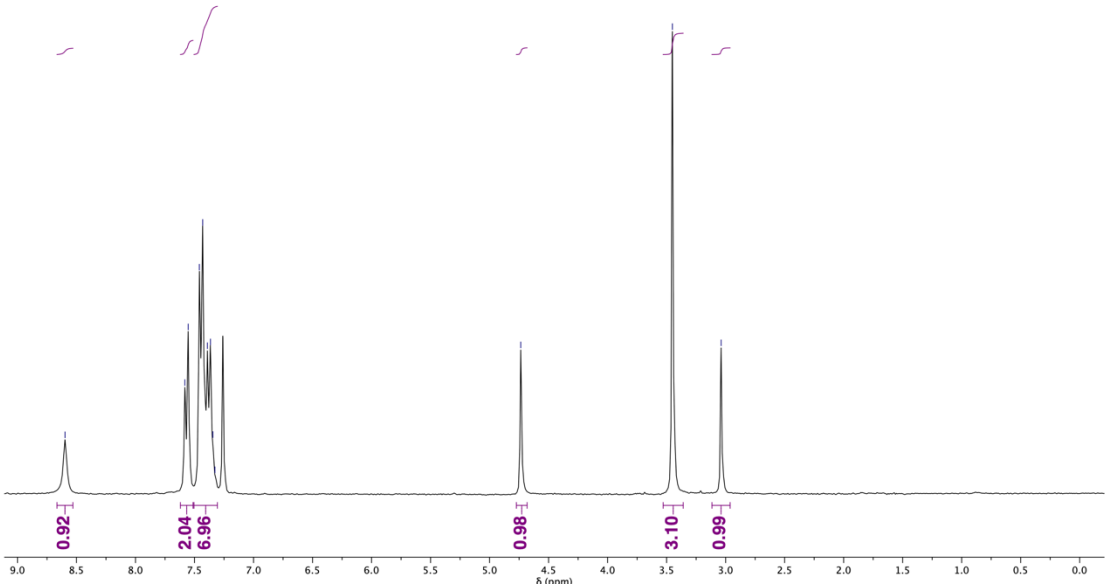


Figure S59. ^{1}H-NMR spectrum of (*R*)-**1** ($CDCl_3$, 300 MHz).

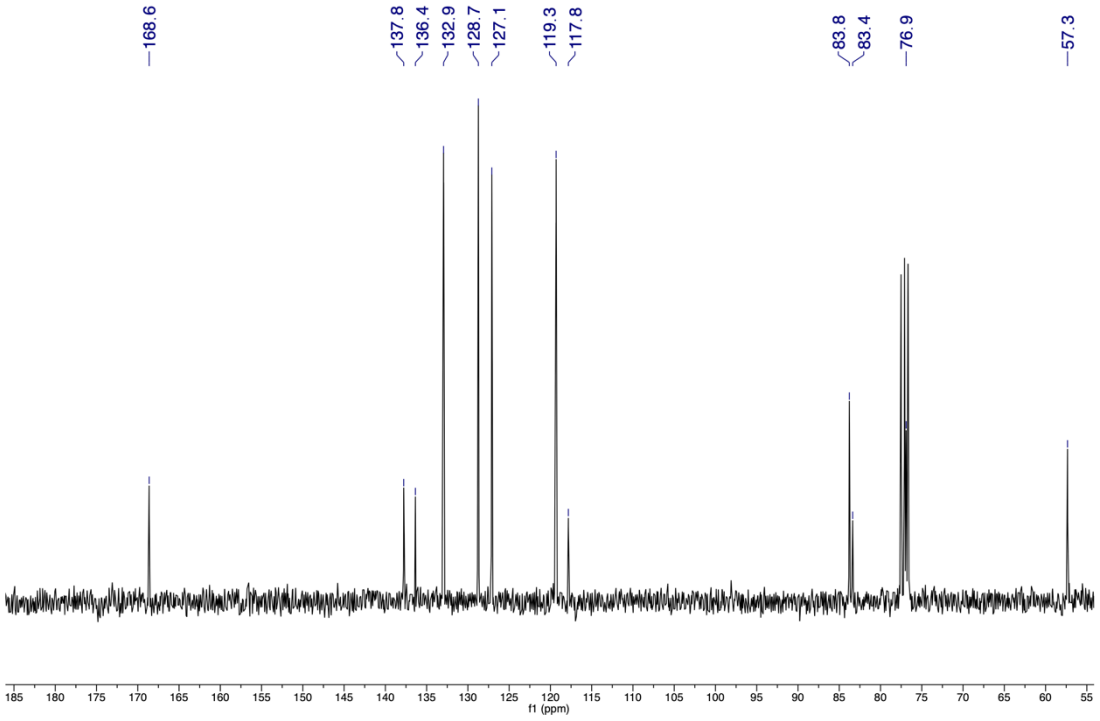
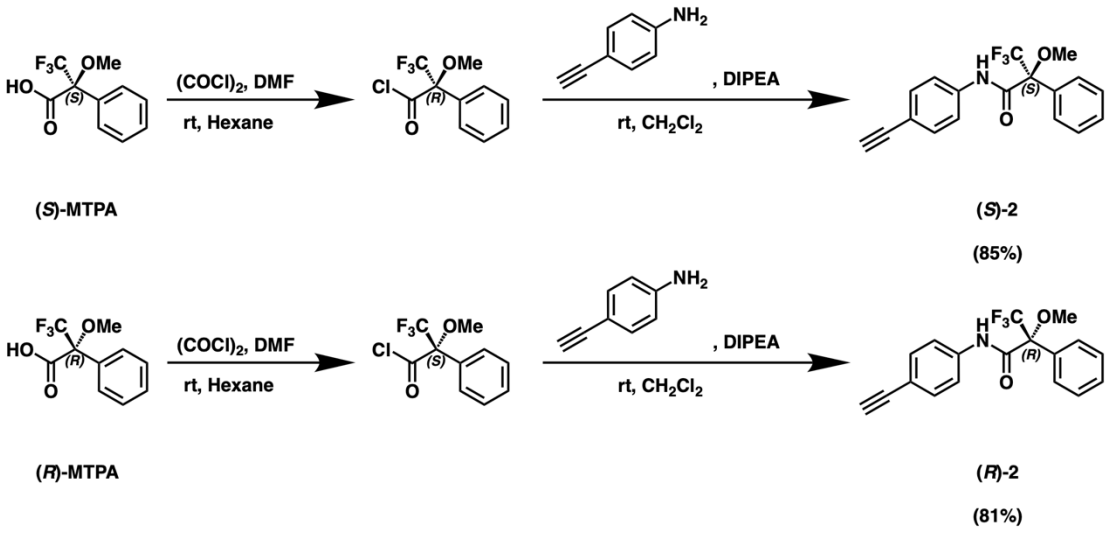


Figure S60. ^{13}C-NMR spectrum of (*R*)-**1** ($CDCl_3$, 75 MHz).

USC
UNIVERSIDADE DE SANTIAGO DE COMPOSTELA

5.3.4. Synthesis of monomer (*S*)-2 and (*R*)-2



Oxalyl chloride (2.50 mL, 29.5 mmol, 6.83 equiv) was added dropwise to a solution of (*S*)-(-)- or (*R*)-(+)-methoxy (trifluoromethyl) phenylacetic acid 1.00 g, 4.27 mmol, 1.00 equiv) in dry hexane and DMF (0.33 mL, 4.27 mmol, 1.00 equiv) at 0 ºC under an Ar atm. After 4 h stirring at rt, the reaction mixture was filtered and the solution obtained dried under vacuum to give the acetyl chloride as a colorless oil.

The (*R*)-(+)-methoxy (trifluoromethyl) phenylacetic acid obtained, was dissolved in CH2Cl2 (40.0 mL) and diisopropyltriethylamine (DIPEA, 1.19 mL, 6.83 mmol, 1.60 equiv) and 4-ethynilaniline (0.50 g, 4.27 mmol, 1 equiv) were added to the solution. The reaction mixture was stirred at rt overnight. The residue was diluted with CH_2Cl_2 and the organic solution was washed with HCl 1M, a saturated Na(HCO_3) aq. solution and a saturated NaCl aq. solution; then the organic layer was dried over anhydrous Na_2SO_4. After filtration, the solution was evaporated and the residue was chromatographed on silica gel with hexane/ethyl acetate (8/2) as the eluent [1.21 g (*S*)-**2** and 1.15 g (*R*)-**2**], yields 85 and 81% respectively of pure product.

Spectroscopic data:

$[\alpha]_D^{20}$ = -67 (c = 10 mg/mL, $CHCl_3$, (*S*)-**2**).

$[\alpha]_D^{20}$ = +68 (c = 10 mg/mL, $CHCl_3$, (*R*)-**2**).

^{1}H-NMR (300 MHz, $CDCl_3$) δ_H (ppm): 8.62 (s, 1H, -NH-, amide), 7.57 (d, 4H, -CH=, *ortho* and *meta* to amide), 7.45 (m, 5H, -CH=, phenyl), 3.50 (s, 3H, -OCH3), 3.06 (s, 1H, HC≡C-).

USC UNIVERSIDADE DE COMPOSTELA

^{13}C-NMR (75 MHz, $CDCl_3$) δ_C (ppm): 55.2, 77.3, 83.2, 118.5, 119.6, 127.7, 128.8, 129.8, 132.0, 133.0, 137.2, 164.5.

HRMS (ESI) m/z calcd. for (*S*)-**2** $C_{18}H_{14}F_3NO_2$ $[M+H]^+$: 334.1049, found: 334.1053

HRMS (ESI) m/z calcd. for (*R*)-**2** $C_{18}H_{14}F_3NO_2$ $[M+H]^+$: 334.1049, found: 334.1051

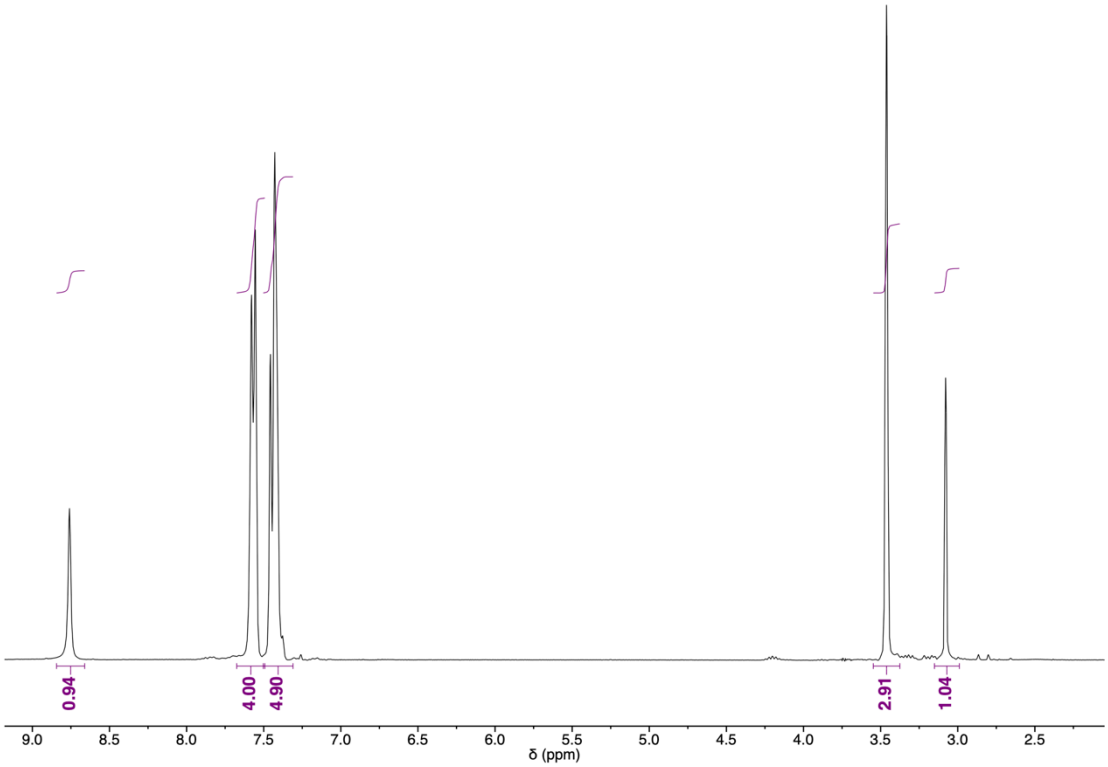


Figure S61. ^{1}H-NMR spectrum of (*S*)-**2** ($CDCl_3$, 300 MHz).

USC
UNIVERSIDADE DE SANTIAGO DE COMPOSTELA

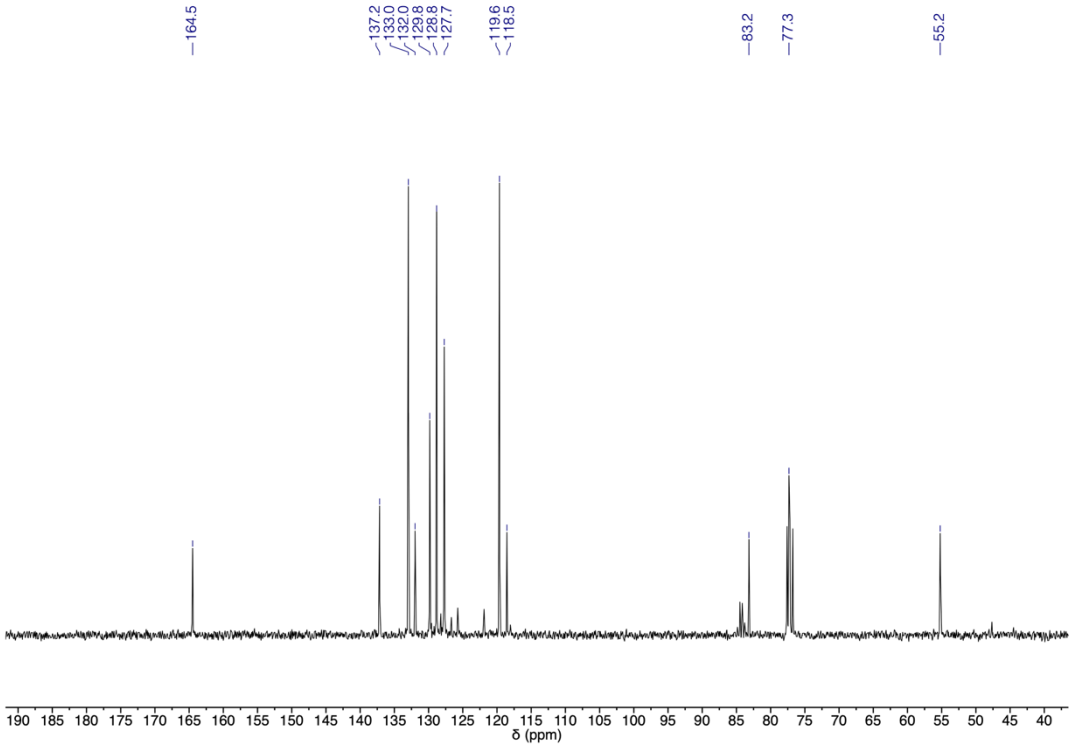


Figure S62. ^{13}C-NMR spectrum of (*S*)-**2** ($CDCl_3$, 75 MHz).

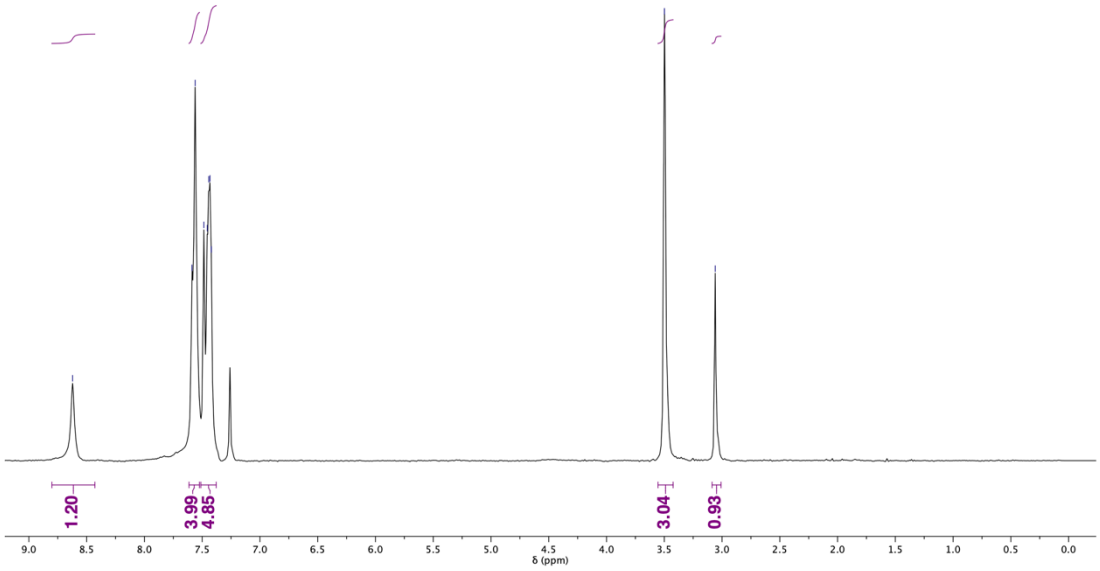


Figure S63. ^{1}H-NMR spectrum of (*R*)-**2** ($CDCl_3$, 300 MHz).

USC UNIVERSIDADE DE SANTIAGO DE COMPOSTELA

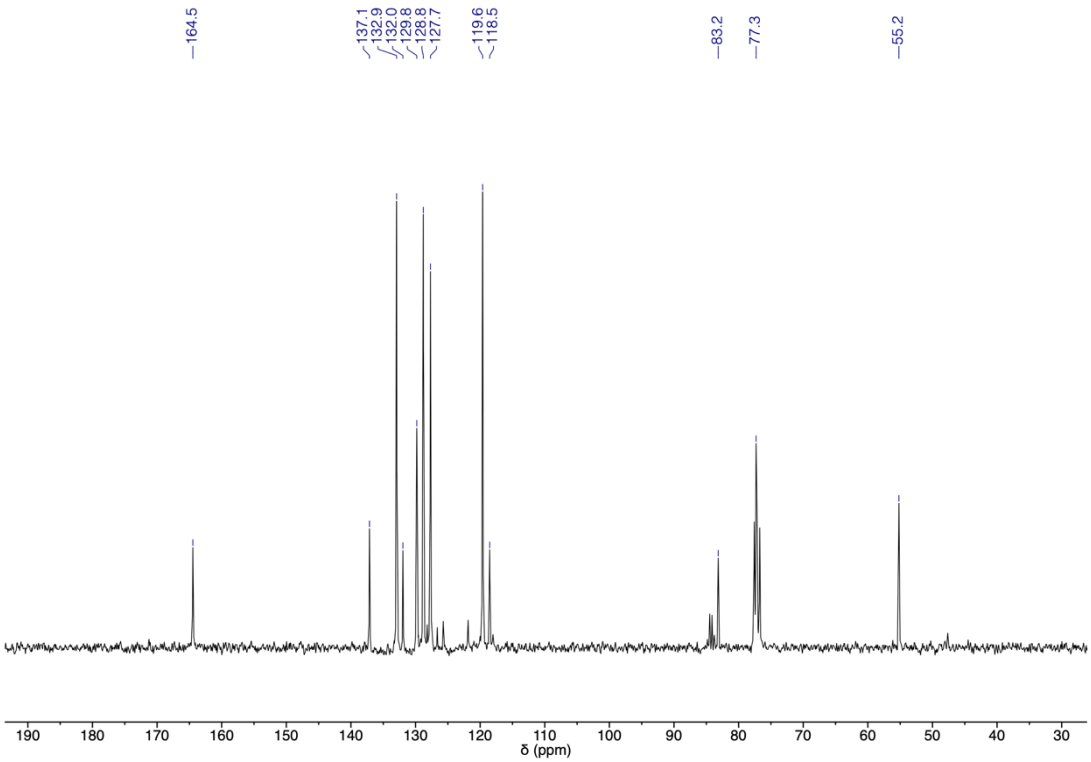
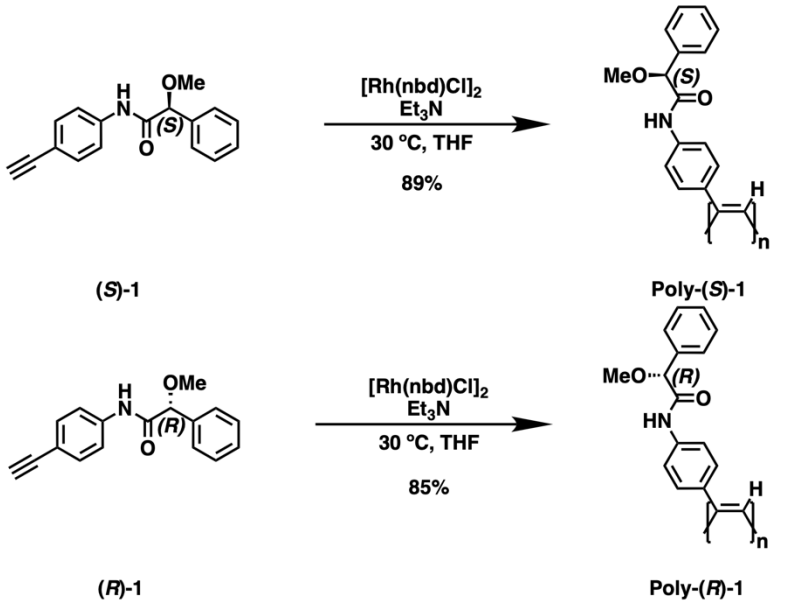


Figure S64. ^{13}C-NMR spectrum of (*R*)-**2** (CDCl3, 75 MHz).

5.3.5. Synthesis of homopolymers Poly-(*S*)-1 and Poly-(*R*)-1



USC
UNIVERSIDADE DE SANTIAGO DE COMPOSTELA

The reaction flask (sealed ampoule) was dried under vacuum and argon flushed for three times before the corresponding monomer (*S*)-**1** or (*R*)-**1** was added as a solid (80.0 mg, 0.30 mmol). Then, the flask was evacuated on the vacuum line and flushed with dry argon (three times). Dry THF (0.50 mL) was added with a syringe and the triethylamine dropwise (5 μL). A solution of rhodium norbornadiene chloride dimer, $[Rh(nbd)Cl]_2$ (1.00 mg, $2.65.10^{-3}$ mmol), in THF was added at 30 ºC. The reaction mixture was stirred at 30 ºC for 6 hours. Then, the resulting polymer was diluted in CH_2Cl_2 and precipitated in a large amount of methanol, centrifuged (2 times) and precipitated in hexane and centrifugated again [70.9 mg (Poly-(*S*)-**1** and 68.0 mg Poly-(*R*)-**1**], 89% and 85% yield respectively of pure products.

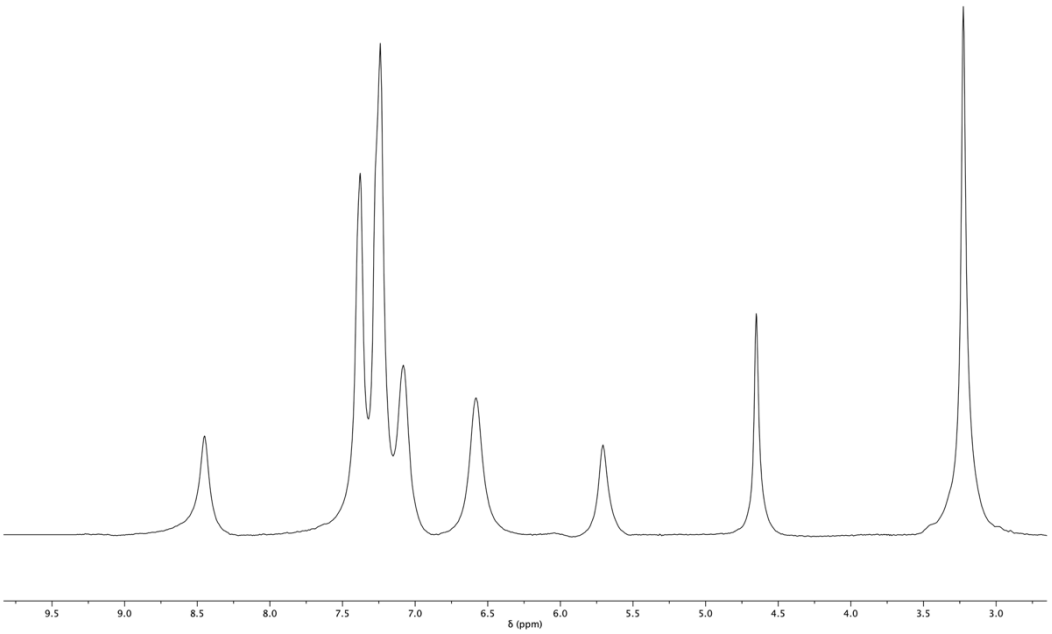


Figure S65. ^{1}H-NMR spectrum of Poly-(*S*)-**1** ($CDCl_3$, 300 MHz).

USC
UNIVERSIDADE DE SANTIAGO DE COMPOSTELA

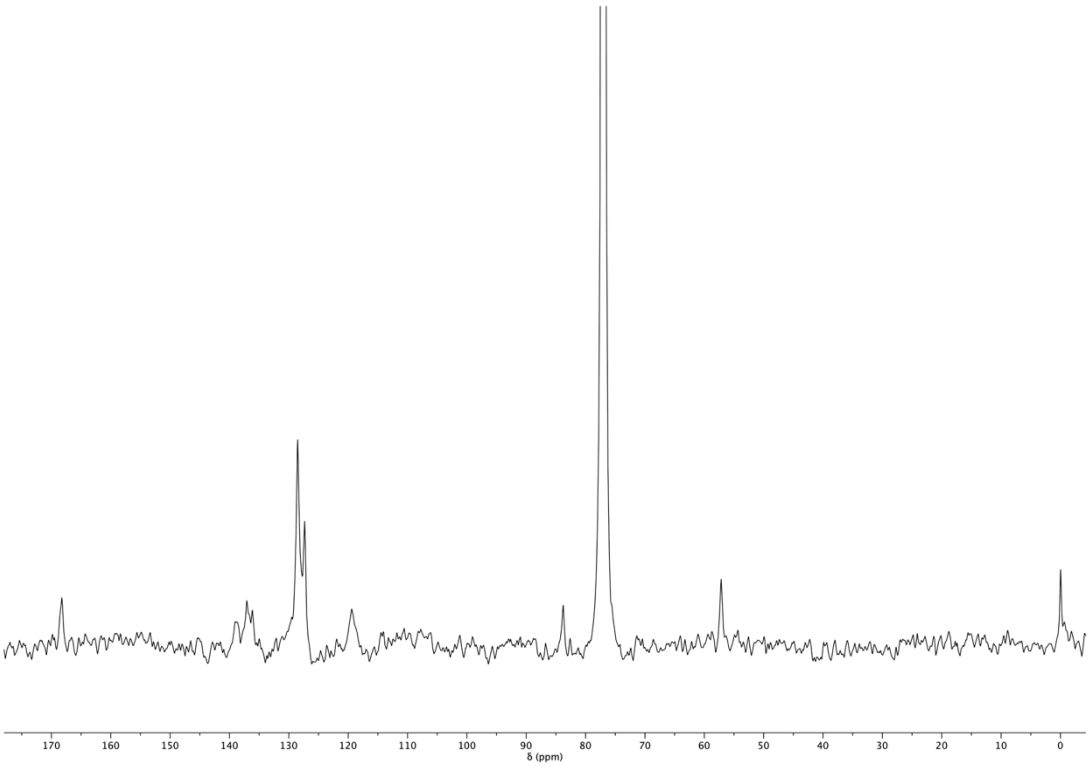


Figure S66. ^{13}C-NMR spectrum of Poly-(*S*)-**1** ($CDCl_3$, 125 MHz).

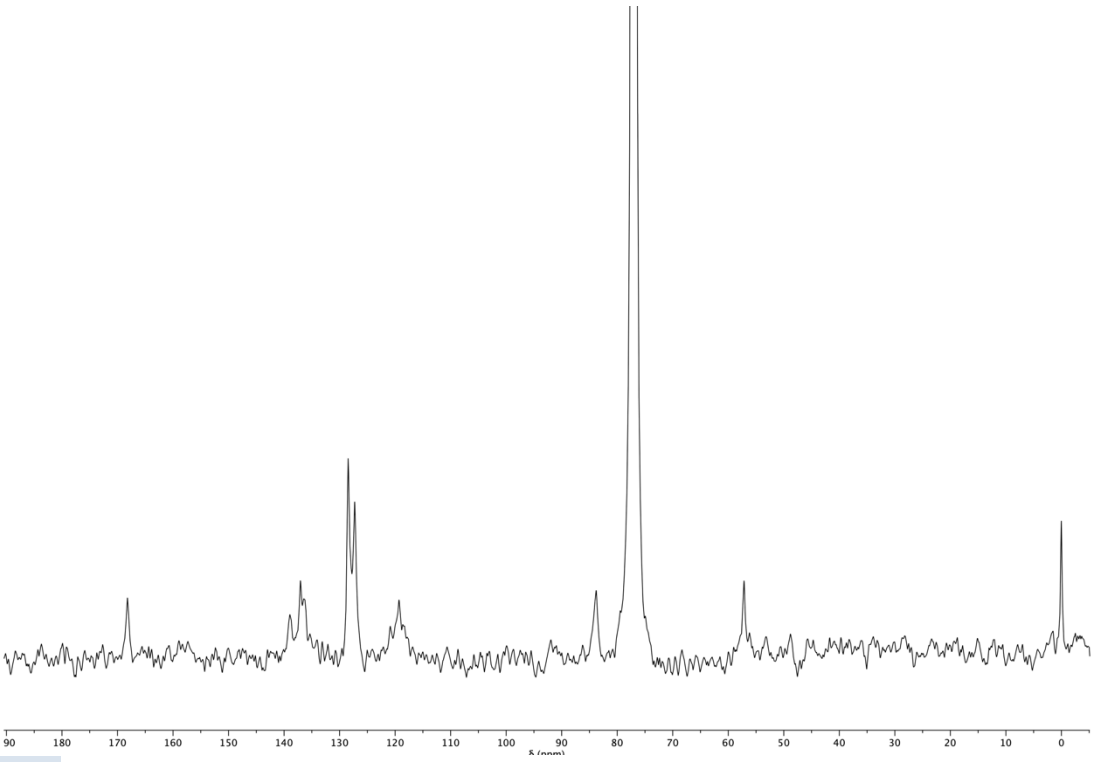


Figure S67. Quantitative ^{13}C-NMR inverse-gated decoupling spectrum of Poly-(*S*)-**1** ($CDCl_3$, 125 MHz).

USC
UNIVERSIDADE
DE SANTIAGO
DE COMPOSTELA

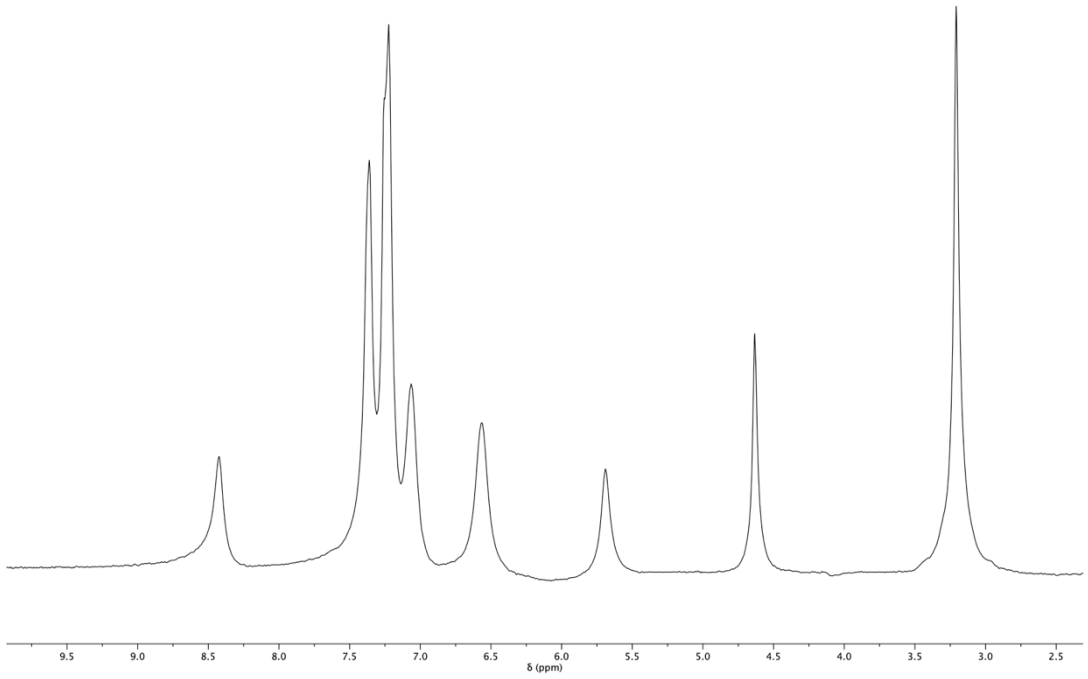
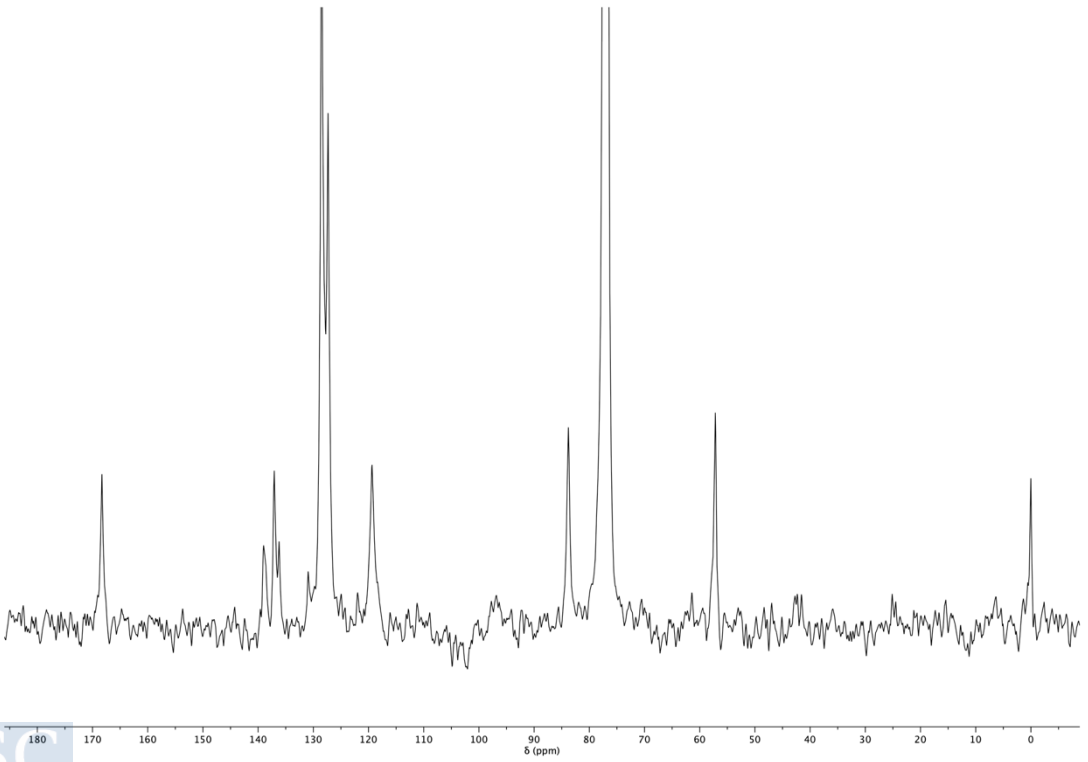


Figure S68. ^{1}H-NMR spectrum of Poly-(*R*)-**1** ($CDCl_3$, 300 MHz).



USC UNIVERSIDADE

Figure S69. ^{13}C-NMR spectrum of Poly-(*R*)-**1** ($CDCl_3$, 125 MHz).

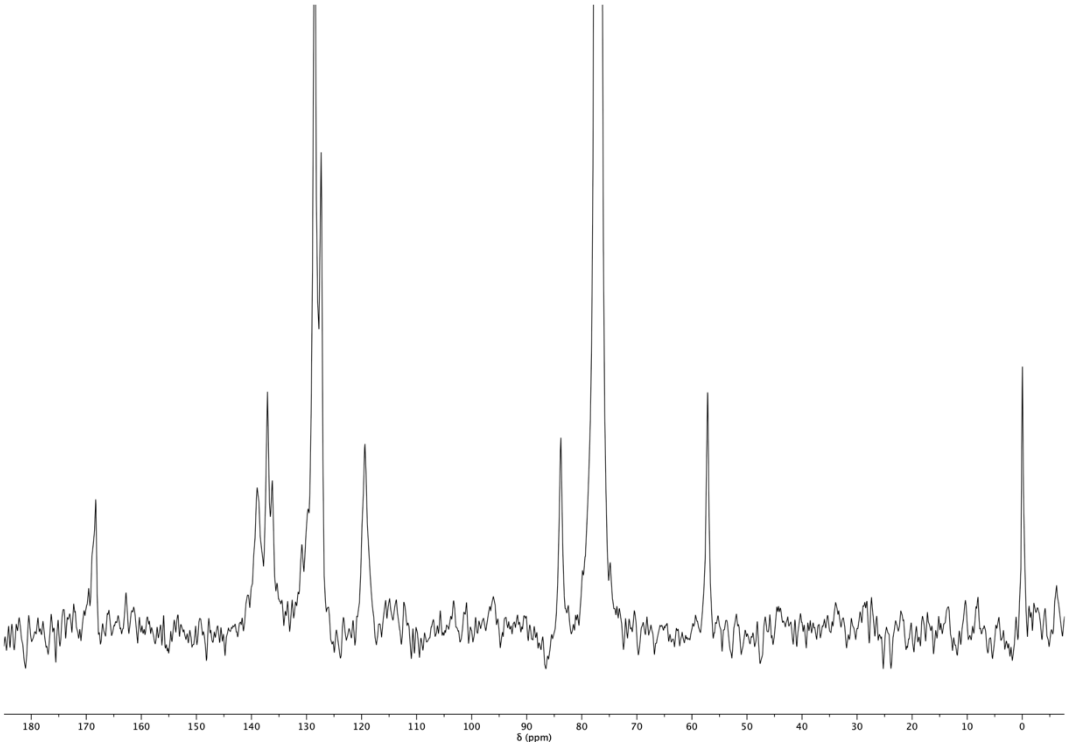
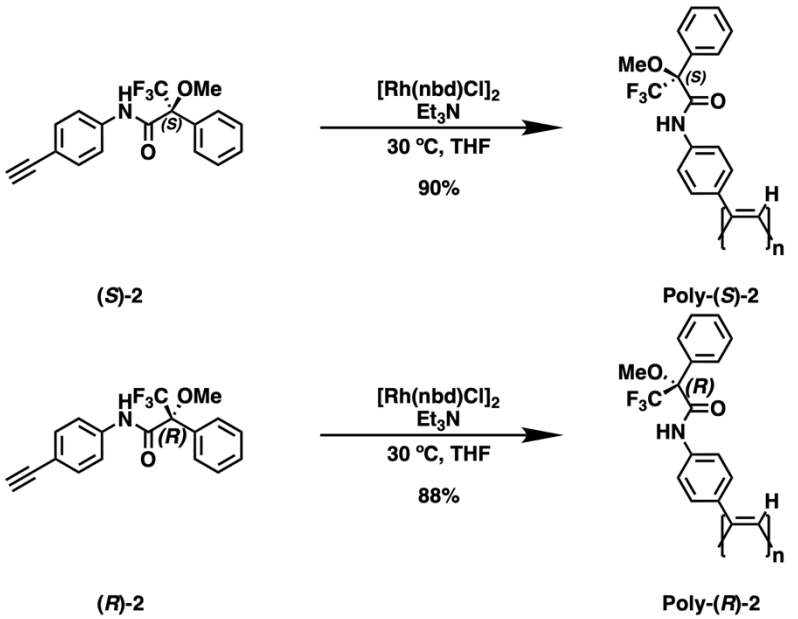


Figure S70. Quantitative ^{13}C-NMR inverse-gated decoupling spectrum of Poly-(*R*)-**1** ($CDCl_3$, 125 MHz).

USC
UNIVERSIDADE
DE SANTIAGO
DE COMPOSTELA

5.3.6. Synthesis of homopolymer Poly-(*S*)-2 and Poly-(*R*)-2



The reaction flask (sealed ampoule) was dried under vacuum and argon flushed for three times before the corresponding monomer (*S*)-**2** or (*R*)-**2** was added as a solid (80.0 mg, 0.30 mmol). Then, the flask was evacuated on the vacuum line and flushed with dry argon (three times). Dry THF (0.50 mL) was added with a syringe and the triethylamine dropwise (5 μL). A solution of rhodium norbornadiene chloride dimer, $[Rh(nbd)Cl]_2$ (1.00 mg, $2.65.10^{-3}$ mmol), in THF was added at 30 ºC. The reaction mixture was stirred at 30 ºC for 6 hours. Then, the resulting polymer was diluted in CH_2Cl_2 and precipitated in a large amount of methanol, centrifuged (2 times) and precipitated in hexane and centrifugated again [90.4 mg Poly-(*S*)-**2** and 88.4 mg Poly-(*R*)-**2**], 90% and 88% yield respectively of pure products.

USC UNIVERSIDADE DE SANTIAGO DE COMPOSTELA

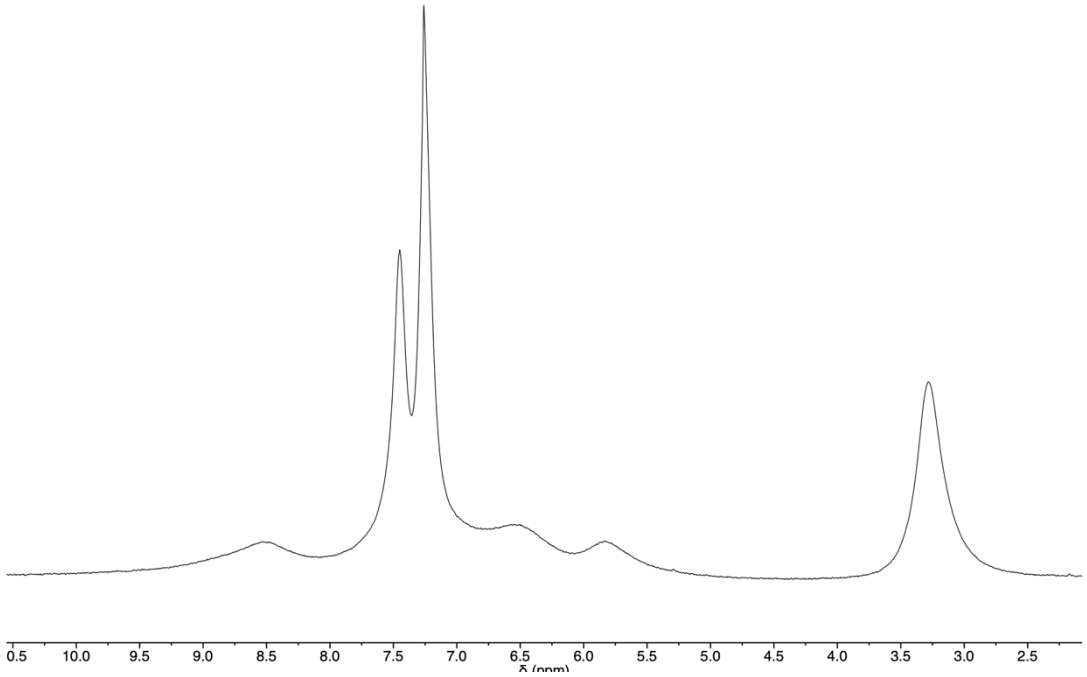


Figure S71. ^{1}H-NMR spectrum of Poly-(*S*)-**2** ($CDCl_3$, 300 MHz).

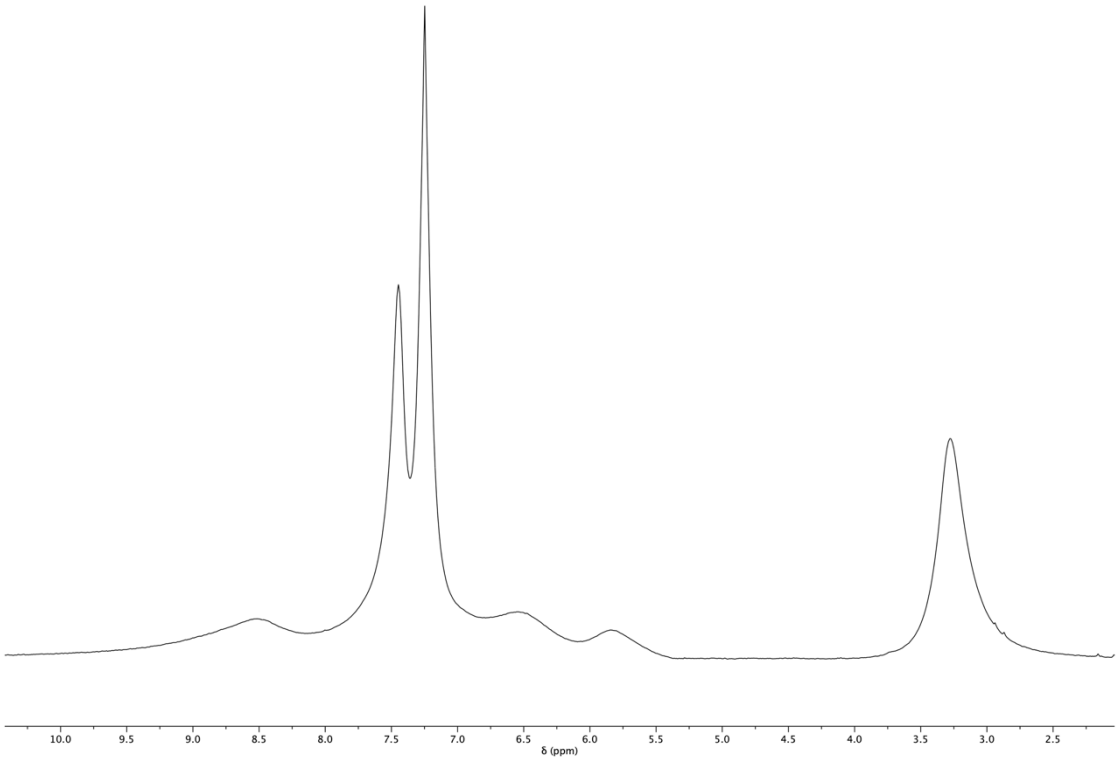


Figure S72. ^{1}H-NMR spectrum of Poly-(*R*)-**2** ($CDCl_3$, 300 MHz).

USC
UNIVERSIDADE DE SANTIAGO DE COMPOSTELA

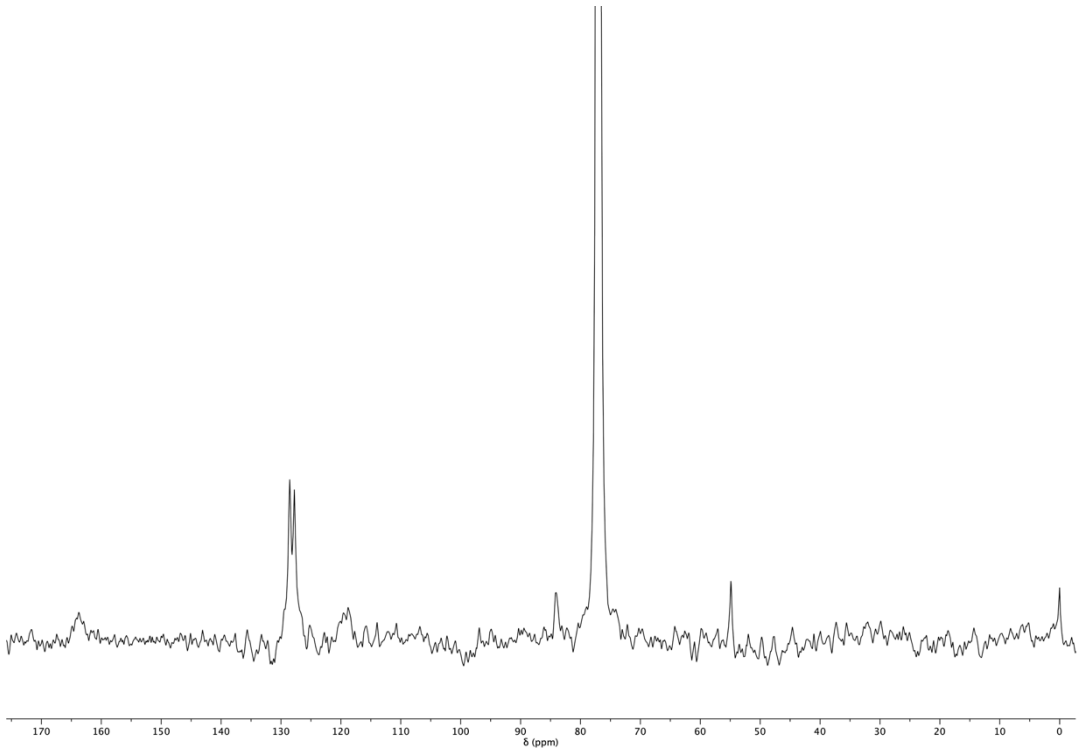


Figure S73. ^{13}C-NMR spectrum of Poly-(*R*)-**2** ($CDCl_3$, 125 MHz).

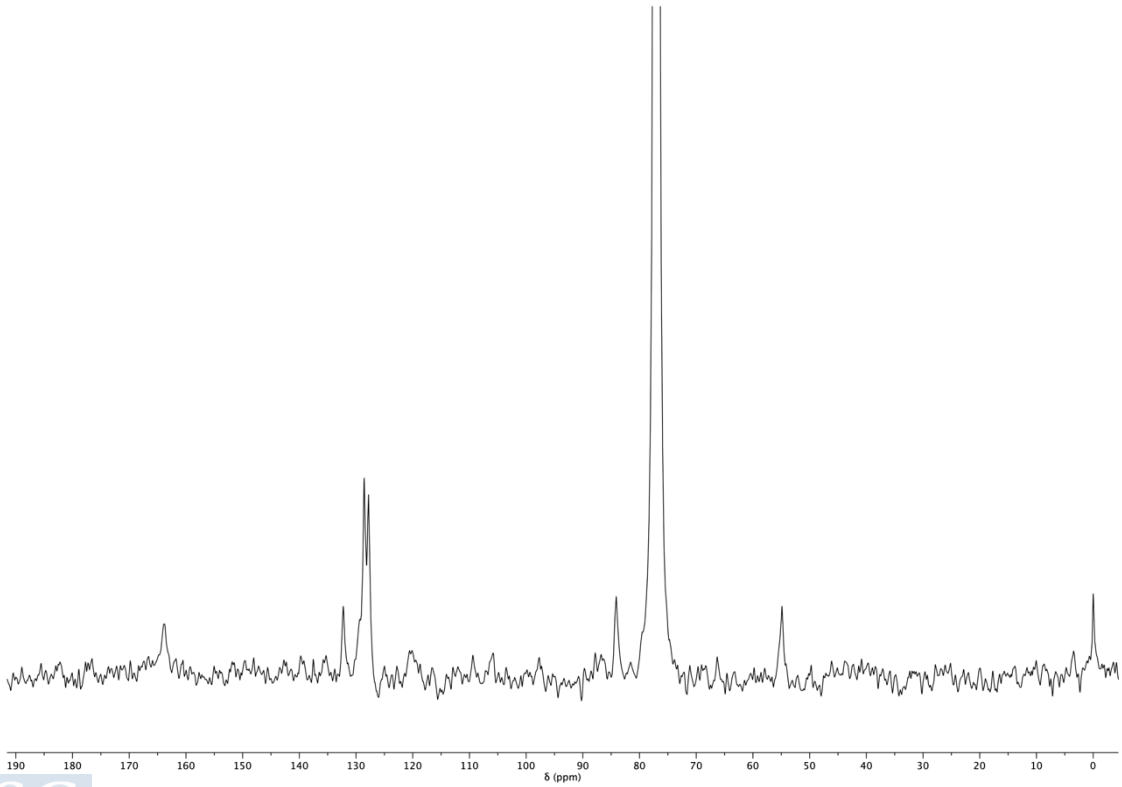
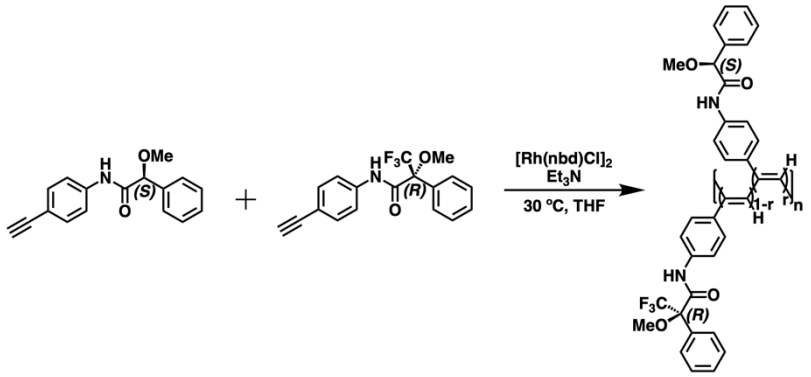


Figure S74. Quantitative ^{13}C-NMR inverse-gated decoupling spectrum of Poly-(*R*)-**2** ($CDCl_3$, 125 MHz).

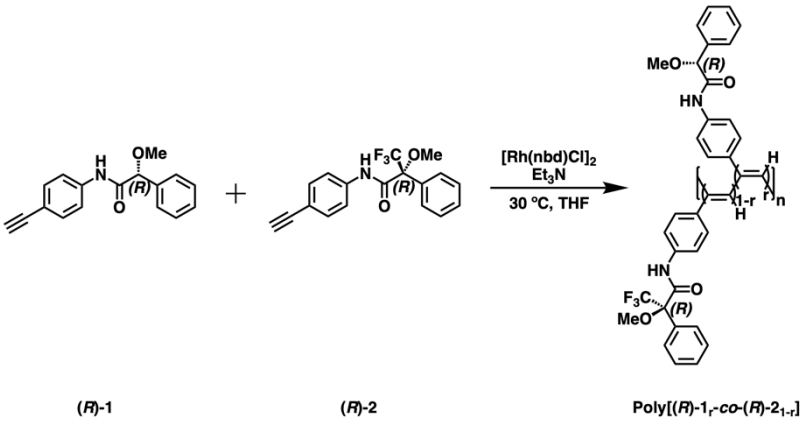
USC UNIVERSIDADE DE SANTIAGO DE COMPOSTELA

5.3.7. Synthesis of copolymers Poly-[(*S*)-1_r-*co*-(*R*)-2_{1-r}]



The reaction flask (sealed ampoule) was dried under vacuum and argon flushed for three times before the corresponding monomers (*S*)-**1** and (*R*)-**2** were added as a solid (see Table S3). Then, the flask was evacuated on the vacuum line and flushed with dry argon (three times). Dry THF (0.50 mL) was added with a syringe and the triethylamine dropwise (5 μL). A solution of rhodium norbornadiene chloride dimer, $[Rh(nbd)Cl]_2$ (1.00 mg, $2.65.10^{-3}$ mmol), in THF was added at 30 ºC. The reaction mixture was stirred at 30 ºC for 6 hours. Then, the resulting polymer was diluted in CH_2Cl_2 and precipitated in a large amount of methanol, centrifuged (2 times) and precipitated in hexane and centrifugated again, yield in Table S3.

5.3.8. Synthesis of copolymers Poly-[(*R*)-1_r-*co*-(*R*)-2_{1-r}]

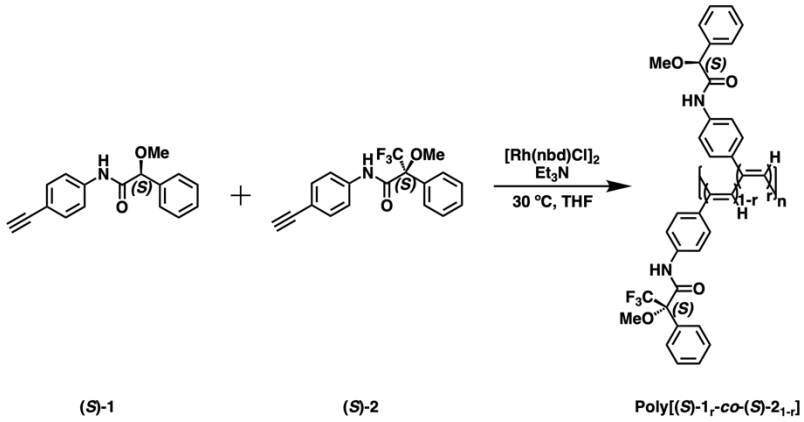


USC UNIVERSIDADE DE SANTIAGO

The reaction flask (sealed ampoule) was dried under vacuum and argon flushed for three times before the corresponding monomers (*R*)-**1** and (*R*)-**2** were added as a solid

(see Table S4). Then, the flask was evacuated on the vacuum line and flushed with dry argon (three times). Dry THF (0.50 mL) was added with a syringe and the triethylamine dropwise (5 μL). A solution of rhodium norbornadiene chloride dimer, $[Rh(nbd)Cl]_2$ (1.00 mg, $2.65.10^{-3}$ mmol), in THF was added at 30 ºC. The reaction mixture was stirred at 30 ºC for 6 hours. Then, the resulting polymer was diluted in CH_2Cl_2 and precipitated in a large amount of methanol, centrifuged (2 times) and precipitated in hexane and centrifugated again, yield in Table S4.

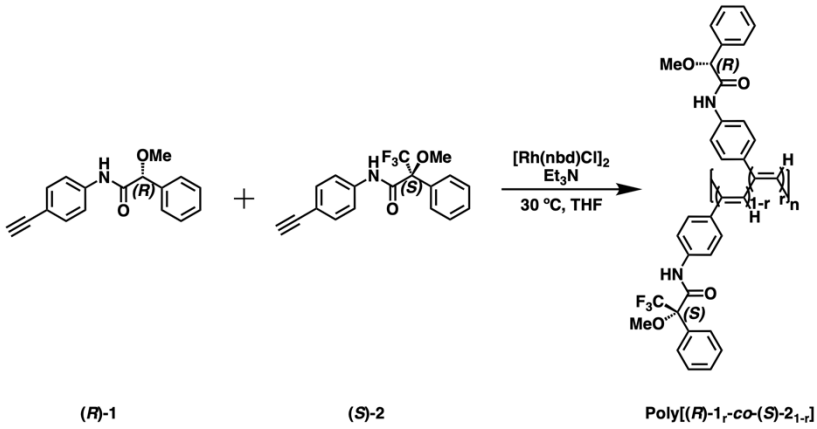
5.3.9. Synthesis of copolymers Poly-[(*S*)-1_r-*co*-(*S*)-2_{1-r}]



The reaction flask (sealed ampoule) was dried under vacuum and argon flushed for three times before the corresponding monomers (*S*)-**1** and (*S*)-**2** were added as a solid (see Table S5). Then, the flask was evacuated on the vacuum line and flushed with dry argon (three times). Dry THF (0.50 mL) was added with a syringe and the triethylamine dropwise (5 μL). A solution of rhodium norbornadiene chloride dimer, $[Rh(nbd)Cl]_2$ (1.00 mg, $2.65.10^{-3}$ mmol), in THF was added at 30 ºC. The reaction mixture was stirred at 30 ºC for 6 hours. Then, the resulting polymer was diluted in CH_2Cl_2 and precipitated in a large amount of methanol, centrifuged (2 times) and precipitated in hexane and centrifugated again, yield in Table S5.

USC UNIVERSIDADE DE SANTIAGO DE COMPOSTELA

5.3.10. Synthesis of copolymers Poly-[(*R*)-1_r-*co*-(*S*)-2_{1-r}]



(*R*)-1 (*S*)-2 Poly[(*R*)-1_r-*co*-(*S*)-2_{1-r}]

The reaction flask (sealed ampoule) was dried under vacuum and argon flushed for three times before the corresponding monomers (*R*)-**1** and (*S*)-**2** were added as a solid (see Table S6). Then, the flask was evacuated on the vacuum line and flushed with dry argon (three times). Dry THF (0.50 mL) was added with a syringe and the triethylamine dropwise (5 μL). A solution of rhodium norbornadiene chloride dimer, $[Rh(nbd)Cl]_2$ (1.00 mg, $2.65.10^{-3}$ mmol), in THF was added at 30 ºC. The reaction mixture was stirred at 30 ºC for 6 hours. Then, the resulting polymer was diluted in CH_2Cl_2 and precipitated in a large amount of methanol, centrifuged (2 times) and precipitated in hexane and centrifugated again, yield in Table S6.

USC UNIVERSIDADE DE SANTIAGO DE COMPOSTELA

Table S3. Amounts of (*S*)-**1** and (*R*)-**2** monomers used to form each copolymer and their yields.

copolymer	Mass of (*S*)-1 (mg)	(*S*)-1 (mmol)	Mass of (*R*)-2 (mg)	(*R*)-2 (mmol)	Yield (%)
Poly-[(*S*)-**1**$_{0.90}$-*co*-(*R*)-**2**$_{0.10}$]	72	0.27	10	0.03	90
Poly-[(*S*)-**1**$_{0.80}$-*co*-(*R*)-**2**$_{0.20}$]	64	0.24	20	0.06	86
Poly-[(*S*)-**1**$_{0.70}$-*co*-(*R*)-**2**$_{0.30}$]	56	0.21	30	0.09	76
Poly-[(*S*)-**1**$_{0.60}$-*co*-(*R*)-**2**$_{0.40}$]	48	0.18	40	0.12	92
Poly-[(*S*)-**1**$_{0.50}$-*co*-(*R*)-**2**$_{0.50}$]	40	0.15	50	0.15	87
Poly-[(*S*)-**1**$_{0.40}$-*co*-(*R*)-**2**$_{0.60}$]	32	0.12	60	0.18	87
Poly-[(*S*)-**1**$_{0.30}$-*co*-(*R*)-**2**$_{0.70}$]	24	0.09	70	0.21	86
Poly-[(*S*)-**1**$_{0.20}$-*co*-(*R*)-2$_{0.80}$]	16	0.06	80	0.24	93
Poly-[(*S*)-**1**$_{0.10}$-*co*-(*R*)-**2**$_{0.90}$]	8	0.03	90	0.27	87

Table S4. Amounts of (*R*)-**1** and (*R*)-**2** monomers used to form each copolymer and their yields.

copolymer	Mass of (*S*)-1 (mg)	(*S*)-1 (mmol)	Mass of (*R*)-2 (mg)	(*R*)-2 (mmol)	Yield (%)
Poly-[(*R*)-**1**$_{0.90}$-*co*-(*R*)-**2**$_{0.10}$]	72	0.27	10	0.03	82
Poly-[(*R*)-**1**$_{0.80}$-*co*-(*R*)-**2**$_{0.20}$]	64	0.24	20	0.06	80
Poly-[(*R*)-**1**$_{0.70}$-*co*-(*R*)-**2**$_{0.30}$]	56	0.21	30	0.09	74
Poly-[(*R*)-**1**$_{0.60}$-*co*-(*R*)-**2**$_{0.40}$]	48	0.18	40	0.12	70
Poly-[(*R*)-**1**$_{0.50}$-*co*-(*R*)-**2**$_{0.50}$]	40	0.15	50	0.15	70
Poly-[(*R*)-**1**$_{0.40}$-*co*-(*R*)-**2**$_{0.60}$]	32	0.12	60	0.18	91
Poly-[(*R*)-**1**$_{0.30}$-*co*-(*R*)-**2**$_{0.70}$]	24	0.09	70	0.21	85
Poly-[(*R*)-**1**$_{0.20}$-*co*-(*R*)-**2**$_{0.80}$]	16	0.06	80	0.24	78
Poly-[(*R*)-**1**$_{0.10}$-*co*-(*R*)-**2**$_{0.90}$]	8	0.03	90	0.27	75

USC UNIVERSIDADE DE SANTIAGO DE COMPOSTELA

Table S5. Amounts of (*S*)-**1** and (*S*)-**2** monomers used to form each copolymer and their yields.

copolymer	Mass of (*S*)-1 (mg)	(*S*)-1 (mmol)	Mass of (*R*)-2 (mg)	(*R*)-2 (mmol)	Yield (%)
Poly-[(*S*)-**1**$_{0.70}$-*co*-(*S*)-**2**$_{0.30}$]	56	0.21	30	0.09	82
Poly-[(*S*)-**1**$_{0.50}$-*co*-(*S*)-**2**$_{0.50}$]	40	0.15	50	0.15	83
Poly-[(*S*)-**1**$_{0.30}$-*co*-(*S*)-**2**$_{0.70}$]	24	0.09	70	0.21	85

Table S6. Amounts of (*R*)-**1** and (*S*)-**2** monomers used to form each copolymer and their yields.

copolymer	Mass of (*S*)-1 (mg)	(*S*)-1 (mmol)	Mass of (*R*)-2 (mg)	(*R*)-2 (mmol)	Yield (%)
Poly-[(*R*)-**1**$_{0.70}$-*co*-(*S*)-**2**$_{0.30}$]	56	0.21	30	0.09	81
Poly-[(*R*)-**1**$_{0.50}$-*co*-(*S*)-**2**$_{0.50}$]	40	0.15	50	0.15	77
Poly-[(*R*)-**1**$_{0.30}$-*co*-(*S*)-**2**$_{0.70}$]	24	0.09	70	0.21	92

USC UNIVERSIDADE DE SANTIAGO DE COMPOSTELA

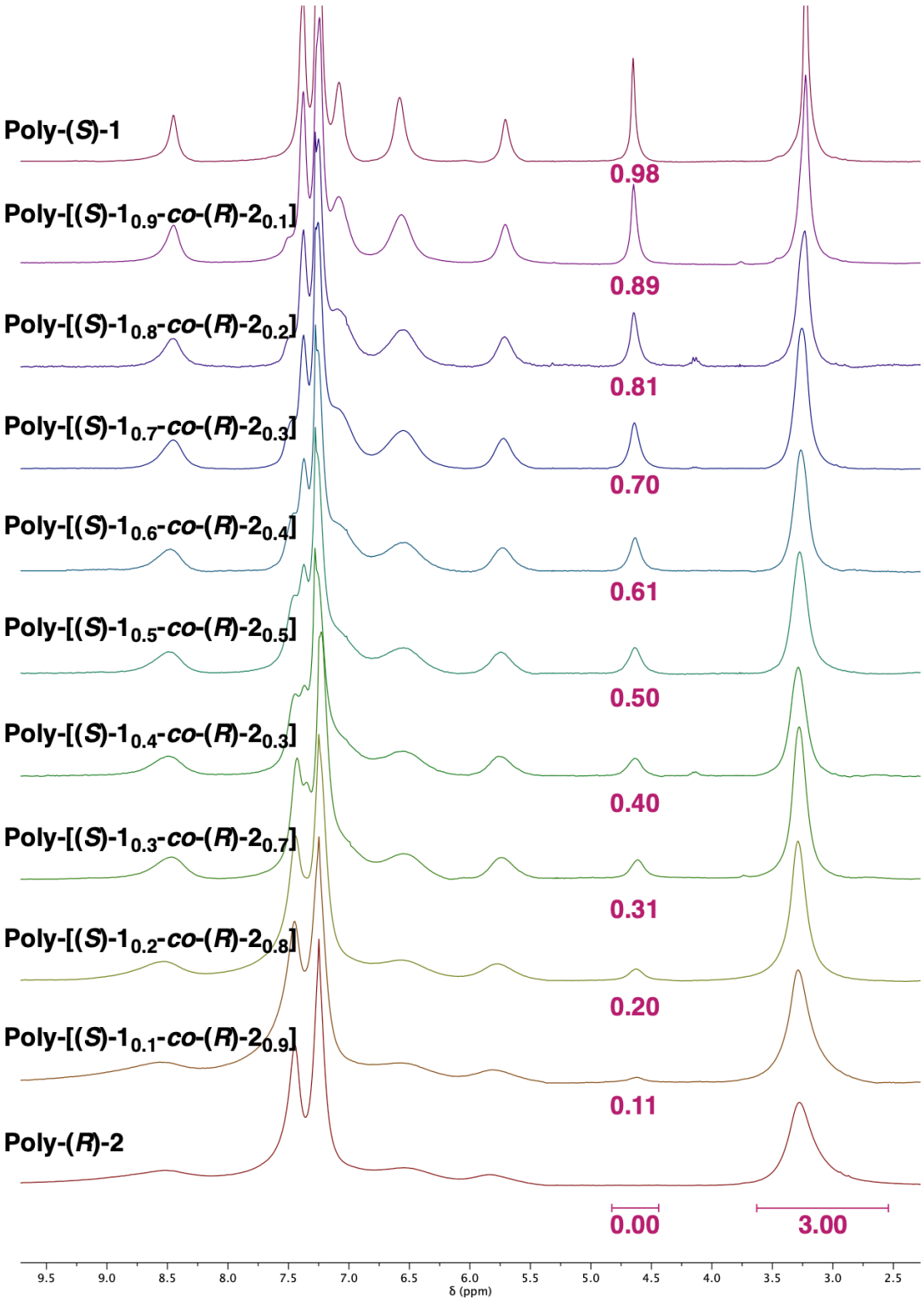


Figure S75. ^{1}H-NMR spectra ($CDCl_3$, 300 MHz) of Poly-(*S*)-**1**, Poly-[(*S*)-**1**$_{0.90}$-*co*-(*R*)-**2**$_{0.10}$], Poly-[(*S*)-**1**$_{0.80}$-*co*-(*R*)-**2**$_{0.20}$], Poly-[(*S*)-**1**$_{0.70}$-*co*-(*R*)-**2**$_{0.30}$], Poly-[(*S*)-**1**$_{0.60}$-*co*-(*R*)-**2**$_{0.40}$], Poly-[(*S*)-**1**$_{0.50}$-*co*-(*R*)-**2**$_{0.50}$], Poly-[(*S*)-**1**$_{0.40}$-*co*-(*R*)-**2**$_{0.60}$], Poly-[(*S*)-**1**$_{0.30}$-*co*-(*R*)-**2**$_{0.70}$], Poly-[(*S*)-**1**$_{0.20}$-*co*-(*R*)-**2**$_{0.80}$], Poly-[(*S*)-**1**$_{0.10}$-*co*-(*R*)-**2**$_{0.90}$], and Poly-(*R*)-**2**. Integration of the Hydrogen in alpha of (*S*)-**1** to the carbonyl compared to the hydrogens of the methoxy groups of (*S*)-**1** + (*R*)-**2**.

USC UNIVERSIDADE DE SANTIAGO DE COMPOSTELA

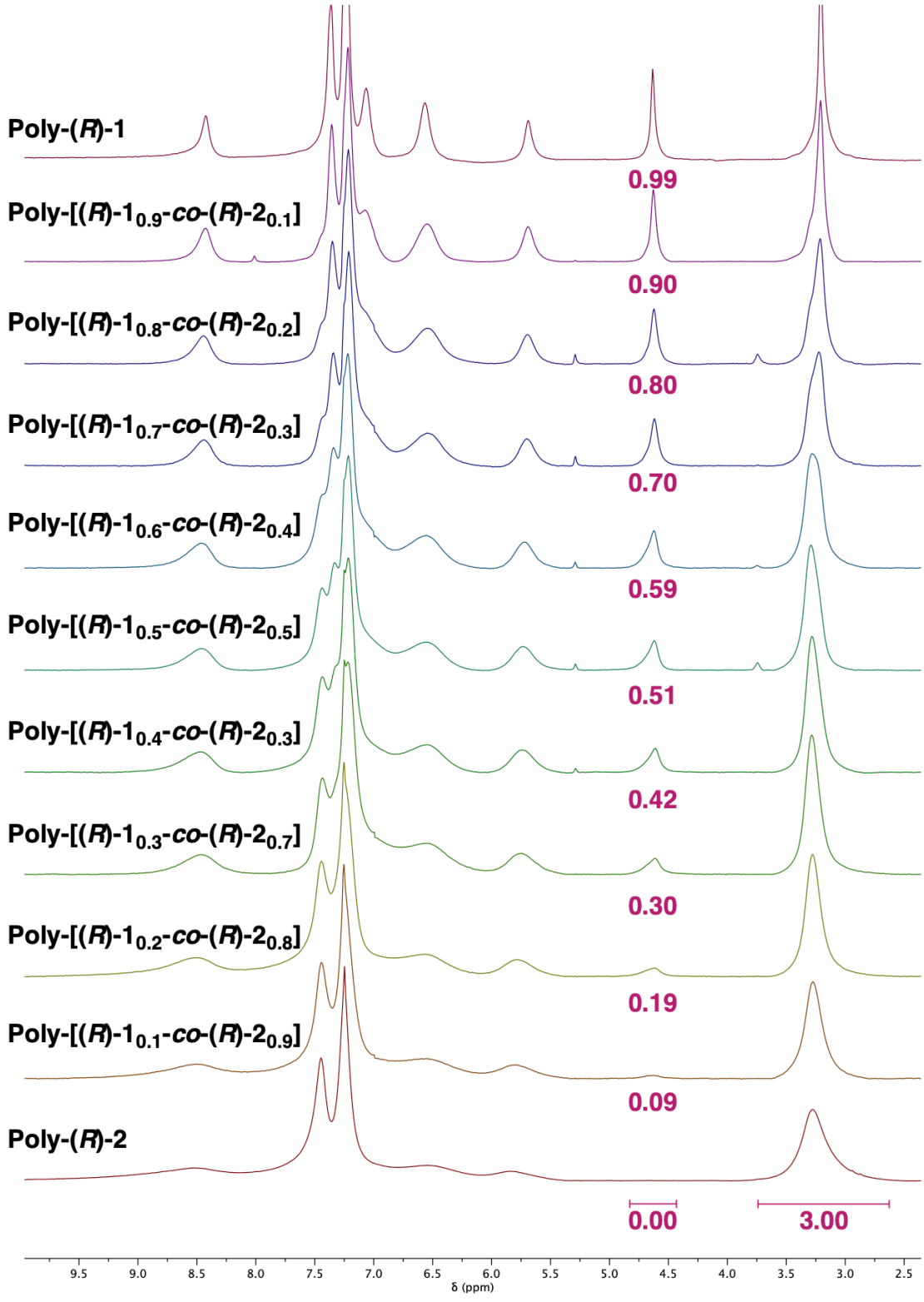


Figure S76. ^{1}H-NMR spectra ($CDCl_3$, 300 MHz) of Poly-(*R*)-**1**, Poly-[(*R*)-**1**$_{0.90}$-*co*-(*R*)-**2**$_{0.10}$], Poly-[(*R*)-**1**$_{0.80}$-*co*-(*R*)-**2**$_{0.20}$], Poly-[(*R*)-**1**$_{0.70}$-*co*-(*R*)-**2**$_{0.30}$], Poly-[(*R*)-**1**$_{0.60}$-*co*-(*R*)-**2**$_{0.40}$], Poly-[(*R*)-**1**$_{0.50}$-*co*-(*R*)-**2**$_{0.50}$], Poly-[(*R*)-**1**$_{0.40}$-*co*-(*R*)-**2**$_{0.60}$], Poly-[(*R*)-**1**$_{0.30}$-*co*-(*R*)-**2**$_{0.70}$], Poly-[(*R*)-**1**$_{0.20}$-*co*-(*R*)-**2**$_{0.80}$], Poly-[(*R*)-**1**$_{0.10}$-*co*-(*R*)-**2**$_{0.90}$], and Poly-(*R*)-**2**. Integration of the Hydrogen in alpha of (*R*)-**1** to the carbonyl compared to the hydrogens of the methoxy groups of (*R*)-**1** + (*R*)-**2**.

USC UNIVERSIDADE DE SANTIAGO DE COMPOSTELA

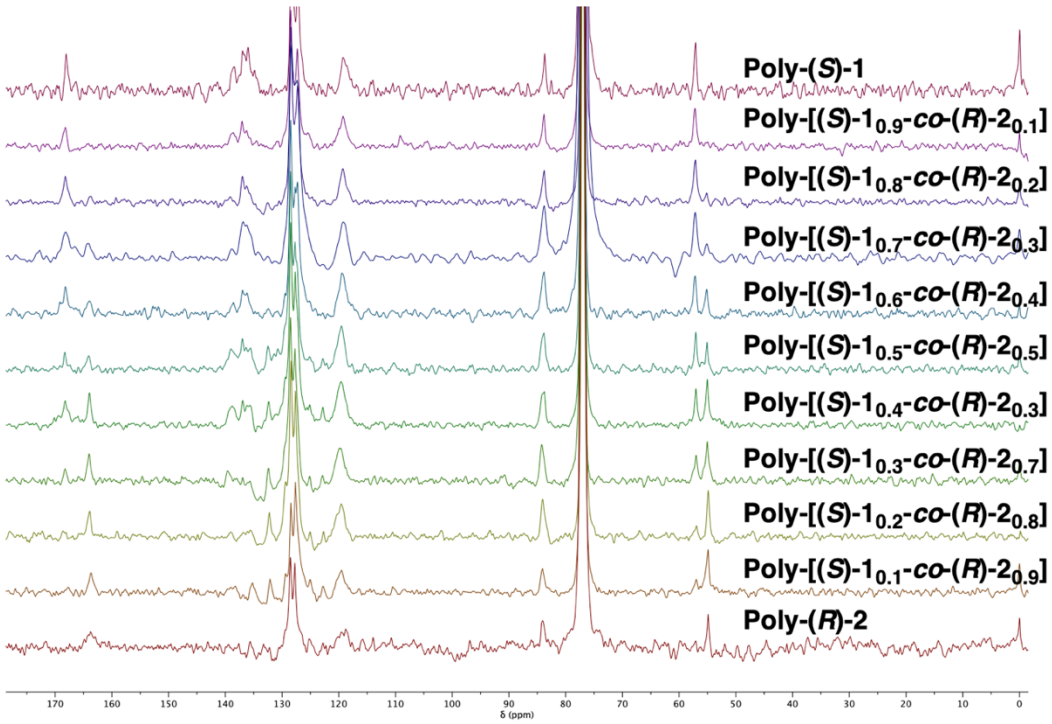


Figure S77. ^{13}C-NMR spectra ($CDCl_3$, 125 MHz) of Poly-(*S*)-**1**, Poly-[(*S*)-**1**$_{0.90}$-*co*-(*R*)-**2**$_{0.10}$], Poly-[(*S*)-**1**$_{0.80}$-*co*-(*R*)-**2**$_{0.20}$], Poly-[(*S*)-**1**$_{0.70}$-*co*-(*R*)-**2**$_{0.30}$], Poly-[(*S*)-**1**$_{0.60}$-*co*-(*R*)-**2**$_{0.40}$], Poly-[(*S*)-**1**$_{0.50}$-*co*-(*R*)-**2**$_{0.50}$], Poly-[(*S*)-**1**$_{0.40}$-*co*-(*R*)-**2**$_{0.60}$], Poly-[(*S*)-**1**$_{0.30}$-*co*-(*R*)-**2**$_{0.70}$], Poly-[(*S*)-**1**$_{0.20}$-*co*-(*R*)-**2**$_{0.80}$], Poly-[(*S*)-**1**$_{0.10}$-*co*-(*R*)-**2**$_{0.90}$], and Poly-(*R*)-**2**.

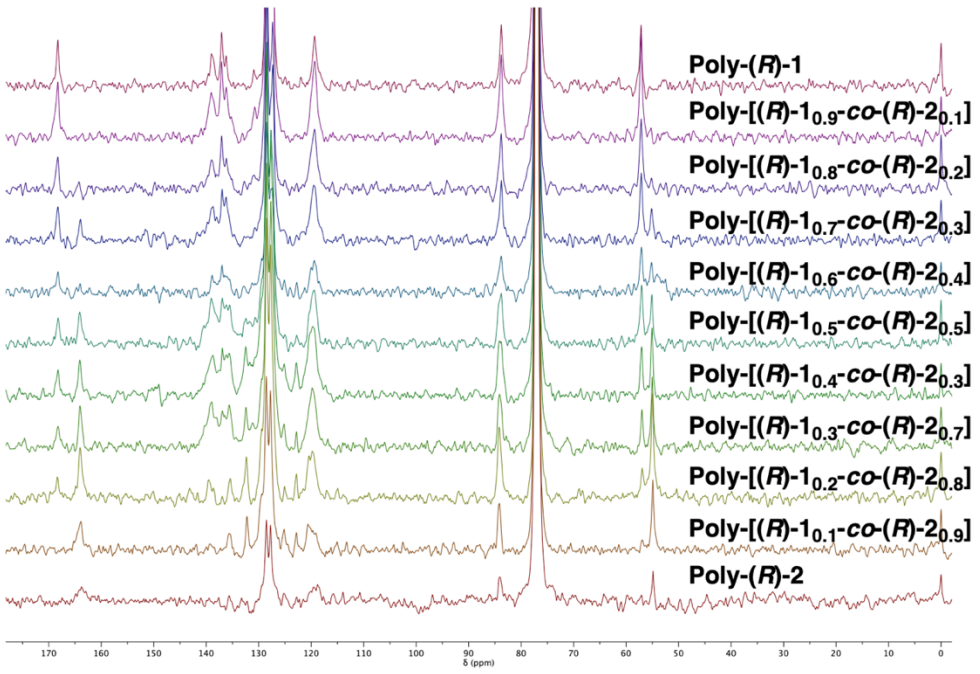


Figure S78. ^{13}C-NMR spectra ($CDCl_3$, 125 MHz) of Poly-(*R*)-**1**, Poly-[(*R*)-**1**$_{0.90}$-*co*-(*R*)-**2**$_{0.10}$], Poly-[(*R*)-**1**$_{0.80}$-*co*-(*R*)-**2**$_{0.20}$], Poly-[(*R*)-**1**$_{0.70}$-*co*-(*R*)-**2**$_{0.30}$], Poly-[(*R*)-**1**$_{0.60}$-*co*-(*R*)-**2**$_{0.40}$], Poly-[(*R*)-**1**$_{0.50}$-*co*-(*R*)-**2**$_{0.50}$], Poly-[(*R*)-**1**$_{0.40}$-*co*-(*R*)-**2**$_{0.60}$], Poly-[(*R*)-**1**$_{0.30}$-*co*-(*R*)-**2**$_{0.70}$], Poly-[(*R*)-**1**$_{0.20}$-*co*-(*R*)-**2**$_{0.80}$], Poly-[(*R*)-**1**$_{0.10}$-*co*-(*R*)-**2**$_{0.90}$], and Poly-(*R*)-**2**.

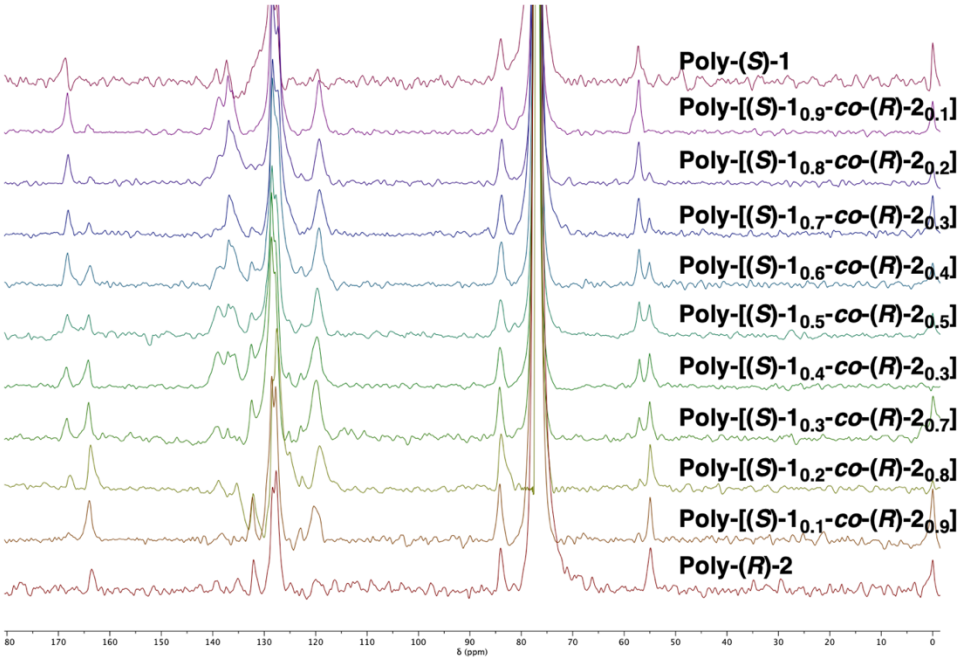


Figure S79. Quantitative ^{13}C-NMR inverse-gated decoupling spectra ($CDCl_3$, 125 MHz) of Poly-(*S*)-**1**, Poly-[(*S*)-**1**$_{0.90}$-*co*-(*R*)-**2**$_{0.10}$], Poly-[(*S*)-**1**$_{0.80}$-*co*-(*R*)-**2**$_{0.20}$], Poly-[(*S*)-**1**$_{0.70}$-*co*-(*R*)-**2**$_{0.30}$], Poly-[(*S*)-**1**$_{0.60}$-*co*-(*R*)-**2**$_{0.40}$], Poly-[(*S*)-**1**$_{0.50}$-*co*-(*R*)-**2**$_{0.50}$], Poly-[(*S*)-**1**$_{0.40}$-*co*-(*R*)-**2**$_{0.60}$], Poly-[(*S*)-**1**$_{0.30}$-*co*-(*R*)-**2**$_{0.70}$], Poly-[(*S*)-**1**$_{0.20}$-*co*-(*R*)-**2**$_{0.80}$], Poly-[(*S*)-**1**$_{0.10}$-*co*-(*R*)-**2**$_{0.90}$], and Poly-(*R*)-**2**.

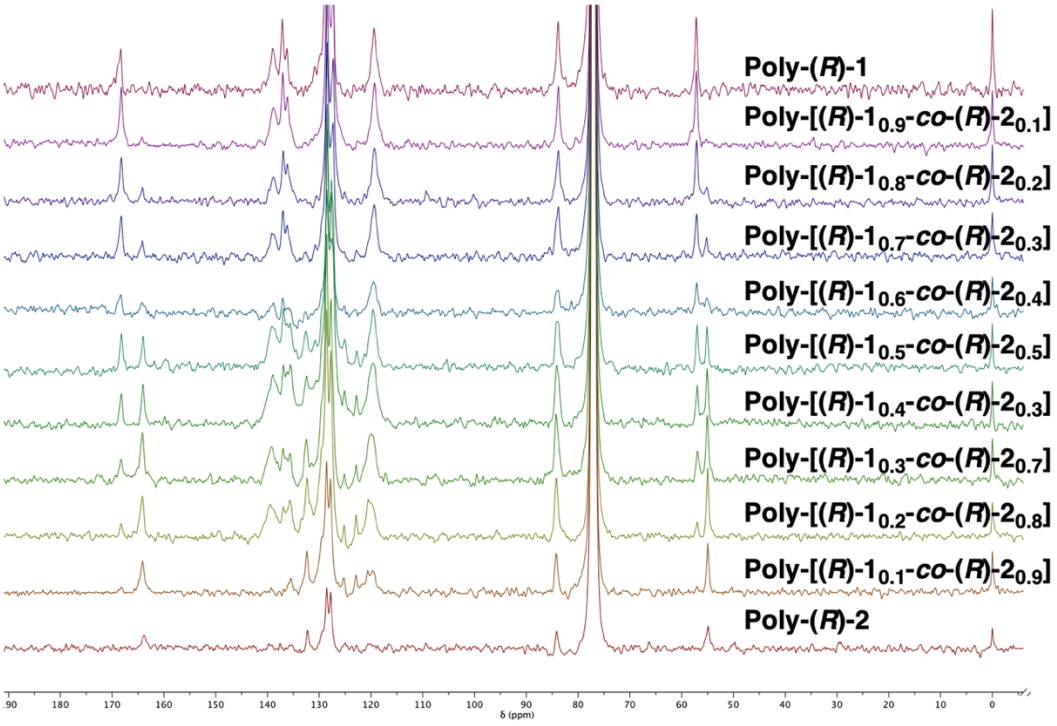


Figure S80. Quantitative ^{13}C-NMR inverse-gated decoupling spectra ($CDCl_3$, 125 MHz) of Poly-(*R*)-**1**, Poly-[(*R*)-**1**$_{0.90}$-*co*-(*R*)-**2**$_{0.10}$], Poly-[(*R*)-**1**$_{0.80}$-*co*-(*R*)-**2**$_{0.20}$], Poly-[(*R*)-**1**$_{0.70}$-*co*-(*R*)-**2**$_{0.30}$], Poly-[(*R*)-**1**$_{0.60}$-*co*-(*R*)-**2**$_{0.40}$], Poly-[(*R*)-**1**$_{0.50}$-*co*-(*R*)-**2**$_{0.50}$], Poly-[(*R*)-**1**$_{0.40}$-*co*-(*R*)-**2**$_{0.60}$], Poly-[(*R*)-**1**$_{0.30}$-*co*-(*R*)-**2**$_{0.70}$], Poly-[(*R*)-**1**$_{0.20}$-*co*-(*R*)-**2**$_{0.80}$], Poly-[(*R*)-**1**$_{0.10}$-*co*-(*R*)-**2**$_{0.90}$], and Poly-(*R*)-**2**.

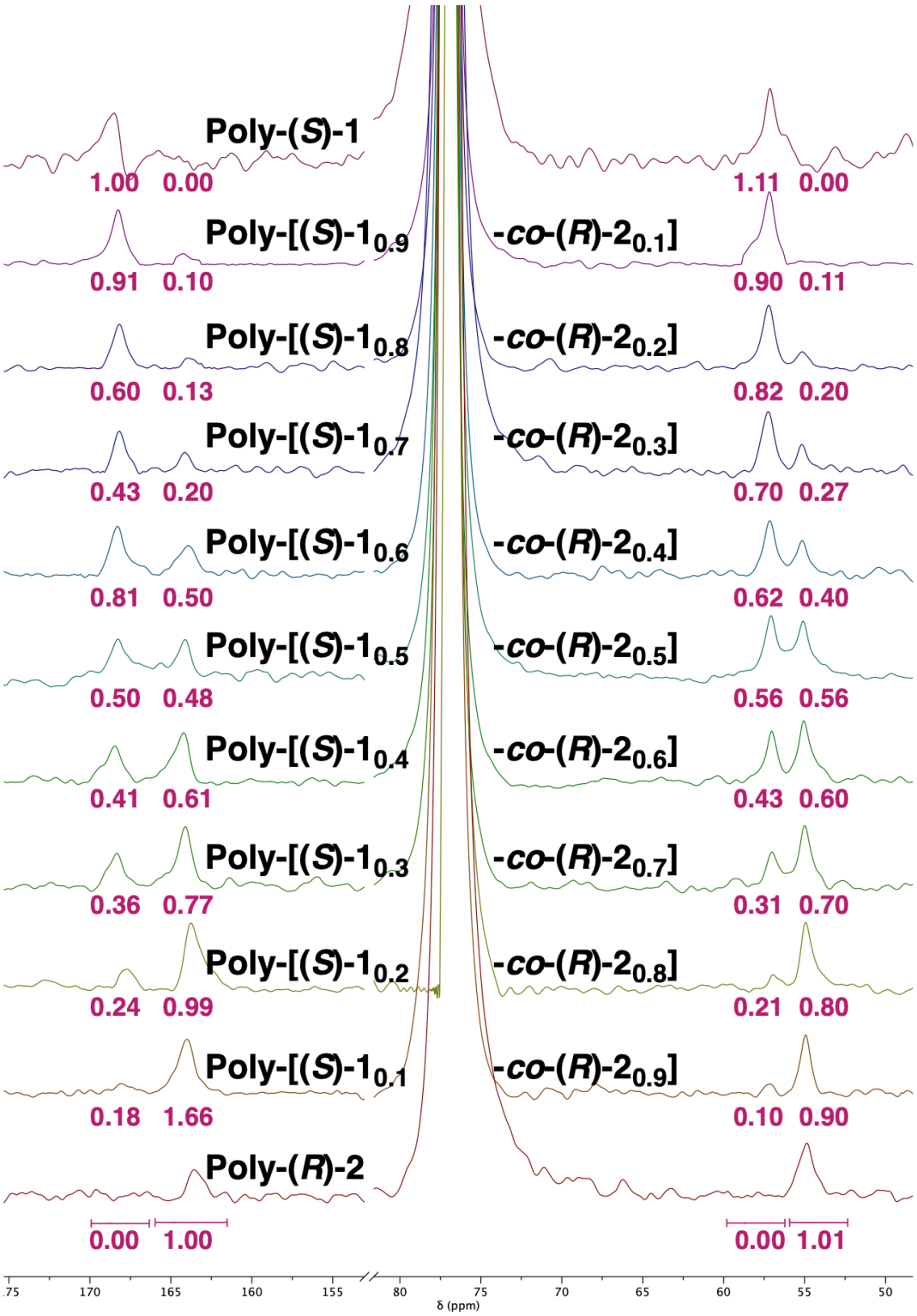


Figure S81. Quantitative ^{13}C-NMR inverse-gated decoupling spectra ($CDCl_3$, 125 MHz) integrated at carbonyl and Methoxy groups of Poly-(*S*)-**1**, Poly-[(*S*)-**1**$_{0.90}$-*co*-(*R*)-**2**$_{0.10}$], Poly-[(*S*)-**1**$_{0.80}$-*co*-(*R*)-**2**$_{0.20}$], Poly-[(*S*)-**1**$_{0.70}$-*co*-(*R*)-**2**$_{0.30}$], Poly-[(*S*)-**1**$_{0.60}$-*co*-(*R*)-**2**$_{0.40}$], Poly-[(*S*)-**1**$_{0.50}$-*co*-(*R*)-**2**$_{0.50}$], Poly-[(*S*)-**1**$_{0.40}$-*co*-(*R*)-**2**$_{0.60}$], Poly-[(*S*)-**1**$_{0.30}$-*co*-(*R*)-**2**$_{0.70}$], Poly-[(*S*)-**1**$_{0.20}$-*co*-(*R*)-**2**$_{0.80}$], Poly-[(*S*)-**1**$_{0.10}$-*co*-(*R*)-**2**$_{0.90}$], and Poly-(*R*)-**2**.

USC UNIVERSIDADE DE SANTIAGO DE COMPOSTELA

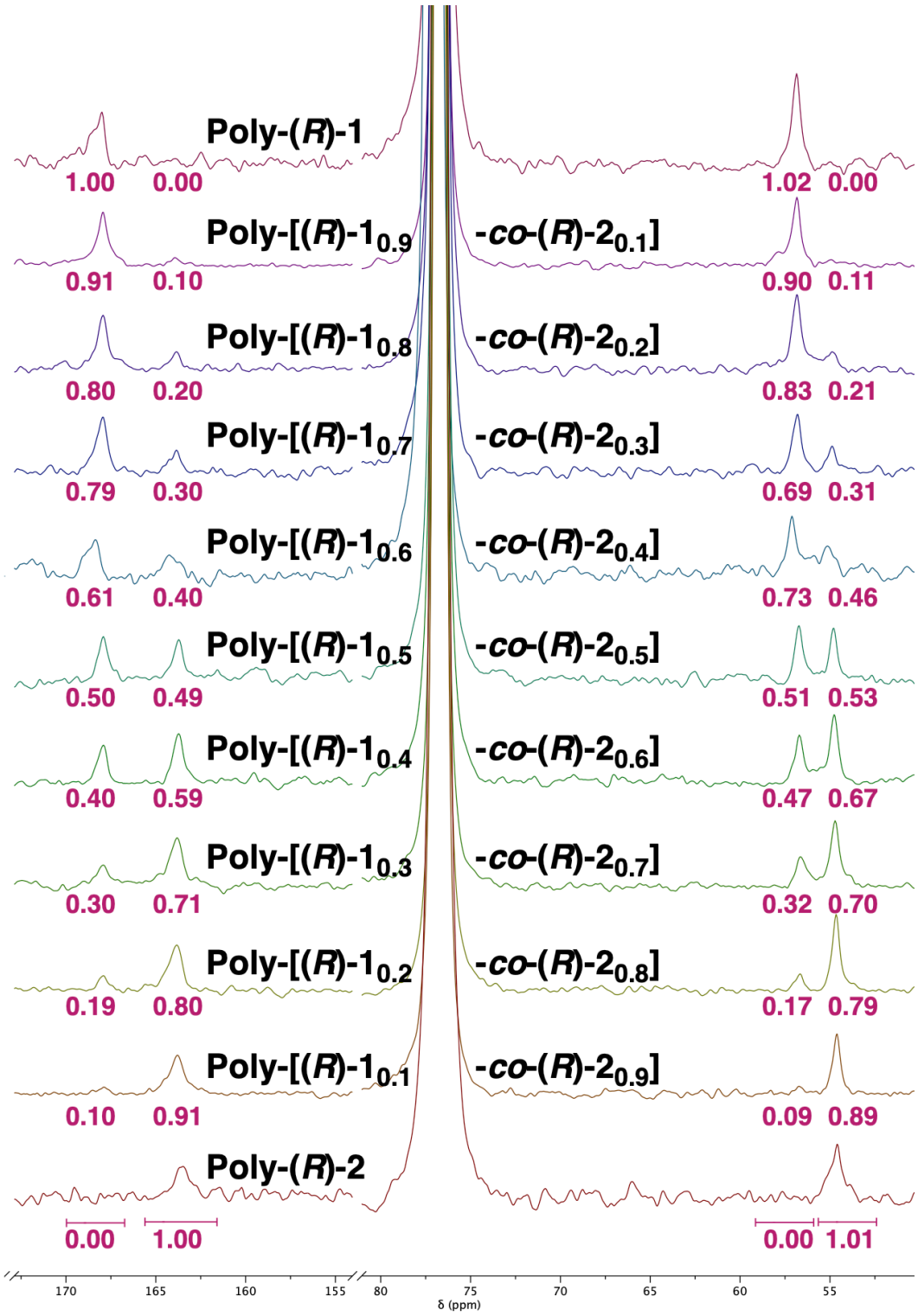


Figure S82. Quantitative ^{13}C-NMR inverse-gated decoupling spectra ($CDCl_3$, 125 MHz) integrated at carbonyl and Methoxy groups of Poly-(*R*)-**1**, Poly-[(*R*)-**1**$_{0.90}$-*co*-(*R*)-**2**$_{0.10}$], Poly-[(*R*)-**1**$_{0.80}$-*co*-(*R*)-**2**$_{0.20}$], Poly-[(*R*)-**1**$_{0.70}$-*co*-(*R*)-**2**$_{0.30}$], Poly-[(*R*)-**1**$_{0.60}$-*co*-(*R*)-**2**$_{0.40}$], Poly-[(*R*)-**1**$_{0.50}$-*co*-(*R*)-**2**$_{0.50}$], Poly-[(*R*)-**1**$_{0.40}$-*co*-(*R*)-**2**$_{0.60}$], Poly-[(*R*)-**1**$_{0.30}$-*co*-(*R*)-**2**$_{0.70}$], Poly-[(*R*)-**1**$_{0.20}$-*co*-(*R*)-**2**$_{0.80}$], Poly-[(*R*)-**1**$_{0.10}$-*co*-(*R*)-**2**$_{0.90}$], and Poly-(*R*)-**2**.

USC UNIVERSIDADE DE SANTIAGO DE COMPOSTELA

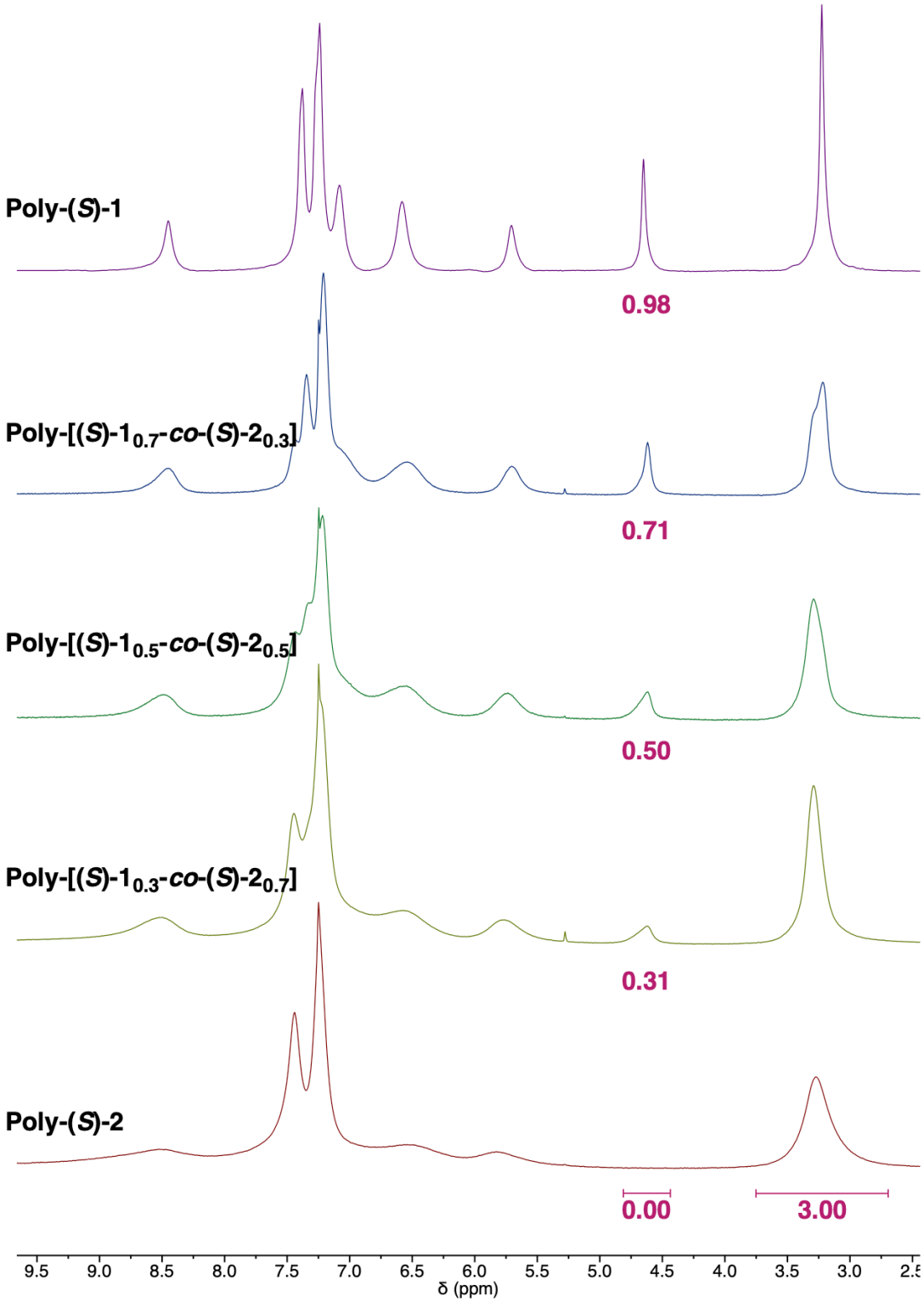


Figure S83. ^{1}H-NMR spectra ($CDCl_3$, 300 MHz) of Poly-(*S*)-**1**, Poly-[(*S*)-**1**$_{0.70}$-*co*-(*S*)-**2**$_{0.30}$], Poly-[(*S*)-**1**$_{0.50}$-*co*-(*S*)-**2**$_{0.50}$], Poly-[(*S*)-**1**$_{0.30}$-*co*-(*S*)-**2**$_{0.70}$], and Poly-(*S*)-**2**. Integration of the Hydrogen in alpha of (*S*)-**1** to the carbonyl compared to the hydrogens of the methoxy groups of (*S*)-**1** + (*S*)-**2**.

USC UNIVERSIDADE DE SANTIAGO DE COMPOSTELA

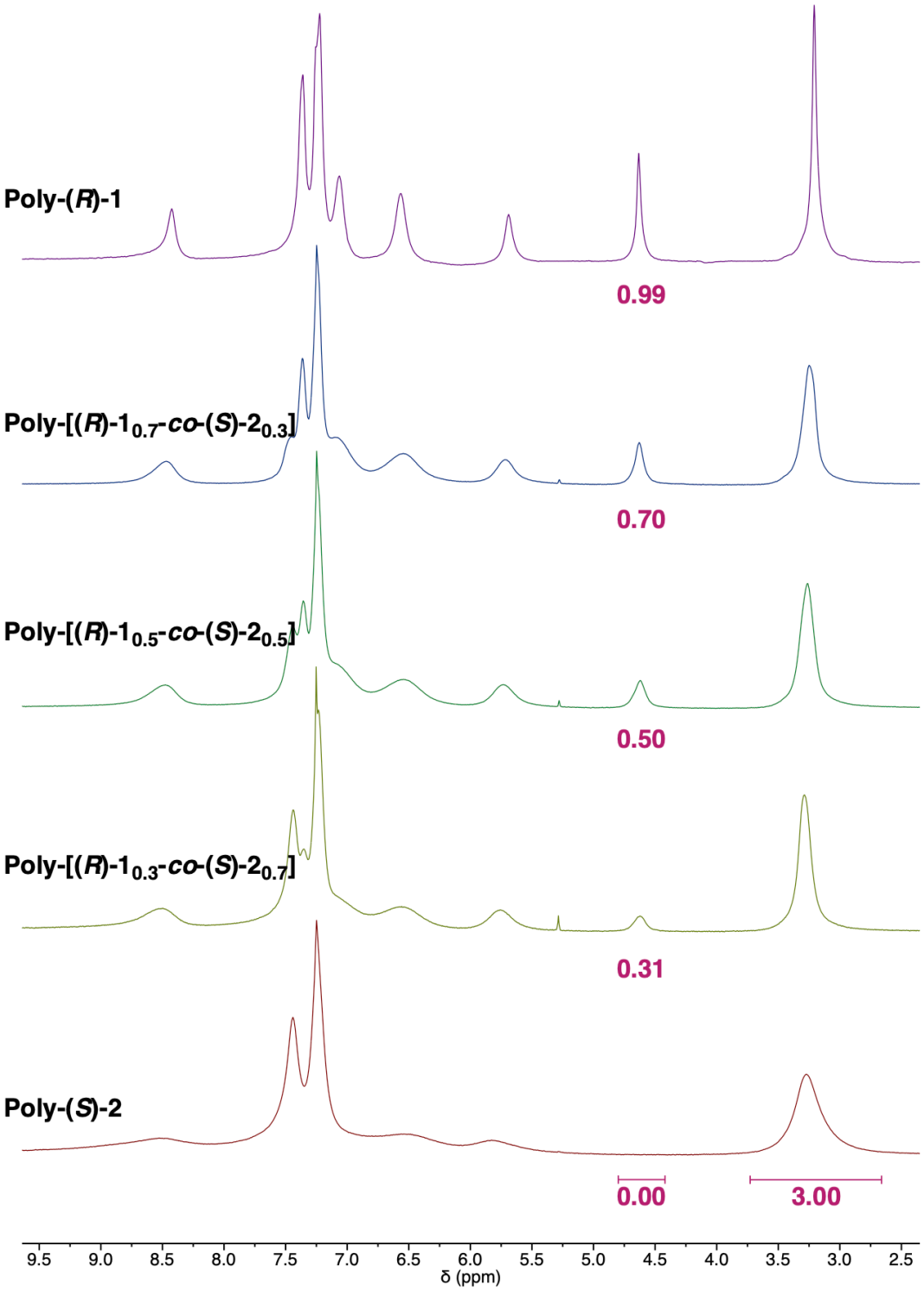


Figure S84. ^{1}H-NMR spectra ($CDCl_3$, 300 MHz) of Poly-(*R*)-**1**, Poly-[(*R*)-**1**$_{0.70}$-*co*-(*S*)-**2**$_{0.30}$], Poly-[(*R*)-**1**$_{0.50}$-*co*-(*S*)-**2**$_{0.50}$], Poly-[(*R*)-**1**$_{0.30}$-*co*-(*S*)-**2**$_{0.70}$], and Poly-(*S*)-**2**. Integration of the Hydrogen in alpha of (*R*)-**1** to the carbonyl compared to the hydrogens of the methoxy groups of (*R*)-**1** + (*S*)-**2**.

USC UNIVERSIDADE DE SANTIAGO DE COMPOSTELA

Table S7. GPC data of Poly-(*S*)-**1**, Poly-(*R*)-**1**, Poly-(*S*)-**2**, and Poly-(*R*)-**2** in THF.

polymer	Mn (Da)	Mw (Da)	PDI
Poly-(*S*)-**1**	281218	486507	1.73
Poly-(*R*)-**1**	299821	467721	1.56
Poly-(*S*)-**2**	512445	681552	1.33
Poly-(*R*)-**2**	652763	757205	1.16

Table S8. GPC data of Poly-[(*S*)-**1**$_r$-*co*-(*R*)-**2**$_{1-r}$] in THF.

polymer	Mn (Da)	Mw (Da)	PDI
Poly-[(*S*)-**1**$_{0.90}$-*co*-(*R*)-**2**$_{0.10}$]	299822	380774	1.27
Poly-[(*S*)-**1**$_{0.80}$-*co*-(*R*)-**2**$_{0.20}$]	322233	406014	1.26
Poly-[(*S*)-**1**$_{0.70}$-*co*-(*R*)-**2**$_{0.30}$]	352313	398114	1.13
Poly-[(*S*)-**1**$_{0.60}$-*co*-(*R*)-**2**$_{0.40}$]	401122	493380	1.23
Poly-[(*S*)-**1**$_{0.50}$-*co*-(*R*)-**2**$_{0.50}$]	482212	622053	1.29
Poly-[(*S*)-**1**$_{0.40}$-*co*-(*R*)-**2**$_{0.60}$]	531241	695926	1.31
Poly-[(*S*)-**1**$_{0.30}$-*co*-(*R*)-**2**$_{0.70}$]	571242	731190	1.28
Poly-[(*S*)-**1**$_{0.20}$-*co*-(*R*)-**2**$_{0.80}$]	619872	805834	1.30
Poly-[(*S*)-**1**$_{0.10}$-*co*-(*R*)-**2**$_{0.90}$]	631241	757489	1.20

Table S9. GPC data of Poly-[(*R*)-**1**$_r$-*co*-(*R*)-**2**$_{1-r}$] in THF.

polymer	Mn (Da)	Mw (Da)	PDI
Poly-[(*R*)-**1**$_{0.90}$-*co*-(*R*)-**2**$_{0.10}$]	311244	389055	1.25
Poly-[(*R*)-**1**$_{0.80}$-*co*-(*R*)-**2**$_{0.20}$]	329766	399017	1.21
Poly-[(*R*)-**1**$_{0.70}$-*co*-(*R*)-**2**$_{0.30}$]	377772	430660	1.14
Poly-[(*R*)-**1**$_{0.60}$-*co*-(*R*)-**2**$_{0.40}$]	411222	522252	1.27
Poly-[(*R*)-**1**$_{0.50}$-*co*-(*R*)-**2**$_{0.50}$]	445433	583517	1.31
Poly-[(*R*)-**1**$_{0.40}$-*co*-(*R*)-**2**$_{0.60}$]	498218	667612	1.34

USC UNIVERSIDADE DE SANTIAGO DE COMPOSTELA

Poly-[(*R*)-**1**$_{0.30}$-*co*-(*R*)-**2**$_{0.70}$]	482124	670152	1.39
Poly-[(*R*)-**1**$_{0.20}$-*co*-(*R*)-**2**$_{0.80}$]	551244	755204	1.37
Poly-[(*R*)-**1**$_{0.10}$-*co*-(*R*)-**2**$_{0.90}$]	569877	678154	1.19

Table S10. GPC data of Poly-[(*S*)-**1**$_{r}$-*co*-(*S*)-**2**$_{1-r}$] in THF.

polymer	Mn (Da)	Mw (Da)	PDI
Poly-[(*S*)-**1**$_{0.70}$-*co*-(*S*)-**2**$_{0.30}$]	411576	460965	1.12
Poly-[(*S*)-**1**$_{0.50}$-*co*-(*S*)-**2**$_{0.50}$]	451125	609019	1.35
Poly-[(*S*)-**1**$_{0.30}$-*co*-(*S*)-**2**$_{0.70}$]	576511	732169	1.27

Table S11. GPC data of Poly-[(*R*)-**1**$_{r}$-*co*-(*S*)-**2**$_{1-r}$] in THF.

polymer	Mn (Da)	Mw (Da)	PDI
Poly-[(*R*)-**1**$_{0.70}$-*co*-(*S*)-**2**$_{0.30}$]	381251	446064	1.17
Poly-[(*R*)-**1**$_{0.50}$-*co*-(*S*)-**2**$_{0.50}$]	501129	636434	1.27
Poly-[(*R*)-**1**$_{0.30}$-*co*-(*S*)-**2**$_{0.70}$]	576512	686049	1.19

5.3.11. FT-IR studies of polymers and copolymers

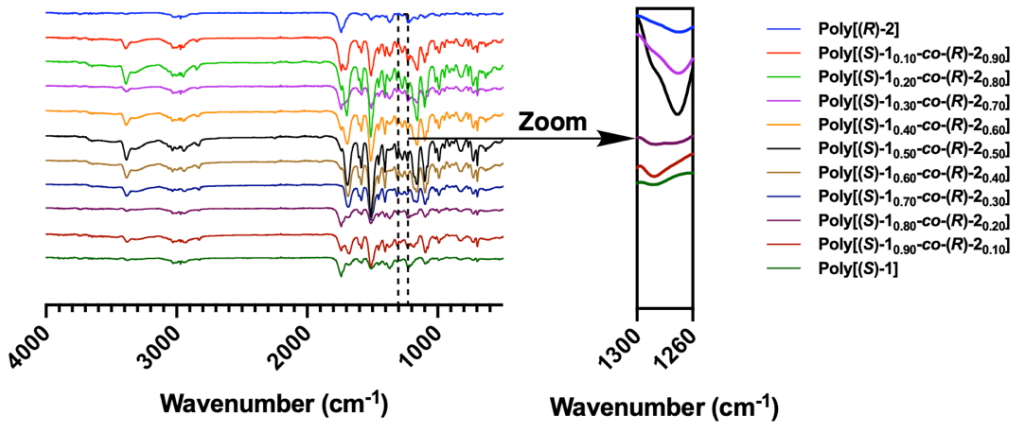


Figure S85. FT-IR/UATR full spectra of Poly-(*R*)-**2**, Poly-[(*S*)-**1**$_{r}$-*co*-(*R*)-**2**$_{1-r}$], and Poly-(*S*)-**1**, and partial spectra at the rocking of the α Hydrogen and the -CF_3 stretching bands.

USC UNIVERSIDADE DE SANTIAGO DE COMPOSTELA

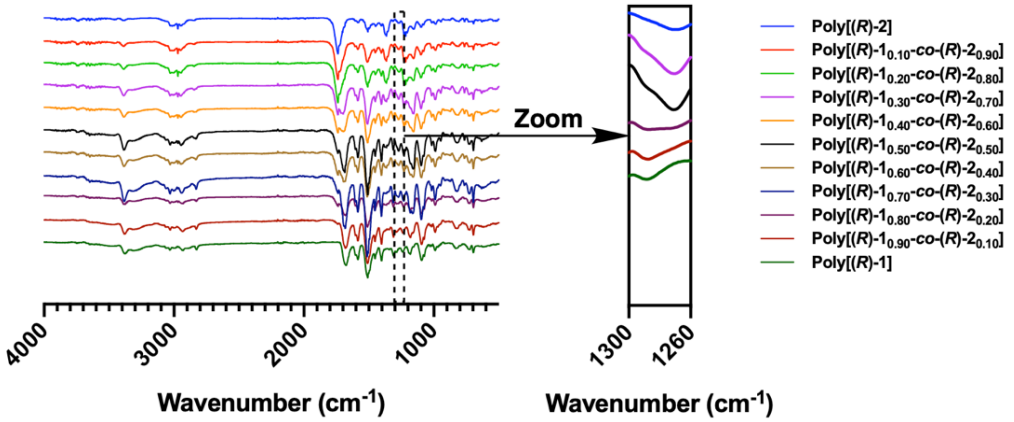


Figure S86. FT-IR/UATR full spectra of Poly-(*R*)-**2**, Poly-[(*R*)-**1**$_r$-*co*-(*R*)-**2**$_{1-r}$], and Poly-(*R*)-**1**, and partial spectra at the rocking of the α Hydrogen and the -CF_3 stretching bands.

Table S12. FT-IR/UATR assignation of the characteristic vibrations in polymers.

$\tilde{\nu}$ (cm-1)	Intensity	Assignation
3384-3372	Medium/weak	N-H stretching
3093-2934	Weak	C-H ring or olefin stretching
2890	Weak	C-H α to the carbonyl stretching in (*R*/*S*)-**1**
2845-2822	Weak	C-H stretching of OMe
1695-1677	Strong	C=O amide stretching
1600-1605	Weak	C=C ring (I) or backbone stretching
1580-1584	Medium	N-H amide (I) bending or C=C backbone stretching
1503-1506	Strong	N-H amide (II) stretching
1440-1445	Medium	C=C ring (II) stretching
1400	Medium	C=C ring (III) stretching
1283	Medium	C-H α to the carbonyl in (*R*/*S*)-**1** rocking

5.3.12. Determination of the monomer reactivity ratios in copolymerization

To estimate the monomer reactivity ratios in the copolymerization of Poly-[(*S*)-**1**$_r$-*co*-(*R*)-**2**$_{1-r}$] [(*S*)-**1** and (*R*)-**2**], and in Poly-[(*R*)-**1**$_r$-*co*-(*R*)-**2**$_{1-r}$] [(*R*)-**1** and (*R*)-**2**], the

copolymerizations of (*S*)-**1** with (*R*)-**2** and (*R*)-**1** with (*R*)-**2** at varying monomer feed ratios were carried out and were terminated at low conversions by adding, in both cases, a solution of HCl 0.05 M in MeOH (5 mL) 10 seconds after the catalyst addition. Subsequently, a solution of NaOH 0.05 M in MeOH (5 mL) was added followed by MeOH (10 mL) containing a small amount of concentrated HCl. The resulting Poly-[(*S*)-$\mathbf{1}_r$-*co*-(*R*)-$\mathbf{2}_{1-r}$] and Poly-[(*R*)-$\mathbf{1}_r$-*co*-(*R*)-$\mathbf{2}_{1-r}$] were collected by centrifugation and dried in vacuo at room temperature overnight. The copolymer compositions were determined from their quantitative ^{13}C-NMR inverse-gated decoupling spectra (Figure S87) peaks of the methoxy and carbonyl groups of (*R*/*S*)-**1** compared to (*R*)-**2** and the results are summarized in Table S13 and Table S14. The copolymer compositions represented by f are almost similar to the corresponding monomer feed ratios represented by F. For the determination of $r_{(S)\text{-}\mathbf{1}}$ and $r_{(R)\text{-}\mathbf{2}}$, and $r_{(R)\text{-}\mathbf{1}}$ and $r_{(R)\text{-}\mathbf{2}}$, the Kellen-Tüdös method was used.[154,408,409] In this method, the following equation (S7) and equation (S8) are employed.

$$\eta = \left(r_{(R)-\mathbf{2}} + \frac{r_{(S)-\mathbf{1}}}{\alpha}\right)\xi - \frac{r_{(S)-\mathbf{1}}}{\alpha} \quad \textbf{(S7)}$$

$$\eta = \left(r_{(R)-\mathbf{2}} + \frac{r_{(R)-\mathbf{1}}}{\alpha}\right)\xi - \frac{r_{(R)-\mathbf{1}}}{\alpha} \quad \textbf{(S8)}$$

To represent the experimental η and ξ and fit a regression curve to extract the reactivity ratios, the parameters are defined by equation (S9) and equation (S10).

$$\eta = \frac{G}{\alpha + H} \quad \textbf{(S9)}$$

$$\xi = \frac{H}{\alpha + H} \quad \textbf{(S10)}$$

USC UNIVERSIDADE DE SANTIAGO DE COMPOSTELA

Where H, G and α values are obtained using the equation (S11), equation (S12), and equation (S13).

$$G = \frac{F \cdot (f - 1)}{f} \quad \textbf{(S11)}$$

$$H = \frac{F^2}{f} \quad \textbf{(S12)}$$

$$\alpha = (F_{min} - F_{max})^{0.5} \quad \textbf{(S13)}$$

The estimated monomer reactivity ratios using the f value measured in the Carbonyl groups for Poly-[(*S*)-**1**$_r$-*co*-(*R*)-**2**$_{1\text{-}r}$] are $r_{(S)\text{-}\mathbf{1}}$ = 1.002 and $r_{(R)\text{-}\mathbf{2}}$ =0.992 and those for the Poly-[(*R*)-**1**$_r$-*co*-(*R*)-**2**$_{1\text{-}r}$] are $r_{(R)\text{-}\mathbf{1}}$ = 0.937 and $r_{(R)\text{-}\mathbf{2}}$ =0.845. While the estimated monomer reactivity ratios using the f value measured in the Methoxy groups for Poly-[(*S*)-**1**$_r$-*co*-(*R*)-**2**$_{1\text{-}r}$] are $r_{(S)\text{-}\mathbf{1}}$ = 1.003 and $r_{(R)\text{-}\mathbf{2}}$ =0.996 and those for the Poly-[(*R*)-**1**$_r$-*co*-(*R*)-**2**$_{1\text{-}r}$] are $r_{(R)\text{-}\mathbf{1}}$ = 0.988 and $r_{(R)\text{-}\mathbf{2}}$ =0.987. The reactivity ratios between the monomers in the two copolymerization are very similar, suggesting that the monomer distribution in copolymers is random.

Table S13. Values of yield, F, and f for Poly-[(*S*)-**1**$_r$-*co*-(*R*)-**2**$_{1\text{-}r}$].

copolymer	F	Yield (%)	f at Carbonyl NMR signal	f at Methoxy NMR signal
Poly-[(*S*)-**1**$_{0.20}$-*co*-(*R*)-**2**$_{0.80}$]	0.20	19	0.20	0.20
Poly-[(*S*)-**1**$_{0.40}$-*co*-(*R*)-**2**$_{0.60}$]	0.40	20	0.40	0.39
Poly-[(*S*)-**1**$_{0.60}$-*co*-(*R*)-**2**$_{0.40}$]	0.60	21	0.59	0.61
Poly-[(*S*)-**1**$_{0.80}$-*co*-(*R*)-**2**$_{0.20}$]	0.80	40	0.80	0.79

USC UNIVERSIDADE DE SANTIAGO DE COMPOSTELA

Table S14. Values of yield, F, and f for Poly-[(*R*)-**1**$_{r}$-*co*-(*R*)-**2**$_{1-r}$].

copolymer	F	Yield (%)	f at Carbonyl NMR signal	f at Methoxy NMR signal
Poly-[(*R*)-**1**$_{0.20}$-*co*-(*R*)-**2**$_{0.80}$]	0.20	30	0.21	0.20
Poly-[(*R*)-**1**$_{0.40}$-*co*-(*R*)-**2**$_{0.60}$]	0.40	25	0.39	0.41
Poly-[(*R*)-**1**$_{0.60}$-*co*-(*R*)-**2**$_{0.40}$]	0.60	34	0.60	0.61
Poly-[(*R*)-**1**$_{0.80}$-*co*-(*R*)-**2**$_{0.20}$]	0.80	38	0.78	0.78

USC UNIVERSIDADE DE SANTIAGO DE COMPOSTELA

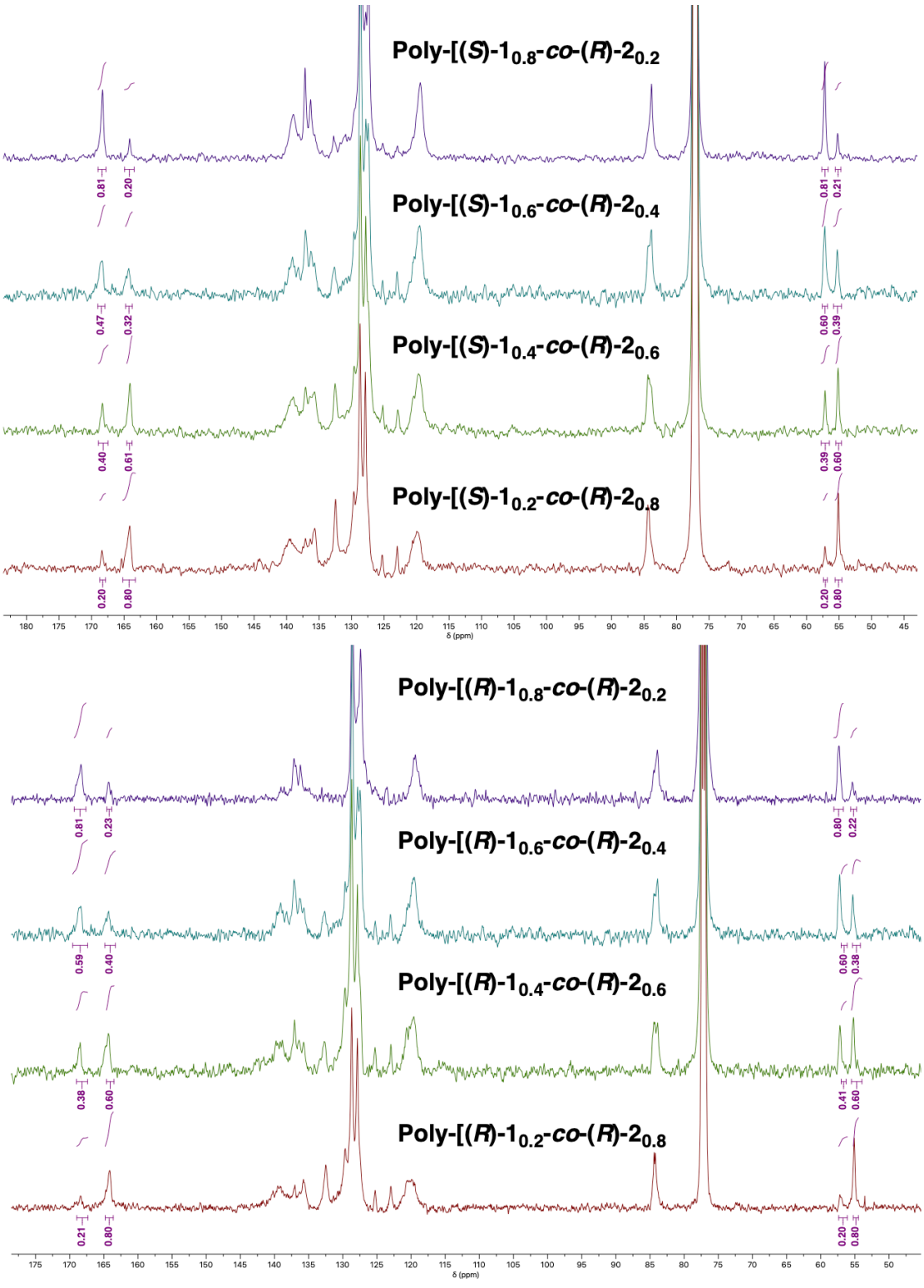


Figure S87. Quantitative ^{13}C-NMR inverse-gated decoupling spectra ($CDCl_3$, 125 MHz) of Kellen-Tüdös Poly-[(*S*)-**1**$_{0.80}$-*co*-(*R*)-**2**$_{0.20}$], Poly-[(*S*)-**1**$_{0.60}$-*co*-(*R*)-**2**$_{0.40}$], Poly-[(*S*)-**1**$_{0.40}$-*co*-(*R*)-**2**$_{0.60}$], Poly-[(*S*)-**1**$_{0.20}$-*co*-(*R*)-**2**$_{0.80}$], Poly-[(*R*)-**1**$_{0.80}$-*co*-(*R*)-**2**$_{0.20}$], Poly-[(*R*)-**1**$_{0.60}$-*co*-(*R*)-**2**$_{0.40}$], Poly-[(*R*)-**1**$_{0.40}$-*co*-(*R*)-**2**$_{0.60}$], and Poly-[(*R*)-**1**$_{0.20}$-*co*-(*R*)-**2**$_{0.80}$]. Integration of the carbons of the carbonyl and the methoxy of (*S*/*R*)-**1** compared to (*R*)-**2**.

USC UNIVERSIDADE DE SANTIAGO DE COMPOSTELA

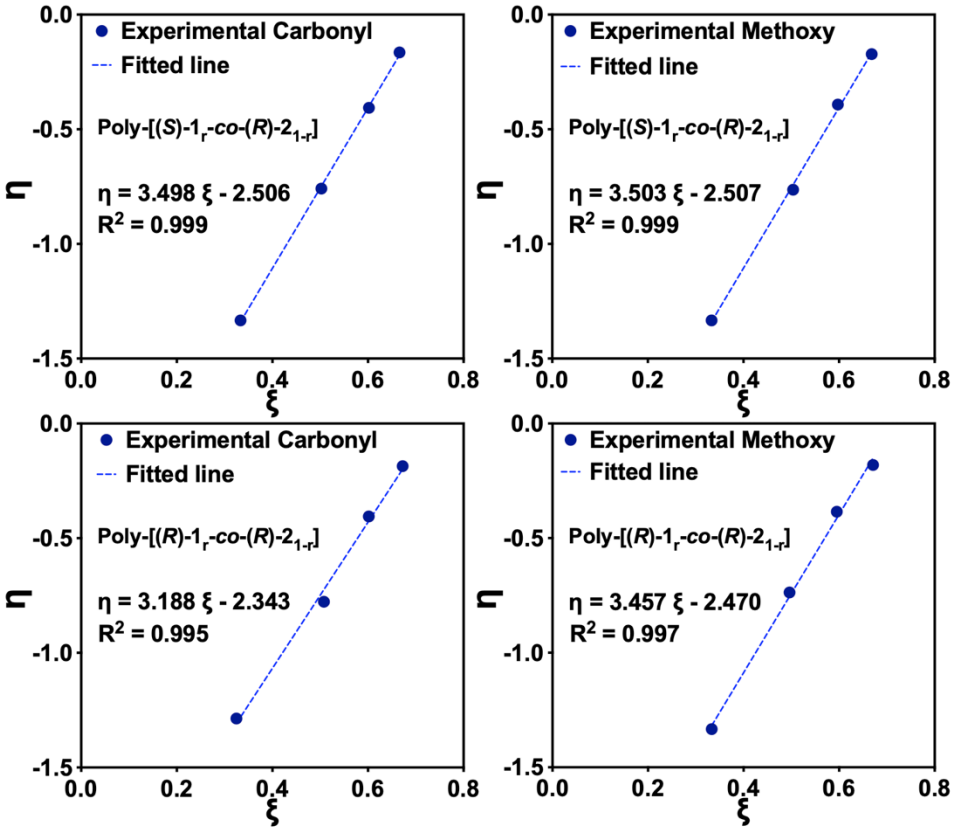


Figure S88. Kellen-Tüdös plots for the polymerization of Poly-[(*S*)-**1**$_r$-*co*-(*R*)-**2**$_{1-r}$],and Poly-[(*R*)-**1**$_r$-*co*-(*R*)-**2**$_{1-r}$] copolymer series.

USC UNIVERSIDADE DE SANTIAGO DE COMPOSTELA

5.3.13. ECD and UV-Vis studies of complexed homopolymers with monovalent and divalent metal ions

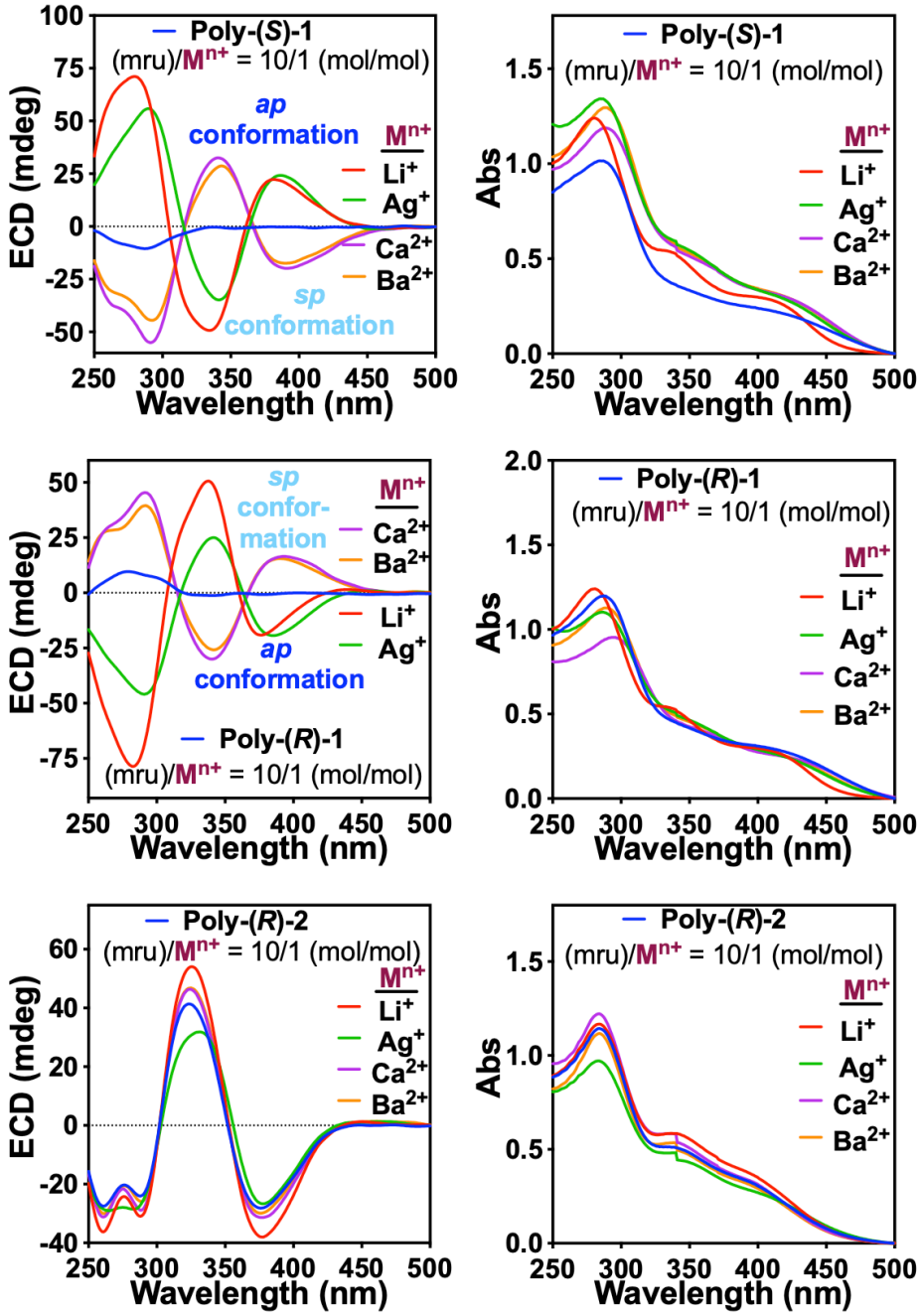


Figure S89. ECD and UV-Vis spectra of Poly-(*S*)-**1**, Poly-(*R*)-**1**, and Poly-(*R*)-**2** (c=0.3 mg/mL $CHCl_3$) coordinated to 0.1 equiv of $LiClO_4$, $AgClO_4$, $Ca(ClO_4)_2$, and $Ba(ClO_4)_2$. (c=10.0 mg/mL MeOH).

USC UNIVERSIDADE DE SANTIAGO DE COMPOSTELA

5.3.14. FT-IR studies of polymers and copolymers complexed with metal ions

First, to a solution of the polymer (c = 0.3 mg·mL^{-1} $CHCl_3$) we added 0.1 equiv of $M(ClO_4)_x$ from a solution of 10 mg·mL^{-1} MeOH. Then this solution was deposited in the FT-IR and we let it dry to obtain a film.

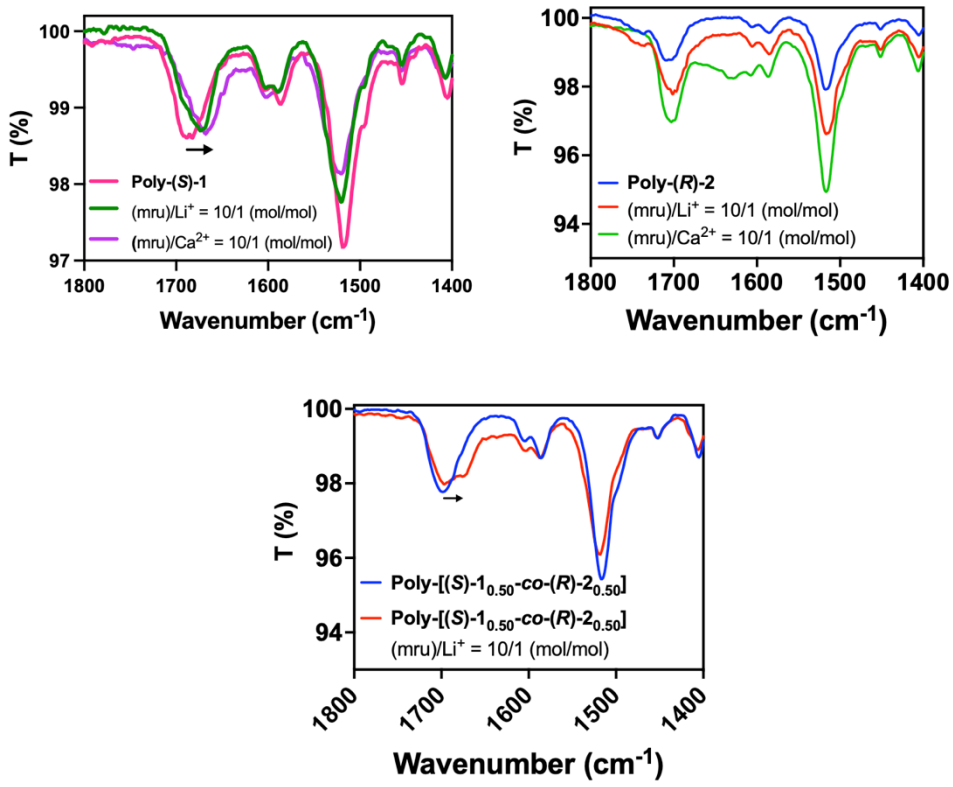


Figure S90. FT-IR/UATR spectra of Poly-(*S*)-**1**, Poly-(*R*)-**2**, and Poly-[(*S*)-$\mathbf{1}_{0.50}$-*co*-(*R*)-$\mathbf{2}_{0.50}$] coordinated to $LiClO_4$ and $Ca(ClO_4)_2$.

5.3.15. VT-UV-Vis studies of Poly-[(*S*)-$\mathbf{1}_{0.6}$-*co*-(*R*)-$\mathbf{2}_{0.4}$] and Poly-[(*R*)-$\mathbf{1}_{0.4}$-*co*-(*R*)-$\mathbf{2}_{0.6}$] complexed with Li^+ and Ca^{2+}

VT-UV-Vis (0.5 ºC·min^{-1}) to a solution of Poly-[(*S*)-$\mathbf{1}_{0.6}$-*co*-(*R*)-$\mathbf{2}_{0.4}$] and Poly-[(*R*)-$\mathbf{1}_{0.6}$-*co*-(*R*)-$\mathbf{2}_{0.4}$] (c = 0.3 mg·mL^{-1} $CHCl_3$) after the addition of 0.1 equiv of $LiClO_4$ or $Ca(ClO_4)_2$ from a solution of 10 mg/mL MeOH.

USC UNIVERSIDADE DE SANTIAGO DE COMPOSTELA

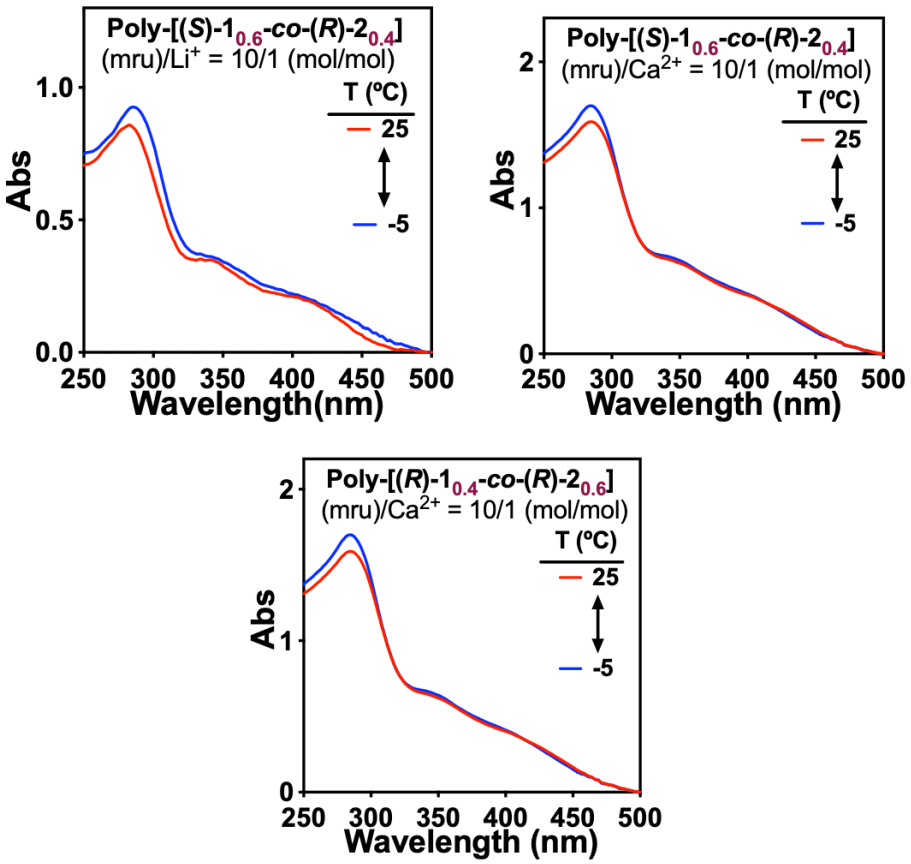


Figure S91. VT-UV-Vis (0.5 ºC·min^{-1}) of Poly-[(*S*)-**1**$_{0.6}$-*co*-(*R*)-**2**$_{0.4}$] and Poly-[(*R*)-**1**$_{0.6}$-*co*-(*R*)-**2**$_{0.4}$] (0.3 mg·mL^{-1} $CHCl_3$) in presence of 0.1 equiv of $LiClO_4$ $Ca(ClO_4)_2$ (10 mg·mL^{-1} MeOH).

5.3.16. VT-ECD studies of Poly-[(*S*)-1$_{0.7}$-*co*-(*R*)-2$_{0.3}$] and Poly-[(*S*)-1$_{0.3}$-*co*-(*R*)-2$_{0.7}$] complexed with Li$^+$ and Ca^{2+}

VT-ECD (0.5 ºC·min^{-1}) of a solution of Poly-[(*S*)-**1**$_{0.7}$-*co*-(*R*)-**2**$_{0.3}$] and Poly-[(*R*)-**1**$_{0.3}$-*co*-(*R*)-**2**$_{0.7}$] (c = 0.3 mg·mL^{-1} $CHCl_3$) after the addition of 0.1 equiv of $LiClO_4$ or $Ca(ClO_4)_2$ from a solution of 10 mg/mL MeOH.

USC UNIVERSIDADE DE SANTIAGO DE COMPOSTELA

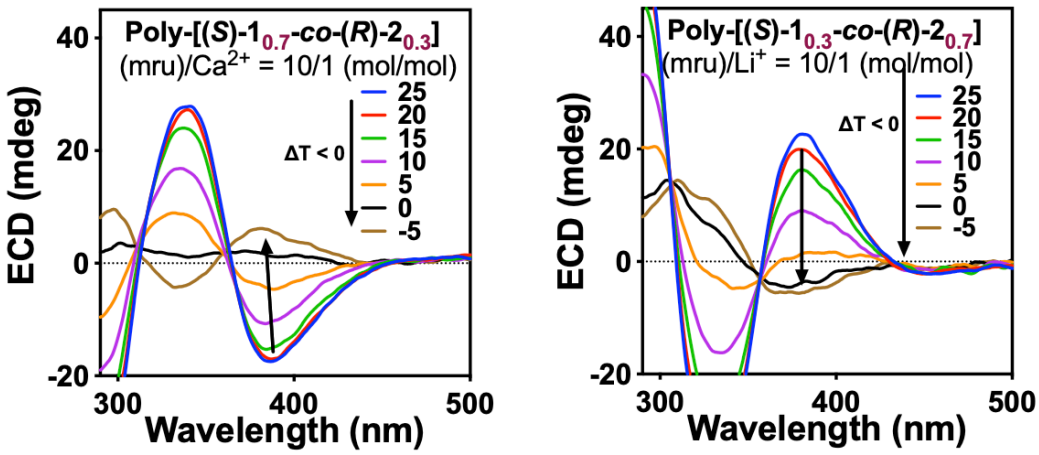


Figure S92. VT-ECD (0.5 ºC·min^{-1}) of a solution of Poly-[(*S*)-**1**$_{0.7}$-*co*-(*R*)-**2**$_{0.3}$] and Poly-[(*R*)-**1**$_{0.3}$-*co*-(*R*)-**2**$_{0.7}$] (c = 0.3 mg·mL^{-1} $CHCl_3$) after the addition of 0.1 equiv of $LiClO_4$ or $Ca(ClO_4)_2$ from a solution of 10 mg/mL MeOH.

USC UNIVERSIDADE DE SANTIAGO DE COMPOSTELA

5.3.17. ECD of the homopolymer Poly-(*S*)-1 or Poly-(*R*)-1 mixtures with Poly-(*R*)-2 in $CHCl_3$ and complexed with Li^+ and Ca^{2+}

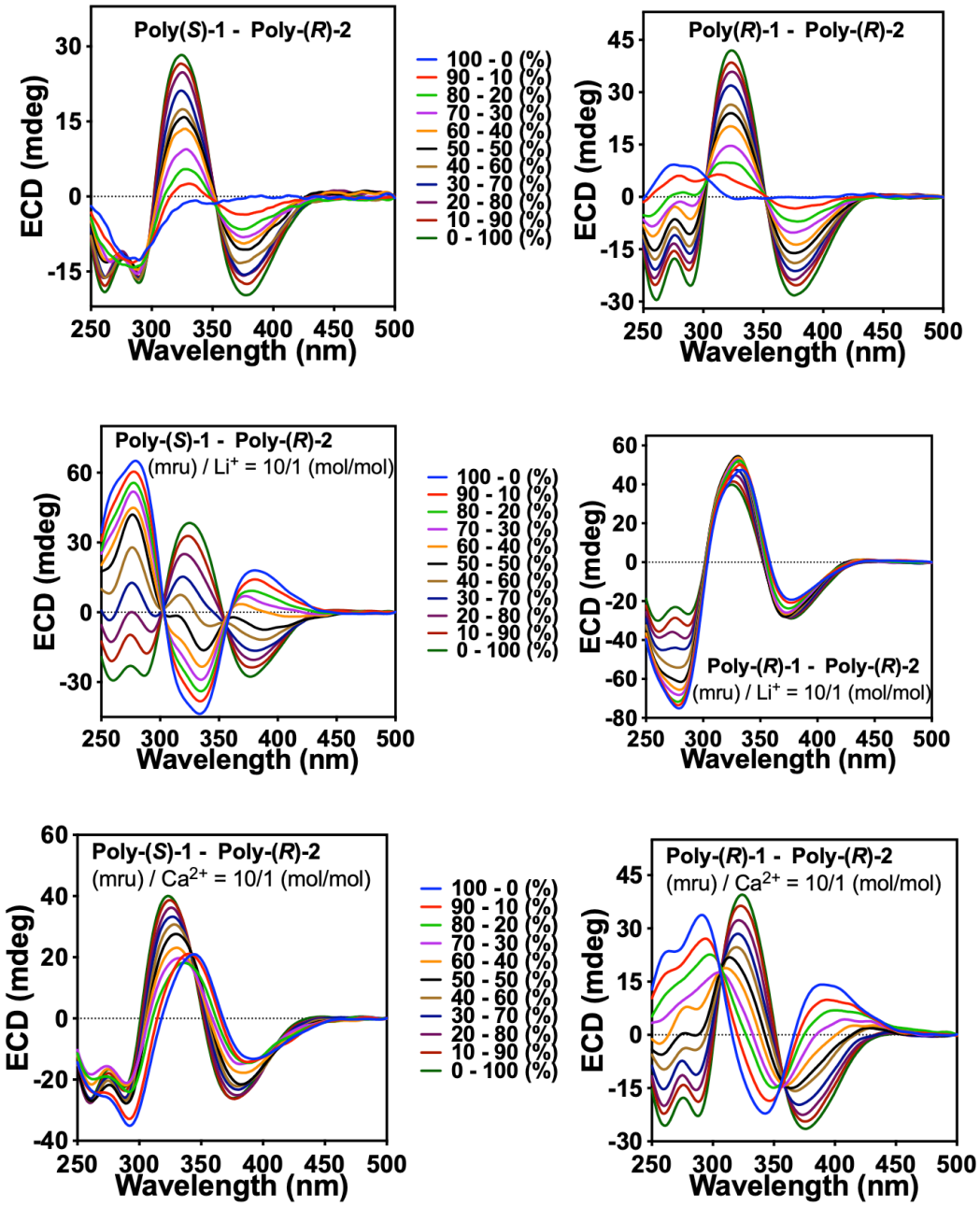


Figure S93. ECD spectra of the homopolymer mixtures of Poly-(*S*)-**1** or Poly-(*R*)-**1** with Poly-(*R*)-**2** in $CHCl_3$ (c=0.3 mg/mL $CHCl_3$) in the absence and in the presence of 0.1 equiv of $LiClO_4$ $Ca(ClO_4)_2$ (10.0 mg/mL MeOH).

USC UNIVERSIDADE DE SANTIAGO DE COMPOSTELA

5.3.18. ECD, UV-Vis and g_{value} of Poly-[(*S*)-1$_r$-*co*-(*R*)-2$_{1-r}$] and Poly-[(*R*)-1$_r$-*co*-(*R*)-2$_{1-r}$] in $CHCl_3$ and complexed with Li^+ and Ca^{2+}

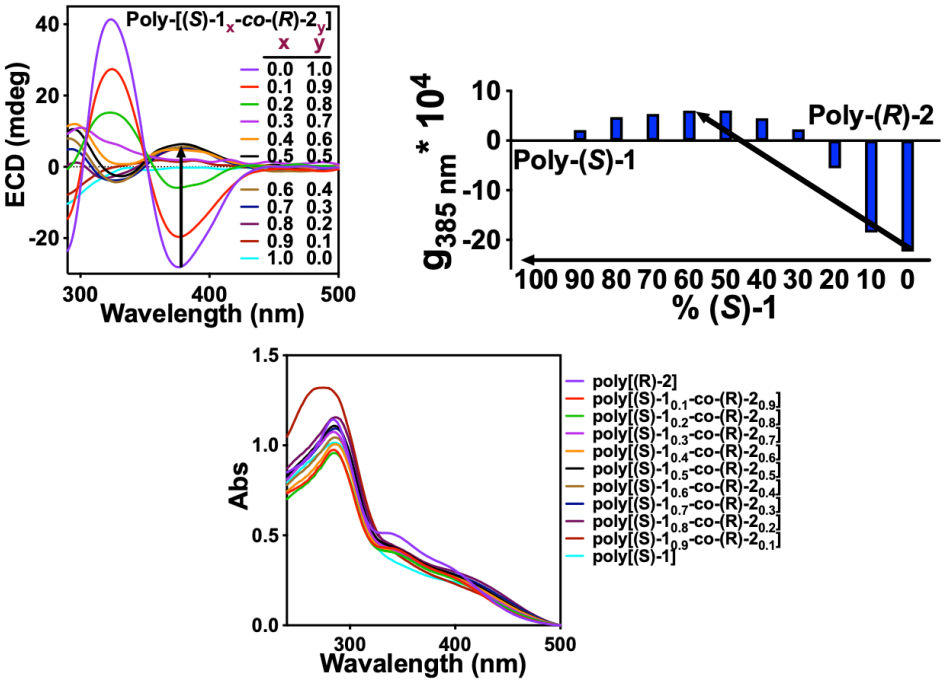


Figure S94. ECD, g_{value}, and UV-Vis spectra of Poly-[(*S*)-**1**$_r$-*co*-(*R*)-**2**$_{1-r}$] (0.3 mg·mL^{-1} $CHCl_3$).

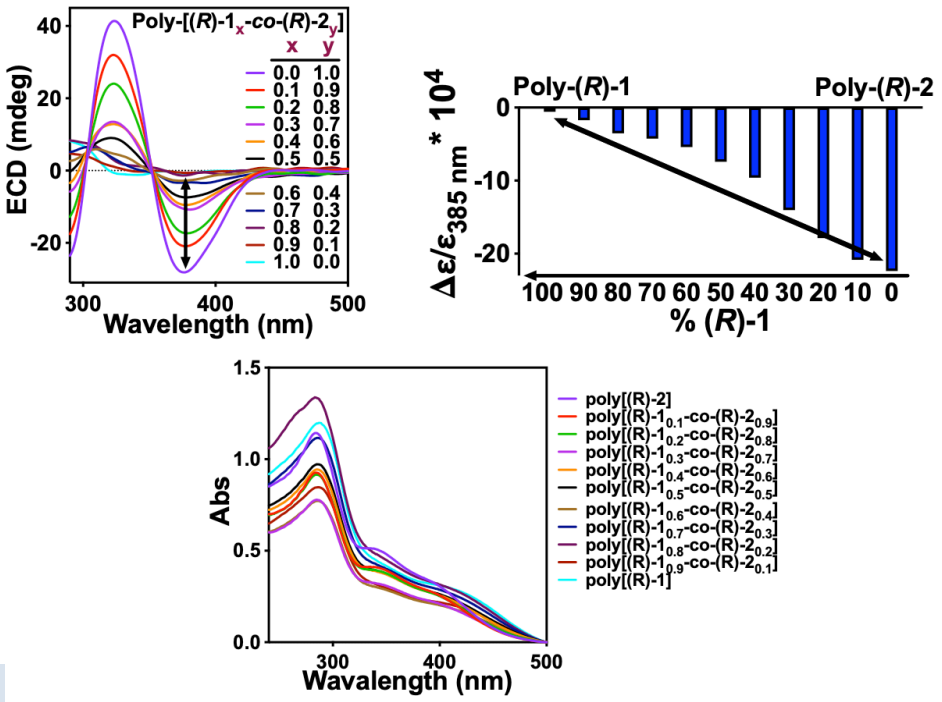


Figure S95. ECD, g_{value}, and UV-Vis spectra of Poly-[(*R*)-**1**$_r$-*co*-(*R*)-**2**$_{1-r}$] (0.3 mg·mL^{-1} $CHCl_3$).

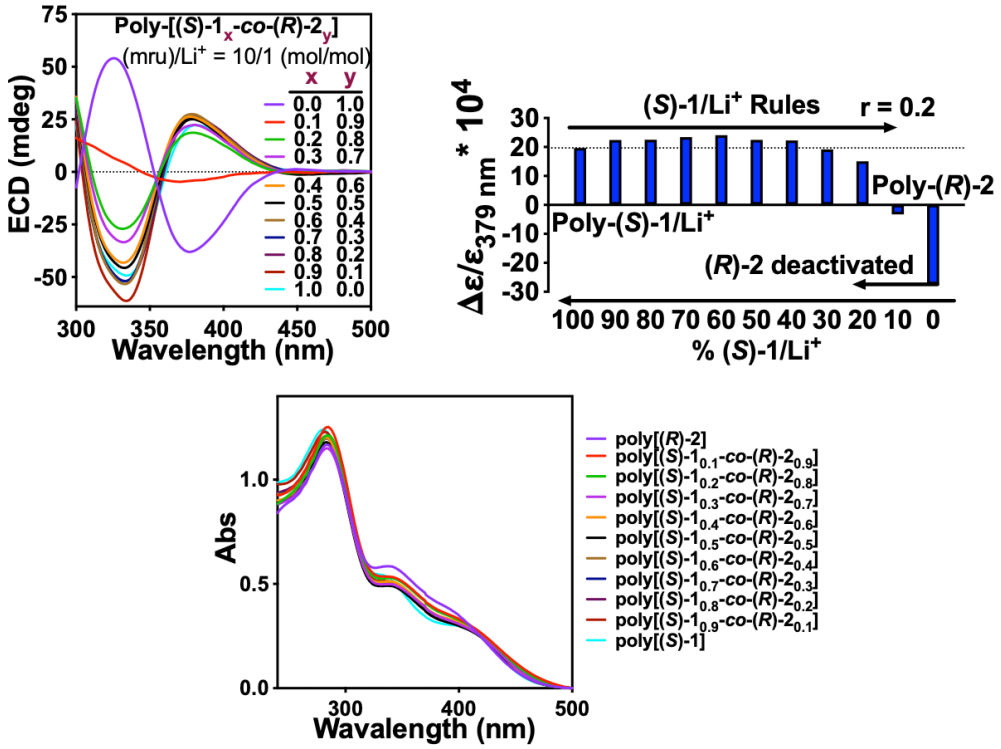


Figure S96. ECD, g_{value}, and UV-Vis spectra of Poly-[(*S*)-**1**$_r$-*co*-(*R*)-**2**$_{1-r}$] (0.3 mg·mL^{-1} $CHCl_3$) in presence of 0.1 equiv of $LiClO_4$ (10 mg·mL^{-1} MeOH).

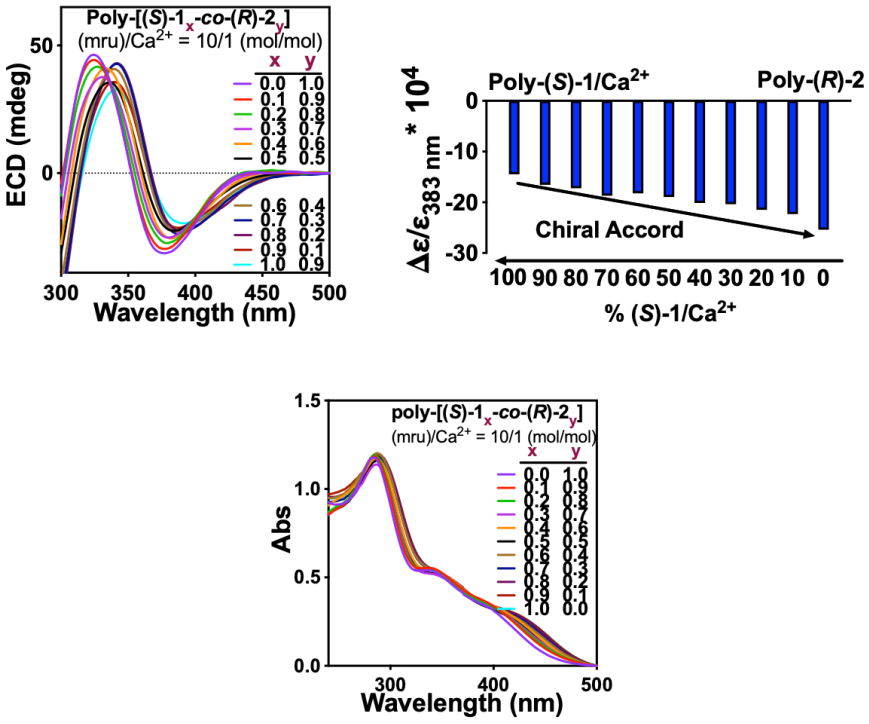


Figure S97. ECD, g_{value}, and UV-Vis spectra of Poly-[(*S*)-**1**$_r$-*co*-(*R*)-**2**$_{1-r}$] (0.3 mg·mL^{-1} $CHCl_3$) in presence of 0.1 equiv of $Ca(ClO_4)_2$ (10 mg·mL^{-1} MeOH).

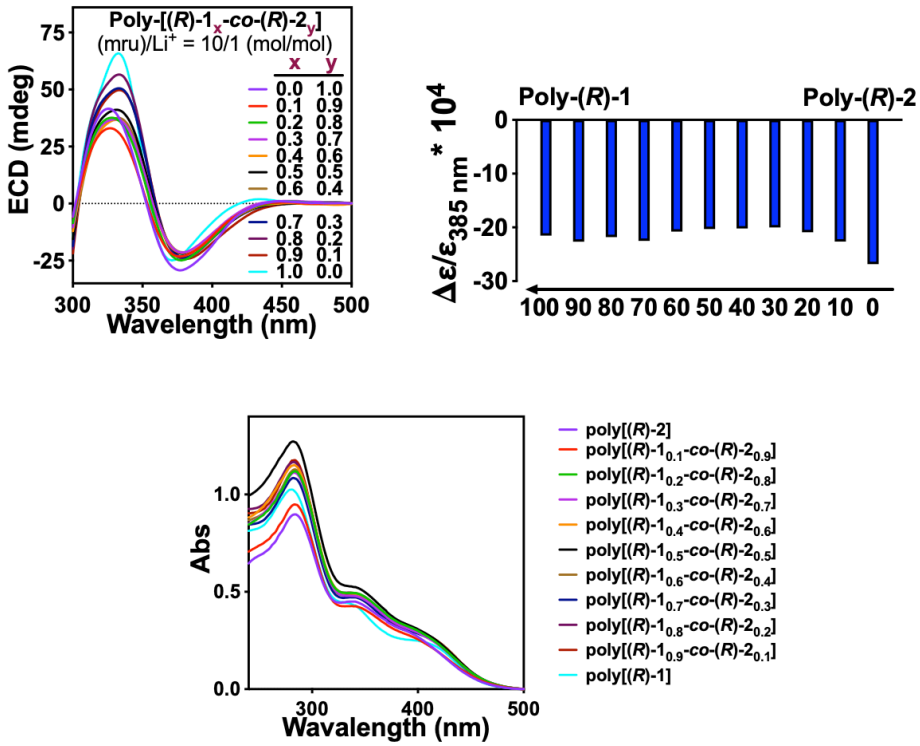


Figure S98. ECD, g_{value}, and UV-Vis spectra of Poly-[(*R*)-**1**$_r$-*co*-(*R*)-**2**$_{1-r}$] (0.3 mg·mL^{-1} $CHCl_3$) in presence of 0.1 equiv of $LiClO_4$ (10 mg·mL^{-1} MeOH).

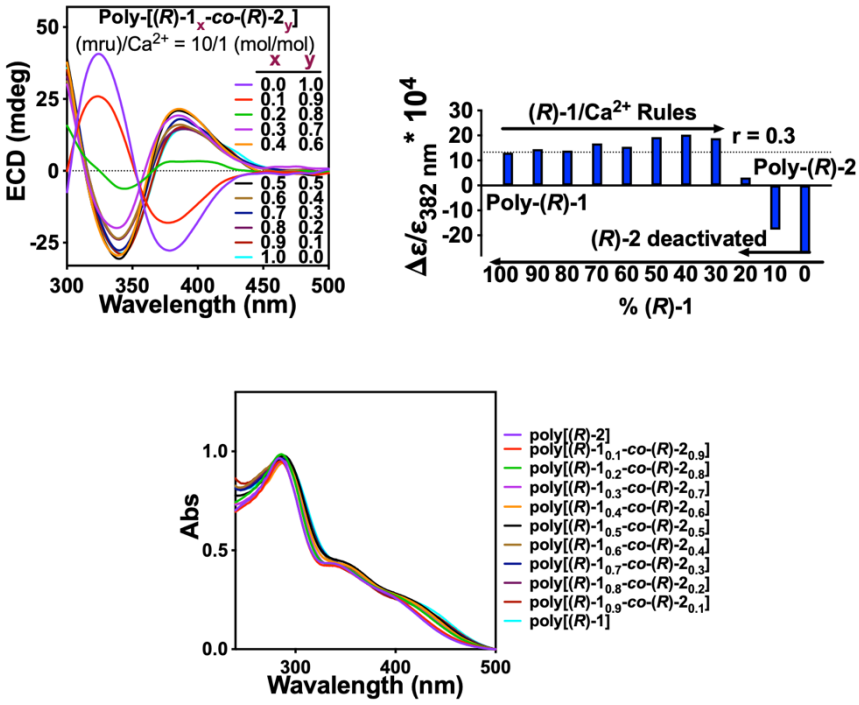


Figure S99. ECD, g_{value}, and UV-Vis spectra of Poly-[(*R*)-**1**$_r$-*co*-(*R*)-**2**$_{1-r}$] (0.3 mg·mL^{-1} $CHCl_3$) in presence of 0.1 equiv of $Ca(ClO_4)_2$ (10 mg·mL^{-1} MeOH).

5.3.19. ECD and UV of Poly-[(*S*)-1$_r$-*co*-(*S*)-2$_{1-r}$] and Poly-[(*R*)-1$_r$-*co*-(*S*)-2$_{1-r}$] in $CHCl_3$ and complexed with Li^+ and Ca^{2+}

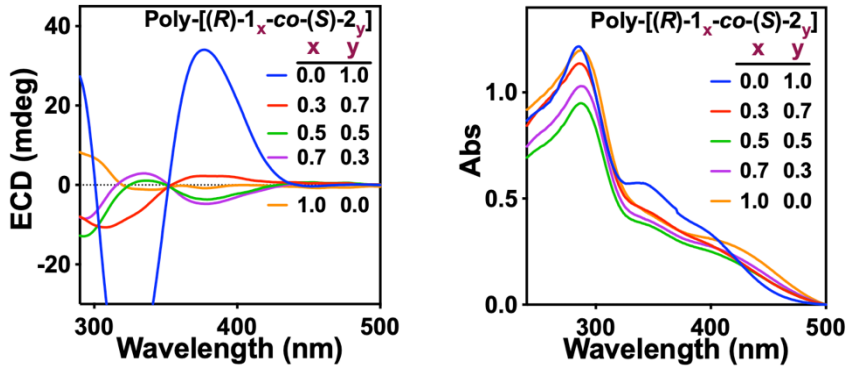


Figure S100. ECD, g_{value}, and UV-Vis spectra of Poly-[(*R*)-**1**$_r$-*co*-(*S*)-**2**$_{1-r}$] (0.3 mg·mL^{-1} $CHCl_3$).

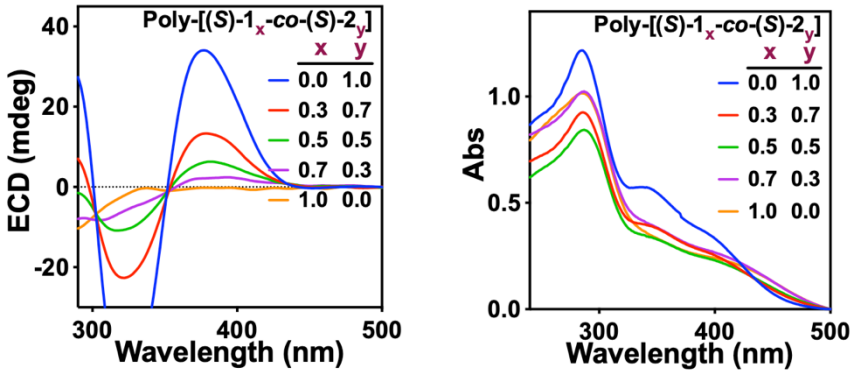


Figure S101. ECD, g_{value}, and UV-Vis spectra of Poly-[(*S*)-**1**$_r$-*co*-(*S*)-**2**$_{1-r}$] (0.3 mg·mL^{-1} $CHCl_3$).

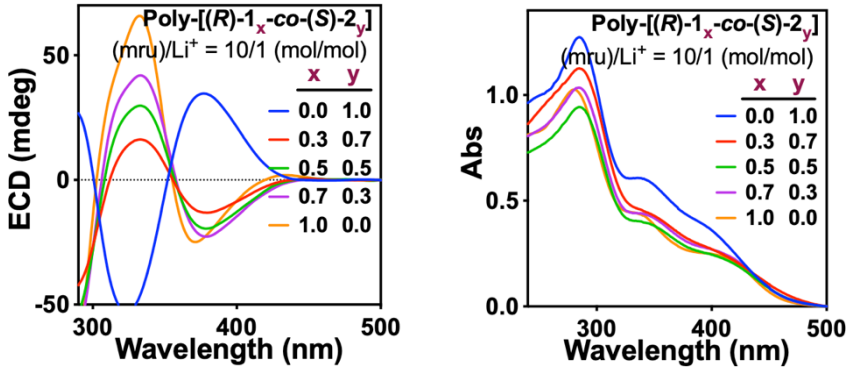


Figure S102. ECD, g_{value}, and UV-Vis spectra of Poly-[(*R*)-**1**$_r$-*co*-(*S*)-**2**$_{1-r}$] (0.3 mg·mL^{-1} $CHCl_3$) in presence of 0.1 equiv of $LiClO_4$ (10 mg·mL^{-1} MeOH).

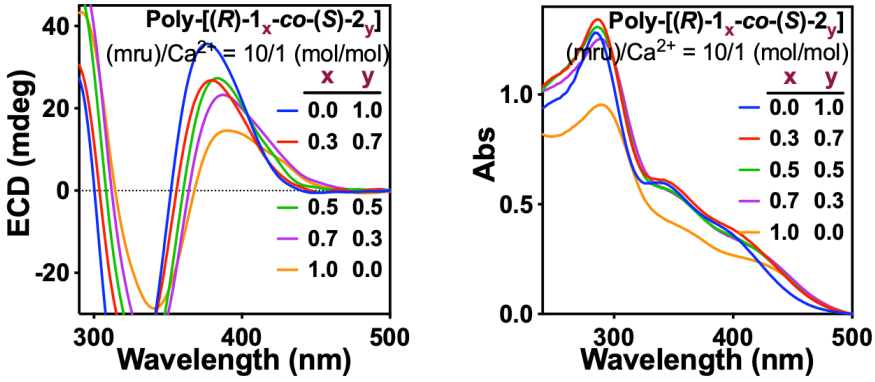


Figure S103. ECD, g_{value}, and UV-Vis spectra of Poly-[(*R*)-**1**$_r$-*co*-(*S*)-**2**$_{1-r}$] (0.3 mg·mL^{-1} $CHCl_3$) in presence of 0.1 equiv of $Ca(ClO_4)_2$ (10 mg·mL^{-1} MeOH).

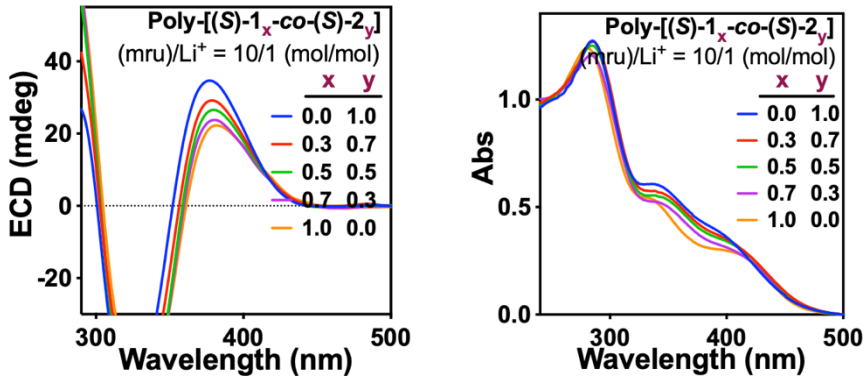


Figure S104. ECD, g_{value}, and UV-Vis spectra of Poly-[(*S*)-**1**$_r$-*co*-(*S*)-**2**$_{1-r}$] (0.3 mg·mL^{-1} $CHCl_3$) in presence of 0.1 equiv of $LiClO_4$ (10 mg·mL^{-1} MeOH).

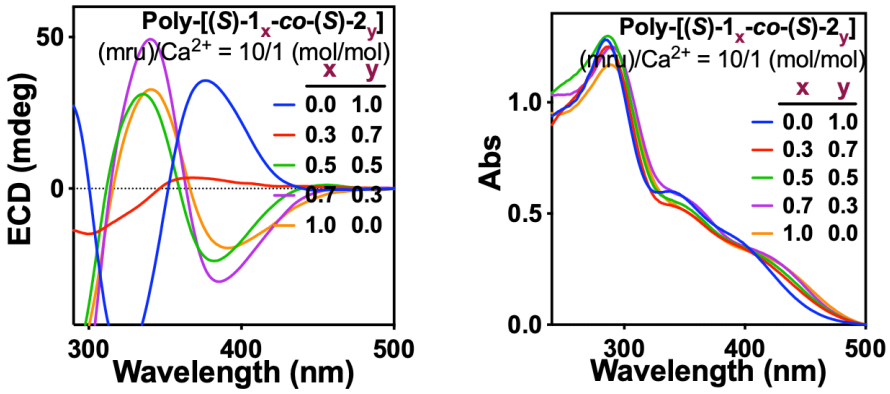


Figure S105. ECD, g_{value}, and UV-Vis spectra of Poly-[(*S*)-**1**$_r$-*co*-(*S*)-**2**$_{1-r}$] (0.3 mg·mL^{-1} $CHCl_3$) in presence of 0.1 equiv of $Ca(ClO_4)_2$ (10 mg·mL^{-1} MeOH).

USC UNIVERSIDADE DE SANTIAGO DE COMPOSTELA

5.3.20. DSC Studies

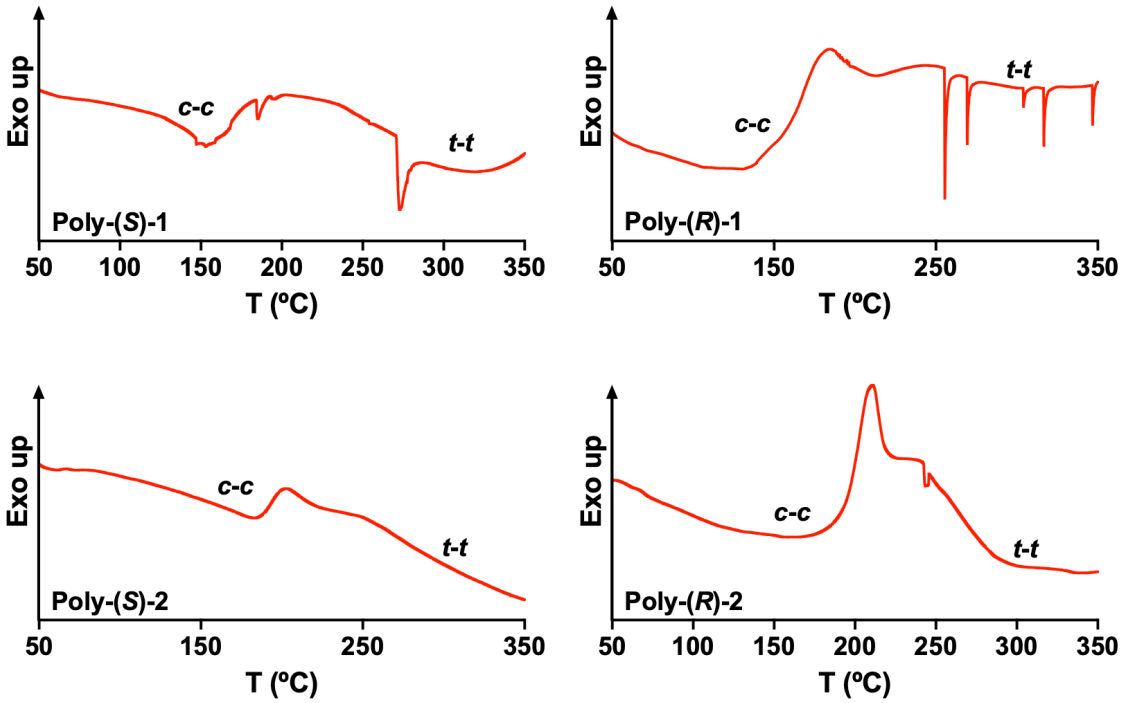


Figure S106. DSC of homopolymers film of Poly-(*S*)-**1**, Poly-(*R*)-**1**, Poly-(*S*)-**2**, and Poly-(*R*)-**2** ($CHCl_3$ film).

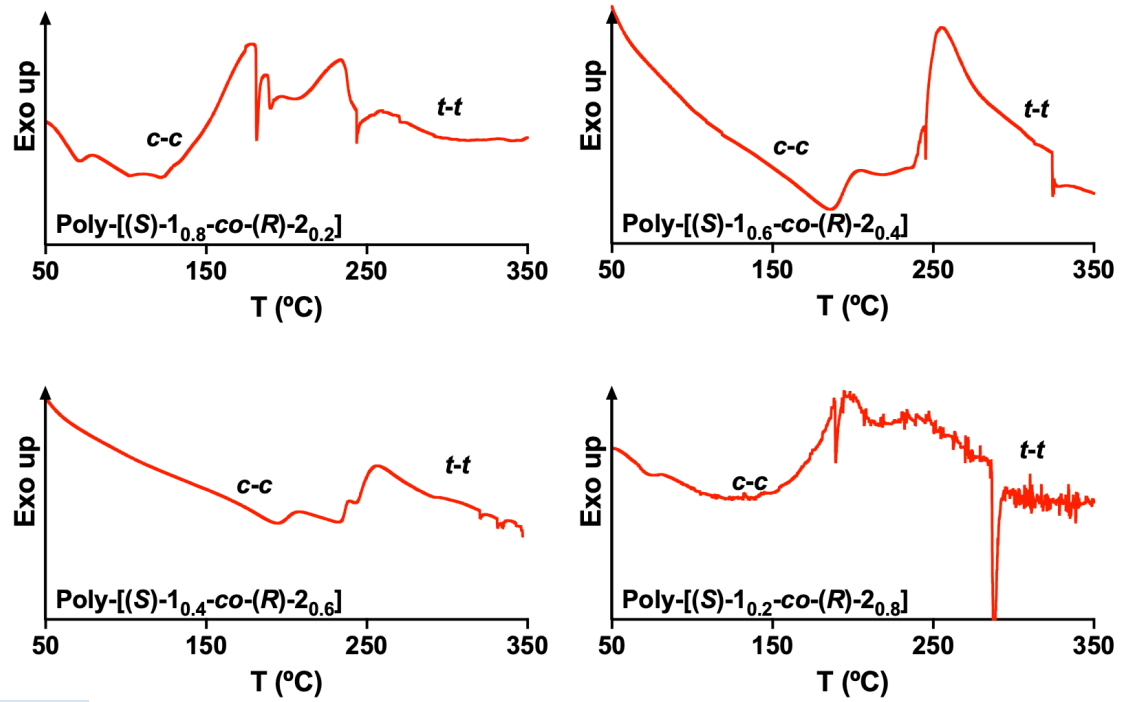


Figure S107. DSC of copolymers of Poly-[(*S*)-**1**$_{0.8}$-*co*-(*R*)-**2**$_{0.2}$], Poly-[(*S*)-**1**$_{0.6}$-*co*-(*R*)-**2**$_{0.4}$], Poly-[(*S*)-**1**$_{0.4}$-*co*-(*R*)-**2**$_{0.6}$], and Poly-[(*S*)-**1**$_{0.2}$-*co*-(*R*)-**2**$_{0.8}$] ($CHCl_3$ film).

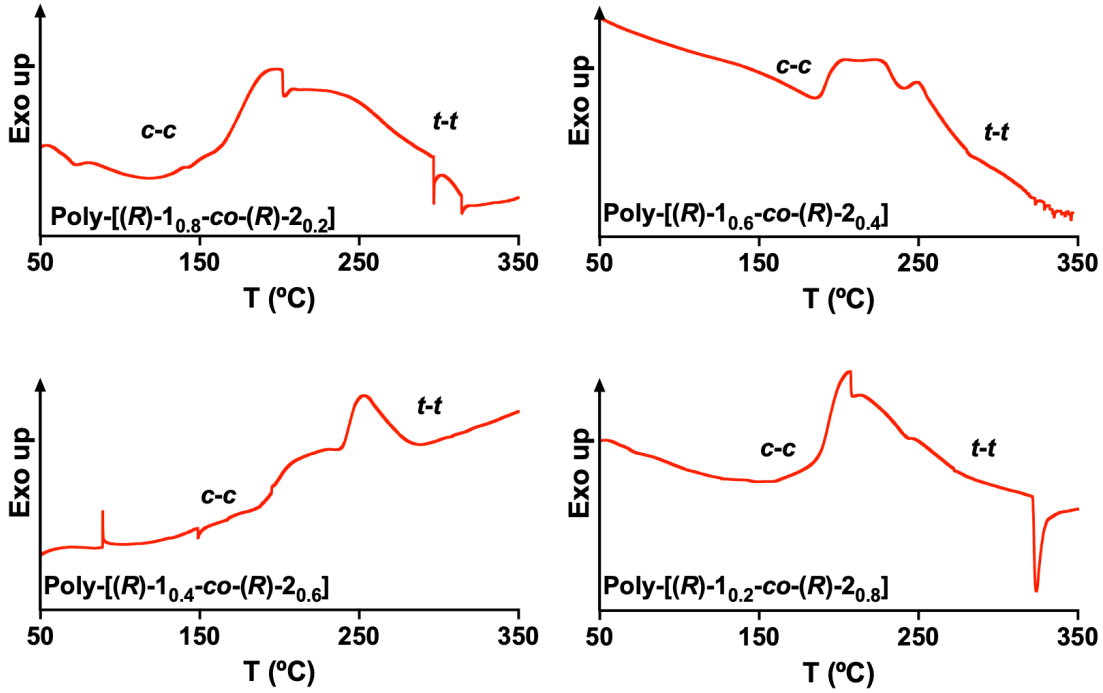


Figure S108. DSC of copolymers of Poly-[(*R*)-**1**$_{0.8}$-*co*-(*R*)-**2**$_{0.2}$], Poly-[(*R*)-**1**$_{0.6}$-*co*-(*R*)-**2**$_{0.4}$], Poly-[(*R*)-**1**$_{0.4}$-*co*-(*R*)-**2**$_{0.6}$], and Poly-[(*R*)-**1**$_{0.2}$-*co*-(*R*)-**2**$_{0.8}$] ($CHCl_3$ film).

5.3.21. Raman Studies

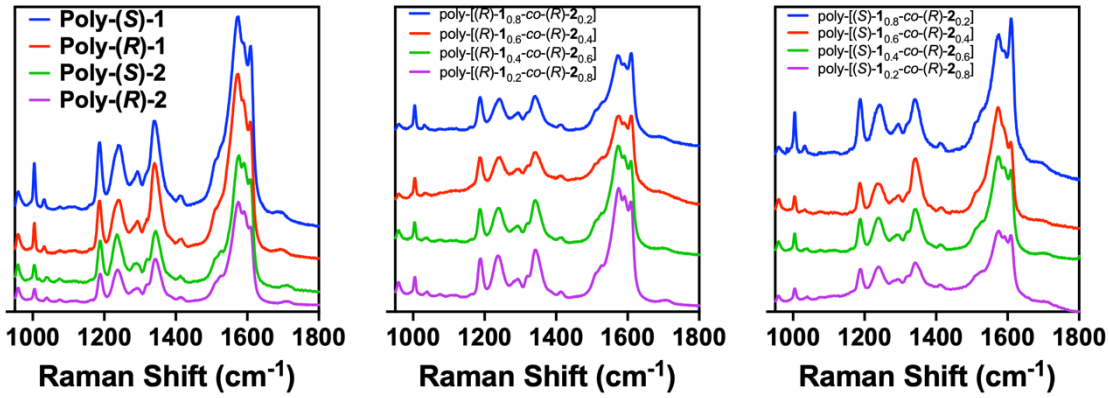


Figure S109. Confocal Raman spectra of Poly-(*S*)-**1**, Poly-(*R*)-**1**, Poly-(*S*)-**2**, Poly-(*R*)-**2**, Poly-[(*R*)-**1**$_{0.8}$-*co*-(*R*)-**2**$_{0.2}$], Poly-[(*R*)-**1**$_{0.6}$-*co*-(*R*)-**2**$_{0.4}$], Poly-[(*R*)-**1**$_{0.4}$-*co*-(*R*)-**2**$_{0.6}$], Poly-[(*R*)-**1**$_{0.2}$-*co*-(*R*)-**2**$_{0.8}$], Poly-[(*S*)-**1**$_{0.8}$-*co*-(*R*)-**2**$_{0.2}$], Poly-[(*S*)-**1**$_{0.6}$-*co*-(*R*)-**2**$_{0.4}$], Poly-[(*S*)-**1**$_{0.4}$-*co*-(*R*)-**2**$_{0.6}$], and Poly-[(*S*)-**1**$_{0.2}$-*co*-(*R*)-**2**$_{0.8}$], (Laser 785 nm) ($CHCl_3$ film).

USC
UNIVERSIDADE DE SANTIAGO DE COMPOSTELA

5.3.22. Abnormal chiral-to-chiral Sergeants and Soldiers Effect in the poly-[(*R*)-**1**$_r$-*co*-(*S*)-**2**$_{1-r}$] copolymer series

In this enantiomeric copolymer series, the same chiral-to-chiral Abnormal Sergeants and Soldiers Effect is observed, although (*S*)-**2** comonomer (Sergeant) which is folded into a *P* helix commands the 90% of (*R*)-**1** comonomer (Soldier) to fold into an *M* helix [$ECD_{380\ nm} < 0$] through the adoption of an *ap*-OMe conformation at the pendant. The helical sense induced by the poly-[(*R*)-**1**$_r$-*co*-(*S*)-**2**$_{1-r}$] copolymer series are opposite to those observed for the poly-[(*S*)-**1**$_r$-*co*-(*R*)-**2**$_{1-r}$] copolymer series due to their enantiomeric relationship (Figure S110b).

DFT Computational studies (geometry optimization, frequency on gaussian 16 and NCI on Multiwfn calculations with wb97xd/6-31+g** PCM=$CHCl_3$) show that within the copolymer, the comonomer (*S*)-**2** (Sergeant), present into an *ap*-CF_3 conformation of the (O=)C-C(-CF_3) bonds, commands an *ap*-OMe conformation of the (O=)C-C(-O) bonds of comonomer (*R*)-**1** to induce a final *M* helix into the copolymer which shows a $\pi-\pi$ stacking between the phenyl rings of adjacent chiral pendants (Figure S110f).

To corroborate the results obtained from computational studies, perchlorate salts of monovalent and divalent metal ions such as $LiClO_4$ (10 mg/mL MeOH) and $Ca(ClO_4)_2$ were added to vials containing a chloroform solution of the copolymer poly-[(*R*)-**1**$_r$-*co*-(*S*)-**2**$_{1-r}$] (r=0.9) (0.3 mg/mL $CHCl_3$) to form poly-[(*R*)-**1**$_r$-*co*-(*S*)-**2**$_{1-r}$]/M^{n+} in a 1.0/0.1 mol/mol ratio. This copolymer was chosen from the copolymer series because it has a large amount of the soldier [(*R*)-**1**] that shows metal ion valence stimuli-responsiveness. As expected, the ECD trace of the poly-[(*R*)-**1**$_r$-*co*-(*S*)-**2**$_{1-r}$]/Li^+ has the same ECD pattern than the one obtained for poly-[(*R*)-**1**$_r$-*co*-(*S*)-**2**$_{1-r}$] in the absence of the metal ion salt. Moreover, the ECD trace of the poly-[(*R*)-**1**$_r$-*co*-(*S*)-**2**$_{1-r}$]/Ca^{2+} produce a helix inversion of the ECD trace regarding to the one obtained for poly-[(*R*)-**1**$_r$-*co*-(*S*)-**2**$_{1-r}$] in the absence of the metal ion salt (Figure S110c and Figure S110d). This different stimuli-responsiveness of the copolymers to metal ions, confirm that monomer (*R*)-**1** adopts a preferred *ap*-OMe conformation when is copolymerized with (*S*)-**2**.

By applying a modification of Sato's model, it was possible to obtain the $\Delta G_{h,R1,R1}$=+0.34 J/mol, $\Delta G_{h,S2,S2}$=+268.00 J/mol, and $\Delta G_{h,R1,S2}$=-41.07 J/mol which agrees with an Abnormal Sergeant and Soldiers Effect (Comm -1.55 [Sergeant x= (*S*)-**2**]),) (Figure S110e).

USC DE COMPOSTELA

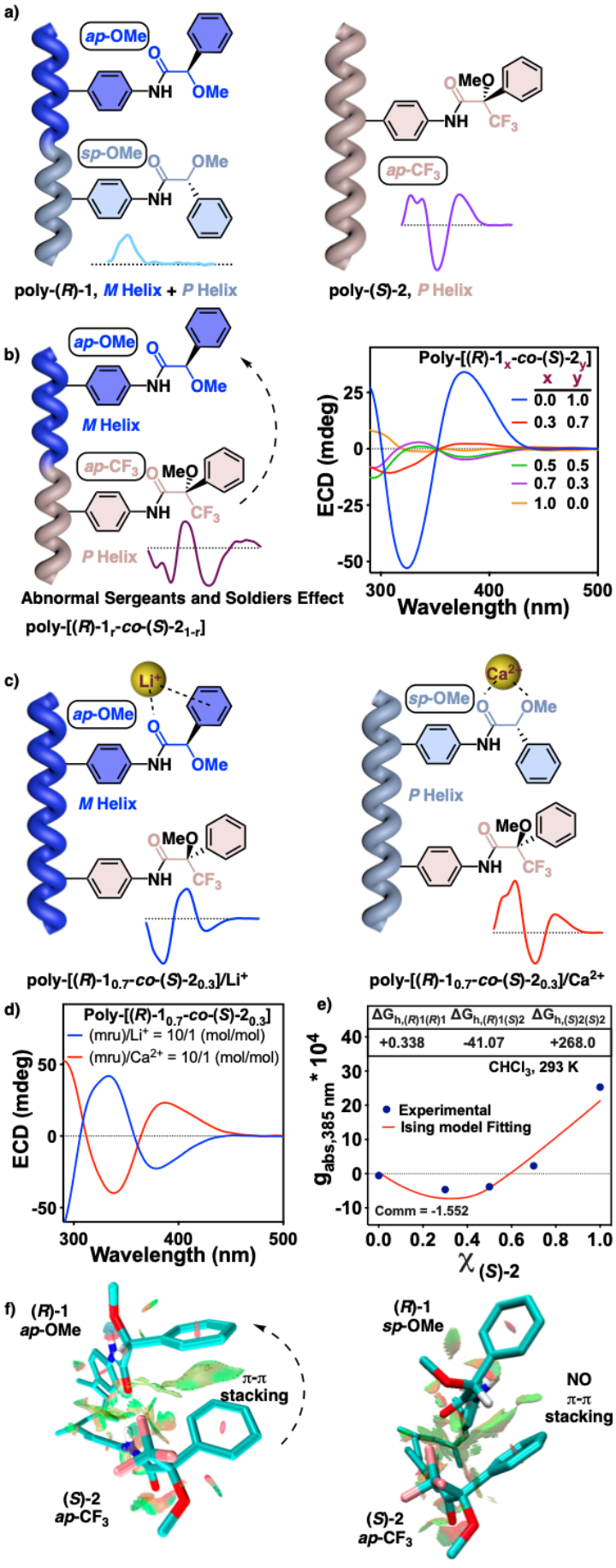

a)
ap-OMe
sp-OMe
poly-(R)-1, M Helix + P Helix
poly-(S)-2, P Helix
b)
M Helix
P Helix
Abnormal Sergeants and Soldiers Effect
poly-[(R)-1r-co-(S)-21-r]
Poly-[(R)-1x-co-(S)-2y]
ECD (mdeg)
Wavelength (nm)
c)
poly-[(R)-10.7-co-(S)-20.3]/Li+
poly-[(R)-10.7-co-(S)-20.3]/Ca2+
d)
(mru)/Li+ = 10/1 (mol/mol)
(mru)/Ca2+ = 10/1 (mol/mol)
e)
CHCl3, 293 K
Experimental
Ising model Fitting
Comm = -1.552
f)
(R)-1 ap-OMe
π-π stacking
(S)-2 ap-CF3
(R)-1 sp-OMe
NO π-π stacking

Figure S110. a) ECD pattern, helical sense, and equilibrium of the conformations or major conformation at the pendants of poly-(*R*)-**1** and poly-(*S*)-**2** in $CHCl_3$. b) ECD studies of the poly-[(*R*)-$\mathbf{1}_r$-*co*-(*S*)-$\mathbf{2}_{1-r}$] series. c,d) illustration of the helical sense adopted by the polyenic backbone of poly-[(*R*)-$\mathbf{1}_{0.9}$-*co*-(*R*)-$\mathbf{2}_{0.1}$] in the presence of a major conformation and ECD spectra of (*R*)-**1** by complexation of 0.1 equiv of $LiClO_4$ and $Ca(ClO_4)_2$ (10 mg/mL MeOH). e) Plot of the g_{abs} at indicated wavelength for poly-[(*R*)-$\mathbf{1}_r$-*co*-(*S*)-$\mathbf{2}_{1-r}$] series against copolymer composition and the corresponding curve fitting based on modified Sato's model to obtain the free energy parameters. f) Optimized structures and NCI calculations (wb97xd/6-31+g**, PCM=$CHCl_3$) of the dimers containing the residues at the nth, nth +3 in an *M* helix with conformation of the Sergeant (*S*)-**2** in *ap*-CF_3 and the two options of the Soldier (*R*)-**1** in *ap*-OMe and *sp*-OMe. Concentration of homopolymers and copolymers = 0.3 mg/mL $CHCl_3$.

5.3.23. Absence of chiral-to-chiral communication in poly-[(*S*)-$\mathbf{1}_r$-*co*-(*S*)-$\mathbf{2}_{1-r}$] copolymer series

In this case, comonomers behave within the copolymer as in their corresponding homopolymers (Figure S111a and Figure S111b). Addition of perchlorate salts of monovalent and divalent metal ions such as $LiClO_4$ (10 mg/mL MeOH) and $Ca(ClO_4)_2$ were added to vials containing a chloroform solution of the copolymer poly-[(*S*)-$\mathbf{1}_r$-*co*-(*S*)-$\mathbf{2}_{1-r}$] (r=0.9) (0.3 mg/mL $CHCl_3$) (Figure S111c), produced the same results than in the enantiomeric version of the copolymer, but with the induction of opposite helical senses (Figure S111).

Thus, comonomer (*S*)-**2**, is present within the copolymer into an *ap*-CF_3 conformation of the (O=)C-C(-CF_3) bonds, which induces a *P* helix into the copolymer, while comonomer (*S*)-**1** adopts an equal mixture of *ap*-OMe and *sp*-OMe conformers, inducing an equal population of both helical senses (Figure S111b).

By applying a modification of Sato's model, it was possible to obtain the $\Delta G_{h,S1,S1}$=+0.01 J/mol, $\Delta G_{h,S2,S2}$=+35.46 J/mol, and $\Delta G_{h,R1,S2}$=-7.21 J/mol which agrees with an absence of communication effect (Comm = -0.203 [x= (*S*)-**2**]) (Figure S111e).

USC UNIVERSIDADE DE SANTIAGO DE COMPOSTELA

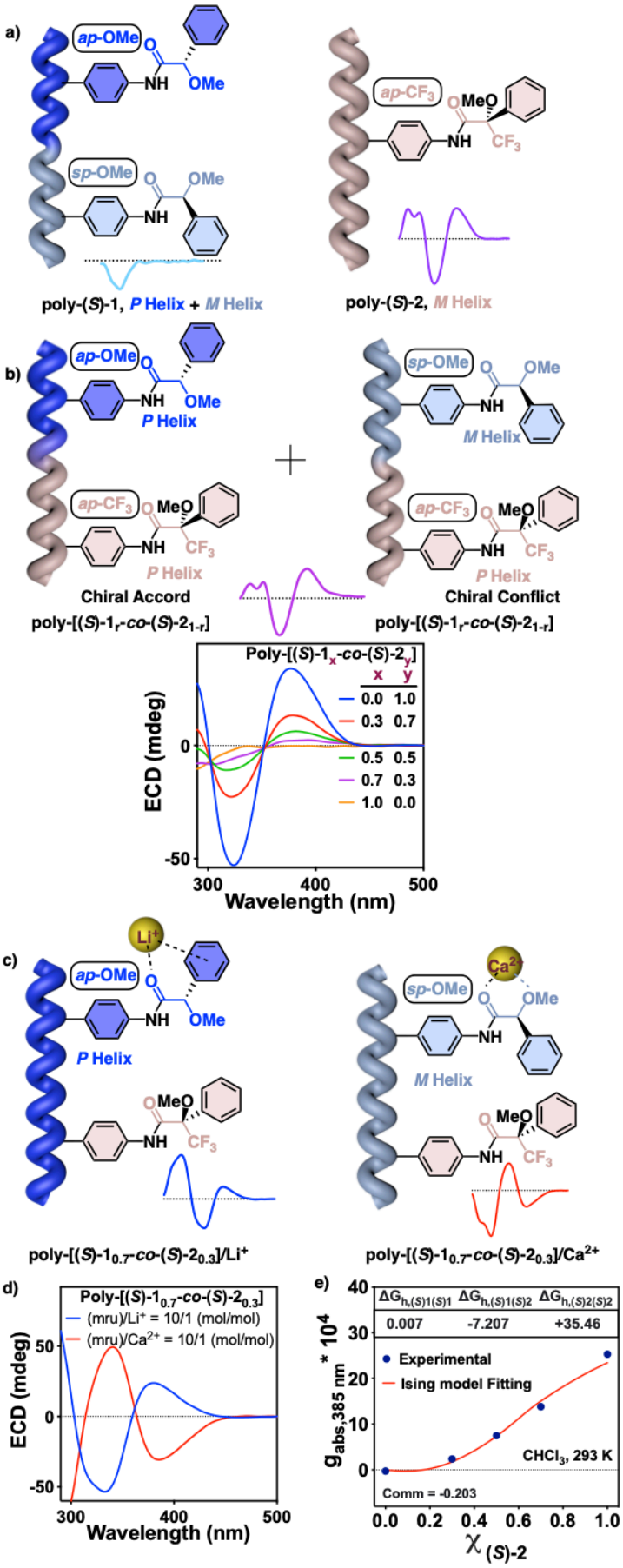

a)
ap-OMe
sp-OMe
poly-(S)-1, P Helix + M Helix
ap-CF3
poly-(S)-2, M Helix
b)
P Helix
M Helix
Chiral Accord
poly-[(S)-1r-co-(S)-21-r]
Chiral Conflict
poly-[(S)-1r-co-(S)-21-r]
Poly-[(S)-1x-co-(S)-2y]
x y
0.0 1.0
0.3 0.7
0.5 0.5
0.7 0.3
1.0 0.0
ECD (mdeg)
Wavelength (nm)
c)
Li+
Ca2+
poly-[(S)-10.7-co-(S)-20.3]/Li+
poly-[(S)-10.7-co-(S)-20.3]/Ca2+
d)
(mru)/Li+ = 10/1 (mol/mol)
(mru)/Ca2+ = 10/1 (mol/mol)
e)
ΔGh,(S)1(S)1
ΔGh,(S)1(S)2
ΔGh,(S)2(S)2
0.007
-7.207
+35.46
Experimental
Ising model Fitting
CHCl3, 293 K
Comm = -0.203
gabs,385 nm * 10^4
χ (S)-2

Figure S111. a) ECD pattern, helical sense, and equilibrium of the conformations or major conformation at the pendants of poly-(*S*)-**1** and poly-(*S*)-**2** in $CHCl_3$. b) ECD studies of the poly-[(*S*)-$\mathbf{1}_r$-*co*-(*S*)-$\mathbf{2}_{1-r}$] series. c,d) illustration of the helical sense adopted by the polyenic backbone of poly-[(*S*)-$\mathbf{1}_{0.9}$-*co*-(*R*)-$\mathbf{2}_{0.1}$] in the presence of a major conformation and ECD spectra of (*S*)-**1** by complexation of 0.1 equiv of $LiClO_4$ and $Ca(ClO_4)_2$ (10 mg/mL MeOH). e) Plot of the g_{abs} at indicated wavelength for poly-[(*S*)-$\mathbf{1}_r$-*co*-(*S*)-$\mathbf{2}_{1-r}$] series against copolymer composition and the corresponding curve fitting based on modified Sato's model to obtain the free energy parameters. Concentration of homopolymers and copolymers = 0.3 mg/mL $CHCl_3$.

5.3.24. From Abnormal to Classic chiral-to-chiral Sergeants and Soldiers Effect in poly-[(*R*)-$\mathbf{1}_r$-*co*-(*S*)-$\mathbf{2}_{1-r}$] (r= 0.0-1.0) m.r.u./Li^+ 1.0/0.1 (mol/mol) ratio

By applying a modification of Sato's model, it was possible to obtain the $\Delta G_{h,R\mathbf{1},R\mathbf{1}}$, $\Delta G_{h,S\mathbf{2},S\mathbf{2}}$, and $\Delta G_{h,R\mathbf{1},S\mathbf{2}}$ which are -50.31, +51.68, and -158.50 J/mol, respectively. These energy helix induction for each possible comonomer pair within the copolymer chain allow us to obtain a value for the communication process, in this case (Comm= +1.45 [sergeant x=(*S*)-**1**]), which indicates the presence of a chiral-to-chiral Classic Sergeants and Soldiers Effect (Figure S112e).

DFT computational studies carried out in a dimeric model (see above for details) show that π–π supramolecular interactions emerge when the copolymer adopts an *M* helix ($ECD_{380\ nm}$>0), being the comonomer (*R*)-**1** present in an *ap*-OMe conformation, while (*S*)-**2** is adopting *sp*-OMe conformation. This π–π interaction is not present when (*R*)-**1** adopts an *ap*-OMe conformation and (*S*)-**2** adopts an *ap*-OMe. Therefore, a conformational change takes place at comonomer (*R*)-**2** when the Li^+ ion is complexed to (*S*)-**1** (Figure S112f).

Low temperature ECD studies (268 K) of the poly-[(*R*)-$\mathbf{1}_r$-*co*-(*S*)-$\mathbf{2}_{1-r}$] m.r.u./Li^+ (r=0.5) complex (0.5 K/min) in a 1.0/0.1 mol/mol ratio show the reversibility of the process were the Sergeant and Soldiers role in the SaS effect can be reverted, recovering the two comonomers their initial status (Figure S112c and Figure S112d). This reversibility of the process allows us to activate/deactivate selectively by temperature different chiral communication effects such as the chiral to chiral Classic Sergeants and Soldiers Effect or the chiral-to-chiral Abnormal Sergeants and Soldiers Effect.

USC UNIVERSIDADE DE SANTIAGO DE COMPOSTELA

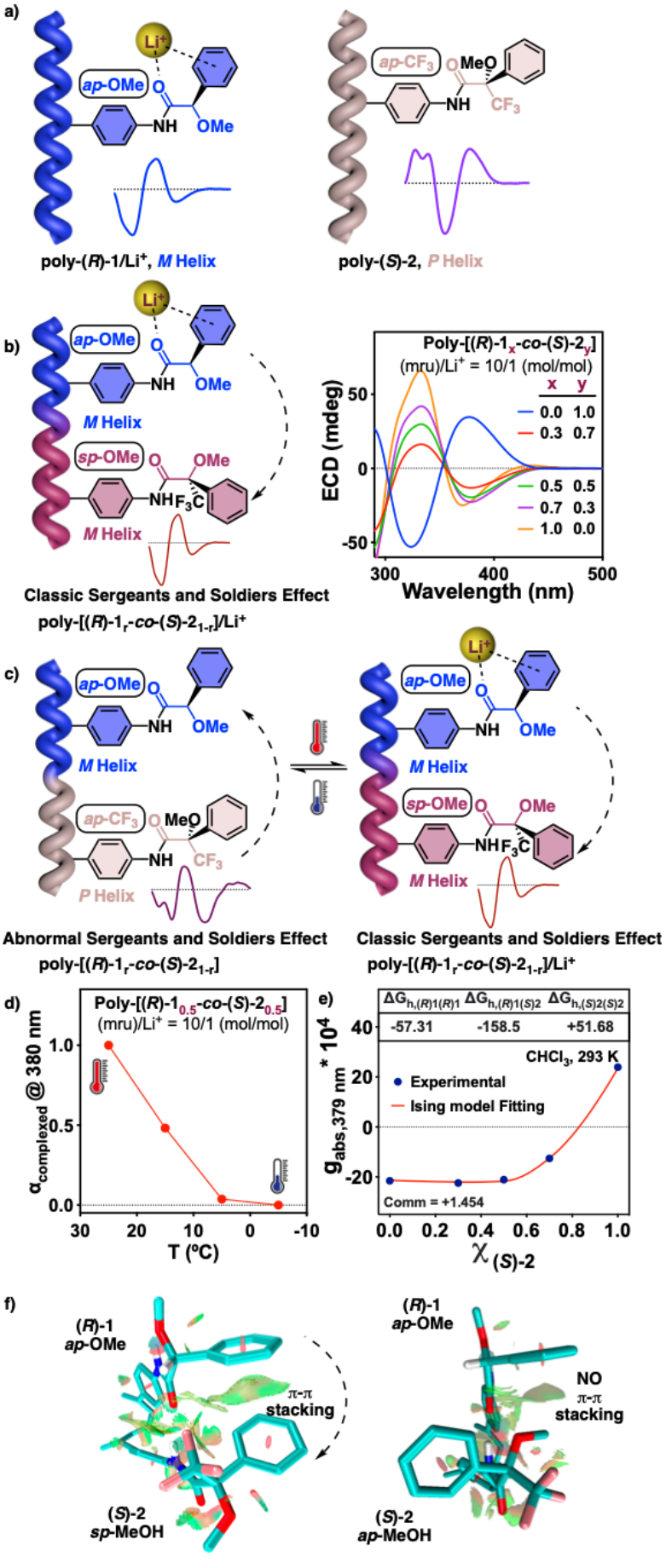

a)
poly-(R)-1/Li+, M Helix
poly-(S)-2, P Helix
b)
Classic Sergeants and Soldiers Effect
poly-[(R)-1r-co-(S)-21-r]/Li+
Poly-[(R)-1x-co-(S)-2y]
(mru)/Li+ = 10/1 (mol/mol)
ECD (mdeg)
Wavelength (nm)
c)
Abnormal Sergeants and Soldiers Effect
poly-[(R)-1r-co-(S)-21-r]
Classic Sergeants and Soldiers Effect
poly-[(R)-1r-co-(S)-21-r]/Li+
d)
Poly-[(R)-10.5-co-(S)-20.5]
(mru)/Li+ = 10/1 (mol/mol)
αcomplexed @ 380 nm
T (°C)
e)
ΔGh,(R)1(R)1 ΔGh,(R)1(S)2 ΔGh,(S)2(S)2
-57.31 -158.5 +51.68
CHCl3, 293 K
Experimental
Ising model Fitting
Comm = +1.454
gabs,379 nm * 10^4
χ (S)-2
f)
(R)-1 ap-OMe
π-π stacking
(S)-2 sp-MeOH
(R)-1 ap-OMe
NO π-π stacking
(S)-2 ap-MeOH

Figure S112. a) ECD pattern, helical sense, and conformations at the pendants of poly-(*R*)-**1** and poly-(*S*)-**2** in $CHCl_3$ complexed with 0.1 equiv $LiClO_4$ (10 mg/mL MeOH). b) ECD studies of the poly-[(*R*)-$\mathbf{1}_r$-*co*-(*S*)-$\mathbf{2}_{1-r}$] series complexed with 0.1 equiv $LiClO_4$ (10 mg/mL MeOH). c,d) illustration of the helical sense adopted by the polyenic backbone and VT-ECD spectra (0.5 ºC/min) of poly-[(*R*)-$\mathbf{1}_r$-*co*-(*S*)-$\mathbf{2}_{1-r}$]/Li^+ responding to temperature: at low temperature Sergeant complexation of (*R*)-**1** is deactivated, while at room temperature complexation is restored to switch the communication mechanism. e) Plot of the g_{abs} at indicated wavelength for poly-[(*R*)-$\mathbf{1}_r$-*co*-(*S*)-$\mathbf{2}_{1-r}$]/Li^+ series against copolymer composition and the corresponding curve fitting based on modified Sato's model to obtain the free energy parameters. f) Optimized structures and NCI calculations (wb97xd/6-31+g**, PCM=$CHCl_3$) of the dimers containing the residues at the nth, nth +3 in an *M* helix with conformation of the Sergeant (*R*)-**1** in *ap*-OMe and the two options of the Soldier (*S*)-**2** in *sp*-OMe and *ap*-OMe. Concentration of homopolymers and copolymers = 0.3 mg/mL $CHCl_3$.

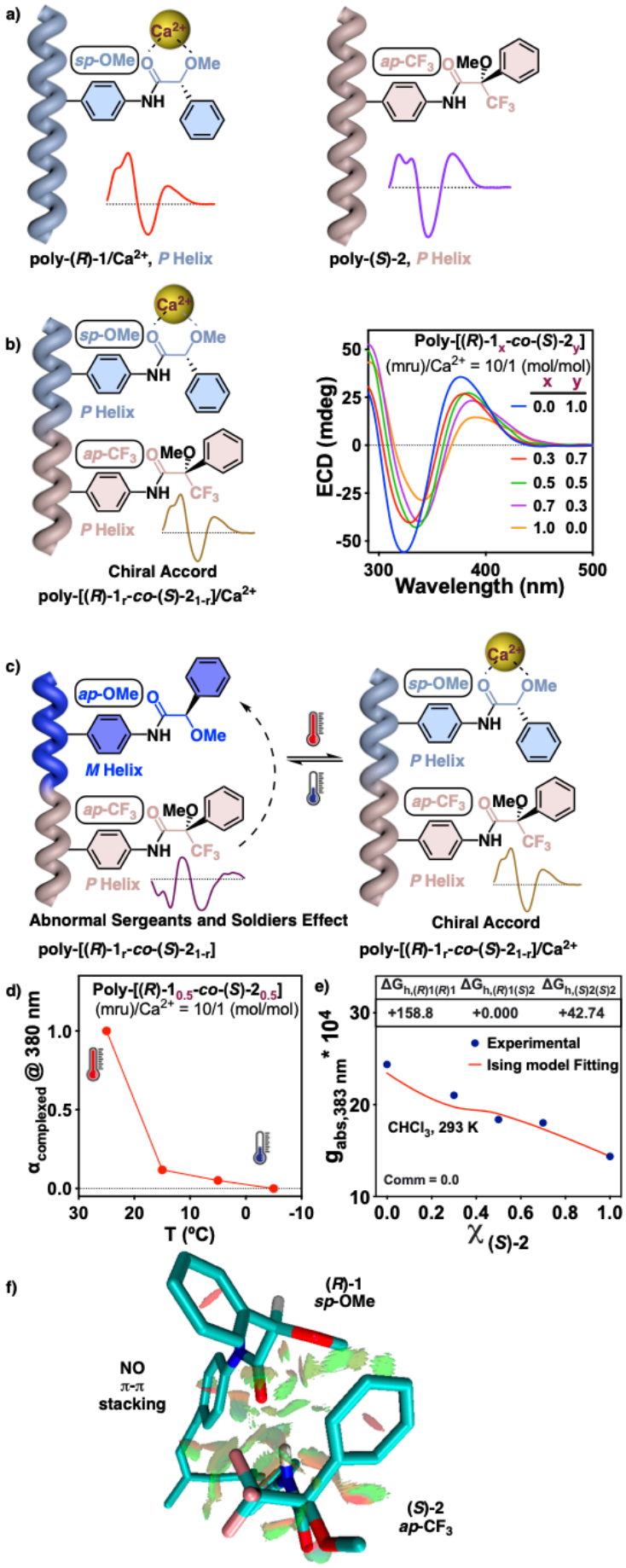
5.3.25. From Abnormal chiral-to-chiral Sergeants and Soldiers Effect to Chiral Accord in poly-[(*R*)-$\mathbf{1}_r$-*co*-(*S*)-$\mathbf{2}_{1-r}$] (r= 0.0-1.0) m.r.u./Ca^{2+} 1.0/0.1 (mol/mol) ratio

By applying a modification of Sato's model it was possible to obtain the $\Delta G_{h,R\mathbf{1},R\mathbf{1}}$, $\Delta G_{h,S\mathbf{2},S\mathbf{2}}$, and $\Delta G_{h,R\mathbf{1},S\mathbf{2}}$ which are +158.80, +42.74, and 0.00 J/mol, respectively. Due to the limited number of data points, $\Delta G_{h,R\mathbf{1},S\mathbf{2}}$ was set to 0.00 J/mol during the fitting procedure. These energy helix induction for each possible comonomer pair within the copolymer chain allow us to obtain a value for the communication process, in this case, Comm= +0.00, which indicates the absence of a chiral-to-chiral communication mechanism (Figure S113e).

DFT computational studies carried out in a dimeric model (see above for details) lack $\pi-\pi$ supramolecular interactions when the copolymer adopts a *P* helix ($ECD_{380\,nm}>0$), being the comonomer (*R*)-**1** present in an *sp*-OMe conformation, while (*S*)-**2** is adopting *ap*-CF_3 conformation (Figure S113f).

Low temperature ECD studies (268 K) of the poly-[(*R*)-$\mathbf{1}_r$-*co*-(*S*)-$\mathbf{2}_{1-r}$] m.r.u./Ca^{2+} (r=0.5) complex (0.5 K/min) in a 1.0/0.1 mol/mol ratio show again a fully reversibility of the chiral-to-chiral communication process between a Chiral Accord and a chiral-to-chiral Abnormal Sergeants and Soldiers Effect (Figure S113c and Figure S113d).

USC UNIVERSIDADE DE SANTIAGO DE COMPOSTELA



USC UNIVERSIDADE DE SANTIAGO DE COMPOSTELA

Figure S113. a) ECD pattern, helical sense, and major conformations at the pendants of poly-(*R*)-**1** and poly-(*S*)-**2** in $CHCl_3$ complexed with 0.1 equiv $Ca(ClO_4)_2$ (10 mg/mL MeOH). b) ECD studies of the poly-[(*R*)-$\mathbf{1}_r$-*co*-(*S*)-$\mathbf{2}_{1-r}$] series complexed with 0.1 equiv $Ca(ClO_4)_2$ (10 mg/mL MeOH). c,d) illustration of the helical sense adopted by the polyenic backbone and VT-ECD spectra (0.5 ºC/min) of poly-[(*R*)-$\mathbf{1}_r$-*co*-(*S*)-$\mathbf{2}_{1-r}$]/Ca^{2+} responding to temperature: at low temperature (*R*)-**1** complexation is deactivated, while at room temperature complexation is restored to switch the communication mechanism. e) Plot of the g_{abs} at indicated wavelength for poly-[(*R*)-$\mathbf{1}_r$-*co*-(*S*)-$\mathbf{2}_{1-r}$]/Ca^{2+} series against copolymer composition and the corresponding curve fitting based on modified Sato's model to obtain the free energy parameters. f) Optimized structure and NCI calculations (wb97xd/6-31+g**, PCM=$CHCl_3$) of the dimer containing the residues at the nth, nth +3 in a *P* helix with conformation of (*R*)-**1** in *sp*-OMe and (*S*)-**2** in *ap*-CF_3. Concentration of homopolymers and copolymers = 0.3 mg/mL $CHCl_3$.

5.3.26. From a mixture of Chiral Accord and Chiral Conflict effect to a selective Chiral Accord in poly-[(*R*)-$\mathbf{1}_r$-*co*-(*R*)-$\mathbf{2}_{1-r}$] (r= 0.0-1.0) m.r.u./Li^+ 1.0/0.1 (mol/mol) ratio

By applying a modification of Sato's model it was possible to obtain the $\Delta G_{h,R\mathbf{1},R\mathbf{1}}$, $\Delta G_{h,R\mathbf{2},R\mathbf{2}}$, and $\Delta G_{h,R\mathbf{1},R\mathbf{2}}$ which are +96.38, +72.29, and 0.00 J/mol, respectively. Due to the limited number of data points, $\Delta G_{h,R\mathbf{1},R\mathbf{2}}$ was set to 0.00 J/mol during the fitting procedure. These energy helix induction for each possible comonomer pair within the copolymer chain allow us to obtain a value for the communication process, in this case, Comm= +0.00, which indicates the absence of a chiral-to-chiral communication mechanism (Figure S114e).

DFT computational studies carried out in a dimeric model (see above for details) lack $\pi-\pi$ supramolecular interactions when the copolymer adopts a *P* helix ($ECD_{380\,nm}>0$), being the comonomer (*R*)-**1** present in an *sp*-OMe conformation, while (*R*)-**2** is adopting *ap*-CF_3 conformation (Figure S114f).

Low temperature ECD studies (268 K) of the poly-[(*R*)-$\mathbf{1}_r$-*co*-(*R*)-$\mathbf{2}_{1-r}$] m.r.u./Ca^{2+} (r=0.5) complex (0.5 K/min) in a 1.0/0.1 mol/mol ratio show again a fully reversibility of the chiral-to-chiral communication process between the Chiral Conflict and Chiral Accord induced in the absence of metal ions (decomplexation) and the Chiral Accord effects (complex) (Figure S114c and Figure S114d).

USC UNIVERSIDADE DE SANTIAGO DE COMPOSTELA

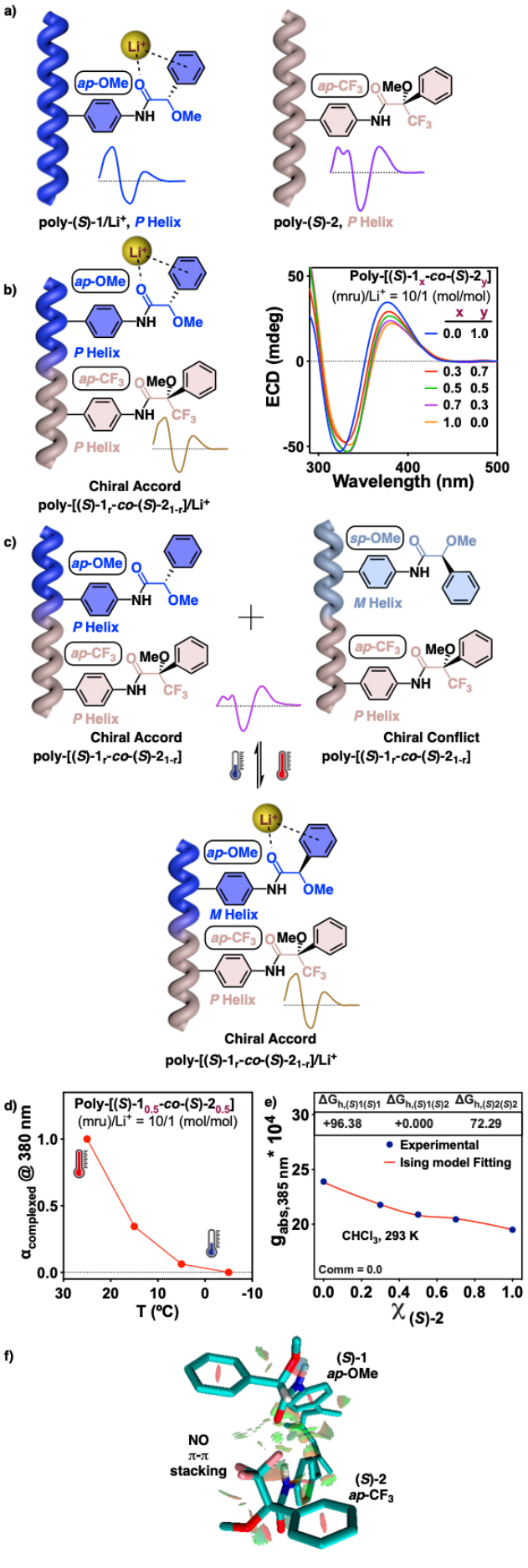

a)
poly-(S)-1/Li+, P Helix
poly-(S)-2, P Helix
b)
Chiral Accord
poly-[(S)-1r-co-(S)-21-r]/Li+
Poly-[(S)-1x-co-(S)-2y]
(mru)/Li+ = 10/1 (mol/mol)
ECD (mdeg)
Wavelength (nm)
c)
Chiral Accord
poly-[(S)-1r-co-(S)-21-r]
Chiral Conflict
poly-[(S)-1r-co-(S)-21-r]
Chiral Accord
poly-[(S)-1r-co-(S)-21-r]/Li+
d)
Poly-[(S)-10.5-co-(S)-20.5]
(mru)/Li+ = 10/1 (mol/mol)
αcomplexed @ 380 nm
T (°C)
e)
ΔGh,(S)1(S)1 ΔGh,(S)1(S)2 ΔGh,(S)2(S)2
+96.38 +0.000 72.29
Experimental
Ising model Fitting
CHCl3, 293 K
Comm = 0.0
gabs,385 nm * 10^4
χ (S)-2
f)
(S)-1
ap-OMe
NO
π-π
stacking
(S)-2
ap-CF3

Figure S114. a) ECD pattern, helical sense, and major conformations at the pendants of poly-(*S*)-**1** and poly-(*S*)-**2** in $CHCl_3$ complexed with 0.1 equiv $LiClO_4$ (10 mg/mL MeOH). b) ECD studies of the poly-[(*S*)-**1**$_r$-*co*-(*S*)-**2**$_{1-r}$] series complexed with 0.1 equiv $LiClO_4$ (10 mg/mL MeOH). c,d) illustration of the helical sense adopted by the polyenic backbone and VT-ECD spectra (0.5 ºC/min) of poly-[(*S*)-**1**$_r$-*co*-(*S*)-**2**$_{1-r}$]/Li^+ responding to temperature: at low temperature (*S*)-**1** complexation is deactivated, while at room temperature complexation is restored to switch the communication mechanism. e) Plot of the g_{abs} at indicated wavelength for poly-[(*S*)-**1**$_r$-*co*-(*S*)-**2**$_{1-r}$]/Li^+ series against copolymer composition and the corresponding curve fitting based on modified Sato's model to obtain the free energy parameters. f) Optimized structure and NCI calculations (wb97xd/6-31+g**, PCM=$CHCl_3$) of the dimer containing the residues at the nth, nth +3 in a *P* helix with conformation of (*S*)-**1** in *ap*-OMe and (*S*)-**2** in *ap*-CF_3. Concentration of homopolymers and copolymers = 0.3 mg/mL $CHCl_3$.

5.3.27. From a mixture of Chiral Accord and Chiral Conflict effect to Classic chiral-to-chiral Sergeants and Soldiers Effect in poly-[(*S*)-1$_r$-*co*-(*S*)-2$_{1-r}$] (r= 0.0-1.0) m.r.u./Ca^{2+} 1.0/0.1 (mol/mol) ratio

In this case, ECD studies show that in all the poly-[(*S*)-**1**$_r$-*co*-(*S*)-**2**$_{1-r}$] (r=0.9-0.1)/Ca^{2+} metal complexes, a strong negative Cotton band is present at 380 nm [$ECD_{380\ nm} < 0$] (Figure S115b), which is identical to the one induced by the monomer (*S*)-**1** interacting with the a divalent metal ion (*sp*-OMe conformer), and opposite to the one commanded by the chiral monomer (*S*)-**2** (*ap*-CF_3 conformation) (Figure S115a).

Thus, a Sergeants and Soldiers Effect is triggered from (*S*)-**1** to (*S*)-**2** in the presence of Ca^{2+} ions, which show that in chiral copolymer series a conformational dispute is produced between chiral monomers, which can be shifted towards one or the other chiral comonomer depending on the external stimuli employed. Thus, in this case, both monomers present in the copolymer series the same conformational composition than in the parent homopolymers, demonstrating an equal chiral strength for both comonomers and results in a lack of communication between them (Figure S115c). However, the addition of divalent metal ions, alters the conformational composition at (*S*)-**1**, which makes a chelate with the metal stabilizing largely the *sp*-OMe conformation. As a result, the conformation strength equilibrium is disrupted allowing to (*S*)-**1**/Ca^{2+} to act as a Sergeant and (*S*)-**2** to act as a Soldier, triggering a Classic chiral to chiral Sergeants and Soldiers effect (Figure S115b and Figure S115c).

DFT computational studies carried out in a dimeric model (see above for details) show that π–π supramolecular interactions emerge when the copolymer adopts an *M* helix ($ECD_{380\ nm}>0$), being the comonomer (*S*)-**1** present in an *sp*-OMe conformation, while (*S*)-**2** is adopting *sp*-OMe conformation. This π–π interaction is not present when

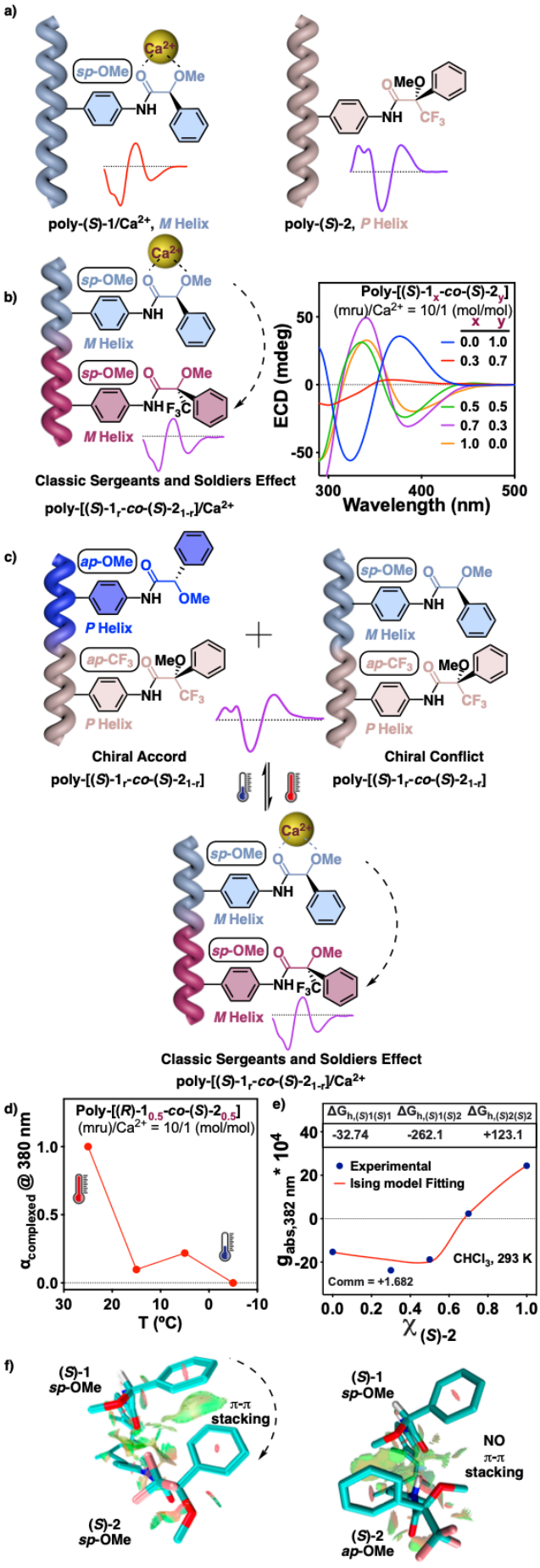
USC UNIVERSIDADE DE SANTIAGO DE COMPOSTELA

(*S*)-**1** adopts an *sp*-OMe conformation and (*S*)-**2** adopts an *ap*-OMe. Therefore, a conformational change takes place at comonomer (*S*)-**2** when the Li^+ ion is complexed to (*S*)-**1** (Figure S115f).

The energy of the helix induction process in copolymers could be obtained by applying a modification of Sato's model, $\Delta G_{h,S1,S1}$, $\Delta G_{h,S2,S2}$, and $\Delta G_{h,S1,S2}$ which are -32.74, +123.10, and -262.10 J/mol, respectively. These energy helix induction for each possible comonomer pair within the copolymer chain allow us to obtain a value for the communication process, in this case, Comm = +1.68 [Sergeant x=(*S*)-**1**]), a value distinct to zero, which indicates the presence of a chiral-to-chiral communication mechanism within the asymmetry amplification process, being in this case a chiral to chiral Classic Sergeants and Soldiers Effect (Figure S115e).

Low temperature ECD studies (268 K) of the poly-[(*S*)-$\mathbf{1}_r$-*co*-(*S*)-$\mathbf{2}_{1-r}$] m.r.u./Ca^{2+} (r=0.6) complex (0.5 K/min) in a 1.0/0.1 mol/mol ratio (Figure S115d) show a fully reversibility between the absence of communication and the chiral-to-chiral Classic Sergeants and Soldiers Effect, demonstrating that a Chiral Dispute with different results effect can be produced between the two chiral monomers in the poly-[(*S*)-$\mathbf{1}_r$-*co*-(*S*)-$\mathbf{2}_{1-r}$] (r=0.9-0.1) whose results depends on the external stimuli employed.

USC
UNIVERSIDADE DE SANTIAGO DE COMPOSTELA



USC UNIVERSIDADE DE SANTIAGO DE COMPOSTELA

Figure S115. a) ECD pattern, helical sense, and major conformations at the pendants of poly-(*S*)-**1** and poly-(*S*)-**2** in $CHCl_3$ complexed with 0.1 equiv $Ca(ClO_4)_2$ (10 mg/mL MeOH). b) ECD studies of the poly-[(*S*)-**1**$_r$-*co*-(*S*)-**2**$_{1\text{-}r}$] series complexed with 0.1 equiv $Ca(ClO_4)_2$ (10 mg/mL MeOH). c,d) illustration of the helical sense adopted by the polyenic backbone and VT-ECD spectra (0.5 ºC/min) of poly-[(*S*)-**1**$_r$-*co*-(*S*)-**2**$_{1\text{-}r}$]/Ca^{2+} responding to temperature: at low temperature Sergeant complexation of (*S*)-**1** is deactivated, while at room temperature complexation is restored to switch the communication mechanism. e) Plot of the g_{abs} at indicated wavelength for poly-[(*S*)-**1**$_r$-*co*-(*S*)-**2**$_{1\text{-}r}$]/Ca^{2+} series against copolymer composition and the corresponding curve fitting based on modified Sato's model to obtain the free energy parameters. f) Optimized structures and NCI calculations (wb97xd/6-31+g**, PCM=$CHCl_3$) of the dimers containing the residues at the nth, nth +3 in an *M* helix with conformation of the Sergeant (*S*)-**1** in *sp*-OMe and the two options of the Soldier (*S*)-**2** in *sp*-OMe and *ap*-OMe. Concentration of homopolymers and copolymers = 0.3 mg/mL $CHCl_3$.

USC UNIVERSIDADE DE SANTIAGO DE COMPOSTELA

USC
UNIVERSIDADE
DE SANTIAGO
DE COMPOSTELA

5.4. Experimental Section and Methodology Chapter 3.4.

5.4.1. Experimental Procedures

Commercially available chemicals have been used as delivered. Solvents were purchased as reagent grade and distilled if necessary. Anhydrous solvents were either purchased as ultra-dry solvent from Acros Organics® or received from solvent purification system. For the coupling and polymerization reactions, dry THF was obtained from MBRAUN SPS 800 solvent purification system. The reactions were done in inert atmospheres.

Column chromatography was performed with silica gel 230-400 mesh (Merck).

Thin-layer chromatography of silica 60F254 Merck was visualized in UV at a wavelength of 254 nm and by heat with Hanessian.

Size exclusion chromatography (SEC/GPC) studies were performed on Alliance 2695 HPLC System (Waters) liquid chromatography system equipped with a UV 2489 detector (Waters). The samples were eluted by three Phenogel columns connected to each other with stationary phases of 10^3, 10^4, and 10^5 Amstrong and packed with a solid support of a cross-linked styrene and p-divinylbenzene copolymer.

The average molecular weights (M_n and M_W) of all polymers were estimated by GPC with THF as eluent at flow rate 1.0 mL/min at concentration 0.5 mg/mL using narrow polystyrene standards (PSS) as calibrants.

The UV/Vis absorption spectra were acquired in the Jasco V-730 spectrophotometer in the range of wavelengths from 240 nm to 500 nm. All samples were prepared at a fixed concentration of 0.3 mg polymer/mL solvent inside quartz glass cuvettes with a light path of 1 mm.

The CD spectra were acquired in the Jasco 720 spectrophotometer in the range of wavelengths from 240 nm to 500 nm. All samples were prepared at a fixed concentration of 0.3 mg polymer/mL solvent inside quartz glass cuvettes with a light path of 1 mm.

The ^{1}H-NMR and ^{13}C-NMR spectra were obtained in a Varian Mercury 300 MHz spectrometer, using $CDCl_3$ solvent.

USC UNIVERSIDADE DE SANTIAGO DE COMPOSTELA

The IR spectra were obtained using the FT-IR PerkinElmer Spectrum Two equipped with the UATR addon.

5.4.2. Monomers and polymers

The preparation of monomers [(*S*)-**1**, (*R*)-**1**, **2**, and **3**] can be found in references.[277,366]

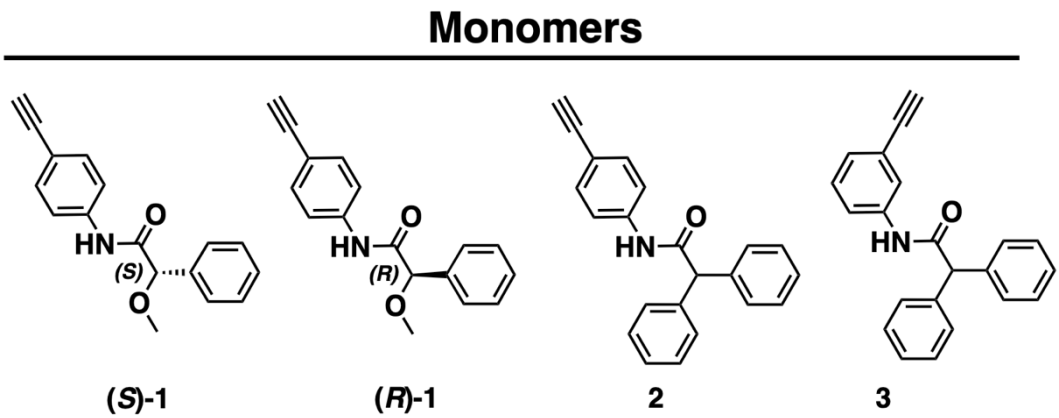
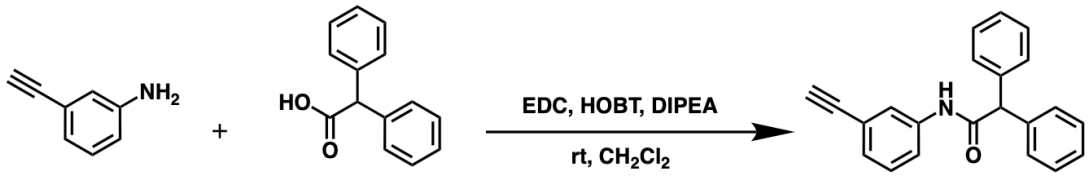


Figure S116. Structure of the monomers.

USC
UNIVERSIDADE DE SANTIAGO DE COMPOSTELA

5.4.3. Synthesis monomer 3



3-ethylinaniline **diphenylacetic acid** **3**

1-Ethyl-3-(3-dimethylaminopropyl)carbodiimide (EDC, 2.06 g, 10.72 mmol, 1.25 equiv), 1-Hydroxybenzotriazole (HOBT, 1.45 g, 10.72 mmol, 1.25 equiv), diphenylacetic acid (2.00 g, 9.43 mmol, 1.10 equiv.) and diisopropyltriethylamine (DIPEA, 1.50 mL, 17.16 mmol, 2.00 equiv) were dissolved in 100 mL of dry CH_2Cl_2, and the mixture was stirred for 10 min. to activate the acid. Then, 3-ethynylaniline (1.01 g, 8.58 mmol, 1.00 equiv) was added and the reaction mixture was stirred overnight. Then, the organic solution was washed with HCl 1M, a saturated solution of $Na(HCO_3)$ and a saturated solution of NaCl. The combined organic layers were dried over anhydrous Na_2SO_4, filtered and the solvent was evaporated at reduced pressure. The crude product was chromatographed on silica gel with hexane/ethyl acetate (8/2) as eluent, 74% yield of pure product [1.98 g of **3**].

Spectroscopic data:

^{1}H-NMR (300 MHz, $CDCl_3$) δ_H (ppm): 7.55 (m, 2H), 7.33 (m, 12H), 5.10 (s, 1H), 3.06 (s, 1H).

^{13}C-NMR (75 MHz, $CDCl_3$) δ_C (ppm): 170.3, 139.0, 137.8, 129.2, 129.1, 129.1, 128.4, 127.8, 123.3, 123.0, 120.5, 83.2, 77.7, 60.3.

HRMS (ESI) m/z calcd. for **3** $C_{22}H_{17}NO$ $[M+H]^+$: 312.1383, found: 312.1388.

USC UNIVERSIDADE DE SANTIAGO DE COMPOSTELA

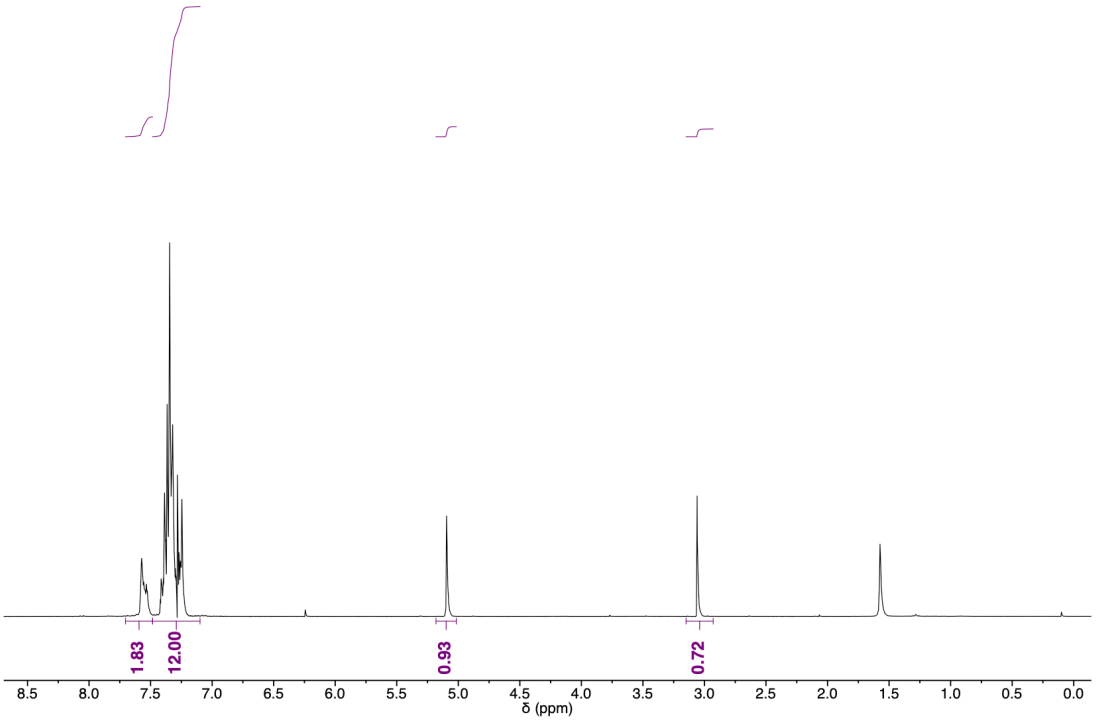


Figure S117. ^{1}H-NMR spectrum of **3** ($CDCl_3$, 300 MHz).

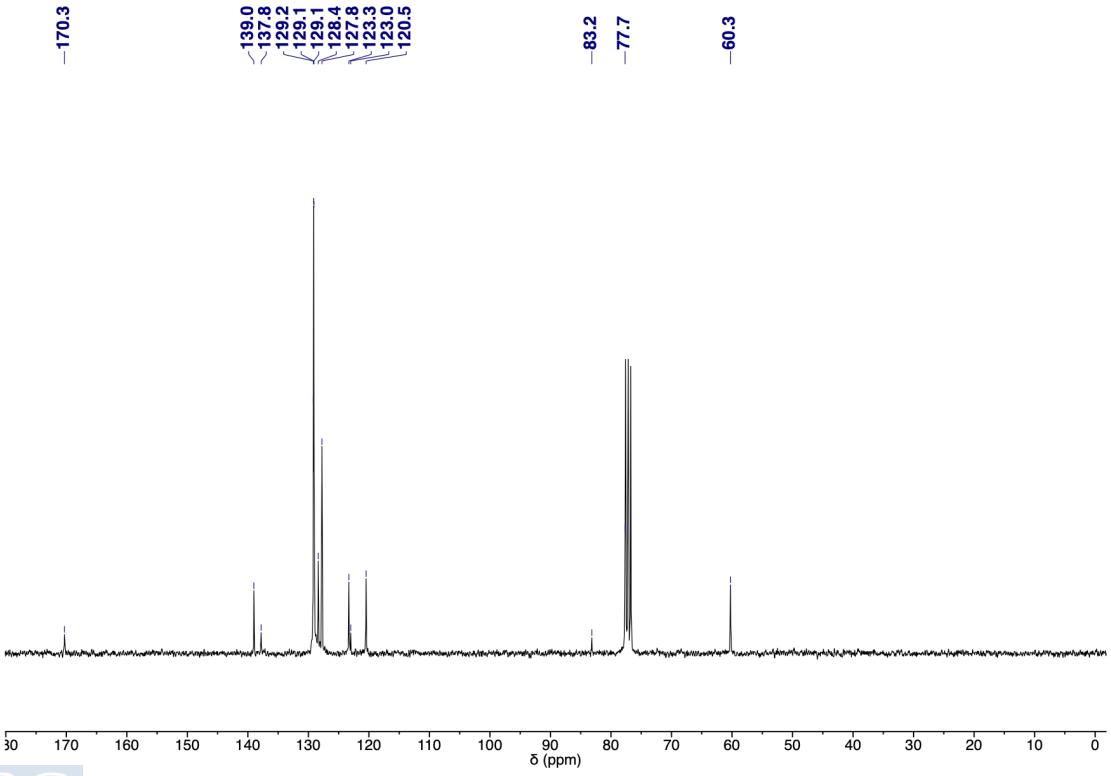
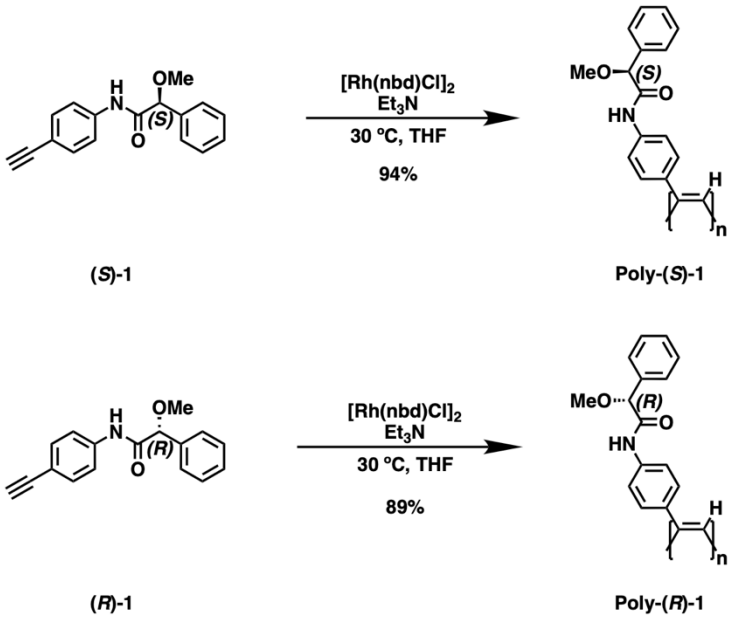


Figure S118. ^{13}C-NMR spectrum of **3** ($CDCl_3$, 75 MHz).

USC DE SANTIAGO DE COMPOSTELA

5.4.4. Synthesis of homopolymers Poly-(*S*)-1 and Poly-(*R*)-1



The reaction flask (sealed ampoule) was dried under vacuum and argon flushed for three times before the corresponding monomer (*S*)-**1** or (*R*)-**1** was added as a solid (42.5 mg, 0.16 mmol). Then, the flask was evacuated on the vacuum line and flushed with dry argon (three times). Dry THF (0.50 mL) was added with a syringe and the triethylamine dropwise (5 μL). A solution of rhodium norbornadiene chloride dimer, $[Rh(nbd)Cl]_2$ (1.00 mg, $2.65.10^{-3}$ mmol), in THF was added at 30 ºC. The reaction mixture was stirred at 30 ºC for 6 hours. Then, the resulting polymer was diluted in CH_2Cl_2 and precipitated in a large amount of methanol, centrifuged (2 times) and precipitated in hexane and centrifugated again [39.8 mg (Poly-(*S*)-**1** and 38.0 mg Poly-(*R*)-**1**], 94% and 89% yield respectively of pure products.

USC UNIVERSIDADE DE SANTIAGO DE COMPOSTELA

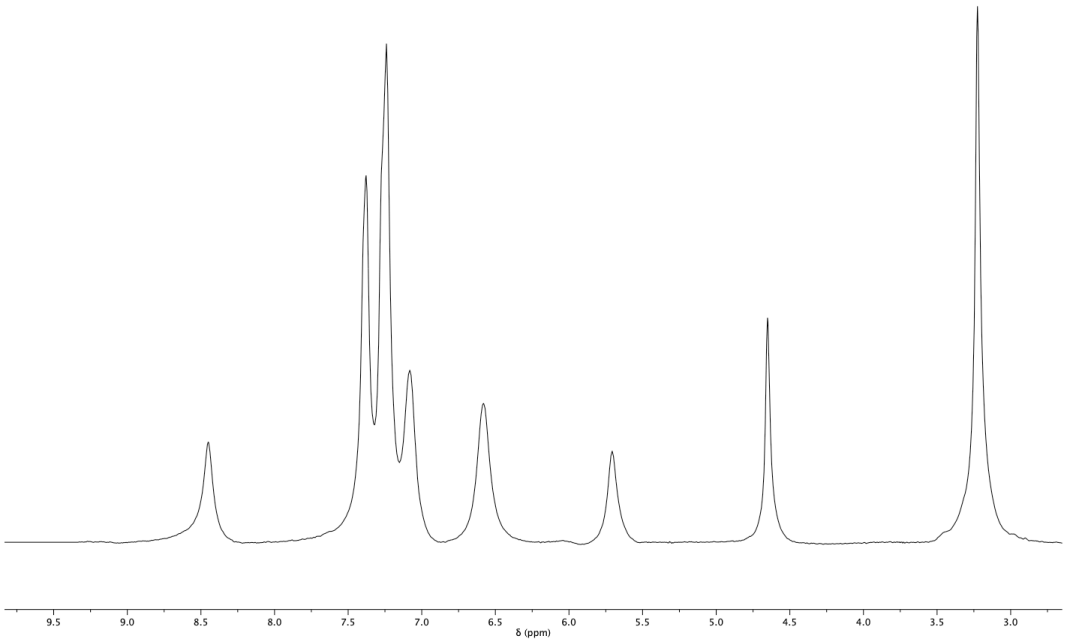


Figure S119. ^{1}H-NMR spectrum of Poly-(*S*)-**1** ($CDCl_3$, 300 MHz).

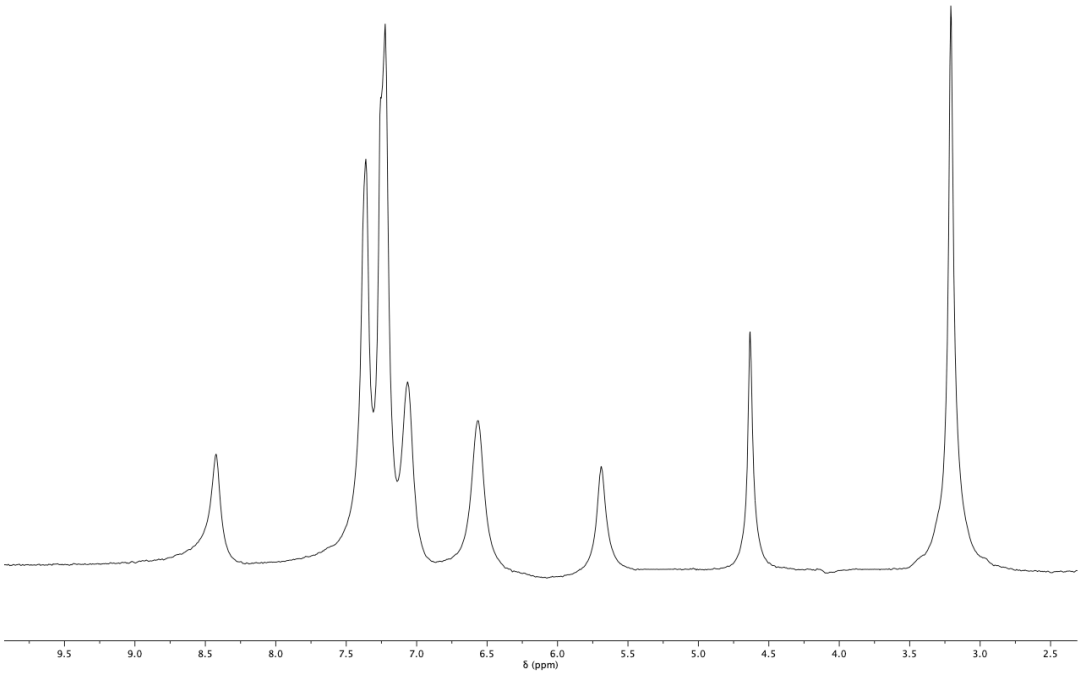
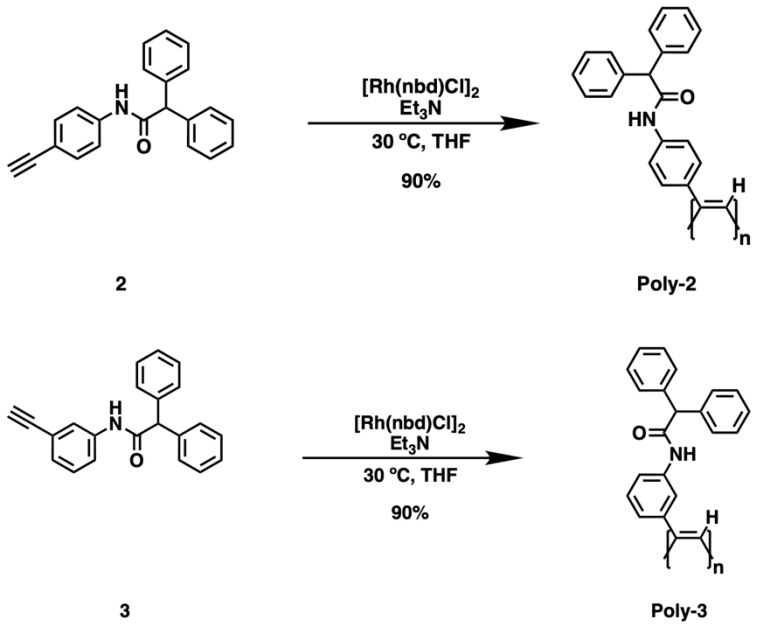


Figure S120. ^{1}H-NMR spectrum of Poly-(*R*)-**1** ($CDCl_3$, 300 MHz).

USC
UNIVERSIDADE
DE SANTIAGO
DE COMPOSTELA

5.4.5. Synthesis of homopolymers Poly-2 and Poly-3



The reaction flask (sealed ampoule) was dried under vacuum and argon flushed for three times before the corresponding monomer **2** or **3** was added as a solid (49.8 mg, 0.16 mmol). Then, the flask was evacuated on the vacuum line and flushed with dry argon (three times). Dry THF (0.50 mL) was added with a syringe and the triethylamine dropwise (5 μL). A solution of rhodium norbornadiene chloride dimer, $[Rh(nbd)Cl]_2$ (1.00 mg, $2.65.10^{-3}$ mmol), in THF was added at 30 ºC. The reaction mixture was stirred at 30 ºC for 6 hours. Then, the resulting polymer was diluted in CH_2Cl_2 and precipitated in a large amount of methanol, centrifuged (2 times) and precipitated in hexane and centrifugated again [45.1 mg Poly-**2** and 43.4 mg Poly-**3**], 96 % and 87 % yield respectively of pure products.

USC UNIVERSIDADE DE SANTIAGO DE COMPOSTELA

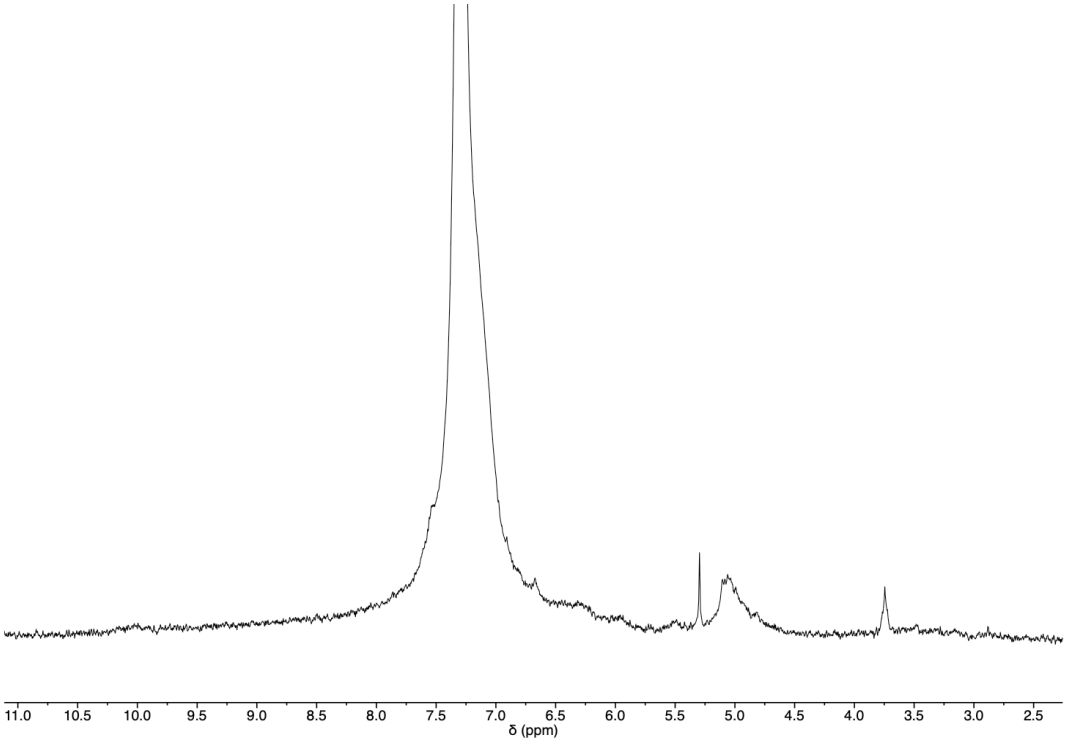
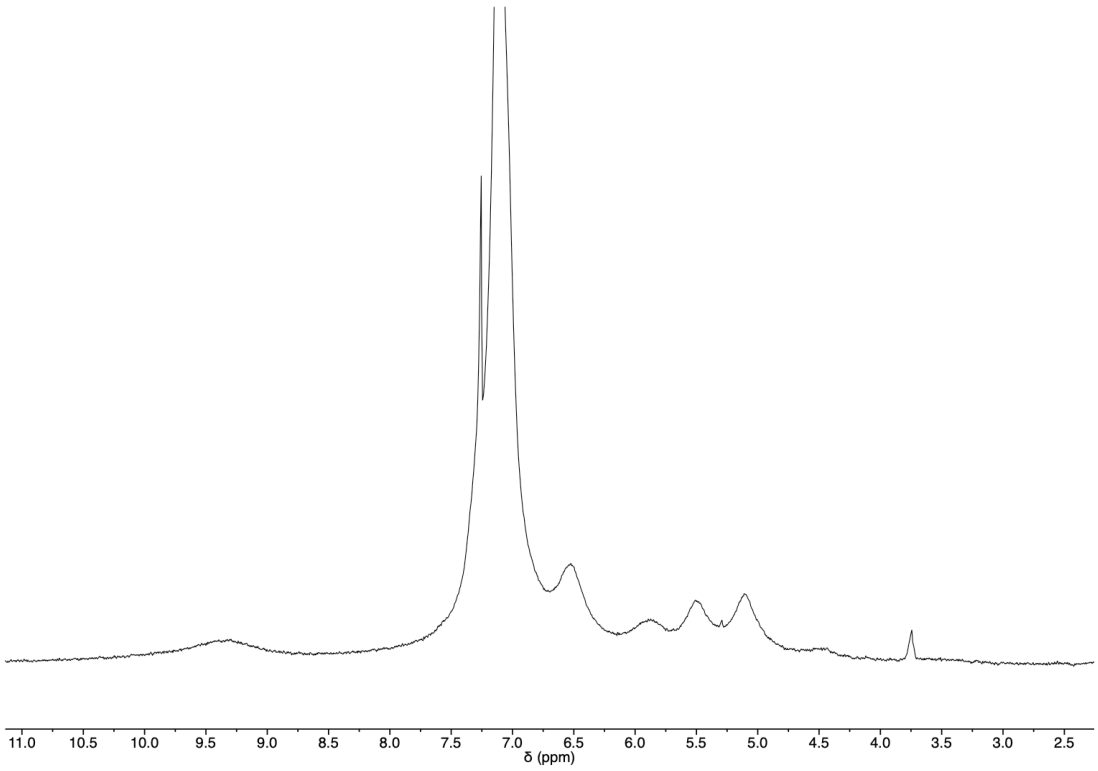


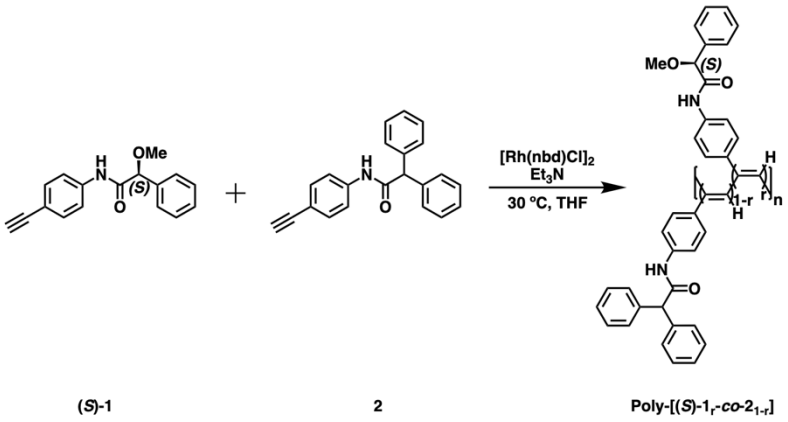
Figure S121. ^{1}H-NMR spectrum of Poly-**2** ($CDCl_3$, 300 MHz).



USC UNIVERSIDADE DE SANTIAGO DE COMPOSTELA

Figure S122. ^{1}H-NMR spectrum of Poly-**3** ($CDCl_3$, 300 MHz).

5.4.6. Synthesis of copolymers Poly-[(*S*)-1_r-*co*-2_{1-r}]

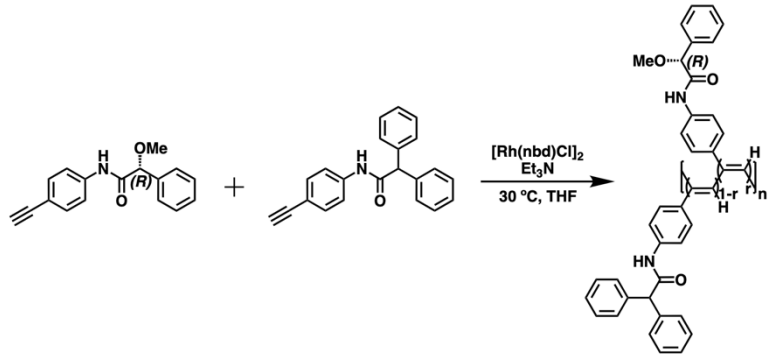


(*S*)-1 2 Poly-[(*S*)-1_r-*co*-2_{1-r}]

The reaction flask (sealed ampoule) was dried under vacuum and argon flushed for three times before the corresponding monomers (*S*)-**1** and **2** were added as a solid (see Table S15). Then, the flask was evacuated on the vacuum line and flushed with dry argon (three times). Dry THF (0.50 mL) was added with a syringe and the triethylamine dropwise (5 μL). A solution of rhodium norbornadiene chloride dimer, $[Rh(nbd)Cl]_2$ (1.00 mg, $2.65.10^{-3}$ mmol), in THF was added at 30 ºC. The reaction mixture was stirred at 30 ºC for 6 hours. Then, the resulting polymer was diluted in CH_2Cl_2 and precipitated in a large amount of methanol, centrifuged (2 times) and precipitated in hexane and centrifugated again, yield in Table S15.

USC UNIVERSIDADE DE SANTIAGO DE COMPOSTELA

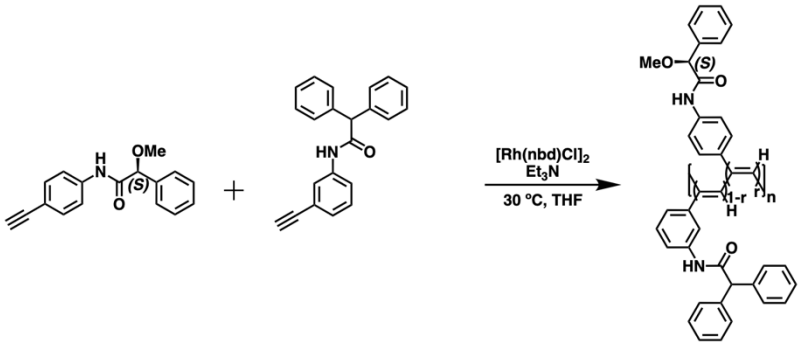
5.4.7. Synthesis of copolymers Poly-[(*R*)-1$_r$-*co*-2$_{1-r}$]



(*R*)-1 2 Poly-[(*R*)-1$_r$-*co*-2$_{1-r}$]

The reaction flask (sealed ampoule) was dried under vacuum and argon flushed for three times before the corresponding monomers (*R*)-**1** and **2** were added as a solid (see Table S16). Then, the flask was evacuated on the vacuum line and flushed with dry argon (three times). Dry THF (0.50 mL) was added with a syringe and the triethylamine dropwise (5 μL). A solution of rhodium norbornadiene chloride dimer, $[Rh(nbd)Cl]_2$ (1.00 mg, $2.65.10^{-3}$ mmol), in THF was added at 30 ºC. The reaction mixture was stirred at 30 ºC for 6 hours. Then, the resulting polymer was diluted in CH_2Cl_2 and precipitated in a large amount of methanol, centrifuged (2 times) and precipitated in hexane and centrifugated again, yield in Table S16.

5.4.8. Synthesis of copolymers Poly-[(*S*)-1$_r$-*co*-3$_{1-r}$]



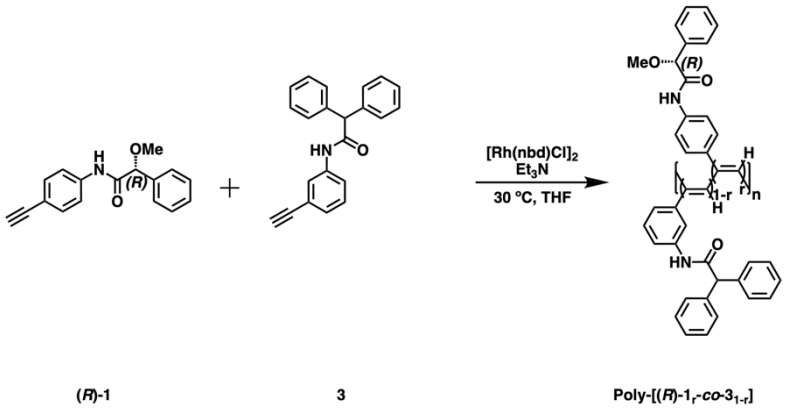
(*S*)-1 3 Poly-[(*S*)-1$_r$-*co*-3$_{1-r}$]

The reaction flask (sealed ampoule) was dried under vacuum and argon flushed for three times before the corresponding monomers (*S*)-**1** and **3** were added as a solid (see

USC DE COMPOSTELA

Table S17). Then, the flask was evacuated on the vacuum line and flushed with dry argon (three times). Dry THF (0.50 mL) was added with a syringe and the triethylamine dropwise (5 μL). A solution of rhodium norbornadiene chloride dimer, $[Rh(nbd)Cl]_2$ (1.00 mg, $2.65.10^{-3}$ mmol), in THF was added at 30 ºC. The reaction mixture was stirred at 30 ºC for 6 hours. Then, the resulting polymer was diluted in CH_2Cl_2 and precipitated in a large amount of methanol, centrifuged (2 times) and precipitated in hexane and centrifugated again, yield in Table S17.

5.4.9. Synthesis of copolymers Poly-[(*R*)-1_r-*co*-3_{1-r}]



(*R*)-1 3 Poly-[(*R*)-1_r-*co*-3_{1-r}]

The reaction flask (sealed ampoule) was dried under vacuum and argon flushed for three times before the corresponding monomers (*R*)-**1** and **3** were added as a solid (see Table S18). Then, the flask was evacuated on the vacuum line and flushed with dry argon (three times). Dry THF (0.50 mL) was added with a syringe and the triethylamine dropwise (5 μL). A solution of rhodium norbornadiene chloride dimer, $[Rh(nbd)Cl]_2$ (1.00 mg, $2.65.10^{-3}$ mmol), in THF was added at 30 ºC. The reaction mixture was stirred at 30 ºC for 6 hours. Then, the resulting polymer was diluted in CH_2Cl_2 and precipitated in a large amount of methanol, centrifuged (2 times) and precipitated in hexane and centrifugated again, yield in Table S18.

USC UNIVERSIDADE DE SANTIAGO DE COMPOSTELA

Table S15. Amounts of (*S*)-**1** and **2** monomers used to form each copolymer and their yields.

copolymer	Mass of (*S*)-1 (mg)	(*S*)-1 (mmol)	Mass of 2 (mg)	2 (mmol)	Yield (%)
Poly-[(*S*)-**1**$_{0.90}$-*co*-**2**$_{0.10}$]	4.20	0.016	44.8	0.144	79
Poly-[(*S*)-**1**$_{0.80}$-*co*-**2**$_{0.20}$]	8.50	0.032	39.8	0.128	76
Poly-[(*S*)-**1**$_{0.70}$-*co*-**2**$_{0.30}$]	12.7	0.048	34.9	0.112	80
Poly-[(*S*)-**1**$_{0.60}$-*co*-**2**$_{0.40}$]	16.9	0.064	29.9	0.096	86
Poly-[(*S*)-**1**$_{0.50}$-*co*-**2**$_{0.50}$]	21.2	0.080	24.9	0.080	84
Poly-[(*S*)-**1**$_{0.40}$-*co*-**2**$_{0.60}$]	25.5	0.096	19.9	0.064	93
Poly-[(*S*)-**1**$_{0.30}$-*co*-**2**$_{0.70}$]	29.7	0.112	15.0	0.048	98
Poly-[(*S*)-**1**$_{0.20}$-*co*-**2**$_{0.80}$]	34.0	0.128	9.96	0.032	94
Poly-[(*S*)-**1**$_{0.10}$-*co*-**2**$_{0.90}$]	38.2	0.144	4.98	0.016	97

Table S16. Amounts of (*R*)-**1** and **2** monomers used to form each copolymer and their yields.

Copolymer	Mass of (*R*)-1 (mg)	(*R*)-1 (mmol)	Mass of 2 (mg)	2 (mmol)	Yield (%)
Poly-[(*R*)-**1**$_{0.90}$-*co*-**2**$_{0.10}$]	4.20	0.016	44.8	0.144	81
Poly-[(*R*)-**1**$_{0.80}$-*co*-**2**$_{0.20}$]	8.50	0.032	39.8	0.128	80
Poly-[(*R*)-**1**$_{0.70}$-*co*-**2**$_{0.30}$]	12.7	0.048	34.9	0.112	80
Poly-[(*R*)-**1**$_{0.60}$-*co*-**2**$_{0.40}$]	16.9	0.064	29.9	0.096	84
Poly-[(*R*)-**1**$_{0.50}$-*co*-**2**$_{0.50}$]	21.2	0.080	24.9	0.080	92
Poly-[(*R*)-**1**$_{0.40}$-*co*-**2**$_{0.60}$]	25.5	0.096	19.9	0.064	88
Poly-[(*R*)-**1**$_{0.30}$-*co*-**2**$_{0.70}$]	29.7	0.112	15.0	0.048	89
Poly-[(*R*)-**1**$_{0.20}$-*co*-**2**$_{0.80}$]	34.0	0.128	9.96	0.032	97
Poly-[(*R*)-**1**$_{0.10}$-*co*-**2**$_{0.90}$]	38.2	0.144	4.98	0.016	89

USC UNIVERSIDADE DE SANTIAGO DE COMPOSTELA

Table S17. Amounts of (*S*)-**1** and **3** monomers used to form each copolymer and their yields.

copolymer	Mass of (*S*)-1 (mg)	(*S*)-1 (mmol)	Mass of 3 (mg)	3 (mmol)	Yield (%)
Poly-[(*S*)-**1**$_{0.90}$-*co*-**3**$_{0.10}$]	4.20	0.016	44.8	0.144	84
Poly-[(*S*)-**1**$_{0.80}$-*co*-**3**$_{0.20}$]	8.50	0.032	39.8	0.128	87
Poly-[(*S*)-**1**$_{0.70}$-*co*-**3**$_{0.30}$]	12.7	0.048	34.9	0.112	95
Poly-[(*S*)-**1**$_{0.60}$-*co*-**3**$_{0.40}$]	16.9	0.064	29.9	0.096	90
Poly-[(*S*)-**1**$_{0.50}$-*co*-**3**$_{0.50}$]	21.2	0.080	24.9	0.080	93
Poly-[(*S*)-**1**$_{0.40}$-*co*-**3**$_{0.60}$]	25.5	0.096	19.9	0.064	97
Poly-[(*S*)-**1**$_{0.30}$-*co*-**3**$_{0.70}$]	29.7	0.112	15.0	0.048	95
Poly-[(*S*)-**1**$_{0.20}$-*co*-**3**$_{0.80}$]	34.0	0.128	9.96	0.032	97
Poly-[(*S*)-**1**$_{0.10}$-*co*-**3**$_{0.90}$]	38.2	0.144	4.98	0.016	90

Table S18. Amounts of (*R*)-**1** and **3** monomers used to form each copolymer and their yields.

Copolymer	Mass of (*R*)-1 (mg)	(*R*)-1 (mmol)	Mass of 3 (mg)	3 (mmol)	Yield (%)
Poly-[(*R*)-**1**$_{0.90}$-*co*-**3**$_{0.10}$]	4.20	0.016	44.8	0.144	91
Poly-[(*R*)-**1**$_{0.80}$-*co*-**3**$_{0.20}$]	8.50	0.032	39.8	0.128	93
Poly-[(*R*)-**1**$_{0.70}$-*co*-**3**$_{0.30}$]	12.7	0.048	34.9	0.112	89
Poly-[(*R*)-**1**$_{0.60}$-*co*-**3**$_{0.40}$]	16.9	0.064	29.9	0.096	85
Poly-[(*R*)-**1**$_{0.50}$-*co*-**3**$_{0.50}$]	21.2	0.080	24.9	0.080	95
Poly-[(*R*)-**1**$_{0.40}$-*co*-**3**$_{0.60}$]	25.5	0.096	19.9	0.064	87
Poly-[(*R*)-**1**$_{0.30}$-*co*-**3**$_{0.70}$]	29.7	0.112	15.0	0.048	95
Poly-[(*R*)-**1**$_{0.20}$-*co*-**3**$_{0.80}$]	34.0	0.128	9.96	0.032	96
Poly-[(*R*)-**1**$_{0.10}$-*co*-**3**$_{0.90}$]	38.2	0.144	4.98	0.016	94

USC UNIVERSIDADE DE SANTIAGO DE COMPOSTELA

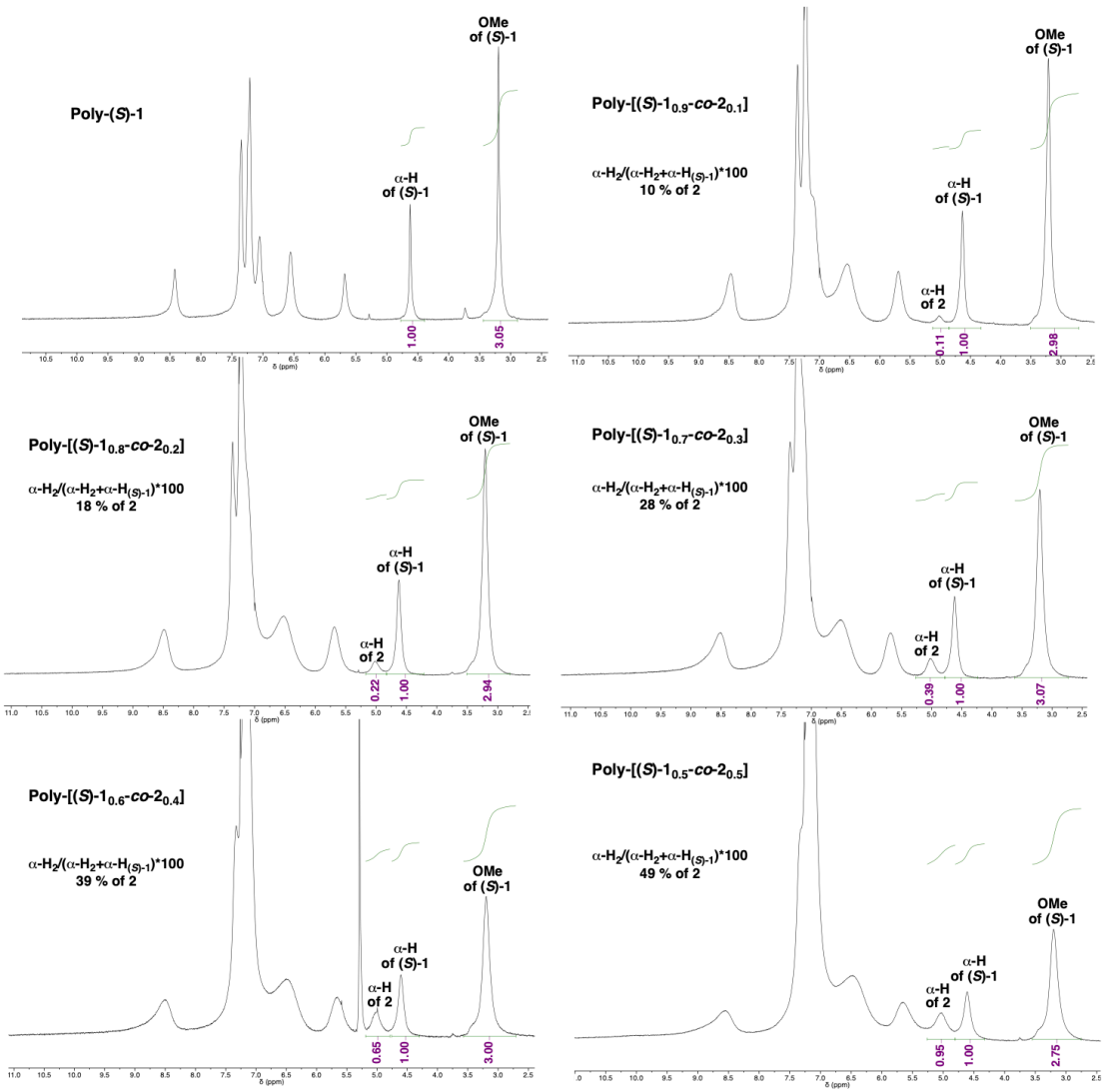


Figure S123. ^{1}H-NMR spectra ($CDCl_3$, 300 MHz) of Poly-(*S*)-**1**, Poly-[(*S*)-**1**$_{0.90}$-*co*-**2**$_{0.10}$], Poly-[(*S*)-**1**$_{0.80}$-*co*-**2**$_{0.20}$], Poly-[(*S*)-**1**$_{0.70}$-*co*-**2**$_{0.30}$], Poly-[(*S*)-**1**$_{0.60}$-*co*-**2**$_{0.40}$], and Poly-[(*S*)-**1**$_{0.50}$-*co*-**2**$_{0.50}$]. Integration of the Hydrogen in alpha to the carbonyl of **2** compared to the one of the (*S*)-**1** and Integration of the methoxy (*S*)-**1**.

USC UNIVERSIDADE DE SANTIAGO DE COMPOSTELA

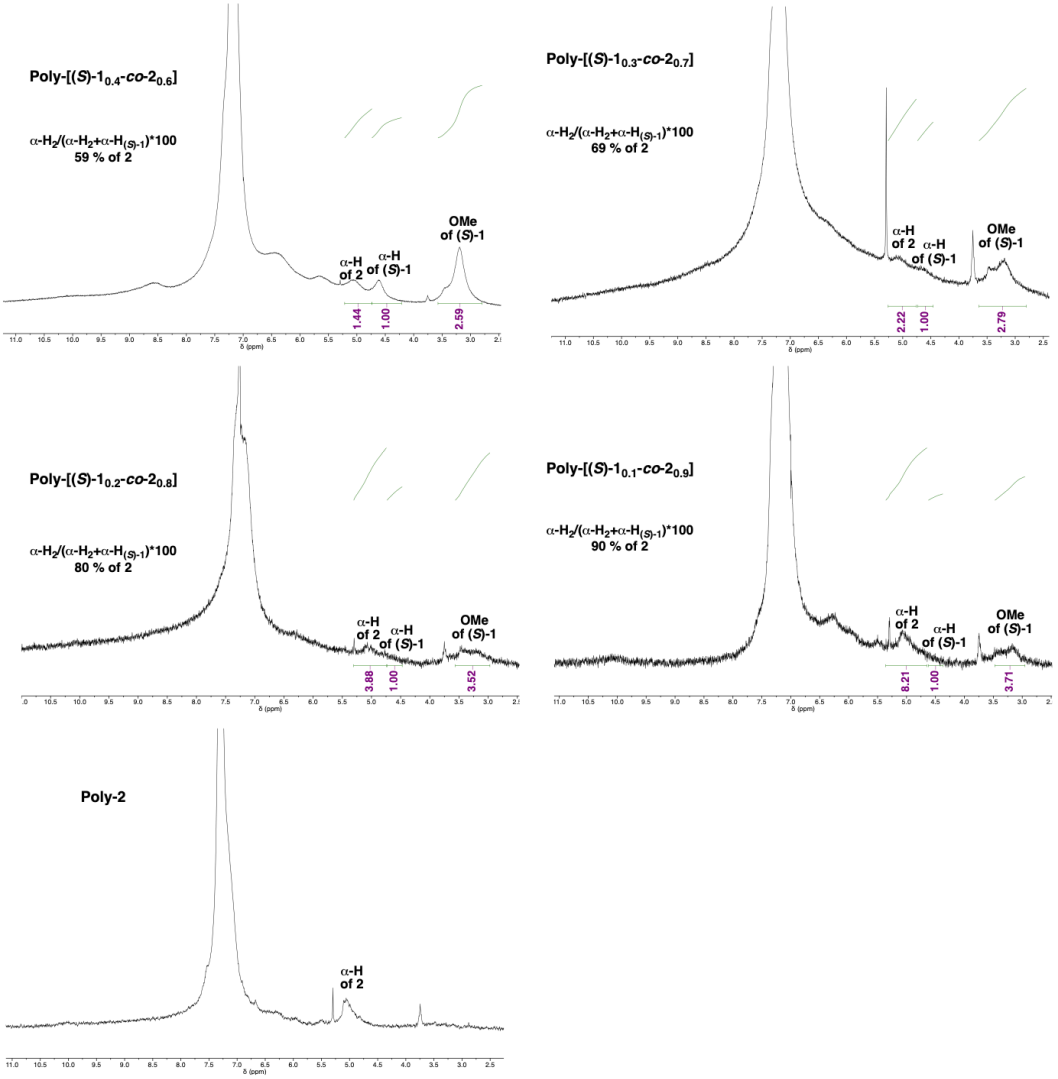


Figure S124. ^{1}H-NMR spectra ($CDCl_3$, 300 MHz) of Poly-[(*S*)-**1**$_{0.40}$-*co*-**2**$_{0.60}$], Poly-[(*S*)-**1**$_{0.30}$-*co*-**2**$_{0.70}$], Poly-[(*S*)-**1**$_{0.20}$-*co*-**2**$_{0.80}$], Poly-[(*S*)-**1**$_{0.10}$-*co*-**2**$_{0.90}$], and Poly-**2**. Integration of the Hydrogen in alpha to the carbonyl of **2** compared to the one of the (*S*)-**1** and Integration of the methoxy (*S*)-**1**.

USC UNIVERSIDADE DE SANTIAGO DE COMPOSTELA

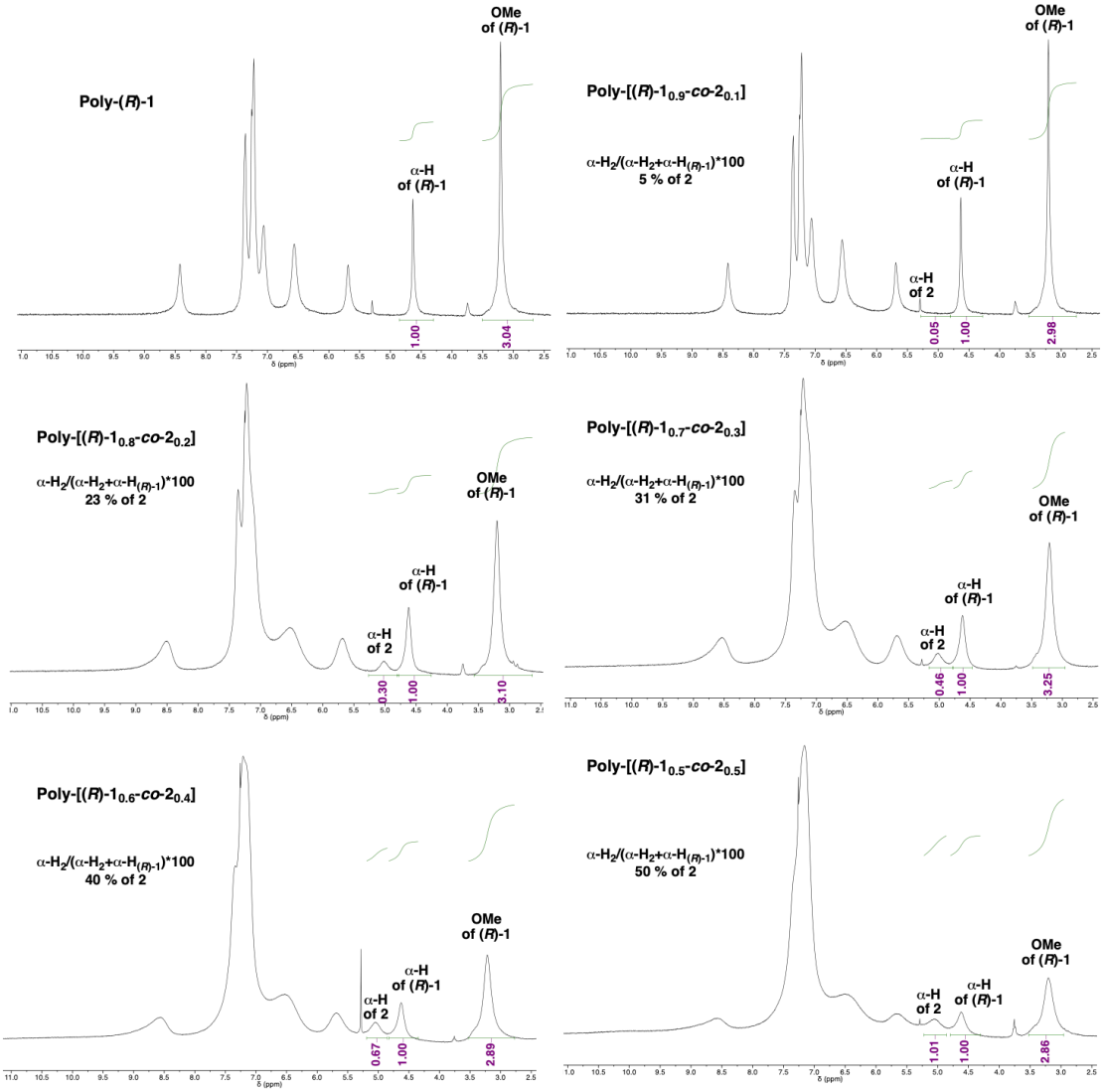


Figure S125. ^{1}H-NMR spectra ($CDCl_3$, 300 MHz) of Poly-(*R*)-**1**, Poly-[(*R*)-**1**$_{0.90}$-*co*-**2**$_{0.10}$], Poly-[(*S*)-**1**$_{0.80}$-*co*-**2**$_{0.20}$], Poly-[(*R*)-**1**$_{0.70}$-*co*-**2**$_{0.30}$], Poly-[(*R*)-**1**$_{0.60}$-*co*-**2**$_{0.40}$], and Poly-[(*R*)-**1**$_{0.50}$-*co*-**2**$_{0.50}$]. Integration of the Hydrogen in alpha to the carbonyl of **2** compared to the one of the (*R*)-**1** and Integration of the methoxy (*R*)-**1**.

USC UNIVERSIDADE DE SANTIAGO DE COMPOSTELA

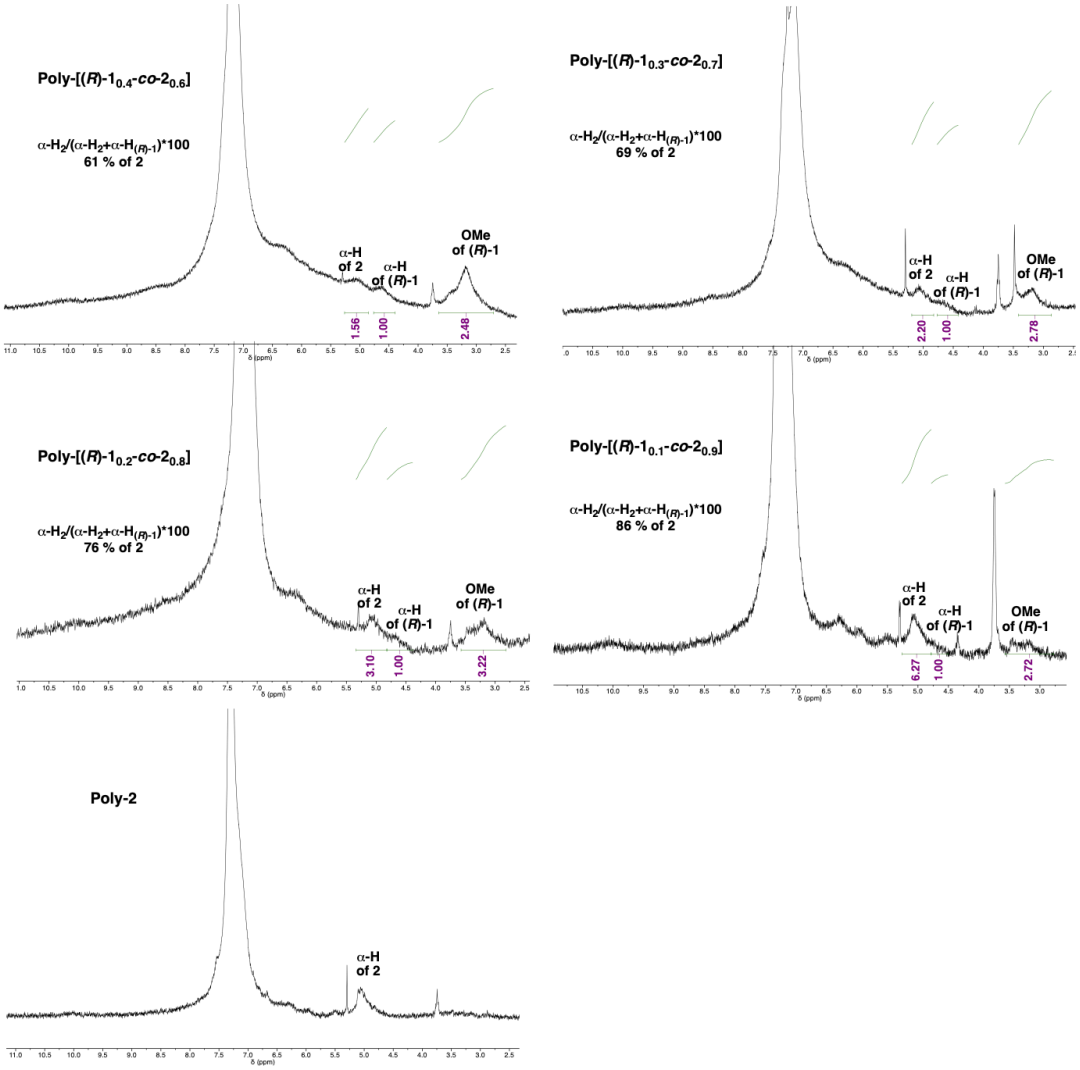


Figure S126. ^{1}H-NMR spectra ($CDCl_3$, 300 MHz) of Poly-[(*R*)-**1**$_{0.40}$-*co*-**2**$_{0.60}$], Poly-[(*R*)-**1**$_{0.30}$-*co*-**2**$_{0.70}$], Poly-[(*R*)-**1**$_{0.20}$-*co*-**2**$_{0.80}$], Poly-[(*R*)-**1**$_{0.10}$-*co*-**2**$_{0.90}$], and Poly-**2**. Integration of the Hydrogen in alpha to the carbonyl of **2** compared to the one of the (*R*)-**1** and Integration of the methoxy (*R*)-**1**.

USC UNIVERSIDADE DE SANTIAGO DE COMPOSTELA

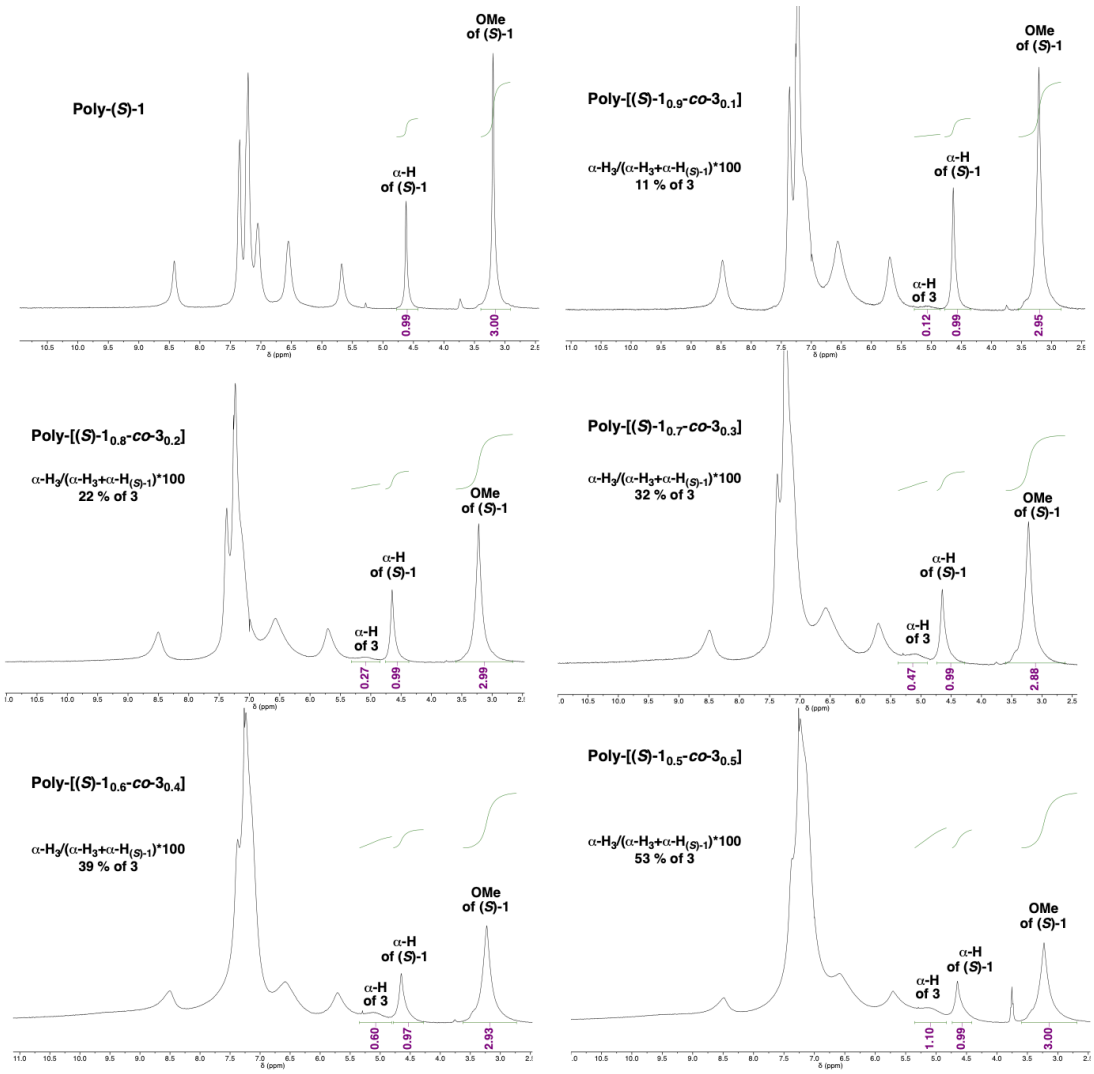


Figure S127. ^{1}H-NMR spectra ($CDCl_3$, 300 MHz) of Poly-(*S*)-**1**, Poly-[(*S*)-**1**$_{0.90}$-*co*-**3**$_{0.10}$], Poly-[(*S*)-**1**$_{0.80}$-*co*-**3**$_{0.20}$], Poly-[(*S*)-**1**$_{0.70}$-*co*-**3**$_{0.30}$], Poly-[(*S*)-**1**$_{0.60}$-*co*-**3**$_{0.40}$], and Poly-[(*S*)-**1**$_{0.50}$-*co*-**3**$_{0.50}$]. Integration of the Hydrogen in alpha to the carbonyl of **3** compared to the one of the (*S*)-**1** and Integration of the methoxy (*S*)-**1**.

USC UNIVERSIDADE DE SANTIAGO DE COMPOSTELA

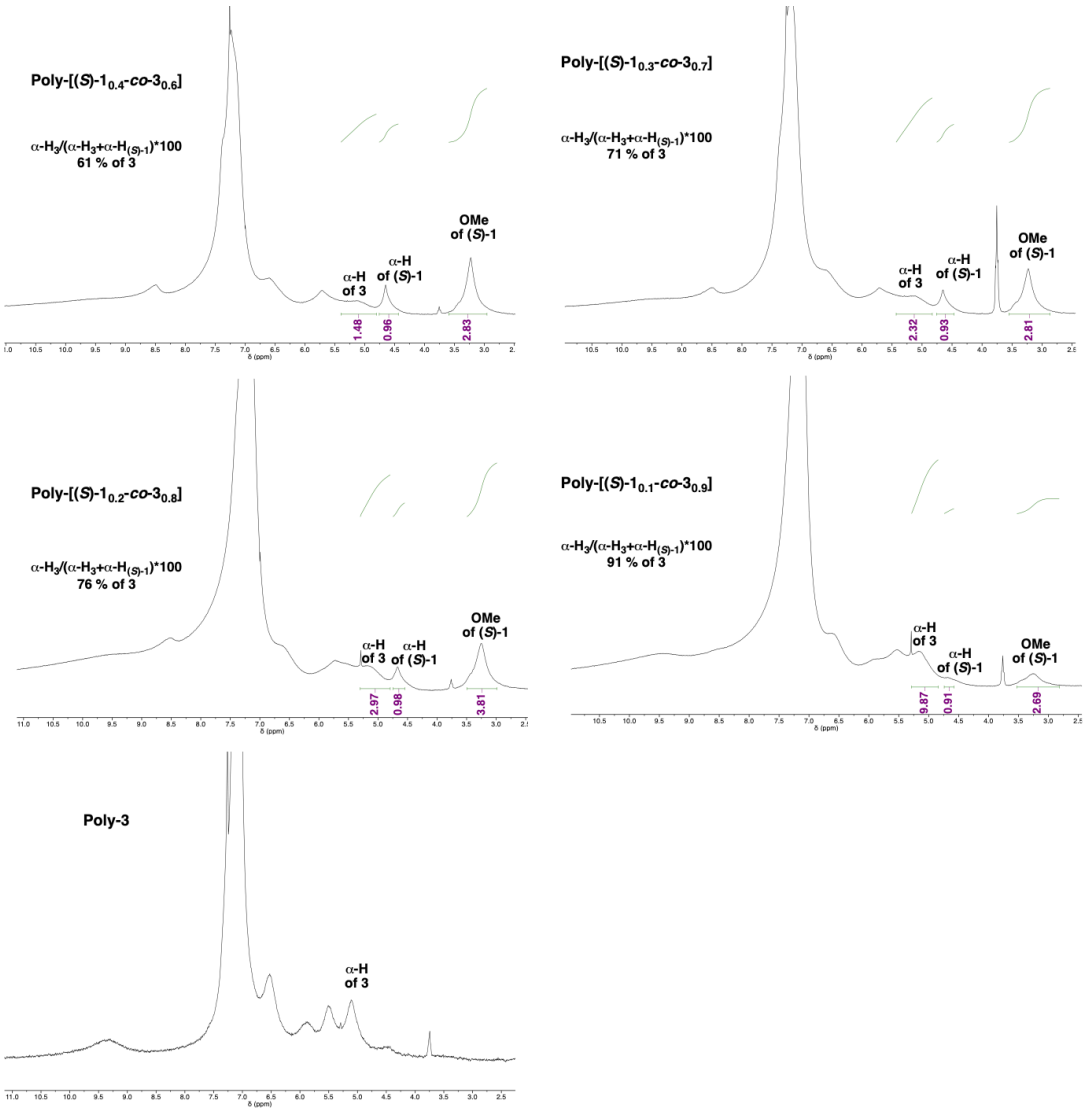


Figure S128. ^{1}H-NMR spectra ($CDCl_3$, 300 MHz) of Poly-[(*S*)-**1**$_{0.40}$-*co*-**3**$_{0.60}$], Poly-[(*S*)-**1**$_{0.30}$-*co*-**3**$_{0.70}$], Poly-[(*S*)-**1**$_{0.20}$-*co*-**3**$_{0.80}$], Poly-[(*S*)-**1**$_{0.10}$-*co*-**3**$_{0.90}$], and Poly-**3**. Integration of the Hydrogen in alpha to the carbonyl of **3** compared to the one of the (*S*)-**1** and Integration of the methoxy (*S*)-**1**.

USC UNIVERSIDADE DE SANTIAGO DE COMPOSTELA

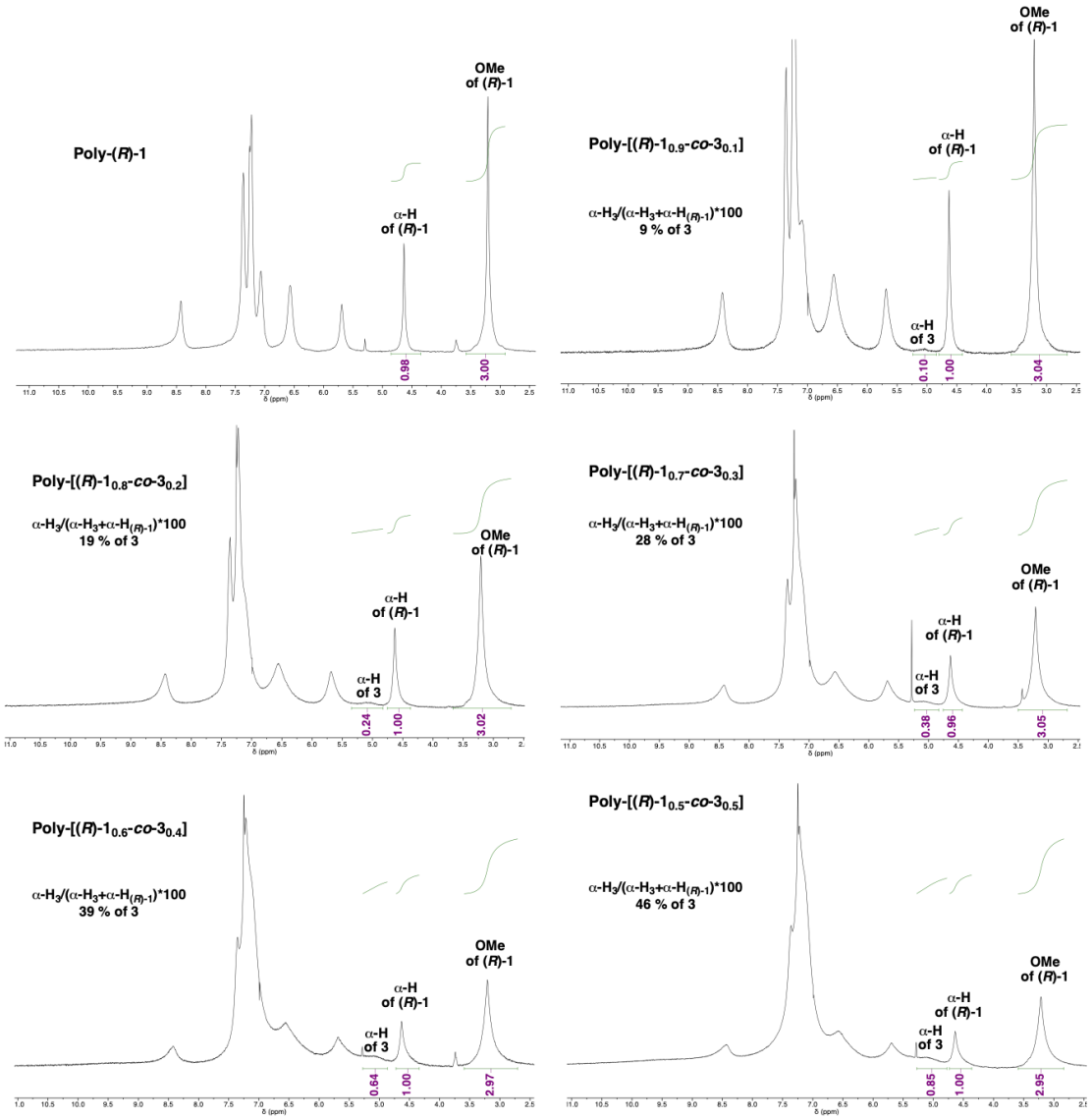


Figure S129. ^{1}H-NMR spectra ($CDCl_3$, 300 MHz) of Poly-(*R*)-**1**, Poly-[(*R*)-**1**$_{0.90}$-*co*-**3**$_{0.10}$], Poly-[(*R*)-**1**$_{0.80}$-*co*-**3**$_{0.20}$], Poly-[(*R*)-**1**$_{0.70}$-*co*-**3**$_{0.30}$], Poly-[(*R*)-**1**$_{0.60}$-*co*-**3**$_{0.40}$], and Poly-[(*R*)-**1**$_{0.50}$-*co*-**3**$_{0.50}$]. Integration of the Hydrogen in alpha to the carbonyl of **3** compared to the one of the (*R*)-**1** and Integration of the methoxy (*R*)-**1**.

USC UNIVERSIDADE DE SANTIAGO DE COMPOSTELA

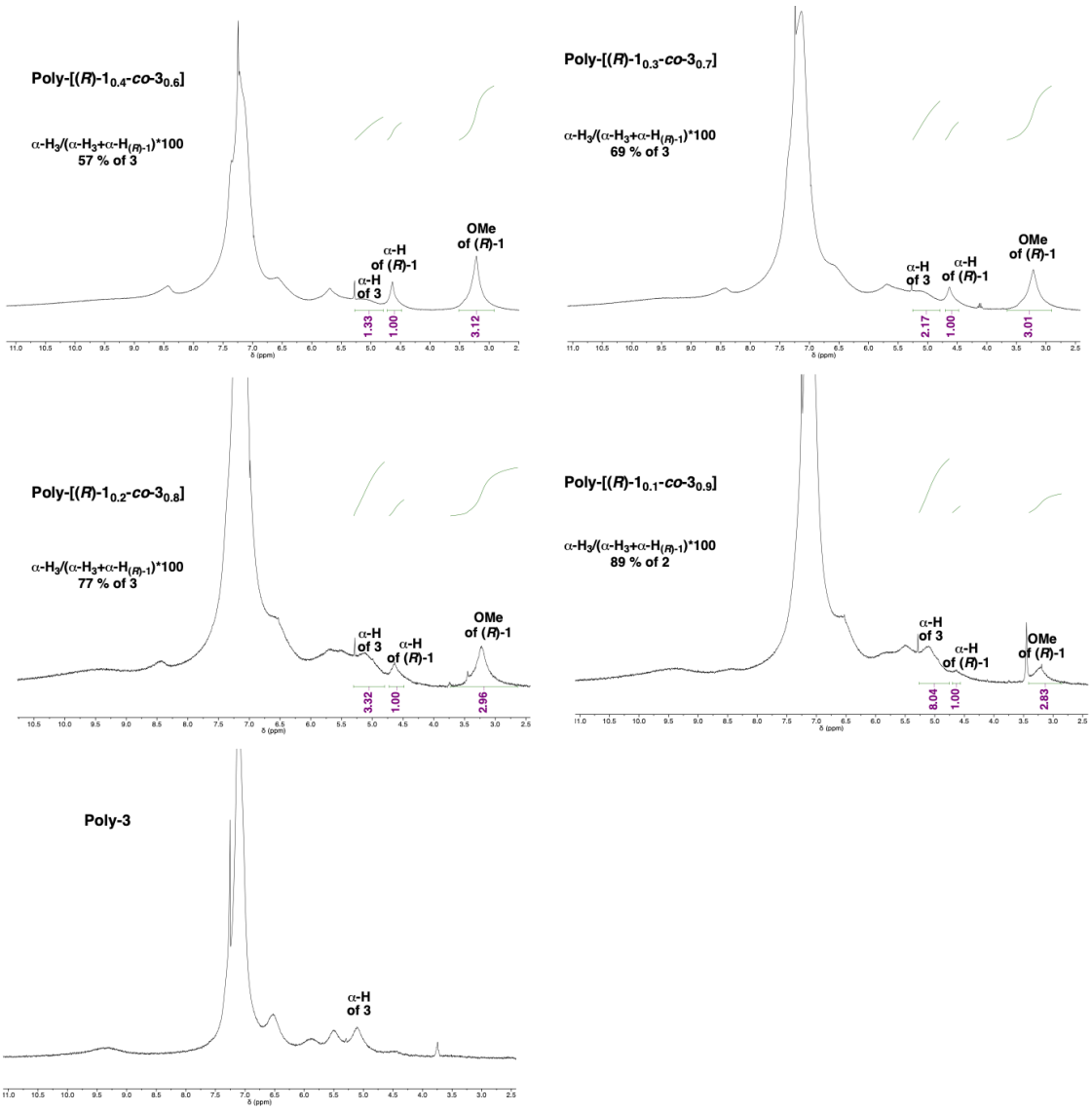


Figure S130. ^{1}H-NMR spectra ($CDCl_3$, 300 MHz) of Poly-[(*R*)-**1**$_{0.40}$-*co*-**3**$_{0.60}$], Poly-[(*R*)-**1**$_{0.30}$-*co*-**3**$_{0.70}$], Poly-[(*R*)-**1**$_{0.20}$-*co*-**3**$_{0.80}$], Poly-[(*R*)-**1**$_{0.10}$-*co*-**3**$_{0.90}$], and Poly-**3**. Integration of the Hydrogen in alpha to the carbonyl of **3** compared to the one of the (*R*)-**1** and Integration of the methoxy (*R*)-**1**.

Table S19. GPC data in Da or g/mol of Poly-(*S*)-**1**, Poly-(*R*)-**1**, Poly-**2**, and Poly-**3** in THF.

polymer	Mn (Da)	Mw (Da)	PDI
Poly-(*S*)-**1**	160480	207338	1.29
Poly-(*R*)-**1**	234160	305563	1.30
Poly-**2**	103819	176492	1.70
Poly-**3**	122969	183061	1.49

USC UNIVERSIDADE DE SANTIAGO DE COMPOSTELA

Table S20. GPC data in Da or g/mol of Poly-[(*S*)-**1**$_r$-*co*-**2**$_{1-r}$] in THF.

polymer	Mn (Da)	Mw (Da)	PDI
Poly-[(*S*)-**1**$_{0.90}$-*co*-**2**$_{0.10}$]	74165	96141	1.30
Poly-[(*S*)-**1**$_{0.80}$-*co*-**2**$_{0.20}$]	82236	116983	1.42
Poly-[(*S*)-**1**$_{0.70}$-*co*-**2**$_{0.30}$]	77585	110535	1.42
Poly-[(*S*)-**1**$_{0.60}$-*co*-**2**$_{0.40}$]	66846	85082	1.27
Poly-[(*S*)-**1**$_{0.50}$-*co*-**2**$_{0.50}$]	69354	88394	1.27
Poly-[(*S*)-**1**$_{0.40}$-*co*-**2**$_{0.60}$]	74665	99377	1.33
Poly-[(*S*)-**1**$_{0.30}$-*co*-**2**$_{0.70}$]	90018	130203	1.45
Poly-[(*S*)-**1**$_{0.20}$-*co*-**2**$_{0.80}$]	122896	207841	1.69
Poly-[(*S*)-**1**$_{0.10}$-*co*-**2**$_{0.90}$]	131819	247167	1.87

Table S21. GPC data in Da or g/mol of Poly-[(*R*)-**1**$_r$-*co*-**2**$_{1-r}$] in THF.

polymer	Mn (Da)	Mw (Da)	PDI
Poly-[(*R*)-**1**$_{0.90}$-*co*-**2**$_{0.10}$]	91755	128437	1.40
Poly-[(*R*)-**1**$_{0.80}$-*co*-**2**$_{0.20}$]	77332	102777	1.33
Poly-[(*R*)-**1**$_{0.70}$-*co*-**2**$_{0.30}$]	83091	115448	1.39
Poly-[(*R*)-**1**$_{0.60}$-*co*-**2**$_{0.40}$]	79691	109524	1.37
Poly-[(*R*)-**1**$_{0.50}$-*co*-**2**$_{0.50}$]	84102	119037	1.42
Poly-[(*R*)-**1**$_{0.40}$-*co*-**2**$_{0.60}$]	92310	137556	1.49
Poly-[(*R*)-**1**$_{0.30}$-*co*-**2**$_{0.70}$]	107717	169736	1.58
Poly-[(*R*)-**1**$_{0.20}$-*co*-**2**$_{0.80}$]	130130	215656	1.66
Poly-[(*R*)-**1**$_{0.10}$-*co*-**2**$_{0.90}$]	156129	272226	1.74

Table S22. GPC data in Da or g/mol of Poly-[(*S*)-**1**$_r$-*co*-**3**$_{1-r}$] in THF.

Polymer	Mn (Da)	Mw (Da)	PDI
Poly-[(*S*)-**1**$_{0.90}$-*co*-**3**$_{0.10}$]	122130	198196	1.62

USC UNIVERSIDADE DE SANTIAGO DE COMPOSTELA

Poly-[(*S*)-**1**$_{0.80}$-*co*-**3**$_{0.20}$]	152082	261142	1.72
Poly-[(*S*)-**1**$_{0.70}$-*co*-**3**$_{0.30}$]	155650	238867	1.53
Poly-[(*S*)-**1**$_{0.60}$-*co*-**3**$_{0.40}$]	199287	292453	1.47
Poly-[(*S*)-**1**$_{0.50}$-*co*-**3**$_{0.50}$]	162273	244212	1.50
Poly-[(*S*)-**1**$_{0.40}$-*co*-**3**$_{0.60}$]	174837	251521	1.44
Poly-[(*S*)-**1**$_{0.30}$-*co*-**3**$_{0.70}$]	150961	207493	1.37
Poly-[(*S*)-**1**$_{0.20}$-*co*-**3**$_{0.80}$]	145694	207158	1.42
Poly-[(*S*)-**1**$_{0.10}$-*co*-**3**$_{0.90}$]	146113	221559	1.52

Table S23. GPC data in Da or g/mol of Poly-[(*R*)-**1**$_{r}$-*co*-**3**$_{1-r}$] in THF.

polymer	Mn (Da)	Mw (Da)	PDI
Poly-[(*R*)-**1**$_{0.90}$-*co*-**3**$_{0.10}$]	181820	269798	1.48
Poly-[(*R*)-**1**$_{0.80}$-*co*-**3**$_{0.20}$]	219809	312181	1.42
Poly-[(*R*)-**1**$_{0.70}$-*co*-**3**$_{0.30}$]	226312	334813	1.48
Poly-[(*R*)-**1**$_{0.60}$-*co*-**3**$_{0.40}$]	220495	295689	1.34
Poly-[(*R*)-**1**$_{0.50}$-*co*-**3**$_{0.50}$]	211692	287549	1.36
Poly-[(*R*)-**1**$_{0.40}$-*co*-**3**$_{0.60}$]	227614	282293	1.24
Poly-[(*R*)-**1**$_{0.30}$-*co*-**3**$_{0.70}$]	183863	256926	1.40
Poly-[(*R*)-**1**$_{0.20}$-*co*-**3**$_{0.80}$]	137474	169847	1.24
Poly-[(*R*)-**1**$_{0.10}$-*co*-**3**$_{0.90}$]	138038	177630	1.29

5.4.10. Determination of the monomer reactivity ratios in copolymerization

To estimate the monomer reactivity ratios in the copolymerization of Poly-[(*S*)-**1**$_{r}$-*co*-**2**$_{1-r}$] [(*S*)-**1** and **2**], and in Poly-[(*S*)-**1**$_{r}$-*co*-**3**$_{1-r}$] [(*S*)-**1** and **3**], the copolymerizations of (*S*)-**1** with **2** and (*S*)-**1** with **3** at varying monomer feed ratios were carried out and were terminated at low conversions by adding, in both cases, a solution of HCl 0.05 M in MeOH (5 mL) 10 seconds after the catalyst addition. Subsequently, a solution of NaOH 0.05 M

in MeOH (5 mL) was added followed by MeOH (10 mL) containing a small amount of concentrated HCl. The resulting Poly-[(*S*)-**1**$_r$-*co*-**2**$_{1-r}$] and Poly-[(*S*)-**1**$_r$-*co*-**3**$_{1-r}$] were collected by centrifugation and dried in vacuo at room temperature overnight. The copolymer compositions were determined from their quantitative ^{13}C-NMR inverse-gated decoupling spectra (Figure S131 and Figure S132) peaks of the methoxy and carbonyl groups of (*R*/*S*)-**1** compared to (*R*)-**2** and the results are summarized in Table S24 and Table S25. The copolymer compositions represented by f are almost similar to the corresponding monomer feed ratios represented by F. For the determination of $r_{(S)\text{-}\mathbf{1}}$ and $r_{\mathbf{2}}$, and $r_{(S)\text{-}\mathbf{1}}$ and $r_{\mathbf{3}}$, the Kellen-Tüdös method was used.[154,408,409] In this method, the following equation (S14) and equation (S15) are employed.

$$\eta = \left(r_{\mathbf{2}} + \frac{r_{(S)-\mathbf{1}}}{\alpha}\right)\xi - \frac{r_{(S)-\mathbf{1}}}{\alpha} \qquad \textbf{(S14)}$$

$$\eta = \left(r_{\mathbf{3}} + \frac{r_{(S)-\mathbf{1}}}{\alpha}\right)\xi - \frac{r_{(S)-\mathbf{1}}}{\alpha} \qquad \textbf{(S15)}$$

To represent the experimental η and ξ and fit a regression curve to extract the reactivity ratios, the parameters are defined by equation (S16) and equation (S17).

$$\eta = \frac{G}{\alpha + H} \qquad \textbf{(S16)}$$

$$\xi = \frac{H}{\alpha + H} \qquad \textbf{(S17)}$$

Where H, G and α values are obtained using the equation (S18), equation (S19), and equation (S20).

USC UNIVERSIDADE DE SANTIAGO DE COMPOSTELA

$$G = \frac{F \cdot (f - 1)}{f} \quad \textbf{(S18)}$$

$$H = \frac{F^2}{f} \quad \textbf{(S19)}$$

$$\alpha = (F_{min} - F_{max})^{0.5} \quad \textbf{(S20)}$$

The estimated monomer reactivity ratios using the f value measured in the Carbonyl groups for Poly-[(*S*)-**1**$_r$-*co*-**2**$_{1-r}$] are $r_{(S)\text{-}1}$ = 0.782 and r_2 =0.666. While the estimated monomer reactivity ratios using the f value measured in the Methoxy groups for Poly-[(*S*)-**1**$_r$-*co*-**3**$_{1-r}$] are $r_{(S)\text{-}1}$ = 0.979 and r_3 =0.840. The reactivity ratios between the monomers in the two copolymerization are very similar, suggesting that the monomer distribution in copolymers is random.

Table S24. Values of yield, F, and f for Poly-[(*S*)-**1**$_r$-*co*-**2**$_{1-r}$].

copolymer	F	Yield (%)	f at H in alpha to carbonyl NMR signal
Poly-[(*S*)-**1**$_{0.20}$-*co*-**2**$_{0.80}$]	0.20	25	0.23
Poly-[(*S*)-**1**$_{0.40}$-*co*-**2**$_{0.60}$]	0.40	23	0.39
Poly-[(*S*)-**1**$_{0.60}$-*co*-**2**$_{0.40}$]	0.60	33	0.65
Poly-[(*S*)-**1**$_{0.80}$-*co*-**2**$_{0.20}$]	0.80	35	0.78

USC UNIVERSIDADE DE SANTIAGO DE COMPOSTELA

Table S25. Values of yield, F, and f for Poly-[(*S*)-**1**$_{r}$-*co*-**3**$_{1-r}$].

copolymer	F	Yield (%)	f at H in alpha to carbonyl NMR signal
Poly-[(*R*)-**1**$_{0.20}$-*co*-**3**$_{0.80}$]	0.20	28	0.20
Poly-[(*R*)-**1**$_{0.40}$-*co*-**3**$_{0.60}$]	0.40	20	0.38
Poly-[(*R*)-**1**$_{0.60}$-*co*-**3**$_{0.40}$]	0.60	37	0.58
Poly-[(*R*)-**1**$_{0.80}$-*co*-**3**$_{0.20}$]	0.80	36	0.76

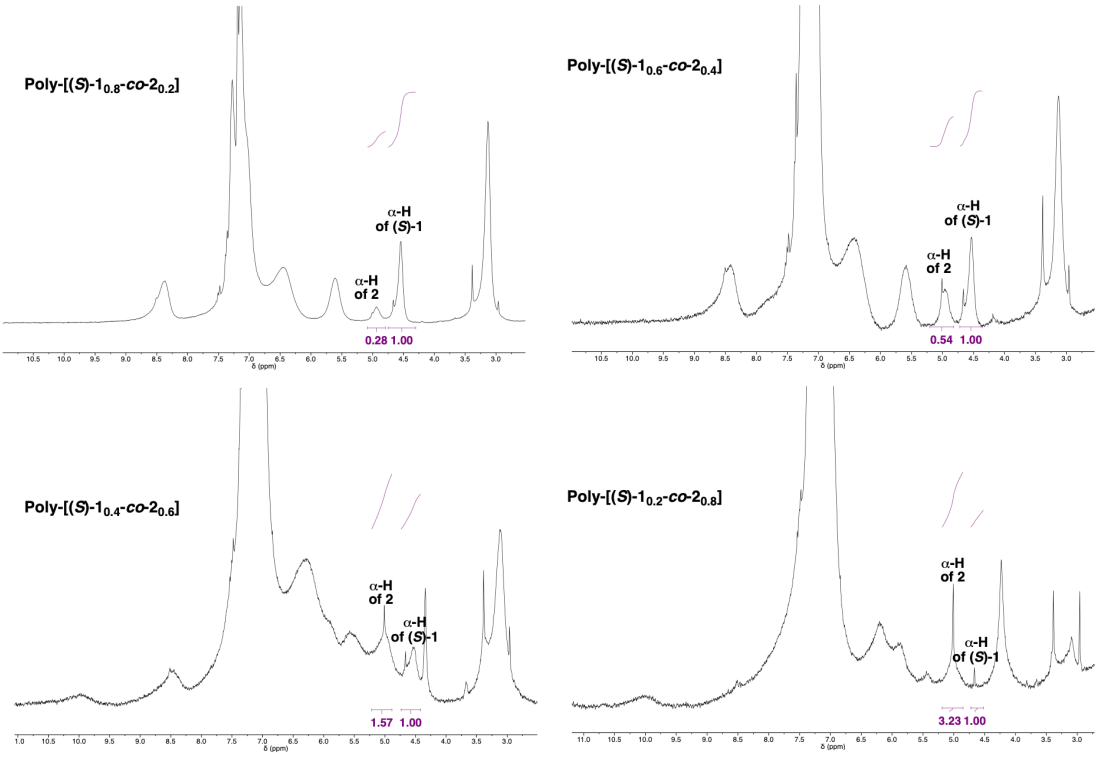


Figure S131. ^{1}H-NMR spectra ($CDCl_3$, 300 MHz) of Kellen-Tüdös Poly-[(*S*)-**1**$_{0.80}$-*co*-**2**$_{0.20}$], Poly-[(*S*)-**1**$_{0.60}$-*co*-**2**$_{0.40}$], Poly-[(*S*)-**1**$_{0.40}$-*co*-**2**$_{0.60}$] and Poly-[(*S*)-**1**$_{0.20}$-*co*-**2**$_{0.80}$].

USC UNIVERSIDADE DE SANTIAGO DE COMPOSTELA

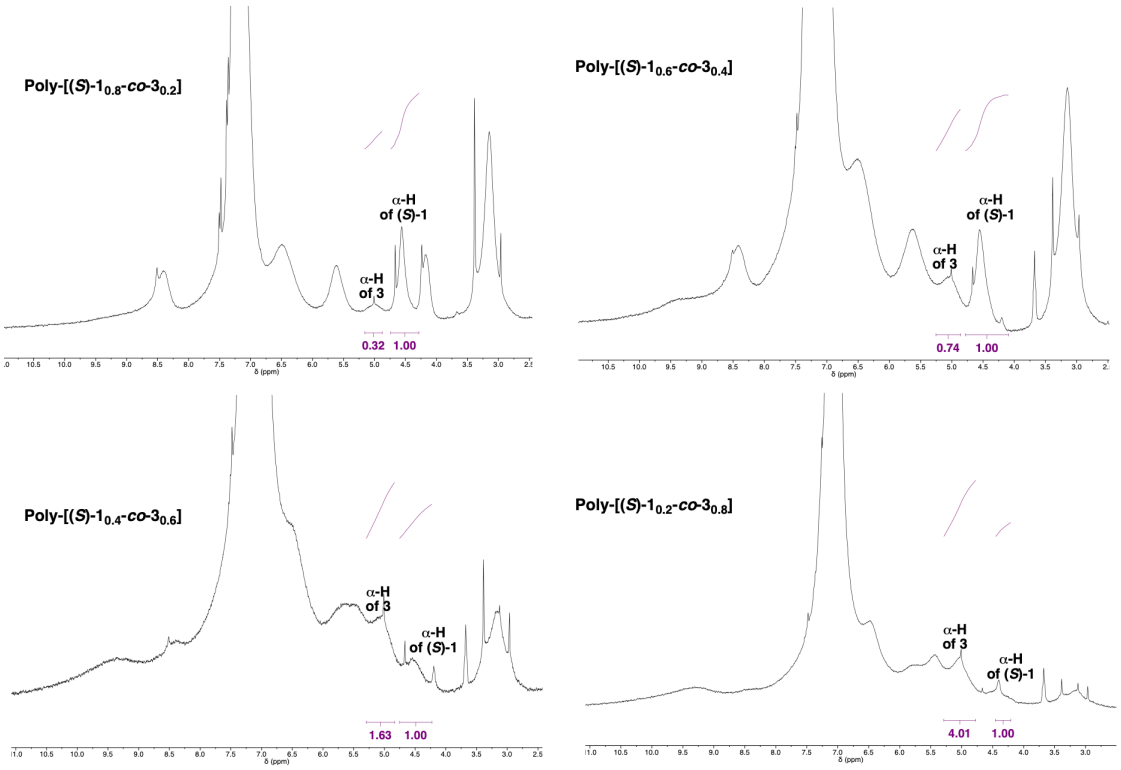


Figure S132. ^{1}H-NMR spectra ($CDCl_3$, 300 MHz) of Kellen-Tüdös Poly-[(*S*)-**1**$_{0.80}$-*co*-**3**$_{0.20}$], Poly-[(*S*)-**1**$_{0.60}$-*co*-**3**$_{0.40}$], Poly-[(*S*)-**1**$_{0.40}$-*co*-**3**$_{0.60}$], and Poly-[(*S*)-**1**$_{0.20}$-*co*-**3**$_{0.80}$].

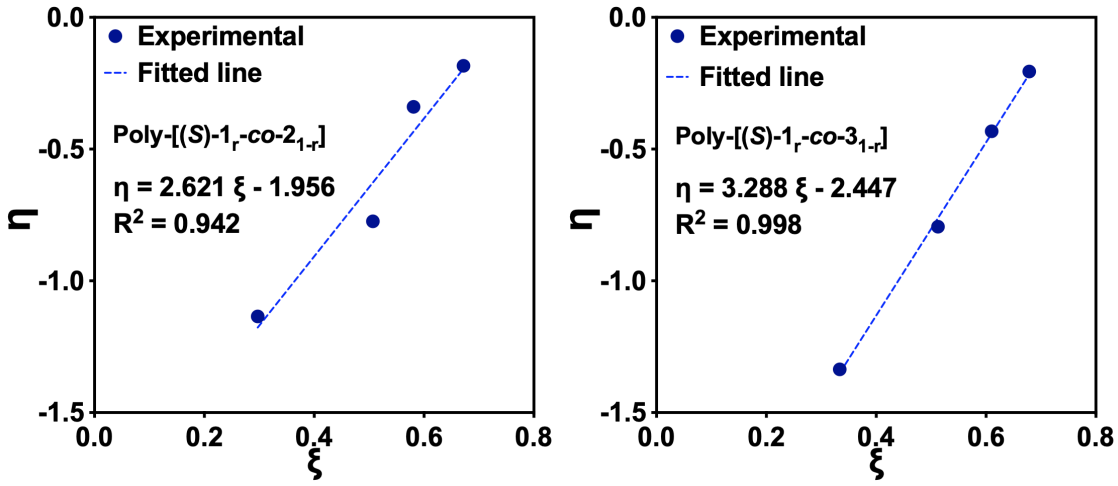


Figure S133. Kellen-Tüdös plots for the polymerization of Poly-[(*S*)-**1**$_r$-*co*-**2**$_{1-r}$],and Poly-[(*S*)-**1**$_r$-*co*-**3**$_{1-r}$] copolymer series.

USC UNIVERSIDADE DE SANTIAGO DE COMPOSTELA

5.4.11. DSC Studies.

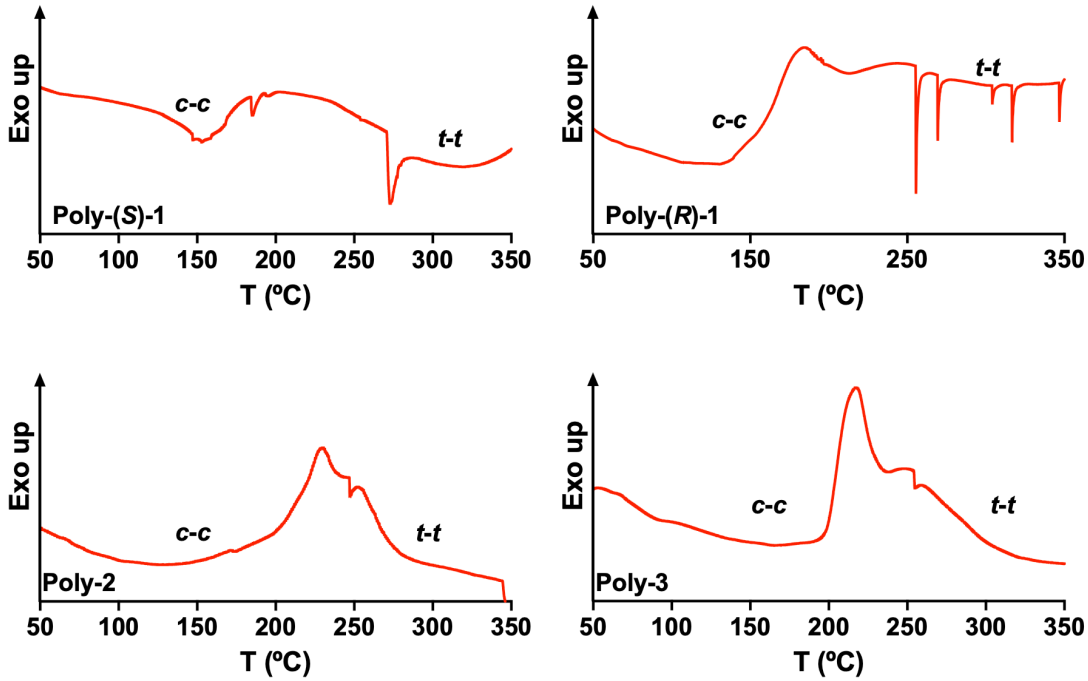


Figure S134. DSC of homopolymers of Poly-(*S*)-**1**, Poly-(*R*)-**1**, Poly-**2**, and Poly-**3** ($CHCl_3$ film).

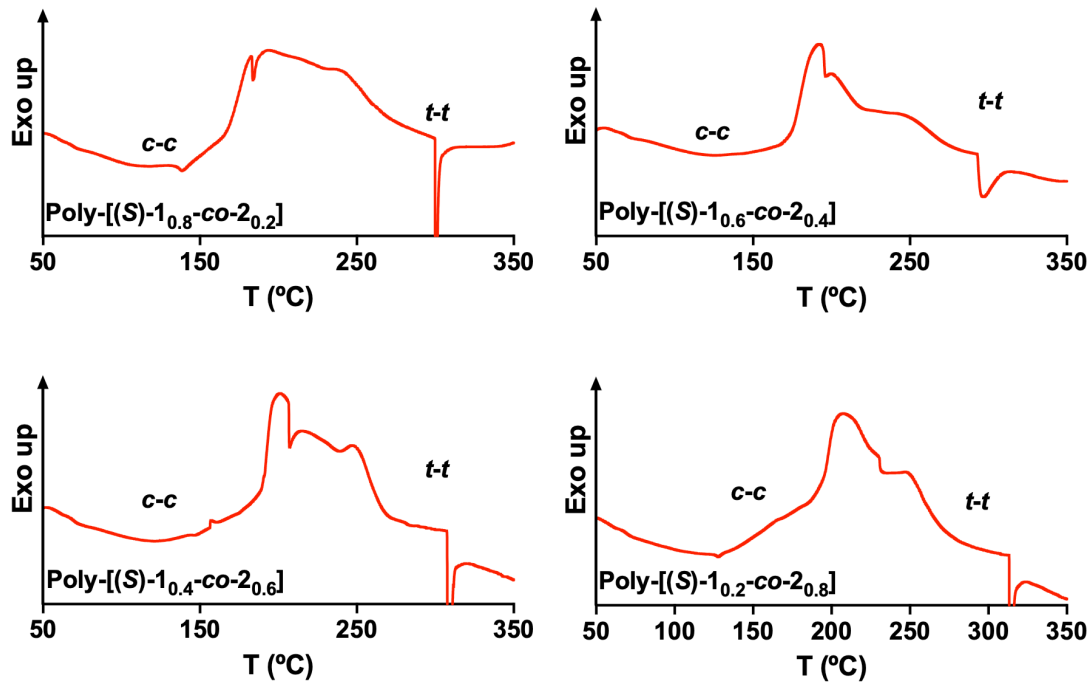


Figure S135. DSC of copolymers of Poly-[(*S*)-**1**$_{0.8}$-*co*-**2**$_{0.2}$], Poly-[(*S*)-**1**$_{0.6}$-*co*-**2**$_{0.4}$], Poly-[(*S*)-**1**$_{0.4}$-*co*-**2**$_{0.6}$], and Poly-[(*S*)-**1**$_{0.2}$-*co*-**2**$_{0.8}$] ($CHCl_3$ film).

USC DE COMPOSTELA

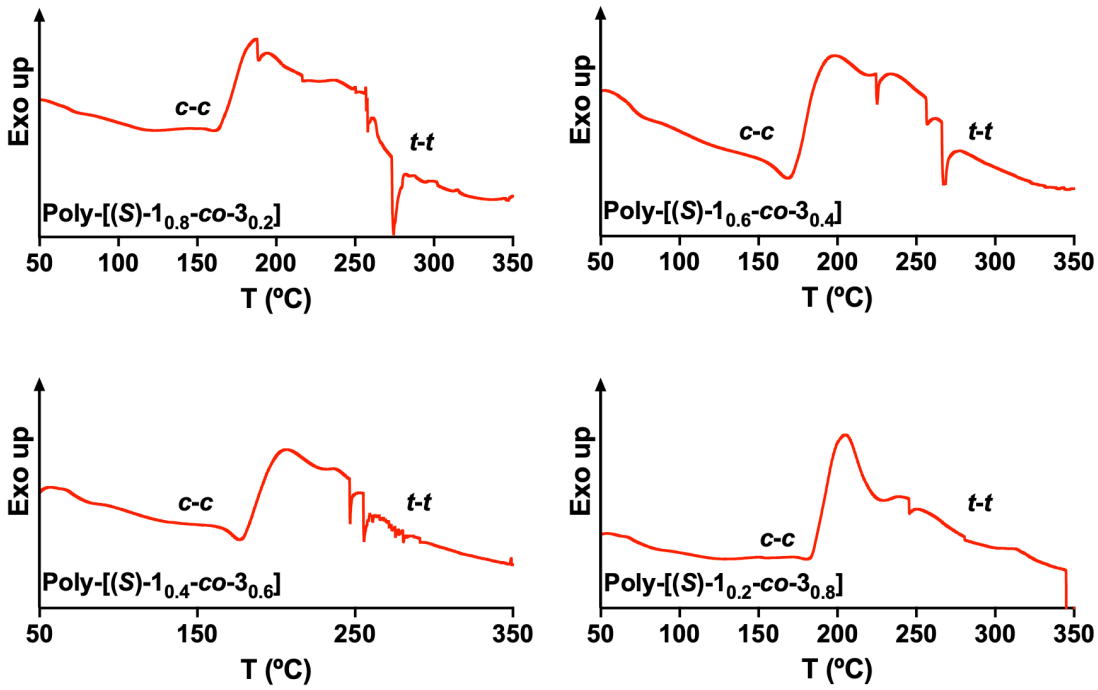


Figure S136. DSC of copolymers of Poly-[(*S*)-**1**$_{0.8}$-*co*-**3**$_{0.2}$], Poly-[(*S*)-**1**$_{0.6}$-*co*-**3**$_{0.4}$], Poly-[(*S*)-**1**$_{0.4}$-*co*-**3**$_{0.6}$], and Poly-[(*S*)-**1**$_{0.2}$-*co*-**3**$_{0.8}$] ($CHCl_3$ film).

5.4.12. Raman Studies

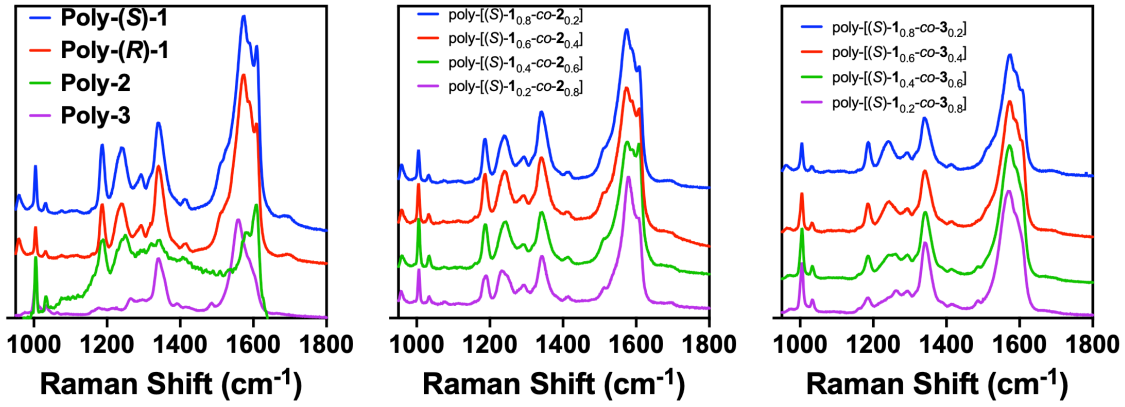


Figure S137. Confocal Raman spectra of Poly-(*S*)-**1**, Poly-(*R*)-**1**, Poly-**2**, Poly-**3**, Poly-[(*R*)-**1**$_{0.8}$-*co*-**2**$_{0.2}$], Poly-[(*R*)-**1**$_{0.6}$-*co*-**2**$_{0.4}$], Poly-[(*R*)-**1**$_{0.4}$-*co*-**2**$_{0.6}$], Poly-[(*R*)-**1**$_{0.2}$-*co*-**2**$_{0.8}$], Poly-[(*R*)-**1**$_{0.8}$-*co*-**3**$_{0.2}$], Poly-[(*R*)-**1**$_{0.6}$-*co*-**3**$_{0.4}$], Poly-[(*R*)-**1**$_{0.4}$-*co*-**3**$_{0.6}$], and Poly-[(*R*)-**1**$_{0.2}$-*co*-**3**$_{0.8}$], (Laser 785 nm) ($CHCl_3$ film).

USC UNIVERSIDADE DE SANTIAGO DE COMPOSTELA

5.4.13. ECD and UV-Vis spectra of Poly-(*S*)-1 in different solvents or in the presence of metal ions

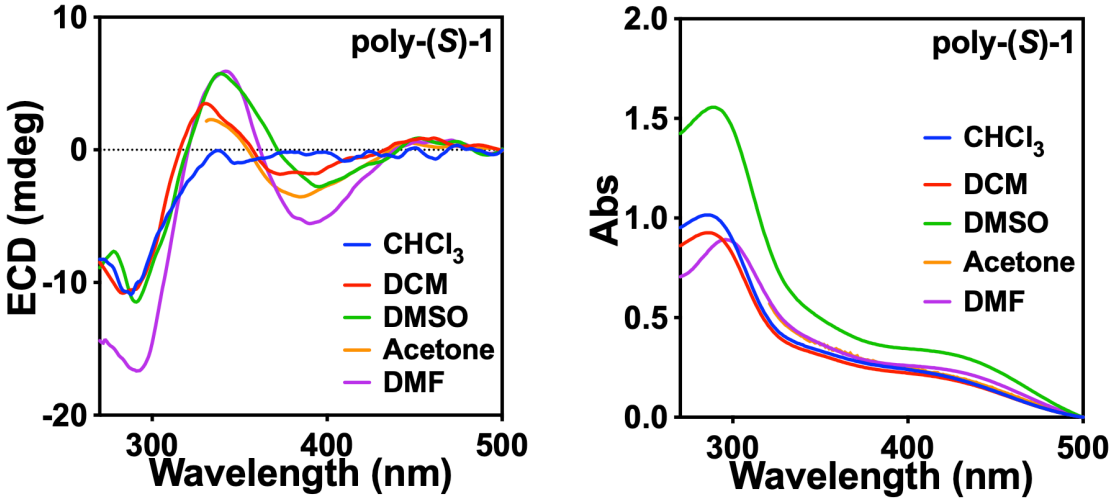


Figure S138. ECD and UV-Vis of Poly-(*S*)-**1** in different solvents (c=0.3 mg/mL).

USC
UNIVERSIDADE DE SANTIAGO DE COMPOSTELA

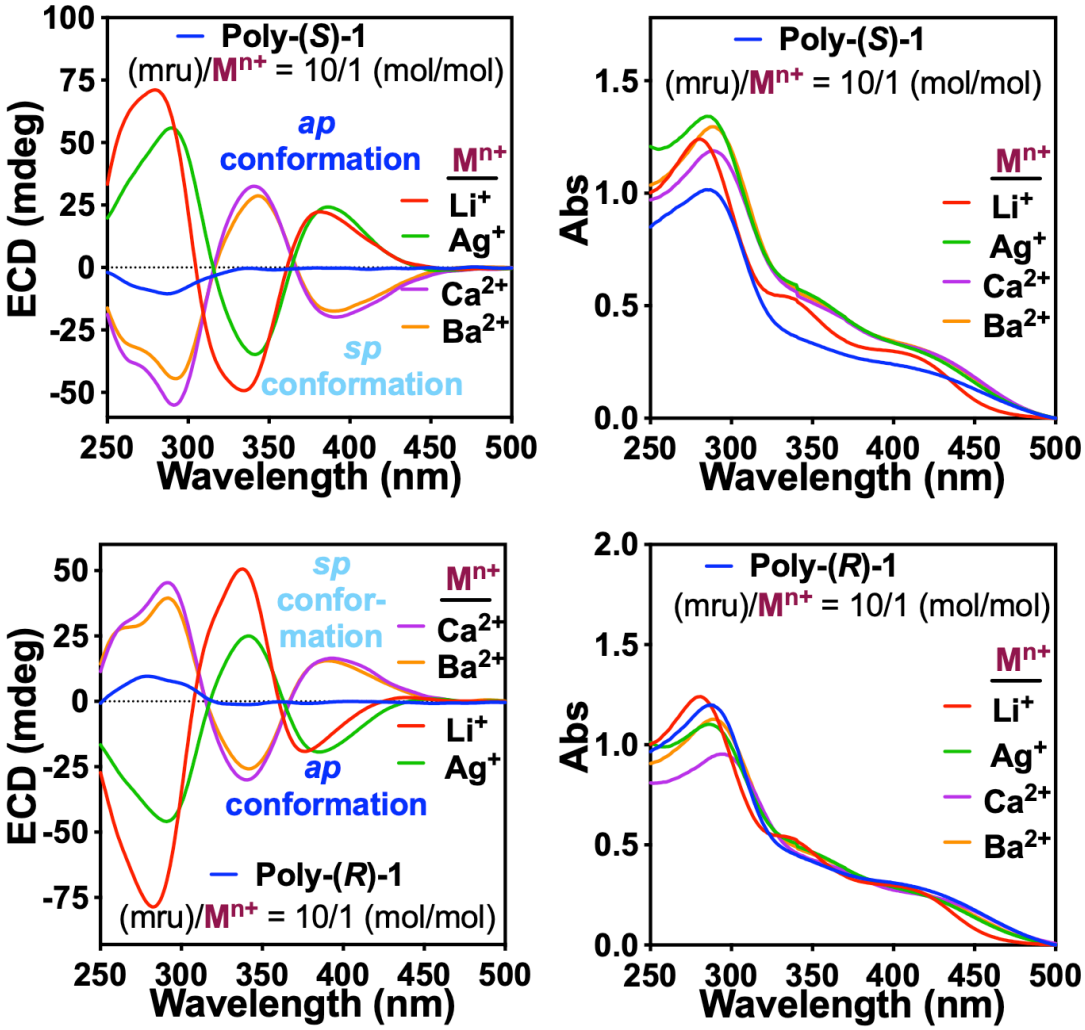


Figure S139. ECD and UV-Vis spectra of Poly-(*S*)-**1**, Poly-(*R*)-**1** (c=0.3 mg/mL $CHCl_3$) coordinated to 0.1 equiv of $LiClO_4$, $AgClO_4$, $Ca(ClO_4)_2$, and $Ba(ClO_4)_2$. (c=10.0 mg/mL MeOH).

USC UNIVERSIDADE DE SANTIAGO DE COMPOSTELA

5.4.14. ECD and UV-Vis spectra of enantiomeric series Poly-[(*R*)-1_r-*co*-2_{1-r}] and Poly-[(*R*)-1_r-*co*-3_{1-r}] in DFM and $CHCl_3$

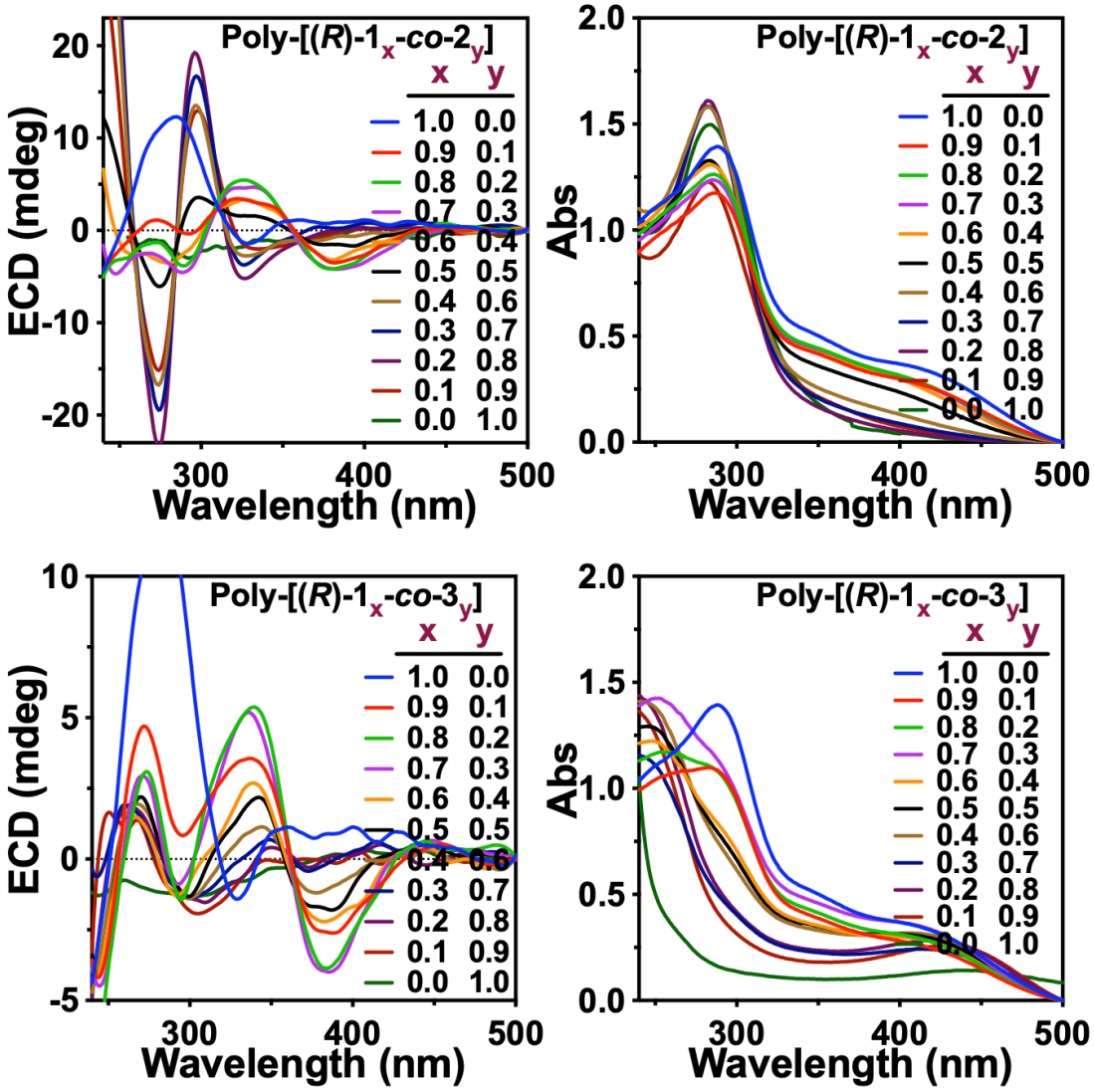


Figure S140. ECD and UV-Vis of Poly-[(*R*)-**1**$_r$-*co*-**2**$_{1-r}$] and Poly-[(*R*)-**1**$_r$-*co*-**3**$_{1-r}$] in $CHCl_3$ (c=0.3 mg/mL).

USC UNIVERSIDADE DE SANTIAGO DE COMPOSTELA

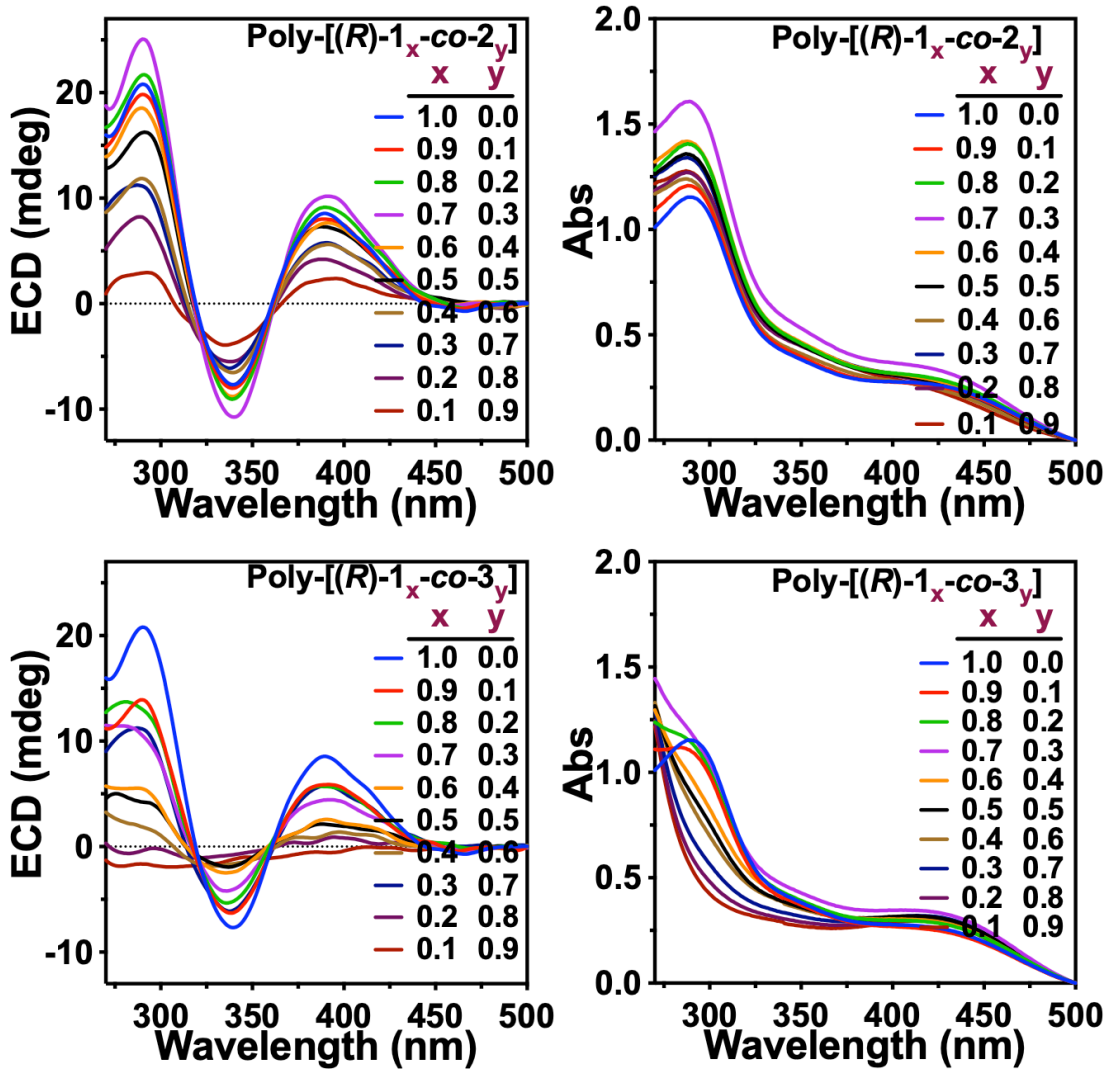


Figure S141. ECD and UV-Vis of Poly-[(*R*)-**1**$_r$-*co*-**2**$_{1-r}$] and Poly-[(*R*)-**1**$_r$-*co*-**3**$_{1-r}$] in DMF (c=0.3 mg/mL).

USC UNIVERSIDADE DE SANTIAGO DE COMPOSTELA

USC
UNIVERSIDADE
DE SANTIAGO
DE COMPOSTELA

5.5. Experimental Section and Methodology Chapter 3.5.

5.5.1. Materials and Methods

The Commercially available chemicals have been used as delivered. Solvents were purchased as reagent grade and distilled if necessary. Anhydrous solvents were either purchased as ultra-dry solvent from Acros Organics® or received from solvent purification system. For the coupling and polymerization reactions, dry THF was obtained from MBRAUN SPS 800 solvent purification system. The reactions were done in inert atmospheres.

Column chromatography was performed with silica gel 230-400 mesh (Merck).

Thin-layer chromatography of silica 60F254 Merck was visualized in UV at a wavelength of 254 nm and by heat with Hanessian.

The IR spectra were obtained using the FT-IR PerkinElmer Spectrum Two equipped with the UATR addon.

NMR experiments were measured in a Varian 300 operating at 300 MHz for proton NMR, 75 MHz for carbon. TMS signal (δ= 0 ppm) was used as internal reference for ^{1}H NMR experiments; $CDCl_3$ signal (δ= 77.2 ppm) was used as standard for ^{13}C experiments.

The UV/Vis absorption spectra were acquired in the Jasco V-730 spectrophotometer in the range of wavelengths from 240 nm to 500 nm. All samples were prepared at a fixed concentration of 0.3 mg polymer/mL solvent inside quartz glass cuvettes with a light path of 1 mm.

The ECD spectra were acquired in the Jasco 720 spectrophotometer in the range of wavelengths from 240 nm to 500 nm. All samples were prepared at a fixed concentration of 0.3 mg polymer/mL solvent inside quartz glass cuvettes with a light path of 1 mm. pH studies were carried out with a concentration of 0.03 mg polymer/mL inside quartz glass cuvettes with a light path of 10 mm.

DLS measurements were performed on a Nano-ZS 90 (Malvern) equipped with a He-Ne laser (λ = 633 nm) under scattering angle of 173º. The samples were maintained at the designed temperature for 5 min before testing.

USC DE COMPOSTELA

SEM samples were performed on a LEO-435VP electron microscope. A drop of sample was settled on a silicon wafer chip and allowed to dry at rt for 12 h.

TEM measurements were performed on a Phillips CM-12 electron microscope. A drop of sample was settled on a silicon wafer chip and allowed to dry at rt for 12 h.

Irradiation experiments were done in an Asahi Spectra Xenon light model MAX-303. The light was filtered using a short pass filter / Vis 550 nm 25 dia.

Gaussian curve fitting was performed with Solver from excel for the electron microscopy measured sizes with the equation (S21).

$$Freq = Amplitude \cdot e^{\frac{-(D_{size}-D_{mean})^2}{2 \cdot SD^2}} \quad \textbf{(S21)}$$

5.5.2. Monomers and polymers

The preparation of monomers (*L*)-**1** and polymers poly-(*L*)-**1** can be found in literature.[59] The preparation of monomer (*D*)-**1** and polymer poly-(*D*)-**1** followed the same synthesis procedures as (*L*)-**1** and poly-(*L*)-**1**.

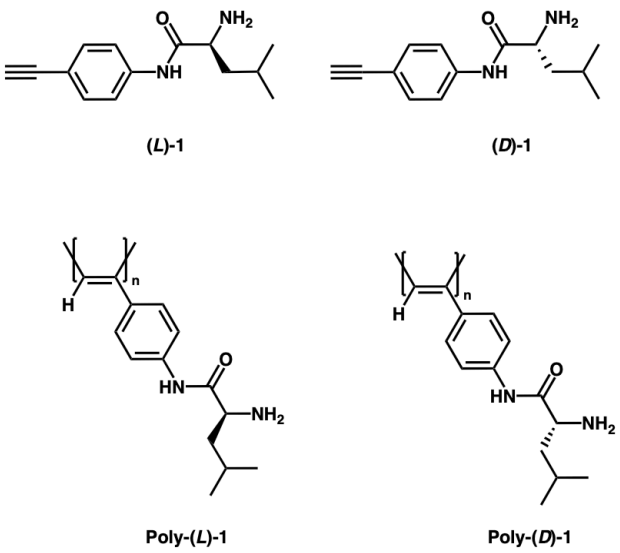
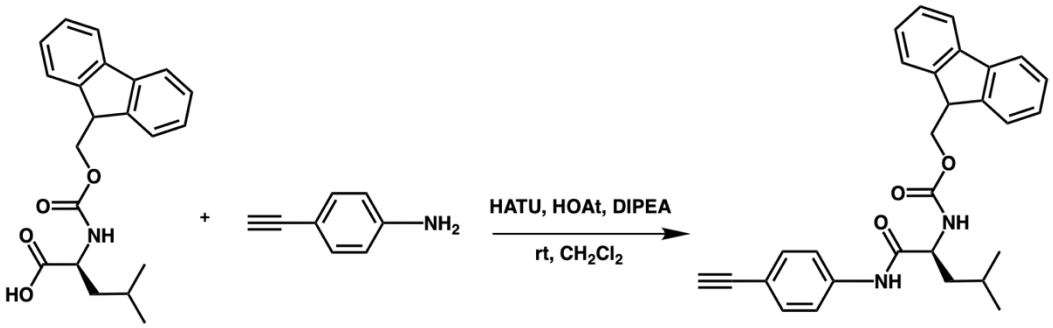


Figure S142. Structures of monomers and Polymers.

5.5.3. Synthetic procedure of intermediate derived from 4-ethynylaniline



2-(7-Aza-1H-benzotriazole-1-yl)-1,1,3,3-tetramethyluronium (0.55 g, HATU, 1.2 equiv.), 1-hydroxy-7-azabenzotriazole (0,19 g, HOAt, 1.2 equiv.), Fmoc-(L)-Leu (0.5 g, 1.2 equiv.) and diisopropylethylamine (DIPEA, 0.5 mL, 1.4 equiv.) were dissolved in 20 mL of dry CH_2Cl_2, and the mixture was stirred for 15 min to activate the acid. Then, 4-ethynylaniline (0.14 g, 1.0 equiv.) was added and the reaction mixture was stirred overnight. Then, the organic layer was washed with HCl 1M and brine. The combined organic layers were dried over anhydride Na_2SO_4, filtered and the solvent was evaporated at reduced pressure. The crude product was chromatographed on silica gel (70-230 mesh) with hexane/ethyl acetate (8/2) as eluent, yields 82% of pure product (0.53 g).

Spectroscopic data:

^{1}H-NMR (300 MHz, $CDCl_3$) δ_H (ppm): 0.89 (m, 6H), 1.68 (m, 3H), 3.03 (s, 1H), 4.10 (m, 1H), 4.32 (m, 3H), 5.83 (m, 1H), 7.17- 7.49 (m, 9H), 7.50-7.73 (m, 3H), 8.95 (s, 1H).

^{13}C-NMR (75 MHz, $CDCl_3$) δ_C (ppm): 21.9, 22.9, 24.7, 40.9, 47.0, 54.4, 67.4, 76.8, 83.4, 113.7,117.8, 119.5, 120.0, 127.1, 127.8, 130.8, 132.8, 138.2, 141.3, 143.4, 156.9, 171.1.

HRMS (ESI) m/z calcd. for $C_{29}H_{28}N_2O_3$ $[M+H]^+$ 453.2173, found 453.2175.

$[\alpha]_D^{20}$ = -24 (c= 15 mg/mL, $CHCl_3$).

USC UNIVERSIDADE DE SANTIAGO DE COMPOSTELA

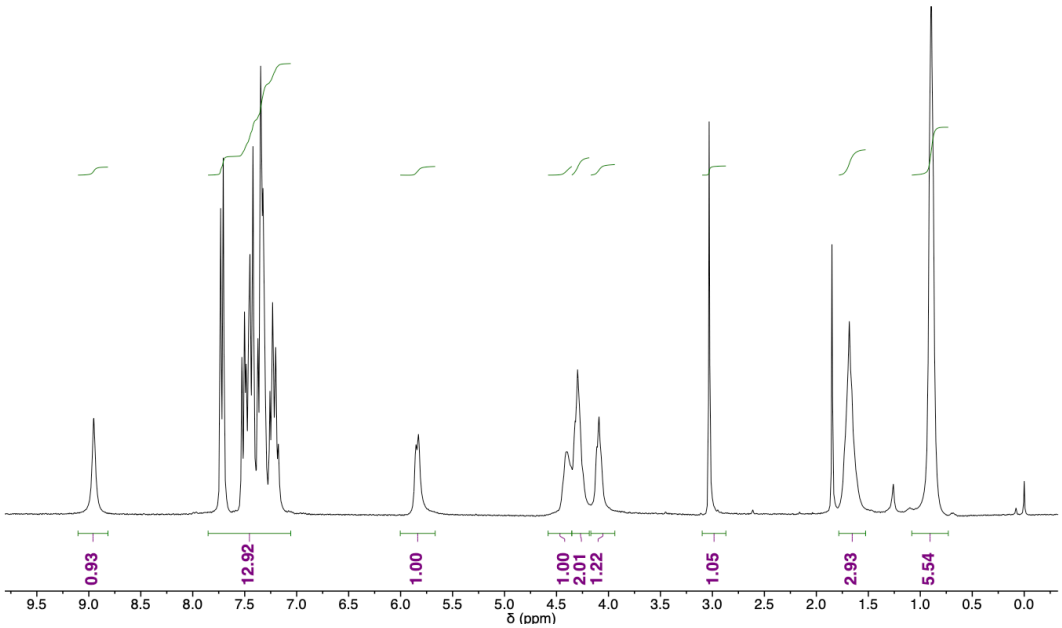


Figure S143. ^{1}H-NMR spectrum of intermediate derived from 4-ethynylaniline ($CDCl_3$, 300 MHz).

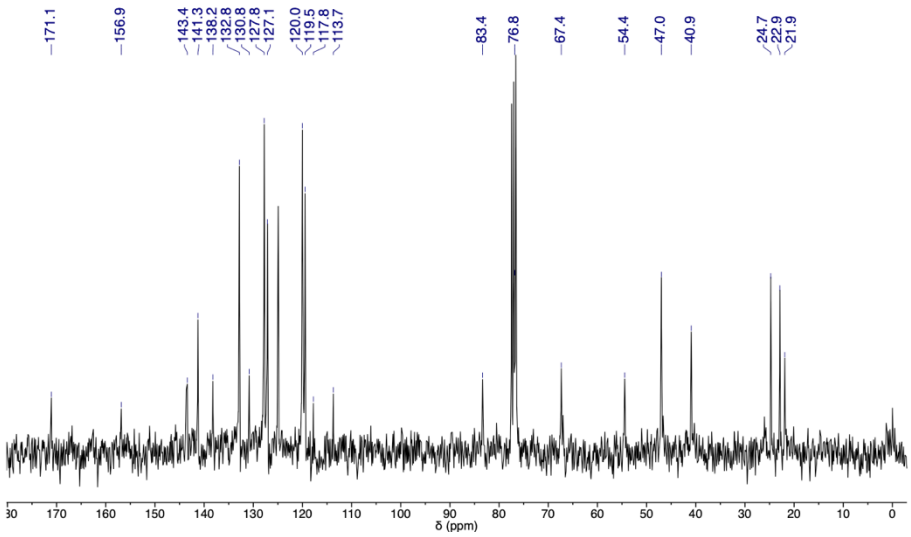
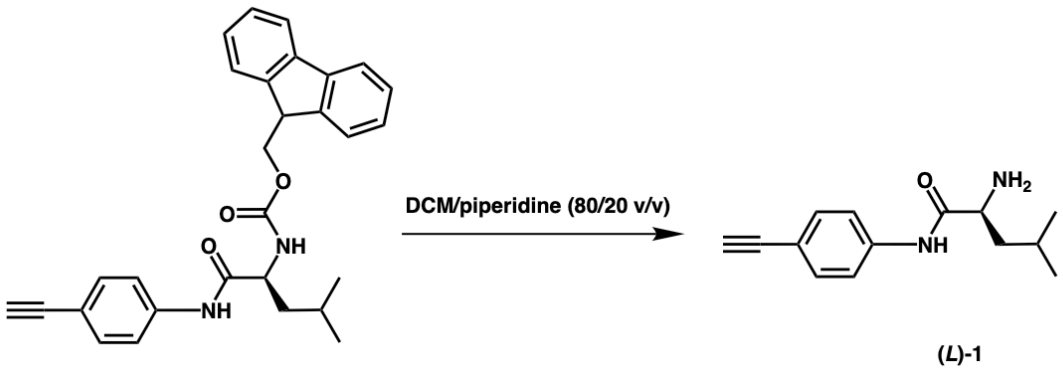


Figure S144. ^{13}C-NMR spectrum of intermediate derived from 4-ethynylaniline ($CDCl_3$, 75 MHz).

USC
UNIVERSIDADE DE SANTIAGO DE COMPOSTELA

5.5.4. Deprotection protocol and synthesis of (*L*)-1



The Fmoc group of the intermediate derived from 4-ethynylaniline was removed in a mixture of DCM/piperidine (80/20 v/v) 20%. The reaction mixture was stirred at room temperature until the reaction ended (1h). After the completion, the crude products were chromatographed on silica gel (70- 230 mesh) with hexane/ethyl acetate (1/1) as eluent, yields 72% of pure product (0.201 g).

Spectroscopic data:

^{1}H-NMR (300 MHz, $CDCl_3$) δ_H (ppm): 0.96 (m, 6H), 1.44 (m, 2H), 1.78 (m, 2H), 2.56 (s, 2H), 3.03 (s, 1H), 3.60 (m, 1H), 7.43 (d, 2H), 7.54 (d, 2H), 9.69 (s, 1H).

^{13}C-NMR (75 MHz, $CDCl_3$) δ_C (ppm): 21.3, 23.4, 24.9, 43.8, 53.9, 76.7, 83.5, 117.2, 118.9, 129.7, 132.8, 138.4, 173.9.

HRMS (ESI) m/z calcd. for $C_{14}H_{18}N_2O$ $[M+H]^+$ 231.1492, found 231.1491.

$[\alpha]_D^{20}$ = -43 (c= 15 mg/mL, $CHCl_3$).

USC UNIVERSIDADE DE SANTIAGO DE COMPOSTELA

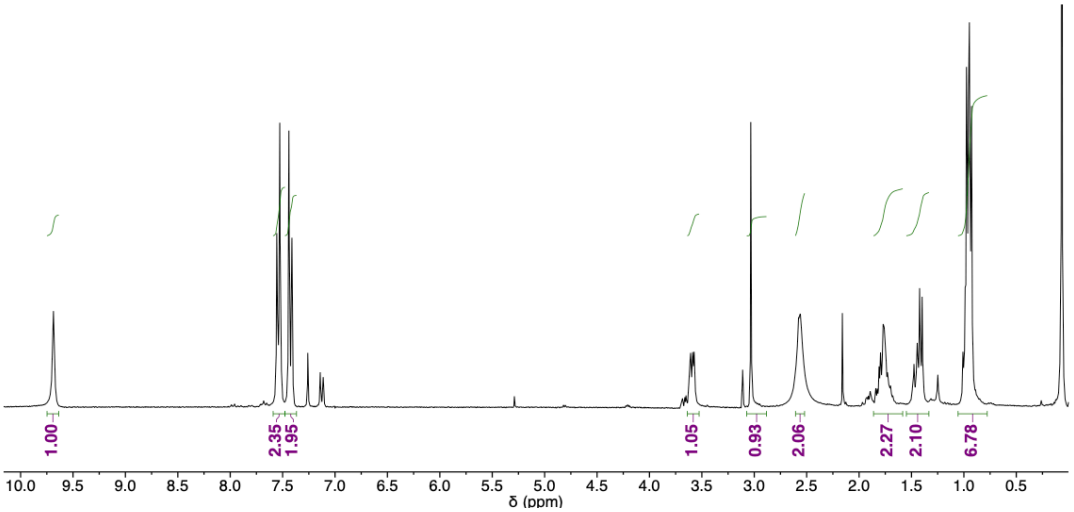


Figure S145. ^{1}H-NMR spectrum of (*L*)-**1** ($CDCl_3$, 300 MHz).

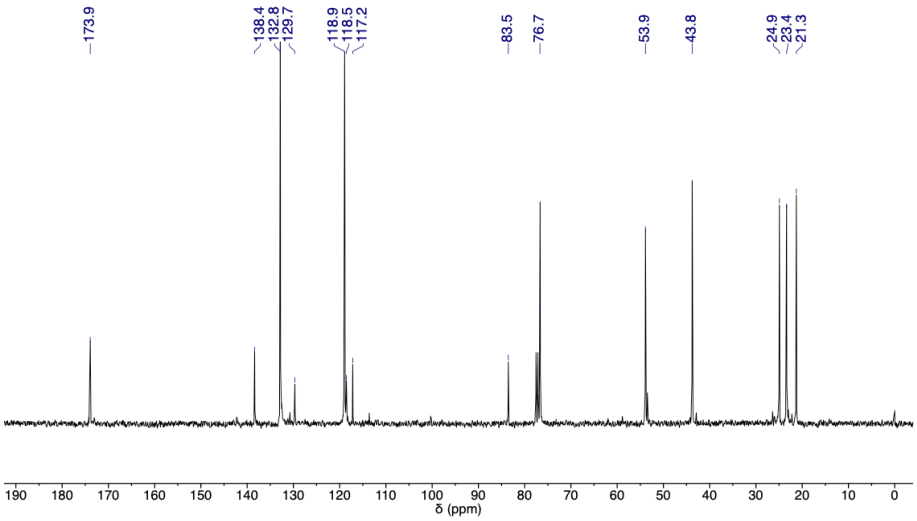


Figure S146. ^{13}C-NMR spectrum of (*L*)-**1** ($CDCl_3$, 75 MHz).

5.5.5. Polymer synthesis

monomer (*L*)-**1** (60 mg) was added as a solid in a flask. Water (459 μL) and HCl (21.5 μL from 11 M, 1.0 eq.) were added in order to protonate the amino group and avoid the catalyst poisoning. Next, a solution of $[Rh(cod)_2]BF_4$ in (0,525 mg) water at r.t. The reaction mixture was stirred at r.t. for 36 h. Next, the resulting polymers were diluted in water and lyophilized. After that, the polymers were dissolved in MeOH and precipitated in large amount of ethyl acetate and centrifuged twice (53.3 mg Poly-(*L*)-**1**), yields 89% of pure product.

USC UNIVERSIDADE DE SANTIAGO

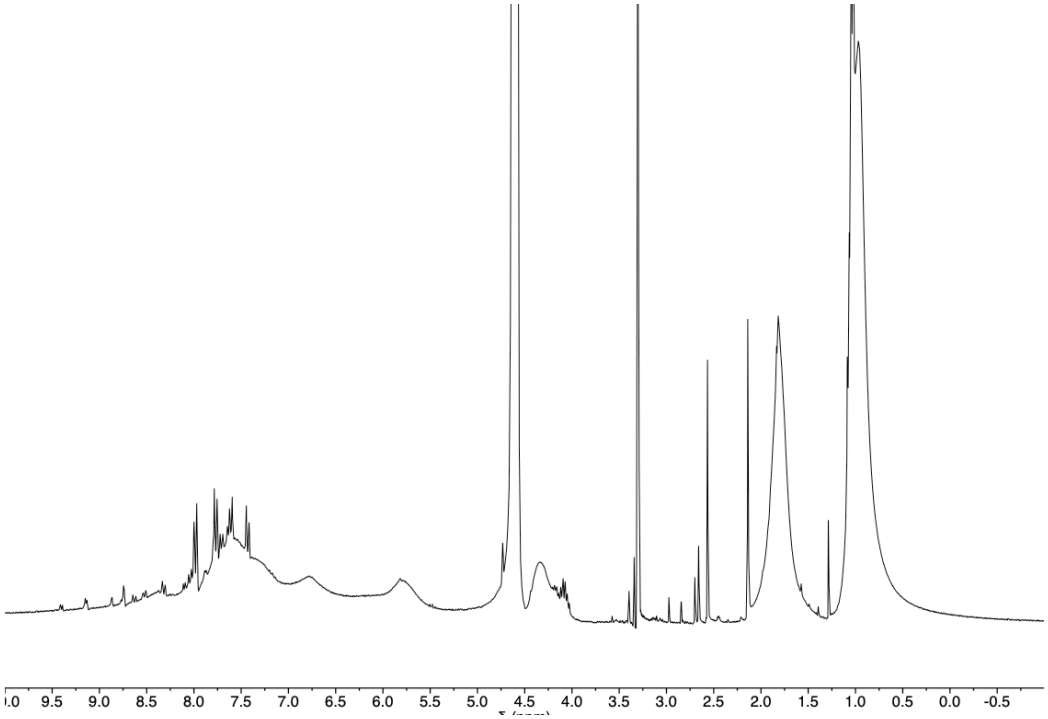


Figure S147. ^{1}H-NMR spectrum of Poly-(*L*)-**1** (methanol-d4, 300 MHz).

Table S26. Regression Parameters and Standard Deviations.

Compound	M_n	M_w	M_p	M_z	Đ
Poly-(*L*)-**1**	67796	217186	236216	330460	3.20

USC UNIVERSIDADE DE SANTIAGO DE COMPOSTELA

5.5.6. CD and UV-Vis of Monomer (*L*)-1 and addition of $AgClO_4$ followed by $NaBH_4$

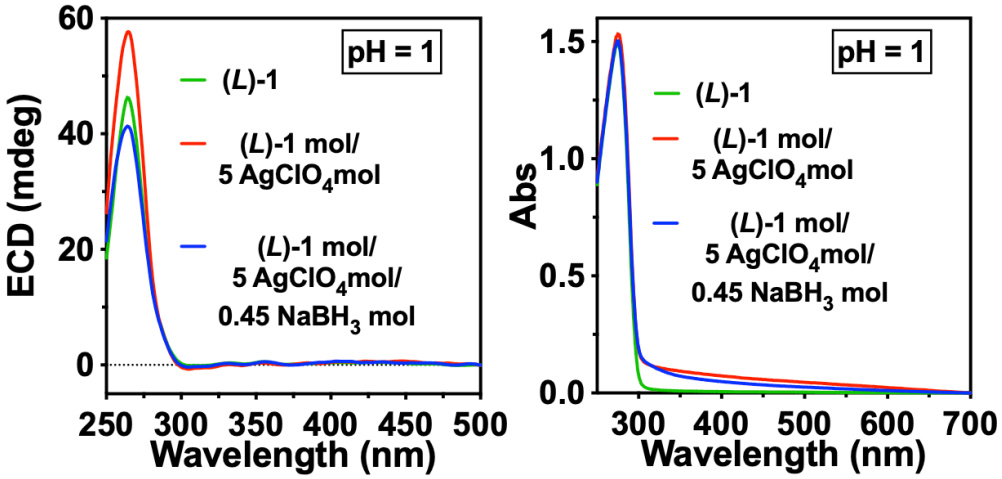


Figure S148. ECD and UV-Vis of (*L*)-**1** at pH = 1 in presence of 5 equivalents of $AgClO_4$ salt (10 mg·mL^{-1} H_2O MQ) and 0.45 equivalents of $NaBH_4$ (10 mg·mL^{-1} H_2O MQ).

5.5.7. Screening of poly-(*L*)-1 at pH = 7 with $AgClO_4$

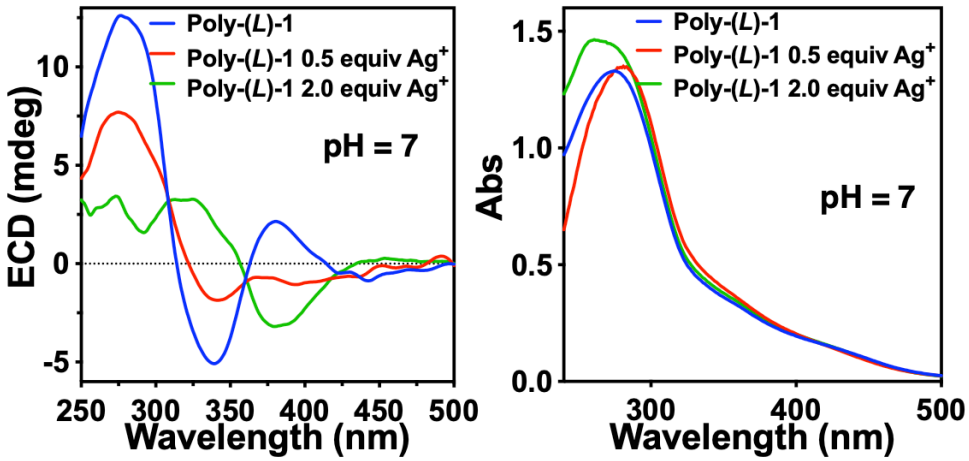


Figure S149. ECD and UV-Vis of poly-(*L*)-**1** (0.3 mg·mL^{-1} H_2O MQ pH = 7) in presence of 0.5 and 2.0 equivalents of $AgClO_4$ (10 mg·mL^{-1} H_2O MQ).

USC UNIVERSIDADE DE SANTIAGO DE COMPOSTELA

5.5.8. ECD and UV-Vis studies of Poly-(*L*/*D*)-1/Ag^+ Complexes and AgNP@Poly-(*L*/*D*)-1 or AgNPs@Poly-(*L*/*D*)-1 nanocomposites

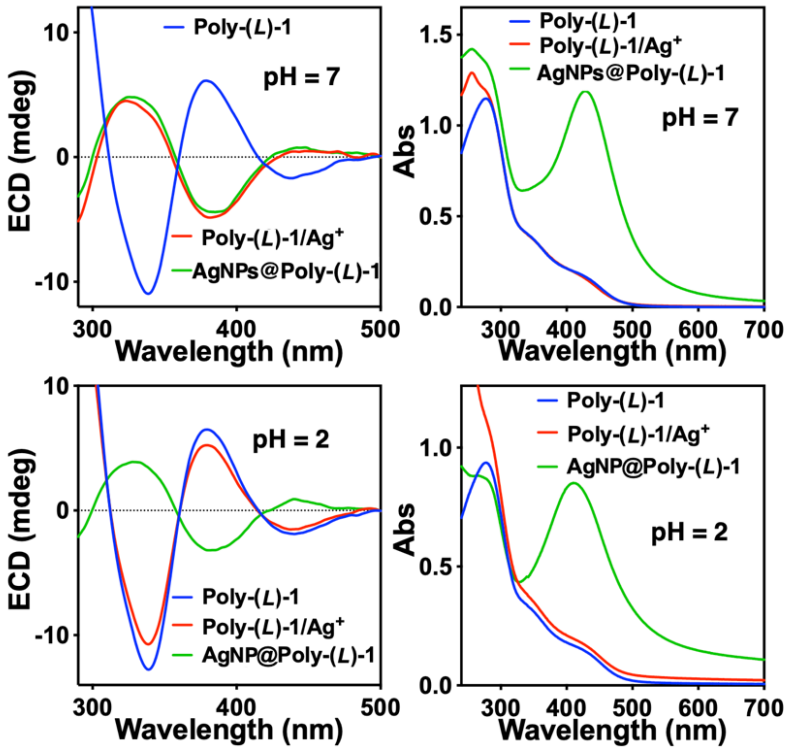


Figure S150. ECD and UV-Vis of poly-(*L*)-**1** (0.3 mg3mL^{-1} H_2O MQ pH = 2 and 7) in presence of 1.5 equivalents of $AgClO_4$ (10 mg·mL^{-1} H_2O MQ) and after the reduction with 0.45 equivalents of $NaBH_4$ (0.5 mg·mL^{-1} H_2O MQ).

USC UNIVERSIDADE DE SANTIAGO DE COMPOSTELA

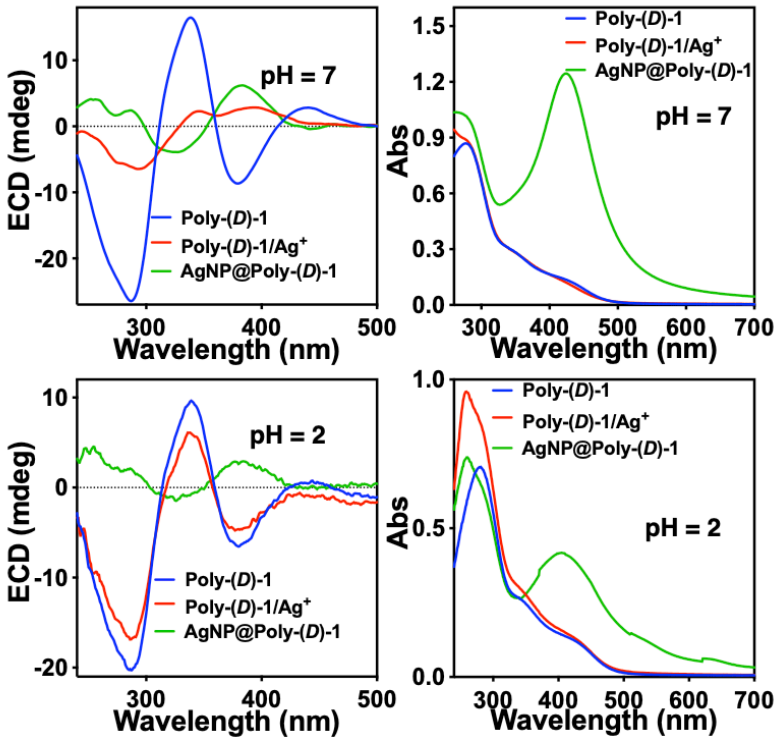


Figure S151. CD and UV-Vis of poly-(*D*)-**1** (0.3 mg·mL^{-1} H_2O MQ pH = 2 and 7) in presence of 1.5 equivalents of $AgClO_4$ (10 mg·mL^{-1} H_2O MQ) and after the reduction with 0.45 equivalents of $NaBH_4$ (0.5 mg·mL^{-1} H_2O MQ).

5.5.9. Synthesis of AgNP@Poly-(*L*)-1 with more equivalents of $AgClO_4$

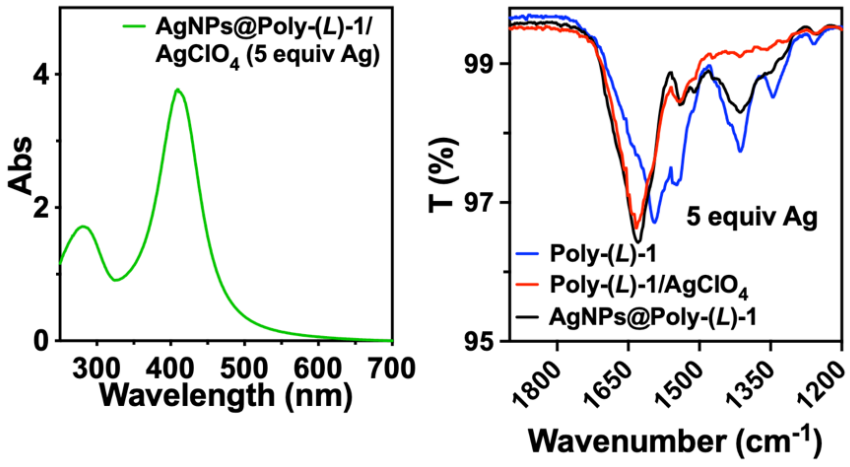


Figure S152. UV-Vis and FT-IR of Poly-(*L*)-**1** in presence of 5 equivalents of $AgClO_4$ salt (10 mg·mL^{-1} H_2O MQ) and 0.45 equivalents of $NaBH_4$ (10 mg·mL^{-1} H_2O MQ).

USC UNIVERSIDADE DE SANTIAGO DE COMPOSTELA

5.5.10. Thermal, Time and Photo Stability studies of Poly-(*L*)-1 and AgNPs@Poly-(*L*)-1

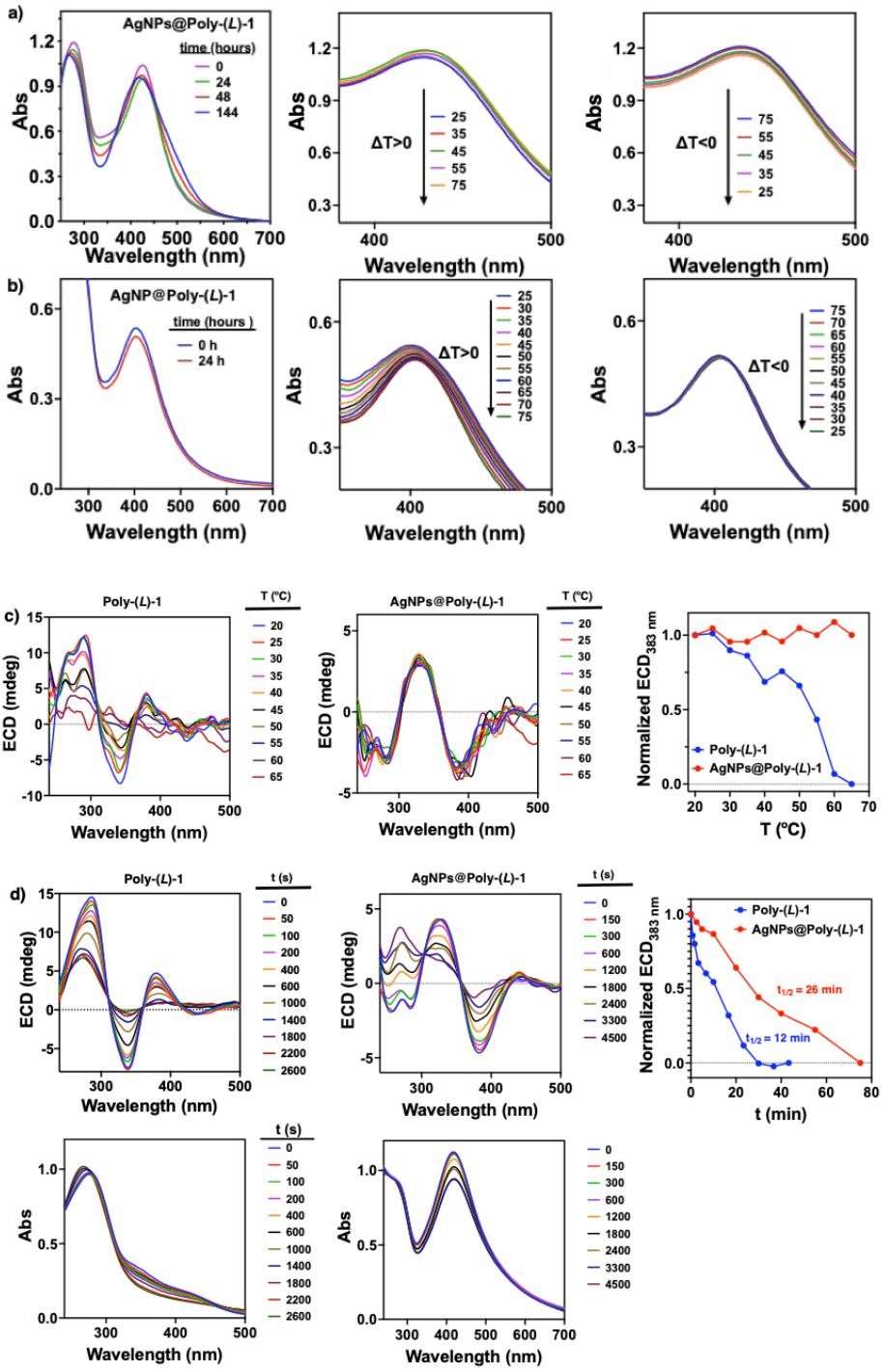


Figure S153. UV-Vis of (a) AgNPs@Poly-(*L*)-**1** prepared at pH=7 (b) AgNP@Poly-(*L*)-**1** prepared at pH=2 evolution by Time and Temperature (increase and decrease at 0.5 K·min^{-1}). (c) VT-ECD studies of Poly-(*L*)-**1** and AgNPs@Poly-(*L*)-**1** prepared at pH=7 (increase and decrease at 0.5 K·min^{-1}). (d) ECD and UV-Vis spectra of Poly-(*L*)-**1** and AgNPs@Poly-(*L*)-**1** under light irradiation with time. (d) ECD and UV-Vis studies of Poly-(*L*)-**1** and AgNPs@Poly-(*L*)-**1** prepared at pH=7) at different irradiation times under visible light.

USC
DE COMPOSTELA

5.5.11. ECD and UV-Vis studies of the oxidation of AgNP@Poly-(*L*)-1 with $Fe(ClO_4)_3$, $Hg(ClO_4)_2$, and $Ce(SO_4)_2$

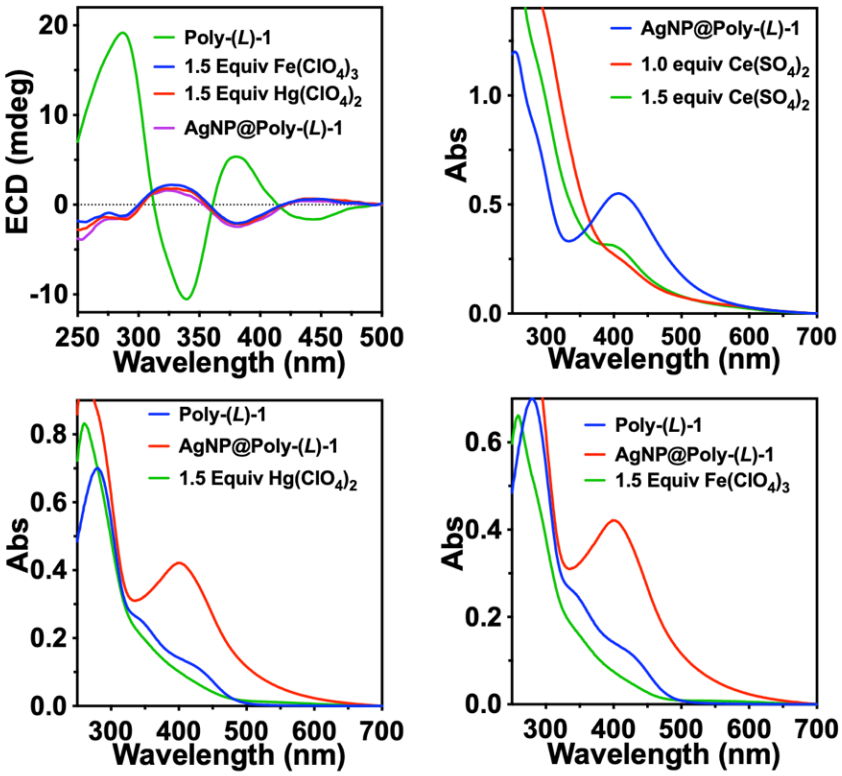


Figure S154. ECD and UV-Vis of AgNP@Poly-(*L*)-**1** in presence of $Fe(ClO_4)_3$, $Hg(ClO_4)_2$, $Ce(SO_4)_2$ (10 mg·mL^{-1} H_2O MQ).

USC UNIVERSIDADE DE SANTIAGO DE COMPOSTELA

5.5.12. ECD, UV-Vis and DLS studies of the oxidation of AgNPs@Poly-(*L*)-1 with $Fe(ClO_4)_3$, $Hg(ClO_4)_2$, and $Ce(SO_4)_2$

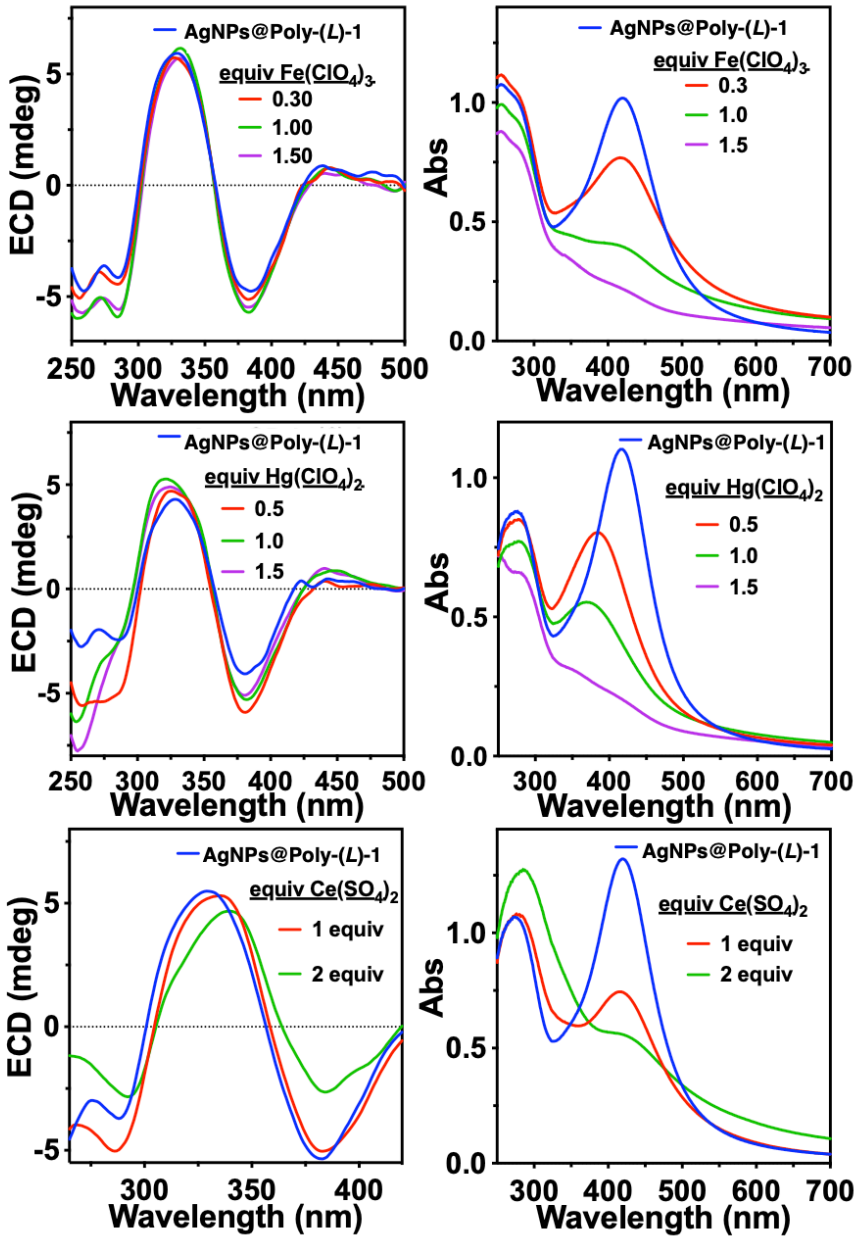


Figure S155. ECD and UV-Vis of AgNPs@Poly-(*L*)-**1** in presence of $Fe(ClO_4)_3$, $Hg(ClO_4)_2$, $Ce(SO_4)_2$ (10 mg·mL^{-1} H_2O MQ).

USC UNIVERSIDADE DE SANTIAGO DE COMPOSTELA

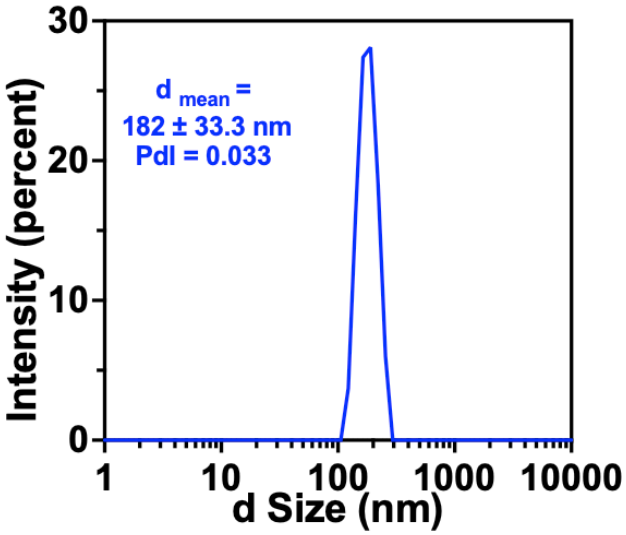


Figure S156. DLS of the obtained HPMC of AgNPs@Poly-(*L*)-**1** after the oxidation with $Fe(ClO_4)_3$ (10 mg·mL^{-1} H_2O MQ).

5.5.13. ECD and UV-Vis studies of AgNPs@Poly-(*L*)-1 in the presence of ultrapure $FeCl_2$ and not ultrapure $Fe(ClO_4)_2$

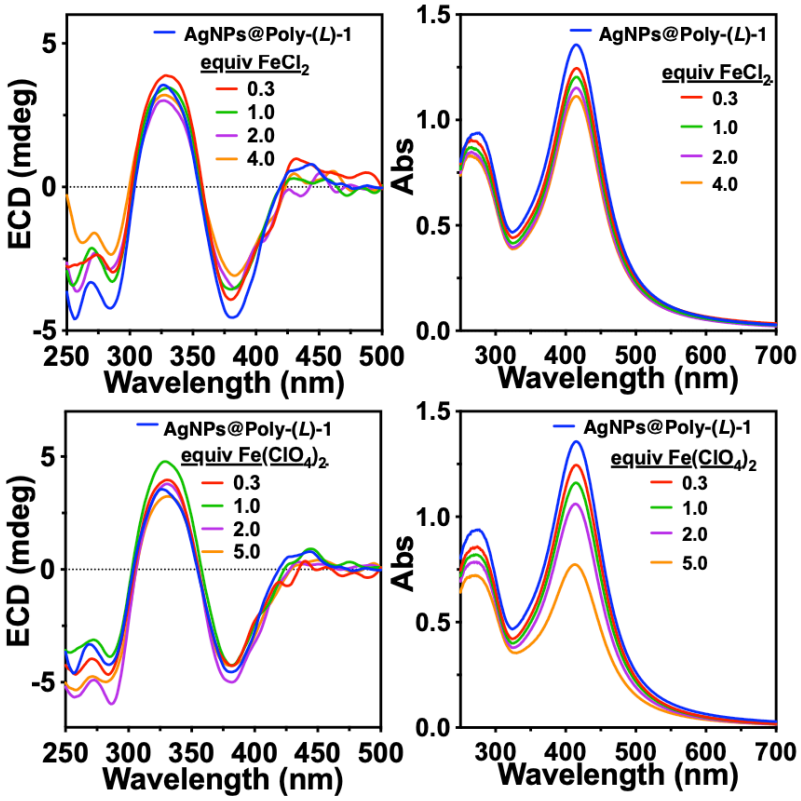


Figure S157. ECD and UV-Vis of AgNPs@Poly-(*L*)-**1** in presence of oxidated $Fe(ClO_4)_2$ and ultrapure $FeCl_2$ (10 mg·mL^{-1} H_2O MQ).

5.5.14. ECD and UV-Vis studies of AgNPs@Poly-(*L*)-1 in the presence of salts

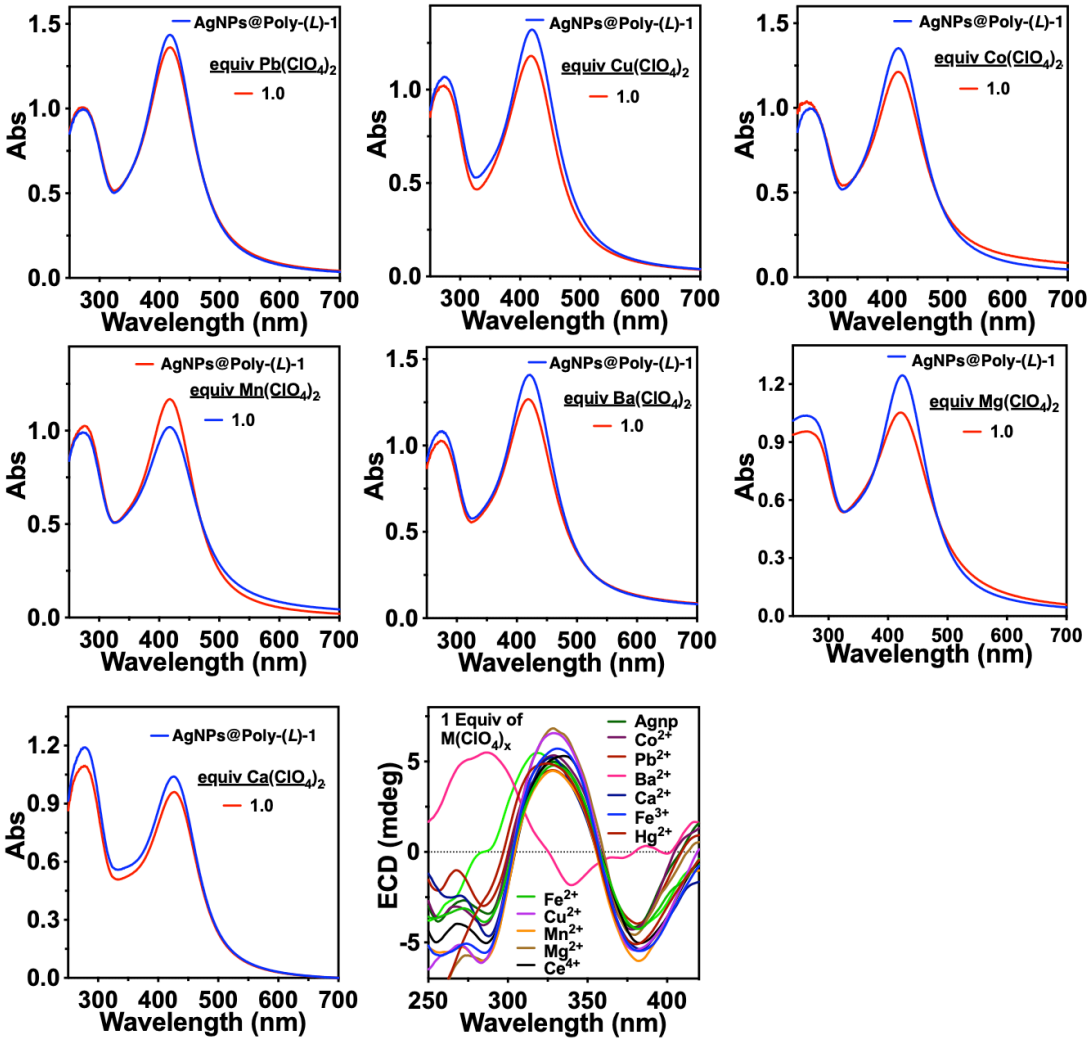


Figure S158. UV-Vis of AgNPs@Poly-(*L*)-**1** in presence of 1 equivalent of $M(ClO_4)_2$ salts (10 mg·mL^{-1} H_2O MQ). ECD of AgNPs@Poly-(*L*)-**1** in presence of 1 equivalent of $M(ClO_4)_n$ and $Ce(SO_4)_2$ salts (10 mg·mL^{-1} H_2O MQ).

5.5.15. ECD study of Poly-(*L*)-1 interaction with $Ba(ClO_4)_2$

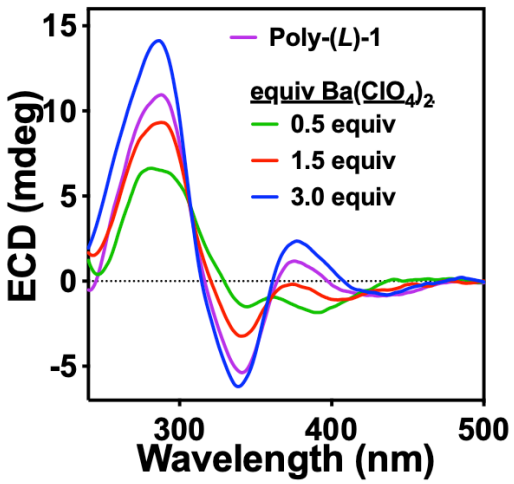


Figure S159. ECD of Poly-(*L*)-**1** in presence of $Ba(ClO_4)_2$ (10 mg·mL^{-1} H_2O MQ).

5.5.16. Chiroptical study of AgNPs@Poly-(*L*)-1 and of AgNP@Poly-(*L*)-1 nanocomposites in the presence of divalent perchlorate salts

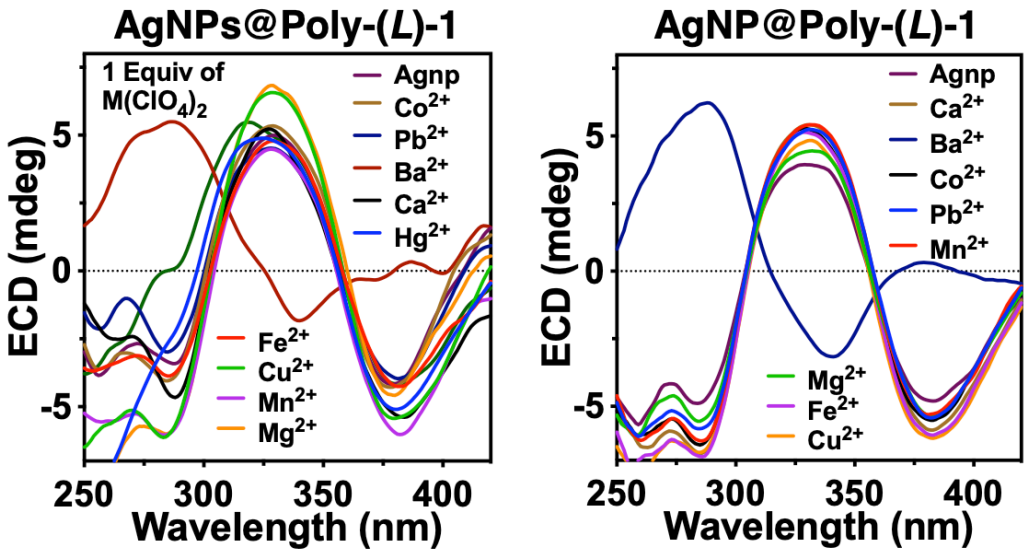


Figure S160. ECD of the nanocomposites AgNPs@Poly-(*L*)-**1** and AgNP@Poly-(*L*)-**1** in presence of $M(ClO_4)_2$ (10 mg·mL^{-1} H_2O MQ).

USC UNIVERSIDADE DE SANTIAGO DE COMPOSTELA

5.5.17. UV-Vis of the nanocomposites after basification

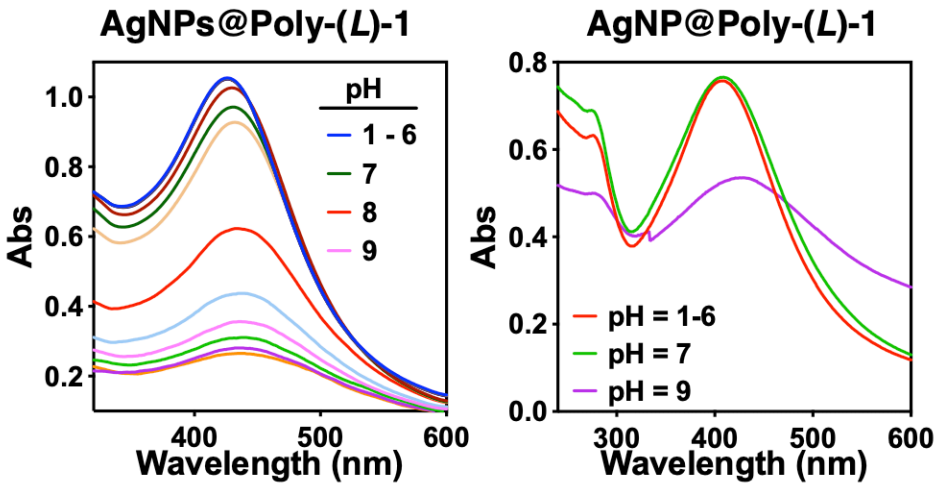


Figure S161. UV-Vis of the nanocomposites AgNPs@Poly-(*L*)-**1** and AgNP@Poly-(*L*)-**1** at different pH (basifying with NaOH 1M). NaOH 1M added in AgNP(s)@Poly-(*L*)-**1** with a microfluidic equipment.

5.5.18. UV-Vis and DLS of the nanocomposite following cycles of basification and acidification

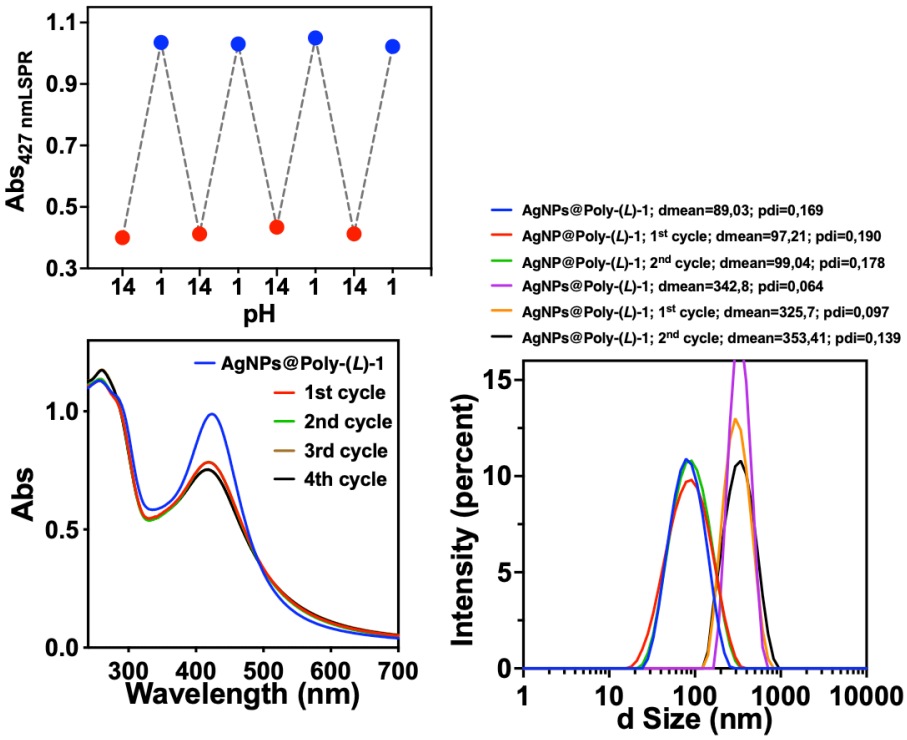


Figure S162. UV-Vis of nanocomposites AgNPs@Poly-(*L*)-**1** and DLS of the nanocomposites AgNP(s)@Poly-(*L*)-**1** after precipitation by basification with NaOH 1M followed by acidification with HCl 1M to pH = 1.

5.5.19. Poly-(*L*)-1 at different pH

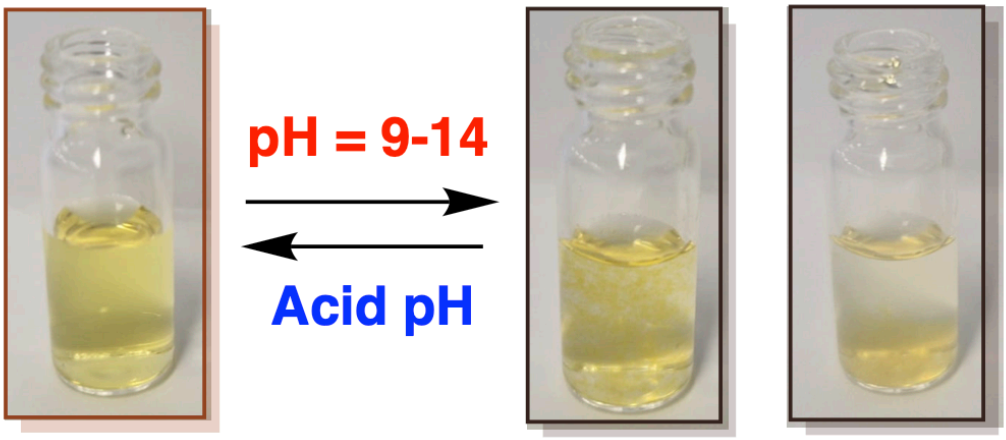


Figure S163. Precipitation of Poly-(*L*)-**1** at basic pH, and recovery after acidification.

5.5.20. Scanning electron microscopy images of Poly-(*L*)-1/$AgClO_4$ pH = 7

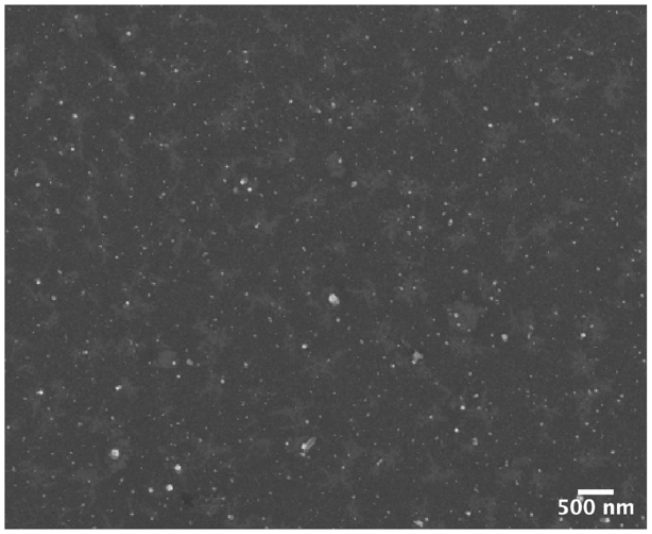


Figure S164. Scanning electron microscopy images of Poly-(*L*)-**1**/$AgClO_4$ (1/1.5 mol/mol) HPMC.

USC UNIVERSIDADE DE SANTIAGO DE COMPOSTELA

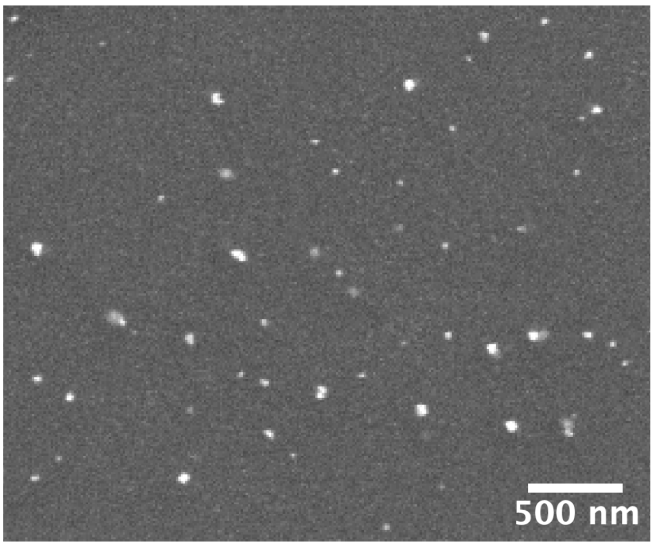


Figure S165. Scanning electron microscopy images of Poly-(*L*)-**1**/$AgClO_4$ (1/1.5 mol/mol) HPMC.

5.5.21. Scanning electron microscopy images of AgNP@Poly-(*L*)-1 synthetized at pH = 2

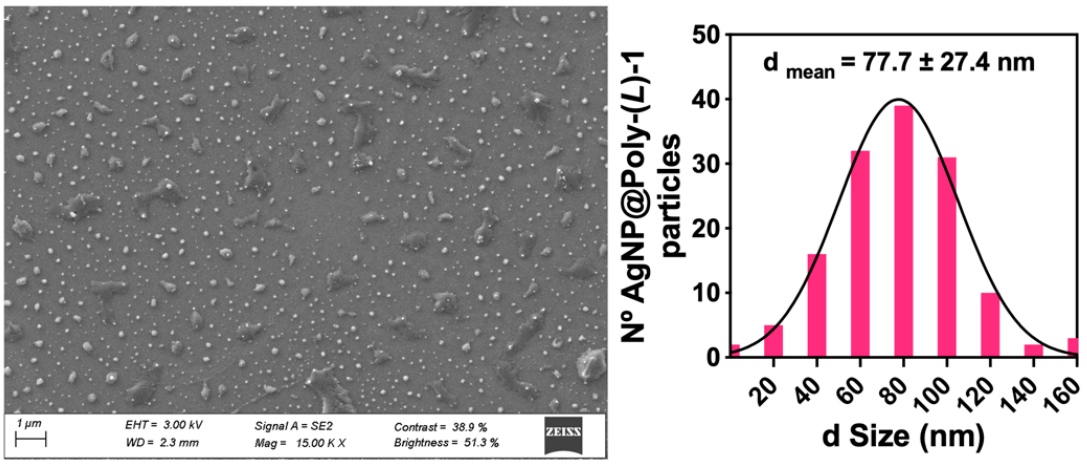


Figure S166. Scanning electron microscopy images of AgNP@Poly-(*L*)-**1** nanocomposite used for the gaussian size distribution nanocomposites synthetized at pH = 2 (140 nanocomposites measured).

USC UNIVERSIDADE DE SANTIAGO DE COMPOSTELA

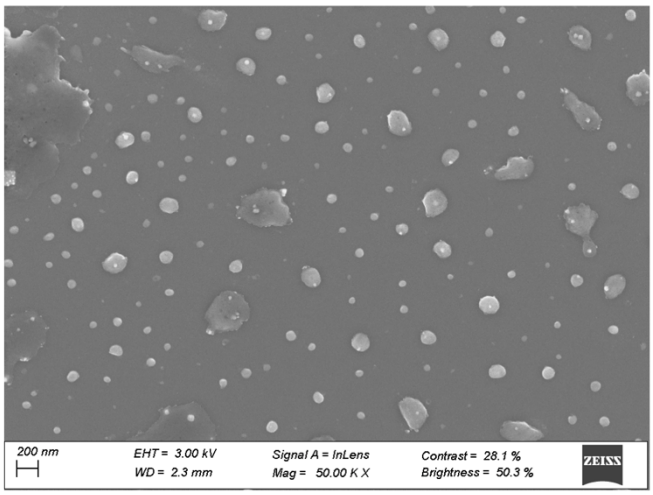


Figure S167. Scanning electron microscopy images of AgNP@Poly-(*L*)-**1** nanocomposite synthetized at pH = 2.

5.5.22. Transmission electron microscopy images of AgNP@ Poly-(*L*)-1 synthetized at pH = 2

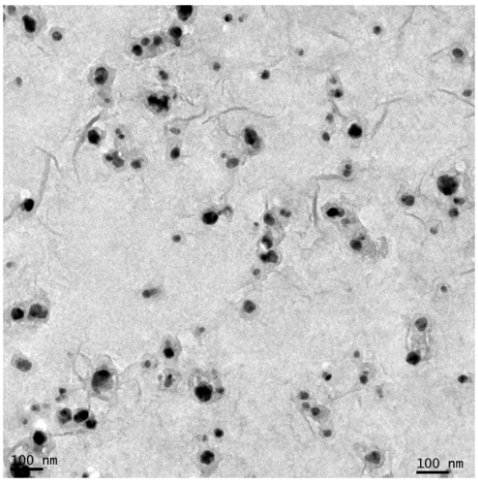


Figure S168. Transmission electron microscopy images of AgNP@Poly-(*L*)-**1** nanocomposite synthetized at pH = 2 used for the gaussian size distribution of the AgNPs (50 AgNPs measured).

USC
UNIVERSIDADE DE SANTIAGO DE COMPOSTELA

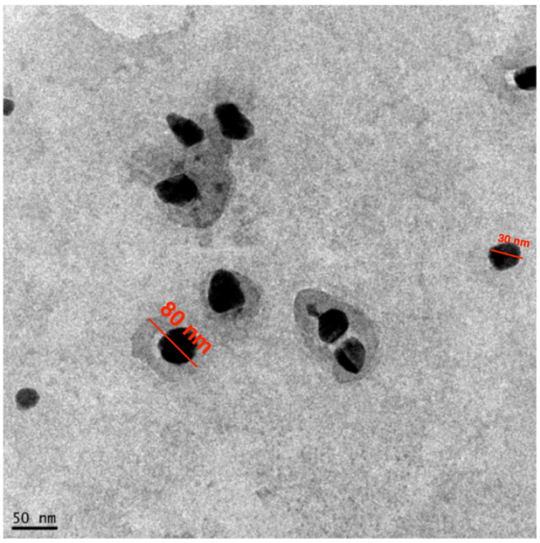


Figure S169. Transmission electron microscopy images of AgNP@Poly-(*L*)-**1** nanocomposite synthetized at pH = 2.

5.5.23. Scanning electron microscopy images of AgNPs@ Poly-(*L*)-1 synthetized at pH = 7

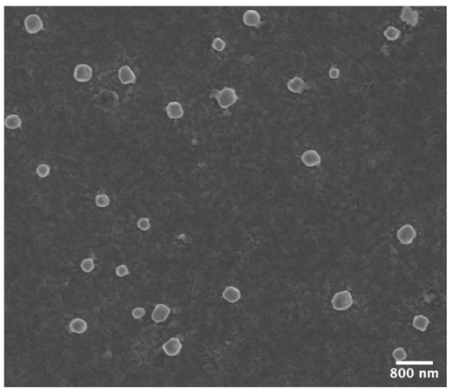


Figure S170. Scanning electron microscopy images of AgNPs@Poly-(*L*)-**1** nanocomposite synthetized at pH = 7.

USC UNIVERSIDADE DE SANTIAGO DE COMPOSTELA

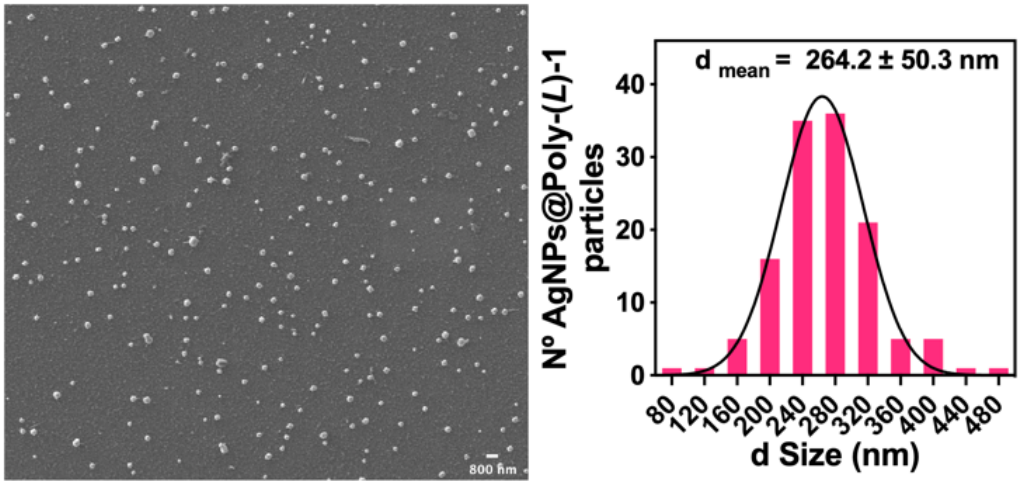


Figure S171. Scanning electron microscopy images of AgNPs@Poly-(*L*)-**1** nanocomposite synthetized at pH = 7 used for the gaussian size distribution of the nanocomposites (140 nanocomposites measured).

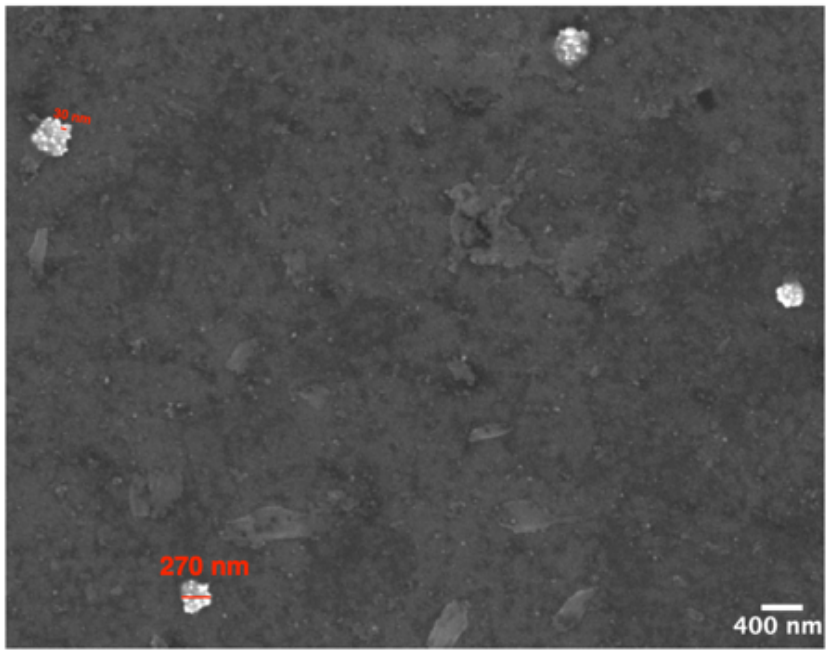


Figure S172. Scanning electron microscopy images of AgNPs@Poly-(*L*)-**1** nanocomposite synthetized at pH = 7.

USC
UNIVERSIDADE DE SANTIAGO DE COMPOSTELA

5.5.24. Scanning electron microscopy images of Poly-(L)-1/AgClO4 pH = 7

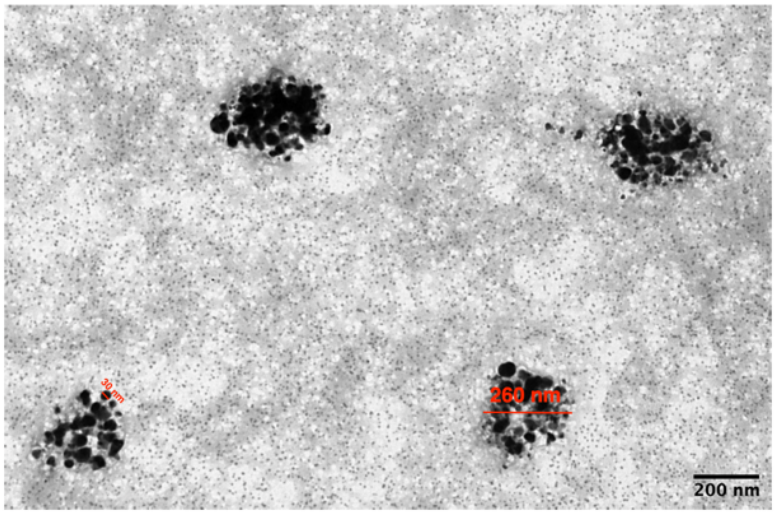


Figure S173. Transmission electron microscopy images of AgNPS@Poly-(*L*)-**1** nanocomposite synthetized at pH = 7 used for the gaussian size distribution of the AgNPs (100 AgNPs measured).

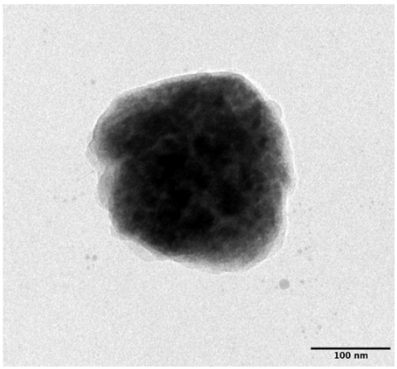


Figure S174. Transmission electron microscopy images of AgNPs@Poly-(*L*)-**1** nanocomposite synthetized at pH = 7.

USC UNIVERSIDADE DE SANTIAGO DE COMPOSTELA

5.5.25. Scanning electron microscopy images of AgNPs@ Poly-(*L*)-1 synthetized at pH = 7 before after precipitation with NaOH 1M and recovery with HCl 1M

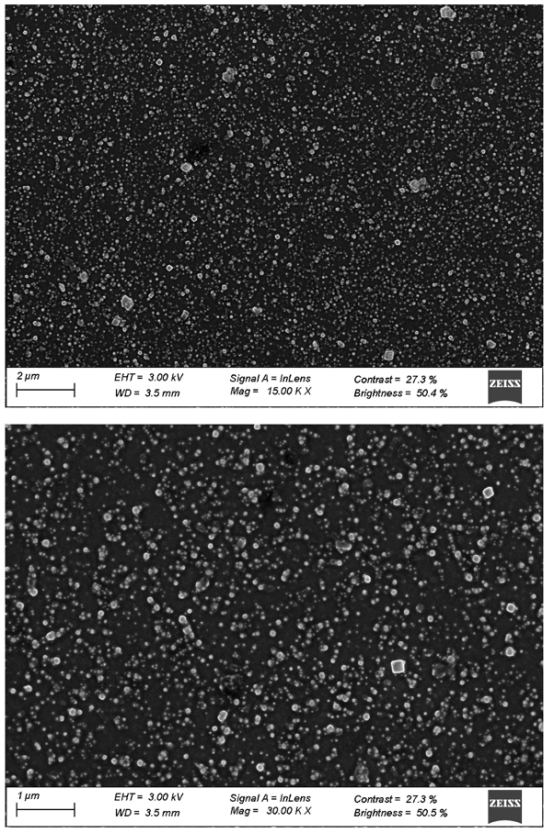


Figure S175. Scanning electron microscopy images of AgNPs@Poly-(*L*)-**1** nanocomposite synthetized at pH = 7 before precipitation with NaOH 1M.

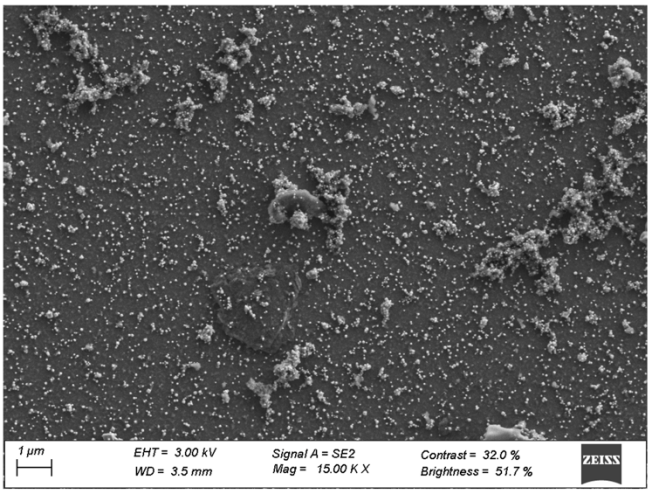


Figure S176. Scanning electron microscopy images of AgNPs@Poly-(*L*)-**1** nanocomposite synthetized at pH = 7 after precipitation with NaOH 1M and redispersion with HCl 1M two times.

USC UNIVERSIDADE DE SANTIAGO DE COMPOSTELA

5.5.26. Scanning electron microscopy images of AgNP@ Poly-(*L*)-1 synthetized at pH = 2 before after precipitation with NaOH 1M and recovery with HCl 1M

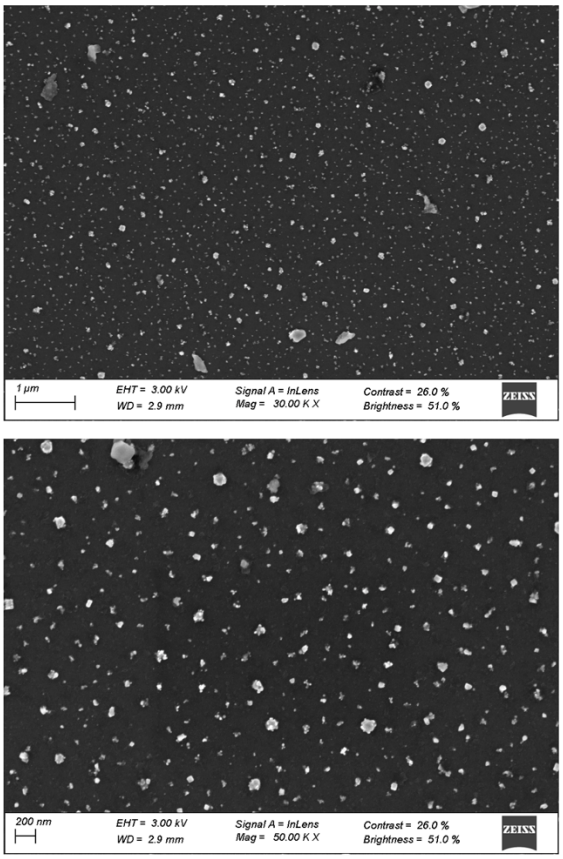


Figure S177. Scanning electron microscopy images of AgNP@Poly-(*L*)-**1** nanocomposite synthetized at pH = 2 before precipitation with NaOH 1M.

USC UNIVERSIDADE DE SANTIAGO DE COMPOSTELA

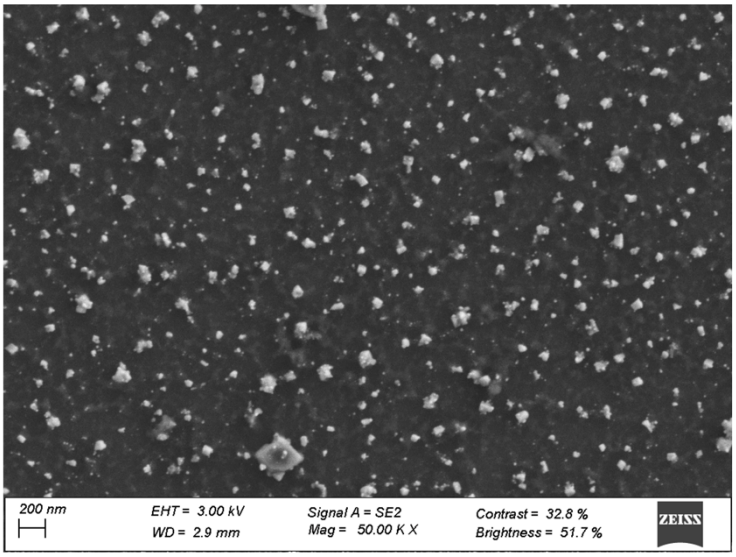


Figure S178. Scanning electron microscopy images of AgNP@Poly-(*L*)-**1** nanocomposite synthetized at pH = 2 after precipitation with NaOH 1M and redispersion with HCl 1M two times.

USC
UNIVERSIDADE DE SANTIAGO DE COMPOSTELA

5.5.27. UV-Vis and TEM studies of AgNP@Poly-(*L*)-1 nanocomposite prepared (a) at pH = 7 and measured at pH = 2 (b) prepared at pH = 2 and measured at pH = 7

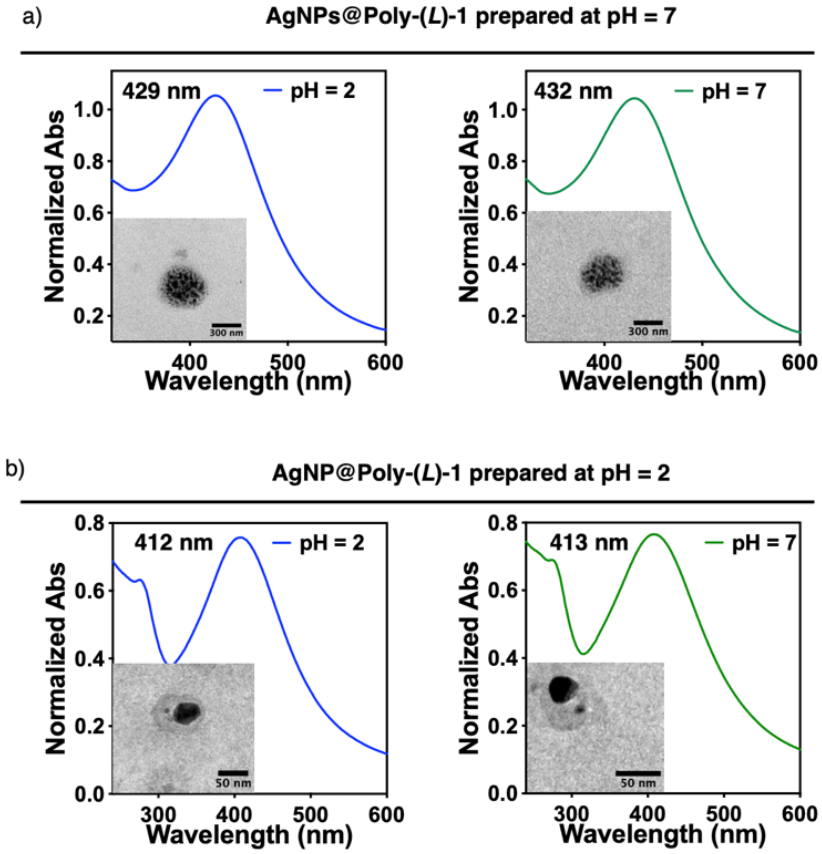


Figure S179. UV-Vis spectra and TEM images of AgNP@Poly-(*L*)-**1** nanocomposite (a) synthetized at pH = 7 and measured at pH = 2 and (b) prepared at pH = 2 and measured at pH = 7.

5.5.28. Calculation of the limits of detection

To confirm the mechanism described, DFT calculations were performed with Gaussian 16 Rec.01c.[413] The optimization and frequency calculations were performed in the monomer (*L*)-**1** using the method set B3LYP[415] with a modification to add a grimme Dispersion 3[551] and the basis set 6-311+g(d,p)[127] for H,C,O, and N and cc-pVDZ-PP[552] for silver[553] obtained from Basis Set Exchange (BSE)[554] in a polarizable continuum model (PCM) of water. The Free energies (G) of (*L*)-**1**, (*L*)-**1**/Ag^{+} and (L)-1/Ag^{0}_{7} with different conformations are compilated in the Table S27. The possible coordination mechanisms or pathways with the Free energy difference are represented in Figure S180 and Figure

S183. The interaction with silver cation and Ag_0^7 that represents the facet of AgNP was followed by the electron localization function (ELF) and Non-Covalent Interaction (NCI) analysis of the checkfile from gaussian using Multiwfn.[420] The NCI represents with blue color the strong interactions, red color for repulsion and green color for VdW (Figure S181 and Figure S182).

Table S27. Free energies of the optimized molecules used to calculate the Free Energy difference (B3LYP-D3 with 6-311+g(d,p) for H,C,O, and N and cc-pVDZ-PP for silver). The most stable structures are underlined.

Compound	G (kcal/mol)
Ag^+	92150.26754
Cl^-	288919.7102
Ag^0_7 (111)	645811.8223
<u>(*L*)-1-NH_2 *ap*</u>	-457461.8779
(*L*)-1-NH_2 *sp*	-457457.6724
<u>(*L*)-1-$NH_3^+Cl^-$ *ap*</u>	-746649,5965
(*L*)-1-$NH_3^+Cl^-$ *sp*	-746510,1798
<u>(*L*)-1-NH_2 *sp* BiChelate C=O···Ag^+···NH_2</u>	-549622.0129
(*L*)-1-NH_2 *sp* MonoChelate O=C—HN···Ag^+	-549605,0403
(*L*)-1-NH_2 *ap* BiChelate H_2N···Ag^+···NH—C=O	-549619,9032
(*L*)-1-NH_2 *ap* MonoChelate C=O ···Ag^+	-549617,2815
<u>(*L*)-1-NH_3^+···Ag^0_7 *sp*</u>	-1103555,133
(*L*)-1-NH_3^+···Ag^0_7 *ap*	-1103549,017
(*L*)-1-NH_2···Ag^0_7 *sp*	-1103278,29
<u>(*L*)-1-NH_2···Ag^0_7 *ap*</u>	-1103280,638

USC UNIVERSIDADE DE SANTIAGO DE COMPOSTELA

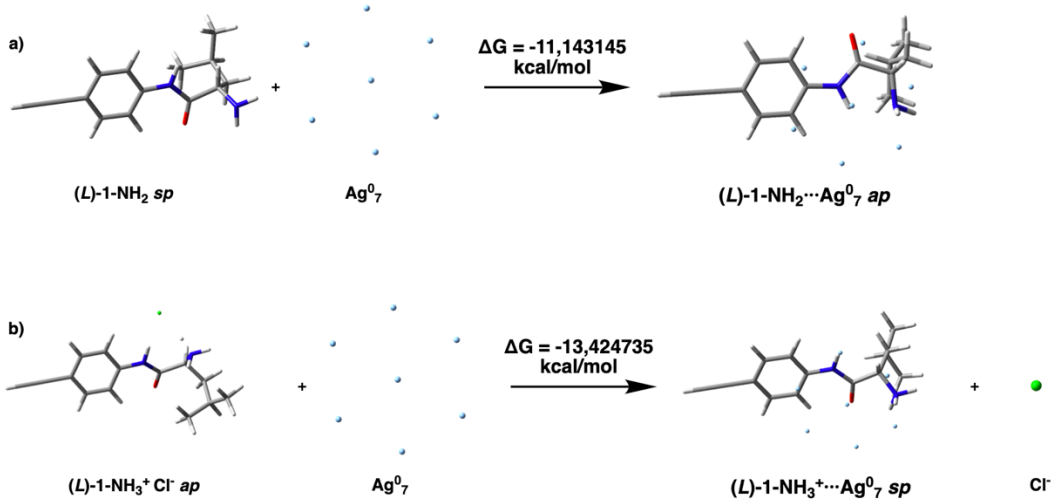


Figure S180. Free Energy difference and optimized geometries (B3LYP-D3 with 6-311+g(d,p) for H,C,O, and N and cc-pVDZ-PP for silver) of (a) (*L*)-**1**-NH_2 in *sp* conformation, Ag^0_7 and (*L*)-**1**-NH_2---Ag^0_7 in *ap* conformation (b) (*S*)-**1**-$NH_3^+Cl^-$ in *ap* conformation, Ag^0_7, (*L*)-**1**-NH_3^+---Ag^0_7 in *ap* conformation and Cl^-.

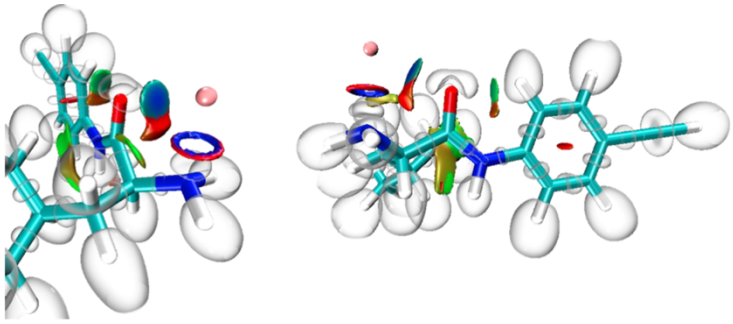


Figure S181. NCI and ELF representation of the Ag cation interacting with the carbonyl and the free electron pair of NH_2 in (*L*)-**1**-NH_2 in *sp* conformation.

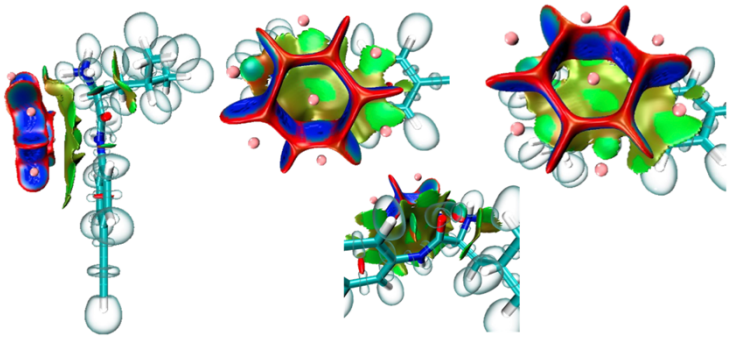


Figure S182. NCI and ELF representation of the Ag^0_7 facet of a AgNP interacting with the carbonyl and a proton of NH_3^+ in (*L*)-**1**-NH_3^+ in *sp* conformation.

USC UNIVERSIDADE DE SANTIAGO DE COMPOSTELA

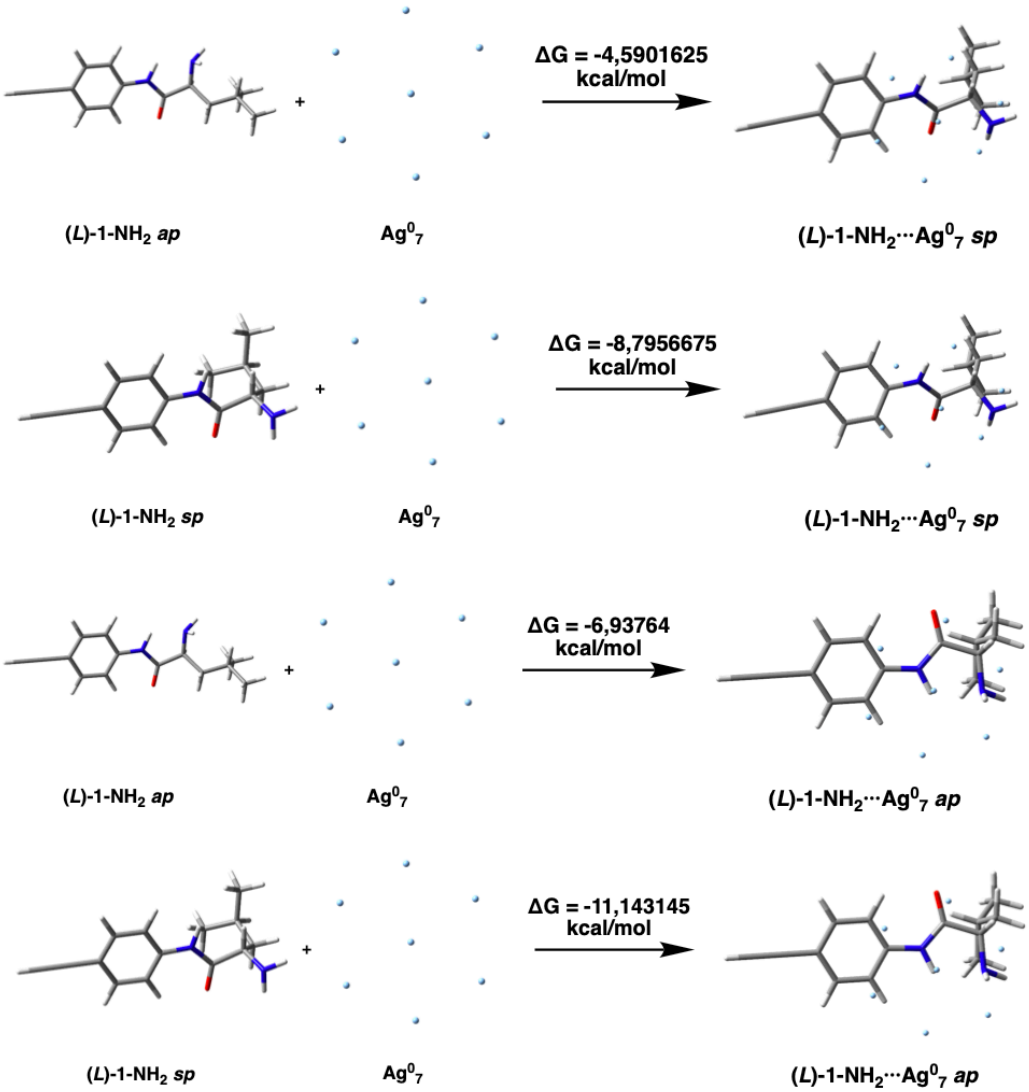


Figure S183. Optimized geometries (B3LYP-D3 with 6-311+g(d,p) for H,C,O, and N and cc-pVDZ-PP for silver) and alternative proposed mechanisms that are less likely to occur due to smaller Free energy difference.

USC UNIVERSIDADE DE SANTIAGO DE COMPOSTELA

5.6. Experimental Section and Methodology Chapter 3.6.

5.6.1. Materials and methods

Chemicals. Commercially available chemicals have been used as delivered. Solvents were purchased as reagent grade and distilled if necessary. Anhydrous solvents were either purchased as ultra-dry solvent from Acros Organics® or received from solvent purification system. For the coupling and polymerization reactions, dry THF was obtained from MBRAUN SPS 800 solvent purification system. Water was purified by Millipore water purification system. Coupling reagents (2-(7-Aza-1H-benzotriazole-1-yl)-1,1,3,3-tetramethyluronium hexafluorophosphate) (HATU), 4-ethynylbenzoic acid, 3-ethynylbezoic acid, 4-ethynylaniline, 3-ethynylaniline and 2-ethynylaniline were purchased from AnaSpec Inc. (*S*)-α-methoxy-α-trifluoromethylphenylacetic acid, (*R*)-α-methoxyphenylacetic acid, oxalyl chloride, 1-Ethyl-3-(3-dimethylaminopropyl)carbodiimide (EDC), hydroxybenzotriazole (HOBt), (L)-alanine methyl ester hydrochloride, (*L*)-valine methyl ester hydrochloride, (*L*)-isoleucine methyl ester hydrochloride, (*L*)-leucine methyl ester hydrochloride, rhodium norbornadiene chloride dimer [Rh(nbd)Cl]2, diisopropyltriethylamine (DIPEA), potassium hydroxide (KOH), triethylamine (TEA, 99%), glacial acetic acid, triphenylphosphine (PPh_3) and diphenylacetylene were purchased from Aldrich. 4-(Methylthio)phenylboronic acid was purchased from BLDpharm.

Instrumentations and Characterizations. NMR experiments were carried out in a Varian Inova 300 (300 MHz resonance 1H). Size exclusion chromatography studies were performed on Alliance 2695 HPLC System (Waters) liquid chromatography system equipped with a UV 2489 detector (Waters). The samples were eluted by three Phenogel columns connected to each other with stationary phases of 10^3, 10^4, and 10^5 Amstrong and packed with a solid support of a cross-linked styrene and *p*-divinylbenzene copolymer. CD and UV measurements were registered in a Jasco-720 spectropolarimeter and a Jasco-730 spectrophotometer respectively. Cuvettes of 1 mm were used unless indicated cases with 1 cm. Irradiation experiments were done in an Asahi Spectra Xenon light model MAX-303. The light was filtered using a short pass filter / Vis 550 nm 25 dia.

USC UNIVERSIDADE DE SANTIAGO DE COMPOSTELA

5.6.2. Monomers and polymers

The preparation of monomers [(*R*)-**1**, (*S*)-**2**, (*S*)-**3**, (*S*)-**4,** and (*S*)-**5**] can be found in references.[84,102,169]

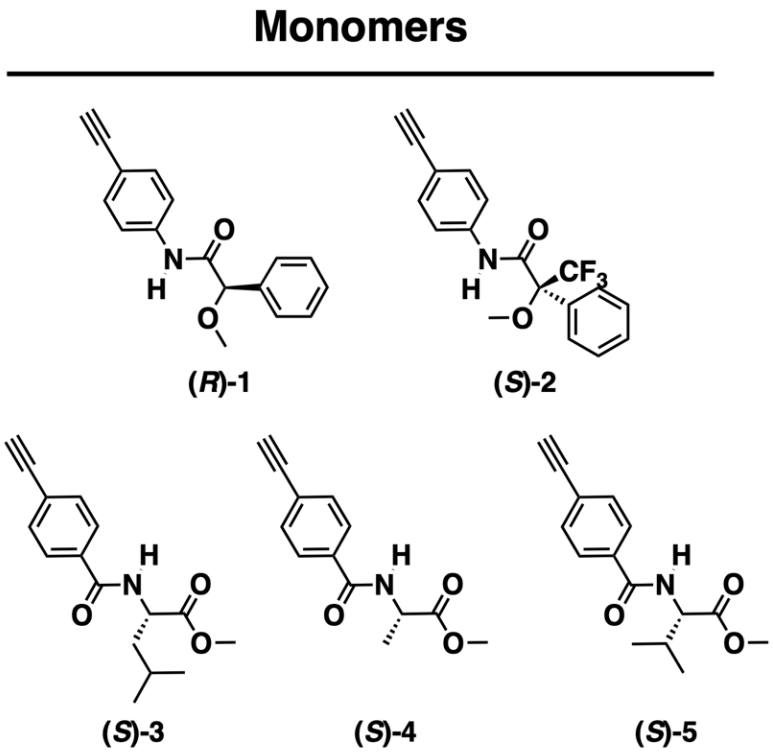


Figure S184. Structures of monomers with anilide and bezamide connection.

5.6.3. Synthesis of polymers

The general procedure to obtain the polymer was already described.[84,102] The polymers were synthesized in a reaction flask (sealed ampoule) that was dried under vacuum and flushed with argon for three times before monomers were added as a solid. Then, the flask was evacuated on a vacuum line and flushed with dry argon (three times). Dry THF was added with a syringe and then, Et_3N (5 μL). A solution of rhodium norbornadiene chloride dimer, $[Rh(nbd)Cl]_2$, in THF was added at 30 ºC. The reaction mixture was stirred at 30 ºC for 24 h. Next, the resulting polymers were diluted in CH_2Cl_2 and they were precipitated in a large amount of diethyl ether, centrifuged (twice) and re-precipitated in hexane and centrifuged again. From GCP poly-(*S*)-**2** we obtained M_n=336 kDa, Đ=1.26 and estimated DP = 1008, while poly-(*S*)-**3** we obtained M_n=325 kDa, Đ=1.39 and estimated DP = 1188.

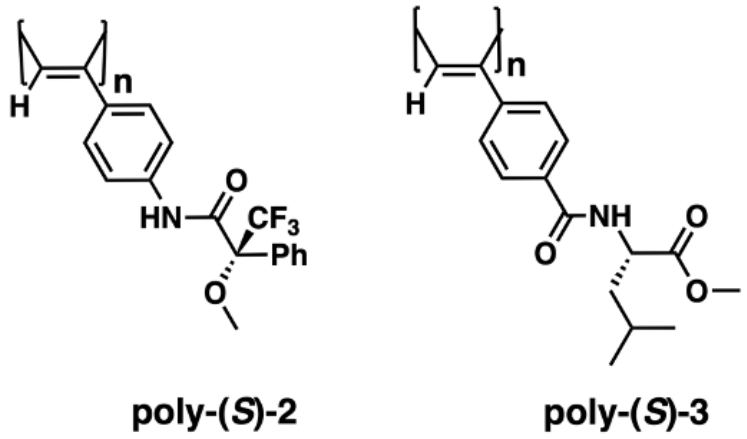


Figure S185. Structures of poly-(*S*)-**2** and poly-(*S*)-**3**.

Table S28. Amount of monomers, catalyst, Et_3N in the polymerization.

Compound	Mass/mg	THF/μL	Et_3N/μL	Catalyst/mg	Yield %
Poly-(*S*)-**2**	100	400	5	1.2	93
Poly-(*S*)-**3**	82	400	5	1.2	95

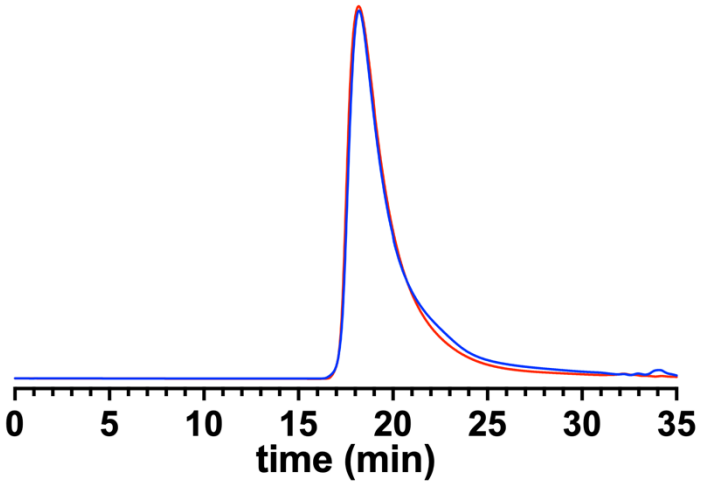


Figure S186. GPC profiles of poly-(*S*)-**2** and poly-(*S*)-**3**.

5.6.4. Synthesis of oligomers

A solution of $[Rh(nbd)Cl]_2$ (18.4 mg, 0.04 mmol), 4-(Methylthio)phenylboronic acid (20.25 mg, 0.12 mmol), and diphenylacetylene (57.6 mg, 0.32 mmol) in THF (0.4 mL)

was cooled to 0 °C. An aqueous solution of KOH (50% (w/v), 23 μL, 0.20 mmol) was added to this yellow solution, and the resultant brown solution was stirred for 5 min at 0 °C. After that, PPh_3 (63.0 mg, 0.24 mmol) was rapidly added, and the solution was stirred for 2 min at 0 °C. Oligomerization was performed by adding 20 μL of this solution (catalyst) to another solution of monomer (mass and [monomer]/[Rh] feed ratio in Table S29, Table S30, Table S31, Table S32, and Table S33) in THF (0.40 mL). After stirring for 2 h at 30 °C the oligomerization reaction was stopped by adding acetic acid (a few drops) to the oligomerization mixture. The resultant mixture was precipitated in a large amount of hexane and centrifuged.

Control oligomer size is established by fine-tuning the [monomer]/[Rh] feed ratio during the synthesis process. Gel Permeation Chromatography (GPC) was employed to validate the degree of polymerization, given the remarkable monodispersity exhibited by these oligomers in terms of molecular weight distribution. M_n, derived from GPC analysis using polystyrene calibration standards, serves as a dependable indicator of oligomer weight. To calculate precisely the oligomer size, we subtract the initiator's weight contribution from M_n and subsequently divide the resulting M_n by the molar weight of the monomer (Table S29, Table S30, Table S31, Table S32, and Table S33). The initiator, in this case, consists of 4-(Methylthio)phenyl (124 Da) with 2 or 3 diphenylacetylene units. To achieve a conservative estimate, we consider an average of 2.5 diphenylacetylene units (2.5 x 178 Da) in the initiator. Therefore, the calculation is performed as follows: DP = M_n – [124 Da + (2.5 x 178Da)] / Mw of the monomer.

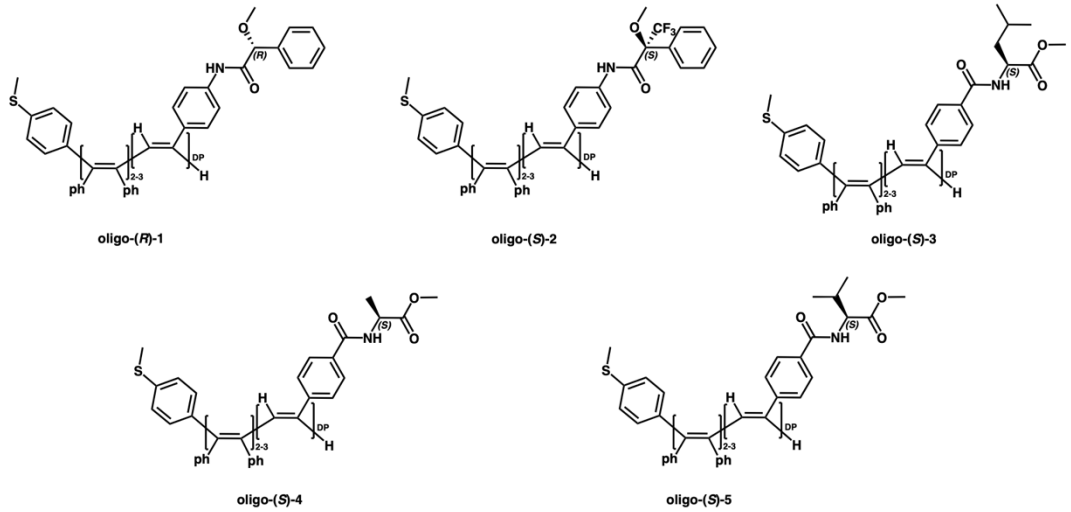


Figure S187. Structures of oligo-(*R*)-**1**, oligo-(*S*)-**2**, oligo-(*S*)-**3**, oligo-(*S*)-**4**, and oligo-(*S*)-**5**.

USC UNIVERSIDADE DE SANTIAGO DE COMPOSTELA

Table S29. Amount of monomer (*R*)-**1**, [monomer]/[Rh] feed ratio and yield of the oligomerizations of oligo-(*R*)-**1**. M_n, M_w, Đ from GPC and calculated DP from M_n.

Mass (mg)	[(*R*)-1]/[Rh]	Yield %	M_n (kDa)	M_w (kDa)	Đ	DP
5.00	4.71	98	1.90	1.99	1.05	5.0
10.0	9.43	95	2.92	3.07	1.05	8.9
20.0	18.9	97	5.67	5.86	1.03	19.3
40.0	37.7	96	9.81	10.0	1.02	34.9
80.0	75.4	96	18.9	19.3	1.02	69.2

Table S30. Amount of monomer (*S*)-**2**, [monomer]/[Rh] feed ratio and yield of the oligomerizations of oligo-(*S*)-**2**. M_n, M_w, Đ from GPC and calculated DP from M_n.

Mass (mg)	[(*S*)-2]/[Rh]	Yield %	M_n (kDa)	M_w (kDa)	Đ	DP
6.25	4.71	95	2.23	2.32	1.04	5.0
12.5	9.43	98	3.48	3.63	1.04	8.7
25.0	18.9	93	6.40	6.61	1.03	17.5
50.0	37.7	99	13.0	13.7	1.05	37.4
100	75.4	98	90.7	177	1.95	309

Table S31. Amount of monomer (*S*)-**3**, [monomer]/[Rh] feed ratio and yield of the oligomerizations of oligo-(*S*)-**3**. M_n, M_w, Đ from GPC and calculated DP from M_n.

Mass (mg)	[(*S*)-3]/[Rh]	Yield %	M_n (kDa)	M_w (kDa)	Đ	DP
5.15	4.71	97	1.69	1.76	1.04	4.1
10.3	9.43	96	2.98	3.06	1.03	8.8
20.6	18.9	96	5.18	5.36	1.03	16.9
41.2	37.7	96	9.92	10.1	1.02	34.2
82.4	75.4	93	24.9	25.2	1.01	89.2

USC UNIVERSIDADE DE SANTIAGO DE COMPOSTELA

Table S32. Amount of monomer (*S*)-**4**, [monomer]/[Rh] feed ratio and yield of the oligomerizations of oligo-(*S*)-**4**. M_n, M_w, Đ from GPC and calculated DP from M_n.

Mass (mg)	[(*S*)-4]/[Rh]	Yield %	M_n (kDa)	M_w (kDa)	Đ	DP
4.36	4.71	95	1.93	2.01	1.04	5.9
8.72	9.43	93	3.41	3.53	1.04	12.3
17.4	18.9	94	6.06	6.19	1.02	23.7
35.0	37.7	95	12.0	12.1	1.01	49.3
70.0	75.4	97	22.9	23.3	1.02	96.4

Table S33. Amount of monomer (*S*)-**5**, [monomer]/[Rh] feed ratio and yield of the oligomerizations of oligo-(*S*)-**5**. M_n, M_w, Đ from GPC and calculated DP from M_n.

Mass (mg)	[(*S*)-5]/[Rh]	Yield %	M_n (kDa)	M_w (kDa)	Đ	DP
4.89	4.71	91	1.37	1.42	1.03	3.1
9.29	9.43	97	2.39	2.47	1.03	7.0
19.6	18.9	95	4.87	5.01	1.02	16.6
39.1	37.7	97	8.54	8.71	1.01	30.8
78.2	75.4	98	16.2	16.3	1.02	60.2

USC UNIVERSIDADE DE SANTIAGO DE COMPOSTELA

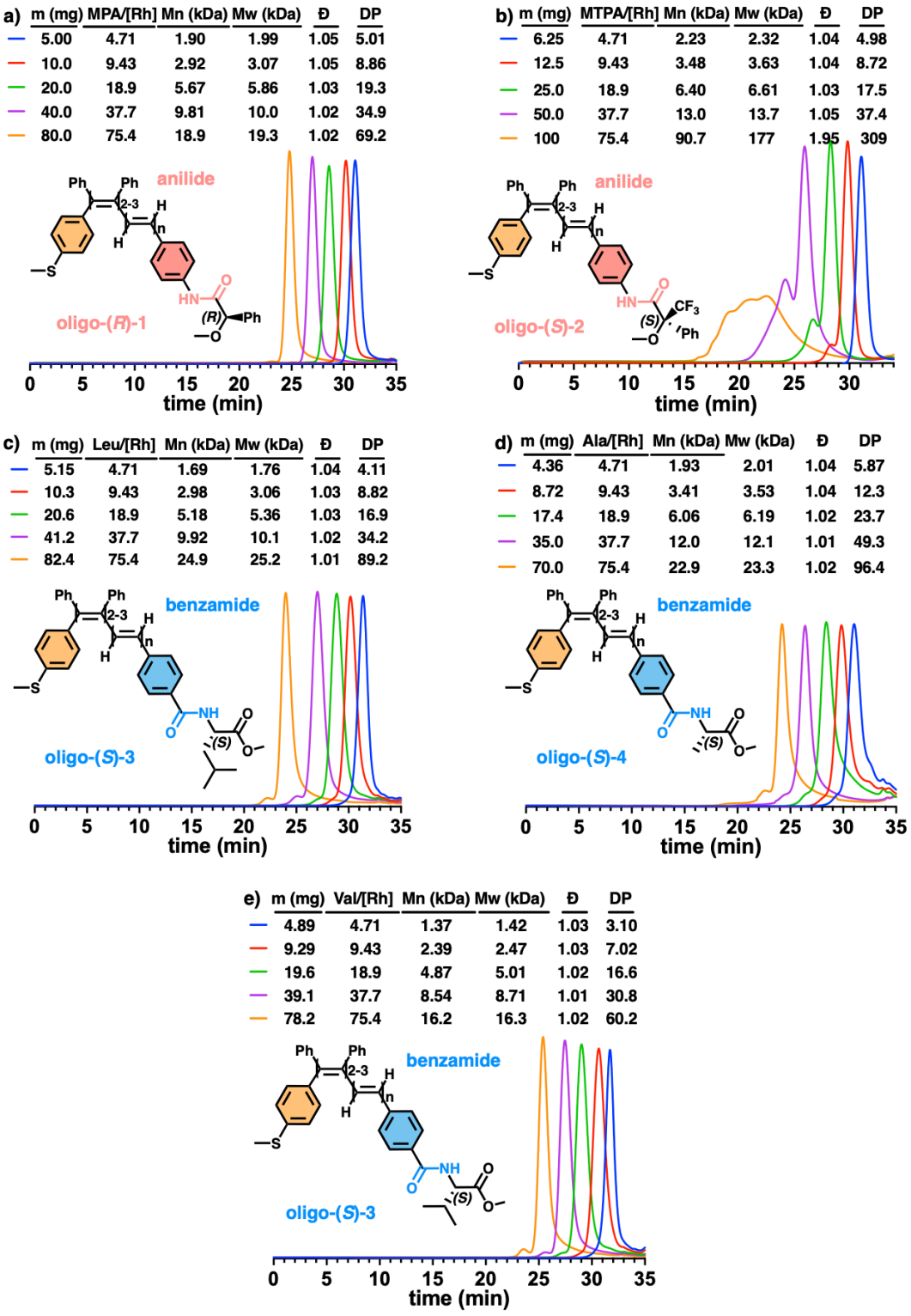


Figure S188. GPC profiles of oligos with different degrees of polymerization (DPs) for a) oligo-(*R*)-**1** b) oligo-(*S*)-**2** c) oligo-(*S*)-**3** d) oligo-(*S*)-**4** e) oligo-(*S*)-**5**.

USC UNIVERSIDADE DE SANTIAGO DE COMPOSTELA

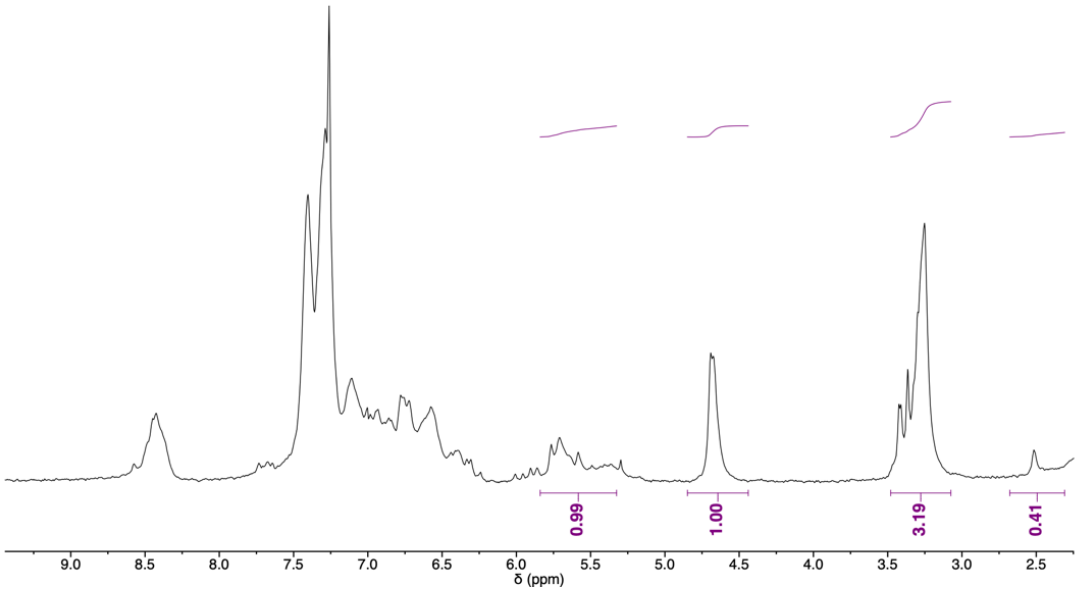


Figure S189. ^{1}H-NMR spectrum of oligo-(*R*)-**1** DP (GPC)= 5 ($CDCl_3$, 300 MHz).

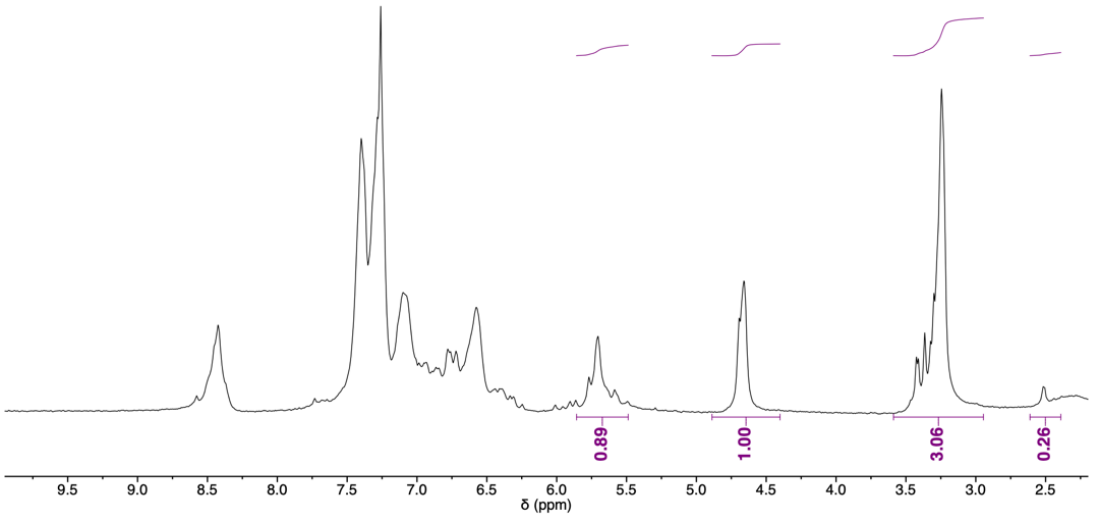


Figure S190. ^{1}H-NMR spectrum of oligo-(*R*)-**1** DP (GPC)= 9 ($CDCl_3$, 300 MHz).

USC
UNIVERSIDADE DE SANTIAGO DE COMPOSTELA

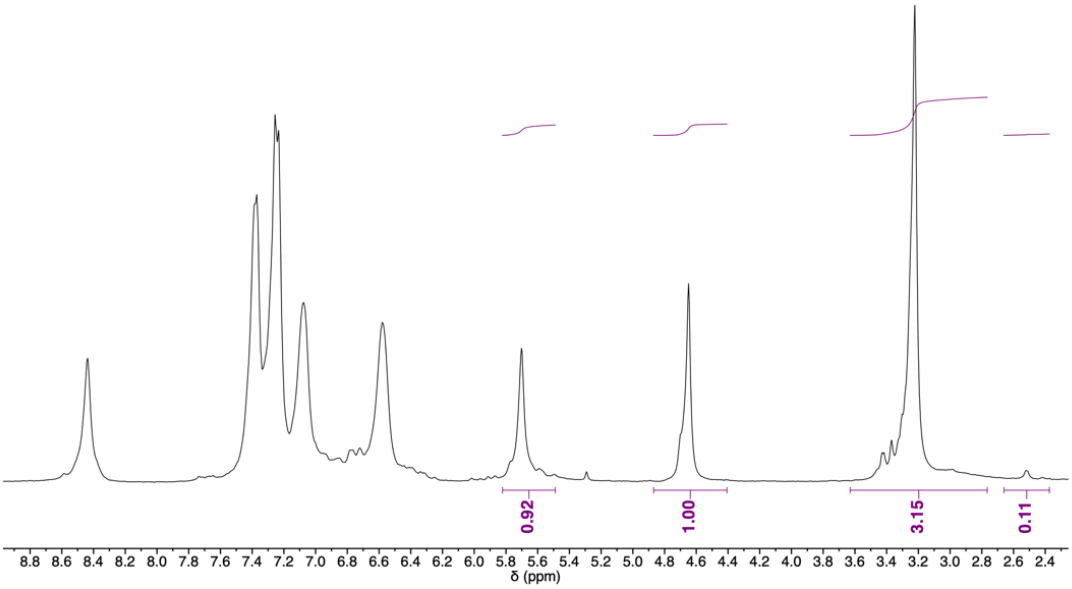


Figure S191. ^{1}H-NMR spectrum of oligo-(*R*)-**1** DP (GPC)= 19 ($CDCl_3$, 300 MHz).

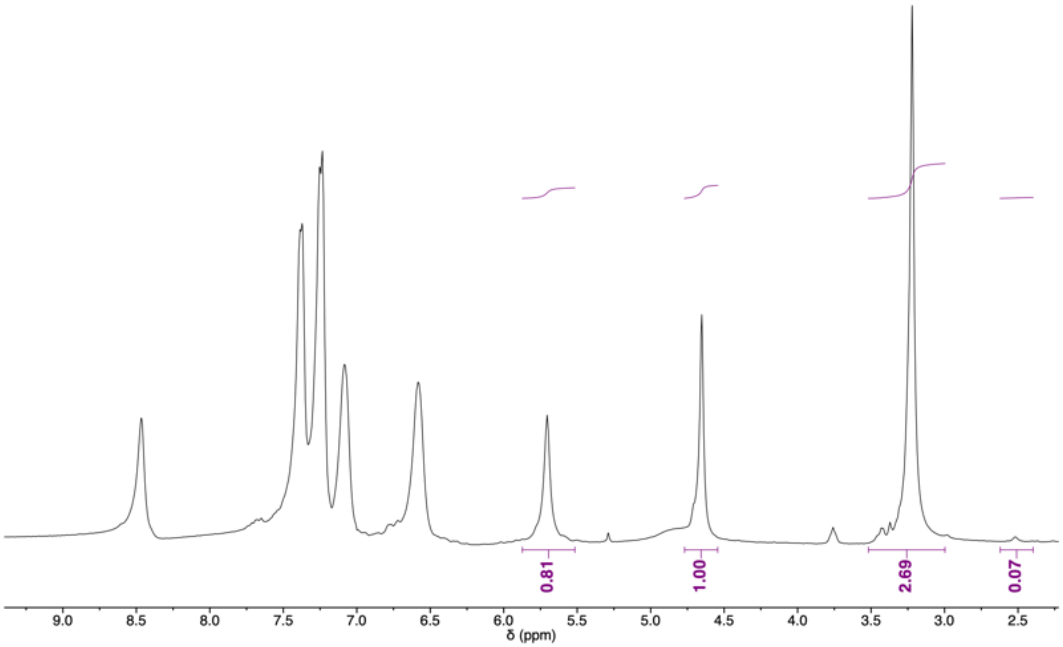


Figure S192. ^{1}H-NMR spectrum of oligo-(*R*)-**1** DP (GPC)= 35 ($CDCl_3$, 300 MHz).

USC
UNIVERSIDADE DE SANTIAGO DE COMPOSTELA

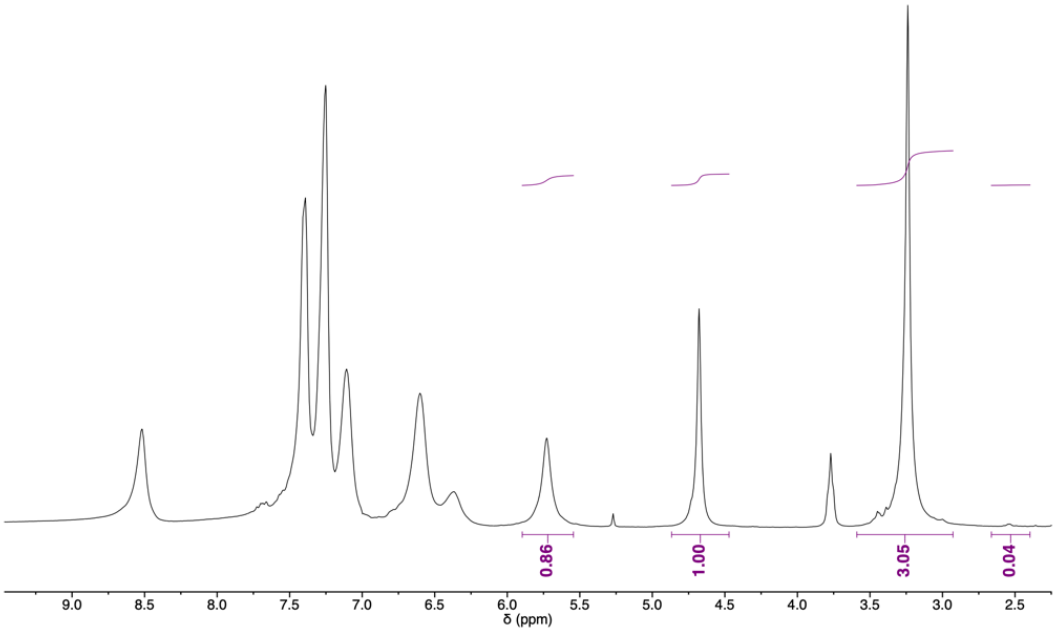


Figure S193. ^{1}H-NMR spectrum of oligo-(*R*)-**1** DP (GPC)= 69 ($CDCl_3$, 300 MHz).

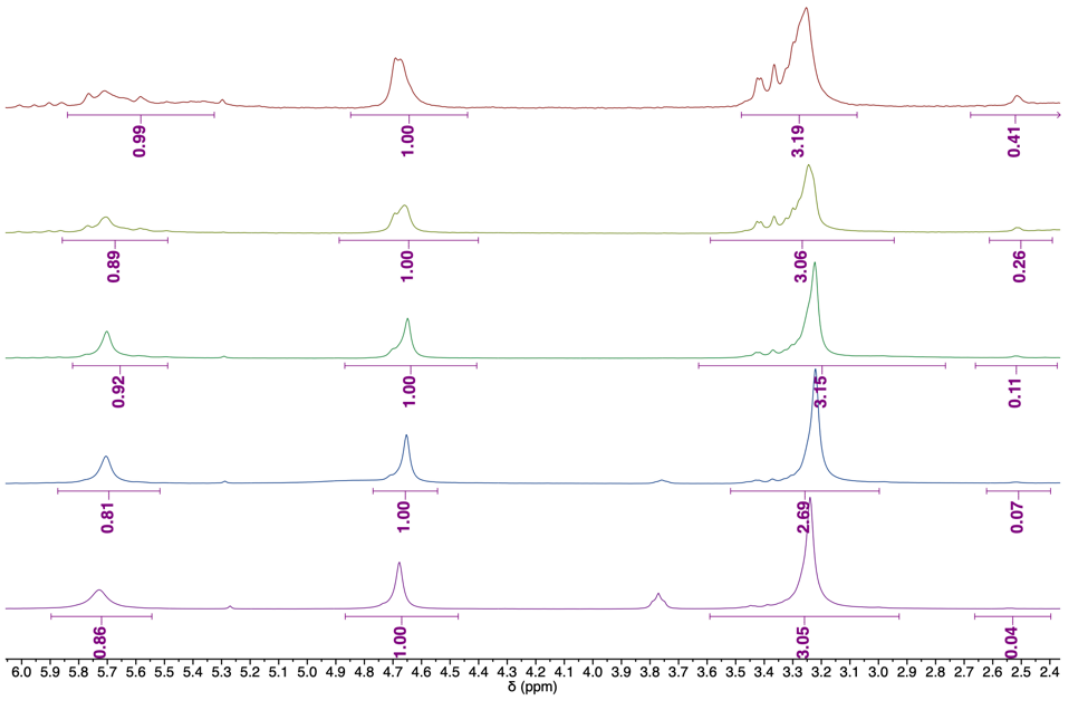


Figure S194. ^{1}H-NMR spectra of oligo-(*R*)-**1** DP (GPC)= 5, 9, 19, 35, and 69 ($CDCl_3$, 300 MHz).

USC UNIVERSIDADE DE SANTIAGO DE COMPOSTELA

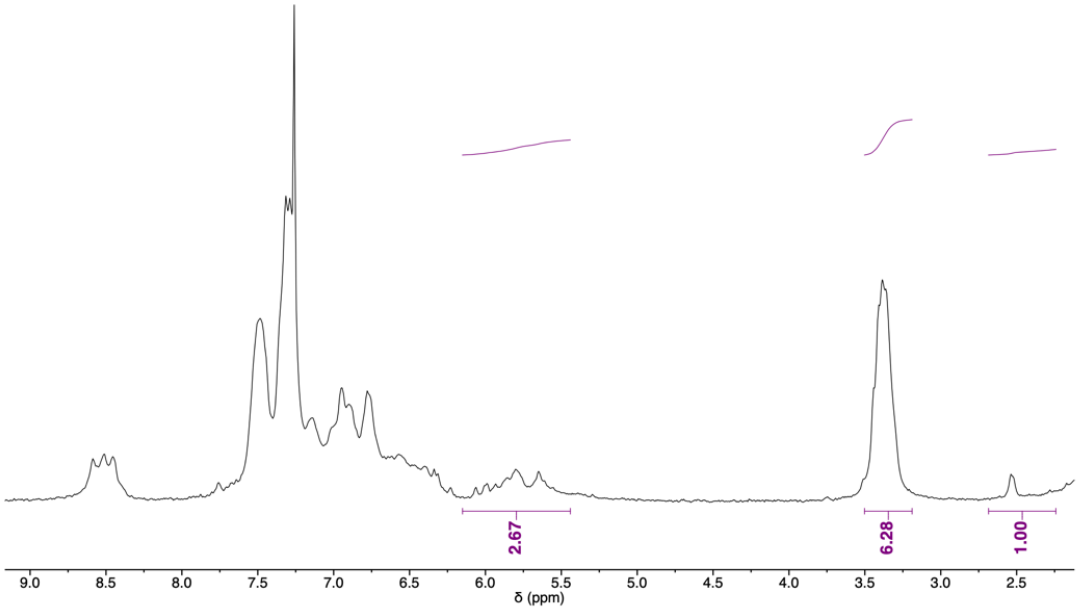


Figure S195. ^{1}H-NMR spectrum of oligo-(*S*)-**2** DP (GPC)= 5 ($CDCl_3$, 300 MHz).

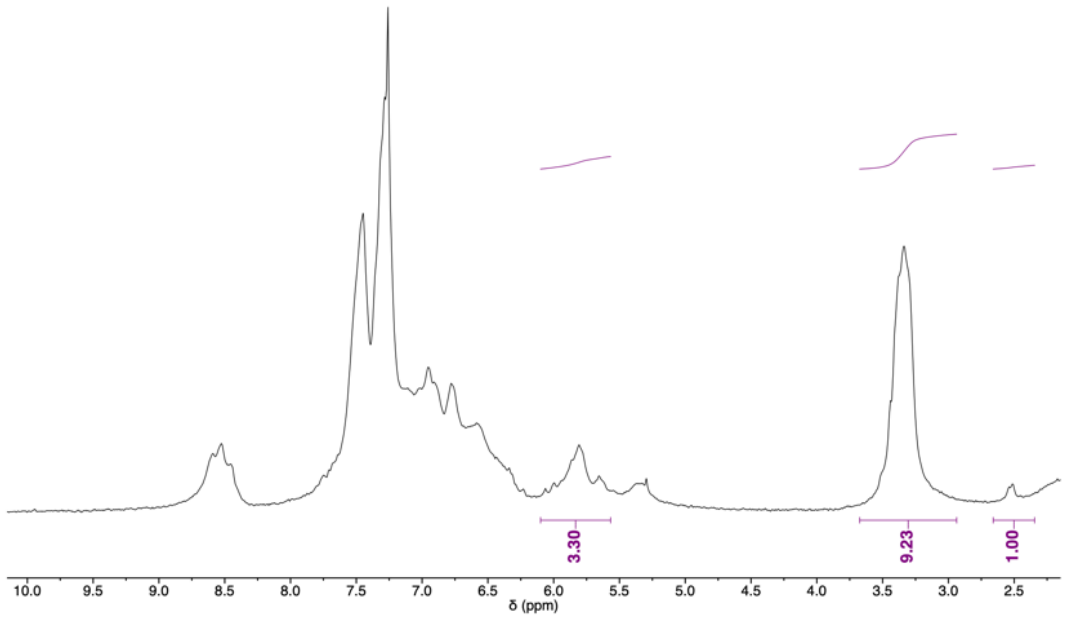


Figure S196. ^{1}H-NMR spectrum of oligo-(*S*)-**2** DP (GPC)= 9 ($CDCl_3$, 300 MHz).

USC
UNIVERSIDADE DE SANTIAGO DE COMPOSTELA

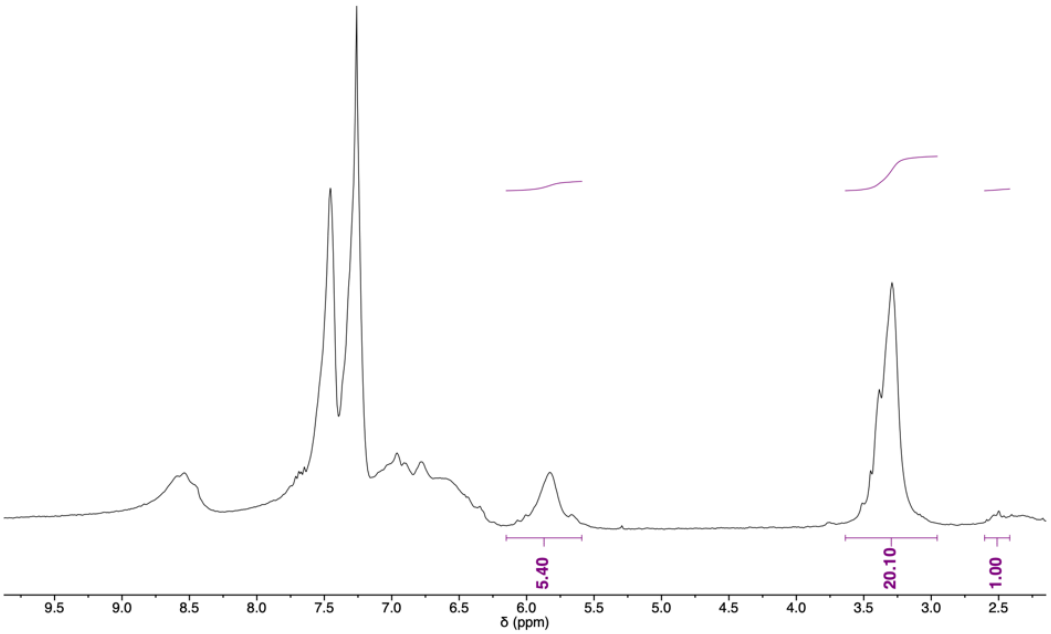


Figure S197. ^{1}H-NMR spectrum of oligo-(*S*)-**2** DP (GPC)= 18 ($CDCl_3$, 300 MHz).

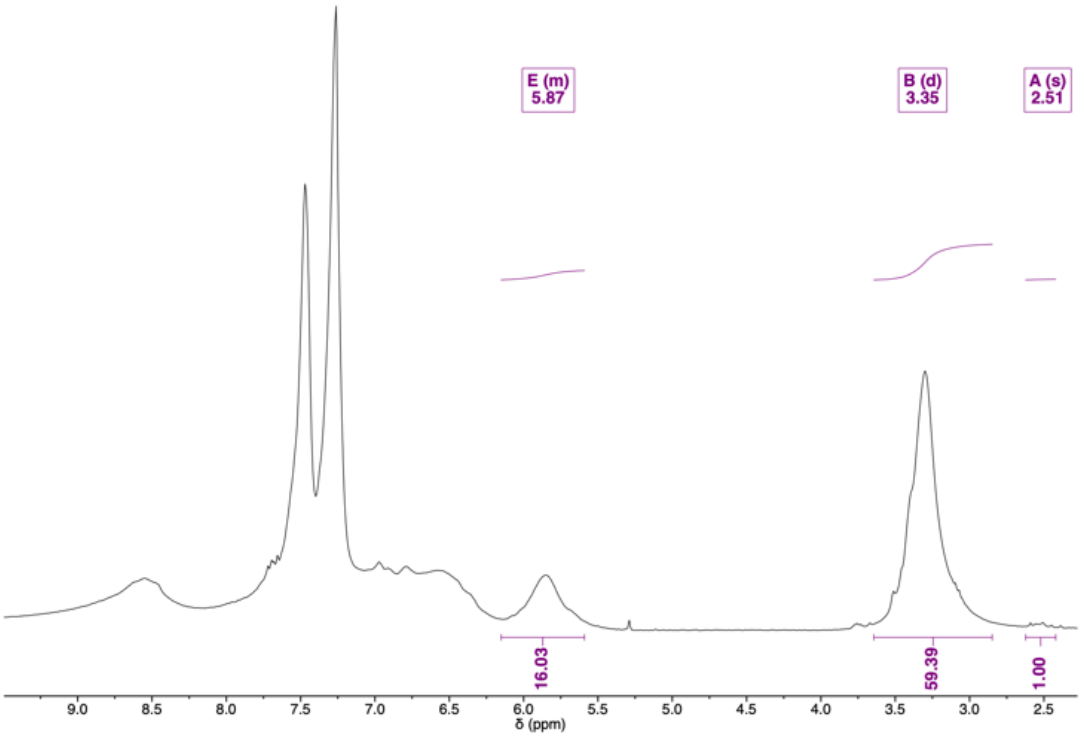


Figure S198. ^{1}H-NMR spectrum of oligo-(*S*)-**2** DP (GPC)= 37 ($CDCl_3$, 300 MHz).

USC
UNIVERSIDADE DE SANTIAGO DE COMPOSTELA

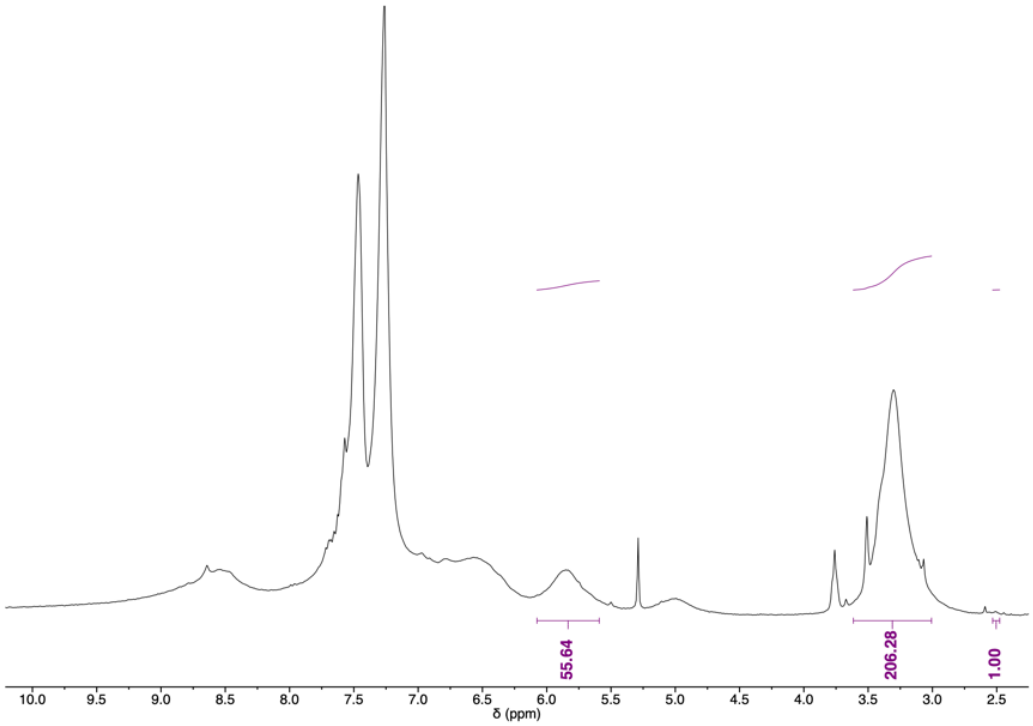


Figure S199. ^{1}H-NMR spectrum of oligo-(*S*)-**2** DP (GPC)= 309 ($CDCl_3$, 300 MHz).

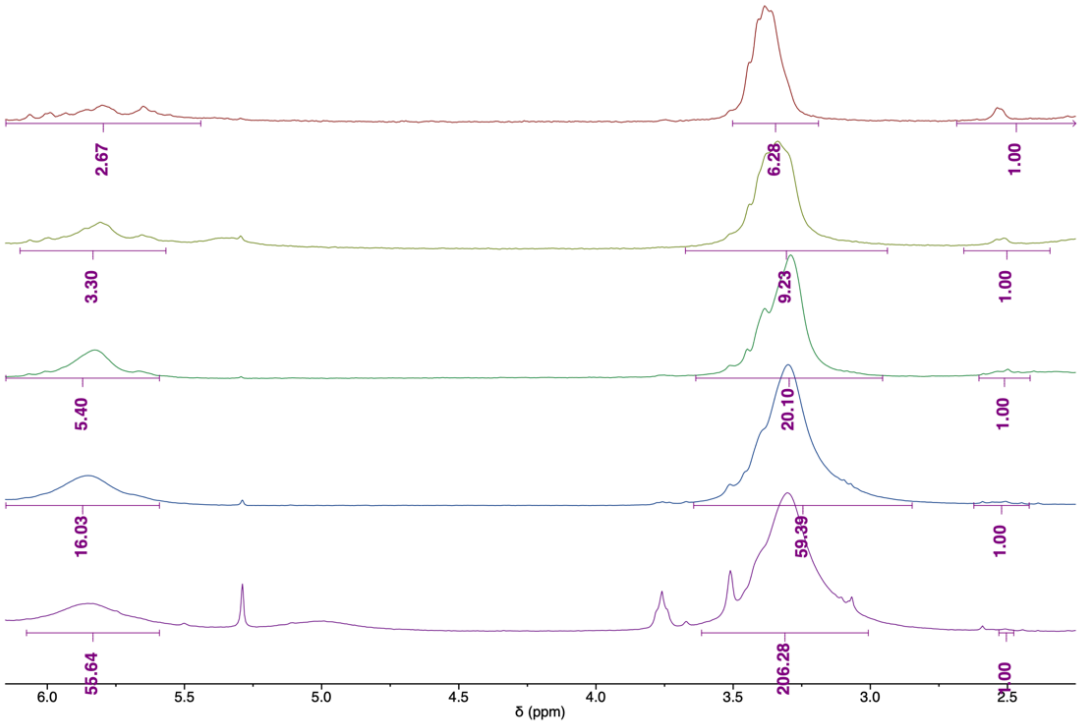


Figure S200. ^{1}H-NMR spectra of oligo-(*S*)-**2** DP (GPC)= 5, 9, 18, 37, and 309 ($CDCl_3$, 300 MHz).

USC UNIVERSIDADE DE SANTIAGO DE COMPOSTELA

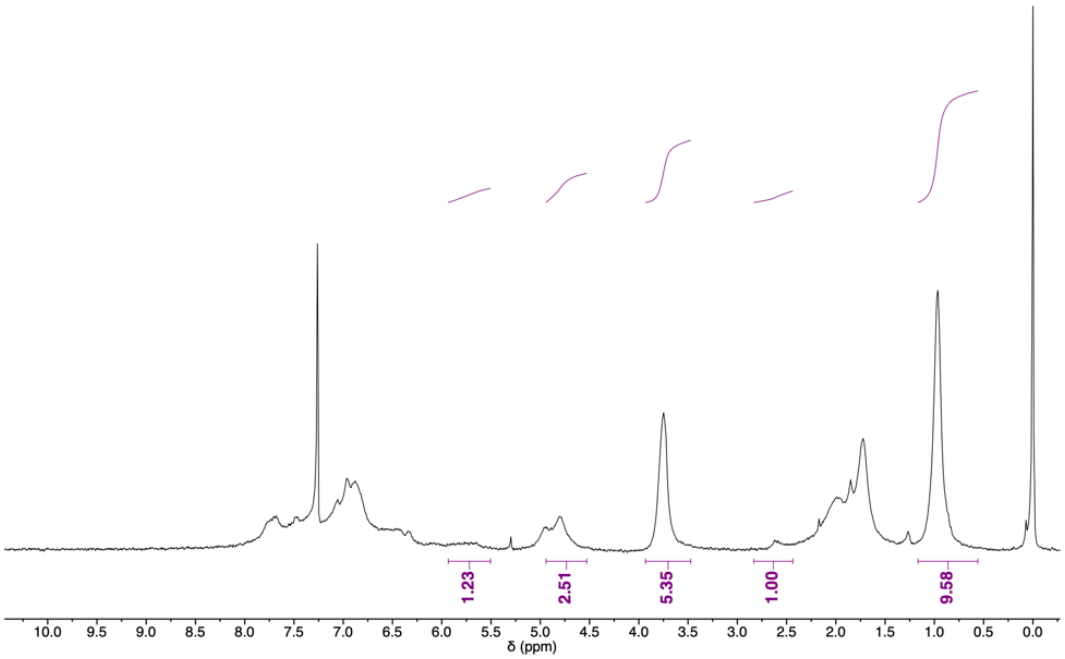


Figure S201. ^{1}H-NMR spectrum of oligo-(*S*)-**3** DP (GPC)= 4 ($CDCl_3$, 300 MHz).

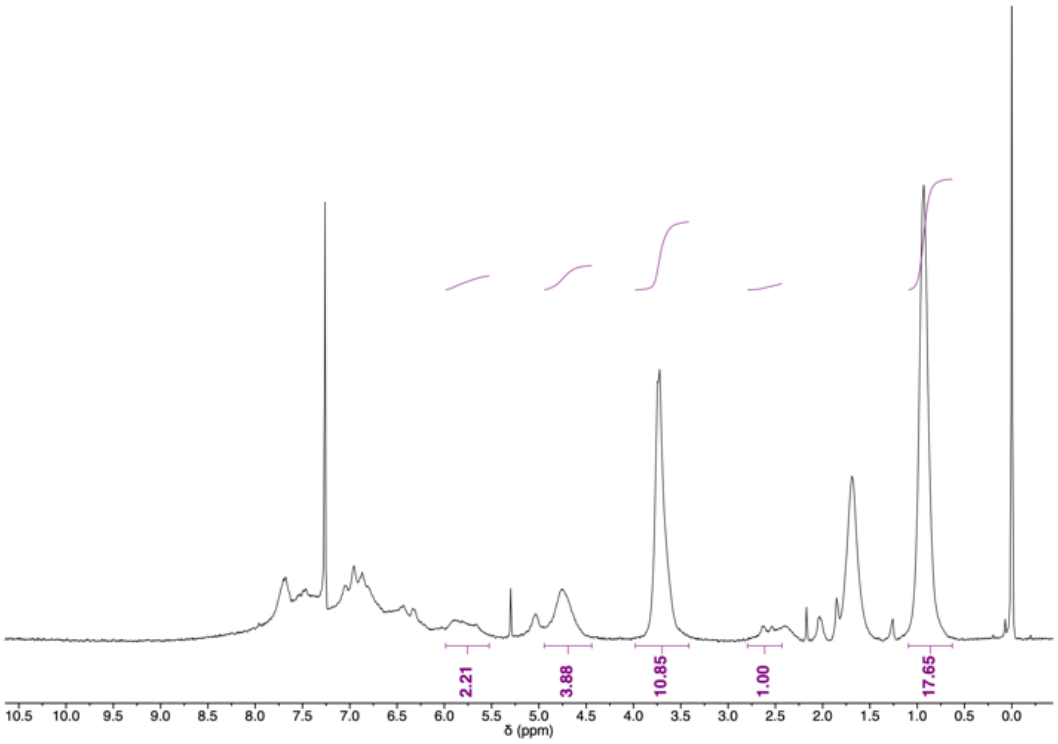


Figure S202. ^{1}H-NMR spectrum of oligo-(*S*)-**3** DP (GPC)= 9 ($CDCl_3$, 300 MHz).

USC
UNIVERSIDADE DE SANTIAGO DE COMPOSTELA

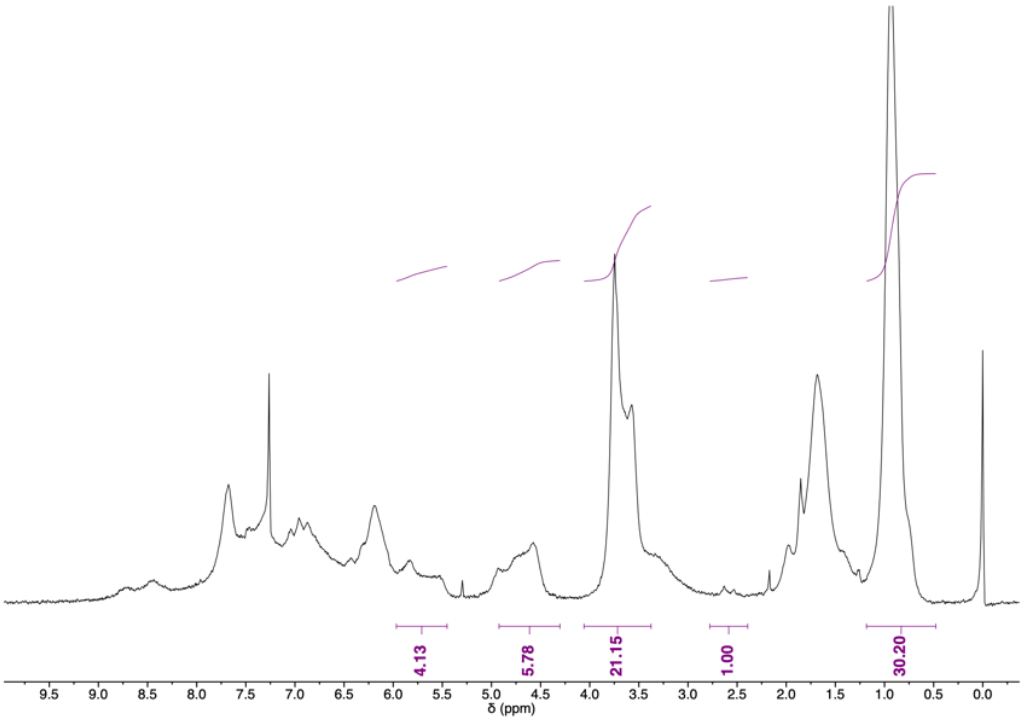


Figure S203. ^{1}H-NMR spectrum of oligo-(*S*)-**3** DP (GPC)= 17 ($CDCl_3$, 300 MHz).

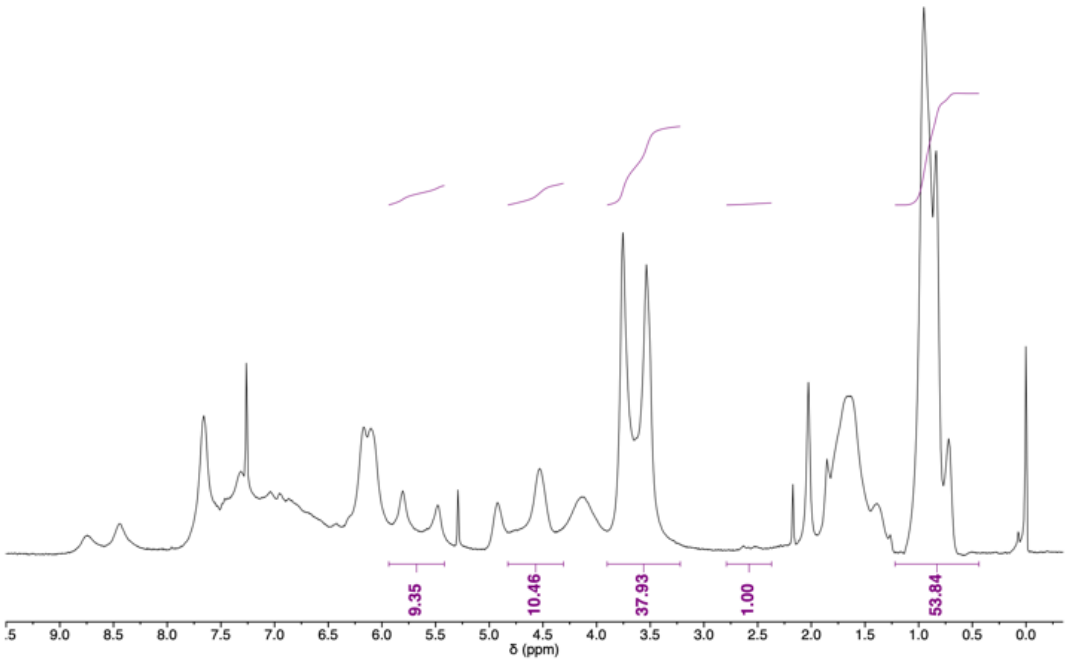


Figure S204. ^{1}H-NMR spectrum of oligo-(*S*)-**3** DP (GPC)= 34 ($CDCl_3$, 300 MHz).

USC UNIVERSIDADE DE SANTIAGO DE COMPOSTELA

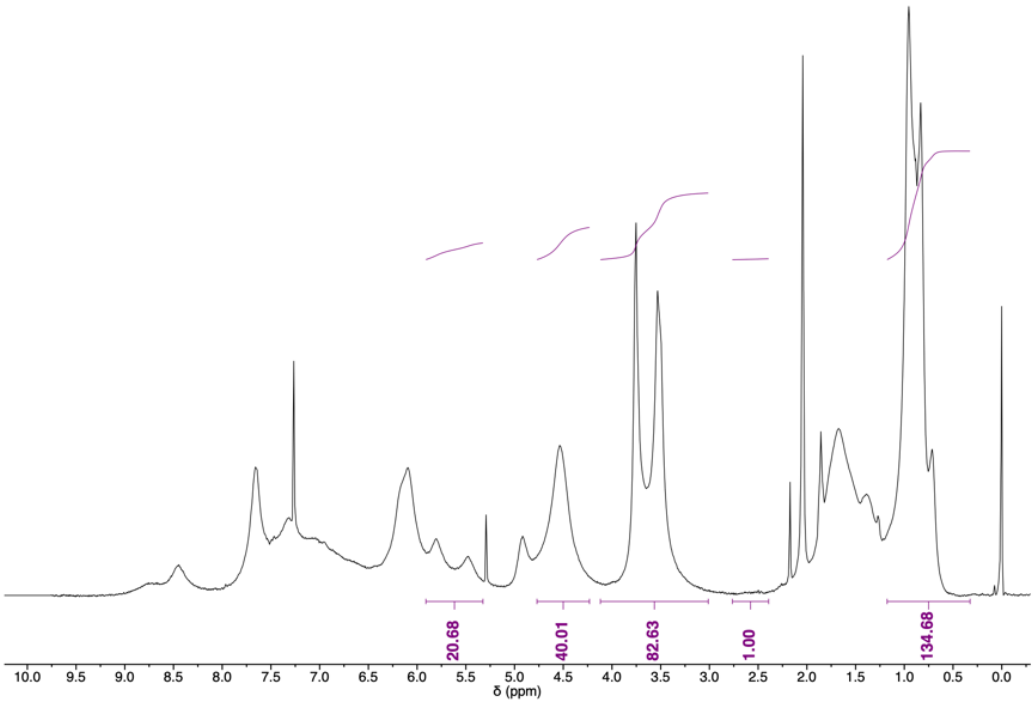


Figure S205. ^{1}H-NMR spectrum of oligo-(*S*)-**3** DP (GPC)= 89 ($CDCl_3$, 300 MHz).

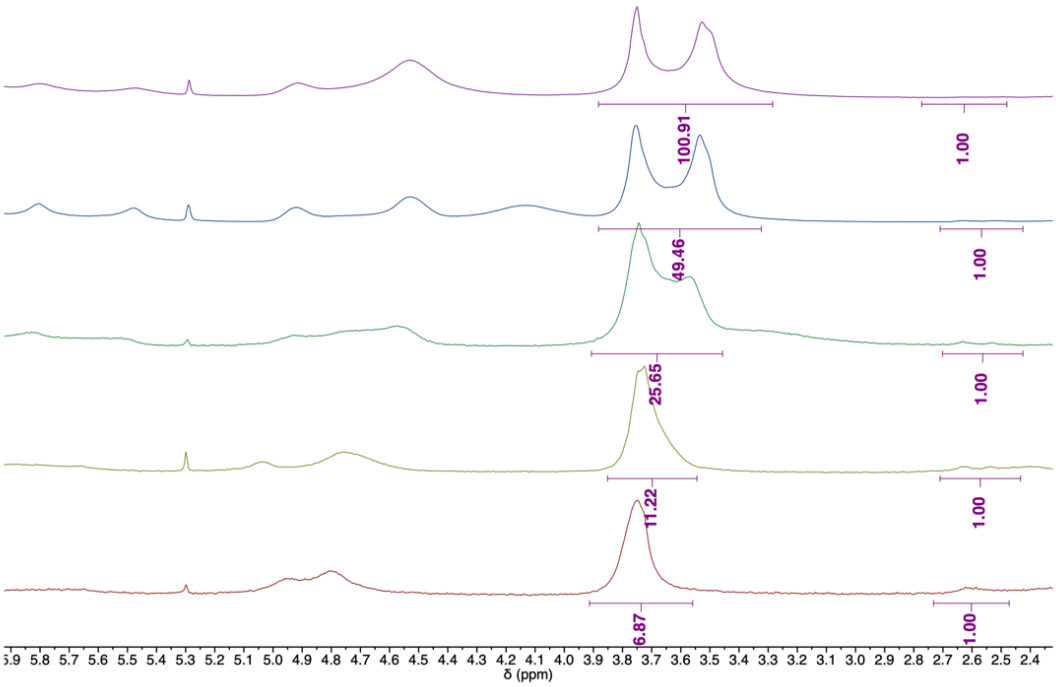


Figure S206. ^{1}H-NMR spectra of oligo-(*S*)-**3** DP (GPC)= 4, 9, 17, 34, and 89 ($CDCl_3$, 300 MHz).

USC
UNIVERSIDADE DE SANTIAGO DE COMPOSTELA

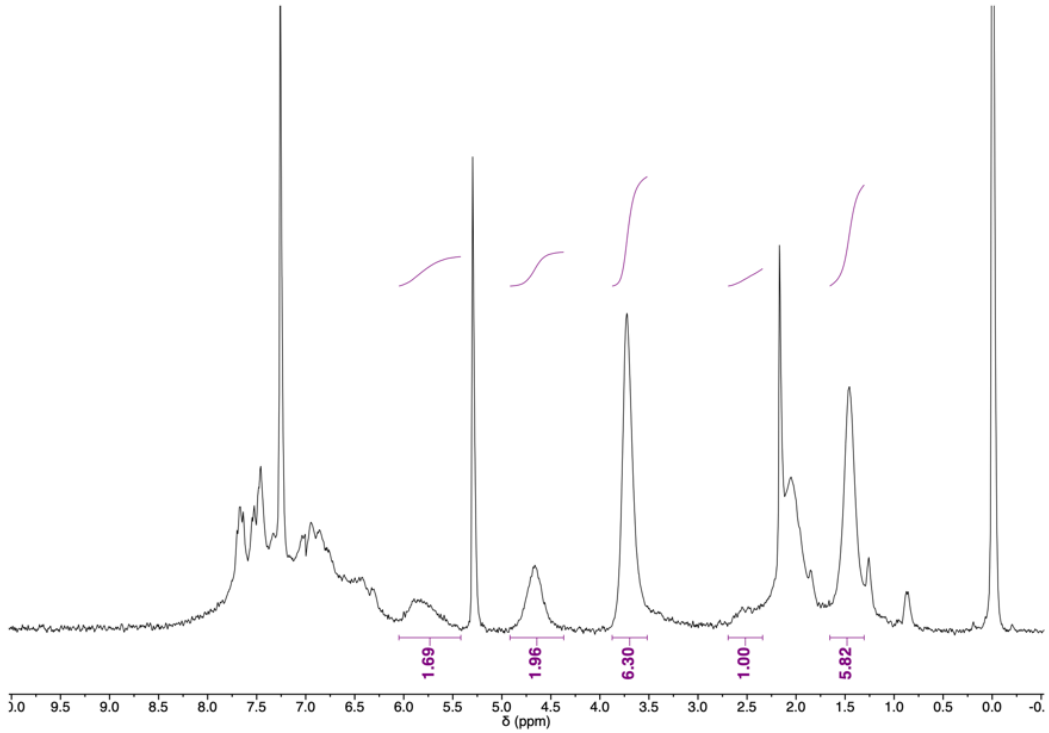


Figure S207. ^{1}H-NMR spectrum of oligo-(*S*)-**4** DP (GPC)= 6 ($CDCl_3$, 300 MHz).

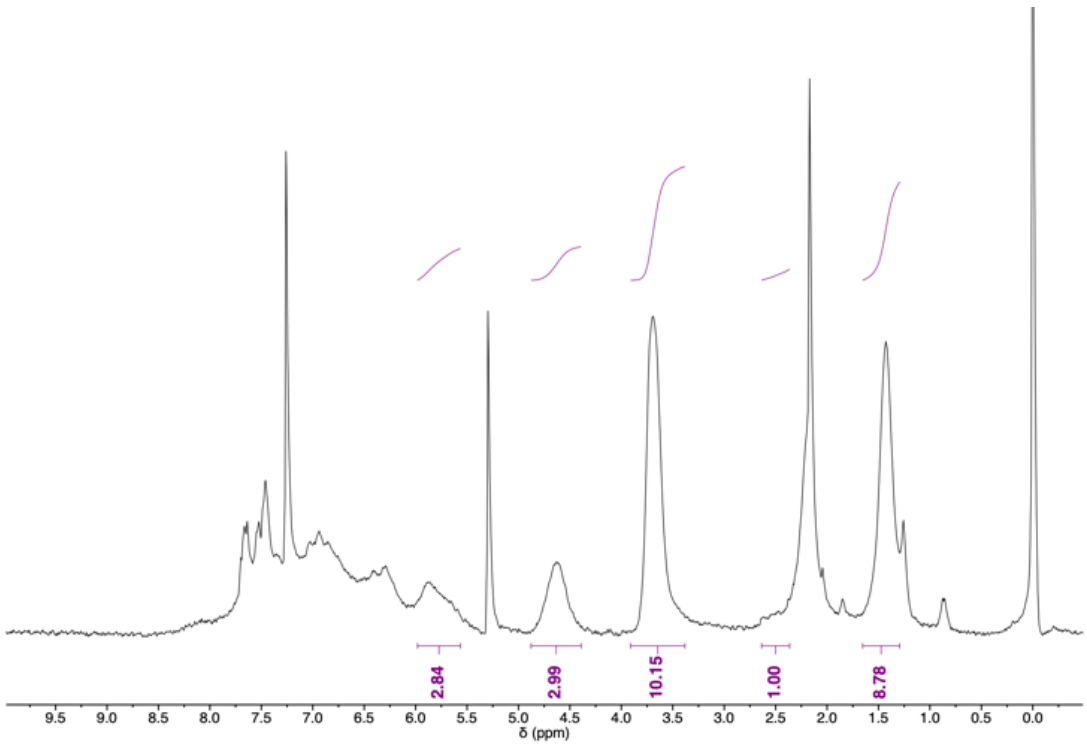


Figure S208. ^{1}H-NMR spectrum of oligo-(*S*)-**4** DP (GPC)= 12 ($CDCl_3$, 300 MHz).

UNIVERSIDADE DE SANTIAGO DE COMPOSTELA

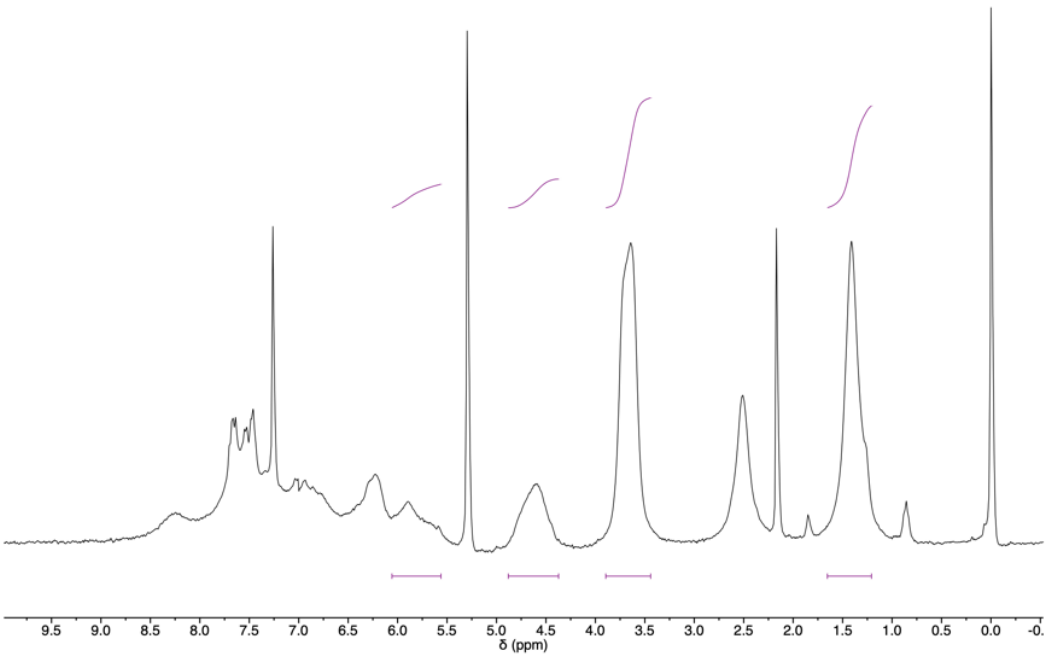


Figure S209. ^{1}H-NMR spectrum of oligo-(*S*)-**4** DP (GPC)= 24 ($CDCl_3$, 300 MHz).

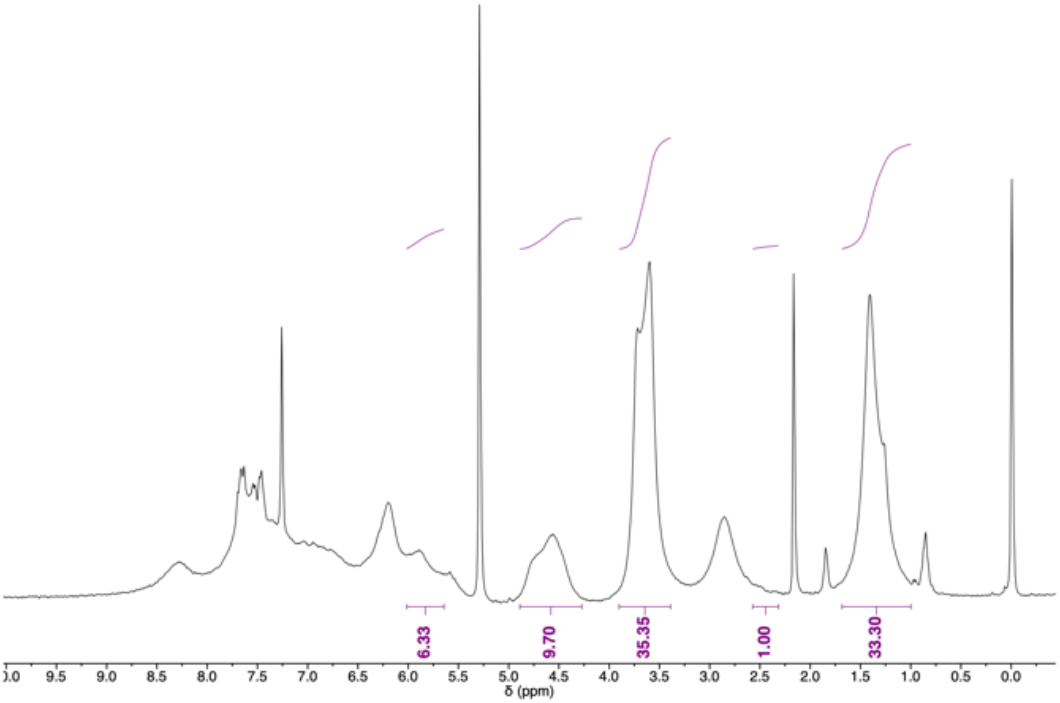


Figure S210. ^{1}H-NMR spectrum of oligo-(*S*)-**4** DP (GPC)= 49 ($CDCl_3$, 300 MHz).

USC UNIVERSIDADE DE SANTIAGO DE COMPOSTELA

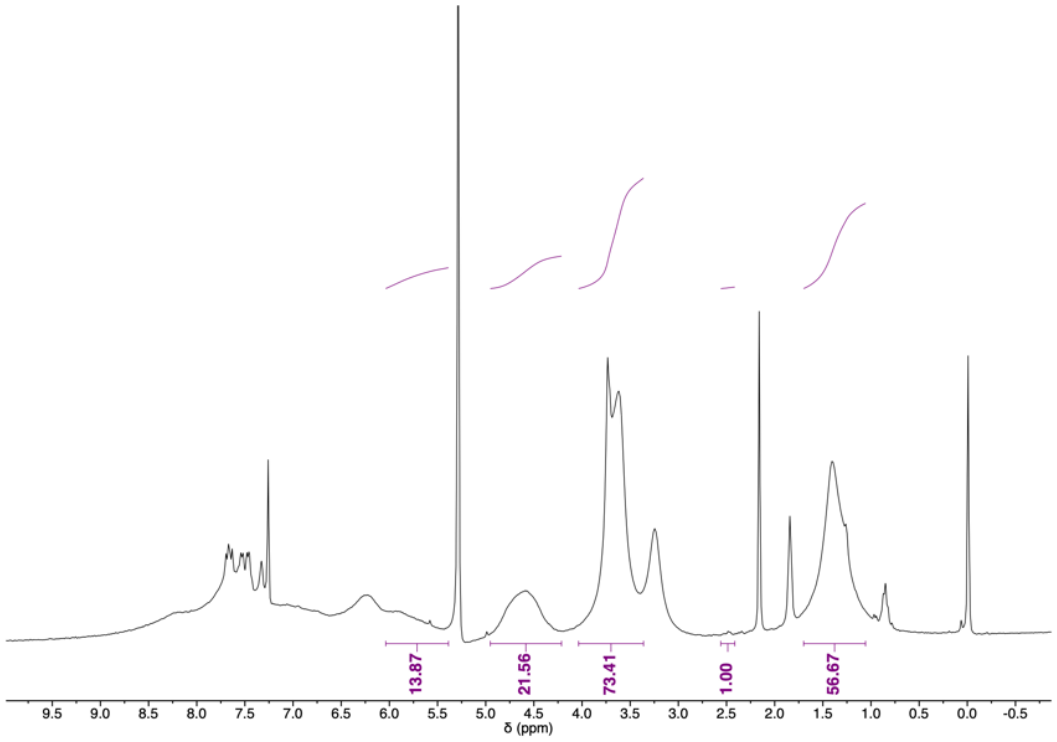


Figure S211. ^{1}H-NMR spectrum of oligo-(*S*)-**4** DP (GPC)= 96 ($CDCl_3$, 300 MHz).

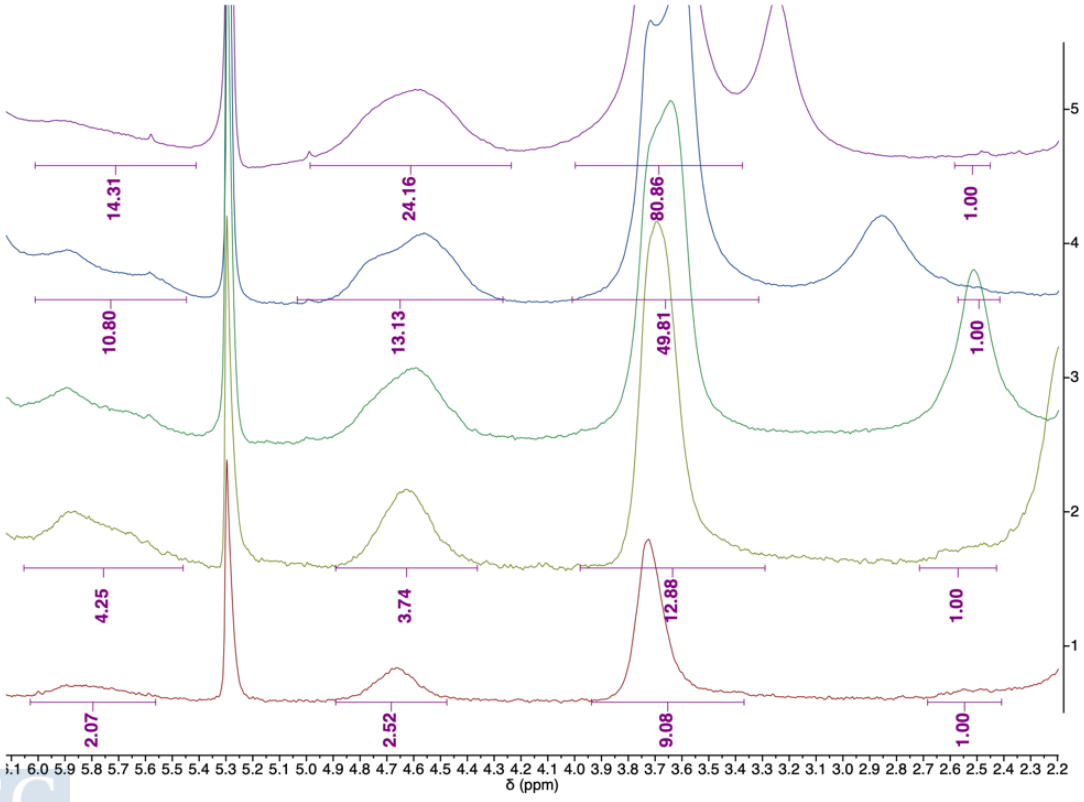


Figure S212. ^{1}H-NMR spectra of oligo-(*S*)-**4** DP (GPC)= 6, 12, 24, 49, and 96 ($CDCl_3$, 300 MHz).

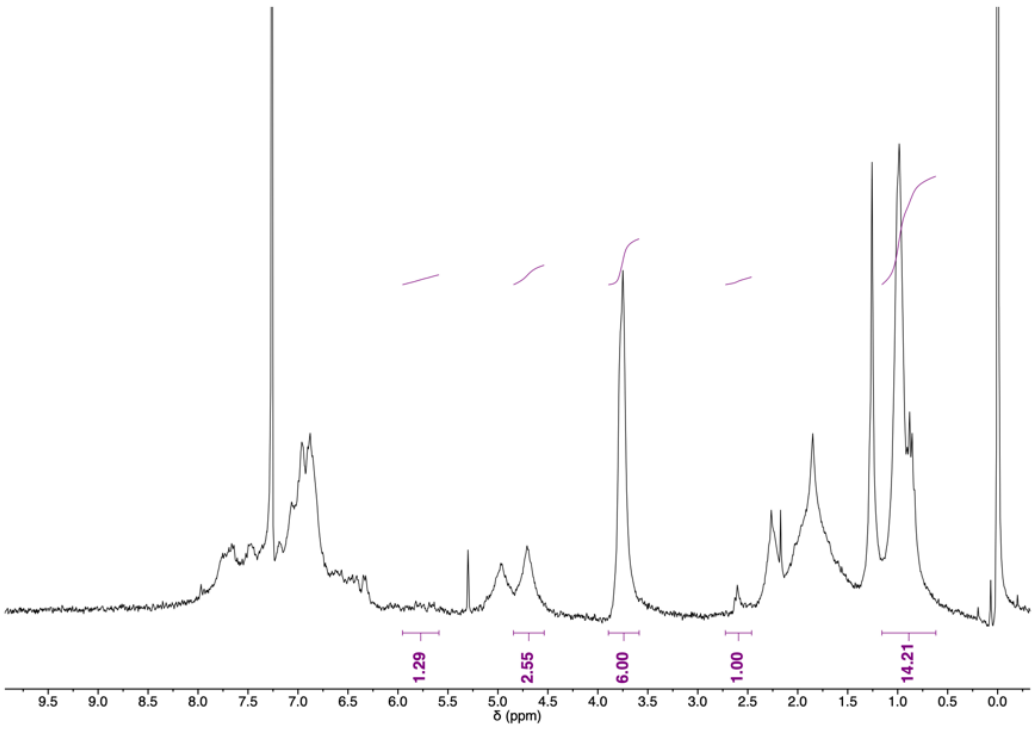


Figure S213. ^{1}H-NMR spectrum of oligo-(*S*)-**5** DP (GPC)= 3 ($CDCl_3$, 300 MHz).

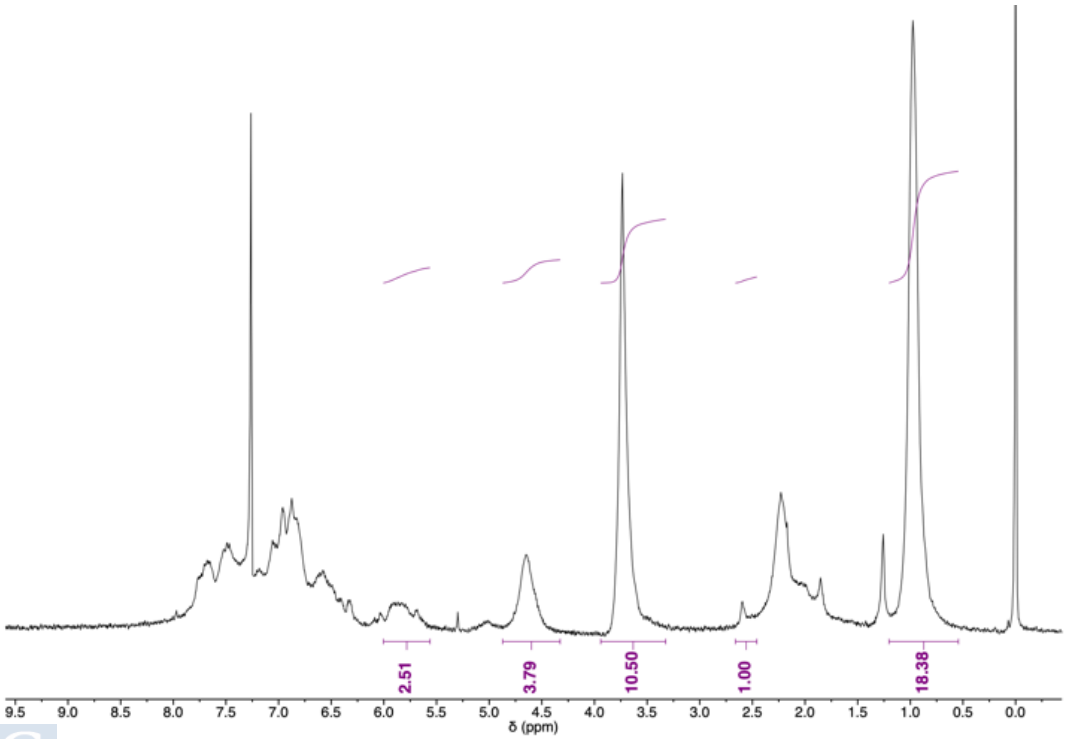


Figure S214. ^{1}H-NMR spectrum of oligo-(*S*)-**5** DP (GPC)= 7 ($CDCl_3$, 300 MHz).

USC DE COMPOSTELA

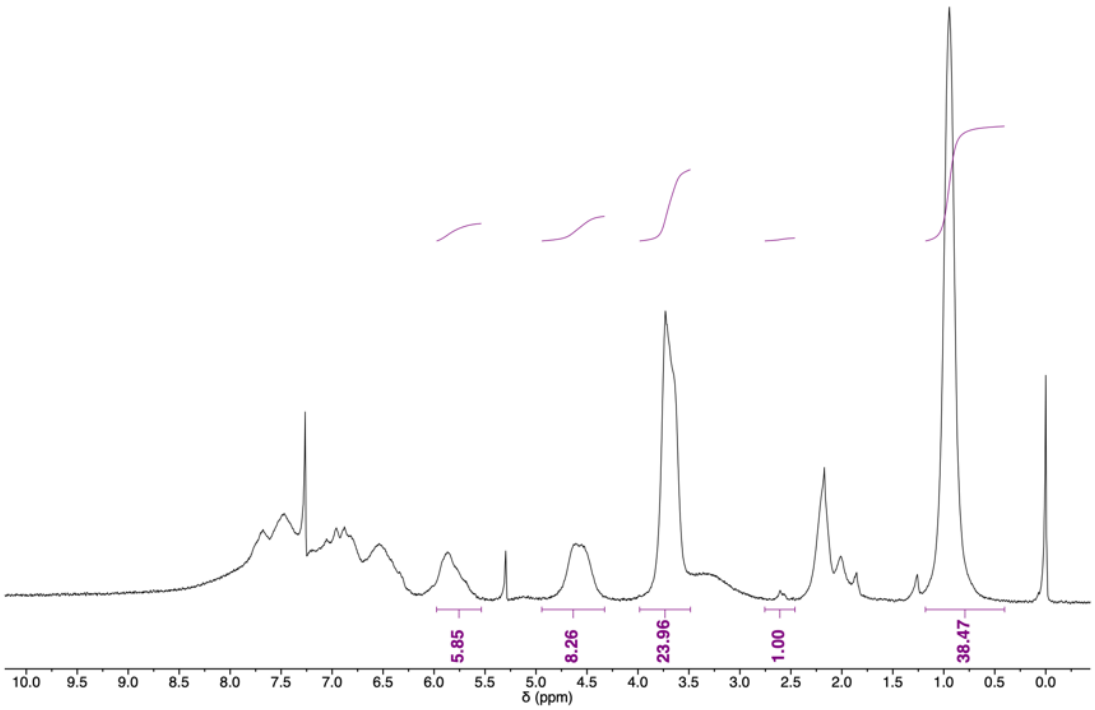
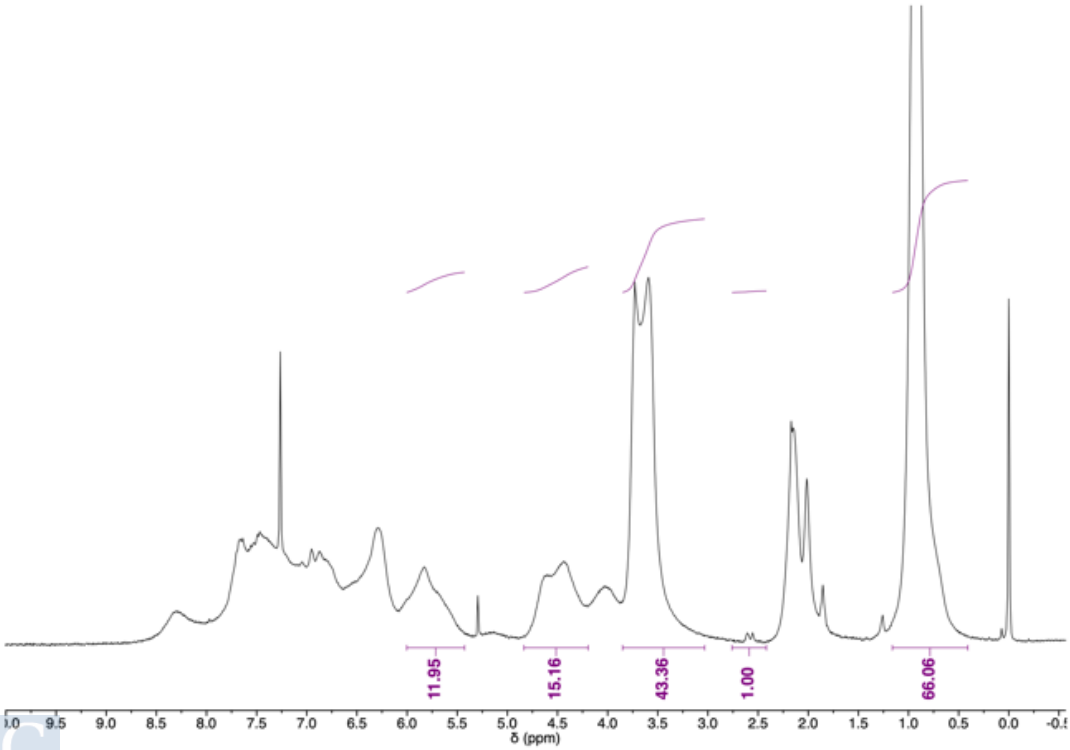


Figure S215. ^{1}H-NMR spectrum of oligo-(*S*)-**5** DP (GPC)= 17 ($CDCl_3$, 300 MHz).



USC UNIVERSIDADE DE SANTIAGO

Figure S216. ^{1}H-NMR spectrum of oligo-(*S*)-**5** DP (GPC)= 31 ($CDCl_3$, 300 MHz).

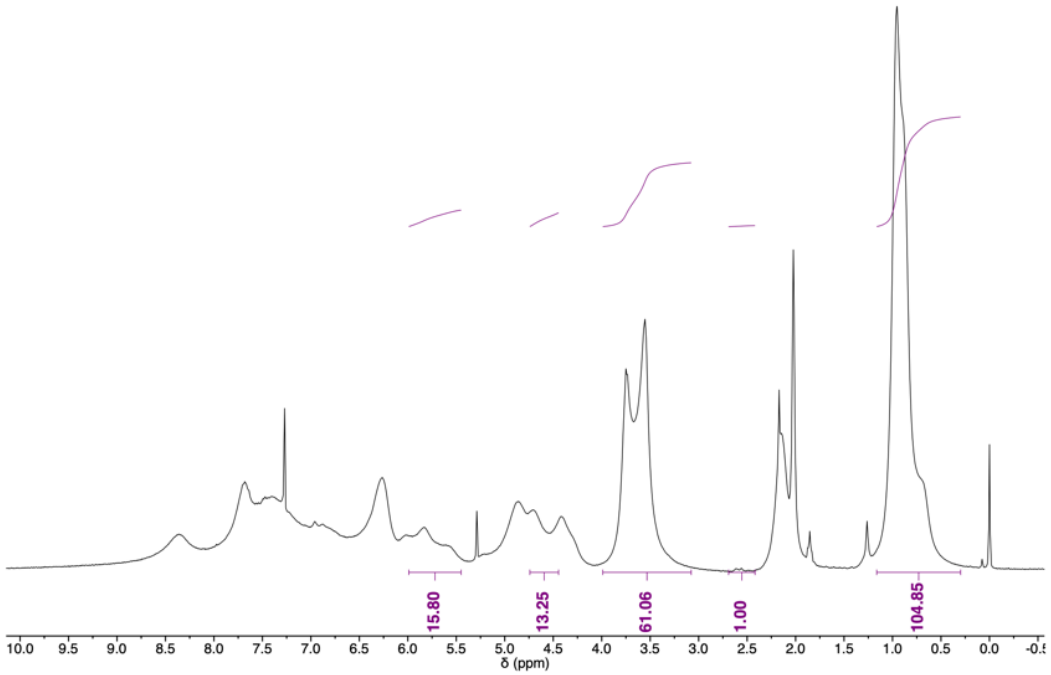


Figure S217. ^{1}H-NMR spectrum of oligo-(*S*)-**5** DP (GPC)= 60 ($CDCl_3$, 300 MHz).

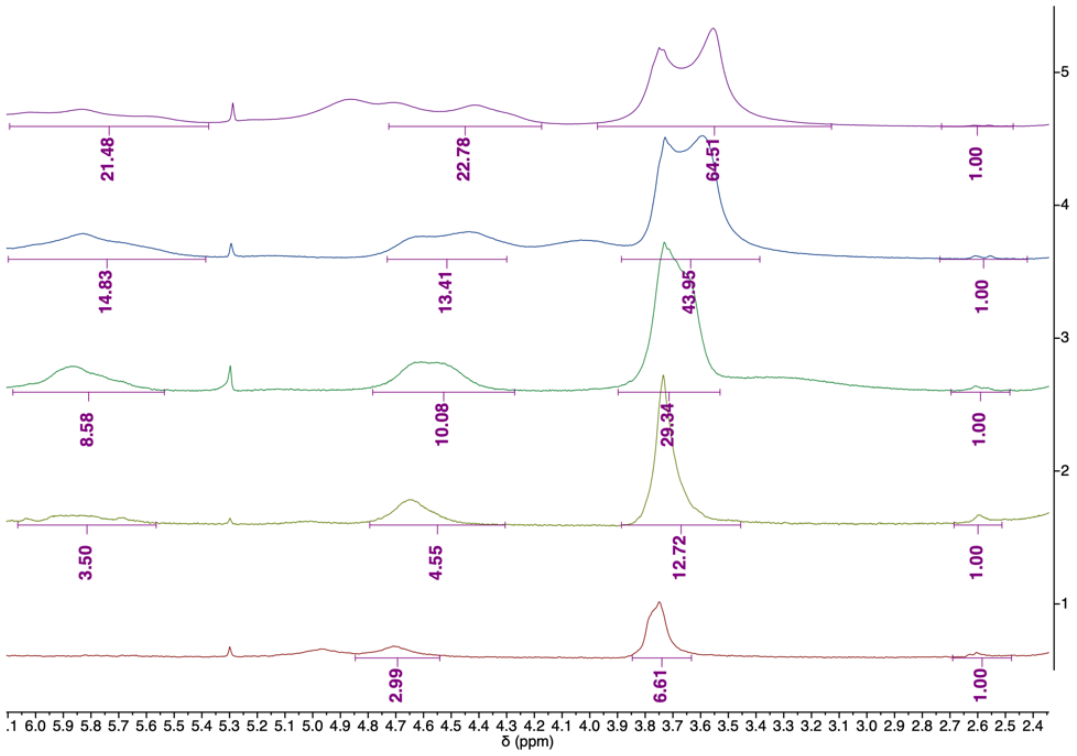


Figure S218. ^{1}H-NMR spectra of oligo-(*S*)-**5** DP (GPC)= 3, 7, 17, 31, and 60 ($CDCl_3$, 300 MHz).

5.6.5. ECD and UV-Vis spectra of oligomers

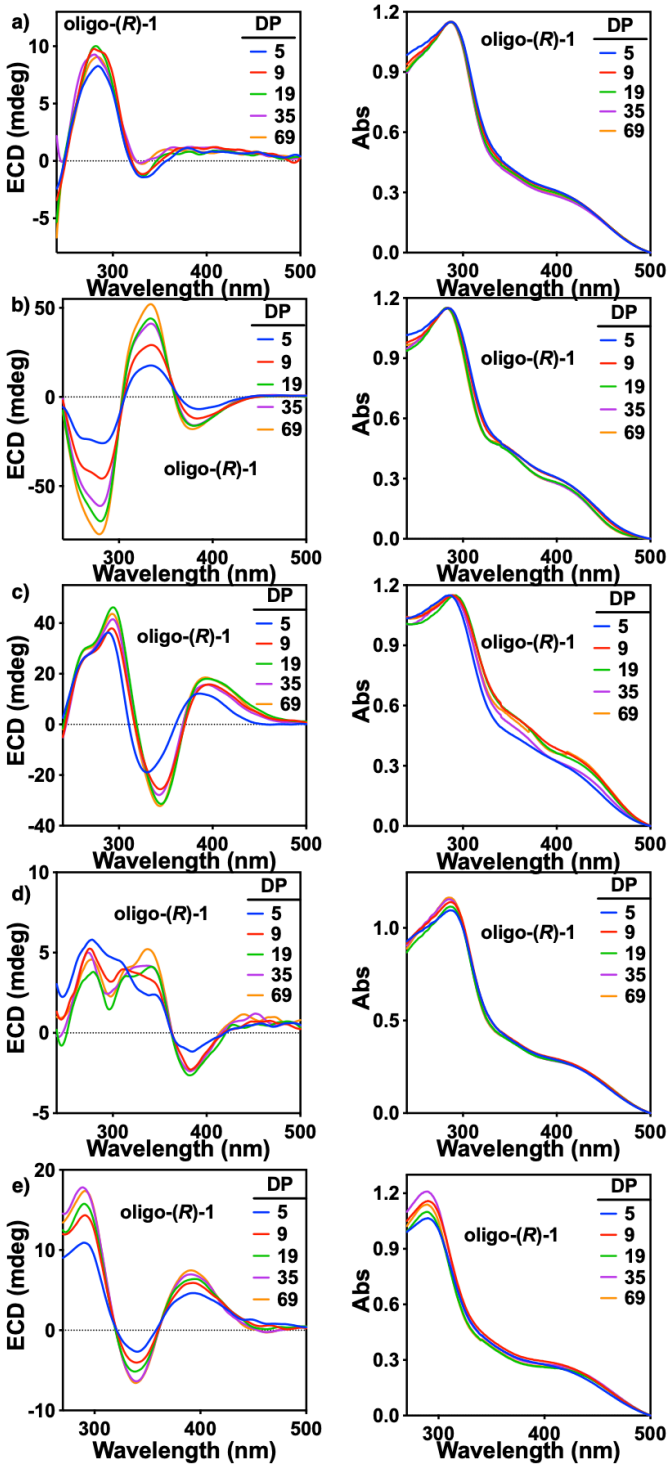


Figure S219. ECD and UV-Vis spectra (c=0.3mg/mL) of oligo-(*R*)-**1** (DP=5, 9, 19, 35, and 69 from GPC) in a) $CHCl_3$ b) $CHCl_3$ in presence of 0.1 equiv of $LiClO_4$ (10 mg·mL^{-1} MeOH) c) in presence of 0.1 equiv of $Ca(ClO_4)_2$ (10 mg·mL^{-1} MeOH) d) THF e) DMF.

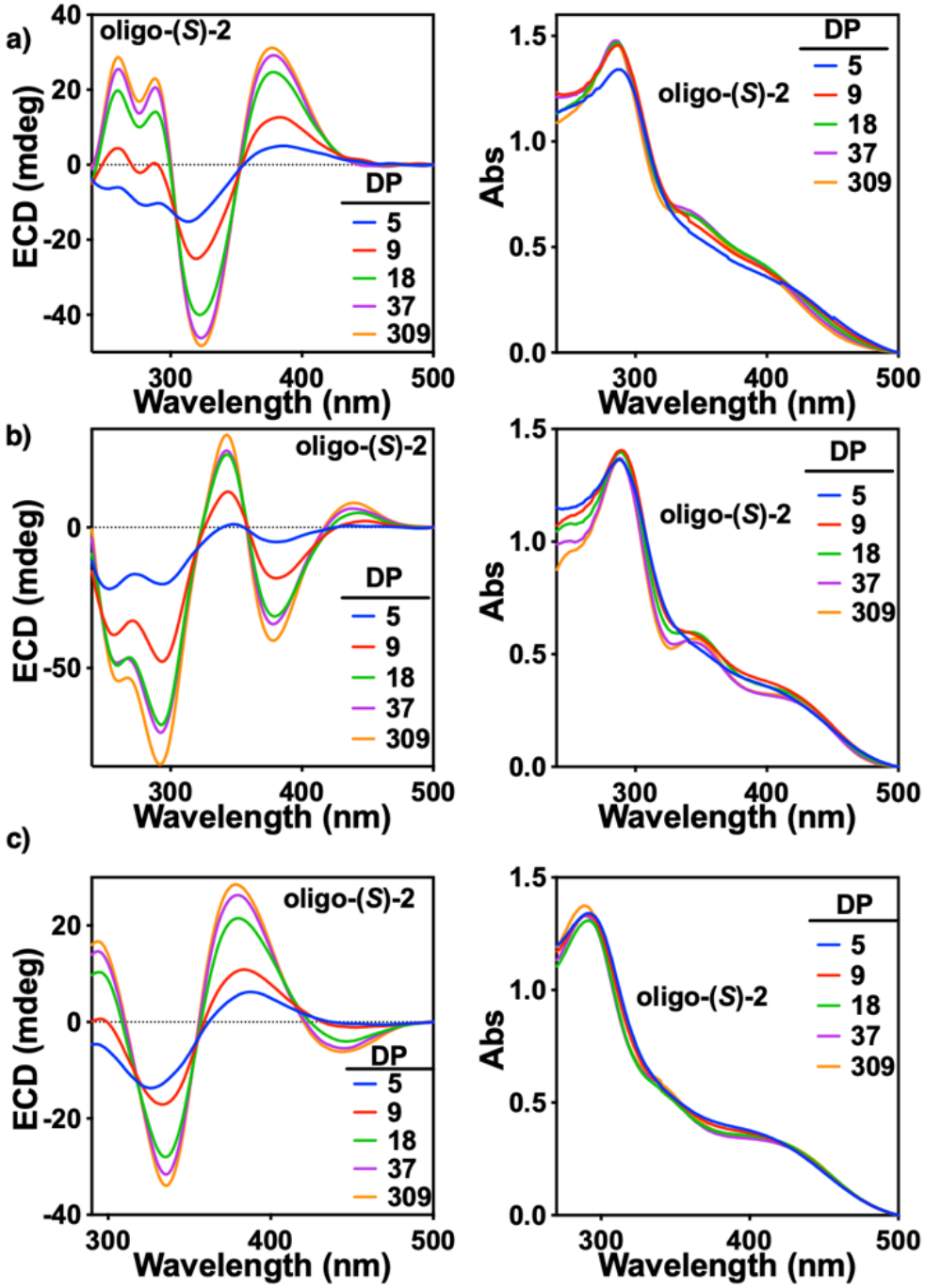


Figure S220. ECD and UV-Vis spectra (c=0.3mg/mL) of oligo-(*S*)-**2** (DP=5, 9, 18, 37, and 309 from GPC) in a) $CHCl_3$ b) THF c) DMF.

USC UNIVERSIDADE DE SANTIAGO DE COMPOSTELA

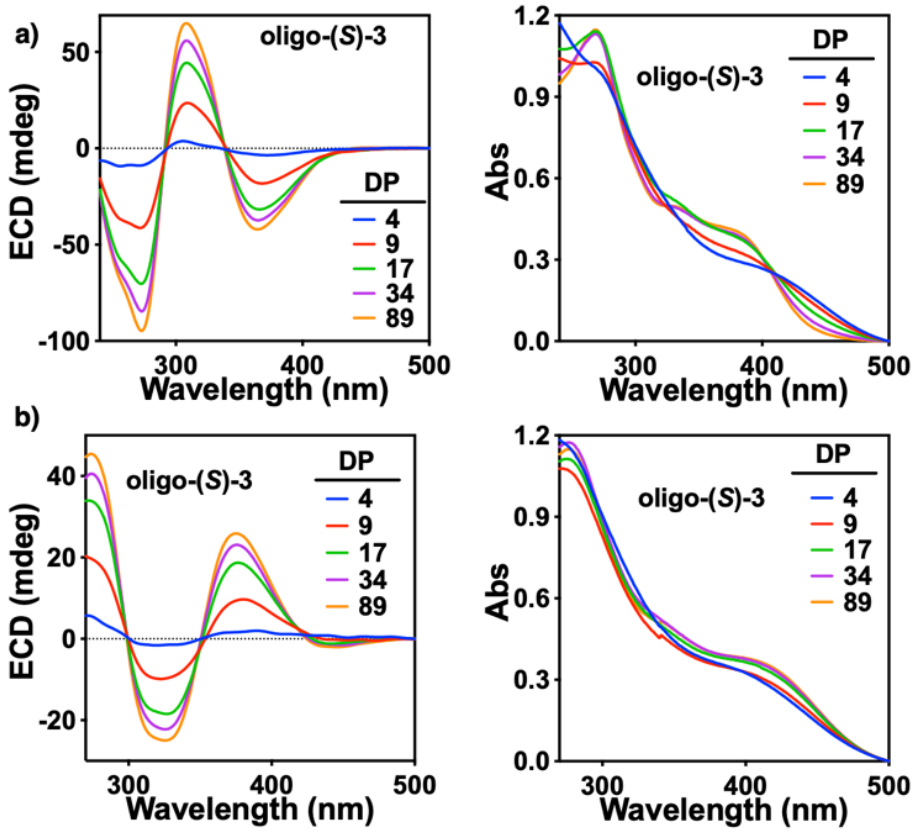


Figure S221. ECD and UV-Vis (c=0.3mg/mL) spectra of oligo-(*S*)-**3** (DP=4, 9, 17, 34, and 89 from GPC) in a) $CHCl_3$ b) DMF.

USC
UNIVERSIDADE DE SANTIAGO DE COMPOSTELA

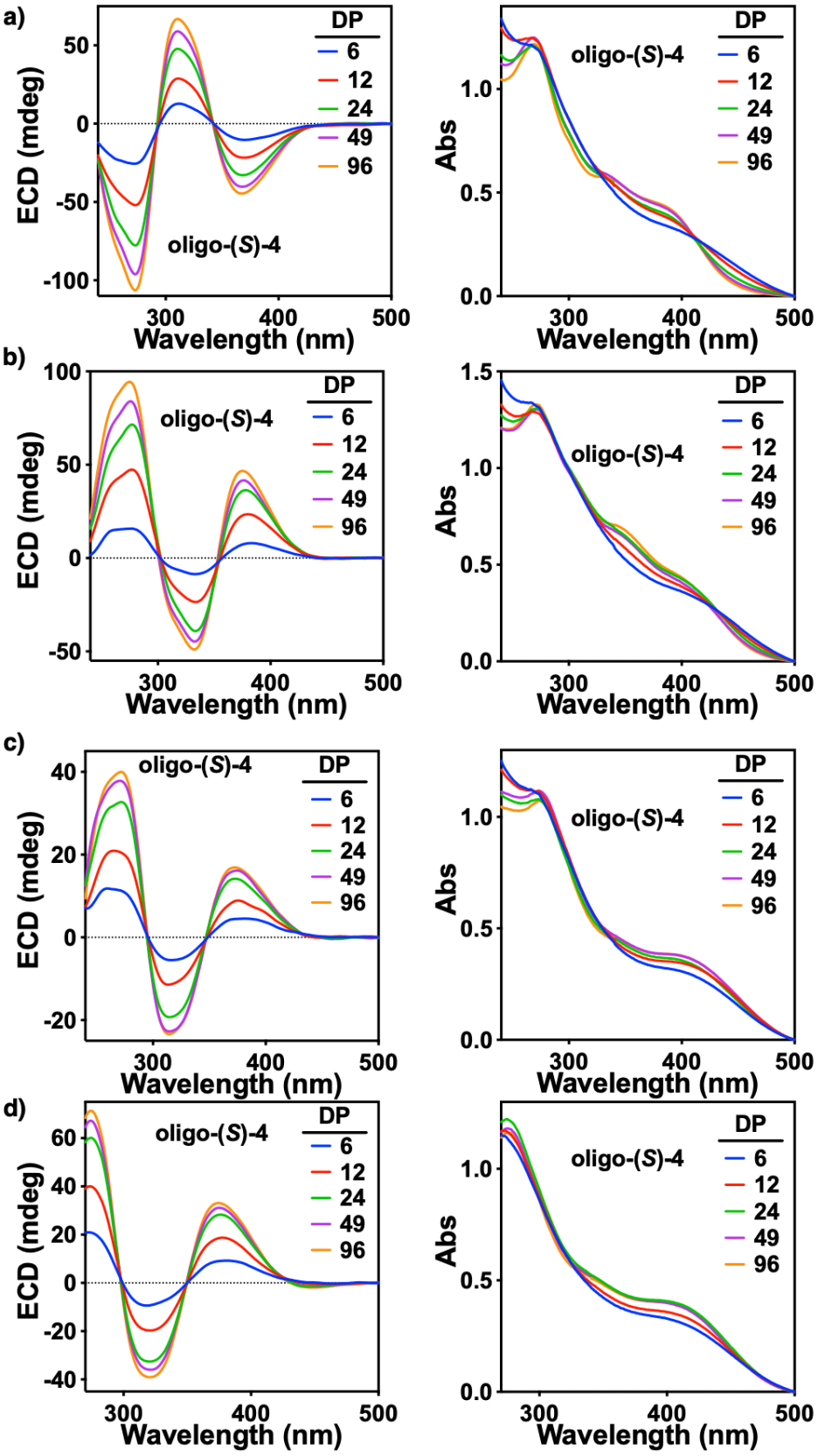


Figure S222. ECD and UV-Vis spectra (c=0.3mg/mL) of oligo-(*S*)-**4** (DP=6, 12, 24, 49, and 96 from GPC) in a) $CHCl_3$ b) $CHCl_3$ in presence of 0.5 equiv of $LiClO_4$ (10 mg·mL^{-1} MeOH) c) THF d) DMF.

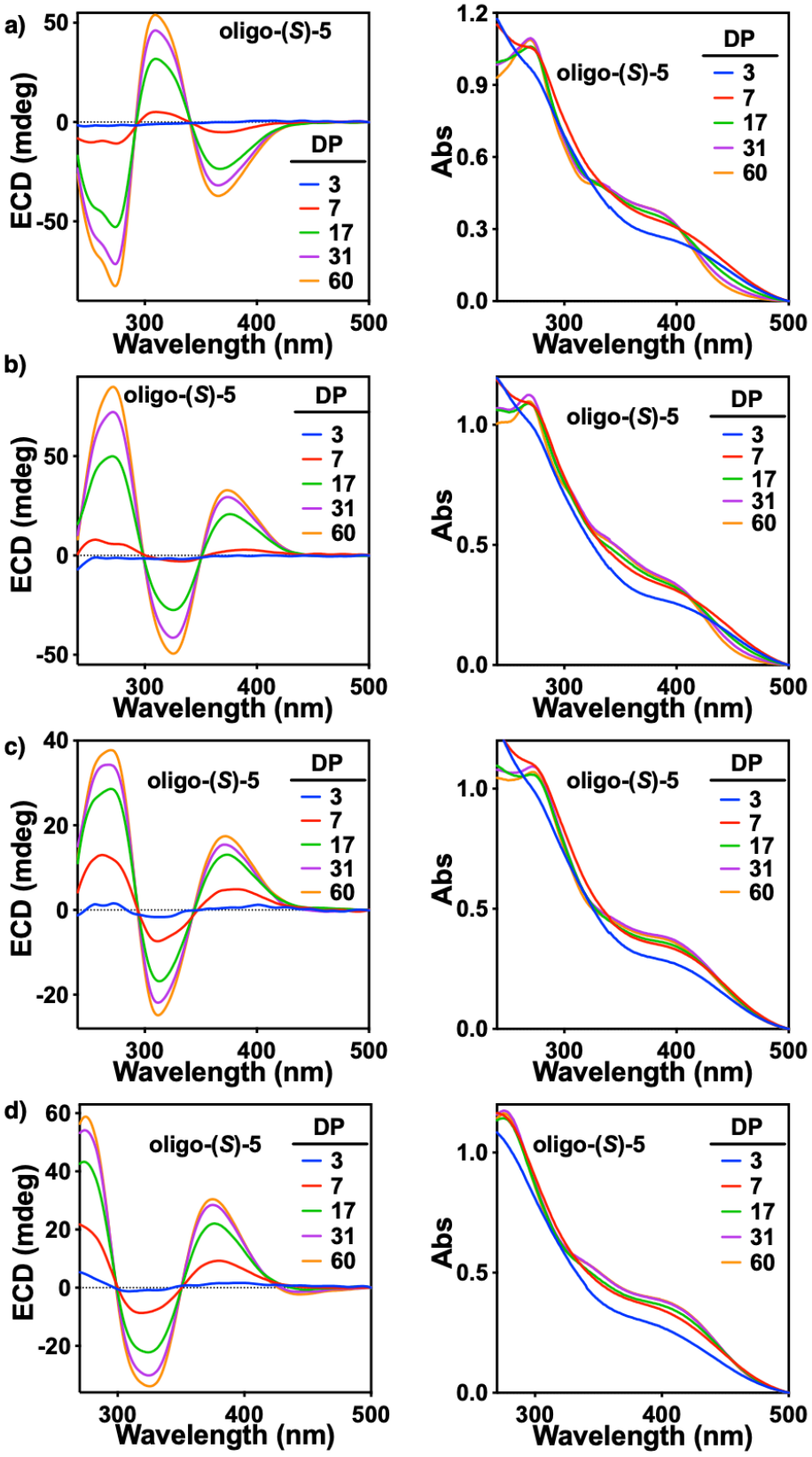


Figure S223. ECD and UV-Vis spectra (c=0.3mg/mL) of oligo-(*S*)-**5** (DP=3, 7, 17, 31, and 60 from GPC) in a) $CHCl_3$ b) $CHCl_3$ in presence of 0.5 equiv of $LiClO_4$ (10 mg·mL^{-1} MeOH) c) THF d) DMF.

USC DE SANTIAGO DE COMPOSTELA

5.6.6. Experimental g-value and Ising model fit

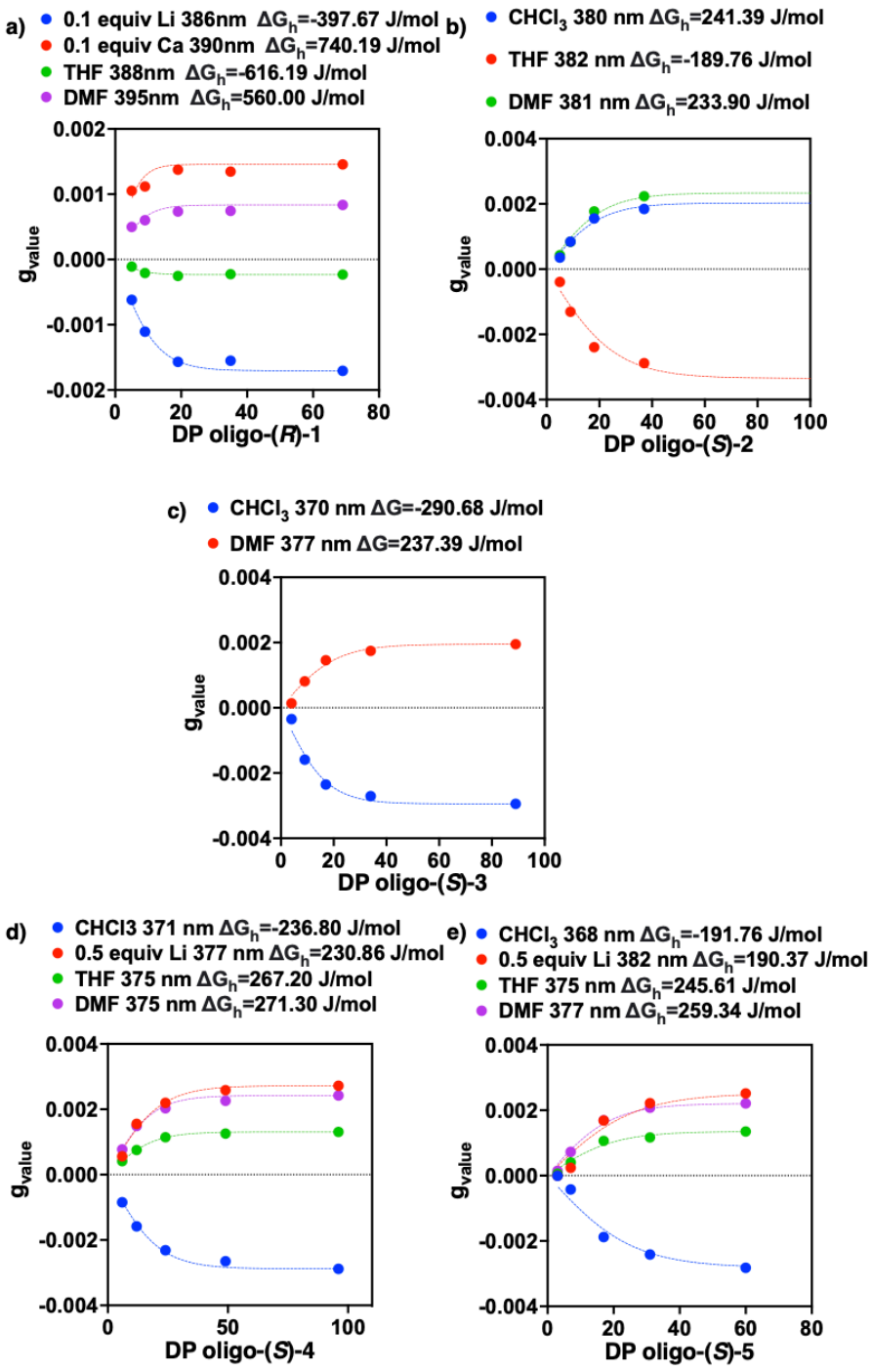


Figure S224. g_{value} calculated at maximum absorbance of the polyenic backbone and the ΔG_h from the fitting of the Ising model described for short polymers dependent on the N (DP from GPC) at 293 K with g_{max} from the g_{value} of the bigger oligomer in each solvent for a) oligo-(*R*)-**1** in $CHCl_3$ in presence of 0.1 equiv of $LiClO_4$ or $Ca(ClO_4)_2$ (10 mg·mL^{-1} MeOH), THF, and DMF b) oligo-(*S*)-**2** $CHCl_3$, THF, and DMF c) oligo-(*S*)-**3** $CHCl_3$ and DMF d) oligo-(*S*)-**4** in $CHCl_3$ in presence of 0.5 equiv of $LiClO_4$ (10 mg·mL^{-1} MeOH), THF, and DMF e) oligo-(*S*)-**5** in $CHCl_3$ in presence of 0.5 equiv of $LiClO_4$ (10 mg·mL^{-1} MeOH), THF, and DMF.

USC UNIVERSIDADE DE SANTIAGO DE COMPOSTELA

5.6.7. Irradiation PEC Studies

The oligomers were irradiated with light filtered using a short pass filter (Vis 550 nm, 25 dia.) for all the DPs. Using the $t_{ECD50\%}$, we can extract the %SSE. We represented %SSE over the DP and the number of terminal parts. To obtain the terminals, we first obtained the molarity of each sample prepared at 0.3 mg/mL, knowing the molar weight from GPC for each DP of each oligomer. Then, we multiplied by Avogadro's number to obtain the number of oligomers and multiplied by two, as these oligomers or polymers have only 2 terminal parts.

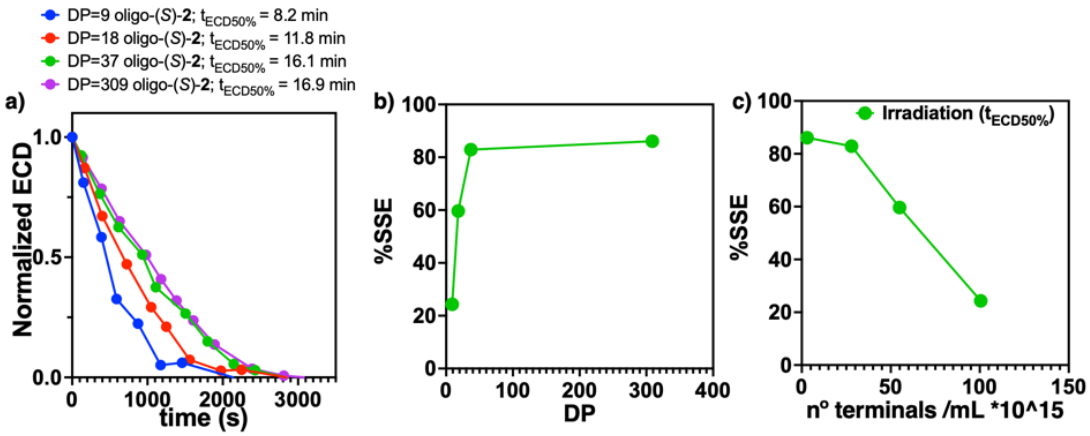


Figure S225. a) Normalized ECD at 380 nm for each oligo-(*S*)-**2** (DP 9, 18, 37, and 309) in $CHCl_3$ (c=0.3mg/mL) as a function of time while being irradiated with the lamp b) %SSE calculated using $t_{ECD50\%}$ as a function of DP. c) %SSE as a function of the concentration of terminal numbers.

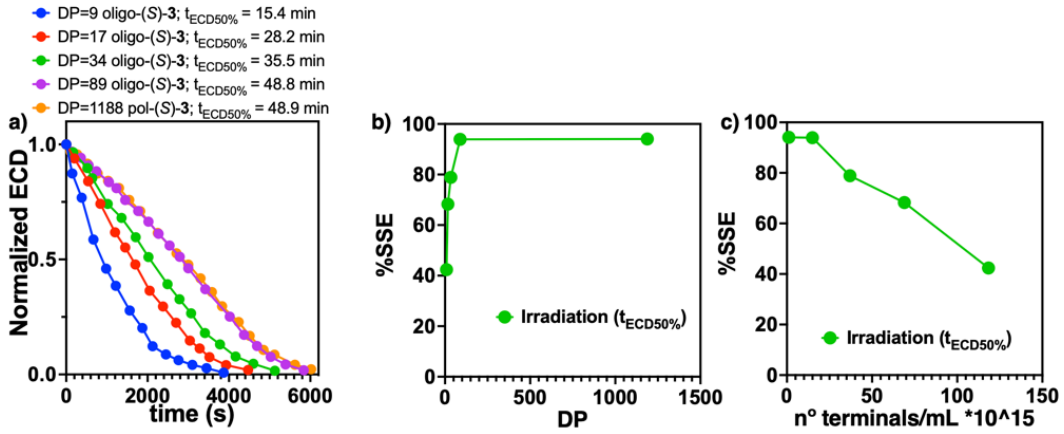


Figure S226. a) Normalized ECD at 368 nm for each oligo-(*S*)-**3** (DP 9, 17, 34, and 89) and poly-(*S*)-**3** (DP=1188) in $CHCl_3$ (c=0.3mg/mL) as a function of time while being irradiated with the lamp b) %SSE calculated using $t_{ECD50\%}$ as a function of DP. c) %SSE as a function of the concentration of terminal numbers.

USC UNIVERSIDADE DE SANTIAGO DE COMPOSTELA

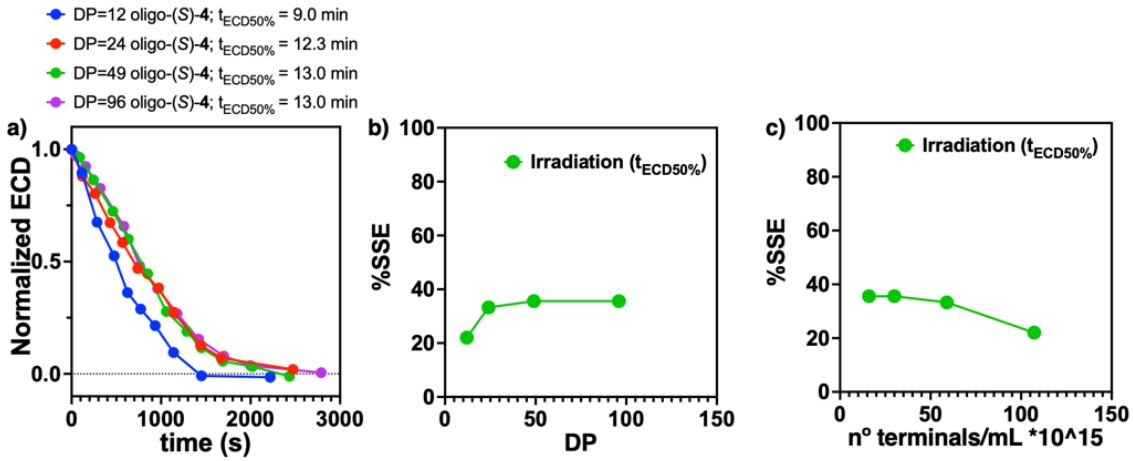


Figure S227. a) Normalized ECD at 382 nm for each oligo-(*S*)-**4** (DP 12, 24, 49, and 96) in THF (c=0.3mg/mL) as a function of time while being irradiated with the lamp b) %SSE calculated using $t_{ECD50\%}$ as a function of DP. c) %SSE as a function of the concentration of terminal numbers.

USC UNIVERSIDADE DE SANTIAGO DE COMPOSTELA

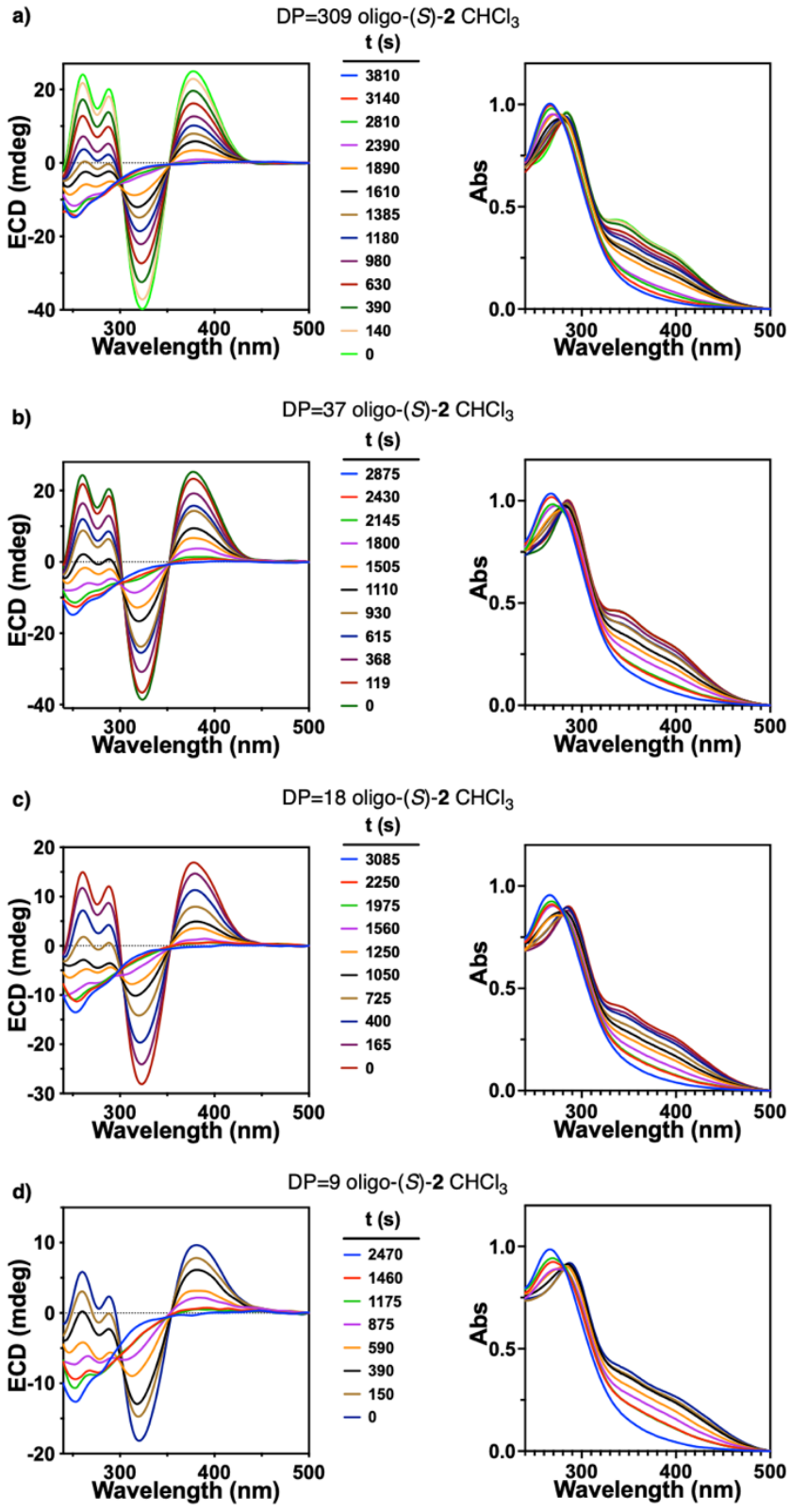


Figure S228. ECD and UV-Vis spectra for each oligo-(*S*)-**2** (DP 309, 37, 18, and 9) in $CHCl_3$ (c=0.3mg/mL) as a function of time while being irradiated with the lamp.

USC UNIVERSIDADE DE SANTIAGO DE COMPOSTELA

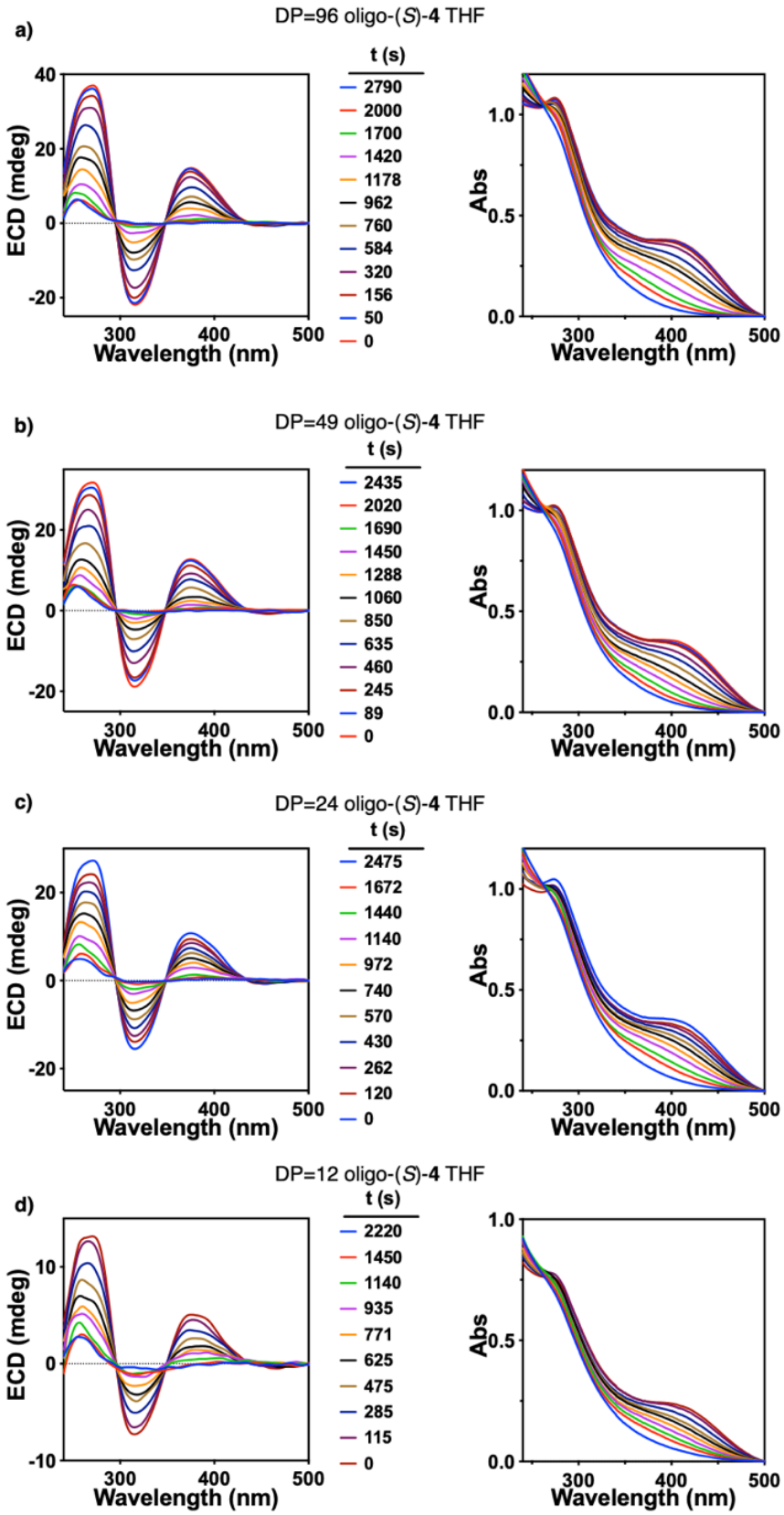


Figure S229. ECD and UV-Vis spectra for each oligo-(*S*)-**4** (DP 12, 24, 49, and 96) in THF (c=0.3mg/mL) as a function of time while being irradiated with the lamp.

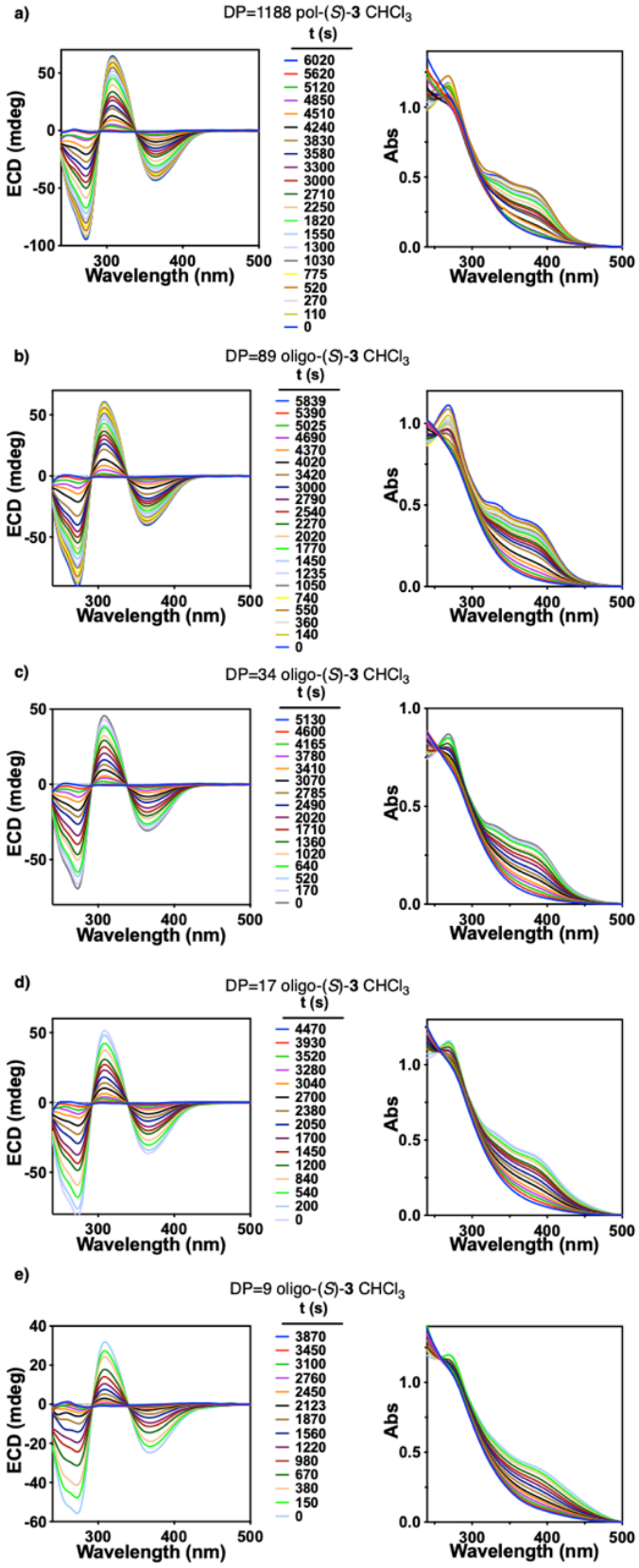


Figure S230. ECD and UV-Vis spectra for each oligo-(*S*)-**3** (DP 9, 17, 34, and 89) and poly-(*S*)-**3** (DP=1188) in $CHCl_3$ (c=0.3mg/mL) as a function of time while being irradiated with the lamp.

5.6.8. Color dependence with the DP in Anilides

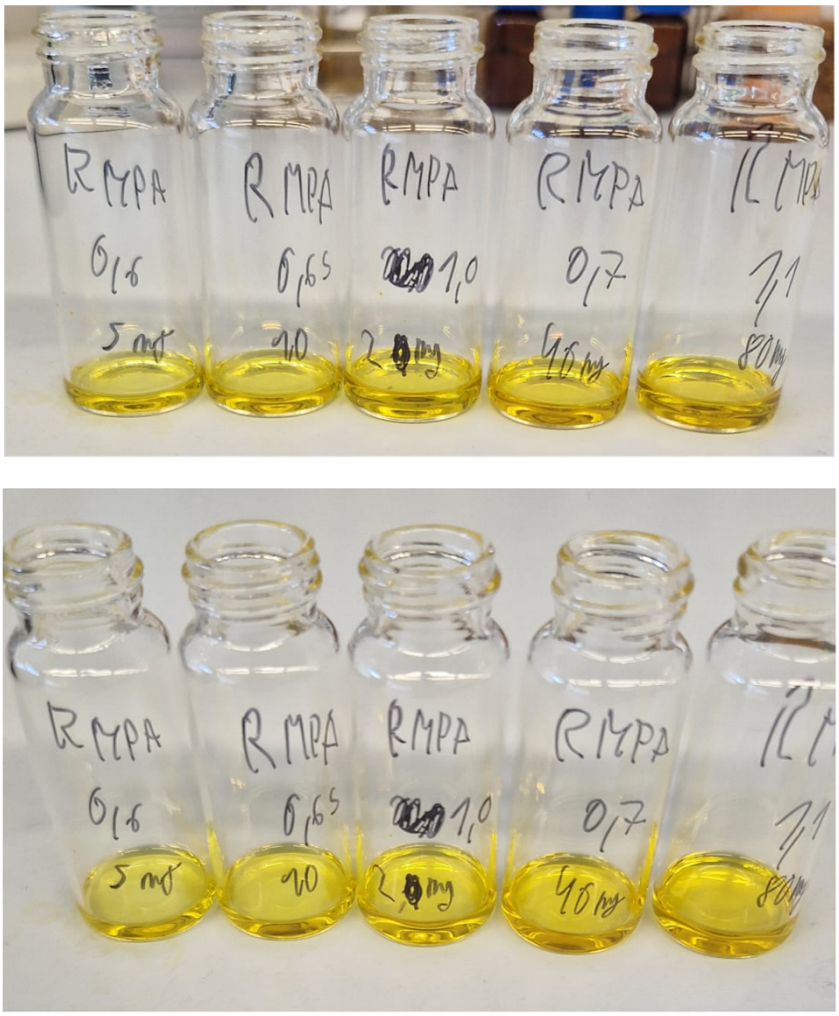
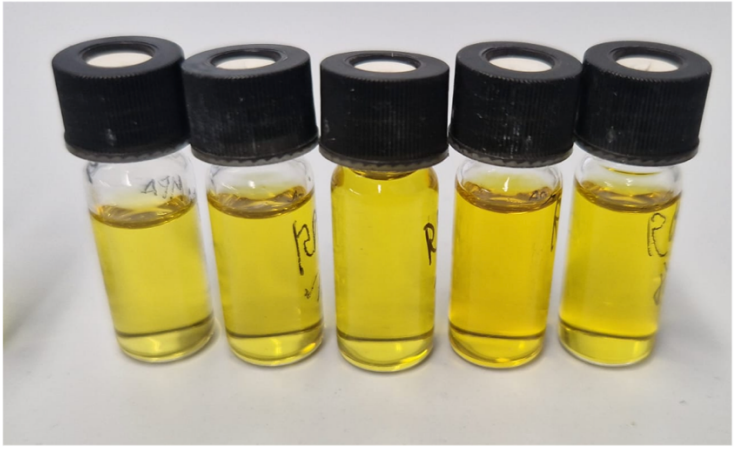


Figure S231. oligo-(*R*)-**1** (DP=5, 9, 19, 35, and 69 from GPC, left to right) in $CHCl_3$ (c=1.0 mg/mL).



USC UNIVERSIDADE

Figure S232. oligo-(*R*)-**1** (DP=5, 9, 19, 35, and 69 from GPC, left to right) in THF (c=0.5 mg/mL).

5.6.9. Color and morphology dependence with the DP in Benzamides

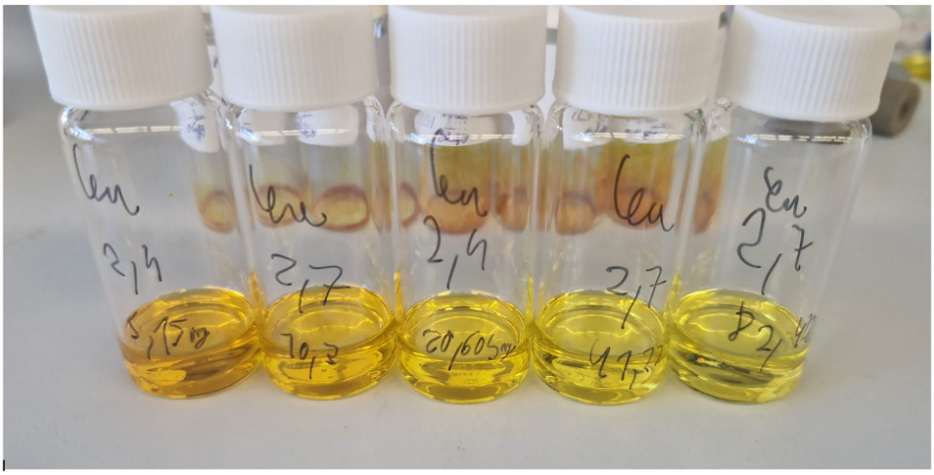


Figure S233. oligo-(*S*)-**3** (DP=4, 9, 17, 34, and 89 from GPC, left to right) in $CHCl_3$ (c=1.0 mg/mL).

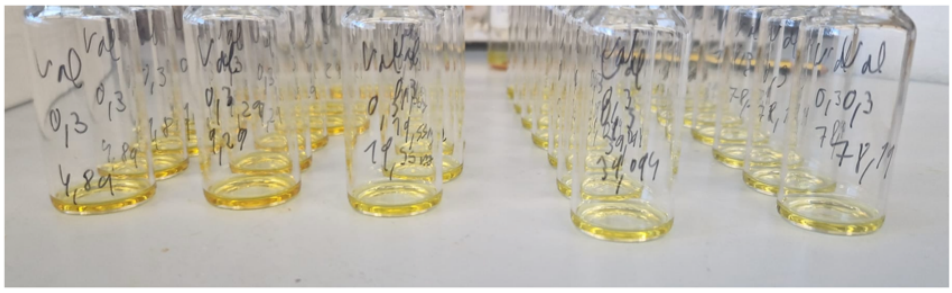


Figure S234. oligo-(*S*)-**5** (DP=3, 7, 17, 31, and 60 from GPC, left to right) in $CHCl_3$ (c=1.0 mg/mL).

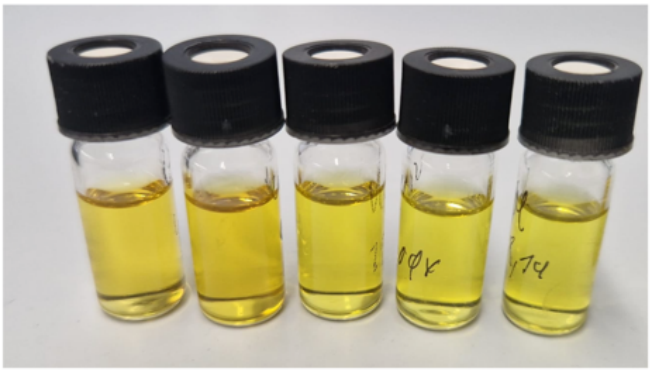


Figure S235. oligo-(*S*)-**5** (DP=3, 7, 17, 31, and 60 from GPC, left to right) in THF (c=0.5 mg/mL).

USC UNIVERSIDADE DE SANTIAGO DE COMPOSTELA

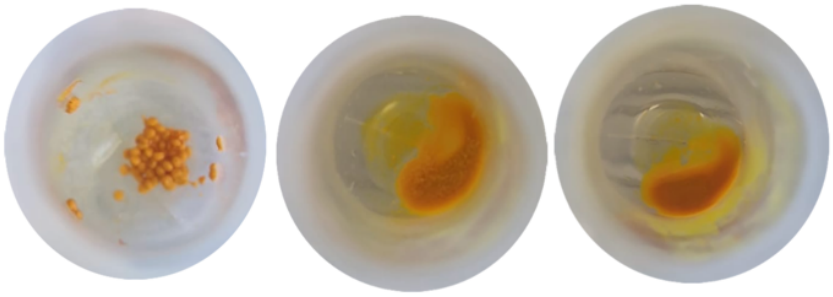


Figure S236. Photographs of oligo-(*S*)-**4** (DP=96, 49, and 12 from GPC) precipitated in Hexane.

5.6.10. VT-ECD spectra of oligomers

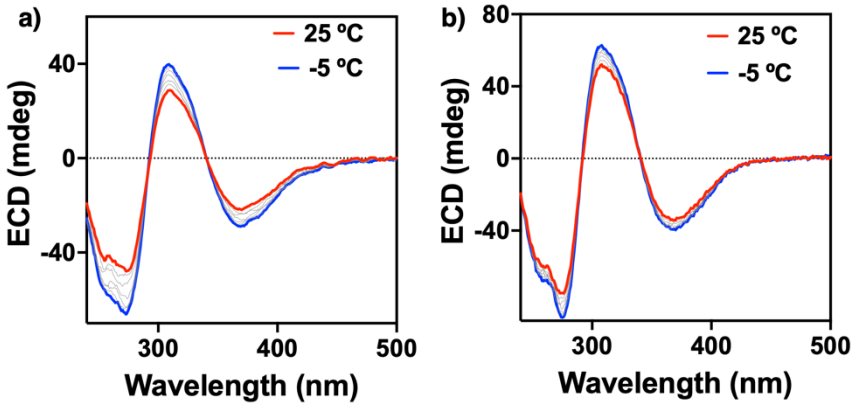


Figure S237. VT-ECD cooling spectra of oligo-(*S*)-**3** in $CHCl_3$ (c=0.3mg/mL) a) DP = 9 b) DP = 17.

USC
UNIVERSIDADE DE SANTIAGO DE COMPOSTELA

5.7. Experimental Section and Methodology Chapter 3.7.

5.7.1. Materials and methods

Chemicals. Commercially available chemicals have been used as delivered. Solvents were purchased as reagent grade and distilled if necessary. Anhydrous solvents were either purchased as ultra-dry solvent from Acros Organics® or received from solvent purification system. For the coupling and polymerization reactions, dry THF was obtained from MBRAUN SPS 800 solvent purification system. Water was purified by Millipore water purification system. 1-Ethyl-3-(3-dimethylaminopropyl)carbodiimide (EDC), hydroxybenzotriazole (HOBt), (*L*)-phenylalanine methyl ester hydrochloride, (*L*)-valine methyl ester hydrochloride, (*L*)-isoleucine methyl ester hydrochloride, (*L*)-leucine methyl ester hydrochloride, rhodium norbornadiene chloride dimer $[Rh(nbd)Cl]_2$, diisopropyltriethylamine (DIPEA), potassium hydroxide (KOH), triethylamine (TEA, 99%), glacial acetic acid, triphenylphosphine (PPh_3), and diphenylacetylene were purchased from Aldrich. 4-(Methylthio)phenylboronic acid was purchased from BLDpharm.

Instrumentations and Characterizations. NMR experiments were carried out in a Varian Inova 300 (300 MHz resonance 1H). Size exclusion chromatography studies were performed on Alliance 2695 HPLC System (Waters) liquid chromatography system equipped with a UV 2489 detector (Waters). The samples were eluted by three Phenogel columns connected to each other with stationary phases of 10^3, 10^4, and 10^5 Amstrong and packed with a solid support of a cross-linked styrene and *p*-divinylbenzene copolymer. CD and UV measurements were registered in a Jasco-720 spectropolarimeter and a Jasco-730 spectrophotometer respectively. Cuvettes of 1 mm were used unless indicated cases with 1 cm. Irradiation experiments were done in an Asahi Spectra Xenon light model MAX-303. The light was filtered using a short pass filter / Vis 550 nm 25 dia.

5.7.2. Monomers and polymers

USC UNIVERSIDADE

The preparation of monomers (*S*)-**1**, (*S*)-**2**, (*S*)-**3**, (*S*)-**4** can be found in references.[169,269]

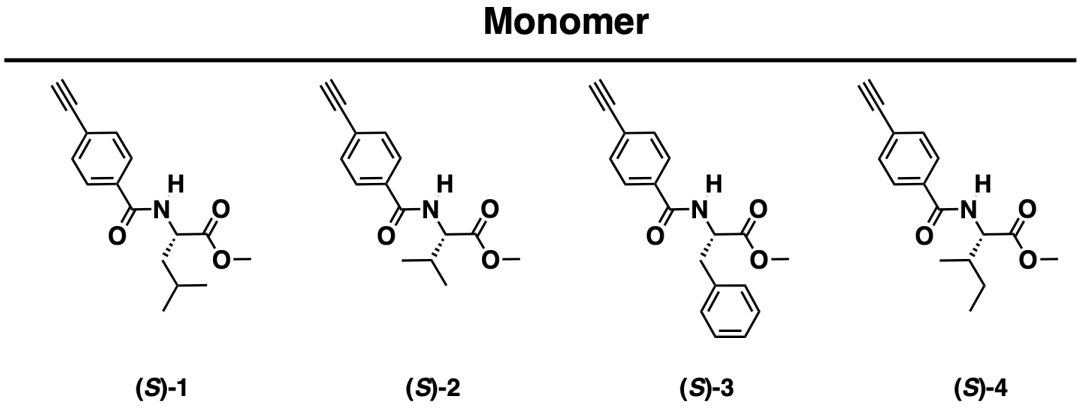


Figure S238. Structure of monomers (*S*)-**1**, (*S*)-**2**, (*S*)-**3**, and (*S*)-**4**.

5.7.3. Synthesis of polymers

The general procedure to obtain the polymer was already described.[169,269] The polymers were synthesized in a reaction flask (sealed ampoule) that was dried under vacuum and flushed with argon for three times before monomers were added as a solid. Then, the flask was evacuated on a vacuum line and flushed with dry argon (three times). Dry THF was added with a syringe and then, Et_3N (5 μL). A solution of rhodium norbornadiene chloride dimer, $[Rh(nbd)Cl]_2$, in THF was added at 30 ºC. The reaction mixture was stirred at 30 ºC for 24 h. Next, the resulting polymers were diluted in CH_2Cl_2 and they were precipitated in a large amount of diethyl ether, centrifuged (twice) and re-precipitated in hexane and centrifuged again.

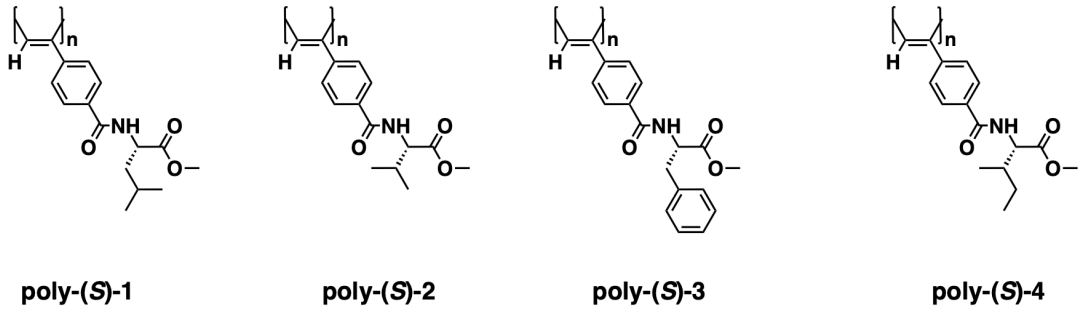


Figure S239. Structure of poly-(*S*)-**1**, poly-(*S*)-**2**, poly-(*S*)-**3**, and poly-(*S*)-**4**.

USC UNIVERSIDADE DE SANTIAGO DE COMPOSTELA

Table S34. Monomer amount, catalyst, and Et_3N in the polymerization.

Compound	Mass/mg	THF/μL	Et_3N/μL	Catalyst/mg	Yield %
Poly-(*S*)-**1**	82	400	5	1.2	95
Poly-(*S*)-**2**	78	400	5	1.2	93
Poly-(*S*)-**3**	92	400	5	1.2	82
Poly-(*S*)-**4**	82	400	5	1.2	86

Table S35. GPC M_n, M_w, Đ from GPC, and calculated DP from M_n for the polymers.

Compound	M_n (kDa)	M_w (kDa)	Đ	DP
Poly-(*S*)-**1**	730	1181	1.62	2675
Poly-(*S*)-**2**	113	135	1.20	435
Poly-(*S*)-**3**	349	539	1.54	1192
Poly-(*S*)-**4**	72	108	1.50	312

5.7.4. Synthesis of oligomers

A solution of $[Rh(nbd)Cl]_2$ (18.4 mg, 0.04 mmol), 4-(Methylthio)phenylboronic acid (20.25 mg, 0.12 mmol), and diphenylacetylene (57.6 mg, 0.32 mmol) in THF (0.4 mL) was cooled to 0 °C. An aqueous solution of KOH (50% (w/v), 23 μL, 0.20 mmol) was added to this yellow solution, and the resultant brown solution was stirred for 5 min at 0 °C. After that, PPh_3 (63.0 mg, 0.24 mmol) was rapidly added, and the solution was stirred for 2 min at 0 °C. Oligomerization was performed by adding 20 μL of this solution (catalyst) to another solution of monomer (mass and [monomer]/[Rh] feed ratio in Table S36 and Table S37) in THF (0.40 mL). After stirring for 2 h at 30 °C the oligomerization reaction was stopped by adding acetic acid (a few drops) to the oligomerization mixture. The resultant mixture was precipitated in a large amount of hexane and centrifuged (Table S36 and Table S37).

Control oligomer size is established by fine-tuning the [monomer]/[Rh] feed ratio during the synthesis process. Gel Permeation Chromatography (GPC) was employed to

USC DE SANTIAGO DE COMPOSTELA

validate the degree of polymerization, given the remarkable monodispersity exhibited by these oligomers in terms of molecular weight distribution. M_n, derived from GPC analysis using polystyrene calibration standards, serves as a dependable indicator of oligomer weight. To calculate precisely the oligomer size, we subtract the initiator's weight contribution from M_n and subsequently divide the resulting Mn by the molar weight of the monomer (Table S36 and Table S37). The initiator, in this case, consists of 4-(Methylthio)phenyl (124 Da) with 2 or 3 diphenylacetylene units. To achieve a conservative estimate, we consider an average of 2.5 diphenylacetylene units (2.5 x 178 Da) in the initiator. Therefore, the calculation is performed as follows: DP = M_n – [124 Da + (2.5 x 178 Da)] / Mw of the monomer.

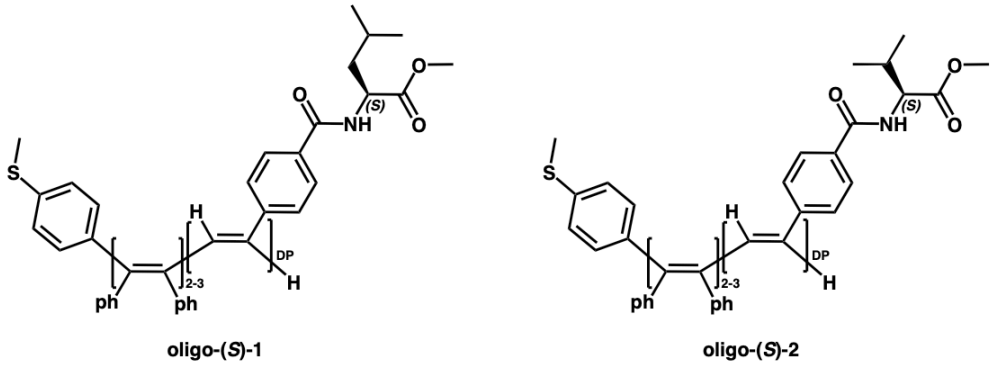


Figure S240. Structures of the oligomer series oligo-(*S*)-**1** and oligo-(*S*)-**2**

Table S36. Amount of monomer (*S*)-**1**, [monomer]/[Rh] feed ratio and yield of the oligomerizations of oligo-(*S*)-**3**. M_n, M_w, Đ from GPC, and calculated DP from M_n.

Mass (mg)	[(*S*)-1]/[Rh]	Yield %	M_n (kDa)	M_w (kDa)	Đ	DP
5.15	4.71	97	1.69	1.76	1.04	4.1
10.3	9.43	96	2.98	3.06	1.03	8.8
20.6	18.9	96	5.18	5.36	1.03	16.9
41.2	37.7	96	9.92	10.1	1.02	34.2
82.4	75.4	93	24.9	25.2	1.01	89.2

USC UNIVERSIDADE DE SANTIAGO DE COMPOSTELA

Table S37. Amount of monomer (*S*)-**2**, [monomer]/[Rh] feed ratio and yield of the oligomerizations of oligo-(*S*)-**3**. M_n, M_w, Đ from GPC, and calculated DP from M_n.

Mass (mg)	[(*S*)-2]/[Rh]	Yield %	M_n (kDa)	M_w (kDa)	Đ	DP
4.89	4.71	91	1.37	1.42	1.03	3.1
9.29	9.43	97	2.30	2.47	1.03	7.0
19.6	18.9	95	4.87	5.01	1.02	16.6
39.1	37.7	97	8.54	8.71	1.01	30.8
78.2	75.4	98	16.2	16.3	1.02	60.2

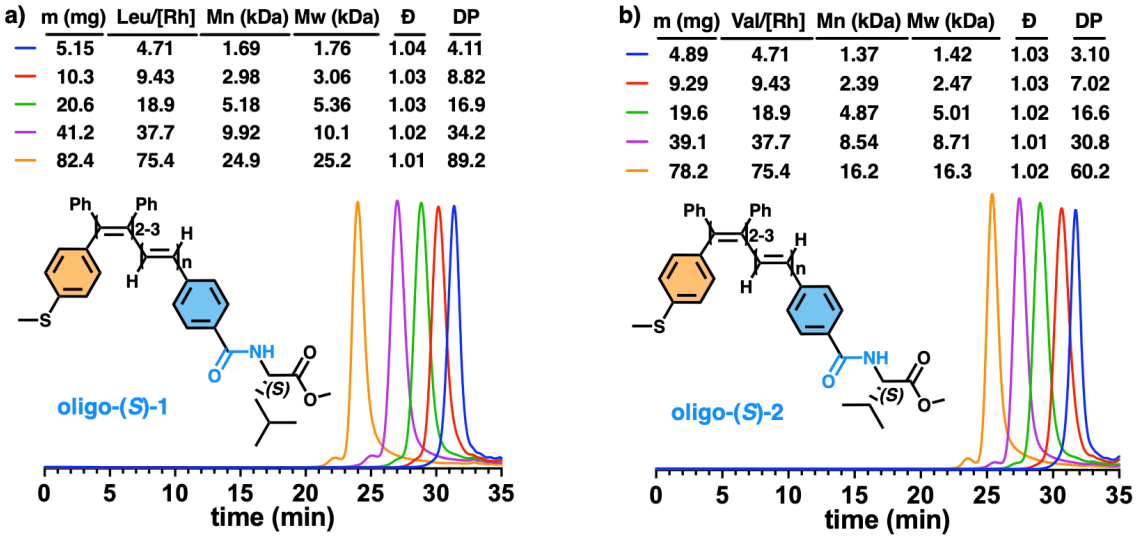


Figure S241. GPC profiles of oligos with different degrees of polymerization (DPs) for a) oligo-(*S*)-**1** and b) oligo-(*S*)-**2**.

USC UNIVERSIDADE DE SANTIAGO DE COMPOSTELA

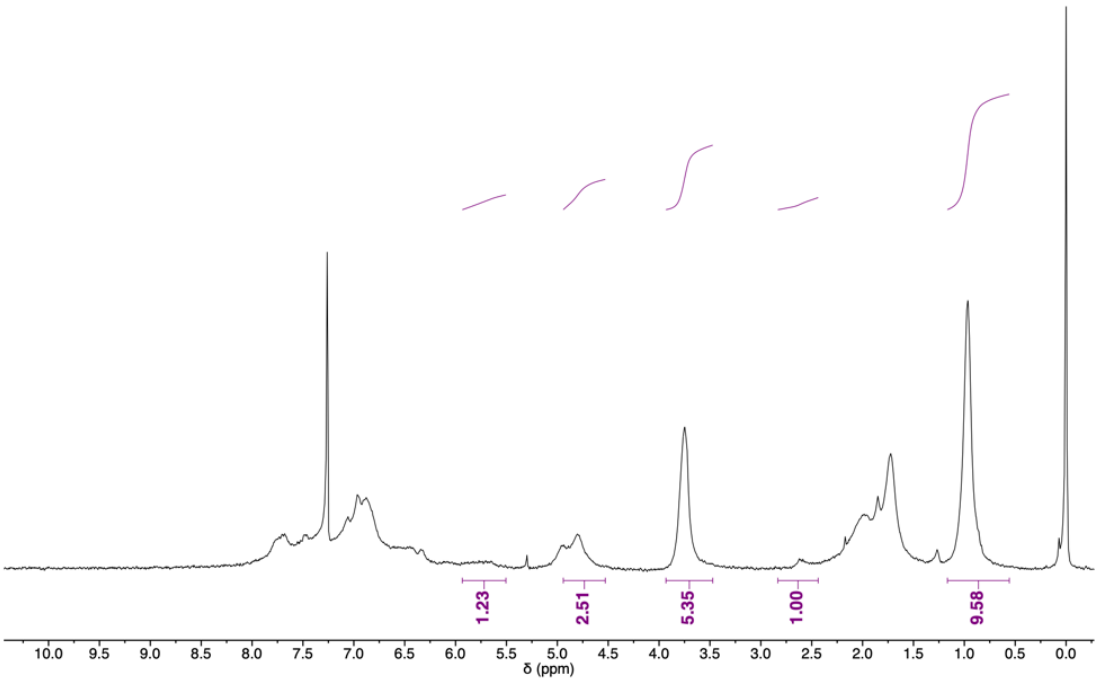


Figure S242. ^{1}H-NMR spectrum of oligo-(*S*)-**1** DP (GPC)= 4 ($CDCl_3$, 300 MHz).

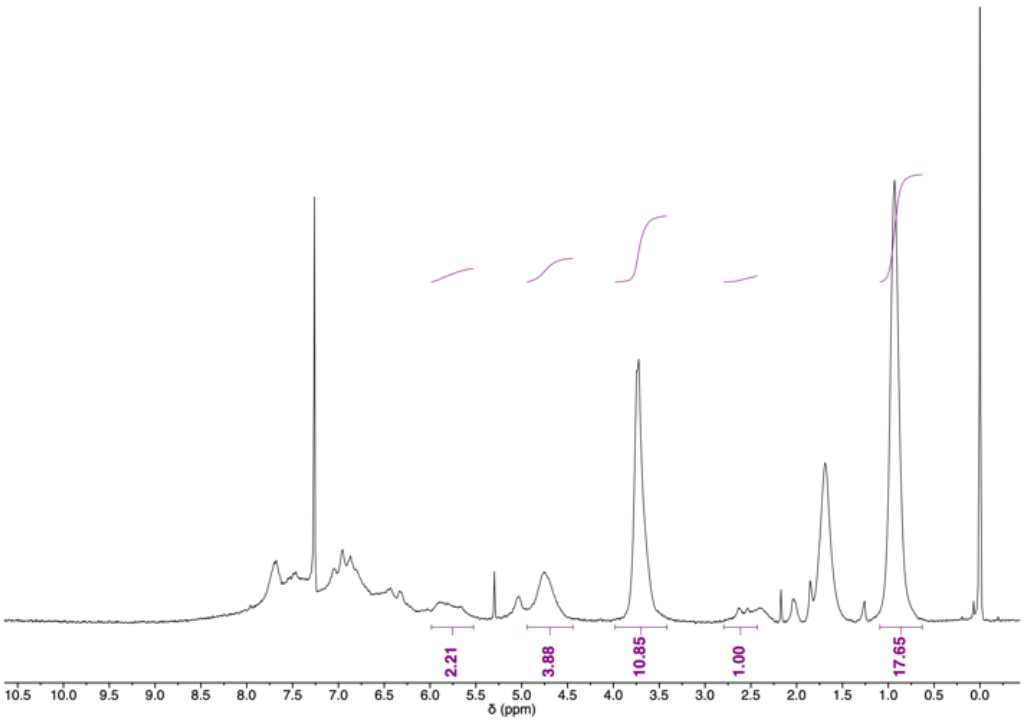


Figure S243. ^{1}H-NMR spectrum of oligo-(*S*)-**1** DP (GPC)= 9 ($CDCl_3$, 300 MHz).

USC
UNIVERSIDADE DE SANTIAGO DE COMPOSTELA

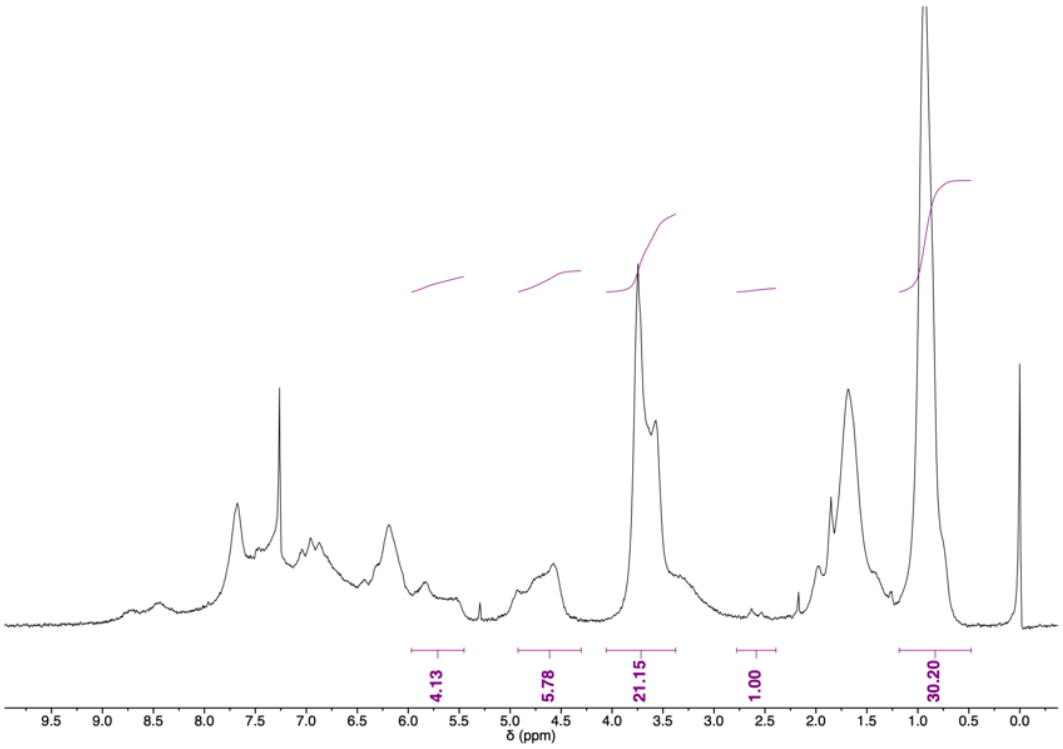


Figure S244. ^{1}H-NMR spectrum of oligo-(*S*)-**1** DP (GPC)= 17 ($CDCl_3$, 300 MHz).

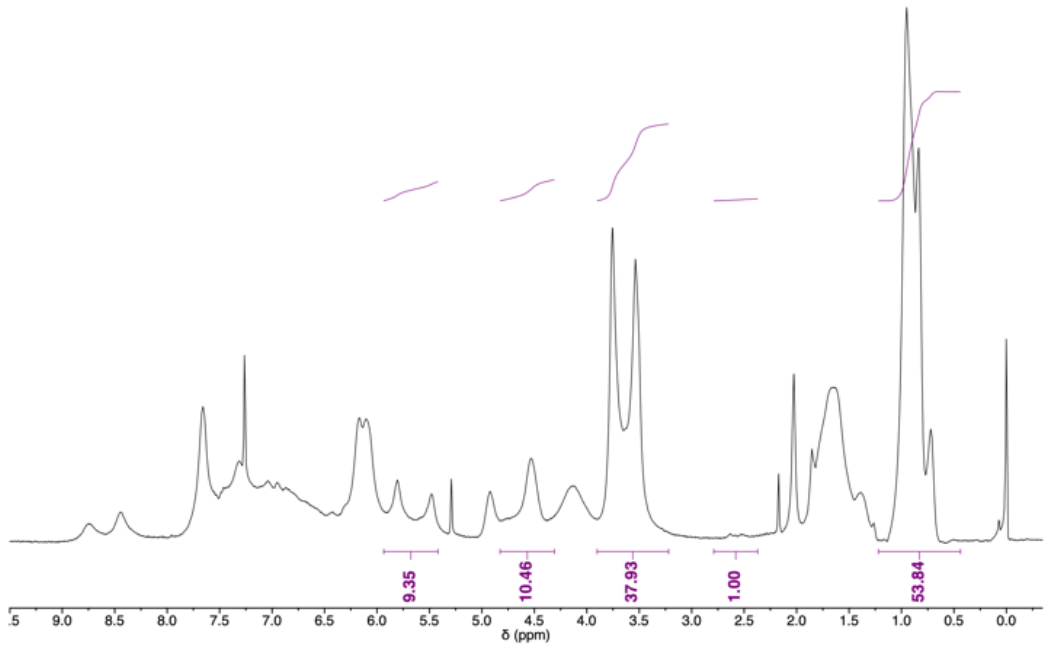


Figure S245. ^{1}H-NMR spectrum of oligo-(*S*)-**1** DP (GPC)= 34 ($CDCl_3$, 300 MHz).

USC
UNIVERSIDADE DE SANTIAGO DE COMPOSTELA

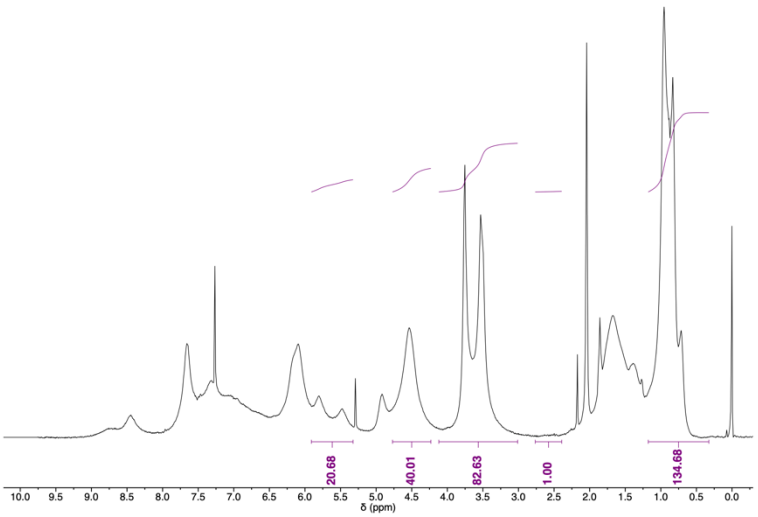


Figure S246. ^{1}H-NMR spectrum of oligo-(*S*)-**1** DP (GPC)= 89 ($CDCl_3$, 300 MHz).

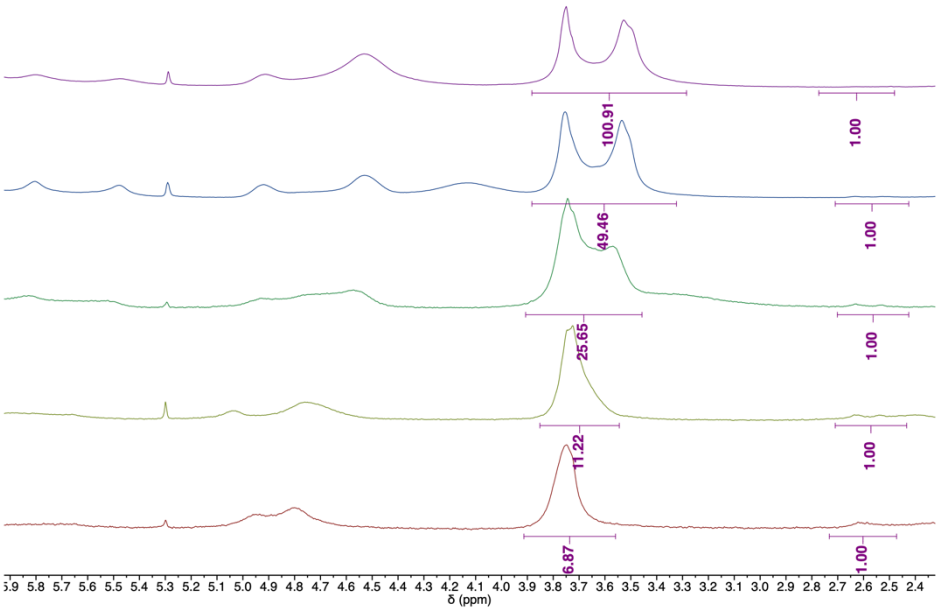


Figure S247. ^{1}H-NMR spectra of oligo-(*S*)-**1** DP (GPC)= 4, 9, 17, 34, and 89 ($CDCl_3$, 300 MHz).

USC
UNIVERSIDADE DE SANTIAGO DE COMPOSTELA

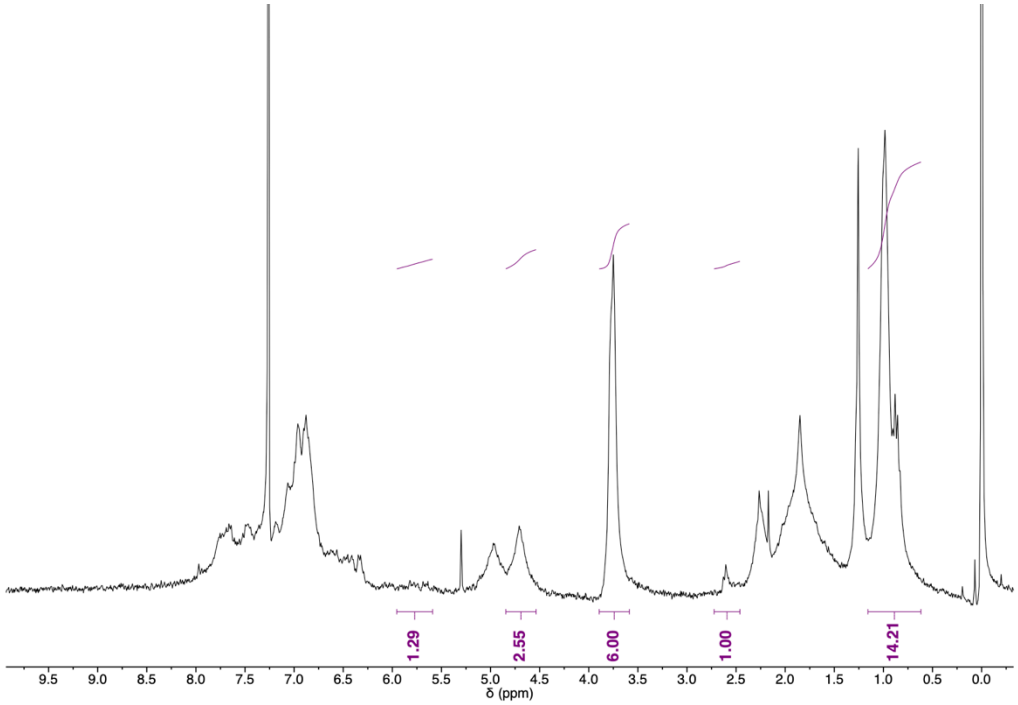


Figure S248. ^{1}H-NMR spectrum of oligo-(*S*)-**2** DP (GPC)= 3 ($CDCl_3$, 300 MHz).

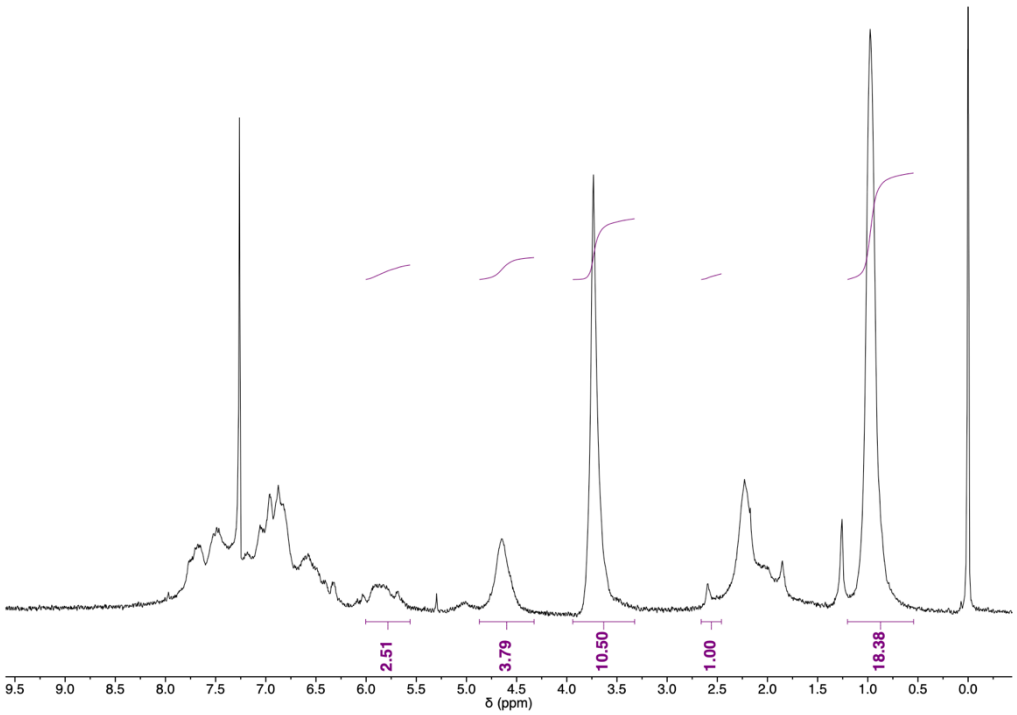


Figure S249. ^{1}H-NMR spectrum of oligo-(*S*)-**2** DP (GPC)= 7 ($CDCl_3$, 300 MHz).

USC
UNIVERSIDADE DE SANTIAGO DE COMPOSTELA

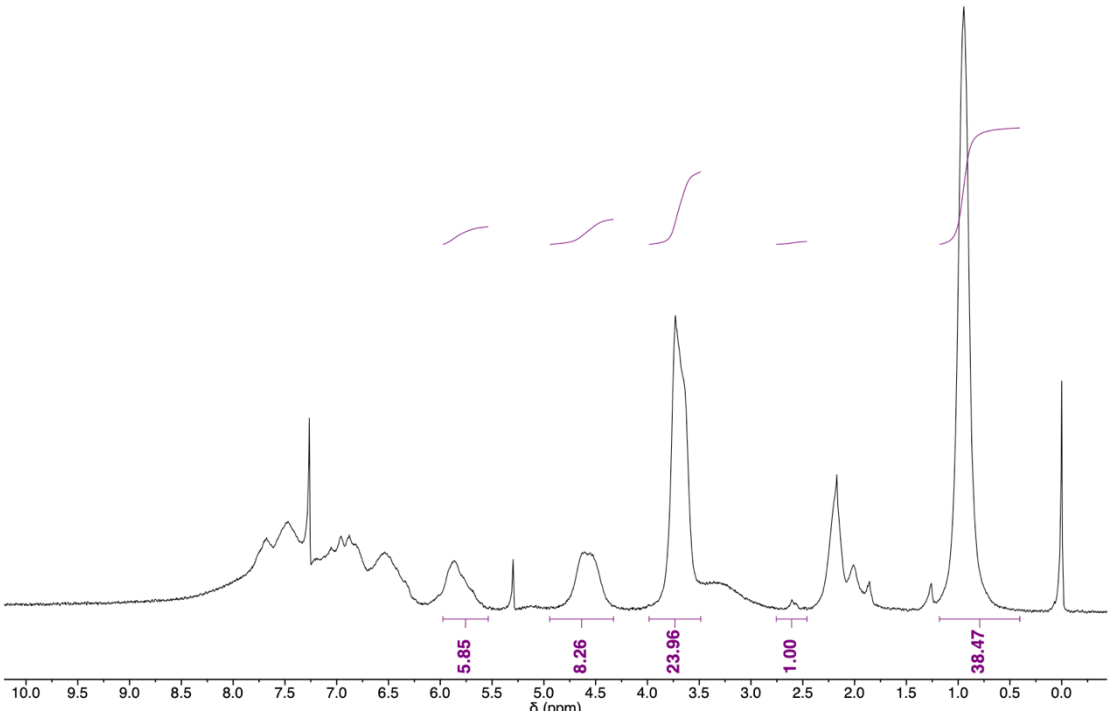


Figure S250. ^{1}H-NMR spectrum of oligo-(*S*)-**2** DP (GPC)= 17 ($CDCl_3$, 300 MHz).

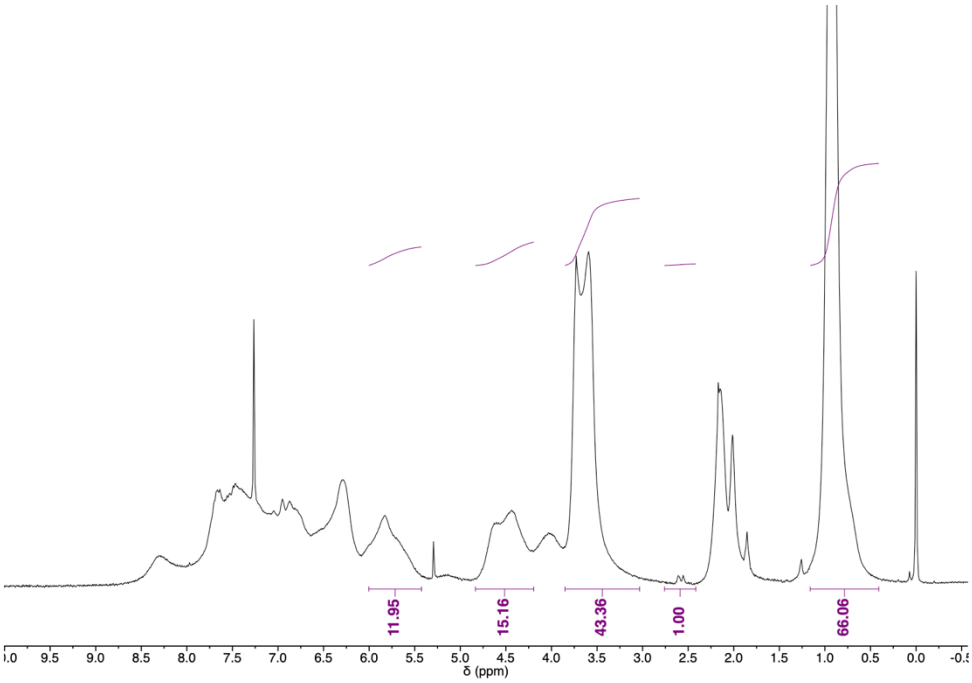


Figure S251. ^{1}H-NMR spectrum of oligo-(*S*)-**1** DP (GPC)= 31 ($CDCl_3$, 300 MHz).

USC UNIVERSIDADE DE SANTIAGO DE COMPOSTELA

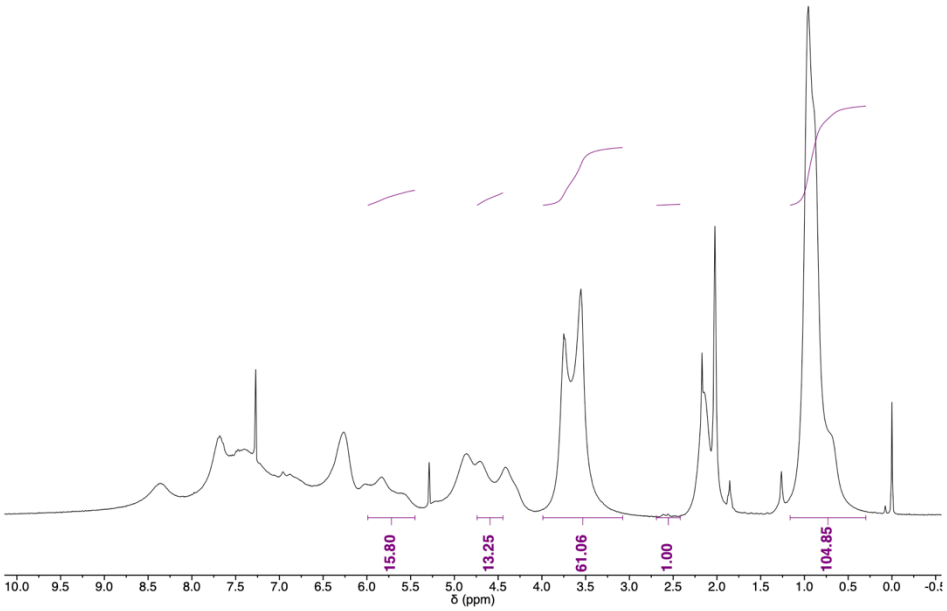


Figure S252. ^{1}H-NMR spectrum of oligo-(*S*)-**2** DP (GPC)= 60 ($CDCl_3$, 300 MHz).

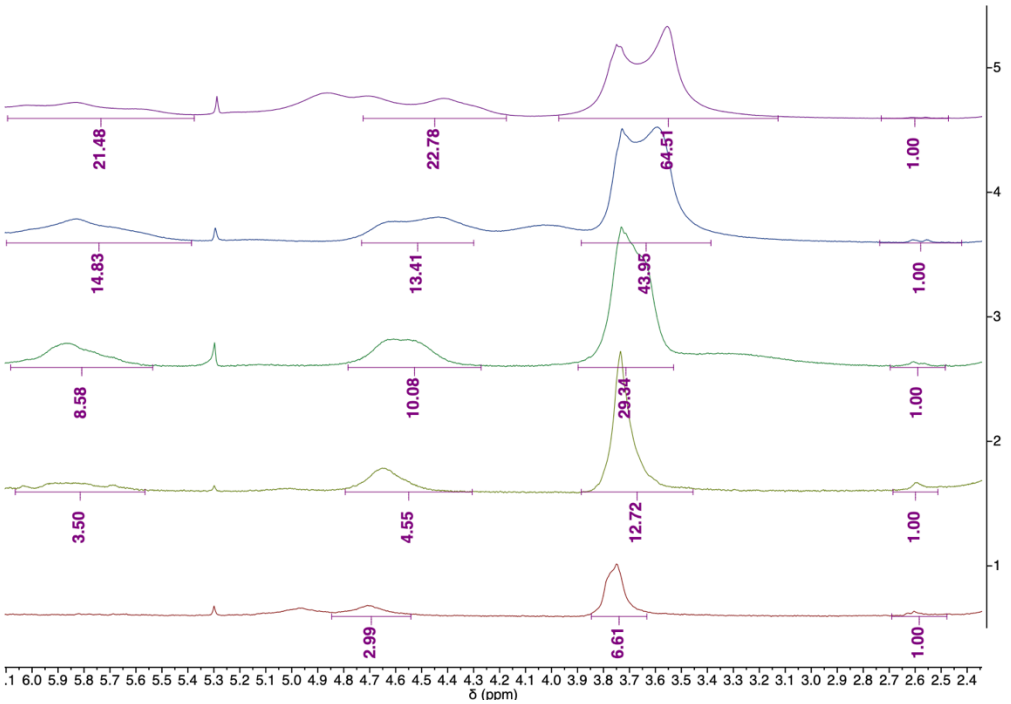


Figure S253. ^{1}H-NMR spectra of oligo-(*S*)-**2** DP (GPC)= 3, 7, 17, 31, and 60 ($CDCl_3$, 300 MHz).

USC
UNIVERSIDADE DE SANTIAGO DE COMPOSTELA

5.7.5. ECD and UV-Vis spectra of oligomers oligo-(*S*)-1

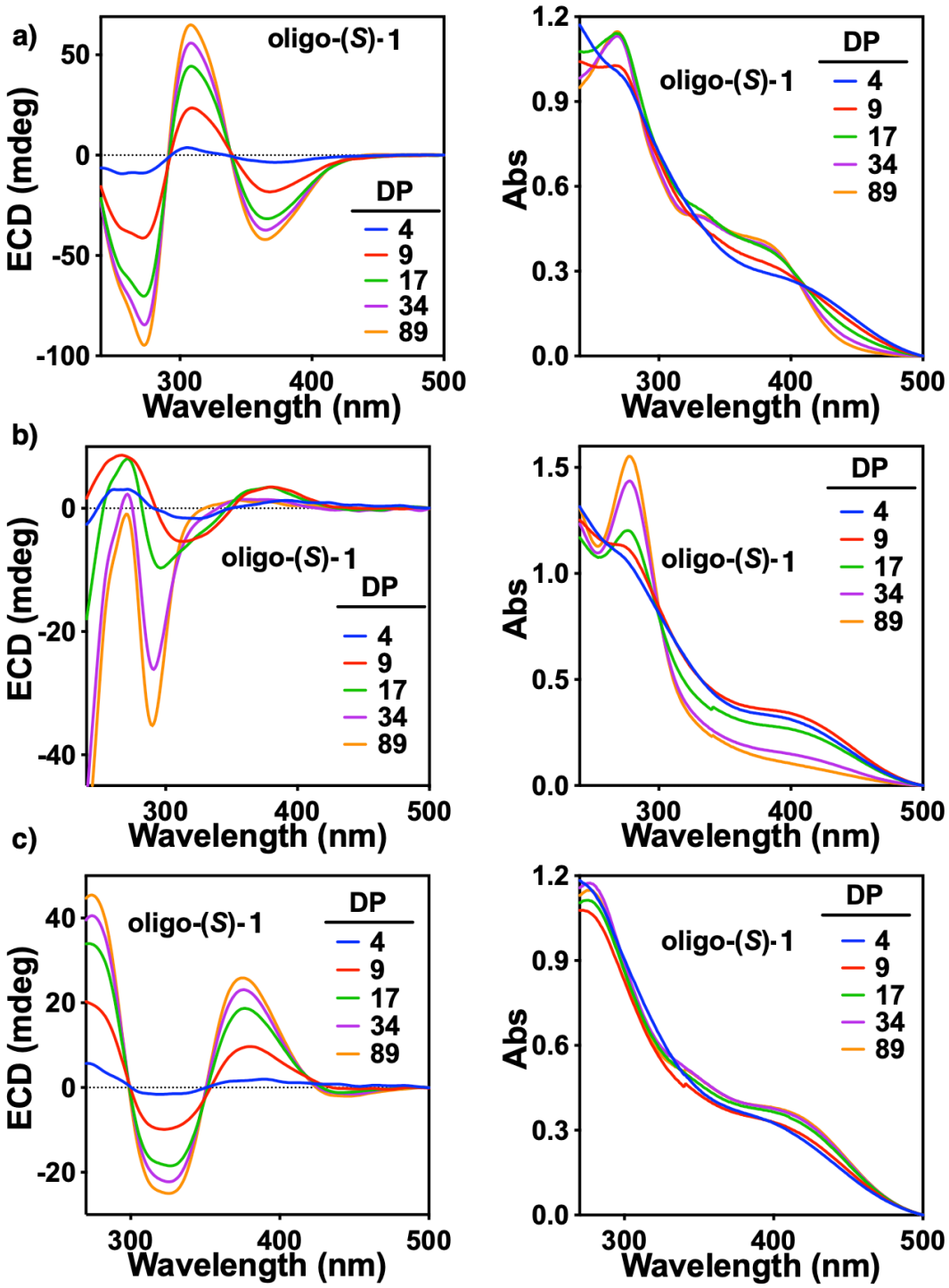


Figure S254. ECD and UV-Vis spectra of oligo-(*S*)-**1** (DP=4, 9, 17, 34, and 89 from GPC) in a) $CHCl_3$ b) THF c) DMF (c=0.3 mg/mL).

USC UNIVERSIDADE DE SANTIAGO DE COMPOSTELA

5.7.6. Color dependence with the DP of oligomers oligo-(*S*)-1

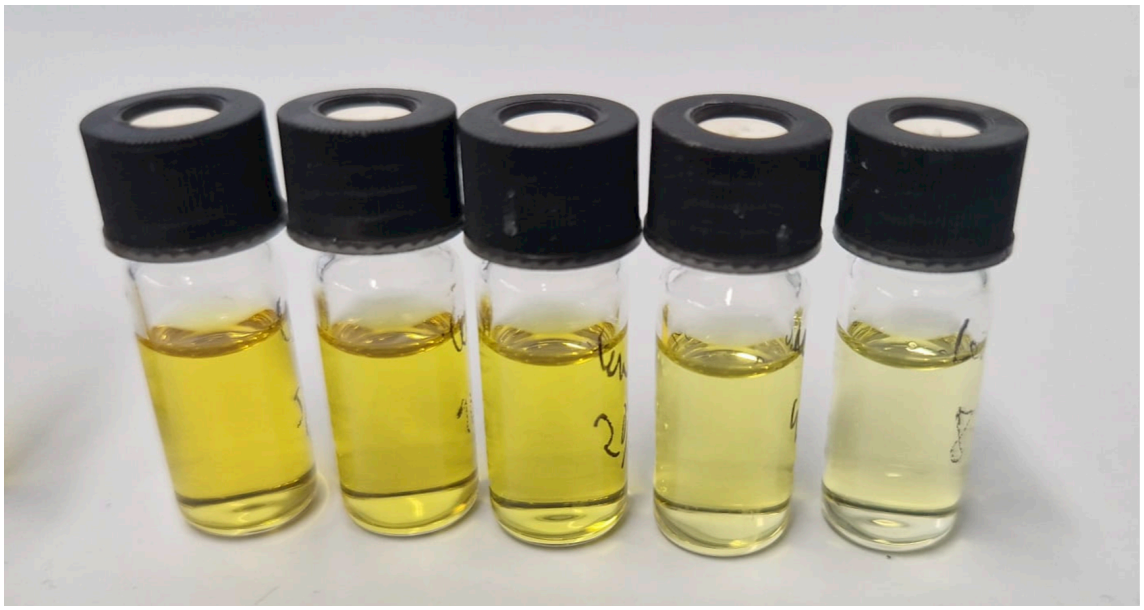


Figure S255. Photograph of oligo-(*S*)-**1** (DP=4, 9, 17, 34, and 89 from GPC, left to right) in THF (c=0.5 mg /mL).

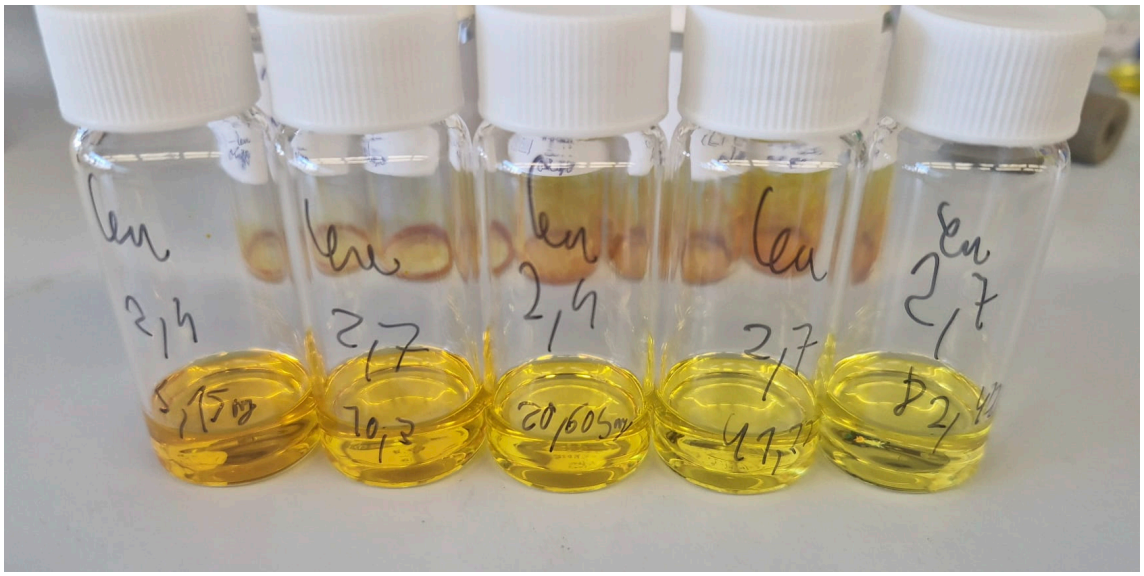


Figure S256. Photograph of oligo-(*S*)-**1** (DP=4, 9, 17, 34, and 89 from GPC, left to right) in $CHCl_3$ (c=1.0 mg/mL).

USC UNIVERSIDADE DE SANTIAGO DE COMPOSTELA

5.7.7. ECD and UV-Vis of Polymers in Solvents

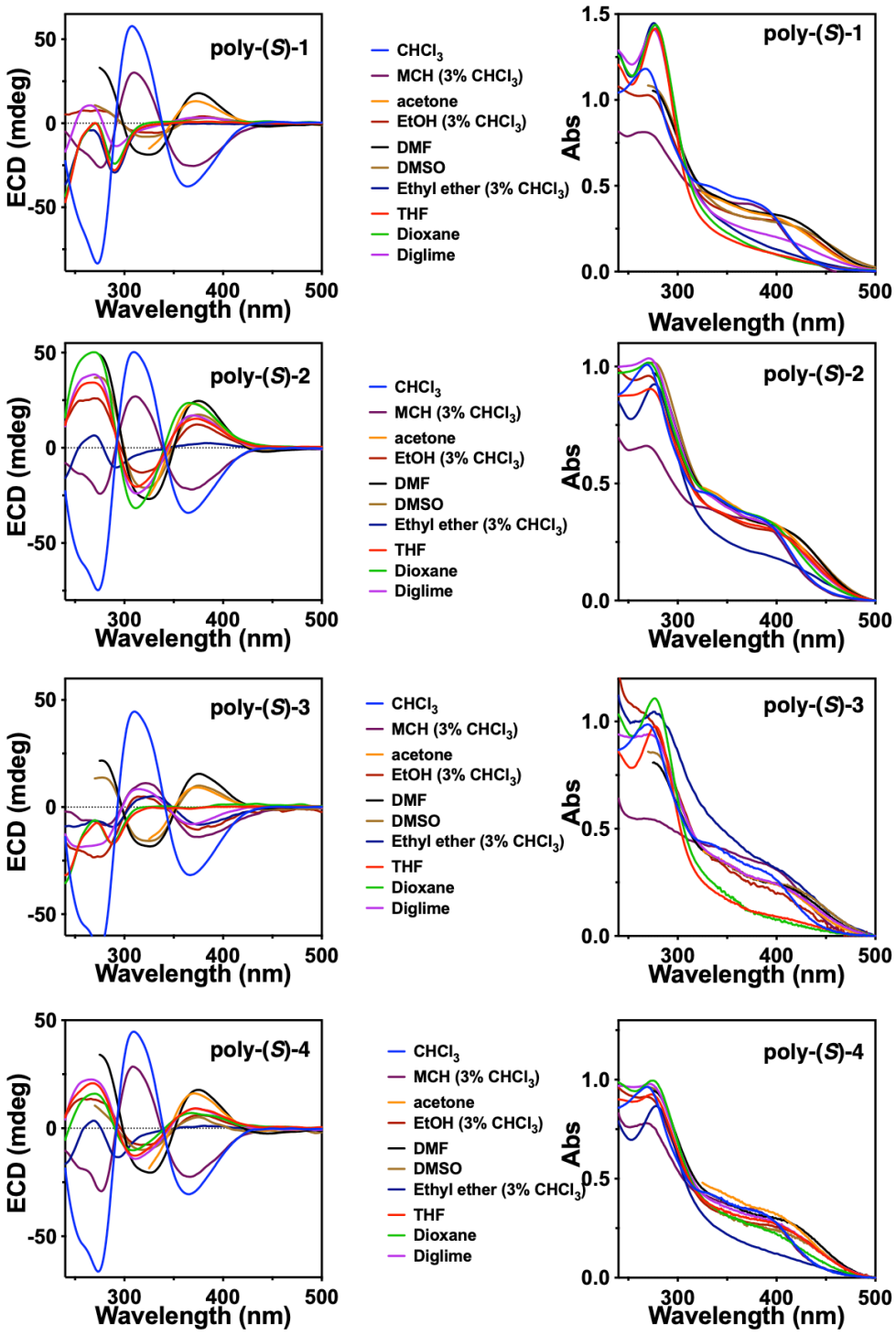


Figure S257. a) Normalized ECD at 380 nm for each oligo-(*S*)-**2** (DP 9, 18, 37, and 309) in $CHCl_3$ (c=0.3mg/mL) as a function of time while being irradiated with the lamp b) %SSE calculated using $t_{ECD50\%}$ as a function of DP. c) %SSE as a function of the concentration of terminal numbers.

USC UNIVERSIDADE DE SANTIAGO DE COMPOSTELA

5.7.8. ECD and UV-Vis of Poly-(*S*)-1 under the addition of $CHCl_3$ to visualize the elongation of a compressed structure in THF

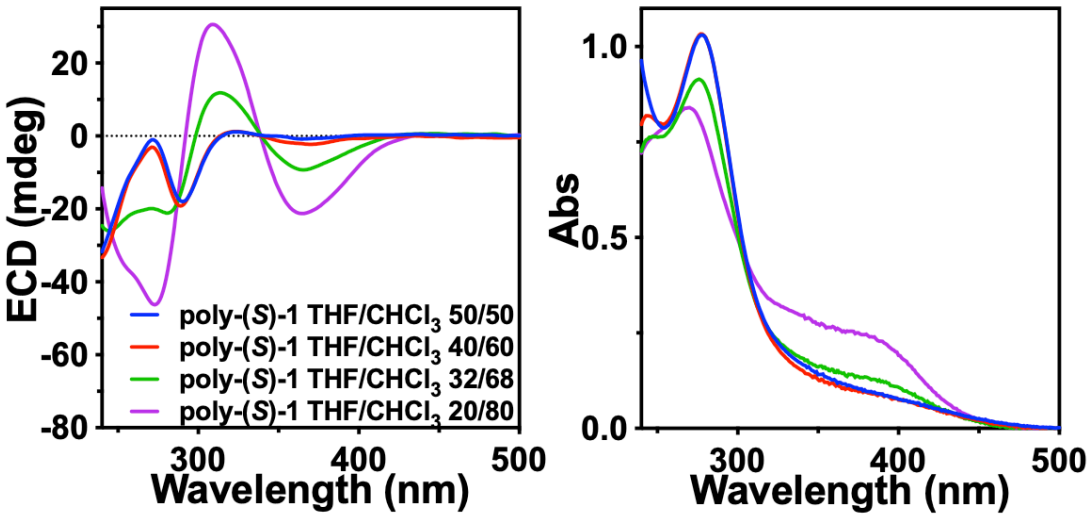


Figure S258. ECD and UV-Vis spectra of Poly-(*S*)-**1** (c=0.3 mg/mL) in different mixtures THF/$CHCl_3$ (v/v).

USC UNIVERSIDADE DE SANTIAGO DE COMPOSTELA

5.7.9. ECD and UV-Vis upon irradiation of oligo-(*S*)-1 DP=89, Poly-(*S*)-1, Poly-(*S*)-3 in THF

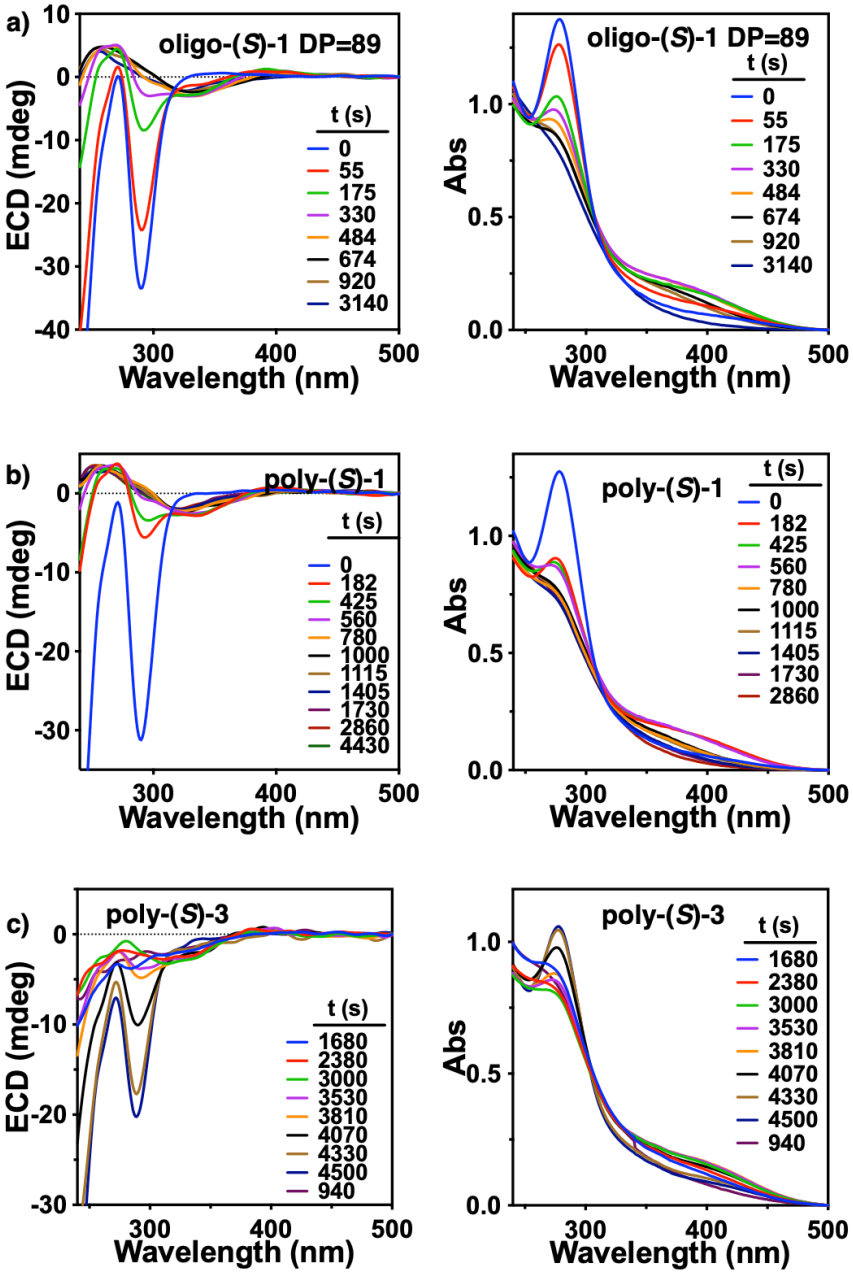


Figure S259. VT-ECD cooling spectra of oligo-(*S*)-**3** in $CHCl_3$ (c=0.3mg/mL) a) DP = 9 b) DP = 17.

USC UNIVERSIDADE DE SANTIAGO DE COMPOSTELA

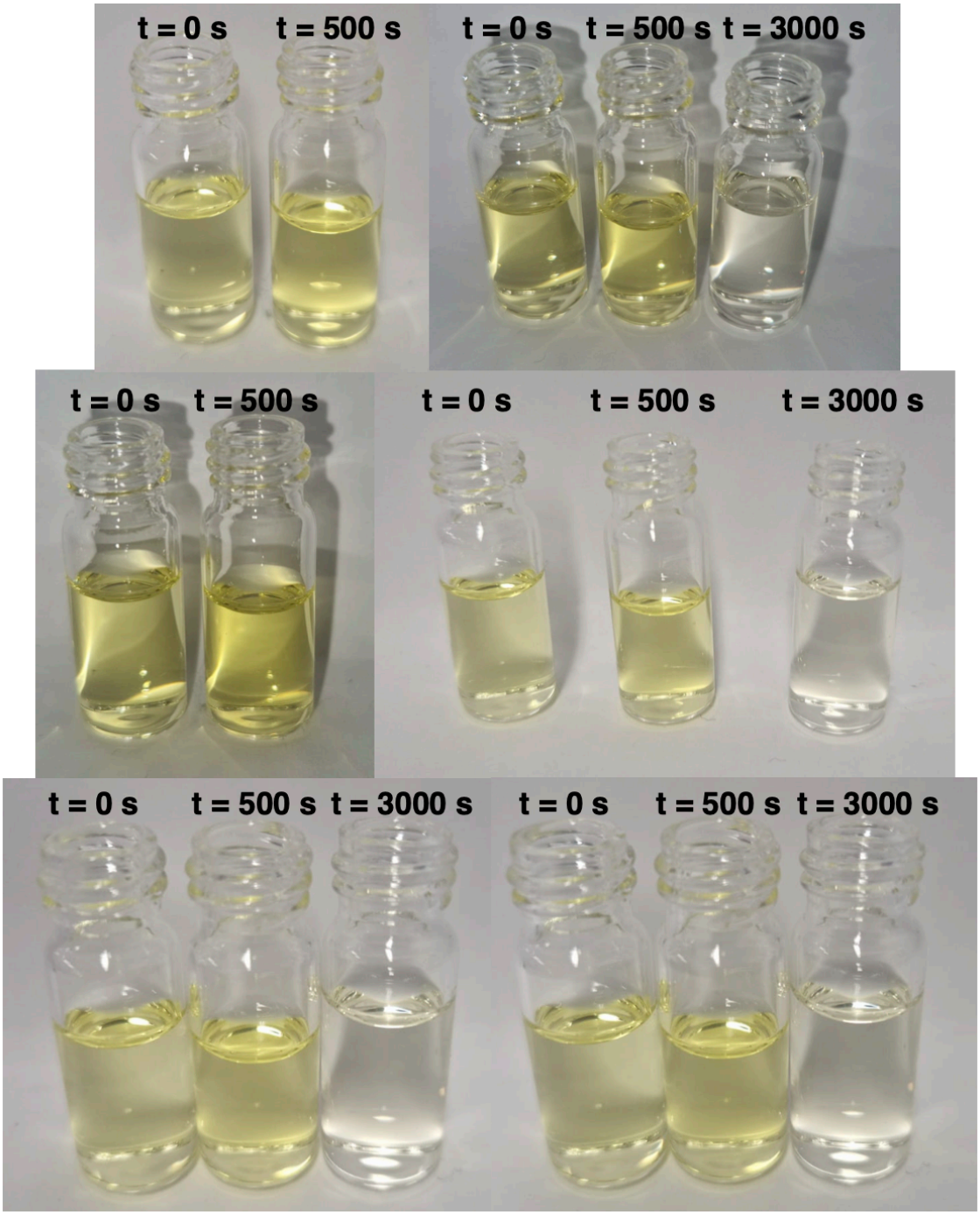


Figure S260. Photographs of oligo-(*S*)-**1** DP=89 upon irradiation of short pass filter 550 nm 25 dia. In THF (c=0.3 mg/mL).

USC
UNIVERSIDADE DE SANTIAGO DE COMPOSTELA

5.7.10. ECD and UV-Vis upon irradiation of oligo-(*S*)-1 DP=89, Poly-(*S*)-1, Poly-(*S*)-3 in Dioxane

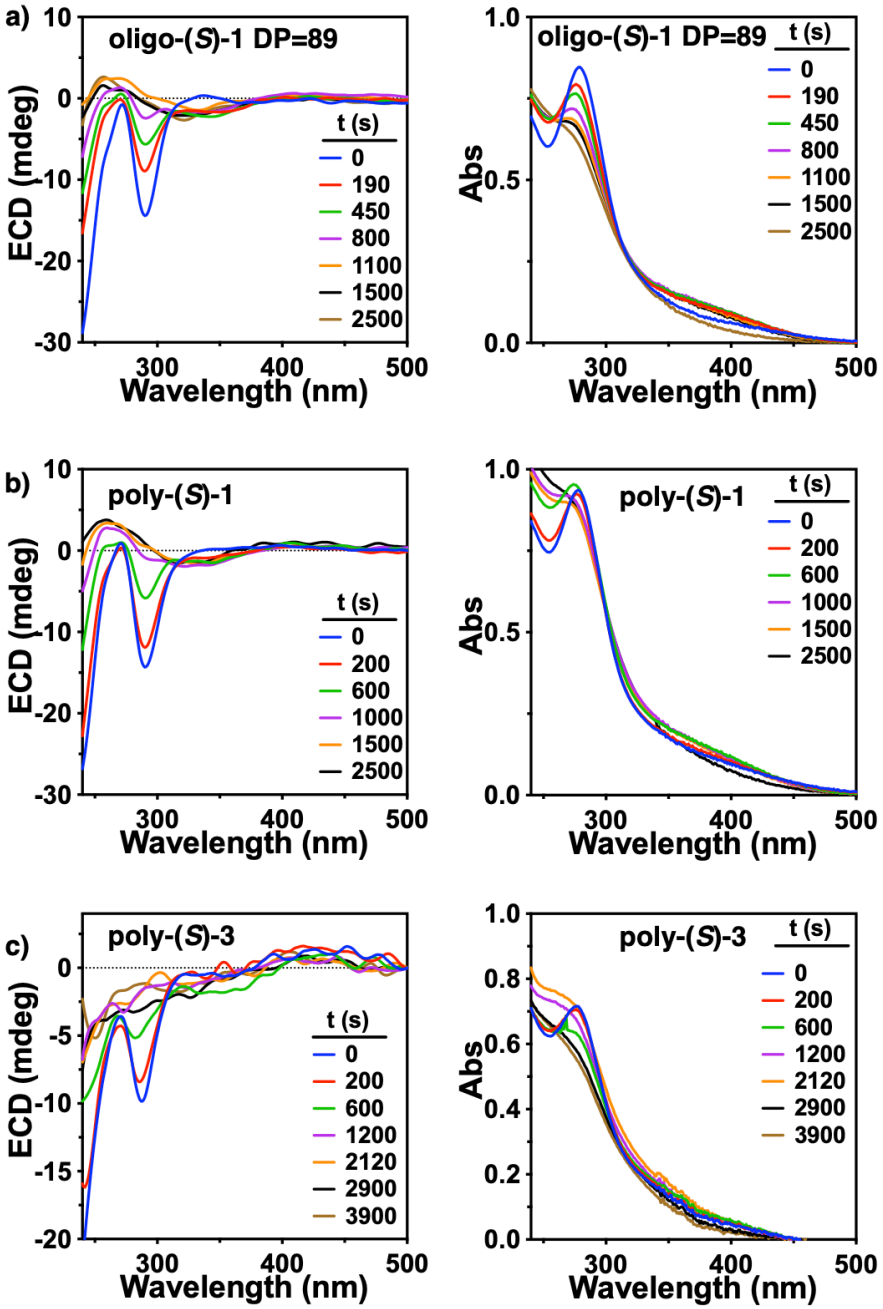


Figure S261. ECD and UV-Vis spectra upon irradiation of short pass filter 550 nm 25 dia. in Dioxane (c=0.3 mg/mL) of a) oligo-(*S*)-**1** DP=89, b) Poly-(*S*)-**1** c) Poly-(*S*)-**3**.

USC UNIVERSIDADE DE SANTIAGO DE COMPOSTELA

5.7.11. ECD of oligo-(*S*)-1 DP=89 and Poly-(*S*)-1 in $CHCl_3$

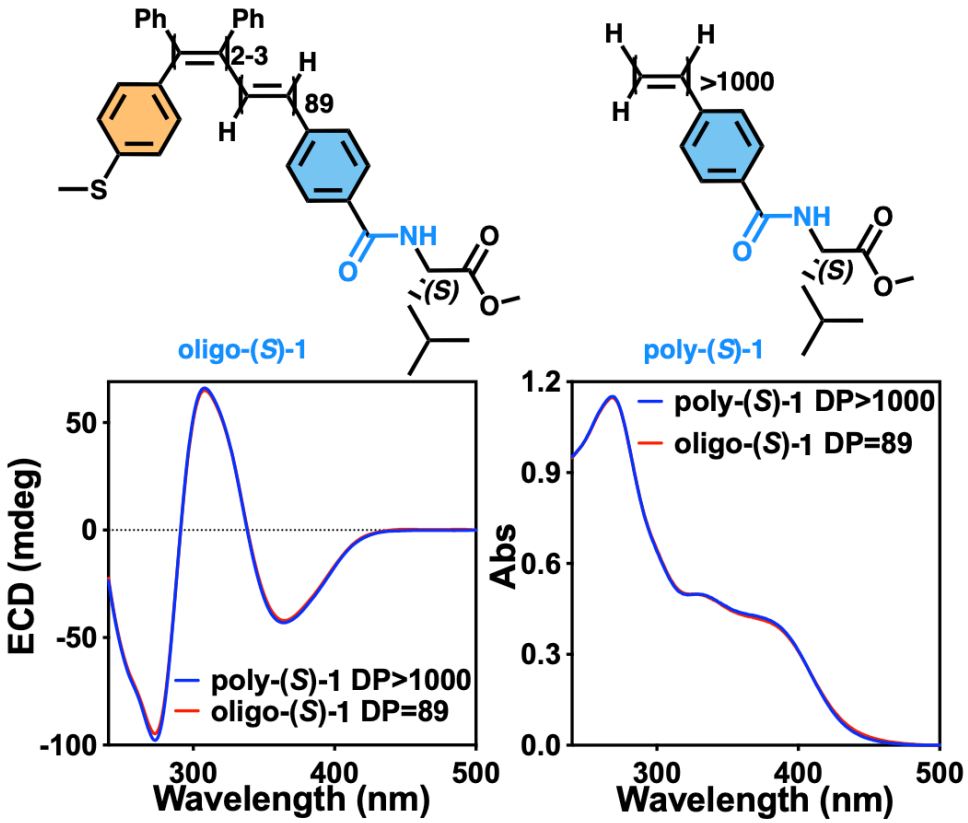


Figure S262. ECD and UV-Vis spectra (c=0.3 mg/mL $CHCl_3$) of the largest oligomer oligo-(*S*)-**1** (DP = 89) and a large polymer poly-(*S*)-**1** (DP > 1000).

USC
UNIVERSIDADE DE SANTIAGO DE COMPOSTELA

5.7.12. ECD and UV-Vis spectra of oligomers oligo-(*S*)-2 in Et_2O (3% $CHCl_3$)

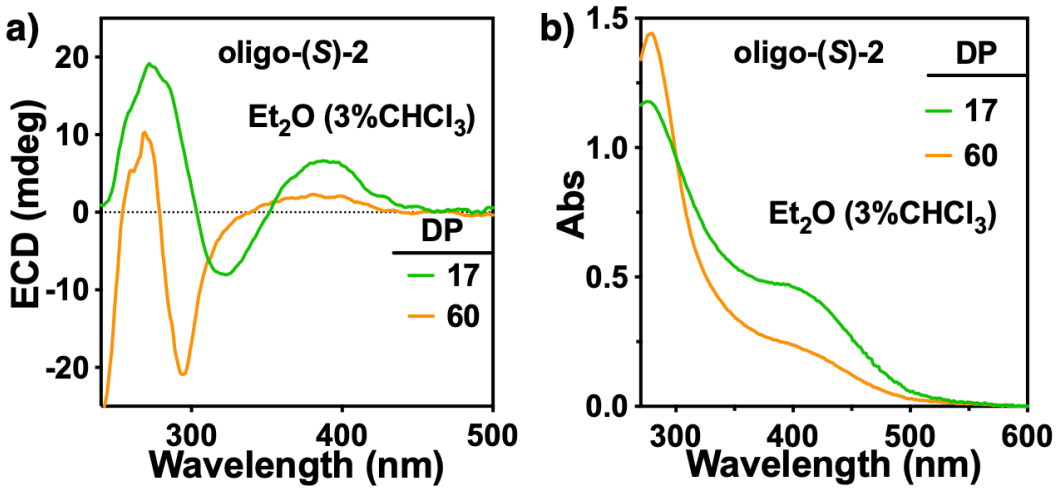


Figure S263. a) ECD and b) UV-Vis spectra of oligo-(*S*)-**2** (DP=17 and 60 from GPC) (c=0.03 mg/mL, cuvette of 1 cm path length).

USC UNIVERSIDADE DE SANTIAGO DE COMPOSTELA

5.7.13. ECD and UV-Vis spectra of oligo-(*S*)-1

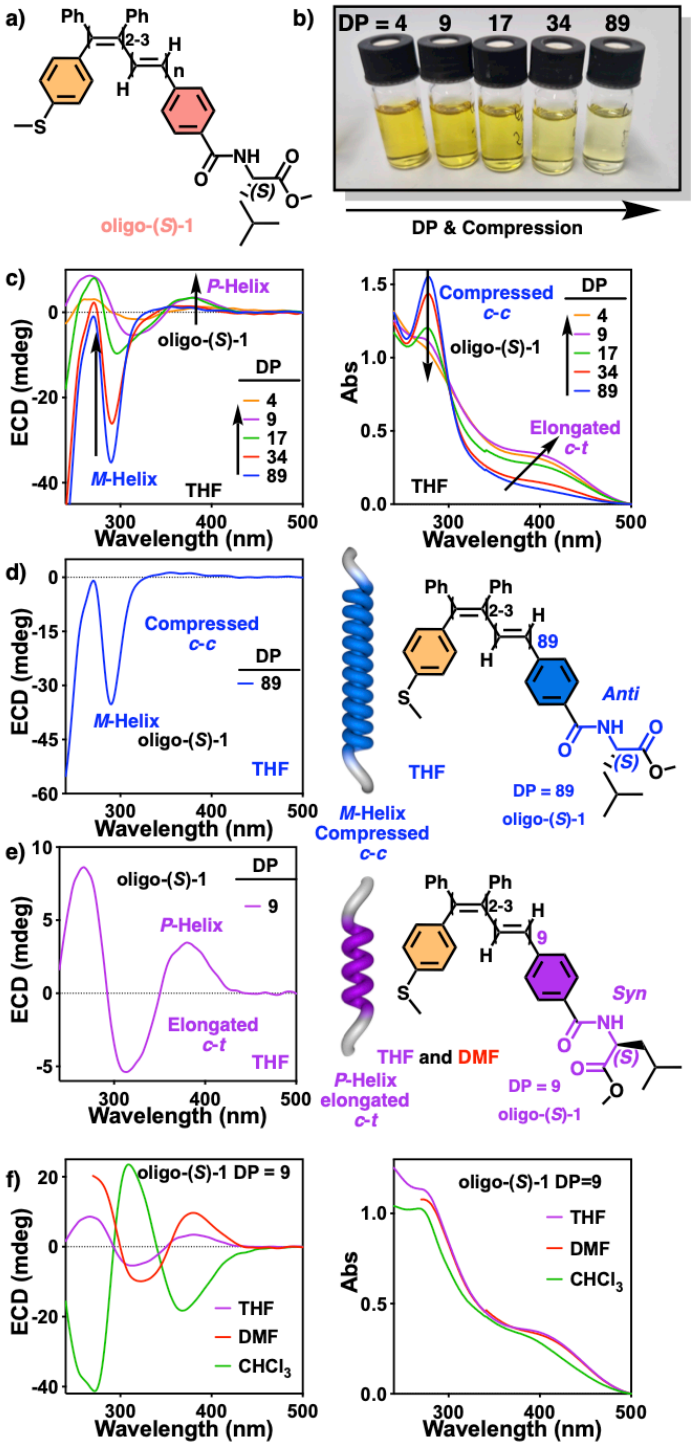


Figure S264. a) Chemical Structure of the oligomer series oligo-(*S*)-**1** with DP=4, 9, 17, 34, and 89. b) photograph of the oligomer series oligo-(*S*)-**1** with DP=4, 9, 17, 34, and 89 (c=0.5 mg/mL THF). c) ECD and UV-Vis spectra of the oligomer series oligo-(*S*)-**1** with DP=4, 9, 17, 34, and 89 (c=0.5 mg/mL THF). d) ECD spectrum and conformation adopted by the pendant of the oligomer series oligo-(*S*)-**1** with DP= 89 (c=0.3 mg/mL THF). e) ECD spectrum and conformation adopted by the pendant of the oligomer series oligo-(*S*)-**1** with DP=9 (c=0.3 mg/mL THF). f) ECD and UV-Vis spectra of oligo-(*S*)-**1** with DP=9 in THF, DMF, and $CHCl_3$ (c=0.3 mg/mL).

5.7.14. Irradiation studies of oligo-(*S*)-1 at DP=9 in THF

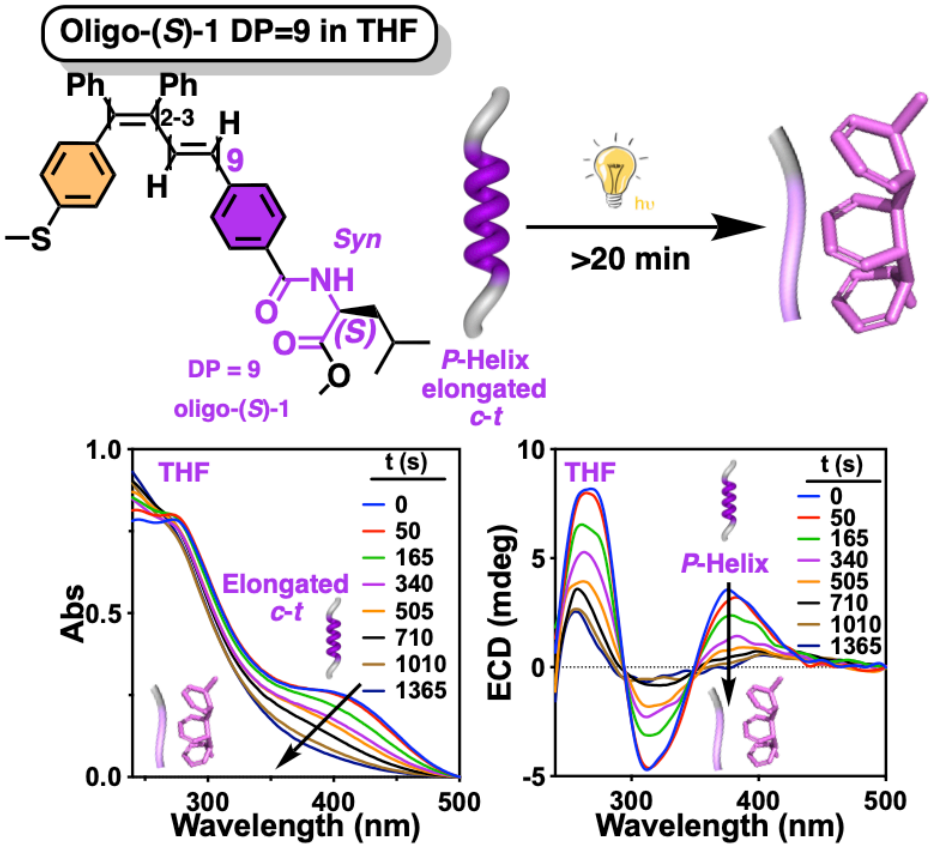


Figure S265. a) Schematic representation, ECD, and UV-Vis spectra of the irradiation PEC (short pass filter / Vis 550 nm 25 dia) over time of the oligo-(*S*)-**1** with DP=9 (c=0.3 mg/mL THF).

USC
UNIVERSIDADE DE SANTIAGO DE COMPOSTELA

5.7.15. Second step process comparison of oligo-(*S*)-1 between DP=9 and DP=89

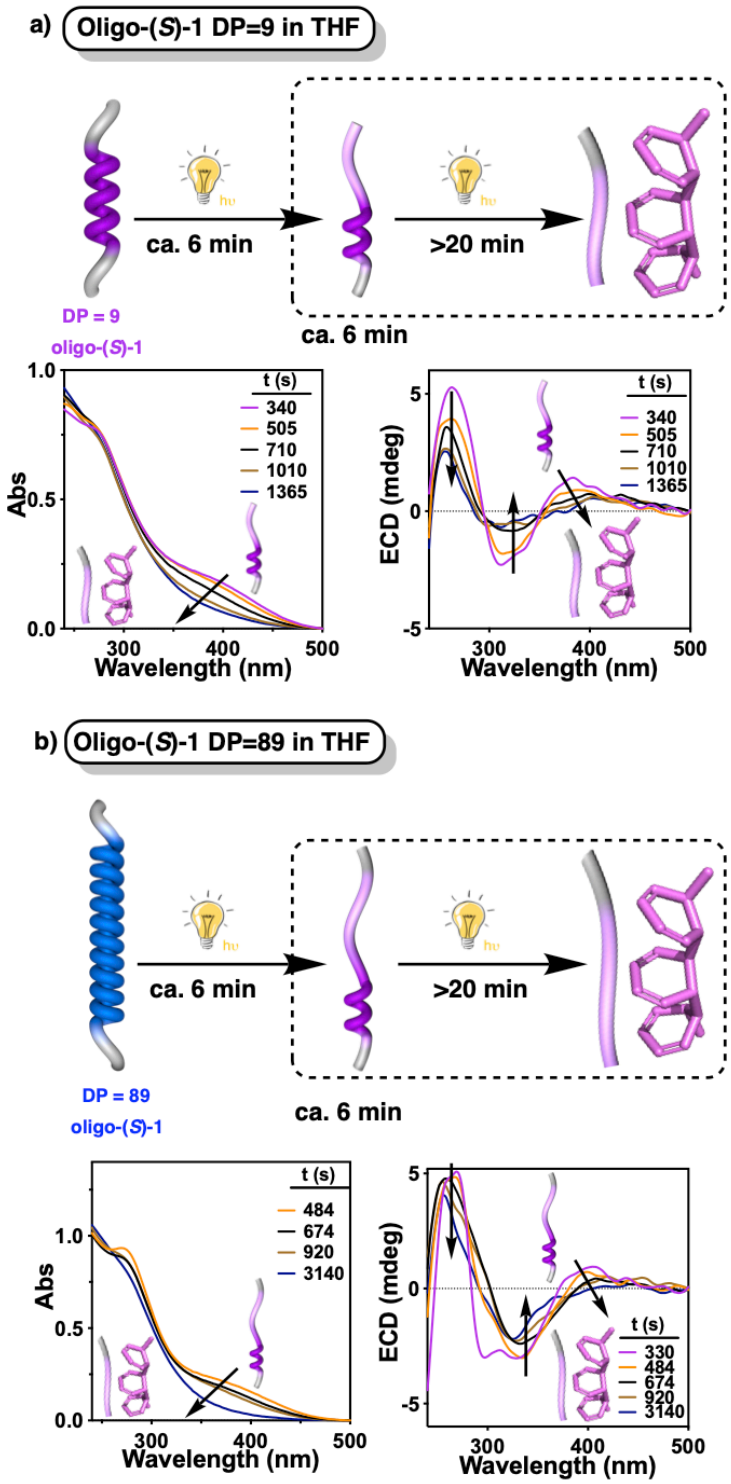


Figure S266. a) Schematic representation, ECD, and UV-Vis spectra of the irradiation PEC (short pass filter / Vis 550 nm 25 dia) over time of the oligo-(*S*)-**1** with DP=9 (c=0.3 mg/mL THF). b) Schematic representation, ECD and UV-Vis spectra of the irradiation PEC (short pass filter / Vis 550 nm 25 dia) over time of the oligo-(*S*)-**1** with DP=89 (c=0.3 mg/mL THF).

5.7.16. Irradiation studies of poly-(*S*)-1 and poly-(*S*)-3 in THF

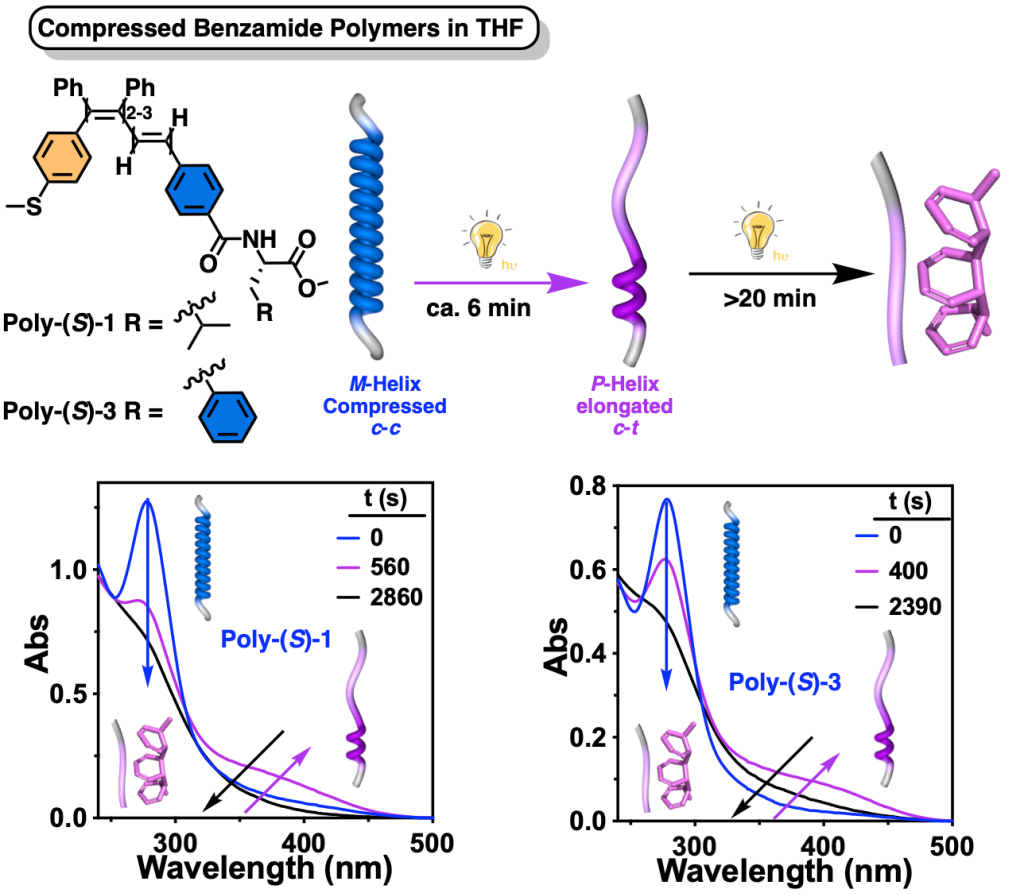


Figure S267. a) Schematic representation, ECD, and UV-Vis spectra of the irradiation PEC (short pass filter / Vis 550 nm 25 dia) over time of the poly-(*S*)-**1** and poly-(*S*)-**3** (c=0.3 mg/mL THF).

USC UNIVERSIDADE DE SANTIAGO DE COMPOSTELA

5.8. Experimental Section and Methodology Chapter 3.8.

5.8.1. Experimental Procedures

The ECD measurements were done in a Jasco J-1500. UV spectra were registered in a Jasco V-750. The cuvette used for general measurements was 1 mm of pathlength unless otherwise specified; in such cases, a 1 cm cuvette was used.

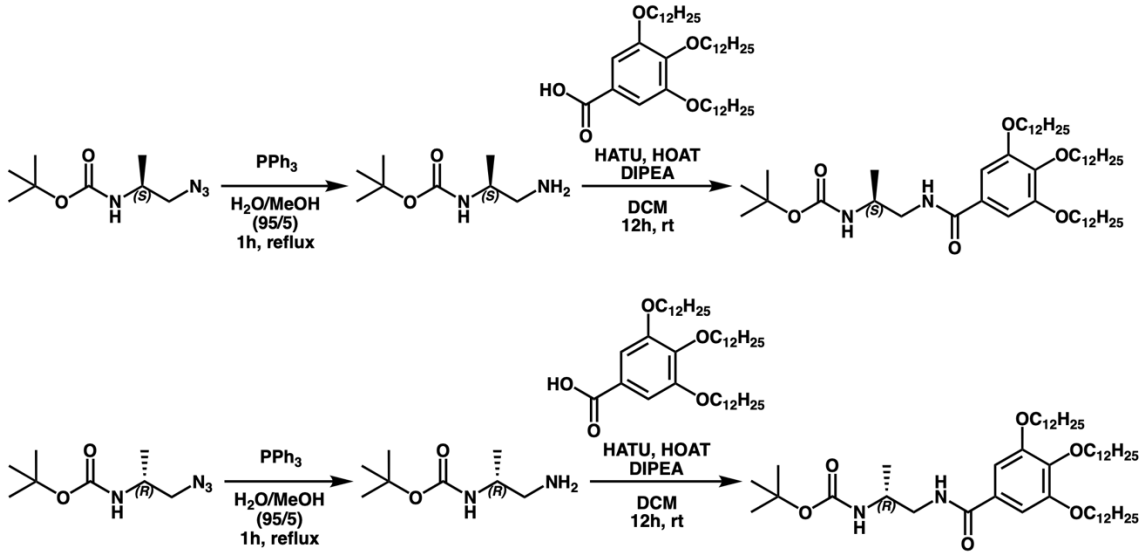
NMR experiments were measured in a Varian 300 operating at 300 MHz for proton NMR and 75 MHz for carbon.

IR spectra were recorded in Jasco FT-IR 4600 apparatus using a cell equipped with BaF2 lens and a Teflon spacer generating a 150 μm path length.

Emission spectra and quantum yields were measured using a Jasco Spectrofluorometer FP-8550 with the accessory PCT-818 and coumarin 1 as standard.

USC
UNIVERSIDADE DE SANTIAGO DE COMPOSTELA

5.8.2. Synthesis of tert-butyl (*S*)- and (*R*)-(1-(3,4,5-tris(dodecyloxy)benzamido)propan-2-yl)carbamate



tert-butyl (*S*/*R*)-(1-azidopropan-2-yl)carbamate (1.00 g, 5.00 mmol, 1.00 equiv) and triphenylphosphane (PPh_3, 1.44 g, 5.50 mmol, 1.10 equiv) were dissolved in H_2O/MeOH (5/95, 30 mL) and the mixture was refluxed for one hour. After this time the organic solvent was removed, and the crude was extracted with 10 mL of DCM. The organic phase was dried over anhydrous Na_2SO_4.

2-(7-Aza-1H-benzotriazole-1-yl)-1,1,3,4-tetramethyluronium hexafluorophosphate) (HATU, 2.28 g, 6.00 mmol, 1.20 equiv), 1-hydroxy-7-azabenzotriazole (HOAt, 0.81 g, 6.00 mmol, 1.20 equiv), (3,4,5-tris(dodecyloxy)benzoic acid (3.37 g, 5.00 mmol, 1.0 equiv.) and diisopropyltriethylamine (DIPEA, 1.05 mL, 6.00 mmol, 1.20 equiv) were dissolved in 100 mL of dry CH_2Cl_2, and the mixture was stirred for 15 min. to activate the acid. Then, DCM solution containing tert-butyl (*S*/*R*)-(1-aminopropan-2-yl)carbamate was added and the reaction mixture was stirred overnight. Then, the organic solution was washed with HCl 1M, a saturated solution of $NaHCO_3$ and a saturated solution of NaCl. The combined organic layers were dried over anhydrous Na_2SO_4, filtered and the solvent was evaporated at reduced pressure. The crude product was chromatographed on silica gel with hexane/ethyl acetate (8/2) as eluent [2.71 g (*S*)-*N*-(2-aminopropyl)-3,4,5-tris(dodecyloxy)benzamide and 2.60 g (*R*)-*N*-(2-aminopropyl)-3,4,5-tris(dodecyloxy)benzamide], 65% and 63% yield respectively of pure products.

USC UNIVERSIDADE DE SANTIAGO DE COMPOSTELA

Spectroscopic data:

^{1}H-NMR (300 MHz, $CDCl_3$) (*S*)-*N*-(2-aminopropyl)-3,4,5-tris(dodecyloxy)benzamide δ_H (ppm): 7.46 (s, 1H), 7.05 (s, 2H), 4.76 (d, J = 7.6 Hz, 1H), 3.98 (m, 6H), 3.88 (s, 1H), 3.43 (m, 2H), 1.74 (m, 6H), 1.29 (m, 64H), 0.86 (t, J = 6.7 Hz, 8H).

^{13}C-NMR (75 MHz, $CDCl_3$) (*S*)-*N*-(2-aminopropyl)-3,4,5-tris(dodecyloxy)benzamide δ_C (ppm): 167.5, 157.2, 153.1, 141.2, 129.2, 105.9, 80.0, 73.6, 69.4, 48.2, 46.9, 32.1, 30.5, 29.9, 29.8, 29.8, 29.7, 29.5, 29.5, 28.5, 26.2, 22.8, 18.9, 14.2.

HRMS (MALDI-TOF) m/z calcd. for (*S*)-*N*-(2-aminopropyl)-3,4,5-tris(dodecyloxy)benzamide $C_{51}H_{94}N_2O_6$ $[M+Na]^+$: 853.700 found: 853.659.

^{1}H-NMR (300 MHz, $CDCl_3$) (*R*)-*N*-(2-aminopropyl)-3,4,5-tris(dodecyloxy)benzamide δ_H (ppm): 7.52 (s, 1H), 7.05 (s, 2H), 4.83 (d, J = 7.5 Hz, 1H), 3.97 (m, 6H), 3.87 (s, 1H), 3.42 (m, 2H), 1.74 (m, 6H), 1.30 (m, 64H), 0.86 (t, J = 6.6 Hz, 8H).

^{13}C-NMR (75 MHz, $CDCl_3$) (*R*)-*N*-(2-aminopropyl)-3,4,5-tris(dodecyloxy)benzamide δ_C (ppm): 167.5, 157.1, 153.1, 141.2, 129.1, 105.9, 79.9, 73.5, 69.3, 48.2, 46.9, 32.0, 30.4, 29.8, 29.8, 29.7, 29.7, 29.5, 29.5, 28.4, 26.2, 22.8, 18.9, 14.2.

HRMS (MALDI-TOF) m/z calcd. for (*R*)-*N*-(2-aminopropyl)-3,4,5-tris(dodecyloxy)benzamide $C_{51}H_{94}N_2O_6$ $[M+Na]^+$: 853.700 found: 853.637.

USC UNIVERSIDADE DE SANTIAGO DE COMPOSTELA

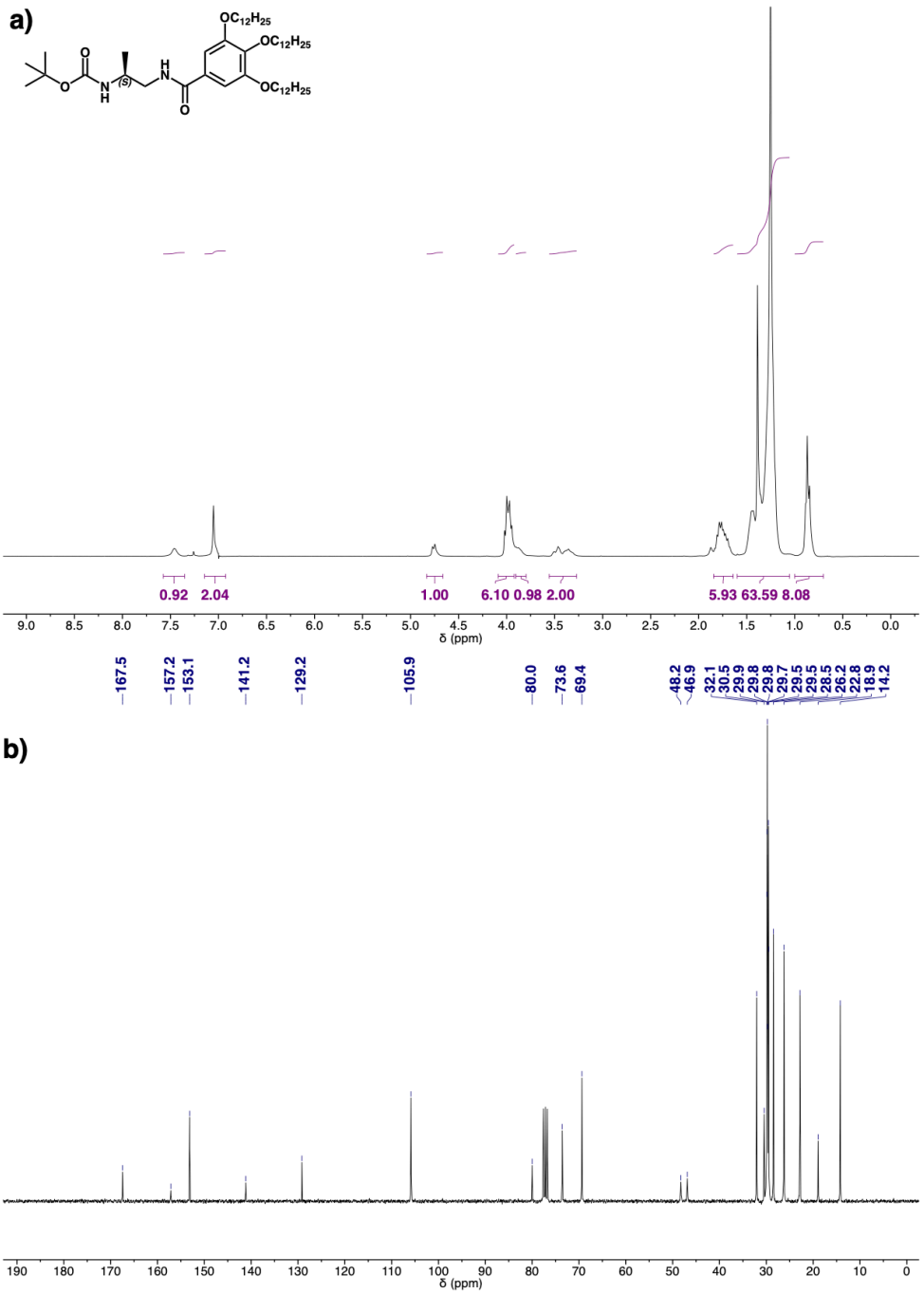


Figure S268. a) ^{1}H-NMR and b) ^{13}C-NMR spectra of *tert*-butyl (*S*)-(1-(3,4,5-tris(dodecyloxy)benzamido)propan-2-yl)carbamate ($CDCl_3$, 300 and 75 MHz, respectively).

USC
UNIVERSIDADE DE SANTIAGO DE COMPOSTELA

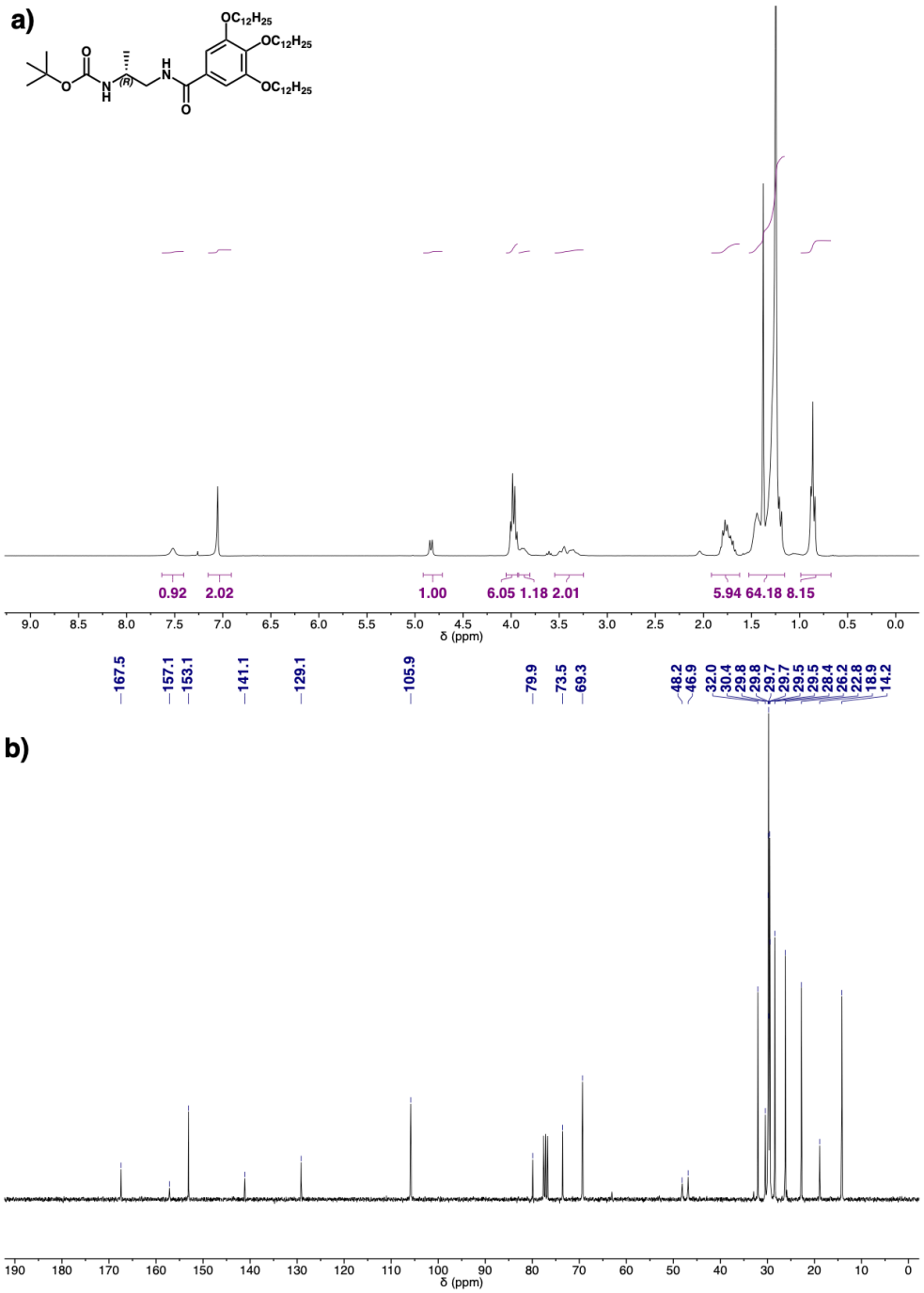
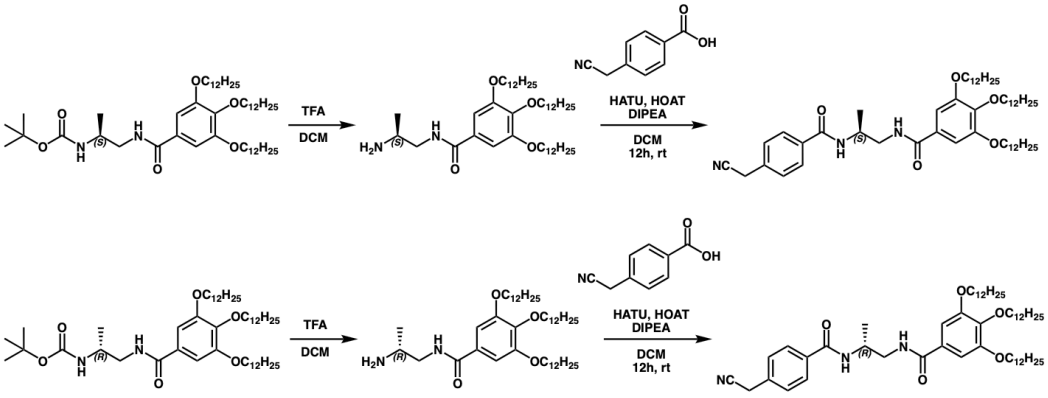


Figure S269. a) ^{1}H-NMR and b) ^{13}C-NMR spectra of *tert*-butyl (*R*)-(1-(3,4,5-tris(dodecyloxy)benzamido)propan-2-yl)carbamate ($CDCl_3$, 300 and 75 MHz, respectively).

USC
UNIVERSIDADE DE SANTIAGO DE COMPOSTELA

5.8.3. Synthesis of (*S*) and (*R*)-*N*-(2-(4-(cyanomethyl)benzamido)propyl)-3,4,5-tris(dodecyloxy)benzamide



tert-butyl (*S*/*R*)-(1-azidopropan-2-yl)carbamate (1.40 g, 1.69 mmol, 1.00 equiv) was dissolved in 2,2,2-trifluoroacetic acid (TFA, 10 mL) and DCM (30 mL) and the mixture was stirred for one hour at room temperature followed by evaporation of the solvents.

In other round bottom flask 2-(7-Aza-1H-benzotriazole-1-yl)-1,1,3,4-tetramethyluronium hexafluorophosphate) (HATU, 0.77 g, 2.02 mmol, 1.20 equiv), 1-hydroxy-7-azabenzotriazole (HOAt, 0.27 g, 2.02 mmol, 1.20 equiv), 4-(cyanomethyl)benzoic acid (0.26 g, 1.69 mmol, 1.0 equiv.) and diisopropyltriethylamine (DIPEA, 0.29 mL, 1.69 mmol, 1.20 equiv) were dissolved in 100 mL of dry CH_2Cl_2, and the mixture was stirred for 15 min. to activate the acid. Then, the crude from the boc deprotection previously prepared —(*S*/*R*)-*N*-(2-aminopropyl)-3,4,5-tris(dodecyloxy)benzamide— was dissolved in 10 mL of DCM and added to the reaction mixture, that was further stirred overnight. Then, the organic solution was washed with HCl 1M, a saturated solution of $NaHCO_3$ and a saturated solution of NaCl. The combined organic layers were dried over anhydrous Na_2SO_4, filtered and the solvent was evaporated at reduced pressure. The crude product was chromatographed on silica gel with DCM/MeOH (99/1) as eluent [0,63 g (*S*)-*N*-(2-(4-(cyanomethyl)benzamido)propyl)-3,4,5-tris(dodecyloxy)benzamide and 0.88 g (*R*)-*N*-(2-(4-(cyanomethyl)benzamido)propyl)-3,4,5-tris(dodecyloxy)benzamide], 43% and 60% yield respectively of pure products.

Spectroscopic data:

^{1}H-NMR (300 MHz, $CDCl_3$) (*S*)-*N*-(2-(4-(cyanomethyl)benzamido)propyl)-3,4,5-tris(dodecyloxy)benzamide δ_H (ppm): 7.75 (d, J = 8.2 Hz, 2H), 7.32 (d, J = 8.3 Hz, 2H),

7.16 (t, J = 5.4 Hz, 1H), 6.98 (s, 2H), 6.91 (d, J = 7.4 Hz, 1H), 4.38 (m, 1H), 3.97 (m, 6H), 3.69 (s, 2H), 3.49 (m, 2H), 1.76 (m, 6H), 1.44 (q, J = 7.1 Hz, 6H), 1.28 (m, 49H), 0.86 (t, J = 6.5 Hz, 8H).

^{13}C-NMR (75 MHz, $CDCl_3$) (*S*)-*N*-(2-(4-(cyanomethyl)benzamido)propyl)-3,4,5-tris(dodecyloxy)benzamide δ_C (ppm): 171.4, 168.7, 168.0, 153.2, 152.0, 141.2, 137.8, 133.1, 129.6, 129.0, 127.5, 121.2, 105.7, 84.6, 73.6, 69.3, 52.2, 47.2, 47.0, 41.0, 32.0, 30.4, 29.8, 29.8, 29.7, 29.5, 29.5, 26.2, 26.2, 22.8, 18.5, 14.2.

HRMS (MALDI-TOF) m/z calcd. for (*S*)-*N*-(2-(4-(cyanomethyl)benzamido)propyl)-3,4,5-tris(dodecyloxy)benzamide $C_{55}H_{91}N_3O_5$ $[M+Na]^+$: 896.685 found: 896.659.

^{1}H-NMR (300 MHz, $CDCl_3$) (*R*)-*N*-(2-(4-(cyanomethyl)benzamido)propyl)-3,4,5-tris(dodecyloxy)benzamide δ_H (ppm): 7.75 (d, J = 8.0 Hz, 2H), 7.32 (d, J = 8.3 Hz, 2H), 7.20 (t, J = 5.3 Hz, 1H), 6.98 (s, 2H), 6.94 (s, J = 7.3 Hz, 1H), 4.37 (m, 1H), 3.98 (m, 6H), 3.68 (s, 2H), 3.51 (m, 2H), 1.75 (m, 7H), 1.44 (q, J = 7.1 Hz, 6H), 1.28 (m, 52H), 0.87 (t, J = 6.4 Hz, 9H).

^{13}C-NMR (75 MHz, $CDCl_3$) (*R*)-*N*-(2-(4-(cyanomethyl)benzamido)propyl)-3,4,5-tris(dodecyloxy)benzamide δ_C (ppm): 171.4, 168.7, 168.0, 153.2, 152.7, 141.3, 137.9, 133.1, 129.7, 129.0, 127.5, 121.7, 105.7, 84.5, 73.6, 69.4, 52.3, 47.2, 47.1, 41.1, 32.1, 30.5, 29.9, 29.8, 29.7, 29.6, 29.5, 26.3, 26.2, 22.8, 18.6, 14.2.

HRMS (MALDI-TOF) m/z calcd. for (*R*)-*N*-(2-(4-(cyanomethyl)benzamido)propyl)-3,4,5-tris(dodecyloxy)benzamide $C_{55}H_{91}N_3O_5$ $[M+Na]^+$: 896.685 found: 896.671

USC UNIVERSIDADE DE SANTIAGO DE COMPOSTELA

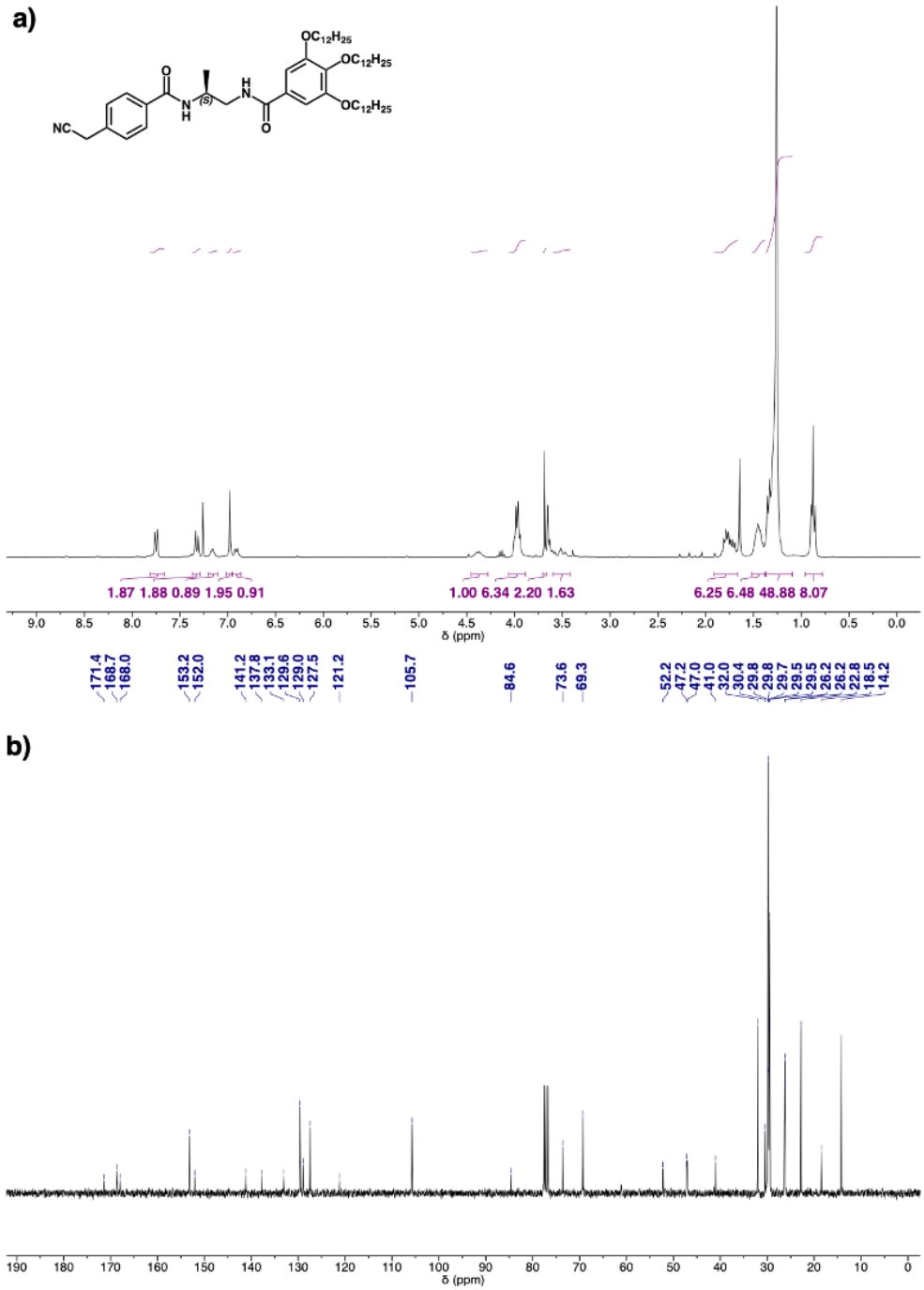


Figure S270. a) ^{1}H-NMR and b) ^{13}C-NMR spectra of (*S*)-*N*-(2-(4-(cyanomethyl)benzamido)propyl)-3,4,5-tris(dodecyloxy)benzamide ($CDCl_3$, 300 and 75 MHz, respectively).

USC UNIVERSIDADE DE SANTIAGO DE COMPOSTELA

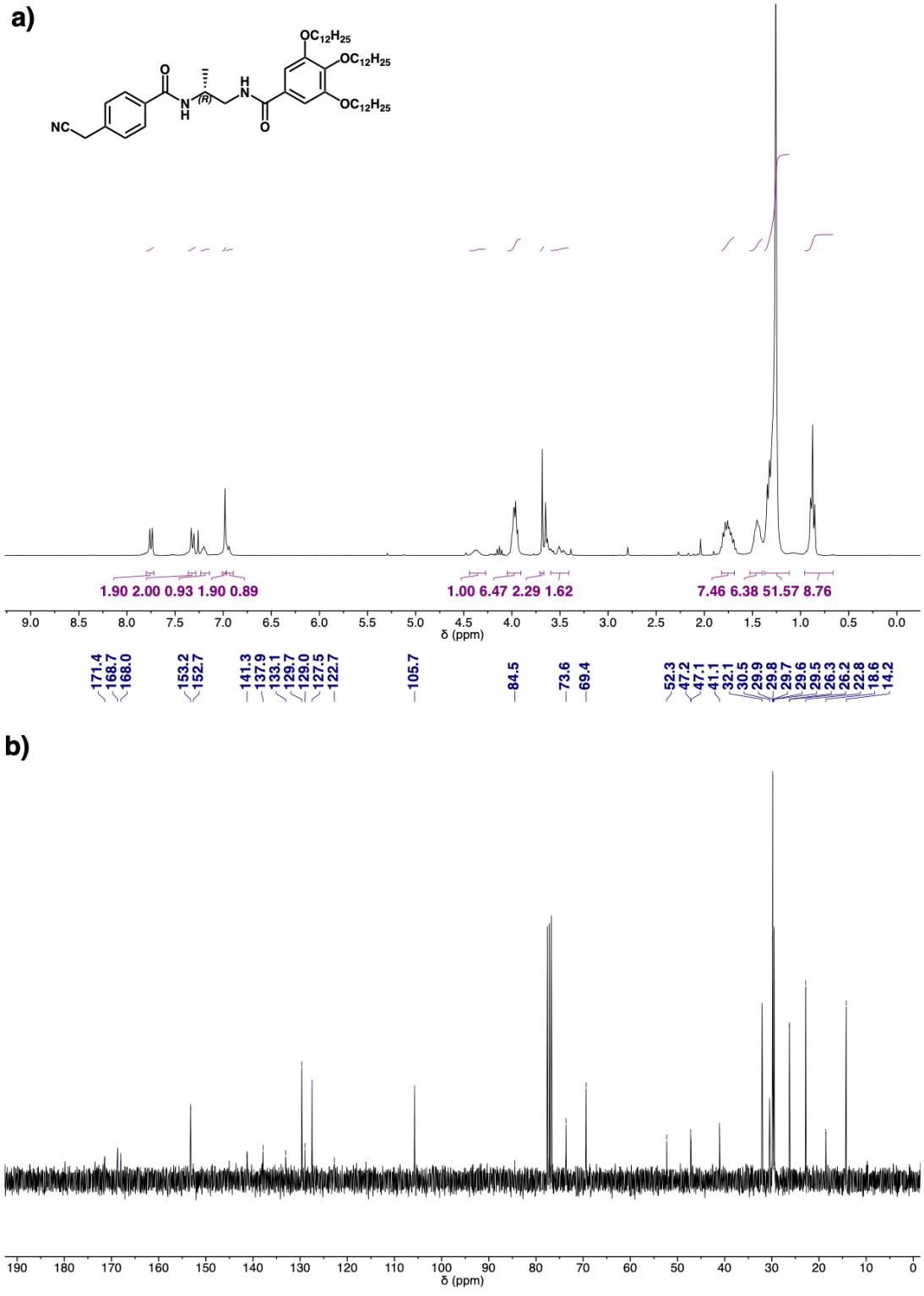
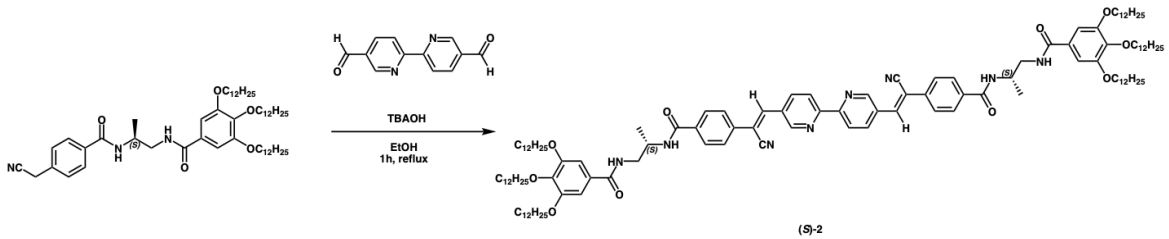


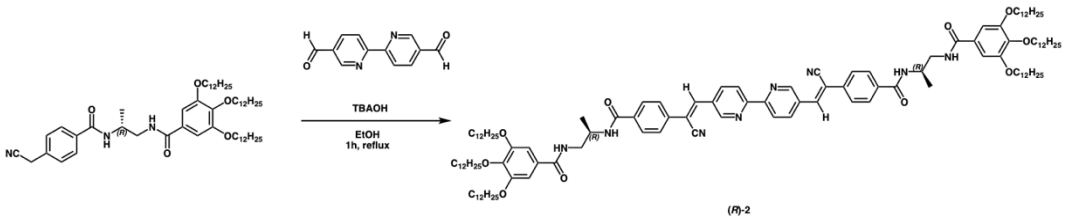
Figure S271. a) ^{1}H-NMR and b) ^{13}C-NMR spectra of (*R*)-*N*-(2-(4-(cyanomethyl)benzamido)propyl)-3,4,5-tris(dodecyloxy)benzamide ($CDCl_3$, 300 and 75 MHz, respectively).

USC
UNIVERSIDADE DE SANTIAGO DE COMPOSTELA

5.8.4. Synthesis of *N*,*N*'-((2*S*/*R*,2'*S*/*R*)-((4,4'-((1*Z*,1'*Z*)-[2,2'-bipyridine]-5,5'-diylbis(1-cyanoethene-2,1-diyl))bis(benzoyl))bis(azanediyl))bis(propane-2,1-diyl))bis(3,4,5-tris(dodecyloxy)benzamide)



(*S*)-*N*-(2-(4-(cyanomethyl)benzamido)propyl)-3,4,5-tris(dodecyloxy)benzamide (0.50 g, 0.57 mmol, 2.00 equiv) and [2,2'-bipyridine]-5,5'-dicarbaldehyde (0.06 g, 0.29 mmol, 1.00 equiv) were dissolved in boiling ethanol. Upon solution of both molecules a catalytic amount of TBAOH was added, and the mixture was further refluxed for 30 min. The reaction mixture was cooled down and poured into ice cold MeCN. The precipitates were centrifuged, and the supernatant was discarded. The obtained solid was dissolved in the minimum amount of DCM and reprecipitated in cold MeCN (2 cycles) affording pure *N*,*N*'-((2*S*,2'*S*)-((4,4'-((1*Z*,1'*Z*)-[2,2'-bipyridine]-5,5'-diylbis(1-cyanoethene-2,1-diyl))bis(benzoyl))bis(azanediyl))bis(propane-2,1-diyl))bis(3,4,5-tris(dodecyloxy)benzamide) in 54% yield (0.30 g).



The same protocol was applied for the preparation of *N*,*N*'-((2*R*,2*R*)-((4,4'-((1*Z*,1'*Z*)-[2,2'-bipyridine]-5,5'-diylbis(1-cyanoethene-2,1-diyl))bis(benzoyl))bis(azanediyl))bis(propane-2,1-diyl))bis(3,4,5-tris(dodecyloxy)benzamide), starting from (*R*)-*N*-(2-(4-(cyanomethyl)benzamido)propyl)-3,4,5-tris(dodecyloxy)benzamide (0.50 g, 0.57 mmol, 2.00 equiv) and [2,2'-bipyridine]-5,5'-dicarbaldehyde (0.06 g, 0.29 mmol, 2.00 equiv). Obtaining the desired product in 34% yield (0.19 g).

Spectroscopic data:

^{1}H-NMR (300 MHz, CDCl3) (*S*)-**2** δ_H (ppm): 8.90 (s, 1H), 8.51 (s, 2H), 7.80 (d, J = 8.2 Hz, 2H), 7.62 (d, J = 8.1 Hz, 2H), 7.58 (s, 1H), 7.52 (d, J = 7.4 Hz, 1H), 7.15 (s, 1H), 7.00 (s, 2H), 4.37 (s, 1H), 3.95 (m, 6H), 3.78 (m, 1H), 3.49 (d, J = 13.8 Hz, 1H), 1.74 (m, 7H), 1.32 (m, 63H), 0.85 (d, J = 7.1 Hz, 8H).

^{13}C-NMR (75 MHz, $CDCl_3$) (*S*)-**2** δ_C (ppm): 169.2, 167.0, 156.4, 153.3, 151.4, 141.5, 138.8, 136.5, 135.9, 135.3, 129.8, 129.0, 128.1, 126.1, 121.7, 117.2, 113.1, 105.9, 73.7, 69.5, 47.8, 46.4, 32.1, 30.5, 29.9, 29.8, 29.8, 29.6, 29.5, 26.3, 26.2, 22.8, 18.4, 14.2.

HRMS (MALDI-TOF) m/z calcd. for (*S*)-**2** $C_{122}H_{186}N_8O_{10}$ $[M+Na]^+$: 1946.418, found: 1946.477.

^{1}H-NMR (300 MHz, $CDCl_3$) (*R*)-**2** δ_H (ppm): 8.95 (s, 1H), 8.57 (s, 2H), 7.86 (d, J = 8.2 Hz, 2H), 7.69 (d, J = 8.0 Hz, 2H), 7.61 (s, 1H), 7.37 (d, J = 7.1 Hz, 1H), 7.00 (s, 2H), 6.98 (s, 1H), 4.38 (s, 1H), 3.98 (m, 6H), 3.75 (m, 1H), 3.51 (d, J = 14.0 Hz, 1H), 1.75 (m, 7H), 1.36 (m, 66H), 0.87 (t, J = 6.5 Hz, 8H).

^{13}C-NMR (75 MHz, $CDCl_3$) (*R*)-**2** δ_C (ppm): 169.2, 167.1, 156.4, 153.3, 151.4, 141.4, 138.8, 136.4, 135.9, 135.3, 129.7, 128.9, 128.1, 126.1, 121.6, 117.2, 113.0, 105.8, 73.7, 69.4, 47.7, 46.3, 32.1, 30.5, 29.9, 29.8, 29.7, 29.6, 29.5, 26.3, 26.2, 22.8, 18.4, 14.2.

HRMS (MALDI-TOF) m/z calcd. for (*R*)-**2** $C_{122}H_{186}N_8O_{10}$ $[M+Na]^+$: 1946.418, found: 1946.462

USC UNIVERSIDADE DE SANTIAGO DE COMPOSTELA

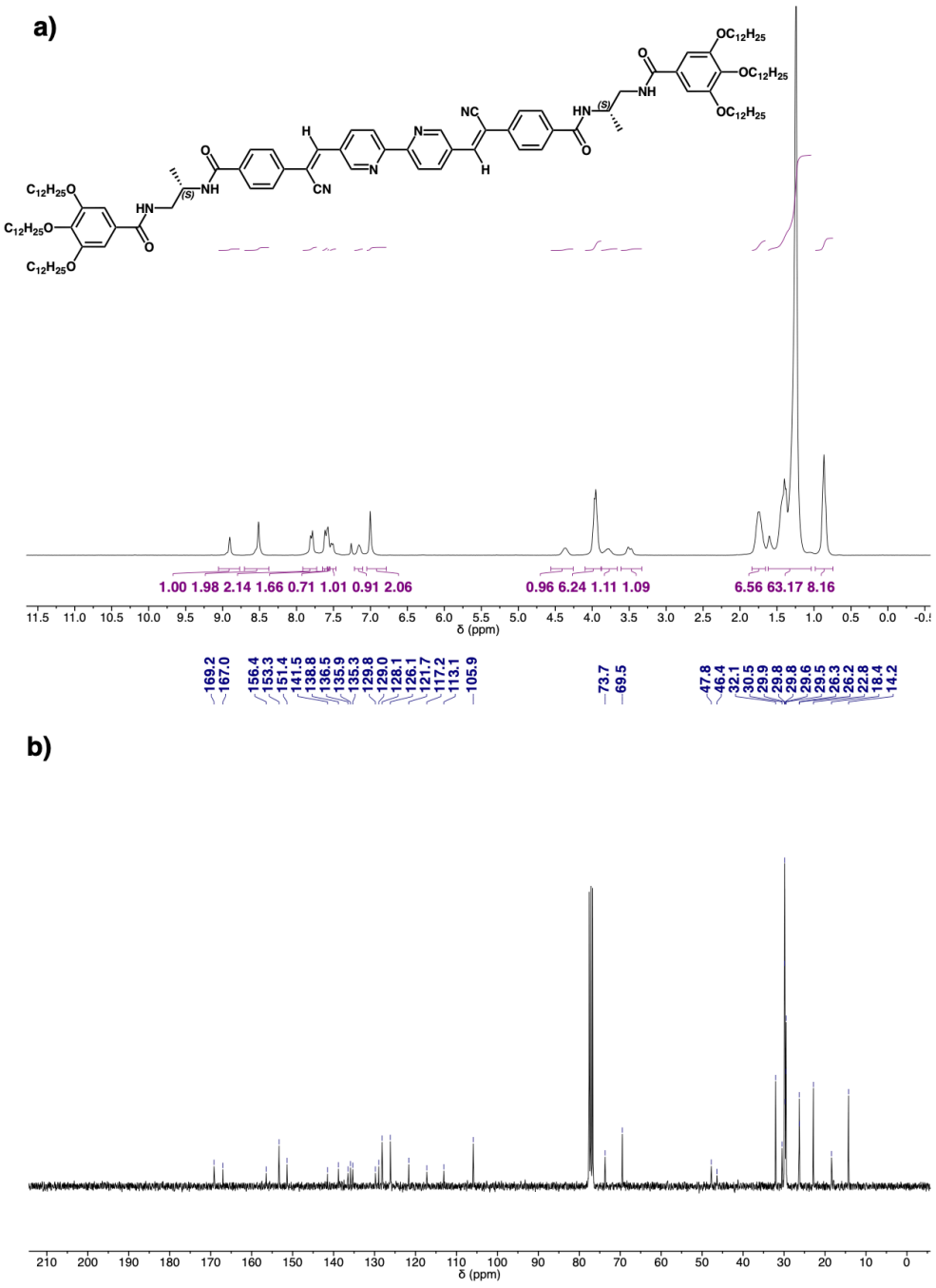


Figure S272. a) ^{1}H-NMR and b) ^{13}C-NMR spectra of (*S*)-**2** ($CDCl_3$, 300 and 75 MHz, respectively).

USC UNIVERSIDADE DE SANTIAGO DE COMPOSTELA

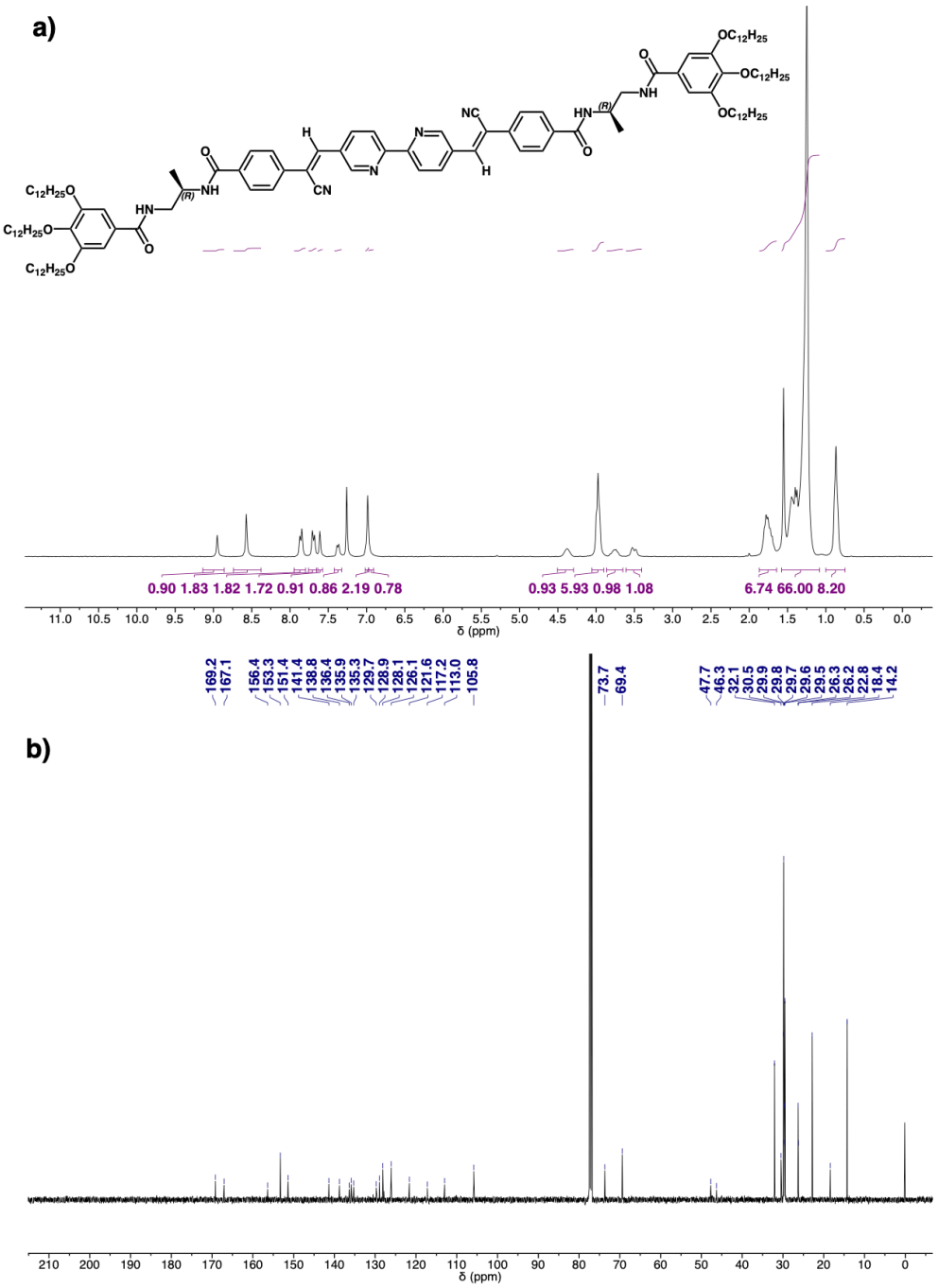
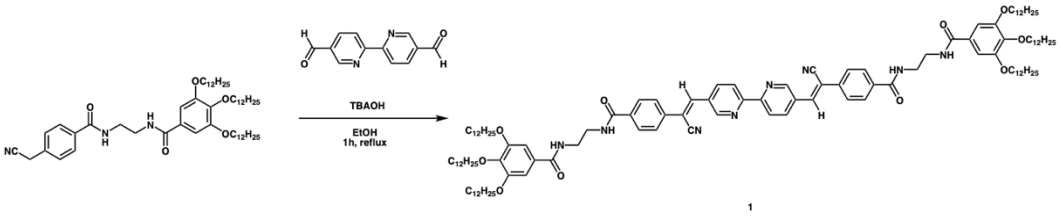


Figure S273. a) ^{1}H-NMR and b) ^{13}C-NMR spectra of (*R*)-**2** ($CDCl_3$, 300 and 75 MHz, respectively).

USC UNIVERSIDADE DE SANTIAGO DE COMPOSTELA

5.8.5. Synthesis of *N,N'*-(((4,4'-((1*Z*,1'*Z*)-[2,2'-bipyridine]-5,5'-diylbis(1-cyanoethene-2,1-diyl))bis(benzoyl))bis(azanediyl))bis(ethane-2,1-diyl))bis(3,4,5-tris(dodecyloxy)benzamide)



N-(2-(4-(cyanomethyl)benzamido)ethyl)-3,4,5-tris(dodecyloxy)benzamide (0.50 g, 0.59 mmol, 2.00 equiv) and [2,2'-bipyridine]-5,5'-dicarbaldehyde (0.06 g, 0.30 mmol, 1.00 equiv) were dissolved in boiling ethanol. Upon solution of both molecules a catalytic amount of TBAOH was added, and the mixture was further refluxed for 30 min. The reaction mixture was cooled down and poured into ice cold MeCN. The precipitates were centrifuged, and the supernatant was discarded. The obtained solid was dissolved in the minimum amount of DCM and reprecipitated in cold MeCN (2 cycles) affording pure *N,N'*-(((4,4'-((1*Z*,1'*Z*)-[2,2'-bipyridine]-5,5'-diylbis(1-cyanoethene-2,1-diyl))bis(benzoyl))bis(azanediyl))bis(ethane-2,1-diyl))bis(3,4,5-tris(dodecyloxy)benzamide) in 69% yield (0.39 g).

Spectroscopic data:

^{1}H-NMR (300 MHz, $CDCl_3$) δ_H (ppm): 8.92 (d, J = 7.0 Hz, 1H), 8.54 (d, J = 7.0 Hz, 2H), 7.82 (d, J = 8.3 Hz, 2H), 7.66 (d, J = 8.5 Hz, 3H), 7.61 (s, 1H), 7.15 (s, 1H), 7.05 (s, 2H), 3.98 (t, J = 6.4 Hz, 7H), 3.72 (s, 5H), 1.76 (m, 7H), 1.59 (s, 9H), 1.26 (m, 59H), 0.87 (m, 9H).

^{13}C-NMR (75 MHz, $CDCl_3$) δ_C (ppm): 167.6, 153.3, 152.7, 151.4, 150.2, 135.9, 128.9, 128.2, 126.2, 125.1, 123.5, 121.7, 118.0, 105.9, 73.7, 69.5, 47.8, 46.4, 32.1, 30.5, 29.8, 29.5, 26.3, 22.8, 14.3.

HRMS (MALDI-TOF) m/z calcd. for **1** $C_{120}H_{182}N_8O_{10}$ $[M+Na]^+$: 1918.387 found: 1918.468.

USC UNIVERSIDADE DE SANTIAGO DE COMPOSTELA

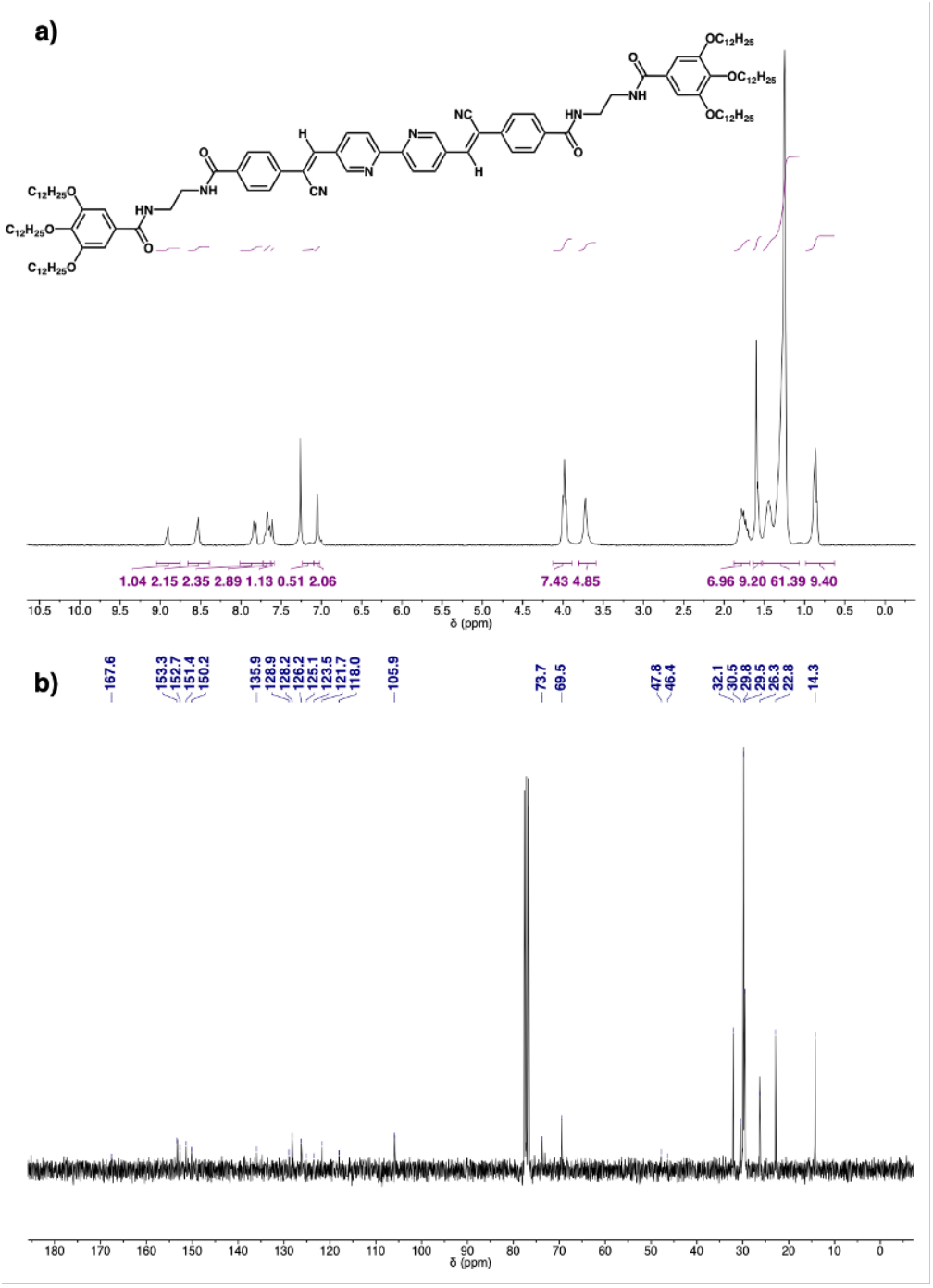


Figure S274. a) ^{1}H-NMR and b) ^{13}C-NMR spectra of **1** ($CDCl_3$, 300 and 75 MHz, respectively).

USC UNIVERSIDADE DE SANTIAGO DE COMPOSTELA

5.8.6. IR experiments

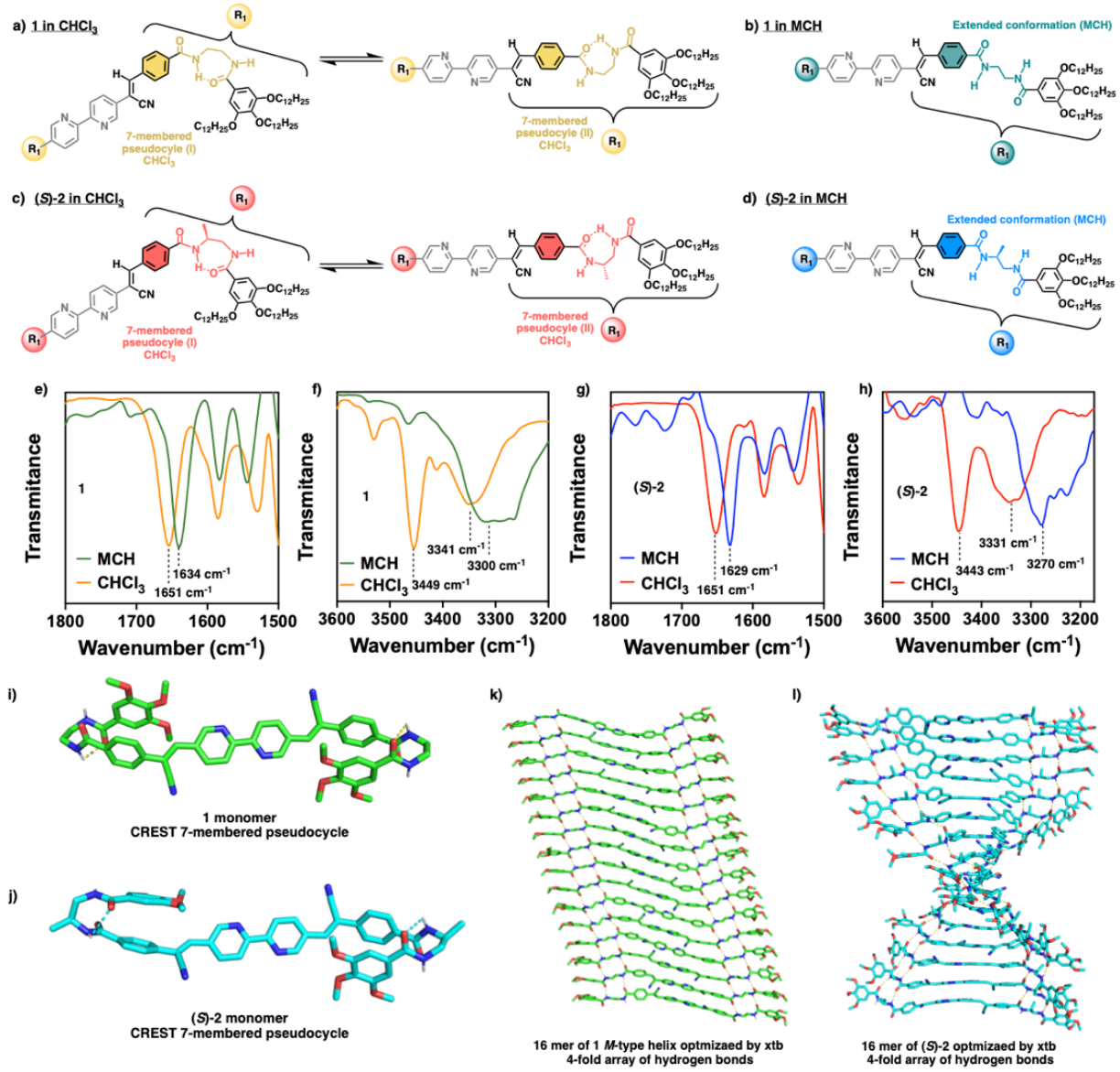


Figure S275. Chemical Structure of **1** and (*S*)-**2** with the ethylenediamide bridge forming (a,c) the two possible 7-membered pseudocycles or (b,d) the extended conformation that promoted effective aggregation. IR spectra of (e,f) **1** and (g,h) (*S*)-**2** in $CHCl_3$ and MCH (c_T = 0.5 μM) confirming the presence of the abovementioned structures. Monomers stabilizing pseudocycles calculated by CREST and the aggregated 16-mer optimized by GFN2-xTB of **1** (l,k) and (*S*)-**2** (j,l).

USC UNIVERSIDADE DE SANTIAGO DE COMPOSTELA

5.8.7. Temperature dependent NMR experiments

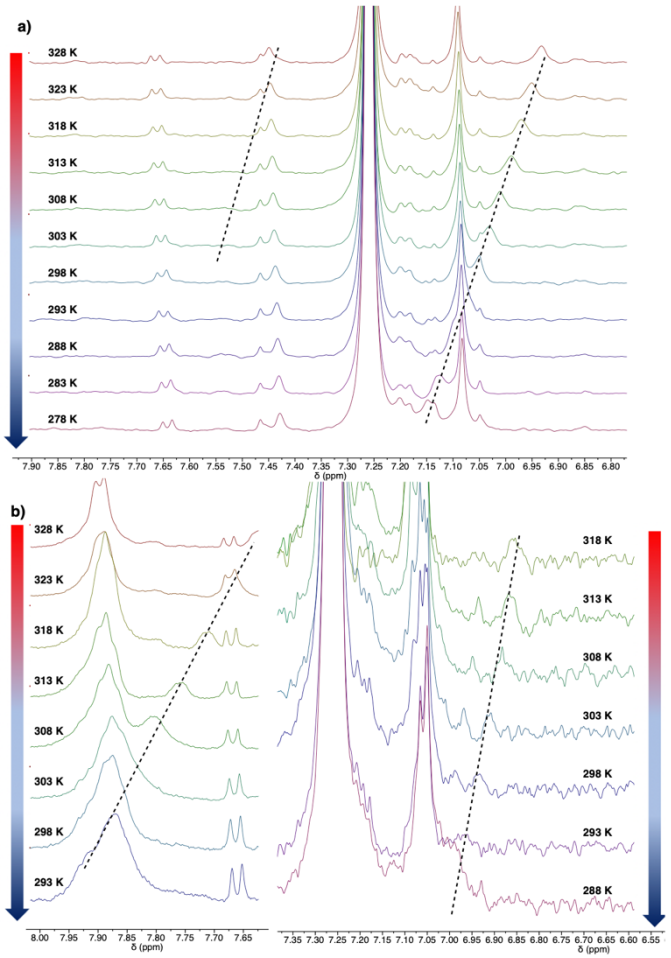


Figure S276. Temperature dependent at $CHCl_3$/MCH (4/6) of (a) **1** and (b) (*S*)-**2** ($CDCl_3$, 500 MHZ).

5.8.8. Additional Spectra

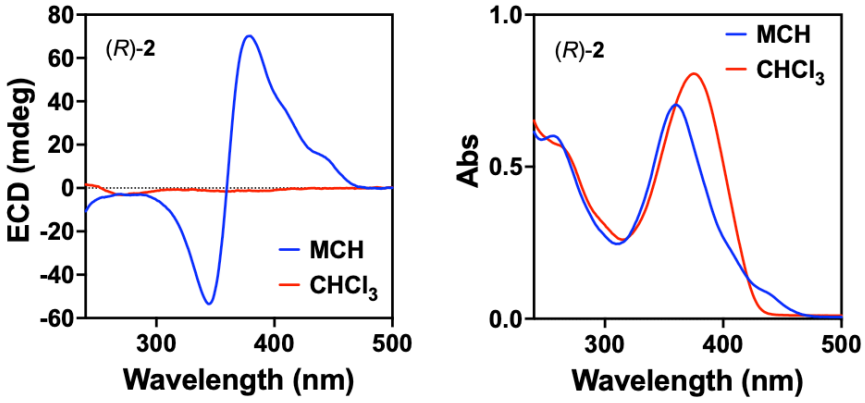


Figure S277. (a) ECD and (b) UV-Vis spectra of (*R*)-**2** in MCH and $CHCl_3$ (c_T= 100 μM).

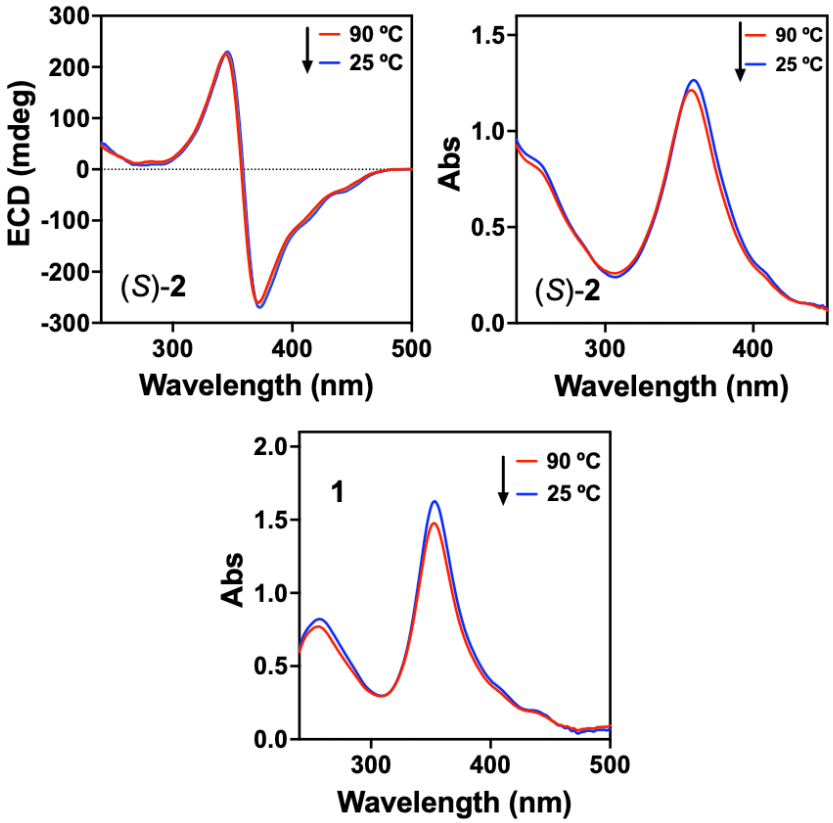


Figure S278. (a) VT-ECD and (b) VT-UV-Vis spectra of (*S*)-**2** in MCH (c_T= 250 μM). (c) VT-UV-Vis spectra of **1** in MCH (c_T= 250 μM).

USC
UNIVERSIDADE DE SANTIAGO DE COMPOSTELA

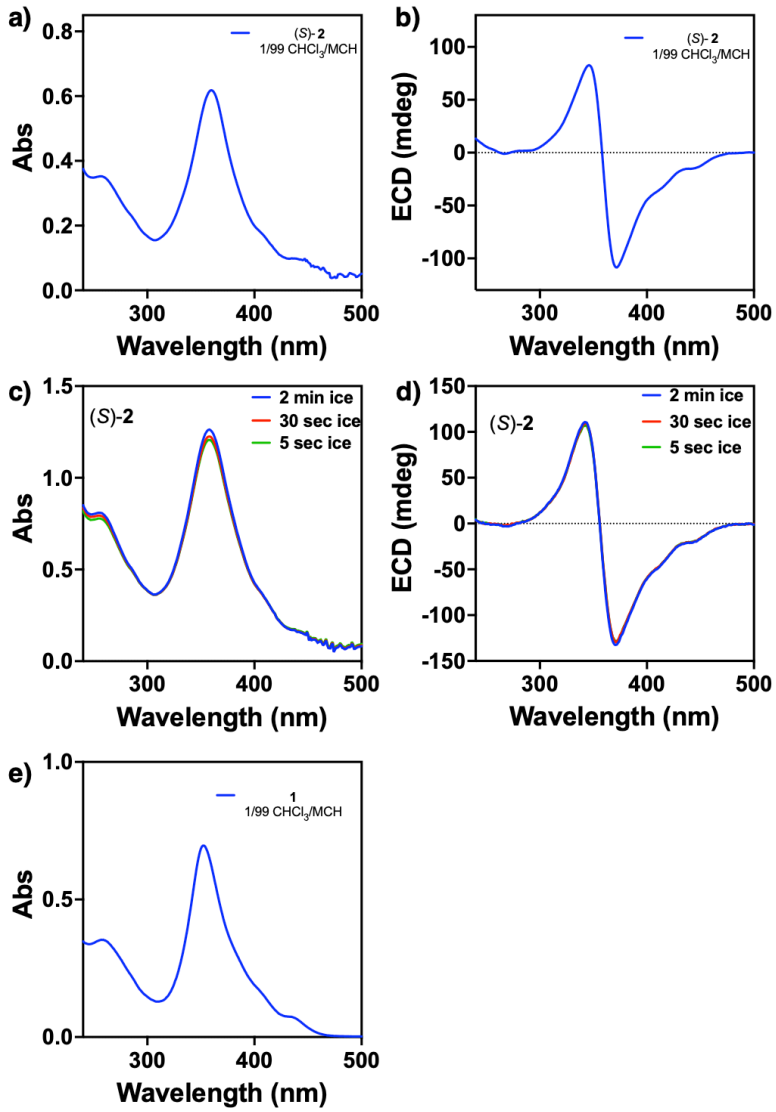


Figure S279. Solvophobic quenching (c_T= 100 μM) of (*S*)-**2** in 1/99 $CHCl_3$/MCH (a) UV-Vis and (b) ECD. Thermal quenching (c_T= 200 μM) of (*S*)-**2** (a) UV-Vis (b) ECD. (e) Solvophobic quenching (c_T= 100 μM) of **1** in 1/99 $CHCl_3$/MCH UV-Vis.

USC UNIVERSIDADE DE SANTIAGO DE COMPOSTELA

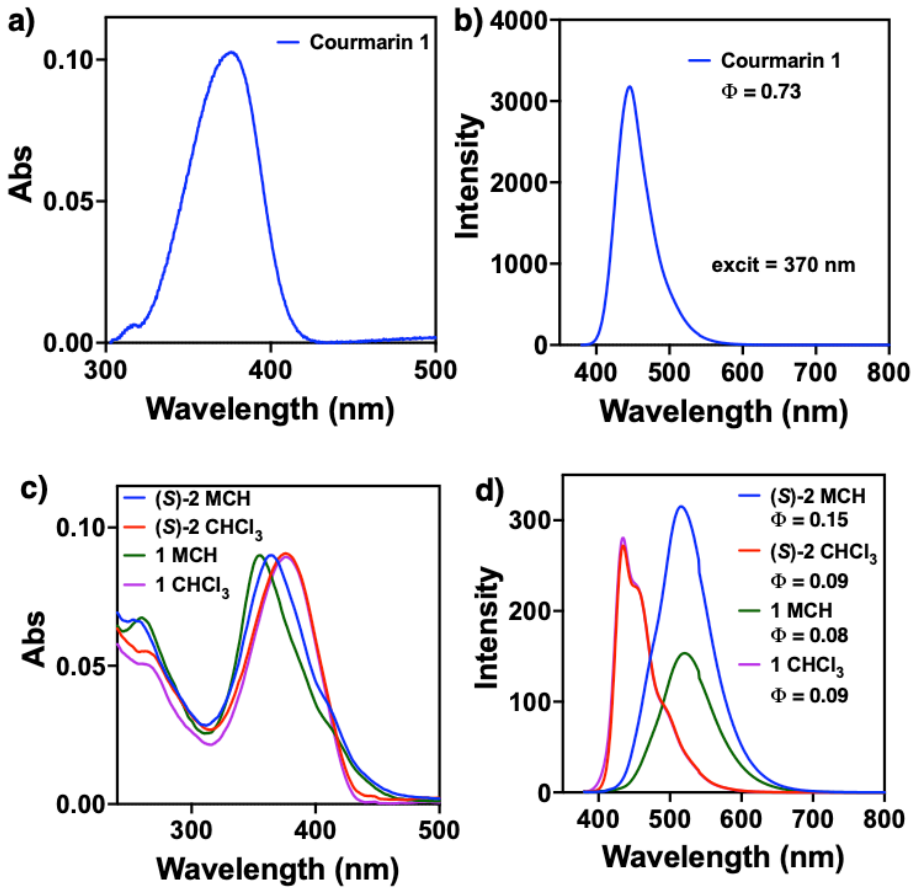


Figure S280. (a) UV-Vis, (b) emission spectra and quantum yield of coumarin 1 in ethanol (c_T = 20 μM, 298 K, exc= 370 nm, sensitivity low, emission slit = 5.0 nm and excitation slit=2.5 nm). (c) UV-Vis, (d) emission spectra and quantum yield of **1** and (*S*)-**2** in MCH and $CHCl_3$ (c_T = 10 μM, 298 K, exc= 370 nm, sensitivity low, emission slit = 5.0 nm and excitation slit=2.5 nm).

USC
UNIVERSIDADE DE SANTIAGO DE COMPOSTELA

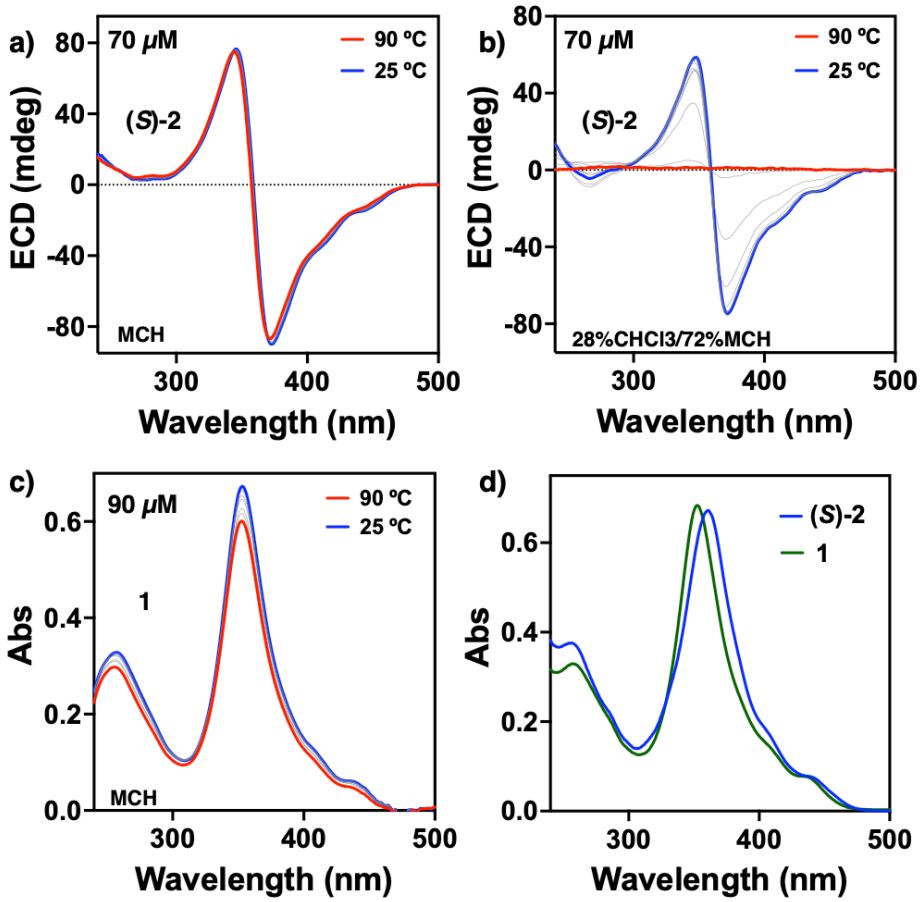


Figure S281. (a,b) VT-ECD cooling curve 1 K/min of (*S*)-**2** in MCH and 28/72 $CHCl_3$/MCH. (c) VT-UV-Vis cooling curve 1 K/min of 1 in MCH (d) UV-Vis of (*S*)-**2** and **1** in MCH.

USC UNIVERSIDADE DE SANTIAGO DE COMPOSTELA

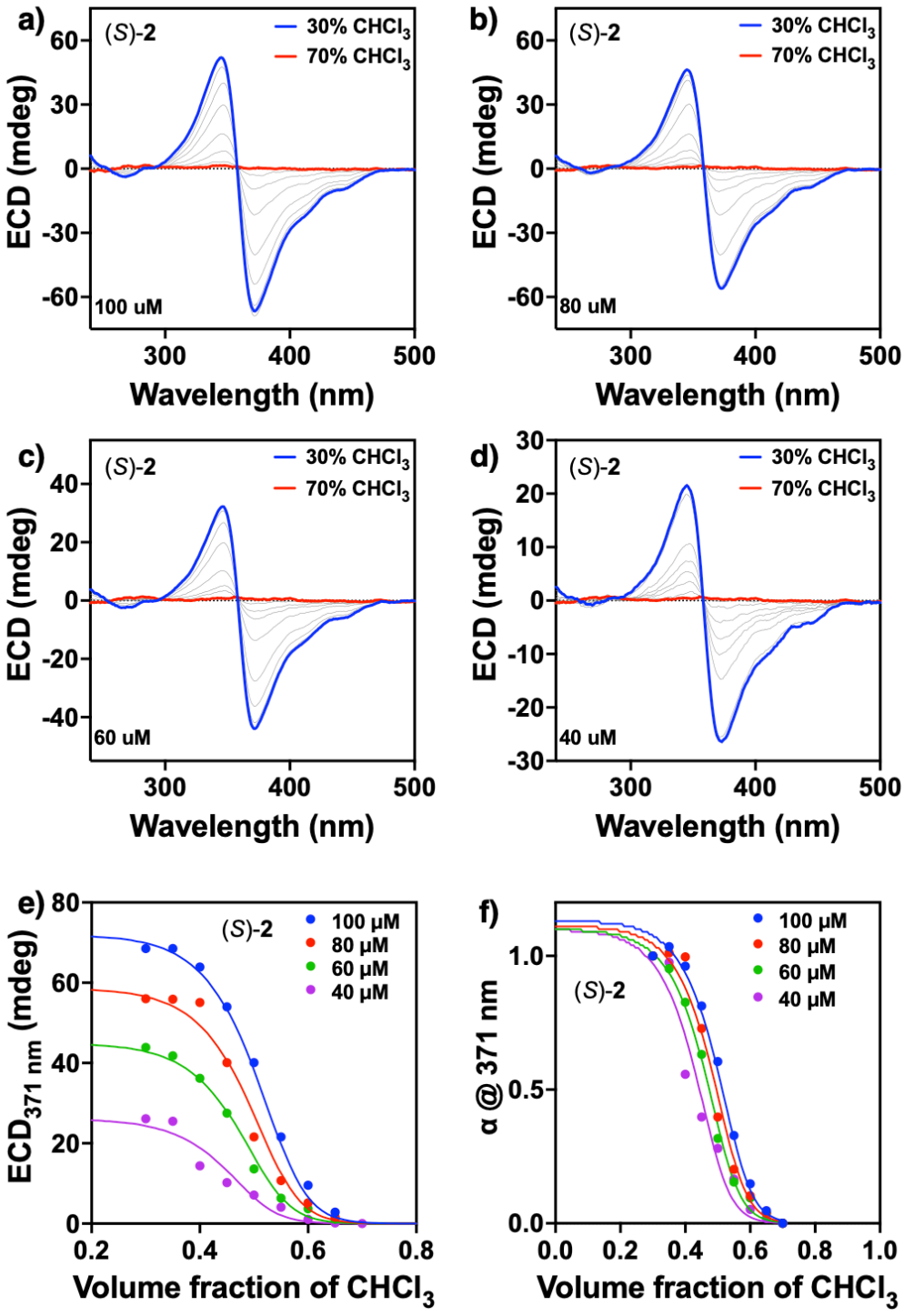


Figure S282. Solvent denaturation ECD spectra of (*S*)-**2** in $CHCl_3$/MCH: (a) c_T= 100 µM; (b) c_T= 80 µM; (c) c_T= 60 µM; (d) c_T= 40 M. (e, f) Solvent denaturation fitting of the ECD spectra for (*S*)-**2** in $CHCl_3$/MCH at different concentrations.

USC UNIVERSIDADE DE SANTIAGO DE COMPOSTELA

Table S38. Thermodynamic parameters of the supramolecular polymerization process of (*S*)-**2** in $CHCl_3$/MCH mixture obtained by solvent denaturation followed by ECD spectroscopy (c_T = 100, 80, 60, and 40 μM, 298 K).

$\Delta G^{0\prime}$ (kJ/mol)	m
$-4.10 \cdot 10^1$	$3.38 \cdot 10^1$

USC UNIVERSIDADE DE SANTIAGO DE COMPOSTELA

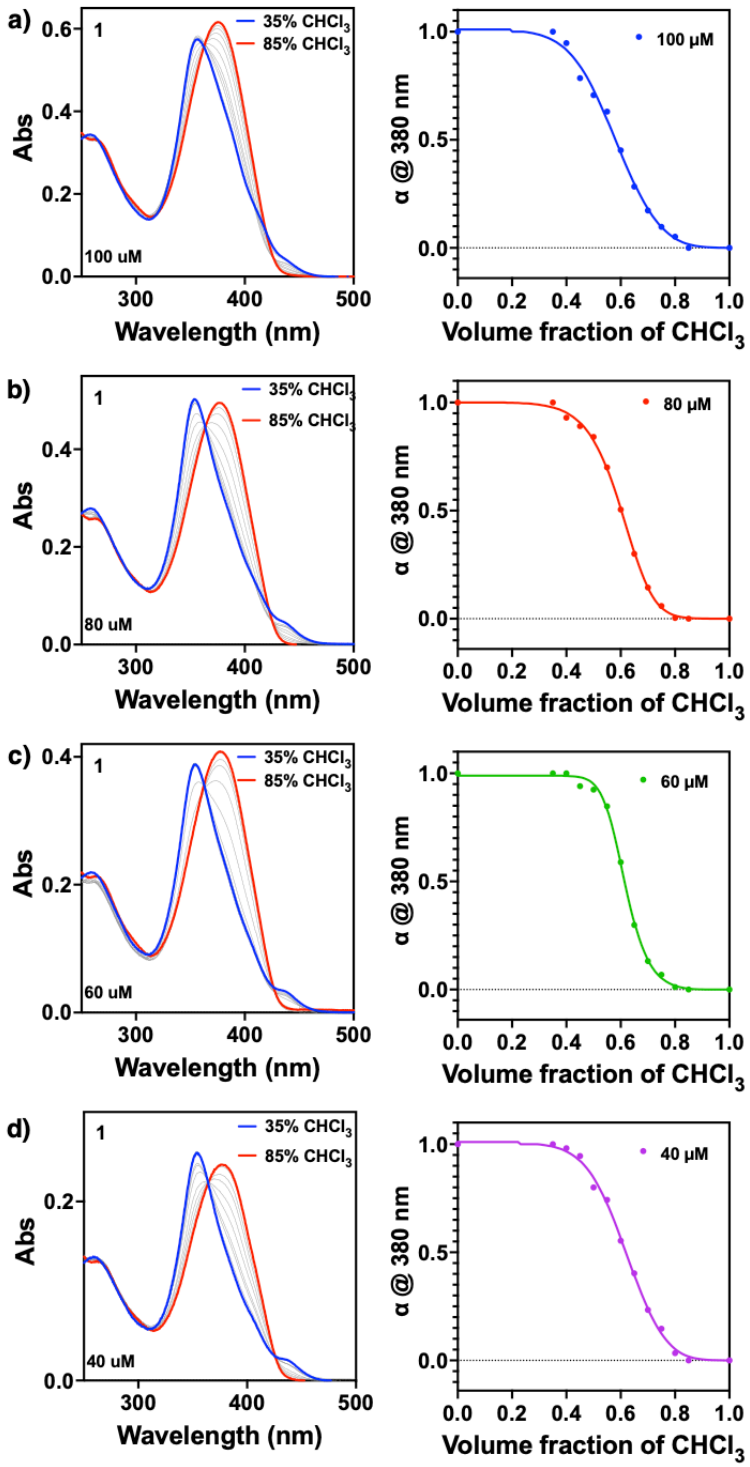


Figure S283. Solvent denaturation UV-Vis spectra and fitting of α_{Agg} for **1** in $CHCl_3$/MCH: (a) c_T= 100 µM; (b) c_T= 80 µM; (c) c_T= 60 µM; (d) c_T= 40 µM.

USC UNIVERSIDADE DE SANTIAGO DE COMPOSTELA

Table S39. Thermodynamic parameters of the supramolecular polymerization process of **1** in $CHCl_3$/MCH mixture obtained by solvent denaturation followed by UV-Vis spectroscopy (c_T = 100, 80, 60, and 40 μM, 298 K).

c_T (*μ*M)	$DG^{0'}$ (kJ/mol)	m
100	$-4.96 \cdot 10^1$	$4.00 \cdot 10^1$
80	$-4.79 \cdot 10^1$	$3.81 \cdot 10^1$
60	$-5.00 \cdot 10^1$	$3.82 \cdot 10^1$
40	$-5.55 \cdot 10^1$	$4.40 \cdot 10^1$
ϕ	$-5.08 \cdot 10^1$	$4.01 \cdot 10^1$

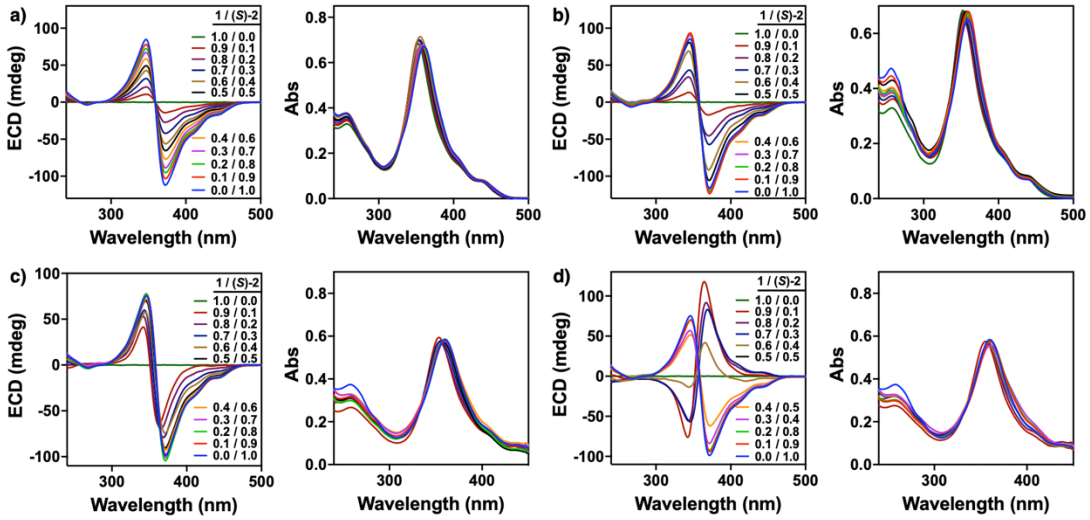


Figure S284. Copolymer communication experiments illustrated through ECD and UV-Vis spectra of various **1**/(*S*)-**2** mixtures (c_T= 100 μM, 25 ºC): (a) individual solutions of **1** and (*S*)-**2** prepared in MCH, followed by measurement of the mixture in MCH; (b) individual solutions of **1** and (*S*)-**2** prepared in $CHCl_3$, mixed, evaporated to remove $CHCl_3$, and then dissolved in MCH; (c) individual solutions of **1** and (*S*)-**2** prepared in $CHCl_3$, mixed, followed by the addition of MCH to obtain a 32% $CHCl_3$ / 68% MCH mixture; (d) individual solutions of **1** and (*S*)-**2** prepared in $CHCl_3$, mixed, followed by the addition of MCH to obtain a 32% $CHCl_3$ / 68% MCH mixture, subjected to a heating-cooling cycle, and measured in the resulting solvent mixture.

USC UNIVERSIDADE DE SANTIAGO DE COMPOSTELA

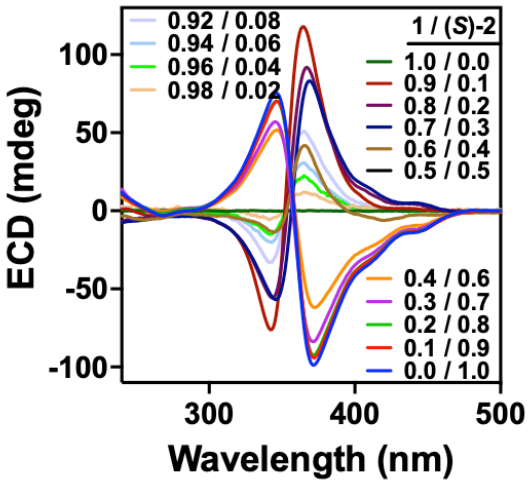


Figure S285. Copolymer communication experiments illustrated through ECD spectra of various **1**/(*S*)-**2** mixtures (c_T= 100 μM, 25 ºC) prepared in $CHCl_3$, mixed, followed by the addition of MCH to obtain a 32% $CHCl_3$ / 68% MCH mixture after VT heating until disassembly and cooling 1 K/min cycle.

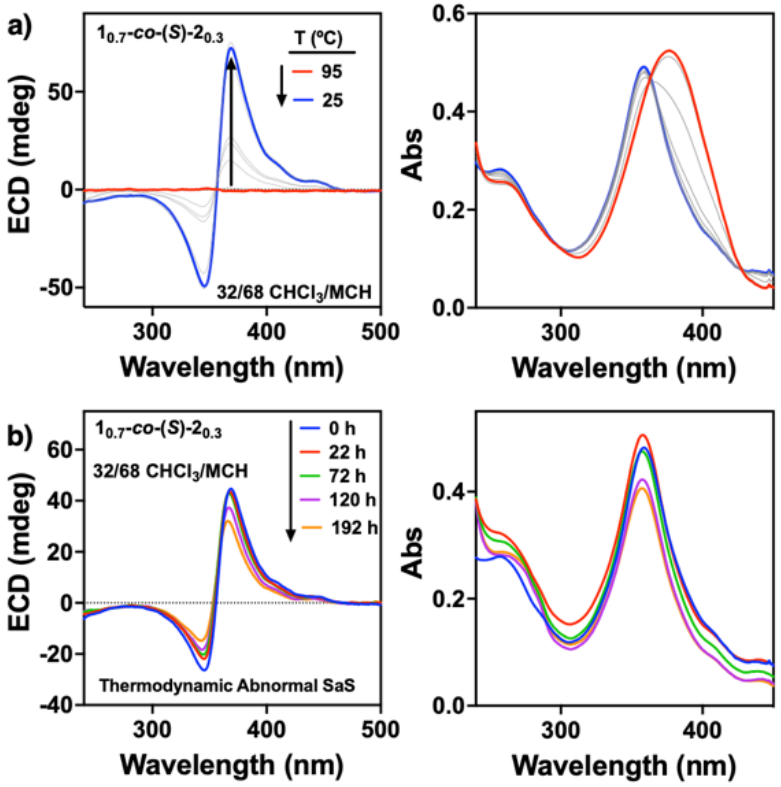


Figure S286. Thermal and temporal studies of the Abnormal Sergeants and Soldiers Effect in a **1**/(*S*)-**2** mixture (70% **1**, 30% (*S*)-**2**, c_T= 100 μM) in 32% $CHCl_3$ / 68% MCH: (a) VT-ECD and VT-UV-Vis spectra during a temperature ramp from 90 ºC (monomeric state) to 25 ºC (aggregated state), showcasing the thermodynamically driven Abnormal Sergeants and Soldiers Effect; (b) time-dependent stability study of the thermodynamic aggregate at 25 ºC, monitored by ECD and UV-Vis to assess persistence of the Abnormal Sergeants and Soldiers Effect.

USC UNIVERSIDADE DE SANTIAGO DE COMPOSTELA

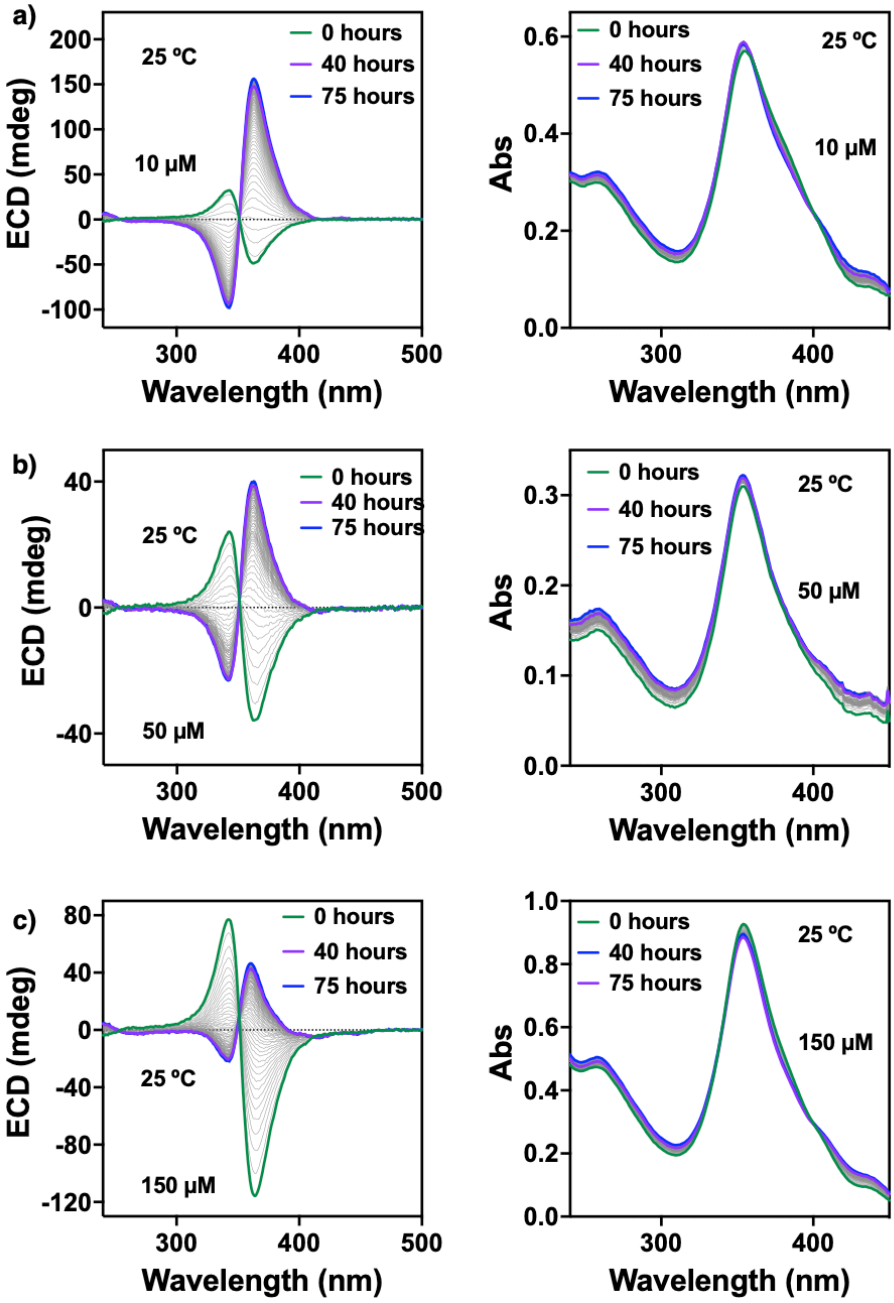


Figure S287. Kinetic studies of the evolution of *M*-helices from a kinetically Sergeants and Soldiers Effect to a thermodynamically Abnormal Sergeants and Soldiers Effect in a 80% **1** 20% (*S*)-**2** mixture in 32% $CHCl_3$ / 68% MCH at 25ºC, monitored by ECD and UV-Vis: (a) time-dependent measurements c_T= 10 µM using a 1 cm pathlength cuvette; (b) time-dependent measurements at c_T= 50 µM. using a 1 mm pathlength cuvette; (c) time-dependent measurements at c_T= 150 µM using a 1 mm pathlength cuvette.

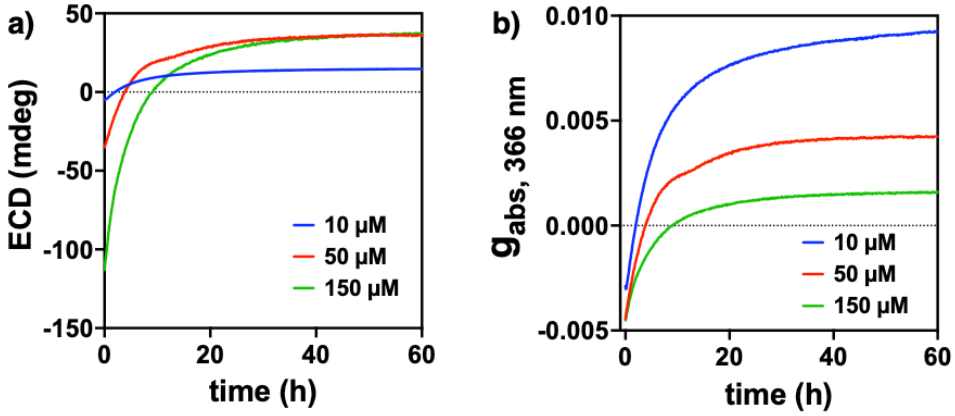


Figure S288. Kinetic studies of the evolution of *M*-helices from a kinetically Sergeants and Soldiers Effect to a thermodynamically Abnormal Sergeants and Soldiers Effect in 80% **1**, 20% (*S*)-**2** mixtures in 32% $CHCl_3$ / 68% MCH at 25ºC at different concentrations, monitored by (a)ECD (b) g_{abs}.

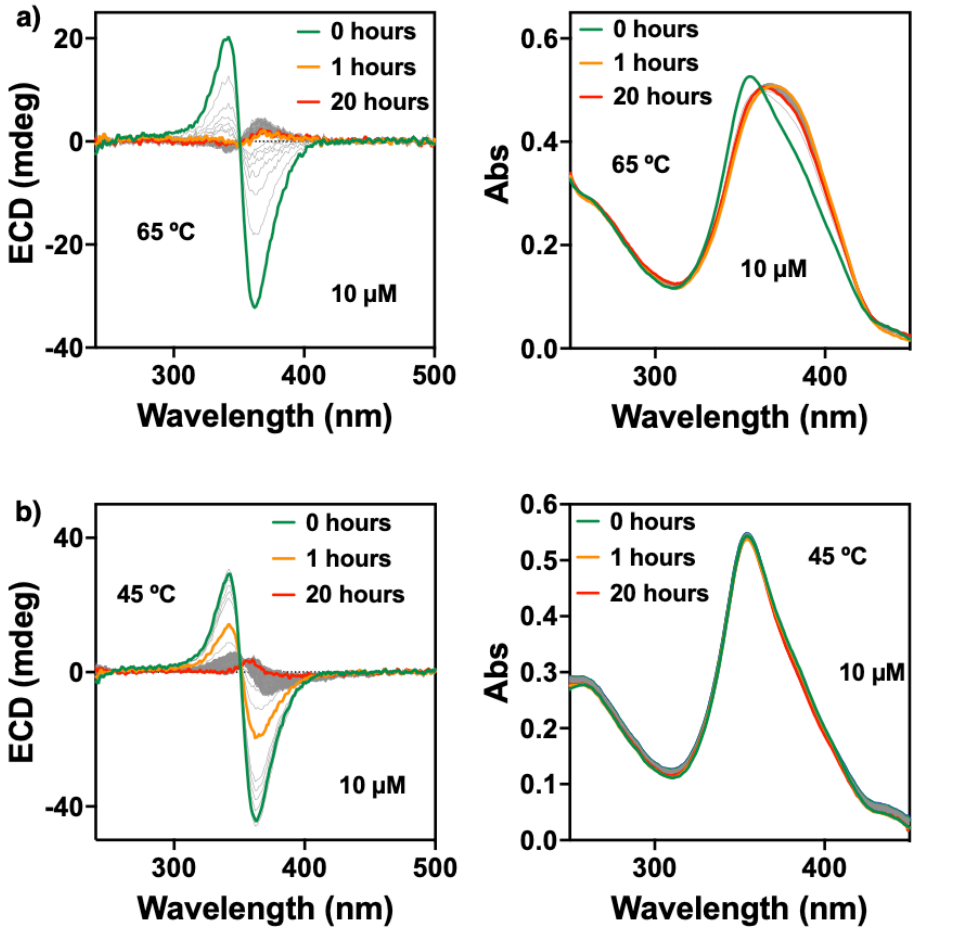


Figure S289. Kinetic studies in 80% **1**, 20% (*S*)-**2** mixture c_T= 100 µM in 32% $CHCl_3$ / 68% MCH using a 1 cm pathlength cuvette, monitored by ECD and UV-Vis: (a) time-dependent at 65 ºC (b) time-dependent at 45 ºC.

USC UNIVERSIDADE DE SANTIAGO DE COMPOSTELA

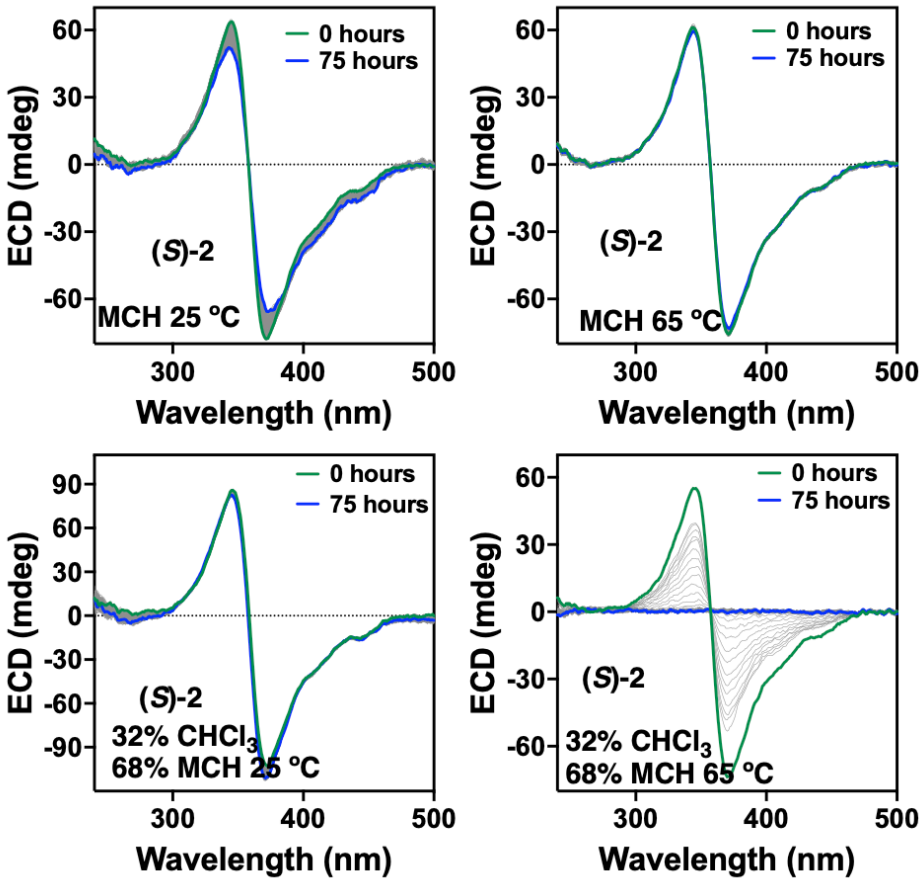


Figure S290. Kinetic studies of the homopolymer of (*S*)-**2** at c_T= 100 μM in 32% $CHCl_3$ / 68% MCH and 100% MCH at 25 or 65 ºC.

USC UNIVERSIDADE DE SANTIAGO DE COMPOSTELA

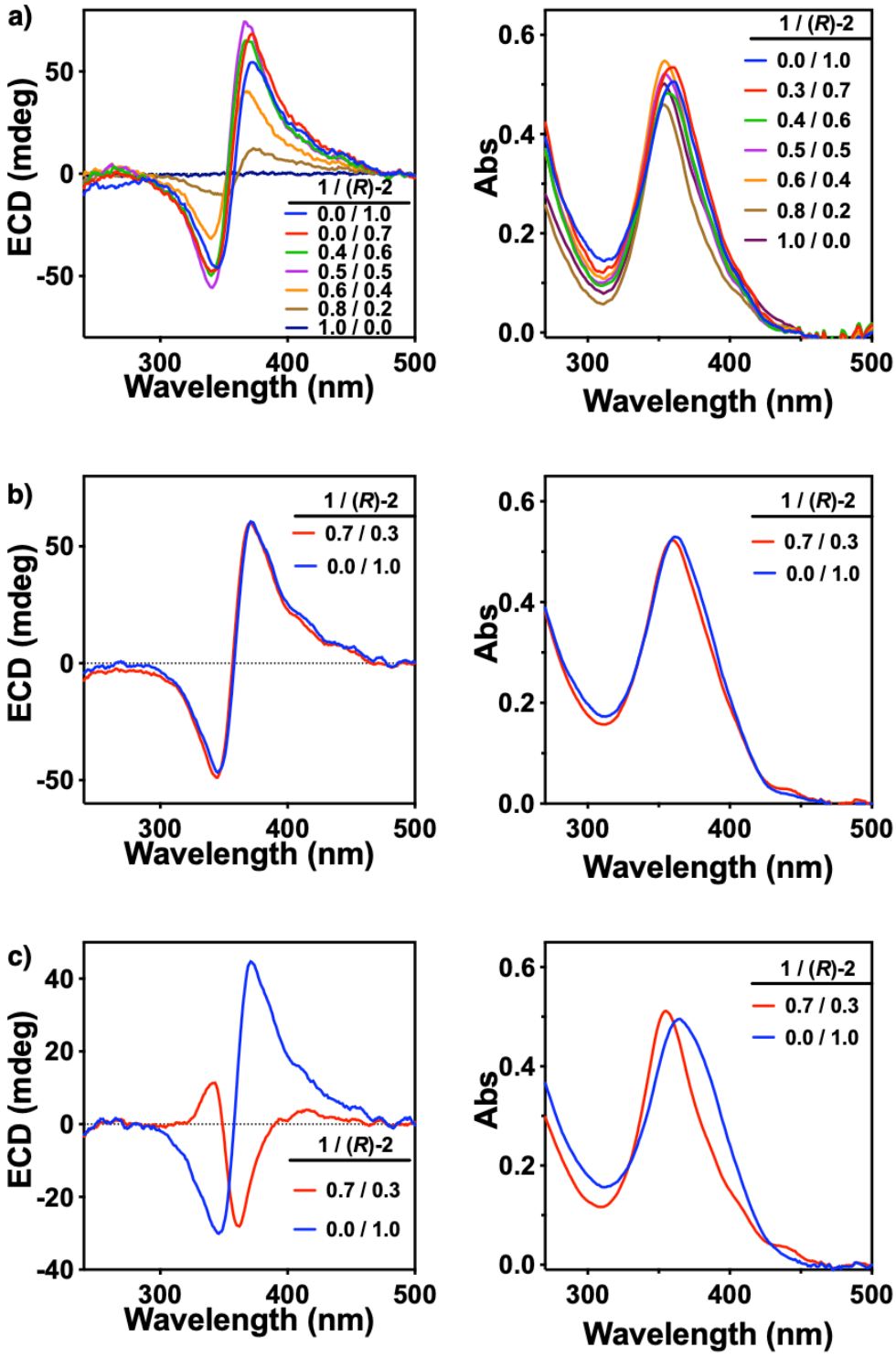


Figure S291. Copolymer communication experiments illustrated through ECD and UV-Vis spectra of various **1**/(*R*)-**2** mixtures (c_T= 100 μM, 25 ºC): (a) individual solutions of **1** and (*R*)-**2** prepared in $CHCl_3$, mixed, evaporated to remove $CHCl_3$, and then dissolved in MCH; (b) individual solutions of **1** and (*R*)-**2** prepared in $CHCl_3$, mixed, followed by the addition of MCH to obtain a 32% $CHCl_3$ / 68% MCH mixture; (c) individual solutions of **1** and (*R*)-**2** prepared in $CHCl_3$, mixed, followed by the addition of MCH to obtain a 32% $CHCl_3$ / 68% MCH mixture, subjected to a heating-cooling cycle, and measured in the resulting solvent mixture.

USC UNIVERSIDADE DE SANTIAGO DE COMPOSTELA

5.8.9. AFM Studies

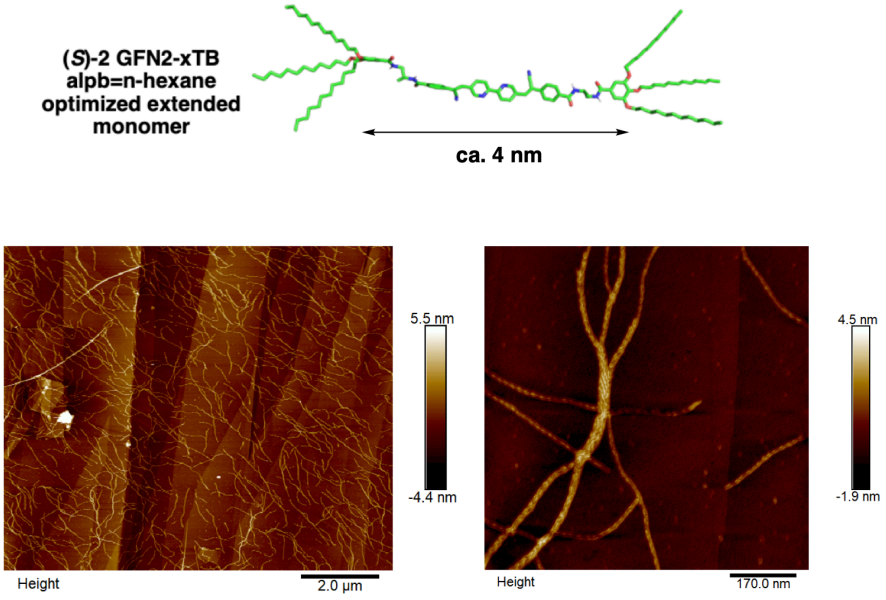


Figure S292. Additional AFM images for (*S*)-**2**.

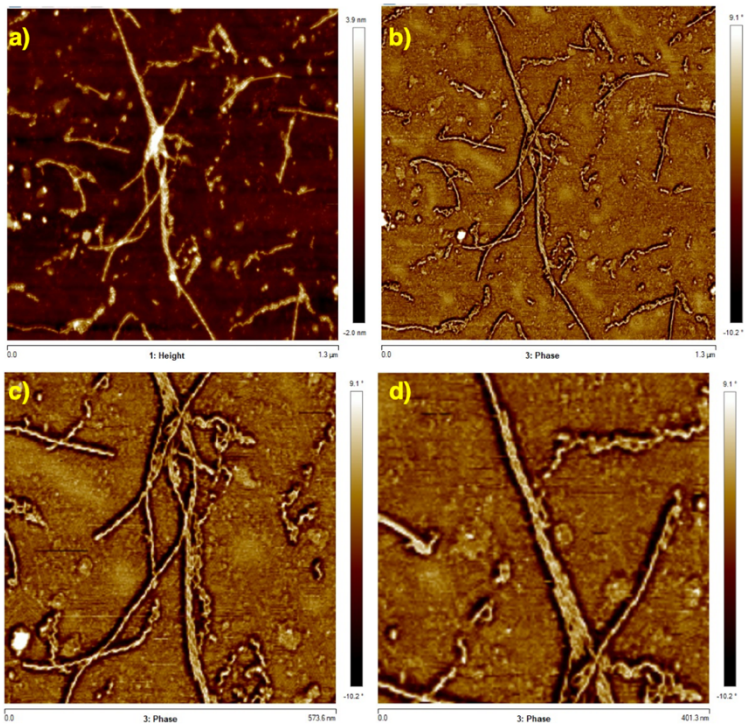


Figure S293. a) Height and b) phase image images of the thermodynamic structure of Poly-[**1**$_{0.2}$-*co*-(*S*)-**2**$_{0.2}$]. c) and d) magnifications of image.

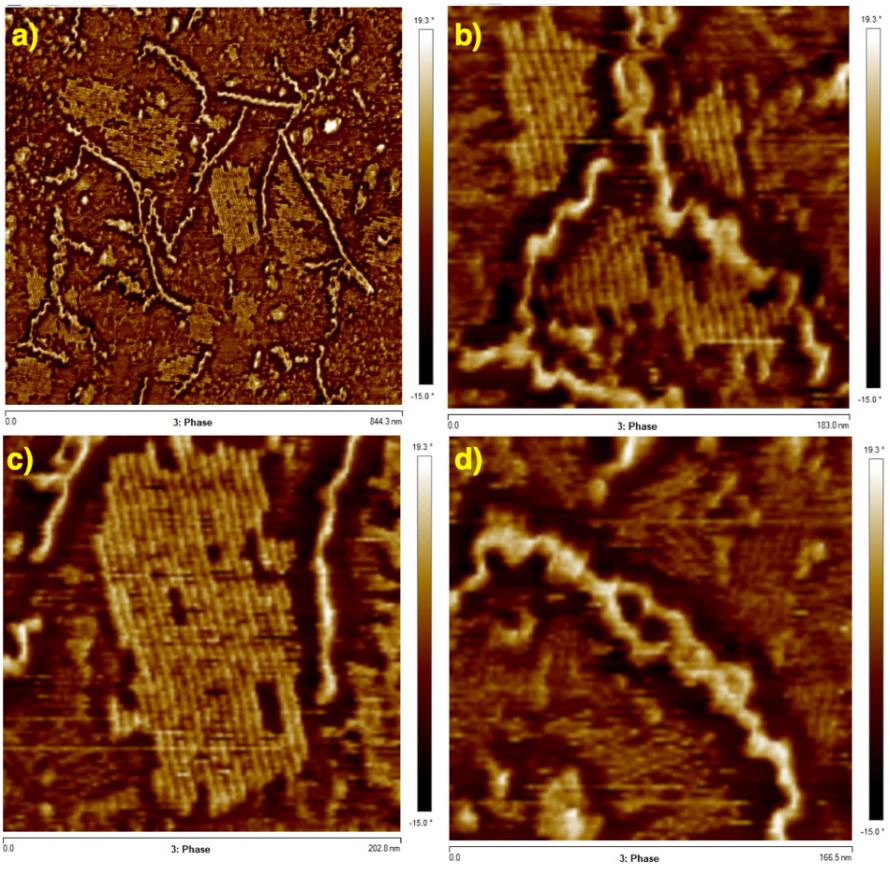


Figure S294. AFM images of thermodynamic structure of Poly-[**1**$_{0.2}$-*co*-(*S*)-**2**$_{0.2}$] a) large scale image showing the presence on unimolecular helical structures among higher fiber-like aggregates. b) to d) magnifications of image a) showing unimolecular right-handed helical structures.

5.8.10. Density functional theory-based computations

The conformational space of a simplified monomeric unit of **1** and (*S*)-**2** (where peripheral dodecyl side chains are replaced by methyl groups) was explored using the Conformer–Rotamer Ensemble Sampling Tool (CREST 3.0.1),[536] implemented in the xtb-6.6.0 program package.[555] Chloroform ($CHCl_3$) was included as the solvent using the analytical linearized Poisson-Boltzmann (ALPB) model.[556] The most stable conformers for (*S*)-**2** in $CHCl_3$ were identified using the semiempirical GFN2-xTB method, which operates with a Hamiltonian like DFTB3, employing a minimal valence basis set (STO-mG) and density-dependent D4 dispersion corrections.[557] The monomers of **1** and (*S*)-**2** exhibited their most stable conformations through the formation of pseudocycles via bisamide interactions. For the dimerization process, only the molecular core (up to the

first amide group of the bisamide) was considered to identify the most stable packing arrangement. CREST calculations in alpb=*n*-hexane revealed that the dimers adopt an H-aggregate structure, with alternating bipyridine trans nitrogens and cyanostilbene groups to minimize steric overlap between stacked monomers. The energy difference between cyanostilbene groups in cis and trans configurations relative to the nearest bipyridine nitrogen was negligible. Afterwards, DFT optimization and frequency calculations of the dimer were performed using Gaussian-16.C01.[413] in the wb97XD/6-31+g(d,p) functional with a PCM solvent model for methylcyclohexane (MCH).

To confirm the H-aggregate nature of the dimer, time-dependent density functional theory (TD-DFT) calculations of the optimized ground state by DFT. At the wb97xd/6-31+G** level of theory with PCM (methylcyclohexane),[126,414-418] the calculated and processed by Multiwfn[558] electronic transition dipole moments (TDMs) revealed that the lowest-energy transition (to the first excited singlet) had antiparallel TDMs between monomers, canceling the total TDM and resulting in low absorption. In contrast, the second excited singlet transition exhibited parallel TDMs, summing to a total TDM and leading to higher absorption. These results align with Kasha's Rules for H-aggregates, where transitions to the lowest-energy excited state are symmetry-forbidden, leading to reduced absorption. To confirm these findings, DFT (wb97xd/6-31+G** PCM = methylcyclohexane) was used to obtain the MOs of HOMO-1, HOMO, LUMO, and LUMO+1. NTOs for the first two transitions were computed in TD-DFT (wb97xd/6-31+G** PCM = methylcyclohexane) and matched with the MOs to elucidate the transitions. The first NTO was a forbidden transition between the symmetric HOMO and asymmetric LUMO because their symmetry mismatch prevents sufficient orbital overlap. The second allowed transition occurred due to an interaction between HOMO and LUMO asymmetric orbitals, which share the same general symmetry or have sufficient overlap, making the transition allowed (Figure S295).

Using the optimized dimer structure, trimers of (*S*)-**2** with either *M*- or *P*-type helicity were modeled. The structures were constructed as mirror images, with methyl groups ensuring the same (*S*)-chirality across monomers. By optimizing these structures at the GFN2-xTB level, we avoided the computational cost of DFT-level optimizations, which require extensive dispersion, polarization, and diffuse basis set considerations. The M-type helix was found to be the most stable (ΔE = 1.39 kcal/mol). Simulated ECD spectra of the trimers using TD-DFT (cam-b3lyp/3-21g, PCM=methylcyclohexane)[415] showed a

USC DE COMPOSTELA

bisignate (-/+) signal for (*S*)-**2**, consistent with the experimental ECD of the aggregate in MCH and confirming the *M*-type helical sense as the preferred conformation. This stability is attributed to steric hindrance: in the *M*-type helix, chiral methyl groups point into free space, while in the *P*-type helix, steric clashes occur between methyl groups and adjacent monomers in the stack.

Building on the dimer and trimer findings, a supramolecular hexadecamer (16-mer) was constructed using achiral **1** or the *M*-type helix of (*S*)-**2** (with dodecyl chains replaced by methyl groups). The minimum-energy structure of the 16-mer was calculated at the GFN2-xTB level. To investigate the polymerization mechanism, single-point calculations were performed for $(\mathbf{1})_n$ and $((S)\text{-}\mathbf{2})_n$ oligomers of increasing length (n = 2–12), extracted from the central portion of the optimized 16-mer to minimize terminal effects. Binding energy per molecular pair ($\Delta E_{bind,n-1}$) was calculated using equation (S22).

$$\Delta E_{bind,n-1} = \frac{E_{stack} - n \cdot E_{monomer}}{n-1} \qquad \textbf{(S22)}$$

Where E_{stack} is the total energy of the stacked $(\mathbf{1})_n$ or $((S)\text{-}\mathbf{2})_n$ aggregate bearing n monomeric units and $E_{monomer}$ is the energy calculated for the monomer. Theoretical calculations reveal that $\Delta_{Ebind,n-1}$ decreases with the oligomer size, which is indicative of a cooperative supramolecular polymerization mechanism.

Finally, the approximation of Achiral Soldiers (**1**) to Chiral Sergeants ((*S*)-**2**) was examined by optimizing four possible structures of the *M*- and *P*-type helices, each incorporating two methyl groups in one of the monomers to represent different interactions. The structures were constructed as mirror images, with methyl groups ensuring the same (*S*)-chirality in only the Sergeant monomer. Models were done in Avogadro 1.2.0,[559] the optimized structures represented in Pymol 2.5.2 and the TDMs represented in VMD.[560]

USC UNIVERSIDADE DE SANTIAGO DE COMPOSTELA

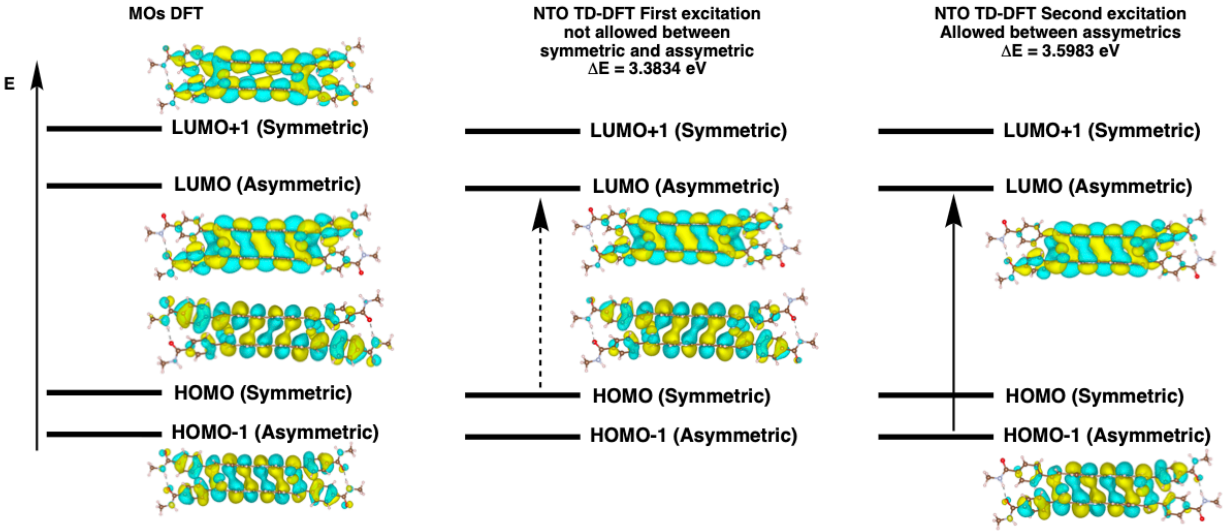


Figure S295. MOs calculated by DFT wb97xd/6-31+G** for a simplified H-type dimer. NTOs and ΔE calculated by TD-DFT wb97xd/6-31+G** (PCM=methylcyclohexane) in the two first transitions for the HOMOs and LUMOs.

USC
UNIVERSIDADE
DE SANTIAGO
DE COMPOSTELA

USC
UNIVERSIDADE
DE SANTIAGO
DE COMPOSTELA

Chapter 6. Bibliography

USC
UNIVERSIDADE
DE SANTIAGO
DE COMPOSTELA

USC
UNIVERSIDADE
DE SANTIAGO
DE COMPOSTELA

[1] B. Alberts, Ed., *Molecular Biology of the Cell*, Garland Science, New York, **2002**.

[2] W. Saenger, *Principles of Nucleic Acid Structure*, Springer New York, New York, NY, **1984**.

[3] G. E. Schulz, R. H. Schirmer, *Principles of Protein Structure*, Springer New York, New York, NY, **1979**.

[4] L. Pauling, R. B. Corey, H. R. Branson, *Proc. Natl. Acad. Sci.* **1951**, *37*, 205-211.

[5] J. D. Watson, F. H. C. Crick, *Nature* **1953**, *171*, 737-738.

[6] D. Hirose, A. Isobe, E. Quiñoá, F. Freire, K. Maeda, *J. Am. Chem. Soc.* **2019**, *141*, 8592-8598.

[7] T. Haino, *Polym. J.* **2019**, *51*, 303-318.

[8] E. Yashima, N. Ousaka, D. Taura, K. Shimomura, T. Ikai, K. Maeda, *Chem. Rev.* **2016**, *116*, 13752-13990.

[9] E. Schwartz, M. Koepf, H. J. Kitto, R. J. M. Nolte, A. E. Rowan, *Polym. Chem.* **2011**, *2*, 33-47.

[10] Y. Okamoto, T. Nakano, *Chem. Rev.* **1994**, *94*, 349-372.

[11] G. Natta, P. Pino, P. Corradini, F. Danusso, E. Mantica, G. Mazzanti, G. Moraglio, *J. Am. Chem. Soc.* **1955**, *77*, 1708-1710.

[12] P. Pino, G. P. Lorenzi, *J. Am. Chem. Soc.* **1960**, *82*, 4745-4747.

[13] R. J. M. Nolte, A. J. M. Van Beijnen, W. Drenth, *J. Am. Chem. Soc.* **1974**, *96*, 5932-5933.

[14] Y. Okamoto, K. Suzuki, K. Ohta, K. Hatada, H. Yuki, *J. Am. Chem. Soc.* **1979**, *101*, 4763-4765.

[15] M. M. Green, Christopher. Andreola, Beth. Munoz, M. P. Reidy, Karl. Zero, *J. Am. Chem. Soc.* **1988**, *110*, 4063-4065.

[16] I. Louzao, J. M. Seco, E. Quiñoá, R. Riguera, *Angew. Chem. Int. Ed.* **2010**, *49*, 1430-1433.

[17] F. Ciardelli, E. Benedetti, O. Pieroni, *Makromol. Chem.* **1967**, *103*, 1-18.

[18] F. Ciardelli, S. Lanzillo, O. Pieroni, *Macromolecules* **1974**, *7*, 174-179.

USC UNIVERSIDADE DE SANTIAGO DE COMPOSTELA

[19] K. Maeda, E. Yashima, in *Supramolecular Chirality* (Eds.: M. Crego-Calama, D.N. Reinhoudt), Springer-Verlag, Berlin/Heidelberg, **2006**, pp. 47-88.

[20] C. I. Simionescu, V. Percec, S. Dumitrescu, *J. Polym. Sci. Polym. Chem. Ed.* **1977**, *15*, 2497-2509.

[21] C. I. Simionescu, V. Percec, *Prog. Polym. Sci.* **1982**, *8*, 133-214.

[22] M. Tabata, T. Sone, Y. Sadahiro, *Macromol. Chem. Phys.* **1999**, *200*, 265-282.

[23] K. Shimomura, T. Ikai, S. Kanoh, E. Yashima, K. Maeda, *Nat. Chem.* **2014**, *6*, 429-434.

[24] Y. Zhou, C. Zhang, Q. Geng, L. Liu, H. Dong, T. Satoh, Y. Okamoto, *Polymer* **2017**, *131*, 17-24.

[25] M. Lago-Silva, M. Fernández-Míguez, R. Rodríguez, E. Quiñoá, F. Freire, *Chem. Soc. Rev.* **2024**, *53*, 793-852.

[26] Y. Nagata, T. Nishikawa, M. Suginome, *J. Am. Chem. Soc.* 2015, 137, 4070-4073.

[27] T. Ikai, M. Ando, M. Ito, R. Ishidate, N. Suzuki, K. Maeda, E. Yashima, *J. Am. Chem. Soc.* **2021**, *143*, 12725-12735.

[28] Y. Nagata, R. Takeda, M. Suginome, *ACS Cent. Sci.* **2019**, *5*, 1235-1240.

[29] J. Liu, J. W. Y. Lam, B. Z. Tang, *Chem. Rev.* **2009**, *109*, 5799-5867.

[30] E. Yashima, K. Maeda, H. Iida, Y. Furusho, K. Nagai, *Chem. Rev.* **2009**, *109*, 6102-6211.

[31] Y. Kishimoto, P. Eckerle, T. Miyatake, T. Ikariya, R. Noyori, *J. Am. Chem. Soc.* **1994**, *116*, 12131-12132.

[32] K. Hirao, Y. Ishii, T. Terao, Y. Kishimoto, T. Miyatake, T. Ikariya, R. Noyori, *Macromolecules* **1998**, *31*, 3405-3408.

[33] Y. Kishimoto, P. Eckerle, T. Miyatake, M. Kainosho, A. Ono, T. Ikariya, R. Noyori, *J. Am. Chem. Soc.* **1999**, *121*, 12035-12044.

[34] Y. Kishimoto, M. Itou, T. Miyatake, T. Ikariya, R. Noyori, *Macromolecules* **1995**, *28*, 6662-6666.

[35] Y. Kishimoto, T. Miyatake, T. Ikariya, R. Noyori, *Macromolecules* **1996**, *29*, 5054-5055.

USC UNIVERSIDADE DE SANTIAGO DE COMPOSTELA

[36] Z. Ke, S. Abe, T. Ueno, K. Morokuma, *J. Am. Chem. Soc.* **2011**, *133*, 7926-7941.

[37] N. S. L. Tan, A. B. Lowe, *Angew. Chem. Int. Ed.* **2020**, *59*, 5008-5021.

[38] M. Angoy, M. V. Jiménez, F. J. Lahoz, E. Vispe, J. J. Pérez-Torrente, *Polym. Chem.* **2022**, *13*, 1411-1421.

[39] M. Tabata, W. Yang, K. Yokota, *Polym. J.* **1990**, *22*, 1105-1107.

[40] W. Yang, M. Tabata, S. Kobayashi, K. Yokota, A. Shimizu, *Polym. J.* **1991**, *23*, 1135-1138.

[41] M. Tabata, Y. Tanaka, Y. Sadahiro, T. Sone, K. Yokota, I. Miura, *Macromolecules* **1997**, *30*, 5200-5204.

[42] F. Freire, J. M. Seco, E. Quiñoá, R. Riguera, *J. Am. Chem. Soc.* **2012**, *134*, 19374-19383.

[43] F. Freire, J. M. Seco, E. Quiñoá, R. Riguera, *Angew. Chem. Int. Ed.* **2011**, *50*, 11692-11696.

[44] K. Huang, Y. Mawatari, A. Miyasaka, Y. Sadahiro, M. Tabata, Y. Kashiwaya, *Polymer* **2007**, *48*, 6366-6373.

[45] M. Goto, M. Minami, H. Sogawa, F. Sanda, *Polymer* **2021**, *229*, 124013.

[46] T. Miyagawa, M. Yamamoto, R. Muraki, H. Onouchi, E. Yashima, *J. Am. Chem. Soc.* **2007**, *129*, 3676-3682.

[47] K. Nagai, K. Maeda, Y. Takeyama, T. Sato, E. Yashima, *Chem. Asian J.* **2007**, *2*, 1314-1321.

[48] K. Maeda, K. Morino, Y. Okamoto, T. Sato, E. Yashima, *J. Am. Chem. Soc.* **2004**, *126*, 4329-4342.

[49] K. Maeda, M. Ishikawa, E. Yashima, *J. Am. Chem. Soc.* **2004**, *126*, 15161-15166.

[50] W. Z. Yuan, L. Tang, H. Zhao, J. K. Jin, J. Z. Sun, A. Qin, H. P. Xu, J. Liu, F. Yang, Q. Zheng, E. Chen, B. Z. Tang, *Macromolecules* **2009**, *42*, 52-61.

[51] M. A. Saito, K. Maeda, H. Onouchi, E. Yashima, *Macromolecules* **2000**, *33*, 4616-4618.

[52] I. Saeed, F. Z. Khan, M. Shiotsuki, T. Masuda, *J. Polym. Sci. A Polym. Chem.* **2009**, *47*, 1853-1863.

USC UNIVERSIDADE DE SANTIAGO DE COMPOSTELA

[53] J. Liu, J. W. Y. Lam, B. Z. Tang, in *Encyclopedia of Polymer Science and Technology* (Ed.: H.F. Mark), Wiley, **2011**.

[54] K. Echizen, T. Taniguchi, T. Nishimura, K. Maeda, *Angew. Chem. Int. Ed.* **2022**, *61*, e202202676.

[55] E. Yashima, Y. Maeda, T. Matsushima, Y. Okamato, *Chirality* **1997**, *9*, 593-600.

[56] H. Kawamura, Y. Takeyama, M. Yamamoto, H. Kurihara, K. Morino, E. Yashima, *Chirality* **2011**, *23*, E35-E42.

[57] K. Maeda, S. Okada, E. Yashima, Y. Okamoto, *J. Polym. Sci. A Polym. Chem.* **2001**, *39*, 3180-3189.

[58] W. Z. Yuan, H. Zhao, X. Y. Shen, F. Mahtab, J. W. Y. Lam, J. Z. Sun, B. Z. Tang, *Macromolecules* **2009**, *42*, 9400-9411.

[59] E. Suárez-Picado, E. Quiñoá, R. Riguera, F. Freire, *Chem. Mater.* **2018**, *30*, 6908-6914.

[60] S. Sakamoto, T. Taniguchi, Y. Sakata, S. Akine, T. Nishimura, K. Maeda, *Angew. Chem. Int. Ed.* **2021**, *60*, 22201-22206.

[61] T. Taniguchi, T. Yoshida, K. Echizen, K. Takayama, T. Nishimura, K. Maeda, *Angew. Chem. Int. Ed.* **2020**, *59*, 8670-8680.

[62] T. Taniguchi, T. Nishimura, K. Maeda, *J. Synth. Org. Chem. Jpn.* **2023**, *81*, 594-606.

[63] S. Mishra, A. K. Mondal, E. Z. B. Smolinsky, R. Naaman, K. Maeda, T. Nishimura, T. Taniguchi, T. Yoshida, K. Takayama, E. Yashima, *Angew. Chem. Int. Ed.* **2020**, *59*, 14671-14676.

[64] K. Echizen, T. Taniguchi, T. Nishimura, K. Maeda, *J. Am. Chem. Soc.* **2021**, *143*, 3604-3612.

[65] S. Kumazawa, J. Rodriguez Castanon, M. Shiotsuki, T. Sato, F. Sanda, *Polym. Chem.* **2015**, *6*, 5931-5939.

[66] M. Goto, A. Nito, Y. Miyagi, F. Sanda, *Macromol. Mater. Eng.* **2019**, *304*, 1900275.

[67] L. Liu, T. Namikoshi, Y. Zang, T. Aoki, S. Hadano, Y. Abe, I. Wasuzu, T. Tsutsuba, M. Teraguchi, T. Kaneko, *J. Am. Chem. Soc.* **2013**, *135*, 602-605.

USC UNIVERSIDADE DE SANTIAGO DE COMPOSTELA

[68] M. Miyata, M. Teraguchi, H. Endo, T. Kaneko, T. Aoki, *Chem. Lett.* **2014**, *43*, 1476-1477.

[69] R. B. Woodward, R. Hoffmann, *J. Am. Chem. Soc.* **1965**, *87*, 395-397.

[70] F. Rey-Tarrío, R. Rodríguez, E. Quiñoá, F. Freire, *Nat. Commun.* **2023**, *14*, 1742.

[71] F. Rey-Tarrío, S. Guisán-Ceinos, J. M. Cuerva, D. Miguel, M. Ribagorda, E. Quiñoá, F. Freire, *Angew. Chem. Int. Ed.* **2022**, *61*, e202207623.

[72] T. Masuda, B. Z. Tang, T. Higashimura, H. Yamaoka, *Macromolecules* **1985**, *18*, 2369-2373.

[73] J. Sedlacek, J. Vohlidal, Z. Grubisic-Gallot, *Makromol. Chem. Rapid Commun.* **1993**, *14*, 51-53.

[74] X. Kong, J. W. Y. Lam, B. Z. Tang, *Macromolecules* **1999**, *32*, 1722-1730.

[75] S. M. A. Karim, R. Nomura, T. Masuda, *J. Polym. Sci. A Polym. Chem.* **2001**, *39*, 3130-3136.

[76] V. Percec, J. G. Rudick, P. Nombel, W. Buchowicz, *J. Polym. Sci. A Polym. Chem.* **2002**, *40*, 3212-3220.

[77] V. Percec, J. G. Rudick, *Macromolecules* **2005**, *38*, 7241-7250.

[78] J. Vohlídal, D. Rédrová, M. Pacovská, J. Sedláček, Collect. Czechoslov. *Chem. Commun.* **1993**, *58*, 2651-2662.

[79] S. Matsunami, T. Watanabe, H. Kamimura, T. Kakuchi, F. Ishii, K. Tsuda, *Polymer* **1996**, *37*, 4853-4855.

[80] E. Ohta, H. Sato, S. Ando, A. Kosaka, T. Fukushima, D. Hashizume, M. Yamasaki, K. Hasegawa, A. Muraoka, H. Ushiyama, K. Yamashita, T. Aida, *Nat. Chem.* **2011**, *3*, 68-73.

[81] H. Iida, T. Mizoguchi, S.-D. Oh, E. Yashima, *Polym. Chem.* **2010**, *1*, 841-848.

[82] E. Gomar-Nadal, J. Veciana, C. Rovira, D. B. Amabilino, *Adv. Mater.* **2005**, *17*, 2095-2098.

[83] A. Miyasaka, Y. Mawatari, T. Sone, M. Tabata, *Polym. Degrad. Stab.* **2007**, *92*, 253-259.

USC UNIVERSIDADE DE SANTIAGO DE COMPOSTELA

[84] S. Leiras, F. Freire, J. M. Seco, E. Quiñoá, R. Riguera, *Chem. Sci.* **2013**, *4*, 2735-2743.

[85] P. Salvadori, C. Rosini, L. Di Bari, in *The Chemistry of Dienes and Polyenes* (Ed.: Z. Rappoport), Wiley, **1997**, pp. 111-147.

[86] B. Fernández, R. Rodríguez, E. Quiñoá, R. Riguera, F. Freire, *ACS Omega* **2019**, *4*, 5233-5240.

[87] C. I. Simionescu, V. Percec, *J. Polym. Sci. Polym. Chem. Ed.* **1980**, *18*, 147-155.

[88] C. I. Simionescu, V. Percec, *J. Polym. Sci. Polym. Lett. Ed.* **1979**, *17*, 421-429.

[89] A. Motoshige, Y. Mawatari, Y. Yoshida, R. Motoshige, M. Tabata, *Polym Chem* **2014**, *5*, 971-978.

[90] A. Motoshige, Y. Mawatari, R. Motoshige, Y. Yoshida, M. Tabata, *J. Polym. Sci. A Polym. Chem.* **2013**, *51*, 5177-5183.

[91] Y. Yoshida, Y. Mawatari, A. Motoshige, R. Motoshige, T. Hiraoki, M. Wagner, K. Müllen, M. Tabata, *J. Am. Chem. Soc.* **2013**, *135*, 4110-4116.

[92] F. Rey-Tarrío, R. Rodríguez, E. Quiñoá, R. Riguera, F. Freire, *Angew. Chem. Int. Ed.* **2021**, *60*, 8095-8103.

[93] A. Miyasaka, T. Sone, Y. Mawatari, S. Setayesh, K. Müllen, M. Tabata, *Macromol. Chem. Phys.* **2006**, *207*, 1938-1944.

[94] H. Shirakawa, S. Ikeda, *Polym. J.* **1971**, *2*, 231-244.

[95] T. Ito, H. Shirakawa, S. Ikeda, *J. Polym. Sci. Polym. Chem. Ed.* **1974**, *12*, 11-20.

[96] A. Motoshige, Y. Mawatari, Y. Yoshida, C. Seki, H. Matsuyama, M. Tabata, *J. Polym. Sci. A Polym. Chem.* **2012**, *50*, 3008-3015.

[97] V. Percec, M. Peterca, J. G. Rudick, E. Aqad, M. R. Imam, P. A. Heiney, *Chem. Eur. J.* **2007**, *13*, 9572-9581.

[98] V. Percec, J. G. Rudick, M. Peterca, E. Aqad, M. R. Imam, P. A. Heiney, *J. Polym. Sci. A Polym. Chem.* **2007**, *45*, 4974-4987.

[99] V. Percec, E. Aqad, M. Peterca, J. G. Rudick, L. Lemon, J. C. Ronda, B. B. De, P. A. Heiney, E. W. Meijer, *J. Am. Chem. Soc.* **2006**, *128*, 16365-16372.

USC UNIVERSIDADE DE SANTIAGO DE COMPOSTELA

[100] V. Percec, J. G. Rudick, M. Peterca, M. Wagner, M. Obata, C. M. Mitchell, W.-D. Cho, V. S. K. Balagurusamy, P. A. Heiney, *J. Am. Chem. Soc.* **2005**, *127*, 15257-15264.

[101] J. Clayden, N. Greeves, S. Warren, *Organic Chemistry*, Oxford University Press, Oxford, **2012**.

[102] R. Rodríguez, E. Quiñoá, R. Riguera, F. Freire, *J. Am. Chem. Soc.* **2016**, *138*, 9620-9628.

[103] F. Sellmaier, T. Uhlig, M. Schmidhuber, Eds. , *Spacecraft Operations*, Springer International Publishing, Cham, **2022**.

[104] J. M. Herbert, in *Theoretical and Computational Photochemistry*, Elsevier, **2023**, pp. 69-118.

[105] M. Soltani Nejad, M. Alipour, *Phys. Chem. Chem. Phys.* **2024**, *26*, 879-894.

[106] R. C. Hilborn, *Am. J. Phys.* **1982**, *50*, 982-986.

[107] S. S. Andrews, J. Tretton, *J. Chem. Educ.* **2020**, *97*, 4370-4376.

[108] L. Rosenfeld, *Z. Phys.* **1929**, *52*, 161-174.

[109] L. A. Nafie, T. B. Freedman, *J. Mol. Struct.* **1990**, *224*, 121-132.

[110] J. A. Schellman, Chem. Rev. **1975**, *75*, 323-331.

[111] E. Freytag, M. Holzapfel, A. Swain, G. Bringmann, M. Stolte, F. Würthner, C. Lambert, *Chem. Sci.* **2022**, *13*, 12229-12238.

[112] G. Mazzeo, S. Ghidinelli, R. Ruzziconi, M. Grandi, S. Abbate, G. Longhi, *ChemPhotoChem* **2022**, *6*, e202100222.

[113] L. Frédéric, A. Desmarchelier, L. Favereau, G. Pieters, *Adv. Funct. Mater.* **2021**, *31*, 2010281.

[114] B. H. Jhun, S. Y. Park, Y. You, *Dyes and Pigments* **2023**, *208*, 110786.

[115] P. Changenet, F. Hache, *Eur. Phys. J. Spec. Top.* **2023**, *232*, 2117-2129.

[116] M. Scott, D. R. Rehn, S. Coriani, P. Norman, A. Dreuw, *J. Chem. Phys.* **2021**, *154*, 064107.

[117] G. Pescitelli, L. Di Bari, N. Berova, *Chem. Soc. Rev.* **2011**, *40*, 4603-4625.

USC UNIVERSIDADE DE SANTIAGO DE COMPOSTELA

[118] E. C. Jordan, K. G. Balmain*, Electromagnetic Waves and Radiating Systems*, Prentice-Hall, Englewood Cliffs, NJ, **1968**.

[119] B. Fernández, R. Rodríguez, A. Rizzo, E. Quiñoá, R. Riguera, F. Freire, *Angew. Chem. Int. Ed.* **2018**, *57*, 3666-3670.

[120] J. Autschbach, *Chirality* **2009**, *21*, E116-E152.

[121] J. Autschbach, L. Nitsch-Velasquez, M. Rudolph, in Electronic and Magnetic Properties of Chiral Molecules and Supramolecular Architectures (Eds.: R. Naaman, D.N. Beratan, D. Waldeck), Springer Berlin Heidelberg, Berlin, Heidelberg, **2010**, pp. 1–98.

[122] M. Kwit, M. D. Rozwadowska, J. Gawroński, A. Grajewska, *J. Org. Chem.* **2009**, *74*, 8051-8063.

[123] A. K. Wilson, T. Van Mourik, T. H. Dunning, *J. Mol. Struct. THEOCHEM* **1996**, *388*, 339-349.

[124] R. A. Kendall, T. H. Dunning, R. J. Harrison, *J. Chem. Phys.* **1992**, *96*, 6796-6806.

[125] T. Yanai, D. P. Tew, N. C. Handy, *Chem. Phys. Lett.* **2004**, *393*, 51-57.

[126] J.-D. Chai, M. Head-Gordon, *Phys. Chem. Chem. Phys.* **2008**, *10*, 6615-6620.

[127] V. A. Rassolov, M. A. Ratner, J. A. Pople, P. C. Redfern, L. A. Curtiss, *J. Comput. Chem.* **2001**, *22*, 976-984.

[128] J. S. Binkley, J. A. Pople, W. J. Hehre, *J. Am. Chem. Soc.* **1980**, *102*, 939-947.

[129] M. Scott, D. R. Rehn, P. Norman, A. Dreuw, *J. Phys. Chem. Lett.* **2021**, *12*, 5132-5137.

[130] N. Berova, L. D. Bari, G. Pescitelli, *Chem. Soc. Rev.* **2007**, *36*, 914-931.

[131] H. Watarai, K. Adachi, *Anal. Bioanal. Chem.* **2009**, *395*, 1033-1046.

[132] G. Pescitelli, *Chirality* **2022**, *34*, 333-363.

[133] S. G. Telfer, T. M. McLean, M. R. Waterland, *Dalton Trans.* **2011**, *40*, 3097-3108.

[134] K. Ishii, S. Hattori, Y. Kitagawa, *Photochem. Photobiol. Sci.* **2020**, *19*, 9-19.

[135] B. Nieto-Ortega, R. Rodríguez, S. Medina, E. Quiñoá, R. Riguera, J. Casado, F. Freire, F. J. Ramírez, *J. Phys. Chem. Lett.* **2018**, *9*, 2266-2270.

USC UNIVERSIDADE DE SANTIAGO DE COMPOSTELA

[136] K. P. C. Vollhardt, N. E. Schore, *Organic Chemistry: Structure and Function*, W.H. Freeman, New York, NY, **2007**.

[137] L. Palomo, R. Rodríguez, S. Medina, E. Quiñoá, J. Casado, F. Freire, F. J. Ramírez, *Angew. Chem. Int. Ed.* **2020**, *59*, 9080-9087.

[138] G. Binnig, C. F. Quate, Ch. Gerber, *Phys. Rev. Lett.* **1986**, *56*, 930-933.

[139] C. F. Quate, *Surf. Sci.* **1994**, *299-300*, 980-995.

[140] J. Kumaki, S. Sakurai, E. Yashima, *Chem. Soc. Rev.* **2009**, *38*, 737-746.

[141] T. Nishimura, K. Takatani, S. Sakurai, K. Maeda, E. Yashima, *Angew. Chem. Int. Ed.* **2002**, *41*, 3602-3604.

[142] S. Sakurai, K. Okoshi, J. Kumaki, E. Yashima, *Angew. Chem. Int. Ed.* **2006**, *45*, 1245-1248.

[143] G. Roberts, Ed. , *Langmuir-Blodgett Films*, Springer US, Boston, MA, **1990**.

[144] A. Ulman, in *An Introduction to Ultrathin Organic Films*, Elsevier, **1991**, pp. 1-99.

[145] B. S. Li, J. W. Y. Lam, Z.-Q. Yu, B. Z. Tang, *Langmuir* **2012**, *28*, 5770-5774.

[146] B. S. Li, S. Z. Kang, K. K. L. Cheuk, L. Wan, L. Ling, C. Bai, B. Z. Tang, *Langmuir* **2004**, *20*, 7598-7603.

[147] R. Rodríguez, J. Ignés-Mullol, F. Sagués, E. Quiñoá, R. Riguera, F. Freire, *Nanoscale* **2016**, *8*, 3362-3367.

[148] V. Percec, Ed. , *Hierarchical Macromolecular Structures: 60 Years after the Staudinger Nobel Prize I*, Springer International Publishing, Cham, **2013**.

[149] J. Lehn, *Supramolecular Chemistry: Concepts and Perspectives*, Wiley, **1995**.

[150] J. W. Steed, J. L. Atwood, *Supramolecular Chemistry*, Wiley, Hoboken, NJ Chichester, West Sussex, **2022**.

[151] M. Liu, L. Zhang, T. Wang, *Chem. Rev.* **2015**, *115*, 7304-7397.

[152] L. Zhang, L. Qin, X. Wang, H. Cao, M. Liu, *Adv. Mater.* **2014**, *26*, 6959-6964.

[153] Y. Yang, Y. Zhang, Z. Wei, *Adv. Mater.* **2013**, *25*, 6039-6049.

[154] S. Leiras, F. Freire, E. Quiñoá, R. Riguera, *Chem. Sci.* **2015**, *6*, 246-253.

USC UNIVERSIDADE DE SANTIAGO DE COMPOSTELA

[155] K. Shinohara, S. Yasuda, G. Kato, M. Fujita, H. Shigekawa, *J. Am. Chem. Soc.* **2001**, *123*, 3619-3620.

[156] K. Maeda, H. Mochizuki, K. Osato, E. Yashima, *Macromolecules* **2011**, *44*, 3217-3226.

[157] K. K. L. Cheuk, B. S. Li, J. W. Y. Lam, Y. Xie, B. Z. Tang, *Macromolecules* **2008**, *41*, 5997-6005.

[158] B. S. Li, K. K. L. Cheuk, D. Yang, J. W. Y. Lam, L. J. Wan, C. Bai, B. Z. Tang, *Macromolecules* **2003**, *36*, 5447-5450.

[159] K. Maeda, Y. Matsushita, M. Ezaka, E. Yashima, *Chem. Commun.* **2005**, 4152-4154.

[160] F. Freire, E. Quiñoá, R. Riguera, *Chem. Rev.* **2016**, *116*, 1242-1271.

[161] Y. Zhang, X. Luo, J. Deng, W. Yang, *Macromol. Chem. Phys.* **2011**, *212*, 353-360.

[162] C. Song, X. Liu, D. Liu, C. Ren, W. Yang, J. Deng, *Macromol. Rapid Commun.* **2013**, *34*, 1426-1445.

[163] W. Li, H. Huang, Y. Li, J. Deng, *Polym. Chem.* **2014**, *5*, 1107-1118.

[164] B. Chen, X. Liu, C. Xu, C. Song, X. Luo, W. Yang, J. Deng, *Macromol. Chem. Phys.* **2012**, *213*, 603-609.

[165] X. Luo, J. Deng, W. Yang, *Angew. Chem. Int. Ed.* **2011**, *50*, 4909-4912.

[166] D. Liu, Y. Li, J. Deng, W. Yang, *Polymer* **2014**, *55*, 840-847.

[167] C. J. Martínez Rivas, M. Tarhini, W. Badri, K. Miladi, H. Greige-Gerges, Q. A. Nazari, S. A. Galindo Rodríguez, R. Á. Román, H. Fessi, A. Elaissari, *Int. J. Pharm.* **2017**, *532*, 66-81.

[168] Y. Zhang, J. Deng, K. Pan, *Macromolecules* **2018**, *51*, 8878-8886.

[169] M. Núñez-Martínez, M. Fernández-Míguez, E. Quiñoá, F. Freire, *Angew. Chem. Int. Ed.* **2024**, *63*, e202403313.

[170] S. Arias, F. Freire, E. Quiñoá, R. Riguera, Angew. Chem. Int. Ed. 2014, 53, 13720-13724.

USC UNIVERSIDADE DE SANTIAGO DE COMPOSTELA

[171] S. Arias, M. Núñez-Martínez, E. Quiñoá, R. Riguera, F. Freire, *Polym. Chem.* **2017**, *8*, 3740-3745.

[172] D. P. Dubal, O. Ayyad, V. Ruiz, P. Gómez-Romero, *Chem. Soc. Rev.* **2015**, *44*, 1777-1790.

[173] U. Díaz, D. Brunel, A. Corma, *Chem. Soc. Rev.* **2013**, *42*, 4083-4097.

[174] S. Wang, Y. Kang, L. Wang, H. Zhang, Y. Wang, Y. Wang, S*ens. Actuators B Chem.* **2013**, *182*, 467-481.

[175] M. Srinivasan, M. Rajabi, S. Mousa, *Nanomaterials* **2015**, *5*, 1690-1703.

[176] C. M. Cobley, J. Chen, E. C. Cho, L. V. Wang, Y. Xia, *Chem. Soc. Rev.* **2011**, *40*, 44-56.

[177] G. Magdy, E. Aboelkassim, S. M. Abd Elhaleem, F. Belal, *Microchem. J.* **2024**, *196*, 109615.

[178] M. Jeyaraj, S. Gurunathan, M. Qasim, M.-H. Kang, J.-H. Kim, *Nanomaterials* **2019**, *9*, 1719.

[179] A. Chen, C. Ostrom, *Chem. Rev.* **2015**, *115*, 11999-12044.

[180] M. B. Gawande, A. Goswami, F.-X. Felpin, T. Asefa, X. Huang, R. Silva, X. Zou, R. Zboril, R. S. Varma, *Chem. Rev.* **2016**, *116*, 3722-3811.

[181] B. Le Ouay, F. Stellacci, *Nano Today* **2015**, *10*, 339-354.

[182] M. T. Yilmaz, H. İspirli, O. Taylan, E. Dertli, *LWT* **2020**, *128*, 109497.

[183] M. Hasanin, M. A. Elbahnasawy, A. M. Shehabeldine, A. H. Hashem, *BioMetals* **2021**, *34*, 1313-1328.

[184] K. Naumenko, S. Zahorodnia, C. V. Pop, N. Rizun, *J. Virus Erad.* **2023**, *9*, 100330.

[185] G. S. Zeedan, K. A. A. EL-Razik, A. M. Allam, A. M. Abdalhamed, H. A. A. Zeina, *Adv. Anim. Vet. Sci.* **2020**, *8*, 433-443.

[186] M. Seong, D. G. Lee, *Curr. Microbiol.* **2017**, *74*, 661-670.

[187] J. He, Y. Ma, X. Niu, J. Pei, R. Yan, F. Xu, J. Ma, X. Ma, S. Jia, W. Ma, *Toxicology* **2024**, *502*, 153734.

USC UNIVERSIDADE DE SANTIAGO DE COMPOSTELA

[188] A. Rinna, Z. Magdolenova, A. Hudecova, M. Kruszewski, M. Refsnes, M. Dusinska, *Mutagenesis* **2015**, *30*, 59-66.

[189] H. M. Ali, K. Karam, T. Khan, S. Wahab, S. Ullah, M. Sadiq, *3 Biotech* **2023**, *13*, 414.

[190] M. Seo, T. Oh, S. Bae, *Vet. Med. Sci.* **2021**, *7*, 1551-1557.

[191] N. S. Swidan, Y. A. Hashem, W. F. Elkhatib, M. A. Yassien, *Sci. Rep.* **2022**, *12*, 3869.

[192] A. B. Asha, R. Narain, in *Polymer Science and Nanotechnology*, Elsevier, **2020**, pp. 343-359.

[193] K. Phatanodom, C. Angthong, *Pol. J. Surg.* **2022**, *96*, 46-52.

[194] P. Velmurugan, S.-M. Lee, M. Cho, J.-H. Park, S.-K. Seo, H. Myung, K.-S. Bang, B.-T. Oh, *Appl. Microbiol. Biotechnol.* **2014**, *98*, 8179-8189.

[195] T. K. C. Poon, K. P. Iyengar, V. K. Jain, J. Clin. *Orthop. Trauma* **2021**, *21*, 101536.

[196] A. Almatroudi, *Pharmaceutics* **2024**, *16*, 1232.

[197] T. Akpobolokemi, E. Chung, R. T. Martinez-Nunez, G. Ren, B. T. Raimi Abraham, A. Griffiths, *RSC Pharm.* **2025**, *2*, 353-368.

[198] J. Hühn, C. Carrillo-Carrion, M. G. Soliman, C. Pfeiffer, D. Valdeperez, A. Masood, I. Chakraborty, L. Zhu, M. Gallego, Z. Yue, M. Carril, N. Feliu, A. Escudero, A. M. Alkilany, B. Pelaz, P. Del Pino, W. J. Parak, *Chem. Mater.* **2017**, *29*, 399-461.

[199] K. Zhang, J. M. Suh, J.-W. Choi, H. W. Jang, M. Shokouhimehr, R. S. Varma, *ACS Omega* **2019**, *4*, 483-495.

[200] G. Suriati, M. Mariatti, A. Azizan, *Int. J. Automot. Mech. Eng.* **2022**, *10*, 1920-1927.

[201] M. Rehan, A. Barhoum, G. Van Assche, A. Dufresne, L. Gätjen, R. Wilken, *Int. J. Biol. Macromol.* **2017**, *98*, 877-886.

[202] Z. Zhang, X. Yang, M. Shen, Y. Yin, J. Liu, *J. Environ. Sci.* **2015**, *35*, 62-68.

[203] A. Dhaka, S. Chand Mali, S. Sharma, R. Trivedi, *Results Chem.* **2023**, *6*, 101108.

[204] A. Rónavári, P. Bélteky, E. Boka, D. Zakupszky, N. Igaz, B. Szerencsés, I. Pfeiffer, Z. Kónya, M. Kiricsi, *Int. J. Mol. Sci.* **2021**, *22*, 8673.

USC UNIVERSIDADE DE SANTIAGO DE COMPOSTELA

[205] M. Tejamaya, I. Römer, R. C. Merrifield, J. R. Lead, *Environ. Sci. Technol.* **2012**, *46*, 7011-7017.

[206] J. Wu, Y. Xu, P. Xu, Z. Pan, S. Chen, Q. Shen, L. Zhan, Y. Zhang, W. Ni, *Nanoscale* **2015**, *7*, 17529-17537.

[207] J. Ding, Z. Li, O. Kodra, M. Couillard, J. Ouyang, F. Lapointe, P. R. L. Malenfant, *ACS Omega* **2023**, *8*, 14219-14232.

[208] W. Nie, X. Dai, D. Li, D. McCoul, G. J. Gillispie, Y. Zhang, B. Yu, C. He, *ACS Biomater. Sci. Eng.* **2018**, *4*, 3588-3599.

[209] A. Arenas-Vivo, G. Amariei, S. Aguado, R. Rosal, P. Horcajada, *Acta Biomater.* **2019**, *97*, 490-500.

[210] D. Tanaka, K. Imazu, J. Sung, C. Park, K. Okamoto, K. Tamada, *Nanoscale* **2015**, *7*, 15310-15320.

[211] S. Myung, P. T. Yin, C. Kim, J. Park, A. Solanki, P. I. Reyes, Y. Lu, K. S. Kim, K. Lee, *Adv. Mater.* **2012**, *24*, 6081-6087.

[212] T. Fernandes, A. L. Daniel-da-Silva, T. Trindade, *Coord. Chem. Rev.* **2022**, *460*, 214483.

[213] Y.-H. Tseng, Y. He, L. Que, *The Analyst* **2013**, *138*, 3053-3057.

[214] X. Lan, X. Zhou, L. A. McCarthy, A. O. Govorov, Y. Liu, S. Link, *J. Am. Chem. Soc.* **2019**, *141*, 19336-19341.

[215] A. Kunnummal, R. A. Parambil, S. Maniappan, J. Kumar, *ACS Appl. Opt. Mater.* **2024**, *2*, 2451-2458.

[216] A. Amirjani, F. Firouzi, D. F. Haghshenas, *Plasmonics* **2020**, *15*, 1077-1082.

[217] K. B. Mogensen, K. Kneipp, *J. Phys. Chem. C* **2014**, *118*, 28075-28083.

[218] P. K. Jain, S. Eustis, M. A. El-Sayed, *J. Phys. Chem. B* **2006**, *110*, 18243-18253.

[219] J. W. Barr, S. Gomrok, E. Chaffin, X. Huang, Y. Wang, *J. Phys. Chem. C* **2021**, *125*, 5260-5268.

[220] P. del Pino, F. Yang, B. Pelaz, Q. Zhang, K. Kantner, R. Hartmann, N. Martinez de Baroja, M. Gallego, M. Möller, B. B. Manshian, S. J. Soenen, R. Riedel, N. Hampp, W. J. Parak, Angew. *Chem. Int. Ed.* **2016**, *55*, 5483-5487.

USC UNIVERSIDADE DE SANTIAGO DE COMPOSTELA

[221] B. A. Manning, S. R. Kanel, E. Guzman, S. W. Brittle, I. E. Pavel, *J. Nanoparticle Res.* **2019**, *21*, 213.

[222] T. Chen, S. Wang, P. Shao, *J. Mater. Sci. Mater. Electron.* **2017**, *28*, 9387-9394.

[223] C. F. Bohren, D. R. Huffman, *Absorption and Scattering of Light by Small Particles*, Wiley-VCH, Weinheim, **2004**.

[224] B. O. Aljohny, A. A. A. Almaliki, Y. Anwar, M. Ul-Islam, T. Kamal, *J. Polym. Environ.* **2021**, *29*, 3252-3262.

[225] J. M. Pettibone, J. M. Gorham, J. Liu, *J. Nanoparticle Res.* **2018**, *20*, 312.

[226] Z. Shi, J. Tang, L. Chen, C. Yan, S. Tanvir, W. A. Anderson, R. M. Berry, K. C. Tam, *J. Mater. Chem. B* **2015**, *3*, 603-611.

[227] H. Li, Y. Ren, M. He, H. Qi, *Phys. Chem. Chem. Phys.* **2024**, *26*, 17860-17868.

[228] V. E. Bochenkov, T. I. Shabatina, *Biosensors* **2018**, *8*, 120.

[229] J. Kumar, H. Eraña, E. López-Martínez, N. Claes, V. F. Martín, D. M. Solís, S. Bals, A. L. Cortajarena, J. Castilla, L. M. Liz-Marzán, Proc. *Natl. Acad. Sci.* **2018**, *115*, 3225-3230.

[230] M. Hentschel, M. Schäferling, X. Duan, H. Giessen, N. Liu, *Sci. Adv.* **2017**, *3*, e1602735.

[231] C. Zhang, C. Song, W. Yang, J. Deng, *Macromol. Rapid Commun.* **2013**, *34*, 1319-1324.

[232] D. Liu, H. Chen, J. Deng, W. Yang, *J. Mater. Chem. C* **2013**, *1*, 8066-8074.

[233] J. Bergueiro, M. Núñez-Martínez, S. Arias, E. Quiñoá, R. Riguera, F. Freire, *Nanoscale Horiz.* **2020**, *5*, 495-500.

[234] M. Núñez-Martínez, S. Arias, E. Quiñoá, R. Riguera, F. Freire, *Chem. Mater.* **2021**, *33*, 4805-4812.

[235] M. Núñez-Martínez, S. Arias, J. Bergueiro, E. Quiñoá, R. Riguera, F. Freire, *Macromol. Rapid Commun.* **2022**, *43*, 2100616.

[236] M. Núñez-Martínez, E. Quiñoá, F. Freire, *Nanoscale* **2022**, *14*, 13066-13072.

[237] M. Núñez-Martínez, E. Quiñoá, F. Freire, *Chem. Mater.* **2023**, *35*, 4865-4872.

[238] E. Yashima, K. Maeda, Y. Okamoto, *Nature* **1999**, *399*, 449-451.

USC UNIVERSIDADE DE SANTIAGO DE COMPOSTELA

[239] Y. Ke, Y. Nagata, T. Yamada, M. Suginome, *Angew. Chem. Int. Ed.* **2015**, *54*, 9333-9337.

[240] R. Rodríguez, E. Suárez-Picado, E. Quiñoá, R. Riguera, F. Freire, *Angew. Chem. Int. Ed.* **2020**, *59*, 8616-8622.

[241] Z. Fernández, B. Fernández, E. Quiñoá, R. Riguera, F. Freire, *Chem. Sci.* **2020**, *11*, 7182-7187.

[242] J. J. L. M. Cornelissen, J. J. J. M. Donners, R. De Gelder, W. S. Graswinckel, G. A. Metselaar, A. E. Rowan, N. A. J. M. Sommerdijk, R. J. M. Nolte, *Science* **2001**, *293*, 676-680.

[243] E. Suárez-Picado, E. Quiñoá, R. Riguera, F. Freire, *Angew. Chem. Int. Ed.* **2020**, *59*, 4537-4543.

[244] R. Rodríguez, E. Rivadulla-Cendal, M. Fernández-Míguez, B. Fernández, K. Maeda, E. Quiñoá, F. Freire, *Angew. Chem. Int. Ed.* **2022**, *61*, e202209953.

[245] M. Lago-Silva, M. M. Cid, E. Quiñoá, F. Freire, *Angew. Chem. Int. Ed.* **2023**, *62*, e202303329.

[246] Y. Inai, Y. Ishida, K. Tagawa, A. Takasu, T. Hirabayashi, *J. Am. Chem. Soc.* **2002**, *124*, 2466-2473.

[247] N. Ousaka, Y. Inai, J. Org. Chem. 2009, *74*, 1429-1439.

[248] M. Fukuda, R. Rodríguez, Z. Fernández, T. Nishimura, D. Hirose, G. Watanabe, E. Quiñoá, F. Freire, K. Maeda, *Chem. Commun.* **2019**, *55*, 7906-7909.

[249] Y. Inai, H. Komori, N. Ousaka, *Chem. Rec.* **2007**, *7*, 191-202.

[250] H. Nakako, R. Nomura, T. Masuda, *Macromolecules* **2001**, *34*, 1496-1502.

[251] X. Guan, S. Wang, G. Shi, J. Zhang, X. Wan, *Macromolecules* **2021**, *54*, 4592-4600.

[252] Y. Zhou, C. Zhang, Y. Qiu, L. Liu, T. Yang, H. Dong, T. Satoh, Y. Okamoto, *Molecules* **2016**, *21*, 1583.

[253] S. Arias, F. Freire, M. Calderón, J. Bergueiro, *Angew. Chem. Int. Ed.* **2017**, *56*, 11420-11425.

USC UNIVERSIDADE DE SANTIAGO DE COMPOSTELA

[254] T. Miyagawa, A. Furuko, K. Maeda, H. Katagiri, Y. Furusho, E. Yashima, *J. Am. Chem. Soc.* **2005**, *127*, 5018-5019.

[255] N. Zhu, K. Nakazono, T. Takata, *Chem. Commun.* **2016**, *52*, 3647-3649.

[256] S. Wang, S. Xie, H. Du, H. Zeng, J. Zhang, X. Wan, *Sci. China Chem.* **2023**, *66*, 887-895.

[257] R. Kakuchi, S. Nagata, R. Sakai, I. Otsuka, H. Nakade, T. Satoh, T. Kakuchi, *Chem. Eur. J.* **2008**, *14*, 10259-10266.

[258] Y. Qu, J. Hua, Y. Jiang, H. Tian, *J. Polym. Sci. A Polym. Chem.* **2009**, *47*, 1544-1552.

[259] R. Kakuchi, Y. Tago, R. Sakai, T. Satoh, T. Kakuchi, *Macromolecules* **2009**, *42*, 4430-4435.

[260] R. Kakuchi, R. Shimada, Y. Tago, R. Sakai, T. Satoh, T. Kakuchi, *J. Polym. Sci. A Polym. Chem.* **2010**, *48*, 1683-1689.

[261] S. Leiras, E. Suárez-Picado, E. Quiñoá, R. Riguera, F. Freire, *Giant* **2021**, *7*, 100068.

[262] Y. Gao, T. Gao, L. Wang, X. Ma, R. Jin, C. Kang, L. Gao, *New J. Chem.* **2021**, *45*, 5093-5098.

[263] Y. Qiu, Y. Zhang, Q. Jiang, H. Wang, Y. Liao, H. Zhou, X. Xie, *Macromolecules* **2022**, *55*, 9057-9065.

[264] M. H.-Y. Chan, S. Y.-L. Leung, V. W.-W. Yam, *J. Am. Chem. Soc.* **2019**, *141*, 12312-12321.

[265] F. Freire, J. M. Seco, E. Quiñoá, R. Riguera, in *Hierarchical Macromolecular Structures: 60 Years after the Staudinger Nobel Prize II* (Ed.: V. Percec), Springer International Publishing, Cham, **2013**, pp. 123–140.

[266] R. Rodríguez, S. Arias, E. Quiñoá, R. Riguera, F. Freire, *Nanoscale* **2017**, *9*, 17752-17757.

[267] S. Arias, F. Freire, E. Quiñoá, R. Riguera, *Polym. Chem.* **2015**, *6*, 4725-4733.

[268] M. Fukuda, T. Nishimura, D. Hirose, K. Maeda, *Chem. Lett.* **2023**, *52*, 136-139.

USC UNIVERSIDADE DE SANTIAGO DE COMPOSTELA

[269] M. Alzubi, S. Arias, I. Louzao, E. Quiñoá, R. Riguera, F. Freire, *Chem. Commun.* **2017**, *53*, 8573-8576.

[270] T. Van Leeuwen, G. H. Heideman, D. Zhao, S. J. Wezenberg, B. L. Feringa, *Chem. Commu.* **2017**, *53*, 6393-6396.

[271] M. M. Green, M. P. Reidy, R. D. Johnson, G. Darling, D. J. O'Leary, G. Willson, *J. Am. Chem. Soc.* **1989**, *111*, 6452-6454.

[272] M. M. Green, N. C. Peterson, T. Sato, A. Teramoto, R. Cook, S. Lifson, *Science* **1995**, *268*, 1860-1866.

[273] H. Gu, Y. Nakamura, T. Sato, A. Teramoto, M. M. Green, S. K. Jha, C. Andreola, M. P. Reidy, *Macromolecules* **1998**, *31*, 6362-6368.

[274] M. M. Green, J.-W. Park, T. Sato, A. Teramoto, S. Lifson, R. L. B. Selinger, J. V. Selinger, *Angew. Chem. Int. Ed.* **1999**, *38*, 3138-3154.

[275] Y. Nagata, T. Nishikawa, M. Suginome, *Chem. Commun.* **2018**, *54*, 6867-6870.

[276] K. Cobos, E. Quiñoá, R. Riguera, F. Freire, *J. Am. Chem. Soc.* **2018**, *140*, 12239-12246.

[277] S. Arias, R. Rodríguez, E. Quiñoá, R. Riguera, F. Freire, *J. Am. Chem. Soc.* **2018**, *140*, 667-674.

[278] M. M. Green, B. A. Garetz, B. Munoz, H. Chang, S. Hoke, R. G. Cooks, J. *Am. Chem. Soc.* **1995**, *117*, 4181-4182.

[279] K. Cobos, R. Rodríguez, E. Quiñoá, R. Riguera, F. Freire, *Angew. Chem. Int. Ed.* **2020**, *59*, 23724-23730.

[280] V. Jain, K. Cheon, K. Tang, S. Jha, M. M. Green, *Isr. J. Chem.* **2011**, *51*, 1067-1074.

[281] M. Alzubi, S. Arias, R. Rodríguez, E. Quiñoá, R. Riguera, F. Freire, *Angew. Chem. Int. Ed.* **2019**, *58*, 13365-13369.

[282] M. Goto, S. Mino, H. Sogawa, F. Sanda, *J. Polym. Sci.* **2023**, *61*, 1270-1278.

[283] S. I. Stupp, R. H. Zha, L. C. Palmer, H. Cui, R. Bitton, *Faraday Discuss.* **2013**, *166*, 9-30.

USC UNIVERSIDADE DE SANTIAGO DE COMPOSTELA

[284] Z. Chen, A. Lohr, C. R. Saha-Möller, F. Würthner, *Chem. Soc. Rev.* **2009**, *38*, 564-584.

[285] L. Brunsveld, B. J. B. Folmer, E. W. Meijer, R. P. Sijbesma, *Chem. Rev.* **2001**, *101*, 4071-4098.

[286] M. Peterca, M. R. Imam, C.-H. Ahn, V. S. K. Balagurusamy, D. A. Wilson, B. M. Rosen, V. Percec, *J. Am. Chem. Soc.* **2011**, *133*, 2311-2328.

[287] T. F. A. De Greef, M. M. J. Smulders, M. Wolffs, A. P. H. J. Schenning, R. P. Sijbesma, E. W. Meijer, *Chem. Rev.* **2009**, *109*, 5687-5754.

[288] R. B. Martin, *Chem. Rev.* **1996**, *96*, 3043-3064.

[289] M. M. J. Smulders, M. M. L. Nieuwenhuizen, T. F. A. de Greef, P. van der Schoot, A. P. H. J. Schenning, E. W. Meijer, *Chem. Eur. J.* **2010**, *16*, 362-367.

[290] M. Wehner, F. Würthner, *Nat. Rev. Chem.* **2019**, *4*, 38-53.

[291] C. Kulkarni, E. W. Meijer, A. R. A. Palmans, *Acc. Chem. Res.* **2017**, *50*, 1928-1936.

[292] C. Naranjo, A. Doncel-Giménez, R. Gómez, J. Aragó, E. Ortí, L. Sánchez, *Chem. Sci.* **2023**, *14*, 9900-9909.

[293] M. Kasha, H. R. Rawls, M. Ashraf El-Bayoumi, *Pure Appl. Chem.* **1965**, *11*, 371-392.

[294] M. Kasha, *Radiat. Res.* **1963**, *20*, 55-70.

[295] S. Ma, S. Du, G. Pan, S. Dai, B. Xu, W. Tian, *Aggregate* **2021**, *2*, e96.

[296] M. S. Barclay, C. K. Wilson, S. K. Roy, O. A. Mass, O. M. Obukhova, R. P. Svoiakov, A. L. Tatarets, A. U. Chowdhury, J. S. Huff, D. B. Turner, P. H. Davis, E. A. Terpetschnig, B. Yurke, W. B. Knowlton, J. Lee, R. D. Pensack, *ChemPhotoChem* **2022**, *6*, e202200039.

[297] E. Fuentes, M. Gerth, J. A. Berrocal, C. Matera, P. Gorostiza, I. K. Voets, S. Pujals, L. Albertazzi, *J. Am. Chem. Soc.* **2020**, *142*, 10069-10078.

[298] C. Otsuka, S. Takahashi, A. Isobe, T. Saito, T. Aizawa, R. Tsuchida, S. Yamashita, K. Harano, H. Hanayama, N. Shimizu, H. Takagi, R. Haruki, L. Liu, M. J. Hollamby, T. Ohkubo, S. Yagai, *J. Am. Chem. Soc.* **2023**, *145*, 22563-22576.

USC UNIVERSIDADE DE SANTIAGO DE COMPOSTELA

[299] C. Otsuka, S. Imai, T. Ohkubo, S. Yagai, *Chem. Commun.* **2024**, *60*, 1108-1111.

[300] A. Lohr, M. Lysetska, F. Würthner, *Angew. Chem. Int. Ed.* **2005**, *44*, 5071-5074.

[301] A. Lohr, F. Würthner, *Angew. Chem. Int. Ed.* **2008**, *47*, 1232-1236.

[302] F. Würthner, S. Yao, U. Beginn, *Angew. Chem. Int. Ed.* **2003**, *42*, 3247-3250.

[303] P. A. Korevaar, C. Schaefer, T. F. A. De Greef, E. W. Meijer, *J. Am. Chem. Soc.* **2012**, *134*, 13482-13491.

[304] P. A. Korevaar, S. J. George, A. J. Markvoort, M. M. J. Smulders, P. A. J. Hilbers, A. P. H. J. Schenning, T. F. A. De Greef, E. W. Meijer, *Nature* **2012**, *481*, 492-496.

[305] P. Jonkheijm, P. Van Der Schoot, A. P. H. J. Schenning, E. W. Meijer, *Science* **2006**, *313*, 80-83.

[306] B. Maiti, S. Bhattacharjee, S. Bhattacharya, *Nanoscale* **2019**, *11*, 2223-2230.

[307] M. H.-Y. Chan, M. Ng, S. Y.-L. Leung, W. H. Lam, V. W.-W. Yam, J*. Am. Chem. Soc.* **2017**, *139*, 8639-8645.

[308] X. Yu, Z. Wang, Y. Li, L. Geng, J. Ren, G. Feng, *Inorg. Chem.* **2017**, *56*, 7512-7518.

[309] F. Wang, C. Feng, *Angew. Chem. Int. Ed.* **2018**, *57*, 5655-5659.

[310] S. Akine, H. Nagumo, T. Nabeshima, *Inorg. Chem.* **2012**, *51*, 5506-5508.

[311] C. Liu, K. Fu, S. Zheng, L. Yao, W. Zhou, G. Liu, *Adv. Opt. Mater.* **2023**, *11*, 2300019.

[312] H. Maeda, W. Hane, Y. Bando, Y. Terashima, Y. Haketa, H. Shibaguchi, T. Kawai, M. Naito, K. Takaishi, M. Uchiyama, A. Muranaka, *Chem. Eur. J.* **2013**, *19*, 16263-16271.

[313] J. Yan, J. Liu, H. Lei, Y. Kang, C. Zhao, Y. Fang, *J. Colloid Interface Sci.* **2015**, *448*, 374-379.

[314] B. Adhikari, H.-B. Kraatz, *Chem. Commun.* **2014**, *50*, 5551-5553.

[315] S. Kawano, N. Fujita, S. Shinkai, *Chem. Eur. J.* **2005**, *11*, 4735-4742.

[316] J. Kim, J. Lee, W. Y. Kim, H. Kim, S. Lee, H. C. Lee, Y. S. Lee, M. Seo, S. Y. Kim, *Nat. Commun.* **2015**, *6*, 6959.

USC UNIVERSIDADE DE SANTIAGO DE COMPOSTELA

[317] J. S. Kang, S. Kang, J.-M. Suh, S. M. Park, D. K. Yoon, M. H. Lim, W. Y. Kim, M. Seo, *J. Am. Chem. Soc.* **2022**, *144*, 2657-2666.

[318] Q. Sallembien, P. Aoun, S. Blanchard, L. Bouteiller, M. Raynal, *Chem. Eur. J.* **2023**, *29*, e202203199.

[319] A. Kousar, J. Liu, N. Mehwish, F. Wang, A. Y. Dang-i, C. Feng, Mater. *Today Chem.* **2019**, *11*, 217-224.

[320] S. Goskulwad, D. D. La, M. A. Kobaisi, S. V. Bhosale, V. Bansal, A. Vinu, K. Ariga, S. V. Bhosale, *Sci. Rep.* **2018**, *8*, 11220.

[321] M. Pandeeswar, T. Govindaraju, *Mol. Syst. Des. Eng.* **2016**, *1*, 202-207.

[322] H. Frisch, Y. Nie, S. Raunser, P. Besenius, *Chem. Eur. J.* **2015**, *21*, 3304-3309.

[323] E. E. Greciano, R. Rodríguez, K. Maeda, L. Sánchez, *Chem. Commun.* **2020**, *56*, 2244-2247.

[324] M. M. J. Smulders, P. J. M. Stals, T. Mes, T. F. E. Paffen, A. P. H. J. Schenning, A. R. A. Palmans, E. W. Meijer, *J. Am. Chem. Soc.* **2010**, *132*, 620-626.

[325] L. N. J. De Windt, Z. Fernández, M. Fernández-Míguez, F. Freire, A. R. A. Palmans, *Chem. Eur. J.* **2022**, *28*, e202103691.

[326] M. Lago-Silva, M. Fernández-Míguez, Z. Fernández, M. M. Cid, E. Quiñoá, R. Rodríguez, F. Freire, *Angew. Chem. Int. Ed.* **2025**, *64*, e202421310.

[327] S. Wang, J. Chen, X. Feng, G. Shi, J. Zhang, X. Wan, *Macromolecules* **2017**, *50*, 4610-4615.

[328] V. Percec, Q. Xiao, *Isr. J. Chem.* **2021**, *61*, 530-556.

[329] E. Yashima, K. Maeda, Y. Furusho, *Acc. Chem. Res.* **2008**, *41*, 1166-1180.

[330] L. Zhou, C.-L. Li, R.-T. Gao, S.-M. Kang, L. Xu, X.-H. Xu, N. Liu, Z.-Q. Wu, *Macromolecules* **2021**, *54*, 679-686.

[331] Z.-Q. Wu, X. Song, Y.-X. Li, L. Zhou, Y.-Y. Zhu, Z. Chen, N. Liu, *Nat. Commun.* **2023**, *14*, 566.

[332] K. Maeda, M. Nozaki, K. Hashimoto, K. Shimomura, D. Hirose, T. Nishimura, G. Watanabe, E. Yashima, *J. Am. Chem. Soc.* **2020**, *142*, 7668-7682.

USC UNIVERSIDADE DE SANTIAGO DE COMPOSTELA

[333] T. Ikai, K. Nakamura, K. Mizumoto, K. Oki, E. Yashima, *Angew. Chem. Int. Ed.* **2023**, *62*, e202301127.

[334] M. Fernández-Míguez, M. Núñez-Martínez, E. Suárez-Picado, E. Quiñoá, F. Freire, *ACS Nano* **2024**, *18*, 28822-28833.

[335] M. Lago-Silva, M. M. Cid, E. Quiñoá, F. Freire, *J. Am. Chem. Soc.* **2024**, *146*, 752-759.

[336] R. Rodríguez, E. Rivadulla-Cendal, E. Quiñoá, F. Freire, *Chirality* **2023**, *35*, 172-177.

[337] M. Núñez-Martínez, M. Fernández-Míguez, E. Quiñoá, F. Freire, *Nanoscale* **2025**, *17*, 4439-4443.

[338] X.-X. Lu, H.-S. Tang, C.-C. Ko, J. Ka-Yan Wong, N. Zhu, V. W.-W. Yam, *Chem. Commun.* **2005**, 1572-1574.

[339] V. Amendola, L. Fabbrizzi, L. Mosca, F. Schmidtchen, *Chem. Eur. J.* **2011**, *17*, 5972-5981.

[340] C. Caltagirone, G. W. Bates, P. A. Gale, M. E. Light, *Chem. Commun.* **2008**, 61-63.

[341] J. De Jong, J. E. Bos, S. J. Wezenberg, *Chem. Rev.* **2023**, *123*, 8530-8574.

[342] R. Sakai, E. B. Barasa, N. Sakai, S. Sato, T. Satoh, T. Kakuchi, *Macromolecules* **2012**, *45*, 8221-8227.

[343] R. Sakai, N. Sakai, T. Satoh, W. Li, A. Zhang, T. Kakuchi, *Macromolecules* **2011**, *44*, 4249-4257.

[344] R. Sakai, S. Okade, E. B. Barasa, R. Kakuchi, M. Ziabka, S. Umeda, K. Tsuda, T. Satoh, T. Kakuchi, *Macromolecules* **2010**, *43*, 7406-7411.

[345] R. Kakuchi, S. Nagata, Y. Tago, R. Sakai, I. Otsuka, T. Satoh, T. Kakuchi, *Macromolecules* **2009**, *42*, 1476-1481.

[346] R. Kakuchi, T. Kodama, R. Shimada, Y. Tago, R. Sakai, T. Satoh, T. Kakuchi, *Macromolecules* **2009**, *42*, 3892-3897.

[347] C. Poderi, I. Neira, P. Franchi, E. Mezzina, I. Baù, P. Neviani, M. Lucarini, *Chem. Eur. J.* **2023**, *29*, e202301508.

USC UNIVERSIDADE DE SANTIAGO DE COMPOSTELA

[348] C. J. Pedersen, H. K. Frensdorff, *Angew. Chem. Int. Ed.* **1972**, *11*, 16-25.

[349] J. Li, D. Yim, W.-D. Jang, J. Yoon, *Chem. Soc. Rev.* **2017**, *46*, 2437-2458.

[350] J. M. Haider, Z. Pikramenou, *Chem. Soc. Rev.* **2005**, *34*, 120-132.

[351] T. Kameda, M. Takaizumi, S. Kumagai, Y. Saito, T. Yoshioka, *Soft Mater.* **2021**, *19*, 139-147.

[352] G. T. Selvan, S. Poomalai, S. Ramasamy, P. M. Selvakumar, I. V. Muthu Vijayan Enoch, S. G. Lanas, A. Melchior, *Anal. Chem.* **2018**, *90*, 13607-13615.

[353] D. Prochowicz, A. Kornowicz, J. Lewiński, *Chem. Rev.* **2017**, *117*, 13461-13501.

[354] H. Liu, Y. Tan, Q. Dai, H. Liang, J. Song, J. Qu, W.-Y. Wong, *Dyes and Pigments* **2018**, *158*, 312-318.

[355] E. Pluhařová, M. D. Baer, C. J. Mundy, B. Schmidt, P. Jungwirth, *J. Phys. Chem. Lett.* **2014**, *5*, 2235-2240.

[356] N. Kaur, B. Kaur, *J. Coord. Chem.* **2021**, *74*, 575-583.

[357] K. Maeda, T. Miyagawa, A. Furuko, H. Onouchi, E. Yashima, *Macromolecules* **2015**, *48*, 4281-4293.

[358] H. Onouchi, T. Hasegawa, D. Kashiwagi, H. Ishiguro, K. Maeda, E. Yashima, *Macromolecules* **2005**, *38*, 8625-8633.

[359] K. Nagai, K. Maeda, Y. Takeyama, K. Sakajiri, E. Yashima, *Macromolecules* **2005**, *38*, 5444-5451.

[360] K. Maeda, Y. Takeyama, K. Sakajiri, E. Yashima, *J. Am. Chem. Soc.* **2004**, *126*, 16284-16285.

[361] K. Maeda, D. Hirose, M. Nozaki, Y. Shimizu, T. Mori, K. Yamanaka, K. Ogino, T. Nishimura, T. Taniguchi, M. Moro, E. Yashima, *Sci. Adv.* **2021**, *7*, eabg5381.

[362] A. Zhang, Y. Guo, *Chem. Eur. J.* **2008**, *14*, 8939-8946.

[363] L. Ren, X. Lu, W. Li, J. Yan, A. K. Whittaker, A. Zhang, *J. Am. Chem. Soc.* **2023**, *145*, 24906-24921.

[364] Y. Cao, L. Ren, Y. Zhang, X. Lu, X. Zhang, J. Yan, W. Li, T. Masuda, A. Zhang, *Macromolecules* **2021**, *54*, 7621-7631.

[365] H. Komori, Y. Inai, *J. Org. Chem.* **2007**, *72*, 4012-4022.

USC UNIVERSIDADE DE SANTIAGO DE COMPOSTELA

[366] S. Arias, J. Bergueiro, F. Freire, E. Quiñoá, R. Riguera, *Small* **2016**, *12*, 238-244.

[367] J. Bergueiro, F. Freire, E. P. Wendler, J. M. Seco, E. Quiñoá, R. Riguera, *Chem. Sci.* **2014**, *5*, 2170-2176.

[368] P. P. N. Syamala, B. Soberats, D. Görl, S. Gekle, F. Würthner, *Chem. Sci.* **2019**, *10*, 9358-9366.

[369] N. J. Greenfield, *Nat. Protoc.* **2006**, *1*, 2527-2535.

[370] L. A. Freiburger, K. Auclair, A. K. Mittermaier, *Thermochim. Acta* **2012**, *527*, 148-157.

[371] S. Lany, *J. Am. Chem. Soc.* **2024**, *146*, 14114-14127.

[372] U. Pal, S. K. Pramanik, B. Bhattacharya, B. Banerji, N. C. Maiti, *SpringerPlus* **2015**, *4*, 548.

[373] H. Kwon, G. Mpourmpakis, *J. Chem. Theory Comput.* **2023**, *19*, 3652-3663.

[374] N. Liu, R.-T. Gao, Z.-Q. Wu, *Acc. Chem. Res.* **2023**, *56*, 2954-2967.

[375] C. Zhao, S. Meng, H. Chan, X. Wang, H. Li, M. C. W. Chan, *Angew. Chem. Int. Ed.* **2022**, *61*, e202115712.

[376] F. S. A. Khan, N. M. Mubarak, Y. H. Tan, M. Khalid, R. R. Karri, R. Walvekar, E. C. Abdullah, S. Nizamuddin, S. A. Mazari, *J. Hazard. Mater.* **2021**, *413*, 125375.

[377] B. Tutunaru, A. Samide, C. Tigae, B. Oprea, *Int. J. Electrochem. Sci.* **2024**, *19*, 100561.

[378] M. Li, Q. Shi, N. Song, Y. Xiao, L. Wang, Z. Chen, T. D. James, *Chem. Soc. Rev.* **2023**, *52*, 5827-5860.

[379] L. M. S. Takata, H. Iida, K. Shimomura, K. Hayashi, A. A. Dos Santos, E. Yashima, *Macromol. Rapid Commun.* **2015**, *36*, 2047-2054.

[380] H. Iida, Z. Tang, E. Yashima*, J. Polym. Sci. A Polym. Chem.* **2013**, *51*, 2869-2879.

[381] K. Vikrant, K.-H. Kim, *Chem. Eng. J.* **2019**, *358*, 264-282.

[382] R. Li, H. Wu, J. Ding, W. Fu, L. Gan, Y. Li, *Sci. Rep.* **2017**, *7*, 46545.

[383] A. B. Tabrizi, *J. Hazard. Mater.* **2007**, *139*, 260-264.

USC UNIVERSIDADE DE SANTIAGO DE COMPOSTELA

[384] Md. R. Awual, M. Ismael, T. Yaita, S. A. El-Safty, H. Shiwaku, Y. Okamoto, S. Suzuki, *Chem. Eng. J.* **2013**, *222*, 67-76.

[385] T. J. Huat, J. Camats-Perna, E. A. Newcombe, N. Valmas, M. Kitazawa, R. Medeiros, *J. Mol. Biol.* **2019**, *431*, 1843-1868.

[386] M. Halon-Golabek, A. Borkowska, A. Herman-Antosiewicz, J. Antosiewicz, *Front. Neurosci.* **2019**, *13*, 165.

[387] J. Pan, J. Li, R. Huang, X. Zhang, H. Shen, Y. Xiong, X. Zhu, *Tetrahedron* **2015**, *71*, 5341-5346.

[388] X. Shi, X. Ren, Z. Ren, J. Li, Y. Wang, S. Yang, J. Gu, Q. Gao, G. Huang, *Eur. J. Org. Chem.* **2014**, 2014, 5083–5088.

[389] M. D. Peeks, C. E. Tait, P. Neuhaus, G. M. Fischer, M. Hoffmann, R. Haver, A. Cnossen, J. R. Harmer, C. R. Timmel, H. L. Anderson, *J. Am. Chem. Soc.* **2017**, *139*, 10461-10471.

[390] G. Moise, L. Tejerina, M. Rickhaus, H. L. Anderson, C. R. Timmel, *J. Phys. Chem. Lett.* **2019**, *10*, 5708-5712.

[391] Y. Yang, O. Blacque, S. Sato, M. Juríček, *Angew. Chem. Int. Ed.* **2021**, *60*, 13529-13535.

[392] C. R. Jacob, M. Reiher, *Int. J. Quantum Chem.* **2012**, *112*, 3661-3684.

[393] J. J. Tarrío, B. Hermida, R. Rodríguez, J. Crassous, E. Quiñoá, F. Freire, *Small* **2025**, *21*, 2409379.

[394] F. Rey- Tarrío, E. Quiñoá, G. Fernández, F. Freire, *Nat. Commun.* **2023**, *14*, 3348.

[395] Z. Fernández, B. Fernández, E. Quiñoá, F. Freire, *J. Am. Chem. Soc.* **2021**, *143*, 20962-20969.

[396] A. Xu, T. Masuda, A. Zhang, *Polym. Rev.* **2017**, *57*, 138-158.

[397] R. Rodríguez, E. Quiñoá, R. Riguera, F. Freire, *Small* **2019**, *15*, 1805413.

[398] R. Rodríguez, E. Quiñoá, R. Riguera, F. Freire, *Chem. Mater.* **2018**, *30*, 2493-2497.

[399] J. G. Rudick, V. Percec, *Acc. Chem. Res.* **2008**, *41*, 1641-1652.

USC UNIVERSIDADE DE SANTIAGO DE COMPOSTELA

[400] E. Yashima, K. Maeda, *Macromolecules* **2008**, *41*, 3-12.

[401] R. Ishidate, A. J. Markvoort, K. Maeda, E. Yashima, *J. Am. Chem. Soc.* **2019**, *141*, 7605-7614.

[402] T. Ikai, R. Ishidate, K. Inoue, K. Kaygisiz, K. Maeda, E. Yashima, *Macromolecules* **2020**, *53*, 973-981.

[403] E. Yashima, K. Maeda, O. Sato, *J. Am. Chem. Soc.* **2001**, *123*, 8159-8160.

[404] M. Fernández-Míguez, E. Quiñoá, F. Freire, *Angew. Chem. Int. Ed.* **2025**, *64*, e202503949.

[405] Z. Tang, H. Iida, H.-Y. Hu, E. Yashima, *ACS Macro Lett.* **2012**, *1*, 261-265.

[406] T. Sato, K. Terao, A. Teramoto, M. Fujiki, *Macromolecules* **2002**, *35*, 5355-5357.

[407] Z. Yan, S. Cai, J. Tan, J. Zhang, C. Yan, T. Xu, X. Wan, *ACS Macro Lett.* **2019**, 8, 789-794.

[408] T. Kelen, F. TÜdös, *J. Macromol. Sci. Part A Chem.* **1975**, *9*, 1-27.

[409] K. Maeda, M. Muto, T. Sato, E. Yashima, *Macromolecules* **2011**, *44*, 8343-8349.

[410] M. G. Mayershofer, O. Nuyken, *J. Polym. Sci. A Polym. Chem.* **2005**, *43*, 5723-5747.

[411] B. S. Li, K. K. L. Cheuk, L. Ling, J. Chen, X. Xiao, C. Bai, B. Z. Tang, *Macromolecules* **2003**, *36*, 77-85.

[412] K. K. L. Cheuk, J. W. Y. Lam, L. M. Lai, Y. Dong, B. Z. Tang, *Macromolecules* **2003**, *36*, 9752-9762.

[413] Gaussian 16, Revision C.01, M. J. Frisch, G. W. Trucks, H. B. Schlegel, G. E. Scuseria, M. A. Robb, J. R. Cheeseman, G. Scalmani, V. Barone, G. A. Petersson, H. Nakatsuji, X. Li, M. Caricato, A. V. Marenich, J. Bloino, B. G. Janesko, R. Gomperts, B. Mennucci, H. P. Hratchian, J. V. Ortiz, A. F. Izmaylov, J. L. Sonnenberg, D. Williams-Young, F. Ding, F. Lipparini, F. Egidi, J. Goings, B. Peng, A. Petrone, T. Henderson, D. Ranasinghe, V. G. Zakrzewski, J. Gao, N. Rega, G. Zheng, W. Liang, M. Hada, M. Ehara, K. Toyota, R. Fukuda, J. Hasegawa, M. Ishida, T. Nakajima, Y. Honda, O. Kitao, H. Nakai, T. Vreven, K. Throssell, J. A. Montgomery Jr., J. E. Peralta, F. Ogliaro, M. J. Bearpark, J. J. Heyd, E. N. Brothers, K. N. Kudin, V. N. Staroverov, T. A. Keith, R. Kobayashi, J. Normand, K.

USC UNIVERSIDADE DE SANTIAGO DE COMPOSTELA

Raghavachari, A. P. Rendell, J. C. Burant, S. S. Iyengar, J. Tomasi, M. Cossi, J. M. Millam, M. Klene, C. Adamo, R. Cammi, J. W. Ochterski, R. L. Martin, K. Morokuma, O. Farkas, J. B. Foresman, D. J. Fox, Gaussian, Inc., Wallingford CT, **2016**.

[414] C. Lee, W. Yang, R. G. Parr, *Phys. Rev. B* **1988**, *37*, 785-789.

[415] A. D. Becke, *J. Chem. Phys.* **1993**, *98*, 5648-5652.

[416] T. Stein, L. Kronik, R. Baer, *J. Am. Chem. Soc.* **2009**, *131*, 2818-2820.

[417] M. M. Francl, W. J. Pietro, W. J. Hehre, J. S. Binkley, M. S. Gordon, D. J. DeFrees, J. A. Pople, *J. Chem. Phys.* **1982**, *77*, 3654-3665.

[418] J. Tomasi, B. Mennucci, R. Cammi, *Chem. Rev.* **2005**, *105*, 2999-3094.

[419] T. Lu, *Angew. Chem. Int. Ed.* **2025**, *64*, e202504895.

[420] T. Lu, F. Chen, *J. Comput. Chem.* **2012**, *33*, 580-592.

[421] S. Lifson, M. M. Green, C. Andreola, N. C. Peterson, *J. Am. Chem. Soc.* **1989**, *111*, 8850-8858.

[422] J. V. Selinger, R. L. B. Selinger, *Phys. Rev. E* **1997**, *55*, 1728-1731.

[423] H. Gu, T. Sato, A. Teramoto, L. Varichon, M. M. Green, *Polym. J.* **1997**, *29*, 77-84.

[424] A. Teramoto, *Prog. Polym. Sci.* **2001**, *26*, 667-720.

[425] K. Cobos, R. Rodríguez, O. Domarco, B. Fernández, E. Quiñoá, R. Riguera, F. Freire, *Macromolecules* **2020**, *53*, 3182-3193.

[426] F. Freire, E. Quiñoá, R. Riguera, *Chem. Commun.* **2017**, *53*, 481-492.

[427] S. Arias, M. Núñez-Martínez, E. Quiñoá, R. Riguera, F. Freire, *Small* **2017**, *13*, 1602398.

[428] S. Arias, J. Bergueiro, F. Freire, E. Quiñoá, R. Riguera, *Small* **2016**, *12*, 237-237.

[429] K. Tang, M. M. Green, K. S. Cheon, J. V. Selinger, B. A. Garetz, *J. Am. Chem. Soc.* **2003**, *125*, 7313-7323.

[430] D. Jaque, L. Martínez Maestro, B. Del Rosal, P. Haro-Gonzalez, A. Benayas, J. L. Plaza, E. Martín Rodríguez, J. García Solé, *Nanoscale* **2014**, *6*, 9494-9530.

USC UNIVERSIDADE DE SANTIAGO DE COMPOSTELA

[431] C. J. Kirubaharan, D. Kalpana, Y. S. Lee, A. R. Kim, D. J. Yoo, K. S. Nahm, G. G. Kumar, *Ind. Eng. Chem. Res.* **2012**, *51*, 7441-7446.

[432] T. Mitsudome, A. Noujima, Y. Mikami, T. Mizugaki, K. Jitsukawa, K. Kaneda, *Angew. Chem. Int. Ed.* **2010**, *49*, 5545-5548.

[433] M. Grzelczak, J. Vermant, E. M. Furst, L. M. Liz-Marzán, *ACS Nano* **2010**, *4*, 3591-3605.

[434] R. M. Choueiri, A. Klinkova, H. Thérien-Aubin, M. Rubinstein, E. Kumacheva, *J. Am. Chem. Soc.* **2013**, *135*, 10262-10265.

[435] M. Grzelczak, L. M. Liz-Marzán, R. Klajn, Chem. Soc. Rev. 2019, 48, 1342–1361.

[436] J. Zhang, P. J. Santos, P. A. Gabrys, S. Lee, C. Liu, R. J. Macfarlane, *J. Am. Chem. Soc.* **2016**, *138*, 16228-16231.

[437] C.-C. Li, S.-J. Chang, F.-J. Su, S.-W. Lin, Y.-C. Chou, *Colloids Surf. Physicochem. Eng. Asp.* **2013**, *419*, 209-215.

[438] C. Pigliacelli, R. Sánchez-Fernández, M. D. García, C. Peinador, E. Pazos, *Chem. Commun.* **2020**, *56*, 8000-8014.

[439] H.-E. Lee, H.-Y. Ahn, J. Mun, Y. Y. Lee, M. Kim, N. H. Cho, K. Chang, W. S. Kim, J. Rho, K. T. Nam, *Nature* **2018**, *556*, 360-365.

[440] G. González-Rubio, J. Mosquera, V. Kumar, A. Pedrazo-Tardajos, P. Llombart, D. M. Solís, I. Lobato, E. G. Noya, A. Guerrero-Martínez, J. M. Taboada, F. Obelleiro, L. G. MacDowell, S. Bals, L. M. Liz-Marzán, *Science* **2020**, *368*, 1472-1477.

[441] J. Lu, Y. Xue, K. Bernardino, N.-N. Zhang, W. R. Gomes, N. S. Ramesar, S. Liu, Z. Hu, T. Sun, A. F. De Moura, N. A. Kotov, K. Liu, *Science* **2021**, *371*, 1368-1374.

[442] N.-N. Zhang, H.-R. Sun, S. Liu, Y.-C. Xing, J. Lu, F. Peng, C.-L. Han, Z. Wei, T. Sun, B. Yang, K. Liu, *CCS Chem.* **2022**, *4*, 660-670.

[443] J.-S. Lee, A. K. R. Lytton-Jean, S. J. Hurst, C. A. Mirkin, *Nano Lett.* **2007**, *7*, 2112-2115.

[444] E. Pazos, E. Sleep, C. M. Rubert Pérez, S. S. Lee, F. Tantakitti, S. I. Stupp, *J. Am. Chem. Soc.* **2016**, *138*, 5507-5510.

USC UNIVERSIDADE DE SANTIAGO DE COMPOSTELA

[445] D. Porrelli, M. Mardirossian, L. Musciacchio, M. Pacor, F. Berton, M. Crosera, G. Turco, *ACS Appl. Mater. Interfaces* **2021**, *13*, 17255-17267.

[446] Z. Szakács, M. Kraszni, B. Noszál, *Anal. Bioanal. Chem.* **2004**, *378*, 1428-1448.

[447] J. Weisell, M. T. Hyvönen, J. Vepsäläinen, L. Alhonen, T. A. Keinänen, A. R. Khomutov, P. Soininen, *Amino Acids* **2010**, *38*, 501-507.

[448] B. Noszal, W. Guo, D. L. Rabenstein, *J. Org. Chem.* **1992**, *57*, 2327-2334.

[449] S. T. Schneebeli, A. D. Bochevarov, R. A. Friesner, *J. Chem. Theory Comput.* **2011**, *7*, 658-668.

[450] M. Khavani, A. Mehranfar, M. Izadyar, *Sci. Rep.* **2021**, *11*, 23422.

[451] E. R. Johnson, S. Keinan, P. Mori-Sánchez, J. Contreras-García, A. J. Cohen, W. Yang, *J. Am. Chem. Soc.* **2010**, *132*, 6498-6506.

[452] P. V. Nhat, N. T. Si, M. T. Nguyen, *J. Comput. Chem.* **2019**, *40*, 1990-1993.

[453] P. L. Rodríguez-Kessler, A. R. Rodríguez-Domínguez, D. MacLeod Carey, A. Muñoz-Castro, *Phys. Chem. Chem. Phys.* **2020**, *22*, 27255-27262.

[454] P. V. Nhat, N. T. Si, M. T. Nguyen, *J. Mol. Model.* **2018**, *24*, 209.

[455] R. A. Boto, J. Contreras-García, M. Calatayud, *Comput. Theor. Chem.* **2015**, *1053*, 322-327.

[456] S. Balasurya, A. Syed, A. M. Thomas, N. Marraiki, A. M. Elgorban, L. L. Raju, A. Das, S. S. Khan, Spectrochim. *Acta. A. Mol. Biomol. Spectrosc.* **2020**, *228*, 117712.

[457] Y. Zou, J. Pang, F. Zhang, F. Chai, *ChemistrySelect* **2021**, *6*, 6077-6082.

[458] I. Schiesaro, L. Burratti, C. Meneghini, I. Fratoddi, P. Prosposito, J. Lim, C. Scheu, I. Venditti, G. Iucci, C. Battocchio, *J. Phys. Chem. C* **2020**, *124*, 25975-25983.

[459] M. Maity, K. Bera, U. Pal, K. Khamaru, N. C. Maiti, *ACS Appl. Nano Mater.* **2018**, *1*, 6099-6111.

[460] S. H. Gellman, *Acc. Chem. Res.* **1998**, *31*, 173–180.

[461] J. W. Y. Lam, B. Z. Tang, *Acc. Chem. Res.* **2005**, *38*, 745–754.

[462] Y.-J. Jin, G. Kwak, *Polym. Rev.* **2017**, *57*, 175–199.

USC UNIVERSIDADE DE SANTIAGO DE COMPOSTELA

[463] H. Shirakawa, E. J. Louis, A. G. MacDiarmid, C. K. Chiang, A. J. Heeger, *J. Chem. Soc. Chem. Commun.* **1977**, *1*, 578-580.

[464] J. Solà, S. P. Fletcher, A. Castellanos, J. Clayden, *Angew. Chem. Int. Ed.* **2010**, *49*, 6836–6839.

[465] J. Solà, M. Helliwell, J. Clayden, *J. Am. Chem. Soc.* **2010**, *132*, 4548–4549.

[466] Y. Inai, N. Ousaka, T. Okabe, *J. Am. Chem. Soc.* **2003**, *125*, 8151–8162.

[467] Y. Inai, K. Tagawa, A. Takasu, T. Hirabayashi, T. Oshikawa, M. Yamashita, *J. Am. Chem. Soc.* **2000**, *122*, 11731–11732.

[468] Y. Inai, H. Komori, *Biomacromolecules* **2004**, *5*, 1231–1240.

[469] S. Sakamoto, T. Taniguchi, Y. Sakata, S. Akine, T. Nishimura, K. Maeda, *Organometallics* **2022**, *41*, 472–479.

[470] P. C. Knipe, S. Thompson, A. D. Hamilton, *Chem. Sci.* **2015**, *6*, 1630–1639.

[471] B. L. Feringa, *J. Org. Chem.* **2007**, *72*, 6635–6652.

[472] J. Su, Y. Song, Z. Zhu, X. Huang, J. Fan, J. Qiao, F. Mao, *Sig. Transduct. Target Ther.* **2024**, *9*, 196.

[473] X. Xu, C. Gao, R. Emusani, C. Jia, D. Xiang, *Adv. Sci.* **2024**, *11*, 2400877.

[474] E. Moulin, L. Faour, C. C. Carmona-Vargas, N. Giuseppone, *Adv. Mater.* **2020**, *32*, 1906036.

[475] C. M. Goodman, S. Choi, S. Shandler, W. F. DeGrado, *Nat. Chem. Biol.* **2007**, *3*, 252–262.

[476] N. Bajpayee, T. Vijayakanth, S. Rencus-Lazar, S. Dasgupta, A. V. Desai, R. Jain, E. Gazit, R. Misra, *Angew. Chem. Int. Ed.* **2023**, *62*, e202214583.

[477] S. Kwon, B. J. Kim, H.-K. Lim, K. Kang, S. H. Yoo, J. Gong, E. Yoon, J. Lee, I. S. Choi, H. Kim, H.-S. Lee, *Nat. Commun.* **2015**, *6*, 8747.

[478] R. Rodríguez, E. Suárez-Picado, E. Quiñoá, R. Riguera, F. Freire, *Angew. Chem. Int. Ed.* **2020**, *59*, 8616-8622.

[479] V. Koehler, A. Roy, I. Huc, Y. Ferrand, *Acc. Chem. Res.* **2022**, *55*, 1074–1085.

[480] A. R. Davis, S. Ozturk, C. C. Seaton, L. Male, S. J. Pike, *Chem. – Eur. J.* **2024**, *30*, e202402892.

USC UNIVERSIDADE DE SANTIAGO DE COMPOSTELA

[481] D. T. J. Morris, J. Clayden, *Chem. Soc. Rev.* **2023**, *52*, 2480–2496.

[482] J. E. Jones, V. Diemer, C. Adam, J. Raftery, R. E. Ruscoe, J. T. Sengel, M. I. Wallace, A. Bader, S. L. Cockroft, J. Clayden, S. J. Webb, *J. Am. Chem. Soc.* **2016**, *138*, 688–695.

[483] F. G. A. Lister, N. Eccles, S. J. Pike, R. A. Brown, G. F. S. Whitehead, J. Raftery, S. J. Webb, J. Clayden, *Chem. Sci.* **2018**, *9*, 6860–6870.

[484] B. A. F. Le Bailly, J. Clayden, *Chem. Commun.* **2016**, *52*, 4852–4863.

[485] D. Mazzier, M. Crisma, M. De Poli, G. Marafon, C. Peggion, J. Clayden, A. Moretto*, J. Am. Chem. Soc.* **2016**, *138*, 8007–8018.

[486] E. Yashima, *Proc. Jpn. Acad. Ser. B* **2023**, *99*, 438–459.

[487] T. Ikai, Y. Morita, T. Majima, S. Takeda, R. Ishidate, K. Oki, N. Suzuki, H. Ohtani, H. Aoi, K. Maeda, K. Okoshi, E. Yashima, *J. Am. Chem. Soc.* **2023**, *145*, 24862–24876.

[488] K. Maeda, K. Shimomura, T. Ikai, S. Kanoh, E. Yashima, *Macromolecules* **2017**, *50*, 7801–7806.

[489] C. Reichardt, T. Welton, Solvents and Solvent Effects in Organic Chemistry, Wiley-VCH, Weinheim, Germany, **2011**.

[490] F. Huang, O. A. Scherman, *Chem. Soc. Rev.* **2012**, *41*, 5879-5880.

[491] T. Aida, E. W. Meijer, *Isr. J. Chem.* **2020**, *60*, 33–47.

[492] P. K. Hashim, J. Bergueiro, E. W. Meijer, T. Aida, *Prog. Polym. Sci.* **2020**, *105*, 101250.

[493] T. Aida, E. W. Meijer, S. I. Stupp, *Science* **2012**, *335*, 813–817.

[494] M. Hartlieb, E. D. H. Mansfield, S. Perrier, *Polym. Chem.* **2020**, *11*, 1083–1110.

[495] C. Rest, R. Kandanelli, G. Fernández, *Chem. Soc. Rev.* **2015**, *44*, 2543–2572.

[496] S. Cantekin, T. F. A. De Greef, A. R. A. Palmans, *Chem. Soc. Rev.* **2012**, *41*, 6125-6137.

[497] S. Cantekin, H. M. M. Ten Eikelder, A. J. Markvoort, M. A. J. Veld, P. A. Korevaar, M. M. Green, A. R. A. Palmans, E. W. Meijer, *Angew. Chem. Int. Ed.* **2012**, *51*, 6426–6431.

USC UNIVERSIDADE DE SANTIAGO DE COMPOSTELA

[498] P. J. M. Stals, J. F. Haveman, R. Martín-Rapún, C. F. C. Fitié, A. R. A. Palmans, E. W. Meijer, *J. Mater. Chem.* **2009**, *19*, 124–130.

[499] R. Van Hameren, A. M. Van Buul, M. A. Castriciano, V. Villari, N. Micali, P. Schön, S. Speller, L. Monsù Scolaro, A. E. Rowan, J. A. A. W. Elemans, R. J. M. Nolte, *Nano Lett.* **2008**, *8*, 253–259.

[500] T.-Q. Nguyen, R. Martel, P. Avouris, M. L. Bushey, L. Brus, C. Nuckolls, *J. Am. Chem. Soc.* **2004**, *126*, 5234–5242.

[501] M. L. Bushey, A. Hwang, P. W. Stephens, C. Nuckolls, *Angew. Chem. Int. Ed.* **2002**, *41*, 2828–2831.

[502] M. L. Bushey, A. Hwang, P. W. Stephens, C. Nuckolls, J*. Am. Chem. Soc.* **2001**, *123*, 8157–8158.

[503] M. A. Martínez, A. Doncel-Giménez, J. Cerdá, J. Calbo, R. Rodríguez, J. Aragó, J. Crassous, E. Ortí, L. Sánchez, *J. Am. Chem. Soc.* **2021**, *143*, 13281–13291.

[504] M. Wehner, M. I. S. Röhr, M. Bühler, V. Stepanenko, W. Wagner, F. Würthner, *J. Am. Chem. Soc.* **2019**, *141*, 6092–6107.

[505] C. Roche, H.-J. Sun, P. Leowanawat, F. Araoka, B. E. Partridge, M. Peterca, D. A. Wilson, M. E. Prendergast, P. A. Heiney, R. Graf, H. W. Spiess, X. Zeng, G. Ungar, V. Percec, *Nat. Chem.* **2016**, *8*, 80–89.

[506] F. Würthner, C. R. Saha-Möller, B. Fimmel, S. Ogi, P. Leowanawat, D. Schmidt, *Chem. Rev.* **2016**, *116*, 962–1052.

[507] L. Wang, B. E. Partridge, N. Huang, J. T. Olsen, D. Sahoo, X. Zeng, G. Ungar, R. Graf, H. W. Spiess, V. Percec, *J. Am. Chem. Soc.* **2020**, *142*, 9525–9536.

[508] B. E. Partridge, L. Wang, D. Sahoo, J. T. Olsen, P. Leowanawat, C. Roche, H. Ferreira, K. J. Reilly, X. Zeng, G. Ungar, P. A. Heiney, R. Graf, H. W. Spiess, V. Percec, *J. Am. Chem. Soc.* **2019**, *141*, 15761–15766.

[509] B. E. Partridge, P. Leowanawat, E. Aqad, M. R. Imam, H.-J. Sun, M. Peterca, P. A. Heiney, R. Graf, H. W. Spiess, X. Zeng, G. Ungar, V. Percec, *J. Am. Chem. Soc.* **2015**, *137*, 5210–5224.

[510] R. Manha Veedu, N. Niemeyer, N. Bäumer, K. Kartha Kalathil, J. Neugebauer, G. Fernández, *Angew. Chem. Int. Ed.* **2023**, *62*, e202314211.

USC UNIVERSIDADE DE SANTIAGO DE COMPOSTELA

[511] N. Bäumer, S. Ogi, L. Borsdorf, S. Yamaguchi, G. Fernández, *Chem. Commun.* **2023**, *59*, 8937–8940.

[512] B. Matarranz, S. Díaz-Cabrera, G. Ghosh, I. Carreira-Barral, B. Soberats, M. García-Valverde, R. Quesada, G. Fernández, *Angew. Chem. Int. Ed.* **2023**, *62*, e202218555.

[513] I. Helmers, M. S. Hossain, N. Bäumer, P. Wesarg, B. Soberats, L. S. Shimizu, G. Fernández, *Angew. Chem. Int. Ed.* **2022**, *61*, e202200390.

[514] B. Matarranz, G. Fernández, *Chem. Phys. Rev.* **2021**, *2*, 041304.

[515] H. Wang, Y. Zhang, Y. Chen, H. Pan, X. Ren, Z. Chen, *Angew. Chem. Int. Ed.* **2020**, *59*, 5185–5192.

[516] K. V. Rao, M. F. J. Mabesoone, D. Miyajima, A. Nihonyanagi, E. W. Meijer, T. Aida, *J. Am. Chem. Soc.* **2020**, *142*, 598–605.

[517] N. Sasaki, M. F. J. Mabesoone, J. Kikkawa, T. Fukui, N. Shioya, T. Shimoaka, T. Hasegawa, H. Takagi, R. Haruki, N. Shimizu, S. Adachi, E. W. Meijer, M. Takeuchi, K. Sugiyasu, *Nat. Commun.* **2020**, *11*, 3578.

[518] M. F. J. Mabesoone, A. J. Markvoort, M. Banno, T. Yamaguchi, F. Helmich, Y. Naito, E. Yashima, A. R. A. Palmans, E. W. Meijer, *J. Am. Chem. Soc.* **2018**, *140*, 7810–7819.

[519] K. Venkata Rao, D. Miyajima, A. Nihonyanagi, T. Aida, Nat. Chem. 2017, 9, 1133–1139.

[520] S. Ogi, K. Sugiyasu, S. Manna, S. Samitsu, M. Takeuchi, *Nat. Chem.* **2014**, *6*, 188–195.

[521] H. Lee, H. Park, D. Y. Ryu, W.-D. Jang, *Chem. Soc. Rev.* **2023**, *52*, 1947–1974.

[522] Z. Fernández, B. Fernández, E. Quiñoá, F. Freire, *Angew. Chem. Int. Ed.* **2021**, *60*, 9919–9924.

[523] B. Matarranz, G. Ghosh, R. Kandanelli, A. Sampedro, K. K. Kartha, G. Fernández, *Chem. Commun.* **2021**, *57*, 4890–4893.

[524] G. Das, R. Thirumalai, B. Vedhanarayanan, V. K. Praveen, A. Ajayaghosh, *Adv. Opt. Mater.* **2020**, *8*, 2000173.

USC UNIVERSIDADE DE SANTIAGO DE COMPOSTELA

[525] S. K. Albert, H. V. P. Thelu, M. Golla, N. Krishnan, S. Chaudhary, R. Varghese, *Angew. Chem. Int. Ed.* **2014**, *53*, 8352–8357.

[526] F. García, L. Sánchez, *J. Am. Chem. Soc.* **2012**, *134*, 734–742.

[527] F. García, R. Gómez, L. Sánchez, *Chem. Soc. Rev.* **2023**, *52*, 7524–7548.

[528] E. E. Greciano, J. Calbo, J. Buendía, J. Cerdá, J. Aragó, E. Ortí, L. Sánchez, *J. Am. Chem. Soc.* **2019**, *141*, 7463–7472.

[529] M. M. J. Smulders, I. A. W. Filot, J. M. A. Leenders, P. Van Der Schoot, A. R. A. Palmans, A. P. H. J. Schenning, E. W. Meijer, *J. Am. Chem. Soc.* **2010**, *132*, 611–619.

[530] N. J. Van Zee, M. F. J. Mabesoone, B. Adelizzi, A. R. A. Palmans, E. W. Meijer, *J. Am. Chem. Soc.* **2020**, *142*, 20191–20200.

[531] E. E. Greciano, S. Alsina, G. Ghosh, G. Fernández, L. Sánchez, *Small Methods* **2020**, *4*, 1900715.

[532] A. Gao, Q. Wang, H. Wu, J.-W. Zhao, X. Cao, *Coord. Chem. Rev.* **2022**, *471*, 214753.

[533] S.-Y. Chen, Y.-W. Chiu, G.-S. Liou, *Nanoscale* **2019**, *11*, 8597–8603.

[534] F. Ito, J. Fujimori, N. Oka, M. Sliwa, C. Ruckebusch, S. Ito, H. Miyasaka, *Faraday Discuss.* **2017**, *196*, 231–243.

[535] M. K. Dhinakaran, W. Gong, Y. Yin, A. Wajahat, X. Kuang, L. Wang, G. Ning, *Polym. Chem.* **2017**, *8*, 5295–5302.

[536] P. Pracht, F. Bohle, S. Grimme, *Phys. Chem. Chem. Phys.* **2020**, *22*, 7169–7192.

[537] M. Zhang, Y. Zhou, B. Wu, C. Lu, G. Quan, Z. Huang, C. Wu, X. Pan, *Mater. Adv.* **2023**, *4*, 5420–5430.

[538] E. Runge, E. K. U. Gross, *Phys. Rev. Lett.* **1984**, *52*, 997–1000.

[539] H. M. M. Ten Eikelder, A. J. Markvoort, T. F. A. De Greef, P. A. J. Hilbers, *J. Phys. Chem. B* **2012**, *116*, 5291–5301.

[540] A. J. Markvoort, H. M. M. Ten Eikelder, P. A. J. Hilbers, T. F. A. De Greef, E. W. Meijer, *Nat. Commun.* **2011**, *2*, 509.

USC UNIVERSIDADE DE SANTIAGO DE COMPOSTELA

[541] Y. Dorca, C. Naranjo, G. Ghosh, B. Soberats, J. Calbo, E. Ortí, G. Fernández, L. Sánchez, *Chem. Sci.* **2022**, *13*, 81–89.

[542] W. R. Henderson, R. K. Castellano, *Polym. Int.* **2021**, *70*, 897–910.

[543] S. Bujosa, A. Doncel-Giménez, N. Bäumer, G. Fernández, E. Ortí, A. Costa, C. Rotger, J. Aragó, B. Soberats, *Angew. Chem. Int. Ed.* **2022**, *61*, e202213345.

[544] F. García, P. M. Viruela, E. Matesanz, E. Ortí, L. Sánchez, *Chem. – Eur. J.* **2011**, *17*, 7755–7759.

[545] E. E. Greciano, J. Calbo, E. Ortí, L. Sánchez, *Angew. Chem. Int. Ed.* **2020**, *59*, 17517–17524.

[546] J. Matern, K. K. Kartha, L. Sánchez, G. Fernández, *Chem. Sci.* **2020**, *11*, 6780–6788.

[547] P. Hohenberg, W. Kohn, *Phys. Rev.* **1964**, *136*, B864–B871.

[548] F. Neese, *WIREs Comput. Mol. Sci.* **2012**, *2*, 73–78.

[549] V. Barone, in *Recent Advances in Computational Chemistry,* WORLD SCIENTIFIC, **1995**, pp. 287–334.

[550] S. Stoll, A. Schweiger, *J. Magn. Reson.* **2006**, *178*, 42–55.

[551] S. Grimme, J. Antony, S. Ehrlich, H. Krieg, *J. Chem. Phys.* **2010**, 132, 154104.

[552] D. Figgen, G. Rauhut, M. Dolg, H. Stoll, *Chem. Phys.* **2005**, *311*, 227–244.

[553] K. A. Peterson, C. Puzzarini, *Theor. Chem. Acc.* **2005**, *114*, 283–296.

[554] B. P. Pritchard, D. Altarawy, B. Didier, T. D. Gibson, T. L. Windus, *J. Chem. Inf. Model.* **2019**, *59*, 4814–4820.

[555] C. Bannwarth, E. Caldeweyher, S. Ehlert, A. Hansen, P. Pracht, J. Seibert, S. Spicher, S. Grimme, *WIREs Comput. Mol. Sci.* **2021**, *11*, e1493.

[556] S. Ehlert, M. Stahn, S. Spicher, S. Grimme, *J. Chem. Theory Comput.* **2021**, *17*, 4250–4261.

[557] C. Bannwarth, S. Ehlert, S. Grimme, *J. Chem. Theory Comput.* **2019**, *15*, 1652–1671.

[558] T. Lu, *J. Chem. Phys.* **2024**, *161*, 082503.

USC UNIVERSIDADE DE SANTIAGO DE COMPOSTELA

[559] M. D. Hanwell, D. E. Curtis, D. C. Lonie, T. Vandermeersch, E. Zurek, G. R. Hutchison, *J. Cheminformatics* **2012**, *4*, 17.

[560] W. Humphrey, A. Dalke, K. Schulten*, J. Mol. Graph.* **1996**, *14*, 33–38.

USC
UNIVERSIDADE DE SANTIAGO DE COMPOSTELA

USC
UNIVERSIDADE
DE SANTIAGO
DE COMPOSTELA

Appendix

USC
UNIVERSIDADE
DE SANTIAGO
DE COMPOSTELA

USC
UNIVERSIDADE
DE SANTIAGO
DE COMPOSTELA

A.1. List of publications derived from this Doctoral Thesis and partially reproduced

1) Manuel Núñez-Martínez[+], Manuel Fernández-Míguez[+], Emilio Quiñoá, Félix Freire,* Size Control of Chiral Nanospheres Obtained via Nanoprecipitation of Helical Poly(phenylacetylene)s in the Absence of Surfactants, *Angew. Chem. Int. Ed.* **2024**, *63*, e202403313. DOI: 10.1002/anie.202403313.

[+]These authors contributed equally to this work.

Reproduced in: Section 1.6.3.

Impact factor: 16.9 (2024 Journal Citation Reports).

CiteScore: 27.6 (2024 Scopus).

SJR: 5.550 (2024 SJR).

Category: Chemistry, Multidisciplinary (Q1,D1) (2024 Journal Citation Reports).

General Chemistry (Q1,D1) (2024 Scopus).

Chemistry (Miscellaneous) (Q1) (2024 SJR).

M. F.-M. contributed to the experimental part (synthesis and characterization), the discussion of results, and the writing of the manuscript.

This publication is licensed under CC BY-NC 4.0. As it can be read in the following text for thesis and dissertation not permission is required.

USC UNIVERSIDADE DE SANTIAGO DE COMPOSTELA

CC BY-NC 4.0

Attribution-NonCommercial 4.0 International

Deed

Canonical URL : https://creativecommons.org/licenses/by-nc/4.0/

See the legal code

You are free to:

Share — copy and redistribute the material in any medium or format

Adapt — remix, transform, and build upon the material

The licensor cannot revoke these freedoms as long as you follow the license terms.

Under the following terms:

Attribution — You must give appropriate credit , provide a link to the license, and indicate if changes were made . You may do so in any reasonable manner, but not in any way that suggests the licensor endorses you or your use.

NonCommercial — You may not use the material for commercial purposes .

No additional restrictions — You may not apply legal terms or technological measures that legally restrict others from doing anything the license permits.

Notices:

You do not have to comply with the license for elements of the material in the public domain or where your use is permitted by an applicable exception or limitation .

No warranties are given. The license may not give you all of the permissions necessary for your intended use. For example, other rights such as publicity, privacy, or moral rights may limit how you use the material.

USC UNIVERSIDADE DE SANTIAGO DE COMPOSTELA

2) María Lago-Silva, Manuel Fernández-Míguez, Rafael Rodríguez, Emilio Quiñoá, Félix Freire,* Stimuli-responsive synthetic helical polymers, *Chem. Soc. Rev.* **2024**, *53*, 793-852. DOI: 10.1039/D3CS00952A

Reproduced in: Section 1.8.

Impact factor: 39.0 (2024 Journal Citation Reports).

CiteScore: 73.2 (2024 Scopus).

SJR: 11.467 (2024 SJR).

Category: Chemistry, Multidisciplinary (Q1,D1) (2024 Journal Citation Reports).

General Chemistry (Q1,D1) (2024 Scopus).

Chemistry (Miscellaneous) (Q1) (2024 SJR).

M. F.-M. contributed to the planning and the writing of the manuscript.

This publication is licensed under CC BY 3.0. As it can be read in the following text for thesis and dissertation not permission is required.

USC UNIVERSIDADE DE SANTIAGO DE COMPOSTELA

CC BY 3.0

Attribution 3.0 Unported

Deed

Notice

This is an older version of this license. Compared to previous versions, the 4.0 versions of all CC licenses are more user-friendly and more internationally robust. If you are licensing your own work, we strongly recommend the use of the 4.0 license instead: Deed - Attribution 4.0 International

Canonical URL : https://creativecommons.org/licenses/by/3.0/

See the legal code

You are free to:

Share — copy and redistribute the material in any medium or format for any purpose, even commercially.

Adapt — remix, transform, and build upon the material for any purpose, even commercially.

The licensor cannot revoke these freedoms as long as you follow the license terms.

Under the following terms:

Attribution — You must give appropriate credit, provide a link to the license, and indicate if changes were made. You may do so in any reasonable manner, but not in any way that suggests the licensor endorses you or your use.

No additional restrictions — You may not apply legal terms or technological measures that legally restrict others from doing anything the license permits.

Notices:

You do not have to comply with the license for elements of the material in the public domain or where your use is permitted by an applicable exception or limitation.

No warranties are given. The license may not give you all of the permissions necessary for your intended use. For example, other rights such as publicity, privacy, or moral rights may limit how you use the material.

USC UNIVERSIDADE DE SANTIAGO DE COMPOSTELA

3) Rafael Rodríguez, Elena Rivadulla-Cendal, Manuel Fernández-Míguez, Berta Fernández, Katsuhiro Maeda, Emilio Quiñoá, and Félix Freire,* Full Control of the Chiral Overpass Effect in Helical Polymers: *P*/*M* Screw Sense Induction by Remote Chiral Centers After Bypassing the First Chiral Residue, *Angew. Chem. Int. Ed.* **2022**, *61*, e202209953. DOI: 10.1002/anie.202209953

Reproduced in: Section 1.8.1.3.

Impact factor: 16.6 (2022 Journal Citation Reports).

CiteScore: 26.3 (2022 Scopus).

SJR: 5.573 (2022 SJR).

Category: Chemistry, Multidisciplinary (Q1,D1) (2022 Journal Citation Reports).

General Chemistry (Q1,D1) (2022 Scopus).

Chemistry (Miscellaneous) (Q1) (2022 SJR).

M. F.-M. contributed to the computational studies.

This publication is licensed under CC B-NC 4.0. As it can be read in the following text for thesis and dissertation not permission is required.

USC UNIVERSIDADE DE SANTIAGO DE COMPOSTELA

CC BY-NC 4.0

Attribution-NonCommercial 4.0 International

Deed

Canonical URL : https://creativecommons.org/licenses/by-nc/4.0/

See the legal code

You are free to:

Share — copy and redistribute the material in any medium or format

Adapt — remix, transform, and build upon the material

The licensor cannot revoke these freedoms as long as you follow the license terms.

Under the following terms:

Attribution — You must give appropriate credit , provide a link to the license, and indicate if changes were made . You may do so in any reasonable manner, but not in any way that suggests the licensor endorses you or your use.

NonCommercial — You may not use the material for commercial purposes .

No additional restrictions — You may not apply legal terms or technological measures that legally restrict others from doing anything the license permits.

Notices:

You do not have to comply with the license for elements of the material in the public domain or where your use is permitted by an applicable exception or limitation .

No warranties are given. The license may not give you all of the permissions necessary for your intended use. For example, other rights such as publicity, privacy, or moral rights may limit how you use the material.

USC UNIVERSIDADE DE SANTIAGO DE COMPOSTELA

4) Lafayette N. J. de Windt, Zulema Fernández, Manuel Fernández-Míguez, Félix Freire,* Anja R. A. Palmans,* Elucidating the Supramolecular Copolymerization of N- and C-Centered Benzene-1,3,5-Tricarboxamides: The Role of Parallel and Antiparallel Packing of Amide Groups in the Copolymer Microstructure, *Chem. Eur. J.* **2022**, *18*, e202103691. DOI: 10.1002/chem.202103691.

Reproduced in: Section 1.9.5.1.

Impact factor: 4.3 (2022 Journal Citation Reports).

CiteScore: 8.8 (2022 Scopus).

SJR: 1.229 (2022 SJR).

Category: Chemistry, Multidisciplinary (Q2) (2022 Journal Citation Reports).

Chemistry – Organic Chemistry (Q1) (2022 Scopus).

Chemistry (Miscellaneous) (Q1) (2022 SJR).

M. F.-M. contributed to the computational studies.

This publication is licensed under CC BY-NC 4.0. As it can be read in the following text for thesis and dissertation not permission is required.

USC UNIVERSIDADE DE SANTIAGO DE COMPOSTELA

CC BY-NC 4.0

Attribution-NonCommercial 4.0 International

Deed

Canonical URL : https://creativecommons.org/licenses/by-nc/4.0/

See the legal code

You are free to:

Share — copy and redistribute the material in any medium or format

Adapt — remix, transform, and build upon the material

The licensor cannot revoke these freedoms as long as you follow the license terms.

Under the following terms:

Attribution — You must give appropriate credit , provide a link to the license, and indicate if changes were made . You may do so in any reasonable manner, but not in any way that suggests the licensor endorses you or your use.

NonCommercial — You may not use the material for commercial purposes .

No additional restrictions — You may not apply legal terms or technological measures that legally restrict others from doing anything the license permits.

Notices:

You do not have to comply with the license for elements of the material in the public domain or where your use is permitted by an applicable exception or limitation .

No warranties are given. The license may not give you all of the permissions necessary for your intended use. For example, other rights such as publicity, privacy, or moral rights may limit how you use the material.

USC UNIVERSIDADE DE SANTIAGO DE COMPOSTELA

5) María Lago-Silva[+], Manuel Fernández-Míguez[+], Zulema Fernández, María Magdalena Cid, Emilio Quiñoá, Rafael Rodríguez,* Félix Freire,* Coaxial Helices in Chiral Supramolecular Aggregates from Highly Hindered Chiral Allenes, *Angew. Chem. Int. Ed.* **2024**, *64*, e202421310. DOI: 10.1002/anie.202421310.

[+]These authors contributed equally to this work.

Reproduced in: Section 1.9.6.

Impact factor: 16.9 (2024 Journal Citation Reports).

CiteScore: 27.6 (2024 Scopus).

SJR: 5.550 (2024 SJR).

Category: Chemistry, Multidisciplinary (Q1,D1) (2024 Journal Citation Reports).

General Chemistry (Q1,D1) (2024 Scopus).

Chemistry (Miscellaneous) (Q1) (2024 SJR).

M. F.-M. contributed to the experimental part (Characterization, and computational studies), the discussion of results, and the writing of the manuscript.

This publication is licensed under CC-BY-NC 4.0. As it can be read in the following text for thesis and dissertation not permission is required.

USC UNIVERSIDADE DE SANTIAGO DE COMPOSTELA

CC BY-NC 4.0

Attribution-NonCommercial 4.0 International

Deed

Canonical URL : https://creativecommons.org/licenses/by-nc/4.0/

See the legal code

You are free to:

Share — copy and redistribute the material in any medium or format

Adapt — remix, transform, and build upon the material

The licensor cannot revoke these freedoms as long as you follow the license terms.

Under the following terms:

Attribution — You must give appropriate credit , provide a link to the license, and indicate if changes were made . You may do so in any reasonable manner, but not in any way that suggests the licensor endorses you or your use.

NonCommercial — You may not use the material for commercial purposes .

No additional restrictions — You may not apply legal terms or technological measures that legally restrict others from doing anything the license permits.

Notices:

You do not have to comply with the license for elements of the material in the public domain or where your use is permitted by an applicable exception or limitation .

No warranties are given. The license may not give you all of the permissions necessary for your intended use. For example, other rights such as publicity, privacy, or moral rights may limit how you use the material.

USC UNIVERSIDADE DE SANTIAGO DE COMPOSTELA

6) Manuel Fernández-Míguez, Emilio Quiñoá, Félix Freire,* Thermal Activation of Asymmetry Amplification Effects in Helical Polymer-Metal Complexes, *Angew. Chem. Int. Ed.* **2025**, *64*, e202503949. DOI: 10.1002/anie.202503949.

Reproduced in: Chapter 3.1. and 5.1.

Impact factor: 16.9 (2024 Journal Citation Reports).

CiteScore: 27.6 (2024 Scopus).

SJR: 5.550 (2024 SJR).

Category: Chemistry, Multidisciplinary (Q1,D1) (2024 Journal Citation Reports).

General Chemistry (Q1,D1) (2024 Scopus).

Chemistry (Miscellaneous) (Q1) (2024 SJR).

M. F.-M. contributed to the experimental part (synthesis, characterization, and computational studies), the discussion of results, and the writing of the manuscript.

Authorization from the journal:

USC
UNIVERSIDADE DE SANTIAGO DE COMPOSTELA

License Details

This Agreement between Manuel Fernández Míguez, Universidade de Santiago de Compostela (USC) ("You") and John Wiley and Sons ("John Wiley and Sons") consists of your license details and the terms and conditions provided by John Wiley and Sons and Copyright Clearance Center.

Print Copy

License Number	6033170000784
License date	May 20, 2025
Licensed Content Publisher	John Wiley and Sons
Licensed Content Publication	Angewandte Chemie International Edition
Licensed Content Title	Thermal Activation of Asymmetry Amplification Effects in Helical Polymer–Metal Complexes
Licensed Content Author	Manuel Fernández-Míguez, Emilio Quiñoá, Félix Freire
Licensed Content Date	Mar 21, 2025
Licensed Content Volume	64
Licensed Content Issue	21
Licensed Content Pages	8
Type of Use	Dissertation/Thesis
Requestor type	Author of this Wiley article
Format	Print and electronic
Portion	Full article
Will you be translating?	No
Title of new work	Dynamic Helical Polymers: Exploring the Complexity of Responses to Stimuli
Institution name	Universidad de Santiago de Compostela (USC)
Expected presentation date	Oct 2025
The Requesting Person / Organization to Appear on the License	Manuel Fernández Míguez, Universidade de Santiago de Compostela (USC)
Requestor Location	Mr. Manuel Fernández Míguez c/ Jenaro de la Fuente s/n Santiago De Compostela, 15782 Spain
Publisher Tax ID	EU826007151
Total	**0.00 EUR**

USC UNIVERSIDADE DE SANTIAGO DE COMPOSTELA

7) Manuel Núñez-Martínez[+], Manuel Fernández-Míguez[+], Emilio Quiñoá, Félix Freire,* Colorimetric detector of oxidizing metal ions by anilide-poly(phenylacetylene)s, *Nanoscale* **2025**, *17*, 4439–4443. DOI: 10.1039/D4NR03662J.

[+]These authors contributed equally to this work.

Reproduced in: Chapter 3.2 and 5.2.

Impact factor: 5.1 (2024 Journal Citation Reports).

CiteScore: 9.9 (2024 Scopus).

SJR: 1.245 (2024 SJR).

Category: Physics, Applied (Q1) (2024 Journal Citation Reports).

General Materials Science (Q1) (2024 Scopus).

Materials Science (Miscellaneous) (Q1) (2024 SJR).

M. F.-M. contributed to the experimental part (synthesis, characterization, and computational studies), the discussion of results, and the writing of the manuscript.

This publication is licensed under CC BY-NC 3.0. As it can be read in the following text for thesis and dissertation not permission is required.

USC UNIVERSIDADE DE SANTIAGO DE COMPOSTELA

CC BY-NC 3.0

Attribution-NonCommercial 3.0 Unported

Deed

Notice

This is an older version of this license. Compared to previous versions, the 4.0 versions of all CC licenses are more user-friendly and more internationally robust. If you are licensing your own work, we strongly recommend the use of the 4.0 license instead: Deed - Attribution-NonCommercial 4.0 International

Canonical URL : https://creativecommons.org/licenses/by-nc/3.0/

See the legal code

You are free to:

Share — copy and redistribute the material in any medium or format

Adapt — remix, transform, and build upon the material

The licensor cannot revoke these freedoms as long as you follow the license terms.

Under the following terms:

Attribution — You must give appropriate credit, provide a link to the license, and indicate if changes were made. You may do so in any reasonable manner, but not in any way that suggests the licensor endorses you or your use.

NonCommercial — You may not use the material for commercial purposes.

No additional restrictions — You may not apply legal terms or technological measures that legally restrict others from doing anything the license permits.

Notices:

You do not have to comply with the license for elements of the material in the public domain or where your use is permitted by an applicable exception or limitation.

No warranties are given. The license may not give you all of the permissions necessary for your intended use. For example, other rights such as publicity, privacy, or moral rights may limit how you use the material.

8) Manuel Fernández-Míguez, Manuel Núñez-Martínez, Esteban Suárez-Picado, Emilio Quiñoá, Félix Freire,* Optical and Chiroptical Stimuli-Responsive Chiral AgNPs@H-Leu-Poly(phenylacetylene) Nanocomposites in Water, *ACS Nano* **2024**, *18*, 28822–28833. DOI: 10.1021/acsnano.4c08622.

[+]These authors contributed equally to this work.

Reproduced in: Chapter 3.5 and 5.5.

Impact factor: 16.0 (2024 Journal Citation Reports).

CiteScore: 24.2 (2024 Scopus).

SJR: 4.497 (2024 SJR).

Category: Chemistry, Multidisciplinary (Q1,D1) (2024 Journal Citation Reports).

General Materials Science (Q1,D1) (2024 Scopus).

Materials Science (Miscellaneous) (Q1) (2024 SJR).

M. F.-M. contributed to the experimental part (synthesis, characterization, and computational studies), the discussion of results, and the writing of the manuscript.

This publication is licensed under CC BY 4.0. As it can be read in the following text for thesis and dissertation not permission is required.

USC UNIVERSIDADE DE SANTIAGO DE COMPOSTELA

CC BY 4.0

Attribution 4.0 International

Deed

Canonical URL : https://creativecommons.org/licenses/by/4.0/

See the legal code

You are free to:

Share — copy and redistribute the material in any medium or format for any purpose, even commercially.

Adapt — remix, transform, and build upon the material for any purpose, even commercially.

The licensor cannot revoke these freedoms as long as you follow the license terms.

Under the following terms:

Attribution — You must give appropriate credit , provide a link to the license, and indicate if changes were made . You may do so in any reasonable manner, but not in any way that suggests the licensor endorses you or your use.

No additional restrictions — You may not apply legal terms or technological measures that legally restrict others from doing anything the license permits.

Notices:

You do not have to comply with the license for elements of the material in the public domain or where your use is permitted by an applicable exception or limitation .

No warranties are given. The license may not give you all of the permissions necessary for your intended use. For example, other rights such as publicity, privacy, or moral rights may limit how you use the material.

USC UNIVERSIDADE DE SANTIAGO DE COMPOSTELA

A.2. Conflict of Interest

The PhD candidate Manuel Fernández Míguez declares no conflict of interest in relation to the doctoral thesis.

Santiago de Compostela, July 1st 2025.

A.3. Rights and Permissions of the images

Figure 6:

License Details

This Agreement between Manuel Fernández Míguez, Universidade de Santiago de Compostela (USC) ("You") and John Wiley and Sons ("John Wiley and Sons") consists of your license details and the terms and conditions provided by John Wiley and Sons and Copyright Clearance Center.

Print Copy

License Number	6032960958287
License date	May 20, 2025
Licensed Content Publisher	John Wiley and Sons
Licensed Content Publication	Angewandte Chemie
Licensed Content Title	Facile and Versatile Synthesis of End-Functionalized Poly(phenylacetylene)s: A Multicomponent Catalytic System for Well-Controlled Living Polymerization of Phenylacetylenes
Licensed Content Author	Tsuyoshi Taniguchi, Takumi Yoshida, Kensuke Echizen, et al
Licensed Content Date	Mar 19, 2020
Licensed Content Volume	132
Licensed Content Issue	22
Licensed Content Pages	11
Type of Use	Dissertation/Thesis
Requestor type	University/Academic
Format	Print and electronic
Portion	Figure/table
Number of figures/tables	1
Will you be translating?	No
Title of new work	Dynamic Helical Polymers: Exploring the Complexity of Responses to Stimuli
Institution name	Universidad de Santiago de Compostela (USC)
Expected presentation date	Oct 2025
Portions	Figure 1
The Requesting Person / Organization to Appear on the License	Manuel Fernández Míguez, Universidade de Santiago de Compostela (USC)
Requestor Location	Mr. Manuel Fernández Míguez c/ Jenaro de la Fuente s/n Santiago De Compostela, 15782 Spain
Publisher Tax ID	EU826007151
Billing Type	Invoice
Billing address	Universidade de Santiago de Compostela c/ Jenaro de la Fuente s/n Santiago De Compostela, Spain 15782
Total	**0.00 EUR**

USC UNIVERSIDADE DE SANTIAGO DE COMPOSTELA

Figure 7:

License Details

This Agreement between Manuel Fernández Míguez, Universidade de Santiago de Compostela (USC) ("You") and John Wiley and Sons ("John Wiley and Sons") consists of your license details and the terms and conditions provided by John Wiley and Sons and Copyright Clearance Center.

Print Copy

License Number	6032960763426
License date	May 20, 2025
Licensed Content Publisher	John Wiley and Sons
Licensed Content Publication	Angewandte Chemie International Edition
Licensed Content Title	Photochemical Electrocyclization of Poly(phenylacetylene)s: Unwinding Helices to Elucidate their 3D Structure in Solution
Licensed Content Author	Félix Freire, Ricardo Riguera, Emilio Quiñoá, et al
Licensed Content Date	Feb 19, 2021
Licensed Content Volume	60
Licensed Content Issue	15
Licensed Content Pages	9
Type of Use	Dissertation/Thesis
Requestor type	University/Academic
Format	Print and electronic
Portion	Figure/table
Number of figures/tables	1
Will you be translating?	No
Title of new work	Dynamic Helical Polymers: Exploring the Complexity of Responses to Stimuli
Institution name	Universidad de Santiago de Compostela (USC)
Expected presentation date	Oct 2025
Portions	Figure 3
The Requesting Person / Organization to Appear on the License	Manuel Fernández Míguez, Universidade de Santiago de Compostela (USC)
Requestor Location	Mr. Manuel Fernández Míguez c/ Jenaro de la Fuente s/n Santiago De Compostela, 15782 Spain
Publisher Tax ID	EU826007151
Total	**0.00 EUR**

USC UNIVERSIDADE DE SANTIAGO DE COMPOSTELA

Figure 8:

License Details

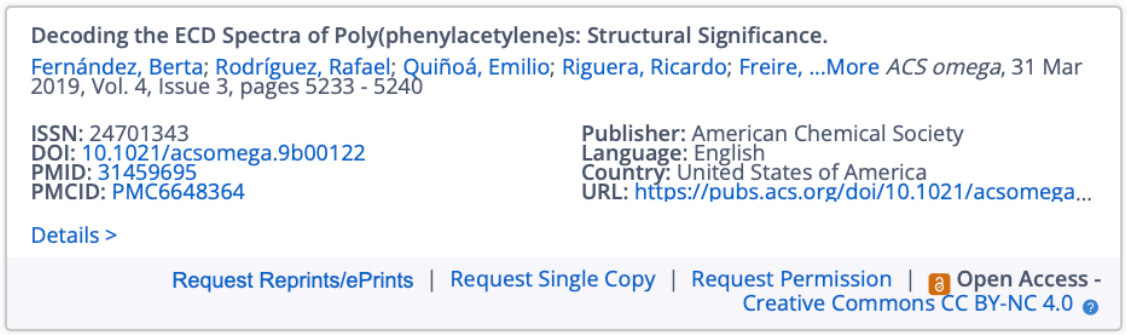
This Agreement between Manuel Fernández Míguez, Universidade de Santiago de Compostela (USC) ("You") and John Wiley and Sons ("John Wiley and Sons") consists of your license details and the terms and conditions provided by John Wiley and Sons and Copyright Clearance Center.

Print Copy

License Number	6032961138087
License date	May 20, 2025
Licensed Content Publisher	John Wiley and Sons
Licensed Content Publication	Journal of Polymer Science Part A: Polymer Chemistry
Licensed Content Title	Dramatic decrease of the cis content and molecular weight of cis-transoidal polyphenylacetylene at 23 °C in solutions prepared in air
Licensed Content Author	Wlodzimierz Buchowicz, Paul Nombel, Jonathan G. Rudick, et al
Licensed Content Date	Aug 13, 2002
Licensed Content Volume	40
Licensed Content Issue	19
Licensed Content Pages	9
Type of Use	Dissertation/Thesis
Requestor type	University/Academic
Format	Print and electronic
Portion	Figure/table
Number of figures/tables	1
Will you be translating?	No
Title of new work	Dynamic Helical Polymers: Exploring the Complexity of Responses to Stimuli
Institution name	Universidad de Santiago de Compostela (USC)
Expected presentation date	Oct 2025
Portions	Scheme 1
The Requesting Person / Organization to Appear on the License	Manuel Fernández Míguez, Universidade de Santiago de Compostela (USC)
Requestor Location	Mr. Manuel Fernández Míguez c/ Jenaro de la Fuente s/n Santiago De Compostela, 15782 Spain
Publisher Tax ID	EU826007151
Total	**0.00 EUR**

USC UNIVERSIDADE DE SANTIAGO DE COMPOSTELA

Figure *10*:



Decoding the ECD Spectra of Poly(phenylacetylene)s: Structural Significance.

Fernández, Berta; Rodríguez, Rafael; Quiñoá, Emilio; Riguera, Ricardo; Freire, ...More *ACS omega*, 31 Mar 2019, Vol. 4, Issue 3, pages 5233 - 5240

ISSN: 24701343
DOI: 10.1021/acsomega.9b00122
PMID: 31459695
PMCID: PMC6648364

Publisher: American Chemical Society
Language: English
Country: United States of America
URL: https://pubs.acs.org/doi/10.1021/acsomega...

Details >

Request Reprints/ePrints | Request Single Copy | Request Permission | Open Access - Creative Commons CC BY-NC 4.0

CC BY-NC 4.0

Attribution-NonCommercial 4.0 International

Deed

Canonical URL : https://creativecommons.org/licenses/by-nc/4.0/

See the legal code

You are free to:

Share — copy and redistribute the material in any medium or format

Adapt — remix, transform, and build upon the material

The licensor cannot revoke these freedoms as long as you follow the license terms.

Under the following terms:

Attribution — You must give appropriate credit , provide a link to the license, and indicate if changes were made . You may do so in any reasonable manner, but not in any way that suggests the licensor endorses you or your use.

NonCommercial — You may not use the material for commercial purposes .

No additional restrictions — You may not apply legal terms or technological measures that legally restrict others from doing anything the license permits.

Notices:

You do not have to comply with the license for elements of the material in the public domain or where your use is permitted by an applicable exception or limitation .

No warranties are given. The license may not give you all of the permissions necessary for your intended use. For example, other rights such as publicity, privacy, or moral rights may limit how you use the material.

USC UNIVERSIDADE DE SANTIAGO DE COMPOSTELA

Figure 11:

CCC Marketplace

This is a License Agreement between Manuel Fernández Míguez, Universidade de Santiago de Compostela (USC) ("User") and Copyright Clearance Center, Inc. ("CCC") on behalf of the Rightsholder identified in the order details below. The license consists of the order details, the Marketplace Permissions General Terms and Conditions below, and any Rightsholder Terms and Conditions which are included below.
All payments must be made in full to CCC in accordance with the Marketplace Permissions General Terms and Conditions below.

Order Date	20-May-2025	**Type of Use**	Republish in a thesis/dissertation
Order License ID	1611604-1	**Publisher**	Royal Society of Chemistry
ISSN	2041-6539	**Portion**	Chart/graph/table/figure

LICENSED CONTENT

Publication Title	Chemical science	**Rightsholder**	Royal Society of Chemistry
Article Title	Controlled modulation of the helical sense and the elongation of poly(phenylacetylene)s by polar and donor effects	**Publication Type**	e-Journal
		Start Page	2735
		Issue	7
		Volume	4
Author / Editor	Royal Society of Chemistry (Great Britain)	**URL**	http://www.rsc.org/Publishin...
Date	01/01/2010		
Language	English		
Country	United Kingdom of Great Britain and Northern Ireland		

REQUEST DETAILS

Portion Type	Chart/graph/table/figure	**Distribution**	Worldwide
Number of Charts / Graphs / Tables / Figures Requested	2	**Translation**	Original language of publication
Format (select all that apply)	Print, Electronic	**Copies for the Disabled?**	No
Who Will Republish the Content?	Author of requested content	**Minor Editing Privileges?**	No
		Incidental Promotional Use?	No
Duration of Use	Life of current edition	**Currency**	EUR
Lifetime Unit Quantity	Up to 499		
Rights Requested	Main product		

NEW WORK DETAILS

Title	Dynamic Helical Polymers: Exploring the Complexity of Responses to Stimuli	**Institution Name**	Universidade de Santiago de Compostela
		Expected Presentation Date	2025-10-30
Instructor Name	Manuel Fernández Míguez		

ADDITIONAL DETAILS

Order Reference Number	N/A	**The Requesting Person / Organization to Appear on the License**	Manuel Fernández Míguez, Universidade de Santiago de Compostela (USC)

REQUESTED CONTENT DETAILS

Title, Description or Numeric Reference of the Portion(s)	Figure 11 and Figure 12	**Title of the Article / Chapter the Portion Is From**	Controlled modulation of the helical sense and the elongation of poly(phenylacetylene)s by polar and donor effects
Editor of Portion(s)	Leiras, Seila; Freire, Félix; Seco, José M.; Quiñoá, Emilio; Riguera, Ricardo	**Author of Portion(s)**	Leiras, Seila; Freire, Félix; Seco, José M.; Quiñoá, Emilio; Riguera, Ricardo
Volume / Edition	4	**Issue, if Republishing an Article From a Serial**	7
Page or Page Range of Portion	2735	**Publication Date of Portion**	2013-06-04

USC UNIVERSIDADE DE SANTIAGO DE COMPOSTELA

Figure 12:

License Details

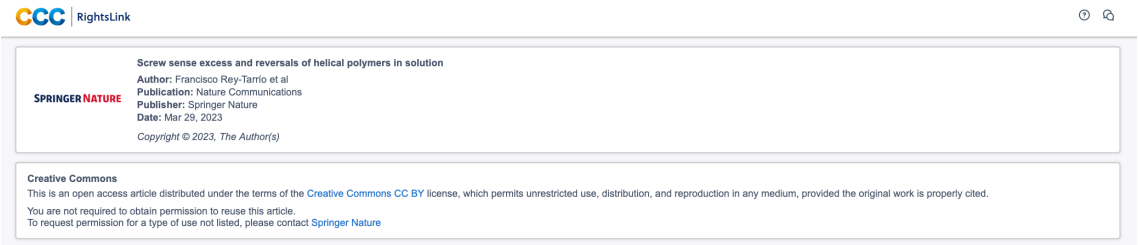
This Agreement between Manuel Fernández Míguez, Universidade de Santiago de Compostela (USC) ("You") and John Wiley and Sons ("John Wiley and Sons") consists of your license details and the terms and conditions provided by John Wiley and Sons and Copyright Clearance Center.

Print Copy

License Number	6032981394769
License date	May 20, 2025
Licensed Content Publisher	John Wiley and Sons
Licensed Content Publication	Angewandte Chemie International Edition
Licensed Content Title	Photochemical Electrocyclization of Poly(phenylacetylene)s: Unwinding Helices to Elucidate their 3D Structure in Solution
Licensed Content Author	Francisco Rey-Tarrío, Rafael Rodríguez, Emilio Quiñoá, et al
Licensed Content Date	Feb 19, 2021
Licensed Content Volume	60
Licensed Content Issue	15
Licensed Content Pages	9
Type of Use	Dissertation/Thesis
Requestor type	University/Academic
Format	Print and electronic
Portion	Figure/table
Number of figures/tables	1
Will you be translating?	No
Title of new work	Dynamic Helical Polymers: Exploring the Complexity of Responses to Stimuli
Institution name	Universidad de Santiago de Compostela (USC)
Expected presentation date	Oct 2025
Portions	Figure 8
The Requesting Person / Organization to Appear on the License	Manuel Fernández Míguez, Universidade de Santiago de Compostela (USC)
Requestor Location	Mr. Manuel Fernández Míguez c/ Jenaro de la Fuente s/n Santiago De Compostela, 15782 Spain
Publisher Tax ID	EU826007151
Total	**0.00 EUR**

USC UNIVERSIDADE DE SANTIAGO DE COMPOSTELA

Figure 13:



CCC | RightsLink

SPRINGER NATURE

Screw sense excess and reversals of helical polymers in solution

Author: Francisco Rey-Tarrío et al
Publication: Nature Communications
Publisher: Springer Nature
Date: Mar 29, 2023

Copyright © 2023, The Author(s)

Creative Commons

This is an open access article distributed under the terms of the Creative Commons CC BY license, which permits unrestricted use, distribution, and reproduction in any medium, provided the original work is properly cited.

You are not required to obtain permission to reuse this article.
To request permission for a type of use not listed, please contact Springer Nature



CC BY 4.0

Attribution 4.0 International

Deed

Canonical URL : https://creativecommons.org/licenses/by/4.0/

See the legal code

You are free to:

Share — copy and redistribute the material in any medium or format for any purpose, even commercially.

Adapt — remix, transform, and build upon the material for any purpose, even commercially.

The licensor cannot revoke these freedoms as long as you follow the license terms.

Under the following terms:

Attribution — You must give appropriate credit , provide a link to the license, and indicate if changes were made . You may do so in any reasonable manner, but not in any way that suggests the licensor endorses you or your use.

No additional restrictions — You may not apply legal terms or technological measures that legally restrict others from doing anything the license permits.

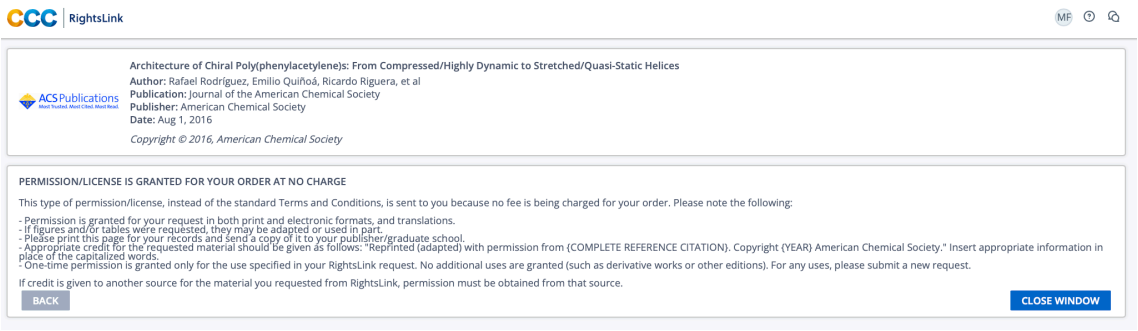
Notices:

You do not have to comply with the license for elements of the material in the public domain or where your use is permitted by an applicable exception or limitation .

No warranties are given. The license may not give you all of the permissions necessary for your intended use. For example, other rights such as publicity, privacy, or moral rights may limit how you use the material.

USC UNIVERSIDADE DE SANTIAGO DE COMPOSTELA

Figure *14*b:



CCC | RightsLink

Architecture of Chiral Poly(phenylacetylene)s: From Compressed/Highly Dynamic to Stretched/Quasi-Static Helices

Author: Rafael Rodríguez, Emilio Quiñoá, Ricardo Riguera, et al
Publication: Journal of the American Chemical Society
Publisher: American Chemical Society
Date: Aug 1, 2016

Copyright © 2016, American Chemical Society

PERMISSION/LICENSE IS GRANTED FOR YOUR ORDER AT NO CHARGE

This type of permission/license, instead of the standard Terms and Conditions, is sent to you because no fee is being charged for your order. Please note the following:

- Permission is granted for your request in both print and electronic formats, and translations.
- If figures and/or tables were requested, they may be adapted or used in part.
- Please print this page for your records and send a copy of it to your publisher/graduate school.
- Appropriate credit for the requested material should be given as follows: "Reprinted (adapted) with permission from {COMPLETE REFERENCE CITATION). Copyright {YEAR} American Chemical Society." Insert appropriate information in place of the capitalized words.
- One-time permission is granted only for the use specified in your RightsLink request. No additional uses are granted (such as derivative works or other editions). For any uses, please submit a new request.

If credit is given to another source for the material you requested from RightsLink, permission must be obtained from that source.

BACK CLOSE WINDOW

Figure 15:



CCC Marketplace

This is a License Agreement between Manuel Fernández Míguez, Universidade de Santiago de Compostela (USC) ("User") and Copyright Clearance Center, Inc. ("CCC") on behalf of the Rightsholder identified in the order details below. The license consists of the order details, the Marketplace Permissions General Terms and Conditions below, and any Rightsholder Terms and Conditions which are included below.

All payments must be made in full to CCC in accordance with the Marketplace Permissions General Terms and Conditions below.

Order Date	20-May-2025	Type of Use	Republish in a thesis/dissertation
Order License ID	1611637-1	Publisher	Springer International Publishing
ISBN-13	9783030885922	Portion	Chart/graph/table/figure

LICENSED CONTENT

Publication Title	Spacecraft Operations	Rightsholder	Springer Nature BV
Article Title	Telemetry, Commanding and Ranging System. Chapter 18	Publication Type	Book
		Start Page	357
Date	06/16/2023	End Page	375
Language	English		
Country	Switzerland		

REQUEST DETAILS

Portion Type	Chart/graph/table/figure	Distribution	Worldwide
Number of Charts / Graphs / Tables / Figures Requested	1	Translation	Original language of publication
Format (select all that apply)	Print, Electronic	Copies for the Disabled?	No
Who Will Republish the Content?	Academic institution	Minor Editing Privileges?	No
		Incidental Promotional Use?	No
Duration of Use	Life of current edition	Currency	EUR
Lifetime Unit Quantity	Up to 499		
Rights Requested	Main product		

NEW WORK DETAILS

Title	Dynamic Helical Polymers: Exploring the Complexity of Responses to Stimuli	Institution Name	Universidade de Santiago de Compostela (USC)
		Expected Presentation Date	2025-10-30
Instructor Name	Manuel Fernández Míguez		

ADDITIONAL DETAILS

The Requesting Person / Organization to Appear on the License	Manuel Fernández Míguez, Universidade de Santiago de Compostela (USC)

REQUESTED CONTENT DETAILS

Title, Description or Numeric Reference of the Portion(s)	Figure 18.1	Title of the Article / Chapter the Portion Is From	Telemetry, Commanding and Ranging System. Chapter 18
Editor of Portion(s)	Schmidhuber, Michael; Lopez-Delgado, Tarsicio	Author of Portion(s)	Schmidhuber, Michael; Lopez-Delgado, Tarsicio
Volume / Edition	Second Edition 2022	Publication Date of Portion	2022-06-15
Page or Page Range of Portion	357-375		

USC UNIVERSIDADE DE SANTIAGO DE COMPOSTELA

Figure 17a:



This is a License Agreement between Manuel Fernández Míguez, Universidade de Santiago de Compostela (USC) ("User") and Copyright Clearance Center, Inc. ("CCC") on behalf of the Rightsholder identified in the order details below. The license consists of the order details, the Marketplace Permissions General Terms and Conditions below, and any Rightsholder Terms and Conditions which are included below.
All payments must be made in full to CCC in accordance with the Marketplace Permissions General Terms and Conditions below.

Order Date	20-May-2025	**Type of Use**	Republish in a thesis/dissertation
Order License ID	1611623-1		
ISSN	1474-9092	**Publisher**	ROYAL SOCIETY OF CHEMISTRY
		Portion	Chart/graph/table/figure

LICENSED CONTENT

Publication Title	Photochemical & photobiological sciences	**Publication Type**	e-Journal
Article Title	Recent advances in studies on the magneto-chiral dichroism of organic compounds.	**Start Page**	8
		End Page	19
		Issue	1
Author / Editor	European Photochemistry Association., European Society for Photobiology., Asia and Oceania Society for Photobiology., Korean Society of Photoscience.	**Volume**	19
		URL	http://xlink.rsc.org/jumptojou...
Date	01/01/2002		
Language	English		
Country	United Kingdom of Great Britain and Northern Ireland		
Rightsholder	Springer Nature BV		

REQUEST DETAILS

Portion Type	Chart/graph/table/figure	**Distribution**	Worldwide
Number of Charts / Graphs / Tables / Figures Requested	1	**Translation**	Original language of publication
Format (select all that apply)	Print, Electronic	**Copies for the Disabled?**	No
Who Will Republish the Content?	Academic institution	**Minor Editing Privileges?**	No
		Incidental Promotional Use?	No
Duration of Use	Life of current edition	**Currency**	EUR
Lifetime Unit Quantity	Up to 499		
Rights Requested	Main product		

NEW WORK DETAILS

Title	Dynamic Helical Polymers: Exploring the Complexity of Responses to Stimuli	**Institution Name**	Universidade de Santiago de Compostela (USC)
		Expected Presentation Date	2025-10-30
Instructor Name	Manuel Fernández Míguez		

ADDITIONAL DETAILS

The Requesting Person / Organization to Appear on the License	Manuel Fernández Míguez, Universidade de Santiago de Compostela (USC)

REQUESTED CONTENT DETAILS

Title, Description or Numeric Reference of the Portion(s)	Figure 7	**Title of the Article / Chapter the Portion Is From**	Recent advances in studies on the magneto-chiral dichroism of organic compounds.
Editor of Portion(s)	Ishii, Kazuyuki; Hattori, Shingo; Kitagawa, Yuichi	**Author of Portion(s)**	Ishii, Kazuyuki; Hattori, Shingo; Kitagawa, Yuichi
Volume / Edition	19		
Page or Page Range of Portion	8-19	**Publication Date of Portion**	2020-10-27

USC UNIVERSIDADE DE SANTIAGO DE COMPOSTELA

Figure 17b:

License Details

This Agreement between Manuel Fernández Míguez, Universidade de Santiago de Compostela (USC) ("You") and Springer Nature ("Springer Nature") consists of your license details and the terms and conditions provided by Springer Nature and Copyright Clearance Center.

Print Copy

License Number	6033010643186
License date	May 20, 2025
Licensed Content Publisher	Springer Nature
Licensed Content Publication	Analytical and Bioanalytical Chemistry
Licensed Content Title	Measuring the optical chirality of molecular aggregates at liquid–liquid interfaces
Licensed Content Author	Hitoshi Watarai et al
Licensed Content Date	Aug 29, 2009
Type of Use	Thesis/Dissertation
Requestor Type	academic/university or research institute
Format	print and electronic
Portion	figures/tables/illustrations
Number of figures/tables/illustrations	1
Will you be translating?	no
Circulation/distribution	1 - 29
Author of this Springer Nature content	no
Title of new work	Dynamic Helical Polymers: Exploring the Complexity of Responses to Stimuli
Institution name	Universidad de Santiago de Compostela (USC)
Expected presentation date	Oct 2025
Portions	scheme 1
The Requesting Person / Organization to Appear on the License	Manuel Fernández Míguez, Universidade de Santiago de Compostela (USC)
Requestor Location	Mr. Manuel Fernández Míguez c/ Jenaro de la Fuente s/n Santiago De Compostela, 15782 Spain
Billing Type	Invoice
Billing address	Universidade de Santiago de Compostela c/ Jenaro de la Fuente s/n Santiago De Compostela, Spain 15782
Total	**0.00 EUR**

USC UNIVERSIDADE DE SANTIAGO DE COMPOSTELA

Figure 17c:

CCC Marketplace

This is a License Agreement between Manuel Fernández Míguez, Universidade de Santiago de Compostela (USC) ("User") and Copyright Clearance Center, Inc. ("CCC") on behalf of the Rightsholder identified in the order details below. The license consists of the order details, the Marketplace Permissions General Terms and Conditions below, and any Rightsholder Terms and Conditions which are included below.
All payments must be made in full to CCC in accordance with the Marketplace Permissions General Terms and Conditions below.

Order Date	20-May-2025	**Type of Use**	Republish in a thesis/dissertation
Order License ID	1611642-1	**Publisher**	ROYAL SOCIETY OF CHEMISTRY, ETC.]
ISSN	0306-0012	**Portion**	Chart/graph/table/figure

LICENSED CONTENT

Publication Title	Chemical Society reviews	**Rightsholder**	Royal Society of Chemistry
Article Title	Application of electronic circular dichroism in configurational and conformational analysis of organic compounds.	**Publication Type**	Journal
		Start Page	914
		Issue	6
		Volume	36
Author / Editor	CHEMICAL SOCIETY (GREAT BRITAIN)		
Date	01/01/1972		
Language	English		
Country	United Kingdom of Great Britain and Northern Ireland		

REQUEST DETAILS

Portion Type	Chart/graph/table/figure	**Distribution**	Worldwide
Number of Charts / Graphs / Tables / Figures Requested	1	**Translation**	Original language of publication
Format (select all that apply)	Print, Electronic	**Copies for the Disabled?**	No
Who Will Republish the Content?	Academic institution	**Minor Editing Privileges?**	No
		Incidental Promotional Use?	No
Duration of Use	Life of current edition	**Currency**	EUR
Lifetime Unit Quantity	Up to 499		
Rights Requested	Main product		

NEW WORK DETAILS

Title	Dynamic Helical Polymers: Exploring the Complexity of Responses to Stimuli	**Institution Name**	Universidade de Santiago de Compostela (USC)
		Expected Presentation Date	2025-10-30
Instructor Name	Manuel Fernández Míguez		

ADDITIONAL DETAILS

Order Reference Number	N/A	**The Requesting Person / Organization to Appear on the License**	Manuel Fernández Míguez, Universidade de Santiago de Compostela (USC)

REQUESTED CONTENT DETAILS

Title, Description or Numeric Reference of the Portion(s)	Figure 6	**Title of the Article / Chapter the Portion Is From**	Application of electronic circular dichroism in configurational and conformational analysis of organic compounds.
Editor of Portion(s)	Berova, Nina; Bari, Lorenzo Di; Pescitelli, Gennaro	**Author of Portion(s)**	Berova, Nina; Bari, Lorenzo Di; Pescitelli, Gennaro
Volume / Edition	36	**Issue, if Republishing an Article From a Serial**	6
Page or Page Range of Portion	914	**Publication Date of Portion**	2007-06-01

USC UNIVERSIDADE DE SANTIAGO DE COMPOSTELA

Figure 17d:

CCC Marketplace

This is a License Agreement between Manuel Fernández Míguez, Universidade de Santiago de Compostela (USC) ("User") and Copyright Clearance Center, Inc. ("CCC") on behalf of the Rightsholder identified in the order details below. The license consists of the order details, the Marketplace Permissions General Terms and Conditions below, and any Rightsholder Terms and Conditions which are included below.
All payments must be made in full to CCC in accordance with the Marketplace Permissions General Terms and Conditions below.

Order Date	20-May-2025	**Type of Use**	Republish in a thesis/dissertation
Order License ID	1611639-1		
ISSN	1520-636X	**Publisher**	JOHN WILEY & SONS, INC.
		Portion	Chart/graph/table/figure

LICENSED CONTENT

Publication Title	Chirality	**Publication Type**	e-Journal
Article Title	ECD exciton chirality method today: a modern tool for determining absolute configurations	**Start Page**	333
		End Page	363
		Issue	2
Date	01/01/1989	**Volume**	34
Language	English	**URL**	http://www3.interscience.wil...
Country	United States of America		
Rightsholder	John Wiley & Sons - Books		

REQUEST DETAILS

Portion Type	Chart/graph/table/figure	**Distribution**	Worldwide
Number of Charts / Graphs / Tables / Figures Requested	1	**Translation**	Original language of publication
Format (select all that apply)	Print, Electronic	**Copies for the Disabled?**	No
Who Will Republish the Content?	Academic institution	**Minor Editing Privileges?**	No
		Incidental Promotional Use?	No
Duration of Use	Life of current edition	**Currency**	EUR
Lifetime Unit Quantity	Up to 499		
Rights Requested	Main product		

NEW WORK DETAILS

Title	Dynamic Helical Polymers: Exploring the Complexity of Responses to Stimuli	**Institution Name**	Universidade de Santiago de Compostela (USC)
		Expected Presentation Date	2025-10-30
Instructor Name	Manuel Fernández Míguez		

ADDITIONAL DETAILS

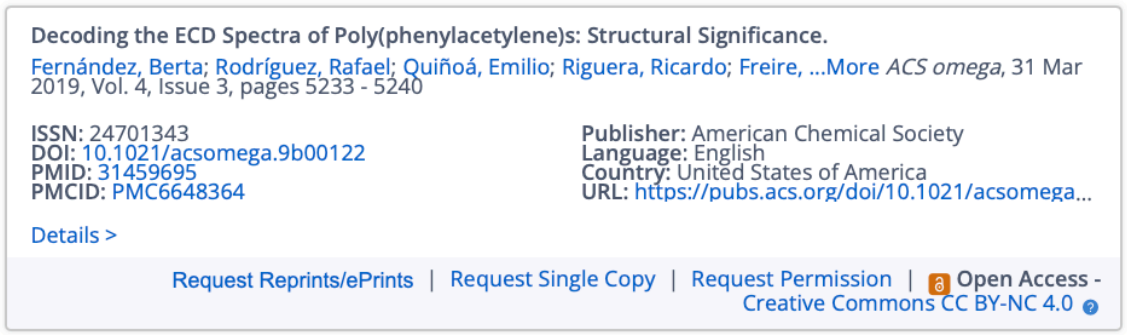
The Requesting Person / Organization to Appear on the License	Manuel Fernández Míguez, Universidade de Santiago de Compostela (USC)		

REQUESTED CONTENT DETAILS

Title, Description or Numeric Reference of the Portion(s)	Figure 1	**Title of the Article / Chapter the Portion Is From**	ECD exciton chirality method today: a modern tool for determining absolute configurations
Editor of Portion(s)	Pescitelli, Gennaro		
Volume / Edition	34	**Author of Portion(s)**	Pescitelli, Gennaro
Page or Page Range of Portion	333-363	**Publication Date of Portion**	2022-02-01

USC UNIVERSIDADE DE SANTIAGO DE COMPOSTELA

Figure 18:



Decoding the ECD Spectra of Poly(phenylacetylene)s: Structural Significance.

Fernández, Berta; Rodríguez, Rafael; Quiñoá, Emilio; Riguera, Ricardo; Freire, ...More *ACS omega*, 31 Mar 2019, Vol. 4, Issue 3, pages 5233 - 5240

ISSN: 24701343
DOI: 10.1021/acsomega.9b00122
PMID: 31459695
PMCID: PMC6648364

Publisher: American Chemical Society
Language: English
Country: United States of America
URL: https://pubs.acs.org/doi/10.1021/acsomega...

Details >

Request Reprints/ePrints | Request Single Copy | Request Permission | Open Access - Creative Commons CC BY-NC 4.0

CC BY-NC 4.0

Attribution-NonCommercial 4.0 International

Deed

Canonical URL : https://creativecommons.org/licenses/by-nc/4.0/

See the legal code

You are free to:

Share — copy and redistribute the material in any medium or format

Adapt — remix, transform, and build upon the material

The licensor cannot revoke these freedoms as long as you follow the license terms.

Under the following terms:

Attribution — You must give appropriate credit , provide a link to the license, and indicate if changes were made . You may do so in any reasonable manner, but not in any way that suggests the licensor endorses you or your use.

NonCommercial — You may not use the material for commercial purposes .

No additional restrictions — You may not apply legal terms or technological measures that legally restrict others from doing anything the license permits.

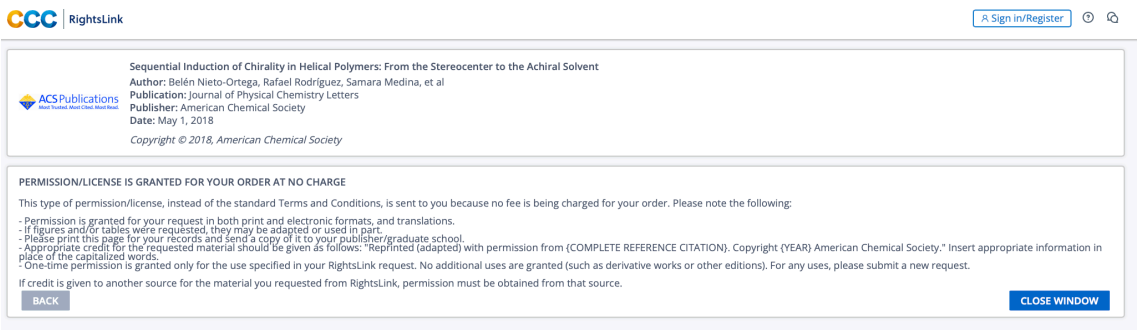
Notices:

You do not have to comply with the license for elements of the material in the public domain or where your use is permitted by an applicable exception or limitation .

No warranties are given. The license may not give you all of the permissions necessary for your intended use. For example, other rights such as publicity, privacy, or moral rights may limit how you use the material.

USC UNIVERSIDADE DE SANTIAGO DE COMPOSTELA

Figure 19:



CCC | RightsLink

Sign in/Register

ACS Publications

Sequential Induction of Chirality in Helical Polymers: From the Stereocenter to the Achiral Solvent

Author: Belén Nieto-Ortega, Rafael Rodríguez, Samara Medina, et al
Publication: Journal of Physical Chemistry Letters
Publisher: American Chemical Society
Date: May 1, 2018

Copyright © 2018, American Chemical Society

PERMISSION/LICENSE IS GRANTED FOR YOUR ORDER AT NO CHARGE

This type of permission/license, instead of the standard Terms and Conditions, is sent to you because no fee is being charged for your order. Please note the following:

- Permission is granted for your request in both print and electronic formats, and translations.
- If figures and/or tables were requested, they may be adapted or used in part.
- Please print this page for your records and send a copy of it to your publisher/graduate school.
- Appropriate credit for the requested material should be given as follows: "Reprinted (adapted) with permission from {COMPLETE REFERENCE CITATION}. Copyright {YEAR} American Chemical Society." Insert appropriate information in place of the capitalized words.
- One-time permission is granted only for the use specified in your RightsLink request. No additional uses are granted (such as derivative works or other editions). For any uses, please submit a new request.

If credit is given to another source for the material you requested from RightsLink, permission must be obtained from that source.

BACK CLOSE WINDOW

Figure 21:



CCC Marketplace

This is a License Agreement between Manuel Fernández Míguez, Universidade de Santiago de Compostela (USC) ("User") and Copyright Clearance Center, Inc. ("CCC") on behalf of the Rightsholder identified in the order details below. The license consists of the order details, the Marketplace Permissions General Terms and Conditions below, and any Rightsholder Terms and Conditions which are included below.

All payments must be made in full to CCC in accordance with the Marketplace Permissions General Terms and Conditions below.

Order Date	20-May-2025	Type of Use	Republish in a thesis/dissertation
Order License ID	1611713-1	Publisher	JOHN/WILEY & SONS, INC.
ISSN	1521-3773	Portion	Chart/graph/table/figure

LICENSED CONTENT

Publication Title	Angewandte Chemie	Publication Type	e-Journal
Article Title	Raman Optical Activity (ROA) as a New Tool to Elucidate the Helical Structure of Poly(phenylacetylene)s.	Start Page	9080
		End Page	9087
		Issue	23
Author / Editor	Gesellschaft Deutscher Chemiker.	Volume	59
		URL	http://www3.interscience.wil...
Date	01/01/1962		
Language	English		
Country	Germany		
Rightsholder	John Wiley & Sons - Books		

REQUEST DETAILS

Portion Type	Chart/graph/table/figure	Distribution	Worldwide
Number of Charts / Graphs / Tables / Figures Requested	1	Translation	Original language of publication
Format (select all that apply)	Print, Electronic	Copies for the Disabled?	No
Who Will Republish the Content?	Academic institution	Minor Editing Privileges?	No
		Incidental Promotional Use?	No
Duration of Use	Life of current edition	Currency	EUR
Lifetime Unit Quantity	Up to 499		
Rights Requested	Main product		

NEW WORK DETAILS

Title	Dynamic Helical Polymers: Exploring the Complexity of Responses to Stimuli	Institution Name	Universidade de Santiago de Compostela (USC)
		Expected Presentation Date	2025-10-30
Instructor Name	Manuel Fernández Míguez		

ADDITIONAL DETAILS

The Requesting Person / Organization to Appear on the License	Manuel Fernández Míguez, Universidade de Santiago de Compostela (USC)

REQUESTED CONTENT DETAILS

Title, Description or Numeric Reference of the Portion(s)	TOC	Title of the Article / Chapter the Portion Is From	Raman Optical Activity (ROA) as a New Tool to Elucidate the Helical Structure of Poly(phenylacetylene)s.
Editor of Portion(s)	Palomo, Luis; Rodríguez, Rafael; Medina, Samara; Quiñoá, Emilio; Casado, Juan; Freire, Félix; Ramirez, Francisco Javier	Author of Portion(s)	Palomo, Luis; Rodríguez, Rafael; Medina, Samara; Quiñoá, Emilio; Casado, Juan; Freire, Félix; Ramirez, Francisco Javier
Volume / Edition	59 / International ed. in English.		
Page or Page Range of Portion	9080-9087	Publication Date of Portion	2020-06-02

USC UNIVERSIDADE DE SANTIAGO DE COMPOSTELA

Figure 22a:



This is a License Agreement between Manuel Fernández Míguez, Universidade de Santiago de Compostela (USC) ("User") and Copyright Clearance Center, Inc. ("CCC") on behalf of the Rightsholder identified in the order details below. The license consists of the order details, the Marketplace Permissions General Terms and Conditions below, and any Rightsholder Terms and Conditions which are included below.

All payments must be made in full to CCC in accordance with the Marketplace Permissions General Terms and Conditions below.

Order Date	20-May-2025	**Type of Use**	Republish in a thesis/dissertation
Order License ID	1611746-1		
ISSN	1521-3773	**Publisher Portion**	JOHN/WILEY & SONS, INC. Chart/graph/table/figure

LICENSED CONTENT

Publication Title	Angewandte Chemie	**Publication Type**	e-Journal
Article Title	A helical array of pendant fullerenes on an optically active polyphenylacetylene.	**Start Page**	3602
		End Page	4, 3515
Author / Editor	Gesellschaft Deutscher Chemiker.	**Issue**	19
		Volume	41
Date	01/01/1962	**URL**	http://www3.interscience.wil...
Language	English		
Country	Germany		
Rightsholder	John Wiley & Sons - Books		

REQUEST DETAILS

Portion Type	Chart/graph/table/figure	**Distribution**	Worldwide
Number of Charts / Graphs / Tables / Figures Requested	1	**Translation**	Original language of publication
Format (select all that apply)	Print, Electronic	**Copies for the Disabled?**	No
Who Will Republish the Content?	Academic institution	**Minor Editing Privileges?**	No
		Incidental Promotional Use?	No
Duration of Use	Life of current edition	**Currency**	EUR
Lifetime Unit Quantity	Up to 499		
Rights Requested	Main product		

NEW WORK DETAILS

Title	Dynamic Helical Polymers: Exploring the Complexity of Responses to Stimuli	**Institution Name**	Universidade de Santiago de Compostela (USC)
		Expected Presentation Date	2025-10-30
Instructor Name	Manuel Fernández Míguez		

ADDITIONAL DETAILS

The Requesting Person / Organization to Appear on the License	Manuel Fernández Míguez, Universidade de Santiago de Compostela (USC)

REQUESTED CONTENT DETAILS

Title, Description or Numeric Reference of the Portion(s)	Figure 3	**Title of the Article / Chapter the Portion Is From**	A helical array of pendant fullerenes on an optically active polyphenylacetylene.
Editor of Portion(s)	Nishimura, Tatsuya; Takatani, Kohei; Sakurai, Shin-ichiro; Maeda, Katsuhiro, Dr.; Yashima, Eiji, Prof. Dr.	**Author of Portion(s)**	Nishimura, Tatsuya; Takatani, Kohei; Sakurai, Shin-ichiro; Maeda, Katsuhiro, Dr.; Yashima, Eiji, Prof. Dr.
Volume / Edition	41 / International ed. in English.	**Publication Date of Portion**	2002-10-04
Page or Page Range of Portion	3602-4, 3515		

USC UNIVERSIDADE DE SANTIAGO DE COMPOSTELA

Figure 22b:

CCC Marketplace

This is a License Agreement between Manuel Fernández Míguez, Universidade de Santiago de Compostela (USC) ("User") and Copyright Clearance Center, Inc. ("CCC") on behalf of the Rightsholder identified in the order details below. The license consists of the order details, the Marketplace Permissions General Terms and Conditions below, and any Rightsholder Terms and Conditions which are included below.
All payments must be made in full to CCC in accordance with the Marketplace Permissions General Terms and Conditions below.

Order Date	20-May-2025	**Type of Use**	Republish in a thesis/dissertation
Order License ID	1611752-1	**Publisher**	ANGEWANDTE CHEMIE
ISSN	1521-3757	**Portion**	Chart/graph/table/figure

LICENSED CONTENT

Publication Title	Angewandte Chemie. Ausgabe A, Wissenschaftlicher Teil	**Rightsholder**	John Wiley & Sons - Books
Article Title	Two-Dimensional Hierarchical Self-Assembly of One-Handed Helical Polymers on Graphite	**Publication Type**	e-Journal
		Start Page	1267
Author / Editor	Gesellschaft Deutscher Chemiker.	**End Page**	1270
		Issue	8
Date	01/01/1949	**Volume**	118
Language	German		
Country	Germany		

REQUEST DETAILS

Portion Type	Chart/graph/table/figure	**Distribution**	Worldwide
Number of Charts / Graphs / Tables / Figures Requested	1	**Translation**	Original language of publication
Format (select all that apply)	Print, Electronic	**Copies for the Disabled?**	No
Who Will Republish the Content?	Academic institution	**Minor Editing Privileges?**	No
		Incidental Promotional Use?	No
Duration of Use	Life of current edition	**Currency**	EUR
Lifetime Unit Quantity	Up to 499		
Rights Requested	Main product		

NEW WORK DETAILS

Title	Dynamic Helical Polymers: Exploring the Complexity of Responses to Stimuli	**Institution Name**	Universidade de Santiago de Compostela (USC)
		Expected Presentation Date	2025-10-30
Instructor Name	Manuel Fernández Míguez		

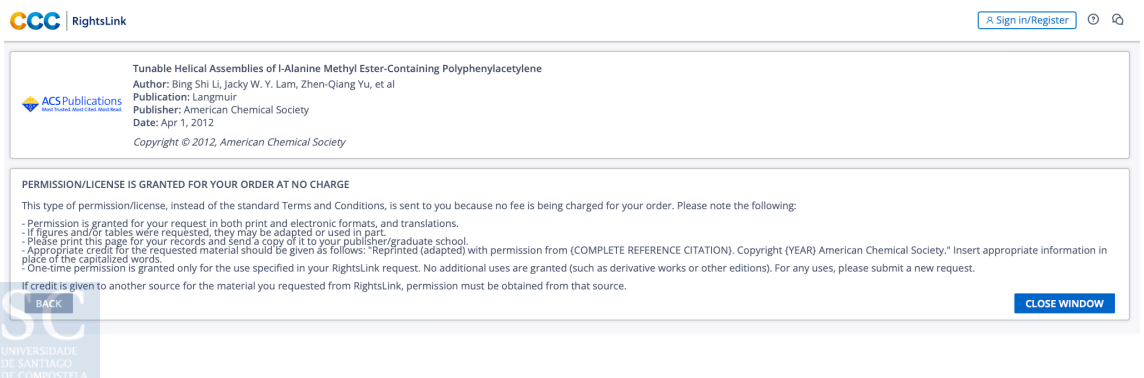
ADDITIONAL DETAILS

The Requesting Person / Organization to Appear on the License	Manuel Fernández Míguez, Universidade de Santiago de Compostela (USC)

REQUESTED CONTENT DETAILS

Title, Description or Numeric Reference of the Portion(s)	TOC	**Title of the Article / Chapter the Portion Is From**	Two-Dimensional Hierarchical Self-Assembly of One-Handed Helical Polymers on Graphite
Editor of Portion(s)	Sakurai, Shin-ichiro, Dr.; Okoshi, Kento, Dr.; Kumaki, Jiro, Dr.; Yashima, Eiji, Prof.	**Author of Portion(s)**	Sakurai, Shin-ichiro, Dr.; Okoshi, Kento, Dr.; Kumaki, Jiro, Dr.; Yashima, Eiji, Prof.
Volume / Edition	118		
Page or Page Range of Portion	1267-1270	**Publication Date of Portion**	2006-02-13

Figure 22c:



USC UNIVERSIDADE DE SANTIAGO DE COMPOSTELA

Figure 22d:

CCC Marketplace

This is a License Agreement between Manuel Fernández Míguez, Universidade de Santiago de Compostela (USC) ("User") and Copyright Clearance Center, Inc. ("CCC") on behalf of the Rightsholder identified in the order details below. The license consists of the order details, the Marketplace Permissions General Terms and Conditions below, and any Rightsholder Terms and Conditions which are included below.
All payments must be made in full to CCC in accordance with the Marketplace Permissions General Terms and Conditions below.

Order Date	20-May-2025	Type of Use	Republish in a thesis/dissertation
Order License ID	1611758-1		
ISSN	2040-3372	Publisher	RSC Pub
		Portion	Chart/graph/table/figure

LICENSED CONTENT

Publication Title	Nanoscale	Publication Type	e-Journal
Article Title	Helical sense selective domains and enantiomeric superhelices generated by Langmuir-Schaefer deposition of an axially racemic chiral helical polymer.	Start Page	3362
		End Page	3367
		Issue	6
		Volume	8
Author / Editor	Royal Society of Chemistry (Great Britain), National Center for Nanoscience and Technology.	URL	http://www.rsc.org/Publishin...
Date	01/01/2009		
Language	English		
Country	United Kingdom of Great Britain and Northern Ireland		
Rightsholder	Royal Society of Chemistry		

REQUEST DETAILS

Portion Type	Chart/graph/table/figure	Distribution	Worldwide
Number of Charts / Graphs / Tables / Figures Requested	1	Translation	Original language of publication
Format (select all that apply)	Print, Electronic	Copies for the Disabled?	No
Who Will Republish the Content?	Academic institution	Minor Editing Privileges?	No
		Incidental Promotional Use?	No
Duration of Use	Life of current edition	Currency	EUR
Lifetime Unit Quantity	Up to 499		
Rights Requested	Main product		

NEW WORK DETAILS

Title	Dynamic Helical Polymers: Exploring the Complexity of Responses to Stimuli	Institution Name	Universidade de Santiago de Compostela (USC)
		Expected Presentation Date	2025-10-30
Instructor Name	Manuel Fernández Míguez		

ADDITIONAL DETAILS

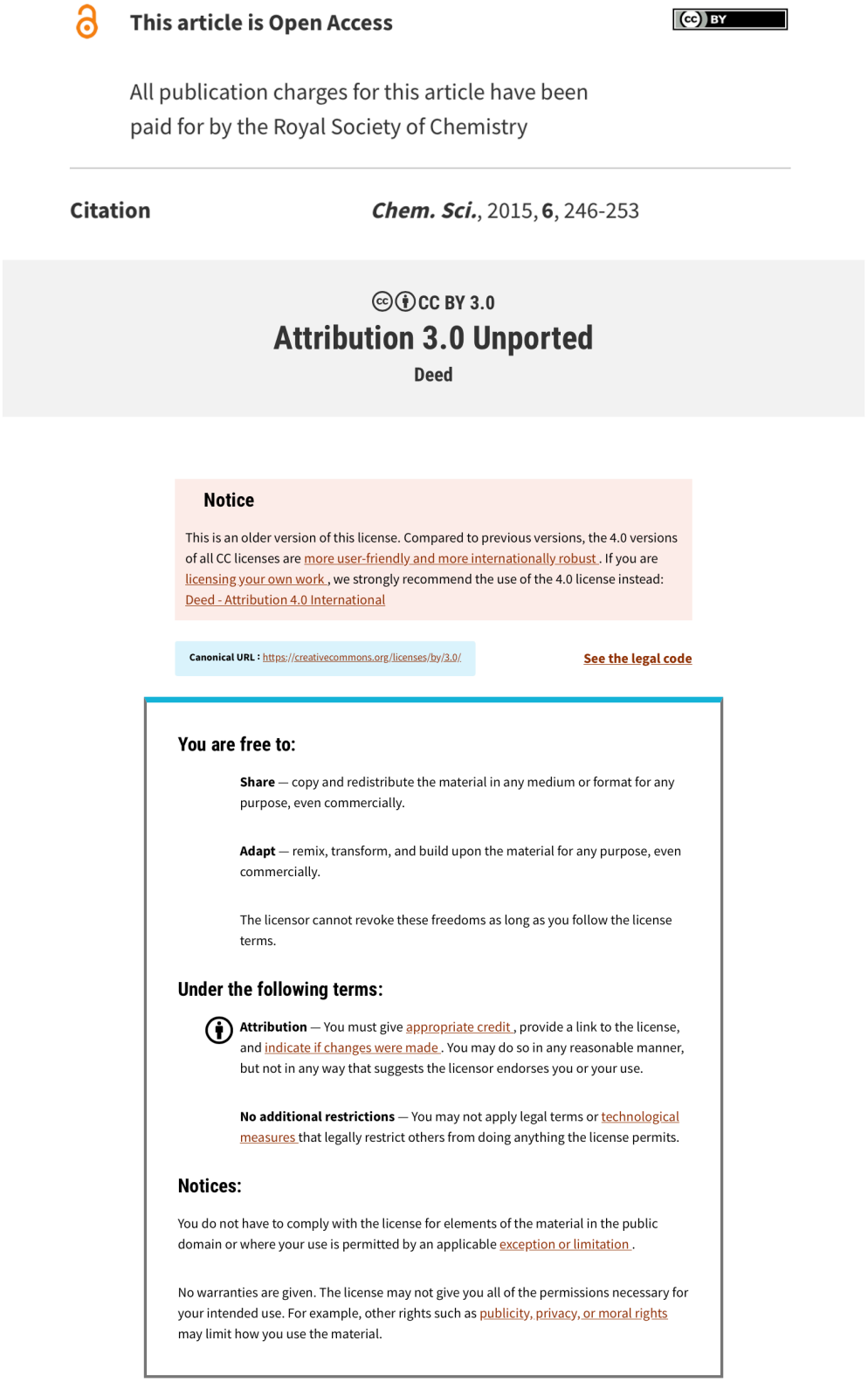
Order Reference Number	N/A	The Requesting Person / Organization to Appear on the License	Manuel Fernández Míguez, Universidade de Santiago de Compostela (USC)

REQUESTED CONTENT DETAILS

Title, Description or Numeric Reference of the Portion(s)	Figure 3	Title of the Article / Chapter the Portion Is From	Helical sense selective domains and enantiomeric superhelices generated by Langmuir-Schaefer deposition of an axially racemic chiral helical polymer.
Editor of Portion(s)	Rodríguez, R.; Ignés-Mullol, J.; Sagués, F.; Quiñoá, E.; Riguera, R.; Freire, F.		
		Author of Portion(s)	Rodríguez, R.; Ignés-Mullol, J.; Sagués, F.; Quiñoá, E.; Riguera, R.; Freire, F.
Volume / Edition	8		
Page or Page Range of Portion	3362-3367	Issue, if Republishing an Article From a Serial	6
		Publication Date of Portion	2016-02-14

USC UNIVERSIDADE DE SANTIAGO DE COMPOSTELA

Figure 23:



This article is Open Access

All publication charges for this article have been paid for by the Royal Society of Chemistry

Citation *Chem. Sci.*, 2015, **6**, 246-253

CC BY 3.0

Attribution 3.0 Unported

Deed

Notice

This is an older version of this license. Compared to previous versions, the 4.0 versions of all CC licenses are more user-friendly and more internationally robust. If you are licensing your own work, we strongly recommend the use of the 4.0 license instead: Deed - Attribution 4.0 International

Canonical URL: https://creativecommons.org/licenses/by/3.0/

See the legal code

You are free to:

Share — copy and redistribute the material in any medium or format for any purpose, even commercially.

Adapt — remix, transform, and build upon the material for any purpose, even commercially.

The licensor cannot revoke these freedoms as long as you follow the license terms.

Under the following terms:

Attribution — You must give appropriate credit, provide a link to the license, and indicate if changes were made. You may do so in any reasonable manner, but not in any way that suggests the licensor endorses you or your use.

No additional restrictions — You may not apply legal terms or technological measures that legally restrict others from doing anything the license permits.

Notices:

You do not have to comply with the license for elements of the material in the public domain or where your use is permitted by an applicable exception or limitation.

No warranties are given. The license may not give you all of the permissions necessary for your intended use. For example, other rights such as publicity, privacy, or moral rights may limit how you use the material.

USC UNIVERSIDADE DE SANTIAGO DE COMPOSTELA

Figure 24:

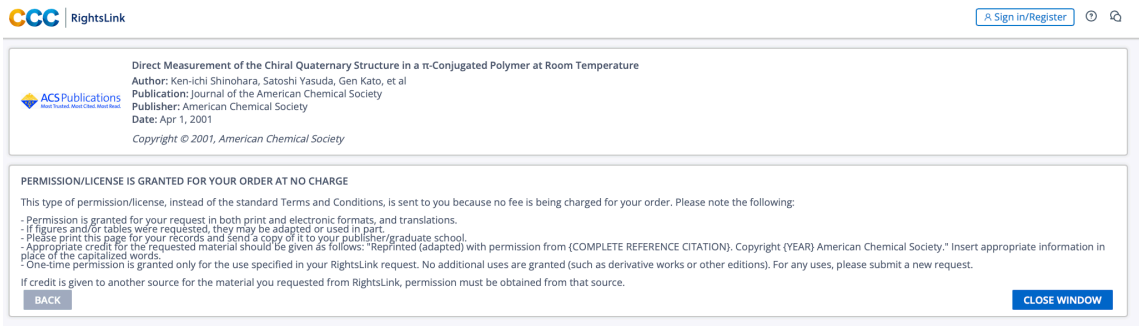
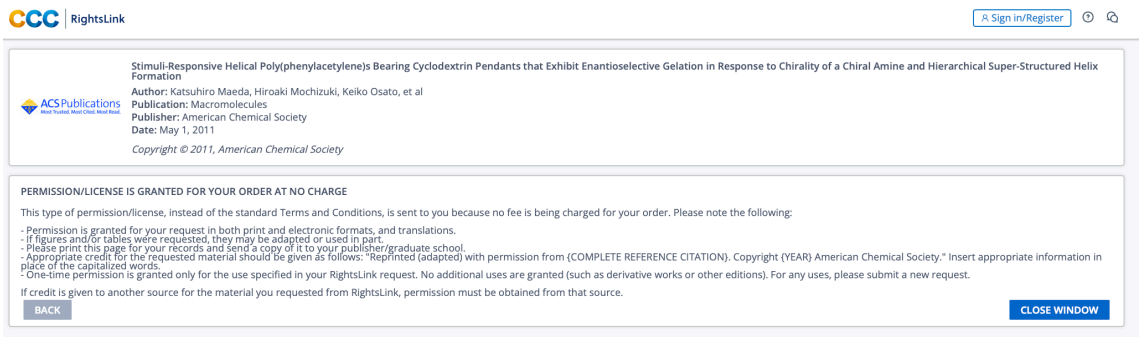


Figure 25:



USC UNIVERSIDADE DE SANTIAGO DE COMPOSTELA

Figure 26:

CCC Marketplace

This is a License Agreement between Manuel Fernández Míguez, Universidade de Santiago de Compostela (USC) ("User") and Copyright Clearance Center, Inc. ("CCC") on behalf of the Rightsholder identified in the order details below. The license consists of the order details, the Marketplace Permissions General Terms and Conditions below, and any Rightsholder Terms and Conditions which are included below.
All payments must be made in full to CCC in accordance with the Marketplace Permissions General Terms and Conditions below.

Order Date	20-May-2025	Type of Use	Republish in a thesis/dissertation
Order License ID	1611768-1		
ISSN	1364-548X	Publisher	ROYAL SOCIETY OF CHEMISTRY
		Portion	Chart/graph/table/figure

LICENSED CONTENT

Publication Title	Chemical communications	Rightsholder	Royal Society of Chemistry
Article Title	Layer-by-layer assembly of charged poly(phenylacetylene)s with induced macromolecular helicity.	Publication Type	e-Journal
		Start Page	4152
		Issue	33
		Volume	0
Author / Editor	Royal Society of Chemistry (Great Britain)		
Date	01/01/1996		
Language	English		
Country	United Kingdom of Great Britain and Northern Ireland		

REQUEST DETAILS

Portion Type	Chart/graph/table/figure	Distribution	Worldwide
Number of Charts / Graphs / Tables / Figures Requested	1	Translation	Original language of publication
Format (select all that apply)	Print, Electronic	Copies for the Disabled?	No
Who Will Republish the Content?	Academic institution	Minor Editing Privileges?	No
		Incidental Promotional Use?	No
Duration of Use	Life of current edition	Currency	EUR
Lifetime Unit Quantity	Up to 499		
Rights Requested	Main product		

NEW WORK DETAILS

Title	Dynamic Helical Polymers: Exploring the Complexity of Responses to Stimuli	Institution Name	Universidade de Santiago de Compostela (USC)
		Expected Presentation Date	2025-10-30
Instructor Name	Manuel Fernández Míguez		

ADDITIONAL DETAILS

Order Reference Number	N/A	The Requesting Person / Organization to Appear on the License	Manuel Fernández Míguez, Universidade de Santiago de Compostela (USC)

REQUESTED CONTENT DETAILS

Title, Description or Numeric Reference of the Portion(s)	Figure 1	Title of the Article / Chapter the Portion Is From	Layer-by-layer assembly of charged poly(phenylacetylene)s with induced macromolecular helicity.
Editor of Portion(s)	Maeda, Katsuhiro; Matsushita, Yasuaki; Ezaka, Muneyoshi; Yashima, Eiji	Author of Portion(s)	Maeda, Katsuhiro; Matsushita, Yasuaki; Ezaka, Muneyoshi; Yashima, Eiji
Volume / Edition	0		
Page or Page Range of Portion	4152	Issue, if Republishing an Article From a Serial	33
		Publication Date of Portion	2005-09-07

USC UNIVERSIDADE DE SANTIAGO DE COMPOSTELA

Figure 27:

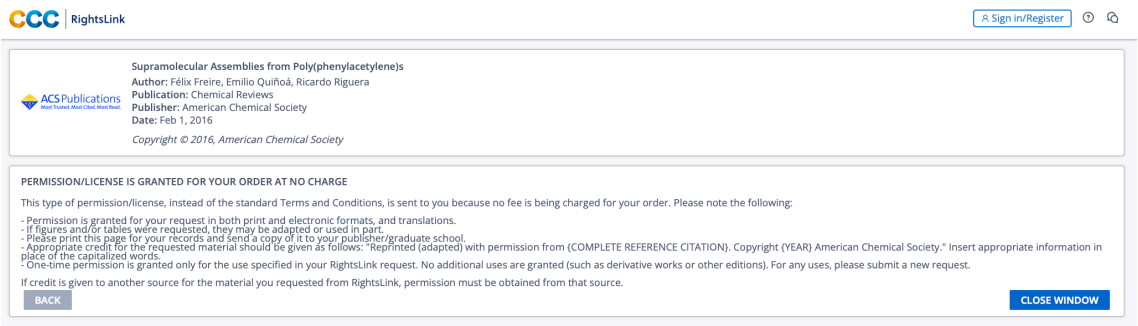


Figure 28:

CCC Marketplace

This is a License Agreement between Manuel Fernández Míguez, Universidade de Santiago de Compostela (USC) ("User") and Copyright Clearance Center, Inc. ("CCC") on behalf of the Rightsholder identified in the order details below. The license consists of the order details, the Marketplace Permissions General Terms and Conditions below, and any Rightsholder Terms and Conditions which are included below.
All payments must be made in full to CCC in accordance with the Marketplace Permissions General Terms and Conditions below.

Order Date	20-May-2025	**Type of Use**	Republish in a thesis/dissertation
Order License ID	1611772-1		
ISSN	0032-3861	**Publisher**	ELSEVIER LTD.
		Portion	Chart/graph/table/figure

LICENSED CONTENT

Publication Title	Polymer	**Publication Type**	Journal
Article Title	Helix-sense-selective polymerization of achiral substituted acetylene in chiral micelles for preparing optically active polymer nanoparticles: Effects of chiral emulsifiers	**Start Page**	840
		End Page	847
		Issue	3
		Volume	55
Date	01/01/1992		
Language	English		
Country	United Kingdom of Great Britain and Northern Ireland		
Rightsholder	Elsevier Science & Technology Journals		

REQUEST DETAILS

Portion Type	Chart/graph/table/figure	**Distribution**	Worldwide
Number of Charts / Graphs / Tables / Figures Requested	1	**Translation**	Original language of publication
Format (select all that apply)	Print, Electronic	**Copies for the Disabled?**	No
Who Will Republish the Content?	Author of requested content	**Minor Editing Privileges?**	No
		Incidental Promotional Use?	No
Duration of Use	Life of current edition	**Currency**	EUR
Lifetime Unit Quantity	Up to 499		
Rights Requested	Main product		

NEW WORK DETAILS

Title	Dynamic Helical Polymers: Exploring the Complexity of Responses to Stimuli	**Institution Name**	Universidade de Santiago de Compostela (USC)
		Expected Presentation Date	2025-10-30
Instructor Name	Manuel Fernández Míguez		

ADDITIONAL DETAILS

Order Reference Number	N/A	**The Requesting Person / Organization to Appear on the License**	Manuel Fernández Míguez, Universidade de Santiago de Compostela (USC)

REQUESTED CONTENT DETAILS

Title, Description or Numeric Reference of the Portion(s)	Scheme 1	**Title of the Article / Chapter the Portion Is From**	Helix-sense-selective polymerization of achiral substituted acetylene in chiral micelles for preparing optically active polymer nanoparticles: Effects of chiral emulsifiers
Editor of Portion(s)	Liu, Dong; Li, Yan; Deng, Jianping; Yang, Wantai		
Volume / Edition	55		
Page or Page Range of Portion	840-847	**Author of Portion(s)**	Liu, Dong; Li, Yan; Deng, Jianping; Yang, Wantai
		Issue, if Republishing an Article From a Serial	3
		Publication Date of Portion	2014-02-12

USC UNIVERSIDADE DE SANTIAGO DE COMPOSTELA

Figure 29:

Angewandte International Edition Chemie | GDCh A Journal of the German Chemical Society

Research Article | Open Access

Size Control of Chiral Nanospheres Obtained via Nanoprecipitation of Helical Poly(phenylacetylene)s in the Absence of Surfactants

Dr. Manuel Núñez-Martínez, Manuel Fernández-Míguez, Prof. Emilio Quiñoá, Prof. Félix Freire

First published: 14 May 2024 | https://doi.org/10.1002/anie.202403313 | Citations: 7

CC BY-NC 4.0

Attribution-NonCommercial 4.0 International

Deed

Canonical URL : https://creativecommons.org/licenses/by-nc/4.0/

See the legal code

You are free to:

Share — copy and redistribute the material in any medium or format

Adapt — remix, transform, and build upon the material

The licensor cannot revoke these freedoms as long as you follow the license terms.

Under the following terms:

Attribution — You must give appropriate credit , provide a link to the license, and indicate if changes were made . You may do so in any reasonable manner, but not in any way that suggests the licensor endorses you or your use.

NonCommercial — You may not use the material for commercial purposes .

No additional restrictions — You may not apply legal terms or technological measures that legally restrict others from doing anything the license permits.

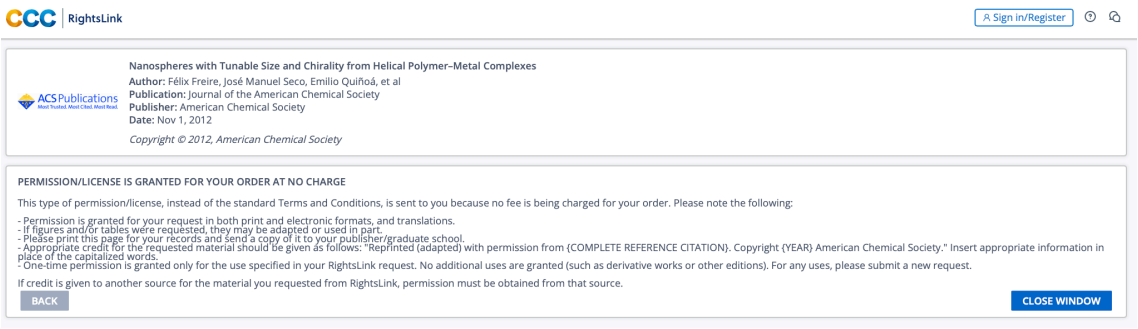
Notices:

You do not have to comply with the license for elements of the material in the public domain or where your use is permitted by an applicable exception or limitation .

No warranties are given. The license may not give you all of the permissions necessary for your intended use. For example, other rights such as publicity, privacy, or moral rights may limit how you use the material.

USC UNIVERSIDADE DE SANTIAGO DE COMPOSTELA

Figure 30 left:



CCC | RightsLink

Sign in/Register

Nanospheres with Tunable Size and Chirality from Helical Polymer–Metal Complexes
Author: Félix Freire, José Manuel Seco, Emilio Quiñoá, et al
Publication: Journal of the American Chemical Society
Publisher: American Chemical Society
Date: Nov 1, 2012

Copyright © 2012, American Chemical Society

PERMISSION/LICENSE IS GRANTED FOR YOUR ORDER AT NO CHARGE

This type of permission/license, instead of the standard Terms and Conditions, is sent to you because no fee is being charged for your order. Please note the following:

- Permission is granted for your request in both print and electronic formats, and translations.
- If figures and/or tables were requested, they may be adapted or used in part.
- Please print this page for your records and send a copy of it to your publisher/graduate school.
- Appropriate credit for the requested material should be given as follows: "Reprinted (adapted) with permission from {COMPLETE REFERENCE CITATION}. Copyright {YEAR} American Chemical Society." Insert appropriate information in place of the capitalized words.
- One-time permission is granted only for the use specified in your RightsLink request. No additional uses are granted (such as derivative works or other editions). For any uses, please submit a new request.

If credit is given to another source for the material you requested from RightsLink, permission must be obtained from that source.

BACK CLOSE WINDOW

Figure 30 right:



CCC Marketplace

This is a License Agreement between Manuel Fernández Míguez, Universidade de Santiago de Compostela (USC) ("User") and Copyright Clearance Center, Inc. ("CCC") on behalf of the Rightsholder identified in the order details below. The license consists of the order details, the Marketplace Permissions General Terms and Conditions below, and any Rightsholder Terms and Conditions which are included below.
All payments must be made in full to CCC in accordance with the Marketplace Permissions General Terms and Conditions below.

Order Date	20-May-2025	Type of Use	Republish in a thesis/dissertation
Order License ID	1611777-1		
ISSN	1521-3773	Publisher	JOHN/WILEY & SONS, INC.
		Portion	Chart/graph/table/figure

LICENSED CONTENT

Publication Title	Angewandte Chemie	Publication Type	e-Journal
Article Title	Nanospheres, nanotubes, toroids, and gels with controlled macroscopic chirality.	Start Page	13720
		End Page	13724
		Issue	50
Author / Editor	Gesellschaft Deutscher Chemiker.	Volume	53
		URL	http://www3.interscience.wil...
Date	01/01/1962		
Language	English		
Country	Germany		
Rightsholder	John Wiley & Sons - Books		

REQUEST DETAILS

Portion Type	Chart/graph/table/figure	Distribution	Worldwide
Number of Charts / Graphs / Tables / Figures Requested	1	Translation	Original language of publication
Format (select all that apply)	Print, Electronic	Copies for the Disabled?	No
Who Will Republish the Content?	Academic institution	Minor Editing Privileges?	No
		Incidental Promotional Use?	No
Duration of Use	Life of current edition	Currency	EUR
Lifetime Unit Quantity	Up to 499		
Rights Requested	Main product		

NEW WORK DETAILS

Title	Dynamic Helical Polymers: Exploring the Complexity of Responses to Stimuli	Institution Name	Universidade de Santiago de Compostela (USC)
		Expected Presentation Date	2025-10-30
Instructor Name	Manuel Fernández Míguez		

ADDITIONAL DETAILS

The Requesting Person / Organization to Appear on the License	Manuel Fernández Míguez, Universidade de Santiago de Compostela (USC)

REQUESTED CONTENT DETAILS

Title, Description or Numeric Reference of the Portion(s)	TOC	Title of the Article / Chapter the Portion Is From	Nanospheres, nanotubes, toroids, and gels with controlled macroscopic chirality.
Editor of Portion(s)	Arias, Sandra; Dr., Freire, Félix; Prof. Dr., Quiñoá, Emilio; Prof. Dr., Riguera, Ricardo	Author of Portion(s)	Arias, Sandra; Dr., Freire, Félix; Prof. Dr., Quiñoá, Emilio; Prof. Dr., Riguera, Ricardo
Volume / Edition	53 / International ed. in English.		
Page or Page Range of Portion	13720-13724	Publication Date of Portion	2014-12-08

USC UNIVERSIDADE DE SANTIAGO DE COMPOSTELA

Figure 31:

License Details

This Agreement between Manuel Fernández Míguez, Universidade de Santiago de Compostela (USC) ("You") and Springer Nature ("Springer Nature") consists of your license details and the terms and conditions provided by Springer Nature and Copyright Clearance Center.

Print Copy

License Number	6033120026729
License date	May 20, 2025
Licensed Content Publisher	Springer Nature
Licensed Content Publication	Plasmonics
Licensed Content Title	Predicting the Size of Silver Nanoparticles from Their Optical Properties
Licensed Content Author	Amirmostafa Amirjani et al
Licensed Content Date	Jan 28, 2020
Type of Use	Thesis/Dissertation
Requestor Type	academic/university or research institute
Format	print and electronic
Portion	figures/tables/illustrations
Number of figures/tables/illustrations	2
Will you be translating?	no
Circulation/distribution	1 - 29
Author of this Springer Nature content	no
Title of new work	Dynamic Helical Polymers: Exploring the Complexity of Responses to Stimuli
Institution name	Universidad de Santiago de Compostela (USC)
Expected presentation date	Oct 2025
Portions	Figure 1 and Figure 3
The Requesting Person / Organization to Appear on the License	Manuel Fernández Míguez, Universidade de Santiago de Compostela (USC)
Requestor Location	Mr. Manuel Fernández Míguez c/ Jenaro de la Fuente s/n Santiago De Compostela, 15782 Spain
Billing Type	Invoice
Billing address	Universidade de Santiago de Compostela c/ Jenaro de la Fuente s/n Santiago De Compostela, Spain 15782
Total	**0.00 EUR**

USC UNIVERSIDADE DE SANTIAGO DE COMPOSTELA

Figure 32:

CCC Marketplace

This is a License Agreement between Manuel Fernández Míguez, Universidade de Santiago de Compostela (USC) ("User") and Copyright Clearance Center, Inc. ("CCC") on behalf of the Rightsholder identified in the order details below. The license consists of the order details, the Marketplace Permissions General Terms and Conditions below, and any Rightsholder Terms and Conditions which are included below.
All payments must be made in full to CCC in accordance with the Marketplace Permissions General Terms and Conditions below.

Order Date	20-May-2025	**Type of Use**	Republish in a thesis/dissertation
Order License ID	1611782-1		
ISSN	2055-6764	**Publisher Portion**	Royal Society of Chemistry Chart/graph/table/figure

LICENSED CONTENT

Publication Title	Nanoscale Horizons	**Rightsholder**	Royal Society of Chemistry
Article Title	Chiral gold-PPA nanocomposites with tunable helical sense and morphology.	**Publication Type**	e-Journal
		Start Page	495
Author / Editor	Royal Society of Chemistry (Great Britain),, Guo jia na mi ke xue zhong xin (China),	**End Page**	500
		Issue	3
		Volume	5
Date	01/01/2016		
Language	English		
Country	United Kingdom of Great Britain and Northern Ireland		

REQUEST DETAILS

Portion Type	Chart/graph/table/figure	**Distribution**	Worldwide
Number of Charts / Graphs / Tables / Figures Requested	1	**Translation**	Original language of publication
Format (select all that apply)	Print, Electronic	**Copies for the Disabled?**	No
Who Will Republish the Content?	Academic institution	**Minor Editing Privileges?**	No
		Incidental Promotional Use?	No
Duration of Use	Life of current edition	**Currency**	EUR
Lifetime Unit Quantity	Up to 499		
Rights Requested	Main product		

NEW WORK DETAILS

Title	Dynamic Helical Polymers: Exploring the Complexity of Responses to Stimuli	**Institution Name**	Universidade de Santiago de Compostela (USC)
		Expected Presentation Date	2025-10-30
Instructor Name	Manuel Fernández Míguez		

ADDITIONAL DETAILS

Order Reference Number	N/A	**The Requesting Person / Organization to Appear on the License**	Manuel Fernández Míguez, Universidade de Santiago de Compostela (USC)

REQUESTED CONTENT DETAILS

Title, Description or Numeric Reference of the Portion(s)	Figure 4	**Title of the Article / Chapter the Portion Is From**	Chiral gold-PPA nanocomposites with tunable helical sense and morphology.
Editor of Portion(s)	Freire, Felix; Riguera, Ricardo; Quiñoá, Emilio; Arias, Sandra; Núñez-Martínez, Manuel; Bergueiro Álvarez, Julian	**Author of Portion(s)**	Freire, Felix; Riguera, Ricardo; Quiñoá, Emilio; Arias, Sandra; Núñez-Martínez, Manuel; Bergueiro Álvarez, Julian
Volume / Edition	5		
Page or Page Range of Portion	495-500	**Issue, if Republishing an Article From a Serial**	3
		Publication Date of Portion	2020-03-02

USC UNIVERSIDADE DE SANTIAGO DE COMPOSTELA

Figure 33 left:

Chemistry of Materials

Cite this: *Chem. Mater.* 2021, 33, 12, 4805–4812

https://doi.org/10.1021/acs.chemmater.1c00805

Published May 12, 2021

Copyright © 2021 American Chemical Society.
This publication is licensed under CC-BY 4.0 .

CC BY 4.0

Attribution 4.0 International

Deed

Canonical URL : https://creativecommons.org/licenses/by/4.0/

See the legal code

You are free to:

Share — copy and redistribute the material in any medium or format for any purpose, even commercially.

Adapt — remix, transform, and build upon the material for any purpose, even commercially.

The licensor cannot revoke these freedoms as long as you follow the license terms.

Under the following terms:

Attribution — You must give appropriate credit , provide a link to the license, and indicate if changes were made . You may do so in any reasonable manner, but not in any way that suggests the licensor endorses you or your use.

No additional restrictions — You may not apply legal terms or technological measures that legally restrict others from doing anything the license permits.

Notices:

You do not have to comply with the license for elements of the material in the public domain or where your use is permitted by an applicable exception or limitation .

No warranties are given. The license may not give you all of the permissions necessary for your intended use. For example, other rights such as publicity, privacy, or moral rights may limit how you use the material.

Figure 33 right:



Research Article | Open Access

The Role of Polymer–AuNP Interaction in the Stimuli-Response Properties of PPA–AuNP Nanocomposites

Manuel Núñez-Martínez, Sandra Arias, Julián Bergueiro, Emilio Quiñoá, Ricardo Riguera, Félix Freire

First published: 10 November 2021 | https://doi.org/10.1002/marc.202100616 | Citations: 4

CC BY-NC-ND 4.0

Attribution-NonCommercial-NoDerivatives 4.0 International

Deed

Canonical URL : https://creativecommons.org/licenses/by-nc-nd/4.0/

See the legal code

You are free to:

Share — copy and redistribute the material in any medium or format

The licensor cannot revoke these freedoms as long as you follow the license terms.

Under the following terms:

Attribution — You must give appropriate credit , provide a link to the license, and indicate if changes were made . You may do so in any reasonable manner, but not in any way that suggests the licensor endorses you or your use.

NonCommercial — You may not use the material for commercial purposes .

NoDerivatives — If you remix, transform, or build upon the material, you may not distribute the modified material.

No additional restrictions — You may not apply legal terms or technological measures that legally restrict others from doing anything the license permits.

Notices:

You do not have to comply with the license for elements of the material in the public domain or where your use is permitted by an applicable exception or limitation .

No warranties are given. The license may not give you all of the permissions necessary for your intended use. For example, other rights such as publicity, privacy, or moral rights may limit how you use the material.

USC UNIVERSIDADE DE SANTIAGO DE COMPOSTELA

Figure 34:

CCC Marketplace

This is a License Agreement between Manuel Fernández Míguez, Universidade de Santiago de Compostela (USC) ("User") and Copyright Clearance Center, Inc. ("CCC") on behalf of the Rightsholder identified in the order details below. The license consists of the order details, the Marketplace Permissions General Terms and Conditions below, and any Rightsholder Terms and Conditions which are included below.
All payments must be made in full to CCC in accordance with the Marketplace Permissions General Terms and Conditions below.

Order Date	20-May-2025	**Type of Use**	Republish in a thesis/dissertation
Order License ID	1611800-1		
ISSN	2040-3372	**Publisher**	RSC Pub
		Portion	Chart/graph/table/figure

LICENSED CONTENT

Publication Title	Nanoscale	**Publication Type**	e-Journal
Article Title	Chiroptical and Colorimetric Switches Based on Helical Polymer-Metal Nanocomposites Prepared via Redox Metal Translocation of Helical Polymer Metal Complexes	**Start Page**	13066
		End Page	13072
		Issue	36
		Volume	14
		URL	http://www.rsc.org/Publishin...
Author / Editor	Royal Society of Chemistry (Great Britain), National Center for Nanoscience and Technology.		
Date	01/01/2009		
Language	English		
Country	United Kingdom of Great Britain and Northern Ireland		
Rightsholder	Royal Society of Chemistry		

REQUEST DETAILS

Portion Type	Chart/graph/table/figure	**Distribution**	Worldwide
Number of Charts / Graphs / Tables / Figures Requested	1	**Translation**	Original language of publication
Format (select all that apply)	Print, Electronic	**Copies for the Disabled?**	No
Who Will Republish the Content?	Academic institution	**Minor Editing Privileges?**	No
		Incidental Promotional Use?	No
Duration of Use	Life of current edition	**Currency**	EUR
Lifetime Unit Quantity	Up to 499		
Rights Requested	Main product		

NEW WORK DETAILS

Title	Dynamic Helical Polymers: Exploring the Complexity of Responses to Stimuli	**Institution Name**	Universidade de Santiago de Compostela (USC)
		Expected Presentation Date	2025-10-30
Instructor Name	Manuel Fernández Míguez		

ADDITIONAL DETAILS

Order Reference Number	N/A	**The Requesting Person / Organization to Appear on the License**	Manuel Fernández Míguez, Universidade de Santiago de Compostela (USC)

REQUESTED CONTENT DETAILS

Title, Description or Numeric Reference of the Portion(s)	Figure 4	**Title of the Article / Chapter the Portion Is From**	Chiroptical and Colorimetric Switches Based on Helical Polymer-Metal Nanocomposites Prepared via Redox Metal Translocation of Helical Polymer Metal Complexes
Editor of Portion(s)	Núñez-Martínez, Manuel; Quiñoá, Emilio; Freire, Felix	**Author of Portion(s)**	Núñez-Martínez, Manuel; Quiñoá, Emilio; Freire, Felix
Volume / Edition	14	**Issue, if Republishing an Article From a Serial**	36
Page or Page Range of Portion	13066-13072	**Publication Date of Portion**	2022-09-22

USC UNIVERSIDADE DE SANTIAGO DE COMPOSTELA

Figure 35:

Chemistry of Materials

Cite this: *Chem. Mater.* 2023, 35, 12, 4865–4872

https://doi.org/10.1021/acs.chemmater.3c00912

Published June 9, 2023

Copyright © 2023 The Authors. Published by American Chemical Society. This publication is licensed under **CC-BY 4.0** .

CC BY 4.0

Attribution 4.0 International

Deed

Canonical URL : https://creativecommons.org/licenses/by/4.0/

See the legal code

You are free to:

Share — copy and redistribute the material in any medium or format for any purpose, even commercially.

Adapt — remix, transform, and build upon the material for any purpose, even commercially.

The licensor cannot revoke these freedoms as long as you follow the license terms.

Under the following terms:

Attribution — You must give appropriate credit , provide a link to the license, and indicate if changes were made . You may do so in any reasonable manner, but not in any way that suggests the licensor endorses you or your use.

No additional restrictions — You may not apply legal terms or technological measures that legally restrict others from doing anything the license permits.

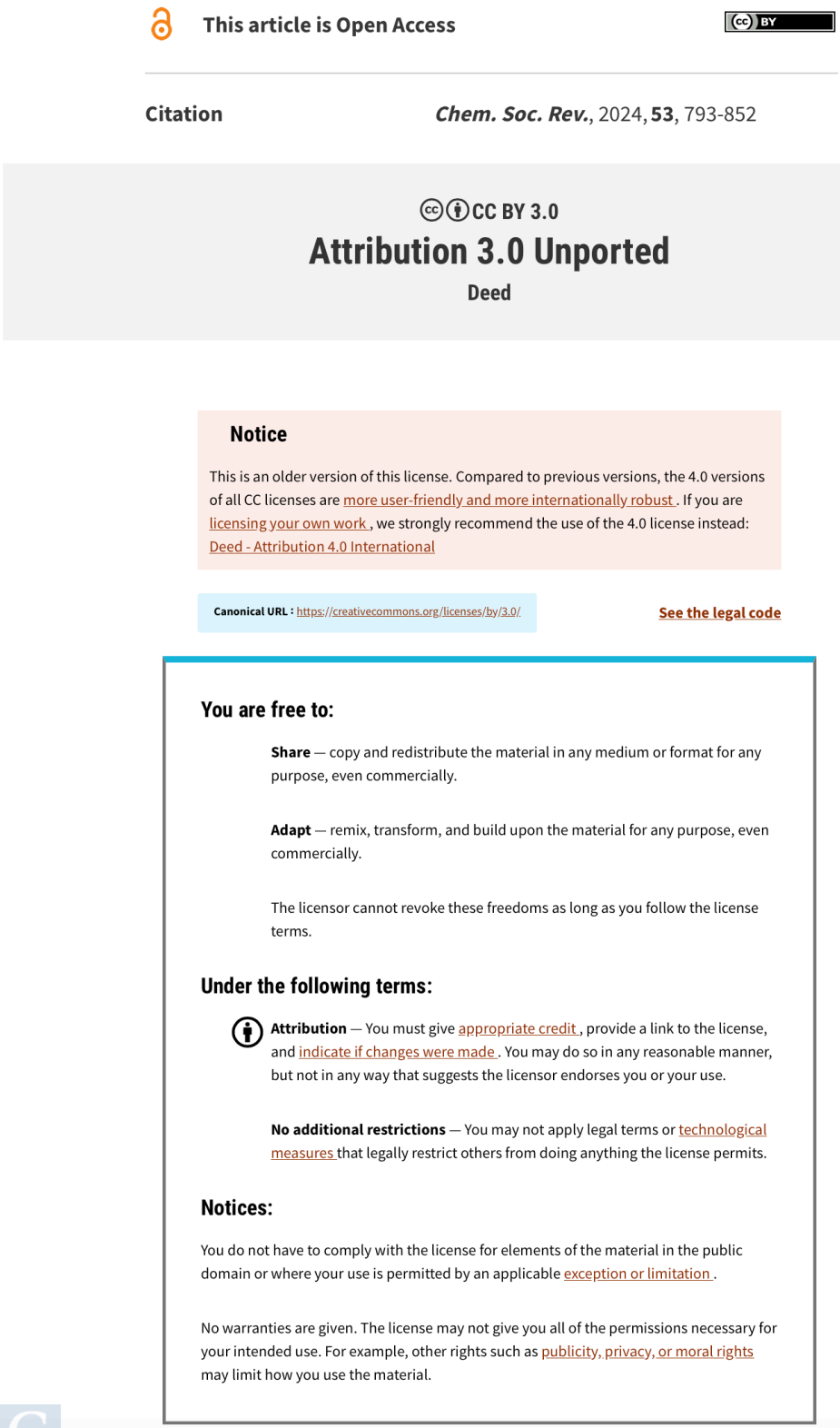
Notices:

You do not have to comply with the license for elements of the material in the public domain or where your use is permitted by an applicable exception or limitation .

No warranties are given. The license may not give you all of the permissions necessary for your intended use. For example, other rights such as publicity, privacy, or moral rights may limit how you use the material.

USC UNIVERSIDADE DE SANTIAGO DE COMPOSTELA

Figure 36, Figure 37, Figure 38, Figure 39, Figure 41, Figure 42, Figure 43, Figure 44, and Figure 46:



This article is Open Access

Citation *Chem. Soc. Rev.*, 2024, **53**, 793-852

CC BY 3.0

Attribution 3.0 Unported

Deed

Notice

This is an older version of this license. Compared to previous versions, the 4.0 versions of all CC licenses are more user-friendly and more internationally robust. If you are licensing your own work, we strongly recommend the use of the 4.0 license instead: Deed - Attribution 4.0 International

Canonical URL: https://creativecommons.org/licenses/by/3.0/

See the legal code

You are free to:

Share — copy and redistribute the material in any medium or format for any purpose, even commercially.

Adapt — remix, transform, and build upon the material for any purpose, even commercially.

The licensor cannot revoke these freedoms as long as you follow the license terms.

Under the following terms:

Attribution — You must give appropriate credit, provide a link to the license, and indicate if changes were made. You may do so in any reasonable manner, but not in any way that suggests the licensor endorses you or your use.

No additional restrictions — You may not apply legal terms or technological measures that legally restrict others from doing anything the license permits.

Notices:

You do not have to comply with the license for elements of the material in the public domain or where your use is permitted by an applicable exception or limitation.

No warranties are given. The license may not give you all of the permissions necessary for your intended use. For example, other rights such as publicity, privacy, or moral rights may limit how you use the material.

USC UNIVERSIDADE DE SANTIAGO DE COMPOSTELA

Figure 40:

CCC Marketplace

This is a License Agreement between Manuel Fernández Míguez, Universidade de Santiago de Compostela (USC) ("User") and Copyright Clearance Center, Inc. ("CCC") on behalf of the Rightsholder identified in the order details below. The license consists of the order details, the Marketplace Permissions General Terms and Conditions below, and any Rightsholder Terms and Conditions which are included below.
All payments must be made in full to CCC in accordance with the Marketplace Permissions General Terms and Conditions below.

Order Date	20-May-2025	**Type of Use**	Republish in a thesis/dissertation
Order License ID	1611809-1		
ISSN	1364-548X	**Publisher Portion**	ROYAL SOCIETY OF CHEMISTRY Chart/graph/table/figure

LICENSED CONTENT

Publication Title	Chemical communications	**Rightsholder**	Royal Society of Chemistry
Article Title	Macromolecular helicity control of poly(phenyl isocyanate)s with a single stimuli-responsive chiral switch.	**Publication Type**	e-Journal
		Start Page	7906
		End Page	7909
		Issue	55
Author / Editor	Royal Society of Chemistry (Great Britain)	**Volume**	55
Date	01/01/1996		
Language	English		
Country	United Kingdom of Great Britain and Northern Ireland		

REQUEST DETAILS

Portion Type	Chart/graph/table/figure	**Distribution**	Worldwide
Number of Charts / Graphs / Tables / Figures Requested	2	**Translation**	Original language of publication
Format (select all that apply)	Print, Electronic	**Copies for the Disabled?**	No
Who Will Republish the Content?	Academic institution	**Minor Editing Privileges?**	No
		Incidental Promotional Use?	No
Duration of Use	Life of current edition	**Currency**	EUR
Lifetime Unit Quantity	Up to 499		
Rights Requested	Main product		

NEW WORK DETAILS

Title	Dynamic Helical Polymers: Exploring the Complexity of Responses to Stimuli	**Institution Name**	Universidade de Santiago de Compostela (USC)
		Expected Presentation Date	2025-10-30
Instructor Name	Manuel Fernández Míguez		

ADDITIONAL DETAILS

Order Reference Number	N/A	**The Requesting Person / Organization to Appear on the License**	Manuel Fernández Míguez, Universidade de Santiago de Compostela (USC)

REQUESTED CONTENT DETAILS

Title, Description or Numeric Reference of the Portion(s)	Figure 1 and Figure 2	**Title of the Article / Chapter the Portion Is From**	Macromolecular helicity control of poly(phenyl isocyanate)s with a single stimuli-responsive chiral switch.
Editor of Portion(s)	Fukuda, Mayu; Rodríguez, Rafael; Fernandez, Zulema; Nishimura, Tatsuya; Hirose, Daisuke; Watanabe, Go; Quiñoá, Emilio; Freire, Felix; Maeda, Katsuhiro	**Author of Portion(s)**	Fukuda, Mayu; Rodríguez, Rafael; Fernandez, Zulema; Nishimura, Tatsuya; Hirose, Daisuke; Watanabe, Go; Quiñoá, Emilio; Freire, Felix; Maeda, Katsuhiro
Volume / Edition	55	**Issue, if Republishing an Article From a Serial**	55
Page or Page Range of Portion	7906-7909	**Publication Date of Portion**	2019-07-04

USC UNIVERSIDADE DE SANTIAGO DE COMPOSTELA

Figure 47:

License Details

This Agreement between Manuel Fernández Míguez, Universidade de Santiago de Compostela (USC) ("You") and Springer Nature ("Springer Nature") consists of your license details and the terms and conditions provided by Springer Nature and Copyright Clearance Center.

Print Copy

License Number	6033130505782
License date	May 20, 2025
Licensed Content Publisher	Springer Nature
Licensed Content Publication	Nature Reviews Chemistry
Licensed Content Title	Supramolecular polymerization through kinetic pathway control and living chain growth
Licensed Content Author	Marius Wehner et al
Licensed Content Date	Dec 21, 2019
Type of Use	Thesis/Dissertation
Requestor Type	academic/university or research institute
Format	print and electronic
Portion	figures/tables/illustrations
Number of figures/tables/illustrations	1
Would you like a high resolution image with your order?	no
Will you be translating?	no
Circulation/distribution	1 - 29
Author of this Springer Nature content	no
Title of new work	Dynamic Helical Polymers: Exploring the Complexity of Responses to Stimuli
Institution name	Universidad de Santiago de Compostela (USC)
Expected presentation date	Oct 2025
Portions	Figure 2
The Requesting Person / Organization to Appear on the License	Manuel Fernández Míguez, Universidade de Santiago de Compostela (USC)
Requestor Location	Mr. Manuel Fernández Míguez c/ Jenaro de la Fuente s/n Santiago De Compostela, 15782 Spain
Billing Type	Invoice
Billing address	Universidade de Santiago de Compostela c/ Jenaro de la Fuente s/n Santiago De Compostela, Spain 15782
Total	**0.00 EUR**

USC UNIVERSIDADE DE SANTIAGO DE COMPOSTELA

Figure 48:



This is a License Agreement between Manuel Fernández Míguez, Universidade de Santiago de Compostela (USC) ("User") and Copyright Clearance Center, Inc. ("CCC") on behalf of the Rightsholder identified in the order details below. The license consists of the order details, the Marketplace Permissions General Terms and Conditions below, and any Rightsholder Terms and Conditions which are included below.
All payments must be made in full to CCC in accordance with the Marketplace Permissions General Terms and Conditions below.

Order Date	20-May-2025	**Type of Use**	Republish in a thesis/dissertation
Order License ID	1611818-1	**Publisher**	Wiley
ISSN	2692-4560	**Portion**	Chart/graph/table/figure

LICENSED CONTENT

Publication Title	AGGREGATE	**Publication Type**	e-Journal
Article Title	Organic molecular aggregates: From aggregation structure to emission property	**Start Page**	n/a
		End Page	n/a
Author / Editor	Hua nan li gong da xue	**Issue**	4
Date	01/01/2020	**Volume**	2
Language	English	**URL**	https://onlinelibrary.wiley.co...
Country	United States of America		
Rightsholder	John Wiley & Sons - Books		

REQUEST DETAILS

Portion Type	Chart/graph/table/figure	**Distribution**	Worldwide
Number of Charts / Graphs / Tables / Figures Requested	1	**Translation**	Original language of publication
Format (select all that apply)	Print, Electronic	**Copies for the Disabled?**	No
Who Will Republish the Content?	Academic institution	**Minor Editing Privileges?**	No
		Incidental Promotional Use?	No
Duration of Use	Life of current edition	**Currency**	EUR
Lifetime Unit Quantity	Up to 499		
Rights Requested	Main product		

NEW WORK DETAILS

Title	Dynamic Helical Polymers: Exploring the Complexity of Responses to Stimuli	**Institution Name**	Universidade de Santiago de Compostela (USC)
		Expected Presentation Date	2025-10-30
Instructor Name	Manuel Fernández Míguez		

ADDITIONAL DETAILS

The Requesting Person / Organization to Appear on the License	Manuel Fernández Míguez, Universidade de Santiago de Compostela (USC)		

REQUESTED CONTENT DETAILS

Title, Description or Numeric Reference of the Portion(s)	Figure 1	**Title of the Article / Chapter the Portion Is From**	Organic molecular aggregates: From aggregation structure to emission property
Editor of Portion(s)	Ma, Suqian; Du, Sijia; Pan, Guocui; Dai, Shuting; Xu, Bin; Tian, Wenjing	**Author of Portion(s)**	Ma, Suqian; Du, Sijia; Pan, Guocui; Dai, Shuting; Xu, Bin; Tian, Wenjing
Volume / Edition	2		
Page or Page Range of Portion	n/a-n/a	**Publication Date of Portion**	2021-08-31

USC UNIVERSIDADE DE SANTIAGO DE COMPOSTELA

Figure 49:

ChemPhotoChem

Chemistry Europe
European Chemical Societies Publishing

Research Article | Open Access

Oblique Packing and Tunable Excitonic Coupling in DNA-Templated Squaraine Rotaxane Dimer Aggregates

Dr. Matthew S. Barclay, Christopher K. Wilson, Simon K. Roy, Dr. Olga A. Mass, Olena M. Obukhova, Rostyslav P. Svoiakov ... See all authors

First published: 11 April 2022 |
https://doi.org/10.1002/cptc.202200039 | Citations: 10

CC BY-NC-ND 4.0

Attribution-NonCommercial-NoDerivatives 4.0 International

Deed

Canonical URL : https://creativecommons.org/licenses/by-nc-nd/4.0/

See the legal code

You are free to:

Share — copy and redistribute the material in any medium or format

The licensor cannot revoke these freedoms as long as you follow the license terms.

Under the following terms:

Attribution — You must give appropriate credit , provide a link to the license, and indicate if changes were made . You may do so in any reasonable manner, but not in any way that suggests the licensor endorses you or your use.

NonCommercial — You may not use the material for commercial purposes .

NoDerivatives — If you remix, transform, or build upon the material, you may not distribute the modified material.

No additional restrictions — You may not apply legal terms or technological measures that legally restrict others from doing anything the license permits.

Notices:

You do not have to comply with the license for elements of the material in the public domain or where your use is permitted by an applicable exception or limitation .

No warranties are given. The license may not give you all of the permissions necessary for your intended use. For example, other rights such as publicity, privacy, or moral rights may limit how you use the material.

USC UNIVERSIDADE DE SANTIAGO DE COMPOSTELA

Figure 50:

CCC Marketplace

This is a License Agreement between Manuel Fernández Míguez, Universidade de Santiago de Compostela (USC) ("User") and Copyright Clearance Center, Inc. ("CCC") on behalf of the Rightsholder identified in the order details below. The license consists of the order details, the Marketplace Permissions General Terms and Conditions below, and any Rightsholder Terms and Conditions which are included below.
All payments must be made in full to CCC in accordance with the Marketplace Permissions General Terms and Conditions below.

Order Date	20-May-2025	**Type of Use**	Republish in a thesis/dissertation
Order License ID	1611820-1		
ISSN	0143-7208	**Publisher**	PERGAMON
		Portion	Chart/graph/table/figure

LICENSED CONTENT

Publication Title	Dyes and pigments : an international journal	**Rightsholder**	Elsevier Science & Technology Journals
Article Title	Molecular sensors producing circularly polarized luminescence responses	**Publication Type**	Journal
		Start Page	110786
		Volume	208
Date	01/01/1980		
Language	English		
Country	United Kingdom of Great Britain and Northern Ireland		

REQUEST DETAILS

Portion Type	Chart/graph/table/figure	**Distribution**	Worldwide
Number of Charts / Graphs / Tables / Figures Requested	1	**Translation**	Original language of publication
Format (select all that apply)	Print, Electronic	**Copies for the Disabled?**	No
Who Will Republish the Content?	Academic institution	**Minor Editing Privileges?**	No
		Incidental Promotional Use?	No
Duration of Use	Life of current edition	**Currency**	EUR
Lifetime Unit Quantity	Up to 499		
Rights Requested	Main product		

NEW WORK DETAILS

Title	Dynamic Helical Polymers: Exploring the Complexity of Responses to Stimuli	**Institution Name**	Universidade de Santiago de Compostela (USC)
		Expected Presentation Date	2025-10-30
Instructor Name	Manuel Fernández Míguez		

ADDITIONAL DETAILS

Order Reference Number	N/A	**The Requesting Person / Organization to Appear on the License**	Manuel Fernández Míguez, Universidade de Santiago de Compostela (USC)

REQUESTED CONTENT DETAILS

Title, Description or Numeric Reference of the Portion(s)	Figure 3	**Title of the Article / Chapter the Portion Is From**	Molecular sensors producing circularly polarized luminescence responses
Editor of Portion(s)	Jhun, Byung Hak; Park, Soo Young; You, Youngmin	**Author of Portion(s)**	Jhun, Byung Hak; Park, Soo Young; You, Youngmin
Volume / Edition	208		
Page or Page Range of Portion	110786	**Issue, if Republishing an Article From a Serial**	N/A
		Publication Date of Portion	2023-01-01

USC UNIVERSIDADE DE SANTIAGO DE COMPOSTELA

Figure 51:

CCC Marketplace

This is a License Agreement between Manuel Fernández Míguez, Universidade de Santiago de Compostela (USC) ("User") and Copyright Clearance Center, Inc. ("CCC") on behalf of the Rightsholder identified in the order details below. The license consists of the order details, the Marketplace Permissions General Terms and Conditions below, and any Rightsholder Terms and Conditions which are included below.
All payments must be made in full to CCC in accordance with the Marketplace Permissions General Terms and Conditions below.

Order Date	20-May-2025	**Type of Use**	Republish in a thesis/dissertation
Order License ID	1611824-1		
ISSN	1521-3773	**Publisher**	JOHN/WILEY & SONS, INC.
		Portion	Chart/graph/table/figure

LICENSED CONTENT

Publication Title	Angewandte Chemie	**Publication Type**	e-Journal
Article Title	Supramolecular stereomutation in kinetic and thermodynamic self-assembly of helical merocyanine dye nanorods.	**Start Page**	5071
		End Page	5074
		Issue	32
		Volume	44
Author / Editor	Gesellschaft Deutscher Chemiker.	**URL**	http://www3.interscience.wil...
Date	01/01/1962		
Language	English		
Country	Germany		
Rightsholder	John Wiley & Sons - Books		

REQUEST DETAILS

Portion Type	Chart/graph/table/figure	**Distribution**	Worldwide
Number of Charts / Graphs / Tables / Figures Requested	4	**Translation**	Original language of publication
Format (select all that apply)	Print, Electronic	**Copies for the Disabled?**	No
Who Will Republish the Content?	Academic institution	**Minor Editing Privileges?**	No
		Incidental Promotional Use?	No
Duration of Use	Life of current edition	**Currency**	EUR
Lifetime Unit Quantity	Up to 499		
Rights Requested	Main product		

NEW WORK DETAILS

Title	Dynamic Helical Polymers: Exploring the Complexity of Responses to Stimuli	**Institution Name**	Universidade de Santiago de Compostela (USC)
		Expected Presentation Date	2025-10-30
Instructor Name	Manuel Fernández Míguez		

ADDITIONAL DETAILS

The Requesting Person / Organization to Appear on the License	Manuel Fernández Míguez, Universidade de Santiago de Compostela (USC)		

REQUESTED CONTENT DETAILS

Title, Description or Numeric Reference of the Portion(s)	Figures 1, 2, 3, and 4	**Title of the Article / Chapter the Portion Is From**	Supramolecular stereomutation in kinetic and thermodynamic self-assembly of helical merocyanine dye nanorods.
Editor of Portion(s)	Lohr, Andreas; Lysetska, Marina, Dr.; Würthner, Frank, Prof. Dr.		
		Author of Portion(s)	Lohr, Andreas; Lysetska, Marina, Dr.; Würthner, Frank, Prof. Dr.
Volume / Edition	44 / International ed. in English.		
Page or Page Range of Portion	5071-5074	**Publication Date of Portion**	2005-08-12

USC UNIVERSIDADE DE SANTIAGO DE COMPOSTELA

Figure 52:

License Details

This Agreement between Manuel Fernández Míguez, Universidade de Santiago de Compostela (USC) ("You") and Springer Nature ("Springer Nature") consists of your license details and the terms and conditions provided by Springer Nature and Copyright Clearance Center.

Print Copy

License Number	6033150026563
License date	May 20, 2025
Licensed Content Publisher	Springer Nature
Licensed Content Publication	Nature
Licensed Content Title	Pathway complexity in supramolecular polymerization
Licensed Content Author	Peter A. Korevaar et al
Licensed Content Date	Jan 18, 2012
Type of Use	Thesis/Dissertation
Requestor Type	academic/university or research institute
Format	print and electronic
Portion	figures/tables/illustrations
Number of figures/tables/illustrations	2
Would you like a high resolution image with your order?	no
Will you be translating?	no
Circulation/distribution	1 - 29
Author of this Springer Nature content	no
Title of new work	Dynamic Helical Polymers: Exploring the Complexity of Responses to Stimuli
Institution name	Universidad de Santiago de Compostela (USC)
Expected presentation date	Oct 2025
Portions	Figures 1 and 4
The Requesting Person / Organization to Appear on the License	Manuel Fernández Míguez, Universidade de Santiago de Compostela (USC)
Requestor Location	Mr. Manuel Fernández Míguez c/ Jenaro de la Fuente s/n Santiago De Compostela, 15782 Spain
Billing Type	Invoice
Billing address	Universidade de Santiago de Compostela c/ Jenaro de la Fuente s/n Santiago De Compostela, Spain 15782
Total	**0.00 EUR**

Figure 53a:

SPRINGER NATURE

Dynamic multistimuli-responsive reversible chiral transformation in supramolecular helices

Author: Santosh Goskulwad et al
Publication: Scientific Reports
Publisher: Springer Nature
Date: Jul 25, 2018

Copyright © 2018, The Author(s)

Creative Commons

This is an open access article distributed under the terms of the Creative Commons CC BY license, which permits unrestricted use, distribution, and reproduction in any medium, provided the original work is properly cited.

You are not required to obtain permission to reuse this article.
To request permission for a type of use not listed, please contact Springer Nature

USC UNIVERSIDADE DE SANTIAGO DE COMPOSTELA

Figure 53b:

CCC Marketplace

This is a License Agreement between Manuel Fernández Míguez, Universidade de Santiago de Compostela (USC) ("User") and Copyright Clearance Center, Inc. ("CCC") on behalf of the Rightsholder identified in the order details below. The license consists of the order details, the Marketplace Permissions General Terms and Conditions below, and any Rightsholder Terms and Conditions which are included below.
All payments must be made in full to CCC in accordance with the Marketplace Permissions General Terms and Conditions below.

Order Date	20-May-2025	Type of Use	Republish in a thesis/dissertation
Order License ID	1611832-1	Publisher	ROYAL SOCIETY OF CHEMISTRY
ISSN	1364-548X	Portion	Chart/graph/table/figure

LICENSED CONTENT

Publication Title	Chemical communications	Rightsholder	Royal Society of Chemistry
Article Title	Disclosing chirality in consecutive supramolecular polymerizations: chiral induction by light in N-annulated perylenetetracarboxamides.	Publication Type	e-Journal
		Start Page	2244
		End Page	2247
		Issue	15
		Volume	56
Author / Editor	Royal Society of Chemistry (Great Britain)		
Date	01/01/1996		
Language	English		
Country	United Kingdom of Great Britain and Northern Ireland		

REQUEST DETAILS

Portion Type	Chart/graph/table/figure	Distribution	Worldwide
Number of Charts / Graphs / Tables / Figures Requested	2	Translation	Original language of publication
Format (select all that apply)	Print, Electronic	Copies for the Disabled?	No
Who Will Republish the Content?	Academic institution	Minor Editing Privileges?	No
		Incidental Promotional Use?	No
Duration of Use	Life of current edition	Currency	EUR
Lifetime Unit Quantity	Up to 499		
Rights Requested	Main product		

NEW WORK DETAILS

Title	Dynamic Helical Polymers: Exploring the Complexity of Responses to Stimuli	Institution Name	Universidade de Santiago de Compostela (USC)
		Expected Presentation Date	2025-10-30
Instructor Name	Manuel Fernández Míguez		

ADDITIONAL DETAILS

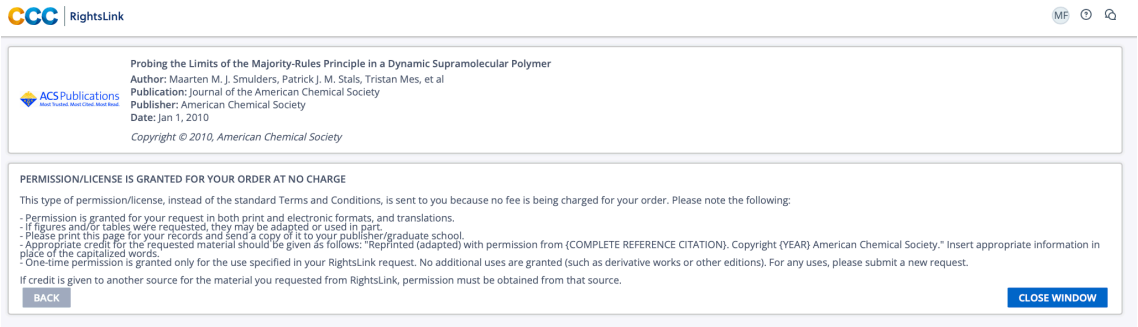
Order Reference Number	N/A	The Requesting Person / Organization to Appear on the License	Manuel Fernández Míguez, Universidade de Santiago de Compostela (USC)

REQUESTED CONTENT DETAILS

Title, Description or Numeric Reference of the Portion(s)	Figures 1 and 4	Title of the Article / Chapter the Portion Is From	Disclosing chirality in consecutive supramolecular polymerizations: chiral induction by light in N-annulated perylenetetracarboxamides.
Editor of Portion(s)	Greciano, Elisa E.; Rodríguez, Rafael; Maeda, Katsuhiro; Sanchez, Luis	Author of Portion(s)	Greciano, Elisa E.; Rodríguez, Rafael; Maeda, Katsuhiro; Sanchez, Luis
Volume / Edition	56	Issue, if Republishing an Article From a Serial	15
Page or Page Range of Portion	2244-2247	Publication Date of Portion	2020-02-20

USC UNIVERSIDADE DE SANTIAGO DE COMPOSTELA

Figure 54:



USC UNIVERSIDADE DE SANTIAGO DE COMPOSTELA

Figure 55:



Research Article | Open Access

Elucidating the Supramolecular Copolymerization of N- and C-Centered Benzene-1,3,5-Tricarboxamides: The Role of Parallel and Antiparallel Packing of Amide Groups in the Copolymer Microstructure

Lafayette N. J. de Windt, Dr. Zulema Fernández, Dr. Manuel Fernández-Míguez, Prof. Dr. Félix Freire, Prof. Dr. Anja R. A. Palmans

First published: 12 November 2021 |
https://doi.org/10.1002/chem.202103691 | Citations: 14

CC BY-NC 4.0

Attribution-NonCommercial 4.0 International

Deed

Canonical URL : https://creativecommons.org/licenses/by-nc/4.0/

See the legal code

You are free to:

Share — copy and redistribute the material in any medium or format

Adapt — remix, transform, and build upon the material

The licensor cannot revoke these freedoms as long as you follow the license terms.

Under the following terms:

Attribution — You must give appropriate credit , provide a link to the license, and indicate if changes were made . You may do so in any reasonable manner, but not in any way that suggests the licensor endorses you or your use.

NonCommercial — You may not use the material for commercial purposes .

No additional restrictions — You may not apply legal terms or technological measures that legally restrict others from doing anything the license permits.

Notices:

You do not have to comply with the license for elements of the material in the public domain or where your use is permitted by an applicable exception or limitation .

No warranties are given. The license may not give you all of the permissions necessary for your intended use. For example, other rights such as publicity, privacy, or moral rights may limit how you use the material.

USC UNIVERSIDADE DE SANTIAGO DE COMPOSTELA

Figure 56:



Research Article | Open Access

Coaxial Helices in Chiral Supramolecular Aggregates from Highly Hindered Chiral Allenes

Dr. María Lago-Silva, Manuel Fernández-Míguez, Dr. Zulema Fernández, Prof. María Magdalena Cid, Prof. Emilio Quiñoá, Dr. Rafael Rodríguez, Prof. Félix Freire

First published: 10 December 2024 | https://doi.org/10.1002/anie.202421310 | Citations: 1

CC BY-NC 4.0

Attribution-NonCommercial 4.0 International

Deed

Canonical URL : https://creativecommons.org/licenses/by-nc/4.0/

See the legal code

You are free to:

Share — copy and redistribute the material in any medium or format

Adapt — remix, transform, and build upon the material

The licensor cannot revoke these freedoms as long as you follow the license terms.

Under the following terms:

Attribution — You must give appropriate credit , provide a link to the license, and indicate if changes were made . You may do so in any reasonable manner, but not in any way that suggests the licensor endorses you or your use.

NonCommercial — You may not use the material for commercial purposes .

No additional restrictions — You may not apply legal terms or technological measures that legally restrict others from doing anything the license permits.

Notices:

You do not have to comply with the license for elements of the material in the public domain or where your use is permitted by an applicable exception or limitation .

No warranties are given. The license may not give you all of the permissions necessary for your intended use. For example, other rights such as publicity, privacy, or moral rights may limit how you use the material.

USC UNIVERSIDADE DE SANTIAGO DE COMPOSTELA

USC
UNIVERSIDADE
DE SANTIAGO
DE COMPOSTELA

Helical polymers, covalent and supramolecular, have attracted the attention of the scienti ic community for their structure-function relationship as found in helical biomacromolecules such as peptides, proteins, or DNA, among others. Inspired by these systems, this thesis explores synthetic helical poly(phenylacetylene)s and supramolecular polymers. These polymers exhibit dynamism, and their structure can be modulated by multi-response to stimuli such as temperature, metal ions, pH, photochemical electrocyclization, and copolymerization. Furthermore, the synthesis and mechanism of the PPA response in the process of nanocomposite formation with metal nanoparticles were also studied. Thus, new helical systems, covalent and supramolecular, were prepared and studied, resulting in novel multi-responsive materials.